AIRFLOW IN THE URBAN ENVIRONMENT

An evaluation of the relationship between urban aspect ratios and patterns of airflow, wind velocity and direction in urban areas, and coefficient of pressure distribution on building envelopes

A Thesis Submitted in Fulfilment of the Requirement for the Degree of Doctor of Philosophy - PhD

THE CARDIFF UNIVERSITY

THE WELSH SCHOOL OF ARCHITECTURE

ARCHITECTURAL SCIENCE GROUP

Candidate: Luciano Caruggi de Faria

Supervisor: Professor Phil Jones

January, 2012

AIRFLOW IN THE URBAN ENVIRONMENT

An evaluation of the relationship between urban aspect ratios and patterns of airflow, wind velocity and direction in urban areas, and coefficient of pressure distribution on building envelopes

A Thesis Submitted in Fulfilment of the Requirement for the Degree of Doctor of Philosophy - PhD

THE CARDIFF UNIVERSITY

THE WELSH SCHOOL OF ARCHITECTURE

ARCHITECTURAL SCIENCE GROUP

Candidate: Luciano Caruggi de Faria

Supervisor: Professor Phil Jones

January, 2012

Planning is always involved in making choices between alternatives. In the case of designing for street climate the objectives may be mutually exclusive. For example, whilst open geometry is conductive to air pollution dispersion and solar access, a more densely clustered arrangement is favourable for shelter and energy conservation (Oke, 1988).

Summary

This thesis addresses the relationship between the physical dimensions and aspect ratios of urban areas and the airflow below the urban canopy height. The aim is to investigate the link between these aspect ratios and the resulting airflow patterns, wind speed and direction, and pressure coefficients on the envelope of target buildings.

The research method involves several steps which seek to explore the airflow in four urban scenarios, simplified simulation using two parallel bricks; several complex urban prototype scenarios; and two actual urban areas used as case studies situated on the Cardiff Cathays Campus and the Paulista Avenue - São Paulo. The research methods employed are: atmospheric boundary layer wind tunnel (WT), steady-state standard k-e CFD simulation and field measurements (FM). Three prevailing wind directions were investigated: parallel, orthogonal and oblique. The outputs are guiven in terms of: Cp and ΔCp data displayed as graphs, tables and/ or contour plots; airflow patterns and velocity magnitude and direction, displayed as vertical profile graphs and visualized by means of CFD pathlines or WT helium bubble pathlines; and correlation displayed as scatter diagrams and matrices.

A relationship was found between the urban aspect ratios and the ΔCp results. This was demonstrated by statistical methods using the data on the variables concerned, thus verifying the strength of the correlation between them. Strong correlation was found between the investigations into similar scenarios of the urban prototypes and the two case studies as regards both the aspect ratios and the ΔCp results. On the other hand, low correlation for the same variables were identified when contrasting dissimilar urban prototype scenarios. Moreover, good levels of comparison were found between the FM and the CFD simulations in Case Study 01 for both the decrease in wind velocity magnitude and direction in urban areas.

Key words: Urban Environment; Urban Canyon; Aspect Ratio; Airflow Pattern; Wind Speed and Direction; Cp; ΔCp; CFD; k-e; Wind Tunnel; Field Measurement; and Correlation Coefficient.

Acknowledgements

Here I intend to express my gratitude to all those who helped and supported me in accomplishing this thesis. First I want to thank the Welsh School of Architecture from the Cardiff University, for offering me a place in the postgraduate programme, and the Professor Phil Jones, supervisor of this investigation, for his orientation and thoughts so important to this work. I also want to thank him for all the opportunities for learning and working in this institution.

I would like to thank both the Senior Lecturer Don Alexander, for his essential guidance related to the simulation methods employed on this investigation and the support from the Research Assistant Dylan Dixon to carry-out the experiments. I would like to thank also the Senior Teaching Fellow Mike Fedeski, for the opportunity of working with him as MSc Teaching Assistant, and the WSA/ CRiBE staff Huw Jenkins, Yan Wang, Simon Lannon, Julie Gwilliam, and Ian Knight, for their support.

Special appreciation has to be given to the Research Executive Officer Katrina Lewis, always so kind and helpful with the postgraduate students, the Post Graduate Officer Christine Heywood, and to the Personal Assistant to the Head of the School Anne Evans, which is also extended to the WSA Facilities Managers Dave Bull and Carole Creasey, Dom Sleeman (IT Technician), Dan Tilbury (Craftsperson) and Sylvia Harris (WSA Librarian Representative). Further, I need to mention the Law School Facilities Manager Julie McCarthy, for allowing the field measurements to happen, and the Cardiff University Graduate Centre, for valuable workshops offered.

I would like to mention also my dear PhD colleagues Jignesh, Spyros, Lu Sun, Li Qian, Shan Shan, Heleni, Ziad, Clarice, and Shiyu, just to mention a few, in addition to the 2007-08 MSc students with whom I had the chance to work, teach and learn so much.

From my country of origin I thank Professor Marcelo de Andrade Romero, Head of the FAU-USP, my former academic supervisor, for all the advices and support; Dr. Lucia Pirró, for her belief in me as a researcher; and Professor Augusto José Pereira Filho, Head of the EM IAG-USP, for supplying weather data for this thesis investigations. I would like to thank also Mr. Arthur Anthony Boorne, a true gentleman who proofread this thesis with incontestable dedication, and has become a friend since then. Furthermore, I am grateful to the architect Jonas Birger, for the learning and opportunities related to architectural design and for having faith in my work as both architect and researcher. I also thank my dear professional practise colleagues for their friendship.

I want to show thankfulness to my parents and great friends, David and Sônia who raised me with love, care, principles, and provided me with the best education they could afford. I want to thank also my dear sisters, Gláucia and Cecília, and brothers, Duda and André, for their companionship and for giving me two lovely nephew and niece. I couldn't let to mention also my grandparents: José, Olga, Julio and Angelina for truly spoiling me during my childhood!

I owe also good and true thanks to my wife's side of my family: Maria Alice, Livia, Claudia, Neto, Teté, dona Nídia, Ré, Ricardo, Miguel, Giordano, Alaor, and Carmem; for having always embraced me as one of them.

Finally, I want to show immense gratitude to Tânia, my precious and loved wife, my best friend, for all the moments which we shared together. She was, is, and will always be my source of inspiration. Without her companionship and support- and patience- I would never have been able to accomplish this enterprise.

...this work is dedicated to the memory of a brave, wise and loved lady, who taught me once how important is celebrating inevitable defeats in life in order to make victorious moments much more tasteful...

LIST OF CONTENTS

List of Appendices

List of Figures

Chapter 2

Chapter 3

Chapter 4

Chapter 5

Chapter 6

Chapter 7

Chapter 8

Chapter 9

Appendix 2

Appendix 4

Appendix 5

List of Tables

Chapter 1

Chapter 2

Chapter 4

Chapter 5

Chapter 6

Chapter 7

Chapter 8

Chapter 9

Chapter 10

Appendix 3

Appendix 4

Appendix 5

Appendix 6

List of Equations

Chapter 2

Chapter 3

Chapter 4

Chapter 5

Part 01: Introduction

Chapter 1: Introduction

1.1. Background introduction

The main purpose of buildings is to provide shelter for human activities. In the light of today's reality, where global climate change and sustainability are central issues, efficient buildings are considered those whose construction, operation and maintenance produce reduced carbon footprints in the environment without compromising the users' comfort and production. The users are the ultimate goal of and the reason for the creation of built spaces.

Mega-cities and large conurbations such as New York, Tokyo, Delhi, São Paulo, London, and many others, can be seen as indicators, or 'thermometers', of changes in the natural climate of a region. These changes are revealed through various urban climate effects, such as heat and cooling islands, greenhouse effects and thermal inversions, acid rain and the general deterioration of air quality.

The interaction between local environment and urban development results in diverse urban micro-climates. According to Monteiro and Mendonça (2003) the urban space, constrained within its own boundaries, is the core of a system that interacts closely with the immediately surrounding natural micro-climate, and which works instantaneously and without interruption.

Since the urban structure is susceptible to policies and directives, it is necessary to direct its occupation with a view to improving inhabitants' comfort both inside and outside buildings and so reduce the energy consumption of buildings (Givoni, 1998). However, these concepts were hardly ever employed during the growth of the existing conurbations and consequently, measures to mitigate the harmful effects of local urban microclimates have had to be taken instead.

A key point to achieving sustainable solutions for new building developments is related to the quality of the architectonic design, and its suitability to the local micro-climate. This quality is sought during the initial stages of design fright from the plot's occupation, the floor plan design, and the external volumetric shape to the selection of construction materials and façade elements. Thus the building's external volume, envelope, and internal spaces are all to be integrated and adapted to the microclimate. The aim is to diminish the impact of the construction on the environment and also to improve the efficiency of the building operation, providing thermal comfort, natural light and indoor air quality for the occupants with reduced dependence on artificial systems.

The process of building design involves making decisions about external shape and internal layout, combining passive design strategies, building legislation, and the client project brief. Misguided decisions at any one of these stages may impact the building's-lifetime performance, operational cost, or result in user dissatisfaction.

1.2. Natural ventilation - role and strategies

Natural ventilation has a major role to play in ensuring indoor air quality by supplying fresh air to dilute pollutants. Further, the increase in controlled air change will remove internal heat by natural convection, contributing to the occupant's thermal comfort and, consequently, improving in their performance and productivity (CIBSE B2, 2001). The selection of ventilation strategies should at first exhaust the natural potential of the site, after which, it should combine hybrid natural and mechanical systems and, only when the previous strategies' response to the external environment is unable to achieve comfort limits, make use of artificial systems.

For instance, free-running buildings without mechanical heating and/ or cooling systems and which rely instead only on passive design strategies, are intended to be at least as comfortable as the external environment can be, but also aim at mitigating extreme outdoor climates (Roulet, 2005). In this way, natural ventilation can minimise the energy consumption of the built environment replacing artificial heating and air conditioning with natural convection techniques whenever possible.

Passive design strategies for keeping internal mean air temperature within the limits of thermal comfort are based on the control of direct solar radiation and heat exchanges between indoor and outdoor environments (Givoni, 1994). While requirements change according to the local climate, the passive techniques which are usually employed are: comfort ventilation, nocturnal ventilation, radiant and evaporative cooling, ground cooling, thermal mass storage and shading control. Strategies for both heating and cooling purposes are derived from these techniques.

Drawbacks to natural ventilation systems include: external urban noise, external air pollution concentration dispersion and smoke control (for both vehicular paths and fire safety), burglary, and the health and comfort of users' which is affected by drafts and internal air contaminants (CIBSE AM10, 2005).

1.3. The potential of urban environments for natural ventilation

Improving the quality of the environment in established urban centres has become a challenge which demands the attention of today's architects and urban planners. However, within the established urban environment the scope of intervention is mostly related to integrating new buildings into settled urban scenes. To attain this task it is necessary to comprehend the urban microclimate's mechanisms as a whole.

The free and undisturbed airflow above the urban skyline becomes highly turbulent below the urban canopy height. The urban terrain's roughness determines the atmospheric boundary layer and the built geometry and topography induces airflow acceleration and deceleration, creating turbulent and sheltered zones and ultimately defining pressure differences across buildings. This chaotic behaviour can undermine natural ventilation strategies which are based in façade openings and so compromise efficiency. The air changes (ACH) for indoor air quality may be reached, but will not the ACH rates required to mitigate internal temperatures and thus ensure thermal comfort.

It is necessary to know beforehand not only the prevailing wind direction and velocity but also how wind interacts locally with the surrounding built-up area to design building's volumetric shape, choose façade materials, size and type of openings, and plan internal layout, shafts, atriums and other vertical space connections. Only thus it is possible to define natural ventilation strategies for buildings in the urban environment.

1.4. About this thesis

This research project will investigate the relationship between urban areas physical dimensions and the resulting airflow patterns, wind speed and direction, and pressure coefficient on the envelope of target buildings. By investigating this relationship it will be possible, for instance, to identify the potential of dense urban areas to provide (or not) the requisite minimal conditions for the application of natural ventilation systems in buildings. The main analyses concentrate on assessing wind effects and pressure distribution in urban areas and how they can either hinder or improve ventilation strategies for office environments. The case studies presented are located in Cardiff and São Paulo.

1.5. Gaps in the subject

According to weather data analysis for the City of São Paulo (Tarifa and Azevedo, 2001; Bastos and Barroso-Krause, 2008) there is potential to achieving thermal comfort during working hours in summer season when external air temperatures do not surpass 28 to 32^{o}C, the day temperature ranges around10^{o}C, and also 2m/s light breezes are achievable in urban areas. Under such circumstances, the application of passive techniques related to natural ventilation strategies is viable up to 85% of the time when day ventilation and exposed thermal mass associated with night ventilation are combined. If these techniques are used in separate, this potential drops to 80% and 58% respectively. For the just quoted climate characteristics, there is potential for future high-rise office buildings in such climates to become more sustainable and energy efficient by applying natural ventilation strategies for passive cooling during most of the year. On the other hand, a preference for high-rise towers with fully glazed envelopes and a lack of instruments available for architects and building designers for predicting both the external airflow speed and direction in high-density urban areas and the resulting performance of natural ventilation strategies contribute to the preference for, and consequent dependence on, HVAC for providing thermal comfort in office environments.

Cook (1985) states that although external airflow in complex urban environments is not yet fully understood it is necessary to produce tools that are suitable for the urban planners, architects and system designer's needs. Georgakis and Santamouris (2004) point out that most of the research which has been done in this field has used simulations of single rows of buildings forming symmetrical canyon shapes, and addressed mainly orthogonal and parallel wind direction scenarios. On the other hand, field measurement studies conducted by those and other authors have reported that oblique winds account for 50% or more of the total wind direction in urban areas. Further, the authors report that the resultant airflow speed and direction of oblique winds in urban areas has been less studied and less well understood than those of parallel and orthogonal ones. The literature review which was undertaken at the outset of this research project indicates that most of the research which has been conducted so far has focused either on wind effects on isolated buildings, or on arrangements of single brick volumes and arrays of prismatic volumes with the aim of studying pollution concentration dispersion.

To date, few studies have recommended methods for the identification of a relationship between the variation of pressure coefficient on buildings façades with the iteration of the surrounding urban area and the airflow below the urban canopy height.

1.6. Purposes of this research

The main purpose of this research is:

- To examine the relationship between the urban fabric and the airflow below the urban canopy height, based on the physical urban aspect ratios and the wind speed and direction and pressure distribution on the building envelope;

The proposed aim of this research will initially be achieved through the analysis of results from experiments by which wind flow effects around simplified urban volumetric shapes are tested. Then, the input information will be integrated into more complex models of a large number of urban prototypes and two actual urban areas, in which one particular target building will be investigated in greater detail.

1.7. Research objectives

1.7.1. Main objective

The main objective of this research is to investigate the relationship between urban areas physical dimensions and the resulting airflow patterns and wind speed and direction and pressure coefficient distribution on the envelope of target buildings.

1.7.2. Secondary objectives

The secondary objectives of this thesis are:

- To study airflow patterns and wind speed and direction changes in urban areas;
- To map the pressure coefficient distribution on external built surfaces;
- To relate the differences in pressure coefficient between windward/ leeward sides of blocks and/ or buildings within the investigated urban areas; and
- To explore the link between external airflow and urban canyon dimensions for the two specific case-bases addressed in this investigation.

1.7.3. Indirect objectives

The following are considered indirect objectives of this thesis:

- The assessment of the effectiveness of modelling external airflows in urban areas in computational fluid dynamics (CFD) software by comparing these results with those of sets of wind tunnel experiments and field measurement data; and
- The highlighting in the methodology of how to set-up the input information and parameters for the 3D models in order to achieve proper CFD simulation results so as to assist further studies which are in the same field of this research.

1.8. Research hypotheses

Since urban areas tend to present canyon-like shapes whose aspect ratios between dimensions, areas and volumes can be determined, the study of airflow speed and direction around simple 3D volumes proportional to real size ratios can be a useful tool to better understand airflow in the urban environment.

1.8.1. Main hypotheses

The main hypotheses of this research are:

- For urban areas where regional wind patterns are known, the resultant air flow below the urban canopy layer can be associated with the urban dimension aspect ratios;
- Due to this association, it is possible to estimate pressure coefficient differences over the building envelopes;
- The mapping of potential spots of pressure coefficient variation on building façades can assist in the design process of selecting strategies for wind-driven natural ventilation systems; and
- A scale may be created

1.9. Research questions

- To what extent do the physical aspect ratios of urban centres affect the airflow and the pressure coefficient over building façades?
- Is it possible to produce a rule-of-thumb or scale for providing the potential for the application of natural ventilation strategies in urban buildings based on the analysis of a given urban fabric's physical dimensions and the information for the prevailing wind speed and direction in the region?

1.10. Rationale of the research

Existing large urban centres provide few options for large scale intervention with a view to improving environmental conditions through the use of sustainable approaches which aim to enhance both energy efficiency and quality of life.

Furthermore, the analysis of a considerable sample of existing high-rise office buildings in the city of São Paulo (Romero and de Faria, 2004) has shown that fully glazed homogeneous envelopes are prevalent, despite their unsuitability for hot and dry or hot and humid climates. Such architectonic solutions rely on full air conditioning systems to achieve air quality and thermal comfort. Moreover, they imply a high level of energy waste, even if high-tech HVAC and high-performance glass are employed.

Passive architectural strategies are, on the other hand, available for application to each new building development or refurbishment/ retrofit project. For such climates cooling by natural ventilation is an option that can be incorporated during most of the year, thereby reducing mechanical cooling loads and improving occupants' satisfaction and health levels.

Specific information and guidance on airflow in urban areas for designing naturally ventilated buildings has been emphasized as determinative in the implementation of such strategy. This occurs because turbulent wind effects below the urban canopy height can reduce the potential for natural ventilation and may thus become a significant obstacle to this strategy.

This proposed research project may help to contribute to this question, as the design of naturally ventilated buildings in areas of similar urban canyon aspect ratios can be assisted by the results achieved here. It is to be expected that future building design should incorporate this information during the initial design stages in order to be more suitable for its micro-climate and thus produce more sustainable and energy efficient working and living areas.

1.11. Methodology overview

In order to achieve the objectives proposed this research project uses several methods of investigation which involves different stages of analysis. These methods include theoretical research, field measurement data, laboratory scale-model tests in a wind tunnel, and computational fluid dynamics (CFD) simulations. The stages are associated with the physical scale of the object analysed:

- Urban airflow: based on an assessment of the external airflow patterns for a given wind direction around simplified models of urban areas, defined by aspect ratios relative to real urban environments;
- Building envelope: related to pressure variation caused by wind forces acting on the inlet/ outlet sides of the building; and
- Building ventilation strategies: the arrangement of internal vertical connections (shafts and atriums) in a case-base tower combined with the building envelope results in pressure variation and airflow across the building.

The methods of investigation and the results are listed below:

Table 1-1: Scope and focus of the methods of investigation at each stage of the investigation.

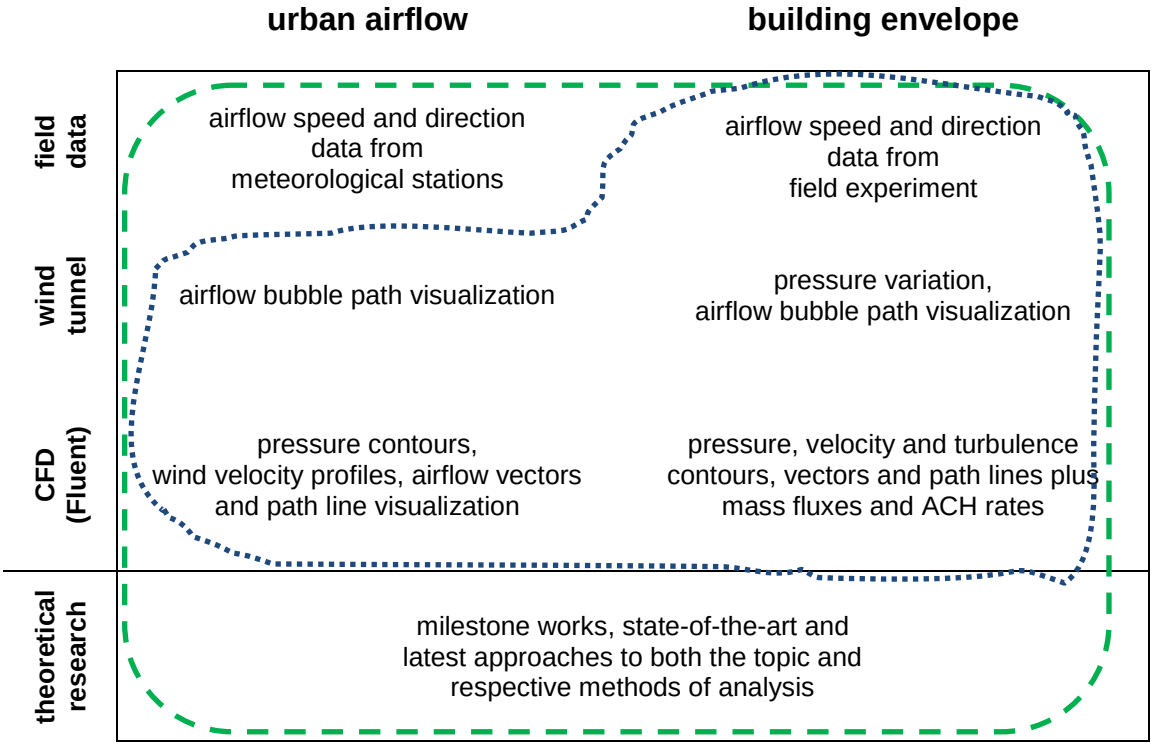

Source: This study.

The broad scope of this investigation will consist of the application of each method in all of the stages proposed. The applications focused on are those whose results are essential for either reaching the proposed objectives or validating the hypotheses suggested by this thesis.

There will follow a part dedicated to the literature review, which will be comprised mainly of milestone publications and state-of-the-art research reviews. In decreasing order of significance, the main sources of information used in this investigation where:

- Books;
- Journals: Building & Environment, Energy & Buildings, Indoor and Built Environment, Solar Energy, Renewable Energy, the International Journal of Ventilation, Atmospheric Environment, and others;
- Technical publications, guidelines, legislation and by-laws;
- Conference papers;
- Others: including suppliers, newspapers and magazines; and
- Internet pages.

Database searches of the above mentioned on-line journals were undertaken as part of the literature review. Around 600 papers were scanned using the following Boolean combinations of keywords:

- ‘Ventilation’, added to the words ‘urban’, ‘single’, ‘double’, ‘cross’, ‘nocturnal’ or ‘night;
- ‘Airflow’, followed by ‘urban’, ‘atmospheric’, ‘internal’;
- ‘Urban’, followed by: ‘canyon’, ‘aspect ratios’, ‘physical dimensions’, ‘fabric’;~
- ‘Air quality’, described as ‘IAQ’, ‘pollution’, ‘urban’, ‘office’;
- ‘Comfort’ or ‘PMV’;
- ‘CFD’, ‘turbulence’, κ-ε, LES;
- ‘Cooling’ plus ‘passive’, ‘ventilative’, ‘evaporative’ and ‘radiative’; and
- ‘Buoyancy’, and the terms ‘stack’, ‘wind-catcher’ and ‘solar chimney’.

1.12. Structure of the thesis

This thesis has five parts, and is subdivided into ten chapters.

1.12.1. Part I: Introduction to the Research

This first part consists of one chapter. In Chapter 1 the background information will be discussed and the subject of the analyses introduced.

1.12.2. Part II: Literature Review

This part will review concepts of airflow and natural ventilation in three chapters: Chapter 2, 'Airflow in the Urban Environment', addresses the theory and the physics of airflow in the external environment; Chapter 3, 'Modelling Airflow in the Urban Environment', presents a panorama of the techniques most widely employed for modelling airflow in the urban areas; and Chapter 4, 'Buildings and Natural Ventilation', discusses natural ventilation strategies for buildings on an internal environment scale.

1.12.3. Part III: Methodology

Chapter 5 gives details of the methods used in this research to analyse the scales of both the urban and the building's environment.

1.12.4. Part IV: Results and Analysis

The results of the simulations are analysed in chapters 6 to 9:

- Chapter 6, 'The Two Bricks: Results and Analysis';
- Chapter 7, 'Urban Prototypes: Results and Analysis';
- Chapter 8, 'Cathays Campus: Results and Analysis'; and
- Chapter 9, 'Paulista Ave.: Results and Analysis'.

1.12.5. Part V: Conclusions

The final conclusions are presented in Chapter 10, which also contains observations on the limitations of the study, its implications for and contributions to the theory. Finally, recommendations and suggestions for further research are included.

1.13. Chapter conclusion

In Chapter 01 the background information and the introduction to the subject for analysis are presented together with: the statement of the research problem and gaps in the area, research aims, purposes, objectives, hypothesis, justification, methodology and structure. Every chapter will contain its own introduction and conclusion to clarify and summarize what is being discussed.

Part 02: Literature Review

Chapter 2: Airflow in the Urban Environment

2.1. Introduction

This chapter presents a picture of studies on airflow field in the urban environment. Starting with the definition of the atmospheric boundary layer and how the terrain roughness affects the urban vertical wind profile, it also describes wind effects around isolated bluff bodies. Finally, it covers the main aspects of airflow in dense urban areas and within urban canyons.

2.2. The Macro-scale system

On a global scale, the seasonal distribution of atmospheric pressure determines wind direction and characteristics. Atmospheric pressure is the action of the air on surfaces. Differences in pressure are to be explained by the temperatures contrast both between the continental land masses and the oceans and the varying intensity of solar radiation due to latitude, in view of the fact that warm air is less dense than cold. If the Earth were stationary, the main movement of air would be from the poles (cold) to the equator (hot). The rotation of the Earth produces a force that deflects these winds (Coriolis forces) which, together with differences of temperature around the globe (day and night) also cause mass movement of the air (Masi and Ochoa, 2005).

There are, over each hemisphere, high and low pressure belts, both permanent and seasonal. The equatorial belt is one of permanent low pressure. In the tropics, there are high pressure belts that move towards the poles during summer and the equator during winter. The polar zones are of permanent high pressure. Between these belts, there is the Global or Geostrophic wind, rotating clockwise and anti-clockwise in the North and South hemisphere, respectively. When these forces meet low-pressure centres, strong winds called cyclones are formed. For high-pressure zones, these are named anti-cyclones (Holmes, 2001). For instance, the Trade Winds (Alisios) arise between the tropics and the equator and blow from the NE and SE in the northern and southern hemispheres, respectively. The winds from the West blow from the subtropical regions to the poles. And the poles generate cold winds which blow towards the NE and SE.

2.3. The Atmospheric Boundary Layer (ABL)

The atmospheric boundary layer (ABL) is the region where the 'free atmosphere' characteristics, dictated by the Coriolis and the pressure gradient forces are affected by friction with the surface of the ground. It comprises the vertical distance from the ground level up to the gradient height, where the wind speed is no longer affected by the unevenness of the ground roughness. The ABL is sub-divided into the Interfacial Layer and the Ekman layer, and is characterized by an increase in average upward wind velocity that determines the vertical wind profile. Above the Interfacial layer height the flow tends to stabilize slowly until attaining the wind velocity and direction of the gradient layer. This effect is called the Ekman Spiral, and occurs in the Ekman Layer. Both the wind profile and the ABL height are determined by the terrain roughness features, although they are also susceptible to influences of small-scale weather systems (Cook, 1985, Holmes, 2001).

Figure 2-1: Atmospheric Boundary Layer

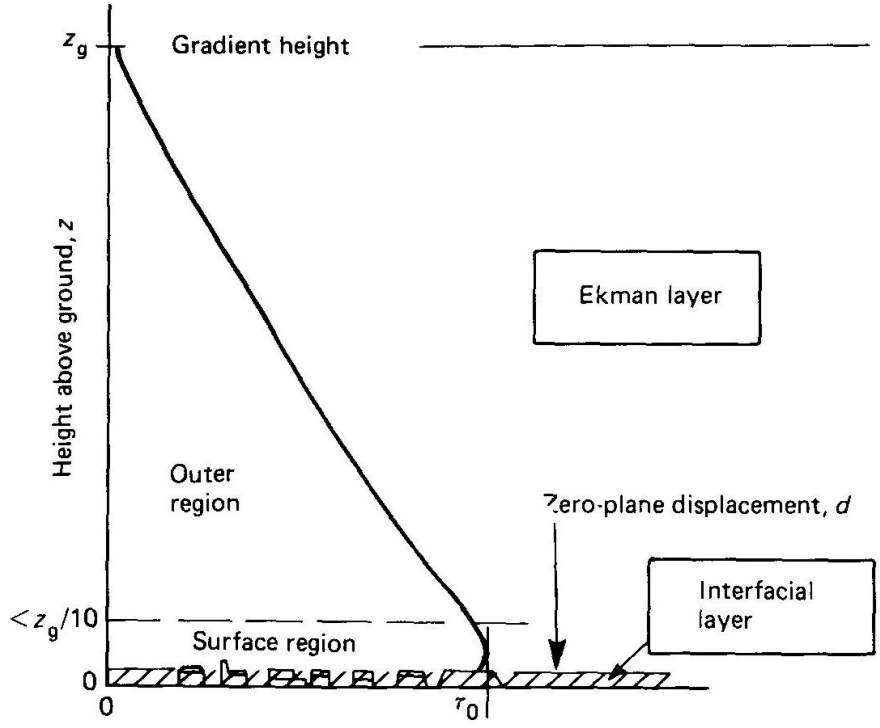

Source: Cook (1985, pp139).

The interfacial layer extends from ground level up to the so-called either 'canopy height' (Oke, 1978 and 1988; Melaragno, 1986; Givoni, 1998) or 'obstructed sub-layer' (Kolokotroni and Santamouris, 2007), meaning the vertical distance from the ground at which the free airflow momentum is transformed into pressure on windward surfaces, thus affecting the surface region and the outer region wind velocity. In a city centre the

urban canopy height is related to the average height of the buildings. In this thesis, the former term will be used in relation to the general description of the urban shape, and the latter will be employed in the specification of the ABL. The 'zero plane displacement' indicates the height in the canopy height on which the pressure is nule (MacDonald, 1975; Cook, 1985; Holmes, 2001). Holmes (2001) indicates that the zero-plane displacement can be considered as standing at three-quarters of the roof height. Cook (1985) provides a more accurate method for calculating it based on the average height of tall buildings and the plan-area density of the urban site.

Equation 2-1: $d = H - [4.3 * Z_o * (1 - a)]$

Where:

- d: is the zero-plane displacement (m);
- H: the average height of the buildings (m); and
- Z_0: the terrain roughness length, a constant of integrations (m); and
- a: is the plan-area density, which is a dimensionless term, calculated as:

Equation 2-2: $a = A_{roof} / A_{urb}$

Where:

- A_{roof}: the total roof area, comprising the sum of the cover area for one or more buildings in an urban site (m^2); and
- A_{urb}: the total urban site area (m^2).

2.3.1. The Beaufort scale for wind speed effects

The Beaufort scale to measure the effects of wind speed has its origin in navigational science and sea surface response to increase in wind velocity, and was later adapted to measure the consequences of the variation in wind speed on land (Cook, 1985; Melaragno, 1986; Masi and Ochoa, 2005). Here, only this adjustment for dry land will be considered.

At ground level and in cities and other urbanized areas the Beaufort scale usually ranges from still air conditions (0) to moderate (4) and fresh breezes (5), and may occur in normal weather. However, strong winds (6-7) may occur sporadically as well, while higher numbers are caused by atypical and extreme weather events, only.

Table 2-1: The Beaufort scale for wind speed effects.

Beaufort scale	wind speed		Description	Land conditions	Dynamic pressure (Pa)	wave lenght
	km/h	m/s				
0	0	0-0.2	Calm	Calm. Smoke rises vertically.	0.2	0
1	1-6	0.3-1.5	Light air	Wind motion visible in smoke.	1.2	0.1
2	7-11	1.6-3.3	Light breeze	Wind felt on exposed skin. Leaves rustle.	6	0.2
3	12-19	3.4-5.4	Gentle breeze	Leaves and smaller twigs in constant motion.	20	0.6
4	20-29	5.5-7.9	Moderate breeze	Dust and loose paper rise. Small branches begin to move.	40	1
5	30-39	8.0-10.7	Fresh breeze	Smaller trees sway.	75	2
6	40-50	10.8-13.8	Strong breeze	Large branches in motion. Whistling heard in overhead wires. Umbrella use becomes difficult.	120	3
7	51-62	13.9-17.1	Near gale	Whole trees in motion. Effort needed to walk against the wind.	170	4
8	63-75	17.2-20.7	Gale	Twigs broken from trees. Cars veer on road.	260	5.5
9	76-87	20.8-24.4	Strong gale	Light structure damage.	350	7
10	88-102	24.5-28.4	Storm	Trees uprooted. Considerable structural damage.	500	9
11	103-119	28.5-32.6	Violent storm	Widespread structural damage.	650	11.5
12	120	32.7-40.8	Hurricane	Considerable and widespread damage to structures.	800+	14+

Source: Masi and Ochoa (2005, pp32).

2.3.2. Terrain Roughness

The decrease of momentum in free air flow due to the roughness of the terrain and subsequent reduction in kinetic energy results in turbulent flow, which is then dissipated by the action of viscosity in the smallest turbulent eddies (Cook 1985). This dragging force retards the flow close to the surface and slows down the mean horizontal wind speed, altering the increase of the upward wind speed. The rougher the ground is, the greater its influence over the ABL depth and gradient height (Oke, 1978).

2.3.3. Wind turbulence in the urban environment

Turbulence is present in most flows. Regarding airflows, it occurs in any atmospheric layer: below or above the ABL; in jet streams in the upper troposphere; in cumulus clouds; and also in the wake of objects in motion (e.g. vehicles and aeroplanes) or is produced by the impact of the airflow against obstacles.

According to Ghiaus and Allard (2005) the laminar free-flow in the atmosphere is an exception, and the wind speed combined with other factors result in a high Reynolds number (Re) and consequent turbulence. The Reynolds stress vertical profile shows that the Re number increases near the ground. This happens since wind loses momentum to overcome the frictional effects of the terrain's roughness and the shear stress thus produced. The consequent loss of kinetic energy is converted into turbulent kinetic energy (Martilli *et al.*, 2002). In the Ekman layer the Re number increases upwards to above the interfacial layer and then starts decreasing again until it reaches the same Re number as is found in the gradient layer (Cook, 1985). Turbulent behaviour is better understood when the dimensional components of the flow vectors are divided into three steady (U, V, W) and three turbulent (u, v, w) sections and described separately. The turbulent components are composed of random and chaotic eddies of different lengths and frequencies (Cook, 1985). Once the wind flow from the open country reaches the suburb or a city centre it tends to skip over the roofs and sides of buildings and its momentum is transformed into pressure on the windward surfaces of solids, creating several types of effect, such as acceleration, down-flow, flow detachment, low wind speed, high and/ or low pressure zones, sheltered areas, and leeward wakes of turbulent vortices. This unsteady behaviour tends to diminish the flow's momentum due to the drag and viscous forces caused by the friction produced between surfaces and air flow. After urban areas, the flow returns to the main streamline, restabilising less turbulent flow behaviour in open country. The surface shear stress value is, therefore, related to the terrain roughness and the friction velocity. The ABL is then set by the energy spent in overcoming the shear stress due to the roughness of the terrain, which is determined by the canopy height. Below this

height, the free airflow momentum is transformed into wind pressure on vertical surfaces. Above this height the flow tends to stabilize slowly until reaching the gradient speed. The atmospheric boundary layer from open areas is transformed on reaching denser locations due to the variation in the shear forces due to the roughness of the terrain and the building surfaces acting as barriers to the free-flow, resulting in more gradual increase of the vertical wind velocity profile and acquiring more turbulent behaviour (Oke, 1978 and 1988; Melaragno, 1982; Cook, 1985).

Figure 2-2: Flow in the interfacial layer:

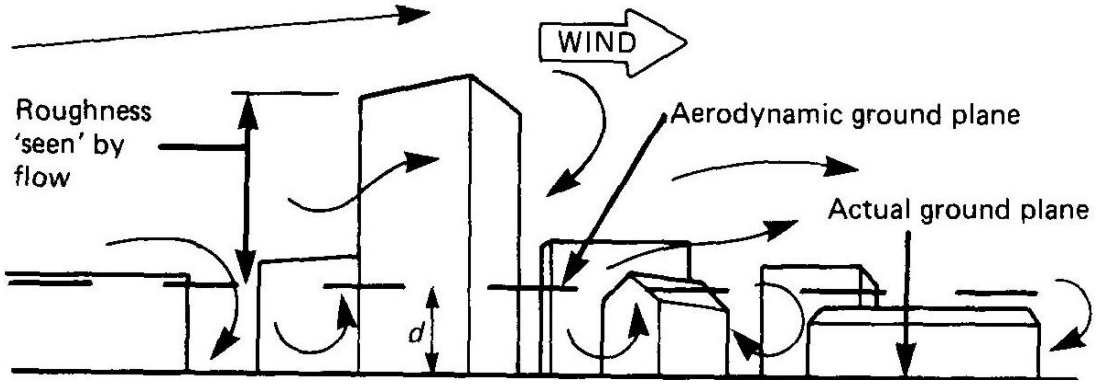

Source: Cook (1985, pp139).

The rougher the terrain, the greater is the shear force and, therefore, the greater the reduction in the speed of the free flow nears the ground. This results in different boundary layer profiles of wind velocity variation and increase with height until reaching the gradient layer, where wind speed is constant and no longer influenced by this ground roughness, although being subject to large scale climatic factors.

2.3.4. Mean wind speed profiles

When the boundary wind from uniformly flat and constant terrain roughness reaches suburban and urban areas, the boundary develops adopting a profile related to its new characteristic terrain roughness (Plate and Kiefer, 2001). Although the complexity of the airflow field and the ABL development over urban areas are not just related to two or three terrain roughness types, since the complex tri-dimensional geometry of urban centres allied to the intermittent nature of the airflow and gust speed and direction provides myriad variables, an assortment of mathematical expressions provide models for calculating a two-dimensional mean wind speed profile. These equations take the terrain roughness into consideration in order to determine the variation in profiles.

Figure 2-3: wind profile development for different terrain roughness:

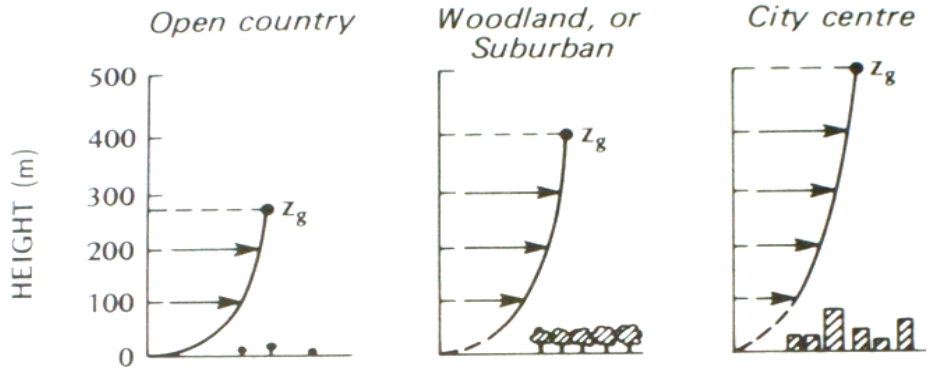

Source: Oke (1978, pp45).

The equations mostly frequently used are the 'power law' and the 'logarithmic law'. These models are detailed in the following items, accompanied by descriptions of positive applications and possible drawbacks.

2.3.5. The Power Law

This model plots the mean wind speed for any height in the ABL above the zero-plane canopy based on the reference wind speed at a certain height, the gradient height and the characteristics of the roughness of the terrain, employed as an exponent of this power law, as follows (Melaragno, 1982; Cook, 1985):

Equation 2-3:
$$\overline{U}_z = \overline{U}_{10}\left[\left(\frac{Z - d}{10}\right)\right]^{a}$$

Where:

- $\underline{U}z$: is the mean wind speed at Z height (m);
- $\underline{U}_{10}$: the mean wind speed at 10 meters height;
- Z: is the height above ground (m);
- d: is the canopy height (m); and
- α: is an exponent, based on the terrain roughness characteristics.

Table 2-2: Terrain roughness parameters 'α':

coastal areas	open terrain 1	open terrain 2	suburban areas 1	suburban areas 2	suburban areas 3	cities 1	cities 2
0.10	0.14	0.16	0.21	0.22	0.28	0.33	0.40

Sources: Cook (1985, p184); and Melaragno (1986, pp48).

According to MacDonald (1975), Cook (1985) and Holmes (2001) there is no theoretical justification for power-law. Since this method is based on empirical

assumptions, it does not represent all the aspects of reality. Further, this model is more accurate in the upper Ekman layer, but inaccurate at low heights and below the canopy height, being considered inadequate to satisfy design needs unless applied for calculating wind loads on high-rise structures and under strong wind conditions. Another drawback highlighted by Cook relates to the fact that, since this model is independent of a linear scale on which any value can be applied for height 'Z-d', the top of the atmospheric boundary layer is never reached. This means that the mean speed continues to increase above the gradient height. In this way, the gradient speed cannot be used as a reference for comparing two profiles of different terrain roughness, and a reference speed at the given height (10m) is used instead. Despite this model's above-mentioned shortcomings, it has been universally accepted and used for determining both mean wind profile and gust speed due to the straightforwardness of its application.

2.3.6. The Log Law

The 'logarithmic law' is considered by some authors to be an accurate method for calculating mean wind speed profiles due to its similarity to a logarithmic decay curve (Oke, 1978). This model can be derived in some ways, and its basic parameter postulates that the wind shear is a function of the upward mean wind speed variation in the Ekman layer. This rate is also a result of the surface shear stress, retarding forces imposed by the aerodynamic roughness of the terrain.

Equation 2-4:
$$\overline{U}_z = \left(\frac{u_*}{k}\right) \ln\left[\left(\frac{Z - d}{Z_0}\right)\right]$$

Where:

- u_*: is the dimensionless friction velocity;
- k: the dimensionless von Karman's constant =0.4, and $1/k$ = 2.5; and
- Z_0: the terrain roughness length, a constant of integrations (m).

The log law avoids the main weakness of the power law, since it has a theoretical basis, is well resolved above the canopy height, and is integrated and scaled based on the extent of the roughness of the terrain. However, Cook (1985) relates that transitions from flatter to rougher terrains are still not well resolved in the higher part of the Ekman layer. It is worthy of mention that, although the log law conforms to the physics of the wind speed profile these ideal conditions are rarely found in nature. MacDonald (1975) adds that below the canopy height the extension and shape of the vertical velocity profile is theoretical only and therefore mathematical models do not conform to reality. This drawback is related to the fact that, in order to apply logarithmic models, the

numbers must be positive, which excludes the possibility of having heights below the canopy height (Holmes, 2001).

2.3.7. The Log-linear Law

A semi-empirical model was developed to fit the log law in the outer region of the Ekman layer with good agreement up to 300m from the canopy height height (Cook, 1985).

Equation 2-5: $\underline{U}z = 2.5 * u_* * \{\ln[(Z-d)/Z_0] + (K*Z/Zg)\}$

Where:

- K is a constant, where $4 < K*Z < 7$; and
- Zg is the gradient height (m).

Table 2-3 presents values for the extent of the terrain roughness and gradient height based on the features of the terrain roughness:

Table 2-3: Terrain roughness parameters:

category	Terrain roughness description	Z_0	d (m)	Zg (m)	Exponent for Z-d	
					<50m	<200m
0	large expanses of water, snow cover, flat land	0.003	0	2210	0.12	0.12
1	flat grassland, parkland, very few isolated obstructions	0.01	0	2380	0.14	0.14
2[1]	farmland, nearly flat or gently undulating countryside, crops, fences, few trees	0.03	0	2550	0.16	0.16
3	farmland, fences, occasional buildings and trees	0.1	2	2770	0.2	0.18
4	suburban areas, domestic housing, dense woodland, 10-20% plan-area density	0.3	10	3000	0.24	0.22
5	urban areas, mostly of 04 storey or higher, 30-50% plan-area density	0.8	25	3250	0.32	0.27
6[2]	City centres	1.0				
7[2]	Metropolis centre	4.0				

Source: Cook (1985, pp203 and 222).

[1] Meteorological standard and basic terrain roughness for sites in the UK (Cook, 1985).
[2] Roughness height introduced by Guiaus and Allard (2005, p.62).

2.3.8. The Deaves and Harris Model

The Deaves and Harris Model overcomes the main drawbacks of the previous log laws: it adapts the mean wind profile due to changes in the terrain roughness characteristics well, since now both the gradient speed and height are obtained from and/or used in the equation (Deaves and Harris, 1978; Deaves, 1981; Cook, 1985). This model sets values for the constant K from the log-linear model and also takes the canopy height into consideration. The last three terms in the equation can be cancelled for heights up to 300m from the canopy height.

Equation 2-6: $\underline{U}z = 2.5*u_**\{\ln[(Z-d)/Z_0]+5.75*(Z-d)/Zg-1.875*[(Z-d)/Zg]^2-4*[(Z-d)/Zg]^3/3+[(Z-d)/Zg]^4/4\}$

2.3.9. Changes in terrain roughness and wind profile adjustment

When the fully developed ABL relating to a specific site encounters a change in the terrain roughness, a velocity and gradient height adjustment takes place from the bottom to the top of the profile until it regains its equilibrium (Holmes, 2001). The fetch is the length term used to describe the radial horizontal dimension from a given terrain with the same roughness characteristics. It specifies terrain roughness changes over distances and their location in the upstream to downstream axis and direction (Cook, 1985). Deaves and Harris (1978) and Deaves (1981) describe two mathematical models to determine the adjustment fetch at a certain height Z for flows from smoother to rougher terrains and vice-versa, as follows:

For $Z_{01} < Z_{02}$:

Equation 2-7: $X_i(Z) = Z_{02}*[Z/(0.36*Z_{02})]^{4/3}$

And for $Z_{01} > Z_{02}$:

Equation 2-8: $X_i(Z) = 14*Z*(Z_{01}/Z_{02})^{1/2}$

Where:

- $X_i(Z)$: is the distance to the inner ABL at Z height (m).

Applying these equations, the distance the adjustment of the ABL from a flat terrain to a suburban area would take to happen would be around 144 m at 10m height. Cook (1985) also provides tables with values of fetch factors where changes from smooth to rough terrains take from 1.00 to 1.79 km to settle down and from rough to smooth terrains this distance varies from 0.42 to 0.99 km at the canopy height. The diversity of real urban fabrics in large urban centres is extremely complex, and such fetch dimensions surpass in most cases the length of regions that traverse homogeneous urban areas. Although the above-mentioned ABL models translate into mathematical equations, in the adjustment of the vertical wind velocity profile across more than two terrain roughness variations, one uses some approximations in the application of these models. For instance, when selecting a stable ABL over a large metropolitan centre, the canopy height should cover a larger area than a few urban blocks with the shape and height of buildings only. It should also take the city's topography as a whole into consideration, within its urban variety from one side to the other with its valleys, hills and urban canyons.

2.3.10. Flow effects due to topography and terrain roughness

Topography, including such features as escarpments, embankments, valleys, ridges, cliffs and hills may increase and/ or decrease the mean wind speed, the gust speed and the turbulence considerably. In his paragraph some of these features will be presented, based on the literature written by various authors (Olgyay, 1973; MacDonald, 1975; Oke, 1978; Cook, 1985; Melaragno, 1986; Holmes, 2001). Topographic dimensions such as vertical, upwind, crosswind, steepness and shape dimension rates are used to define how topography may influence the wind stream, e.g. by flow separation on steep terrains. In order to quantify it, the topography gradient 'Y', a ratio between the horizontal length and the vertical height of tilted terrain is presented. For gradients of less than 5%, no disturbance of the wind flow is considered. From 5%<Y< 30%, the influence of the topography will be noted (e.g. deceleration at the foot and acceleration at the crest), but no flow split occurs. For gradients above 30% significant deceleration and acceleration will be noted, and flow detachment with recirculation bubbles, turbulent wakes and other effects may be observed in sheltered areas. While gradual changes in the zero height, or terrains with smooth and low slope angles, are absorbed by the ABL without changing the wind profile, abrupt changes in the topography, landscaping or large displacements of ground surface are reported to have greater impact on the atmospheric boundary layer than even the urban surface roughness. For upwind slopes with inclination below 17^{o}, the wind starts decelerating at the foot and continues decelerating throughout the uphill length until reaching the crest, where it accelerates. After the terrain becomes flat

again, the wind decelerates once more until its velocity stabilizes. The speed-up ratio from the foot to the crest is around 1.6 at 10m height. For sharper inclinations “skewed to the escarpment”, this same uphill wind will experience, in addition to the deceleration and acceleration just quoted, an upwind separation bubble at the foot of the slope and another downwind separation bubble beyond the crest, since the flow momentum is not enough to overcome the pressure over the up-hill terrain and the shear stress created at the crest. Both these separation bubbles are characterized by low velocity turbulent vortices spinning in the same direction as the airflow. Down-hill flows will experience the mirrored effect for low angle shallow terrains. On the other hand, for flow down on steep escarpments with inclinations greater than 17^{o}, there is no separation bubble at the crest, but it does occur at the foot, with the vortex spinning in the same downhill direction as the main flow. Also, for hills, the flow goes to either side, as well as to the top. The inclination of the slopes is again what determines whether separation bubbles will form, and a leeward wake will probably occur in this case.

Cook (1985) describes wind effects inside valleys, where channelling effects take place if the stream direction is parallel to the predominant axis. Also, funnel shapes at the windward entrance will cause wind acceleration, otherwise the speed along the canyon remains constant. For wind directions orthogonal to the valley length, the flow tends to skip over the canyon, creating a separate bubble of air circulating at low wind speeds within it. The author does not mention either the effects of oblique winds in canyons or internal vortex effects. Several other factors are used to adjust the mean reference wind speed to any specific terrain condition and design assessment. These factors can be equations (based on theoretical or empirical models for ABL or extreme values) or tables and graphs (pre-tabulated terrain roughness).

Equation 2-9: $V\{a, b, c, \ldots, n\} = \underline{V}b \times SaSbSc\ldots Sn$

Where:

- Sa: is the altitude factor, which comprises the consequence of significant slowly changing topography in the wind climate, when the gradient topography is usually below 10%, and is calculated as < Sa = 1+ka*A >, where ka is a constant from 0.0007 to 0.0010 and A is the height difference between the wind data measurement and the project;
- So: the directional factor, which accounts for the effect of local or regional climates in the wind, such as sea breezes or hills;
- Ss: the seasonal factor, on which isopleths contours are a mean value that does not considered the season variation in a parent wind data. Therefore coefficients

are used to adjust the reference mean wind values to specific seasonal variations, ranging from 1.0 for winter to 0.76 for summer;

- Vb: the mean wind speed factor, which determines the adjustment of the reference mean wind speed and other parameters to define the ABL, and:

Equation 2-10: $u = Vb*[2.5*\ln(\text{height}/\text{roughness coefficient})]$

Where,

u: is the frictional velocity.

Deaves and Harris (1978) present a model for calculating the in-wind component intensity of turbulence at any height for a given terrain roughness. Also, the corresponding crosswind and vertical component intensities are described by other authors as almost zero in the gradient height and a ratio of v'/u'=0.68 and w'/u'=0.45 near ground level, e.g., in 'd'.

2.3.11. Gust Wind Speed

The meteorological definition of gust wind speed is the maximum wind velocity recorded in a period of data recording. It should, further, last for a given interval of time. For ordinary anemometers, this time is 1 second for velocities above 20m/s. The basic gust wind speed is, therefore, defined by the hourly-maximum one second duration gust at 10m above basic terrain. Increase of roughness causes an increase in the turbulence components as well, since it involves kinetic energy loss when the mean wind speed is reduced. On the other hand, the gust wind speed seems to present little alteration and, therefore, the comparison between mean wind speed and gust wind speed gives the values of kinetic energy transformed in turbulence (Cook, 1985). Gust wind speed can be calculated based on the mean wind speed added to a peak factor (~3.5) multiplied by a standard deviation. Also, the gust factor is presented by a ratio between the maximum gust speed and the mean wind speed for a given interval of time. This interval should be at least N = 100 hours of data collection for each 30^{o} sector (MacDonald, 1975; Holmes, 2001).

2.4. The wind pressure

Air moving at a constant velocity and direction exerts a potential pressure denominated static pressure (Ps). When wind, characterized as a laminar air movement parallel to the ground, moves towards a building, it produces varying pressure differences on its frontal, lateral, rear and top surfaces. When it reaches a

barrier, the dynamic pressure (Pd) produced is greater than the original potential to windward, and lower to leeward. The dynamic pressure at a specific point of a building's façade is related to the wind velocity and angle of incidence, taking into consideration that both the wind's behaviour and the pressure distribution on a building in the open field and in an urban context are very different (Ghiaus and Roulet, 2005).

2.4.1. The pressure coefficient (Cp)

The wind pressure coefficient (Cp) is a function that allows the identification of the distribution of wind pressure on a building's surfaces and in the spaces between them (CIBSE Guide A, 2006). The Cp is related to the wind velocity at a reference point (V_r), the dynamic pressure on the building's surface (Pd) and the density of the air (ρ_a). Based on the Bernouli principle, the equation for calculating the Cp is (MacDonald, 1975; Cook, 1985; Holmes, 2001; Awbi, 1991, 2003):

Equation 2-11: $$Cp = Pd / (½ \rho_a V_r^2)$$

Where:

- Pd: is the dynamic pressure (Pa);
- ρ_a: the density of the air (average of 1290g/m^3, varying according to temperature, altitude, and relative humidity); and
- V_r: the wind velocity at a given reference point (m/s).

Although there is great variation of the pressure alongside the façade of a building, an average value is used for pressure loads (MacDonald, 1975). Cp's are usually defined either by wind-tunnel experiments or by computational fluid dynamic (CFD) simulations, and are used for calculating wind load on structures and wind-driven ventilation rates across the internal environments of buildings. Usually the Cp's refer to a specific building shape and surrounding characteristics, though there are several databases in the literature that provide pre-established values for a number of situations and examples (MacDonald, 1975; Cook, 1985; Melaragno, 1986; ASHRAE, 2001; Holmes, 2001; Awbi, 2003; CIBSE A, 2006). Cp data are usually extracted from academic works and research centres since wind tunnel and CFD simulations are expensive, time-consuming, highly technical and, therefore, still inaccessible to the majority of building planners and architects' offices. Here the following wind Cp values proposed by Liddament (1996), which are also mentioned by both Awbi (2003) and the CIBSE A (2006), will be used as the Cp reference parameter for this thesis, bearing in mind that these values are valid for detached buildings of up to three storeys, surrounded by others of similar volume, in the urban context.

Figure 2-4: Wind direction towards a square or rectangular bluff body:

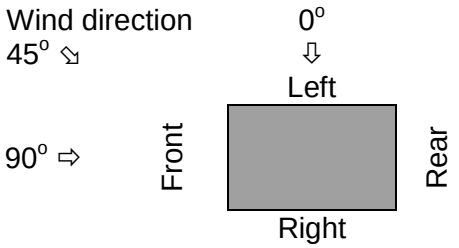

Source: Liddament (1996, pp241).

Table 2-4: Wind Cp values according to the terrain ABL and the wind direction:

Wind Cp averaged values according to the wind direction and surrounding area										
shape	building side v / angle >	Open field			Sub-urban area			Urban area		
		0°	45°	90°	0°	45°	90°	0°	45°	90°
square	Front	-0.50	0.35	0.70	-0.30	0.10	0.40	-0.25	0.05	0.20
	Left side	0.70	0.35	-0.50	0.40	0.10	-0.30	0.20	0.05	-0.25
	Right side	-0.20	-0.40	-0.50	-0.20	-0.35	-0.30	-0.25	-0.30	-0.25
	Rear	-0.50	-0.40	-0.20	-0.30	-0.35	-0.20	-0.25	-0.30	-0.25
rectangular	Front	-0.50	0.25	0.60	-0.35	0.06	0.25	-0.20	0.12	-0.20
	Left side	0.50	0.20	-0.90	0.40	0.20	-0.60	0.18	0.15	0.18
	Right side	-0.35	-0.60	-0.90	-0.30	-0.50	-0.60	-0.20	-0.32	-0.20
	Rear	-0.50	-0.80	-0.70	-0.35	-0.60	-0.50	-0.20	-0.38	-0.20

Source: Liddament (1996, pp241).

2.4.2. The pressure coefficient difference (ΔCp)

The pressure coefficient difference (ΔCp) is based on the difference between the upwind Cp and the downwind Cp values (Ghiaus and Roulet, 2005). The ΔCp is employed to calculating the pressure across a building for a reference wind speed, thus identifying airflow rates through openings and air changes in the internal environment[3].

Equation 2-12: $\Delta Cp = Cp_{ww} - Cp_{lw}$

Where:

Cp_{ww}: is the pressure coefficient on the windward side of the building, and

Cp_{lw}: is the pressure coefficient on the leeward side of the building

[3] For further details in the applications of ΔCp see topic 4.5.3.1. in Chapter 4.

2.5. Airflow around isolated bluff-bodies

Flow patterns around isolated bluff bodies are well-known, and the effects of winds impinging perpendicularly on single blocks have been fully investigated through wind tunnel tests. The results recorded in the literature constitute the basis of knowledge for the calculation of pressure coefficients across buildings and wind loads on structures (Olgyay, 1973; MacDonald 1975; Awbi, 1991 and 2003; Cook 1985; Melaragno, 1986; Holmes 2001).

2.5.1. Windward face

The effects of airflow against bluff bodies are different from those of uniform and variable incident wind profiles. Concisely described, hypothetical orthogonal flow against prismatic sharp-edged shapes, as is the case with most isolated buildings, is related to the impinging boundary wind profile, presenting a front stagnation point (FS) on the windward surface, shear layers in the laterals and flow detachments at the sharp edges, trailing shear layers and turbulent vortex wake of low speed and pressure on the leeward side.

While at the first moment the pressure on the windward surface is evenly distributed and has the same value as in the first case, at the second there is a pressure value gradient that corresponds to the variation of the wind velocity with height, and to the consequent kinetic energy. In the first case, as the streamlines flow over the top, there is a pressure gradient on which the bottom centre is the highest point (1.0), the perimeters being the lowest ones (0.4). In the second case the difference in wind velocity produces a region on the windward surface of high pressure, the FS. From the FS point (which is positioned around 2/3rds of the total height) the flow divides into an upward accelerated flow goes over the top roof, and another downward flow that creates a reverse vortex at ground level until reaching the rest in the separation point on the ground, or ground stagnation GS (1/3rd of the total height).

The centre of the upper pressure sub-zone attains a coefficient of 0.7 and that of the lower 0.4. Both perimeters' coefficient pressures are below 0.4. On tall buildings this downward flow deflects strong high winds to the pedestrian levels, what may incur in pedestrian discomfort and hazard. Also, part of this downward wind is deflected to each side of the building in a horse-shape form. The flow escaping on each side of the building accelerates near the corners by over 50%, which can also be quite hazardous for pedestrians. In high-rise buildings, i.e. those whose height is greater than three times the width, the pressure distribution pattern presents the greatest distribution of pressure in the centre. The FS point is related to 4/5ths of their height and strong downward flows may occur, causing pedestrian hazard or discomfort (Holmes, 2001).

Figure 2-5: Vertical wind profile and Cp distribution of constant (left) and variable (right) vertical wind profile on a cubic volume:

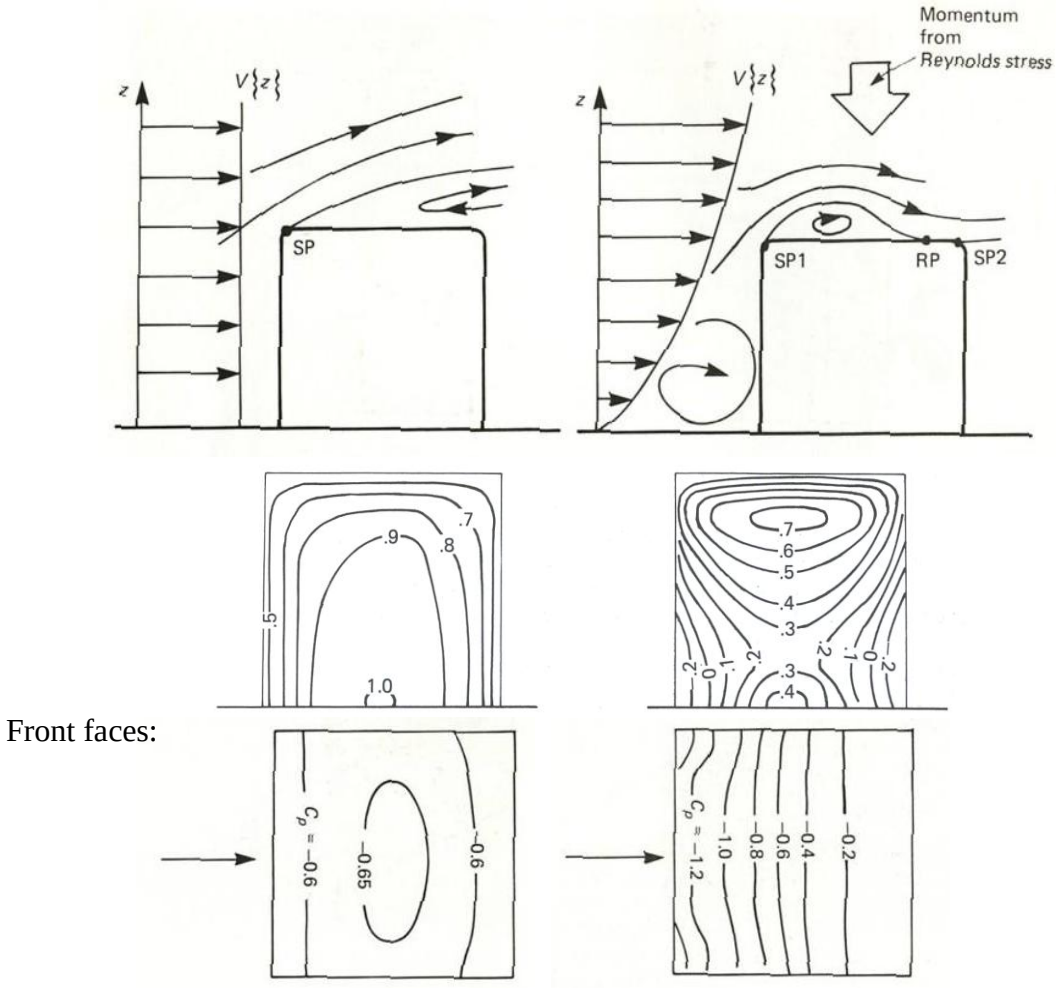

Source: Cook (1985, pp168).

Figure 2-6: Mean, maximum and minimum Cp distribution of constant vertical wind profile on a high-rise volume:

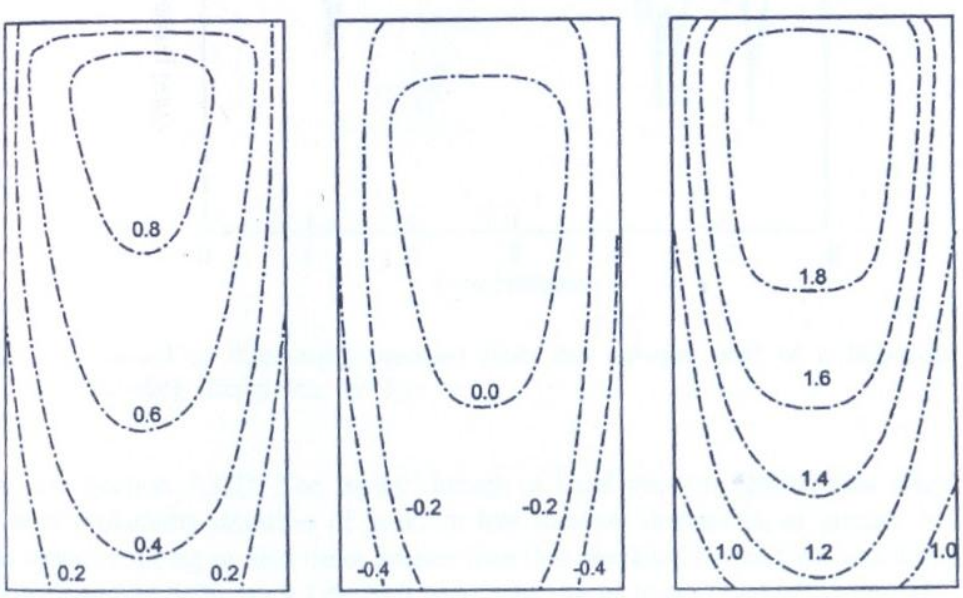

Source: Cheung (1984, *in* Holmes, 2001, pp187).

2.5.2. Flow over the top

The separation bubble at the top of a building is also different for uniform and boundary layer flows. In the first case, all the flow accumulates upwards, creating a sharp detachment. In the second, only the flow in the last 1/3rd of the height of the building goes upwards. This effect, added to the mean wind kinetic energy, contributes to the flow reattachment downstream on the top surface, occurring at the reattachment point RP. There is also a new detachment from the flow at the leeward edge (Cook 1985; Holmes 2001).

2.5.3. Side and leeward faces

The flow separation on the sharp edges of the sides of square buildings creates a separation bubble downwind. The upper 2/3rds part of the lateral flow behaves homogeneously, presenting an accelerated detached flow over a bubble where the low pressure near the upwind edge increases gradually towards the downstream edge. The lower 1/3rd lateral flow is accelerated by the windward horse-shoe shaped vortex.

Figure 2-7: Airflow horse-shoe effect around perpendicular and oblique cubes:

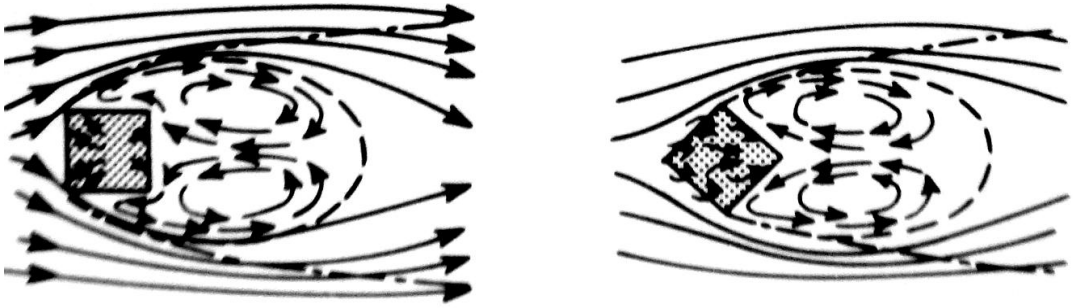

Source: Oke (1978, pp232).

2.5.4. Wake flow

Wakes are formed by the detachment of the flows on sharp edges of a building and have two main components: the near-wake and the far-wake. The near-wake, just beyond the leeward surface, presents a recirculation zone composed of one or more vertical vortices at its centre and spiral upward eddies on each side. The far-wake is represented by the eventual reattachment of the wake to the main airflow streamlines.

Figure 2-8: Streamline sizes around isolated buildings:

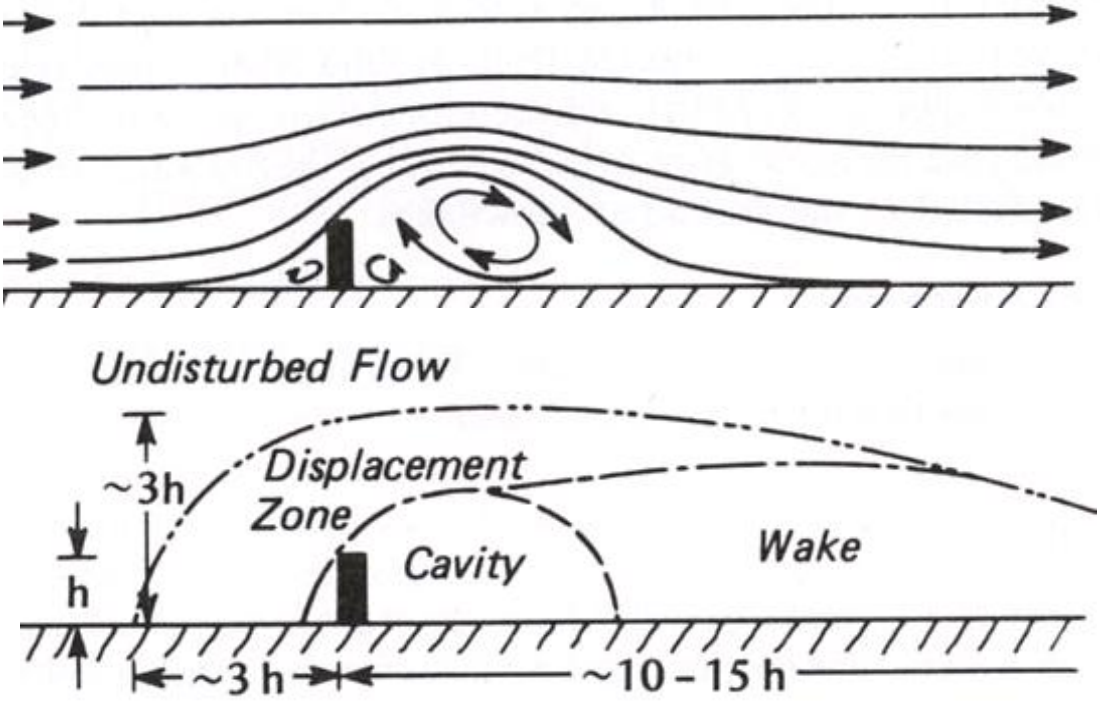

Source: Oke (1978, pp212).

Chandra *et al* (1986) states that, for standard residential neighbourhoods the length of the leeward wake is about four times the ground-to-eave height. In previous studies, Oke (1978) had stated that the total length of the leeward wake to the point at which reattachment flow occurs is from 10 to 15 times the height of isolated high-rise buildings, while the zones of undisturbed flow on the upper and front sides are situated at 02 and 03 times that distance.

Melaragno (1986) has provided a rule-of-thumb for calculating the shielding effects of buildings where the size of the shaded area on the leeward side of the building varies with the shape and height of the construction. This “shadow” is characterized by reduced air speed and eddy formations. Its length varies from three to almost five times the height of the built volume, varying in accordance whit the building’s width and the angle of inclination of the roof, but is only valid for orthogonal winds impinging on detached isolated construction blocks.

Experimentation with simple volumes, such as a cube, prism or brick (or an array of cubes such shapes) has allowed direct comparison of CFD simulation data with those of wind tunnel and/ or field measurements. Such comparisons have been used for verifying, calibrating or validating CFD model input information (for instance, domain and boundary layer, turbulence and viscous modes) and other parameters that may affect the accuracy of such simulations of reality. Examples of CFD and wind tunnel techniques and their application are covered in Chapter 3, while the description of the

models and the parameters employed in the investigations undertaken for this thesis are demonstrated in Chapter 5.

Table 2-5: Building sheltering effects on airflow:

building height	building length	roof angle	shaded size
H	H	flat	3.75 H
H	2 H	flat	3.00 H
H	3 H	flat	3.25 H
H	H	30o	3.25 H
H	H	45o	4.25 H
H	H	60o	4.75 H
H	3 H	30o	3.75 H
H	3 H	45o	4.25 H
H	3 H	60o	4.50 H

Source: Melaragno (1986).

2.6. Airflow in the urban environment

In contrast to the airflow patterns around isolated structures, the wind field in the urban environment is more complex and less predictable, notably below the canopy height of high-density city centres. According to Cook (1985), when the surface roughness is large and packed, as in towns…

> … the wind flow tends to skip over the tops of the buildings, leaving sheltered regions between them… there will be a flow of wind in the region between the ground and the average roof height, but this will be in many different local directions, channelled by the buildings, so that the overall net flow is zero. The flow in this layer at any particular urban spot will be entirely dependent on the local effect of neighbouring buildings and no general characteristics can be expected to apply (Cook, 1985, p.138).

In agreement with this statement, Ghiaus and Allard (2005) mention that the general aspects of wind patterns in the urban environment, as compared to those of undisturbed wind, are: mean speed due to differences in terrain roughness is reduced (by 20 to 30%); turbulence increases in intensity (by 50 to 100%); and there is greater incidence (20%) of weak winds. It is also agreed that the mean wind speed above and inside the canopy height is closely related to certain urban dimensions. For roof-top speeds above 4.0m/s, mean velocity decreases by about 33%, while for speeds below 1.5m/s this coupling between the external main and internal secondary flow is considerably reduces or is lost.

Ahmad *et al.* (2005) relates wind effects to the dispersion of concentrated air pollution. Since the larger part of the flow encounters clustered urban geometry it is not homogeneously distributed, and pollution is trapped in low pressure sheltered areas by localized wind vortices and other channelling effects. By contrast, the connection of open leisure spaces, squares, and parks – and even large or wide urban canyons or areas of low rise buildings comprising 20% of the built density area – creates air paths and/or large breeze ways which lie in the same direction as the prevailing wind and have a direct local impact resulting in a 15 to 20% improvement in the urban airflow circulation (E Ng, 2008). On the other hand, wind acceleration at pedestrian level may happen in clustered areas of city centres due to funnelling, downwind or detachment flow caused by the sharp edges of buildings. The consequence is an increase in turbulence and wind acceleration that, if reaching a factor greater than three times the mean wind speed, causes discomfort and even danger for unaware or disabled pedestrians (Ghiaus, 2005b).

Melaragno (1986) describes several common wind effects in dense urban areas which result in higher mean wind velocities at pedestrian level than those found on the outskirts and in neighbouring countryside:

- Venturi: caused by two blocks higher than 15m arranged as a funnel;
- Pilotis: found in edifices built on columns with a lower gap of more than 14m;
- Cell effect: related to open spaces such as plazas and roundabouts amid urban centre occupations; and
- Setback effect: stepped skyscraper top creating flow deceleration.

2.6.1. Airflow in urban canyons

The so-called ‘urban canyon’ areas are created by the corridors lying between buildings and are formed by the cavities between the road surface and its flanking buildings, up to roof-top level. This term, initially used for describing narrow continuous streets, came to be applied to wider roads as well, although the term ‘avenue canyons’ can also be found in the literature (Vardoulakis *et al.*, 2003).

It is considered that the air volume within an urban canyon plays an active role in the definition of the surrounding urban micro-climate and its interaction with the meso-scale climate (Nakamura and Oke, 1988). Its top also determines the canopy height in the urban surroundings. The effects of airflows within urban canyons are usually explored by investigations focusing on the dispersal of air pollution concentration and urban noise, in addition to natural ventilation systems and building energy efficiency.

Figure 2-9: Schematic cross-section of an urban canyon

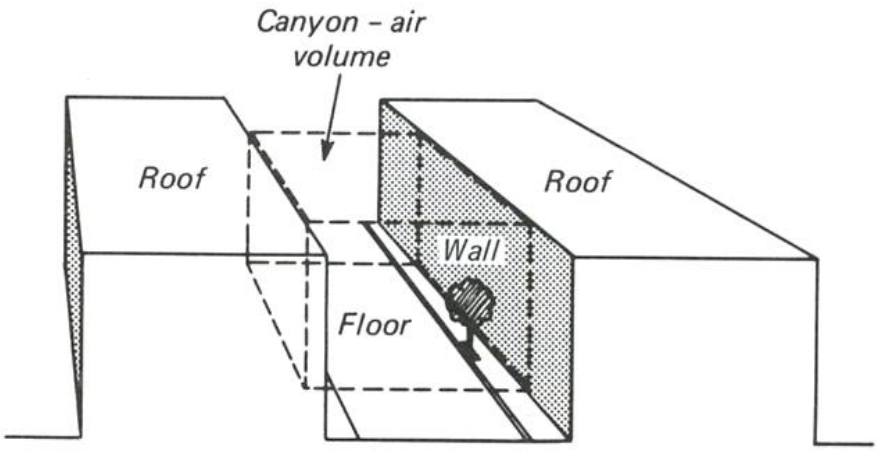

Source: Oke (1978, pp250).

Givoni (1976) states that studies with simple canyon shapes based on urban form give an indication of reality such as avoids the interference of other factors in the outcomes, serving as a parameter for other similar, but more complex, urban arrangements. On the other hand, the author emphasizes that these results are not directly applicable to all real cases, and their utilization thus being limited. Subsequently, Nakamura and Oke (1988) emphasized that interactions between urban canyons and wind effects were still poorly understood and questioned whether urban climate research had provided sufficient quantitative guidelines such as architects and urban planners could apply when deciding on urban and building geometries. Oke (1988) warns about the impossibility of finding universal solutions, since different climates have specific needs and urban geometry can create conflicts of needs. For instance, solar access and pollution dispersal are improved by open geometry, while densely clustered city centres create shade and shelter and lead to more effective use of urban infrastructure, therefore promoting, on one hand, energy efficiency and, on the other, the concentration of pollution. Successful investigations should include airflow aspects such as skimming flow and channelling effect that can hardly be observed through analytical solutions (Johnson and Hunter, 1998, 1999).

2.6.2. Definition of urban aspect ratios

Hunter *et al.* (1991) describe the important role that the urban canyon geometry plays in the near-surface airflow in urban centres. Several geometric paramenters are employed, which are based on linear dimensions, areas and volumes. For instance, flow field simulations in urban canyon geometry usually comprise either two or more parallel bricks or an array of rectangular volumes that physically limits the empty space confined in the canyon. The proportionality between the building and/or block height (H) and building and/or block length (L) and the road width (W) identifies the built

aspect ratio and the type of volumetric canyon within it. It is expected that the resultant airflow speed and direction below the canopy height should be connected to variations in these aspect ratios. For instance, the flow field practically does not interact with distant buildings, although the leeward wakes may not develop completely. This is called ‘isolated roughness regime flow’. Otherwise, for an array of clustered buildings, the leeward wake interacts with the downstream windward bolster and cavity eddies causing secondary flows in the canyon space (Nakamura and Oke, 1988). These urban ratios are given by the relation between the:

- Building aspect ratios between the building and/or block height ‘H’, the road width ‘W’ and building and/or block length ‘L’, such as: H/W and L/H, which are dimensionless terms;
- Plan-area density of the urban site ‘a’ (see Equation 2-2); and
- Built-area density of the urban site ‘b’, defined as follows:

Equation 2-13: $b = A_{built} / A_{urb}$

Where:

- b: is the built-area density, a dimensionless term;
- A_{built}: the total built area above ground level, consisting of the sum of the floor areas for all storeys of one of more buildings in an urban site (m^2); and
- A_{urb}: the total urban site area (m^2).

It is important to highlinght that, while the urban aspect ratio ‘a’ identifies a two dimensional character of the site, since it is related to a proportion between occupied and unoccupied ground area, the urban aspect ratio ‘b’ provides a three dimensional character of the site, since it varies with the number of storeys of a building. For instance, considering a ten storey building which has the same ‘a’ coefficient of a five storey building, it will present a ‘b’ coefficient twice greater than the other. In view of the fact that the first building is possibly twice taller than the second one, its impact on the airflow patterns and velocity and pressure distribution on their envelopes is expected to be different too. For this reason, these two urban aspect ratios are employed in the investigation of the relationship between the urban fabric and the airflow patterns and wind velocity in urban areas.

A canyon can be considered uniform or regular when its cross-sectional H/W ratio approximates to 1.0, deep or narrow when this ratio increases to 2.0 and wide or shallow when it drops to 0.5. Also, the canyon length L/H ratio is considered short,

medium or long for respective ratios of 3.0, 4.5 and 6.0 (Nakamura and Oke, 1988; Vardoulakis *et al.,* 2003). Regarding height, a canyon is considered symmetrical when height is relatively constant and asymmetrical when there is considerable variation in height. Also, windward high-rise buildings are denominated step-up canyons, and the opposite are called step-down. In architectural practice, the terms plan-area and built-area density are related to the building and the plot/ property area. In contrast, here the plot area in fact refers to the urban area surrounding the building(s), comprising the plot area itself but also including the neighbouring plot areas and the surrounding public areas, such as streets, roads, parks and other open spaces. In order to assess the influence of the surrounding built environment in the airflow potential of a given spot, a larger scale is required to verify the urban scale airflow regime. Another indication employed to quantify the blockage condition for the immediate urban surroundings of the target area is the sky-view factor (SVF). This factor is calculated by plotting a 180^{o} view of the sky's dome from a point, a line or an area on a flat 2-D diagram. The sky's dome is sub-divided into parts of either equal area or equal angle on the basis of which a ratio between the seen and the obstructed, ranging from zero for completely covered areas to 1.0 for totally unobstructed ones, is established (Oke, 1978).

Figure 2-10: Stereographic diagram and an SVF projection with a factor of 35.5%.

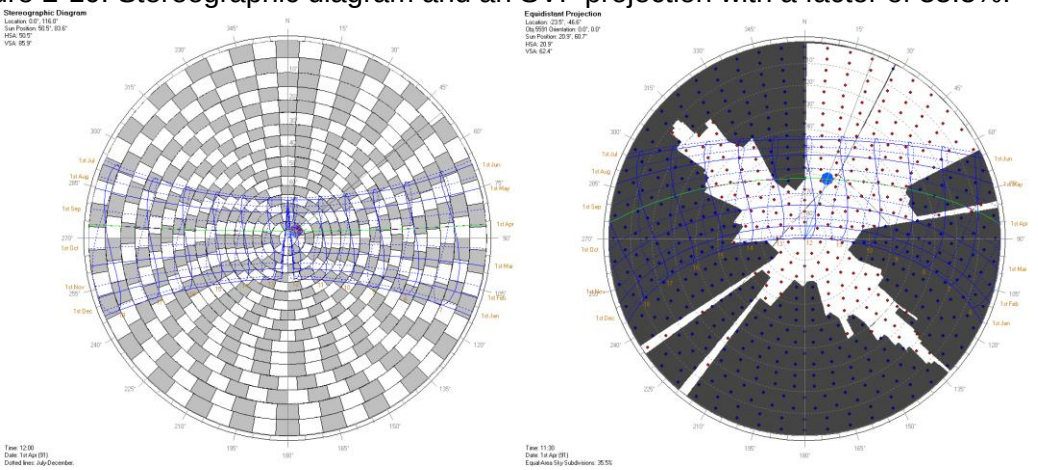

Source: this study.

Although the SVF is largely used to determine the sun-path diagram for daylight and day-factor analysis, Bradley *et al.* (2001) propose a method that applies it to quantify how far the urban geometry's obstructions may influence the surrounding microclimate. The advantage on this method is that a tri-dimensional analysis may provide a better interpretation of an asymmetrical canyon than a two-dimensional H/W schematic section. This method is intended to assess sky luminance efficacy and conditions (Li *et al.,* 2008), though it may be able capable of providing information on airflow potential in urban areas as well.

2.6.3. Modifications of airflow speed and direction as a result of the urban canyon's geometry

Results for parallel, orthogonal and skewed imposed constant flow in simple canyons of infinite length and field measurement investigations found in the literature are described below.

2.6.3.1 Flows parallel to the canyon's axis

Parallel flows create a mean wind component along the canyon's axis with reduced wind speed and possible uplift near the vertical and ground surfaces due to friction (Nakamura and Oke, 1988). In this case the vertical components of velocity tend to be very low and in the stream wise direction, if only wind-drive forces are applied. Further, the flow inside the canyon imitates free flow behaviour, but with reduced intensity. For undisturbed winds above the threshold velocity of 2m/s and parallel to the canyon axis, a secondary circulation flow with a mean wind speed is observed inside it, with low vertical components. The proportional along-canyon wind velocity inside it is linear and related to the angle of incidence of the above-roof airflow. But this coupling is lost for lower speeds, when this proportionality becomes random and scatters (Wedding *et al.*, 1977; Arnfield and Mills, 1994). The same relation was mentioned by Nakamura and Oke (1988) for undisturbed winds from 4 to 5m/s. In addition, for symmetrical canyons, where the mean height of the buildings is the same as the width of the road, or H/W= 1.0, internal velocities are 0.66 to 0.75m/s, when measured internally and externally at heights proportional to 0.06 and 1.20 times the height of the buildings (Santamouris *et al.*, 1999). The same author did not find either this proportionality for deeper canyons (H/W = 2.5) or a clear threshold velocity indicating the existence of coupling, despite statistical analysis's pointing to this correlation. Finally, he concludes that the vertical wind speed at the top of the canyon seems to increase in proportion to the along-canyon free-stream velocity.

2.6.3.2. Flows perpendicular to the canyon's axis

Undoubtedly the most exploited example of airflow regime within canyon geometry, the effects of normal wind direction have been used as a reference for verifying 2-D and 3-D numerical models for airflow field, turbulence and air pollution concentration dispersion. The descriptions below are based on the studies of Georgakis and Santamouris (2004) and Cook (1985). Both studies present airflow speed and direction orthogonal to square canyons (H/W= 1.0). The first author compared wind tunnel data with those of field measurements, obtaining closely similar results.

An important aspect observed in this type of flow is the production of vortices rotating in the mainstream direction below the canopy height and between the two blocks. The vortex occurs as a result of pressure differences between the leeward side of the upstream building (low pressure) and the windward side of the downstream building (high pressure). The pressure difference rises when the free airflow creates an increase in the pressure on the windward surface of the front block and forces a down flow below the frontal stagnation point. The flow separates at the edge of the leeward surface, creating a large wake of low pressure behind the front block. When the detached flow meets the windward surface of the rear block, it tends to be diverted downward, which increases the pressure on the latter block's surface. When, on reaching ground level, the flow turns towards the low pressure area on the leeward side of the frontal block, it gives rise to a flow across the canyon and in a direction reverse to that of the mainstream. From this point the flow is diverted upwards due to its mass conservation and rises, though with a weaker vertical component. When reaching the top edge, where a strong flow detachment takes place, this flow is deflected into the horizontal wind stream direction again. The vortex created in the canyon space therefore presents wind components near the surfaces but little air movement at its centre. DePaul and Shieh (1986) observe that the vortex centre is situated at 0.75H for symmetrical deep canyons, whereas for deeper canyons (H/W>2) several vortices of decreasing intensity are created. Chang *et al* (1971) relate that strong winds orthogonal to a deep canyon create two vortices inside it; an upper one driven by ambient airflow, and a lower one driven in the opposite direction to that of the circulation above it. Also, according to the H/W and L/H ratios and the wind velocity, several phases of airflow speed and direction may be noted, including skimming flow for narrow canyons and, as the H/W ratio increases, transition to wake interference and isolated roughness, as several authors have stated (Oke 1988; Hunter *et al.,* 1991; Sini *et al.,* 1996). Strong winds and/ or narrow canyons cause skimmed flow, which means, that the flow detachment above the canopy height prevents airflow entering downwards into the canyon. Wake interference occurs when the upwind block's leeward wake interferes with the downwind recirculation flow. Finally, isolated roughness is observed when blocks are well separated from each other. Oke (1988) provides also a graph on which lines distinguish the flow regimes orthogonal to the canyon as skimming, wake interference or isolated roughness flow based on the relationship between H/W and L/H. Hunter *et al.* (1991), with a view to contrasting these results with numerical models, provide an extensive analysis of anticipated flow regimes in accordance with the L/H and H/W urban aspect ratios. The results for transition from skimming to wake interferences obtained from Hunter *et al.* agree well with Oke (at H/W~0.7). Also, the

change from wake interference to isolated roughness flow happened at H/W~0.2 for the CFD simulation and at H/W~0.3 for Oke experiment.

Figure 2-11: Airflow speed and direction for canyons with diverse H/W aspect ratios:

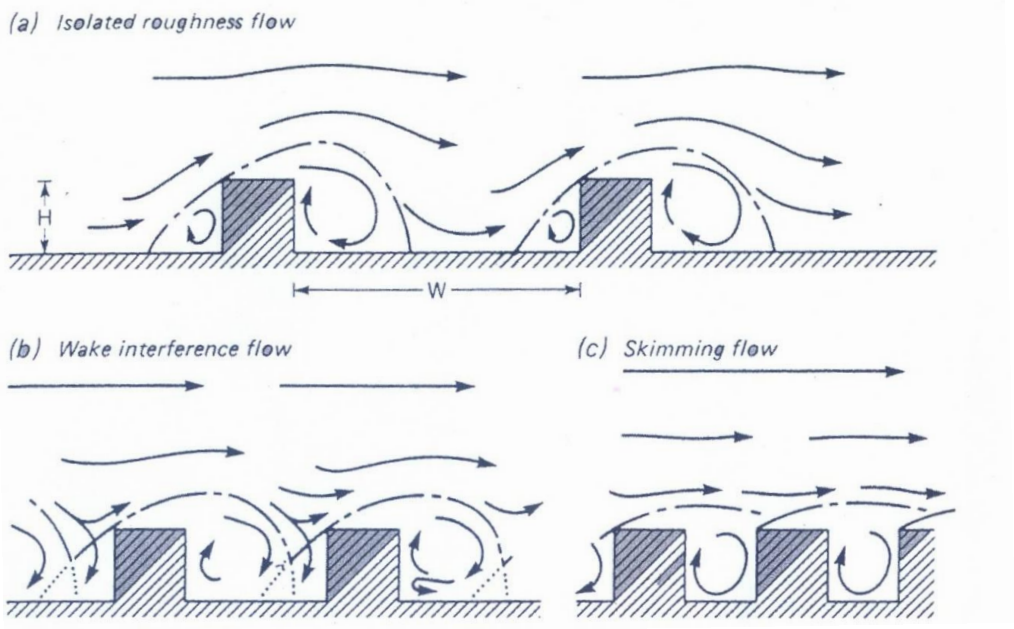

Source: Oke (1988, pp105)

Figure 2-12: Limits of the airflow regimes for diverse H/W aspect ratios:

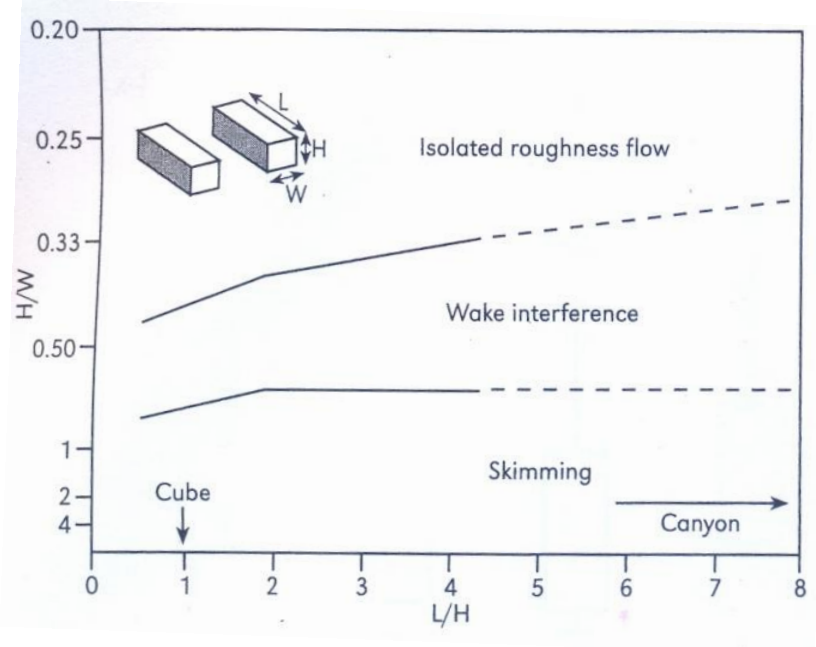

Source: Oke (1988, pp105)

Table 2-6: Airflow speed and direction for diverse H/W aspect ratios:

L/*H* ratios	Width of canyon (m)	*H*/*W* ratios	Type of flow regime anticipated (after Oke [7])
Cubic canyon			
1 (20 m/20 m)	20	1.0	skimming flow
	27	0.74	transition to wake interference
	40	0.5	wake interference
	50	0.4	transition to isolated roughness
	60	0.33	isolated roughness
	80	0.25	isolated roughness
Short canyon			
3 (60 m/20 m)	20	1.0	skimming flow
	40	0.5	wake interference
	60	0.33	transition to isolated roughness
	80	0.25	isolated roughness
Medium-length canyon			
5 (100 m/20 m)	20	1.0	skimming flow
	34	0.6	transition to isolated roughness
	40	0.5	wake interference
	60	0.33	wake interference
	100	0.2	isolated roughness
	140	0.14	isolated roughness
Long canyon			
7 (140 m/20 m)	20	1.0	skimming
	40	0.5	wake interference
	74	0.27	transition to isolated roughness
	100	0.2	isolated roughness
	140	0.14	isolated roughness

Source: Hunter *et al.* (1990, pp318)

Sini *et al.,* (1996) also assessed the effects of winds orthogonal to urban canyons, varying the urban width to building height aspect ratio (W/H, conversely to the more commonly used H/W), to describe both the flow regime and the occurrence of internal vortices:

- For deep canyons (W/H < 0.6) skimming flow and counter clock-wise vortices are observed;
- Skimming flow is seen also for W/H ratios up to 1.5, while only one vortex is described happening inside the canyon under these circumstances;
- For W/H > 5 two clock-wise vortices extending up the whole height of the buildings are found, one on each side of the road; and
- Skimming flow at the top of the buildings is replaced by wake interference flows, isolated roughness flow and fully independent wake flow after W/H> 1.5, > 9 and > 50, respectively.

Oke (1988) also depicts how the aspect ratio may affect urban microclimates:

- H/W <0.4: buildings are too widely spaced, and may be too open to solar radiation and airflow regimes, with varying impact on the environment according to local climate;
- H/W >0.6: canyon becomes too deep, and consequent access to natural light and air pollution dispersion may be critically deficient; and
- 0.4 < H/W < 0.6: seems to be the optimum ratio for urban centres, providing light access, some measure of shelter and renewed air.

Fewer studies have explored airflow in asymmetrical canyons. Hoydysh and Dabberdt (1988) simulated in a wind tunnel the airflow in these canyons. The experiment was based on an array of urban blocks of which the H/W aspect ratio for the first half of the blocks (upwind) was maintained at 1.2 and the ratio for the second half (downwind) varied between 0.5, 1.2 and 2.0. The upwind blocks' L W H dimensions were 60, 20 and 8cm, respectively. A relation is observed between the height of the windward façade of the downstream side of the canyon and the downdraft vertical wind velocity. Flow visualization by tracking bubbles is undertaken. The symmetrical case presented an internal counter-flow vortex escaping from the top after two complete internal rotations. The mean speeds for the descending and ascending flow are 50% and 25% weaker than the reference speed. For the step-up asymmetrical geometry the internal counter-flow showed a vortex escaping from the bottom after from two to up to five complete internal rotations, and both the speeds for the descending and ascending flow were 50% of the reference speed, due to the increase of the downwind effect on high-rise structures. Also, the step-down asymmetrical canyon presented an airflow reduction of 90% in both sides of the canyon. In contrast

to these findings, Arnfield and Mills (1994) state that, for irregular canyons with H/W~ 1.5, vortex circulation speeds are unrelated to the mean wind velocity above the roof level. In addition, step-up asymmetrical canyons show reversed vortices even with external mean wind speeds below 2m/s. The highest wind velocities inside the canyon are observed at both the top and bottom, but there is a general decrease in wind velocity in the horizontal component as compared to the airflow above the roof height. Also, 75% of the areas within the canyon present very low air movement.

2.6.3.3. Flows oblique to the canyon's axis

The effects of flows at an angle to urban canyons are less explored, and...

> …"existing research on this topic is considerably less than the scientific information for perpendicular and along the canyon flows…" (Georgakis and Santamouris, 2004).

Skewed flows usually create a vortex alongside the main axis. The mean flow along the canyon axis presents vertical downwards components causing spiral vortices along the length of the canyon in the upward stream direction but with reduced velocity (Nakamura and Oke, 1988). Also, the transversal component of the flow towards and inside a canyon shape determines the vortex intensity, while the parallel part establishes its length (Yamartino and Wiegang, 1986). For external wind speeds above 1.5m/s, the speed of the vortex increases with the speed of the cross-canyon wind (DePaul, 1986). In symmetrical canyons (H/W=1), the transverse vortex speed inside the canyon is proportional to the above-roof transverse component and independent of the above-roof longitudinal component (Yamartino and Wiegand, 1986).

2.6.3.4. Flows at street intersections

According to Hoydysh and Griffiths (1987, *in* Ahmad *et. Al.*, 2005), street intersection geometry is responsible for channelling, diffusion, deflection, displacement, acceleration, stagnation and recirculation of wind in the urban environment. These wind effects are described affecting the diffusion of air pollution concentration by introducing horizontal wind components at the road cross-sections and thus changing the vertical vortex into a helical eddy that permits diffusion at street intersections. Conversely, away from the block corners, only vertical components of wind cause dispersion.

Figure 2-13: Airflow speed and direction in intersections of urban canyons:

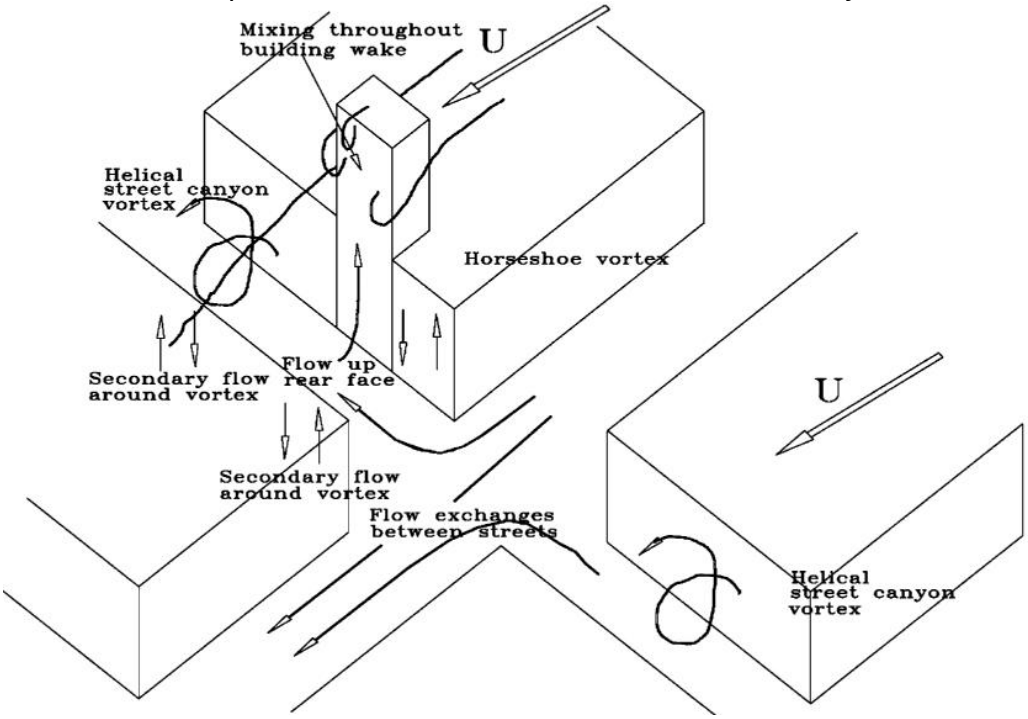

Source: Ahmad *et al*. (2005, pp707).

2.6.4. The influence of the roof shape

Kastner-Klein and Plate (1999) relate the air pollution concentration dispersion to the roof shape, and oblique roofs are linked to a better diffusion of pollutants than is flat roof geometry. Cook (1985) describes how the inclination of the roof changes this flow behaviour as follows: positive pitch angles up to 30^{o} still present flow detachment, a bubble of negative pressure and posterior reattachment; negative pitch angles also create flow detachment, though the reattachment may not occur; and pitched roofs of up to 45^{o} of inclination may not experience detachment, and the flow continues parallel to its surface until detachment occurs at the downwind edge. Further, for winds at a certain angle (skewed) the separation flow along the lower length of the windward top edge is related to the addition of a velocity component to the subsequent separation flows, which will continue to occur until the end point of this edge is reached. This increase in circulation results in a strong conical vortex known as ‘delta-wing’, characterized by extreme negative pressure distribution in the low corner and that may result in uplift forces, which is the same principle as that of the aircraft wing.

2.6.5. Calculating the airflow decrease in urban canyons

Chandra *et al.* (1986) dobserve that for an arrangement of several buildings the effect of the leeward wake can be significant, reducing the potential for natural ventilation considerably. Further, the author presents a method for calculating the decrease of this potential based on a terrain correction factor. Yamartino and Wiegand (1986) provide also a review of existing models, to which components for turbulence were added to the equations for the purpose of calculating pollution dispersion in urban areas. A similar linear model is provided by Nakamura and Oke (1989) in which the airflow reduction inside the canyon (at 0.06H) is related to the mean wind speed above the roof (1.2H) and up to 5m/s, and a factor varying from 0.37 to 0.68 based on the physical dimensions of the surrounding buildings. This model is a 2-D approach that simplifies the complex 3-D airflow characteristic:

Equation 2-14: $$\overline{u}_{canyon} = factor * \overline{u}_{roof}$$

Paciuk (1975, *in* Kolokotroni and Santamouris, 2007) provide another model to calculate the airflow decay in urban environments, based on wind tunnel experiments:

Equation 2-15: $$\overline{U}r_{roof} = 10 + \left(0.6\left(1 - e^{-0.08\left(H \overline{U}_{roof}\right)}\right)\right) - 0.18\left(\left(L + W - 0.5W\right) \overline{\ } W\right)$$

Where:

- $U_{r\ (roof\ )}$: is the percentage of mean air speed inside the urban area compared to the mean air speed above the roof level;
- U_{roof} : the mean air speed above the roof level (m/s);
- *n*: the serial number of the sequence of blocks or buildings;
- *e*: a dimensionless factor; and
- W, H and L: are the length and width of the roads and the height of the canyon/ urban areas (m).

This model seems to deal with two-dimensions only, and its application seems to be linked to the dimensionless factor, which is not provided.

2.6.6. Airflow and temperature inside the canyon

An urban heat island may be described as a phenomenon linked to the size of the cities and urbanized areas. Oke (1973) relates the difference of temperature between urban and rural zones to the cloud-cover sky, the inverse of the regional speed and to a logarithm proportional to the fourth root of the population. Based on field measurements, Rotarch (1994) also stated that the air inside urban canyons is considerably warmer than the mixed air above the roof height. In contrast to this, field research conducted by Nakamura and Oke (1988) revealed that, although air temperatures found near irradiated 'unprotected' surfaces, such as roads in wide canyons, buildings façades and roof covers, were far higher than the mean temperature of the turbulent air in the middle of the canyon, which in its turn was warmer than the air near shaded surfaces, mean air temperature variations below the canopy height were smaller than 1.0K and airflow due to buoyancy effects were imperceptible. Georgakis and Santamouris's (2004) field measurement results agree with this statement. No vertical components of flow patterns due to temperature stratification, i.e. the buoyancy effect, were observed within the canyon environment, since urban canyons present direct solar radiated and shaded areas which vary continuously throughout the day.

2.6.7. Studies on airflow in urban canyons in the literature

Most of the studies mentioned in table 2-7 focuses either on the assessment of heat island effects or airflow regimes in urban areas with a view to assessing air pollution concentration dispersion in the urban environment. The field measurement data and modelling results consists mainly of mean air and surface temperatures, mean wind speed and direction, urban noise and air pollution concentration levels. It may be observed that there have been few investigations associating the resultant air flow below the canopy height with the built urban aspect ratio aiming to map pressure differences on building surfaces. More research and, eventually, guidelines covering this gap, would help architects and designers to maximize the natural resources provided by the external micro-climate and increase the application of natural ventilation systems in the built environment with greater confidence.

Table 2-7: Urban aspect ratios found in the literature:

	source of experimental setup	year	canyon dimensions m			aspect ratio		methods and experiments carried on							
			W	H	L	H / W	L / H	method of research[4]	V m/s	Wind direction	ΔPa	ΔT ^{o}C	Co	κ/ε	dB
1	Nunez and Oke	1977				0.96		FM		0^{o}, 45^{o}, 90^{o}					
2	DePaul and Sheih	1985	24.5	34.5	80.0	1.41	2.32	FM	v	0^{o}, 45^{o}, 90^{o}				v	
3	Yamartion and Wiegang	1986				0.92		FM	v	0^{o}, 45^{o}, 90^{o}			v	v	
4	Nakamura and Oke	1988	16.0	17.0	75.0	1.06	4.41	FM	v	0^{o}, 45^{o}, 90^{o}		v			
5	Oke	1988	0.3 to 5	1.0	6 to 8	0.2 to 4	6 to 8	FM WT AM	v	0^{o}, 90^{o}				v	
6	Hunter *et al.*	1991	59.3	20.0	79.0	0.5	4.0	CFD	v	0^{o}, 90^{o}				v	
7	Arnfield and Mills	1994				1.52		FM		0^{o}, 45^{o}, 90^{o}					
8	Rotarch	1995	15.0	18.3		1.22		FM	v	0^{o}, 45^{o}, 90^{o}		v		v	
9	Johnson and Hunter	1998	30.0	30.0	300.0	1.00	10.00	WT CFD	v	0^{o}, 90^{o}			v		
10	Santamouris *et al.*	1999				2.50		FM		0^{o}, 45^{o}, 90^{o}					
11	Johnson and Hunter	1999	7.5	3.0	68.0	0.40	22.7	FM	v	0^{o}, 45^{o}, 90^{o}				v	
12	Meroney *et al.*	1999	60.0	60.0	60.0	1.00	1.00	WT CFD	v	0^{o}, 45^{o}, 90^{o}					
13	Louka *et al.*	2000				0.70		FM		0^{o}, 45^{o}, 90^{o}					
14	Moussiopoulos	2000				0.96		FM	v	0^{o}, 45^{o}, 90^{o}					
15	Moussiopoulos	2000				1.40		FM	v	0^{o}, 45^{o}, 90^{o}					
16	Kastner-Klein et al	2001	0.50	0.12	0.60	0.24	5.00	FM WT	v	0^{o}, 45^{o}, 90^{o}			v	v	
17	Papadopoulos	2001	8.0	24.0	112.0	3.00	4.67	CFD	v	0^{o}, 45^{o}, 90^{o}		v			
18	Cheng	2003				0.5 to 6		CFD	v	90^{o}					
19	Cheng and Meroney	2003				.2 to 1		CFD	v	0^{o}, 45^{o}, 90^{o}					
18	Georgakis Santamouris	2004	10.0	23.0	50.0	2.30	2.17	FM	v	0^{o}, 45^{o}, 90^{o}					
19	Park *et al.*	2004	10.0	4.2	-	0.42		WT CFD	v	0^{o}, 45^{o}, 90^{o}					
20	Assimakopoulos *et al.*	2006	8.0	23.0	55.0	2.88	2.39	FM CFD		0^{o}, 45^{o}, 90^{o}					
21	Ghiaus	2006	12.6	24.2		2.3		FM	v	0^{o}, 45^{o}, 90^{o}		v	v		v
22	Xiaomin Xie *et al.*	2006	1.0	1.0	-	1.00		WT CFD	v	90^{o}					
23	Eliasson *et al.*	2006	7.1	14.9	50.0	2.10	3.36	FM CFD	v	0^{o}, 45^{o}, 90^{o}		v		v	

Source: this study.

[4] FM= Field Measurements; WT= Wind Tunnel; CFD= Computational Fluid Dynamics; AM= Analytical Model.

2.7. Chapter conclusion

The theory and concepts on the subject of airflow field in the urban environment presented in this chapter will serve as a basis for selecting the real urban scenarios investigated as case studies; for structuring te research project; and finally as a landmark for comparing the results of and the analyses undertaken for this thesis.

Chapter 3: Modelling Airflow in the Urban Environment

3.1. Chapter introduction

This chapter discusses the main concepts of the techniques commonly employed in modelling airflow in the investigation of the urban environment. It discusses initially models of simulation. Then, aspects of physical modelling in wind tunnel are presented. Finally, emphasis is given to computational fluid dynamics (CFD) modelling. The chapter highlights the steps taken and parameters involved in the simulation process, as well as how confidence in the results may be achieved by presenting the verification and validation criteria based on examples given in the literature.

3.2. Airflow modelling

Airflow modelling is necessary to investigate urban wind phenomena in order to evaluate environmental issues in urban areas. Plate (1999) considers it a fundamental tool for assessing the surrounding built environment and the impact that future construction and urban development may have on the urban microclimate. Knowing the wind potential of an urban site is essential for the successful design of naturally ventilated buildings. As in understanding, for example, how the specific air change levels whether for indoor air quality or passive cooling may be achieved.

Despite ventilation rates and efficiency of outside/ inside and inter-zone flows being the focus of internal environment airflow analysis, it is necessary to have a whole understanding of the regional natural winds and local urban airflow patterns in order to carry this analysis through. For this reason, airflow modelling has become a necessary tool for identifying wind patterns and turbulence, wind loads and pressure coefficients on building envelopes, airflow acceleration at the pedestrian level and its potentially hazardous effects, and pollution concentration dispersion in the urban environment.

3.3. Methods to calculate airflow in the urban environment

Investigations of airflow in the urban environment involve interdisciplinary knowledge in meteorology, fluid dynamics, building science and urban planning. Cook (1985) describes four types of models for work with airflow prediction and assessment. While the importance of each of the models in terms of accuracy and complexity is displayed in decreasing order, the creational process is described in crescent order:

- Analytical models: the solution is related to the design problem imposed and solved analytically based on a set of equations;

- Numerical: mathematical equations not soluble analytically but whose results are contrasted with pre-simulated computer-based numerical models and databases;
- Semi-empirical: model described through coefficients and constants of unknown values based on mathematical equations and previous experiments and then compared with new problems imposed;
- Empirical models: based on observation of experiments but without the support of theoretical models. They are by definition restricted to the cases or conditions to which they were originally applied.

Li *et al.* (2006) categorize these model techniques for assessing airflow as either 'diagnostic' or 'prognostic'. In the former group, empiricism and interpolation based on physical measurements prevail; whereas in the latter group the problems are solved by complex mathematical equations.

Kolokotroni and Santamouris (2007) also classify the analytical and numerical models as deterministic techniques which a set of algorithms can change from simplified models, with limited application, to network and computerized models, based on a complex set of equations. In contrast, the semi-empirical and empirical models are said to be data-driven due to their link with the statistical quantitative or qualitative analysis of previous results.

Plate (1999) categorizes these types of models according to the task to be carried out and the accuracy expected in the results:

- Screening models: are either large scale approaches or simplified semi-empirical or empirical models that are useful to evaluate preliminary stages of planning or design. These results, if not accurate enough, will indicate which level of detail should be implemented in the second phase of modelling in order to achieve reliable outcomes;
- Detailed models: can be physical, numerical or analytical. Physical ones reproduce the urban environment and the properties of the flow field on a reduced scale, as in a wind tunnel, where the reproduction of wind effects and turbulences is achieved successfully providing that standard procedures are followed; and
- Numerical and analytical models: simulate the fluid dynamics properties through mathematical equations based on given parameters. Germano *et al.* (2005) present a qualitative method based on a numerical model to assess the natural ventilation potential for new buildings in urban areas based on a comparative analysis between known places and buildings on one hand, and features desired for the new project, on the other. This method is part of the European URBVENT

project (Ghiaus *et al.*, 2004). Computational Fluid Dynamics (CFD) codes are an example of analytical application for solving flow problems. The accuracy of these simulations is related to several criteria adopted for the input information (domain size, grid coarseness, boundary conditions, urban wind profile), and the choice of the governing turbulent energy equation.

During the 1940s, tracer gas decrease experiments for internal space leakage were conducted to identify building ventilation airflow rates, pressure coefficients and differentials, and mean velocities. They also helped to understand heat losses due to cracks and discharge coefficient models (Axley, 2006). Those experiments constituted the basis for building airflow analytical models, in which the laws of flow components are disposed in series or in parallel. These models of airflow analysis are described as macroscopic methods, where...

> ... analytical methods based on modelling buildings as collections of finite-sized control volumes within which mass, momentum or energy transport behaviour is described in terms of algebraic and/ or ordinary differential conservation equations (Axley, 2006, p.42).

In these equations it is assumed that the air input is basically wind-driven and internal buoyancy-driven forces are minimal. Also, internal space flow resistance is negligible and pressure coefficient values from wind-tunnel tests will be extrapolated to real porous façades. The possible variations of the macroscopic methods are described below (Axley, 2006):

- Network method: whole-building flow analysis under isothermal conditions;
- Nodal method: similar to electrical systems, non-dimensional and isothermal, where one value is assigned for each volume, while pseudo-nodes are linked to boundaries and inlet/ outlet sources; and
- Multi-zone, zonal, sub-zonal, multi-cell or multi-room: consider buoyancy-driven, therefore dimensional, forces and divide the 'domain' into cells, small controlled interconnected volumes that exchange mass, momentum, energy and concentration information.

Methods of analysis that investigate the iteration of external bulk airflows with whole-building systems (inlet, outlet, ducts, infiltration, leakage, and inter-space connections) are identified as multi-zone. Basically, each zone or specific point of interest is represented as a cell that provides information and exchanges it with the surrounding ones. Conversely, those limited to airflow in within one zone are so-called sub-zone models. These models can also interact with thermal models that consider

solutions varying over time, named time-domain problems. With the advent of computational science, models developed as multi-zone methods of ventilation and temperature analysis on which each zone, or internal environment space, represents a node in the equation. In contrast to this, new CFD methods have been developed for prediction of detailed airflow patterns, air concentration and temperature distribution between internal and external spaces. These have been denominated microscopic methods, by which...

> ... analytical methods based on continuum descriptions of mass, momentum and energy transport within discrete physical domains of buildings defined in terms of partial differential conservation equations (Axley, 2006, p.42).

Dixon *et al.* (2006) emphasize that micro-scale CFD codes have made possible research of turbulent airflow and air pollution concentration dispersion in dense urban areas. Due to the three-dimensional character of urban airflows, CFD represents an advance as compared to semi-empirical and empirical models. For instance, Kastner-Klein *et al.* (2003) highlights that car traffic has an impact on the air pollution dispersion at the ground level, which escapes detection in airflow investigations with two-dimensional canyon shape' models.

Vardoulakis *et al.* (2003) present a table in which several airflow investigation methods, with focus on pollution concentration dispersion, are related to both the model and the scale of analysis, such as the parametric empirical or semi- empirical, used for statistical or simple box and 2-D street canyon calculations, and numerical Eulerian or Lagrangian models, for more complex 3-D investigations from the micro to the macroscale.

3.4. Airflow modelling in wind tunnel

Investigations which employ physical models in wind tunnel chambers have been endorsed by established methodology and are known to be capable of helping to understand the development of the boundary layer and providing insights and measurement data on the airflow field around scale replicas.

3.4.1. Wind tunnel and the boundary layer

The wind tunnel (WT) consists of a physical chamber of limited dimensions in the interior of which wind flows are simulated, and are used to test the interaction of airflow with physical models. This piece of equipment is composed of inlet fans, flow straighteners, such as screens, a turbulence generator, an airflow adjustment section, the test section itself and finally an outlet surface. A major input parameter for external

environment airflow simulation is the creationt of the expected airflow boundary layer in the test section of the chamber, which should correspond to the wind velocity profile attained in real scale areas (Plate, 1999).

Figure 3-1: Wind tunnel schematic section:

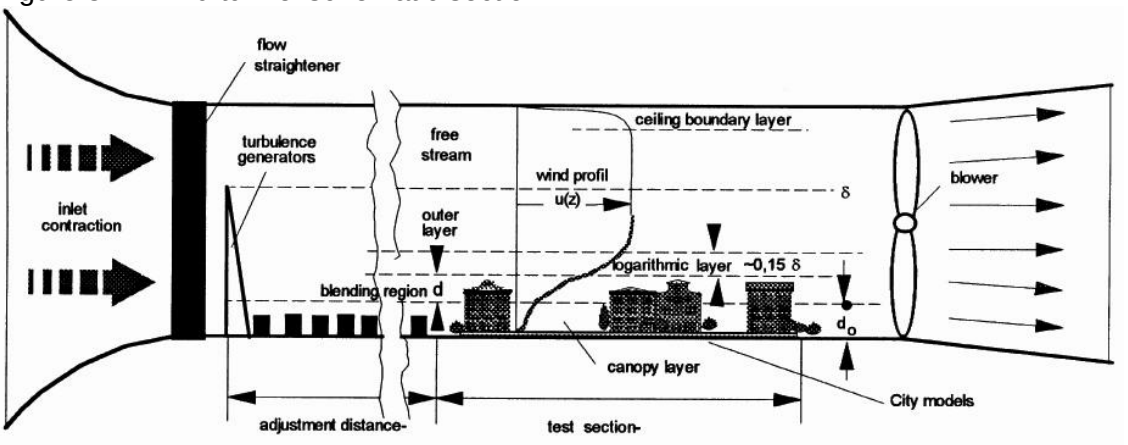

Source: Plate (1999, pp 3,984).

The wind boundary profile is attained throughout the length of the tunnel by setting the proper ground roughness parameters in the adjustment section. Blocks reproduce the urban canopy layer that will create, along this adjustment area, a blending layer in which dragging forces end-up producing shear stress and the vertical stratification of the wind velocity. The result is a wind profile that is equivalent to the real one for the length, width and height of the test section. This proportionality is achieved by the ratio of the wind velocity distribution for a given surface roughness between the natural conditions and the model settings. Large Reynolds numbers above 5,000 ensure that the flow field is stable through the chamber, suffering no effect of variations in velocity. The valid test height is not the total height of the chamber, since the wind profile varies above the reproduced urban boundary layer and ultimately is modified by the influence of the ceiling (Plate, 1999).

Ahmad *et al.* (2005) report that an advantage of this type of simulation lies in the fact that the complex and almost infinite number of variables existing in the natural environment, which can affect results in field measurements, can be isolated and comprehended on a case by case basis. It is necessary to be able to isolate the variables in order to identify which of them are principal, secondary or negligible in determining the airflow regime and related effects in the urban environment. The uncertainties related to the modelling and scaling process are, therefore, plausibly controlled. Such variables may include the mean wind speed and direction, the urban morphology and fabric which affect the topography, for instance, the building geometry and its relationship with street and open spaces (urban aspect ratios), architectonic features (roof shape, canopies, balconies, overhangs), urban equipment (trees,

bushes, walls, cars, urban signs), landscaping and topography. The heat balance is, further, reported to affect the urban airflow.

3.4.2. The scaling law

In order to obtain consistent results in wind tunnel investigations, the flow effects generated by the model have to be proportional to real scale ones. Jensen's scaling laws are usually employed to adapt real atmospheric characteristics for physical scale models in wind tunnels as regards velocity, length, mass and time variations (Armitt and Counihan, 1968; Cook, 1977/ 1978, 1985). Thus, the length and velocities are expressed as ratios, whereas mass variation is related to air density. Other non-dimensional parameters are related to:

- The height above ground (typical length variable);
- The wind speed coefficient (typical velocity variable);
- The roughness number (ground roughness/ structure size);
- The density number (inertia of structure / inertia of air);
- The Re nº. (inertia of the air / viscous forces); and
- The Strouhal nº. for reduced frequency, gravity and elasticity number.

For example, the Reynolds number (Re), which defines the turbulence of the flow, is scaled according to the relationship between the mean airflow velocity (U), the length factor (d) and the kinematic viscosity (ν), as follows (Van der Valk, 2000):

Equation 3-1: $Re = U*d/\nu$

Therefore, equivalence is achieved when the given non-dimensional parameter is the same for both the real and model scales, and is valid for the near flow-field, which comprises airflow below the canopy layer. This is the basis of the boundary profile scaling, which comprises terrain roughness and aerodynamic parameters to scale wind velocity according to height variation. In this way, it is expected that the airflow field inside the wind tunnel chamber should behave like the real size one (Holmes, 2001).

3.4.3. Results and applications

Wind tunnel investigations aim at identifying wind loads and pressure coefficients on surfaces for structural calculation or ventilation rates, air pollution concentration dissipation and wind acceleration at pedestrian level for both comfort and safety purposes (Kastner-Klein and Plate, 1999; Plate, 1999). In addition, several phenomenological features of the airflow field around buildings can be accessed

quantitatively or qualitatively through physical simulation. Flow recirculation, vortices, detachment and reattachment can be either measured by pulse-wire or laser-Doppler anemometers with particle Image visualization (PIV) or visualized by bubble-tracking photographic techniques (Summers *et al*, 1986; Davidson *et al*, 1996). Ground particle erosion allows the visualization and quantification of wind acceleration and gust speed at ground level (Beranek and Van Koten, 1979; Jones *et al.*, 2004). Local averaged pressures can be measured at individual points or as part of a multi-channel electronic system with several hundred positions from which the pressure fluctuations in the model are transmitted by tubing to a decoder (Holmes, 2001).

3.4.4. Model-scale limitations

Successful investigations with the WT rely on scaling the airflow field around the target model to the appropriate atmospheric boundary layer characteristics, including the mean wind speed, turbulence intensity, spectra and integral length parameters on the same linear scale as the real site (Cook, 1985). The model scale ranges from 1:10 up to 1:10,000 in specific cases. It is generally accepted that the use of model scales of up to 1:250 and 1:500 provides accurate results of wind flow velocity and pressure measurements for a building and a block size scale, respectively.

Summers *et al.* (1986) highlight that it is possible to find discrepancies between field measurements and wind tunnel simulations of up to 20%, which are acceptable when the purpose relates to environmental design rather than structural calculation. Most wind tunnels are unable to simulate heat transfer and buoyancy. These factors will not, therefore, be explored in this study, although it does give some examples of simulation in stratified wind tunnels (Uehara *et al.*, 2000).

3.5. Computational fluid dynamics (CFD)

CDF software's provide computer-based numeric solutions for the equations governing the flow fluids and offer detailed picture of the airflow and temperature distribution within the assessed space (CIBSE A, 2006). In this way, it is possible to solve problems involving turbulent flows for incompressible fluids simulated in steady-state and/ or dynamic time-averaged modes. In order to achieve this goal, the Navier-Stokes equations for energy, mass and momentum are applied for all flows, with the addition of further transport equations of turbulent velocity components (Awbi, 1991, 1998a). Recently, unstructured grid and several options for the boundary conditions have allowed the modelling of complex shaped walls and input/ output interfaces which enhance the range of flow problems that can be solved by CFD simulations (Vardoulakis *et al.*, 2003).

3.5.1. CFD simulation steps

It is possible to find descriptions and best practice guides in the literature as to steps to be taken in order to achieve good results with CFD simulation. The 'Best Practice Guideline for the CFD Simulation of Flows in the Urban Environment' Cost Action 732 (Franke *et al.*, 2007) provides a 10 step procedure to be followed in the modelling and calculation process to prevent errors and uncertainties in CFD simulations. These steps comprise the definition of: target variables; approximation equations; geometrical simplification and specification; computational domain; boundary conditions; initial conditions; computational grid; time step size; numerical round-up; and convergence criteria. Coleman and Stern (1997) have grouped these steps into two main categories, 'errors and uncertainties in modelling the physics' and 'numerical errors and uncertainties', covering many aspects related to verification and validation of CFD modelling. Usual steps involved in CFD simulation are (Vardoulakis *et al*, 2003):

- Pre-processing: is related to the three dimensional modelling process, by which the mesh type and size refinement, the fluid properties, the boundary design and other aspects of the input of the problem characteristics are decided;
- Solving: develops the main flow characteristics and adjusts the accuracy of the solution according to the discretization of the flow equations, until satisfactory convergence of results is achieved; and
- Post-processing: provides quantitative (residual plots, reports on mass flow rates and transfers, and forces and moments based on points, lines, surfaces and volumes) and qualitative (contour lines, vectors, path lines) information based on the results achieved which allows the assessment of the solution.

3.5.1.1. Physical parameters

The parameters of interest related to microscale meteorological airflow investigations that suit the urban microclimate assessment provided in the post-processing are:

- Air velocity (magnitude, X, Y, Z, relative, etc);
- Pressure (static, Cp, dynamic, absolute, total and relative);
- Turbulence (intensity, kinetic energy, dissipation rate, viscosity, etc);
- Temperature (static, total, enthalpy, surface, energy, etc); and
- Concentration (mass, diffusion, relative humidity, etc).

3.5.1.2. Governing equations

Computational fluid dynamics work on the basis of numerical codes to solve imposed fluid problems. These codes make use of the laws of physics, derived from basic conservation and transport principles that are interpreted through mathematical equations to solve flow and dispersion problems, providing ultimately information about the parameters of interest in airflow investigation (Vardoulakis *et al.*, 2003). The Navier-Stokes system is the basis for solving analytically incompressible Newtonian flows by approximation (Elman *et al.*, 2005). The governing equations are:

- The mass and conservation continuity equation;
- The three Reynolds-averaged Navier-Stokes (RANS) equations for conservation of mass, energy and momentum; and
- Further transport equations for pollutant concentration.

The general form of the mass and conservation continuity equation is:

Equation 3-2: $$\partial \overline{u}_i / \partial x_i = 0$$

The equations used in standard κ-ε RANS models are (Senthooran *et al.*, 2004):

For momentum:

Equation 3-3: $$\frac{\Delta \overline{u}_i}{\Delta t} = -\frac{1}{\rho}\left(\frac{\partial P}{\partial X_i}\right) + \left(\frac{\partial P}{\partial X_j}\right)\left[\nu + \nu_t\left(\frac{\partial U_i}{\partial X_i} + \frac{\partial U_j}{\partial U_j}\right)\right]$$

For turbulent kinetic energy:

Equation 3-4:
$$\frac{\Delta K}{\Delta_t} = \frac{\partial}{\partial_{X_j}}\left[\left(\nu + \frac{\nu_t}{\sigma_k}\right)\frac{\partial K}{\partial_{X_j}}\right] + P_k - \varepsilon$$

For energy dissipation (diffusion across the boundary):

Equation 3-5:
$$\frac{\Delta \varepsilon}{\Delta_t} = \frac{\partial}{\partial_{X_j}}\left[\left(\nu + \frac{\nu_t}{\sigma_\varepsilon}\right)\frac{\partial \varepsilon}{\partial_{X_j}}\right] + \frac{\varepsilon}{K}(C_1 P_k - C_2 \varepsilon)$$

The Navier-Stokes full equation is analytically unsolvable, although approximation is used to achieve outcomes (Cook, 1985). In generic form, it is represented as (Assimakopoulos *et al.*, 2006):

Equation 3-6:
$$\int(\rho\phi)/\partial t + \int(\rho U_j \phi)/\partial X_j = \int \phi \, grad\ \phi = S\phi$$

The three first terms are related, respectively, to: the change of quantity inside the volume (momentum); the advection across the volume (kinetic energy); and the diffusion across the boundary (energy dissipation).

3.5.2. Attaining confidence in CFD results

Ensuring optimum CFD results is related to the establishment of various criteria at different points during the process. Questions either deriving from the CFD code's limitations or due to misconceptions arising during the stages of the problem description, physical modelling, selection of computation parameters, monitoring the calculation or post-processing the results will result in the analysis of uncertain data and may end up by compromising the conclusions drawn from it. Therefore, a routine that tackles each one of these criteria has to be established, and measures that may influence the reliability of CFD simulations positively are presented below:

- CFD code: since computer calculations are susceptible to programming faults, it is necessary to obtain information about the potential and limitations of the code, how equations are handled, and discretization errors, although users may not have authority to adjust these features. Conversely, several default parameters, such as the control values used in the computation, initial relaxation factors and the calculation round-off approximation, as well as the choice of the turbulence models, have to be known and adjusted by the user;
- Usage error: it is necessary to make sure that the results obtained from the simulation are independent of the characteristics defined during the modelling process. The proper description of the problem involves several steps, such as:

definition of the domain size and its relationship with the blocked geometry, including the level of details to be included; input of the proper data and selection of the correct boundary condition features (e.g., walls, inlet, outlet and interfaces); and balance between grid coarseness and refinement as a whole notably in the target area. Since inexperience or novelty in the use of the CFD programme may result in some or any of these errors, starting simple and building complexity progressively will provide steadiness and confidence in the results and may also sometimes save time;

- Calculation process: the convergence of the solution has to be monitored by both the residual plot and other cell, face or volume variables monitored until low residual errors and steady results are achieved satisfying the criteria adopted for accurate results;
- Time-step scale: LES turbulence mode calculation accuracy involves also specifying the proper time-scale for the intermittent variables;
- Post-processing errors: are related to how the resultant raw data are extracted and interpreted. Errors are associated with both inaccuracy and imprecision in the way the tools handle the data and present them in such a way as to make the analysis and conclusions possible; and
- Verification and validation: are related to two distinct aspects. The CFD code has to be verified and validated in order to ensure that it works in accordance with and is suitable for certain applications, and this information is mainly provided by the software's suppliers. The CFD modelling process has also to be 'verified and validated' in order to confirm the confidence and accuracy of the results and guarantee the reliability to the conclusions, even when the aforementioned steps and decisions related to the CFD process have been followed. This procedure may include checking results with: predictable results calculated manually, standard benchmark cases, comparison against either physical model simulation or field measurement outcomes.

3.5.3. Considerations on CFD simulation process

Several criteria have to be chosen beforehand in order to decide how the algorithms will be applied to the flow problem. Some of them are shown in the following topics, based on information from the commercially available CFD software Fluent 6.2 User's Guide (2005) and CFD guideline Cost Action 732 (Franke *et al.,* 2007).

3.5.3.1. Domain discretization

Due to the unsolvable character of the Navier-Stokes equation, CFD solvers have to formulate a method to make it numerically approachable. This is achieved through the discretization of the solution: the solver makes use of a control-volume based equation to establish a finite-volume with discrete parameters for the continuous physical process, making the application of equations to solve the flow possible.

The finite-volume characteristic of CFD codes implies that an infinite reality has to be constrained in an internal volume of a domain. This domain is defined by physical boundaries and sub-divided into cells, which transmit the flow information calculated by equations through their nodes and faces. Conversely, the domain dimensions and the mesh type and size must not influence or change the characteristics of the resultant flow. Accurate results must be grid and domain independent. In addition, the boundary features have to reproduce the terrain roughness characteristics and maintain them throughout the domain until a modelled barrier is reached in order to enable the required airflow properties to be achieved.

In order to solve the governing integral equations for conservation of mass and momentum, energy and turbulence, the finite-volume method is employed. This means that a given domain area with prearranged boundaries is sub-divided into non-overlapping cells, which subsequently compose the computational grid. Regarding the ratio of fluid and solid volumes within a domain, a good practice consists of allowing a range from 3 to 5% of the total domain composed of blocked volumes, keeping the majority of it as fluid space.

3.5.3.2. Boundary conditions

Since it is through the boundaries of the domain that flow and heat exchanges with the outer-domain take place, the specification of the boundary type and attributions deserves careful consideration. In a basic form, the boundary options generally used can be exemplified as follows:

- Inlet boundaries can be either driven by pressure differential or fluid velocity input. For simulating airflow in the external environment extra attention has to be given to the determination of the velocity-inlet boundary, in order to attain the wind profile as earlier described in Chapter 2.
- Outlet boundaries can be either simple outflow or outlet with previously specified loss coefficient;
- Blocked boundaries (i.e., ground and walls) can present roughness properties varying from no-slip (achieving mirror symmetrical character) to very rough

(representing the canopy height of an urban area). Also, it can allow heat transfer and periodic features;

- Periodic boundaries allow intermittent inlet or outlet of data and occasional change of the boundary features; and
- Interface: allows flow through different domains.

3.5.3.3. Cell and grid topologies

CFD codes differ regarding how internal data is transmitted through cells, faces and grid points. Structured solvers depend on the Cartesian coordinates ‘x, y, z’, or i, j, k’, to situate and keep contact between adjacent cells, since information is related to a cell-node association. In this case, geometry is dependent on an orthogonal grid, as it is the geometry of solid volumes geometry; the domain is made up of hexahedral cells only. Construction of skewed and curved surfaces is only possible via the simplification of their forms, achieved with indented or stepped geometry resolution, which changes the features of the surface and, consequently, the resulting airflow speed and direction.

Unstructured solvers are based on face-node internal data structures to assign instructions to neighbouring cells. In addition to the hexagonal cell volume, it allows also more complex hybrid geometry with tetrahedral, pyramidal and wedge volumes, although some volumetric combinations have proved to perform better than others. For this reason, unstructured solvers allow orthogonal, skewed and curved volume shapes, thus achieving more realistic 3D modelling of the problem to be solved. In an unstructured grid a 3D cell containing several faces will be connected to more than one node. For tetrahedral cells, each triangular face is connected to three nodes, which are shared with the other two faces that constitute its volume. Hexagonal cell faces are linked to four nodes shared among them, while wedge and pyramid faces, which can be triangles or rectangles, share three or four nodes each, respectively.

3.5.3.4. Mesh structure

Mesh quality is related to both the convergence time and the accuracy of results. The mesh should be able to capture the important features of the blocked geometry. Sharp edges and constrained gaps in the domain with coarse cells should be avoided, since the resulting airflow will not be realistic. Initial mesh quality and space discretization are established by the number of node points, faces and cells (density and clustering) and the type of mesh in the fluid domain. Further improvement can be achieved by grid adaption in specific regions of the domain. The nature of the problem will influence its resolution, since turbulent flows, shear areas and mixing areas are more susceptible to the dependence on grid ‘smoothness’ (i.e., maximum aspect ratio between adjacent cells of 1:2 or 1:3, though no larger than 1:5) and ‘skewness’

(asymmetry and angularity between cells) than laminar flows. Taking hexagonal cubic cells as an example, it is important to highlight that, if the aspect ratio between cells is 1:2 or 1:3, the volume ratio between them will be 1:8 or 1:27, respectively. An aspect ratio of 1:2 for tetrahedral cells will result in a volume ratio of approximately 1:7. It is assumed by the research community that coarse mesh will impact the quality of the results more than other factors, such as the turbulence model or the boundary input.

3.5.3.5. Segregated and coupled solution methods

The segregated solution method consists of solving the governing equations sequentially, that is, by segregating one from another. Generally speaking, first momentum equations are solved based on the previous results for pressure and mass fluxes (or on the initial input for the first round), and then having their values updated. The coupled solution follows the structure of the segregated one, but the equations are all solved at the same time. The equations are solved for each cell of the domain, which exchanges values with the surrounding ones. A complete loop of calculation occurs when a solution is given for each cell of the finite-volume, which characterizes one round of iteration. This round repeats either until the predetermined number of iterations is completed or the calculation meets the solution criteria adopted.

3.5.3.6. Linearization method

The linearization method consists of the sequence of the arrangement by which the governing equations will be applied to each cell and from one to other, allowing the development of the flow-field solution (Gauss-Seidel method). The linearization may be either ‘implicit’ or ‘explicit’. In the implicit mode, the solution for each dependent variable calculated is based on the previous and values of the cell itself and the values of the adjacent cells. Since the same thing happens with the neighbouring cells (they use the previously known and unknown values of the others, and so on), the equations must be solved in a package in order to provide the information for each and all of them. Alternatively, the explicit mode considers a relation for the unknown value for each cell, allowing the solution to develop individually.

3.5.3.7. Solution convergence

Convergence is achieved once all discrete conservation equations are attained in the domain to a designated tolerance: the mass, momentum, and energy are in balance and the solution does not improve significantly despite further iterations. The starting point for each cell round of calculations is the determination of its pressure differential. The velocity is determined on the basis of this, as then is the mass exchange. Based on the principle of mass and momentum conservation, if a balance is

not achieved and there is discrepancy between the results of one round of iteration and the next, adjustments in pressure, velocity and energy exchange due to mass flow are called for until the criterion adopted as accurate is satisfied.

3.5.3.8. Monitoring solution progress and the residual plot

The progression of the calculations should lead to a more balanced solution, which is demonstrated by the reduction of the inconsistency among the sequence of the results. At the end of each solver iteration round, the residual differential for each of the conserved variations is plotted on a graph, indicating the level of imbalance of the solution. Due to the infinite precision of computer simulations, the imbalance will continue to exist even when this differential is negligible and further iterations are just a waste of computing time. As a rule-of-thumb, the residual plot drops by 3 orders of magnitude for most of the convergence criteria (and 6 for energy) indicating qualitative convergence if the major flow features are observed. Once the convergence criteria for the solution are assumed, it is possible to monitor their progress dynamically by displaying the residual plot and other monitored variables. The figure below illustrates the progress towards a solution by the residual plot and the monitoring of the velocity magnitude or pressure of a selected cell at a relevant position in the domain.

After 680 iterations, it may be observed that, although the residual plot continues to drop steadily for all the variables calculated, which means that the solution is still seeking conversion, the variations in the velocity magnitude for the monitor cell stabilized well before that, after roughly 100 iterations, presenting a later negligible variation in the velocity value (for an urban external environment scale problem). On the other hand, at 100 iterations not all the variables represented on the residual plot had dropped by 3 orders of magnitude, and stopping calculations at this early stage would possibly lead to inaccuracy in some of the results. Both criteria and prudence have, therefore, to be adopted in order to decide when to stop the iterations without compromise the outcomes.

Figure 3-2: Examples of CFD simulation residual plot (left) and monitor point (right):

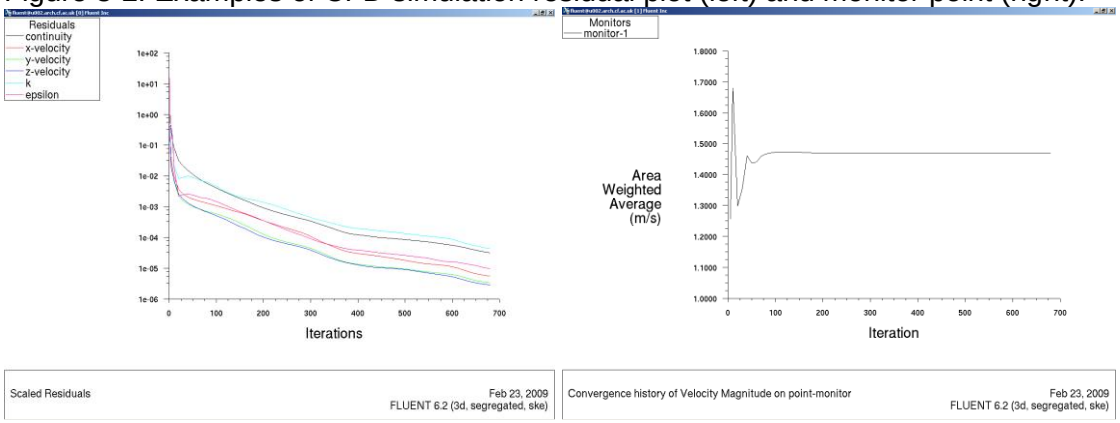

Source: this study.

Figure 3-3: Examples of CFD simulation monitors 1 (left) and 2 (right):

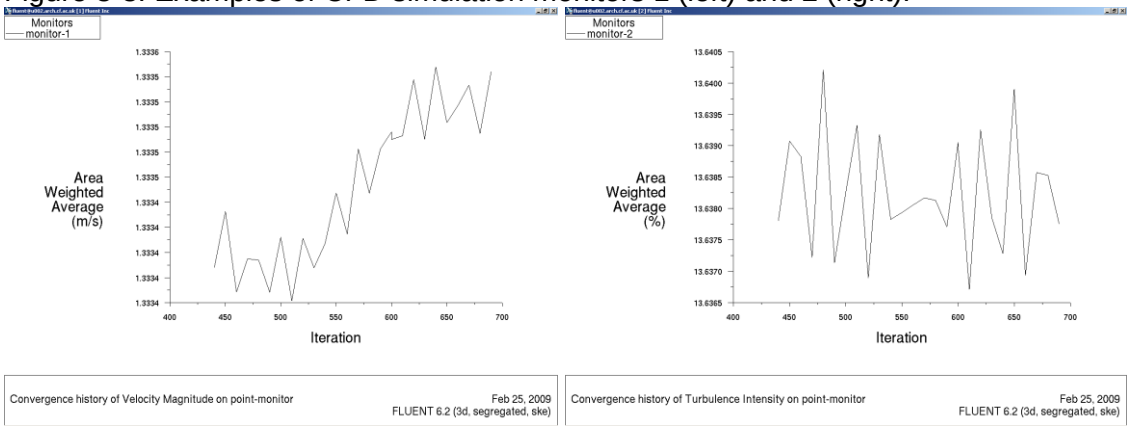

Source: this study.

Also, for the same 690 iterations, it may be seen that the residual plots for velocity magnitude and the turbulence intensity monitoring point still show instability (figure 3-3). Although represented as a continuous line in figure 3-2, this instability is more evident when the range of values displayed is altered, e.g. from 400 to the present number of iterations, and not from the beginning. These variations represent less than 0.001m/s and 0.01% for the variables respectively, and are completely negligible for this scale of model. More detailed examples will be covered on the chapters on the methodology, results and analysis of this thesis.

3.5.3.9. Under-relaxation factors

The sensitiveness in the calculation of the progressive imbalance solution means that, if the discrepancy in the results on a given parameter is greater than the range of acceptable proportionality, the solution will not converge. A continuous rise will be observed in the residual plot, and the calculation may become invalid and eventually come to a stop. By decreasing the under-relaxation factors related to a parameter, the range of acceptable imbalance rises and the calculation progresses, in spite of the increase in both the instability of the results and the calculation time. At the beginning

of the calculations and before the flow-field can be considered fully developed, it is expected that greater imbalance may occur.

Good practice calls for beginning the calculations with low under-relaxation factors (CFD user manuals advice using default values) and, as the calculation progresses, increasing them gradually. Great oscillations raising the residual plots may indicate that the factor was increased too much. In this case, the calculation must be interrupted and its value reduced.

3.5.3.10. Turbulence models

Turbulent flows of small scale and high frequency make the calculation of momentum, energy and concentration transport difficult. Here a comparison between how both the k-e and the LES models tackle this issue and when to use each one of them is presented. Regarding the choice of turbulence models, these are sub-divided into several categories, and have to be selected according to what is expected as a result based on the characteristics of the turbulence for the problem imposed. The most commonly used for airflow modelling in the external environment are:

- Standard k-e model, also defined as Reynolds-averaged Navier-Stokes (RANS) equations;
- Renormalization-group (RNG) k-e model;
- Realizable k-e model; and
- Large Eddy Simulation (LES) model.

Proposed by Launder and Spalding in 1976, the derivations of the k-e semi-empirical model are founded on phenomenological considerations and empiricism (Fluent, 2005). The transport equations for the turbulent kinetic energy ‘k’ and the turbulent dissipation rate ‘e’ are solved separately for all the k-e model closure variations. These equations govern the transport of averaged flow quantities, modelling all the scales of turbulent eddies and determining the turbulence velocity and the length scales independently. The outcome is a steady-state solution of the flow-field (Sini *et al.*, 1996; Fluent, 2005; Dixon *et al.*, 2006).

Both the k-e RNG and Realizable models are improvements of the RANS for specific applications. The first one has an additional term for the turbulent dissipation rate, based on statistical data, to improve the accuracy of strong flows, air jets, and swirls. But the appropriate specifications of the boundary wall roughness and the near-wall mesh resolution have to be mastered in order to achieve the full potential of this approach. For the Realizable model, the turbulent viscosity equation has been reviewed in order to enhance the separation and reattachment flow at sharp edges, among other possibilities (Fluent, 2005).

In reality, turbulent flows are made up of eddies of different length and time scales. While the k-e model makes no distinction for this difference, the LES model, by definition, solves the large eddies and the small eddies separately. The formers are calculated by a time-dependent simulation, the small ones are solved in a steady-state mode. The reason for this method of calculation is related to the fact that large eddies in turbulence are more associated with specific characteristics of the airflow problem imposed, such as the physical geometry, than are the small ones, which are governed by universal models of dissipation. Thus, solving more of the large eddies, e.g. in a greater number of time-steps, will y produce a better statistical representation of their influence on the overall airflow (Fluent, 2005).

3.5.3.11.Comparison between the k-e and the LES models

When comparing the advantages of using either one of the k-e models or the LES model, the pros and cons of each choice have to be taken into consideration in the light of the purpose of the simulation. The k-e models are known to deal well with mean flow-field development on both urban micro-scale and internal environment airflow problems, and their application has been extensively verified and validated by both wind tunnel experiments and field measurements (Hunter *et al.*, 1991; Sini *et al.*, 1996; Holmes, 2001; Jeong and Andrews, 2002). Further, they have been widely employed due to their saving of computing time. Conversely, some of the inherited limitations of k-e models are related to the uncertainty in handling precisely flow separation in sharp eddies and later flow reattachment. LES are used on investigations aiming to identify mixing processes, transient structure of turbulent fields and flow detachment/ reattachment, although some of the limitations of this model are undoubtedly related to the great demand on the computational time so far required. Finally, it is worthy of mention that the usual procedure for undertaking of LES calculations is initially to achieve a fully developed flow-field and statistically acceptable steady-state solution with a k-e model and only then to introduce time-steps for the time-averaged LES computation.

3.5.4. CFD modelling validation and comparisons in the literature

Verification and validation using CFD models are necessary to confirm confidence in results related to the assessment of airflow patterns in the urban environment, and they are usually obtained by comparing the outcomes with those of either WT or field measurement (FM) research (CIBSE A, 2006). Although validation is necessary to identify the level of accuracy obtained in several aspects of the modelling and calculation processes, the literature emphasizes the efficacy of turbulence models in reproducing airflow speed and direction and turbulence, and these are mostly used in investigations focusing on air pollution concentration dispersion.

Yamartino and Wiegand (1986) developed a simple parametric semi-empirical model for predicting airflow and turbulence in urban canyons to highlight air pollution concentration dispersion. The model, Canyon Plume-Box Model (CPBM), was validated with the use of FM data. The CPBM, though incapable of reproducing airflow conditions for above-roof wind speeds below 1m/s, predicted concentrations with reasonable accuracy for parallel and transverse canyon flow.

Summers *et al.* (1986) present possibly one of the first validations of CFD modelling found in the literature, the SWIFT tool (Simulation of Wind Flow in Three Dimensions), although those authors do mention an earlier study performed by Caretto *et al.* dating back to 1972. Airflow around a single brick was compared to the results of that produced in the WT. With a relatively coarse mesh, the results for the windward recirculation was found satisfactory, leeward wake was defined as not well solved, and the normalization of the flow-field took twice the distance of the measurements to occur, possibly due to inconsistency in the turbulence model in dealing with the shear forces and dissipation rates. The author also mentions that WT experiments are able to reproduce airflows with only 20% accuracy and certainty.

Hunter *et al.* (1991) reproduce the WT simulations performed by Oke in 1988 in a numerical model for series of urban canyon H/W aspect ratio variation in order to identify the relationship between the canyons' dimensions and airflow regimes[5]. Sini *et al.* (1996) apply the CHENSI for the same purpose. This validated CFD code uses the standard k-e (RANS) and was reported to reproduce most of the airflow characteristics on the urban environment scale faithfully, although the results under predict recirculation flows by 20%. Jeong and Andrews (2002) also investigated the accuracy of the k-e model to predict airflow speed and direction and pollution dispersion across various H/W canyon ratios in a 2-D domain. Their results corroborate those of Sini's study.

Johnson and Hunter (1998; 1999) have checked the confidence in reproducing airflow of the SCAM k-e model against WT experiments for magnitude of wind speed and turbulence viscosity results (CITY code) focused on pollution dispersion (SCALAR code). Although general agreement was found between the two methods, it was emphasized by the authors that realistic CFD results depend on the accuracy of the flow-field specification. The 2-D approach for canyon investigation considered in previous studies was questioned by these authors, since the airflow-field inside the canyon has components transversal to the stream-wise axis that make it much more complex, and which can only be fully reproduced in 3-D models. In consequence, skimming flow cannot be accurately achieved in 2-D models. Another point concerned

[5] See topic 2.6.3.2 in Chapter 2 for further information.

the inlet boundary condition, which also seemed crucial for achieving a good comparison of results. Considering the wind profile proper to the urban terrains accessed and taking into account the terrain roughness and the canopy height produced almost 100% agreement with the WT results for the windward recirculation features and the leeward wake and reattachment length. Prior to this experiment, the CFD code had been reported to underestimate the first and overestimate the second. Meroney *et al.* (1999) also contrasted CFD and WT results. Their aim was to check whether the commercially available CFD package (FLUENT) using either the RANS or the RNG k-e model could predict the airflow field and pollution concentration dispersion in urban areas when reasonable boundary and inlet information were considered. The wind profile in the numerical calculation was set to reproduce that of the wind tunnel experiment. The results showed that k-e models tend to over-predict flow vortices within the canyon, presenting a wider and longer leeward wake, in close agreement with Hunter *et al.* (1991).

One more fault observed in steady-state solutions is related to the intermittent nature of flow circulations, on which separation and reattachment occur dynamically thus producing backward airflow, and this effect is not totally reproduced in steady-state solutions. For this reason, these models tend to over-predict pollution concentration. By contrast, the horse-shoe detachment flow shape on the windward side edges and top surface detachment bubble and other flow patterns were faithfully reproduced by both the κ-ε models used. Moreover, numerical data output regarding pressure values and velocity magnitudes were accurate enough to allow their realistic use by structure engineers, though Meroney *et al.* (1999) emphasize that consistent results must be grid-independent. Holmes (2001) brings out that k-e models can predict mean pressure values on the building envelope with accuracy, although peak and fluctuating pressures are not obtainable. Similar results regarding the small deviation in the leeward wake recirculation zone and/ or the reasonable agreement with Cp results have also been found in other studies that employed CFD k-e models (Chan *et al.*, 2001; Chan *et al.*, 2003; Cheng and Meroney, 2003a and 2003b; Senthooran *et al*,. 2004; Xie *et al.*, 2005; Wang *et al.*, 2006; Wang and Huang, 2006; Huang *et al.*, 2007; Bady *et al.*, 2008; Yassin *et al.*, 2008), though not all the results were clearly validated by WT experiment.

Studies comparing the performance of the k-e and LES turbulence models have begun to increase in the XXI century due to the advances and availability of faster computer processors and IT facilities. Cheng (2003) and Cheng and Meroney (2003a and 2003b) has explored the airflow over an array of cubic volumes. The emphasis of his research also lays on the comparison between the standard k-e (RANS) and the

LES. This latter was sub-divided into three categories according to the sub-grid scales: the standard Smagorinsky model (SMG, with Cs= 0.10), the Dynamic SGS model with time-averaging procedure (DMT) and the localized dynamic model (LDM). The results of the simulations, when compared to the physical experiments recorded in the literature, have indicated that the LES with LDM is the turbulence model that reproduces the complexity of vortices, reverse flows, separation bubbles, wakes and reattachment processes closer to reality. On the other hand, the k-e model has failed properly to simulate reverse flows to windward and has over-estimated the size of the separation bubbles reattachment to leeward due to the fact that this code does not take unsteady vortices in the airflow calculation into consideration. Conversely, a drawback of LES calculation is its long computational time, two figures greater than that of the steady-state model. By contrast, Walton and Cheng (2002) mention that, although steady-state calculation predicted slightly weaker circulation than did the LES, both yielded results considerably lower than those of the WT experiments recorded in the literature. In addition, none of the models presented secondary vortices for deep H/W ratios, disagreeing with the results obtained by Sini *et al.* (1996). Jiang and Chen (2004) undertook CFD calculations for the same purpose as in the previous examples, but simulating airflow across an isolated cube with a frontal opening, instead. Wind tunnel experiments were also conducted for a similar physical model. Their results agree with those of Cheng (2003) regarding both the more accurate results obtained with LES for reproducing the position and size of the vortex recirculation zone in the leeward wake, on which there was 95% agreement, in contrast with a slight overestimation with the k-e model. In addition, the steady-state calculation over-predicted the air change rates at the frontal opening by approximately 30%, while the time-averaged result reproduced the ACH with 98% agreement.

Recent studies contrasting the k-e and LES models also reported differences between the results of the two options, with the steady-state model frequently over-predicting the leeward recirculation vortex. For Li *et al.* (2005; 2006), Shi *et al.* (2008) and Tominaga *et al.* (2008), the disparity found was roughly 20% greater, though the total length of the leeward wake mentioned by the last was almost twice the size of that given by LES, which subsequently agreed well with the related wind tunnel experiments. Also, Li *et al.* (2005a, 2005b and 2006) mention that ACH results diverged from 5 to 17% for models calculated by time-steady and averaged CFD models and with H/W ratios varying from 0.5 to 2.0, respectively. Moreover, Nozu *et al*. (2008) mention that LES results are more realistic, indicating the attainment of accurate pressure distribution in the complex irregular urban geometry contrasted with the research field in Tokyo.

Some research cases may require a transient component due to the unsteady nature of the airflow. For this reason, investigations focusing on air pollution concentration dispersion in the urban environment that add advection-diffusion equations to the CFD solvers (such as Gaussian plume, Eulerian, Langrarian, Stochastic and hybrid models), have been described as performing better with LES, since it predicts higher turbulence intensity levels at the core of the vortex area and near the walls within urban canyons. Further, the vortex occurs along the length of the canyon, instead of being stationary, which allows more homogeneous, although intermittent, pollution concentration dissipation (Johnson and Hunter, 1998; Walton and Cheng, 2002; Cheng and Meroney, 2003a and 2003b; Jiang and Chen, 2004; Dixon *et al.*, 2006; Li. *et al.*, 2006). Regarding estimating the time-step scale for the calculation of the intermittent variables when using the LES model, Liu *et al.* (2005) provide a method that relates it to the building height and the mean wind speed:

Equation 3-7: $$T = H / \overline{U}$$

For the just mentioned CFD investigations, Liu *et al.* report that 50T is necessary to achieve steady-state resolution and a further 50T to calculate the time-averaged solution at time-steps of 0.1T for analysis, which was related to the time-step scale of 30 to 60 seconds adopted in the LES calculation parameters.

Zuo and Chen (2007a, 2007b and 2008) present a novel airflow modelling technique named ‘Real time or faster-than-real-time (FFD) CFD models’ that proposes an intermediate approach between the simplified nodal models and the time-consuming CFD. Although the FFD model can reproduce some major features of the flow 50 times faster than CFD codes can, it is assumed that it is not yet as accurate as k-e models.

3.6. Chapter Conclusion

This chapter presents the theory behind and the main concepts involved in the most commonly employed techniques for investigating airflow in the urban environment: wind tunnel physical scaled models, and computational fluid dynamics (CFD) calculations. It highlights also the specificities of each of these techniques. The theory presented in this chapter gives support to the investigations carried out for this thesis, which will be covered in Chapter 5: Methodology.

Chapter 4: Buildings and Natural Ventilation

4.1. Introduction

In this chapter the concepts related to natural ventilation systems and the building envelope will be discussed. Starting with the basic role of building internal ventilation and the minimum requirements for health and comfort, it will also cover the definitions of more complex natural ventilation strategies and how to estimate their performance.

4.2. The role of ventilation in the internal environment

Natural ventilation is the process by which fresh air is introduced in the internal environment by using the driven forces of wind and temperature (Liddament *et al.*, 2006). Ventilation is related to quality of health and comfort, since it supplies providing fresh air to the ambient (Awbi, 2003). In indoor spaces, this air supply can act by both diluting and expelling pollutants, improving air quality, and removing internal heat gains (Jones, 2001). Yeang (1996) stresses the value of natural ventilation for structural cooling as a passive cooling technique. Thus, ventilation has a direct impact on the health and comfort levels of a building's users and, as a result, also affects their performance and productivity.

The efficacy of a naturally ventilated internal space is related to the building's design. The choice of ventilation strategy should be made during the early stages of the architectonic design and should consider the regional climate's seasonal variation, the local microclimate and the built-up surroundings all in close relation to the building's occupancy and internal layout. The combined analysis of these factors should provide the guidelines for the ventilation and other passive design strategies to be employed, in order to attain the desirable user's comfort levels associated with a reduced building carbon footprint.

The choice of the ventilation systems should first exhaust all the possibilities of natural ventilation then combine natural and mechanical means in hybrid systems and, when unavoidable, make use of artificial systems only. Such circumstances are observed when the response to external conditions cannot, on the long term, attain the desired comfort limits. When finally the building shape and façade elements are decided on, they integrate the passive design strategies, building legislation and the client's project brief. Wrong decisions at any of these stages imply problems during the building-lifetime performance, operational cost and user satisfaction. According to Yeang (1996), the shape of a building may either enhance natural ventilation or jeopardize the ventilation strategy.

4.2.1. On natural ventilation

It is known that airflow inside buildings occurs due to a combination of wind- and buoyancy-driven forces that create pressure differentials across the internal environment (Olgyay, 1973; Givoni, 1994, 1998; Yeang, 1996). While the former are subject to external wind speed and direction and size and type of openings, the latter are related to solar radiation, internal heat loads, and air temperature stratification. These forces may act alone, together or in opposition one to another.

In order to achieve either indoor air quality or human thermal comfort, two issues have to be addressed: the total amount of airflow and its distribution throughout the internal space. A combination of ventilation strategies and architectonic solutions can be used in order to create differences in pressure between the inlet/ supply and outlet/ exhaust, thus inducing the airflow path through the internal space and determining the internal ventilation rates (Jones and Yeang, 1999).

4.3. Ventilation for health and thermal comfort

Roulet (2005) affirms that the purpose of building ventilation is to guarantee indoor air quality (IAQ) and the user's thermal comfort, and these are achieved by the control of the airflow rates. The demand for air supply obeys the following order in the air changes per hour (ACH) rate: oxygen supply; CO, pollution and odour removal; and convection and evaporation acceleration for thermal comfort. Through the calculation of the ventilation rates it is possible to determine wether the building design meets the requirements for natural ventilation potential (NVP), in terms of IAQ rates, or the passive cooling potential (PCP), related to acceptable levels of the internal environment's thermal comfort. If not, mixed systems or artificial techniques have to be employed in order to achieve the required rates (Germano *et al.*, 2005).

4.3.1. Indoor air quality (IAQ)

The composition of the air in the lower levels of the Earth's atmosphere (troposphere) is nitrogen 78.08% (N_2), oxygen 20.95% (O_2), argon 0.93% (Ar), and carbon dioxide 0.03% (CO_2), water vapor in variable percentage, impure substances and pollution, and fractions of other gases such as helium and hydrogen (Masi and Ochoa, 2005).

The World Health Organization (WHO) alerts that urban center environments are polluted with several harmful chemical components, the maximum concentration limits of which have to be monitored in order to preserve human health. The main pollutants are: sulphur dioxide (SO_2); nitrogen dioxide (NO_2); carbon monoxide (CO); ozone (O_3), suspended air particles and lead (Ghiaus *et al.*, 2005a).

According to Awbi (2003), in internal spaces, such as dwellings, offices, factories or means of transportation, the air composition is added of more than 8,000 other chemical substances, among them being tobacco smoke, formaldehyde, volatile organic compounds, radon, asbestos, suspended particles, ozone and aerosols. Roulet (2005) states that the poorly ventilated indoor spaces of buildings tend to present bad odours, high humidity, carbon dioxide and moisture levels (produced by the users and intensified during the hot season), dust, condensation, mould, aerosols and other toxic gases emitted by users, cleaning products and general maintenance that, as a consequence, compromise air quality and affect users' health. Various authors and guidance books provide information on the acceptable levels of these and other outdoor and indoor contaminants (ASHRAE, 2001; Awbi, 2003; BS EN 13779, 2005; Ghiaus and Allard, 2005; Santamouris, 2006; CIBSE A, 2007).

4.3.1.1. The sick building syndrome (SBS)

When the concentration of one or the combination of several of these chemical pollutants exceeds the maximum recommended levels, building occupants are subject to the effects of the sick building syndrome (SBS). SBS symptoms include allergies, lethargy, irritation of mucous membranes and eyes, headaches and health problems.

In order to minimize heating or air conditioning losses, buildings have become more tightly sealed, with minimum ventilation rates. Nowadays people spend more time living and working in internal environments than they do outdoors, and serious diseases, such as chronic pathologies and cancers, have been increasingly related to IAQ and the SBS. Ghiaus *et al.* (2005a) affirm that, in developed countries, these diseases are more closely associated with the internal contaminant concentration in office buildings than they are to external pollution

4.3.1.2. The air change per hour (ACH)

The air change per hour (ACH) is the unit used to calculate ventilation rates and is based on a complete air change of a given internal environment volume in one hour time. By means of air change indoor and outdoor air concentration levels are mixed, exchanged and diluted. Achieving the minimum ACH per building occupant necessary adequately to dilute these pollutants and provide fresh air has become an important issue associated with health quality (CIBSE A, 2007). The equation for calculating the ACH and the necessary airflow volume are (Ghiaus and Roulet, 2005):

Equation 4-1 ACH = Qflow*Vspace*Timeunit

Where:

- Q_{flow}: is the volume of the flow (m^3/s);
- V_{space}: is the volume of the internal space (floor area x ceiling height, in m^3/s); and
- $Time_{unit}$: 3,600 seconds.

Equation 4-2 $Q_{flow} = 0.5*A_{eff}*V_{ref}$

Where:

- A_{eff}: is the effective area of the window[6] (m^2/s); and
- V_{ref}: is the reference airflow velocity (m/s).

4.3.1.3. ACH and the dissipation of contaminants

The ventilation rate necessary to dissipate internal contamination is related to the intensity, strength and density of a specific contaminant source in both the indoor and outdoor environments, and is given by the following equation (Awbi, 2003):

Equation 4-3 $Q_{flow} = 10G/(C_i–C_o)$

Where:

- G: is the contaminant generation (kg/s);
- C_i: the concentration of the contaminant inside (kg/m^3); and
- C_o: is the concentration of the contaminant outside (kg/m^3).

Further, the airflow rate necessary to dilute the air contaminants should be calculated individually for different pollutants and the highest airflow rate necessary is the one that has to be attained (Roulet, 2005).

In the view of the fact that a person consumes from 0.1 to 0.9 litres of air per second in breathing, depending on the human activity concerned and the consequent metabolic rate, the production of carbon dioxide (CO_2) and necessary ACH can be calculated in accordance with the following equation (Awbi, 2003):

Equation 4-4 $G_{CO_2}= 4*10^{-5}A*M$

[6] As a rule of thumb Pollet and Renson (2008) give a window's effective area ranging from 5 to 20%.

Where:

- G_{CO2}: is the CO_2 production (l/s);
- A: the body's surface area (around 1.8m^2 for an average adult); and
- M: the metabolic rate (from 100 W/m^2 for people at rest, 450 W/m^2 for moderate work, and 800 W/m^2 for very heavy work).

Based on this equation, the ACH for keeping the CO_2 concentration at acceptable levels (0.25%) may vary from 1.8 to 14.0 l/s per occupant. On the other hand, the recommendations for the whole-building ventilation rate for achieving basic IAQ found in non-domestic buildings may vary from 10 l/s up to 36 l/s per person in cases where there are smoke sources (ASHRAE, 2001; Parker and Teekaram, 2005; CIBSE AM10, 2006). According to these guides, this rate can be obtained with a minimum background infiltration rate of 0.1ACH (for unoccupied buildings) plus additional ventilation of 1.5ACH per occupant, varying with activity and clothing levels. However, it is worth noting that ventilation rates necessary for reducing thermal loads exceed this rate by two figures.

4.3.2. Ventilation for thermal comfort

Thermal comfort is influenced by external and internal air temperature and humidity, wind velocity, direction and turbulence, and internal surface temperatures, plus users' activity type and clothing level. The increase in the airflow increases the heat loss from the human body to the surrounding air, thus altering the body's heat balance. This means that the increase in the air's motion in internal environments will improve thermal comfort at high temperatures or cause a chilling effect at low temperatures (Melaragno, 1986).

4.3.2.1. The human body's heat balance

The comfort perception of the human body is a result of the body's energy balance resulting from metabolic rates and of the heat exchanges by convection and conduction twith the air, by evaporation/ transpiration and by radiation to and from surfaces. The comfort perception is affected by air temperature, velocity and humidity rates, and surfaces temperatures (Awbi, 2003; Roulet, 2005).

When exposed to heat discomfort, the imbalance of the body's metabolism makes the skin react to both the warmer (sensible heat and sensible perspiration/ sweating) and the cooler (shivering) climatic conditions of the external environment. These reactions work as warnings that the internal human body is out of the comfort zone and spending energy to maintain its constant temperature of 37^oC. This

mechanism ensures the body's thermal equilibrium by modifying blood circulation, skin temperature and transpiration rates (Givoni, 1998a; Roulet, 2005). Awbi (2003) presents the following equation for calculating the heat balance of the human body:

Equation 4-5 $S= M+W+R+C+K–E–RES$

Where:

- S: is the rate of heat storage of the human body (W/m^2);
- M: the metabolic rate (varies from 100 W/m^2 for people at rest, 450 W/m^2 for moderate work, up to 800 W/m^2 for very heavy work);
- W: the heat generated by the human activity (W/m^2);
- R: the heat change by radiation/ sensible heat (W/m^2);
- C: the heat change by convection (W/m^2);
- K: the heat change by conduction (W/m^2);
- E: the heat loss by evaporation/ sensible perspiration (W/m^2); and
- RES: the heat loss by respiration (W/m^2).

This equation takes into consideration the metabolic rate corresponding to the physical activity performed and clothing level, heat gains or losses by radiation, convection and conduction and heat losses by evaporation and respiration. While positive values indicate a rise in body temperature, negative ones point to heat loss.

4.3.2.2. Scales for assessing thermal comfort

The bioclimatic chart proposed by Olgyay (1963 and 1973) for evaluating the thermal comfort range in temperate climates combines dry bulb temperature, relative humidity, air movement and solar radiation data. The chart defines thermal comfort zones in view also of type of individuals, gender, age, clothing level and activity type. Changes in any of the parameters would modify the perception of thermal comfort. Olgyay's chart has undergone several modifications in the range of air temperature, relative humidity and atmospheric pressure to make it suitable for application in sub-tropical and tropical climates. A shortcoming of such a model is that it focuses on external environments and does not allow adjustments in building strategies for enhancing their thermal and comfort performance (Bogo *et al.,* 1994; Givoni, 1998a). Another scale used for indicating the thermal sensation of warmth or cold was the effective temperature index (ET). The ET combines air flow rates with wet- and dry-bulb thermometers, and used to be adopted by ASHRAE for HVAC system designs. The ET was replaced by the operative temperature scale (TO), which is based on the

mean operative temperature, air humidity, heat changes, clothing and activity level for evaluating the comfort levels, with a maximum of air speed of 0.15 and 0.25m/s, respectively, for winter and summer conditions. The TO is reported to specify HVAC operable conditions creating comfort for up to 80% of building users (Awbi, 2003). On the other hand, Awbi points to a drawback in these scales for assessing thermal comfort: since they are all based on statistical analysis of laboratory data there is a certain limit to their application.

The psychometric chart is possibly the most widely used diagram for measuring and evaluating thermal comfort zones. Using as parameters the dry-bulb temperature (DBT-^{o}C), the wet-bulb temperature (WBT-^{o}C), the dew point (DPT-^{o}C), the relative humidity (RH-%), the humidity ratio (gm of water/ gm of dry air), the enthalpy at saturation (J/gm of dry air) and the specific volume for a given atmospheric pressure, this chart is divided into sub-zones with a thermal sensation for each one of them. When crossing the weather data for a given location it will indicate the resultant comfort condition for the parameters provided. An advantage of the psychometric chart is the possibility it offers of plotting a complete year of weather data on it, and then establishing passive or hybrid mechanical design strategies for attaining or improving the comfort zone in each season of the year or at any specific time of the day.

Figure 4-1: Psychometric chart for summertime in the city of São Paulo showing the design techniques and the respective comfort zones:

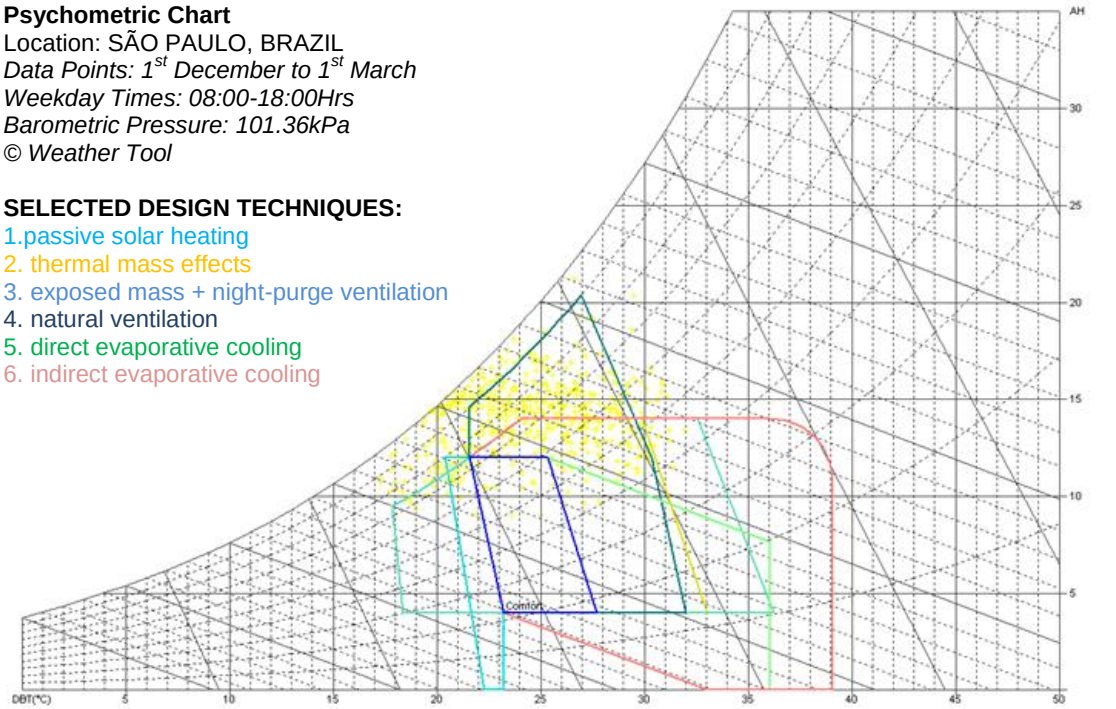

Source: this study.

Figure 4-1 gives, as an example, the psychometric chart for a typical summer day's weather data in the city of São Paulo. This chart was created using the software Ecotect Weather Tool. The initial comfort zone is highlighted in dark blue. It may be observed that most of the time assessed is outside the comfort zone and that therefore some measures have to be taken to improve the comfort conditions. Among the passive design techniques selected to achieve this goal, that of the natural ventilation is the one that encompasses the greater area of the pointed hourly weather data (dark green), followed by the combination of exposed mass and night-ventilation (light blue), and indirect evaporative cooling (pink) as the best strategies for increasing the area of the thermal comfort zone for this weather condition.

According to Roulet (2005), the most frequently used methods for evaluating comfort levels are: questionnaires answered by users showing satisfaction/ dissatisfaction levels; the psychometric chart, and the Fanger method for calculating the predicted mean vote (PMV) and the predicted percentage of dissatisfaction (PPD).

4.3.2.3. Fanger PMV and PPD

Fanger (1972) created a thermal comfort model based on equations derived from controlled physical assessments with human beings in which the environment parameters, such as: the air temperature, the radiant temperature, the relative humidity, the air velocity and the atmospheric pressure; and human characteristics, as for instance: the individual metabolism rate, the clothing level, and the type of physical activity (Awbi, 2003; Charles, 2003). The principle of this model is based on the fact that the human body tends to establish a thermal equilibrium with the environment, which implies that heat is gained or lost in achieving it. The analysis of the experiment observed the skin reaction (sweating/ shivering) to determine comfort balance. Fanger's equation for calculating the thermal comfort is (Awbi, 2003):

Equation 4-6 $f(M,W,I_{cl},t_a,t_r,v,p_a)= 0$

Where:

- M: is the metabolic rate[7] (W/m^2);
- W: the heat generated by the human activity (W/m^2);
- I_{cl}: the clothing level (varies from 0clo for naked people, to 1.0clo for a suit and 1.8clo for heavy clothing);
- t_a: the air temperature (^oC);

[7] The metabolic rate varies from 100 W/m^2 for people at rest to 450 W/m^2 for moderate work to 800 W/m^2 for heavy work (Awbi, 2003).

- t_r: the mean radiant temperature (^oC);
- v: the air velocity magnitude (m/s); and
- p_a: the water vapour pressure in the ambient (Pa).

Based on the results of this experiment, conducted during the 1970's with people of different ages, races, and genders in a controlled indoor space, Fanger created the thermal models of the predicted mean vote (PMV). This thermal sensation scale adopted during the experiment was based on the following seven point psychophysical indicator (ASHRAE, 2001):

Table 4-1: PMV thermal sensation scale:

cold	cool	slightly cool	neutral	slightly warm	warm	hot
-3	-2	-1	0	+1	+2	+3

Source: Givoni (1998a).

Fanger found a link between variations in the terms of the PMV equation for calculating the thermal comfort and the increase in discomfort levels, which resulted in the predicted percentage of dissatisfaction (PPD). This relation is demonstrated by the following simplified equation (Awbi, 2003):

Equation 4-7 $PPD= 5+20.97(PMV)^{1.79}$

By applying the equation for calculating the PPD as a function of the PMV, the more stressing the thermal conditions are, the greater the number of people who show dissatisfaction and move away from the neutral point (zero), as can be visualized in the following chart:

Figure 4-2: Fanger PMV-PPD chart

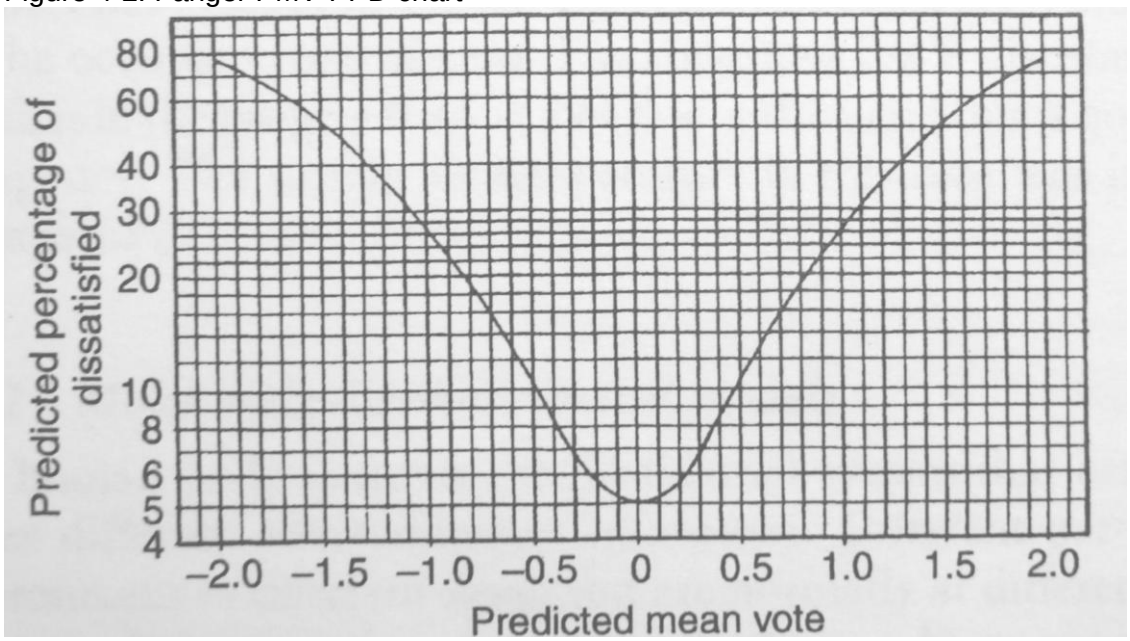

Source: Awbi (2003, pp16).

Many authors have reviewed and commented on Fanger's PMV model. Givoni (1998a) observes that Fanger's method for defining the comfort zone only takes the effect of the air velocity for convective heat changes into consideration and not that for heat loss by evaporation/ sensible perspiration. This means that under conditions of high temperature and relative humidity, variations in the air speed would result in an underestimation of the increase in thermal comfort. For this reason, according to that author, Fanger's model is of limited applicability in hot humid climates, being more suitable for temperate climates.

Delsante and Vik (2001) provide a comprehensive multi-criteria method for calculating the PMV for hybrid ventilation buildings including IAQ, thermal loads and energy consumption as criteria in the equation. Humphreys and Nicol (2002) crossed the PMV with an experiment based on the ASHRAE database. While a good correlation was established between the two methods, the researchers highlight that an average standard deviation of around 0.25 was found. The authors mention that this might be caused by measurement error or contextual assumptions, since the parameters used during the experiment are sometimes difficult to control or replicate.

Difficulties in the control of parameters, mainly related to clothing insulation and metabolic rates, were also mentioned by de Dear and Brager (2002). Their work focused on a review of the ASHRAE and proposed an increase in the range of the comfort zone for naturally ventilated buildings. It also points out that user's of HVAC buildings feel comfortable only within a narrow range of temperature, which matches the PMV well. On the other hand, users of naturally ventilated environments tolerate a

wider range of internal temperature, which is to be explained by self-adaptation of clothing levels, the possibility of controlling the environment through opening windows and also psychological and thermal ability to adapt to the environment.

McCartney and Nicol (2002) propose a review of the Fanger PMV and the ASHRAE range of comfort zone by an adaptive control algorithm. A field measurement and a questionnaire-based research project were conducted in five European countries with considerable climatic differences. The results show that adaptation within the comfort range could result in an economy of energy of up to 30% with HVAC systems without causing thermal discomfort.

Roulet (2005) states that Fanger's equation is valid within certain limits of parameter variation, such as air temperature from 10 to 30^{o}C, mean radiant temperature from 10 to 40^{o}C, water vapour pressure up to 2.7kPa, moderate clothing and activity/ metabolic rate levels and relative air velocity up to 1m/s. As a rule of thumb, the accepted ranges of air temperature are from 20 to 24^{o}C and 23 to 26^{o}C for winter and summer, respectively.

Santamouris (2006b) analyses the relationship between Fanger's equations for the thermoregulation and comfort levels associated with internal airflow. Both PMV and PDD are used to identify the comfort perception in a steady-state indoor climate. The author stresses that steady-state conditions are rare in building's internal environments due to the dynamic iteration of external weather variation, the building materials used and both user activities and clothing levels. For example, when considering passive buildings, monitored internal temperatures seem to fluctuate by from 0.5 to 4.0^{o}C according to changes in the control systems. Roulet (2005) observes that air temperature and radiant surface temperature gradients varying by no more than 4^{o}C from head to ankle and dark/ warm ceilings produce thermal discomfort in office users.

4.3.2.4. Ventilation and thermal comfort

Ventilation helps to enhance thermal comfort in internal environments by ventilating the users, either directly, when airflow increases the cooling sensation, or indirectly, when nocturnal purge ventilation is used to cool the built mass and delay the next day's thermal gains.

4.3.2.4.1. Natural ventilation potential (NVP)

The natural ventilation potential (NVP) is related to the capacity to ensure indoor thermal comfort through the exclusive use of natural ventilation systems. NVP therefore comprises indoor air quality and thermal changes, and reflects in energy savings with HVAC systems. The NVP is related to external microclimate variants (i.e., outdoor air temperature; relative humidity and pollution concentration; airflow speed and direction;

and urban noise) and building variants (i.e., urban density; building shape; solar orientation; façade roughness; type, size and location of openings; indoor air temperature and pollution concentration; internal heat sources; air-tightness; air-path; ventilation systems; building use; and users' activities). A combined assessment of these characteristics identifies the NVP and the most suitable ventilation system for a given location, providing design guidelines (Germano *et al.*, 2005a and 2005b).

4.3.2.4.2. Ventilation for improving thermal comfort

The efficacy of ventilation to ensure thermal comfort is directly related to temperature levels and standards. CIBSE AM 10 (2007) recommends this strategy for those buildings in the UK for which the combined solar radiation and internal heat loads reach a maximum average of 40W/m^2. Under this condition, it is said that non-residential buildings can be naturally ventilated and also meet comfort standards. Additionally, Twinn (1997) indicates a cooling capacity for naturally ventilated buildings of 50W/m^2. Therefore the proper control of the building envelope's solar exposure[8] (up to 25W/m^2) and the decrease of internal heat sources (up to 15W/m^2) are fundamental for reaching this goal. Internal heat loads in office buildings are the result of users' occupancy, machines such as computers, printers and photocopiers, artificial lighting systems, and heat gains from direct solar radiation impinging on façades and structures (Roulet, 2005).

On the other hand, the cooling effect is only perceived by the users if the difference between the inlet and the internal air temperature is greater than 3K (CIBSE AM 10, 2007). This application manual also provides a chart for determining the sensible cooling effect obtained with variations in this temperature differential and the ACH. It may be seen from this chart that the greater the differential, the more ACH is necessary to enhance the cooling capacity of the air in internal environments.

[8] Defined by the Building Regulation Part 2 of the UK.

Figure 4-3: Cooling effect with temperature and ACH variation

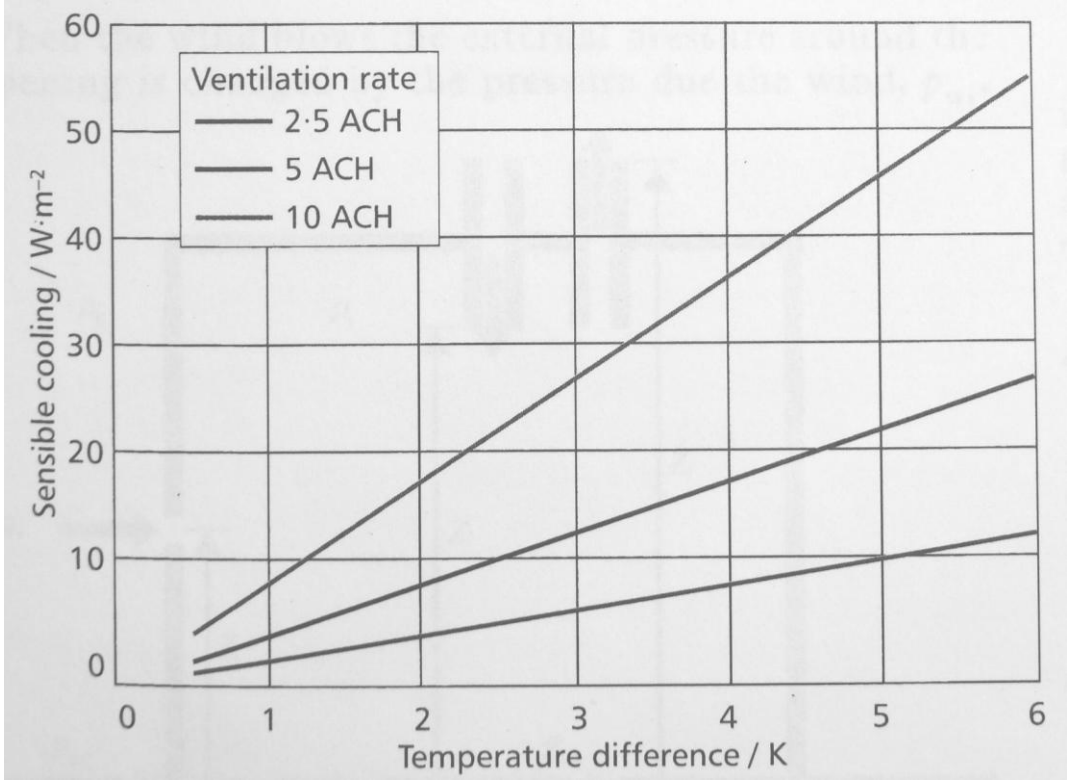

Source: CIBSE AM 10 (2007, pp39).

In contrast to this, it is worthy of note that the ASHRAE (2001) establishes a limiting air speed in HVAC office environments that, if exceeded may cause discomfort. An air speed of 0.8m/s is the limit beyond which higher speeds may be perceived by building occupants as a cold draught at air-conditioned temperatures. The same discomfort is not noticed in free-running buildings, and it will be discussed in section 4.3.2.5.

4.3.2.5. Thermal comfort in free-running buildings

Free-running buildings are those without mechanical HVAC systems whose strategies for achieving internal thermal comfort are based on passive techniques only. Free-running buildings are expected to provide at least as much comfort as the external microclimate conditions, but above all they should minimize extreme outdoor climates within the comfort boundaries (Ghiaus and Allard, 2005 and 2006).

Santamouris (2005) affirms that in such buildings the internal temperature range during the day is expected to be higher than in HVAC ones. Alternatively, comfort can be reached[9] when the maximum temperature is below 28 and 32^{o}C (varying according to the relative humidity of the air), the daily temperature range is less than 10^{o}C, and

[9] This combination of weather conditions can be achieved in most of the months in São Paulo's sub-tropical climate, one of the case studies presented in this thesis (see topic 5.4.2.2. in Chapter 2).

the internal air speed range from 1 to 2m/s, speed that would be considered unacceptable in HVAC environments.

Ghiaus and Allard (2005) add that users of free-running buildings are more adaptable to ambient temperature and other comfort limit variations, accepting thermal conditions that would be classified as non comfortable particularly when they are able to control some of the physical parameters by the adjustment of building controls, operating windows and other devices, and also changing their own clothing levels.

Nonetheless, neither the EN-ISO 7730 nor ASHRAE make any clear distinction between thermal comfort parameters and the requirements between free-running and HVAC buildings. According to Brager and de Dear (2000), this lack of tools and support makes and decision as to the implementation of natural ventilation techniques difficult.

Roulet (2005) reviewed and adapted the PMV equation for free-running building users. His investigation developed an adaptive comfort model in order to identify the operating temperature for naturally ventilated environments. The adaptive comfort is related to the increase in the range of the comfort zone in free-running buildings, considering that the users will adapt to this higher variation of indoor thermal conditions. The results indicate an acceptance by the users of the increase in the temperature by up to + or -2.5^{o}C. In addition, when airflow is introduced into the environment, this range can rise by to an average of + 4.0^{o}C.

Figure 4-4: Accepted air temperature with increase of the air velocity:

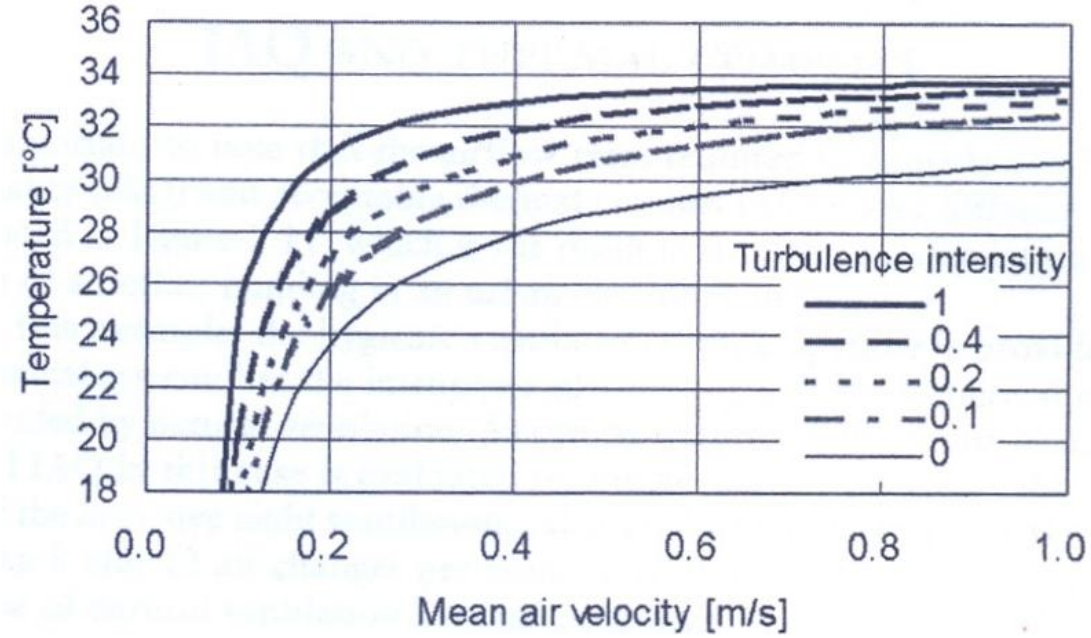

Source: Roulet (2005, pp31).

4.4. Principles of natural ventilation

As has been presented in this chapter, natural ventilation is basically related to air supply, and air extraction or purging (background or concentrated), or both together It also consists of movement of air through an environment, necessary for supplying fresh air at a minimum ACH rate to meet IAQ needs, and for improving the sensation of thermal comfort (Frota, 1995).

4.4.1. The physics of airflow

The air flow inside buildings is a result of the pressure difference between the external and the internal environments. The resistance to this flow is created by both the window inlets and outlets, internal obstructions and partitions, and several other features related to the building's shape and wind properties (Olgyay, 1963 and 1973; Ghiaus and Allard, 2005).

The pressure difference is subject to wind-driven forces (for instance, single or cross-side ventilation, resulting from wind speed and direction) and/ or buoyancy pressure-driven forces (for example, stack effect or ground cooling). The pressure difference may, further, result from the combination of both forces as is used in several ventilation techniques. However, these forces may act one against the other, thus producing air stagnation or reverse flow (CIBSE AM10, 2006). The amount of flow is related to the laws of continuity and mass conservation of fluids, in accordance with which the airflow coming in through the inlet openings must be counterbalanced by the same volume at the outlet (Cook, 1985; Holmes, 2001).

4.4.2. Wind-driven ventilation

Wind-driven ventilation results from the differences of pressure across building's opening's area and the internal environment. Air flows from the higher to the lower pressure side, and the difference in pressure between the inlet/ supply and the outlet/ exhaust determines the airflow path through the internal space and the ventilation rates (Olgyay, 1963).

Free airflow in the external environment has its initial velocity slowed down when it meets an obstacle. This decrease in velocity is counterbalanced by increases in dynamic pressure on the windward surface of the building. The flow around the sides and the top of an obstacle is accelerated, thus reducing the pressure on the stream wise and leeward surfaces (MacDonald, 1975; Cook, 1985; Holmes, 2001).

The wind's dynamic pressure on the surface is a function of the pressure coefficient[10] (Cp), the air density, and the square root of the wind speed, which means that it increases considerably when the wind speed increases with height. Therefore, the differences in pressure between the sides and surfaces of buildings in the urban environment are related to the type and position of the building's opening and shape, and the wind speed and direction (MacDonald, 1975; Cook, 1985; Holmes, 2001; CIBSE AM10, 2006). Conversely, wind is not steady-state; they change their intensity and direction constantly, from still-air to gust speed peaks. Further, airflow speed varies according to its height above the ground, in accordance with the terrain's roughness, and the atmospheric boundary profile. As a consequence, the pressure distribution over a building's envelope also varies (CIBSE A, 2006). For this reason, time-averaged values are usually considered when determining the airflow field in open spaces, in the urban environment, and the resultant dynamic pressure on the building's envelope (CIBSE AM10, 2007).

4.4.2.1. The discharge coefficient (Cd)

The discharge coefficient (Cd) is a dimensionless number that acts through the opening of a building and affects the flow rate between external and internal environments. It is a function defined by differences of temperature, the flow Reynolds number, and the external air speed and direction. The Cd values given in the literature usually range from 0.60 to 0.80 for crossed-side and from 0.25 to 0.60 for single-side ventilation (ASHRAE, 2001; Awbi, 2003; Santamouris, 2006b; CIBSE AM10, 2007; CIBSE A, 2006).

Recent studies conducted by Kurabuchi *et al.* (2004 and 2006) and Ohba *et al.* (2006) explored the relationship between building porosity and the Cd value. The results show that the Cd value increases moderately in accordance with a building's porosity. For building porosity from 0.4% to 64.0% the Cd increase ranges from 0.61 to 0.68, respectively, under stagnant surrounding conditions. On the other hand, Heiselber and Sandberg (2006) have shown that the Cd cannot be considered as a constant and that its number is very difficult to define. Those authors have found Cd values ranging from 0.6 to 0.8 for windows with opening areas of from 0.5 to 0.6m^2. For smaller opening areas the Cd values found ranged from 0.8 to 1.0.

4.4.3. Buoyancy-driven ventilation

A buoyancy-driven force is created by the pressure differences due to air density variation resulting from temperature disparity. Warm air is less dense and thus lighter than cold air and tends to rise, being replaced by cooler air, which creates an airflow

[10] For more details about how to calculate Cp values and wind in urban areas see Topic 2.4 in Chapter 2.

current (Frota, 1995; Awbi, 2003; Masi and Ochoa, 2005). If the indoor air temperature is warmer than the outdoor, the internal air will rise and escape from the existing upper opening, while fresh colder air is supplied by the lower openings. On the other hand, when the indoor air temperature is lower than the outdoor, the flow can be inverted and a negative stack effect occurs, whereby the colder air inside escapes at a lower level and the warm air enter through the higher openings (CIBSE B1, 2002).

The difference in the air density is proportional to the temperature variation from the inside to the outside and from the bottom to the top of a building, and the indoor space's ceiling height, which results in pressure differences and consequently in movement of the air. Usually in buoyancy-driven ventilation systems the air inlet is positioned low down or even under the floor, while the air outlet is positioned much higher, even above the ceiling. In this type of ventilation, air temperature stratification is unavoidable (Awbi, 2003). The maximum recommended vertical gradient of air temperature stratification should vary by 3K from the feet to the head of a seated occupant, or by a maximum of 30 to 50% of the supply-to-exhaustion temperature variation in office applications for a range of 7 to 10K (Fanger, 1988). Otherwise, users may feel a draught and thermal discomfort. Furthermore, it is stated that better results are achieved when the ceiling height is greater than 3 meters and the inlet/ outlet openings are positioned on opposite sides, in order to create a transverse air current across the whole internal environment (CIBSE B1, 2002).

4.4.3.1. The neutral pressure line (NPL)

In an internal environment with temperature stratification, the neutral pressure line (NPL) occurs where the pressure of the cooler air, denser and heavier, and usually lower down, is equal to that of the warmer air, less dense and lighter, and thus above it. According to this picture, below the NPL the air pressure gradually decreases and, conversely, above it the pressure increases (Awbi, 2003; CIBSE AM10, 2007; Ghiaus and Roulet, 2005). If there is no source insufflating or purging air or no air jet in the ambient, then the air flows from the cold side to the warm side below the NPL and from the warm side to the cold side above the NPL. If the inlet and the outlet openings have the same area, the NPL lies exactly equidistant from and between. On the other hand, when the openings are of variable area or a window is open or closed, the airflow tends to create equilibrium according to the physical laws of flow equation and mass conservation and the NPL will adjust its position in accordance with this new pressure difference. Thus, the NPL tends to move towards the larger opening. For example, if the inlet area is greater than the outlet, then the height of the NPL drops (ASHRAE, 2001; Masi and Ochoa, 2005; CIBSE AM10, 2007; Ghiaus and Roulet, 2005).

Figure 4-5: Example of the NPL and the stack pressure in a multi-store building without vertical connection:

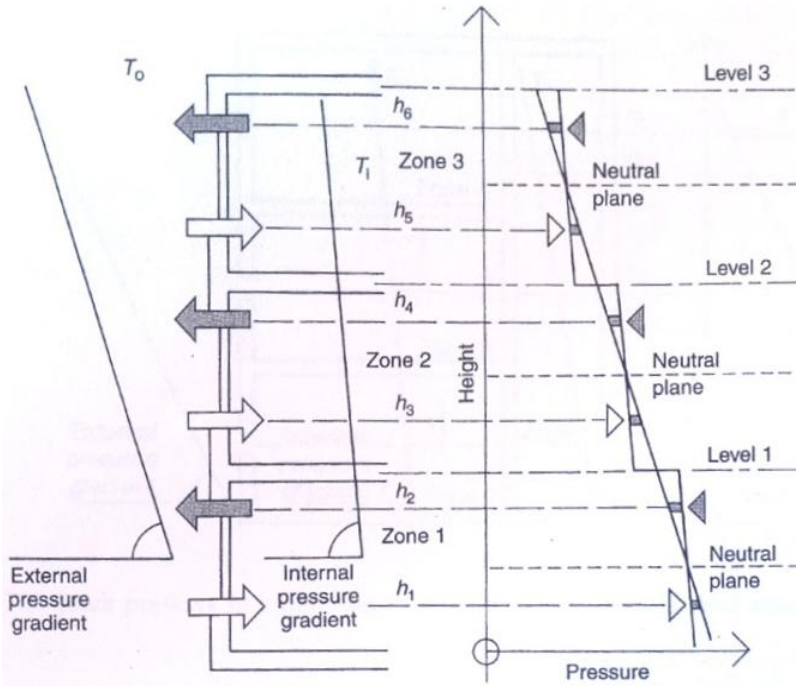

Source: Awbi (2003, pp314).

Figure 4-6: Examples of NPL for stack buoyancy pressure (A), wind pressure (B), and both stack and wind pressures combined (C):

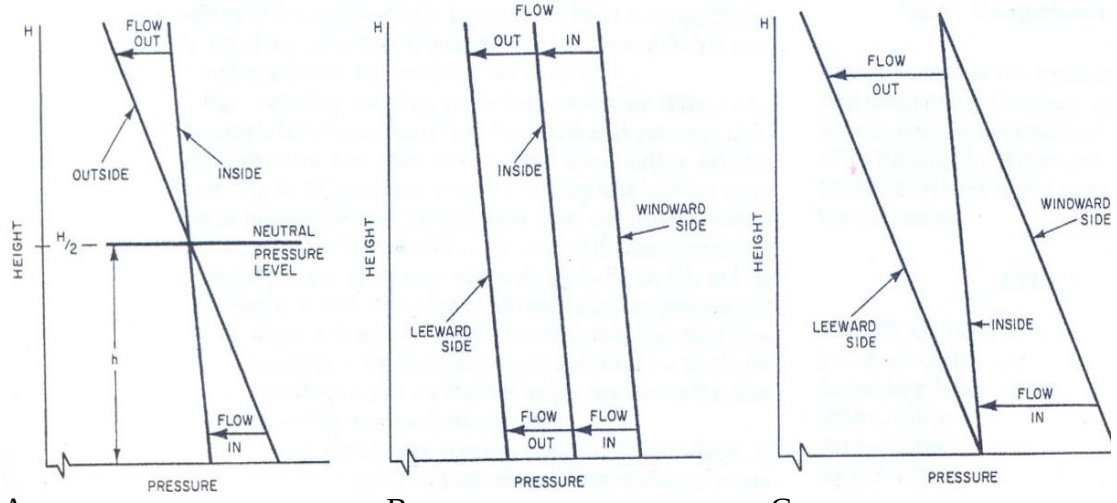

A B C

Source: ASHRAE (2001, pp26.7).

4.5. Natural ventilation strategies

Natural ventilation strategies act as a tool to minimize the built environment's energy consumption by replacing artificial HVAC by natural convection techniques (Keeping and Shiers, 2004). Strategies for natural ventilation comprise: single-sided openings and double-sided cross ventilation openings for wind-driven forces; stacks, solar chimneys, atriums, and wind-catchers for buoyancy-driven forces; and the combination of these two driving forces in several modes.

Most of the passive techniques employed in bioclimatic or free-running buildings make use of one or more of these natural ventilation strategies, directly or indirectly, for example: double-skin façades, night cooling purging, evaporative downdraught cooling, heat recovery, and ground cooling.

A successful choice of the natural ventilation strategy has to take the local microclimate and the prevailing wind directions, the surrounding urban environment, and the internal floor-plan layout into consideration in order to determine which are the forces acting in the system and which approach will be the best for this combination of factors. Eventually, the selection of one or a combination of several natural ventilation strategies will lead to a the decision regarding several aspects of the question, including: window-wall ratio; façade openings and internal volume ratio (porosity); room depth and ceiling height; mechanization and control of openings; and façade composition and elements, such as type and size of openings, sun-breaks and balconies. These choices will be decisive in the functioning of the ventilation strategy.

4.5.1. Ventilation devices commonly used in office buildings

Several authors and guidebooks have described different types and sizes of windows and other ventilation devices commonly used in office buildings, and provide recommendations as to their respective airflow speed and direction and performances (Chandra *et al*., 1986; CIBSE AM10, 2007; Roulet, 2005). The most frequently mentioned types of window and other devices, and their effective opening area (when such data are available), are:

- Trickles and vents for background ventilation;
- Horizontal and vertical sliding sash (effective opening area of 50%);
- Top-hung, side-hung and bottom-hung (effective opening area of 30%);
- Top-hung projection (with effective opening area similar to that of top-hung windows, but since they slide down a little when open, they create a larger opening at the bottom and a smaller one at the top);
- Horizontal and vertical pivot hung (when at 22^{o} the effective opening area is 34%, though it may achieve much more);
- Horizontal louvers;
- Venetian blinds;
- Wind-catchers;
- Stacks, and
- Solar chimneys.

Usually windows are vertically positioned across the façade of office buildings, since external wind moves mostly parallel to the ground. On the other hand, in packed

urban centers, such as urban canyons, vortices and wind effects should be considered as well. Also, skylight top-hung windows may be used in oblique roofs and mansards as ventilation and lighting devices. Wind-catchers and solar chimneys are usually positioned above the line of detachment flow at the top of buildings.

4.5.2. Single-sided single openings

Single-sided ventilation consists of only one opening which connects two environments: the external and the internal. Although this is the most common natural ventilation system used in small office units, single-sided ventilation may not be efficient for cooling purposes if it is not properly designed. Further, when this single opening is closed, ventilation is completely eliminated.

Since the flow through the window can take place as a result either of wind-driven or buoyancy forces, the efficiency of single-side openings is related to the pressure differences they create. In this case, this role is related to the type, shape and size of the window. Therefore, in order to attain the objectives set by the ventilation strategy, the window's characteristics have to be carefully chosen in the light of the internal and external temperature variations, and the external mean wind velocity and direction.

For example, when working with wind-driven forces alone or with a much higher pressure than that of the buoyancy-driven forces, a possible option would be to have two different vertical openings, since they will create positive and negative pressure zones on the same façade, especially as far as oblique wind direction is concerned. This same effect could also be achieved with vertical pivot windows or two lateral panels and even with two or more windows side by side. Vertical sliding sash windows are an option if both panels can move in such a way as to create openings on both sides of the frame. Further, CIBSE AM10 (2007) explains how, due to the continuous variation in the external wind speed and direction in urban areas, the external pressure variation on single-sided windows caused by fluctuation in turbulence will alter the internal/ external pressure difference across the window, resulting in airflow and ACH rates adequate for small spaces.

Further, architectonic façade elements and the building shape can be used as means of enhancing potential single-sided opening ventilation. Buildings of irregular shape and positioning of openings across the building (while maintaining the same areas for inlet and outlet); the roughness and porosity of the surface materials; architectonic elements such as wing-walls, balconies, sashes, sun-breaks, light-shelves and ornaments; and certain indentations on the façade may contribute to the creation of pressure difference between openings, mostly for oblique winds (Olgyay, 1963; Melaragno, 1982; Chandra *et al*., 1986; Givoni, 1998a; Koch-Nielsen, 2002; Masi

and Ochoa, 2005; Ghiaus and Roulet, 2005; Santamouris, 2006b, Khan *et al*, 2008). Given that still-air or weak wind conditions are frequent in urban environments and that, on the other hand, an isothermal state is rare in office buildings, some ventilation mechanism using wind-driven and buoyancy forces alone or combined windows would be the best option for single-side openings. Options in this case would include the use of horizontal pivot hung windows with the top side open to the outside or top-hung projection windows, allowing the wind-driven airflow in on the lower side but blocking it on the higher side, where the warmer air comes out due to air density variation. Two different panels of windows positioned horizontally (horizontal sliding sash windows and horizontal louvers) would produce a similar effect as well, but wind from outside may act against the internal purging of warm air at the top (CIBSE B1, 2002; Ghiaus and Roulet, 2005; Ghiaus and Allard, 2006). Finally, recent studies have shown that the worst type of window for ventilating single-sided single opening internal environments is the top-hung one. On the other hand, this is the most commonly used type of window in skin-glazed office building envelopes nowadays (Romero and de Faria, 2004).

4.5.2. Dimensioning single-sided single opening flows

The ratios of internal space and opening dimensions considered as the limit for single-sided ventilation efficiency are (Awbi, 1998b):

- Maximum of 1/2.5 between ceiling height and room depth; and
- Minimum of 1/20 between window area and floor area.

For wind-driven forces acting only, the equation for single-sided flow is (Bansal *et al.*, 1993; Etheridge, 2000a and 2000b; ASHRAE, 2001; Holmes, 2001; Awbi, 2003; Sandberg, 2004; CIBSE AM10, 2007; Santamouris, 2006):

Equation 4-8 $$Q_{wind} = Cd * A_{eff} |2\Delta P/\rho|^{0.5}$$

Where:

- Q_{wind}: is the airflow due to wind-driven force (m^3/s);
- Cd: the discharge coefficient[11] (from 0.25 to 0.60);
- A_{eff}: the effective opening area (m^2);
- ρ: the air density (kg/m^3); and

[11] This range of Cd values is related to the fact that the single-sided window may have one opening, with inlet and outlet flows opposing each other, or two openings, with separate inlet and outlet flows. Thus it is that the respective Cd values used are 0.25 and 0.60 (CIBSE AM10, 2007).

- ΔP: the pressure difference between inside and outside (Pa), calculated in accordance with the Bernoulli equation as follows (MacDonald, 1975; Cook, 1985; Holmes, 2001; Awbi, 2003):

Equation 4-9 $\Delta P = \frac{1}{2}\rho * \Delta Cp * V_{ref}^2$

Where:

- ΔCp: is the pressure coefficient difference from outside and inside[12];
- ρ: the air density (kg/ m^3); and
- V_{ref}: is the wind velocity at a reference point (m/s).

Further, it is possible to consider an equation from ASHRAE (2001) for calculating airflow rates to adjust the effective open area of a window:

Equation 4-10 $A_{eff} = C_v * A_{opening}$

Where:

- C_v: is the factor of effectiveness of openings, and ranges from 0.50 to 0.60 and from 0.25 to 0.35 for orthogonal and diagonal winds, respectively; and
- $A_{opening}$: is the free area of the inlet opening (m^2).

Buoyancy effects occur where air stratification due to temperature differences occurs. For buoyancy-driven forces acting alone, the equation for single-sided flow is (CIBSE B, 2005; CIBSE AM10, 2007):

Equation 4-11 $Q_{buoyancy} = Cd * A_{eff} |(T_i + 273)/(\Delta T * H * g)|^{0.5}$

Where:

- $Q_{buoyancy}$: is the airflow due to buoyancy-driven force (m^3/s);
- Cd: the discharge coefficient (from 0.25 to 0.60);
- T_i: the inside temperature (^oC);
- ΔT: the difference between outside and inside temperatures (K);

[12] For further information about how to calculate ΔCp see Topic 2.4.1 in Chapter 2.

- H: the height from the bottom of the lower opening to the top of the higher opening (m); and
- g: is the force of gravity (9.81m/s^2 at sea level).

Wide and tall windows present NPL in their open area in a single-sided ventilation internal environment, for example. This means that ventilation through the lower and upper vents of an inlet window are subject to this force, and this can oppose wind- and buoyancy-driven forces on the upper side of the window. In consequence, the desired airflow rate decreases. Awbi (1998) presents an equation for calculating the joint airflow ratio due to wind- and buoyancy-driven forces on single-sided single openings, as follows:

Equation 4-12 $$Q_{total} = 0.5|C_1 * V_{ref}^2 + C_2 * H * \Delta T + C_3|^{0.5} = |Q_{wind}^2 + Q_{buoyancy}^2|^{0.5}$$

Where:

- Q_{total}: is the combined airflow due to wind- and buoyancy-driven forces (m^3/s);
- C_1: a dimensionless coefficient depending on the opening's characteristics (around 0.001);
- C_2: a buoyancy constant (0.0035); and
- C_3: a wind turbulence constant (0.01).

There is also an empirical equation used for calculating air flow due to building envelope leakage, cracks or trickles (ASHRAE, 2001; Awbi, 2003; CIBSE AM10, 2007; CIBSE A, 2006):

Equation 4-13 $$Q_{leakage} = Cd\ A_{eff}\ (\Delta P_{leakage})^n$$

Where:

- $Q_{leakage}$: is the the airflow due to leakage (m^3/s);
- Cd: the discharge coefficient (from 0.60 to 0.70);
- $\Delta P_{leakage}$: the outside to inside pressure difference due to the leakage; and
- n: a dimensionless variable (from 0.60 to 0.70).

4.5.3. Double-sided cross ventilation

Wind induced cross- or double-sided ventilation consists of two or more openings connecting one or more internal environments, in one of the passages on which there is an air inlet and in the other an outlet. External wind across a building creates positive pressure to windward and negative pressure to leeward, thus establishing a pressure difference between the two openings and across the internal space which, consequently, results in the crossed airflow (CIBSE AM10, 2007; Ghiaus and Roulet, 2006). Further, the ceiling height/ room depth 1/5 ratio is considered the limit for efficient cross ventilation to occur (Awbi, 2003). Based on these internal space dimensions, the best ventilation results are obtained either in narrow linear buildings, where windward and leeward pressure differences are considerable, or in robust buildings with internal atriums. In this latter case, the difference of pressure between the inlet on any side of the building and the courtyard must be ensured by openings of such a size as will maintain the direction of flow from the outside to the inside and then on to the atrium, even on the leeward side. Further, the best results are obtained with open-plan layout offices with internal partitions up to 1.6m of height (Givoni, 1994 and 1998a; CIBSE AM10, 2007). Other options for ensuring natural cross ventilation or enhancing its effects include air inflow resulting wind-catchers and outlet with solar chimneys, self-regulated vents for pressure control, and double-skin façades (Ghiaus and Roulet, 2006), all of which are covered later in this chapter.

As for single-sided ventilation systems, when cross-ventilation strategy is under consideration several decisions need to be taken related to the building's design and aspects which may affect the external pressure distribution either positively or negatively and, consequently, affect the cross-building pressure difference. The factors acting against cross ventilation relate to the fact that external winds vary their velocity and direction constantly, changing the pressure coefficient and differences on the façades, resulting in a drop in stable efficiency rates or changing the inlet/ outlet vector direction in consequence (Ghiaus and Roulet, 2006). It is, therefore, essential to be in possession of wind data from close to the project site in order to be able to design cross ventilation adequately, since assessments made on the basis of data from distant sites may lead to error. Moreover, turbulence caused by other buildings and the decrease of wind speed in the urban environment have to be considered in the calculation of the ventilation rates.

Regarding the IAQ, another shortcoming of this technique is that the ACH into the outlet environments will involve the polluted air from the other internal areas of the building. As a result the ACH sum has to consider the dilution of all the internal contaminants and odors through each and every one of the internal spaces (Ghiaus

and Roulet, 2006). The simulation of the airflow pattern due to natural cross-ventilation in an internal space of 5.5x5.5x3.0m was undertaken in a full-scale wind tunnel by Nishizawa *et al.* (2008). The internal space was divided into four equal rooms by a central vertical cross-shaped partition, and the openings were positioned on opposite sides and diagonally, close to the corners of the walls. The focus was on the internal airflow patterns arising between the inlet and the outlet and through the internal division. The results concentrated on ACH rates and internal air velocity distribution. Different external wind directions at the same air velocity were considered as input. The results on the horizontal plane at 1.0 meter height are given in the sequence:

Table 4-2: Airflow distribution on horizontal plane at 1.0m height

Wind Angle	Internal airflow path	ACH	Wind speed in each room (m/s)			
			A	B	C	D
15°	A > B > C	141	0.70	0.70	0.60	0.10
45°	A > (B/D) > C	101	0.80	0.45	0.50	0.45
75°	A > D > C	72	0.25	0.18	0.30	0.17
105°	C > D > A	24	0.20	0.15	0.40	0.28
135°	C > D > B > A	43	0.25	0.35	0.80	0.30
165°	C > D > A	86	0.60	0.20	0.75	0.70

Source: Nishizawa *et al*. (2008).

The results presented show that the internal flow is more homogeneous along the internal path. The airflow distribution is better when the external airflow occurs at 45° incidence to the openings and the internal central column divides the airflow internally symmetrically in two directions. Despite the reduction in ACH as compared with that due to prevailing winds from 15° incidence, the higher mean velocity in all the rooms in this first case indicates that the air is spread uniformly. According to Nishizawa *et al.* (2008), the limitations of this study are related to the external shape of the building (they consider it in isolation from other volumes) the position of the openings selected (only one), the depth of the room (only 5.50m for cross-ventilated space) and the existence of a column dividing the internal environment into four cells (too small for the reality of open-plan buildings). On the other hand, this last characteristic can be exploited as a wind-deflector to control natural ventilation.

4.5.3.1. Dimensioning double-sided single opening flows

For double-sided openings and the wind forces acting, the flow is calculated on the basis of the difference between the pressure at the inlet and that at the outlet. The pressure across the building can be calculated from the difference between the ΔCp to the windward and leeward (or lateral faces), in accordance with the following equation (Ghiaus and Roulet, 2006):

Equation 4-14 $P_{wind} = ½\rho * V^2 (Cp_{ww} – Cp_{lw})$

Where:

- Cp_{ww}: the pressure coefficient on the windward side; and
- Cp_{lw}: the pressure coefficient on the leeward side.

The resultant air flow due to cross ventilation through buildings is a product of the areas of the openings, the discharge coefficient and the ΔCp from the inlet to the outlet, as shown in the following equation (Etheridge, 2002 and 2004; CIBSE AM10, 2007; CIBSE A, 2006):

Equation 4-15 $Q_{wind} = Cd * A_{eff} * V_{ref} |Cp_{WW} – Cp_{LW}|^{0.5}$

Where:

- Q_{wind}: is the airflow due to wind-driven force (m^3/s);
- Cd: the discharge coefficient (from 0.6 to 0.8);
- A_{eff}: the effective opening area (m^2);
- V_{ref}: the wind velocity at the reference point (m/s);
- Cp_{WW}: the pressure coefficient on the windward side; and
- Cp_{LW}: the pressure coefficient to leeward.

4.5.3.2. The effective open area for cross ventilation

The effective open area for calculating airflow rates due to cross-ventilation takes into consideration all the external and internal openings involved in the airflow path throughout the building. For openings within the internal environment, the effective opening area is inversely proportional to the sum of all the openings displayed in series, as shown in the equation given (Frota, 1995; Awbi, 1998; CIBSE A, 2006):

Equation 4-16 $1/A_{eff}^{2} = 1/A_1^{2}+1/A_2^{2}+1/A_3^{2}+\ldots+1/A_n^{2}$

Where:

- A_{eff}: is the effective opening area (m^2); and
- $A_1, A_2, A_3, \ldots, A_n$: the areas of the several openings within the building (m^2).

On the other hand, for openings that are side by side, the simple sum of their areas provides the effective open area (Awbi, 1998):

Equation 4-17 $A_{eff} = A_1+A_2+A_3+\ldots+ A_n$

Holmes (2001) provides also an equation for calculating the pressure coefficient inside the building based on the external Cp difference and the sum of the effective opening area on both windward and leeward sides:

Equation 4-18 $Cp_{inside} = Cp_{WW}/[1+(A_{LW}/A_{WW})^2+Cp_{LW}/[1+(AW_W/A_{LW})^2$

Where:

- Cp_{inside}: is the internal pressure coefficient;
- Cd: the discharge coefficient (from 0.6 to 0.8);
- A_{WW}: the effective opening area on the windward side (m^2); and
- A_{LW}: the effective opening area to leeward (m^2).

Finally, Sandberg's (2004) research has shown that traditional Cp values are valid for well-sealed envelopes or closed windows (low porosity), since under these conditions the airflow has no alternative but to go round the building. For buildings and structures with large openings or porosity rates, the wind may either go round or pass through the internal environment. Under such conditions both the pressure coefficient value drop and the abbreviation of the leeward wake flow were observed.

Figure 4-7: Pressure drop from inlet to outlet openings[13]:

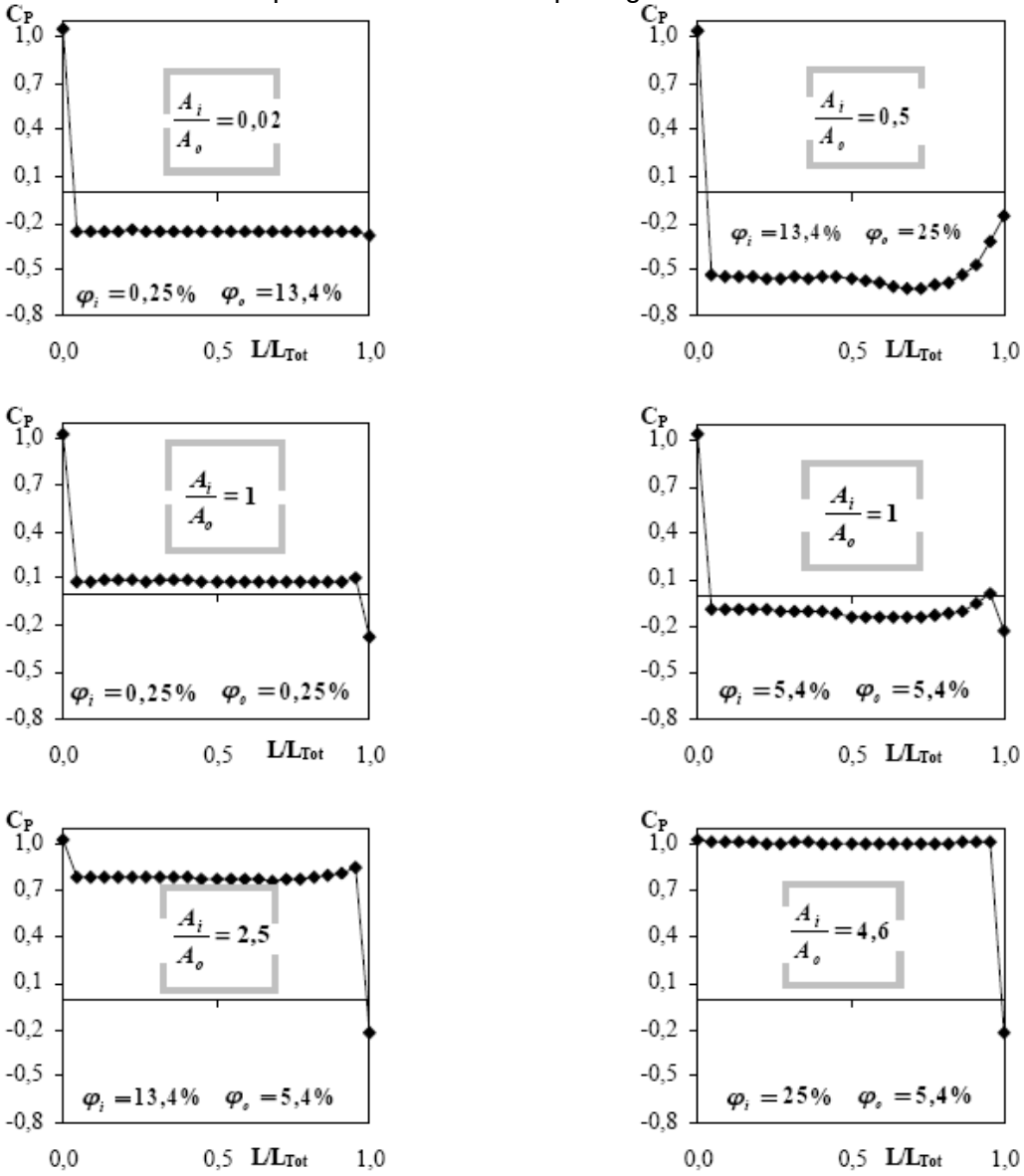

Source: Sandberg (2004, pp416).

4.5.4. Wind catchers

Wind-catchers or scoops are devices placed above the rooftops of the buildings which capture high velocity winds. These devices are another possibility for achieving cross-ventilation in buildings.

The BSRIA Guide for wind-driven natural ventilation systems (Parker and Teekaram, 2005) suggests that the section of the duct of the wind catcher area be subdivided into several vertical panels in such a way that at least one of the open areas of the scoop will be facing the prevailing wind direction orthogonally. The inlet opening will thus receive the cool and fresh air at the inlet and the other openings will be

[13] The parameter L/L_{tot} employed in the graphs presented in Figure 4-7 represents the distance length of building (L) divided by the total length of building (L_{tot}) (Sandberg, 2004, pp418).

naturally positioned to the leeward low pressure side for purging the stale and warmer air. This guide also provides pressure coefficient values at the inlet for orthogonal winds. The values range from 0.50 to 0.99, with an average of 0.85. It is possible to conclude that these Cp values are valid either for open country areas or for scoops positioned at great heights, for instance, above the urban canopy layer. In addition, pressure drops in the ducts have to be taken into consideration in the calculation of the airflow rates when using wind-catcher devices (CIBSE AM10, 2007).

Figure 4-8: Patent of a ventilator and wind cowl from the 19th century:

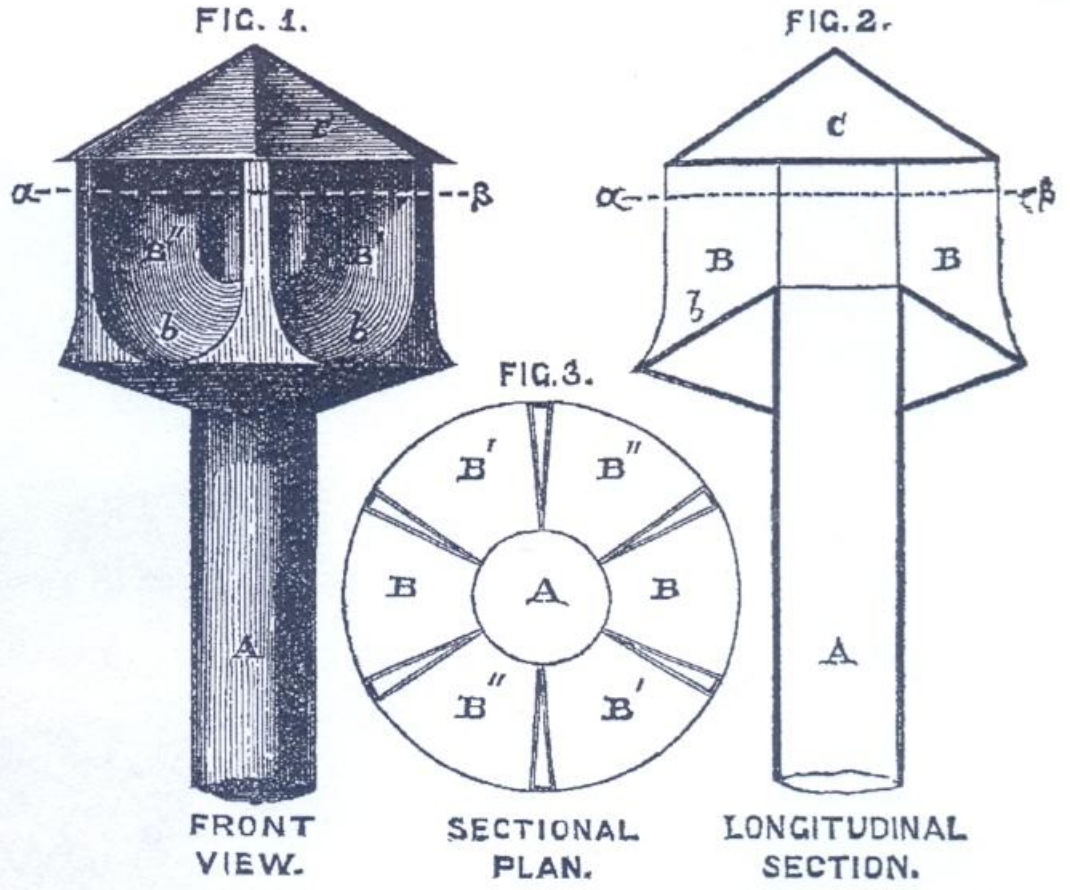

Source: The Lancet (1880, pp462).

Regarding the discharge coefficient for wind-catchers and stacks, investigations conducted by Costola and Etheridge (2008) point out that, for still-air conditions, the Cd ranges from 0.25 to 0.30 on both the windward and leeward sides. For windy conditions Cd values vary according to the airflow Reynolds number. Costola and Etheridge (2008) present windward Cd values ranging from 0.30 to 0.50 with the leeward side maintaining the same initial range of values. In contrast, other researchers (Bansal *et al.,* 1994; Germano *et al.*, 2005a and 2005b) refer to higher windward Cd values, ranging from 0.60 to 0.80 for stack inlet openings under wind conditions. As regards the shape of the inlet opening of wind-catchers, Erell (2007)

also mentions that square openings with oblique internal partitions at 30^{o} or 45^{o} may enhance the down flow, but the author provides no Cd values for this option. Pearlmutter *et al.* (1996) assessed the relationship between the shape of the inlet opening and internal partition for wind-driven and fan-assisted stacks. The results show that curved internal partitions are the most efficient for orthogonal winds.

Figure 4-9: Inlet shape and performance of wind-catchers:

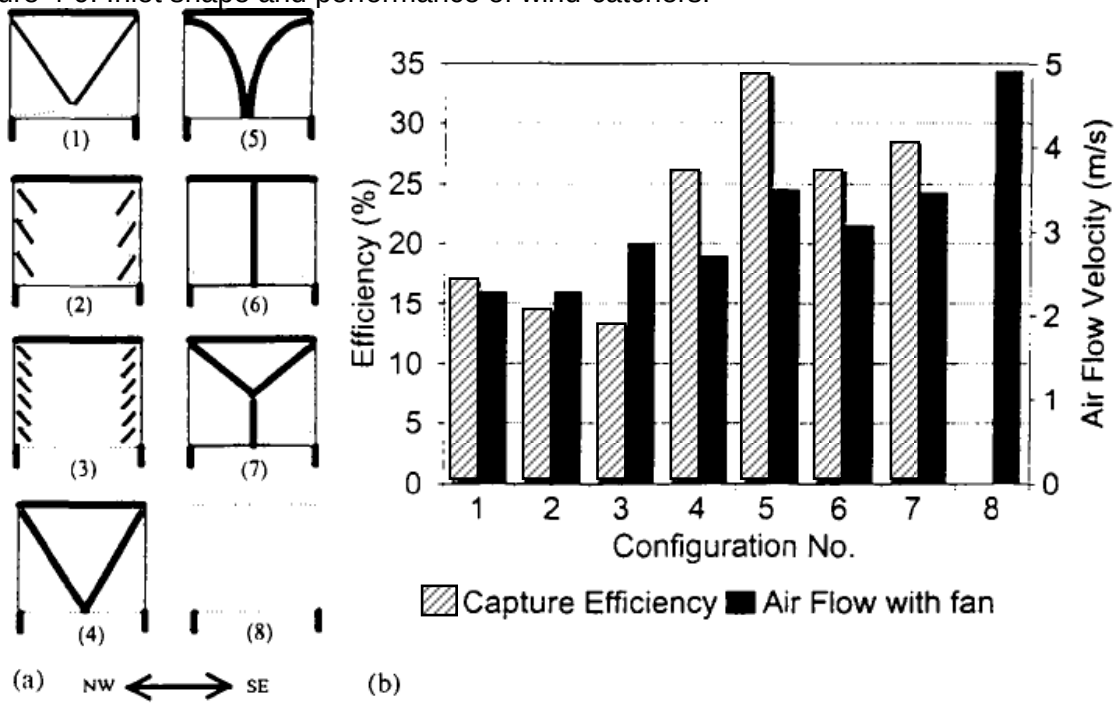

Source: Pearlmutter *et al*. (1996, pp196).

Sun *et al* (2008) who undertook investigations with wind-tunnel and CFD with a wind-catcher of 0.60m diameter and 1.30m height, relate that the performance of airflow rates is practically the same for impinging orthogonal or 45^{o} winds. This experiment considered thermal differences and buoyancy-force in the removal of the air. By analyzing the graphs it may be concluded that the ventilation rate for this type of device is proportional to the external airflow speed. For example, for wind speeds of 2m/s the airflow rate found using the wind tunnel ranged from 10.0 to 16.0l/s while at of the CFD was of 14.0l/s, whether for orthogonal or oblique winds. Another option for wind-catcher devices would have a cowl that enables them to turn into the wind whatever direction it comes from. Finally, the pressure difference and the resultant air flow across the building due to wind forces using wind catchers and scoops can be calculated in accordance with the equations 4-14 and 4-15.

Figure 4-10: airflow variation due to increase of wind speed

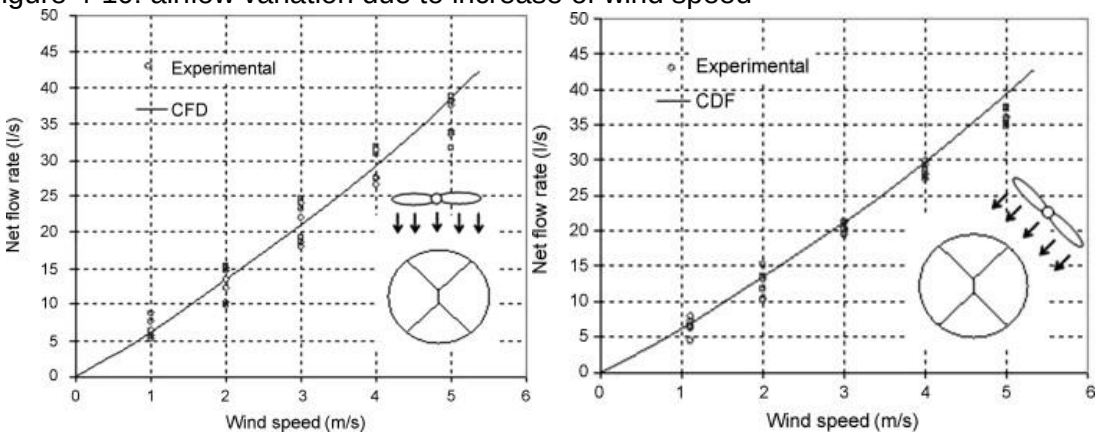

Source: Sun *et al.* (2008, pp1113).

Figure 4-11: Revolving wind-scoop device:

Source: Canadian Architect webpage[14].

4.5.5. Stack ventilation

Stack forces are based on the hydrostatic pressure difference due to air temperature variation. A warm, humid air column is lighter and less dense than a cold, dry one, tending to rise and be replaced by a cooler one. The stack pressure is also related to the distance or height between the inlet and the outlet (ASHRAE, 2001). Usually in this technique the inlet opening is placed low down and the stack outlet is positioned above rooftop height.

Under still-air conditions and when the internal temperature is higher than the external one, the flow is upward. Conversely, when the external environment is warmer than the internal one, the flow is downward. Further, in constrained spaces or with

[14] Link accessed in 09/07/2011: http://www.canadianarchitect.com/asf/principles_of_enclosure/environmental_mediation/environmental_mediation.htm

small, low outlet openings the ascending flow creates a consequent upward and downward vortex (CIBSE AM10, 2007). Under windy conditions, then the airflow inlet should face into the wind and the stack outlet to leeward in such a way that both wind- and buoyancy-driven pressure effects act together, thus increasing the ventilation rates. Since buoyancy pressure alone is small, it requires large ducts and/ or outlet openings in order to be efficient (Germano *et al.*, 2005a and 2005b).

The buoyancy pressure is proportional to the difference in temperature between the bottom and the top of the stack, and increases with temperature and/ or height range. The pressure also increases with the vertical distance to the NPL, which, in its turn, depends on the height of the stack duct.

Several authors present equations for calculating the pressure difference due to stack effect (Bansal *et al.,* 1994; Awbi, 1998 and 2004; Etheridge, 2002; Ghiaus and Roulet, 2006; Germano *et al.*, 2005a and 2005b). All their equations are based on the Bernoulli principle of isothermal condition and steady-state for a reference temperature. Etheridge (2000b) also provides a time-averaged airflow calculation model. Awbi's (2003) equation is presented here:

Equation 4-19 $\Delta P_{stack} = \rho_o * T_o * g * H_{stack}[1/(\Delta T_{outside} - \Delta T_{inside})]$

Where:

- ΔP_{stack}: is pressure difference due to stack effect (Pa);
- ρ_o: the air density reference (kg/ m^3);
- T_o: the temperature reference (K);
- H_{stack}: the height from the bottom to the top of the stack (m).
- $\Delta T_{outside}$: the temperature variation outside (K); and
- ΔT_{inside}: the temperature variation inside (K).

For calculating the airflow rate due to stack pressure there is also difference for equations to be found in the literature (Bansal *et al.,* 1994; Frota, 1995; Gan and Riffat, 1998; Etheridge, 2000a and 2000b; Cook *et al.*, 2003; Hunt and Syrios, 2004; Linden and Kaye, 2006; Ji *et al.*, 2007; Costola and Etheridge, 2008). For instance, the CIBSE Guide AM10 (2007) gives greater weight to the effect of wind-driven forces at the inlet than the buoyancy forces at the outlet. Two sets of equations for stack induced airflow will be presented here: that of Germano *et al.* (2005a and 2005b); and Elmualim *et al.* (1999) in, respectively, equation 4-20 and equation 4-21. The former considers both

the temperature variation and the height differences between the room and the stack. A loss coefficient based on the stack inlet/ outlet area and its discharge coefficient is added to the last equation.

Equation 4-20 $Q_{stack} = Cd * A_{eff} |2 * g * H_s [(T_i - T_o)/(T_o - T_i)]|^{0.5}$

Where:

- Q_{stack}: is the airflow rate due to stack pressure (m^3/s);
- Cd: the discharge coefficient of the air inlet (from 0.6 to 0.8);
- A_{eff}: the air inlet effective opening area (m^2);
- H_s: the height of the stack (m);
- T_i: the temperature inside (K); and
- T_o: the temperature outside (K).

Equation 4-21 $Q_{stack} = Cd_i * A_i |[2g(\Delta T_i * H_i + \Delta T_s * H_s)]/[T_o(1+1/k^2)]|^{0.5}$

Where:

- Cd_i: is the discharge coefficient of the air inlet (from 0.6 to 0.8);
- A_1: the air inlet's effective opening area (m^2);
- ΔT_i: the temperature variation inside the room (K);
- H_i: the height of the air inlet above the bottom of the stack (m);
- ΔT_s: the temperature variation inside the stack (K);
- H_s: the height of the stack[15] (m); and
- k: the loss coefficient, calculated as:

Equation 4-22 $k = (Cd_s * A_s)/(Cd_i * A_i)$

Where:

- Cd_s is the stack[16] discharge coefficient (from 0.25 to 0.30); and
- A_s: the stack inlet's effective opening area (m^2).

A rule of thumb to obtain stack pressure recommends that the stack height should measure at least one and a half times the ceiling height. For example, the

[15] Where Hs ≥ 1 ½ Hi (CIBSE AM10, 2007).
[16] For more information, see Costola and Etheridge (2008) and section 4.4.2.1..

CIBSE AM10 (2007) states that for internal/ external air temperature variations from 1 to 5K, buoyancy-driven forces only can generate internal pressure differences from 0.2 to 0.5Pa and 0.5 to 1.75Pa when ceiling and stack height are of 3 and 10 meters, respectively. The following equation provides the minimum height of the stack above ceiling or roof necessary to avoid back-draught (Awbi, 2003; CIBSE AM10, 2007):

Equation 4-23 $H_o = d[0.5+0.16(R_{angle}-23)]$

Where:

- H_o: is the stack height outside (m);
- d: the distance from the stack outlet to the highest point of the roof;
- 0.5: the minimum height of the stack above the roof (m); and
- R_{angle}: the inclination of the roof.

4.5.5.1. Solar chimneys

Solar chimneys are devices that enhance the performance of stacks by concentrating the heat gains from direct solar radiation on the top (outflow) surface of the stack. When its surface is heated, the internal air is warmed by convection and radiation, thus increasing the vertical pressure difference in the system (Bansal *et al.,* 1994; Awbi, 2003; Santamouris, 2006 Kolokotroni and Santamouris, 2007). These devices were called sirocco rooms in Italian Renaissance architecture, in allusion to the hot Saharan wind blowing from North Africa. Nowadays some such device is under consideration for improving the performance of stack ventilation under low wind speed conditions by up to 50% (Santamouris, 2006).

For cooling ventilation purposes, when internal air is warmer than external, cool air will enter by the lower opening and warm air exit through the upper opening. The use of solar chimneys in warm climates keeps the air temperature close to that of the outlet stack and above that of the already external hot air. This avoids the undesirable reverse flow: when the internal cooler air exits from the lower opening, being replaced by warmer external air from the upper opening, in accordance with to the law of the conservation of mass (CIBSE AM10, 2007). Further, Kolokotroni and Santamouris (2007) mention that, in order to be effective, the solar chimney has to be somewhat longer than a simple stack so as to ensure air layer stratification sufficient to raise the pressure difference. Equation 4-20 does, therefore, seem more suitable for the consideration of the separate stack height and temperature variation for each floor.

Santamouris's (2006) findings show that the solar chimney provides a substantial improvement to the stack's performance especially when displaced at an angle of from 135^{o} to 180^{o} to the direction of the prevailing wind. The proper orientation towards the sun and the avoidance of external shading are also fundamental for ensuring the projected performance of this device.

4.5.6. Combining wind- and buoyancy-driven systems

Combining wind- and buoyancy-driven systems can achieve acceptable ventilation rates, though, if certain measures are not observed, one force may counteract the other, and thus hinder the performance of the system. Therefore, taking this fact into consideration and/ or combining both strategies in the building design will reinforce the positive results of both techniques.

Figure 4-12: Single- and cross-sided openings and the NPL:

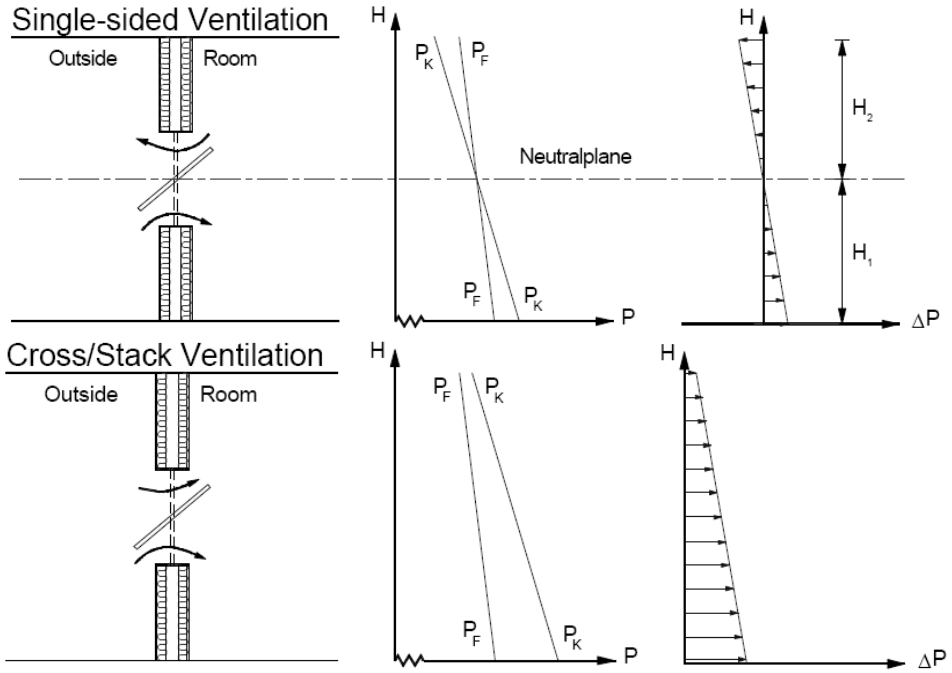

Source: Awbi (2003, pp321).

This concern implies setting both the windward and the inlet on the same side, which is valid also for the leeward and the outflow position[17]. Otherwise the flow may be reduced, canceled or even inverted. Also, the inlet should be placed at a low and the outflow at a greater height, in order to increase the temperature gradient and, in consequence, the pressure difference (Awbi, 2003). In this way, the ideal pressure loop

[17] For alternatives of stacks and chimneys openings and their performances regarding the wind direction see Figures 4-9 and 4-10 in section 4.5.4.

for the combined ventilation system has to consider also the difference of pressure throughout the internal space, as follows (Ghiaus and Roulet, 2005):

Equation 4-24 $P_{inlet\ -o} > P_{inlet-i} > P_{internal} > P_{outlet-o} > P_{outlet-i}$

Where:

- $_{-o}$: means outside; and
- $_{-i}$: inside.

In addition, according to Awbi (1998), and Ghiaus and Roulet (2005), the final pressure difference for both combined wind- and buoyancy-driven forces in this cycle can be represented as:

Equation 4-25 $\Delta P_{total} = \Delta P_{wind} + \Delta P_{stack} = \Delta P_{inlet} + \Delta P_{inlternal} + \Delta P_{outlet}$

Where:

- ΔP_{total}: is the total pressure difference in the system (Pa);
- ΔP_{wind}: the pressure difference due to wind forces (Pa);
- ΔP_{stack}: the pressure difference due to buoyancy forces (Pa);
- ΔP_{inlet}: the pressure difference at the inlet (Pa);
- $\Delta P_{internal}$: the internal environment pressure difference (Pa); and
- ΔP_{outlet}: the pressure difference at the outlet (Pa).

This equation can also be interpreted as the sum of terms of equations 4-13 and 4-17 for simple systems, as follows:

Equation 4-26 $\Delta P_{total} = ½\rho * \Delta Cp * V^2 + \rho_o * T_o * g * H_{stack}[1/(T_o - T_i)]$

Finally, it is possible to find the total airflow rates due to combined wind- and buoyancy-driven pressure differences by means of the equation (Awbi, 1998[18] and 2003; CIBSE B, 2005):

Equation 4-27 $Q_{total} = |Q_{wind}^2 + Q_{stack}^2|^{0.5}$

[18] Awbi (1998) also presents a specific equation for calculating the total airflow ratio for single-sided single openings.

Figure 4-13: Examples of combined wind- and buoyancy-driven ventilation techniques:

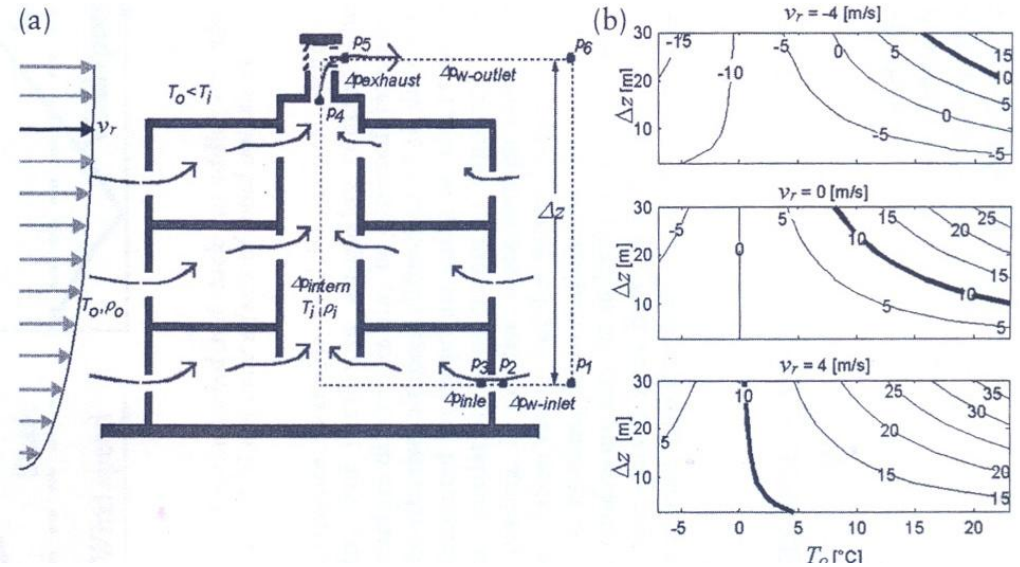

Source: Axley (2001) *in* Ghiaus and Roulet (2005, pp144).

4.5.6.1. Strategies for multi-connected internal spaces

Multi-storey buildings in which there are internal spaces connecting the floors are defined as multi-zonal ones. This integration between two or more floors may occur vertically (via a stairwell or a mezzanine) or horizontally, which means laterally, via atrium, stack, solar chimney, or double skin-glazed façade (Awbi, 2003).

As a consequence of this connection, air will flow from outside to inside through each floor window and/ or wind-catcher, cross an internal environment, pass through one or more of these connecting volumes of air and then either leave the building or go to another internal environment and eventually be purged through an outlet opening. In the first scenario, the pressure loop presented in equation 4-24 is preserved. On the other hand, in the second case, this loop allows air recirculation from one floor to another. This is regarded as an adverse effect for a ventilation system, since it destabilizes both IAQ and thermal comfort strategies. In terms of pressure loop, the ideal pressure drop and airflow path can be described by:

Equation 4-28 $P_{inlet\text{-}o} > P_{inlet\text{-}i} > P_{internal} > P_{connection} > P_{outlet\text{-}o} > P_{outlet\text{-}i}$

In accordance with to what was has been described in item 4.4.3 of this chapter, buoyancy acting alone causes the air to flow from the cold side to the warm side below

the NPL and in the inverse direction above the NPL. This means that when the external air temperature at ground level is cooler than the internal temperature, below the NPL the air flows from outside/ inside and above it the opposite prevails. This has to be borne in mind when natural ventilation is adopted for multi-connected zone buildings, since the floors above the NPL will receive warmed air with high rates of pollution concentration from the other internal spaces (Ghiaus and Roulet, 2006).

Therefore, for multi-storey office buildings with multi-connected internal spaces, where the same airflow rate is required for all floors, various considerations have to be addressed. For instance, the NPL must be above the roof of the upper floor, in order to avoid the floors' above the NPL working as airflow outlet. This can be achieved by making the top outlet opening as large as possible and placing it as high as necessary, since it will move the NPL upwards (Awbi, 2003; CIBSE AM10, 2007). In addition, when the top surface of an atrium is covered, the whole volume of air can act as a solar chimney. In this case, solar baffles or vertical fins should be added to increase the absorption of solar radiation. This increase of air temperature at the top of the outlet helps to raise the NPL (CIBSE AM10, 2007).

In addition, the effective area of the windows and openings must vary with both height and wind direction in order to permit the same air flow rates through the occupied internal environment of all the floors. This is necessary since the lower floors present a greater stack pressure gradient than the upper ones. Also the wind pressure is greater on the windward façade than on the lateral and leeward envelopes. As a consequence, the opening sizes have to be counterbalanced throughout the several façades and floors of the building in order to ensure the same airflow rates and the outside/ inside direction (Germano *et al.*, 2005a and 2005b).

The CIBSE Guide B1 (2002) also alerts to the possibility of façade leakage in buildings located in warm climates. Since there is no concern with heat loss, the leakage is not as apparent as it would be in cold weather. But the cracks and vents in the envelope may result in a drop of pressure that affects the NPL. If the building envelope is not as well sealed as was originally intended, the natural ventilation will also differ from the plan.

4.5.6.1.1 Multi-connected vertical zones

Building spaces are connected vertically when two or more floors are directly open to each other through a horizontal gap. This happens with stairwells, horizontal voids and mezzanine floors joined with double floor-height spaces. In this case, it is foreseen that the air will circulate from one zone to another, though this flow has to be maintained within the building.

Figure 4-14: Example of a building with inter-connected vertical zones:

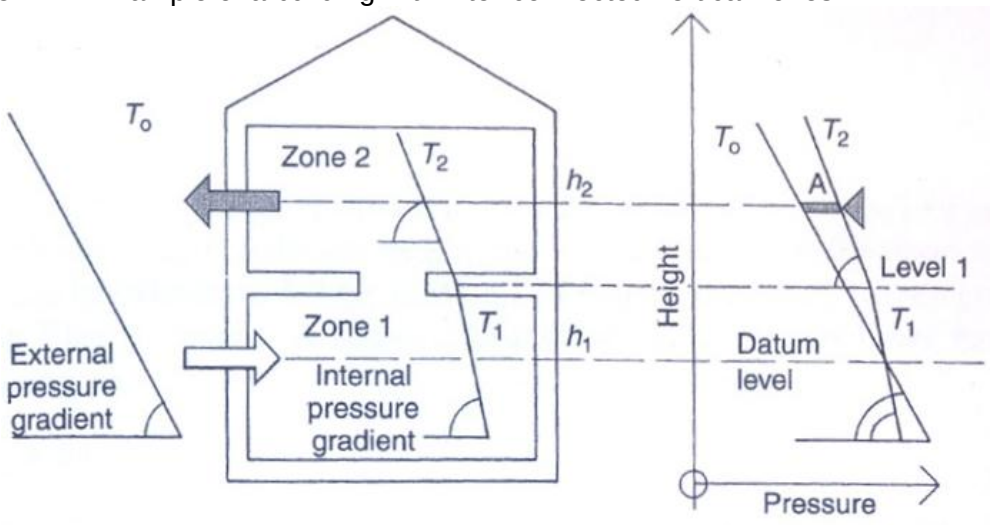

Source: Awbi (2003, pp315).

Awbi (2003) emphasizes that it is to be expected that the mean temperature of from the upper floors or zones should be higher than that of the lower ones, creating a pressure gradient that can be calculated as follows:

Equation 4-29 $\Delta P_{inter\text{-}zones} = \rho o * To * g[(Z_1 - H_1)(1 - T_o/T_1) + (Z_2 - H_2)(1 - (T_o/T_2)]$

Where:

- $\Delta P_{inter\text{-}zone}$: is the pressure difference between the upper and the lower zone due to buoyancy force (Pa);
- H_1: the floor to floor height of zone 1 (m);
- T_1: the mean temperature of zone 1 (K);
- H_2: the floor to floor height of zone 2 (m);
- T_2: the mean temperature of zone 2 (K); and
- T_o: the external reference temperature (K).

4.5.6.1.2. Multi-connected horizontal zones

Multi-connected horizontal spaces are used as part of a cooling strategy to attenuate external climatic extremes. Examples are wind-catchers and courtyards in hot dry climate vernacular architecture, which allow and enhance cross-ventilation. Large and tall contemporary buildings have also been using stacks, solar chimneys, atriums, and double-skin glass façades (Santamouris, 2006).

Nowadays, the use of…

> … stack systems serve to overcome the major limitation of simple cross-ventilation systems… while providing similar airflows in a building's individual rooms. As a result of these advantages, stack ventilation systems – perhaps, most often using a central slot atria as a shared stack – have become the most popular natural ventilation solutions used in commercial buildings during the recent years… (Ghiaus and Roulet, 2005, p145).

In buildings whose floors are connected horizontally, the pressure variation has to be calculated individually for each floor or zone of the building on which the temperature stratification presents variation. This calculation has to consider the inlet and outlet openings within the horizontal internal environment and the inlet and outlet openings in the connecting space, which is a vertical element (Awbi, 2003). The final cycle of pressure difference for a multi-storey building with connected horizontal spaces may, therefore, be represented as:

Equation 4-30 $\Delta P_{total} = \Delta P_{zone\text{-}1} + \Delta P_{zone\text{-}2} + \Delta P_{zone\text{-}3...} + \Delta P_{zone\text{-}n}$

Where:

- $\Delta P_{zone\text{-}1,\ 2,\ 3,\ldots,\ n}$: is the total pressure difference due to air stratification on each of the planned floors or in each zone (Pa).

Awbi (2003) presents a simplified equation that considers the system as having a uniform mean temperature and which can be used to calculate the stack pressure on each of the floors or in each zones of the system:

Equation 4-31 $\Delta P_{stack\text{-}zone} = \rho_o * T_o * g * (H_{o\text{-}zone} - H_{i\text{-}stack})(1-(T_{zone}/T_{stack})]$

Where:

- $\Delta P_{stack\text{-}zone}$: is pressure difference between the zone and the stack due to buoyancy force (Pa);
- $H_{o\text{-}zone}$: the height of the outlet in the zone (m);
- $H_{i\text{-}stack}$: the height of the inlet in the stack (m);
- T_{zone}: the mean temperature in the zone (K); and
- T_{stack}: the mean temperature in the stack (K).

Figure 4-15: Example of a building with inter-connected horizontal zones:

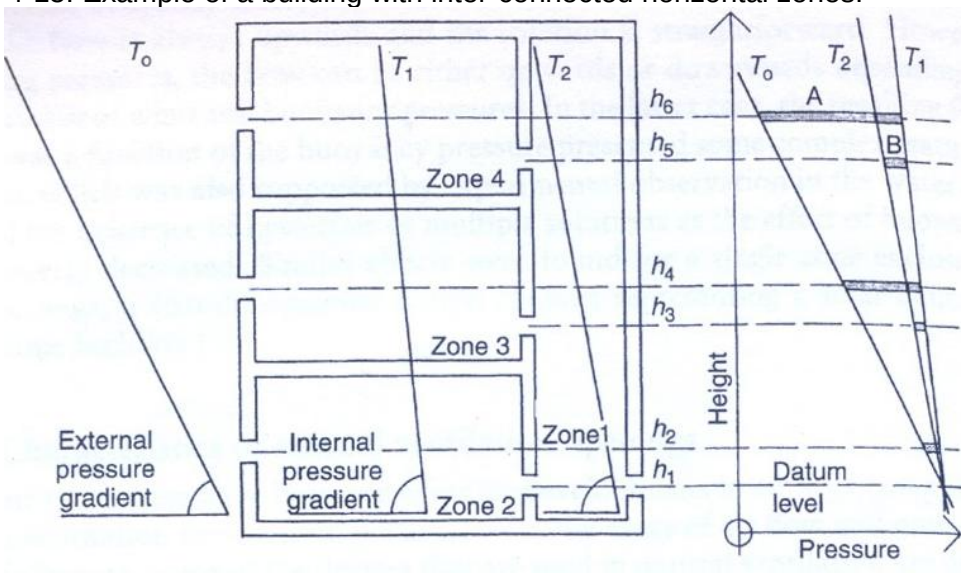

Source: Awbi (2003, pp316).

Awbi (2003) also states that the buoyancy pressure in high-rise buildings' stacks, atriums and double skin-glazed envelopes may exceed the wind-driven pressure and thus become the prevailing pressure force. On the other hand, due to the complexity of this system, the details of the air temperature stratification inside the stack become more significant and pressure losses due to air friction with the duct walls and dampers, together with the inlet/ outlet pressure losses have to be taken into account as well. On occasion, the wind and stack pressures have, together, to exceed the pressure losses for the system to work, as may be seen from the following set of equations (Awbi, 2003):

Equation 4-32 $\Delta P_{sw}=\frac{1}{2}\rho_o * V_m^2[4f(z*K_z/D_h)+K_i(A/A_i)+K_d(A/A_d)+K_e(A/A_e)]$

Where:

- ΔP_{sw}: is the pressure difference in the stack system due both wind- and buoyancy forces (Pa);
- f: the friction factor for the stack walls[19];
- z: the difference in height between the inlet and the outlet openings (m);
- K_z: the pressure loss coefficient through the duct[20];
- D_h: the hydraulic diameter of the stack (m^2);
- A: the cross-sectional area of the stack (m^2);
- K_i: the pressure loss coefficient of the inlet;
- A_i: the inlet area of the stack (m^2);
- K_d: the pressure loss coefficient of the dampers[21];
- A_d: the damper area (m^2);
- K_e: the pressure loss coefficient of the outlet; and
- A_e: the outlet area of the stack (m^2).

The necessary stack height above the rooftop can be calculated by equation 4-23. The hydraulic diameter of the stack is given from the equation (Awbi, 2003):

Equation 4-33 $D_h = 2*w*h/(w+h)$

Where:

- w: is the stack width (m); and
- h: the stack depth (m).

Regarding the shape of the stack section, square ones are reported to perform better than those of hexagonal, octagonal or circular section (Parker and Teekaram, 2005). The airflow rate in multi-spaces connected either horizontally or vertically, combining wind- and buoyancy-driven forces from several openings can be calculated from the following equation (Delsante and Li, 1999):

Equation 4-34 $Q_{w+s} = Cd\Sigma A_{eff}|2g[H_1\Delta T_1 + H_2\Delta T_2 \ldots + H_n\Delta T_n] \pm 2\Delta P_w|^{0.5}$

Where:

[19] Typical friction factor for stack walls is 0.35 (CIBSE A, 2006).
[20] Typical pressure loss coefficient through the stack duct is 0.05 per meter (CIBSE A, 2006).
[21] Typical pressure loss coefficient for dampers and diffusers is 0.25 (CIBSE A, 2006).

- Q_{w+s}: is the airflow rate due to wind and stack pressure (m^3/s);
- Cd: the discharge coefficient of the air inlet (varying in accordance with the opening's characteristics);
- ΣA_{eff}: the sum of all the air inlet's effective opening areas[22] (m^2);
- $H_{1, 2,...n}$: the height of the stack (m);
- ΔP_w: the pressure difference due to wind forces (Pa)- the sign will vary according to whether the forces are added or opposed; and
- $\Delta P_{1,2,...n}$: the difference between inside and outside temperatures (K), calculated by:

Equation 4-35 $\Delta P_1 = (T_i - T_o)/(T_o - T_i)$

Summarizing, all the following features must be considered: inflow and outflow in the direction of the prevailing wind; use of wind- and/or buoyancy-driven forces; inlet/ outlet type, position, operability and dimensions; and cross section and height of wind-catchers, solar chimneys, and atriums. All the possible combinations of them have to be carefully assessed in a holistic manner to determine the place of NPL in the ventilation strategy to be adopted. Ideally, the position of the NPL should be above the highest occupied floor to use this natural ventilation system.

Figure 4-16: The NPL without stack (A), with stack (B) and ideal (C):

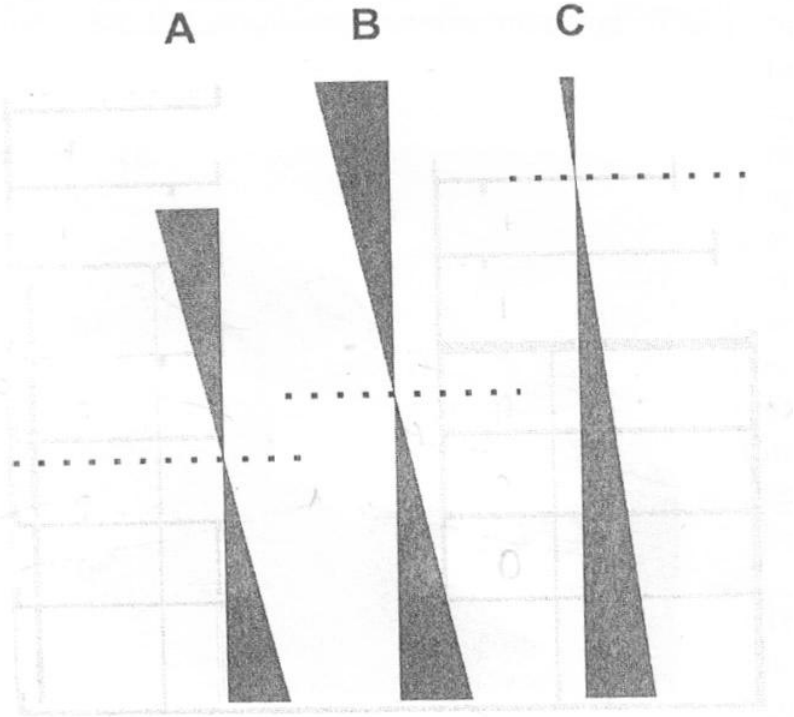

Source: Wagner *et al.* (2008, pp8).

[22] Calculated according to equations 4-15 and 4-16.

4.5.6.1.3. Solar chimneys and double-glazed façades

Stacks and solar chimneys[23] are used in natural ventilation strategies based on both wind- and buoyancy driven forces. The solar chimney relies on solar radiation to heat part of the material of its external surface in order to increase the temperature of the air inside and, in consequence, enhance the cross-ventilation due to the temperature differential within the system (Awbi, 2003; Santamouris, 2006; KoloKOtroni and Santamouris, 2007).

Research conducted by Bansal *et al.* (1994) shows the airflow rates for a combined wind-catcher and solar chimney ventilation strategy used in a six floor building. The stack inlet was positioned windward with a square opening of 1.7x1.7m, while the solar chimney outlet faced leeward[24]. The results show that, when using wind-driven forces alone, the airflow rate is related to the external wind speed, ranging from 0.75 to 3.80m^3/s when external reference airflow velocity ranges from 1.0 to 5.0m/s, respectively. Also, when the solar chimney with a solar radiation load of 700W/m^2 was introduced into the system, the airflow rate increased by 0.70m^3/s for the lowest and 0.15m^3/s for the highest wind speed reported. In conclusion, in this example the buoyancy-driven force alone has a maximum effect, inversely proportional to the external wind speed although, by contrast, solar chimneys can enhance the total airflow ratio when combined with wind-catchers.

If the double-skin glazed façade allows cool air to enter from a bottom inlet and escape from a top outlet, the whole envelope works as a solar chimney inside which there is a rising air current. Under these circumstances, this system embodies a ventilation strategy by cooling down the inner surface convectively while at the same time protecting it from direct solar radiation (CIBSE AM 10, 2007).

According to Gratia and de Helde (2007), this architectonic component is being widely employed nowadays as it attenuates urban noise, controls high external wind speed, and also gives the building a ”green image”. On the other hand, the authors warn that the position of the windward inflow and the leeward outflow have to be carefully planned. Further, the fresh, cool air thus supplied to the internal occupied environments has to come from another source distinct from the double-skin glazed envelope. In addition, if the double-skin’s inner surface is intended for use as an outflow route for the air from the floors, special care has to be taken to avoid any back-flow of heated and polluted air into the internal space of the top floors, as also to avoid any pressure drop in the system. Finally, the operation of the openings has to be

[23] Stack and solar chimney theory has been dealt with in sections 4.5.5. and 4.5.5.1, respectively.
[24] With adopted inlet and outlet discharge coefficients of 0.9 and 0.6, respectively.

planned as their incorrect use can distort the initial flow direction and affect the planned airflow rates within a double-skin glazed envelope.

Figure 4-17: Double skin-glazed envelope used as a solar chimney on leeward (top) and the windward (bottom) sides:

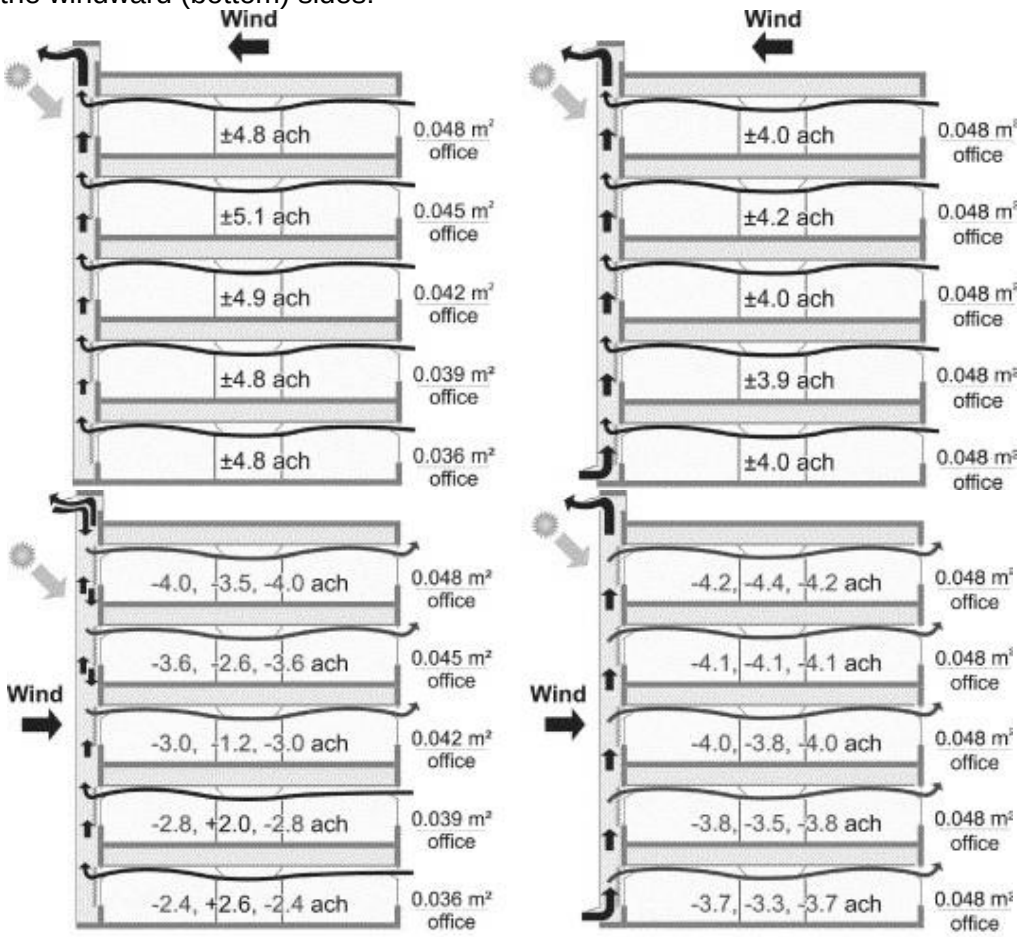

Source: Gratia and de Helde (2007, pp442).

Awbi (2003) proposes an equation to calculate the exit air temperature for solar chimneys and double-skin glazed façades. This equation was based on the calculation of the pressure difference in stack systems due to combined forces having surface heat transfer terms added to it, as follows:

Equation 4-36 $T_e = A/B+(T_i–A/B)^{exp}[-B*w*h/\rho_e*cp*Q]$

Where:

- T_e: is the stack exit air temperature (K);
- T_i: the inlet air temperature (K);
- ρ_e: the air density at the exit (kg/ m^3);

- cp: the specific heat of air (J/Kg.K);
- Q: the airflow rate (m^3/s); and
- A and B: based on the surface heat transfer coefficient and the temperature of the internal surfaces:

Equation 4-37 $A= Ht_1*Tw_1+Ht_2*Tw_2+Ht_3*Tw_3+\ldots+Ht_n*Tw_n$

And,

Equation 4-38 $B= Ht_1+Ht_2+Ht_3+\ldots+Ht_n$

Where:

- $Ht_{1,2,3,\ldots,n}$: are the surface heat transfer coefficients for the materials used in the envelope; and
- $Tw_{1,2,3,\ldots,n}$: the temperatures of the internal surfaces (K).

Equation 4-36 applies to both solar chimney and double-skin glazed façade problems since the number of materials used in the surface envelope can be adjusted to the problem created by the project.

The earlier equation 4-21 (Elmualim *et al.*, 1999) is also appropriate for the calculation of the solar chimney airflow rate due to stack pressure, although the literature gives several other possibilities for the approach to this issue in (Bansal *et al.,* 1994; Frota, 1995; Gan and Riffat, 1998; Etheridge, 2000 b; Awbi, 2003; Cook *et al.*, 2003; Hunt and Syrios, 2004; CIBSE AM10, 2007; Germano *et al.*, 2006; Linden and Kaye, 2006; CIBSE A, 2006; Ji *et al.*, 2007; Costola and Etheridge, 2008). Alternatively, Awbi (2003) proposes the substitution of the air temperature outside (T_o) for the stack exit air temperature (T_e) in the referred equation.

Finally, another option of use for double-skin glazed envelopes is to mantain both the bottom and the top edges and also the internal openings closed. In this scenario the system becomes a passive heating device rather like a large trombe wall, warming the internal environment and delaying the loss of internal heat (Givoni, 1991).

4.6. The cooling capacity of ventilation systems

The performance of a convective cooling system is directly linked to the building material's thermal storage capacity, the internal heat sources, and climatic factors (Lissen *et al.*, 2008). If a high-mass structure presents a temperature higher than that of the surrounding air, it will lose heat from both convective and radiant change. Thus, the relationship between the exposed surface area and the wind speed determines the convective cooling capacity (Givoni, 1994; Geros *et al.*, 2005). Moreover, allied to high ACH rates, the convective cooling will be more efficient if high heat transfer coefficient materials are used as well (Geros *et al.*, 2005).

Lissen *et al.* (2008) developed the storage efficiency (SE) concept, which takes into account the building's thermal mass properties and internal mass distribution and airflow path and rates in order to assess the effectiveness of convective cooling. The SE is related to the ratio of stored heat to the maximum stored heat calculated and is determined by: the climatic characteristics; the set-point temperature; and the position of the air inlet/ outlet that gives rise to the internal airflow. The internal airflow path creates an interaction between storage mass surfaces and convective cooling to define the actual heat transfer variation. In accordance with to this principle, the internal space is surrounded by surfaces directly swapped by the airflow and others conjoining at volumes of stagnated air. Finally, the cooling is more effective if the airflow pattern is stronger over materials with greater inertia/ thermal storage capacity.

Lissen *et al.* (2008) investigated the internal airflow path and the SE using CFD simulations for a 4x4x3m room. Among their findings, the results for the following three scenarios stand out:

- Set 1: inlet set low and outlet high in the same wall. Due to the small size of the space, this opening arrangement allows a nocturnal flow path that swaps most of the surfaces at all heights in the internal environment, optimising the SE of the ventilation system;
- Set 2: low inlet aligned with the floor and high outlet aligned with the ceiling, in opposite walls. This combination creates a diagonal flow that swaps the floor, wall and ceiling close to the outflow directly, while the other regions are cooled by stagnant air; and
- Set 3: both the inlet and outlet openings are set at medium heights in opposite walls. It creates a direct flow in the centre of the space, while both floor and ceiling are cooled by stagnant air.

Finally, the SE calculated for each configuration demonstrates that the more intensely the airflow swaps the internal surfaces, the more efficient the convective

cooling will be. After 10 hours of NVC, the SE results for configurations 1, 2 and 3 were: 0.23, 0.21 and 0.04, respectively.

4.6.1. Heat storage capacity and efficiency of convective cooling.

Most of the convective cooling calculations are computer-based and use the NiteCool or the TRNSYS software. Several authors and guidebooks provide analytical models for estimating the cooling potential or the necessary ACH rates (Santamouris *et al.*, 1996; Santamouris *et al.*, 1997; Givoni, 1998b; ASHRAE, 2001, CIBSE A, 2006). For instance, Pollet and Renson (2008) propose a simplified method for estimating the cooling capacity based on ACH rates and indoor to outdoor temperature variation:

Equation 4-39 $Pc= 0.34ACH*V*\Delta T_{inside-outside}$

Where:

- Pc: is the cooling capacity (W/m^2 of surface area);
- V: the volume of the internal space (m^3); and
- $\Delta T_{inside-outside}$: the inside to outside temperature variation (^oC).

Levermore (2002) provides a detailed model for calculating the heat transfer by ventilation which is also suitable for checking the efficiency of NCV systems:

Equation 4-40 $\Phi_v= 0.34*ACH*V*[T_f-T_o]*[1–1/(1+x)]$

Where:

- Φ_v: is the heat transfer by ventilation (W);
- V: the volume of the internal space (m^3);
- T_f: the fabric's surface temperature (^oC); and
- x: is given by:

Equation 4-41 $x= 4.8A/[(1/3)ACH*V]$

Where:

- A: is the total area of the surfaces over which the air flows (m^2).

Further, the SE model built mass capacity of Lissen *et al.* (2008) can be mathematically described by:

Equation 4-42 $SE= (T_{storage\ initial}–T_{storage\ final})/(T_{storage\ initial}–T_o)$

Where:

- SE: is the dimensionless storage efficiency of the ventilation system;
- $T_{storage\ initial}$: the initial indoor temperature (K);
- $T_{storage\ final}$: the final indoor temperature (K); and
- T_o: ithe outdoor temperature (K).

Equation 4-41 is a simplified model derived from a set of equations presented by Lissen *et al*[25]*.* (2008) for calculating the cooling storage capacity of a given built mass over a given time:

Equation 4-43 $Q_{s-t} = (M_1*cp_1*\Delta\top_1+M_2*cp_2*\Delta\top_2+…+M_n*cp_n*\Delta\top_n)t$

Where:

- Q_{s-t} : is the heat storage or release capacity over an interval of time (W/m^2);
- $M_{1, 2, ..., n}$: the built mass of the materials (m^3);
- $\Delta\top_{1, 2, ..., n}$: the surface temperature difference of the material (K);
- $cp_{1, 2, ..., n}$: the specific heat of the material (J/Kg.K); and
- t: the interval of time (h).

Then, Lissen *et al.* (2008) affirm that the internal/ external thermal balance will be achieved if an infinite interval of time is adopted. This thermal balance defines the maximum, or saturated, heat storage or release capacity of a material (Q_{s-max}). Therefore, the SE can also be seen as a ratio between the heat storage over a certain interval of time and the maximum heat storage capacity of a material. Finally, their analysis incorporates three characteristics of convective heat losses: air change per hour rate, internal flow pattern and thermal mass distribution. When the convective heat losses are included in the above equation, the SE can be determined as follows:

Equation 4-44 $SE=1-\{[M_1*cp_1*\exp(-t/\tau_1)+...+M_n*cp_n*\exp(-t/\tau_n)]/(\Sigma M_i*cp_i)\}$

[25] See Lissen *et al.* (2008) equations [2] to [4].

Where:

- ΣM_i*****cp_i: is related to the sum of the initial thermal state of the materials; and
- $\tau_{1, 2..., n}$: a time constant for each material and expressed as:

Equation 0-45 $\tau_n = [(h_n * A_n + m_n * cp) M_n * cp_n] / (h_n * A_n * m_n * cp)$

Where:

- h_n: is the convective heat transfer of a material (W/m^2);
- m_n: the fraction of airflow in contact with the material surface (m^3);
- A_n: the surface area of a material (m^2); and
- cp: the specific heat of the air (J/Kg.K).

4.7. Night ventilation cooling systems (NVC)

Night ventilation cooling (NVC) is a passive cooling technique based on the fact that during the night the cooler, external air can remove the internal heat stored in the built mass during the day due to both solar radiation and other internal heat gains. NVC can increase the building structure's capacity to act as a heat sink for the following day, cooling the internal environment's air and reducing peak temperatures. In this way, it creates a time lag, delaying the moment of the day when maximum acceptable indoor temperatures are reached and mechanical ventilation systems become unavoidable if thermal comfort temperatures are to be attained (Givoni, 1994 and 1998b; Santamouris, 2006; Lissen *et al.*, 2008).

4.7.1. Parameters and variables for NVC systems

NVC systems can be considered direct: when cooling of the directly exposed built mass occurs by radiation and convection; and indirect: when air circulates in passages over and within the mass element surfaces, as, for example, beneath the floor or in the cavity above the ceiling (Barnard, 2002; Santamouris, 2006).

The direct NVC system is based on heat transfers by radiation and convection. Since it is the thermo-physical properties of materials that determine their heat storing potential during the day its release at night, these materials should be of high density and thermal conductivity. For instance, indoor surfaces should be maximized, having hive-like or rib-like ceiling and concrete slab shapes. High-mass partitions, walls and window frames can also store heat (Givoni, 1994; Eicker *et al.*, 2005). Furthermore, as still-air conditions are more prevalent at night, NVC potential is improved when coupled with cross-ventilation and/or stacks based on buoyancy-driven forces (Eicker *et al.,*

2005; CIBSE AM 10, 2007). Regarding the indirect systems, Givoni (1994) mentions that special channels constructed within the structure can act as NVC “cooling worms” thus avoiding the need to leave windows open at nigh – a matter of security, maintenance, and operability. Givoni (1994) also mentions, as an extension of this technique, the possibility of having air pipes passing through water tanks and/or under the ground, as is to be recommended for places where external air temperature cannot supply the effectiveness of nocturnal ventilation.

The calculation of NVC performance will take into account the total heat loads accumulated throughout the day, the heat storage capacity of the construction materials, and the efficiency of the convective cooling strategy adopted. According to Givoni (1994), the high-mass maximum temperature occurs in the evening. The maximum internal temperature for NVC varies in accordance with air movement (still air to 2m/s) and humidity (dry or semi-dry climate- see table 4-5). There is a maximum surface temperature of the storage mass of 2^{o}C below the upper comfort limit, in order to maintain the heat absorption flow of the structure due to natural convection and long-wave radiation. Finally, since normally external winds cease at night in most hot, humid places, mechanical ventilation is an option for NVC systems (Givoni, 1994).

Table 4-3: Maximum temperature limits for NVC (^{o}C):

Climate	arid		semi-humid	
	still air	2m/s	still air	*2m/s*
Indoor air	28	30	25	*27*
Mass surface	26	29	23	26

Source: Givoni (1994).

4.7.1.1. Climatic boundaries for NVC systems

Several climatic parameters together determine the potential for cooling a building at the close of the night, thus establishing the geographical boundaries for the use of NVC systems. These parameters are: the indoor minimum temperature of the air, the outdoor temperature range and the relative humidity. These parameters determine the upper temperature limit of indoor comfort without daytime ventilation. As a rule of thumb, buildings situated in hot places with a thermal 24-hour fluctuation of between 15 and 20^{o}C that use NVC can expect a maximum indoor/outdoor temperature difference of 8^{o}C (Givoni, 1994 and 1998b; Barnard, 2002). In hot, humid climates, systems coupling natural convective cooling ventilation and mechanical ventilation are recommended for the maintenance of IAQ levels and indoor temperature control for cold and intermediate seasons (Heiselberg, 2006).

4.7.2. Examples of buildings with NVC systems

Experiments conducted by Givoni (1994) show that on hot days with external temperatures above 34^{o}C the internal air temperature of buildings is between 5^{o}C and 9^{o}C below the external one (reaching around 29^{o}C and 25^{o}C) when windows are closed all the time or open for NVC, only. The author concludes that, to effectively achieve the built mass cooling result, the external nocturnal air temperature should not exceed 20^{o}C, and the ultimate storage mass temperature at the end of the process should be higher than that of the external air by a maximum of 2 or 3^{o}C.

Eicker *et al.* (2005) monitored the performance of an NVC system in an office building during the summer. The external daily average temperature was 26^{o}C and thermal amplitude 15^{o}C. It was found that 10- 15 ACH during the night was able to remove thermal loads of 400w/ m^{2}.

Other studies (Geros *et al.*, 1999; Santamouris, 2006) show an NVC capacity to reduce internal environment daytime temperatures by up to 3^{o}C. As a rule of thumb, NVC efficiency is associated with ACH rates. Satisfactory results have been found for 10-30 ACH (Geros *et al.*, 1999) and 10-15 ACH (Santamouris, 2006). Santamouris (2006) also states that NVC buildings registered a decrease in energy consumption with HVAC in of up to 50% and a reduction in peak energy demand of up to 40%.

Figure 4-18: NVC capacity to reduce internal temperatures and ACH rates:

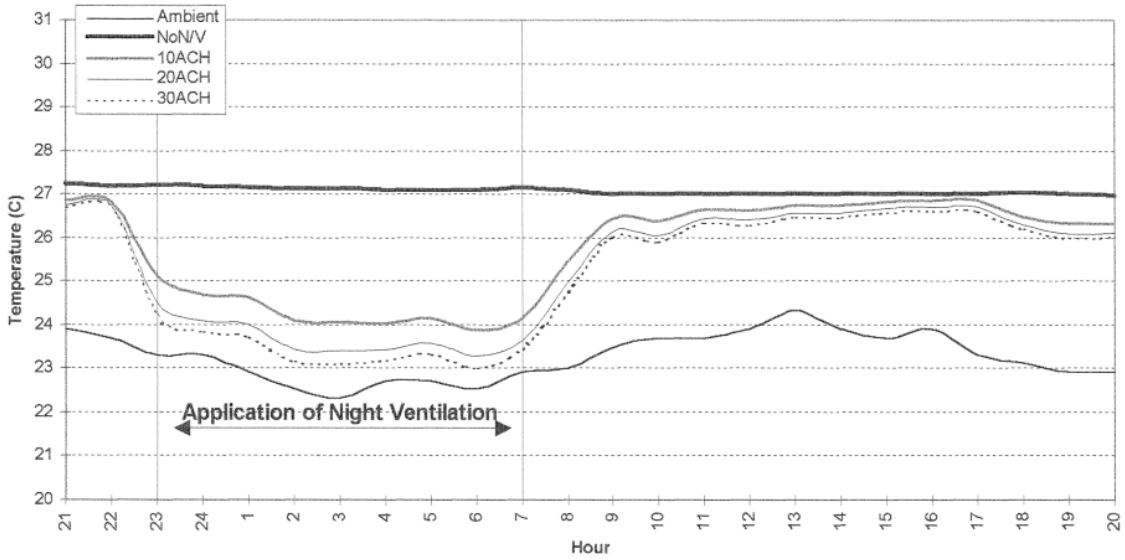

Source: Geros *et al.* (1999, pp149).

Field measurements made by Bouchair (1994) in a dwelling with a wind-catcher inlet and solar chimney outlet provide an example of the performance of an NVC system which combines wind- and buoyancy-driven forces. Results show that, when the stack is continuously open, the internal and the external air temperatures are

equalized during the night, at around 28^{o}C. During the day, when external air temperatures reach 40^{o}C, the internal temperature is lower than the external by up to 8^{o}C. Conversely, without the NVC system, the internal temperature remains practically constant at around 38^{o}C both by day and by night.

Pollet and Renson (2008) investigated a free-running office building in Belgium the ventilation system of which consists of low openings in the façade for inflow and a stack for outflow. The envelope is composed of highly insulating material and equipped with controls for direct solar radiation. Internally, large exposed concrete ceiling surfaces provide thermal mass working as a heat sink during daytime while at night cooling is used to release the heat accumulated during the day.

The analysis of the thermal performance of this building showed that during the summer season, with minimum and maximum external temperatures varying from between 15 and 20^{o}C and 30 and 35^{o}C, respectively, the internal temperatures remained below 26^{o}C during at least 97.5% of the working day. This results in an annual energy consumption of 100kW/m^{2}, a reduction of up to 50% was compared with that of other Belgian office buildings. Pollet and Renson also highlight the importance of having a control system based on outdoor and indoor temperature variation, plus thermal mass temperature and memory register of at least one day, for operating the ventilation system and the solar radiation protection according to pre-established comfort levels. These systems, in their control of the indoor environment, should be subject to the user's options.

4.7.3. Limitations to the application of NVC systems

As the NVC functions during unoccupied periods, external urban noise and draughts do not constitute a problem for this strategy (Lissen *et al.*, 2008). On the other hand, the shortcomings of the system are associated with operability (if not mechanized), maintenance costs of automated openings, and risk of overcooling during the night. Other limitations to the use of NCV are: the reduction in air speed in urban areas at night (of up to 90%), which affects the ACH rates; high external urban air temperatures above the comfort limits (sometimes enhanced by heat island phenomena); urban pollution, moisture control and levels; privacy; and building security (CIBSE AM 10, 2007; Santamouris, 2006).

Regarding the building legislation, Pollet and Renson (2008) state that few EU countries have developed efficient guidelines on NVC to assist building designers. For instance, the French building energy code admits airflow rates for night cooling systems and determines their controlled operation but only from 10pm to 8am. Wouters *et al.* (2006) mention several European agencies and their policies and regulations

related to ventilation standards. Some European projects related to building energy regulations are: JOULE PASCOOL; AIOLOS; NATVENT; IEA projects BCS Annex 28; SHC Task XIII (to name but a few), that study and create building energy regulations. On the other hand, Pollet and Renson (2008) mention that no methods have yet been successfully implemented for calculating NCV capacity or its design parameters.

4.7.4. Heat recovery and NCV systems

Heat recovery systems can remove heat and moisture from air inlet/ outlet, transferring it to the respective outlet/ inlet by using an air handling unit that will harness this potential energy for other uses. These units can be characterized as (Schild, 2006):

- Regenerative (cyclic): by which metallic tube heat exchanges with or without air filters remove heat by conduction and convection and reintroduce the circulated air; and
- Recuperative (static): by which the heat is exchanged by conduction and convection through transitional material surfaces (corrugated or plate) and/ or fluids, and there is no reutilization of the air.

Developed for cold and temperate climates, heat recovery may possibly be applied in hot climates as well. Although under these circumstances no heat recovery system is necessary for matters of thermal comfort, they can still be used for warming water tanks by indirect heat transfer in hotels and high-rise residential buildings. In addition, the harnessing of released heat acts in two ways: it avoids warming of the air of the external environment, thus contributing to reducing the urban heat island effect in urban centres; and it reduces energy consumption in water heating systems for showers and pools. Therefore, although it is not used as a direct ventilation system, it may contribute to the performance of NCV or other natural ventilation systems.

4.8. Passive downdraught evaporative cooling (PDEC) systems

Passive downdraught evaporative cooling systems (PDEC) are based on the cooling of the inlet air by means of a cold water source. In a PDEC system the inflow normally occurs through a wind-catcher tower. This system is based on the vernacular North African *malqaf* (Egypt) and Middle Eastern *badgirs* (arab) or *baud-geers* (farsi) vernacular wind towers and adapted to present reality (Bahadori, 1985; Mathews *et al.*, 1994; Pearlmutter *et al.*, 1997; A'zami, 2005).

Figure 4-19: Natural, hybrid and HVAC strategies domain:

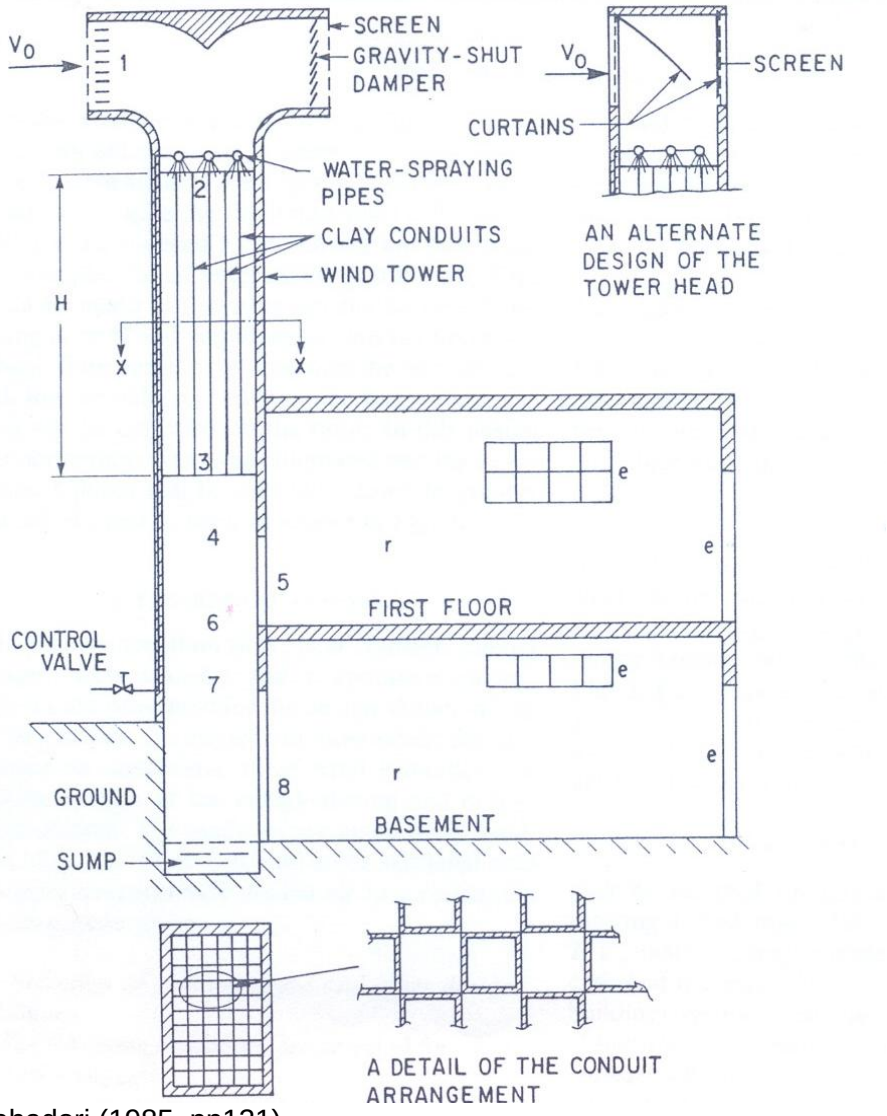

Source: Bahadori (1985, pp121).

According to Erell (2007) PDEC systems may be divided into direct and indirect groups. The direct PDEC system consists of water-spray used to instantly add moisture to the hot, dry air of the inlet. Usually wet clay pads and/ or nozzles are used to mix the air and water. Also, the air inlet may transverse a water pound. The purpose is to induce a process of evaporation by which the hot air inlet is cooled and humidified. By this mechanism, the density of the inlet air increases and, thus, the downflow pressure rises (Bahadori, 1985; Givoni, 1993 and 1994; Pearlmutter *et al.*, 1996; Erell, 2007).

In the indirect PDEC system, the inlet air is cooled by convection with a heat exchanger, consisting either of water pipes with the air passing between them or of air ducts passing through water tank (Givoni, 1994). In this way, the hot air is cooled, but not humidified, at the inlet and its dry-bulb temperature and density reduced.

Finally, when the PDEC is coupled with a solar chimney at the outflow, an increase in the airflow rate in the building is observed (Santamouris, 2006).

4.8.1. Examples of recent use of PDEC systems

Based on the vernacular architecture, Bahadori (1985) created a model that integrated wet pads and other PDEC tower features. A link between the height of this stack and the drop of the DBT was found. As a result, with an outside DBT oscillating from 45 to 25^{o}C, the difference between the outside and the inside DBT varied from 20 to 7^{o}C for an 8.0m height tower. Conversely, the DBT difference ranged only from 10 to 3^{o}C for a lower 2.0m. Finally, results for external wind speed from 5m/s to 15m/s did not vary greatly, there being an average difference of less than 2^{o}C between them.

More recently, Badran (2003) repeated Bahadori's experiment (1985) for the climate in Amman, Jordan. Badran (2003) found the same results as reported for an 8.0m height tower for a 4.0m one. In addition to matching in the air temperature range, the author also mentions an internal air speed of 0.3m/s, which is sufficient to enhance the sensation of thermal comfort. This last finding confirms Givoni's results (1993), from the simulation of the airflow rates and the DBT differences in a wind tower model, as proposed by Cunningham and Thompson (1986). This model was made of a PDEC wind-catcher, a roof-pound attic and a solar chimney. Results show that, for an increase of air speed in the system of from 0.2 to 0.8m/s, the air wet-bulb temperature depression drop remained almost constant varying by from 80 to 90%.

Pearlmutter *et al.* (1996) reported an airflow rate in their experiment with the difference of internal WBT depression for a PDEC system using a fine spray as a source of water supply. The results found were that for ACH differences of 100, 745 and 1150 the corresponding internal WBT depression was of 7.0, 10.9 and 8.0^{o}C. The final conclusions showed that higher ACH does, in fact, reduce the cooling capacity of the system. In addition, when coarse sprays were used, the results were worse than those mentioned above, since they also reduce the evaporative effect.

Tiwari *et al.* (1994) developed a PDEC system for small dwellings in New Delhi, India. The results show that a PDEC tower and a roof garden are sufficient to provide thermal comfort throughout the day and that at night NCV without evaporation may be employed. These results are in line with the previous findings of Nayak *et al.* (1982) and Sodha *et al.* (1986), who also studied the effect of PDEC in buildings in New Delhi, and proposed that the roof-top surface should consist of a green-roof or a roof-pound, and a white-washed highly reflective structure, respectively. Navon and Arkin (1994) also found that, for small buildings in extreme desert conditions, PDEC towers are not only more efficient than air-conditioned systems, but also economically viable.

The Torrent RSB in Ahmedabad, India, built in 1998, used a complex system of central atrium inlet air using PDEC to cool and humidify the external air and several solar chimney towers for the air outlet. Regarding its thermal performance, Erell (2007)

reports that, since the internal atrium height insufficient, the potential cooling effect was reduced. Finally, this author mentions that both the NPL in the PDEC systems and the opening size through the height of the inlet tower have to be considered so as to allow the same airflow rates for all the floors connected to the system. For instance, in the Torrent building, while 9ACH was observed on the ground floor, the upper floor presented 6ACH, which represented a substantial decrease for the top floors. On the basis of this experiment, the author recommends that several stacks for PDEC inflow and solar chimney outflow are more efficient and allow greater control than do centralized systems.

Figure 4-20: A schematic cross-section of the Torrent Research Centre building (Ahmadabad, India) and its PDEC system:

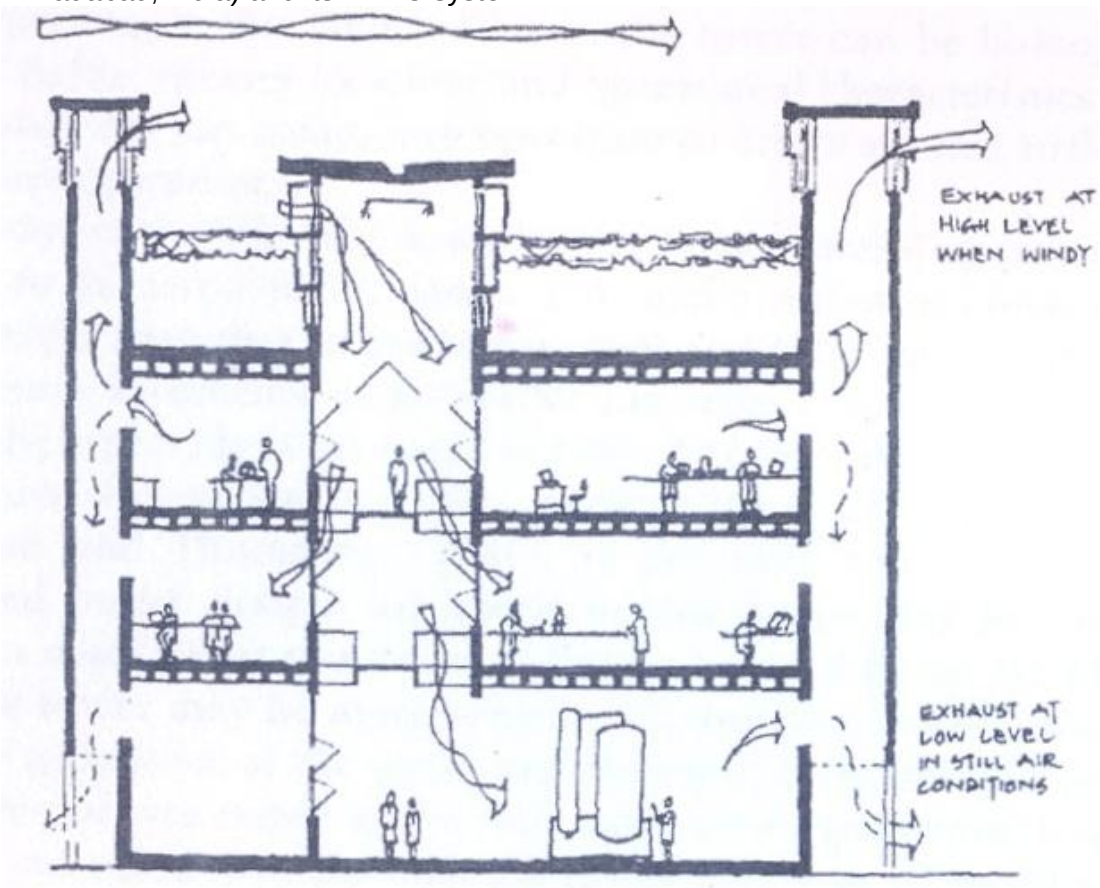

Source: Ford *et al.* (1998) *in* Erell (2007, pp247).

Ghiabaklou's (2003) investigation focused on the thermal comfort prediction of users in an existing commercial building in Teheran, Iran that makes use of a central PDEC system and also has balconies on the façade. By using the Fanger PMV scale, the results showed that 28.7% of the occupants of the building relate a thermal comfort of +0.5 and only 5.4% indicated a slight warm thermal sensation of +1.0. Further, during the experiment, the average internal and external temperatures were 25.4^{o}C and 39.1^{o}C, respectively.

Finally, an example of indirect PDEC is the 'cool recovery' system (Heiselberg, 2006). This system consists of an upper water tank for cooling the air that passes at the inlet through either a cavity or pipes in the water. The tank has to be protected from direct solar radiation during the day and to lose heat to externally at night by radiative cooling, which reduces the water temperature for the following day.

4.8.2. The physical principles of PDEC direct systems

The adiabatic evaporation of water occurs when the pressure of the liquid water is greater than that of the vapour in the surrounding air. The natural process by which liquid water is transformed into gas requires an amount of energy defined as the latent heat of vaporization. This method removes energy from the air, which is cooled in the process (Pearlmutter *et al.*, 1996). According to Erell (2007), the amount of energy required to evaporate 1 litre of water[26] would decrease the temperature of 200m^3 of dry air by 10^{o}C. On the other hand, the author says that this process depends on the initial value of the atmospheric water vapor and pressure. This value can be quantified by the relative humidity of the air which ranges from zero to 100% (when the air is fully saturated with water) or by the wet-bulb temperature that gives the temperature on which the dry air is saturated with water due to adiabatic evaporation.

The difference between the dry-bulb temperature (DBT), i.e., the temperature of the air without water vapor, and the wet-bulb temperature (WBT), or the temperature at which a volume of air becomes saturated with water vapor, is called the wet-bulb temperature depression. This difference gives the potential of the atmosphere for cooling the air by evaporative system, and the lower the WBT is in relation to the DBT the greater is the potential for evaporation (Givoni, 1993 and 1994; Pearlmutter *et al.*, 1996; Erell, 2007). The wet-bulb temperature depression reaches its peak with the maximum DBT of the day and it is lowest during the night, when the DBT also reaches its lower value (Givoni, 1994). In addition, the amplitude of DBT is usually three times that of the WBT (Givoni, 1993). This happens because water has greater thermal inertia than dry air. Alternatively, Erell (2007) affirms that a large wet-bulb temperature depression does not ensure an efficient evaporative system, and the WBT has also to be sufficiently low, since the author affirms that the maximum capacity of air cooling is restricted to 2 or 3K above the ambient WBT at the PDEC system's outlet. PDEC direct systems work, therefore, by decreasing the DBT by the evaporation of water, which transforms sensible heat into latent heat without increasing the WBT (Erell, 2007).

[26] The amount of energy requested is 2.44Mj/kg at 25^{o}C and 10kPa (Erell, 2007).

4.8.3. The PDEC's applicability and efficiency

The forces acting at the airflow inlet of a PDEC tower are: the wind pressure calculated as that for a wind-catcher inlet; the negative buoyancy force as the air is cooled; and the down flow acceleration since the mixed water drops added to the air increase its specific weight, which results in an increase in momentum (Erell, 2007). The sum of these three forces gives the total pressure at the inlet of the PDEC tower. This has the effect of increasing both the pressure difference between the inlet and the outlet openings and, in consequence, the airflow rates in the internal environment. Further, a correlation between the wet pad's cooled surface and the amount of air passing over it was found by Bahadori (1985), who also found that the greater the surface the system provides, the cooler the outlet air will become and the higher the pressure difference will be.

Figure 4-21: Effectiveness of a PDEC system for external wind at 5m/s:

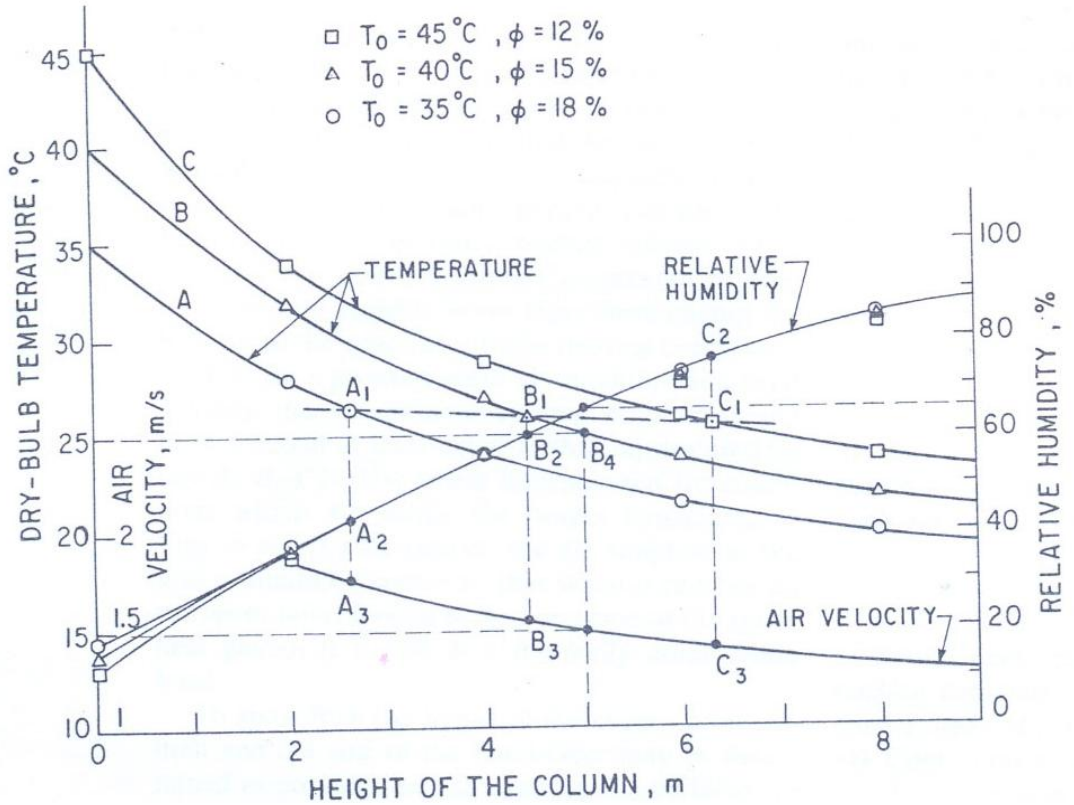

Source: Bahadori (1985, pp127).

On the other hand, Givoni (1993) states that the wet-bulb temperature depression reaches its peak during the day, as also happens with the wind velocity and the performance of joined wind-catcher and solar chimney stacks. Since both the application and efficiency of the PDEC are controlled by the presence of one or a combination of these factors, its inappropriate use would result in a proportional

increase of moisture and mould in the internal environment, which could jeopardize the IAQ. In addition, since the relative humidity at the air inlet is raised in the process, PDEC systems are of restricted use in hot, humid climates.

The difference of pressure due to wind-driven forces may be calculated using equation 4-9, and that to buoyancy-driven forces by the equation 4-19. The difference of pressure due to the negative buoyancy force can be found from a set of two equations. The first equation provides the down flow velocity exclusively due to the difference of temperature in the evaporative system (Erell, 2007):

Equation 4-46 $V_{PDEC} = |2g*H_{PDEC}[(T_o - T_e)/T_o]|^{0.5}$

Where:

- V_{PDEC}: is the negative buoyancy down flow velocity (m/s);
- H_{PDEC} : the height of the PDEC stack (m);
- T_o: the temperature outside (K);
- T_e: the air temperature at the PDEC stack's exit (K); and
- H_i: the height from the air inlet to the bottom of the stack (m).

The second equation gives the air temperature at the PDEC stack's exit (Givoni, 1993), as follows:

Equation 4-47 $T_e = DTB - 0.87(DTB - WTB)$

It is possible, with these two equations, to identify the negative buoyancy down-flow velocity and then to calculate the pressure difference due to the above-mentioned wind-driven force. The combined pressure at the outlet of the PDEC system is given by the sum of these results. Alternatively, Givoni (1993) provides a method for calculating the airflow rate in PDEC systems as a function of the area of the wet pads and the height of the wind tower:

Equation 4-48 $Q_{PDEC} = P_{drop}*A_{pads}|H_{PDEC}(DTB - WTB)|^{0.5}$

Where:

- Q_{PDEC}: is the flow rate in PDEC systems due to the wet pads (m^3/s);
- P_{drop}: the constant pressure drop in the system (0.03);
- A_{pads}: the total surface area of the wet pads (m^2), and
- H_{PDEC}: the height of the PDEC tower (m).

Finally, several researchers (Gan and Riffat, 1999; Gan *et al.,* 2001; Elfatih *et al.*, 2003; Costelloe and Finn, 2003 and 2007; Riffat and Zhu, 2004; Belarbi *et al.,* 2006) present different models for assessing the effectiveness of PDEC systems in buildings.

4.9. Hybrid ventilation systems

Throughout recent history, natural and mechanical ventilation systems have been developed separately, but both are of limited application when so considered (Heiselberg and Tjelflaat, 1999; Delsante and Vik, 2001). Hybrid ventilation systems are an alternative to fill the gap when the external climatic characteristics do not allow IAQ or indoor thermal comfort levels to be attained by natural ventilation strategies and/or other passive techniques alone, and full HVAC are unnecessary (Delsante and Vik, 2001; Heiselberg, 2002 and 2006; Awbi, 2003).

4.9.1. When is a hybrid ventilation system necessary?

The decision regarding a ventilation strategy for a natural, mechanical, hybrid or fully air-conditioned system is related to the correct analysis of the interaction between the surrounding microclimate, the urban environment, and the building itself. This analysis has to be made during the initial design stage and take climate data, solar and wind orientation into consideration in order to decide on the building's shape, façade elements, properties of materials, internal floor-plan and layout (Delsante and Vik, 2001; Liddament *et al.*, 2006)[27].

The next step is the choice of the ventilation system which fulfills both IAQ and thermal comfort requirements. One or more strategies may be chosen for either night or day time and for the different seasons of the year. This approach is also valid for designing other passive strategies for heating and cooling (Delsante and Vik, 2001; Heiselberg, 2002 and 2006; Liddament *et al.*, 2006).

[27] Heiselberg (2002) provides check-lists for decision making regarding natural, hybrid or mechanical ventilation systems; and recommendation and limitation check-list for natural ventilation systems, which are found in Appendix 2.

Figure 4-22: Natural, hybrid and HVAC strategies domain:

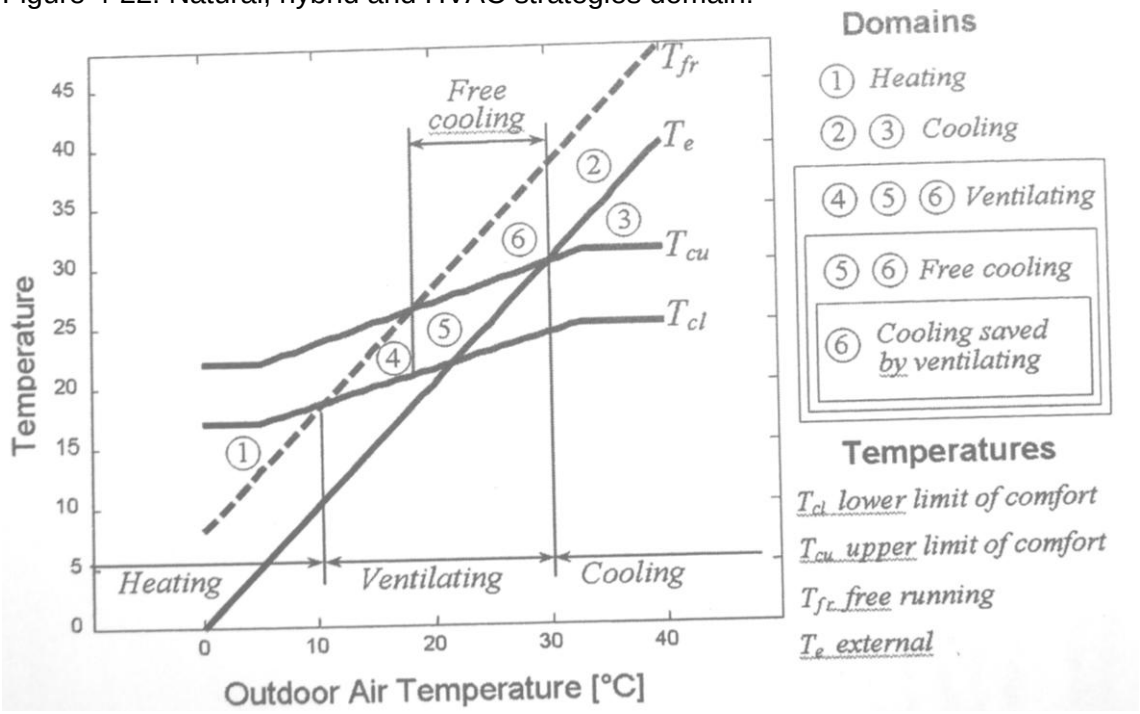

Source: Heiselberg (2006, pp202).

Further steps to consider, after exploiting the potential of the natural resources to the maximum, the design of mechanical systems allied to the previous ones and, later, the description of the periods of the year when only artificial means can provide indoor health and comfort levels. Even in such scenario, hybrid systems allied to air-conditioning can reduce the daily and peak cooling demands on this equipment considerably. Heiselberg (2002 and 2006) provides a chart on which the range of action for each technique is related to the indoor and outdoor air temperatures.

The CIBSE F technical guide (2004) for designing energy efficient buildings presents the following flowchart of ventilation techniques (figure 4-23) in order to assist building designers in their decisions as to which system and strategy should be adopted and their implications.

Heiselberg (2002) also provides a complete check-list that shows the scope of action for natural, hybrid or mechanical ventilation systems for several different conditions or requirement parameters[28]. The performance of each item is subdivided into low, medium or high for each one of the ventilation systems. The aim of this check-list is to help architects and building designers to take decisions as to which particular technique should be approached and when.

[28] See Appendix 2

Figure 4-23: Ventilation design hierarchy and it implications:

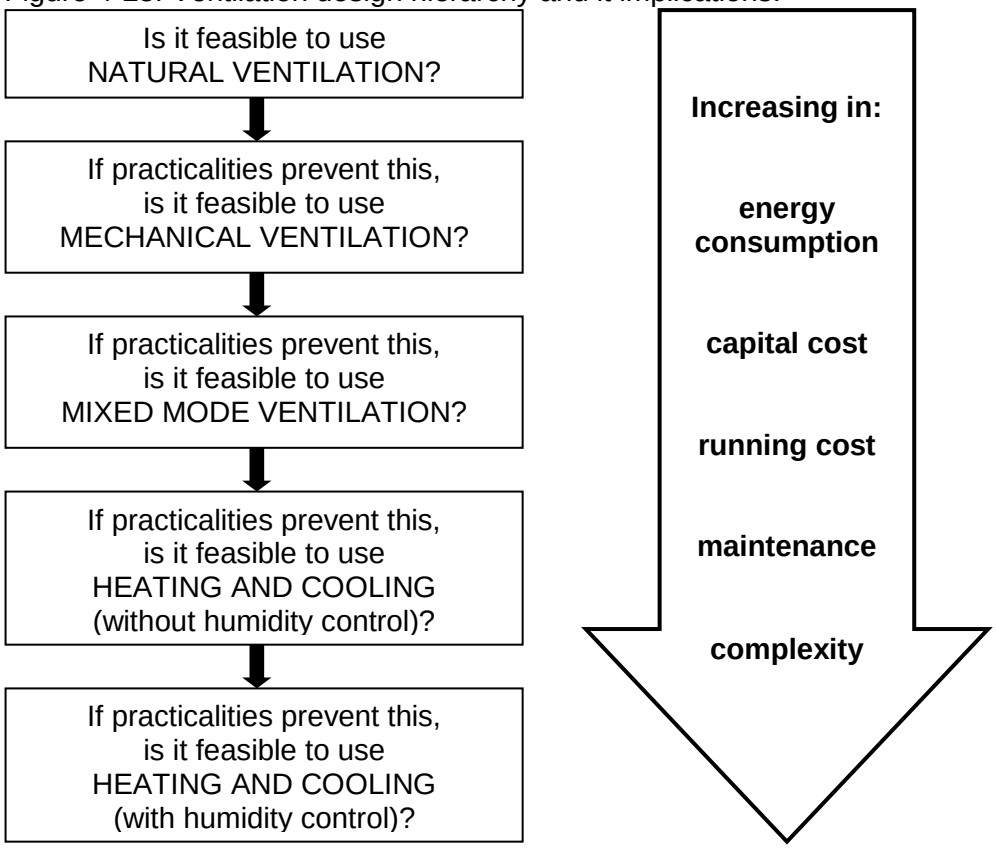

Source: CIBSE F (2004, pp7-1).

4.9.2. Deciding on a hybrid system technique

After recognizing that a hybrid system is necessary, the next step is to decide which combination of ventilation systems will achieve optimum performance. Heiselberg (2006) suggests a design process to guide in this process, which can be schematized in the following steps:

- Conceptual design phase which creates targets to be achieved (including budget limits, building parameters, IAQ and comfort requirements, ventilation and other passive technique strategies);
- Basic design phase (estimating building heat loads and contaminants as well as energy use and how to tackle it); and
- Detailed design phase and design evaluation, where these last are focused on the prediction of thermal loads control and IAQ in order to achieve the levels initially proposed.

Table 4-4: Building comfort system's design steps, parameters and techniques:

	Heating	Cooling	Lighting	Ventilation
Step 1	Conservation	Heat avoidance	daylight	Natural ventilation
Basic design	1. surface to volume ratio 2. insulation 3. infiltration	1. shading 2. exterior colours 3. insulation 4. thermal mass	1. windows 2. glazing 3. interior finishes	1.building form and internal layout 2. location of windows and openings 3. stacks
Step 2	Passive solar	Passive cooling	Daylighting	Natural ventilation
Climatic design	1. direct gain 2. exposed thermal mass 3. sunspace	1. evaporative cooling 2. convective cooling 3. cold air system	1. skylights 2. light shelves 3. light wells 4. solar shading	1. wind introduced ventilation 2. buoyancy induced 3. air distribution 4. control system
Step 3	Heating system	Cooling system	Electric lighting	Mechanical ventilation
Design of mechanical systems	1. radiators 2. radiant heating 3. warm air system	1. refrigeration plant 2. cooled ceiling or floor 3. cold air system	1. lamps 2. fixtures 3. location of fixtures	1. mechanical exhaust 2. mechanical ventilation 3. air conditioning

Source: Heiselberg (2002, pp33).

4.9.3. Types and scope of hybrid systems

The range of hybrid ventilation systems and strategies covers different possible scenarios. The modes of operation are related to the requirement, for instance (Heikkinen *et al.,* 2002; CIBSE A, 2007):

- supplementary systems: mechanical ventilation is activated when natural ventilation alone is unable to supply the prerequisites for IAQ or thermal comfort;
- Complementary systems: have both natural and mechanical ventilation systems working at the same time, with one regulating the other in order to achieve the specifications; and
- Alternate systems: have both natural and mechanical ventilation capacity, but working simultaneously, as needed.

Heiselberg (2002 and 2006) highlights that, since the potential for both natural and mechanical ventilation presents limitations, hybrid systems that combine both systems autonomously can improve their performance and result in better ventilation rates with minimum energy consumption. Further, the link between both modes by control systems is fundamental in the functioning of the ventilation strategy (Heiselberg, 1999). Mutual techniques can operate simultaneously or, otherwise, regardless of need. As regards, for example, maximum internal temperature and air velocity needed to provide comfortable levels, and which coupling decision should be based on the use

of intelligent control systems and/ or user control (Liddament *et al.*, 2006). As a result, according to the requirement, it is possible to have natural ventilation only, fan-assisted ventilation (for air supply and/ or extraction via low-pressure fans), stack wind-supported mechanical ventilation, or balanced ventilation with individual mechanical devices for air supply and extraction (Delsante and Vik, 2001; Heikkinen *et al.,* 2002; Heiselberg, 2002 and 2006; Awbi, 2003; CIBSE A, 2006). The range of hybrid ventilation systems and strategies covers different possible scenarios. Hybrid systems can impel external air directly into the interior, forcing the outflow of warmer air, or pre-cool the air supply by buried pipes and/ or PDEC systems before pumping it into the internal environment (Liddament *et al.*, 2006).

When designing hybrid strategies, the proper dimensioning of the whole airflow path that makes use of building-integrated components (from the air inflow supply, the distribution ducts and the outflow extraction) has to aim at the optimum performance of the ventilation system. Leakages and pressure drops have to be avoided throughout the system (Heiselberg, 2002 and 2006). The success of hybrid systems is also related to the integration of equipment control of and components with sensors. These sensors are usually connected to weather/ comfort databases that activate or indicate how the hybrid system has to work according to the external or internal conditions. Furthermore, different systems and equipment should be used for health and cooling purposes, monitoring the air temperature, solar radiation, relative humidity, rain, pollution levels, and fire/ smoke control. The challenge to the application of convective cooling systems consists of coupling cooling capacity and load with indoor thermal comfort levels and the built thermal mass, bearing in mind that the time taken to respond to any rise in indoor temperature is not instantaneous (Delsante and Vik, 2001; Heiselberg, 1999, 2002 and 2006; Wouters *et al.,* 1999; Liddament *et al.*, 2006).

Figure 4-24: Schematic building section showing a complementary hybrid ventilation system that uses wind-and buoyancy-driven forces allied to supply and exhaust fans:

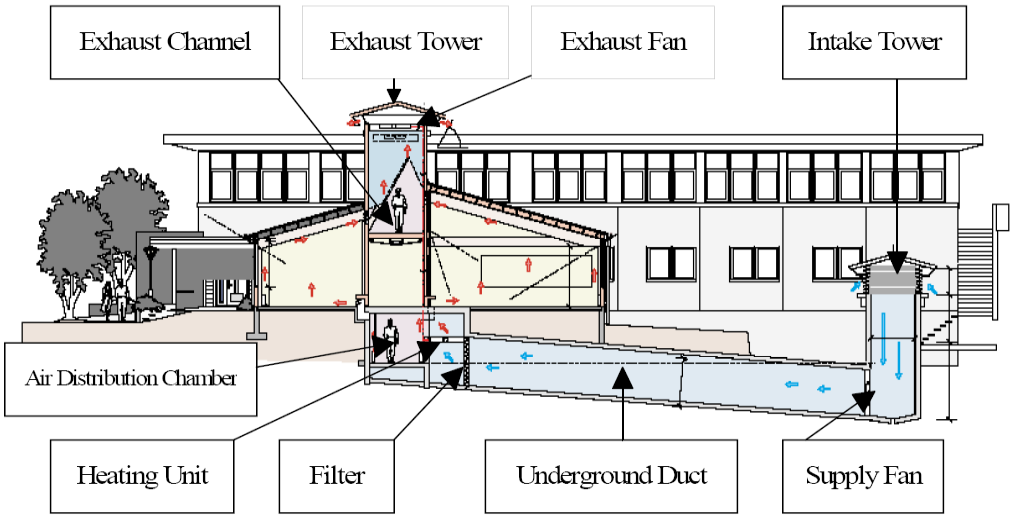

Source: Jeong and Haghighat (2002, pp129).

4.9.4. Calculating the performance of hybrid systems

Equipment and component suppliers must provide information about the performance of their products. This information may cover energy consumption, data on the pressure balance in the system including losses, increase or decrease, and the airflow rate for a given operational mode. Finally, with this information complete, it is possible to make use of equation 4-12, and thus find the total airflow rates due to wind- and buoyancy-driven forces added to the hybrid mechanical ventilation ratios, in accordance with the following equation (Awbi, 1998):

Equation 4-49 $$Q_{total} = |Q_{wind}^2 + Q_{buoyancy}^2 + Q_{mechanical}^2|^{0.5}$$

Where:

- Q_{total}: is the total airflow rate in the ventilation system (m^3/s);
- Q_{wind}: the airflow rate due to wind-driven forces (m^3/s);
- $Q_{buoyancy}$: the airflow rate due to buoyancy-driven forces (m^3/s); and
- $Q_{mechanical}$: the airflow rate added by mechanical sources (m^3/s);

On the other hand, more complex and accurate ways of simulating the performance of hybrid systems involve high technology computer calculations. These simulations, when coupling CFD (steady-state) and DTM (dynamic-state), have the heat gains/ losses through built mass as input for the CFD code and, then, air flow rates and pressure differences as input for the DTM calculation (Delsante and Vik, 2001; Heiselberg, 2002 and 2006).

While CFD calculations have already been covered in Chapter 3, a brief explanation of multi-zone simulations has to be made. This approach consists of dividing the building into several spaces connected by nodes in such a way that air and heat exchanges are analyzed zone by zone at each boundary connection of the airflow trajectory. These can be based on the zone pressure difference (mass balance equations) for each zone, or on the total zone pressure loop equations. The airflow trajectory for assessment and calculation purposes can be divided into the following nodes: external conditions > across envelope openings > through inlet ducts/ shafts > across internal/ room spaces > between different internal/ room spaces > across room outlet openings > through outlet ducts/ shafts > across envelope openings > reintegrated in the external conditions.

Table 4-5: Zone calculation software's areas of applicability:

	Ventilation rates	IAQ	Indoor temperatures	Sizing of openings
Simplified single zone	AIM 2 CEN explicit LBL / VENT			CIBSE Inversed Sizing Model
Simplified thermal+ ventilation	NatVent NITECOOL Summer-build		NatVent NITECOOL	NITECOOL
Single-zone ventilation	AIDA CEN explicit			
Multi-zone ventilation	AIOLOS BREEZE COMIS CONTAM96	NatVent BREEZE COMIS CONTAM96 NavIAQ		
Thermal+ ventilation	Passport Plus SUMMER-Tech.		Passport Plus	

Source: De Gids (2002, pp.6).

Delsante and Vik (2001) provide a comprehensive list of simulated case studies and methods of simulation. De Gids (2002) provides the range of applicability of a number of commercially available softwares which perform zone calculations for ventilation purposes.

4.10. Chapter conclusions

This chapter presented both the concepts related to and the theory of natural ventilation systems. It covers the role of ventilation in the internal environment and how to assess IAQ and thermal comfort. It also presents the method for estimating ventilation rates and ACH for wind- and buoyancy driven forces for several combined ventilation strategies. This theory constitutes the basis for both the methodology (Chapter 5) and the analysis of the experiment conducted in this research.

Part 03: Methodology

Chapter 5: Methodology

5.1. Introduction

This chapter presents the methodology adopted for assessing the airflow field in urban areas, the focus of this thesis. In order to achieve the objectives stated in Chapter 01. Various methods of research on urban fabrics and airflow simulation are employed, comprising: laboratory scale-model tests in a boundary layer wind tunnel (WT), computational fluid dynamics (CFD) models, and field measurements (FM). These methods are detailed in this chapter, and supported by theoretical research presented in Part 2: the literature review.

5.2. The research methods

Designing naturally ventilated building systems to perform at satisfactory levels involves the previous analysis of the airflow field in the external environment. This is necessary to determine whether the site offers the potential for the use of this technique. Thus, the potential is subject to urban environment shape and the airflow field below urban canopy height.

The urban shape can be described in terms of several physical dimensions, areas and volumes that define aspect ratios[29], such as building height to road width (H/W) or length (L/H), plan-area density ($a= A_{roof}/ A_{urb}$), and built-area density ($b= A_{built}/ A_{urb}$). For this reason, the relationship between the resultant airflow field and the urban aspect ratios is the basis of the investigation on an urban scale. The proposed research method is divided into the 4 steps which have been addressed to provide the amount of data for the intended analysis:

- Step 1: Calibration, verification and validation of the input parameters of the CFD models. CFD and WT outputs are compared to ensure the quality and reliability of the numerical simulations in reproducing airflow and identifying wind acceleration and changes in the airflow direction in external urban environments. This step is based on a number of simulations which combine two identical rectangular bricks. The comparisons between the results are aimed at spotting the accuracy and consistency achieved in the CFD simulations undertaken, since the input and calculation parameters will serve as a basis for subsequent more complex investigation using the same CFD

[29] See topic 2.6.2 in Chapter 2 for further information.

code. Three wind directions were defined for these experiments: perpendicular (90˚), parallel (0˚), and oblique (45˚) flows towards the bricks;

- Step 2: Study of urban prototypes with simplified volumetric shape simulated in CFD. A large number of CFD simulations are undertaken for the simplified volumes proposed, which were originally based on ratios of actual urban areas[30]. The systematic variation of the volumetric urban aspect ratio of these prototypes and the simulation for the three wind directions mentioned above allowed finding the relationship between the urban fabric and the airflow speed and direction in order to bring out the potential for natural ventilation in a building's environment. This step is focused on identifying both the airflow speed and direction and the pressure coefficient variation for different sets of urban aspect ratios;
- Step 3: Assessment of case studies. This step covers the assessment of the airflow in two real urban centres (Cardiff Cathays campus area, Wales; and Paulista Avenue, São Paulo, Brazil) carried out via 2 (WT and CFD) or 3 (WT, CFD, and field measurement- FM) techniques combined and for up to 8 wind directions. This aims to verify and validate the results obtained by the techniques in a complex urban scene to identify the level of similarity found between these actual urban areas and the urban prototypes- with comparable aspect ratios- proposed; and
- Step 4: Further investigations of airflow speed and direction in the high-density urban areas and mechanisms of ventilation for high-rise office towers. Using an existing building from the Paulista Avenue case study (the CYK Tower), further tests were carried out in a WT to assess the impact that balconies and vertical architectonic ornaments may have on the Cp distribution in tall urban buildings. Finally, the possibility of using central atriums and top wind catchers to create building design alternatives for allowing both wind-driven (simulated in WT) and buoyancy-driven (calculated via equations) ventilation systems in downtown areas has been explored.

[30] The urban areas analyzed were: the Museum Ave., Cardiff, Wales; the Oxford Street, London, England; the Blvd. Republique, Paris, France; the Paulista Ave., São Paulo, Brazil; and the Hung Hom rd., Hong Kong, HK, which are covered in details in topic 5.4.1.1.

5.2.1. On the outcomes of the research methods

To assist the investigation of airflow in the built environment, both quantitative and qualitative information are necessary. While the results of wind speed and direction, and pressure coefficients provide quantitative numerical information, flow visualization techniques allow a qualitative understanding of airflow behaviour around buildings and other physical barriers. The combined analysis of the outcomes of these techniques compared to the urban aspect ratios may then allow this research to propose a scale to represent the potential for natural ventilation in existing urban areas. Both the quantitative and qualitative data were obtained by experimentation with:

- Scaled physical models in a boundary layer wind tunnel;
- CFD calculations; and
- Field measurements in an actual urban area.

Since this research makes use of CFD calculations for a large part of the analysis, the comparison of the results of the different methods allows the demonstration of the accuracy and confidence levels achieved by each of these processes. Finally, the three techniques were utilized for the same case study permitting the triangulation of the results. Further, the methods used in the verification and validation process and the steps for the CFD modelling found in the literature have already been largely explored in Chapter 3.

5.3. The two bricks experiment

Two rectangular bricks of identical size were used in simulations by both WT and CFD methods in order to assess the airflow around and within a simplified canyon shape. The aim of this simulation was to validate the input parameters used in the CFD models in order to obtain airflow field and pressure output figures comparable to those obtained in the WT physical experiment.

Table 5-1: description of the methods of simulation and output post-processing technique employed for the several combinations of aspect ratio and position vis-à-vis main airflow.

H/W ratio →		0.50	0.66	1.00	2.00
↓ Method		prevailing wind direction			
Wind Tunnel	bubble visualization	90˚	90˚	90˚	90˚
CFD	vectors & pathlines	90˚	90˚	0˚ 45˚ 90˚	90˚
Wind Tunnel	contour plots & data	0˚ 45˚ 90˚	0˚ 45˚ 90˚	0˚ 45˚ 90˚	0˚ 45˚ 90˚
CFD	contour plots & data	90˚	90˚	0˚ 45˚ 90˚	90˚

Source: This study.

Not all the possible combinations between the aspect ratios and the airflow directions were undertaken by both the wind tunnel and the CFD techniques. Good results and comparisons were achieved with the combinations given in Table 5-1. Further simulations would either produce redundant results or be too time-consuming at this stage of the investigation. Moreover, some of these combinations appeared to be impracticable for a number of selected methods of simulation and adopted output post-processing. For instance, the wind tunnel airflow visualization with helium bubbles[31], performed well for perpendicular settings only, since the position of the acrylic brick for parallel and oblique winds produced too much glare and did not allow the analysis of the resultant flow. For instance, a set of parallel bricks was placed orthogonally to the airflow direction.

[31] A technique to be dealt with in topic 5.5.1.3.

Figure 5-1: Example of the set of two parallel bricks placed at 90˚towards the flow (H/W=1. 0).

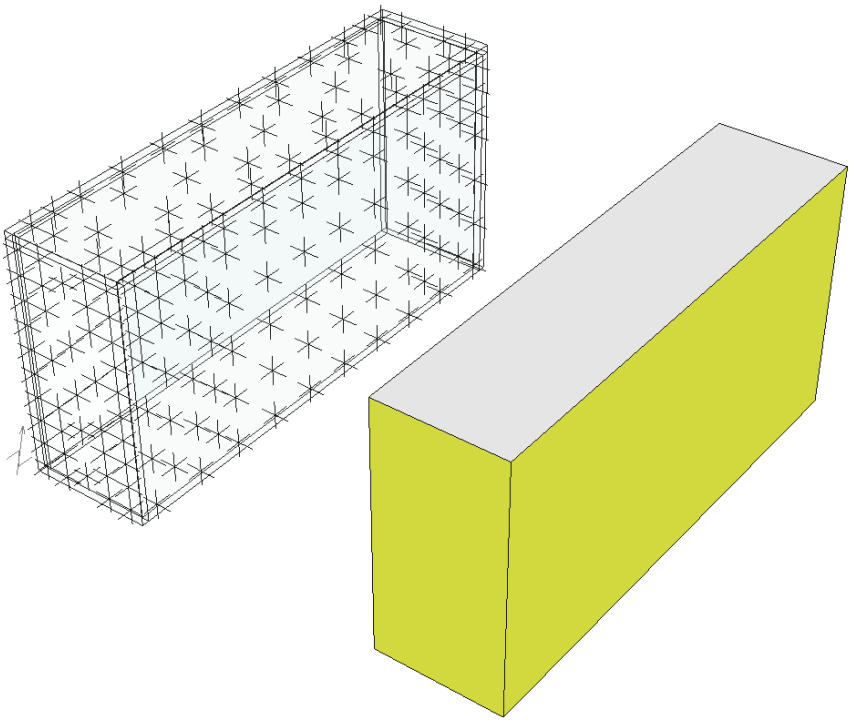

Source: This study.

5.4. The urban environment analysis

The urban environment analysis covers the study of simplified urban prototypes; then examines the case studies of two actual urban areas and finally addresses the assessment of an office tower as built and a proposed tower prototype for one of the urban scenarios investigated.

5.4.1. The urban prototypes

The need to explore non-real urban shapes arose from the recognition of the link between variations in urban shapes and the resultant airflow field. The ultimate goal is to identify the potential of an urban area for applying natural ventilation strategies. Such analyses are only possible for environments with controlled parameters in which aspect ratio changes can be decided by pre-determined criteria. Further, the range in their shapes should cover as many types of urban fabric as possible, from high to low density, from low building centres to downtown skyscrapers. For this reason, the definition of the urban prototype ratios has been based upon the analysis of fractions of five urban areas and canyons of various aspect ratios and landscapes.

5.4.1.1. The urban area analysis

The urban areas that served as the basis for prototypes are here presented. An approximation method was carried out to obtain areas dimensions. This method sought to not to obtain representative dimension aspects that would express the physical features of the canyons selected and their surrounding areas. For instance, the floor area was estimated by drawing polygons on their perimeters on top-view images obtained from Google Earth[32]. Also, the buildings' height was defined by the numbers of floors counted in the Google Street-View and multiplied by the floor-to-floor height. For the cities of Cardiff, London, Paris and São Paulo, on-the-spot photographs were also taken. The floor-to-floor height was estimated by measuring one step height and then multiplying it by the number of steps per floor. This was done for a sample of buildings to which access was allowed. The data for Hong Kong came from the Google source and the CRiBE/ WSA, Cardiff University[33] database.

Figure 5-2: Museum Ave. and and Park Place in the Cathays Campus, Cardiff, Wales (51o 29' N - 3o 10' W):

Source: Google Earth.

Figure 5-3: Oxford Street and the Oxford Circus, London, England (51^{o} 30' N - 0^{o} 8' W):

Source: Google Earth.

[32] The images shown were saved from the free-version of the software Google Earth and the applicative Street-View in March-2011.

[33] This researcher collaborated with an investigation conducted in May, 2008 at CRiBE, WSA, Cardiff University, under the supervision of Prof. Phil Jones. The study was entitled ''Assessment of the wind amplification in the surrounding areas for a proposed new building 'The Hong Kong Community College Development' from 'The Hong Kong Polytechnic University''. The necessary information on the site to create the CFD models was provided by The Hong Kong Polytechnic University.

Figure 5-4: Blvd. Republique, Paris, France (48^{o} 51’ N- 2^{o} 22’ E):

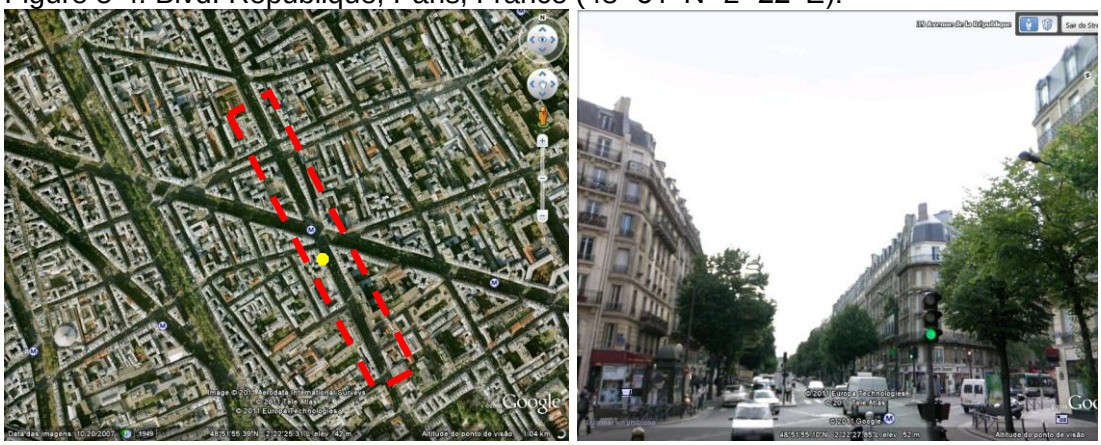

Source: Google Earth.

Figure 5-5: Paulista Ave., São Paulo, Brazil (23o 33’ S - 46o 39’ W):

Source: Google Earth.

Figure 5-6: Hung Hom rd., Hong Kong, HK (22^{o} 18’ N - 114^{o} 11’ E):

Source: Google Earth.

The approach of the urban analysis was not restricted to a specific street or avenue. On the contrary, the purpose was to analyze an area of approximately 196,350m^{2}, equivalent to that of a circle 500m in diameter measured from the spot at the centre of the area. This circular dimension was defined in view of the fact that a distance of 250m in an open field would allow disturbed flows and turbulent wakes to

leeward of vicinity towers of up to 62.5m height to reattach to the flow field before reaching the target area at its centre. This is in accord with the report of Chandra *et al.* (1986) which states that wake flows take four times the height of an isolated high structure to become reestablished.

Figure 5-7: Analyzed perimeter of Paulista Avenue urban area.

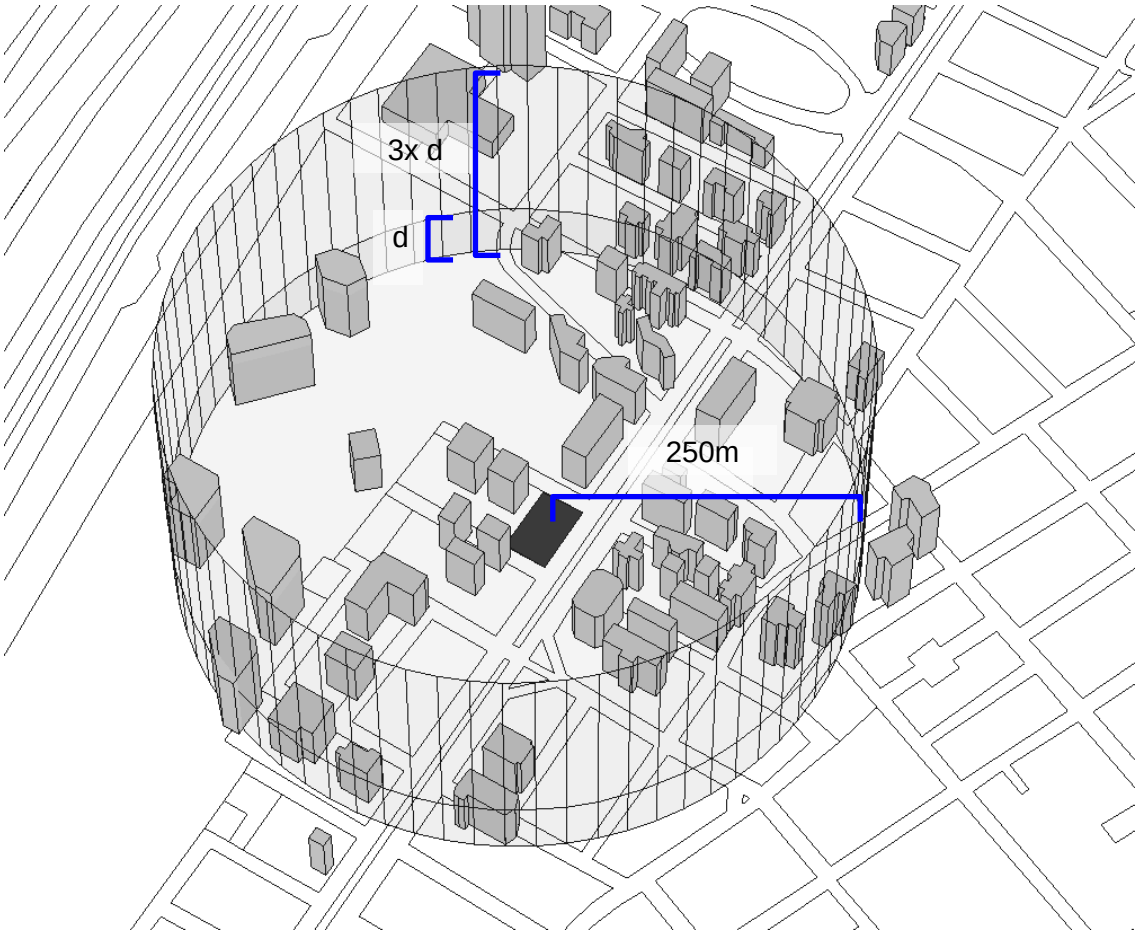

Source: this study.

Figure 5-8: Perimeter marking each of the assessed urban areas:

Cardiff London Paris São Paulo Hong Kong

Source: this study.

Figure 5-9: Shading mask for the assessed urban areas:

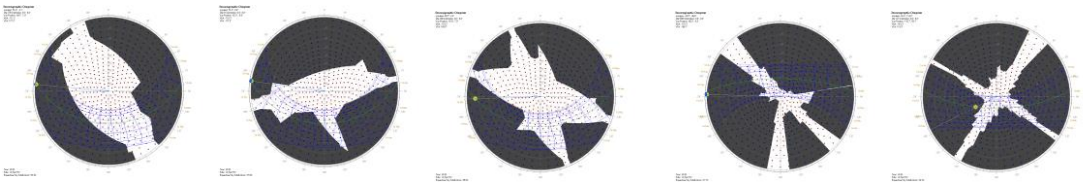

Cardiff London Paris São Paulo Hong Kong

Source: this study.

Table 5-2: Physical dimensions, areas and aspect ratios of the urban areas.

City	floor nº	H	/	W	rate	A_{roof} / A_{urb} A_{roof}	rate	A_{built} / A_{urb} A_{built}	rate
Cardiff	4	18.0	/	32.0	0.56	63,347	0.32	202,710	1.03
London	6	25.0	/	26.0	0.96	127,466	0.65	611,837	3.12
Paris	6	30.0	/	29.2	1.03	143,297	0.73	687,825	3.50
São Paulo	21	68.0	/	62.0	1.10	47,145	0.24	792,042	4.03
Hong Kong	18	68.0 54.0	/	29.0 50.5	2.35[34] 1.07	55,396	0.28	797,702	4.06

Source: this study.

The aspect ratios were also compared to other ratios found in the literature on airflow in urban areas and canyons, presented in Chapter 2. Based on this information, it may be said that the relationship between building height and street width in existing urban centres which have been researched so far ranges from 0.40 to 3.50. This proportionality in the urban landscape has been reported for different places and a great range of building heights. For instance, the building height may vary from 48.3 to 7.5m and from 16.0 to 87.8m, for the previous narrow and large aspect ratios, respectively. Oke (1988) observes that, for cities around the World with more than 100,000 inhabitants, H/W ranges from 0.75 to 1.70, while in the US this ratio varies from 1.15 to 3.3 due to the 'skyscraper culture'. These figures have already been mentioned[35] and are in tune with the findings just quoted.

[34] This ratio refers to the basement and ground floor, usually allowed up to 9m height.

[35] See topic 2.6.3 in Chapter 2 for further information.

5.4.1.2. The groups of urban prototypes

Airflow in urban environment results from a combination of built density and free airflow velocity and direction. In the investigation into urban prototypes many of these features were systematically repeated or modified[36] and simulated on CFD software[37]. The definition of the proposed urban prototypes was based on the aspect ratios of actual urban areas, covering a variety of urban landscapes. The output from these prototypes was organized on a scale such as would allow later comparison between it and that of the case studies with similar aspect ratios. On the other hand, it is not the intention of these sets of prototypes to be generally valid or applicable since they have limitations and were created specifically to answer the hypothesis set out in Chapter 1.

A total of eighteen urban arrangements were simulated using the same ABL for three wind directions: parallel (0^o), orthogonal (90^o), and oblique (45^o), totalling fifty-three different scenarios investigated. The prototypes were divided into four types: 'A', 'B', 'C', and 'D', in accordance with the H/W aspect ratio, and then into four sub-types: 1, 2, 3, and 4, with decreasing plot occupancy density. The reason why a nomenclature was created for each prototype lies in the fact that the airflow in urban areas results from a combination of features, such as: the urban areas, dimensions, and aspect ratios[38] (H/W, L/H, A_{roof}/A_{urb}, and A_{built}/A_{urb}); together with the free airflow velocity and direction. Thus, no presuppositions are made in the assessment of the results. Further, while the first two aspect ratios refer to the respective canyon's linear dimension, the last two refer to areas of several blocks within a pre-established urban perimeter area.

From 'A' to 'C' the scenarios were symmetrical, the height of the blocks was kept constant at 30m, and the division among the types took into account the H/W aspect ratio and the roof and built areas. The length of the blocks also varied from 180m to 30m. The type 'B-Step' was a variation of the 'B-2' in which half of the blocks had their height doubled in order to assess the impact of step-up and step-down airflows in canyons. Type 'D' was also based on the previous sets 'A' and 'B', but it presented random asymmetry due to height variation of up to three times the previous ones in some of its blocks. This set sought to represent a more heterogeneous urban scenario. Finally, the 'D-4' scenario presented several detached blocks of 30, 60 and 90m height, thus resembling a real urban landscape.

[36] The method employed for the definition of the urban prototypes was covered in topics 5.2, 5.4.1, and 5.6.4 of Chapter 5.
[37] For further information about the CFD modelling parameters and definitions see Chapter 3: 'Modelling Airflow in the Urban Environment'.
[38] See topic 2.6.2 in Chapter 2 for further information.

Figure 5-10: Urban prototype scenarios top views and cross sections with the three simulated wind directions.

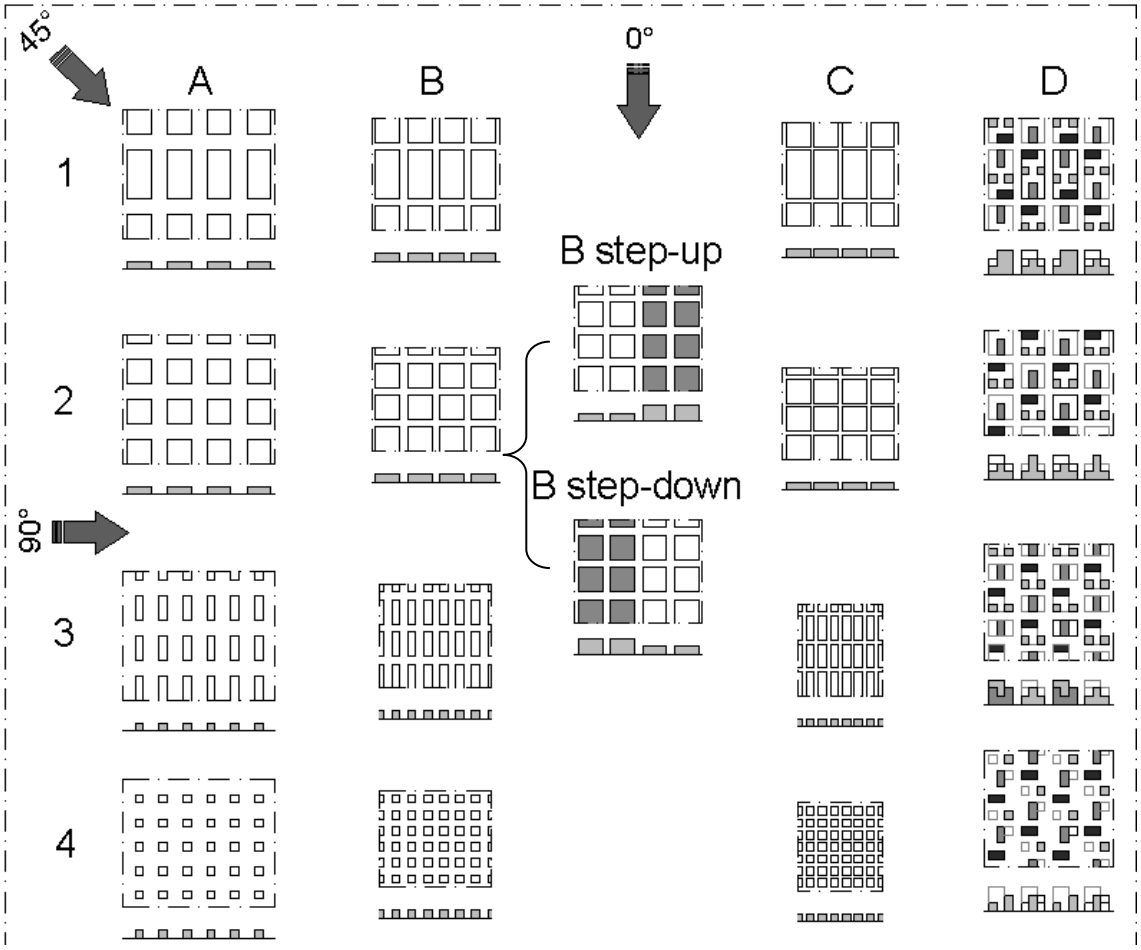

Source: this study.

In order to organize de analysis of the results from the urban prototypes simulation and to permit the access of specific different variables, the prototype scenarios were organized into six groups of similar mandatory features, and will be shown in the sequence.

- Group 01: comprises the A1, B1, and C1 prototypes. This group consists of symmetrical blocks with constant 30m height, 90m width, and 180m length alongside the canyons, which gives the same L/H 6.0 aspect ratio for them. Conversely, the variable canyon width of 60m (wide), 30m (square) and 15m (narrow) provides H/W aspect ratios of 0.5, 1.0, and 2.0, respectively. Also, this group has different A_{roof}/A_{urb} and Ab_{uilt}/A_{urb} ratios in each scenario;

Figure 5-11: Top-view (A1) and cross-section (A1, B1, and C1) of the prototype models simulated for wind incidences at 0o, 45o and 90o and the lines used for extracting numerical data from the canyon's main axis.

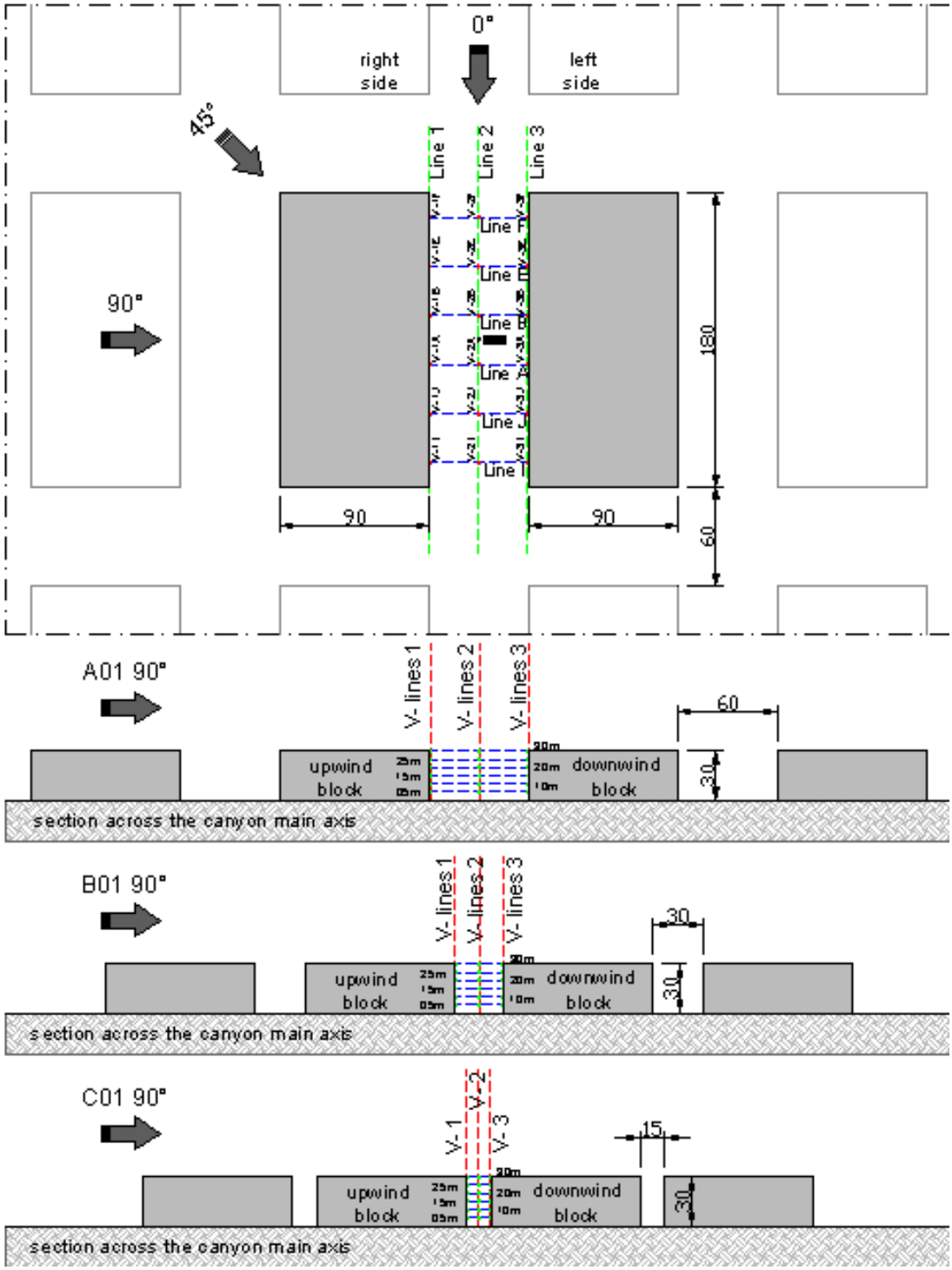

Source: This study.

- Group 02: comprises the A2, B2, and C2 prototypes. This group, also symmetrical, consists of square blocks with constant 30m height, and 90m width and length. While the L/H 3.0 aspect ratio is the same, the different canyon widths of 60m (wide), 30m (square) and 15m (narrow) provide H/W aspect ratios of 0.5, 1.0, and 2.0 and different A_{roof}/A_{urb} and A_{built}/A_{urb} ratios for each scenario;

Figure 5-12: Top-view (A2) and cross-section (A2, B2, and C2) of the prototype models simulated for wind incidences at 0°, 45° and 90° and the lines used for extracting numerical data from the canyon's main axis.

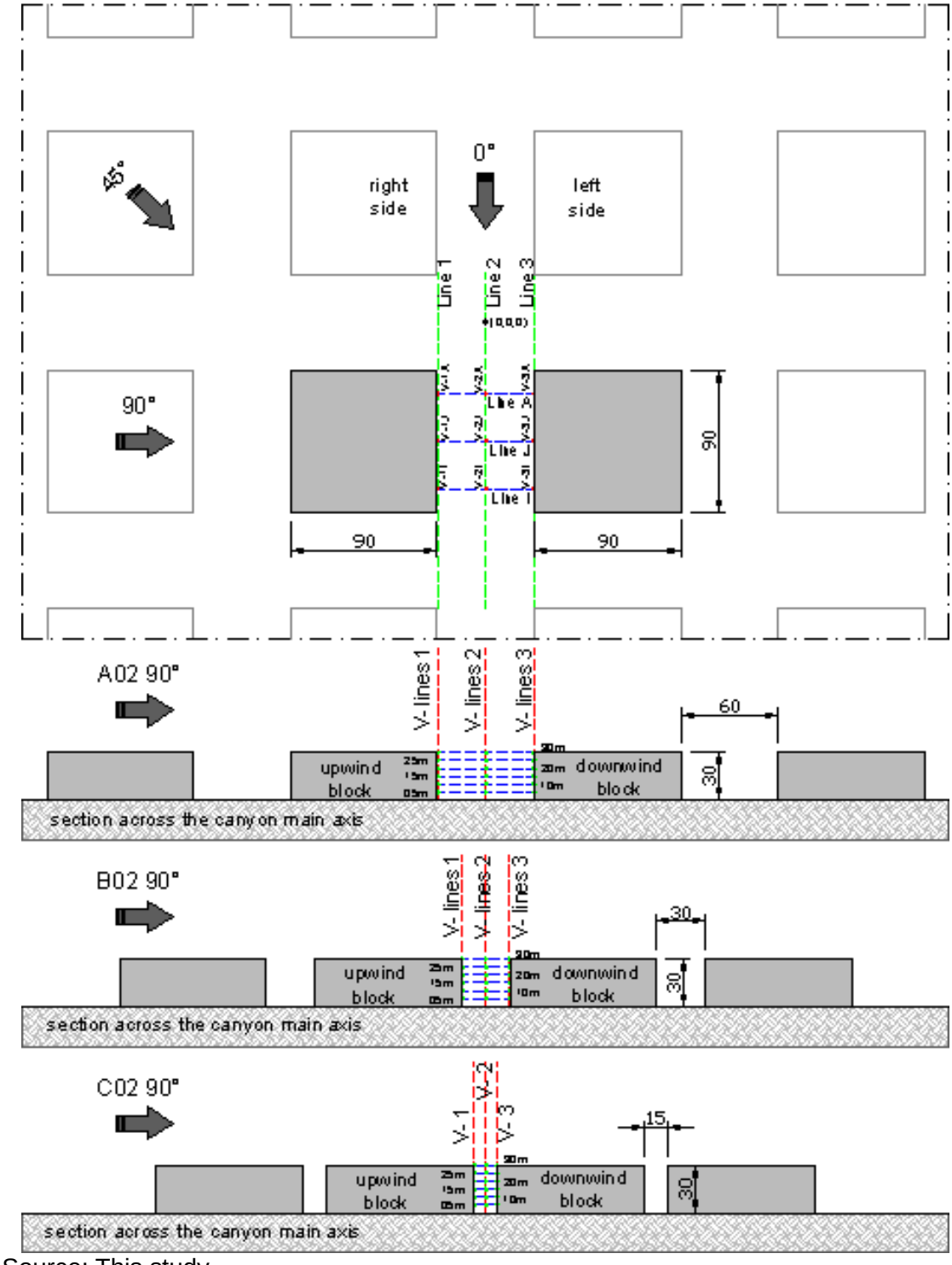

Source: This study.

- Group 03: comprises the A3, B3, and C3 prototypes. This group has the same L/H and H/W aspect ratios as group 02, but with narrower blocks of 30m width instead, providing different A_{roof}/A_{urb} and A_{built}/A_{urb} ratios for the same canyon volumes;

Figure 5-13: Top-view (A3) and cross-section (A3, B3, and C3) of the prototype models simulated for wind incidences at 0^o, 45^o and 90^o and the lines used for extracting numerical data from the canyon's main axis.

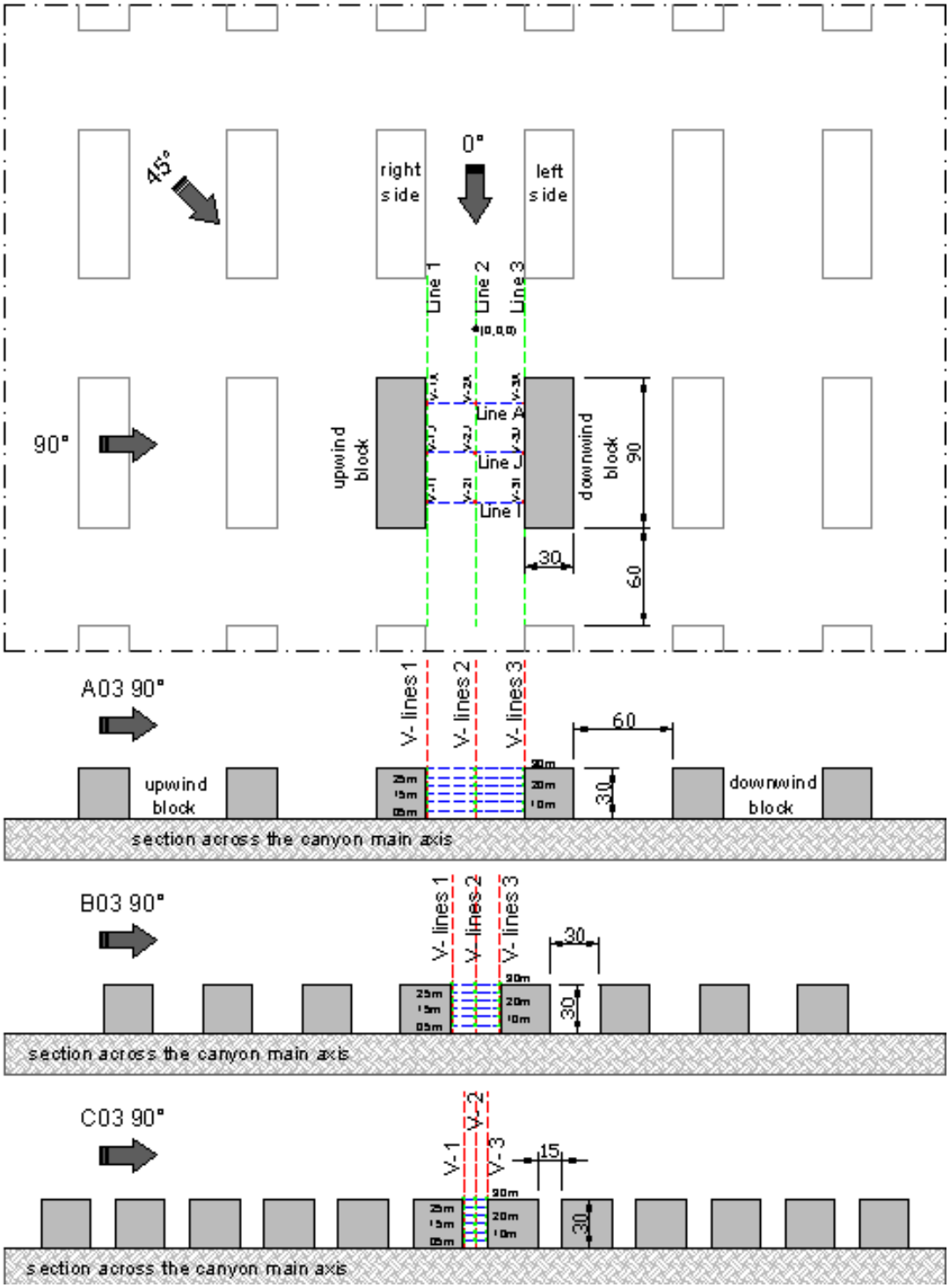

Source: This study.

- Group 04: comprises the A4, B4, and C4 prototypes. This group consist of a symmetrical array of cubes with 30m length, width and height and L/H 1.0 aspect ratio. The variable width of 60m (wide), 30m (square) and 15m (narrow) gives H/W aspect ratios of 0.5, 1.0, and 2.0, with difference in both the A_{roof}/A_{urb} and A_{built}/A_{urb};

Figure 5-14: Top-view (A4) and cross-section (A4, B4, and C4) of the prototype models simulated for wind incidences at 0^o, 45^o and 90^o and the lines used for extracting numerical data from the canyon's main axis.

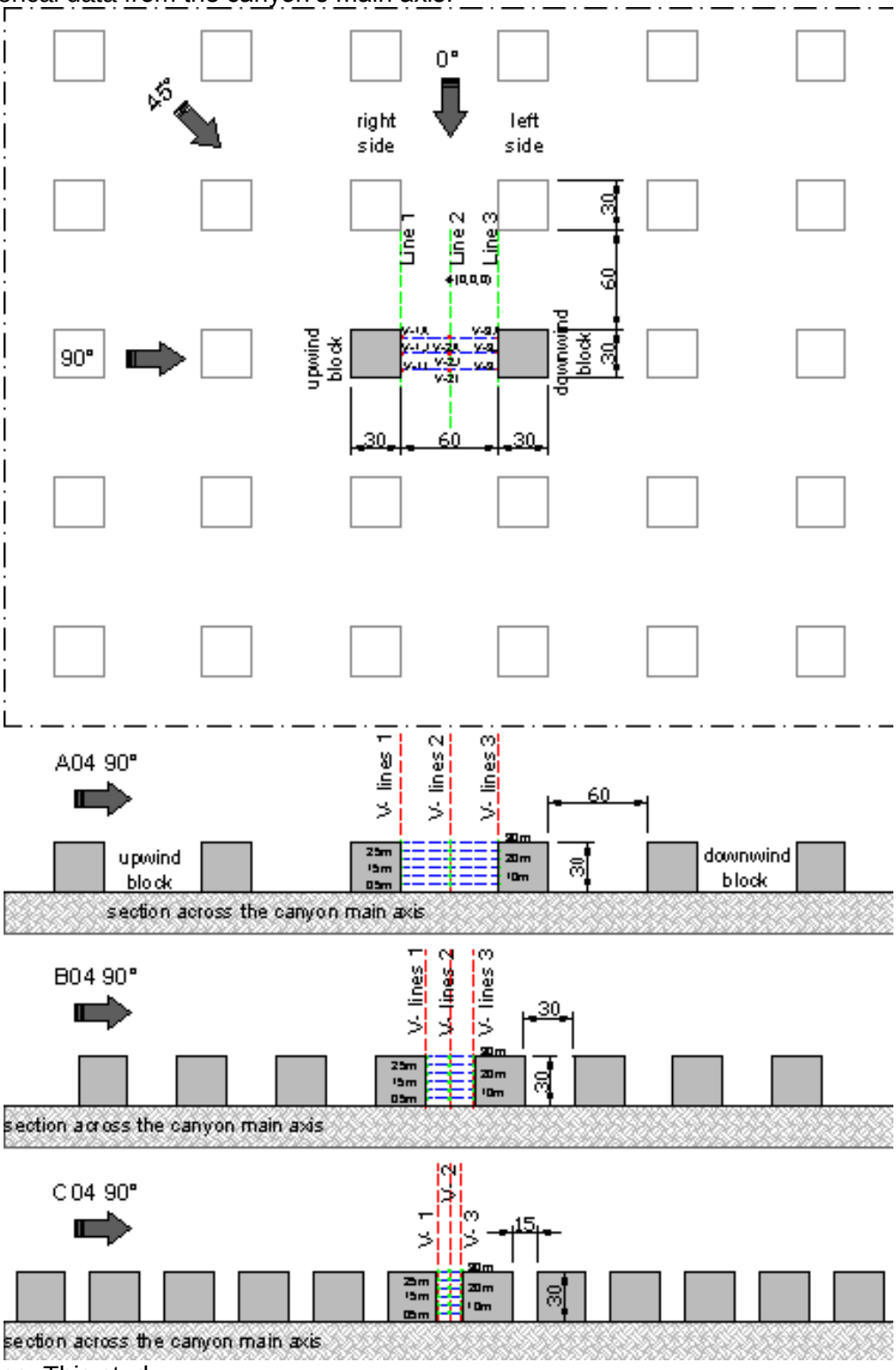

Source: This study.

- Group 05: Based on the square block dimensions of the B2 scenario, this group comprises the B2 Step-up and B2 Step-down prototypes. The difference from the B2 consists of having half of the blocks with 30m height and the other with 60m height, creating a symmetrical difference of level between them. This variation altered the canyon volumes and the Ab_{uilt}/A_{urb} ratios, while the same A_{roof}/A_{urb} ratio was maintained; and

Figure 5-15: Prototype B02 STEP top-view and cross-section for 0^o, 45^o and 90^o winds and the lines used for extracting numerical data from the canyon's main axis.

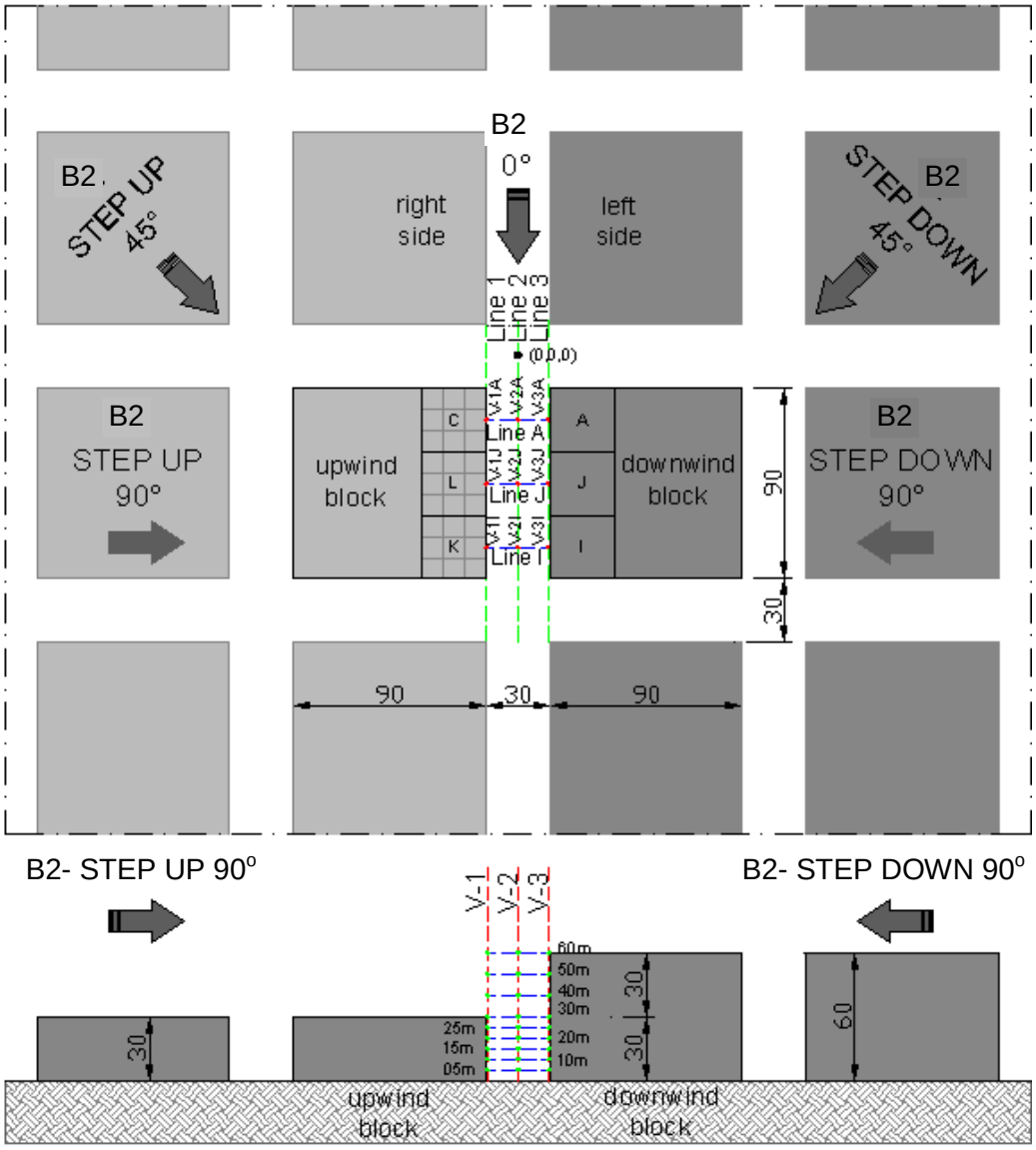

Source: This study.

- Group 06: comprises the D1, D2, D3 and D4 prototypes. This group is an attempt to approximate to high-rise buildings urban scenarios. Based on the previous groups' block sizes, it starts with long blocks, which are then divided in two, and ends in an array similar to detached blocks. The difference consists of having different and asymmetrical heights (30m, 60m and 90m) resembling urban towers throughout the model. The L/H and H/W aspect ratios change block by block and averaged results were, therefore, considered. Both the A_{roof}/A_{urb} and the A_{built}/A_{urb} ratios were comparable to those of real density urban centres.

Figure 5-16: Prototype D01 top-view and cross-section for 0^o, 45^o and 90^o winds and the lines used for extracting numerical data from the canyon's main axis.

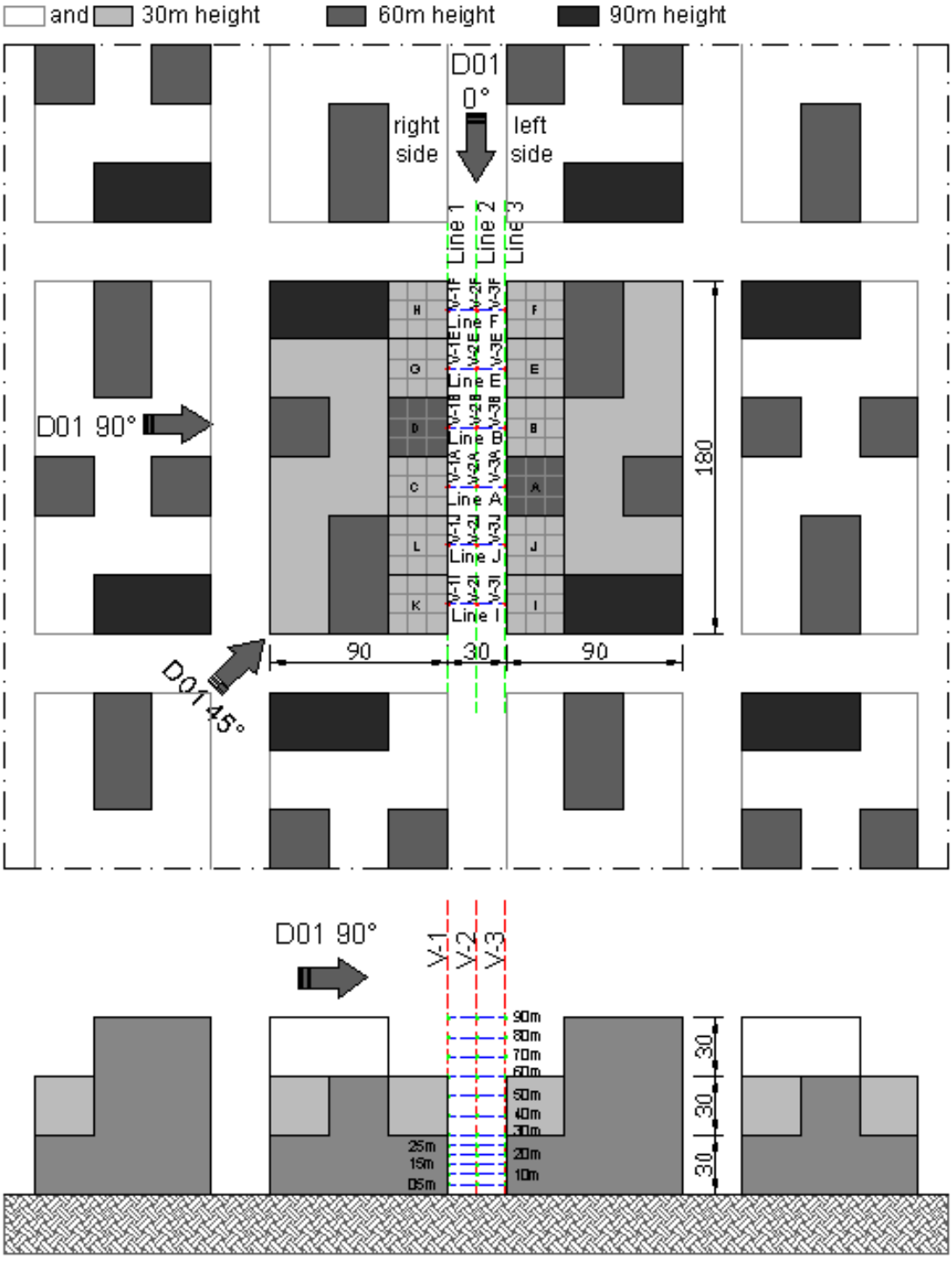

Source: This study.

Figure 5-17: Prototype D02 top-view and cross-section for 0°, 45° and 90° winds and the lines used for extracting numerical data from the canyon's main axis.

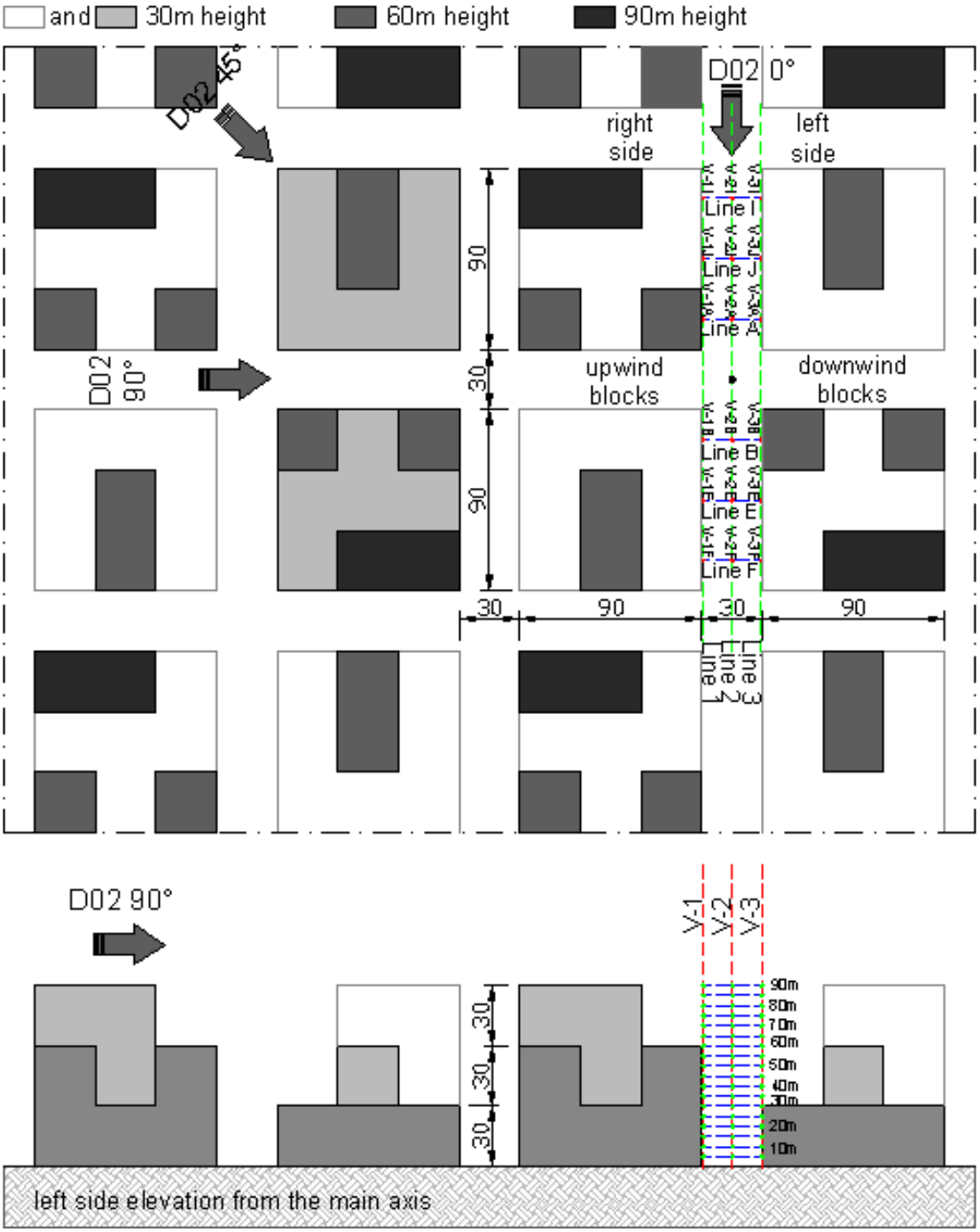

Source: This study.

Figure 5-18: Prototype D03 top-view and cross-section for 0°, 45° and 90° winds and the lines used for extracting numerical data from the canyon's main axis.

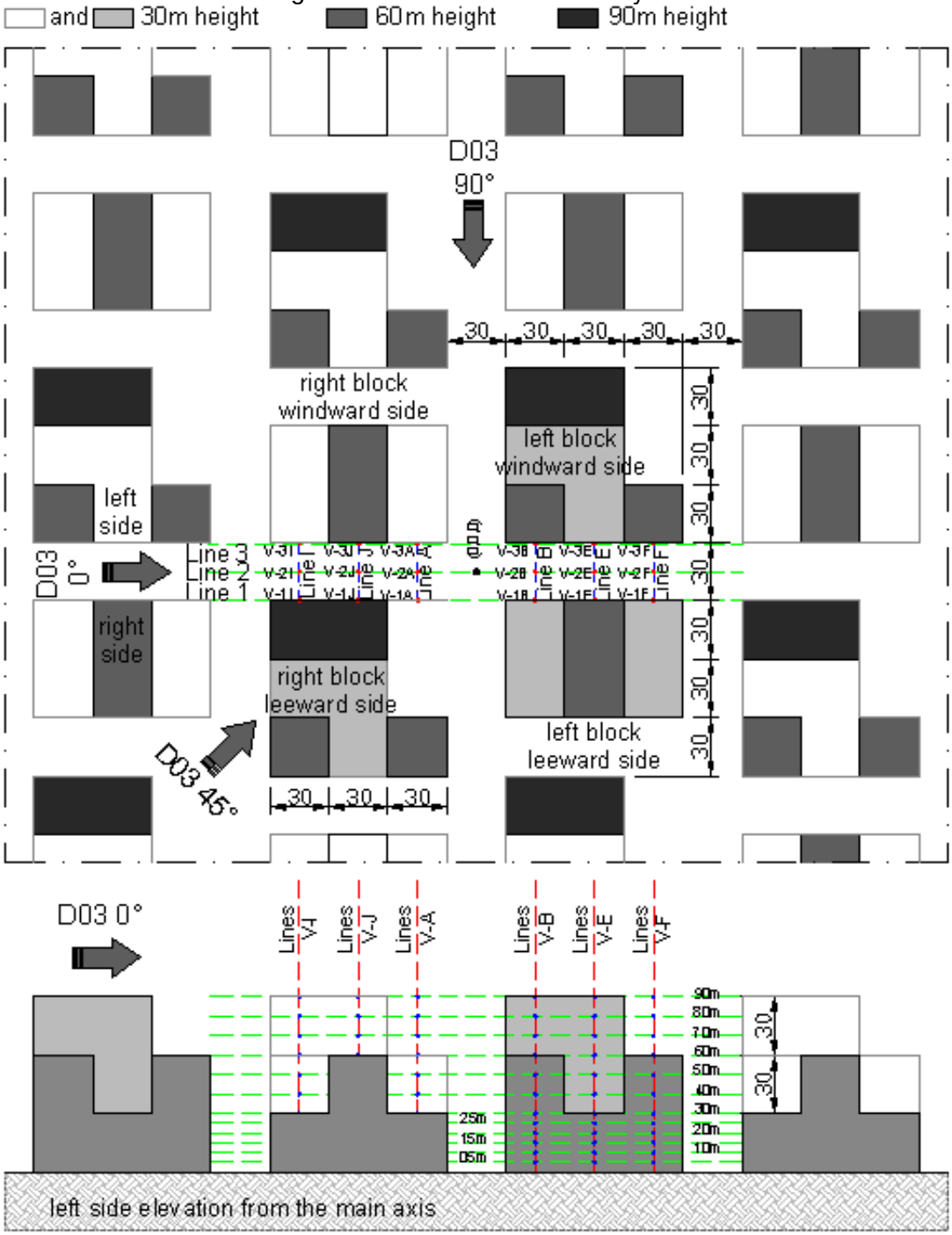

Source: This study.

Figure 5-19: Prototype D04 top-view and cross-section for 0°, 45° and 90° winds and the lines used for extracting numerical data from the canyon's main axis.

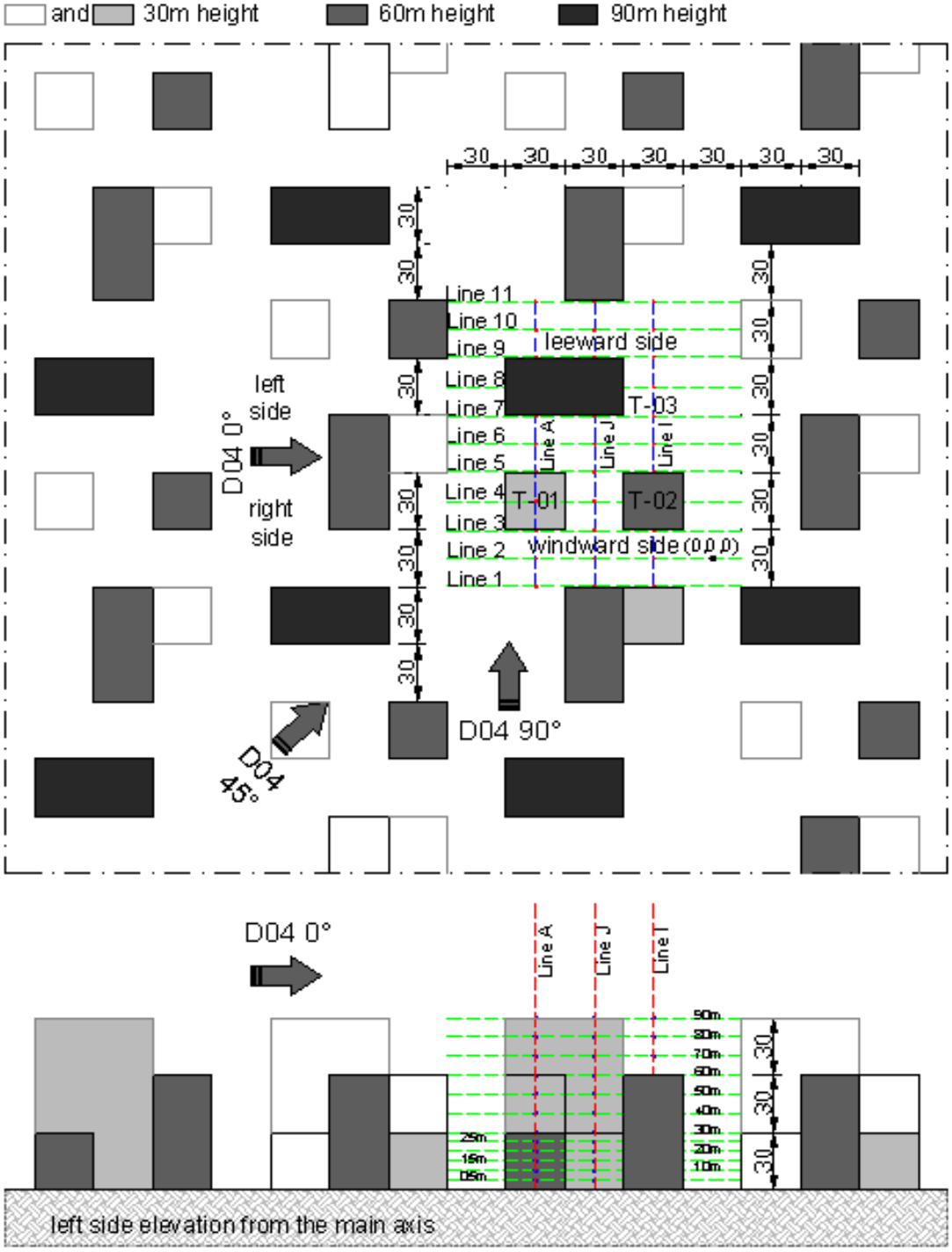

Source: This study.

Table 5-3: Definition and characteristics of the urban prototype models and their equivalence to the real urban canyon assessed.

	Aspect ratio						A_{roof} / A_{urb}				A_{built} / A_{urb}		
Set	H (m)	W (m)	L (m)	H/W rate	L/H rate	similar to	A_{roof} (m^2)	A_{urb} (m^2)	rate	similar to	A_{built} (m^2)	rate	similar to
A1	30	60	180	0.50	6.0	Cardiff	82,557	196,540	0,42	Cardiff	660,456	3,36	Paris, SP
B1	30	30	180	1.00	6.0	London, Paris, SP, HK	122,604	196,540	0,62	London, Paris	980,832	4,99	SP, HK
C1	30	15	180	2.00	6.0	HK	147,857	196,540	0,75	London, Paris	1,182,856	6,06	-
D1 [39]	30-90	30	180	1.0-3.0	2.0-6.0	London, Paris, SP, HK	122,675	196,540	0,62	London, Paris	1,456,600	7,41	-
A2	30	60	90	0.50	3.0	Cardiff	71,457	196,540	0,36	Cardiff	571,656	2,91	London, Paris
B2	30	30	90	1.00	3.0	London, Paris, SP, HK	109,252	196,540	0,56	London	874,016	4,45	SP, HK
$B2_{up}$	30-60	30	90	1.0-2.0	3.0	Cardiff	109,252	196,540	0,56	London	1,311,024	6,67	-
$B2_{down}$	30-60	30	90	1.0-2.0	3.0	Cardiff	109,252	196,540	0,56	London	1,311,024	6,67	-
C2	30	15	90	2.00	3.0	SP	141,298	196,540	0,72	Paris	1,130,352	5,75	-
D2	30-90	30-60	90	0.5-3.0	1.0-3.0	London, Paris, SP, HK	109,252	196,540	0,56	London	1,277,216	6,50	-
A3	30	60	90	0.50	3.0	Cardiff	40,686	196,540	0,21	SP	325,488	1,66	Cardiff
B3	30	30	90	1.00	3.0	London, Paris, SP, HK	72,436	196,540	0,37	Cardiff	579,488	2,95	London, Paris
C3	30	15	90	2.00	3.0	HK	72,436	196,540	0,57	London	894,448	4,55	SP, HK
D3	30-90	30-90	60-90	1.0-3.0	0.66-3.0	London, Paris, SP, HK	79,358	196,540	0,40	-	1,038,064	5,28	-
A4	30	60	30	0.50	1.0	Cardiff	20,825	196,540	0,11	-	166,600	0,85	Cardiff
B4	30	30	30	1.00	1.0	London, Paris, SP, HK	49,568	196,540	0,25	SP, HK	396,544	2,02	-
C4	30	15	30	2.00	1.0	HK	85,606	196,540	0,44	-	684,848	3,48	London, Paris, SP
D4	30-90	30-90	30-60	1.0-3.0	0.33-2.0	London, Paris, SP, HK	58,500	196,540	0,30	Cardiff , SP, HK	979,200	4,98	SP, HK

Source: this study.

[39] Several H/W and L/H ratios can be found in the D1, D2, D3, and D4 prototypes since the geometry and volumes are asymmetrical and heterogeneous. Therefore an averaged value based on the several dimensions in the model is used for calculating the related urban aspect ratios.

Several links between the prototypes and the urban areas may be made. However, when these links are related to one aspect alone there is only a weak connection between them. For instance, if the H/W aspect ratio is considered alone, four urban areas, London, Paris, São Paulo and Hong Kong, have an H/W ratio around 1.0. Conversely, when associated with other criteria, for instance plot occupancy; the first two cities are closer to prototype B1, and the last two to D4, since there is another link as well. In addition, the respective examples present visual compatibility in their urban landscape. In order to confirm whether the built aspect ratio links can be transferred to the results in terms of airflow pressure and velocity decrease within these urban areas, two of these sites, Cardiff and São Paulo, were selected for further investigation. Both of these places could provide essential information to verify the accuracy of the proposed method. Further, neither Cardiff nor São Paulo matched accurately a prototype in all three criteria. This may help to bring out whether one of the criteria is stronger than the other in the relation between built mass and the resultant airflow field.

5.4.2. Introduction to the case studies

Here the two urban areas selected for the case study were: Park Place on the Cardiff University Cathays Campus; and Paulista Avenue, in São Paulo. As case studies, both areas were simulated by CFD and wind tunnel, while field measurements (FM) were only performed in the former. It is worthy of mention that the Cardiff University Cathays Campus area was simulated for the eight prevailing wind directions (N, NE, E, SE, S, SW, W, and NW) by both the CFD and WT methods since, as FM were undertaken in this area, the greater the number of wind directions simulated, the greater the chance of obtaining results comparable with the data measured '*in locus'*. On the other hand, Paulista Ave. was modelled for the five prevailing wind directions in the region: SE; S; NW; N; and NE (in descending order of incidence).

5.4.2.1. The Cardiff University Cathays Campus

The Cathays Campus neighbourhood is considered a low-density area with mostly three-floor low buildings close to open areas such as Alexandria Gardens and Bute Park. The exceptions are the Psychology and the Chemistry School buildings, with 12 and 8 floors, respectively. The sides of the Law School building, which is 4 floors high, are located in Park Place and Museum Avenue. This last road forms, along with the Welsh Assembly building on the other side of the road, a wide urban canyon of H/W= 0.56 aspect ratio. This continuous canyon shape, together with its proximity to the WSA meteorological station (which will be detailed later in this chapter), and the possibility of frequent access to its facilities being granted in order to set-up and carry on data collection, made the Law School building the ideal spot for carrying out the field measurements[40].

Figure 5-20: Views from Museum Avenue and Park Place.

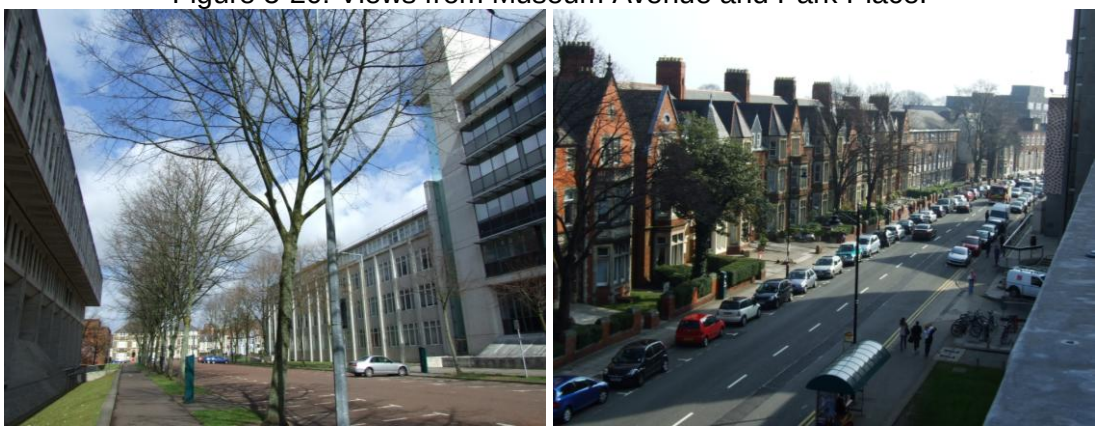

Source: this study.

Table 5-4: Simulation methods and post-processing techniques employed.

↓ Method		prevailing wind direction							
WT	Cp data	N	NE	E	SE	S	SW	W	NW
CFD	Cp data & pathlines	N	NE	E	SE	S	SW	W	NW
FM	wind speed and direction	N	NE	E	SE	S	SW	W	NW

Source: this study.

[40] Special thanks are due to both the WSA Facilities Manager Mr. Dave Bull and the Law School Facilities Manager Ms. Julie McCarthy, for intermediating and permitting this experiment to take place.

Figure 5-21: Cardiff weather wind-roses for the seasons of the year.

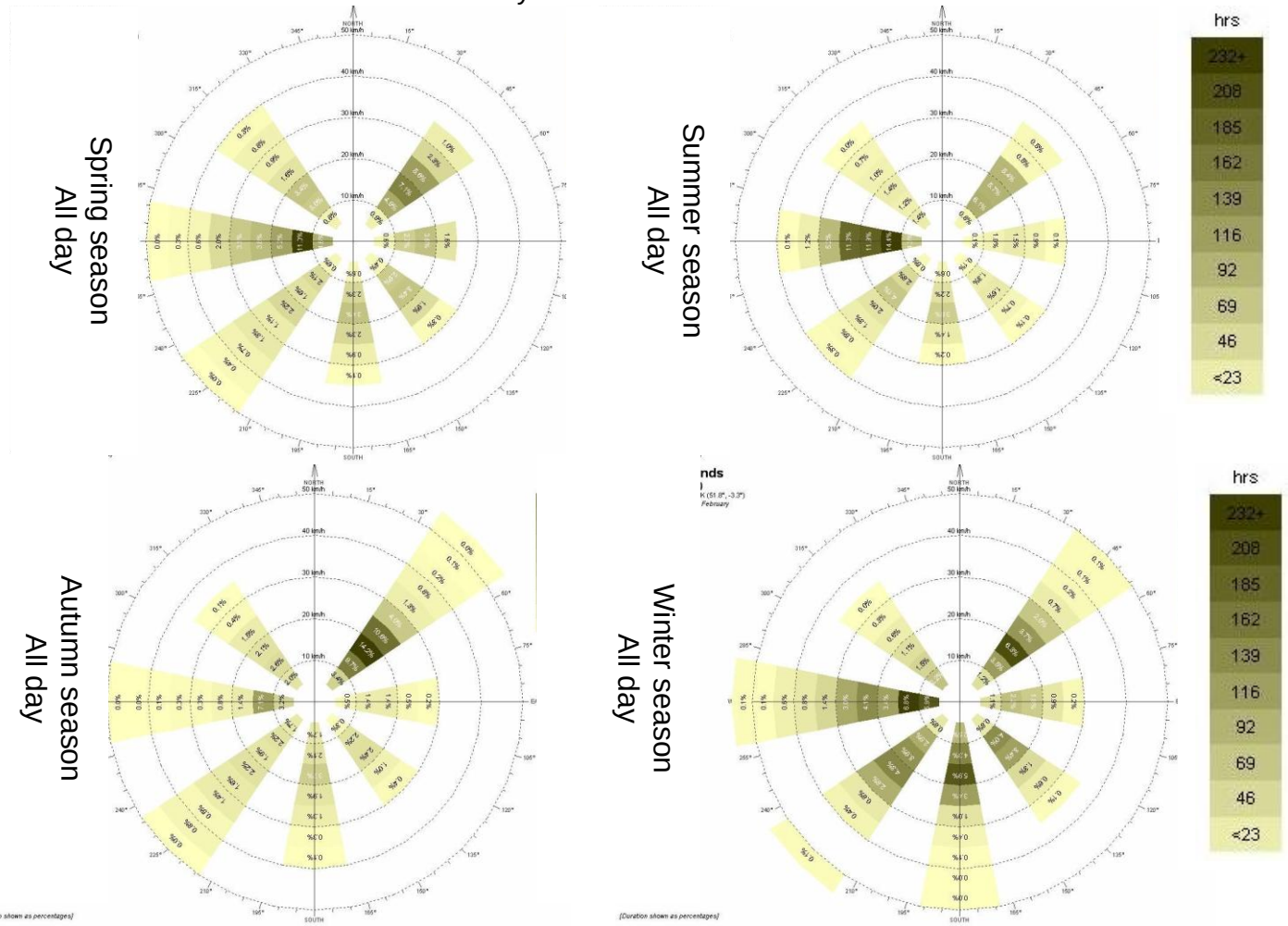

Source: The WSA/ CRiBE.

5.4.2.2. The São Paulo Paulista Avenue

In contrast with the Cathays Campus horizontal landscape, the urban site and immediate surroundings of Paulista Avenue was investigated as the second case study. This urban area, located on a hill-crest at the core of the Metropolitan Region and City of São Paulo, is characterized by high-density land occupation and high-rise buildings, and this avenue is one of the most important financial poles in Brazil.

In 2007, a field research was conducted in Paulista Avenue as part of the wider research project of this thesis and which has provided information on the urban dimensions of this high-rise building urban corridor. One hundred and eighty corporative, institutional, and residential towers along its 2.50km extent were catalogued. The physical average dimensions found in the area were 68.00m for the height, 62.40m and 29.0m for the frontal width between towers and its ground floor, The H/W aspect ratios were respectively 1.10 and 2.08, thus characterizing this area as a constant, irregular but relatively symmetrical urban canyon with a square section. This field research was focused on both physical dimensions, such as areas, aspect ratios and also on façade materials, window-wall ratios (WWR) and carpeted-office energy consumption (KWh/m^2 per year).

The São Paulo conurbation, with approximately 20 million inhabitants, is situated at 770m above sea level and 60 kilometres away from and to the west of the Atlantic coast, at 46^o W. longitude and 23^o S. latitude. Both Bastos and Barroso-Krause (2008) and Tarifa and Azevedo (2001) describe the macroclimate of this region as transitional between mountainous humid tropical and sub-tropical climates, characterized by dry winters and wet summers. It presents monthly-averaged daily temperatures and relative humidity values of 16^oC (minimum) and 74% for the cold season and 22.5^oC (maximum) and 80% for the hot season, with maximum rainfall of 255mm during February (Oliveira *et al.*, 2002).

Prevailing wind circulation results from South Atlantic anti-cyclone masses and continental low-pressure systems on the Southeast/ Northwest axis. Regional wind is induced also by urban roughness, mountain-valley temperature differential and urban heat island phenomena. Wind velocity ranges from 5.5 to 6.5 m/s at 50m height with terrain roughness of 0.45[41].

[41] The weather data was kindly provided in 2002 by the Professor Augusto José Pereira Filho, Head of the EM IAG-USP.

Figure 5-22: Paulista Avenue, at the turn of the 20th century (above); and nowadays: a high-rise tower urban corridor in the city of São Paulo (general view at top-middle and middle-bottom, and schematic longitudinal section at the bottom).

Source: Web site Sampa Art. Accessed in 04/ 03/2001 in: http://www.sampa.art.br/historia/saopaulo.

Figure 5-23: São Paulo weather wind-roses for the seasons of the year.

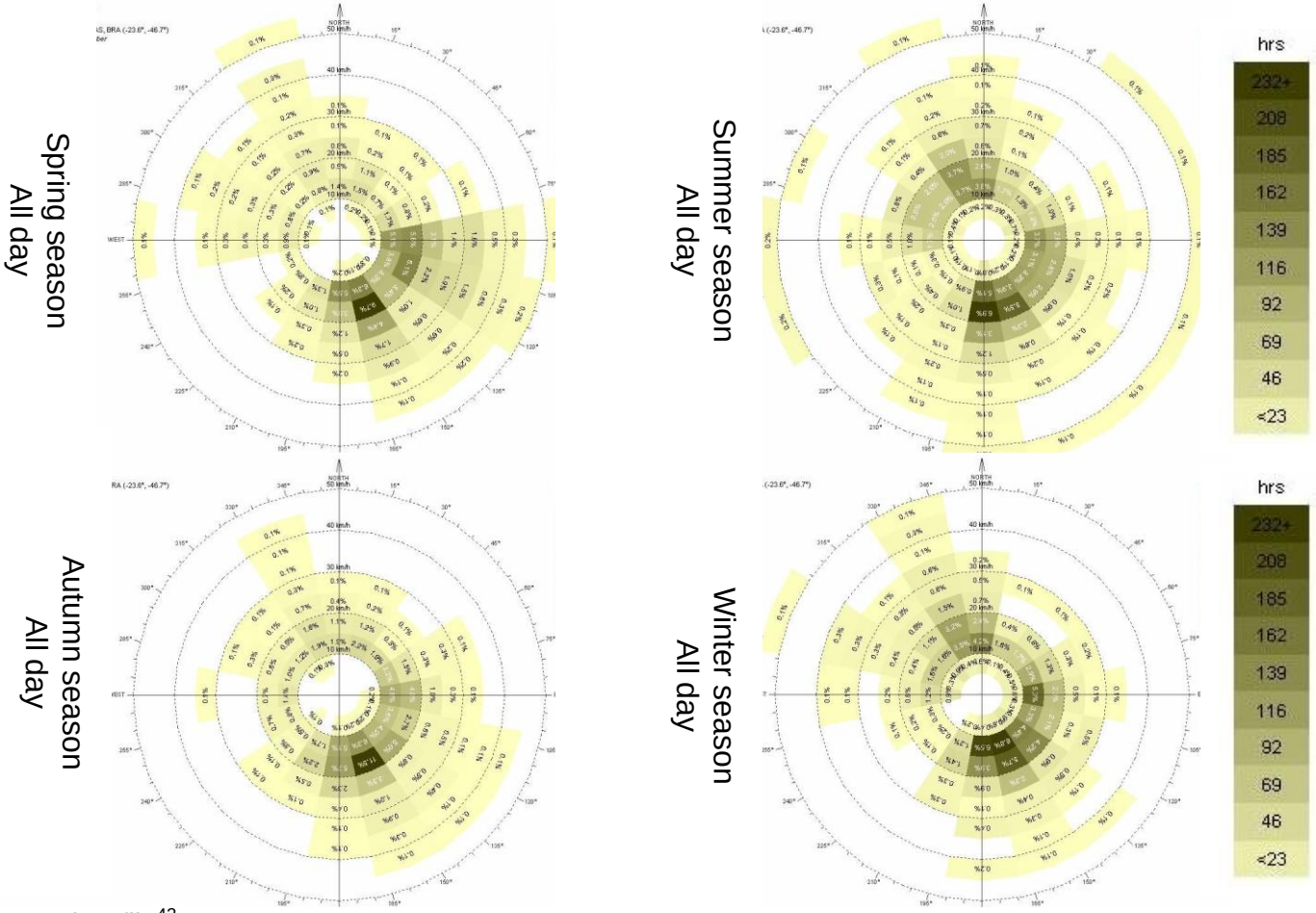

Source: Energy-Plus weather file[42]..

[42] The 'BRA_Sao.Paulo.837800_IWEC.epw' is the Energy-Plus weather file (EPW) from the ASHRAE - IWEC data for Sao Paulo, Brazil, WMO 837800, accessed in 15/09/2011 and available at:
http://apps1.eere.energy.gov/buildings/energyplus/cfm/weather_data3.cfm/region=3_south_america_wmo_region_3/country=BRA/cname=Brazil

Figure 5-24: São Paulo weather wind-roses for the periods of the day during summer season.

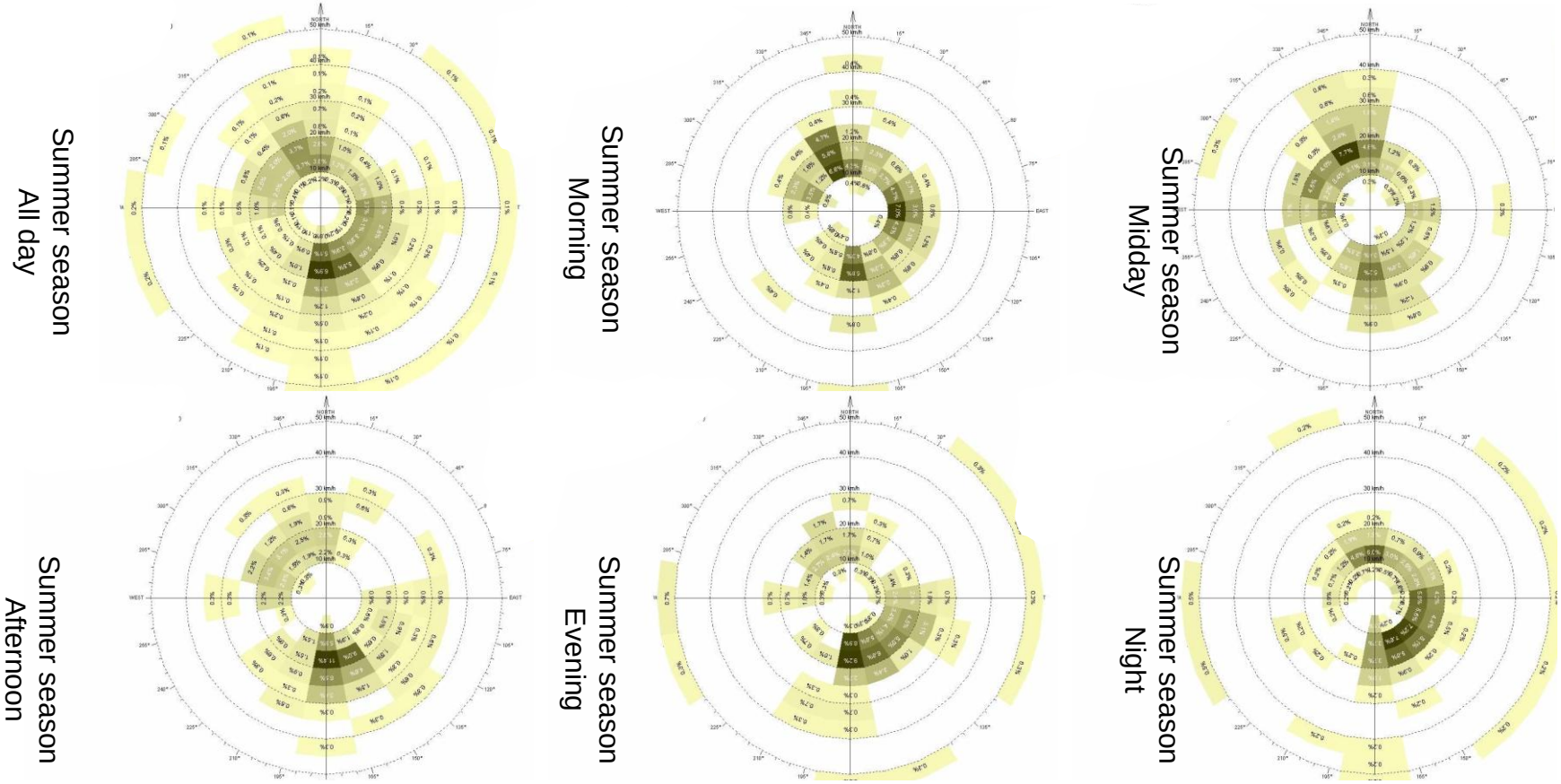

Source: Energy-Plus weather file

5.4.2.2.1. The CYK Tower

The CYK Tower, built in 2003, is an example of contemporary high-rise corporative building architecture[43] in the Paulista Avenue (Paiva, 2003). With a rectangular floor plan fitting the plot's dimensions, it has 20 stores plus the basement and underground parking area. Its skin-glazed façade, with a window-wall ratio (WWR) of approximately 30%, is slightly oblique inwards on the narrow side, is hermetically sealed. This means that the building was not designed to operate with natural ventilation, and the internal office environments rely on full HVAC systems to attain both indoor air quality and thermal comfort levels. On the other hand, its rectangular shape and internal landscape office layout would have been suitable for the application of wind-driven double-side cross natural ventilation systems, if this had been considered as part of the design and ventilation strategies during the initial stages of the architectonic project.

Figure 5-25: The CYK Tower view, cross-sections and floor plan.

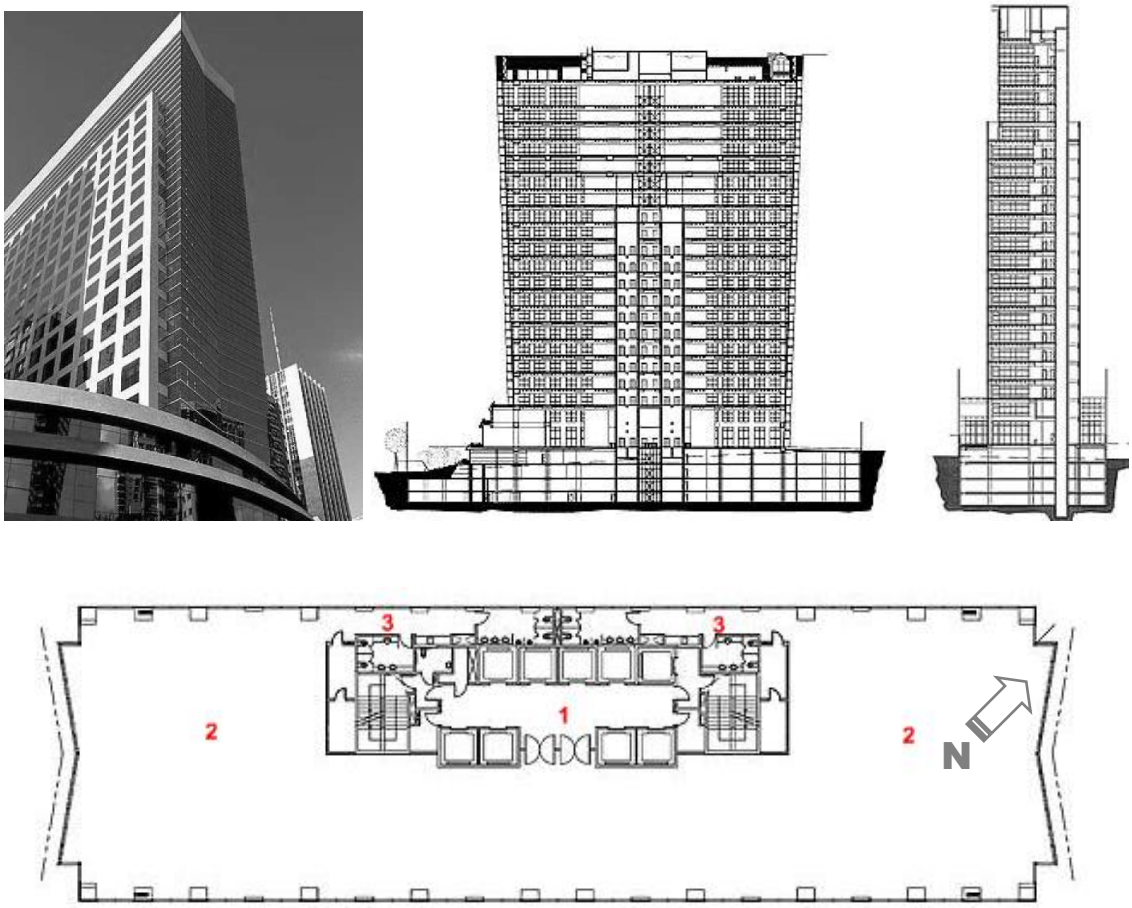

Source: Paiva (2003).

[43] Kogan, Villar & Associados- KV&A Arquitetura.

In order to assess what the potential for the effective application of natural ventilation systems in such an office building would be, a simplified rectangular volume was simulated in both WT and CFD. Additionally, three types of façade component were considered in this analysis: a flat surface; faces with horizontal panels such as balconies or sun-breaks; and finally faces with vertical panels such as exposed column structure or sun-breaks.

Figure 5-26: CYK Tower physical model with the three façades used in the WT experiment: flat surface (left); horizontal panels (middle); and vertical panels (right).

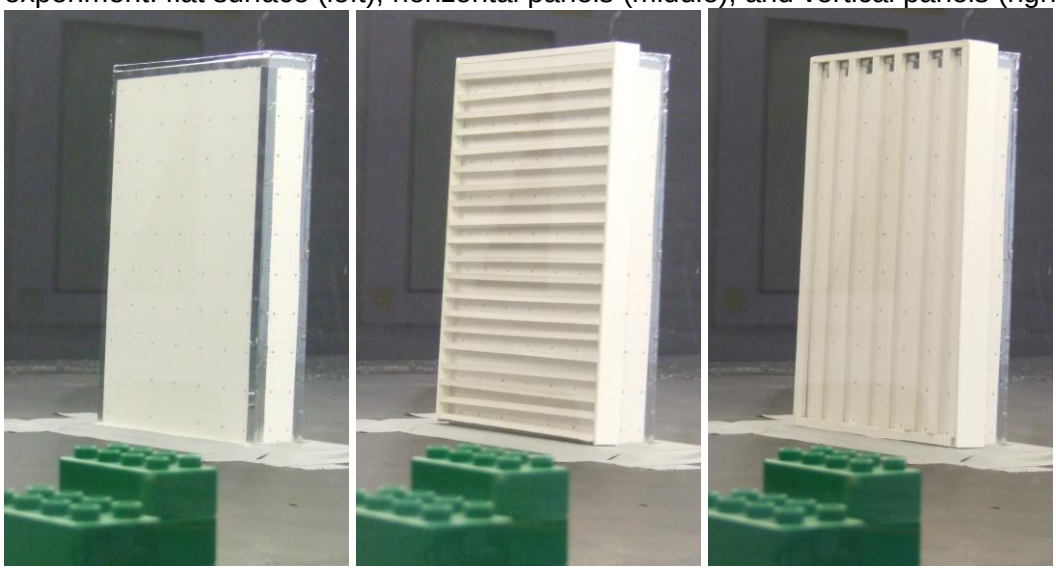

Source: this study.

5.4.2.2.2 The prototype tower

In addition to the simulation of the existing building, a prototype of a high-rise building was investigated. This prototype tower was proposed as an alternative architectonic design to allow cross natural ventilation to occur by using a top wind-catcher with positive and negative pressure sides. This prototype, an exercise in building design for the same site as the CKY Tower, consists of a larger building floor plan with an internal atrium in which two functioning schemes were explored: either with a crossed airflow occurring in separate shafts, each one with independent inlet/ outlet openings (shaft 'A'); or with a single open volume internal atrium (shaft 'B'). Due to the just quoted prototype tower complex geometry and characteristics, it was not viable to create a CFD model for comparison, and its simulations, including airflow field analysis via helium bubbles visualization, were based on isothermal WT physical experiments only.

Figure 5-27: Tower prototype horizontal cross-sections showing shaft ‘A’ partitions.

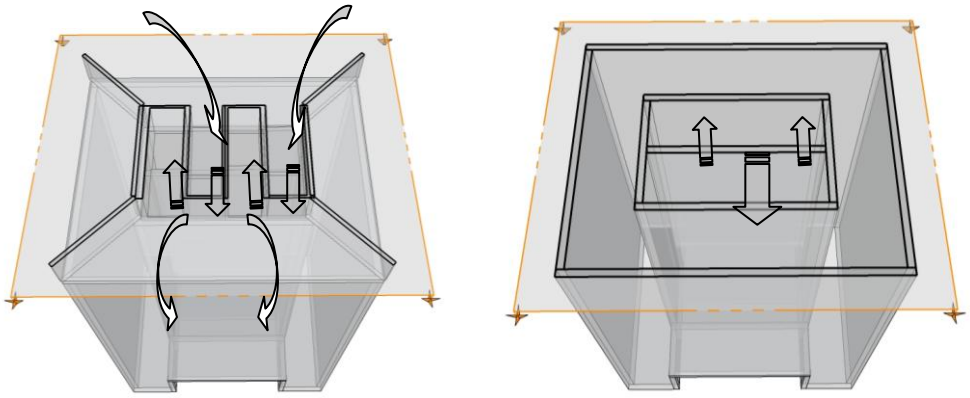

Source: this study.

Figure 5-28: Tower prototype vertical cross-sections showing the two partitions and the inlet/ outlet airflow scheme for shaft ‘A’.

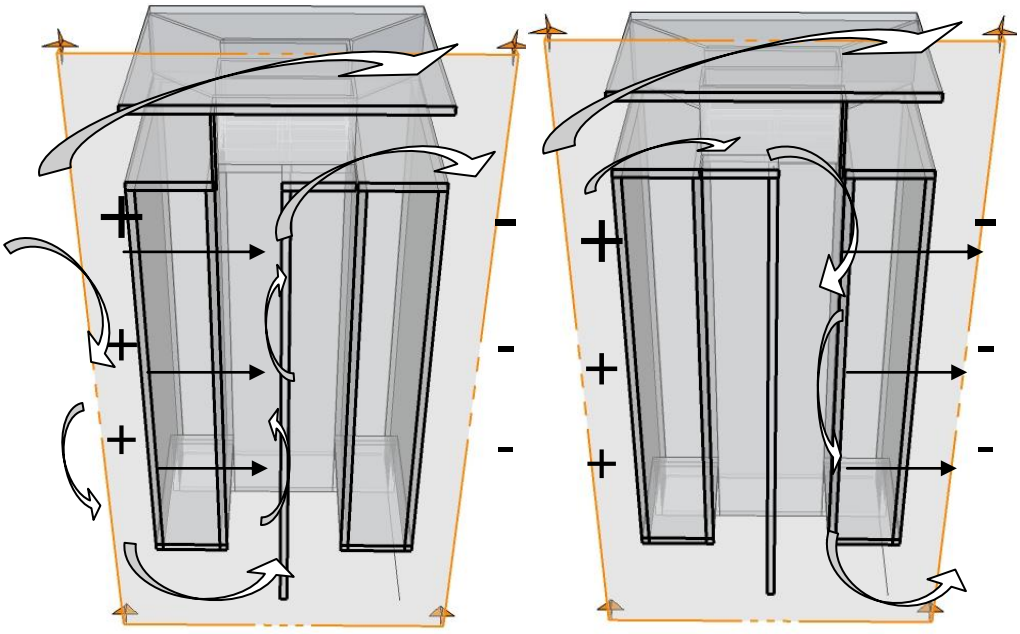

Source: this study.

Shaft ‘A’ would allow wind-driven cross-ventilation utilizing fresh air for both the windward and the leeward sides of the building.

Figure 5-29: Tower prototype horizontal cross-sections showing shaft ‘B’ partitions.

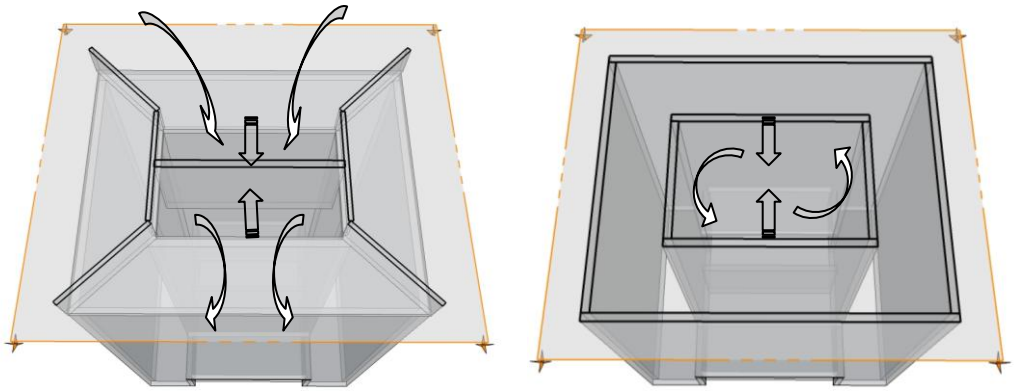

Source: this study.

Figure 5-30: Tower prototype vertical cross-sections showing the internal atrium and the inlet/ outlet airflow scheme for shaft ‘B’.

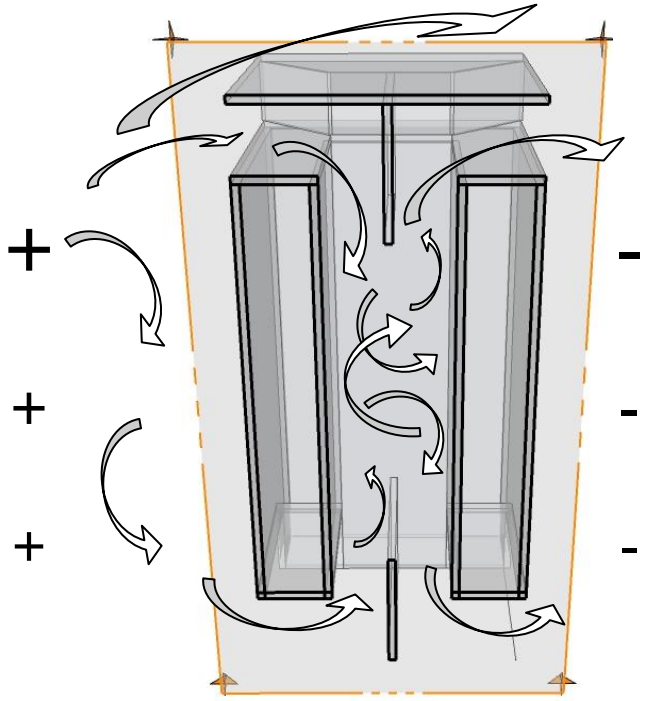

Source: this study.

The aim of shaft ‘B’ is to spot the internal wind pressure in an open central atrium and to evaluate its impact in the windward and the leeward cross-ventilation vector direction and on the NPL inside the building.

5.4.2.2.3. The tower simulation set-up

Both the sets of simulations- for the CYK Tower and the tower prototype- were performed under two different conditions: the first with the tower in isolation and the second with the tower surrounded by the urban neighbourhood. The aims of these series of experiments were:

- To compare both the WT and CFD results and thus verify the accuracy of the numerical model in reproducing airflow around high-rise urban buildings;
- To identify the real potential for natural ventilation in high-rise towers in the urban environment; and
- To check how these results and the respective urban aspect ratios fit into the scale created on the basis of the urban prototype experiment.

Table 5-5: description of the methods of simulation and output post-processing technique employed for the several combinations of aspect ratio and position vis-à-vis the main airflow.

description →		CYK Tower[44] (isolated)	CYK Tower[45] (urban area)	Prototype Tower[46] (isolated)	Prototype Tower (urban area)
↓ method and output		prevailing wind direction			
WT	airflow bubbles	-	-	90˚	90˚
CFD	airflow pathlines	0˚ 45˚ 90˚	0˚ 45˚ 90˚	-	-
WT	Cp data	0˚ 45˚ 90˚	0˚ 45˚ 90˚	0˚ 45˚ 67.5˚ 90˚	0˚ 45˚ 90˚
CFD	Cp data	0˚ 45˚ 90˚	0˚ 45˚ 90˚	-	-

Source: this study.

[44] Simulated for the three surface variations in the WT only: flat surface; with horizontal panels, and with vertical panels.

[45] Simulated for eight wind directions in WT (N, NE, E, SE, S, SW, W, and NW) and for the three surface variations mentioned in the above foot-note. Simulated for five wind directions in CFD (N, NE, SE, S, and NW).

[46] Simulated in both the isolated tower and urban area contexts for the shaft 'A' and shaft 'B' schemes of internal airflow.

5.5. The wind tunnel (WT) experiment

Airflow experiments with a number of physical scale models were undertaken in the WSA boundary layer wind tunnel (WT). First, experiments were carried out with simplified rectangular bricks in order to contrast the results with CFD data and which made it possible to calibrate the computational model inputs, and verify and validate the numerical simulation results. The parameters highlighted at this stage of the investigation were the basis for the further definition of the CFD model input, boundary information and calculation parameters used in the urban prototype investigation, explained in this chapter. Then, a physical scale model representing the urban site and the immediate surroundings of Park Place on the Cathays Campus of Cardiff University was contrasted with both CFD and field measurement data. Finally, another experiment modelling six blocks of Paulista Ave. in São Paulo was performed having as its main target an existing high-rise corporative building: the results of which were compared to those of CFD simulations, as also of a tower prototype, investigated in the WT only.

5.5.1 The WSA WT facility and the parameters adopted

The wind tunnel at the Welsh School of Architecture is an adiabatic atmospheric boundary layer wind tunnel that allows the investigation of scale airflow field around physical models to assess and measure wind speed and turbulence, pressure variation and a number of airflow visualization techniques, such as ground erosion and air bubble tracking. According to the information provided by the CRiBE/ WSA website[47], this equipment has been operated by the British Gas Watson House Research Station in London to the WSA in the early 1970s, was donated to the WSA in the early 1990s, and has undergone several improvements since then. The wind tunnel has a total length of twelve meters and is powered by two 13hp fans providing a maximum speed of approximately 11m/s at up to 1,100 RPM. The imposed airflow field is straightened and the required scale boundary layer achieved over an adjustment area of six meters in length composed of a number of different obstacles and blades, including 'Lego Duplo' blocks on the bottom surface, which reproduces the terrain roughness features and the ABL characteristics. Eventually the lower levels of the atmospheric wind profile are obtained at the modelling section, a rectangular working area in the physical chamber of 2.0m length and side and 1.6m height. The physical models are deployed on a round table of 1.80 m diameter, which allows the exploration of the wind's incidence at any angle. On the other hand, it is to be recommended that the utilizable area of the chamber with no interference of the side and top surfaces on the

[47] The WSA web page: http://www.cardiff.ac.uk/archi , accessed in January 2009.

experiment's results should have a diameter of 1.50m and a height of 1.00m for physical model scales ranging from 1/200 to a maximum of 1/400.

Figure 5-31: Wind tunnel facility at the WSA.

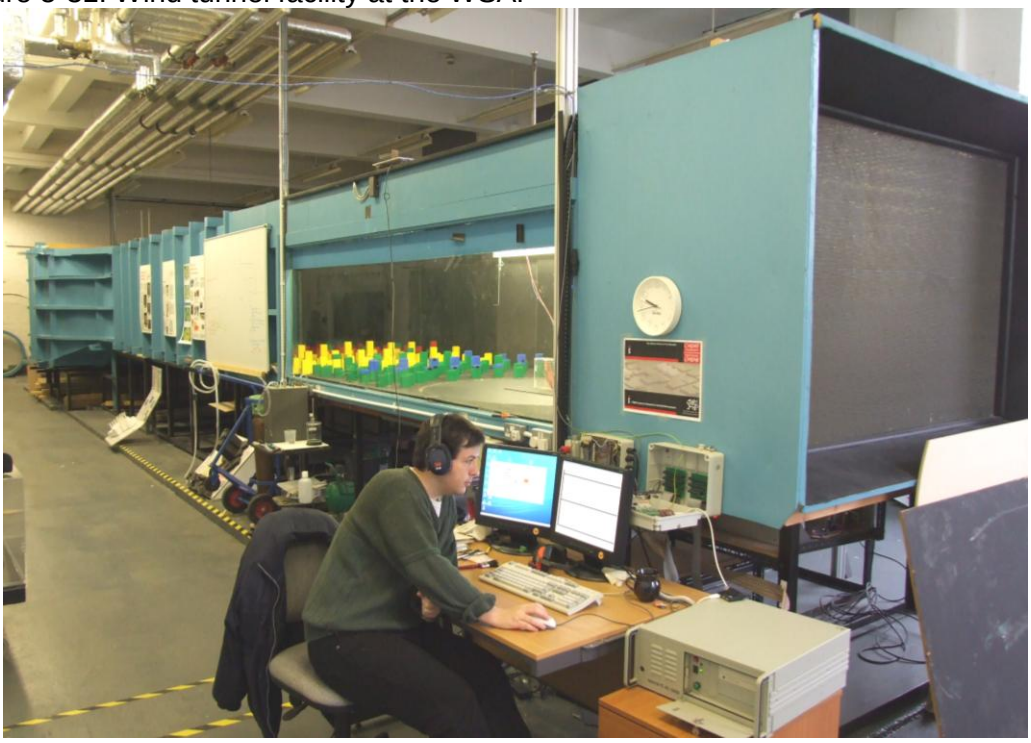

Source: this study.

5.5.1.1. The wind tunnel boundary layer

The wind profile produced in the modelling section was previously checked by measuring the mean wind speed with Dantec hot-wire and laser doppler anemometry equipment at two points at the same instant of time in order to permit comparison of the data. One piece of the equipment was maintained in the same position and the other moved upwards and/ or downwards in its vertical axis. Twenty instantaneous measurements were taken for each set of points, and the average of these values provides the mean wind speed at each one of them. The wind speed inlet adopted in the wind tunnel was approximately 10m/s, created at a constant 900RPM. This experiment was carried out by this researcher with the support and assistance of two staff teams from the CRiBE/ WSA[48]. The ratio between the fixed point ($U_{reference}$) and the point movable on the vertical axis at regular distance intervals (U_{point}) gives a dimensionless variation of the mean upward wind speed, which is comparable to the atmospheric boundary layer.

[48] Special thanks are due to both the WSA Senior Lecturer Don K. Alexander and the Research Assistant Dylan Dixon, for calibrating the wind tunnel at this stage of the investigation.

Equation 5-1: Equation for the scaled Atmospheric Boundary Layer[49]

$$\frac{Z_{point}}{Z_{reference}} = \frac{\overline{U}_{point}}{\overline{U}_{reference}}$$

Source: Cook (1985).

Figure 5-32: The WSA WT chamber and probes used for ABL measuremens.

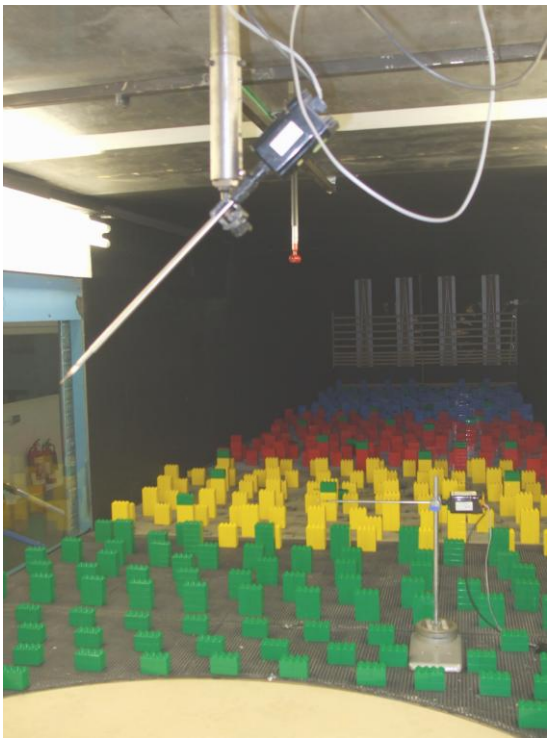

Source: this study.

The Lego blocks in the adjustment area were set up to reproduce a terrain roughness of category 05, reproducing urban areas with a majority of buildings of four or more storeys and a canopy height corresponding to three-quarters of the average building height of 25 meters, and 30-50% of plan-area urban density. Figures 5-33 and 5-34 show the resultant wind profile measured inside the wind tunnel and compare it with other profiles based on the log-law and created by other arrangements of characteristics of terrain roughness. It can be seen that the wind profile resulting from the experiment presents a satisfactory measure of agreement with those based on the terrain roughness characteristics of urban areas.

[49] For further information see topic 2.3 in Chapter 2.

Figure 5-33: ABL achieved in the wind tunnel and compared to diverse terrain roughness factors.

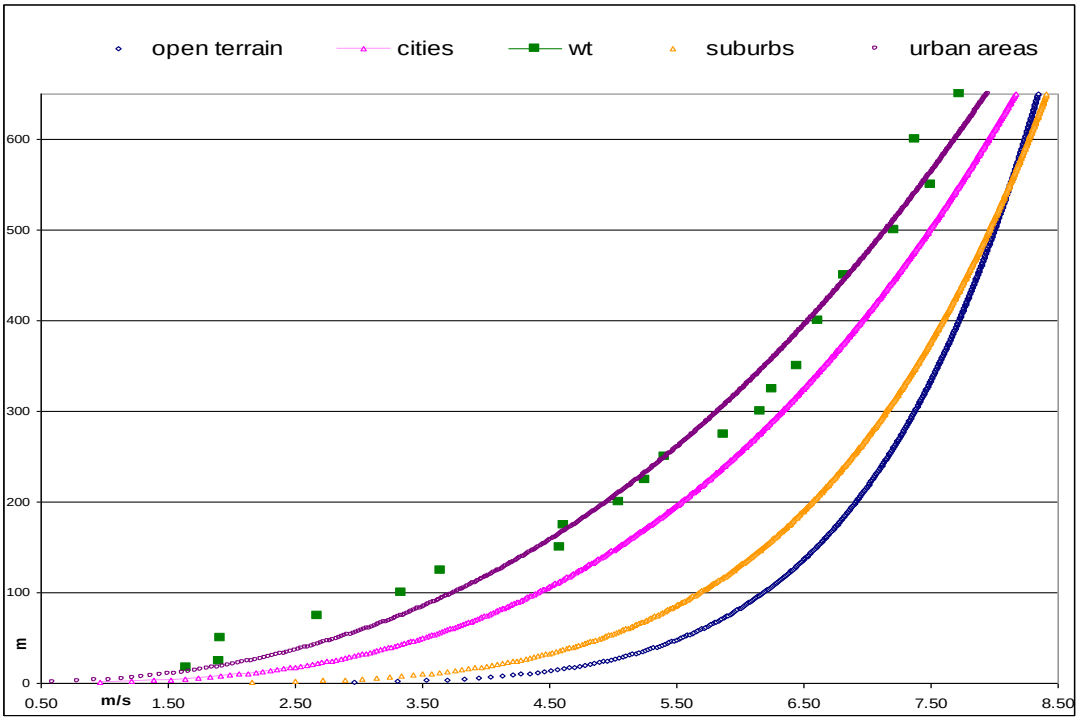

Source: this study.

Figure 5-34: U_{ref} ratios attained in the wind tunnel compared to those resulting from diverse terrain roughness factors.

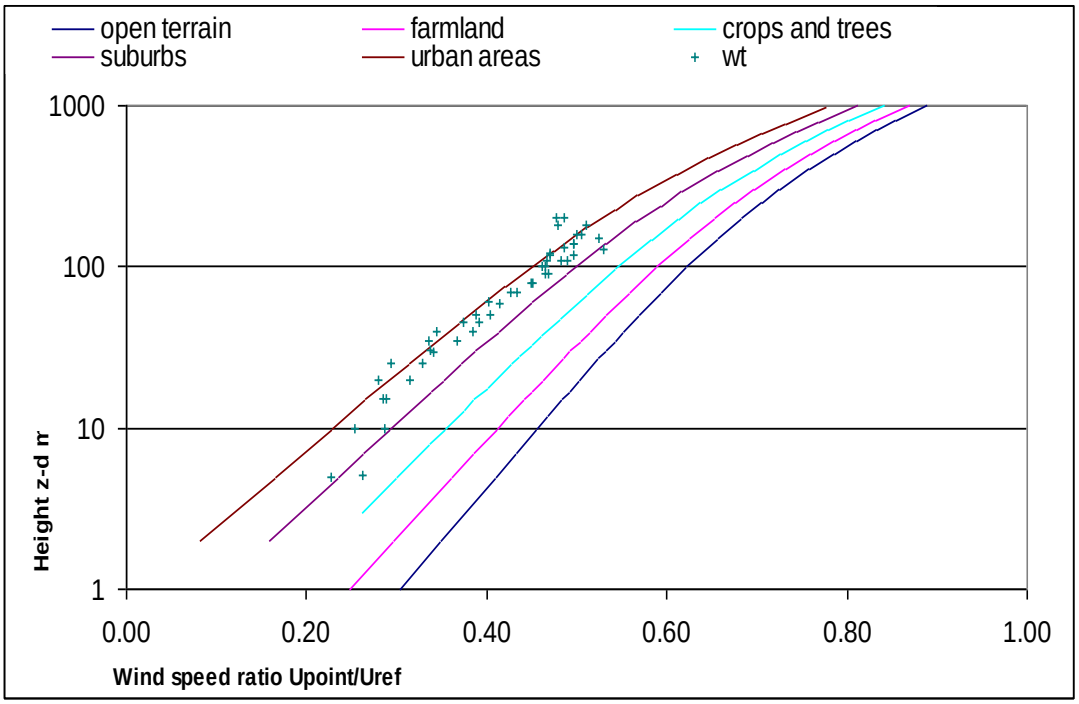

Source: WSA/ CRiBE.

5.5.1.2 Pressure Coefficient (Cp) measurement

The wind pressure coefficient[50] (Cp) is a dimensionless number that can be either positive, for windward forcing pressure, or negative, for leeward suction pressure. The Cp difference at any two points is employed to determine the airflow ratios for natural wind driven ventilation systems in the internal environment. Internal flows are moved by pressure differences and blow from high pressure to low pressure zones. The WSA WT equipment for measuring Cp (Furness low pressure transducers with Scani-valve scanners) allows the measurement of the mean pressure coefficient only, since peak values are not captured. For this research, each of the mean Cp values considered was the average calculated from at least five successive measurements for each point. This was done to avoid the interference of any real random turbulence inside the chamber. When the comparison between these five values indicated a standard deviation greater than 5%, then more runs were performed in order to enhance the accuracy of the Cp value and the reliability of the results. It is worth mentioning that, as the critical literature review in Chapter 3 has highlighted a difference of up to 20% on the results and a wind Cp range of ±0.10 may be acceptable from WT results and field measurement or CFD calculation, when the focus of the investigations is not structural calculation. The wind speed inlet adopted for all wind tunnel experiments was about 10m/s, attained with two fans working at a constant 900 rotations per minute.

Figure 5-35: The WSA transducer and plugs used for measuring Cp's in the WT.

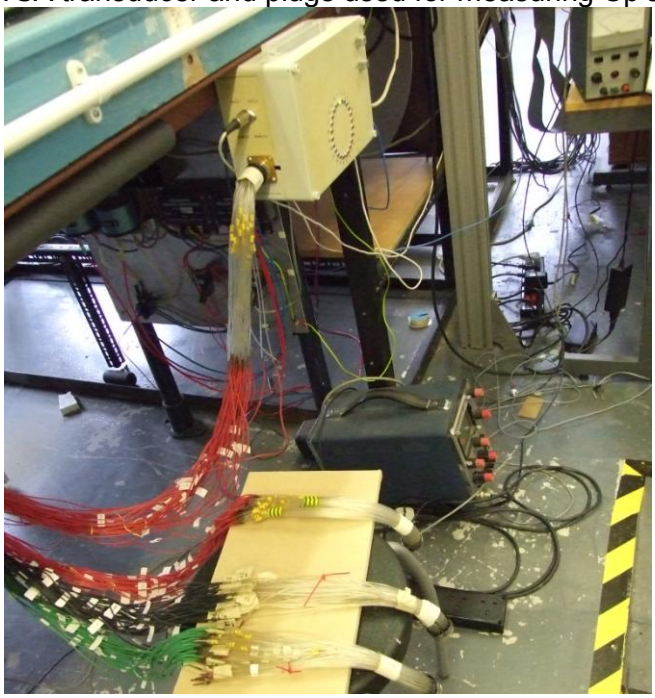

Source: this study.

[50] See topic 2.4 in Chapter 2.

The wind CP at any point of the model was calculated by the ratio between the pressure at each of the measured points (P_{point}) and a free-stream reference pressure ($P_{reference}$). Both the point and the reference pressures are measured and logged instantaneously.

Equation 5-2: The wind Cp equation for WT outputs.

$$Cp_{point} = \frac{P_{point}}{P_{reference}}$$

Source: WSA/ CRiBE.

Hence, due to the scaling laws[51], the Cp is comparable to those obtained in real building envelopes through field measurements. It is further utilized for calculating mean pressures for any given wind speed:

Equation 5-3: Bernoulli pressure equation.

$$P_{envelope} = \frac{1}{2} \rho Cp U^2_{ref}$$

Source: Cook, (1985).

Finally, pressure coefficient contour plots and scattered plot matrices were generated by using the software Axum 6.0 for Windows. The software allows a visual analysis of the Cp distribution and a straightforward qualitative comparison between the wind tunnel measurements and the CFD results.

5.5.1.3 The helium bubble airflow visualization technique

Airflow patterns around translucent models were observed in the WT using the helium bubble flow visualization technique. This technique consists of the injection of a controlled number and size of helium bubbles in a dark chamber that are picked out by a beam of light whilst in movement, carried along by the airflow. The capture of images by both a digital photographic and film camera allows later qualitative analysis of flow detachments, vortices and othermodifications in the airflow speed and direction.

The WSA equipment consists of a 'Sail' trademark bubble generator system for airflow visualization and measurement model 33 with plug-in heads. It mixes helium injected at 20psi with bubble film solution and pressurized air jet at 60psi. The helium-filled neutral buoyant bubbles are filtered in a mini-vortex filter in order to maintain a

[51] For further information see topic 2.3 in Chapter 2.

constant diameter (from 1/32'' to 3/16''). The bubbles are injected into the target area and follow the main airflow path without disintegrating, thus providing a qualitative visualization of the modification on the airflow speed and direction around obstacles.

Figure 5-36: The WSA bubble generator and air compressor for airflow visualization.

Source: this study.

The lights of the laboratory were switched off and the curtains drawn during the experiment so as to create a dark room. A narrow beam of light was created by using a projector positioned downstream. The physical model has to be made of translucent material (e.g., acrylic Perspex) in the light wise. Also, the rubber tube tap from which the bubbles were released was carefully positioned upstream, in such a way as not to interfere with the flow.

Figure 5-37: Set-up of one of the physical models for the airflow visualization.

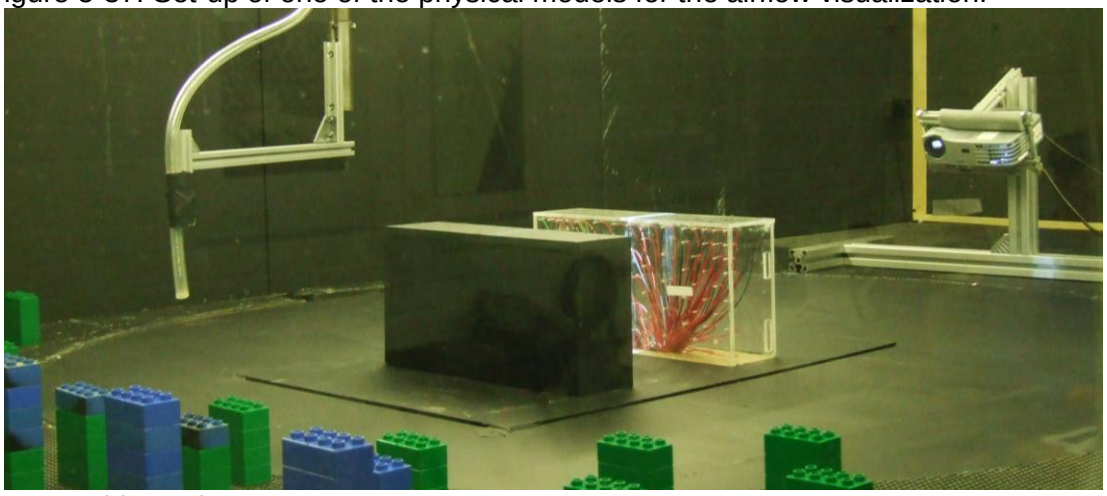

Source: this study.

The airflow visualization images were obtained by using a digital camera model Fujifilm Finepix S6500Fd. For the still pictures the best results were obtained with ISO slow sensitivity speed of 200 to 400, lens aperture of F/5.7 and shutter speed of 1/2 sec. Further enhancement of image visualization was obtained on Photoshop by inverting and editing colours.

5.5.2. The two brick WT experiment set-up

The size of the bricks, 20x40x10cm (height, length, and width) represents urban buildings of 50x100x25m scaled at 1/250. This experiment was set up taking as criterion the H/W aspect ratio between the blocks and the position with regard to the airflow inlet, denominated as follows: parallel (0˚), oblique (45˚), and perpendicular (90˚) flows. It was supposed that this WT experiment reproduced an urban area environment, and the previously measured ABL would be expected to develop in this experiment as well. While the brick with the pressure taps was manufactured with transparent acrylic of 6mm thickness, the other brick was made of MDF and painted in black. A large number of pressure taps (164 altogether) were included in three sides of the acrylic brick in order to measure pressure variations, as follows: 87 points in the front ('xz' axis, 40x20cm), 34 in the left side ('yz' axis, 10x20cm) and 43 in the top surface ('xy' axis, 10x40cm). There was a limit to the equipment available and, therefore, a limit to the number of points that could be measured each round. For this reason, previous CFD simulations for the same size of bricks and WT chamber helped to determine where the pressure taps should be placed in order to give an accurate and homogeneous pressure measurement over the brick's surfaces.

First, WT experiments were carried out with the acrylic brick only. Then, the two bricks were positioned so as to represent four building heights to road width H/W aspect ratios: 0.50, 0.66, 1.00 and 2.00. Experiments were performed with three main wind directions, with the respective stream-flow perpendicular, parallel and oblique to the bricks. Further, in order to measure both the windward and the leeward faces, the turntable was rotated through 180˚ for each set of measurements. The top of this turntable was new and specially made for this set of experiments on MDF and painted in black. This was necessary to reduce the possibility of interference that any undulations on its surface might produce in the result.

Figure 5-38: The acrylic brick with the pressure taps used in the WT experiment.

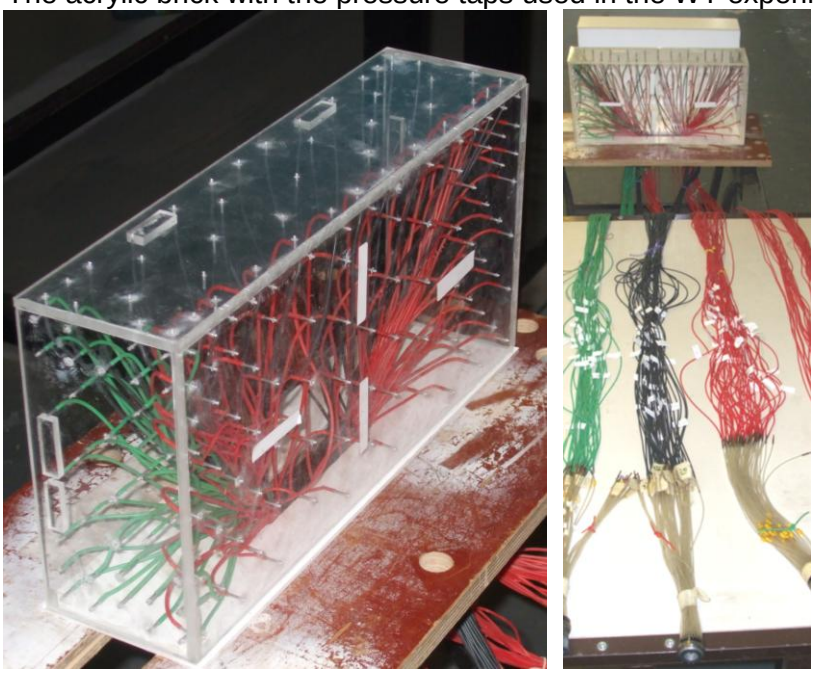

Source: this study.

5.5.3. The Cathays Campus WT experiment set-up

The scale physical model of Cardiff Cathays Campus area which was used in the WT experiment will be detailed here. The model was constructed to a scale of 1/300. The reason why the scale was decreased against that of the previous exercise lay in the fact that a larger urban perimeter could thus be included in the experiment without the interference of chamber side walls in the targeted airflow results. In this way, the 500m diameter of the urban area to be analyzed could be fitted into a 1.66m diameter in the WT, and the canyon area with an actual 32.0m width and 18.0m height was modelled in 10.66cm x 6.00cm, thus reproducing the H/W aspect ratio of 0.56.

Most of the buildings included in the modelled perimeter were created in white Styrofoam, while the side walls of the Law School were made of 2mm transparent acrylic panel. The target building was that of the Law School building, where the pressure was measured. A total of 32 pressure taps were included in both the Park Place and the Museum Ave. façades, with 8 points to each floor of the building, excluding the ground floor. Fifteen points were also placed in each one of the façades facing the internal courtyard. Due to the small size of this model the aluminium tubes had to be curved carefully to fit into the space and thus avoid any bending of the rubber tubes attached to them.

Figure 5-39: The Cathays Campus perimeter used in the WT experiment.

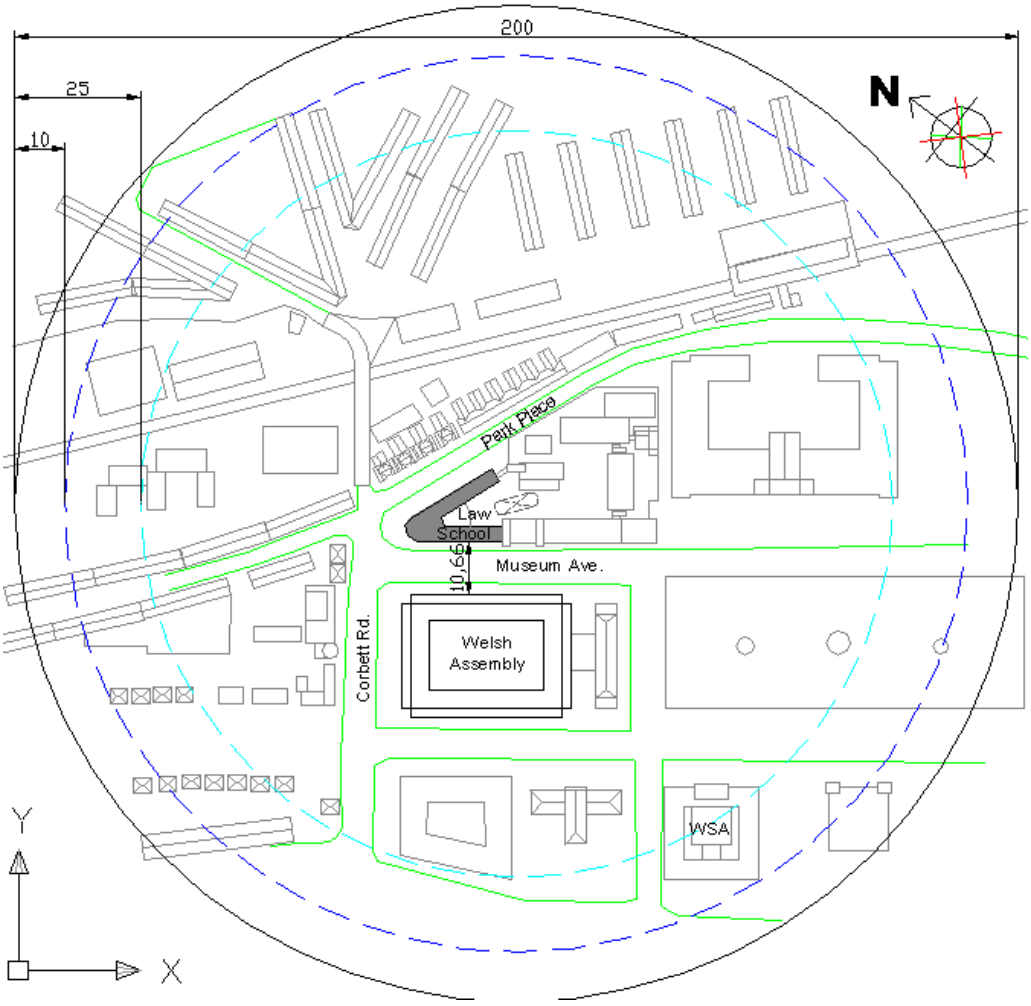

Source: this study.

Figure 5-40: The Law School building scale model used in the WT experiment.

Source: this study.

Figure 5-41: The Cathays Campus eight wind directions simulated in the wind tunnel and three close-ups of the physical models.

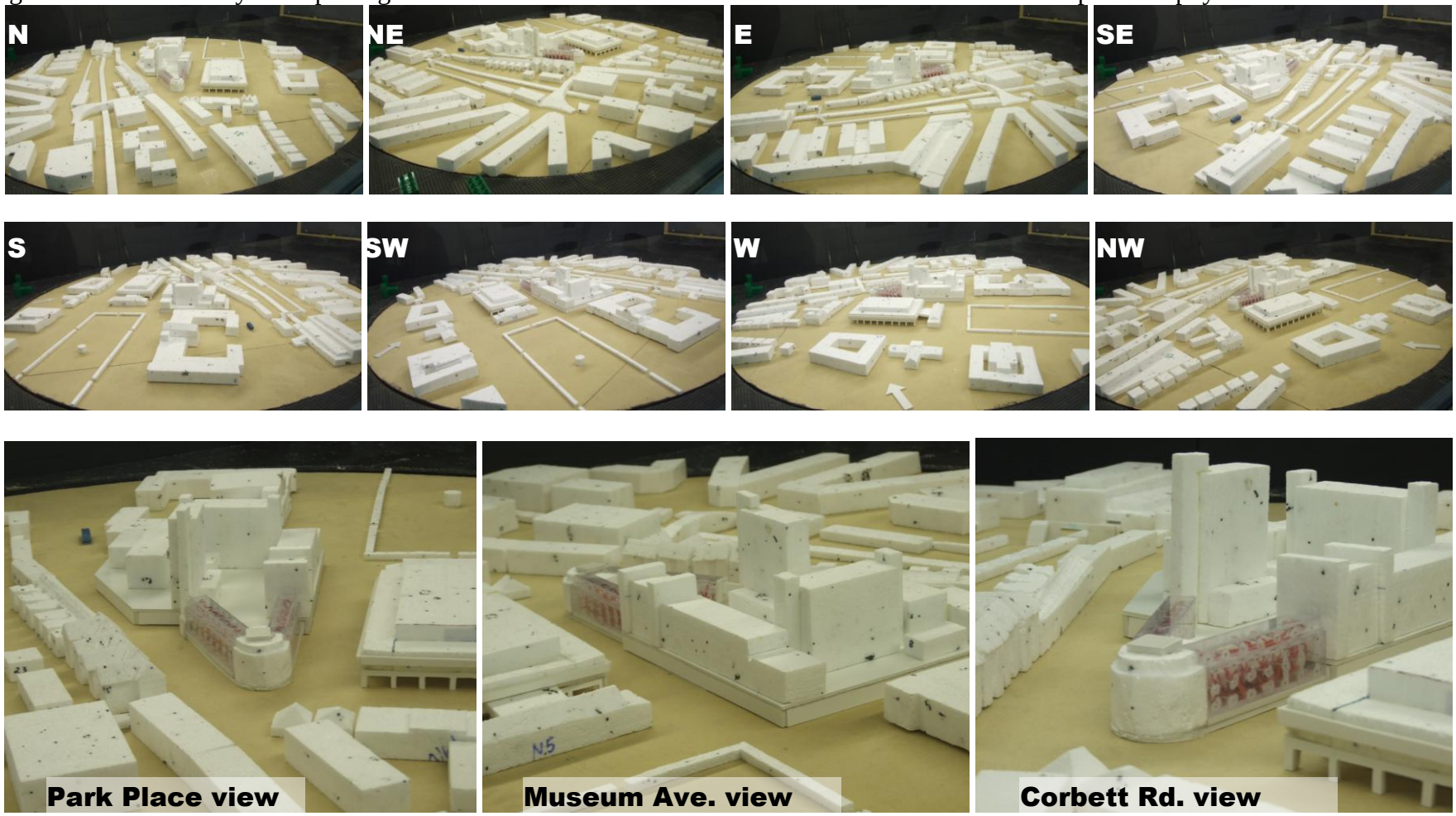

Source: this study.

5.5.4. The São Paulo Paulista Ave. WT experiment set-up

As in the Cathays Campus set-up, the scale used in the Paulista Avenue physical model was 1/300. Since there are towers of up to 35 floors in the perimeter investigated, this scale is suitable both for the needs of this experiment and for the ABL for the urban area produced inside the WT chamber.

Figure 5-42: The Paulista Ave. perimeter simulated in the WT experiment.

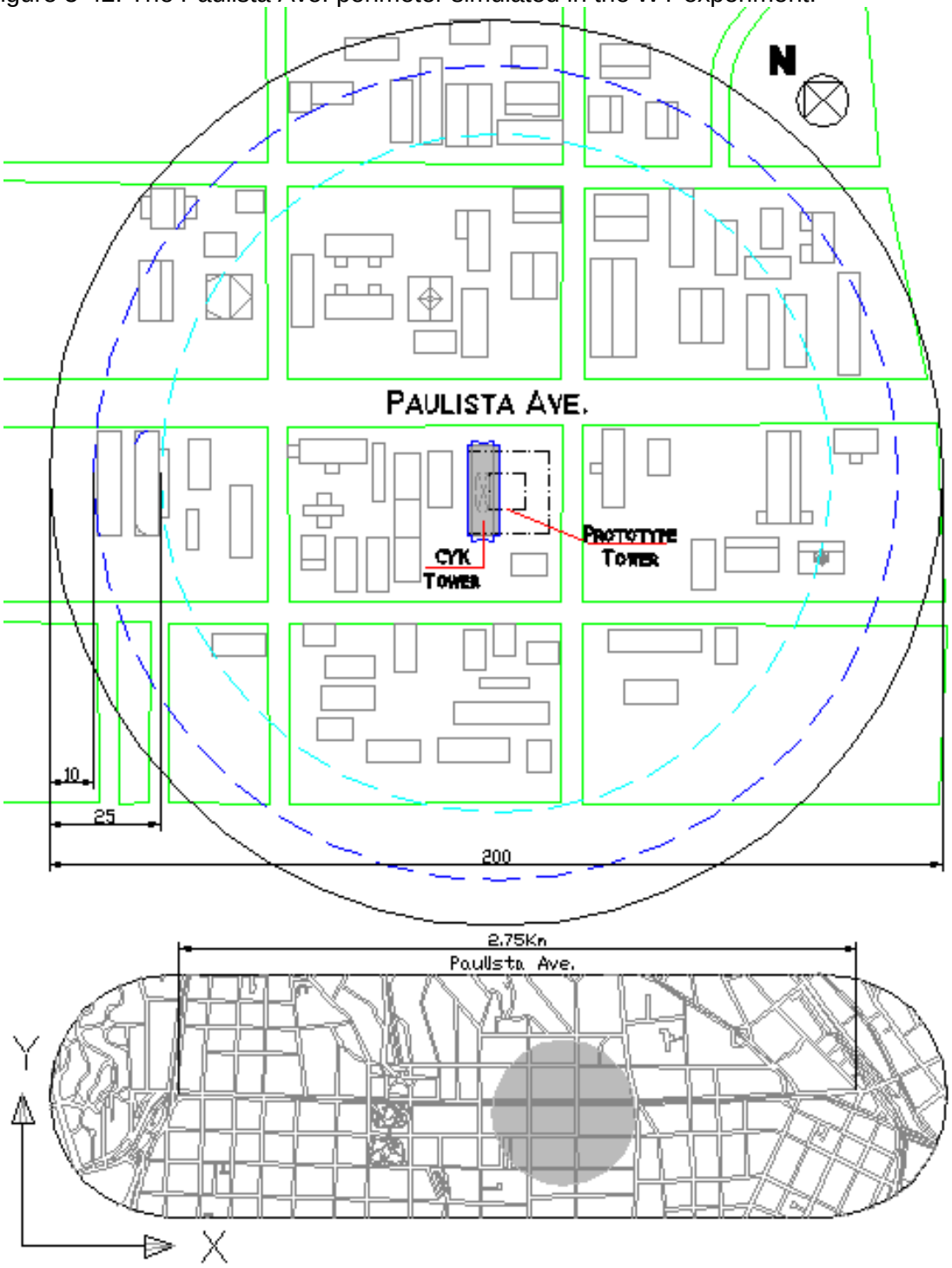

Source: This study.

5.5.4.1 The CYK Tower experiment set-up

For the scale physical model of the Paulista Avenue urban area, the buildings surrounding the target building were made of white Styrofoam. Regarding the CYK Tower, its model size of 33x22x6cm (for height, length, and width, respectively) represents an approximately rectangular building of 100x65x18m scaled at 1/300. A total of 70 pressure taps were included in each wide side of the tower, divided into 10 rows (one for each three floors). Also, the top and the narrow sides received, respectively, 18 and 6 pressure taps. The CYK Tower model was produced in 4mm white cardboard, which is thinner than the acrylic. This was necessary since it is a slender tall building and due to the amount of aluminium tubes and rubber pipes that had to be included inside the model. On the other hand, despite this model's having eventually received a reinforced inner structure to provide it with rigidity and weight, acrylic models have proved to confer greater air tightness and stability during the simulations, though the results have shown that this does not interfere in the quality of the experiment. It is worthy of mention that all the transparent acrylic materials, aluminium tubes and rubber pipes, these last of a total length of almost 400m, were reused in one physical model after another.

Figure 5-43: The CYK Tower making process used in the WT experiment.

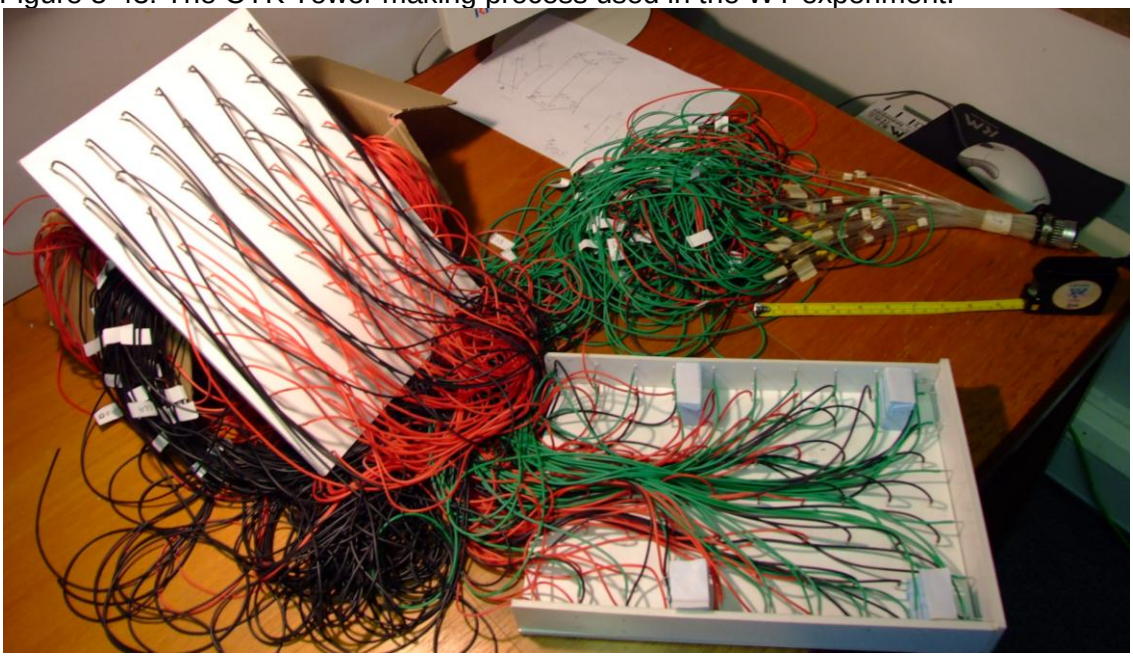

Source: This study.

Figure 5-44: Physical model of the CYK Tower in the urban environment with the three façades employed in the WT experiment: horizontal panels (left); vertical panels (right); and flat surface (bottom).

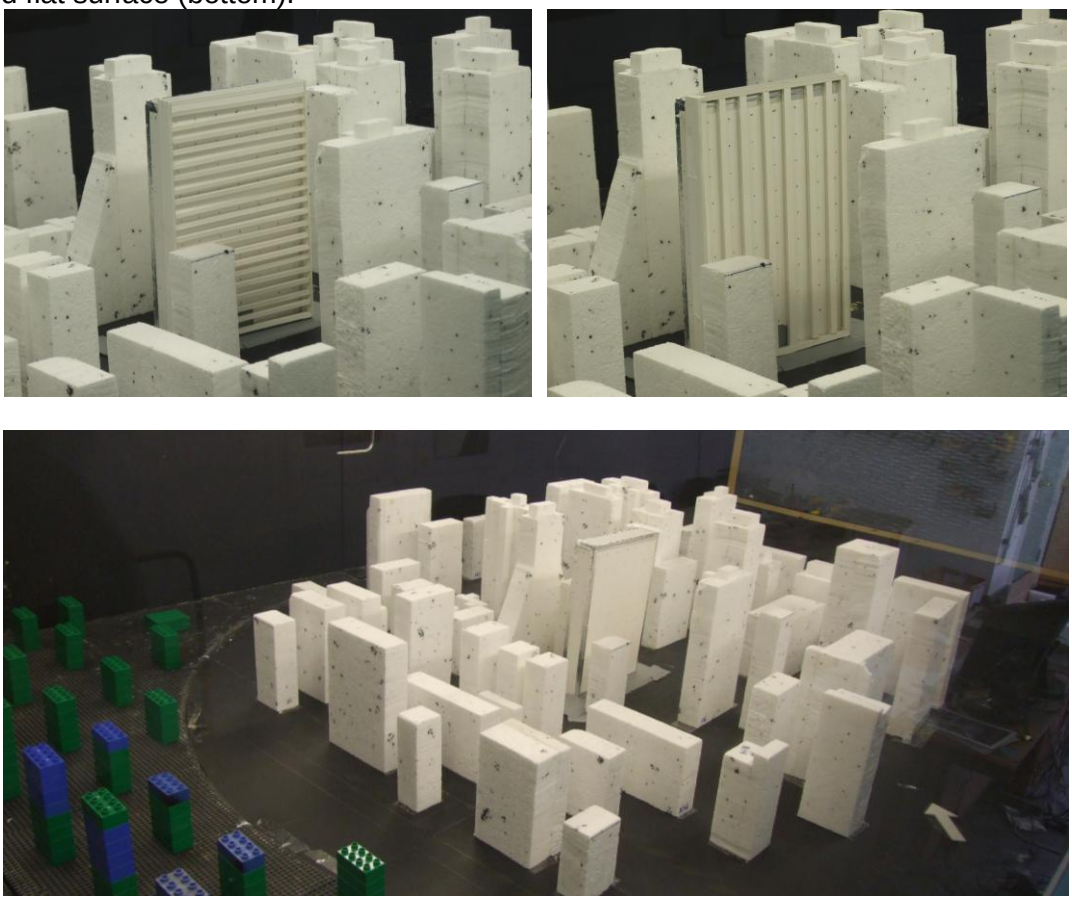

Source: This study.

5.5.4.2 The Prototype tower simulation set-up

As already mentioned in section 5.4.2.2.2., the proposed prototype tower would supposedly occupy the same site as the CYK Tower. This investigation aimed at characterizing the wind-driven natural ventilation performance of a square floor-plan section high-rise tower with a top wind-catcher/ solar chimney. The prototype was designed to allow two internal operation modes: crossed-shafts ‘A’; and open atrium ‘B’. Further, the results give the windward and the leeward external ΔCp only, contrasting with the previous CYK Tower scenarios.

Figure 5-45: Plan (for shaft ‘A’) and close-up of the prototype tower physical model (above) and the model in the Paulista Avenue urban area (below).

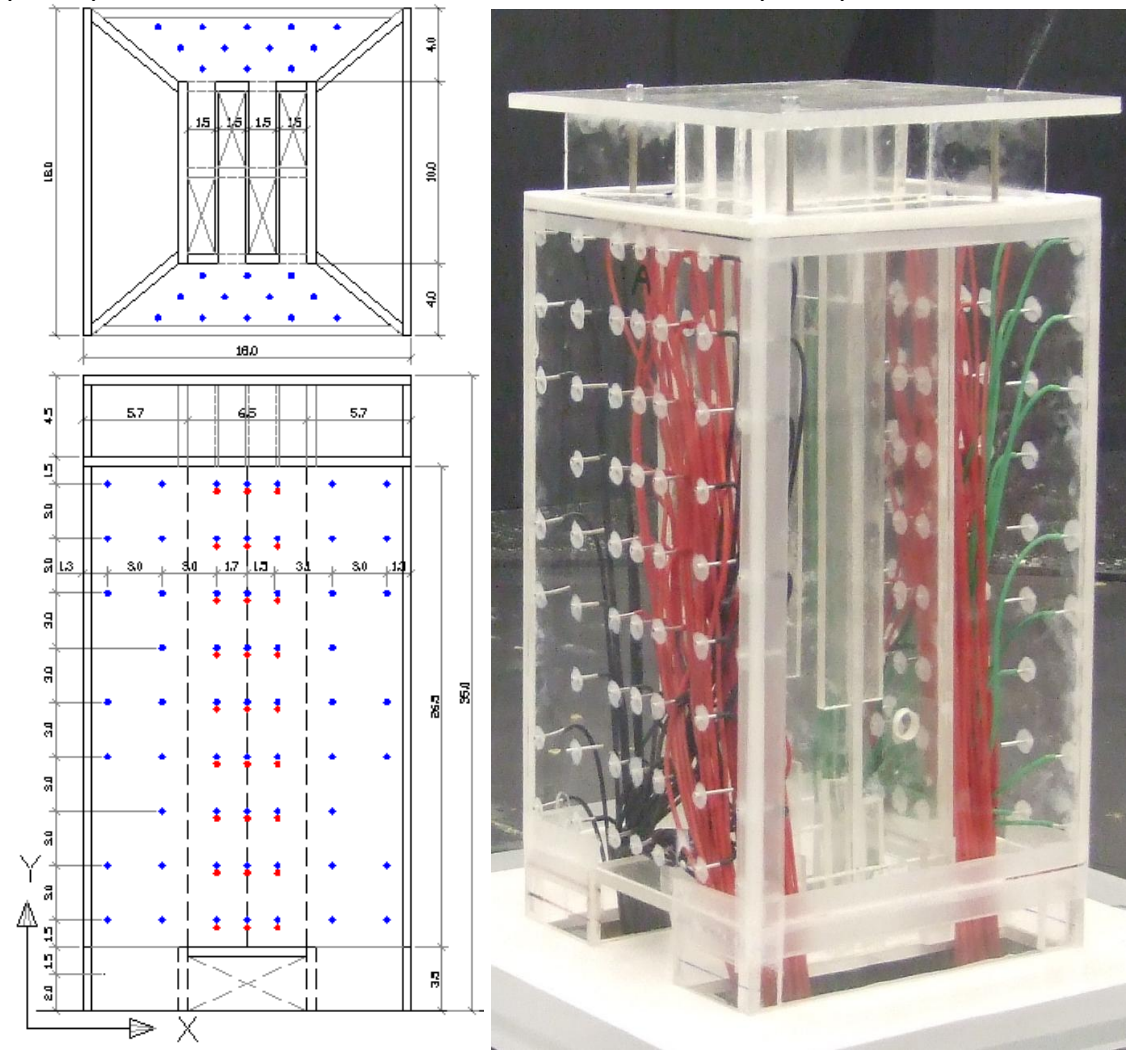

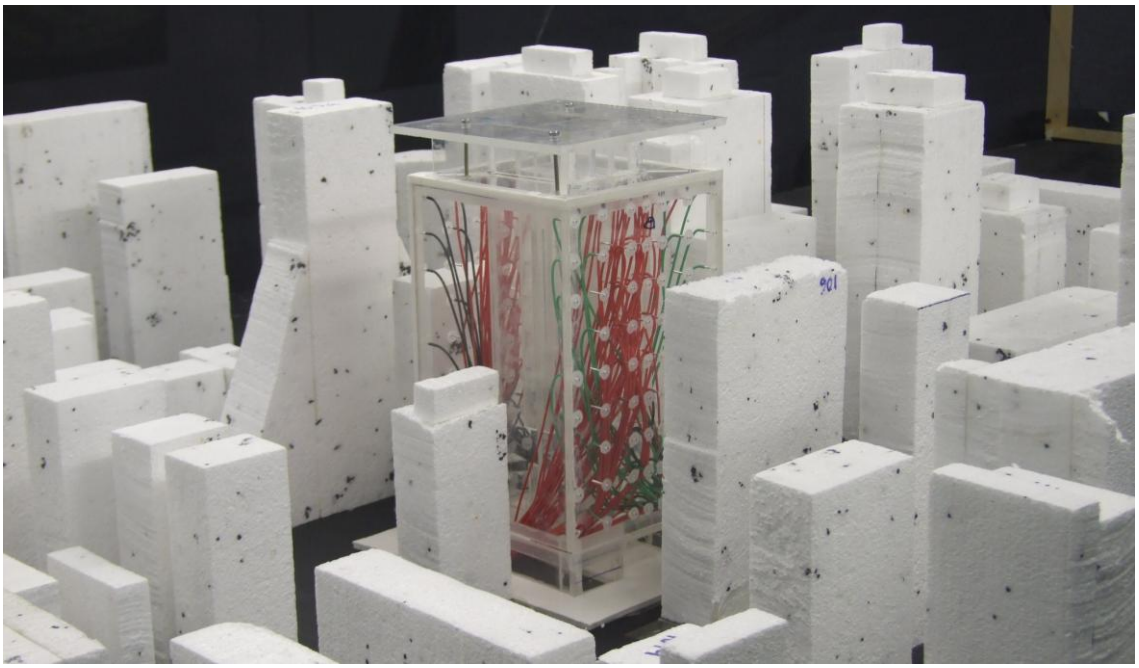

Source: This study.

The prototype tower was made of 6mm transparent acrylic panel with length, width, and height of 18x18x30cm, respectively. The internal shafts presented a plan section of 9x9cm. The wind-catcher on the top was also made of the same material, but with panels 6 and 2mm thick. With the same plan section as the body of the tower, the top device was 4.50cm high, and positioned above the height of most of the surrounding blockages. The real size of this tower would be 60x60x100m with an additional 15m on the top, the internal shaft's dimensions being of 30x30m, with a resulting in internal floor width of 15m- an ideal depth for cross-ventilated spaces. The external windward and leeward faces received 59 pressure taps each, the internal faces of the shafts 27 and the bottom surface of the wind-catchers 12 points on both the windward the leeward sides.

Finally, it is necessary to mention that the wind tunnel experiment with scale physical models is unable to simulate buoyancy-driven forces. In addition, the prototype tower was not simulated in CFD software, which would be able to identify buoyancy pressure values, due to the complexity of creating a physical model with both urban for the ABL full development and the surrounding area, and building (internal space) scales that aggregate both wind- and buoyancy driven forces in a steady-state and non-isothermal condition. On the other hand, the prototype tower performance analysis would be incomplete if only wind-driven forces were considered, given the enhancement that buoyancy-driven forces would bring for shafts and atrium of such a height combined with the use of a solar chimney strategy. For this reason, the Cp and $\triangle$Cp outputs from the wind tunnel will serve as a basis for the wind-driven input in the analytical equations used for calculating the total pressure difference with both forces combined and the resulting airflow rates for low, medium and top height floors.

5.5.5. The standard deviation from the WT outputs

The averaged results from at least five measurements rounds for each pressure tap plug ensured a total averaged standard deviation for all the sets of simulation combined of less than 1.0% (table 5-6). A good level of accuracy was achieved in the wind tunnel experiments carried out in the steps of investigation listed in this Chapter. For further information about the standard deviation on each set of experiment see Appendix 3.

Table 5-6: The averaged standard deviation from the wind tunnel simulations output.

Sets of Experiment	wind angles	nº of experiments	AVG SDEV
Two bricks test	3	12	**1.9%**
Law School	3	16	**0.3%**
Paulista Ave. CKY Tower- isolated	3	9	**1.0%**
Paulista Ave. CKY Tower- urban	3	24	**0.5%**
Paulista Ave. Prot. Tower Shaft 'A'- isolated	3	4	**0.9%**
Paulista Ave. Prot. Tower Shaft 'B'- isolated	3	4	**1.0%**
Paulista Ave. Prot. Tower Shaft 'A'- urban	3	8	**0.5%**
Paulista Ave. Prot. Tower Shaft 'B'- urban	3	8	**0.5%**
Total AVG SDEV from the WT simulations >			**0.8%**

Source: this study.

5.6. The computational fluid dynamics (CFD) simulations

CFD calculation uses a method similar to that employed for the three first steps of the investigation already described in the Methodology Chapter. The ability to simulate the airflow physics in an isothermal environment with controlled accuracy and flexibility in the extraction of data for analysis were decisive in the selection of this method. A total of seventy five CFD calculations were made during the first semester of 2009 in order to provide information for the analysis and corroborate the conclusions of this thesis: 10 for Step 1; 49 for Step 2; and 8 for each of the urban area case studies (Step 3). Several other simulations were carried out throughout the investigation process in order to arrive at this final number.

The CFD programme used in this investigation was a research version of the ANSYS FLUENT 6.2 and the 3D models were built and meshed in the Gambit 2.0 software. The calculations were run in a Linux based computer. This computer was accessed by a Windows desk computer through the Secure Shell (SSH) program that allows this network interface, and the X-Win32.9 application was used for drawing and displaying the graphics on the screen.

Although it is recognized that CFD results are susceptible to uncertainties and approximations, the achievement of consistency and reliability in the outcomes is related to the control of a number of input and calculating parameters[52]. This is usually achieved by following standard procedures and performing pre-test simulations for calibration, verification and validation of the results, as previously described in Chapter 3. The calibration, verification and validation of the parameters used in the CFD

[52] For further information about the steps to attain confidence in CFD results see topic 3.5.1 in Chapter 3.

investigations were attained by calculating the flow field around two parallel rectangular bricks and contrasting the results with those of the wind tunnel physical model. The set-up for the wind tunnel experiment has been described earlier in this chapter. Here the actions for the CFD model set-up will be covered. A number of guide-lines were adopted for the pre-processing, solving and post-processing stages. This practice was used to ensure consistency in the modelling for all the three groups of CFD calculations undertaken: the calibration of the CFD input and modelling parameters itself; the investigation of the urban prototypes; and the assessment of urban areas approached as case studies.

5.6.1. CFD pre-processing parameters

In the CFD pre-processing stage the 3D model input is specified. This involves decision making about the domain size and verifying the impact that the boundaries, the mesh type and size, the fluid properties, the cell blockage and other aspects of the problem description may have on the results. These steps are described in the following sections and are illustrated with information from the simulations performed during the research.

5.6.1.1 Domain discretization

The domain discretization adopted on in the CFD models comprised its sub-division into four or five nested volumes[53]. The domains were classified as: inlet, centre, outlet, and one or two top zones. This allowed different cell treatment for each zone and, therefore, ensured mesh accuracy where necessary without compromising the final outcomes or the calculation time. Also, the total length and volume adopted for these cushion domains have proved to be sufficient to allow full development of the airflow-field without interfering in the flow patterns in the target area.

5.6.1.2 Boundary conditions

The boundary in the CFD model establishes the domain constrains and allows the exchange of mass and heat from outside and inside[54]. The boundary types used in the CFD models performed in this research were: velocity inlet; interface; non-slip walls; symmetry; and outflow boundaries.

[53] For further information about domain discretization in CFD models see topic 3.5.3.1 in Chapter 3.
[54] For further information about boundary conditions in CFD models see topic 3.5.3.2 in Chapter 3.

Figure 5-46: Domain size and description of the boundaries for the two-brick CFD model (H/W=1.0; 90°).

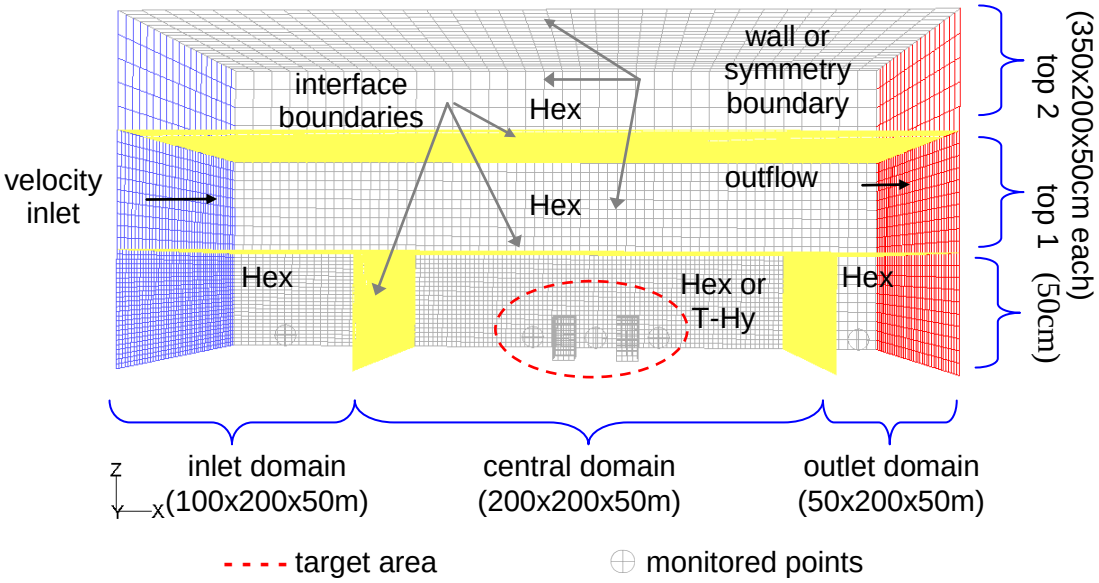

Source: This study.

The fluid field was set for air at constant density (1.225kg/m^3) and viscosity (1.79e-05kg/m-s). The operating pressure conditions of the domain were kept at 101325Pa, the gravitational acceleration at -9.83m/s^2, and an isothermal condition was set for all the models. Also, the proportion of fluid to blocked cells inside the total domain was kept low, with an average value of 3.0% and a maximum of 4.6%.

The upstream boundary was set at 'velocity inlet' and it was through this surface that the ABL was launched into the model. A velocity magnitude was related to each vertical strap on this surface and the resulting airflow normal to the boundary reproduced the type of ABL calculated by a logarithmic profile for a given terrain roughness, in accordance with the description given in the topic 2.3.7 of Chapter 2. The sequence of vertical velocity magnitude development that determines the ABL velocity inlet for the CFD simulations is demonstrated in the sequence. All the outlet boundaries were set as outflow with flow rate weighting equal to 1.

Figure 5-47: Schematic chart for the ABL wind profile log-law development applied in the investigations and as input in the CFD models.

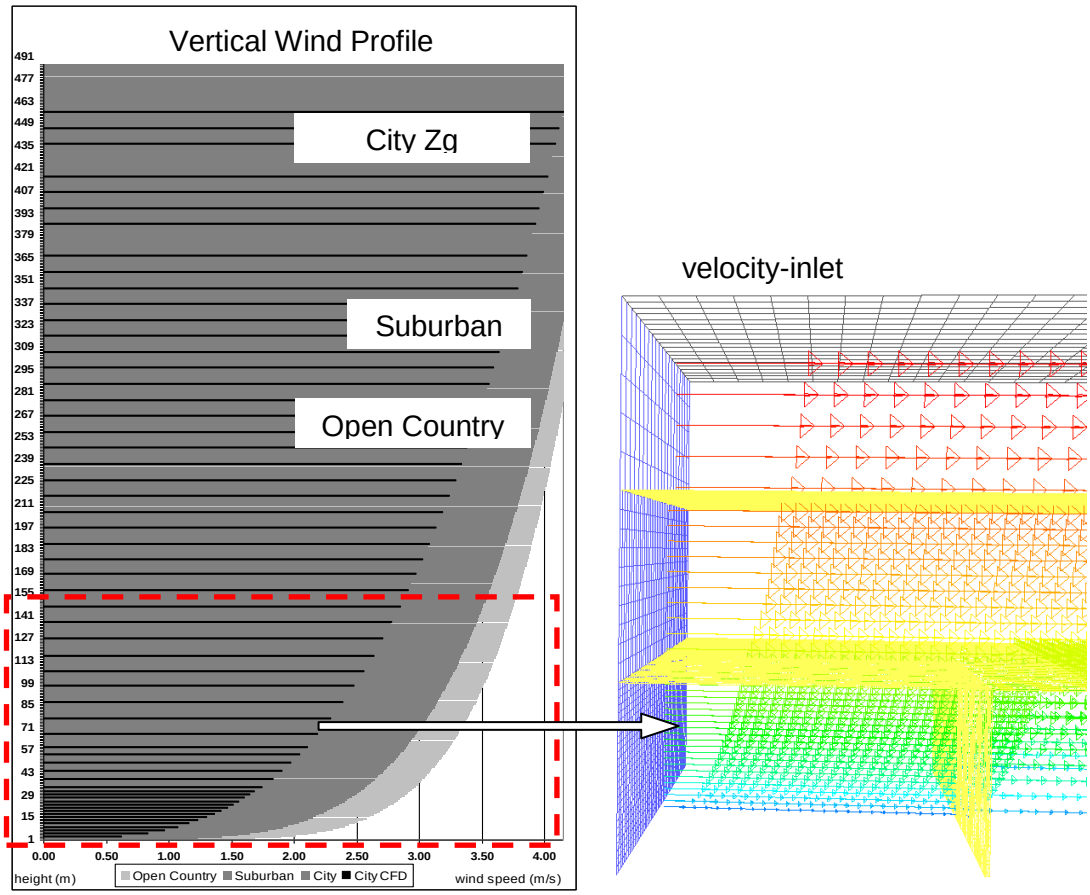

Source: This study.

All the blockage walls and ground were considered stationary with no slip shear condition, wall roughness height of zero meters and roughness constant of 0.5. The exception was the inlet ground, whose wall roughness height was set at 10m and roughness constant at 0.8. For the initial steps of the CFD simulations, the intention of which was to contrast the output with the wind tunnel results, both the size of the chamber and the definition of the walls were kept as similar as possible to those of the physical chamber. In this case, lateral and top boundaries were considered as walls. For the urban prototype and the real urban scenario case studies, symmetry boundaries were adopted for both the lateral and top surfaces of the domain. The nested domains were connected by standard interface boundaries. Neither periodic nor coupled interface was considered in these simulations.

5.6.1.3 Mesh structure

Due to the unstructured feature of the CFD solver adopted in this research, hexagonal or tetrahedral mesh structures were employed in the models, according to need[55]. For instance, the rectangular shape of the several nested volumes that form the domain and the absence of blocked cells allowed the use of hexagonal structured cells through these domains. Further, hexagonal meshes where used thorough the domain where the blocked cells are orthogonal to the grid. On the other hand, tetrahedral meshes formed by pyramidal and wedge-shaped cells were used in the target area mostly in the meshing of non-orthogonal, skewed and curved blocked shapes, which occurred due to the shape's complexity or the rotation of the model in order to simulate 45^{o} oblique winds (see previous figure 5-46 as example given).

In order to achieve reliable results in the CFD simulations during this research, an initial group of CFD simulations was carried out modelling a pair of parallel bricks in an external environment. The aim was to assess the impact of mesh structure on the Cp output and either tetrahedral or hexagonal meshes were utilized. Cp contour plot outputs on the windward face of two parallel bricks were first compared to examples in the literature[56] (de Faria, 2008) and then compared to results from wind tunnel experiments[57]. Figure 5-48 shows how the mesh type and it coarseness/ refinement level influence on the results. The coarsennes and skewness of the mesh structure determine its sensitivity to capture fluid features and are directely related to both the calculation time and the reliability of results in CFD simulation[58]. Initial mesh (A) is too coarse and results are not accurate on both grid options. After first adaption (B) the uneven cell distribution in the tetrahedral mesh solution becomes more apparent, impacting on the pressure distribution and later maesh refinement (C) does not improve this scenery, even with cell volumes are 15x smaller than the initial one. Conversely, when Hex mesh is applied directly on surfaces continuous adaption improves the results until reaching the shape of pressure distribution found in literature. For the chosen initial size of cell, a sequence of two refinements proved to be enough to allow results become independent of mesh size. Further adaption did not improve results, though increased simulation computer time. Table 5-7 shows the number of cells and mesh refinement characteristics adopted for this exercise.

[55] For further information on cells and grid topology in CFD models see topic 3.5.3.3 in Chapter 3.
[56] The Cp contour plot distribution results from classical literature for isolated bricks and used for comparison are found in topic 2.5.1 in Chapter 2.
[57] See topic 5.3 in this chapter and Chapter 6 for further information.
[58] For further information about the mesh structure to be adopted in CFD models and parameters which define its sensitivity see topic 3.5.3.4 in Chapter 3.

Figure 5-48: Impact of mesh refinement on the results for tetrahedral (above) and hexagonal (below) mesh type applied directly to the block surfaces and the domain.

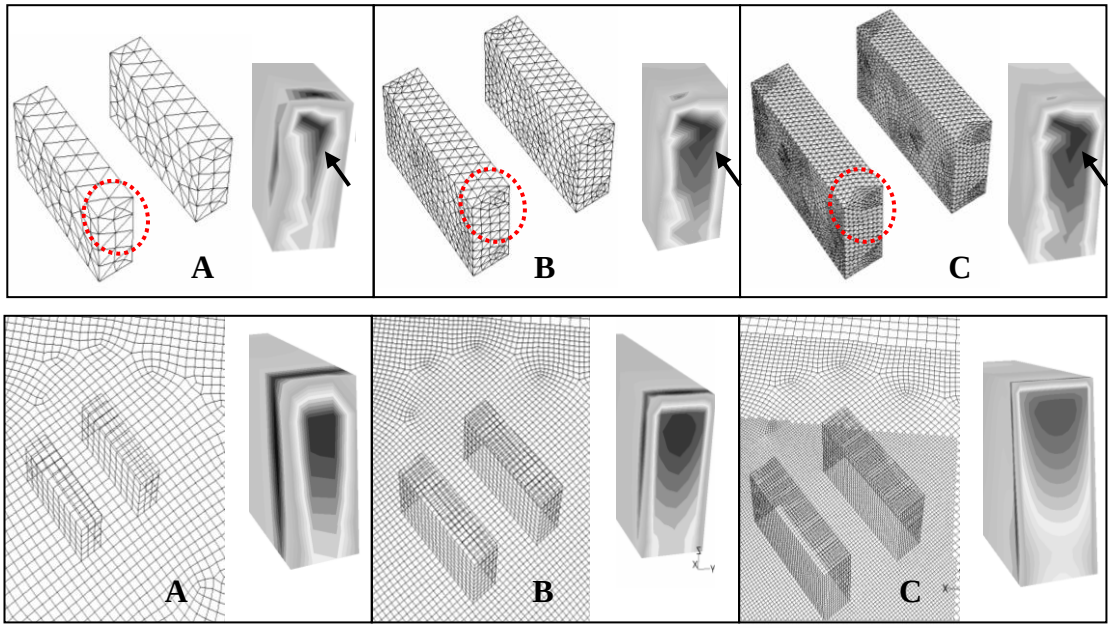

Source: de Faria (2008, pp07).

Table 5-7: Mesh refinement experiment characteristics and steps

grid type		number of cells			volumes (m^3)				
		initial	added	pos-adaption	initial cell	domain volume	max. cell	average cell	min. cell
T-Hy +T-Hy	A	346,467	-	-	5.00	7.20E+06	64.62	20.78	0.78
	B	346,467	463,134	809,601	-	7.20E+06	64.62	8.89	0.36
	C	809,601	625,884	1,435,466	-	7.20E+06	64.62	5.02	0.05
HEX +T-Hy	A	246,100	-	-	5.00	7.20E+06	167.99	29.26	1.17
	B	246,100	324,145	570,245	-	7.20E+06	167.91	12.63	0.18
	C	570,245	623,115	1,193,360	-	7.20E+06	167.91	6.03	0.02

Source: de Faria (2008, p 07).

Based on these previous results some procedures were adopted for all the subsequent CFD models simulated on this investigation. For instance, grids and meshes were applied in the software Gambit in the following order: to the surfaces of the target blocked cells, other blocked cells, ground boundary, inlet boundary, outflow boundary, lateral and top boundaries; and, only then, was the mesh volume applied to the target's central domain, the inlet domain, the outlet domain, and the several top domains, respectively. Further, the initial parameter adopted for the cell size and volume for the subsequent steps of CFD simulation on this investigation was that one drawing unit was considered equivalent to one meter. A cell of 1x1x1 d.u. has, therefore, a volume of $1.0m^3$. Further mesh improvement in the target area was undertaken on Fluent by region adaption, on which an input coordinate limits the hexagonal volume constraint to be refined. By using a maximum level of mesh refinement equal to one and setting a minimum cell volume of $0.125m^3$, an aspect ratio

of 1:2 between adjacent cells was achieved. The horizontal resolution obtained for the grid was a minimum of 20 cells between blockages and canyons in the target area and 10 cells between solid bodies elsewhere in the model. The total number of cells in the CFD models used ranged from 300,000 cells for the two-brick simulations to 1.0 million cells for the complex urban geometry in the case studies and 1.5 million cells for the urban prototype models. Accuracy in the results has proved to be satisfactorily achieved with the mesh refinement of this scale and order of magnitude.

Figure 5-49: Region mesh adaption undertaken for hexagonal and tetrahedral cells.

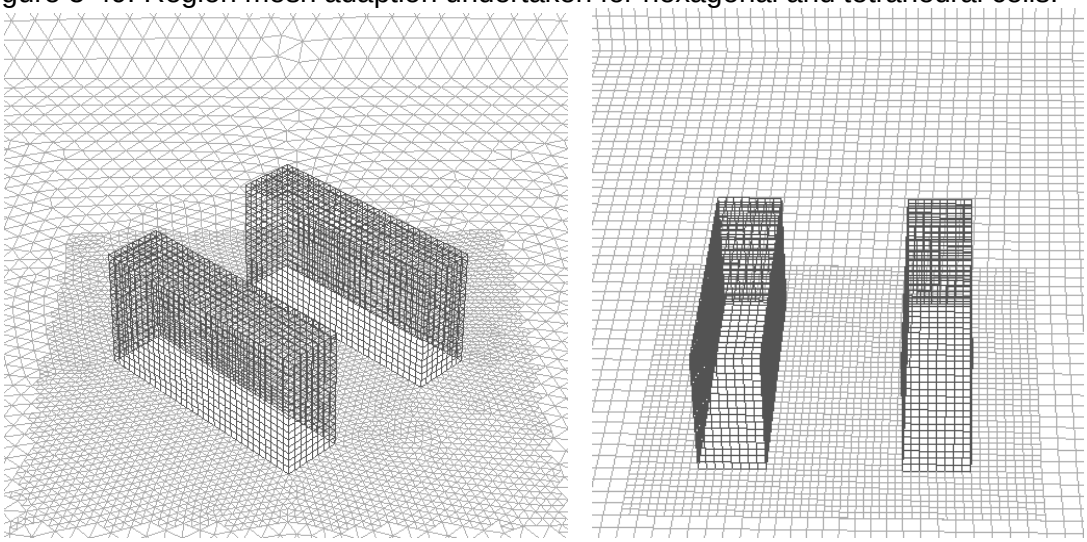

Source: This study.

5.6.2. CFD solving parameters

The solution to the imposed problem is calculated during the CFD solving stage. Several steps involving the solution control parameters, such as the choice of the time mode; thermal mode; turbulence model; solution controls; relaxation factors; monitoring solution progress; and residual plot thresholds, may interfere in the quality of the simulation and, in consequence, in the reliability of the results. The solution control parameters adopted in the CFD calculations are now described and exemplified by the respective software windows. The solution solver was set as pressure based, and the linearization formulation was of implicit mode for steady-time problems.

Figure 5-50: Parameters adopted for the solution solver in the CFD models.

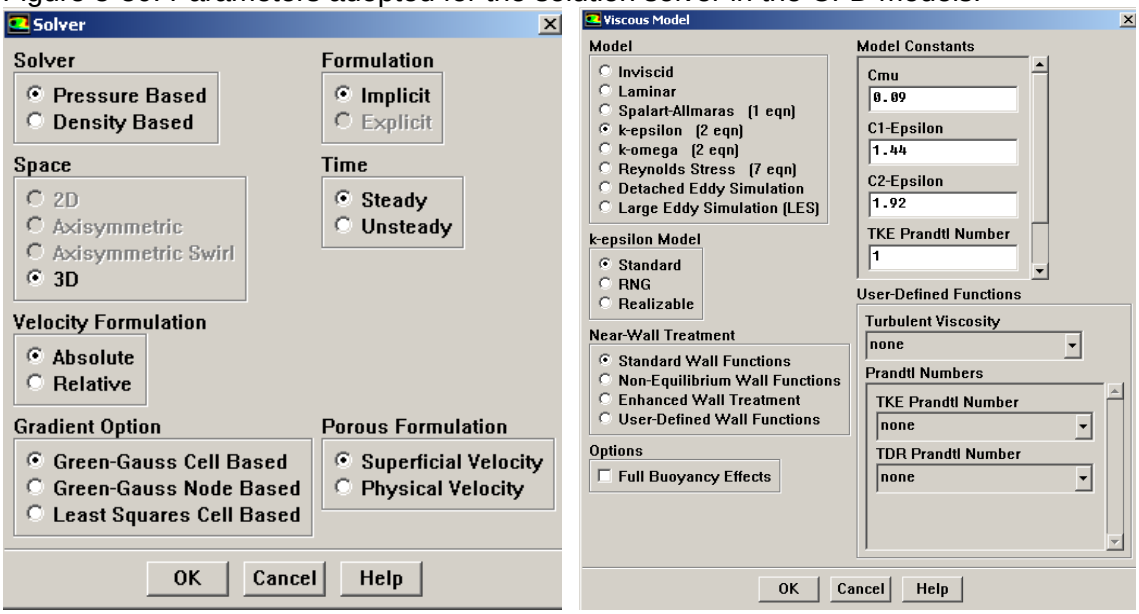

Source: this study (windows from Fluent)

5.6.2.1 The turbulence model

The turbulent viscosity model adopted for all the CFD simulations was the k-e RANS standard[59]. Experiment was carried-out for the purpose of contrasting the results of the standard viscous model used with the k-e RNG; the k-e Realizable; and the LES outputs (de Faria, 2008).

The solver method assigns properties to cells, faces and grid points that compose an unstructured grid constrained in a finite volume, allowing data exchange between neighbour cells. Conservation equations for mass and continuity are applied for all flows, being added of energy equations when the problem involves heat changes or fluid compression. The turbulent kinetic energy 'k' and it rate of dissipation 'e' are the basic components for the equation of turbulent viscosity, 'm_t'. Further transport equations can be added for calculating fluctuating velocity fields of turbulent flows, where eddies of small scale and high frequency make the calculation of momentum, energy and concentration transport difficult to be closed.

Equation 5-4: $\mu_t = p \times C_\mu \times \kappa^2/\varepsilon$

[59] For further information about turbulence equations in CFD models see topic 3.5.3.10 in Chapter 3.

Based on the results from a test on which different turbulence solvers were applied for the same model with a symmetrical boundary domain (see Figure 5-51), and then contrasted to classical results on the literature[60], it is possible to say that the airflow detachment and the separation bubble on the top surface of the model obtained with the default parameters of the k-e RANS were rasonably close to the ones presented by Cook (1985, p 168), while the Realizable model seemed to under-predict the detachment and the RNG model produced a very open and unrealistic top detachment flow and inconsistent leeward wake. The LES model agreed more with the k-e RANS and Realizable ones, although this is the only one capable of capturing recirculation flow on the top separation bubble. LES computational time was 10 times greater than those of the other models. Regarding the Cp contour plot results, all the four models were close to the results from the literature.

Decision about which turbulence solver is the most suitable for modeling external airflow divides the researchers. While some mention that Standard k-e model and LES produces similar acceptable results for most of the applications in urban atmospheric environments (X-X. Li et al, 2005 and 2006), others state that Standard k-e model fails in simulating reverse flows in the windward properly, and, although this drawback was corrected by RANS models, these over-estimates the size of the separation bubbles reattachment on the leeward (Meroney et al, 1999; Cheng, 2003; Tominaga et al, 2008) and recirculation in urban canyons are found slightly weaker as well (Walton and Cheng, 2002). This happens due to the fact that this code does not consider unsteady vortices in the airflow calculation. LES models reproduces closer to reality the complexity of vortices, reverse flows, separation bubbles, wakes and reattachment processes, since it allows a better reproduction of the periodic fluctuation (Tominaga et al, 2008; Shi et al, 2008). On the other hand, all of them agree that a disadvantage for LES calculation is it great computation time, up to 100 times greater than time-steady models.

[60] The Cp contour plot distribution and airflow detachment and leeward wake features from classical literature which were used for comparison are fond in topic 2.5.1 of Chapter 2.

Figure 5-51: Comparison of results obtained with different default turbulence solvers.

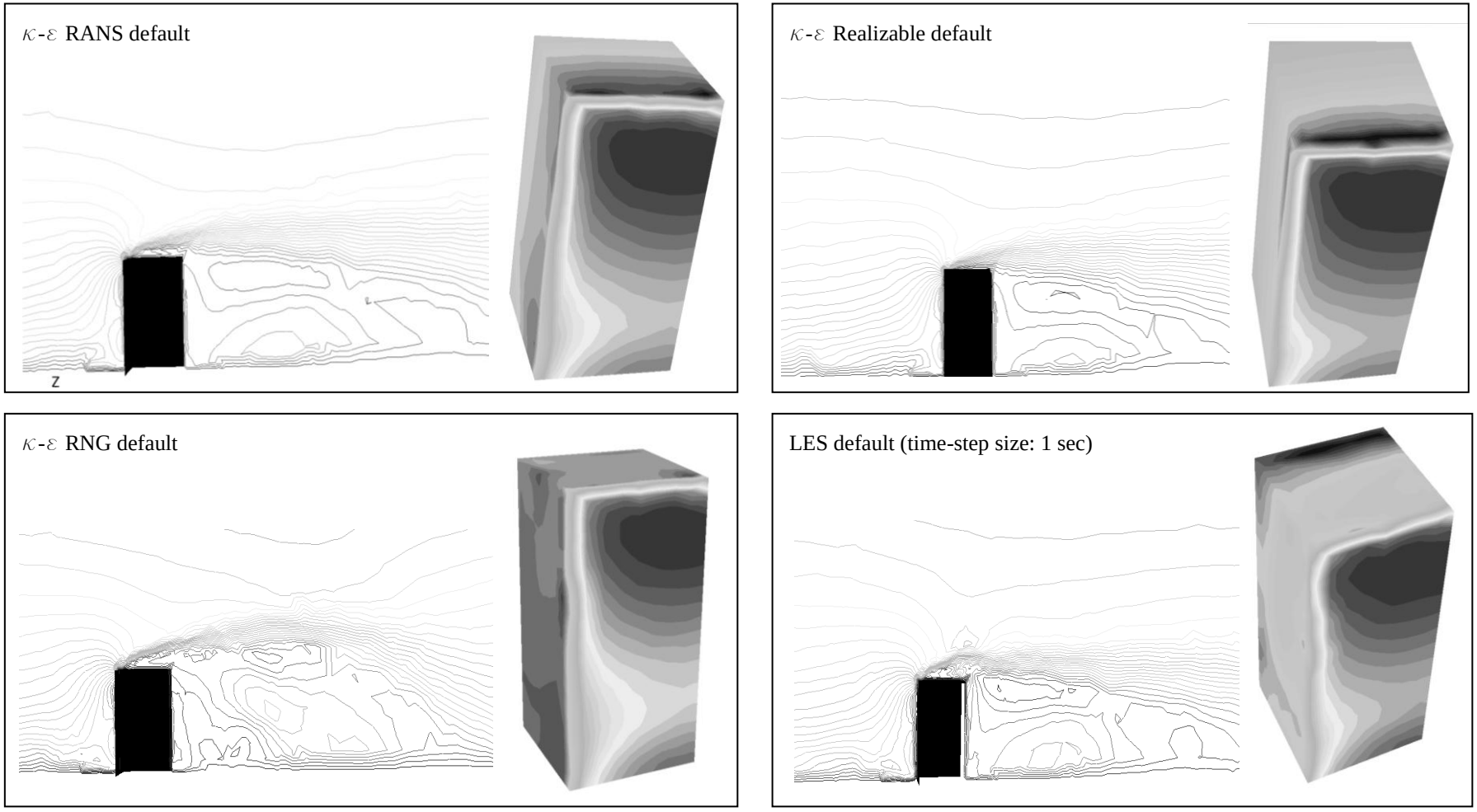

Source: de Faria (2008, pp 07).

5.6.2.2. The solution controls and under-relaxation factors

The solution controls and under-relaxation factors adopted were kept similar to the default values, and no decrease in value was necessary to speed-up or to facilitate the solution to the imposed problems[61].

Figure 5-52: The solution controls and under-relaxation factors used:

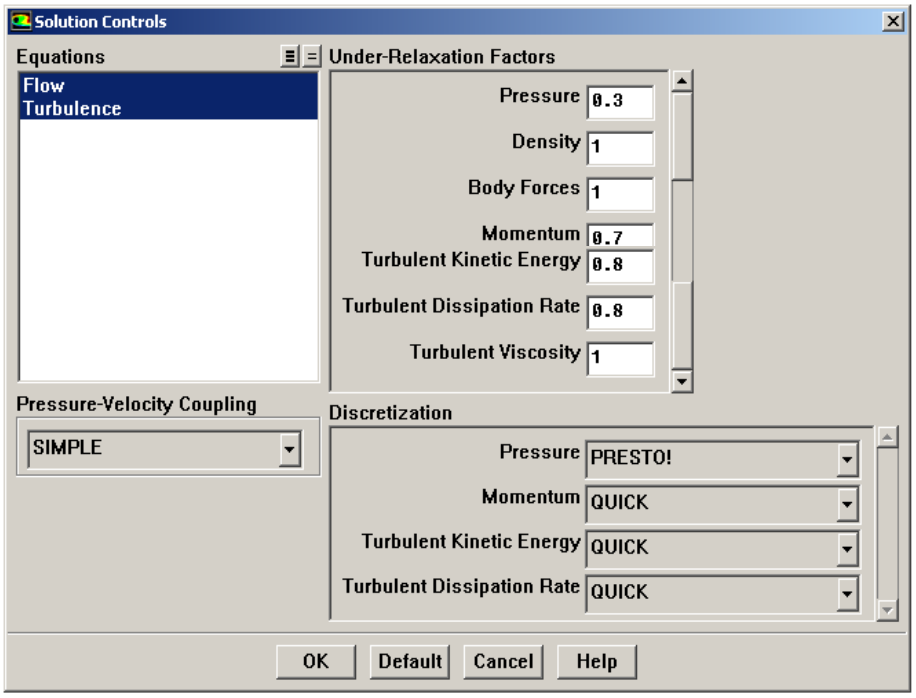

Source: this study (window from Fluent)

The convergence criterion for the continuity, velocity, turbulence and viscosity equations was set at six or seven orders of magnitude, depending on the model. This was necessary since calculations were run at a remote CPU station and, by setting these very low figures, it was possible to allow the calculation to develop while being observed and to determine the moment at which to stop the runs to ensure confidence in the results. Confidence was achieved mostly after the drop of four orders of magnitude for all the residual plot criteria. In addition to the default solution residual plot, the airflow velocity, turbulence and static pressure were monitored at three or five points strategically positioned throughout the domain. Calculations were based on area weighted average results and the results were considered stable when ranges of less than 0.10 unit on the convergence history plot was reached for the following criteria: airflow velocity magnitude (m/s); turbulence kinetic energy (k); and static pressure (Pa).

[61] For further information about solution controls and under-relaxation factors in CFD models see topics 3.5.3.7, 3.5.3.8, and 3.5.3.9 in Chapter 3.

The Cp variation on some of the blocked target surfaces was also monitored during the solution process, results being considered stable for result ranges inferior to 0.05. Monitoring solution progress was achieved through residual plot and the monitoring of specific points and surfaces in the domain:

Figure 5-53: Residual plot convergence criterion window.

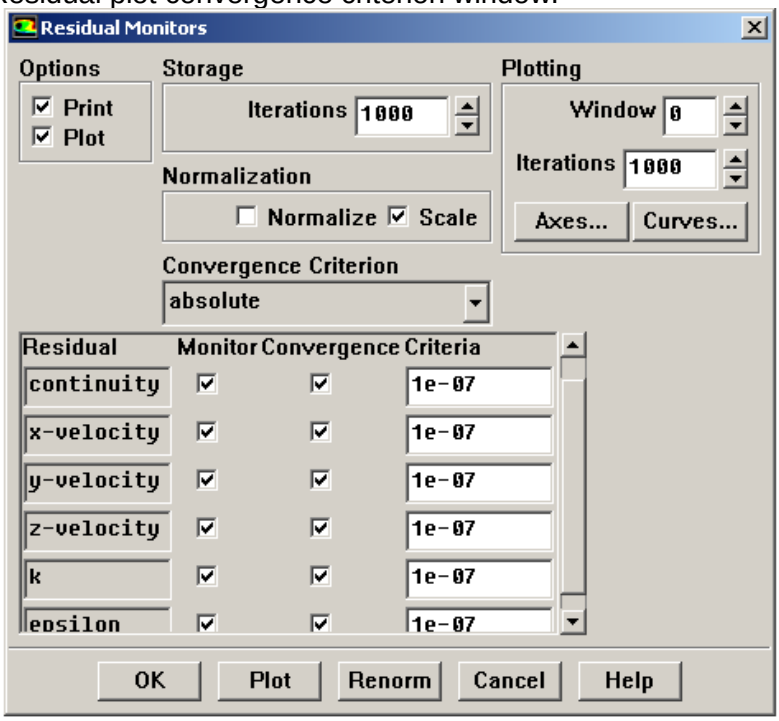

Source: this study (window from Fluent)

Figure 5-54: Example of residual plot from the Urban Prototype CFD simulations.

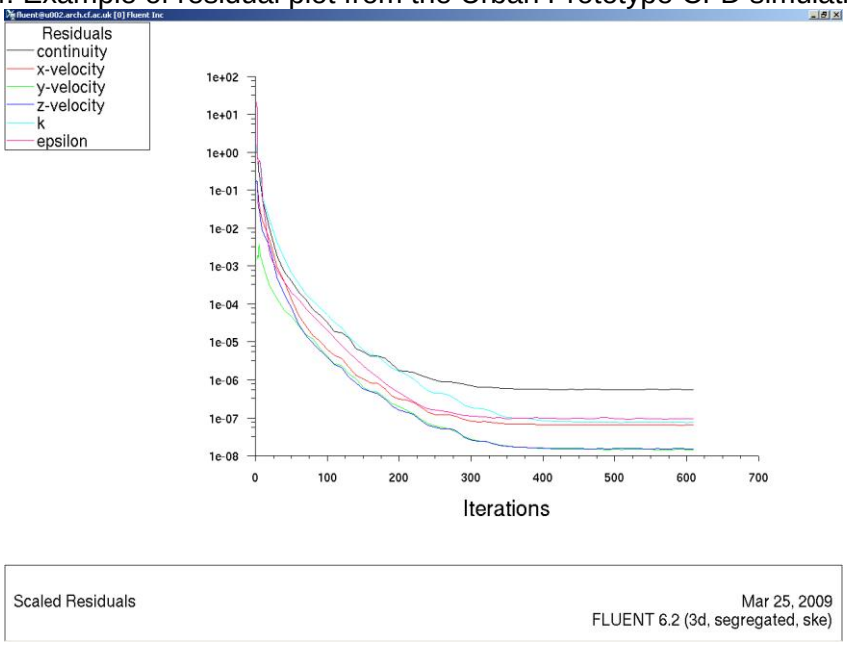

Source: this study (window from Fluent)

Figure 5-55: Selection (above) and definition (below) of a monitored surface or point.

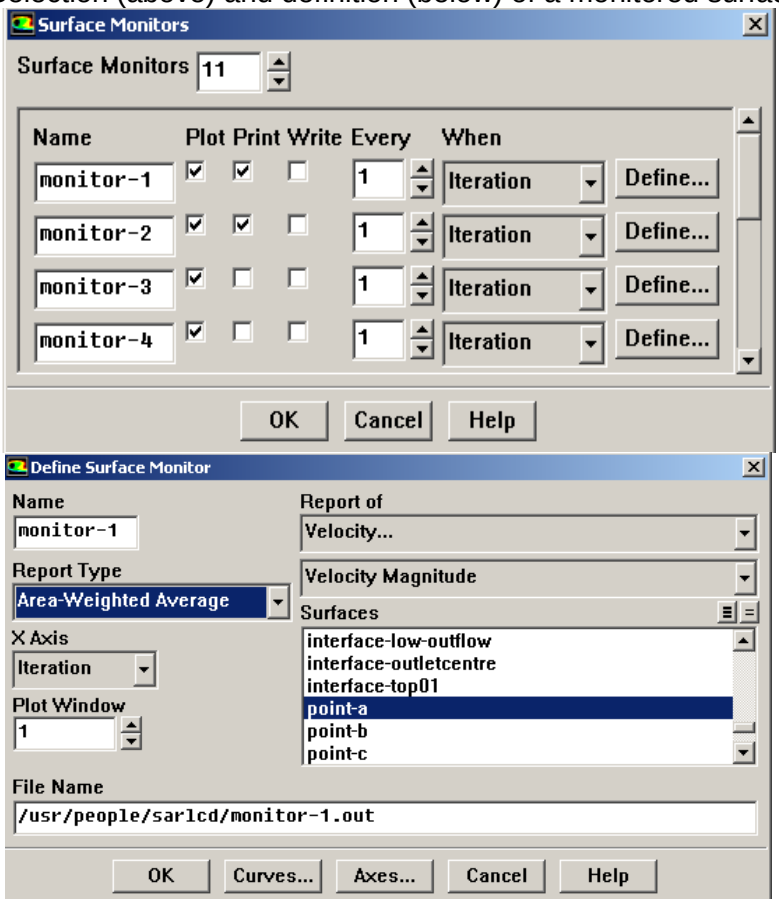

Source: this study (window from Fluent).

Figure 5-56: Examples of monitored points for m/s (top left), k (top right), Pa (bottom left), and Cp (bottom right) during the CFD simulations

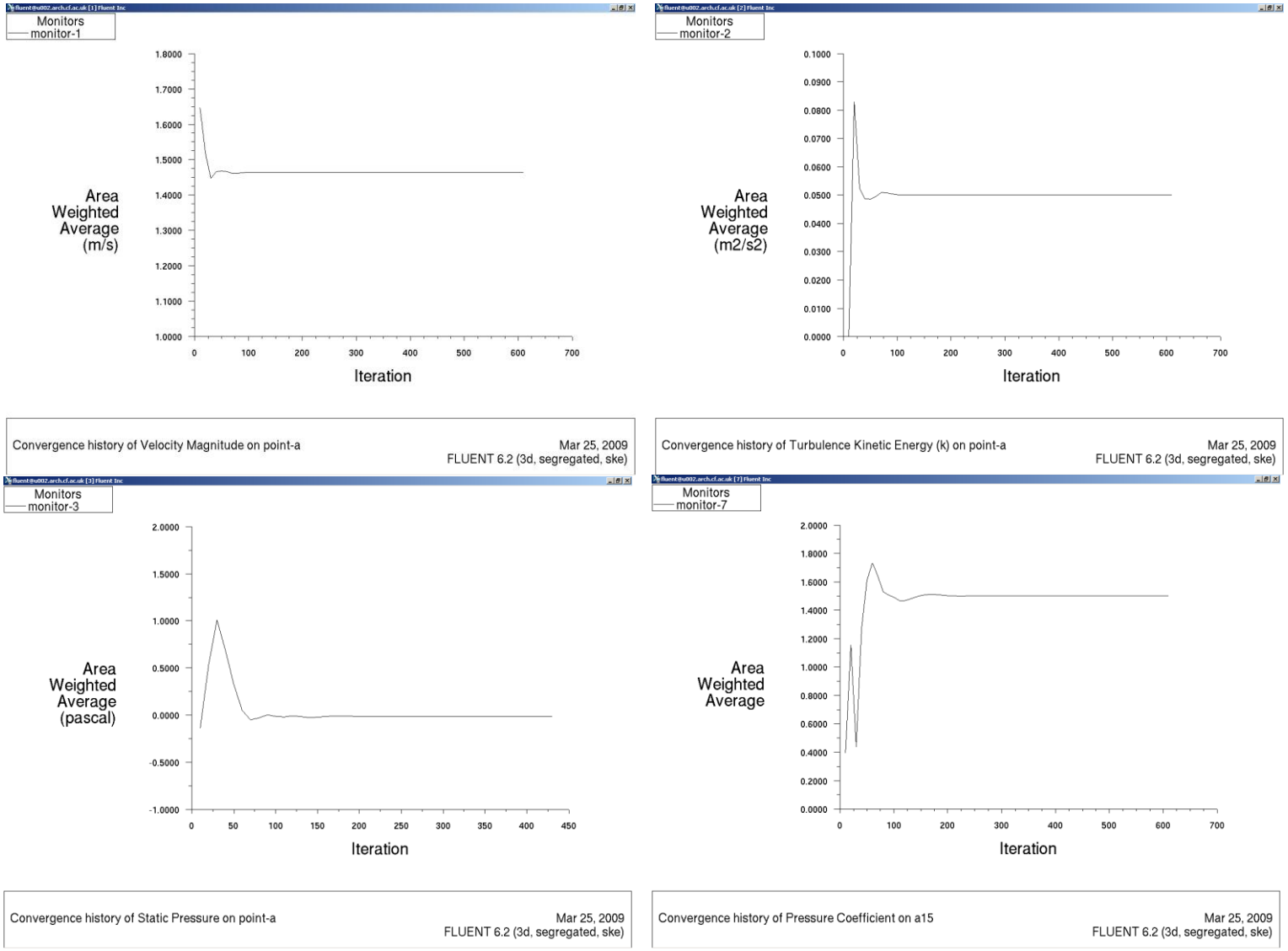

Source: this study (window from Fluent).

5.6.3. The urban prototypes CFD models

In the CFD post-processing stage the calculated output information is extracted from the data file and organized to be analyzed and displayed. Therefore, the proper interpretation of the CFD results depends on how it is done. The CFD software used allows several output display modes and export data formats. The accuracy of the qualitative and quantitative data analysis is associated with the choice of several parameters.

The qualitative visual analysis is related to the display of data of: density, velocity (magnitude, ‘x’, ‘y’, or ‘z’ vectors); pressure (static, dynamic, relative, total, absolute, Cp); turbulence (TKE, intensity, dissipation, viscosity), and several others results. The results can be displayed as contour plots, vectors, pathlines, and particles. For instance, velocity pathlines are related to: the position, size and number of points of a rake whence the flow visualization is released; the range and scale of results to be shown; the pathline style and its attributes (line width, spacing factor and scale); the pathline step size (m), total number and coarseness level; and finally if it is in pulse or single mode. Achieving a good visualization of the resultant airflow is based on several trial and error methods which combine all these parameters. The quantitative data, that is, numerical information that can be analysed and contrasted by means of graphs, equations, averages and total values, can be exported from a point, line, plane or volume within the model domain. The accuracy in the data is related to the mesh refinement of the mesh whence it is extracted. For example, a line across the fluid domain will export as many figures as the total number of cells in the mesh it traverses, and a surface will export one figure for each cell in its area.

5.6.3.1 The qualitative data parameters

In order to analyse the CFD results, both contour plot lines and airflow visualization pathlines were used as qualitative sources of information. Contour plots were used for contrasting Cp results on the block surfaces from the CFD simulations with those from the WT experiment. Also, the range of results for the CFD and the WT contour plot are expected to be related.

Figure 5-57: Example of contour plot parameters window used for displaying Cp results on surfaces.

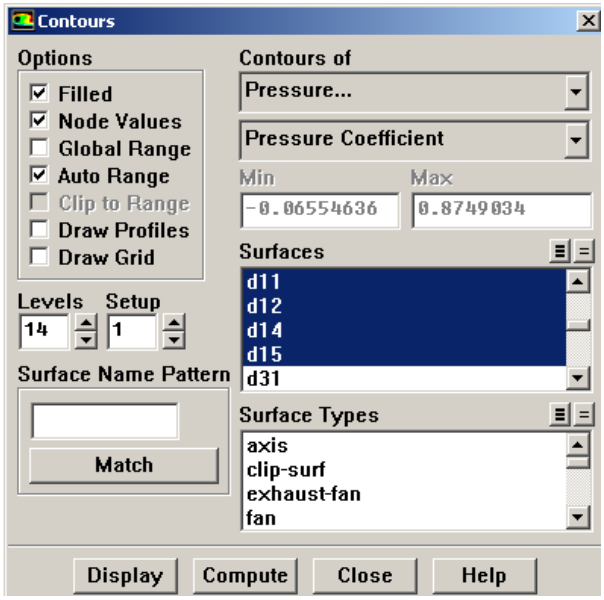

Source: this study (window from Fluent).

Figure 5-58: Example of contour plot image displaying Cp results on a surface.

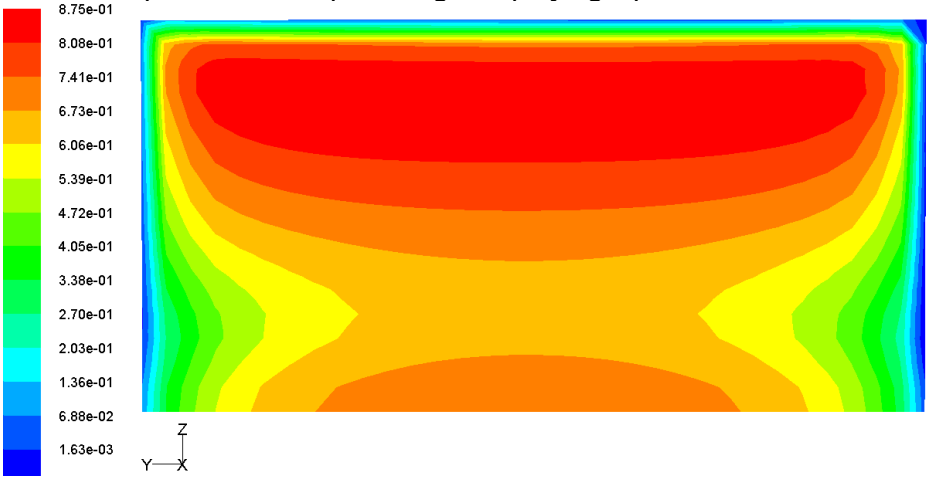

Source: this study.

Velocity magnitude pathlines were used for visualizing the airflow field through the blockages. The pathlines were released either from horizontal rakes placed across the domain or from vertical rakes. Horizontal rakes were created for several heights above ground. Both horizontal and vertical rakes were positioned in the inlet domain and at 2m distance from nodes.

Figure 5-59: Airflow velocity magnitude pathline parameters window.

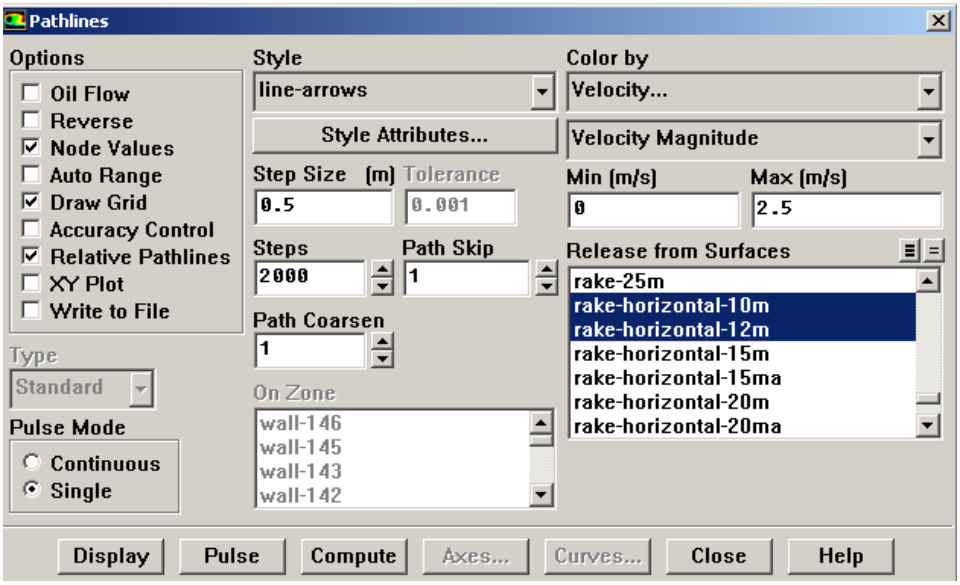

Source: this study (window from Fluent).

Figure 5-60: Example of airflow velocity magnitude pathlines for the two bricks scenario from two horizontal rakes: at 10 and 12m height (H/W= 1.0; m/s; 90°).

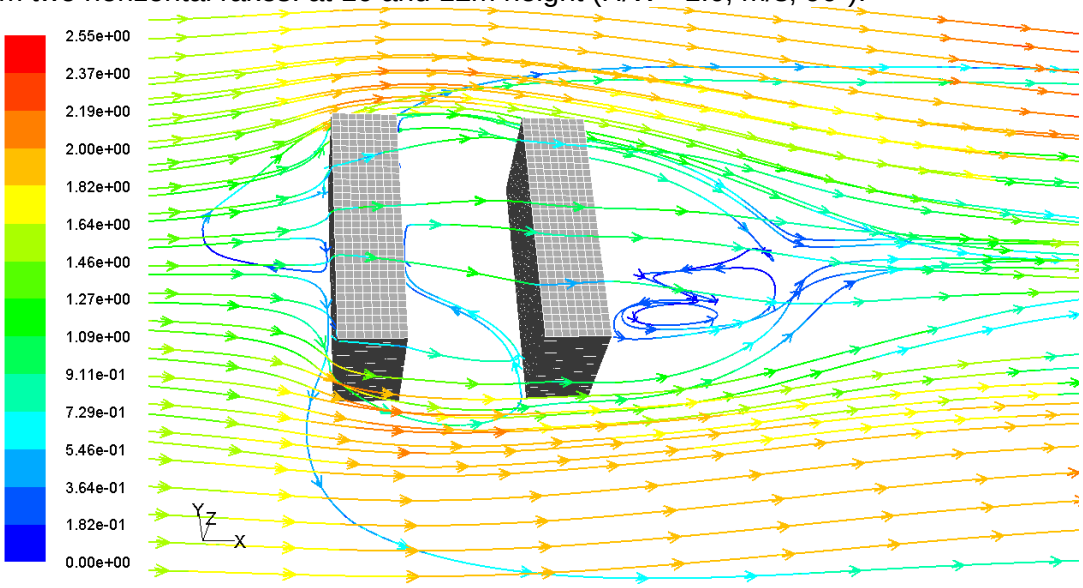

Source: this study.

5.6.3.2 The quantitative data parameters

The quantitative data from the CFD output were extracted either from lines or from surfaces. While the lines provided data about wind velocity (magnitude, 'x', 'y', or 'z' vectors), the surfaces provided basically Cp values, although all extracted data comprised also pressure (static, dynamic, relative, total, absolute, Cp) and turbulence (TKE, intensity, dissipation, viscosity) information. The horizontal lines were strategically positioned either across or alongside the targeted windward and leeward surfaces, and the vertical lines were placed either at 0.50m from these surfaces or

exactly in between the blocks, from the ground to 200m height. Finally, the data were exported from the export panel as comma delimited in the ASCII format and imported into the Excel software. The graphs presented in the results and analysis chapters were developed via Excel.

Figure 5-61: Example of lines and surfaces used for exporting quantitative data (H/W= 1.0; m/s; 90°).

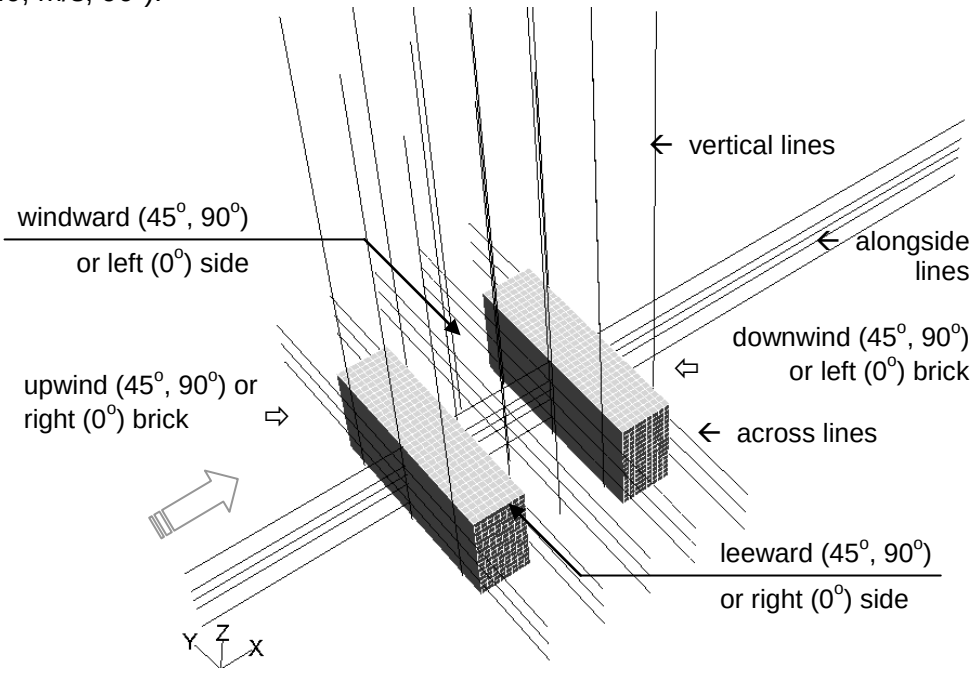

Source: this study.

5.6.4. The urban prototypes CFD models

A large number of urban prototype scenarios (18 in all) were divided into 4 major categories and other 4 sub-types, according to the established parameters already set out in section 5.4.1.2. These scenarios were CFD simulated for three wind directions (0°; 45°; and 90°), totalling therefore 53 scenarios under investigation. The CFD pre-processing, solving and post-processing parameters employed for all these simulations were very similar, all based on the findings of the previous step method. Two samples that represent the extreme opposites within such an assemblage will, therefore, be described here.

While both examples have similar domain extensions (which were split into four zones: inlet; centre; outlet; and top), the first example, the C2 scenario, is characterized by homogeneous low height square blocks and narrow canyons, with aspect ratios of H/W= 2.0 (30x15m, respectively), A_{roof}/A_{urb}= 0.72; and A_{built}/A_{urb}= 5.76; and was simulated for orthogonal winds. For this reason, orthogonal mesh and hexagonal cells were used. In contrast, the second example, the D3 scenario, presents block

asymmetry and height variation (30, 60, and 90m), with aspect ratios of H/W= 0.7, A_{roof}/A_{urb}= 0.45; and A_{built}/A_{urb}= 5.79; and was simulated for oblique winds. Also, orthogonal mesh and hexagonal cells were used in the empty domains, while the centre domain with the blockage was meshed with tetrahedral cells. It is worth noting that, despite the urban landscape differences (the first example is defined by low blocks of large roof area and the second by tall blocks of small roof area) which result in different H/W and plan-area density aspect ratios, the built density is practically the same in both cases.

5.6.4.1. Urban prototype CFD model example 1: C2 (90^o)

Table 5-8: Domain and mesh information for the prototype C2 (H/W= 2.0; 90^o).

Domain zone	domain extent (m) x	y	z	Total volume (m^3)	Fluid volume (m^3)	Blockage %	Type of cells	*n^o of cells*
Total	1,400	600	200	1.68E+08	1.59E+08	5.3%	HEX	*944.067*
Mesh adaption region:	*diagonal: -30,-105,0 / +30,+105,+40*							

Source: This study.

Figure 5-62: Example 1: domain zones and target area for the prototype C2 (H/W= 2.0; 90^o).

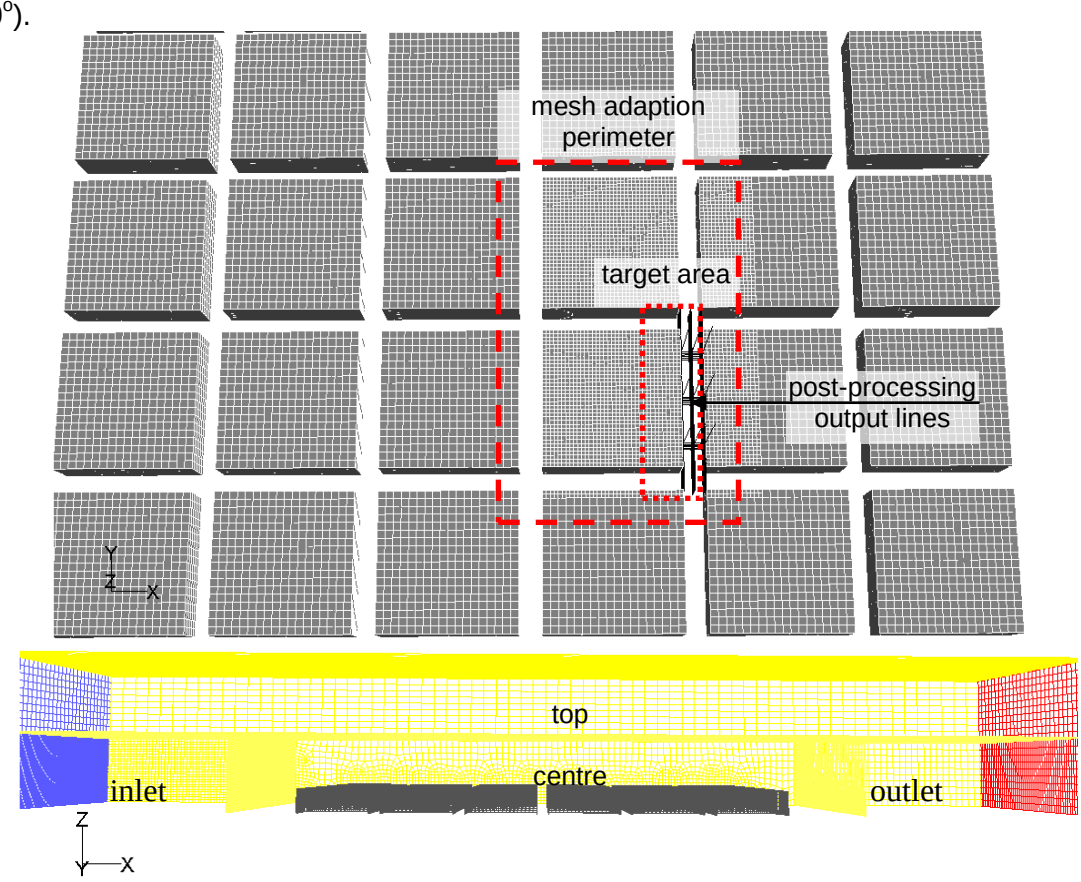

Source: This study.

Figure 5-63: Residual plot (top left), and monitored points (top right: m/s; bottom left: k; and bottom right: Cp) for C2 (H/W= 2.0; 90^{o}).

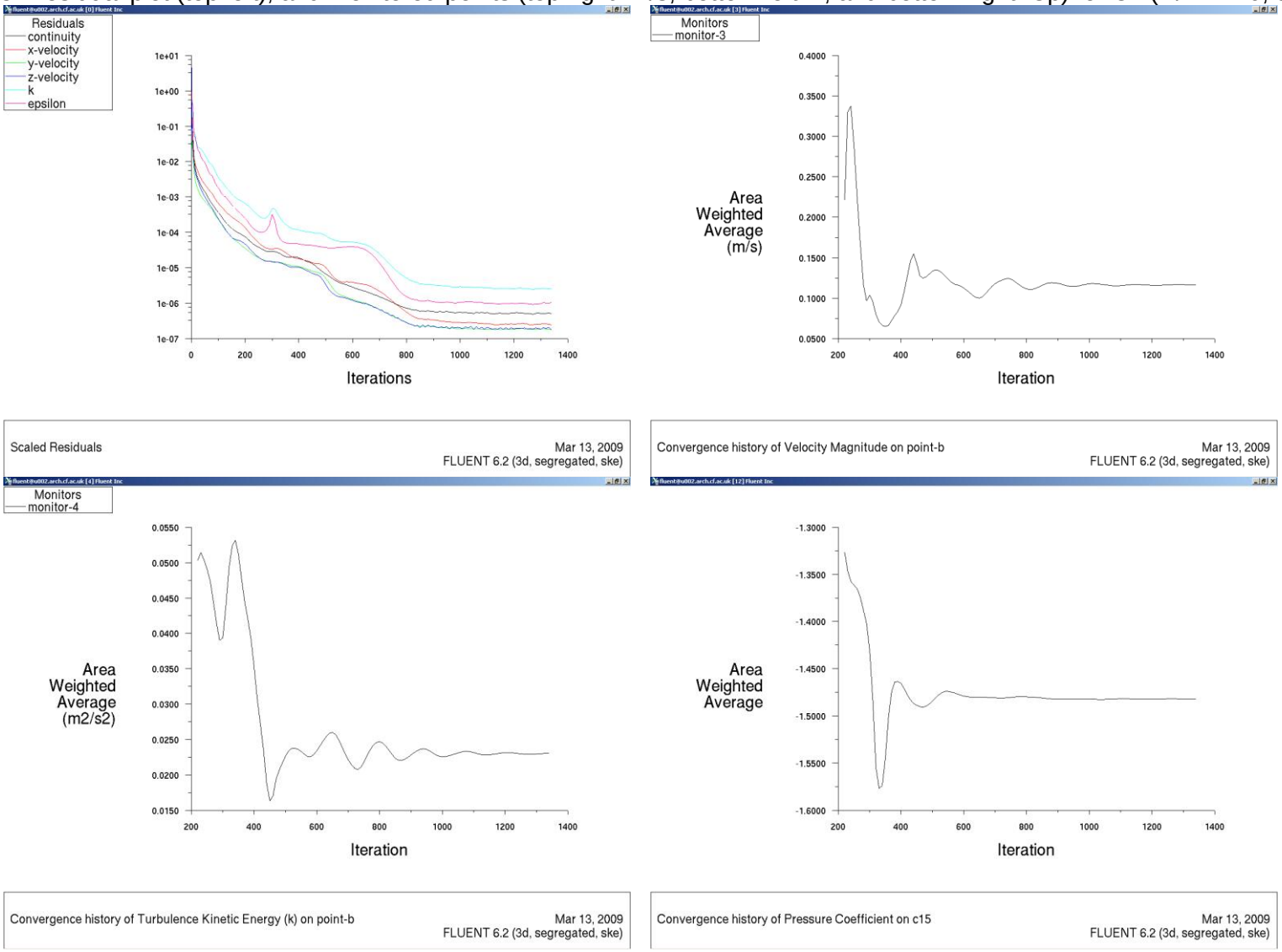

Source: This study.

5.6.4.2. Urban prototype CFD model example 2: D3 (45°)

Table 5-9: Domain and mesh information for the prototype D3 (H/W= 0.7; 45°).

Domain zone	domain extent (m) x	y	z	Total volume (m^3)	Fluid volume (m^3)	Blockage %	Type of cells	*nº of cells*
Total	1,400	600	260	2.18E+08	1.92E+08	14.4%	T-Hy, HEX	*936.767*
Mesh adaption region:				*diagonal: -140,-60,0.0 / 35,140,95*				

Source: This study.

Figure 5-64: Example 2: domain zones and target area for the prototype D3 (H/W= 0.7; 45°).

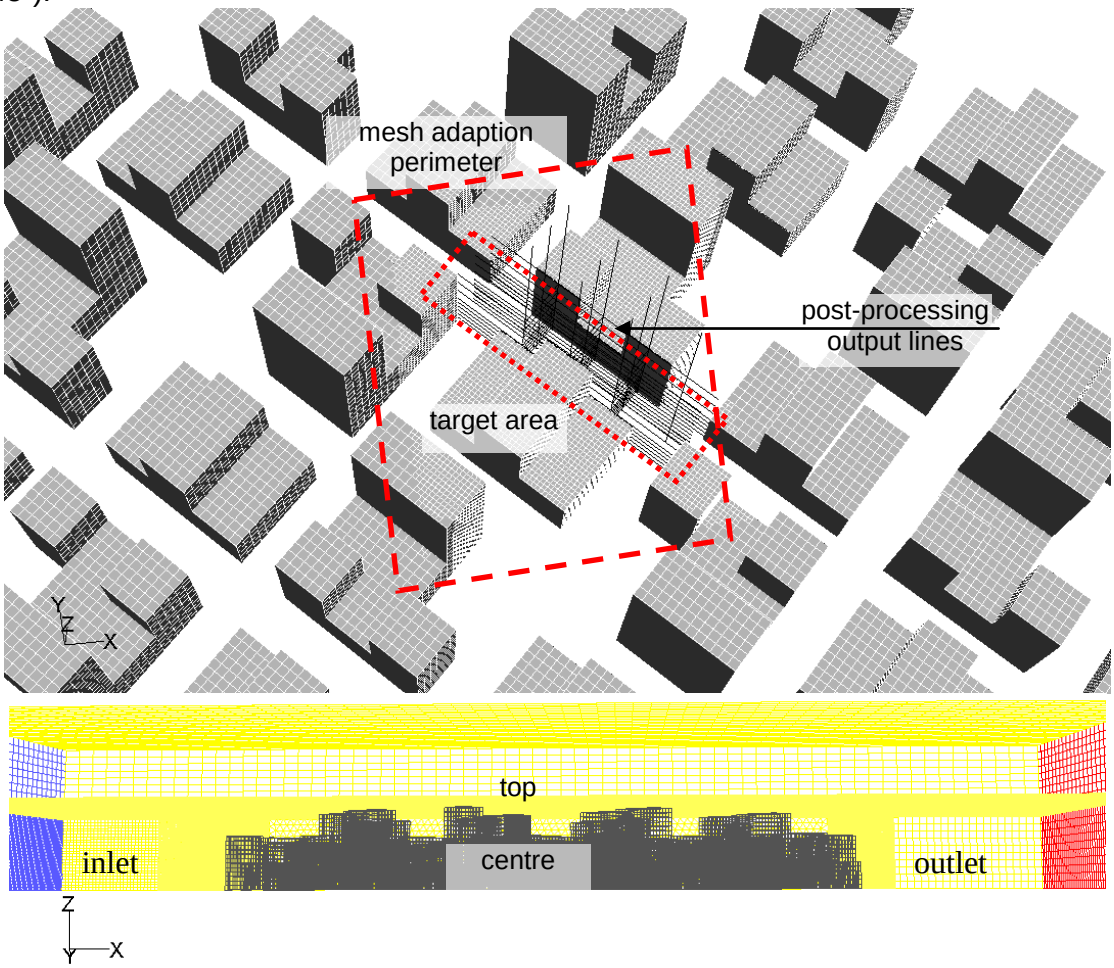

Source: This study.

Figure 5-65: Residual plot (top left), and monitored points (top right: m/s; bottom left: k; and bottom right: Cp) for D3 (H/W= 0.7; 45^{o}).

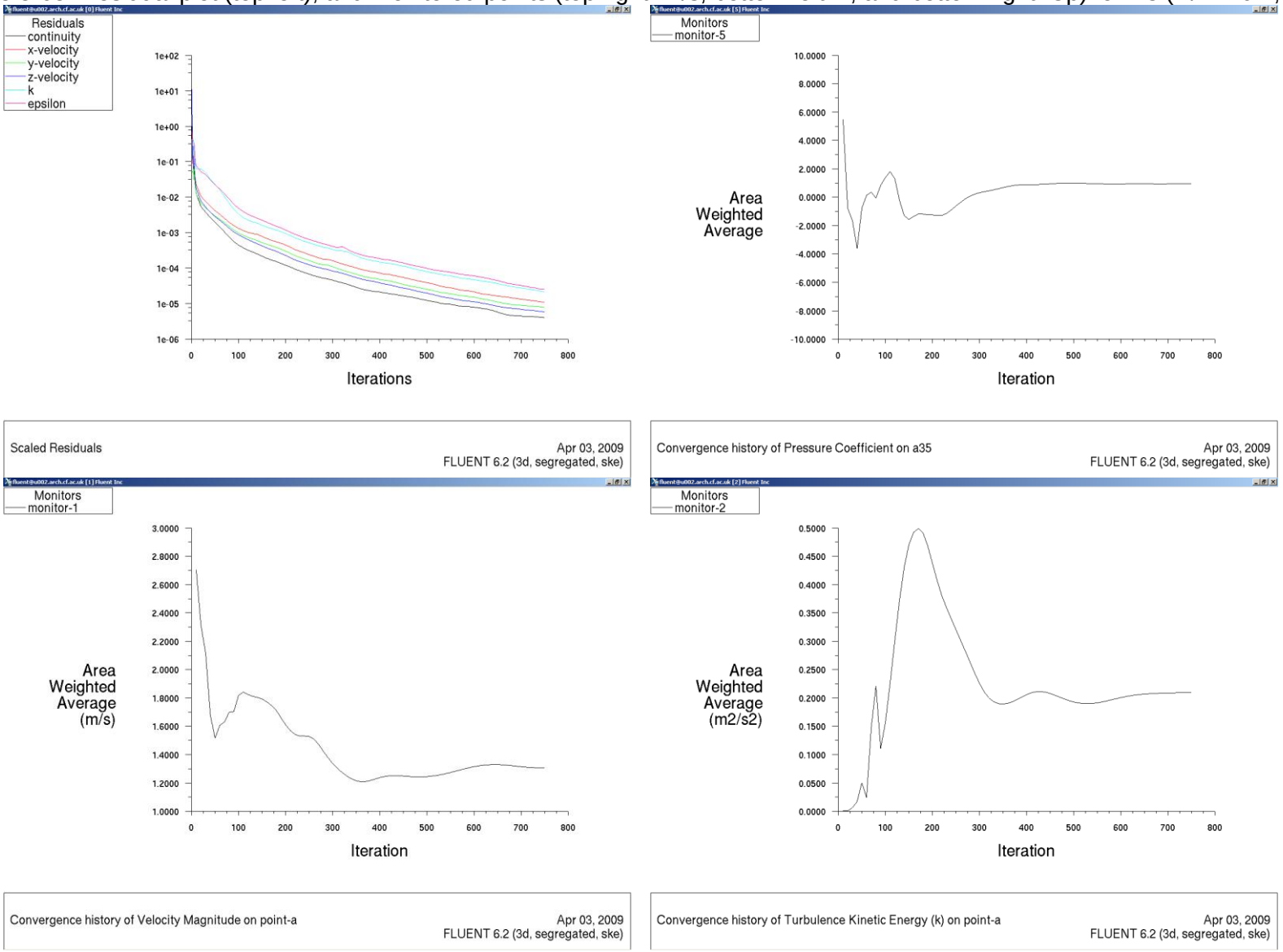

Source: This study.

5.6.5. The Cardiff University Cathays Campus CFD models

A total of eight CFD models were built for the Cathays Campus, and for the same wind directions simulated in the WT. Modeling this urban area was a real challenge as compared to the other prototype and Paulista Avenue CFD models due to the number of detached blocks; building indentations; curved and oblique surfaces; sloped roofs and bridges; and voids, courtyards and gaps involved that had to be replicated to attain maximum fidelity in the model. At first a quite detailed model was built on Gambit. However, its complexity did not allow the grid to be applied to its surfaces or the domain to be meshed, the solution being to work with a simplified model, while at the same time ensuring the highest level of accuracy.

Figure 5-66: Initial detailed attempt (above) and final simplified 3D model (below) for the Cardiff University Cathays Campus CFD models.

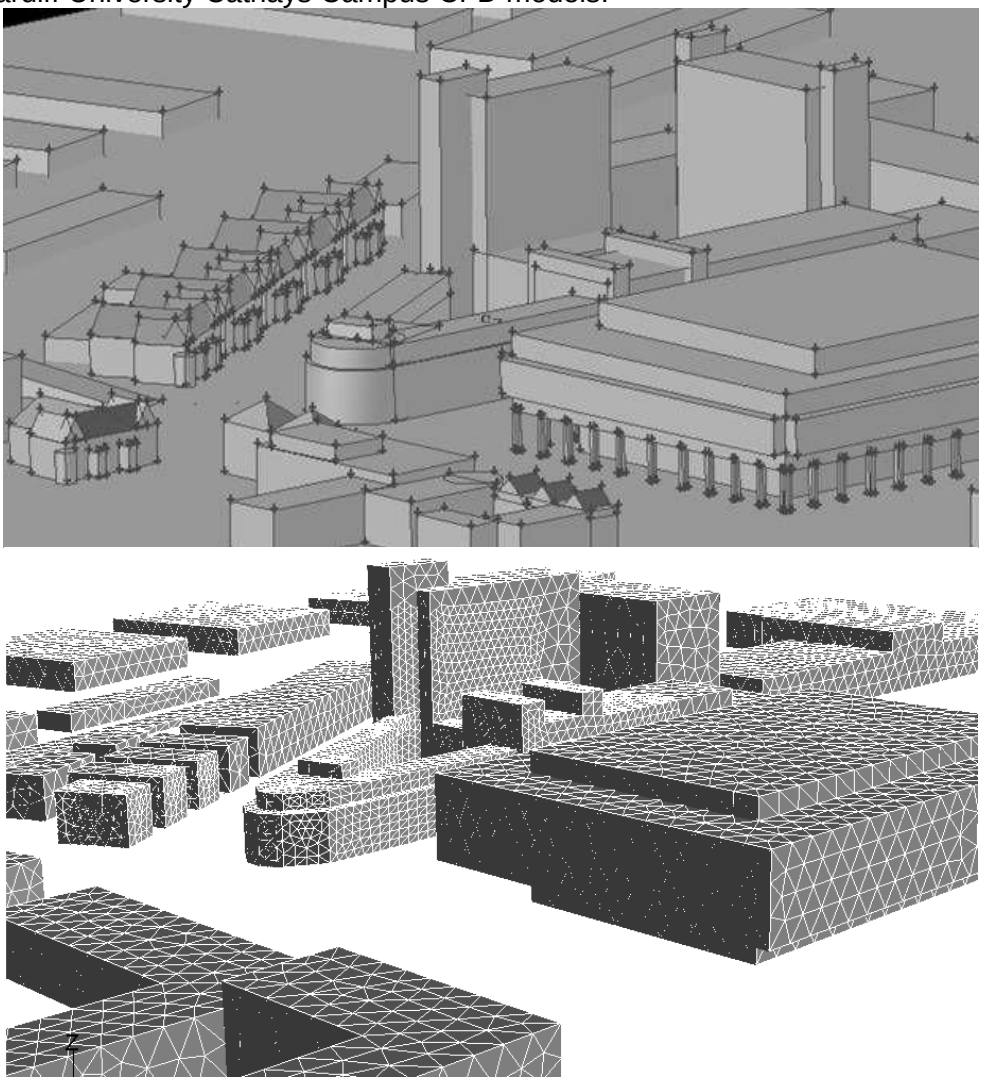

Source: This study.

Table 5-10: Domain and mesh information for the Cathays Campus (SE; 0°).

Domain zone	domain extent (m) x	y	z	Total volume (m^3)	Fluid volume (m^3)	Blockage %	Type of cells	*n° of cells*
Total	1,400	600	200	1.68E+08	1.60E+08	4.9%	T-Hy, HEX	*1.294.844*
Mesh adaption regions: diagonal: -73,-55,0 / 62,37,40 and diagonal: -28,-101,0 / 62,-55,40								

Source: This study.

Figure 5-67: Domain zones and target area for the Cathays Campus (SE; 0°).

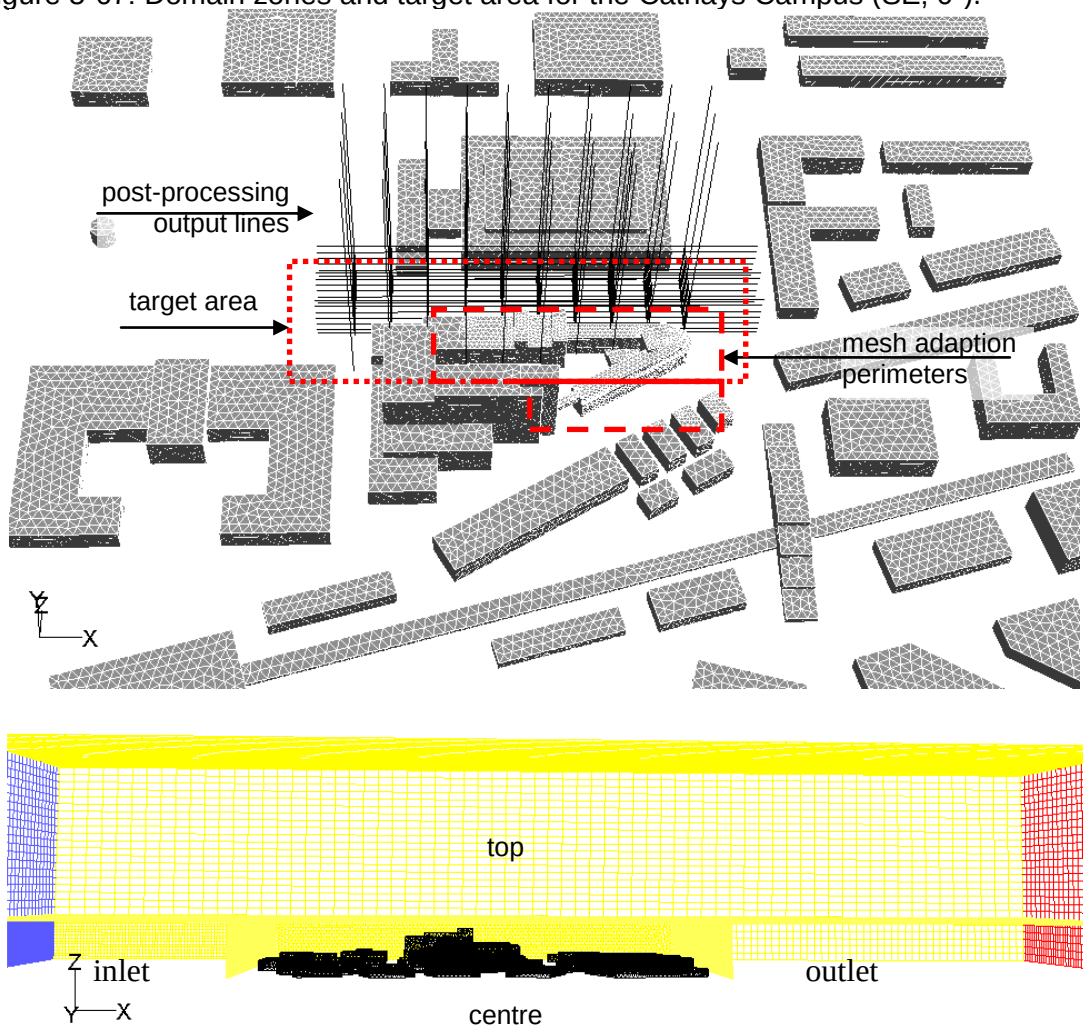

Source: This study.

Figure 5-68: Residual plot (top left), and monitored points (top right: m/s; bottom left: k; and bottom right: Cp) for the Cathays Campus (SE; 0°).

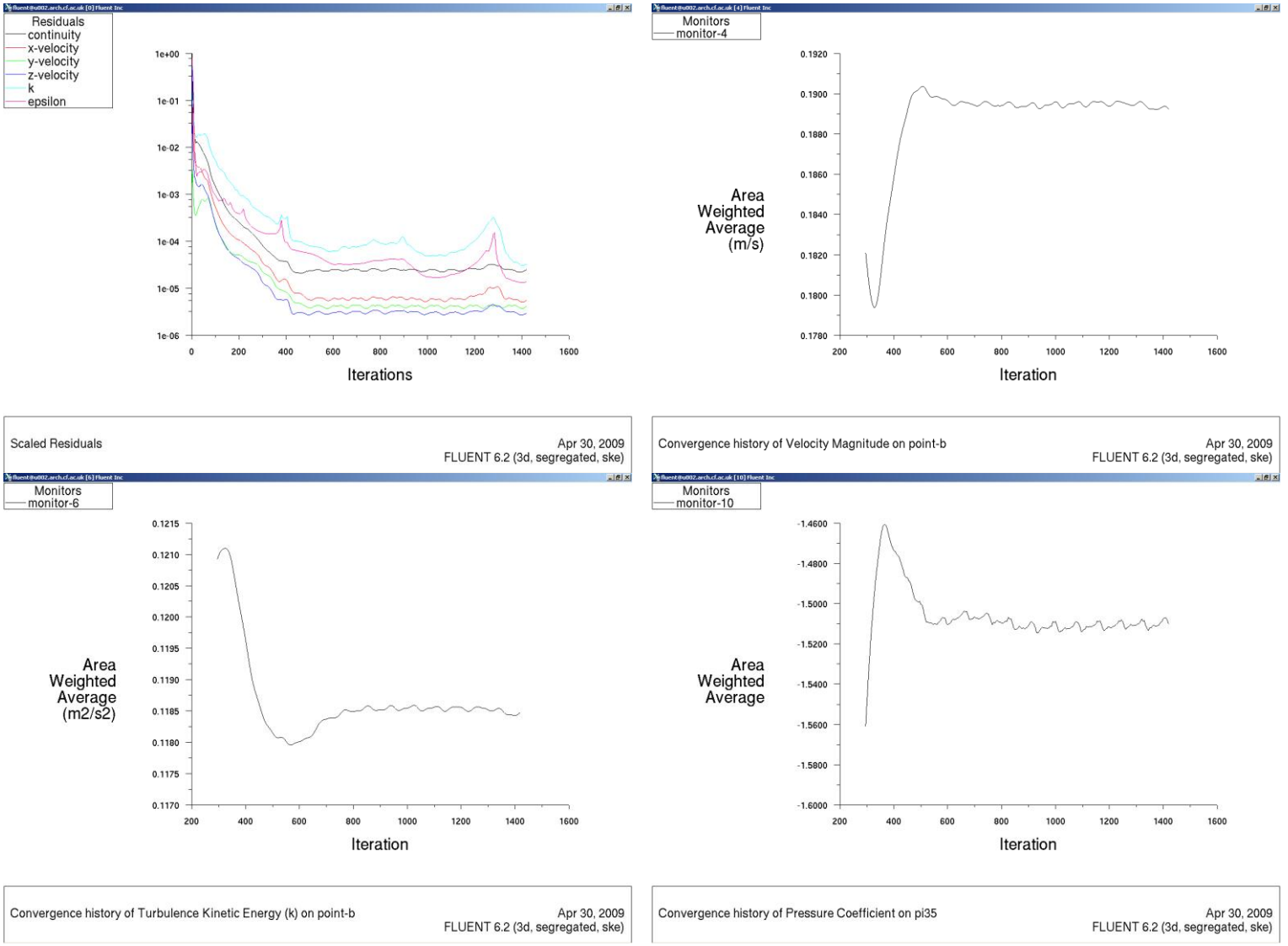

Source: This study.

5.6.6. The Paulista Avenue CFD models

As mentioned earlier in section 5.4.2.2. the Paulista Avenue CFD simulations were performed for the urban area and the CYK Tower and for the following five prevailing wind directions (in descending order): SE; S; NW; N; and NE. In addition, three wind incidences (0^o, 45^o, and 90^o) were simulated for the CYK Tower alone in the domain. On the other hand, neither this tower with the horizontal and the vertical panel variations nor the proposed prototype tower was CFD simulated.

The CYK Tower surfaces were sub-divided into several panels which were named accordingly to the position of the pressure taps used in the WT experiment. In this way, a direct comparison of the Cp area-weighted averaged values was obtained

Figure 5-69: The Paulista Ave. 3D model base with the CYK Tower surface partitions, as developed on Gambit.

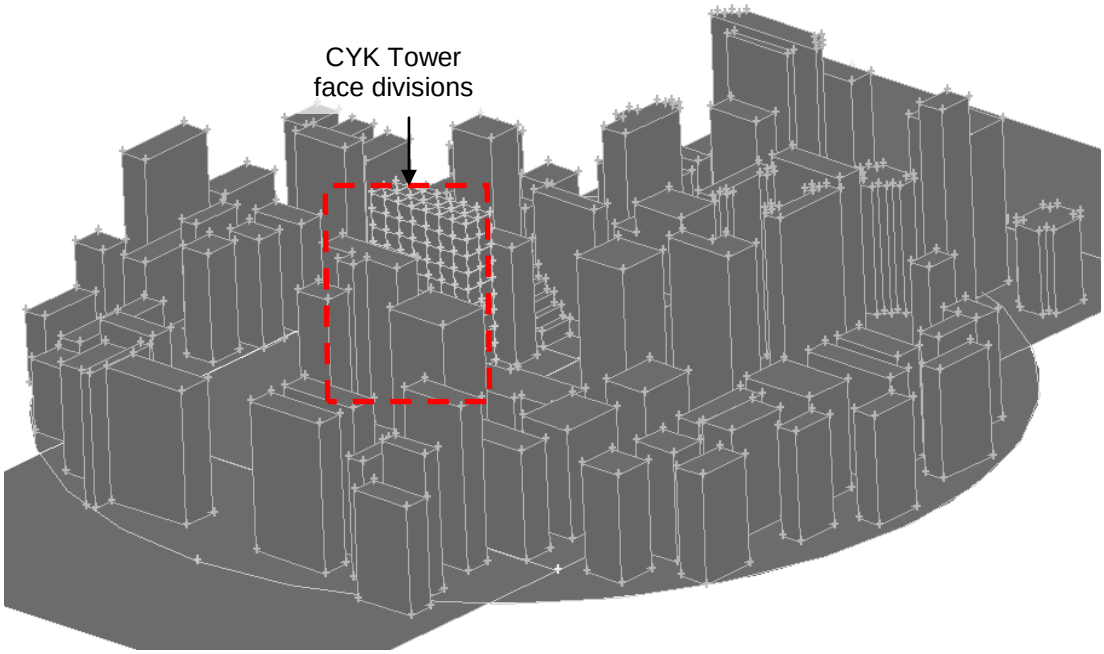

Source: This study.

Table 5-11: Domain and mesh information for Paulista Ave. (SE; 90º).

Domain zone	domain extent (m) x	y	z	Total volume (m^3)	Fluid volume (m^3)	Blockage %	Type of cells	*nº of cells*
Total	750	300	200	4.50E+07	4.34E+07	3.5%	T-Hy, HEX	*1.246.959*
Mesh adaption regions: diagonal: -73,-55,0 / 62,37,40 and diagonal: -28,-101,0 / 62,-55,40								

Source: This study.

Figure 5-70: Domain and target area for Paulista Ave. (SE; 90º).

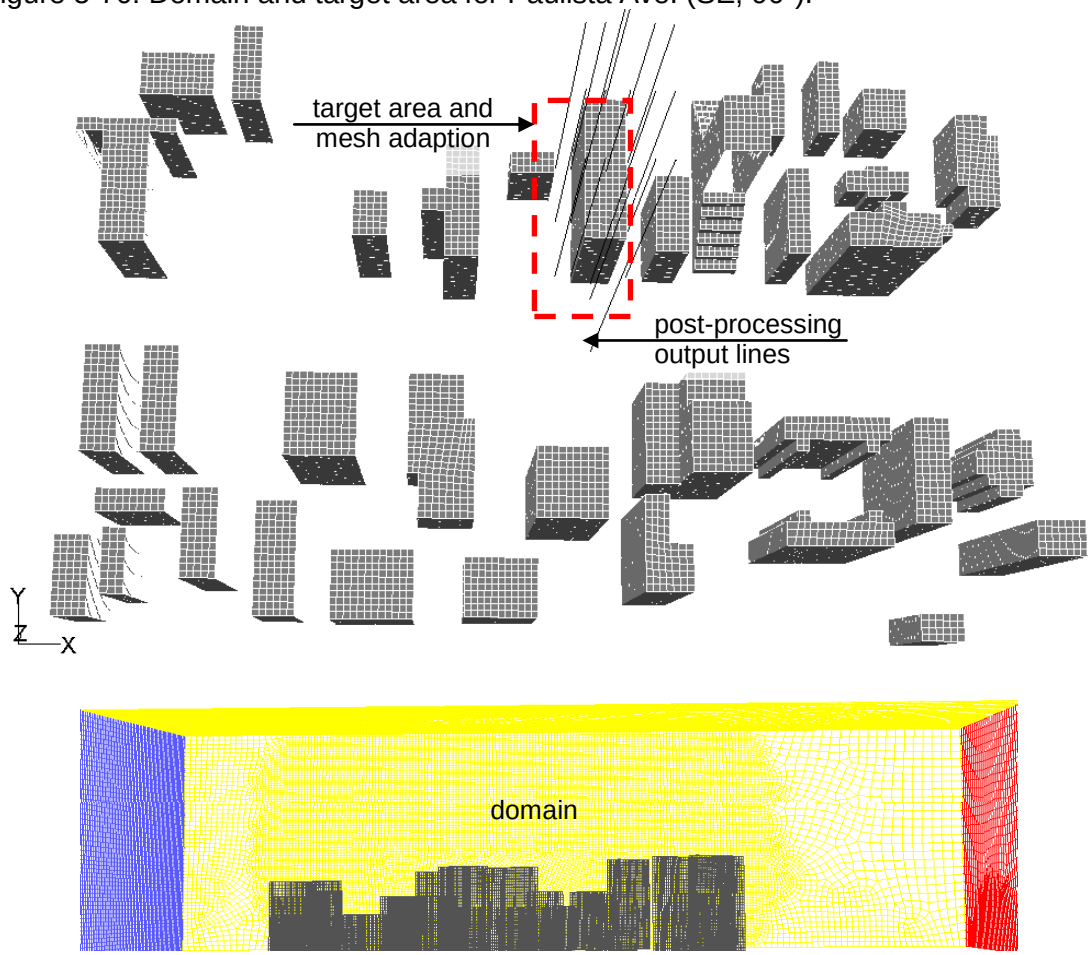

Source: This study.

Finally, although the residual plot presented some peak oscillations even after having dropped below four figures for all the criteria at 1.000 iterations, the monitored cells located at key points in the model indicated steady results with small variation even before reaching 400 iterations.

Figure 5-71: Residual plot (top left), and monitored points (top right: m/s; bottom left: k; and bottom right: Cp) for the Cathays Campus (SE; 0°).

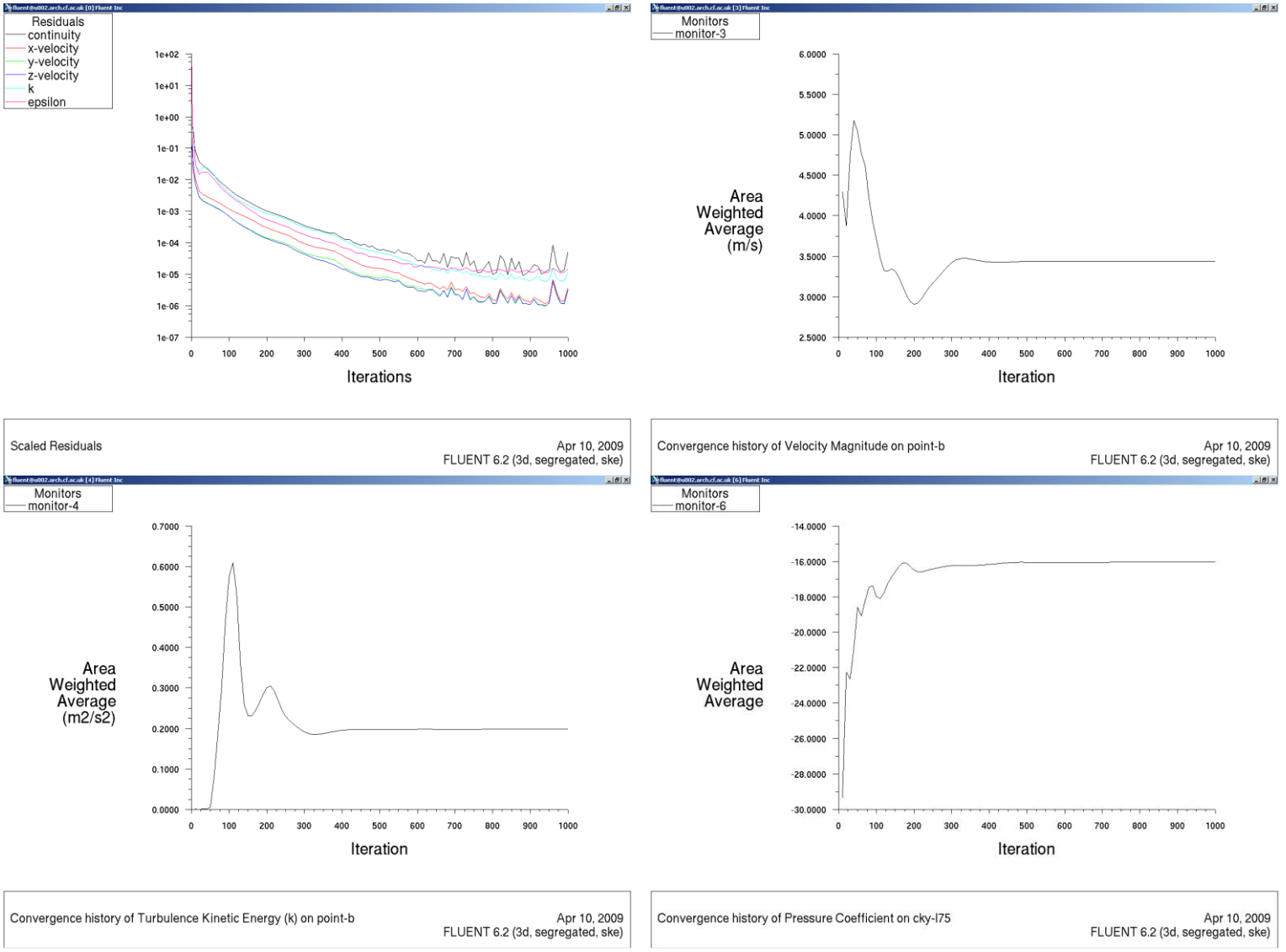

Source: This study.

5.7. The field measurements (FM)

Field measurements (FM) were undertaken at several locations of the external façade on the Law School building of the Cardiff University Cathays Campus. As mentioned in sections 5.4.2 and 5.4.2.1 the data measured '*in locus'* allowed the triangulation of the FM; the CFD, and the WT outputs. A total of seven points were assessed during the experiment, always combined in pairs. There were two sets of probe and laptop that could be used at the same time. The combined pairs were: 01T and 02X; 02X and 03T; 02X and 04T; 02X and 05T; and finally 06T and 07X[62], where 'T' and 'X' stand for the identification of the sets of equipment used. In addition, these pairs were also related to the free airflow information obtained from the WSA meteorological station (see following section for further information about the station's equipment).

Figure 5-72: The 3rd floor Law School floor plan showing the location of the FM equipment:

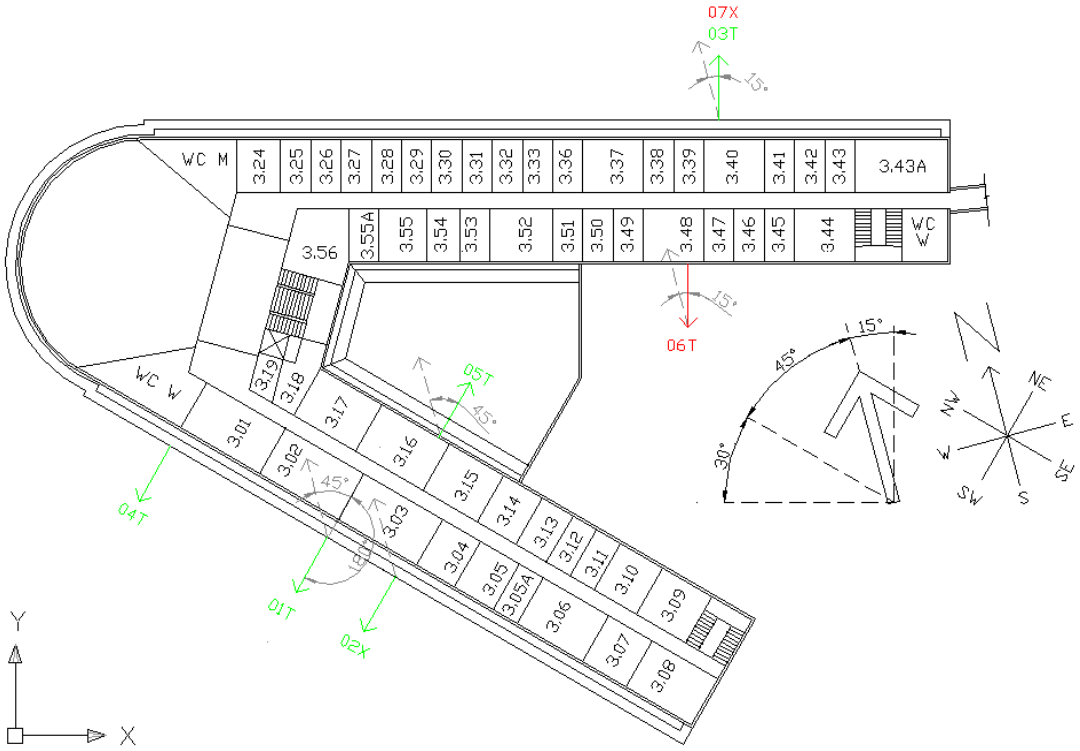

Source: This study.

[62] In the end the data from the last pair of probes were not used in the analysis since an error occurred in the 06T equipment, making the logged data file inaccessible.

Figure 5-73: View of the Law School building (top), and view from the Museum Ave. (bottom left) and the courtyard (bottom right).

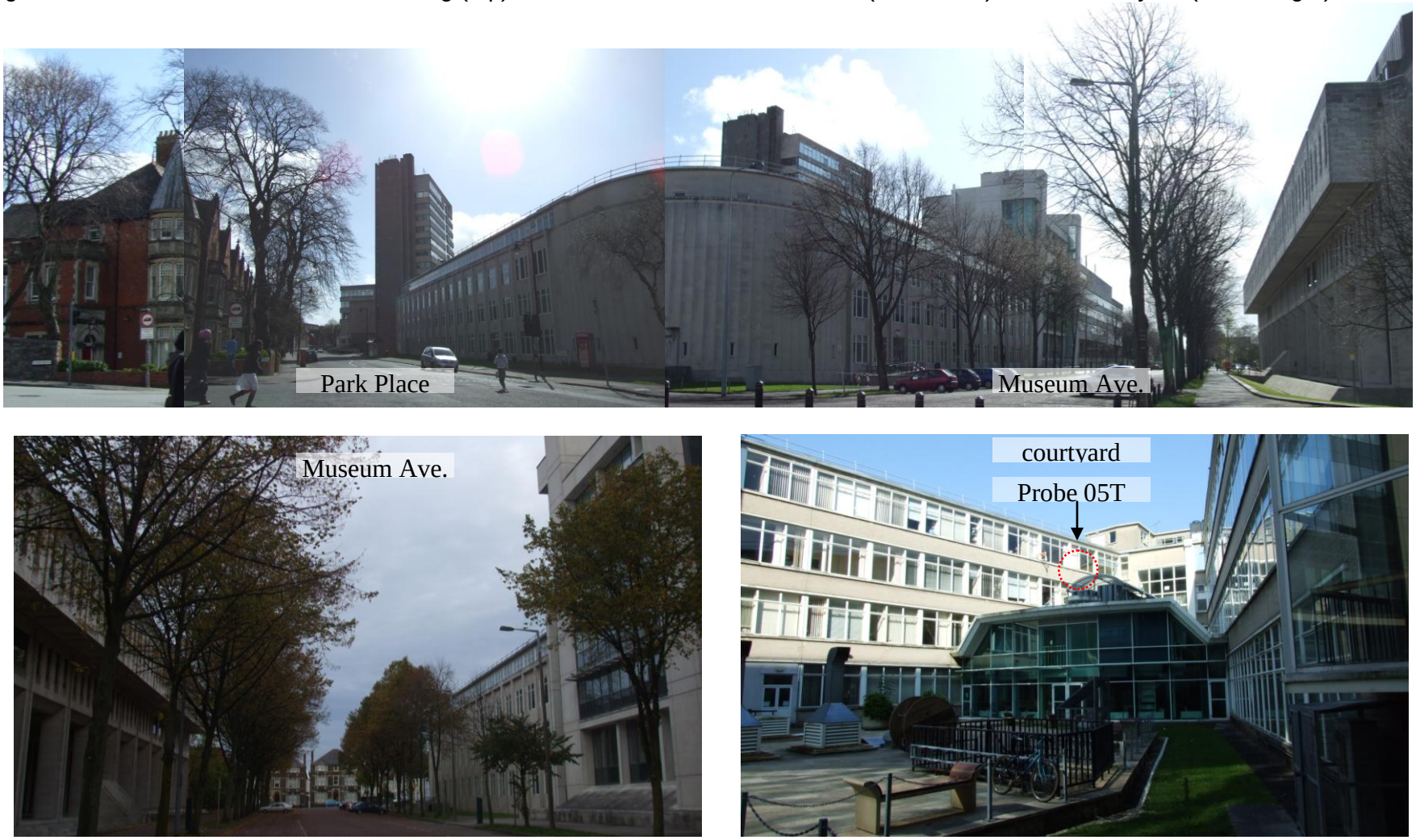

Source: This study.

The points measured were all positioned on the external façade of the building, at around 14m above street level. The points facing towards either Museum Ave. or Park place (01T, 02X, 03T, 04T; and 07X) were fixed on the external parapet of the third floor, and those facing the inner courtyard (05T and 06T) were attached to the window frames and the structural columns.

5.7.1. The FM equipment and set-up

For the field measurement experiment a kit was prepared of an ultrasonic anemometer probe held by an aluminium frame and a laptop for continuous data logging. The model of the probes used was a three axis 'Wind-Master Ultrasonic Anemometer' featured by Gill Equipments and the data logger software was the 'Gill logger v 2.0' supplied with the equipment. This state-of-the-art equipment was tested and calibrated in the WSA laboratory before the field experiment by WSA and CRiBE staff[63]. Parameters and set-up information were based on the equipment user's manual[64]. This ultrasonic anemometer relies on pulse of sounds between two transducers. The interpolation of three sets of transducers determines the wind speed and direction magnitude for the U, V and W axes, and its operation being independent of air temperature. The accuracy of the equipment for wind speed is of 0.01m/s over a range of from 0.0 to 45.0m/s; for wind direction it is 0.1^{o} and for a range of from 0^{o} to 359.9^{o}. The operation conditions in terms of sonic temperature range from -40^{o}C to $+70^{o}$C with accuracy of 0.01^{o}C. In terms of the relative humidity of the air from 5% to 100% and for precipitation up to 300mm per hour.

The data logging was set as the measurement mode 1, which records data in ASCII format for: date and time interval; wind direction (in degrees from the equipment's notch azimuth); wind speed (U, V, W and continuous for the 'M' m/s format); and the sonic temperature (^{o}C). Also, the W vector position was inverted, since the equipment was positioned upside-down. The data was logged for a 3 second time interval. During the experiment, the software window displays on the screen the instantaneous and the averaged 10 and 100 last results. After the experiment, the wind direction logged was related to the North orientation, based on the equipment's notch position. Then the wind direction incidence was calculated. Further, the data time intervals were adjusted to match those logged by the WSA meteorological station: time intervals of 5 minutes and eight wind directions. For instance, the time interval was

[63] This activity and the undertaking of the FM counted on the invaluable assistance and technical support for the calibration of the equipment of the WSA Senior Lecturer Mr. D. K. Alexander and the WSA Research Assistant Dylan Dixon in the setting-up of the equipments and the carrying-out of the measurements.

[64] 'Wind Master & Wind Master-Pro Ultrasonic Anemometer' User Manual Doc. No. 1561-PS-0001 Issue 03. Gill Instruments Limited. Hampshire, March, 2007, and Gill Equipments webpage: www.gill.co.uk

obtained by averaging the 3 second intervals (excluding still-air data). For estimating the direction of the wind, the cut-off range of angles used was:

- α <22.5^{o} or α >337.5^{o} for North wind direction;
- 22.5^{o} < α <67.5^{o}, for Northeast wind direction;
- 67.5^{o} < α <112.5^{o}, for East wind direction;
- 112.5^{o} < α <157.5^{o}.5, for Southeast wind direction;
- 157.5^{o} < α <202.5^{o}, for South wind direction;
- 202.5^{o} < α <247.5^{o}, for Southwest wind direction;
- 247.5^{o} < α <292.5^{o}, for West wind direction; and
- 292.5^{o} < α <337.5^{o}, for Northwest wind direction.

Figure 5-74: Ultrasonic anemometer probe and laptop with the data logger software window.

Source: This study.

With a size of 25x25x75cm and weighing 1.0kg, the probe was fitted into a cage and held firmly and steady by a lightweight aluminium structure. All the structure was designed and built by the researcher in the WSA workshop and WT laboratory, as part of the experiment undertaken.

Figure 5-75: Set of equipment for the inner courtyard and external parapet as planned (above) and as built and fixed during the FM experiment (below).

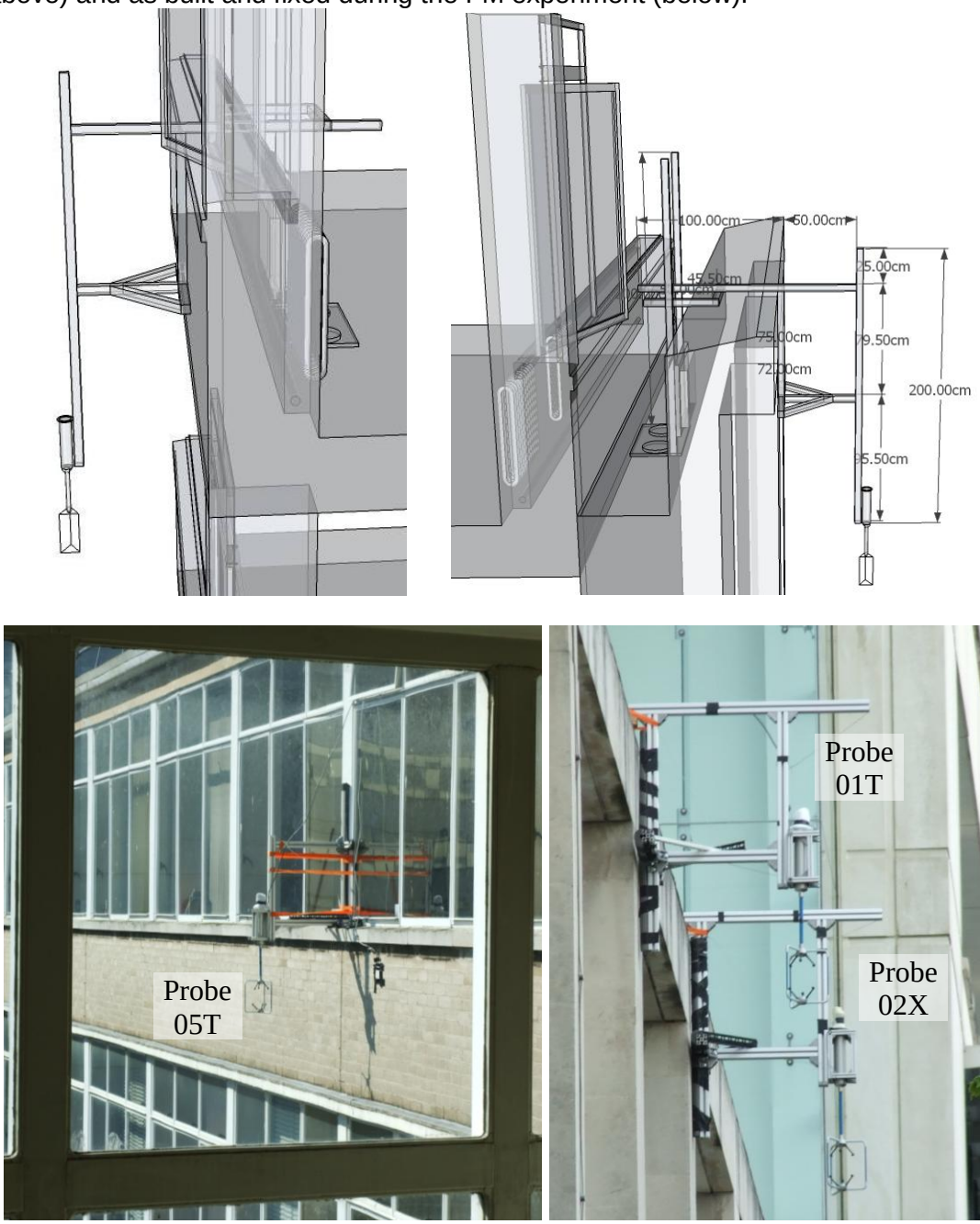

Source: This study.

5.7.2. The WSA meteorological station

The WSA weather monitoring equipment is located on a mast above the rooftop. It follows instantaneous intervals of weather data which are recorded at 5 minute intervals on a CR10 Campbell instrument. The complete list of data types that can be recorded at this meteorological station comprises: air temperature and humidity; global and diffuse horizontal solar radiation and illumination; wind speed and direction;

rainfall; and barometric pressure[65]. The meteorological station of the WSA Bute Building is at approximately 250m from the Law School building, where the field measurements were undertaken. In addition, there are no direct obstructions or towers in between these two places, with the exception of those that compose the assessed canyon in this urban area.

Figure 5-76: View of the WSA monitoring equipments on the Bute Building:

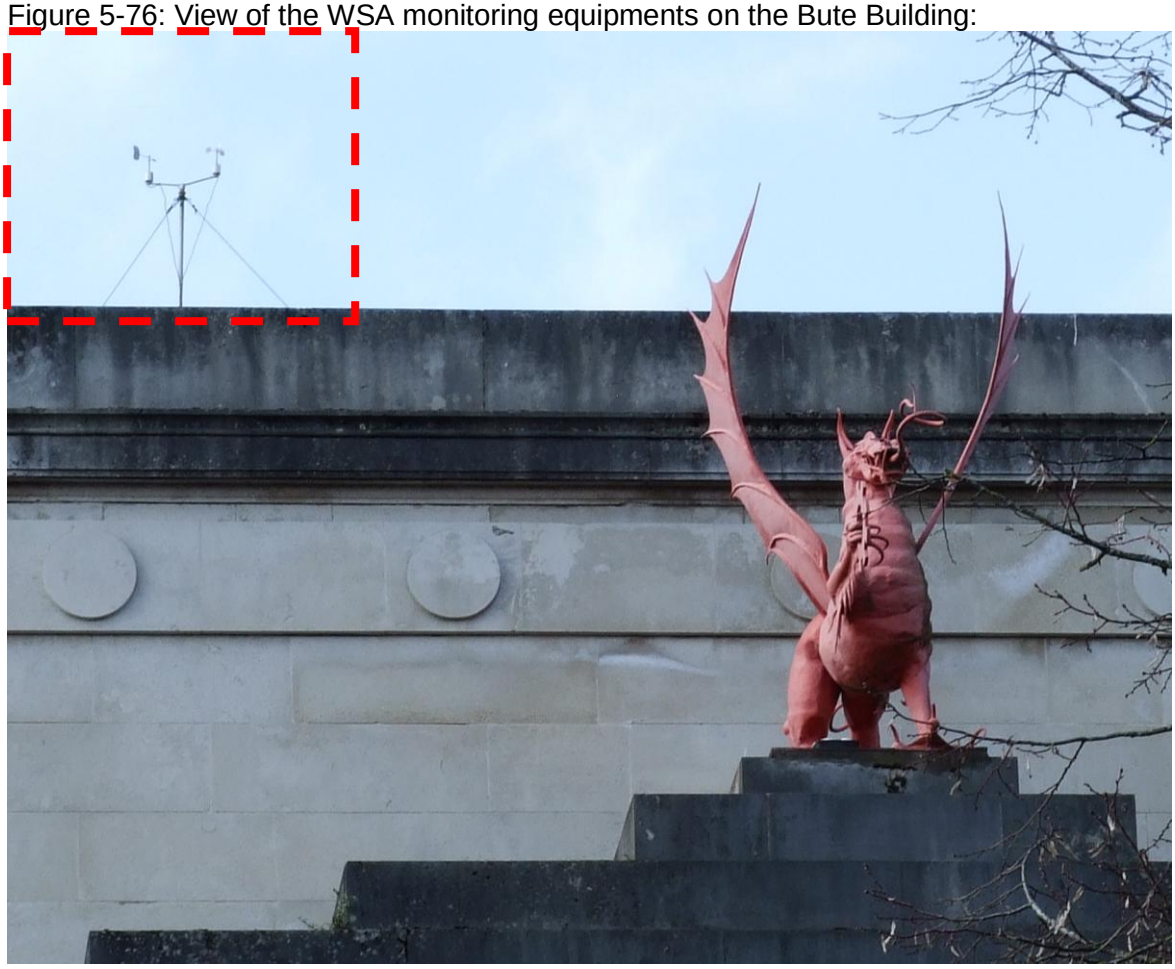

Source: This study.

[65] Information from the WSA webpage: http://www.cardiff.ac.uk/archi accessed in September 2009.

5.8. Correlation coefficients

The correlation coefficient identifies the number of relationship between two sources of quantitative variable data, thus ascertaining the statistical strength between them. The Pearson *r* model provides a scale of significance for correlation coefficients. This scale is a linear association between standard product-moment sources of data. The values on this scale range from +1.00 to -1.00, on which zero means absence of correlation (Warner, 2008; Barrow, 2009; Campbell and Swinscow, 2009; Kottegoda, Renzo Rosso, 2009; Croft and Davidson, 2010).

Equation 5-4: Correlation coefficient '*r'* equation based on series of data 'x' and 'y'.

$r = (n\Sigma xy - \Sigma x\Sigma y)/\text{sqrt}(n\Sigma x^2-(\Sigma x^2)(n\Sigma y^2-(\Sigma y^2)))$

Source: Barrow (2009).

Correlation results are displayed in a scatter diagram (see Figure 5-77 and 5-78) which shows the linear relationship between the sources of data by clustering them around a diagonal line. While the experimental results are usually plot on the vertical axis, the independent or parametrical variable is plot on the horizontal axis (Campbell and Swinscow, 2009). An upwards from left to right line means positive correlation and from right to left line means negative correlation (Croft and Davidson, 2010), and a straight line is related to strong association while a random scatter display is related to a weaker association (Barrow, 2009).

5.8.1. Correlation associations used in this investigation

Several correlation analyses were employed in this investigation in order to reveal a number of associations between different models, such as:

- The level of diversity among the several urban prototype's physical dimensions and aspect ratios adopted;
- The variety of ΔCp results among the several urban prototypes (based on the averaged results of 90% of the data, eliminating the 10% of outliers). [66];
- The urban shape/ aspect ratio's similarity strength between the several urban prototypes and each case study investigated; and
- The ΔCp results' similarity strength between the several urban prototypes and each case study investigated.

The series of data (physical dimensions and aspect ratios, and ΔCp results) and the resultant output scater diagram and correlation matrices, are exemplified in the sequence:

[66]Other ΔCp data (such as peak values, the 8th highest/ lowest results, and the standard deviation) have been displayed in the appendices to provide further information on the results.

Table 5-12: Example of urban area set of data (X', 'Y' and 'Z') employed to determine the strength of the coefficients between the physical dimensions and aspect ratios.

Aspect ratio	X	Y	Z
canyon H (m)	30	30	70,5
canyon W (m)	60	60	54
canyon L (m)	180	90	60
A_{roof} ($k.m^2$)	83	71	59
A_{built} ($k.m^2$)	660	572	979
H/W	0.50	0.50	1.31
L/H	6.00	3.00	0.85
L/W	3.00	1.50	1.11
A_{roof}/ A_{urb}	0.42	0.36	0.30
A_{built}/ A_{urb}	3.36	2.91	4.98
A_{roof}/ H	2.75	2.38	0.83
A_{roof}/ W	1.38	1.19	1.08
A_{roof}/ L	0.46	0.79	0.98
A_{built}/ H	22.02	19.06	13.89
A_{built}/ W	11.01	9.53	18.13
A_{built}/ L	3.67	6.35	16.32

Source: this study.

Figure 5-77: Example of scatter diagram showing correlation level between 'X' urban aspect ratio and 'Y' urban aspect ratio data.

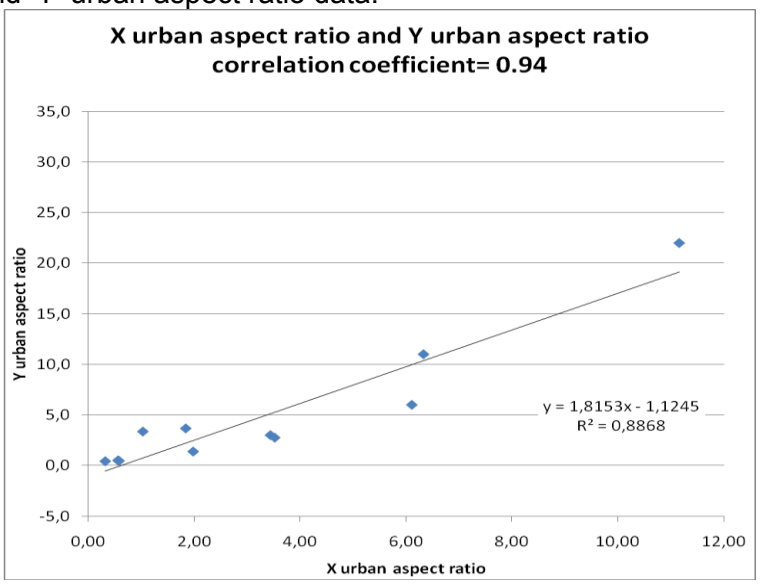

Source: this study.

Table 5-13: Example of correlation coefficient matrix built using urban area (X', 'Y' and 'Z') physical dimensions and aspect ratios set of data.

	X	Y	Z
X			
Y	0.94		
Z	0.65	0.58	

Source: this study.

Table 5-14: Example of urban area set of data (X', 'Y' and 'Z') employed to determine the strength of the coefficients between the ΔCp results for 45° wind incidence.

Wind at 45°	X	Y	Z
ΔCp at top	-0.01	0.20	0.08
	0.06	0.29	0.13
ΔCp at middle	0.05	0.21	0.08
	0.04	0.28	0.05
ΔCp at bottom	0.02	0.24	0.03
	0.02	0.19	0.04
	0.04	0.20	0.03
AVG ΔCp	0.03	0.23	0.06

Source: this study.

Figure 5-78: Example of scatter diagram showing the correlation level between 'X' ΔCp results and 'Y' ΔCp results for 45° wind incidence.

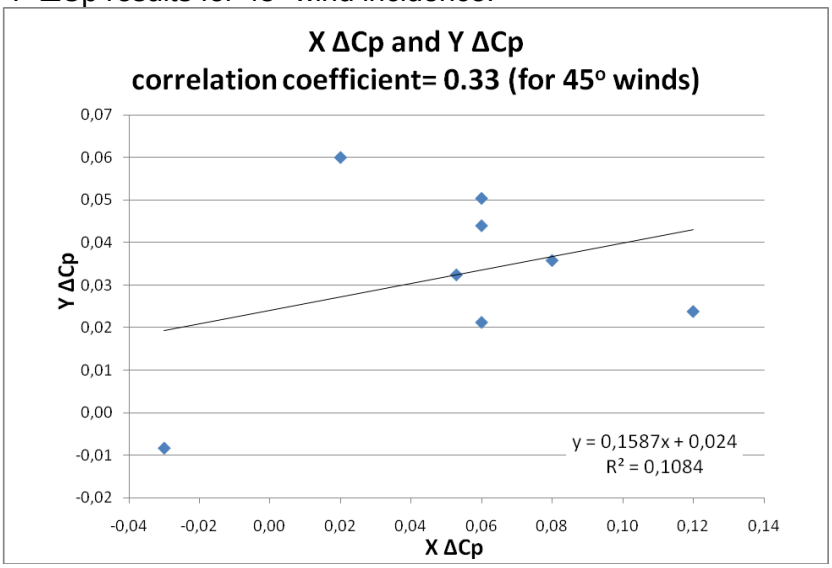

Source: this study.

Table 5-15: Example of correlation matrix built using urban area (X', 'Y' and 'Z') ΔCp results for 45° wind incidence.

	X	Y	Z
X			
Y	0.33		
Z	0.85	0.47	

Source: this study.

5.8.2. Correlation scale of significance

The correlation coefficients for the urban prototype's aspect ratios are presented here for the first time, followed by the correlation coefficients between the urban prototype's and the Cardiff Cathays' aspect ratios and by the correlation coefficients between the urban prototype's and the Paulista Avenue's aspect ratios. Finally, and based on these results, a scale of significance for urban aspect ratios correlation strength is presented.

5.8.2.1. Correlations for the urban prototype's aspect ratios

Here the correlations among aspect ratios for the urban prototype's Groups 01 to 06 are presented and assessed (see table 5-16). The urban prototypes correlation coefficient matrix (table 5-17) shows the comparison of the urban aspect ratios among all the prototype scenarios, and defines which the statistical strength between them is.

From the analysis of the correlation coefficient matrix it is possible to observe that urban prototypes that belong to the same group (e.g. A1, A2 and A3; B1, B2 and B3...) present a correlation relationship from 1.00 to 0.94. Further, the urban prototypes that belong to the adjacent group (e.g. A1 and B1, A2 and B2; A3 and B3...) present a correlation relationship from 0.94 to 0.91. This demonstrates that the systematic variation of the aspect ratios for these simplified scenarios was obtained in a balanced gradient between prototypes both intra and inter-group. On the other hand, when comparing dissimilar scenarios, such as the opposite A1 and D4, and A4 and C1, the relationship found was: 0.66 and 0.45, respectively.

Figure 5-79: Correlation coefficient between C2 aspect ratio and C3 aspect ratio= 0.99

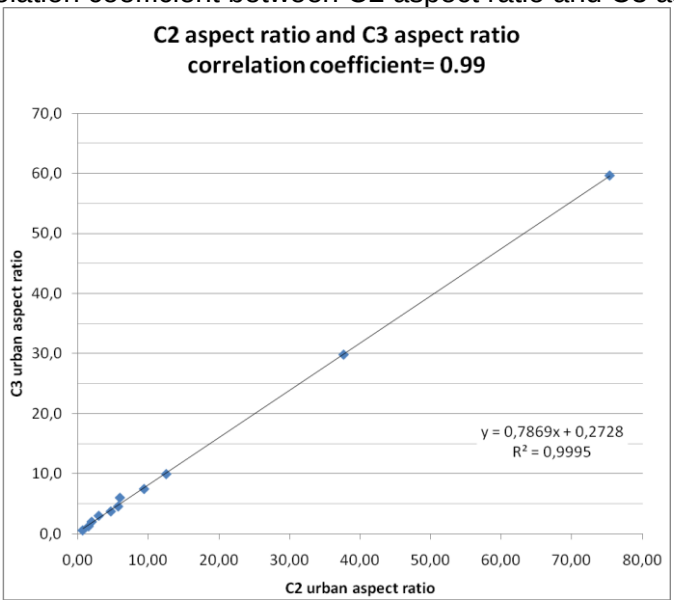

Source: this study

Figure 5-80: Correlation coefficient between A4 aspect ratio and C1 aspect ratio= 0.45

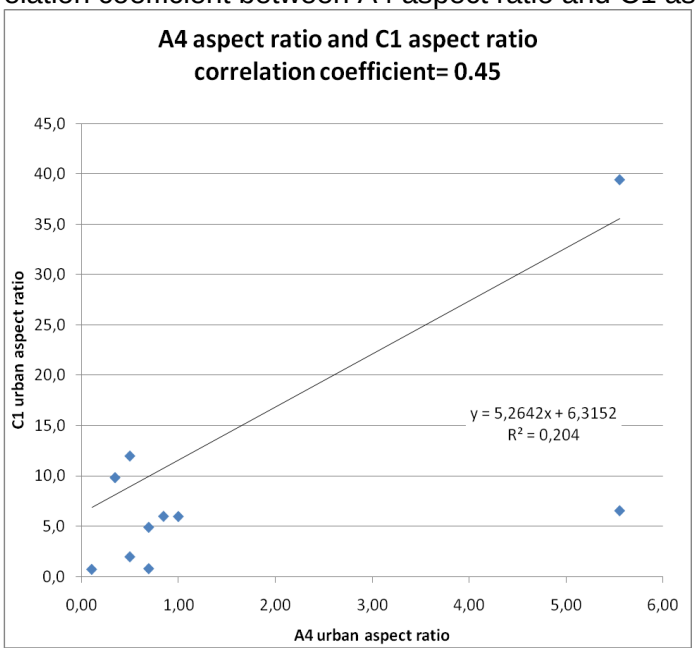

Source: this study

Table 5-16: The urban prototype's physical dimensions and aspect ratios employed to determine the coefficient correlation strength.

Urban Prototypes Physical Dimensions and Aspect Ratios Coefficient Correlation																
	A1	**A2**	**A3**	**A4**	**B1**	**B2**	**B3**	**B4**	**C1**	**C2**	**C3**	**C4**	**D1**	**D2**	**D3**	**D4**
canyon H (m)	30	30	30	30	30	30	30	30	300	30	30	30	36	52	60	70,5
canyon W (m)	60	60	60	60	30	30	30	30	15	15	15	15	30	42	51	54
canyon L (m)	180	90	90	30	180	90	90	30	180	90	90	30	180	90	72	60
A_{roof} ($k.m^2$)	83	71	41	21	123	109	72	50	148	141	112	86	123	109	79	59
A_{built} ($k.m^2$)	660	572	325	167	981	874	579	397	1.183	1.130	894	685	1.457	1.277	1.038	979
H/W	0,50	0,50	0,50	0,50	1,00	1,00	1,00	1,00	2,00	2,00	2,00	2,00	1,20	1,24	1,18	1,31
L/H	6,00	3,00	3,00	1,00	6,00	3,00	3,00	1,00	6,00	3,00	3,00	1,00	5,00	1,73	1,20	0,85
L/W	3,00	1,50	1,50	0,50	6,00	3,00	3,00	1,00	12,00	6,00	6,00	2,00	6,00	2,14	1,41	1,11
A_{roof}/ A_{urb}	0,42	0,36	0,21	0,11	0,62	0,56	0,37	0,25	0,75	0,72	0,57	0,44	0,62	0,56	0,40	0,30
A_{built}/ A_{urb}	3,36	2,91	1,66	0,85	4,99	4,45	2,95	2,02	6,02	5,75	4,55	3,48	7,41	6,50	5,28	4,98
A_{roof}/ H	2,75	2,38	1,36	0,69	4,09	3,64	2,41	1,65	4,93	4,71	3,73	2,85	3,41	2,10	1,32	0,83
A_{roof}/ W	1,38	1,19	0,68	0,35	4,09	3,64	2,41	1,65	9,86	9,42	7,45	5,71	4,09	2,60	1,56	1,08
A_{roof}/ L	0,46	0,79	0,45	0,69	0,68	1,21	0,80	1,65	0,82	1,57	1,24	2,85	0,68	1,21	1,10	0,98
A_{built}/ H	22,02	19,06	10,85	5,55	32,69	29,13	19,32	13,22	39,43	37,68	29,81	22,83	40,46	24,56	17,30	13,89
A_{built}/ W	11,01	9,53	5,42	2,78	32,69	29,13	19,32	13,22	78,86	75,36	59,63	45,66	48,55	30,41	20,35	18,13
A_{built}/ L	3,67	6,35	3,62	5,55	5,45	9,71	6,44	13,22	6,57	12,56	9,94	22,83	8,09	14,19	14,42	16,32

Source: this study.

Table 5-17: Correlation coefficient matrix among the urban prototype scenarios regarding the relationship for aspect ratios[67].

	A1	A2	A3	A4	B1	B2	B3	B4	C1	C2	C3	C4	D1	D2	D3	D4
A1																
A2	0,97															
A3	0,99	0,99														
A4	0,72	0,84	0,83													
B1	0,91	0,90	0,89	0,64												
B2	0,89	0,92	0,90	0,74	0,98											
B3	0,90	0,92	0,91	0,73	0,99	1,00										
B4	0,73	0,84	0,81	0,93	0,79	0,88	0,87									
C1	0,69	0,68	0,66	0,45	0,92	0,91	0,91	0,72								
C2	0,68	0,70	0,67	0,52	0,92	0,92	0,92	0,78	0,99							
C3	0,68	0,69	0,67	0,52	0,92	0,92	0,92	0,77	0,99	1,00						
C4	0,62	0,70	0,67	0,70	0,84	0,90	0,89	0,91	0,90	0,95	0,94					
D1	0,86	0,86	0,84	0,63	0,99	0,99	0,99	0,81	0,96	0,96	0,96	0,89				
D2	0,80	0,86	0,83	0,77	0,94	0,98	0,97	0,93	0,90	0,94	0,93	0,96	0,96			
D3	0,76	0,85	0,82	0,86	0,87	0,93	0,93	0,98	0,82	0,87	0,87	0,95	0,89	0,98		
D4	0,66	0,77	0,74	0,87	0,77	0,86	0,85	0,98	0,75	0,81	0,80	0,94	0,81	0,94	0,99	

Source: this study.

[67] See Table 5-20 for the scale of significance for the urban prototype aspect ratios correlation coefficient (r) strength

5.8.2.2. Correlation coefficients between the urban prototypes and the Cardiff Cathay's aspect ratios

The Law School and the Welsh Assembly buildings form an urban canyon (Museum Ave.) with real dimensions of 110x32x18m[68], and averaged aspect ratio of H/W= 0.56. The correlation coefficient between the Cardiff Cathays aspect ratios and the urban prototypes previously related to have similarities in their landscapes, such as A1; A2; A3; B1; B2 and B3 showed correlation coefficients of 0,94; 0,87; 0,91; 0,85; 0,80 and 0,82, respectively (see Table 5-18). The highest result was found between this real urban area and the first urban prototype in the scale (A1). In contrast, the correlation coefficient between the Cardiff Cathays aspect ratios and the urban prototype with opposite landscape features (D4), on the other edge of the scale, was the lowest found: 0,51.

Figure 5-81: Correlation coefficient between the Cathay's Campus aspect ratio and the Urban Prototype A1 aspect ratios.

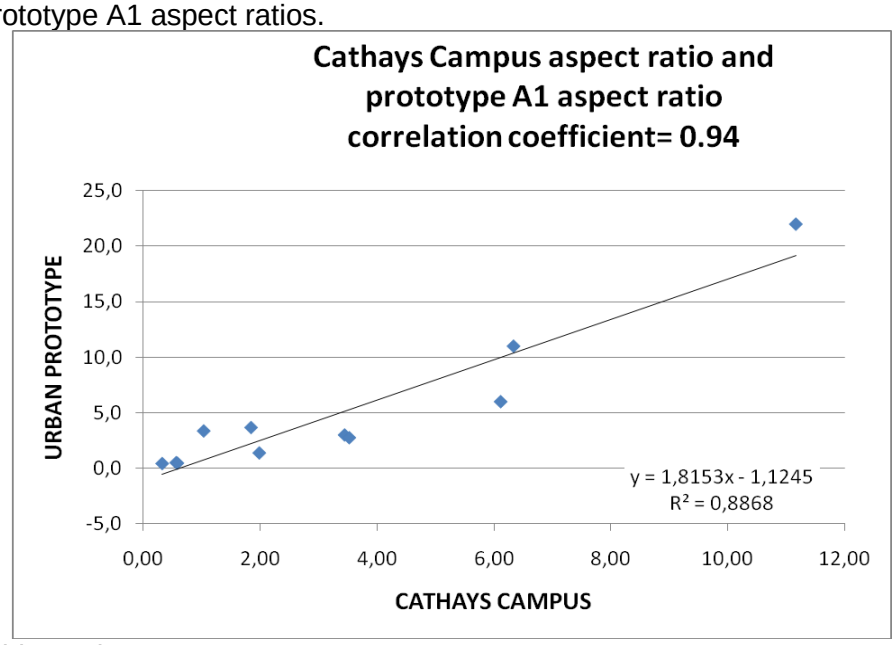

Source: this study.

[68] The dimensions quoted are for length, width and height of the Museum Ave. canyon, respectively.

Figure 5-82: Correlation coefficient between the Cathay's Campus aspect ratio and the Urban Prototype D4 aspect ratios.

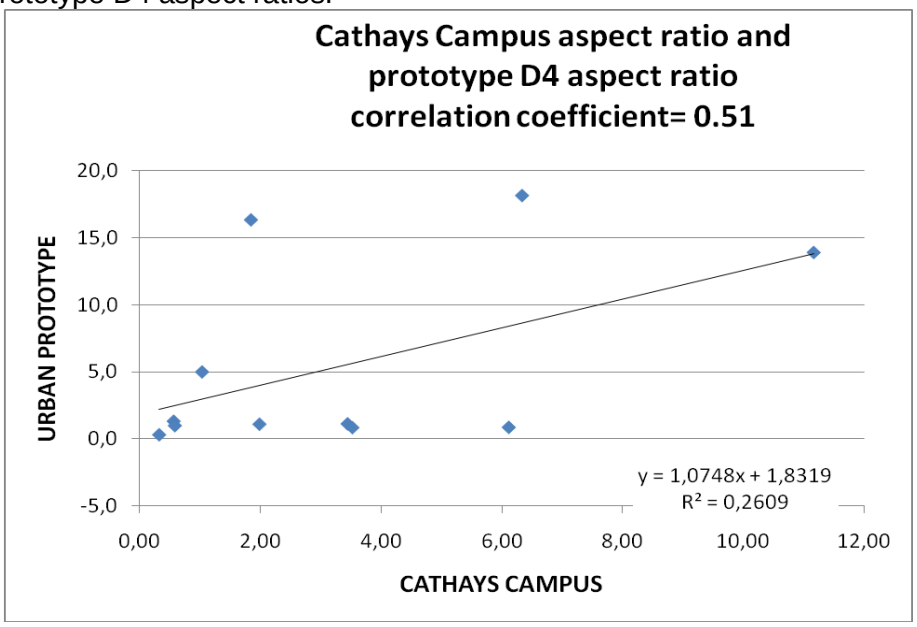

Source: this study.

Table 5-18: The Cathays Campus and Urban Prototypes correlation coefficient for the aspect ratios[69].

Aspect Ratios	Cathays Campus	Urban Prototypes															
		A1	A2	A3	A4	B1	B2	B3	B4	C1	C2	C3	C4	D1	D2	D3	D4
H/W	0,56	0,50	0,50	0,50	0,50	1,00	1,00	1,00	1,00	2,00	2,00	2,00	2,00	1,20	1,24	1,18	1,31
L/H	6,11	6,00	3,00	3,00	1,00	6,00	3,00	3,00	1,00	6,00	3,00	3,00	1,00	5,00	1,73	1,20	0,85
L/W	3,44	3,00	1,50	1,50	0,50	6,00	3,00	3,00	1,00	12,00	6,00	6,00	2,00	6,00	2,14	1,41	1,11
A_{roof}/ A_{urb}	0,32	0,42	0,36	0,21	0,11	0,62	0,56	0,37	0,25	0,75	0,72	0,57	0,44	0,62	0,56	0,40	0,30
A_{built}/ A_{urb}	1,03	3,36	2,91	1,66	0,85	4,99	4,45	2,95	2,02	6,02	5,75	4,55	3,48	7,41	6,50	5,28	4,98
A_{roof}/ H	3,52	2,75	2,38	1,36	0,69	4,09	3,64	2,41	1,65	4,93	4,71	3,73	2,85	3,41	2,10	1,32	0,83
A_{roof}/ W	1,98	1,38	1,19	0,68	0,35	4,09	3,64	2,41	1,65	9,86	9,42	7,45	5,71	4,09	2,60	1,56	1,08
A_{roof}/ L	0,58	0,46	0,79	0,45	0,69	0,68	1,21	0,80	1,65	0,82	1,57	1,24	2,85	0,68	1,21	1,10	0,98
A_{built}/ H	11,16	22,02	19,06	10,85	5,55	32,69	29,13	19,32	13,22	39,43	37,68	29,81	22,83	40,46	24,56	17,30	13,89
A_{built}/ W	6,33	11,01	9,53	5,42	2,78	32,69	29,13	19,32	13,22	78,86	75,36	59,63	45,66	48,55	30,41	20,35	18,13
A_{built}/ L	1,84	3,67	6,35	3,62	5,55	5,45	9,71	6,44	13,22	6,57	12,56	9,94	22,83	8,09	14,19	14,42	16,32
Correlation	**coefficient**	**0,94**	**0,87**	**0,91**	**0,59**	**0,85**	**0,80**	**0,82**	**0,59**	**0,65**	**0,62**	**0,62**	**0,53**	**0,78**	**0,68**	**0,62**	**0,51**

Source: this study

[69] See Table 5-20 for the scale of significance for the Cathays Campus aspect ratios and the urban prototype aspect ratios correlation coefficient (*r*) strength.

5.8.2.3. Correlation coefficients between the urban prototypes and the Paulista Avenue aspect ratios

The urban area surrounding the Paulista Avenue consists of a commercial pole in the city of São Paulo, and one of the highest built density areas in the downtown[70]. Its high-rise towers form a heterogeneous urban canyon with averaged aspect ratio H/W of 1.10. The former Table 5-3 shows links between this actual urban area and several urban prototypes regarding the different aspect ratios utilized. The correlation coefficients between the Paulista Ave. and the Urban Prototype aspect ratios seen on table 5-19 showed a relationship of 0,95 and 0,90 with the urban prototypes D4 and D3, respectively, which belong to the Group 6 prototypes scenarios and were previously described as having the most similar urban landscape features. Once more, the urban prototype previously defined as the opposite one to this high-rise building urban landscape presented the lowest correlation coefficient: 0,53 (A1). This lowest result was followed by the ones obtained with C1 (0,52) and B1 (0,58). Again, it is possible to observe that the similar and the dissimilar urban landscapes were positioned in opposite edges of the scale.

Figure 5-83: Correlation between the Paulista Avenue aspect ratios.and the Urban Prototype D4 aspect ratios.

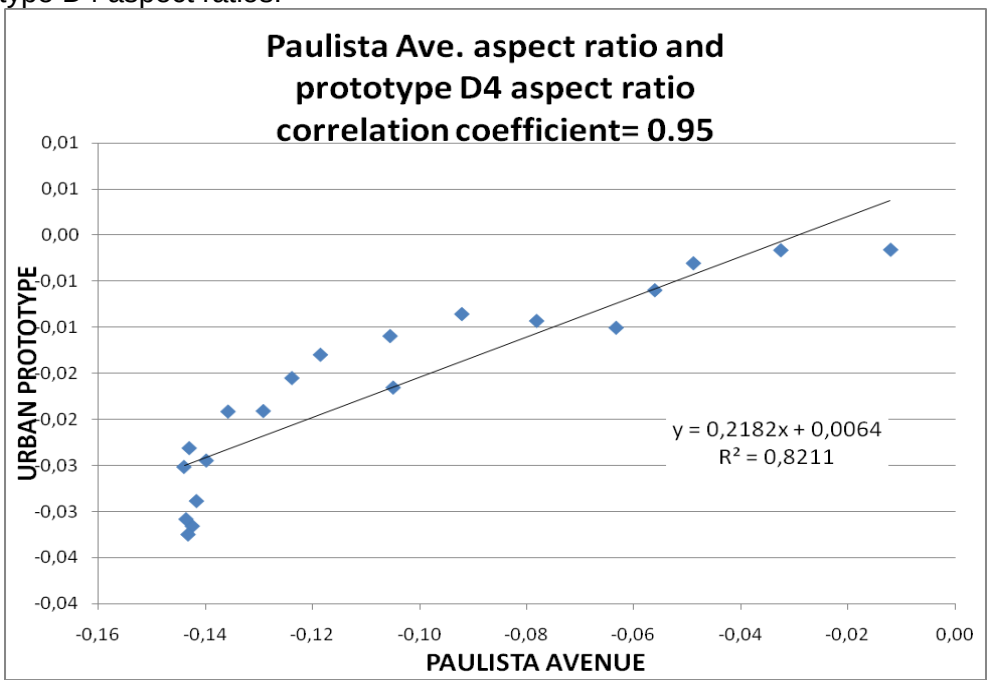

Source: this study.

[70] For further information see topic 5.4.2.2 in this chapter.

Figure 5-84: Correlation between the Paulista Avenue aspect ratios.and the Urban Prototype A1 aspect ratios.

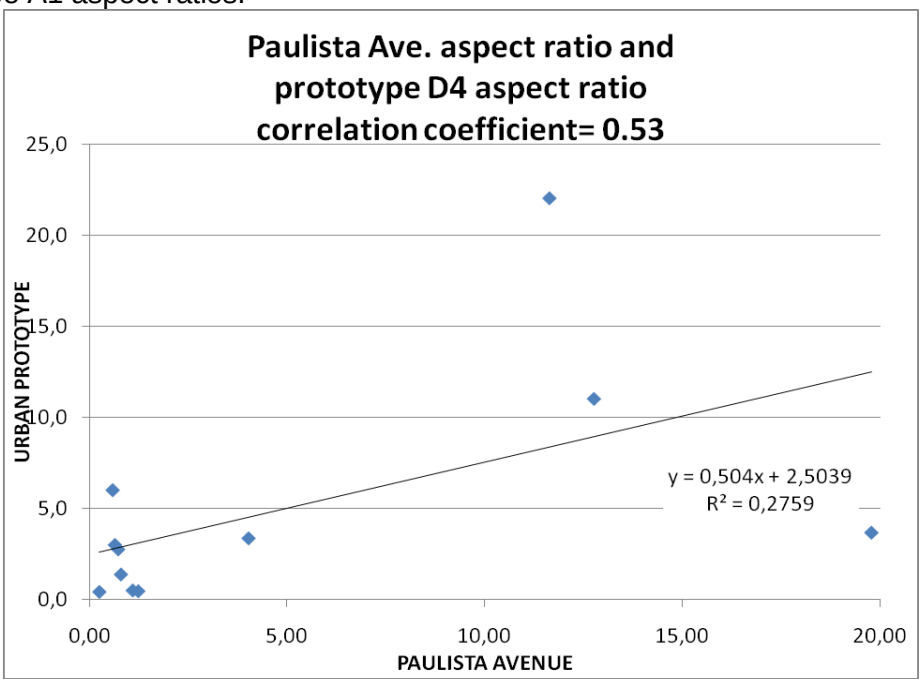

Source: this study.

Table 5-19: The Paulista Avenue CKY Tower and the Urban Prototypes correlation coefficient between the aspect ratios[71].

Aspect Ratios	Paulista Avenue	Urban Prototypes															
		A1	**A2**	**A3**	**A4**	**B1**	**B2**	**B3**	**B4**	**C1**	**C2**	**C3**	**C4**	**D1**	**D2**	**D3**	**D4**
H/W	1,10	0,50	0,50	0,50	0,50	1,00	1,00	1,00	1,00	2,00	2,00	2,00	2,00	1,20	1,24	1,18	1,31
L/H	0,59	6,00	3,00	3,00	1,00	6,00	3,00	3,00	1,00	6,00	3,00	3,00	1,00	5,00	1,73	1,20	0,85
L/W	0,65	3,00	1,50	1,50	0,50	6,00	3,00	3,00	1,00	12,00	6,00	6,00	2,00	6,00	2,14	1,41	1,11
A_{roof}/ A_{urb}	0,25	0,42	0,36	0,21	0,11	0,62	0,56	0,37	0,25	0,75	0,72	0,57	0,44	0,62	0,56	0,40	0,30
A_{built}/ A_{urb}	4,03	3,36	2,91	1,66	0,85	4,99	4,45	2,95	2,02	6,02	5,75	4,55	3,48	7,41	6,50	5,28	4,98
A_{roof}/ H	0,73	2,75	2,38	1,36	0,69	4,09	3,64	2,41	1,65	4,93	4,71	3,73	2,85	3,41	2,10	1,32	0,83
A_{roof}/ W	0,80	1,38	1,19	0,68	0,35	4,09	3,64	2,41	1,65	9,86	9,42	7,45	5,71	4,09	2,60	1,56	1,08
A_{roof}/ L	1,24	0,46	0,79	0,45	0,69	0,68	1,21	0,80	1,65	0,82	1,57	1,24	2,85	0,68	1,21	1,10	0,98
A_{built}/ H	11,65	22,02	19,06	10,85	5,55	32,69	29,13	19,32	13,22	39,43	37,68	29,81	22,83	40,46	24,56	17,30	13,89
A_{built}/ W	12,77	11,01	9,53	5,42	2,78	32,69	29,13	19,32	13,22	78,86	75,36	59,63	45,66	48,55	30,41	20,35	18,13
A_{built}/ L	19,80	3,67	6,35	3,62	5,55	5,45	9,71	6,44	13,22	6,57	12,56	9,94	22,83	8,09	14,19	14,42	16,32
Correlation	**coefficient**	**0,52**	**0,68**	**0,65**	**0,92**	**0,58**	**0,70**	**0,69**	**0,95**	**0,53**	**0,60**	**0,60**	**0,81**	**0,61**	**0,80**	**0,90**	**0,95**

Source: this study

[71] See Table 5-20 for the scale of significance for the Paulista Avenue CKY Tower aspect ratios and the Urban Prototypes aspect ratio's correlation coefficient (*r*) strength

Table 5-20: The scale of significance for urban prototype aspect ratio's and Cardiff/ Paulista aspect ratio's correlation coefficient (*r*) strength.

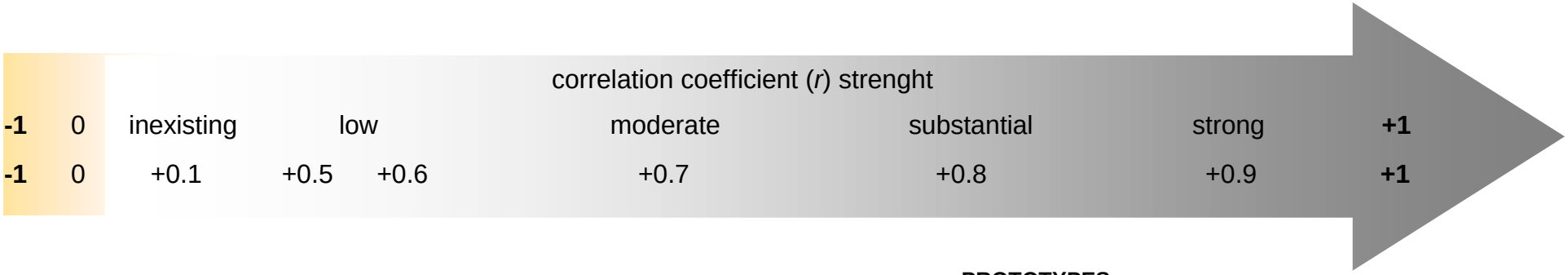

		PROTOTYPES															
		D4	**C4**	**A4**	**B4**	**D3**	**C2**	**C3**	**C1**	**D2**	**D1**	**B2**	**B3**	**B1**	**A2**	**A3**	**A1**
CARDIFF	rank	16	15	14	13	12	11	10	9	8	7	6	5	4	3	2	1
	r	0,51	0,53	0,59	0,59	0,62	0,62	0,62	0,65	0,68	0,78	0,80	0,82	0,85	0,87	0,91	0,94

		PROTOTYPES															
		A1	**C1**	**B1**	**C3**	**C2**	**D1**	**A3**	**A2**	**B3**	**B2**	**D2**	**C4**	**D3**	**A4**	**B4**	**D4**
PAULISTA	*r*	0,52	0,53	0,58	0,60	0,60	0,61	0,65	0,68	0,69	0,70	0,80	0,81	0,90	0,92	0,95	0,95
	rank	16	15	14	13	12	11	10	9	8	7	6	5	4	3	2	1

Source: this study.

5.8.2.4. Scale of significance for urban aspect ratio's correlation coefficient strength

Although Pearson's model is frequently applied in civil and environmental engineering investigations and in the field of the Sciences of Technology, including models for spatial correlation (Kottegoda and Rosso, 2009), a scale such as would determine the strength of the correlation which is compatible with this investigation could not be found in the referenced literature reviewed (Dowdy et al, 2004; Warner, 2008; Barrow, 2009; Campbell and Swinscow, 2009; Croft and Davidson, 2010). Further, the correlation strength scales provided by the literature of the Social or Biological Sciences literature are not appropriate for this application[72], since they are specific to those fields and thus do not match the scale of results from this research area.

On the other hand, it is worthy of mention that the urban prototypes proposed in this investigation were based on urban aspect ratios of actual urban areas, as previously described in topic 5.4.1.1, and that several links between them were identified, based on the analysis of Table 5-3. For instance, when observing the urban landscapes of the two case studies investigated in depth it is possible to associate Cardiff Cathays Campus area (Figures 5-2 and 5-20) with the urban prototypes A (Figure 5-11) and C (Figure 5-13), while the Paulista Avenue area (Figures 5-5 and 5-22) is more closely similar to the urban prototypes D3 (Figure 5-18) and/ or D4 (Figure 5-19). Therefore, for the five cities assessed in the urban area analysis, Cardiff Cathays Campus area would be positioned on one side of the scale, characterized as a low-height built-up area, whilst the Paulista Avenue area would be situated on the other side, as a high-rise built-up area, with both landscapes representing the extremities of this scale. Based on this hypothesis, it is to be expected that results between Cardiff and prototypes A and/ or C will present a strong correlation while results between Cardiff and prototypes D3 and/ or D3 will present a weak correlation, with the opposite occurring with the Paulista.

Therefore, the correlation coefficient found between these will serve as a standard for the scale of significance for this exercise. Based on the findings described in the former topics, a scale of significance for assessing and comparing urban landscapes' physical aspect ratios correlation coefficient strength is proposed here on the basis of the findings described in the former topics.

[72] For instance, De Vaus (2002) ranks the correlation coefficients for Social Science researchers as follows: 1.00= perfect; 0.99 to 0.90= near perfect; 0.89 to 0.80= very strong; 0.79 to 0.70= strong; 0.69 to 0.50= substantial; 0.49 to 0.30= moderate; 0.29 to 0.10= low; 0.09 to 0.00= trivial; while a negative result implies in a reverse correlation, *in* De Vaus, D. 2002. *Analyzing Social Science Data*. London: Sage.

This scale provides four ranks for the Pearson's correlation scale of significance: strong, substantial, moderate, and low (see table 5-20). For the urban aspect ratios analysis, this means a range of correlation coefficient ranging from 0.95 to 0.51.

This scale will serve as a reference for ranking the ΔCp level of association and correlation coefficient strength which will be carried through in Part 4: Results and Analysis of this investigation. It is worth mentioning that the correlation coefficient for ΔCp results is expected to follow the same sequence as this scale, though not of the same order of magnitude.

5.9. Chapter conclusion

This chapter has presented the methodology adopted for assessing the airflow field in urban areas. The urban prototypes and the two real urban area case studies were presented in details. In order to achieve the objectives of this thesis, various research methods on urban fabric and airflow simulation were employed including: laboratory scale-model tests in a boundary layer wind tunnel (WT), computational fluid dynamics (CFD) models, and field measurements (FM). These methods and the various parameters adopted to ensure the accuracy and the effective achievement of valid results in each step of this research project have been detailed here. Finally, the correlation coefficient parameters employed on the assessment of the results is covered. This chapter is supported by the critical literature review presented in Part 2.

Part 04: Results and Analysis

Chapter 6: The Two Bricks: Results and Analysis

6.1. Introduction

This chapter will present and contrast the results of the wind tunnel (WT) and CFD calculations for the two parallel brick experiment and contrast them. This chapter constitutes Step 2 of the proposed investigation methodology. Its aim is to ascertain the accuracy of CFD models in reproducing both external airflow environment patterns and Cp results on buildings surfaces. The CFD input parameters used in these sets of experiments will serve as guidelines for the subsequent CFD models in the other steps of the investigation, in which more complex CFD scenarios are simulated.

6.2. Comparison between the WT and the CFD results

Several sets of simulation were carried out for four different H/W aspect ratios (2.00, 1.00, 0.66 and 0.50) and three wind directions (90˚, 45˚ and 0˚). Further details of the parameters adopted for the CFD and the WT experiments, whose output from each set of simulation performed was assessed, are to be found under topics 5.2, 5.3, 5.5.2, and 5.6 of Chapter 5. The results shown are organized, first according to the wind direction and then the H/W aspect ratio. Cp contour plots for both the wind tunnel and the CFD results are followed by graphs depicting the Cp results on these surfaces at lines of 5.0, 10.0 and 15.0m-high lines. Then velocity vectors and pathlines, from the CFD, and airflow bubble visualization still images, from the wind tunnel, are presented to facilitate the understanding of the modifications of the airflow speed and direction. Finally, the vertical wind profile from the CFD calculation is assessed for each model by 15 strategically positioned vertical lines[73].

[73] See Figure 5-61 under the topic 5.6.3.1. of Chapter 5.

6.3. On the results of the two-brick wind tunnel experiments

Some considerations may be presented on the physical experiments regarding the WT sets of simulation[74] before comparing them with the CFD results. The Cp contour plots obtained on the windward face of the upwind brick will be used as an example. Dynamic pressure was measured by 87 pressure taps on the windward face. Turbulent airflow field fluctuation in the WT chamber did not provide completely symmetrical results as between the left and right sides (Figure 6-1). On the other hand, the standard deviation found between the results was less than 1.9%, which is within an acceptable range[75].

Figure 6-1: Windward face Cp contour plot.

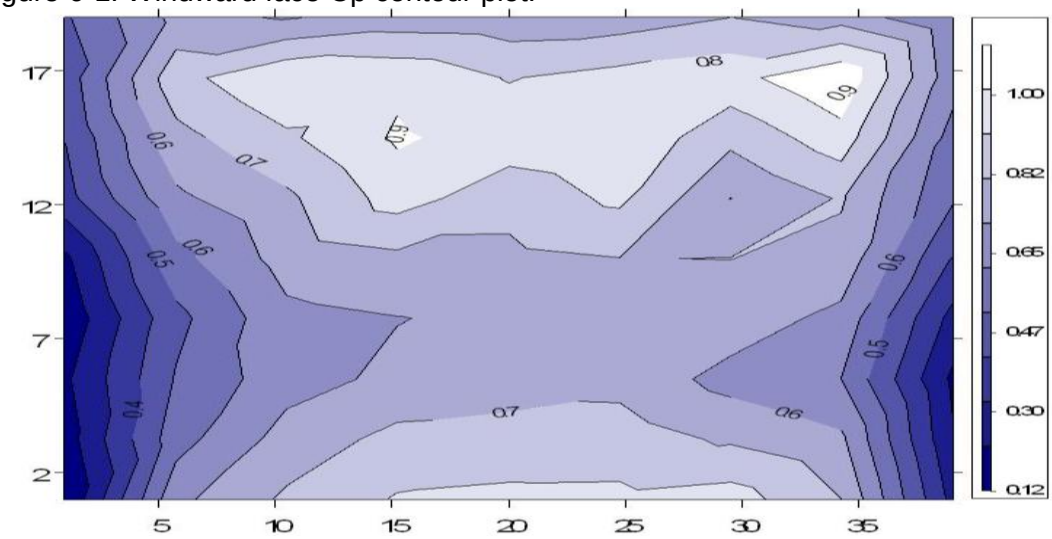

Source: this study.

A symmetrical contour plot image was created by copying the output from the left and the right side. Even with the input data completely identical, contour plots showed indentation due to both the lack of accuracy in representing the curves and the relatively coarse distribution of data due to the restricted number of pressure taps employed (Figure 6-2). Symmetry was also attained with averaged weighting of the results from both sides, which allowed a more even contour plot distribution (Figure 6-3).

[74] For more details about the physical model and the wind tunnel set-up, see topics 5.5.2 and 5.6. in Chapter 5.
[75] See topic 5.5.1.

Figure 6-2: Windward face Cp contour plot showing symmetrical results from the left side.

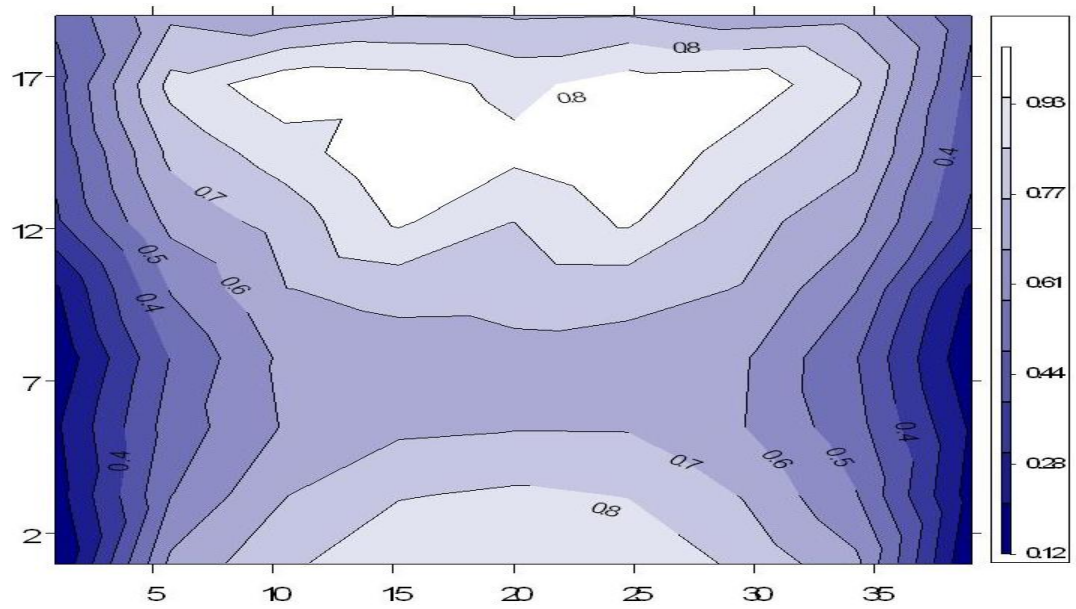

Source: this study.

Figure 6-3: Windward face Cp contour plot showing averaged results.

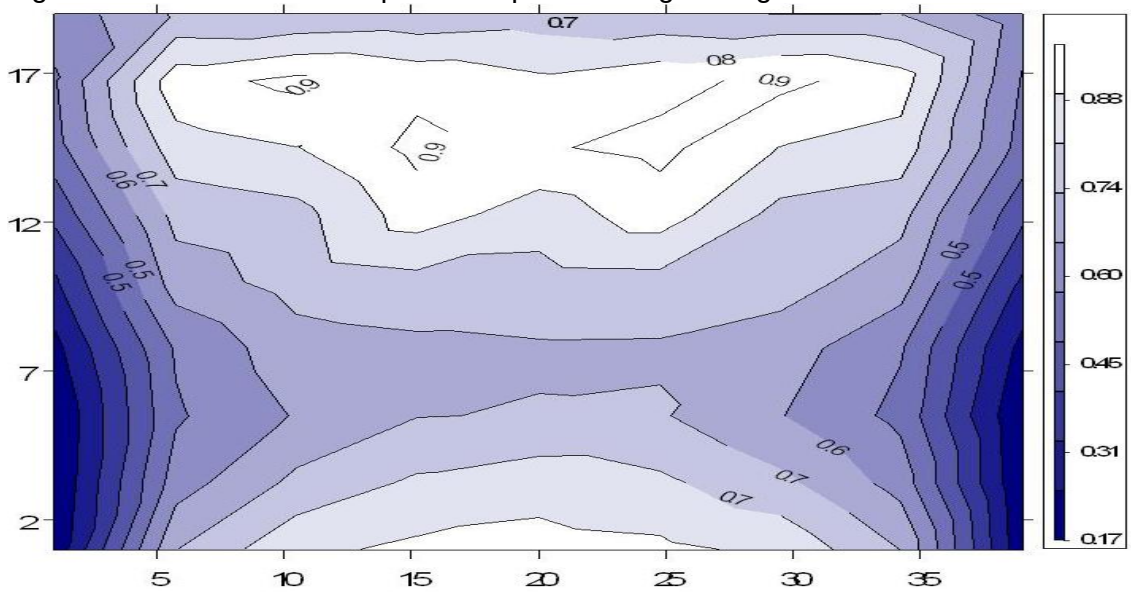

Source: this study.

6.4. Pressure Coefficient (Cp) results

The Cp results are presented here. The Cp CFD contour plots are related to a reference velocity value of 2.35m/s, which corresponds to the airflow velocity at 10m above the canopy height. Further, the range of data on the charts displaying both the WT and the CFD Cp results is the same (from -0.6 to +1.0) in all the figures, to provide an identical basis for the comparison of the results during the analysis.

6.4.1. Bricks perpendicular to the airflow (at 90˚)

The contour plots for the upwind brick top face show similar patterns in both the WT and CFD results. On the other hand, the range of values is slightly greater on the latter. It seems to over predict the pressure on the top surface, which might be explained by the k-e model employed and its limitations in calculating flow detachment on the top horizontal edge followed by a low pressure bubble and flow reattachment[76].

Figure 6-4: WT (top) and CFD (bottom) Cp contour plots for the upwind brick's top face at 90˚ (H/W=1.0).

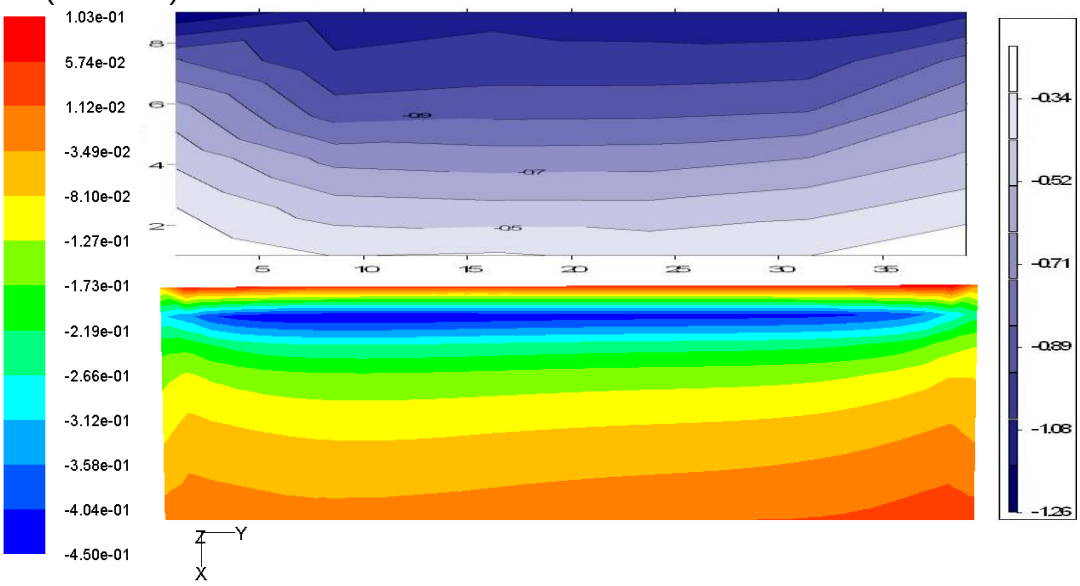

Source: this study.

Few pressure taps were employed on the side of the brick in the WT model since the results on this face are not the main focus of this exercise. For this reason, although there is some resemblance between bthe two contour lines, the WT does not accurately represent the same features of the Cp distribution as the CFD (Figure 6-4). On the other hand, the range of values is equally matched in both sources, in the view of the fact that this range is greater than in the computational calculation due to the large number of cells in a small grid and mesh size.

[76] See topics 3.5.3.10 and 3.5.3.11 in Chapter 3 for further information.

Figure 6-5: CFD (right) and WT (left) Cp contour plots for the upwind brick's right face at 90˚ (H/W=1.0).

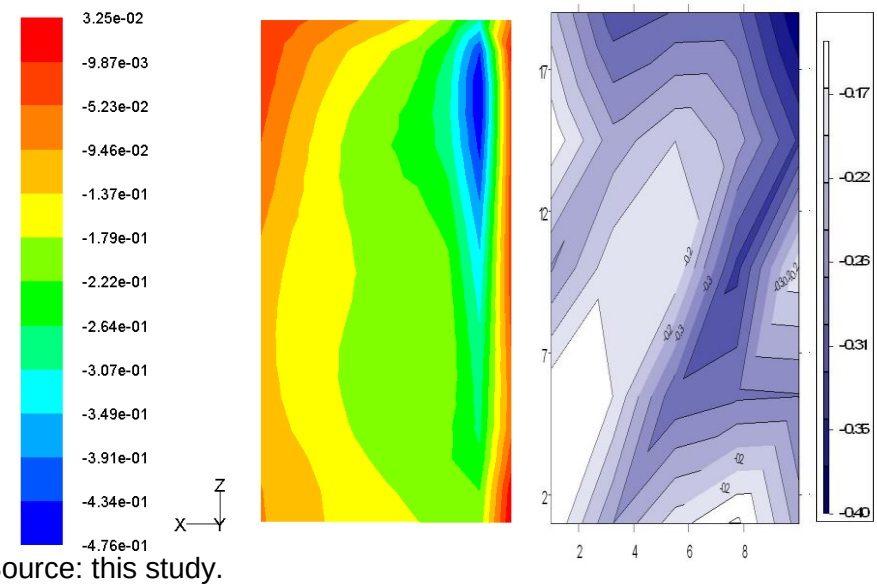

Source: this study.

Figure 6-6 demonstrates that good equivalence was obtained as between the WT and CFD results in both contour plot distribution and Cp results. Both contours present a frontal stagnation point at approximately 4/5ths of the brick's height, which may also be observed also in the airflow pattern analysis. Further, these results correspond well to the descriptions of perpendicular winds impinging on rigid rectangular bodies, found in the literature[77], both in number and shape. It may also be seen and is valid for the following topics, that the CFD output produces fully symmetrical and delineated contour lines, with a great range of values. In contrast, since a limited number of pressure taps was used in the WT measurement, it shows an organic shape with few indentations in the contours. The contour plots for the downwind brick's leeward face follow the same patterns in both wind tunnel and CFD results (Figure 6-7). On the other hand, the range of values is up to 0.30 greater on the latter one. The numerical calculation seems to over predict the pressure on the leeward surface, which could be explained by the nature of the k-e model adopted and its limitations in calculating flow recirculation and leeward wakes.

In the following figures (figure 6-8 to 6-11) Cp results on the rear side of the front brick will be presented for a range of H/W aspect ratios. This side constitutes of the leeward face in a canyon for orthogonal winds. Close similarity was found in the contour plots for each of these pairs. Regarding the range of the results, the wind tunnel numbers are constantly lower than those of the CFD, presenting a difference of between 0.10 and 0.15.

[77] See topic 2.5 in Chapter 2 for further information.

Later, the Cp results from the windward side of the downwind brick are shown for the same range of H/W aspect ratios (figures 6-12 to 6-15). Once again, similar contour plots can be observed for the wind tunnel and the CFD outputs. Regarding the range of the results, it was found that the Cp values from the top height were found to be very close, while those near the ground in the WT were up to 0.10 lower than the CFD ones.

When comparing the impact of the aspect ratio has on the Cp values, it was found that for the bricks with a narrow gap in between (H/W = 2.00) results were quite lower than the others with a square (H/W=1.00), or wide (H/W=0.66 to 0.50) gap, which may be an indicative of the occurrence of skimming flow. Moreover, the results found for the ratios of 1.0, 0.66 and 0.5 were closely similar, although the contour plot shape for the wider ones present in both methods of simulation presented a distortion towards one side, which might indicate wake interference flow.

Figure 6-6: WT (top), CFD (middle) and Cp contours plot and graph (bottom) for the upwind brick's windward face at 90˚ (H/W=1.0).

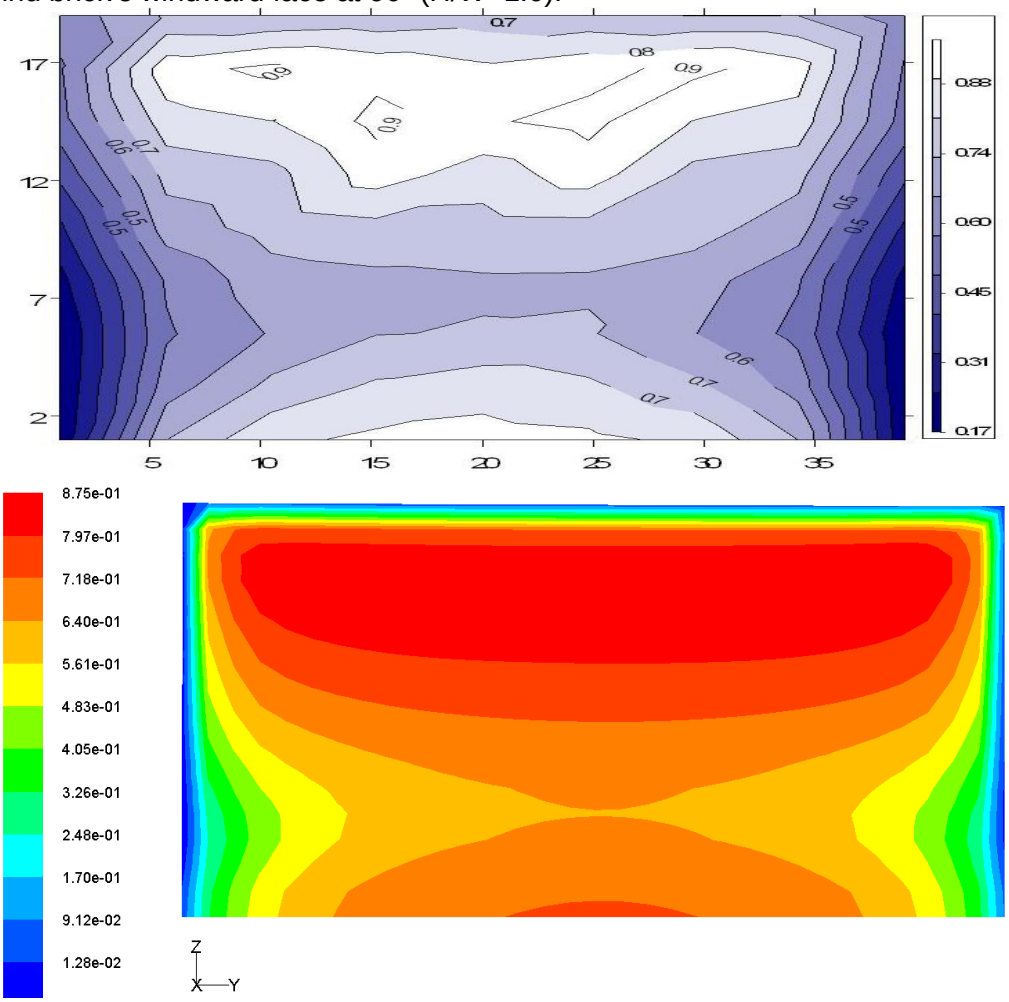

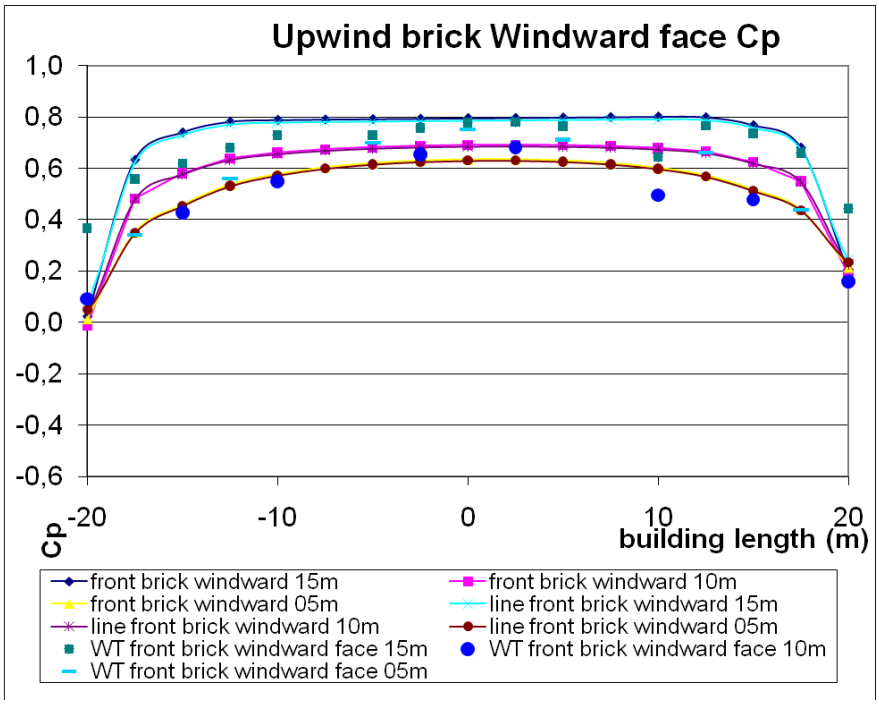

Source: this study.

Figure 6-7: WT (top), CFD (middle) and Cp contours plot and graph (bottom) for the downwind brick's leeward face at 90˚ (H/W=1.0).

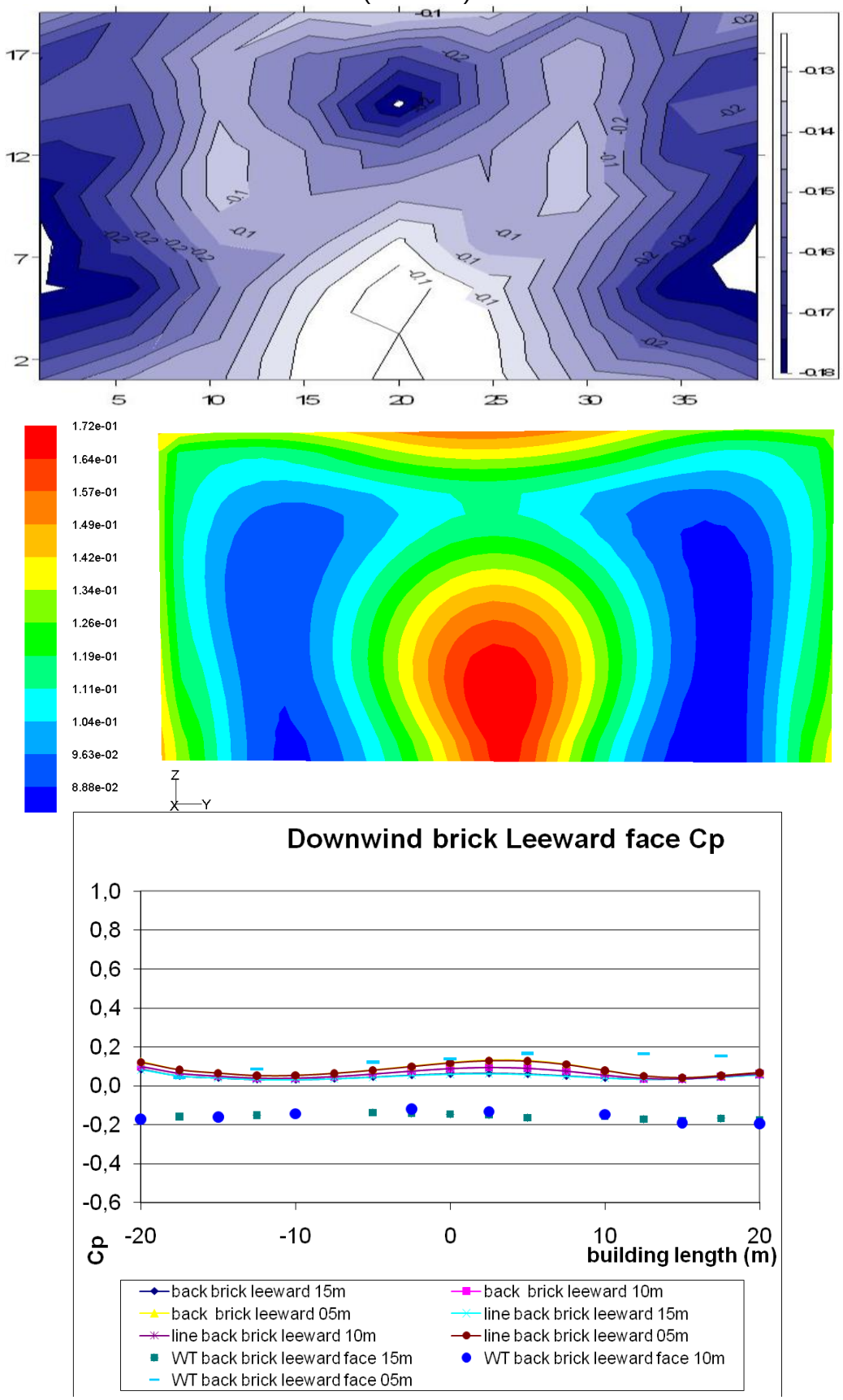

Source: this study.

Figure 6-8: WT (top), CFD (middle) and Cp contours plot and graph (bottom) for the upwind brick's leeward face at 90˚ (H/W=2.00).

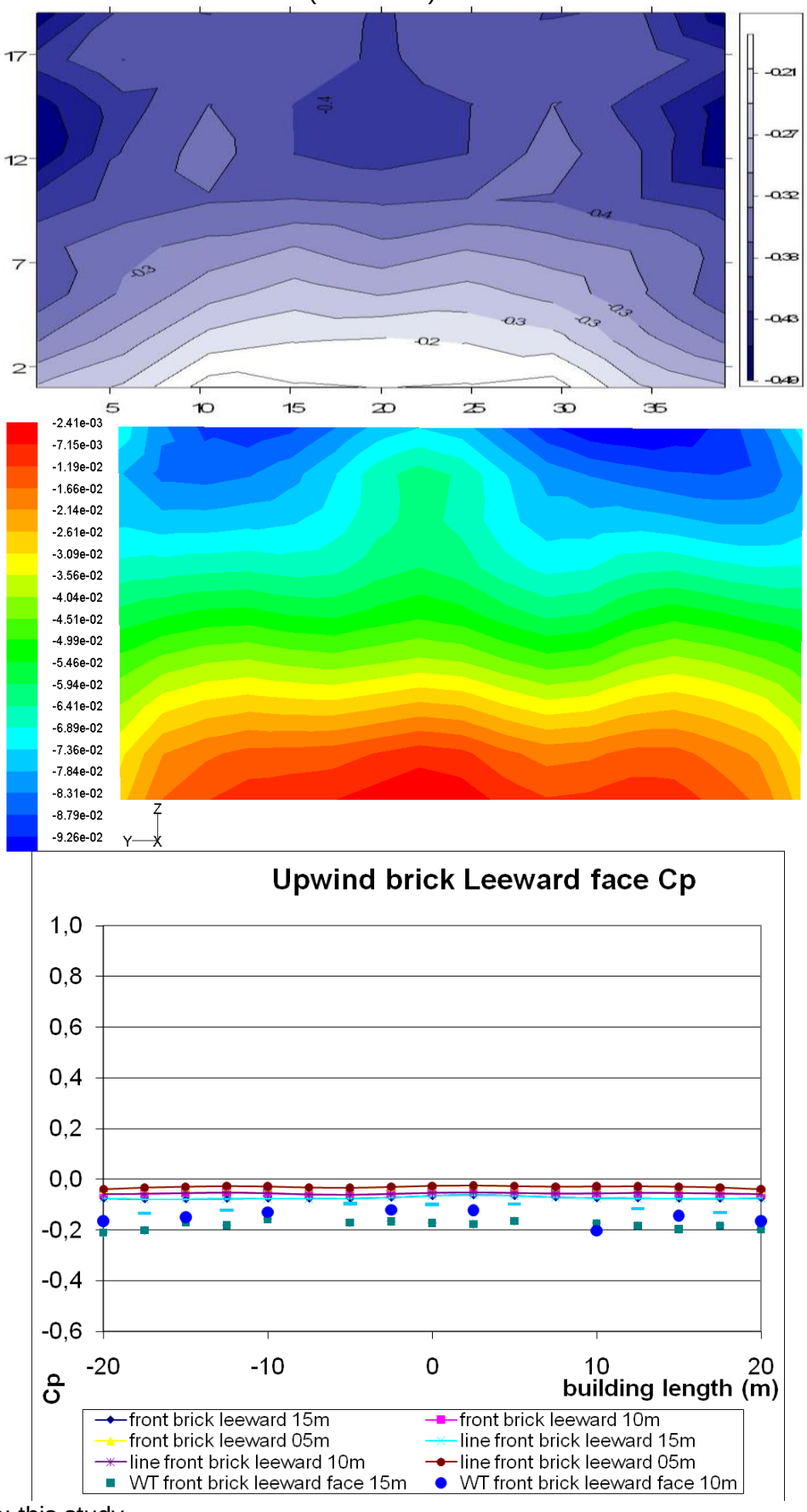

Source: this study.

Figure 6-9: WT (top), CFD (middle) and Cp contours plot and graph (bottom) for the upwind brick's leeward face at 90˚ (H/W=1.00).

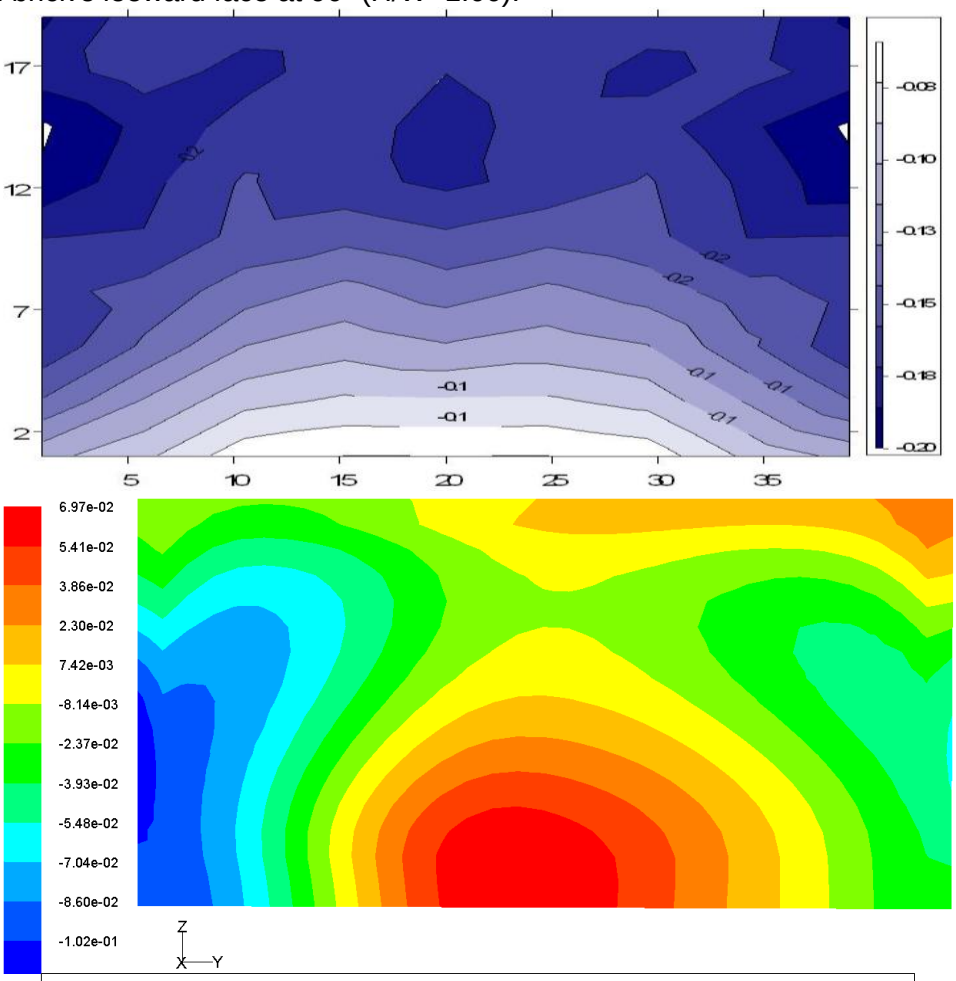

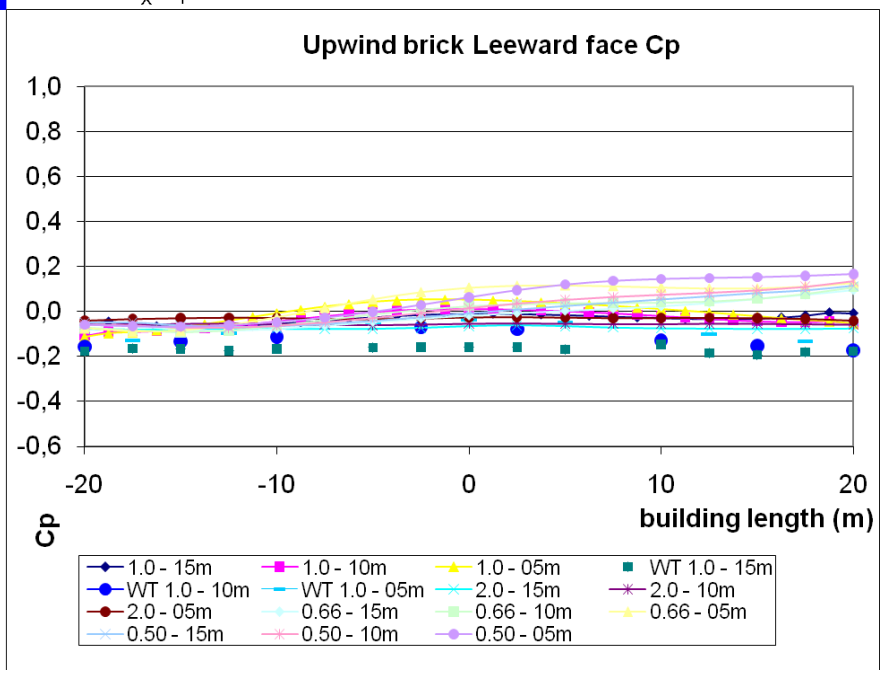

Source: this study.

Figure 6-10: WT (top), CFD (middle) and Cp contours plot and graph (bottom) for the upwind brick's leeward face at 90˚ (H/W=0.66).

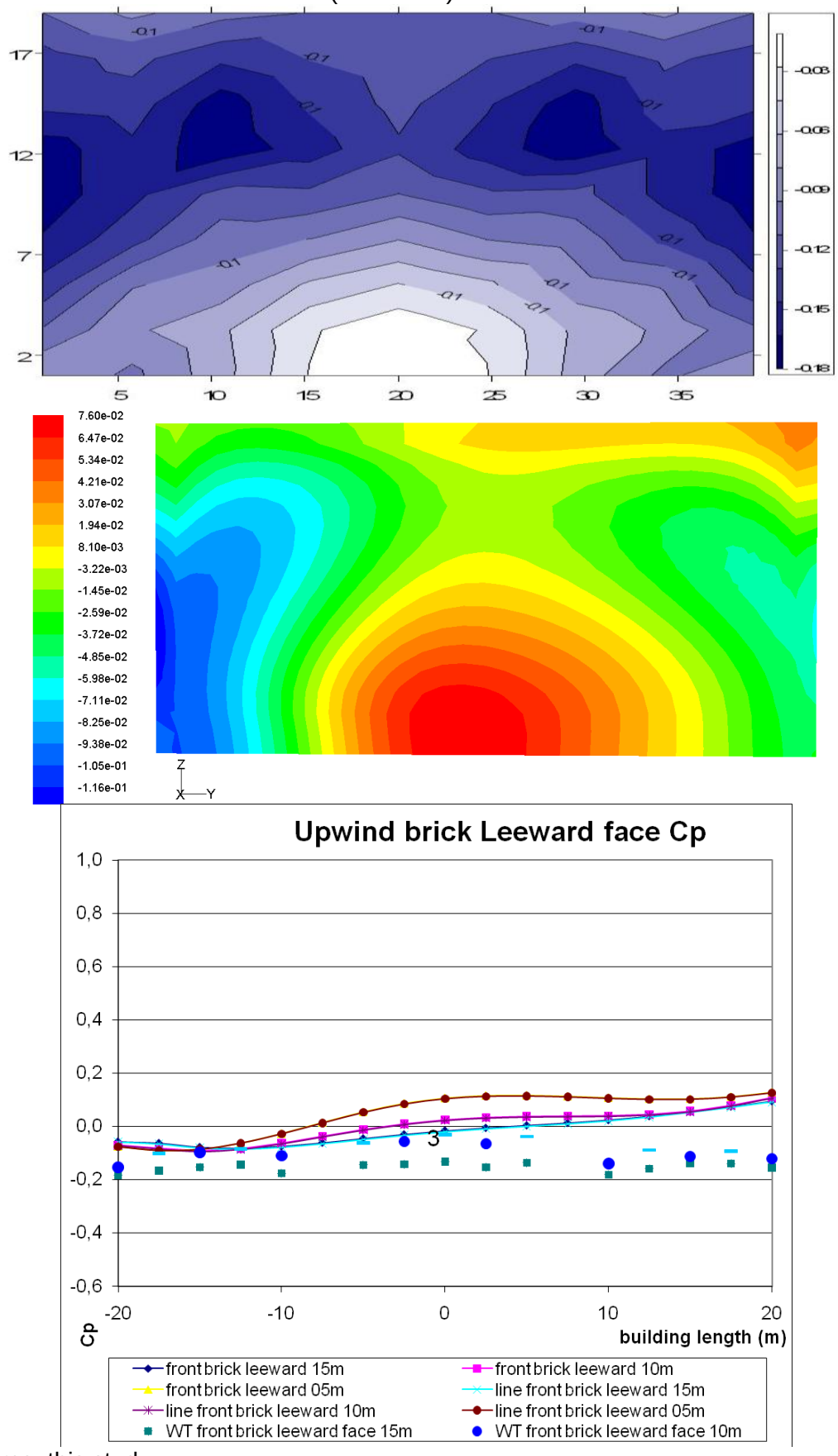

Source: this study.

Figure 6-11: WT (top), CFD (middle) and Cp contours plot and graph (bottom) for the upwind brick's leeward face at 90˚ (H/W=0.50).

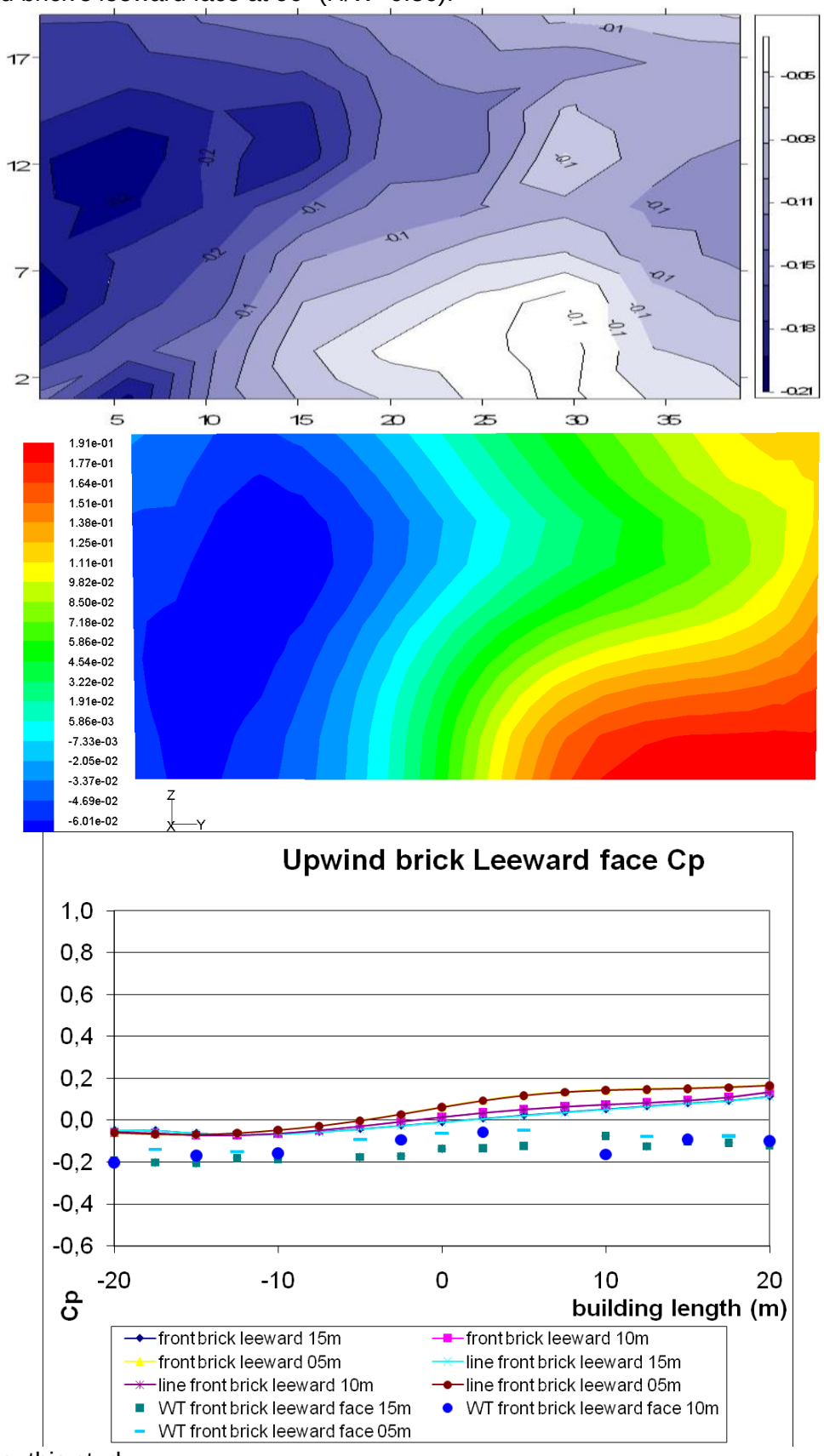

Source: this study.

Figure 6-12: WT (top), CFD (middle) and Cp contours plot and graph (bottom) for the downwind brick's windward face at 90˚ (H/W=2.00).

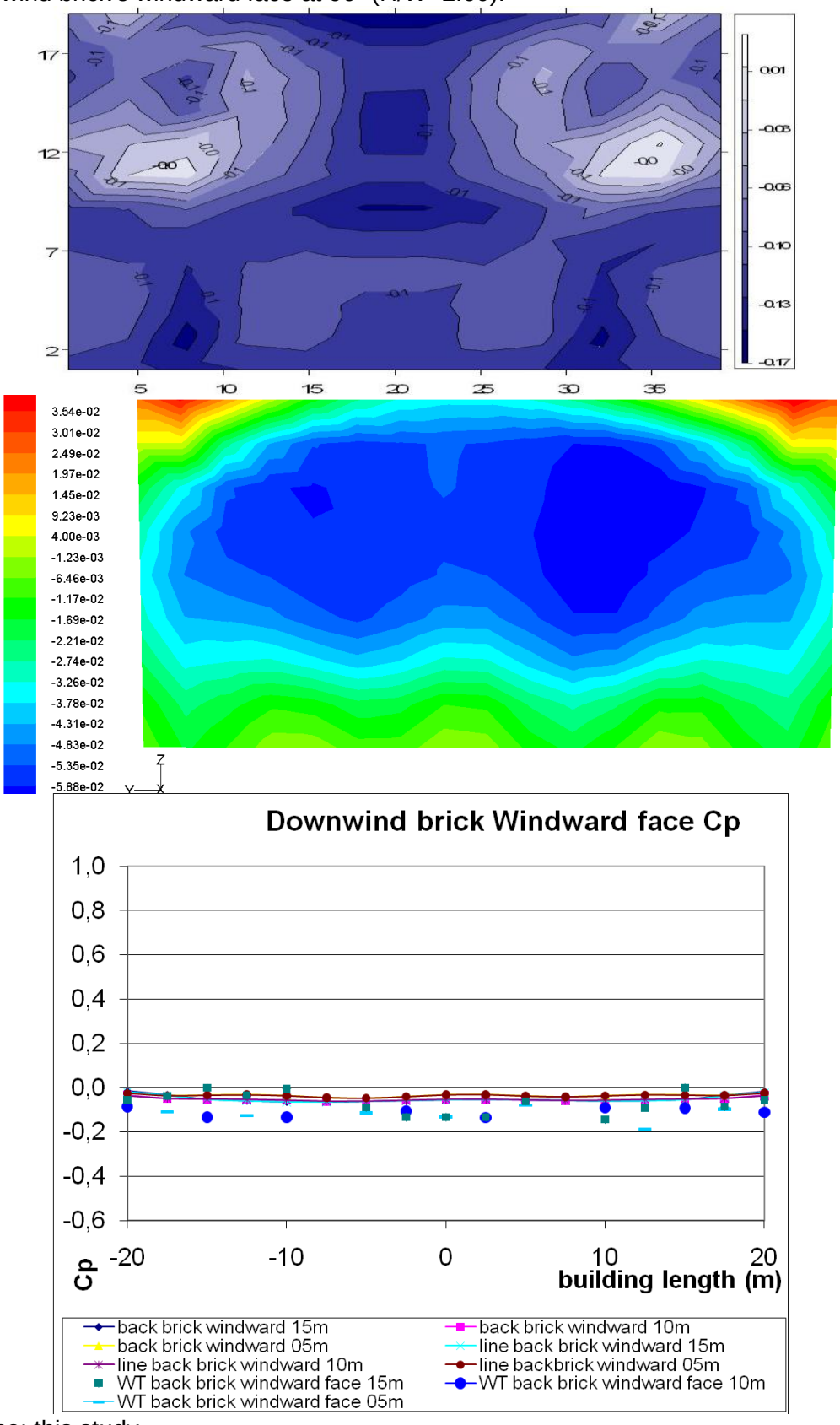

Source: this study.

Figure 6-13: WT (top), CFD (middle) and Cp contours plot and graph (bottom) for the downwind brick's windward face at 90˚ (H/W=1.00).

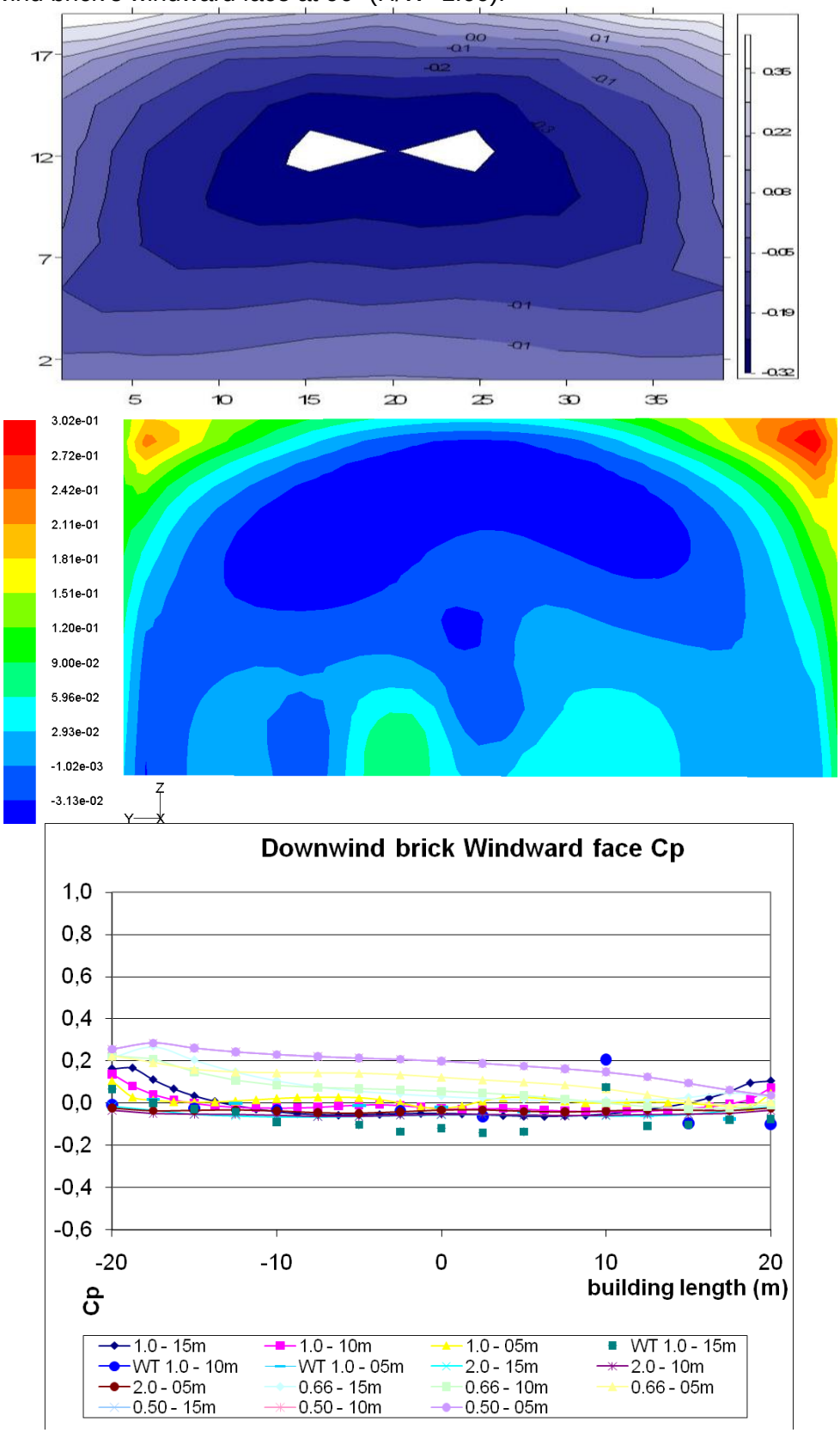

Source: this study.

Figure 6-14: WT (top), CFD (middle) and Cp contours plot and graph (bottom) for the downwind brick's windward face at 90˚ (H/W=0.66).

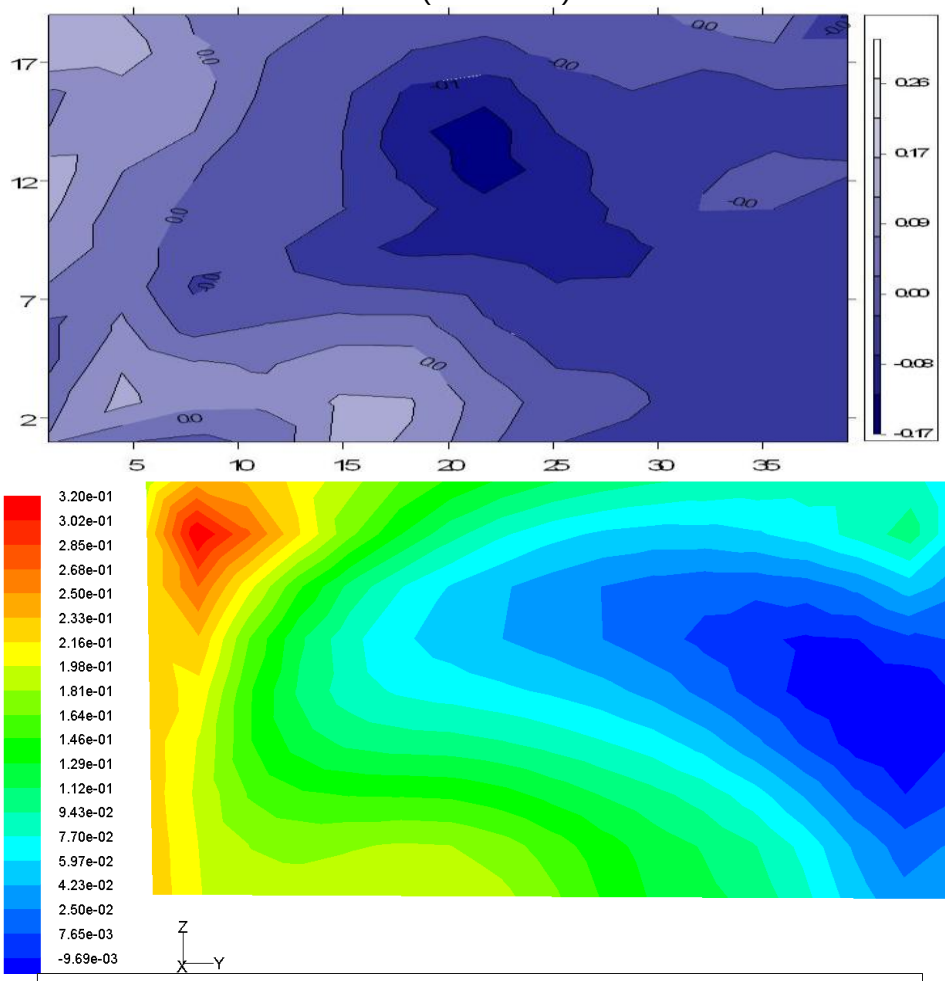

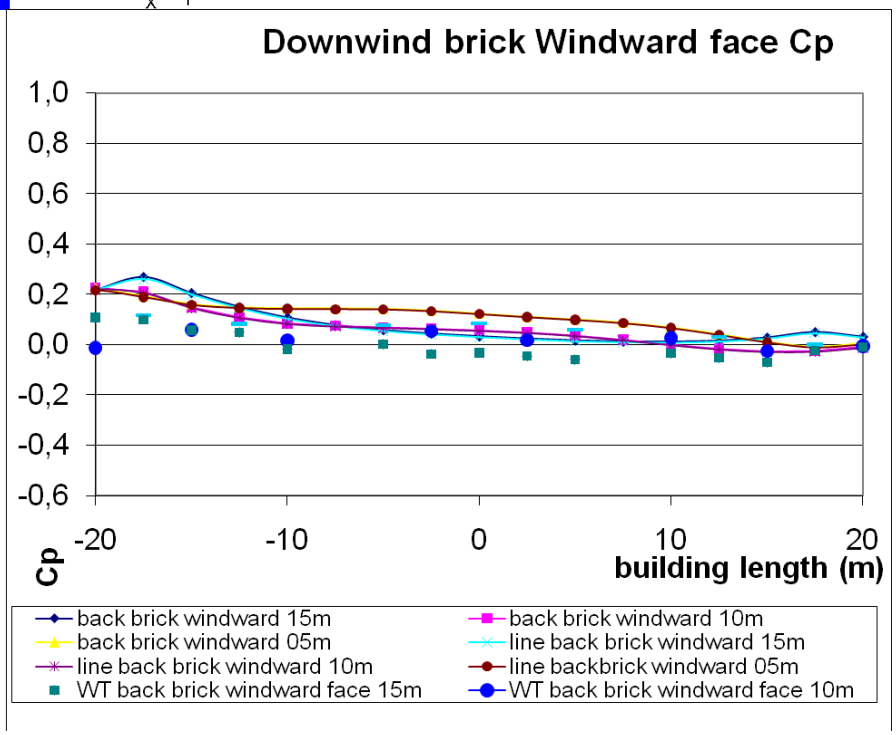

Source: this study.

Figure 6-15: WT (top), CFD (middle) and Cp contours plot and graph (bottom) for the downwind brick's windward face at 90˚ (H/W=0.50).

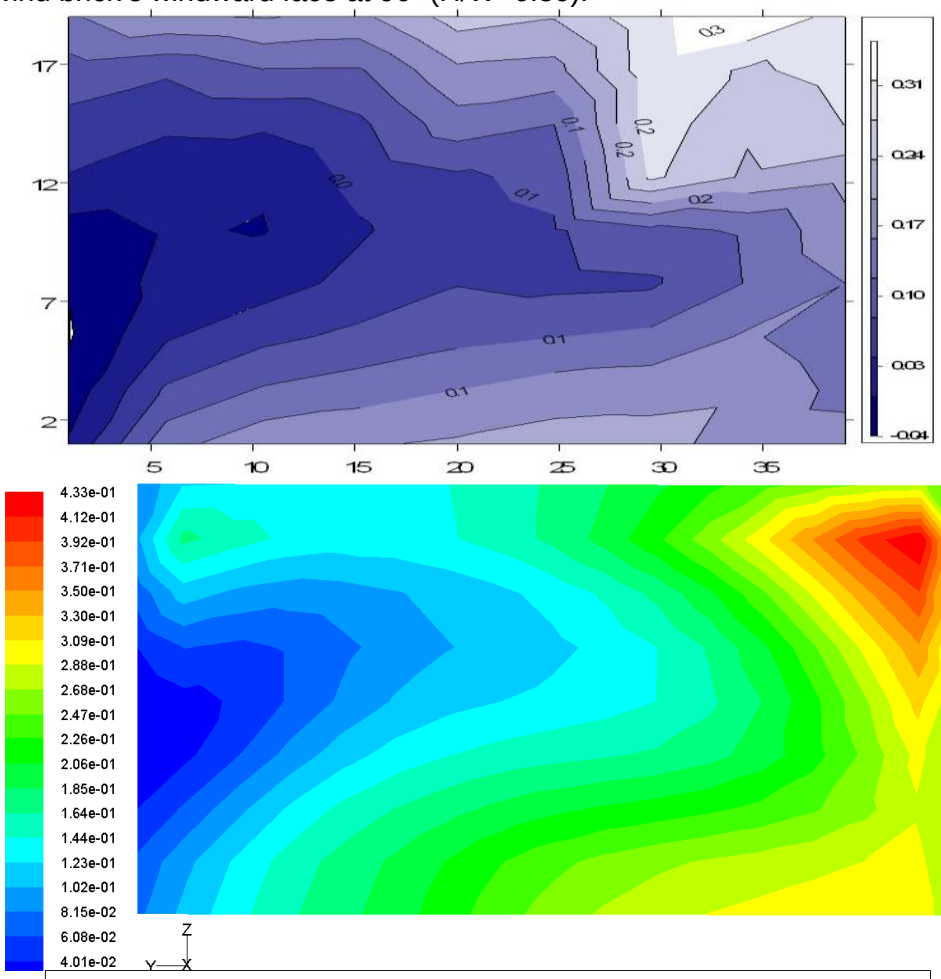

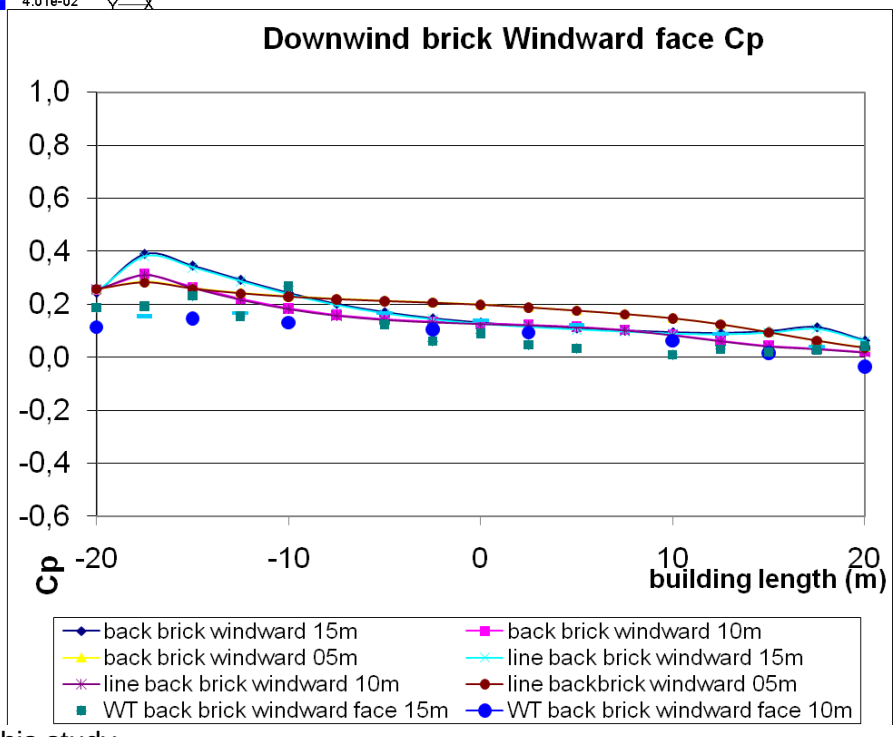

Source: this study.

6.4.2. Bricks parallel to the airflow (at 0˚)

Here the pair of bricks was placed parallel to the airflow, thus corresponding to the inside face of a canyon lying along the main airstream. Four aspect ratios were simulated for this wind direction in WT, while the aspect ratio H/W= 1.0 was observed in both WT and CFD methods.

Figure 6-16: Example of a set of bricks placed at 0˚ (H/W=1.0).

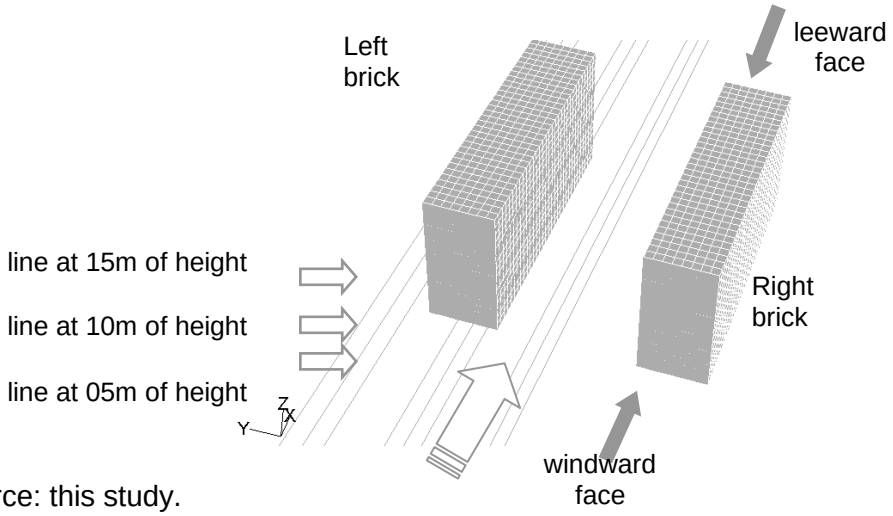

Source: this study.

Figure 6-17: CFD (left) and WT (right) Cp contour plots for the left brick's windward face at 0˚ (H/W=1.0).

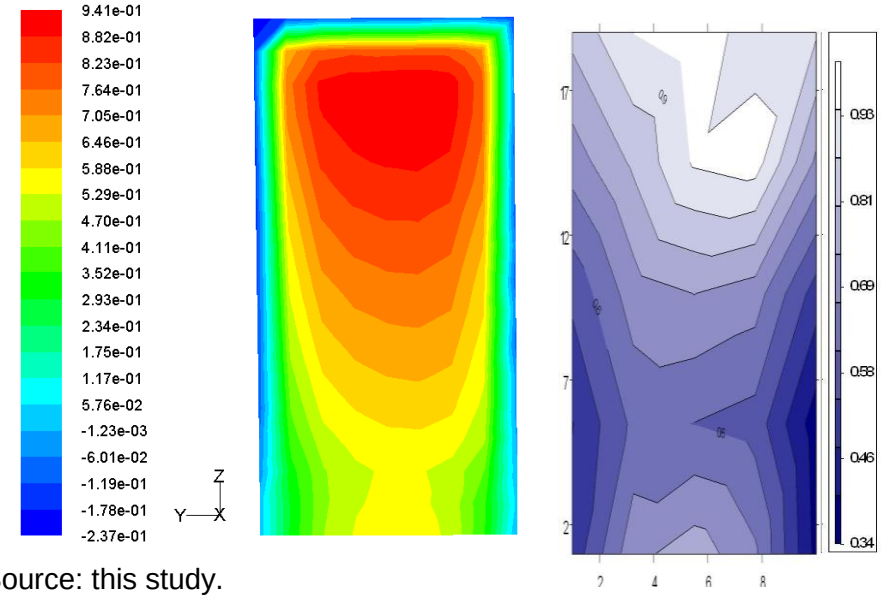

Source: this study.

Figure 6-18: CFD (left) and WT (right) Cp contour plots for the right brick's leeward face at 0˚ (H/W=1.0).

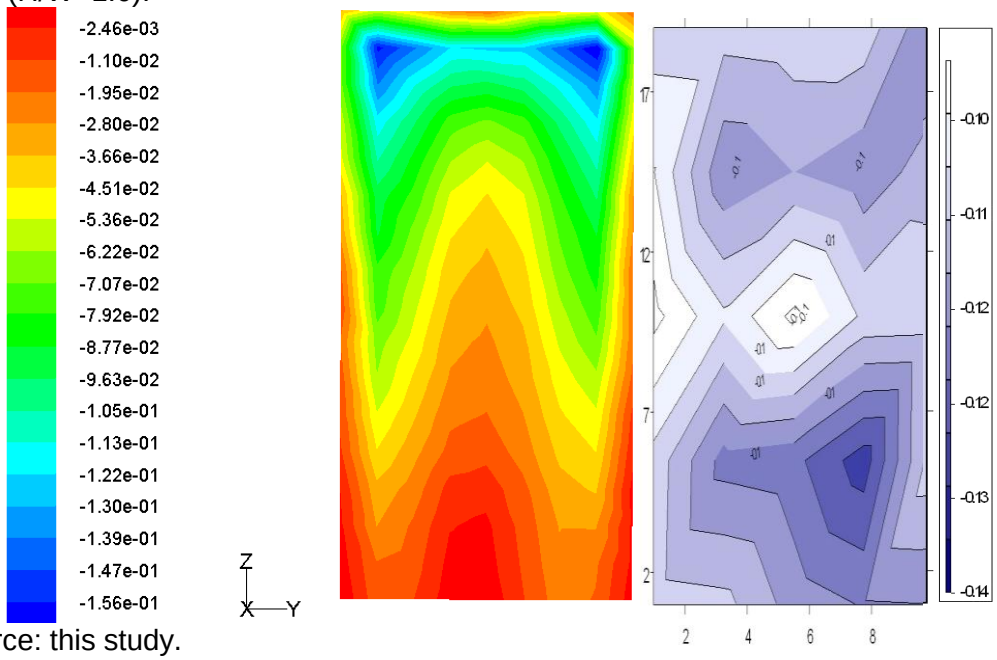

Source: this study.

Figure 6-19: WT (top) and CFD (bottom) Cp contour plots for the left brick's top face at 0˚ (H/W=1.0).

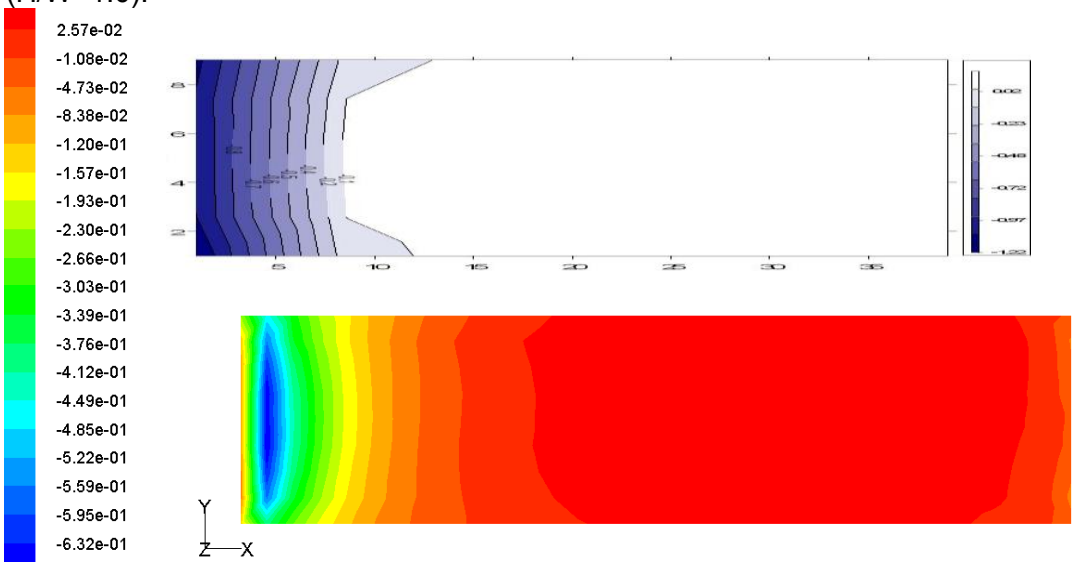

Source: this study.

Similarity is observed between both the windward and the leeward side contour plots from the WT and the CFD simulations, with some low resolution on the WT image due to the few pressure taps used on the front and rear sides (Figures 6-17 and 6-18). On the other hand, the Cp's range of results matches well, with the exception of the lowest ones in the scale. These are lower in the CFD output due to the greater accuracy the software calculation can attain with a fine mesh and grid solution. Moreover, a comparison of the wind tunnel outputs for all the ranges investigated (H/W= 2.00, 1.00, 0.66, and 0.50) did not show much variation in the results between

the narrowest and the widest aspect ratios. The same is valid for the top side, for which both the Cp results and the contour plots from the WT and the CFD match well (Figure 6-18).

Regarding the results for the left brick's right (inside) face for the above-mentioned simulations, a closely range may be observed between the WT and the CFD results for the H/W aspect ratio = 1.00. Further, a sharp drop in pressure right after the upwind vertical corner, which is also clearly to be seen in the graph also, is related to airflow detachment at this edge and its later reattachment after $1/8^{th}$ of the block's length (Figures 6-20). The same features are to be observed in Figures 6-21 to 6-23, although only wind tunnel experiments were performed for this specific set of pair of bricks.

Figure 6-20: WT (top), CFD (middle) and Cp contours plot and graph (bottom) for the left brick's right face at 0˚ (H/W=1.0).

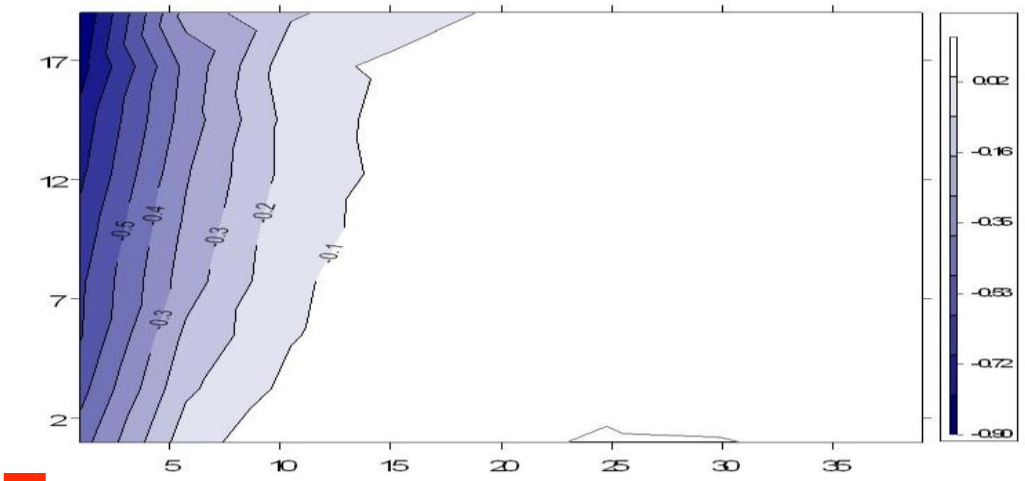

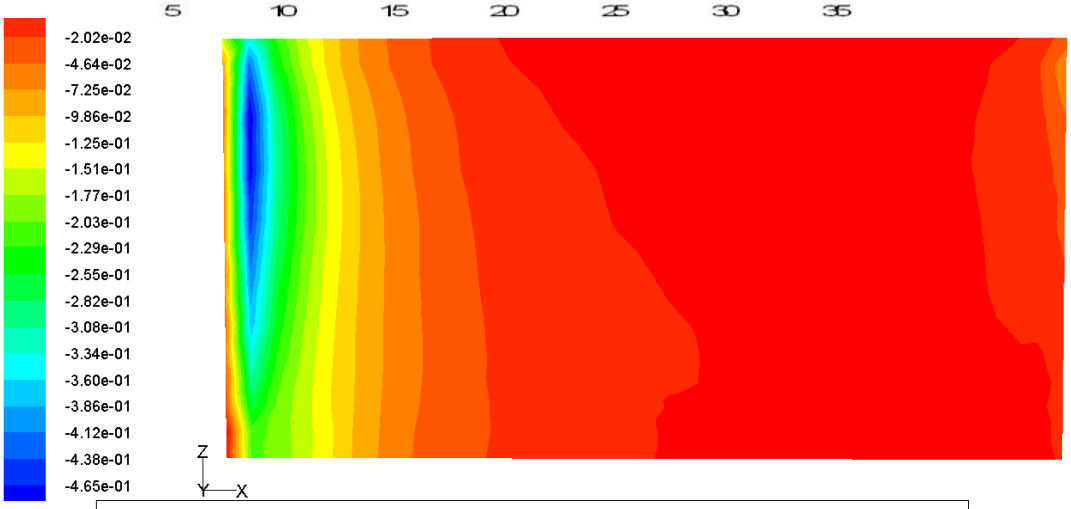

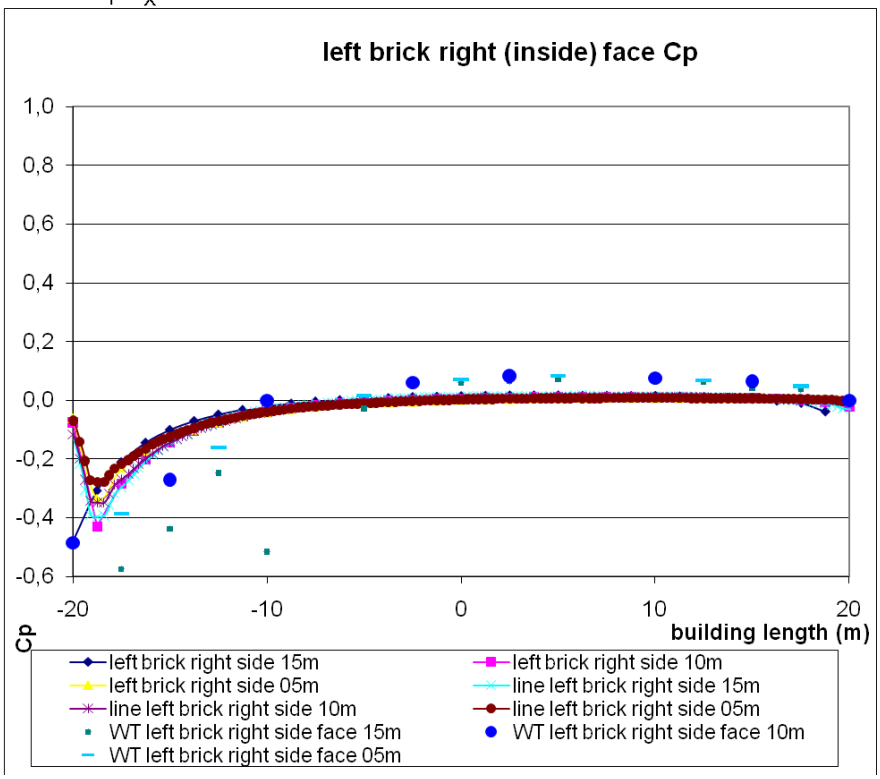

Source: this study.

Figure 6-21: WT (top), CFD (middle) and Cp contours plot and graph (bottom) for the left brick's right face at 0˚ (H/W=2.00).

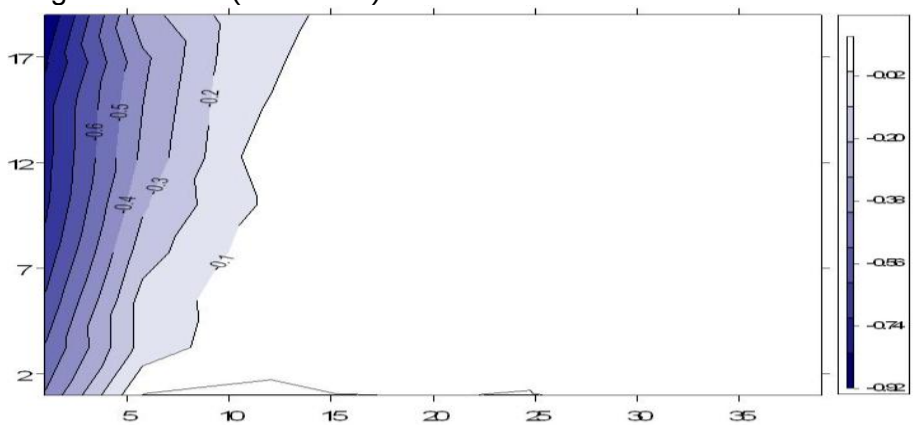

Source: this study.

Figure 6-22: WT (top), CFD (middle) and Cp contours plot and graph (bottom) for the left brick's right face at 0˚ (H/W=0.66).

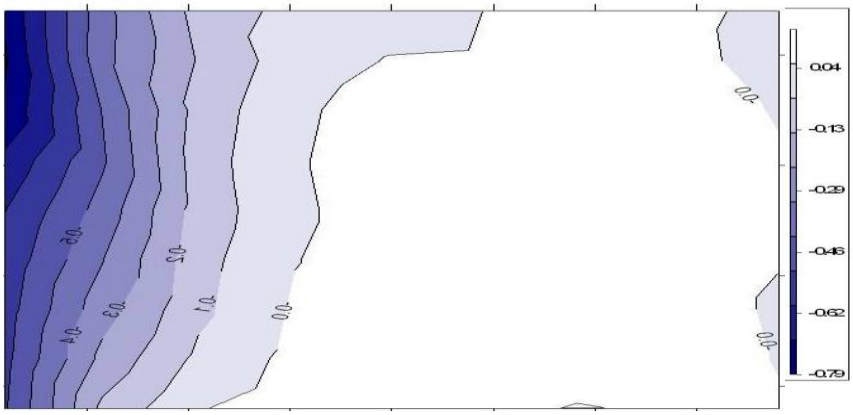

Source: this study.

Figure 6-23: WT (top), CFD (middle) and Cp contours plot and graph (bottom) for the left brick's right face at 0˚ (H/W=0.55).

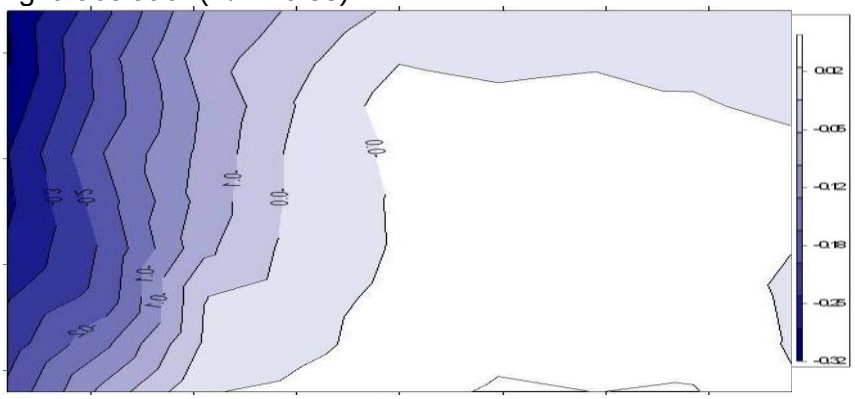

Source: this study.

6.4.3. Bricks oblique to the airflow (at 45˚)

Here the pair of bricks was placed skewed 45˚ to the airflow. The four aspect ratios were simulated for this wind direction in the wind tunnel, while the aspect ratio H/W= 1.0 was used for both WT and CFD methods.

Figure 6-24: Example of a set of bricks placed at 45˚ (H/W=1.0).

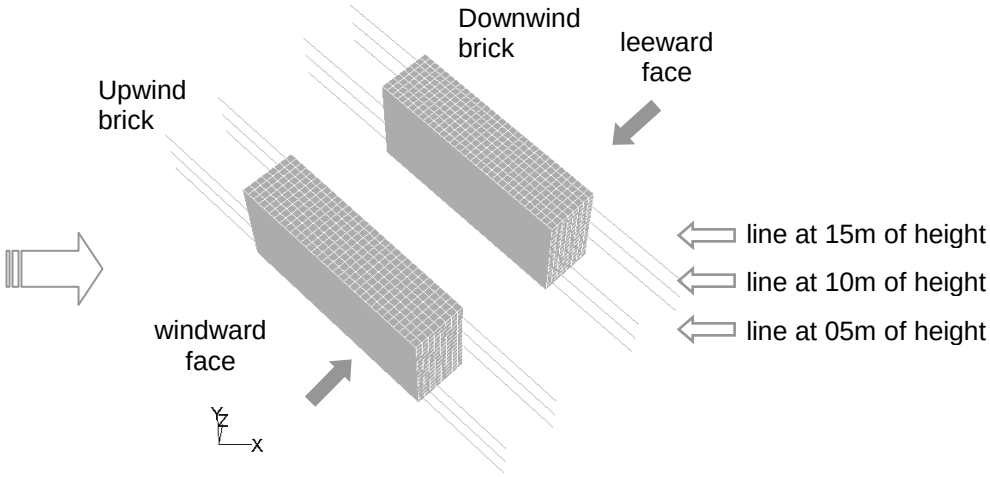

Source: this study.

Figure 6-25: WT (top) and CFD (bottom) Cp contour plots for the right brick's top face at 45˚ (H/W=1.0).

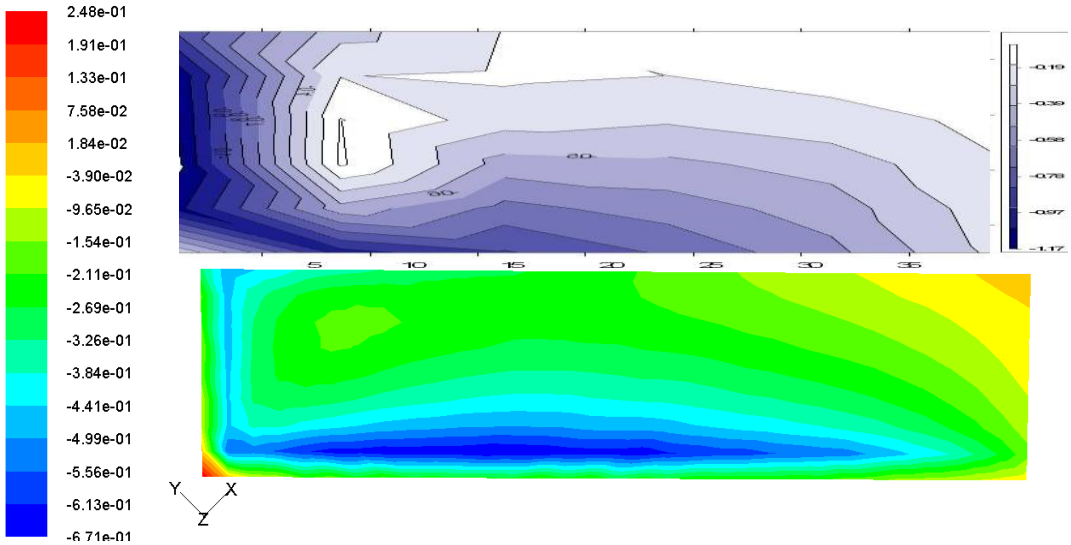

Source: this study.

Figure 6-26: WT (top) and CFD (bottom) Cp contour plots for the left brick's top face at 45° (H/W=1.0).

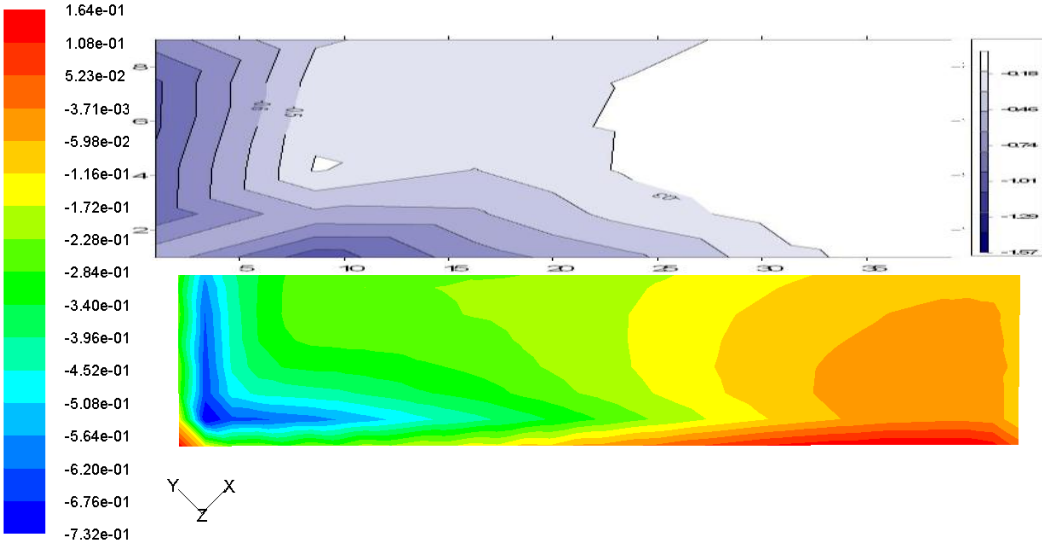

Source: this study.

A comparison of Figures 6-25 and 6-26 shows that a reasonable equivalence was obtained between the wind tunnel and the CFD results on the contour plot of the top surfaces.

The oblique wind on the upper edge of the brick creates a curling flow that results in a diagonal detachment flow. This happens on both the upwind and the downwind bricks since both are exposed to the open flow. Conversely, on the second half of the top surface of the downwind brick this effect is broken due to the wake interference from the first brick. This can also be seen in the airflow visualization pathlines in the next item of analysis.

Regarding the Cp values, again the CFD calculation seems to overestimate the pressure on the top surface, as has already been observed in the previous analysis of the results for the other top surfaces.

Figure 6-27: WT (top), CFD (middle) and Cp contours plot and graph (bottom) for the upwind brick's windward (outside) face at 45˚ (H/W=1.0).

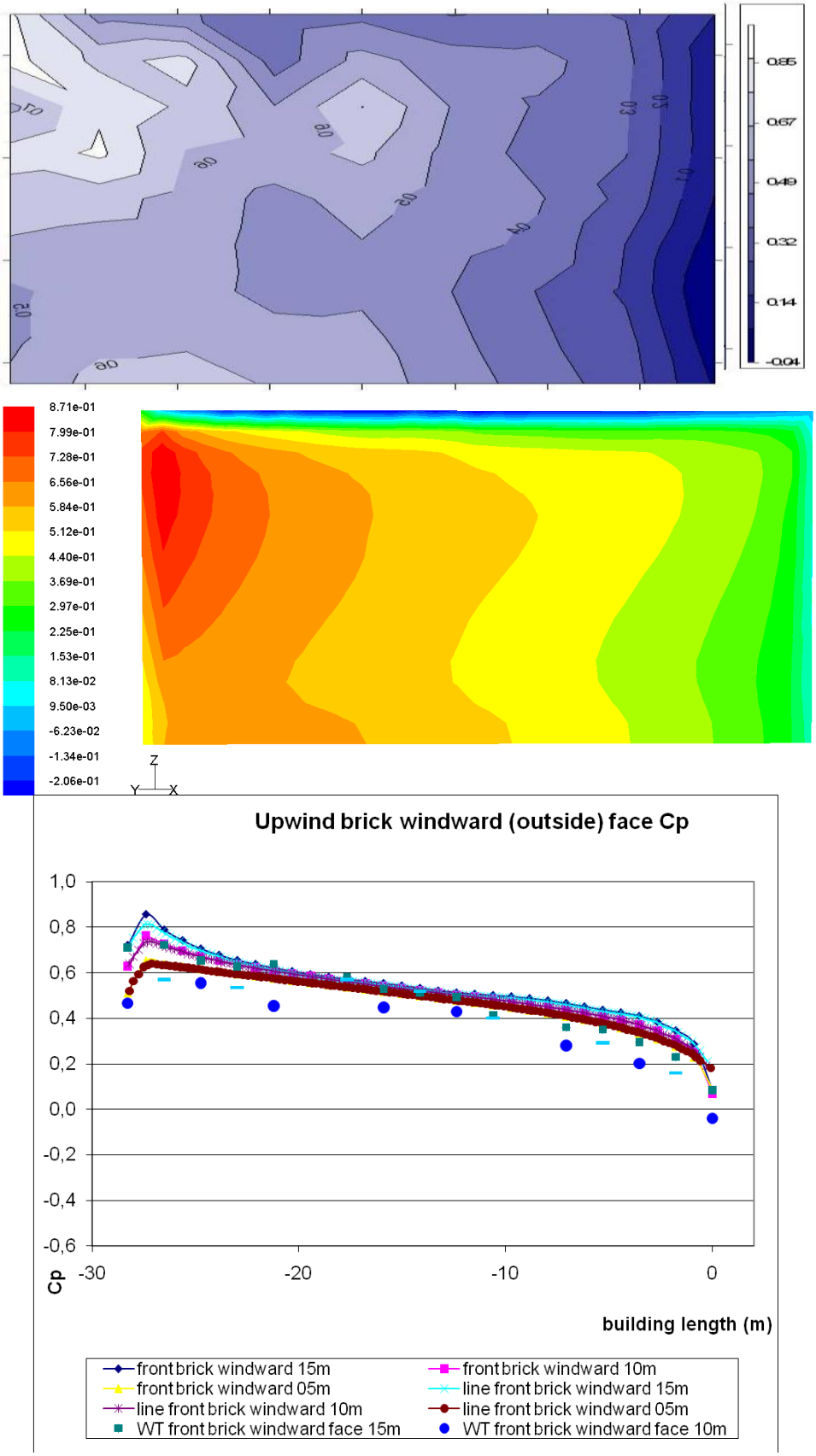

Source: this study.

Figure 6-28: WT (top), CFD (middle) and Cp contours plot and graph (bottom) for the downwind brick's leeward face at 45° (H/W=1.0).

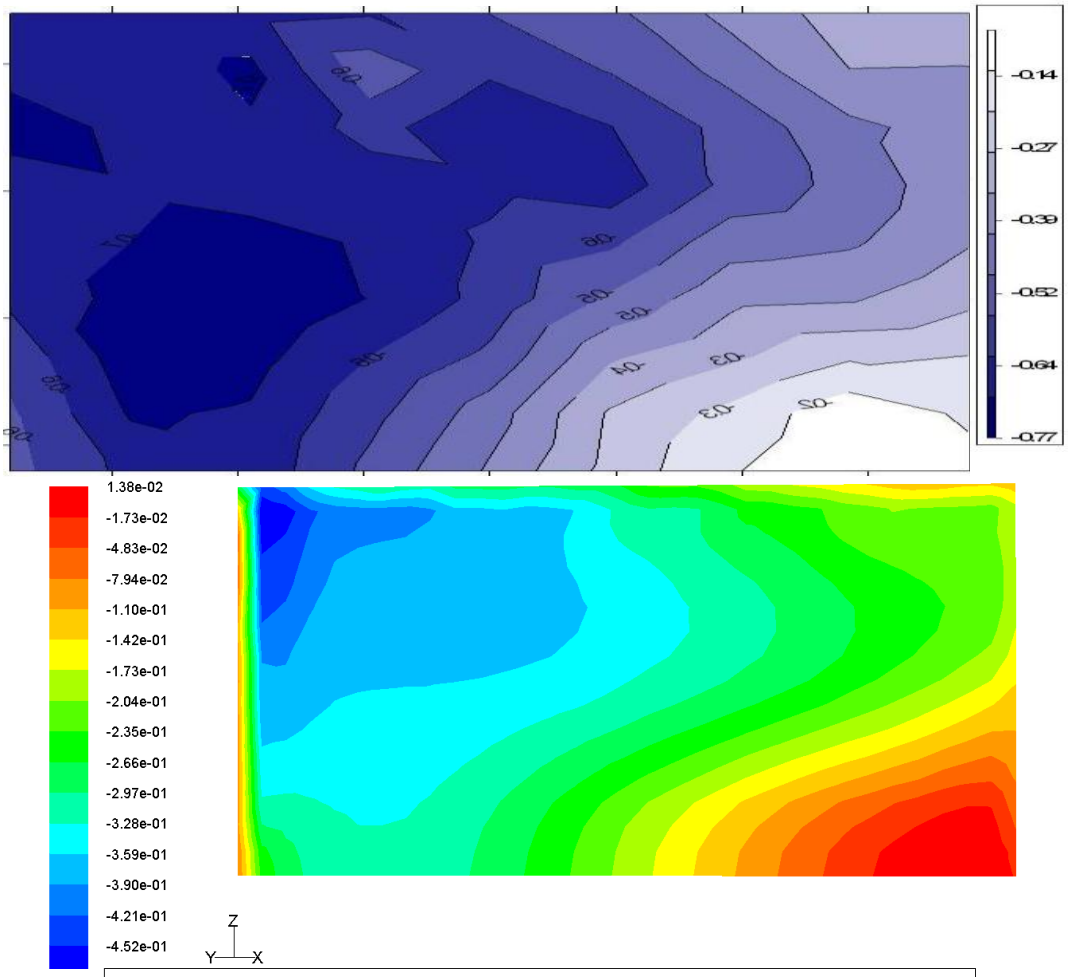

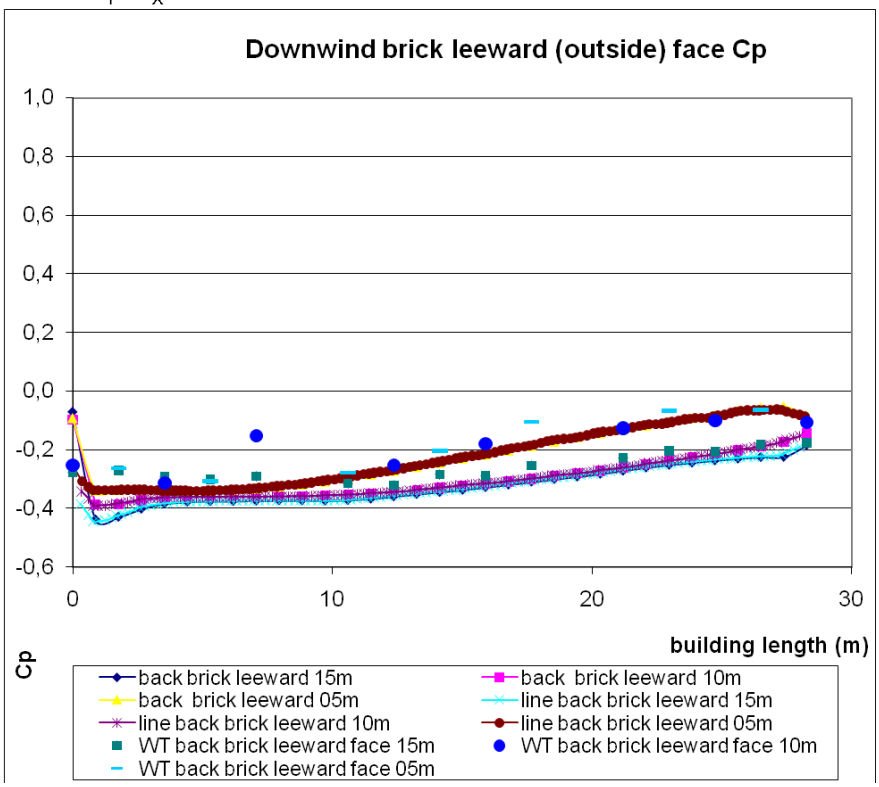

Source: this study.

Figure 6-27 shows the results for the external side of the upwind brick for oblique winds. Although the contour plots from the WT do not mark the FS point as precisely as in the CFD, good equivalence between both for Cp results and contours was found. Figure 6-28 show the results for the rear side of the downwind brick. Here good similarity between the WT and the CFD results is seen as well.

Figure 6-29 shows the results for the rear side of the upwind brick for an aspect ratio of 1.0. Good equivalence between both the WT and CFD contours plot and Cp range of results can once more be observed. When WT results for H/W= 1.0 are contrasted with those for H/W at 2.0, 0.66 and 0.50 aspect ratios (Figures 6-30 to 6-32: only wind tunnel experiments were performed for this specific set of pair of bricks), a quite similar range of results and overall contour patterns may be observed. On the other hand, the area of high pressure on the left side near ground increases gradually from the widest to the narrowest set of bricks.

Good similarity was also found for the windward side of the downwind brick for H/W= 1.0 (Figure 6-33), and its contrast with the other aspect ratios (H/W= 2.0, 0.66 and 0.50- Figures 6-34 to 6-36: only wind tunnel experiments were performed for this specific set of pair of bricks), although the high pressure spot was found on the top right side of the surfaces.

Figure 6-29: WT (top), CFD (middle) and Cp contours plot and graph (bottom) for the upwind brick's leeward (inside) face at 45˚ (H/W=1.0).

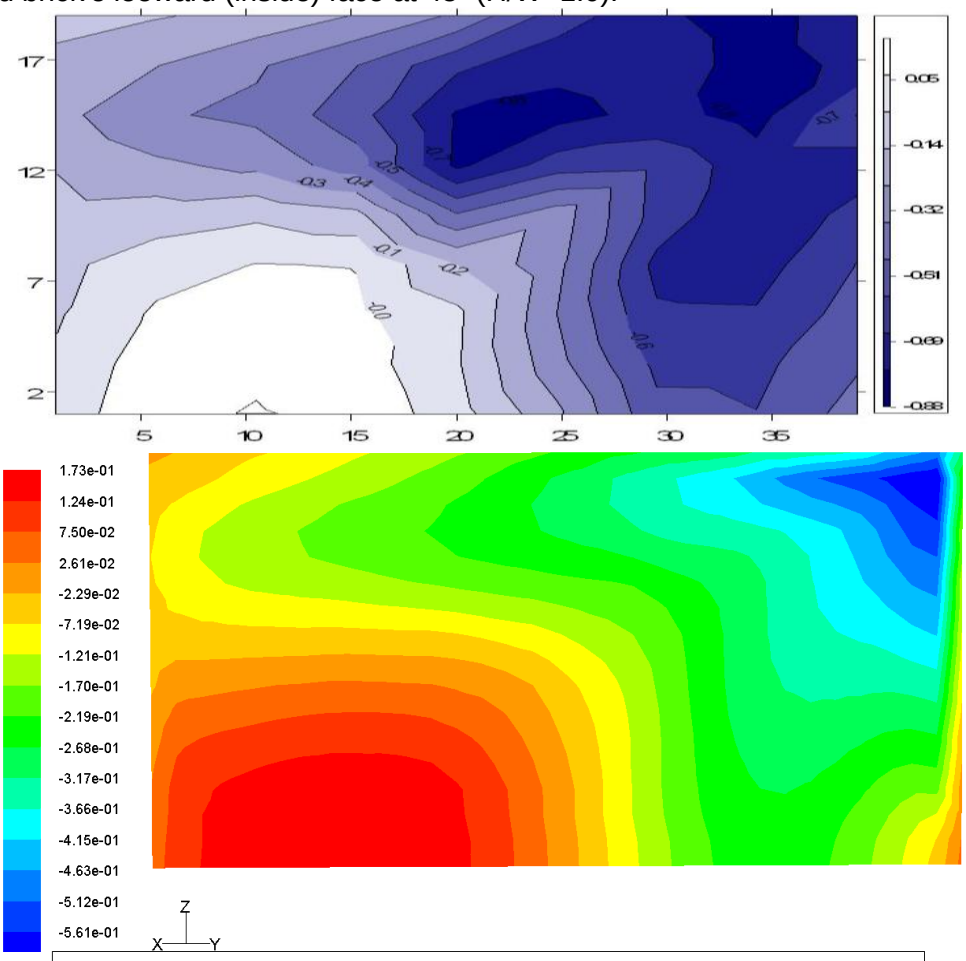

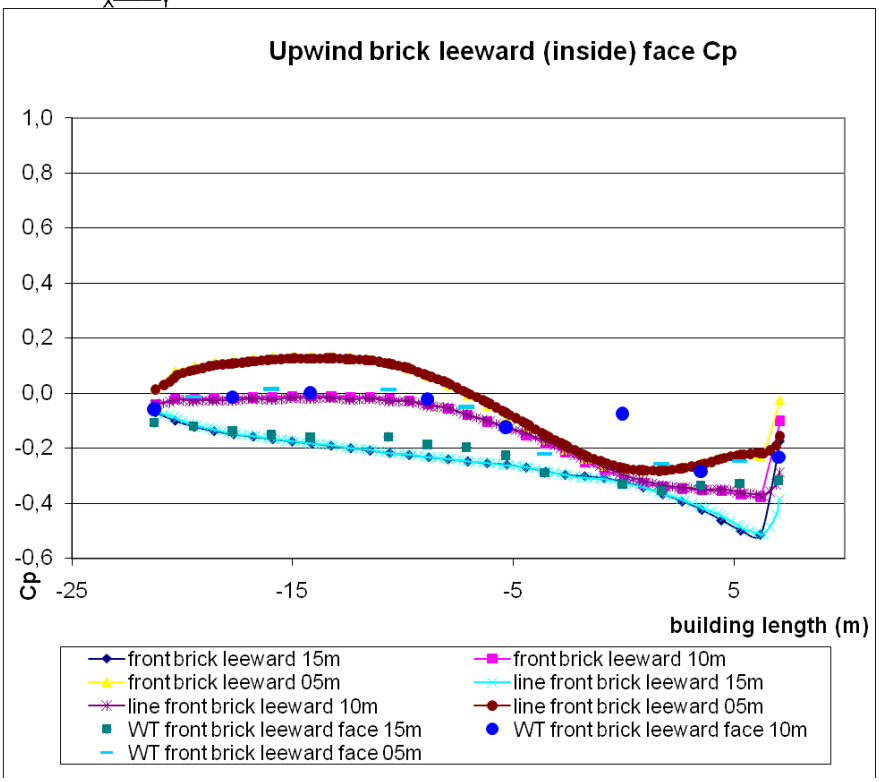

Source: this study.

Figure 6-30: WT (top), CFD (middle) and Cp contours plot and graph (bottom) for the upwind brick's leeward (inside) face at 45˚ (H/W=2.0).

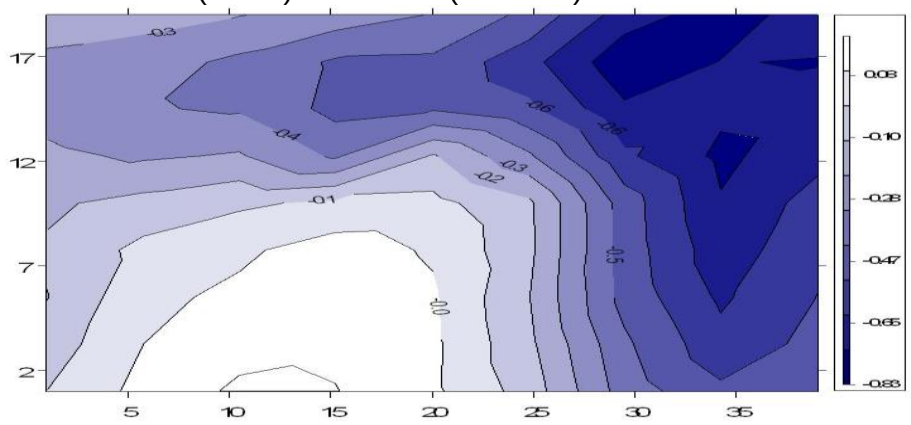

Source: this study.

Figure 6-31: WT (top), CFD (middle) and Cp contours plot and graph (bottom) for the upwind brick's leeward (inside) face at 45˚ (H/W=0.66).

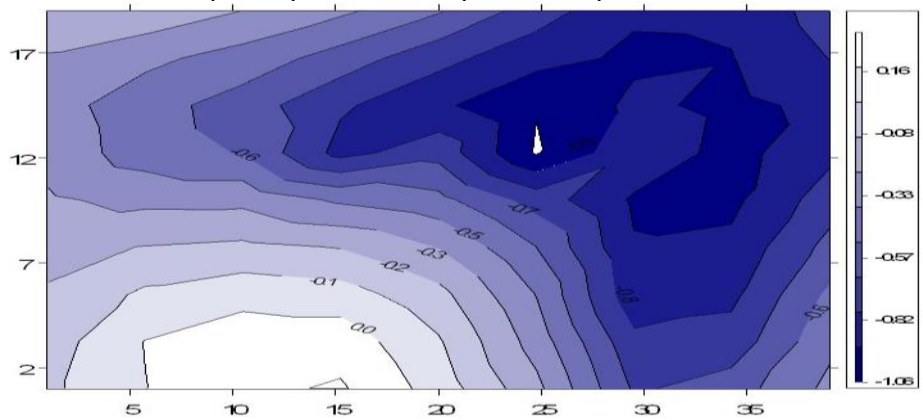

Source: this study.

Figure 6-32: WT (top), CFD (middle) and Cp contours plot and graph (bottom) for the upwind brick's leeward (inside) face at 45˚ (H/W=0.66).

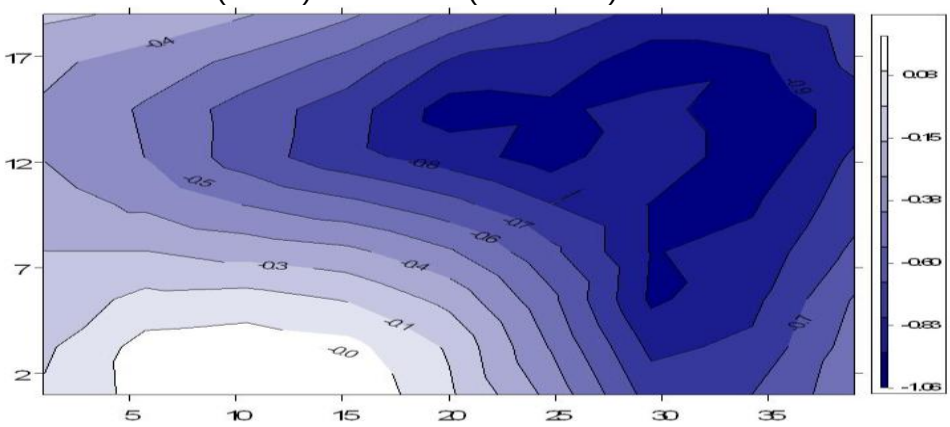

Source: this study.

Figure 6-33: WT (top), CFD (middle) and Cp contours plot and graph (bottom) for the downwind brick's windward (inside) face H/W = 1.00

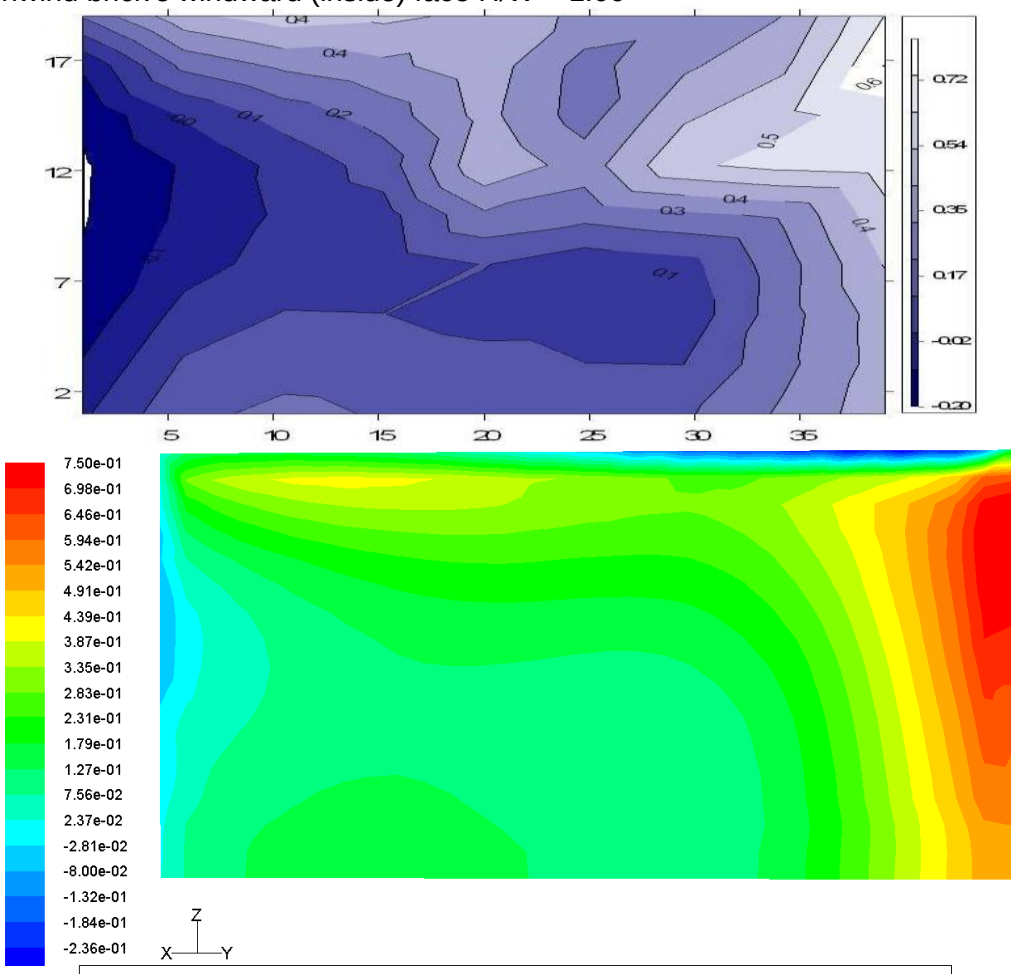

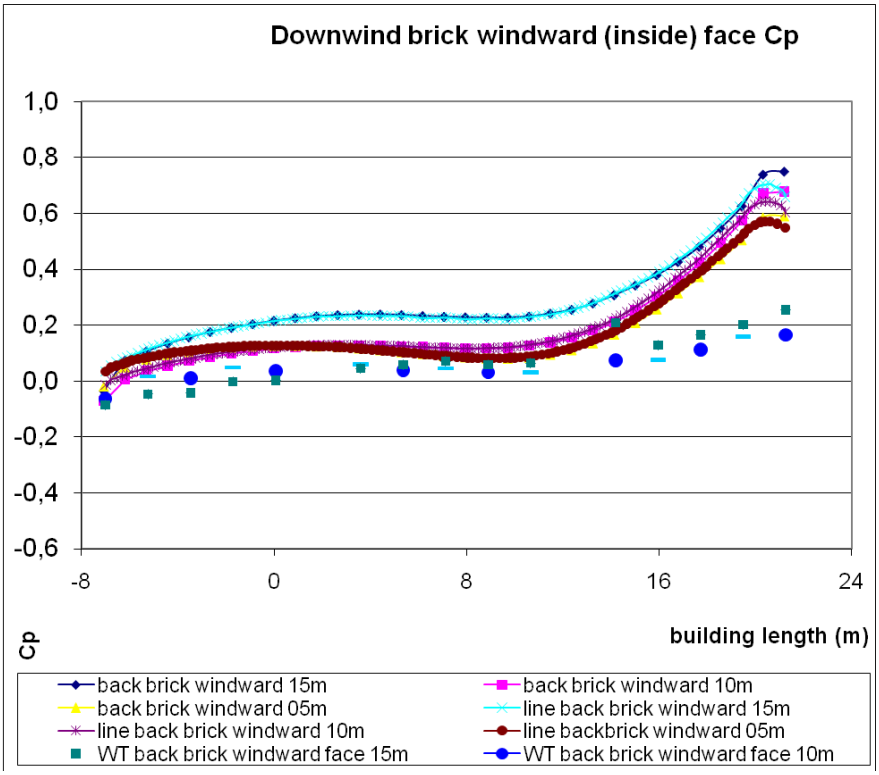

Source: this study.

Figure 6-34: WT (top), CFD (middle) and Cp contours plot and graph (bottom) for the downwind brick's windward face at 45˚ (H/W=2.00).

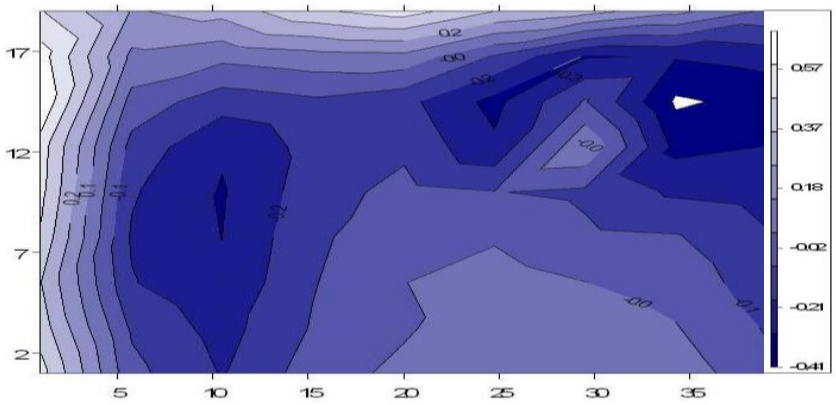

Source: this study.

Figure 6-35: WT (top), CFD (middle) and Cp contours plot and graph (bottom) for the downwind brick's windward face at 45˚ (H/W=0.66).

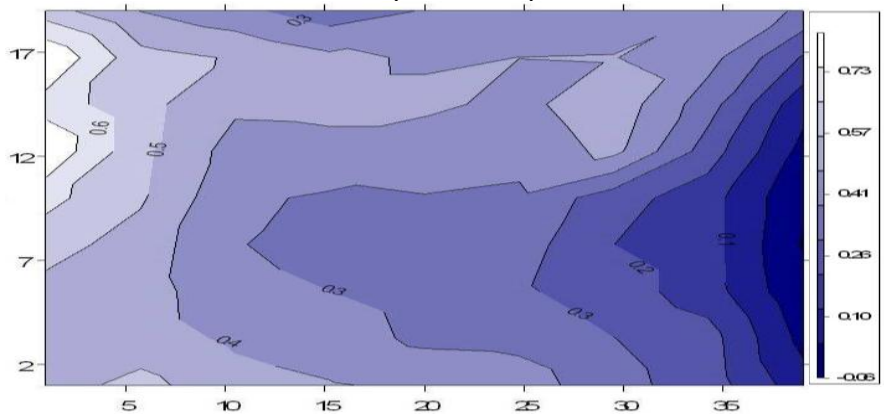

Source: this study.

Figure 6-36: WT (top), CFD (middle) and Cp contours plot and graph (bottom) for the downwind brick's windward face at 45˚ (H/W=0.50).

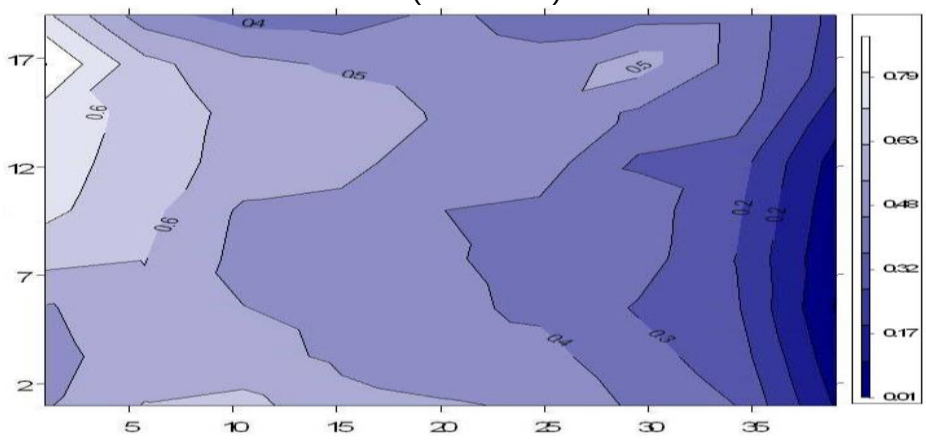

Source: this study.

6.5. WT and Cp: comparison of average results

Here the total averaged Cp results for the windward and the leeward faces of each block and from both WT and CFD experiments will be compared to results given in the literature[78] (Liddament, 1996). As mentioned in Chapter 5, the ABL achieved in the WT experiments and also employed in the CFD simulations is comparable to an urban terrain wind profile. On the other hand, the literature of reference presents results for three types of terrain: open field, sub-urban, and urban areas. Further, while the experiments conducted in this research relate to a set of two parallel rectangular bricks, the results reported in the reference literature are based on an isolated rectangular volume. Finally, not all the sets of H/W bricks that were investigated in the WT were simulated in the CFD.

Regarding the comparison of the Cp total average results, good agreement was found in most of the scenarios. On the other hand, for those sets of comparison where divergent results were observed either between the WT and the CFD or between both and the reference literature, a consistent pattern related to either the H/W aspect ratio or the wind incidence was found. Based on the figures presented, it may be affirmed that there is close agreement between the WT and the CFD Cp average results for the windward side of the upwind brick with orthogonal prevailing winds. These figures also matched those for open field ABL from the reference literature well. Agreement was also found for the same windward side for oblique winds. As for the windward side of the downwind brick (inside the canyon) with orthogonal prevailing winds, the results agree for the 0.50 and 0.66 H/W aspect ratios, which are the widest ones. For the 1.0 and the 2.0 H/W, which are, respectively, square and narrow canyon scenarios, the CFD results were around 0.20 greater than the WT ones. Conversely, for oblique winds the Cp results agree well between both methods of research for the 0.50, 0.66, and the 1.00 H/W scenarios, the CFD result above the WT for the 2.0 H/W narrow canyon maintaining the same Cp difference of 0.20. On the other hand, the Cp results for the leeward side, while the upwind brick's leeward face in the WT and the CFD experiments were contrasted between them, the results for the downwind brick's leeward face from both the WT and the CFD experiments were compared also to the single brick's leeward face as reported in the literature. Regardless of the wind's orientation (45^o or 90^o) and the brick's position, it was found that the CFD Cp results exceeded those of the WT results by a constant 0.35 and 0.30 for the 0.50 and 0.66 H/W, and the 1.0 and 2.0 H/W aspect ratio canyons, respectively. Alternatively, the WT

[78] These Cp values refer to an isolated rectangular-shaped volume found in Liddament (1996) which is also adopted as a reference by both Awbi (2003) and the CIBSE A (2006). For further results and details on this literature see topic 2.4 in Chapter 2 and Table 6-1 below.

Cp results for the downwind brick's leeward face match well with those given in the literature for ABL urban areas.

Furthermore, close agreement of Cp averaged results was also found for parallel winds to the set of bricks between the WT, the CFD, and the reference literature (with ABL for urban areas), although the CFD results were consistently around 0.10 greater than either one of the other sources.

Finally, regarding the difference found between the pressure results of the WT experiments and the CFD, it may be due to either the type of the κ-ε computational steady-state flow solver model adopted and/ or the number of pressure taps used in the WT models - or both[79]. It is acknowledged that the flow solver model used has limitations in reproducing leeward wake flow detachment and in capturing the nuances of the consequent pressure drop on the rear surfaces, even with an increase in mesh refinement. An alternative would be to use a Large Eddy Simulation (LES) time-state flow solver model suggested as an alternative for overcoming this limitation. On the other hand, it is worth mentioning that the time and the computing memory demanded by this alternative solution made it impracticable for the investigation required for this thesis. Regarding the WT experiments, the position and number of pressure taps are directly linked to the resulting data quality; though the literature review shows there is an inaccuracy of up to 20% in WT results as well. A comparison of the quantitative and qualitative data from both WT and CFD is shown below in order to illustrate this question:

[79] For further results and details on this literature see topics 3.5.3.10 and 3.5.3.11 in Chapter 3.

Figure 6-37: WT and CFD Cp contour plot for the upwind brick's windward face (90˚, H/W=1.0): 0.19 to +0.94 (WT), and -0.37 to +0.83 (CFD).

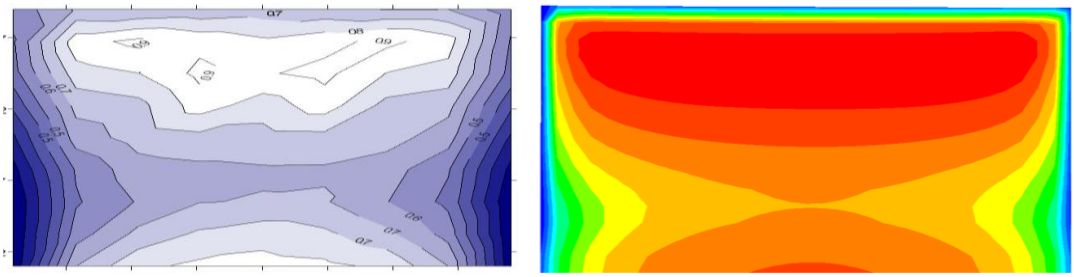

Source: this study.

Figure 6-38: WT and CFD Cp contour plot for the upwind brick's leeward face (90˚, H/W=1.0): -0.20 to -0.08 (WT), and -0.10 to +0.07 (CFD).

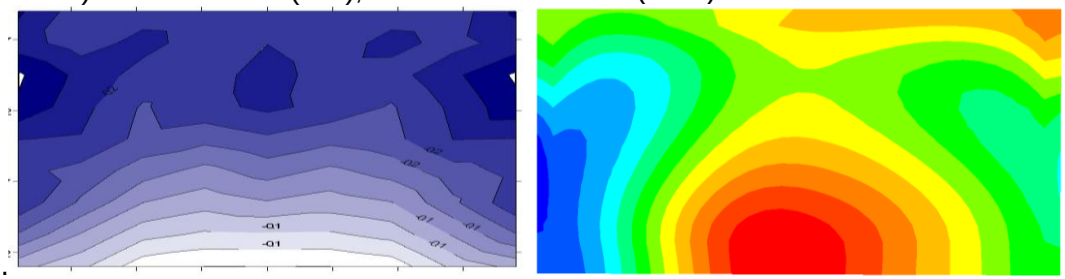

Source: this study.

Figure 6-39: WT and CFD Cp contour plot for the downwind brick's windward face (90˚, H/W=1.0): : -0.32 to +0.40 (WT), and0.03 to +0.30 (CFD).

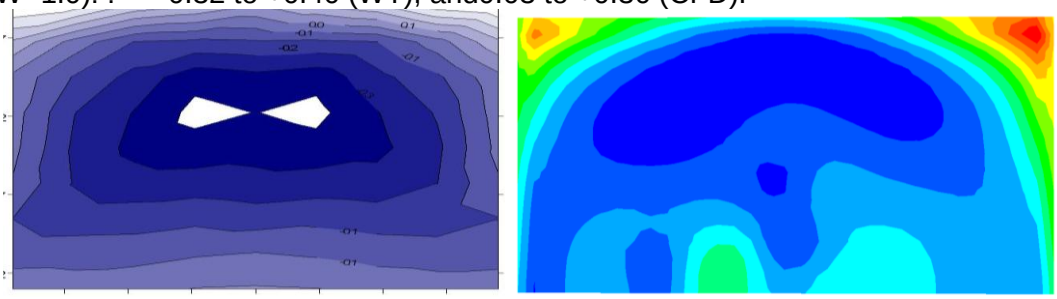

Source: this study.

While the Cp contour plots from both WT and CFD outputs are similar, the range of Cp values seems to be smaller in the CFD simulation than in the WT physical experiments. Nonetheless, the total difference between maximum and minimum values is small and proportional.

Figure 6-40: Comparison of the Cp values for the downwind brick's windward face for the four H/W variations and wind incidence at 90°.

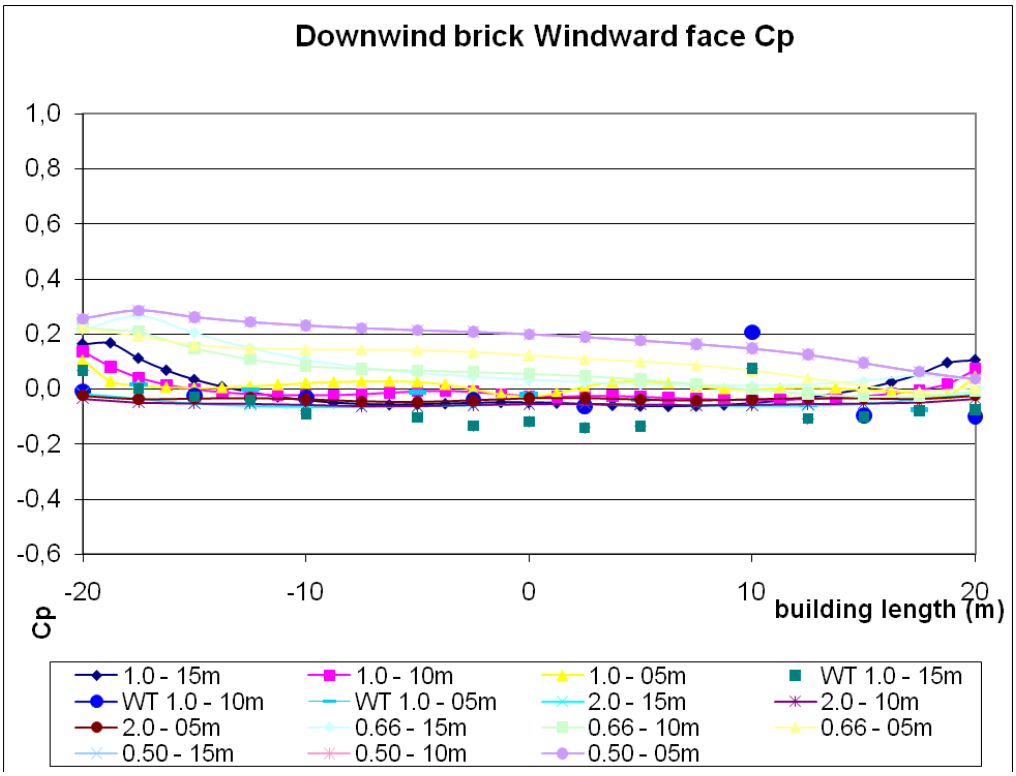

Source: this study.

Figure 6-41: Comparison of the Cp values for the upwind brick's leeward face for the four H/W variations and wind incidence at 90°

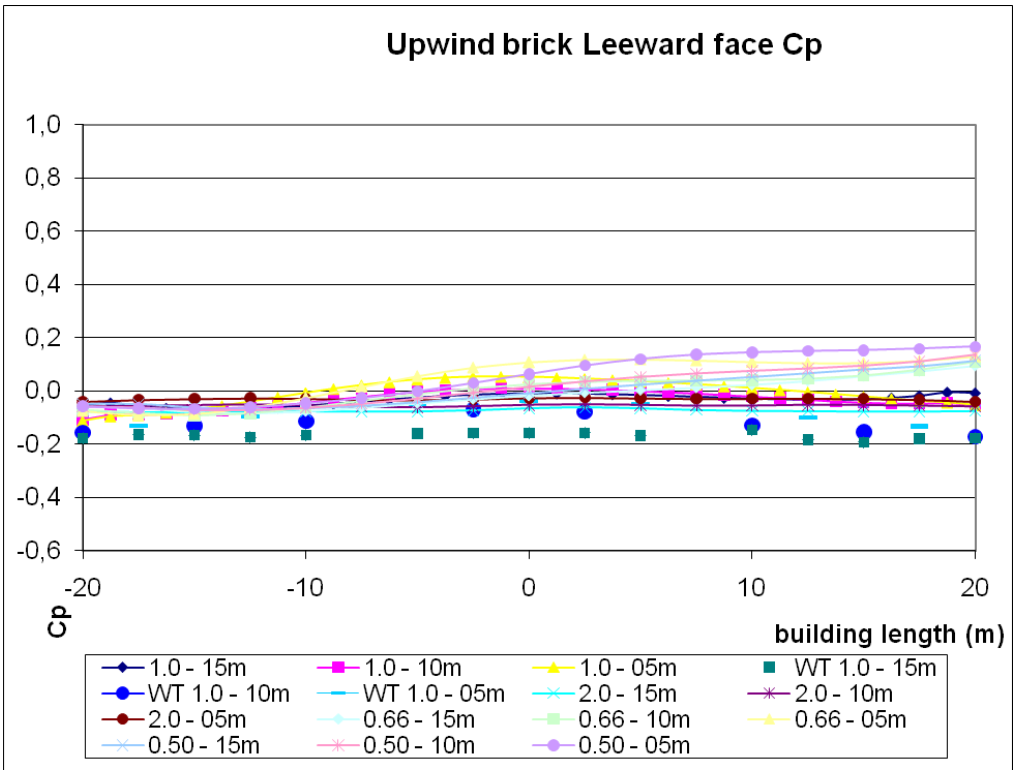

Source: this study.

Figure 6-42: Comparison of the Cp values for the downwind brick's windward face for the H/W= 1.0 and the three wind incidences (90°, 45° and 0°)

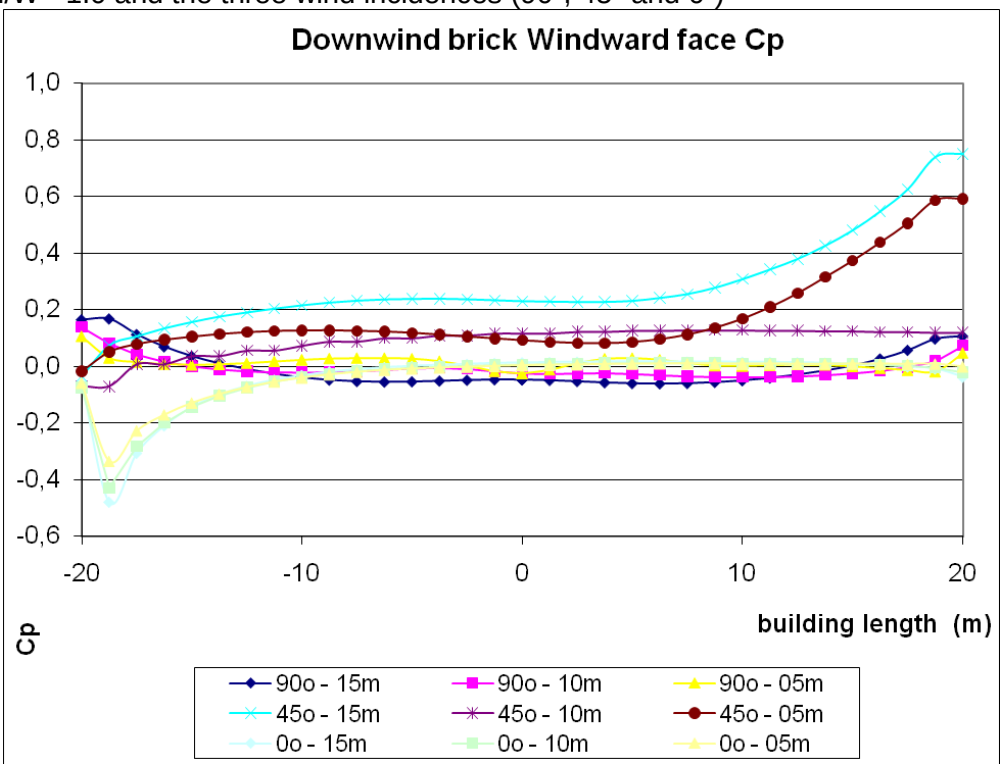

Source: this study.

Figure 6-43: Comparison of the Cp values for the upwind brick's leeward face for the H/W= 1.0 and the three wind incidences (90°, 45° and 0°)

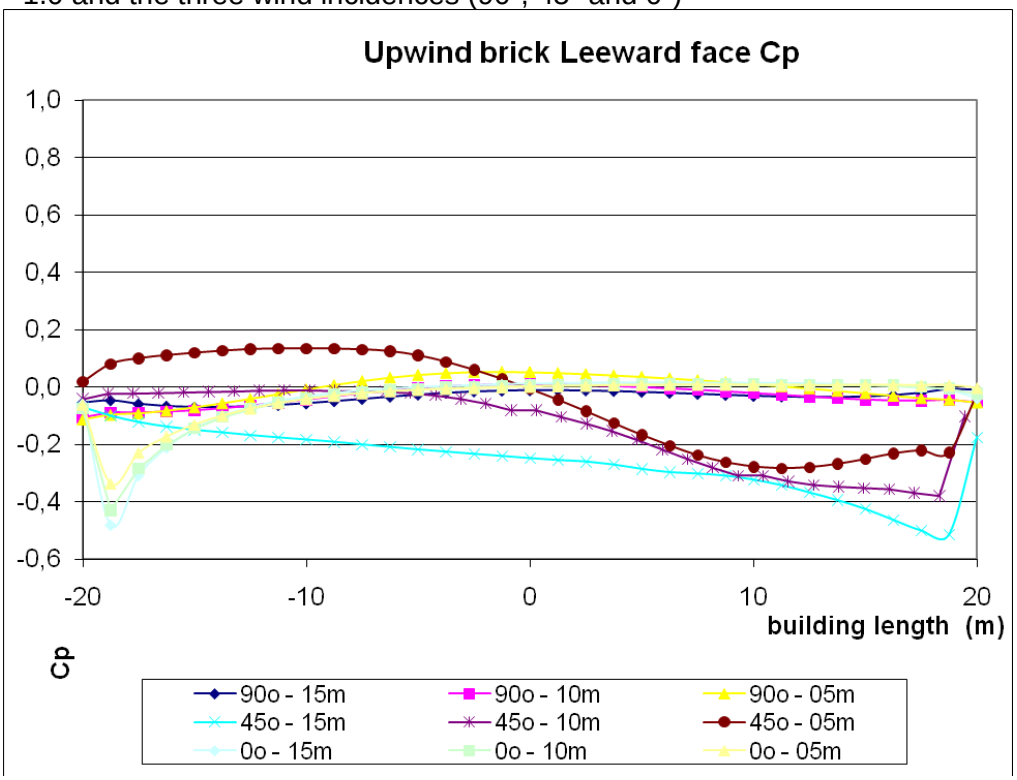

Source: this study.

Table 6-1: Cp results from the sets of WT and CFD experiments and those found in the literature:

Cp averaged results		H/W aspect ratio								Liddament (1996)		
wind α	face	0,50		0,66		1,00		2,00		open field	sub-urban areas	*urban areas*
		WT	CFD	WT	CFD	WT	CFD	WT	CFD			
0˚	left brick inside	-0.19	-	-0.17	-	-0.160	-0.051	-0.16	-	-0.50	-0.35	*-0.20*
	left brick outside	-0.18	-	-0.17	-	-0.170	-0.046	-0.16	-	-	-	-
	right brick inside	-0.19	-	-0.15	-	-0.150	-0.045	-0.18	-	-	-	-
	right brick outside	-0.17	-	-0.17	-	-0.160	-0.049	-0.17	-	-0.50	-0.35	*-0.20*
45˚	front brick windward	0.43	-	0.43	-	0.43	0.540	0.43	-	0.25	0.20	*0.15*
	front brick leeward	-0.57	-	-0.53	-	-0.43	-0.150	-0.37	-	-	-	-
	rear brick windward	0.42	-	0.35	-	0.20	0.234	-0.03	-	-	-	-
	rear brick leeward	-0.54	-	-0.54	-	-0.54	-0.270	-0.54	-	-0.60	-0.50	*-0.32*
90˚	front brick windward	0.64	0.690	0.64	0.690	0.64	0.690	0.64	0.670	0.60	0.25	*0.06*
	front brick leeward	-0.30	0.034	-0.29	0.029	-0.33	-0.013	-0.37	-0.051	-	-	-
	rear brick windward	0.29	0.210	0.10	0.120	-0.06	0.150	-0.25	-0.034	-	-	-
	rear brick leeward	*-0.34*	*0.067*	*-0.34*	*0.090*	*-0.34*	*0.015*	*-0.34*	*0.054*	*-0.70*	*-0.50*	*-0.30*

Source: this study and Liddament (1996).

6.6. Visualization of the airflow patterns

In this topic the airflow patterns resulting from both the CFD simulation and the WT experiments are compared. While in the former the airflow is visualized by vectors and pathlines, in the second the airflow is seen in the still-image pictures taken with the helium bubble visualization technique[80]. This latter technique only permitted the taking of pictures of airflow perpendicular to the flow, only. Therefore, the analysis of the airflow for parallel and oblique winds from CFD simulation will, therefore, be carried out by comparing its wind velocity vectors and pathlines with those given in the literature described in Chapter 2.

6.6.1. Bricks perpendicular to the airflow (at 90˚)

6.6.1.1. Brick's H/W aspect ratio of 1.00

The airflow patterns seen from the right side of the two bricks positioned with an H/W aspect ratio of 1.00 show similar features when contrasting the CFD results (Figures 6-44 and 6-45) with the WT sequence of images (Figure 6-46). An airflow detachment and consequent low pressure bubble is clearly seen on the horizontal top edge of the windward brick in both means of simulation and, above it, streamlines are accelerated. Further, the airflow patterns in the canyon area show a comparable internal clock-wise vortex in both images as regards position and length. The top view (Figure 6-44) shows that these vortices are divided along the two sides flowing almost symmetrically from the centre to the corners of the canyon. The leeward wake also shows vortices forming at the top height immediately beyond the second brick. Finally, the CFD pathlines show a clear FS point on the front side of the first brick which divides the upwards and dondwards flow at approximately three quarters of its height. These descriptions match those given in the literature well both as regards the airflow patterns around isolated bluff-bodies and the airflow perpendicular to the canyon's axis[81].

[80] See topic 5.5.1.3 in Chapter 5 for further information.
[81] See respectively topics 2.5 and 2.6 in Chapter 2.

Figure 6-44: Velocity vectors and pathlines on planes at 5.0 (top) and 10.0m (bottom) high (90˚; H/W=1.00, m/s).

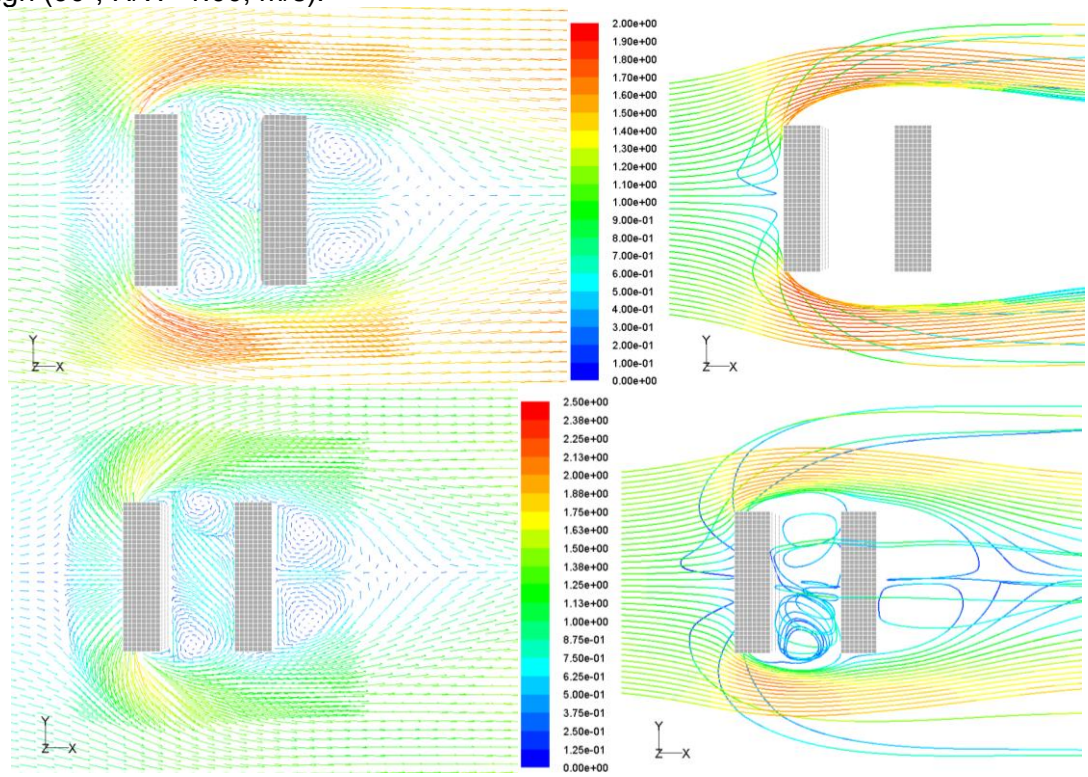

Source: this study.

Figure 6-45: Velocity magnitude pathline view (90˚; H/W=1.00, m/s).

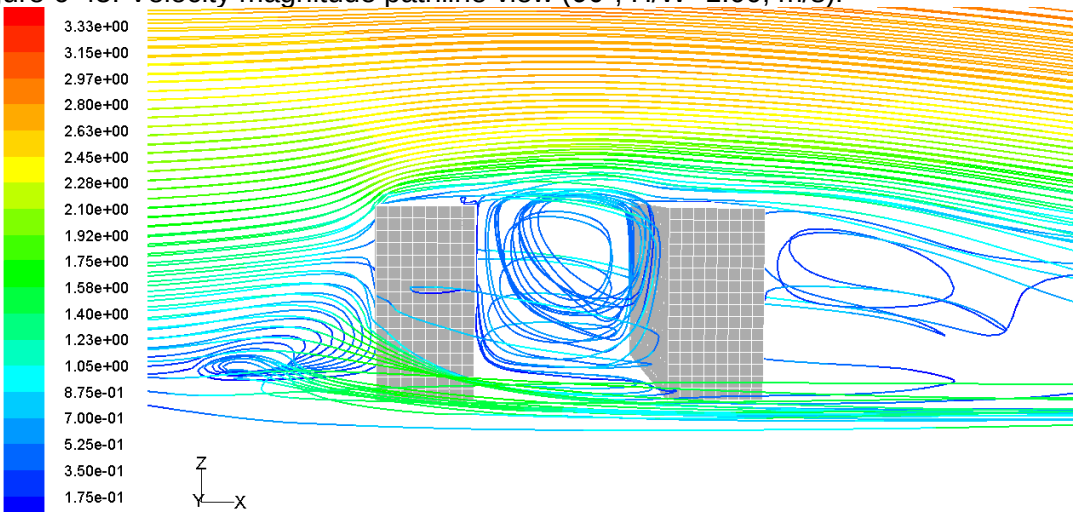

Source: this study.

Figure 6-46: Sequence of airflow visualization by using helium bubbles in the wind tunnel (90˚; H/W=1.0).

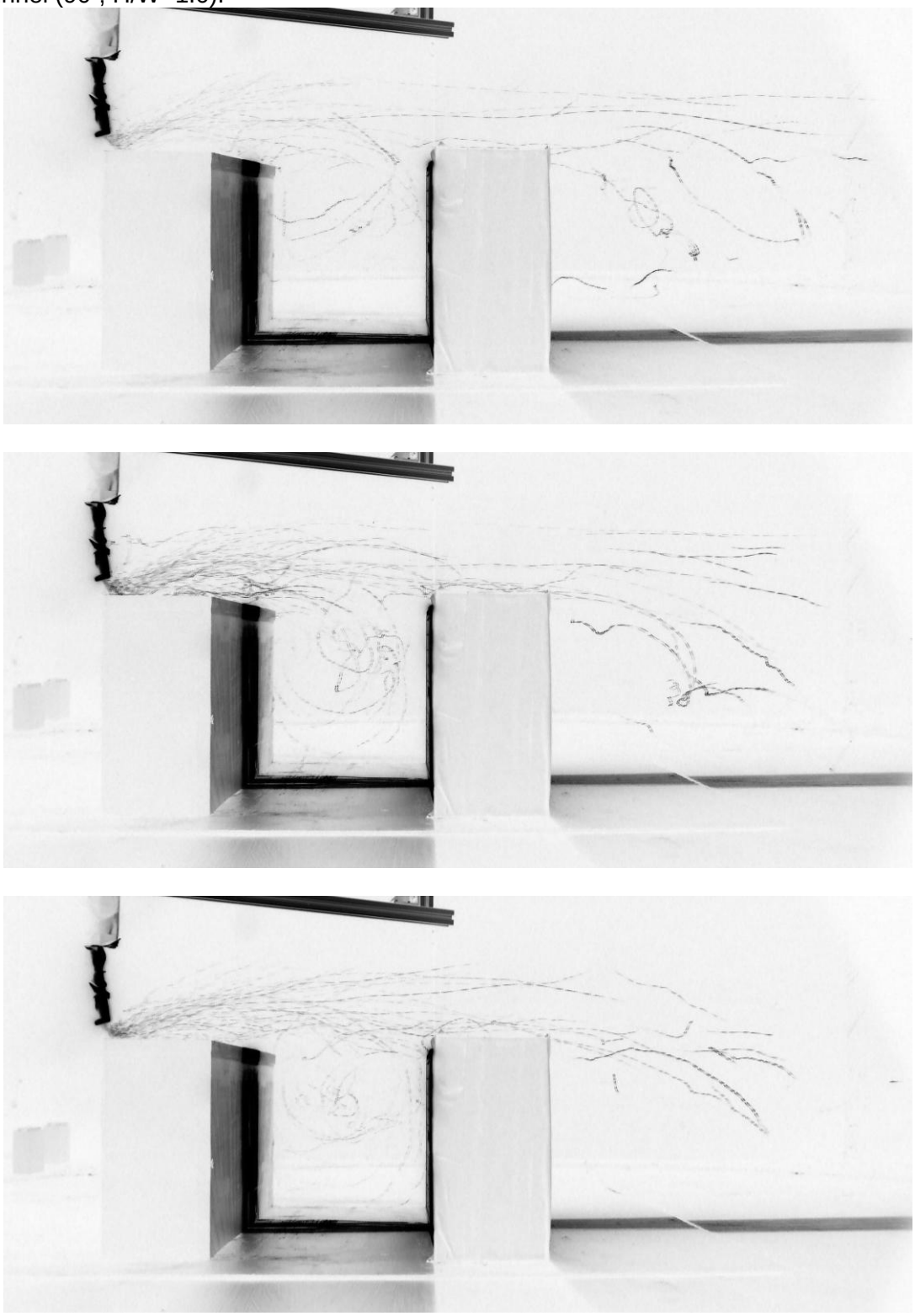

Source: this study.

6.6.1.2. Brick's H/W aspect ratio of 2.00

From the observation of the airflow patterns seen from the right side of the narrowest set of bricks investigated (H/W aspect ratio of 2.00- Figures 6-47 to 6-49) it may be concluded that the bulk of the airflow within the canyon area decreases considerably, which is an evidence of the occurrence of skimming flow. Further, the leeward wake seems to have its vortex elongated on both means of flow visualization.

Figure 6-47: Velocity vectors and pathlines on planes at 10.0 (top) and 15.0m (bottom) high (90˚; H/W=2.00, m/s).

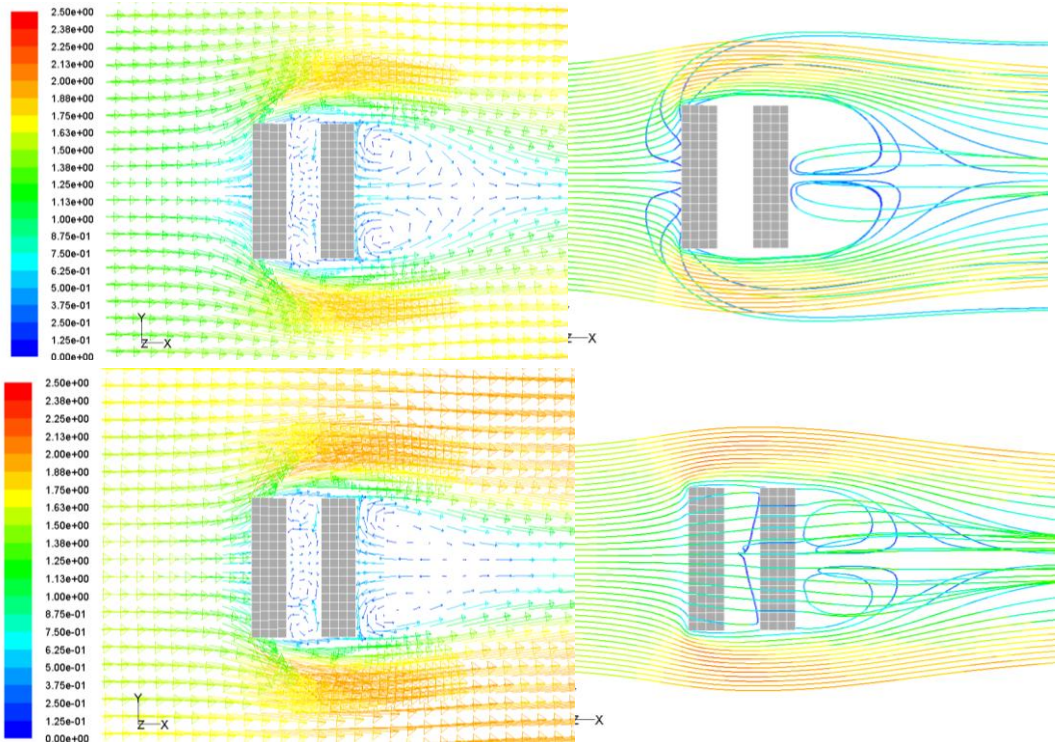

Source: this study.

Figure 6-48: Velocity magnitude pathline view (90˚; H/W=2.00, m/s).

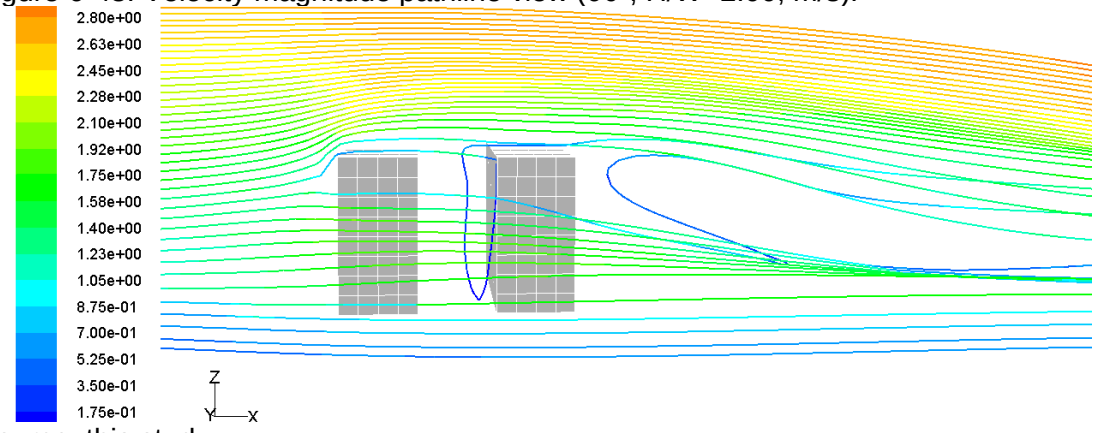

Source: this study.

Figure 6-49: Sequence of airflow visualization by using helium bubbles in the wind tunnel (90˚; H/W=2.0).

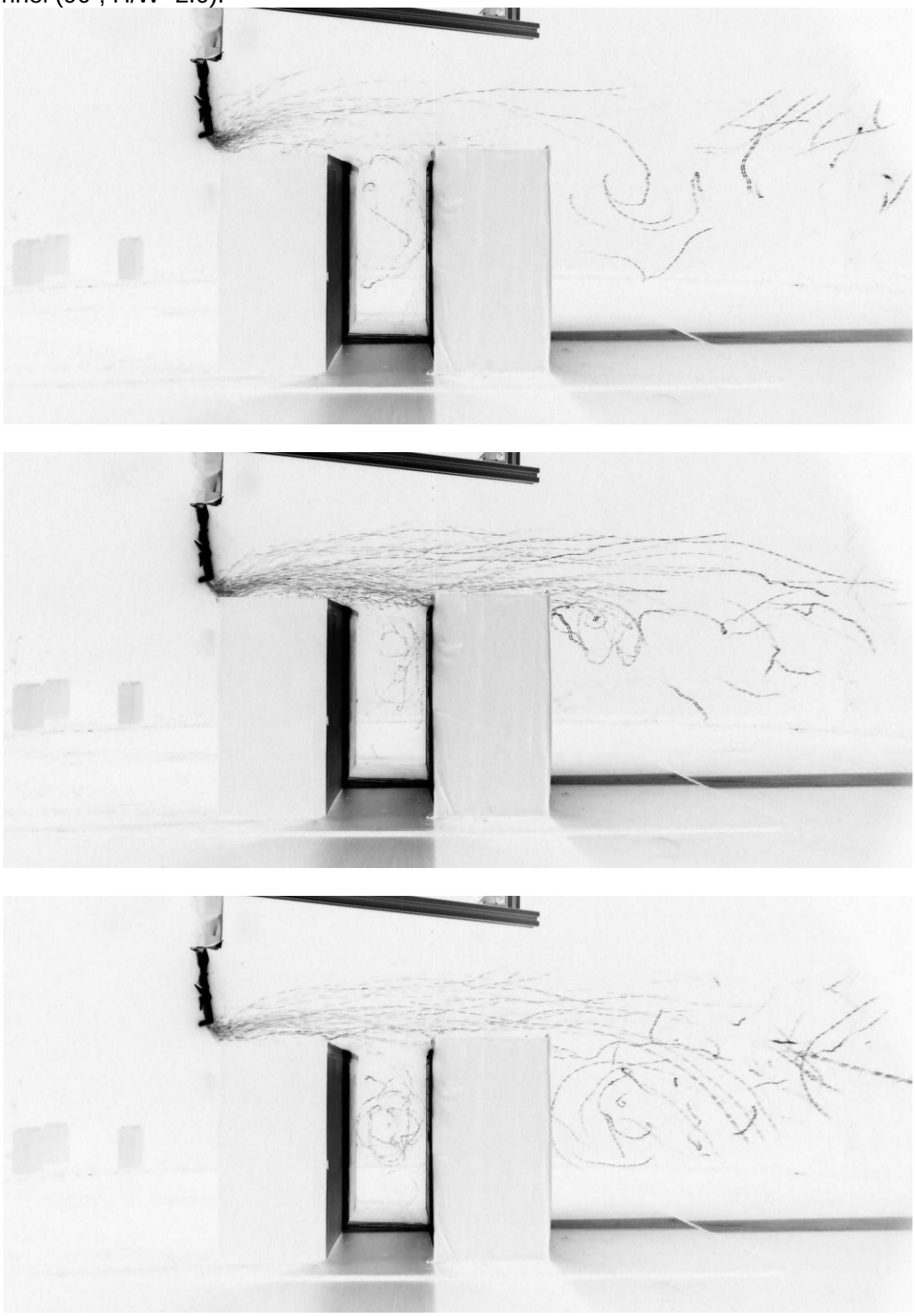

Source: this study.

6.6.1.3. Brick's H/W aspect ratio of 0.66

When compared to those of the square canyon previously analysed, the airflow patterns in the canyon area show an unbalanced internal clock-wise vortex which turns unevenly towards the corners of the canyon. This is clearly seen in Figures 6-50 and 6-51 (CFD), while in the WT image (Figure 6-52) it is blurred. On the other hand, the leeward wake shows similar in the vortices by either means of visualization.

Figure 6-50: Velocity vectors and pathlines on planes at 5.0 (top) and 10.0m (bottom) high (90˚; H/W=0.66, m/s).

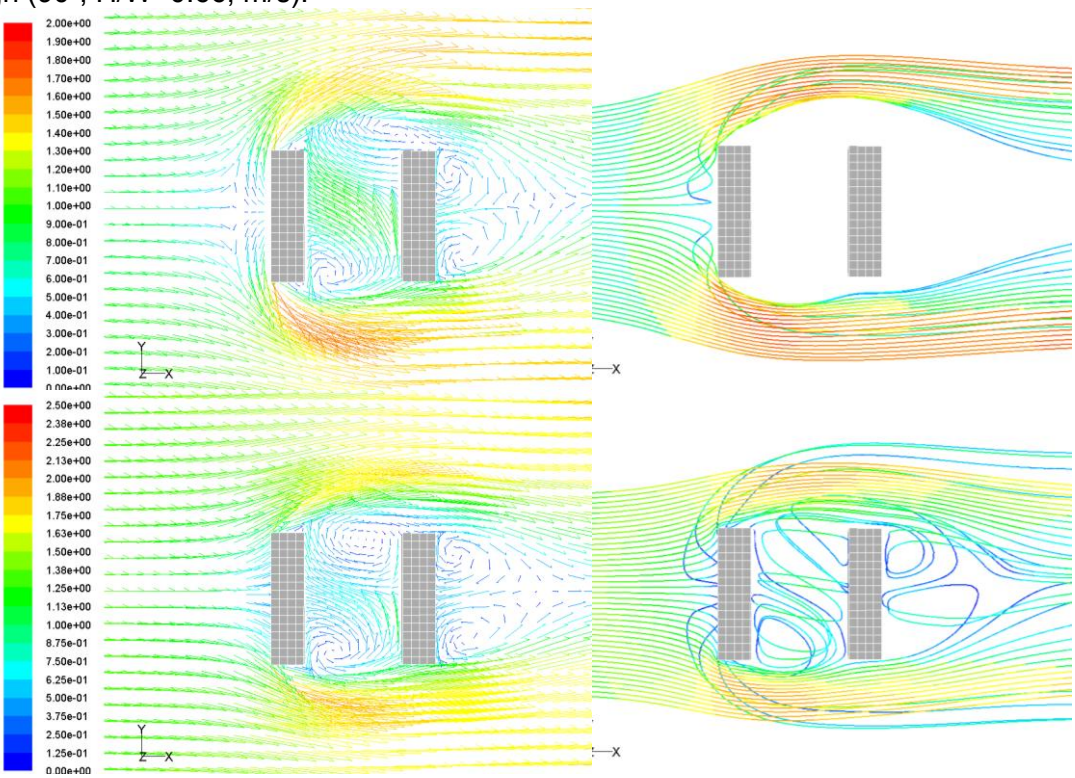

Source: this study.

Figure 6-51: Velocity magnitude pathline view (90˚; H/W=0.66).

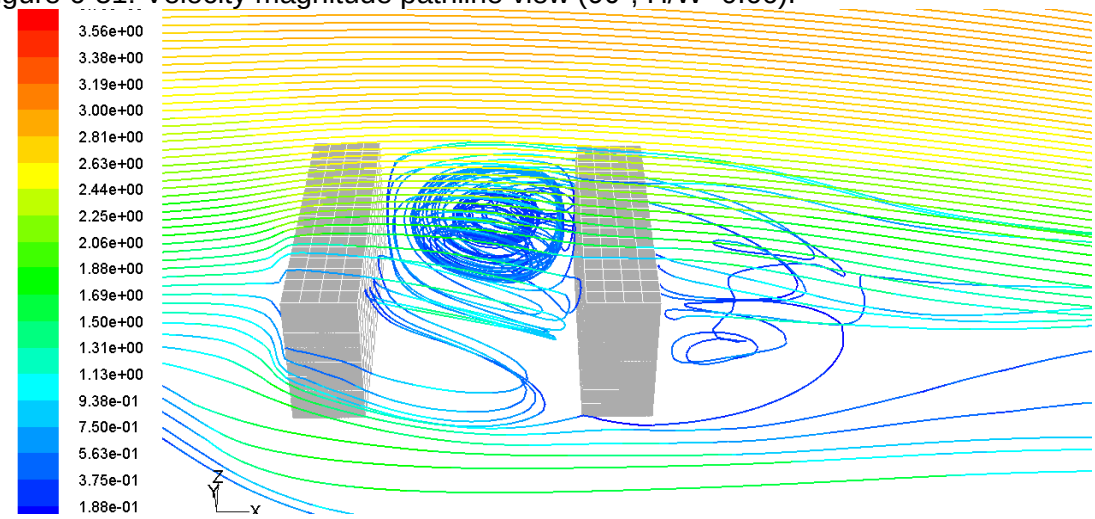

Source: this study.

Figure 6-52: Sequence of airflow visualization by using helium bubbles in the wind tunnel (90˚; H/W=0.66).

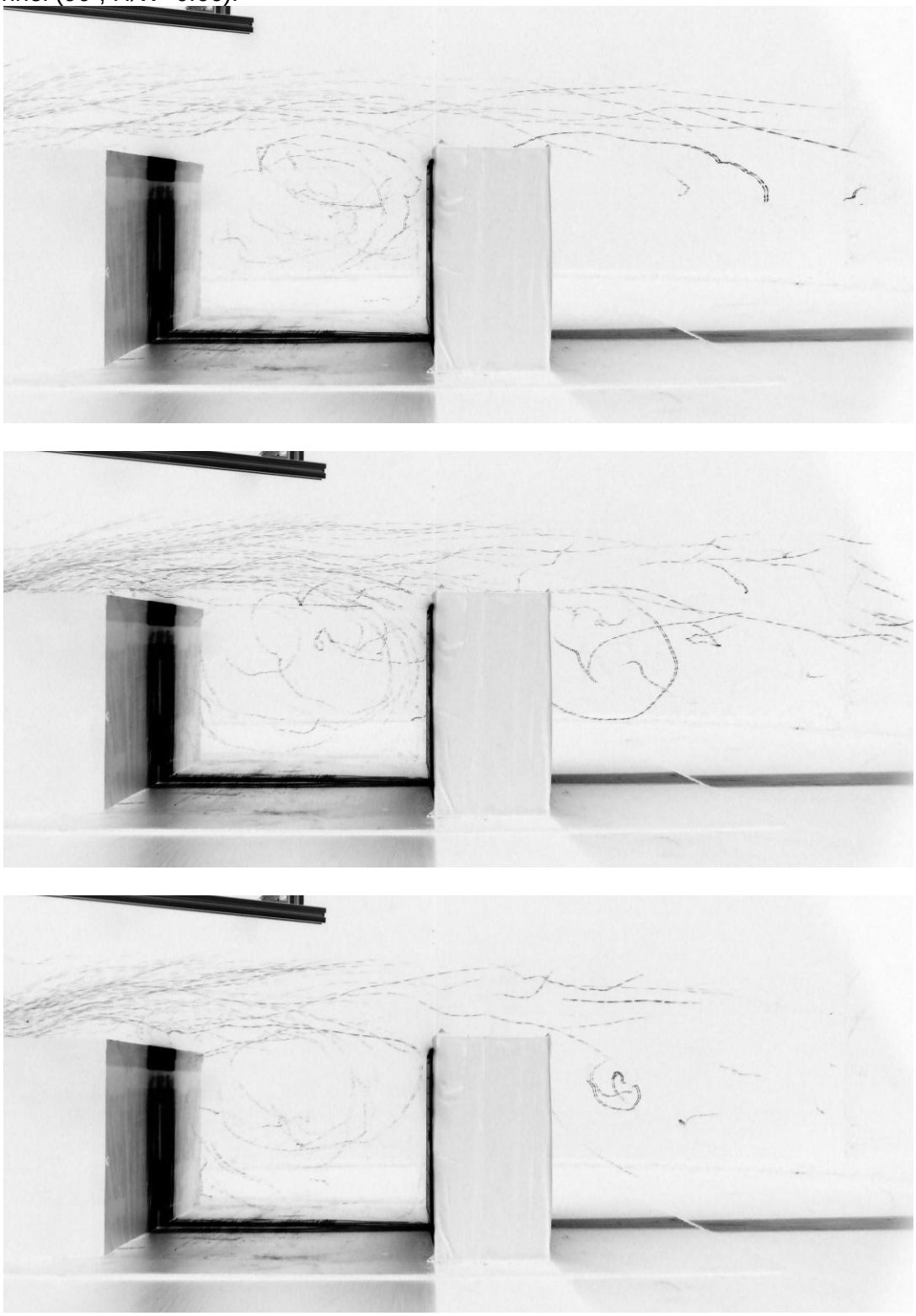

Source: this study.

6.6.1.4. Brick's H/W aspect ratio of 0.50

For wider canyons with an H/W aspect ratio of 0.50, the images from the CFD results (Figures 6-53 and 6-54) show an intensified uneven distribution of the internal vortex, which acquires a diagonal spiral shape across the cavity. It is not possible in the first sequence of images of the WT experiments (Figure 6-55) to identify clearly the internal vortex or determine whether wake interference occurs, although the leeward wake can be seen. On the other hand, the internal vortex becomes clearer in the subsequent WT sets of experiments when the two bricks are separated further to represent an H/W aspect ratio of 0.33 (Figure 6-56), though this aspect ratio was not simulated in CFD.

Figure 6-53: Velocity vectors and pathlines on planes at 5.0 (top) and 10.0m (bottom) high (90˚; H/W=0.50, m/s).

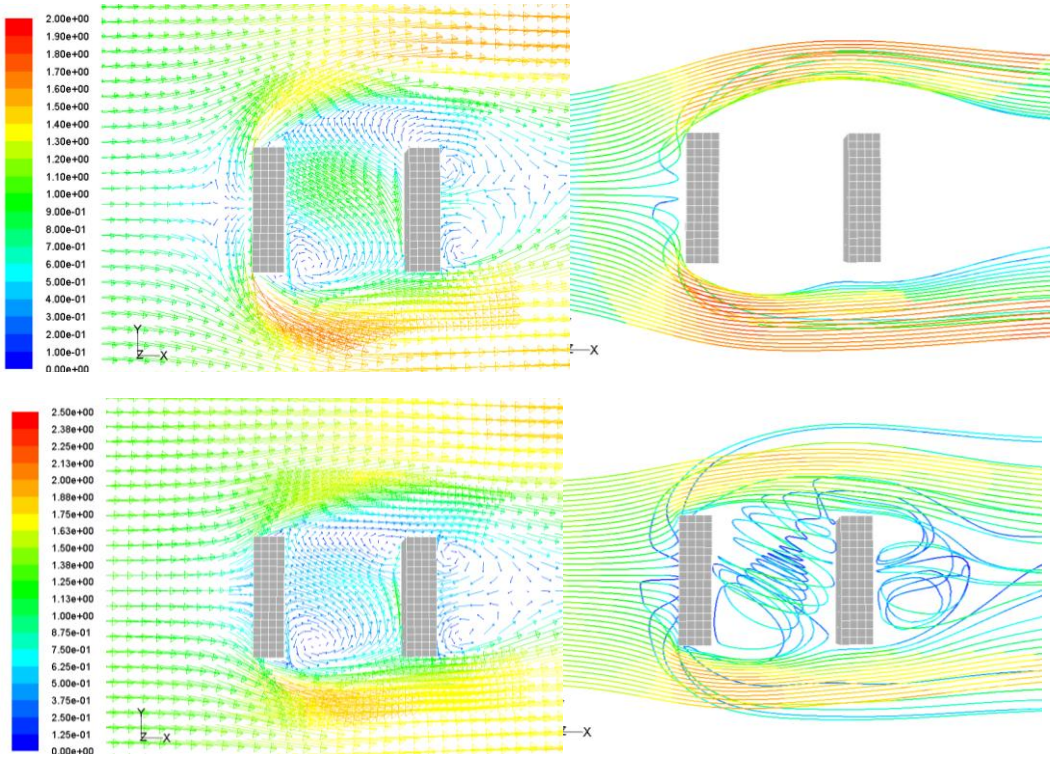

Source: this study.

Figure 6-54: Velocity magnitude pathline view (90˚; H/W=0.50).

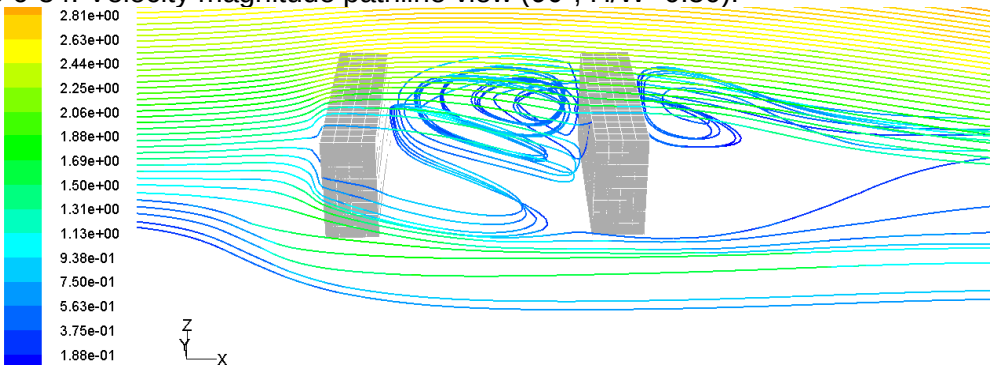

Source: this study.

Figure 6-55: Sequence of airflow visualization by using helium bubbles in the wind tunnel (90˚; H/W=0.50).

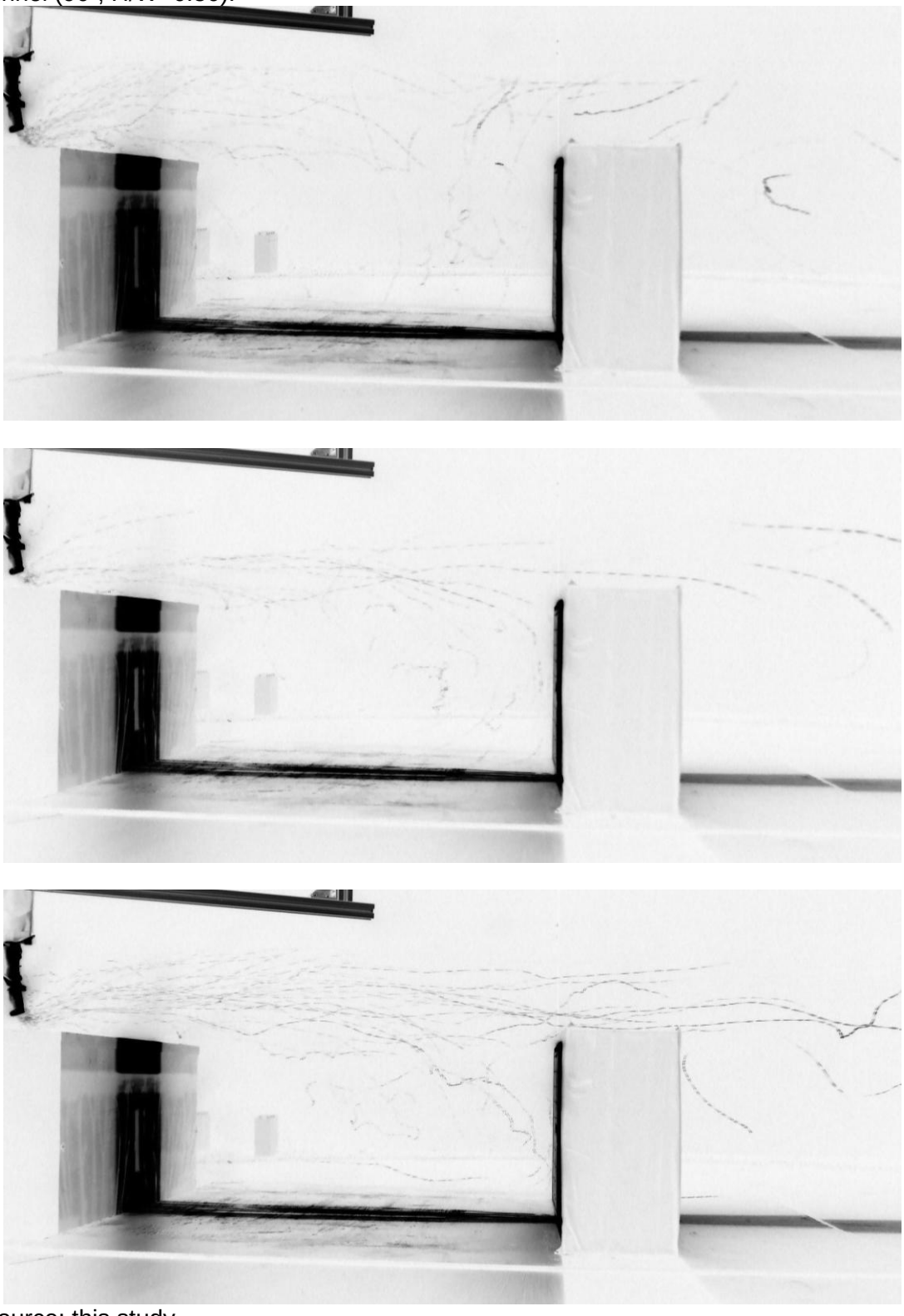

Source: this study.

Figure 6-56: Sequence of airflow visualization by using helium bubbles in the wind tunnel (90˚; H/W=0.33).

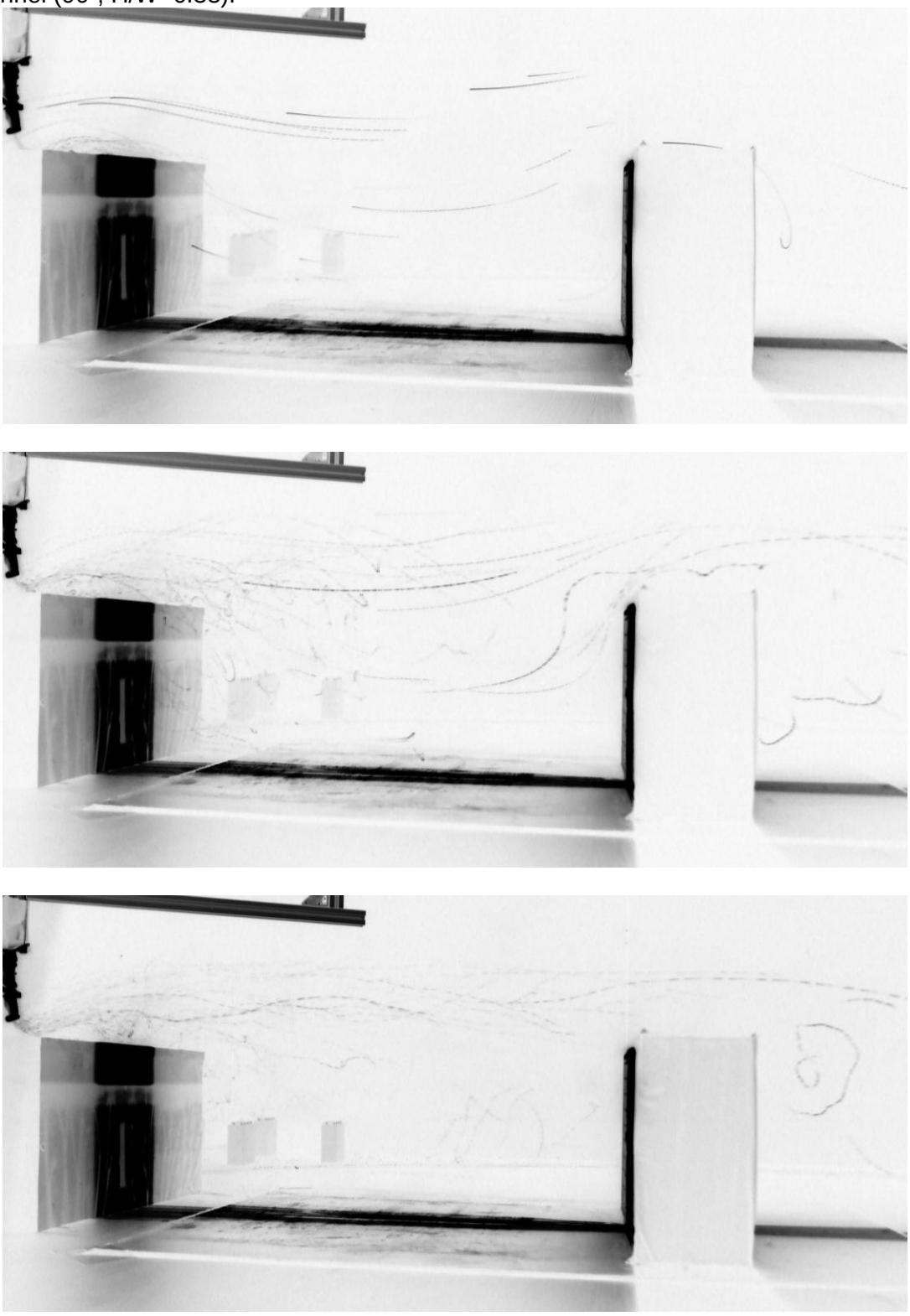

Source: this study.

6.6.2. Bricks parallel to the airflow (at 0˚)

6.6.2.1. Brick's H/W aspect ratio of 1.00

The airflow patterns for the two bricks positioned parallel to the flow and with an H/W aspect ratio of 1.00 show features similar to those described in the literature review regarding flows parallel to the canyon's axis[82], on which both airflow acceleration in the centre and uplift and deceleration near the walls are expected to occur.

Figure 6-57: Velocity vectors and pathlines on planes at 10.0 (top) and 15.0m (bottom) high (0˚; H/W=1.00, m/s).

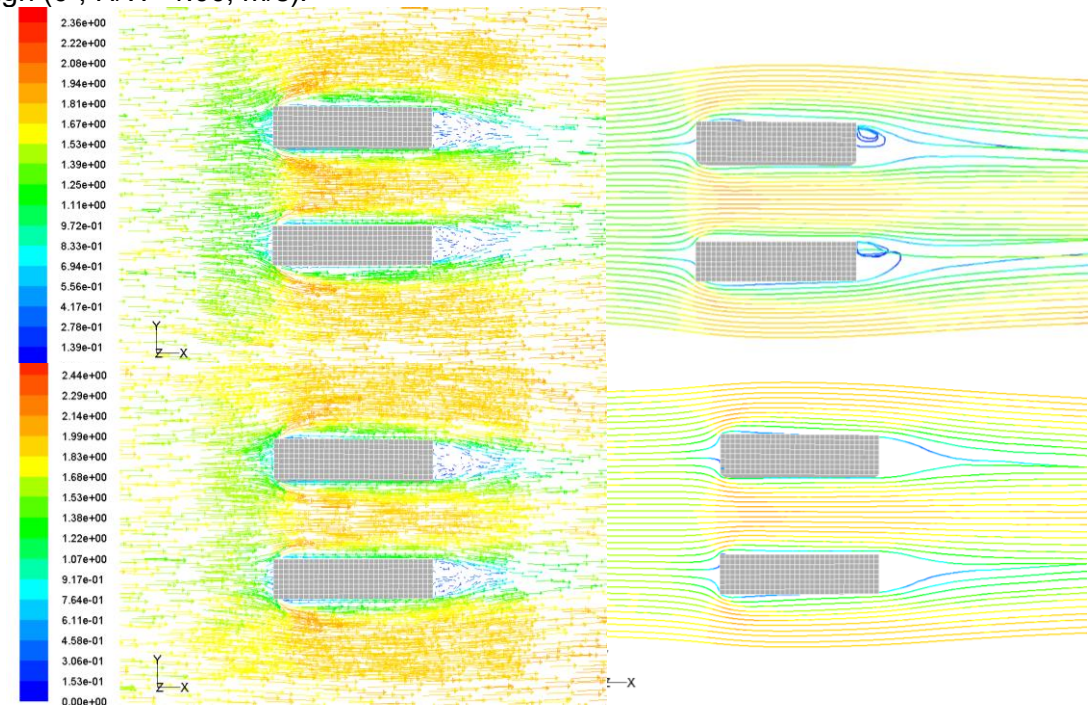

Source: this study.

Figure 6-58: Velocity magnitude pathline view (0˚; H/W=1.00).

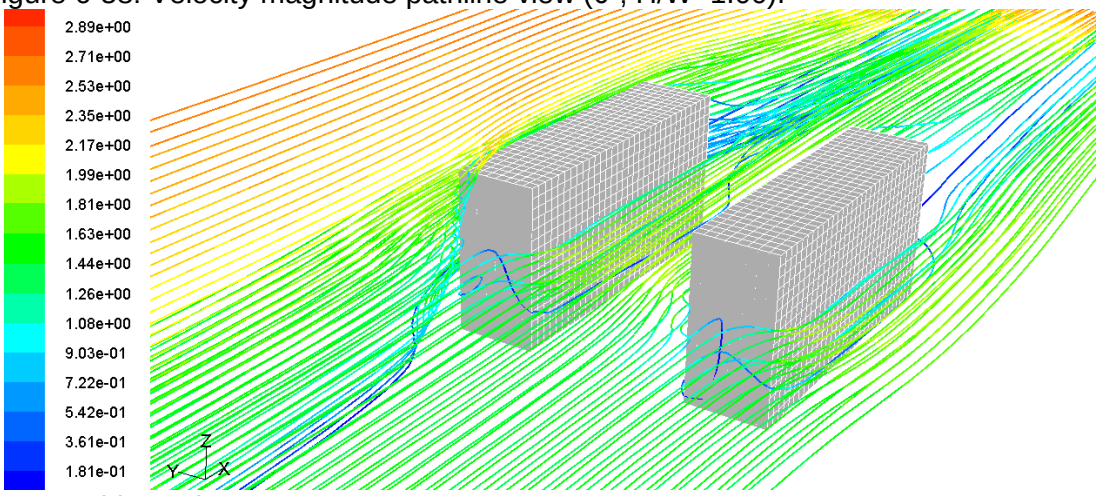

Source: this study.

[82] See topic 2.6.31 in Chapter 2.

6.6.3. Bricks oblique to the airflow (at 45˚)

6.6.3.1. Brick's H/W aspect ratio of 1.00

The airflow patterns for the two bricks positioned obliquely to the flow and with an H/W aspect ratio of 1.00 also present features similar to those described in the literature review[83], as in the example given in the preceding topic on parallel flows. On the other hand, the same literature has already made it clear that there is considerably less information about the effects of non-orthogonal winds in urban areas.

The sequence of airflow velocity pathlines in Figure 6-59 shows the evolution of oblique flow impinging on the two bricks and shown at 5.0, 10.0, 12.5, and 15.0m heights in both top and perspective views. On the basis of this observation it may be affirmed that, after reaching the vertical edge of the upwind brick the flow divides in two directions: part of it turns in downwards on a diagonal washing-out the windward face of the front brick and part accelerates and detaches from the front block, and thus creating a low pressure zone on the latter's rear side before being diverted into the canyon. The same division occurs when the airflow reaches the second block and, when the flow diverted from the first block meets the second one a spiral clock-wise vortex turning is formed along the main axis of the canyon's cavity. The flow accelerates downwards and decelerates upwards.

[83] See topic 2.6.3.3 in Chapter 2.

Figure 6-59: The evolution of airflow velocity pathlines on planes at 5.0, 10.0, 12.5, and 15.0m high (45˚; H/W=1.00, m/s).

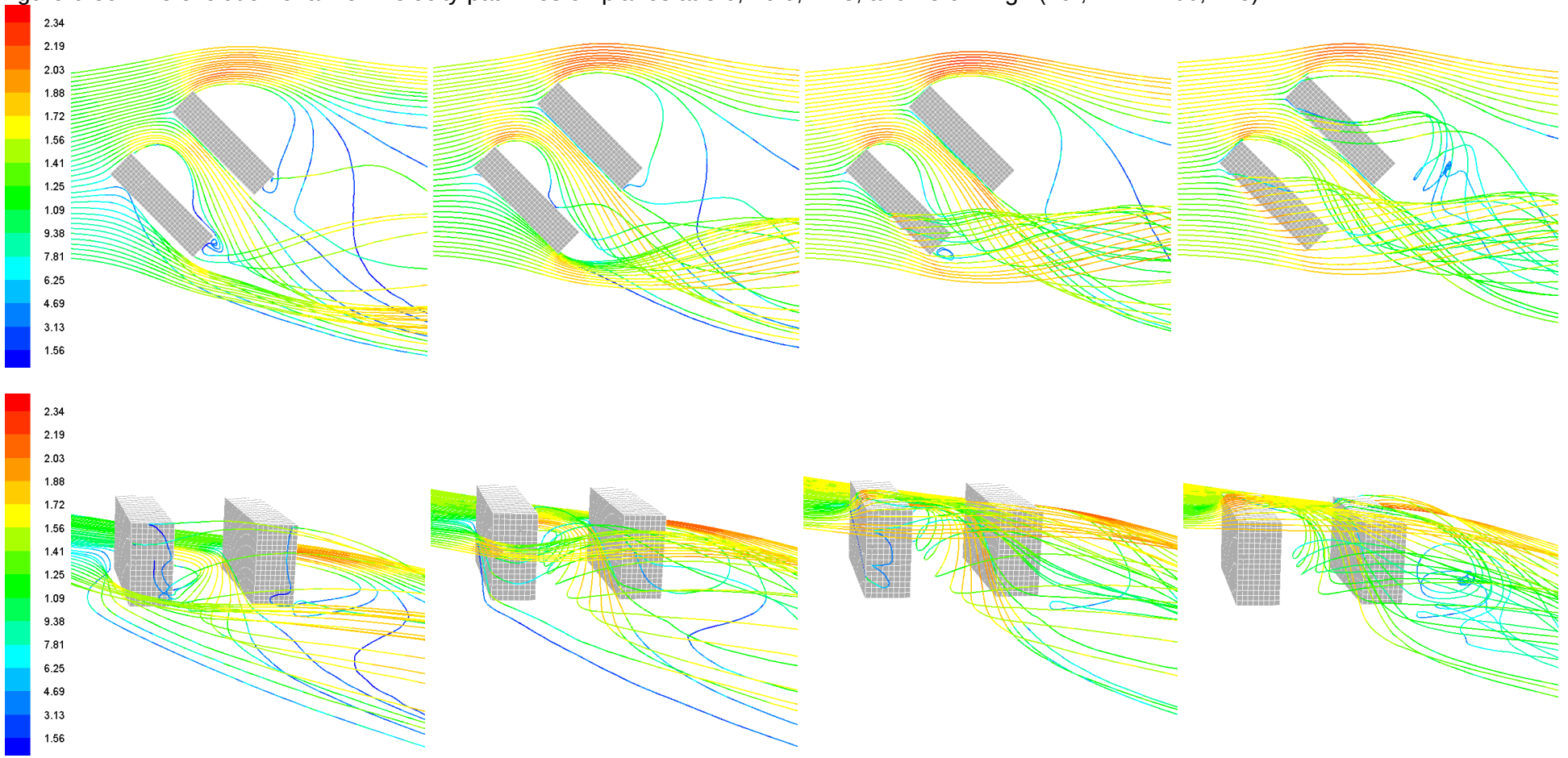

Source: this study.

6.7. Assessment of the wind profile

The velocity magnitude of the CFD results was assessed on each model by 15 vertical strategically-positioned lines (V-1A to V5C; Figure 6-60). This permitted the assessment of several resultant wind velocity profiles near the walls and inside the canyon and the contrast with the free airflow wind profile. This assessment was made for each aspect ratio and incident wind simulated on CFD. Further analysis crossed data of the wind profiles from the simulations for the three wind directions impinging on the H/W=1.0 canyon; and also from the difference between the four H/W ratios for the orthogonal airflow.

Figure 6-60: Top view of a set of bricks showing the vertical profiles and horizontal lines assessed.

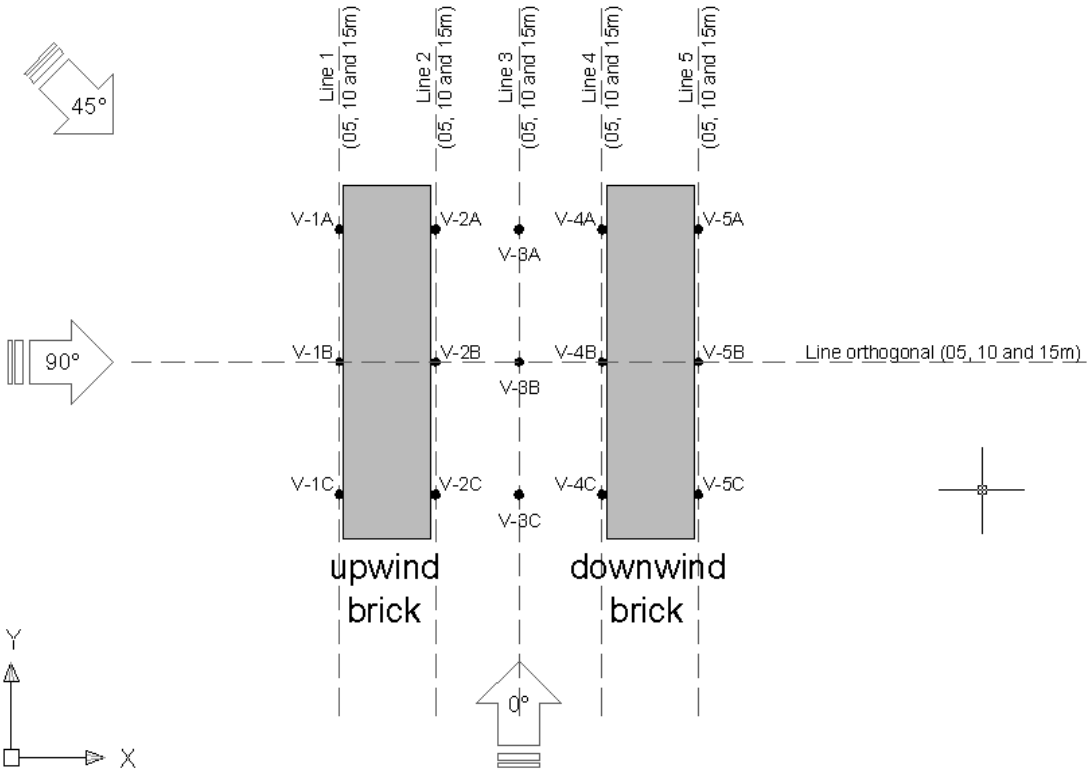

Source: this study.

Figure 6-61: Wind velocity profile for H/W= 2.00 (90˚; m/s).

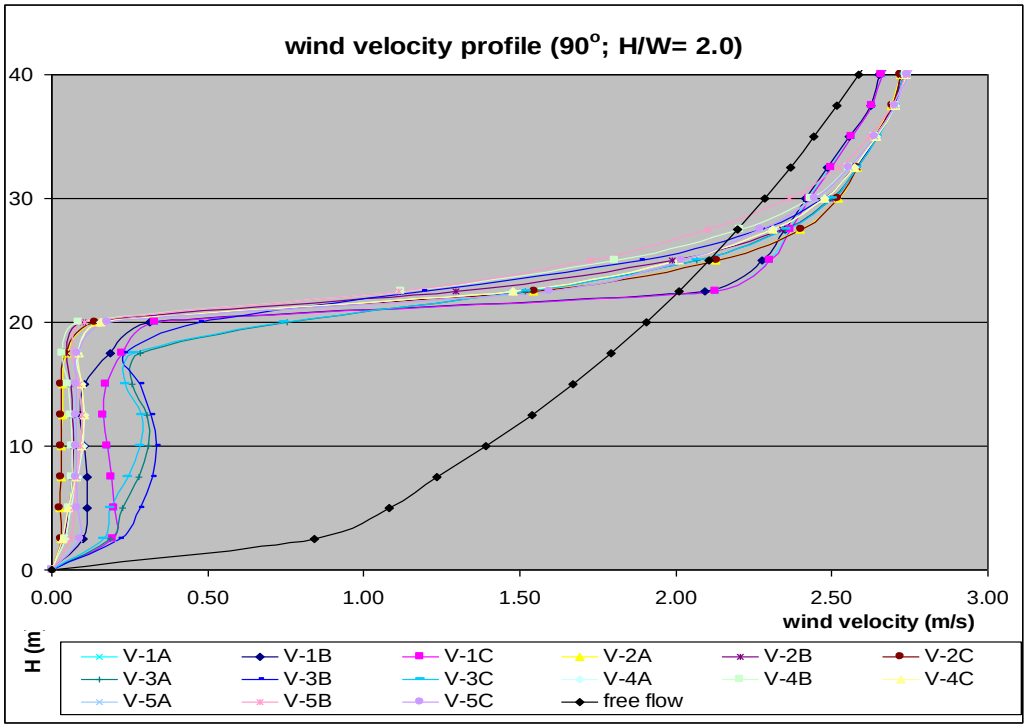

Source: this study.

Figure 6-62: Wind velocity profile for H/W= 1.00 (90˚; m/s).

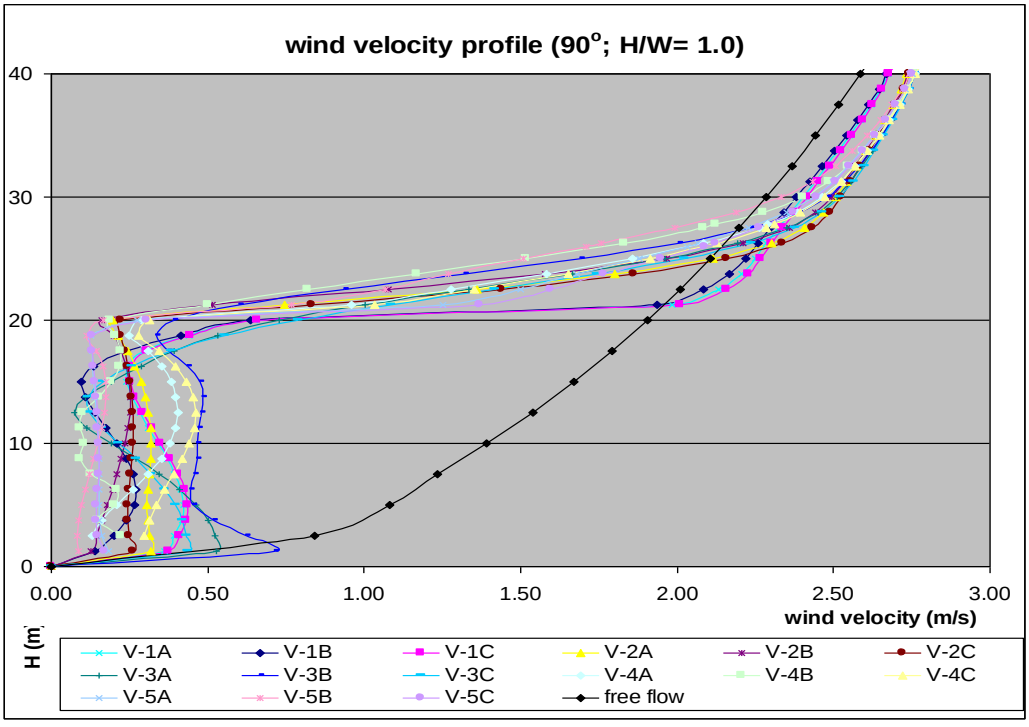

Source: this study.

Figure 6-63: Wind velocity profile for H/W= 0.66 (90˚; m/s).

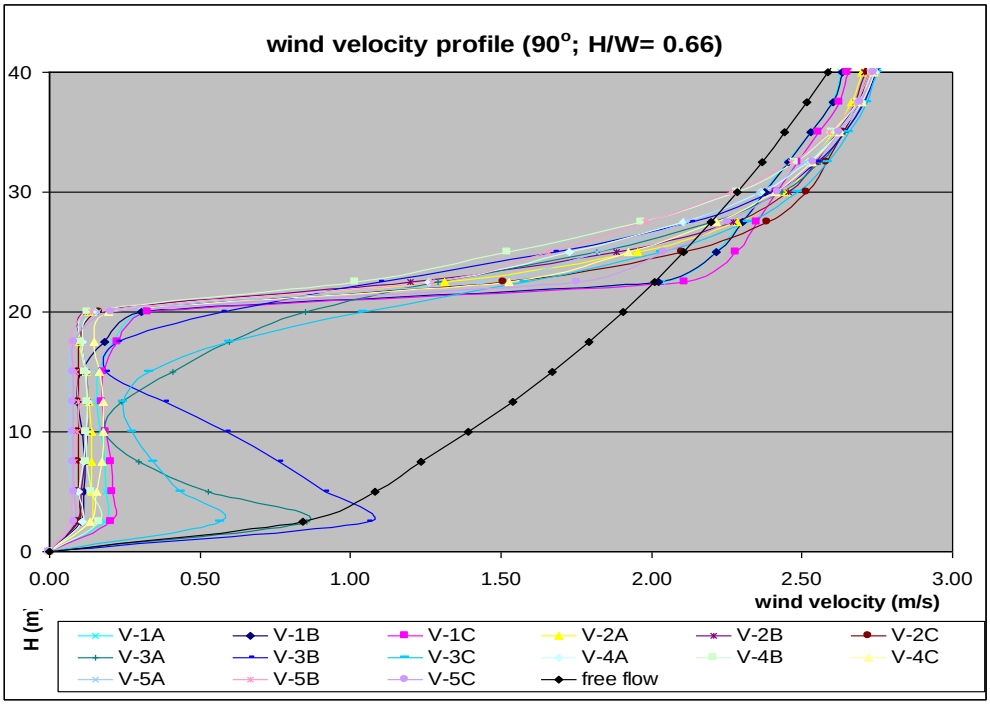

Source: this study.

Figure 6-64: Wind velocity profile for H/W= 0.50 (90˚; m/s).

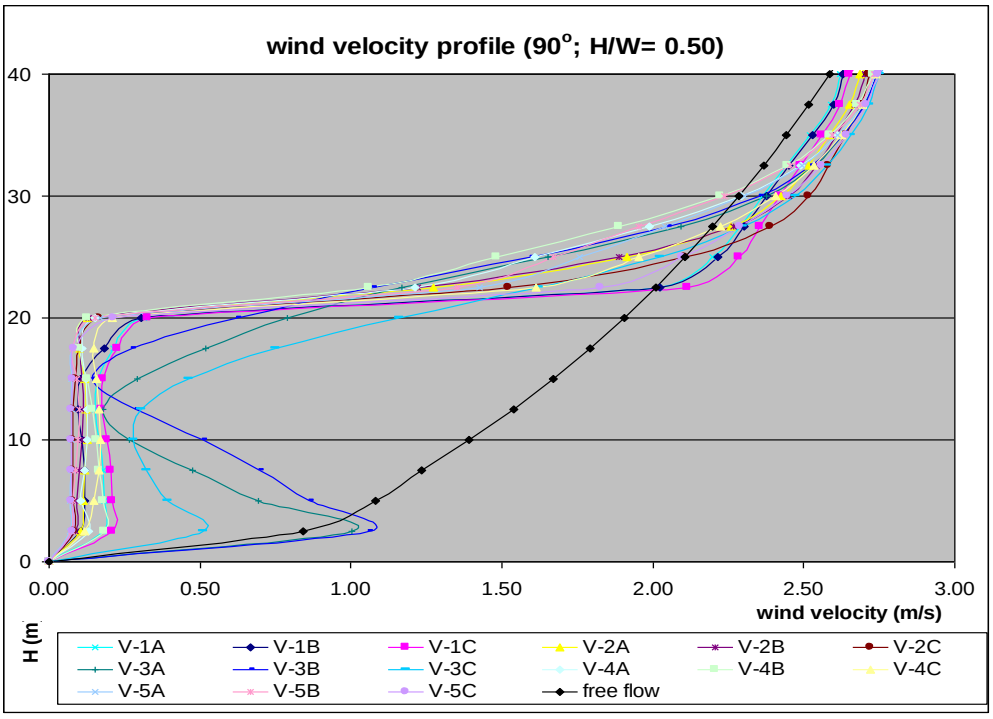

Source: this study.

Figure 6-65: wind profile across the canyon for all H/W ratios (90˚; m/s).

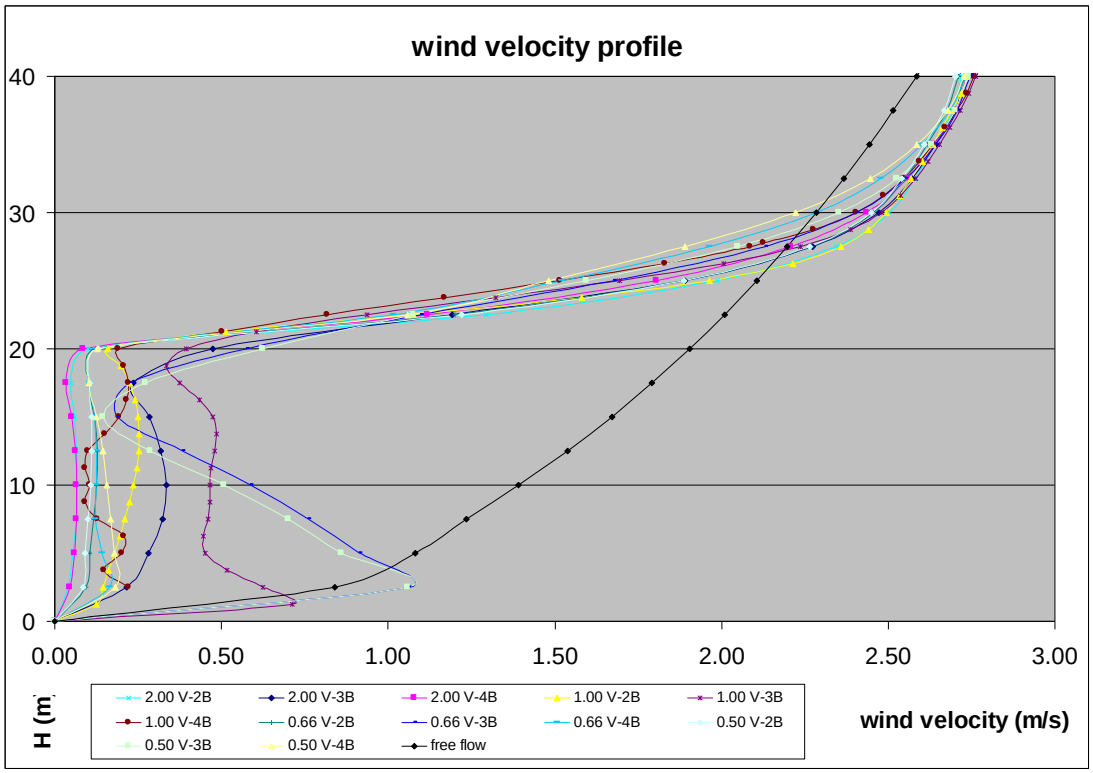

Source: this study.

As seen in Chapter 2, orthogonal winds inside the canyon result in several modifications of airflow speed and direction according to the range of the canyon aspect ratio. These effects range from skimming flow in narrow canyons to wake interference flow in wide ones. However, a clockwise vortex is established inside all these limited spaces. By assessing the wind profiles on the central axes of these canyons it may be said that the wind velocity at 5m height right at its centre (V-3B), when contrasted to that found in the free airflow at the same height, reflects the following influence of the canyon shape: the narrowest set with H/W=2.0 shows a reduction of 65%; the square set with H/W=1.0 has a reduction of 25%; and both the H/W of 0.66 and 0.50 present increases of 25%. This happens due to the skimming flow effect in the first case and wake interference flow in the last two cases. These effects were also highlighted in the airflow visualization analysis and are in agreement with the statement made in the previous paragraph as to the modifications of the airflow speed and direction within canyons.

Figure 6-66: Wind velocity profile for H/W= 1.00 (45˚; m/s).

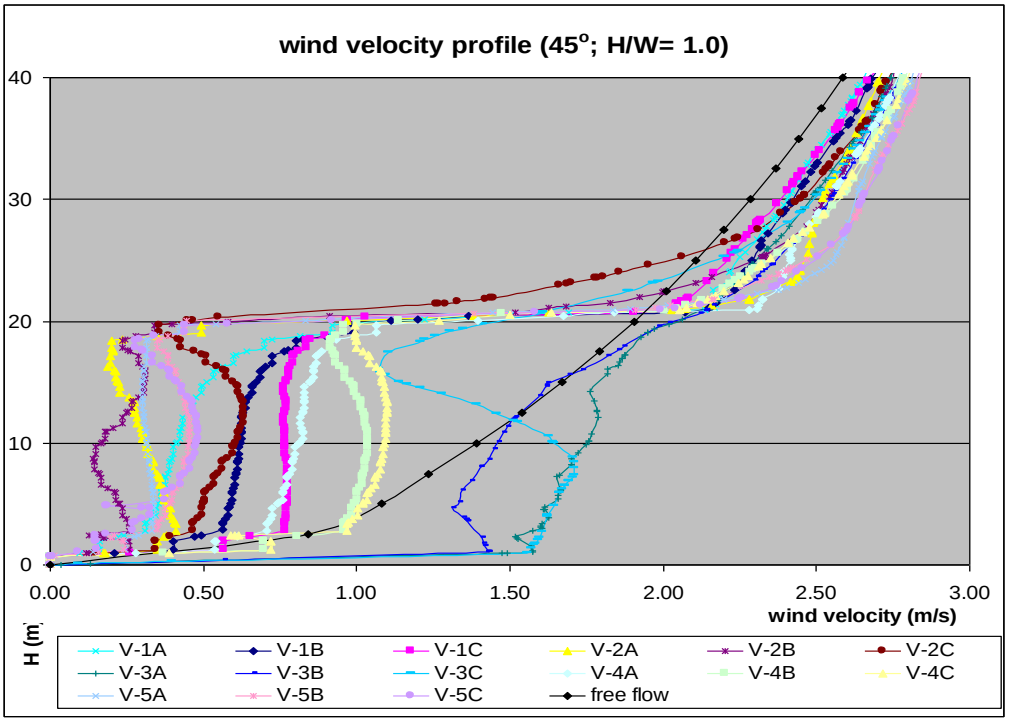

Source: this study.

Figure 6-67: Wind velocity profile for H/W= 1.00 (90˚; m/s).

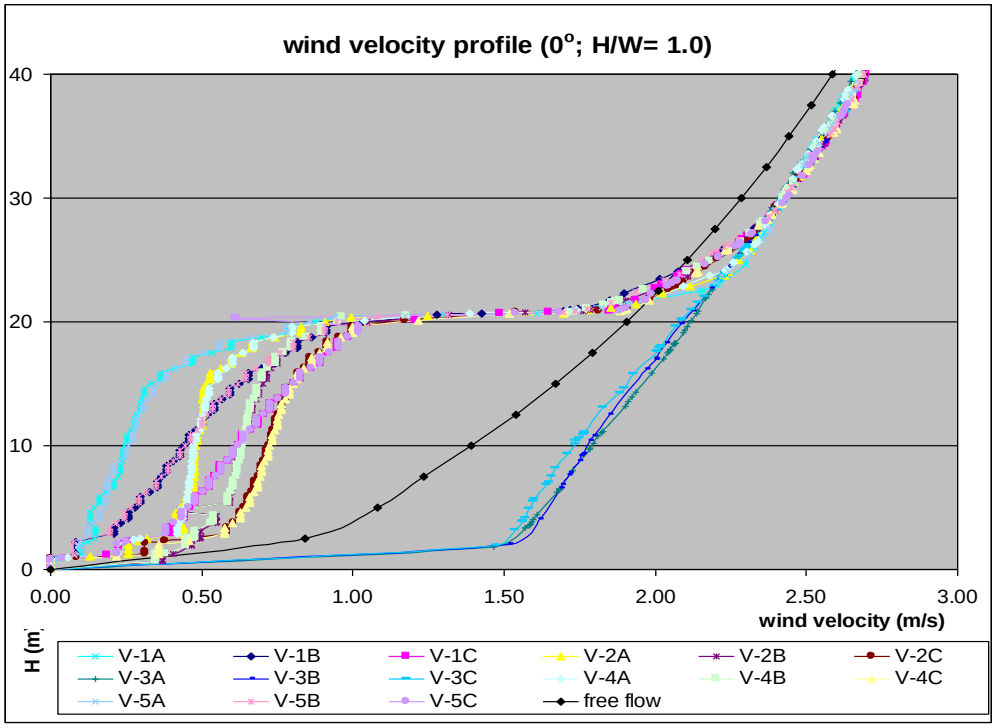

Source: this study.

Figure 6-68: wind profile across the canyon for all wind directions (H/W= 1.0; m/s).

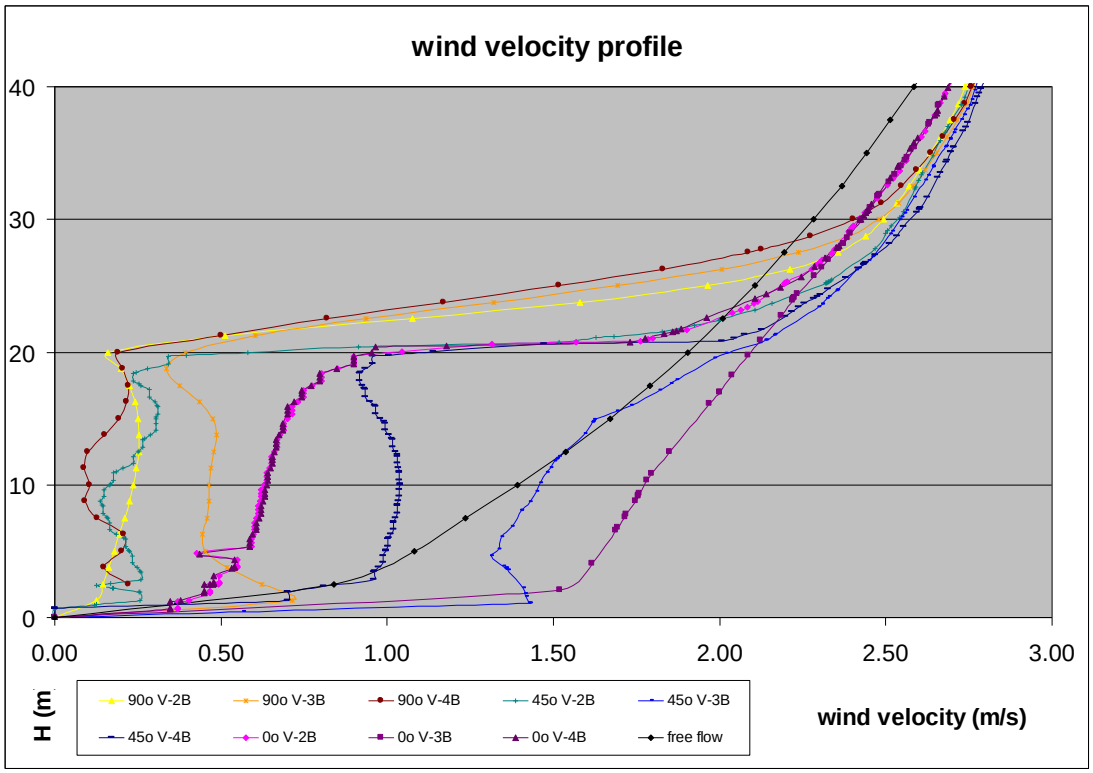

Source: this study.

It may be said that most of the wind profiles presented show a decrease in air velocity inside the canyon. Conversely, it is clear that the oblique winds present a lesser decrease in velocity than do the orthogonal and parallel ones.

At 05m height this decrease ranges from 50% to 80% of the free flow wind profile. The exceptions are the profiles in the centre of the canyon for both the skewed 45˚ flow and that parallel to the bricks (0˚) flows, which show respective increases in velocity of 20% and 60%. These accelerations occur due to the vortex created after the bouncing off the flow on the windward side of the downwind brick in the first case and the Venturi acceleration effect in the second one.

6.8. Chapter conclusion

Simulation of the airflow field around several sets of two parallel bricks was performed for three wind directions in both the wind tunnel and by CFD calculation.

The CFD simulations effectively reproduced the main features of the airflow effectively. This was demonstrated by the assessment of both the numerical and the visual results. For instance, the two methods of simulation produced pressure coefficient contour plots of comparable shape and numerical results.

The limitations of the CFD solver adopted as regards the accurate reproduction of flows detachments and wake reattachment have also been highlighted, although similar airflow patterns were identified for the same set of aspect ratios on both the wind tunnel helium bubble visualization and the CFD airflow visualization by vectors and pathlines.

Further, the CFD software permits the identification of velocity, pressure and turbulence profiles in any direction and region of the model, thus allowing a more complex and accurate assessment of the problem.

In conclusion, the comparison of the CFD output with the wind tunnel results produced a close match. This experiment has, therefore, validated the parameters adopted in the pre-processing, the solving and the post-processing stages of the computational models, which will be carried through in the subsequent investigations of this thesis.

Chapter 7: Urban Prototypes: Results and Analysis

7.1. Introduction

In this chapter the CFD simulation results of the urban prototypes, carried out as part of the Step 2 of this thesis investigation, are presented, analyzed and discussed[84]. The resultant wind field below the canopy height height and the pressure coefficients on the windward and leeward sides are displayed, and compared to references in the literature and among themselves. This analysis aims at finding a correlation between the urban prototypes scenarios aspect ratios and their respective Cp and ΔCp results. Such a correlation may indicate the relationship between aspect ratios and wind-driven ventilation strategies in urban buildings.

7.2. The display and analyses of the results

The groups' assessment took into account the CFD data results from each prototype individually for the three wind direction investigated: 0^o, 45^o, and 90^o. First, the total analysis of the results was based on Cp output data displayed as graphs (see Figure 7-3 for e.g.[85]) and tables depicting the averaged Cp and ΔCp results on both sides of the canyon (right and left faces for parallel winds, or leeward and windward faces for oblique and orthogonal flows - see Table 7-1 for e.g. [86]), which are found in Appendix 4. Further comparison is carried out for the same groups and scenarios results and with the data found in the classical literature and presented in Chapter 2[87]. The wind field and airflow patterns inside the canyons were assessed by the observation of wind velocity magnitude pathlines 3D perspectives showed here (see Figure 7-2 for e.g.). These images allow the qualitative assessment of the airflow field within the canyons to be made through the visualization of wind effects, revealing their connection with the urban environment. Moreover, charts depict the wind velocity magnitude and the wind velocity for the x, y and z vector components on vertical profiles strategically positioned near the canyon walls and on the central axis (see Figure 7-4 for e.g.).

---

[84] For further information regarding the groups of urban prototypes simulated on this investigation see topic 5.4.1 in Chapter 2.

[85] All Cp graphs used in the analyses referring to this chapter are found in Appendix 4.

[86] These tables provide the total averaged Cp maximum and minimum peaks; the 8^{th} maximum and minimum values (discharging extreme values), the averaged results for 90% of the data (omitting the outlying 10%); the standard deviation among the data; and the ΔCp between the faces and at each 5m height from ground level upwards, for both the existing tower and the prototype tower. All tables used in this chapter analyses are found in Appendix 4.

[87] Liddament (1996). For further information see topic 2.4 in Chapter 2.

The urban prototype's ΔCp results were directly compared aiming to identify the statistical correlation coefficient strength between them. Data was plotted in correlation matrix tables which allow a direct comparison between every pair of urban prototype scenario investigated (see Table 7-2 for e.g.). Finally, scatter diagrams[88] show the linear relationship between the sources of data by clustering them around a diagonal line (see Figure 7-5).

Figure 7-1: Example of output lines used for extracting data from the D3 canyon 'A' CFD model for 90^{o} wind incidence.

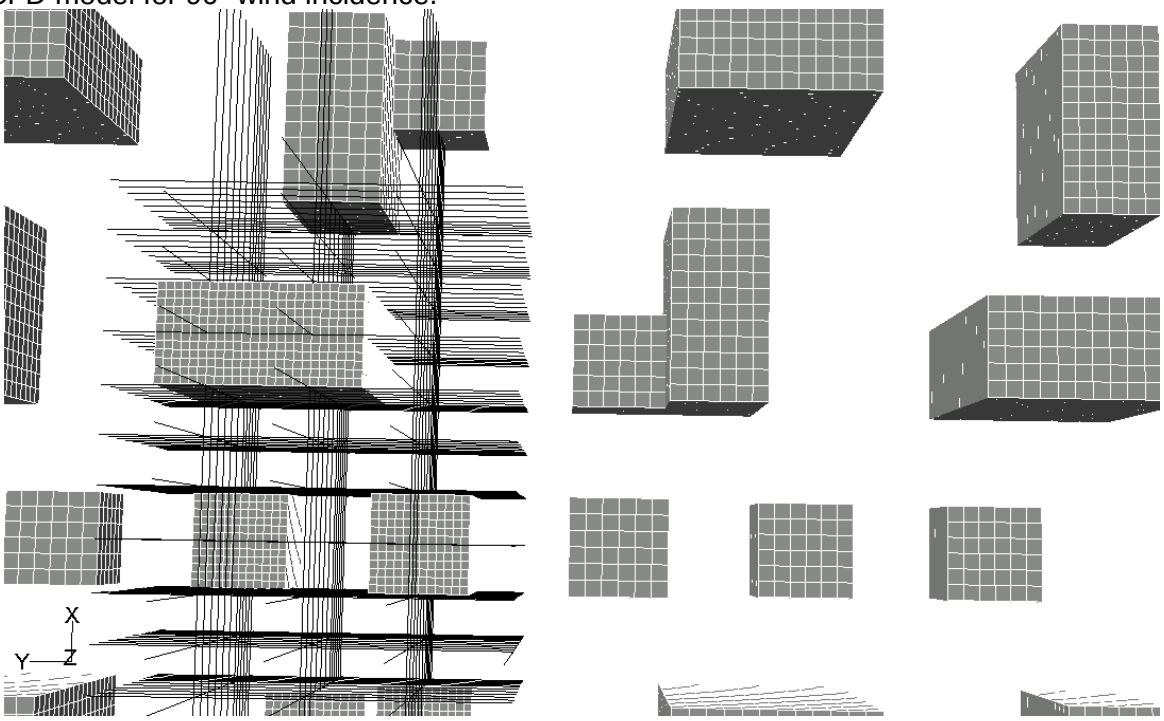

Source: this study.

[88] For further information see topic 5.8 in Chapter 5.

Table 7-1: Example of table showing Cp and ΔCp results for the D1 canyon 'A' scenario for 90° wind incidence (See Appendix 5 for all scenarios).

D1- Canyon 'A'	Orthogonal wind incidence (90°)								
	Windward side Cp				Leeward side Cp				ΔCp
(m)	low 8th	high 8th	avg 90%	sdev	low 8th	high 8th	avg 90%	sdev	
90	0.66	0.70	0.67	0.02	0.79	0.80	0.80	0.00	***-0.12***
85	1.03	1.13	1.10	0.17	0.71	0.74	0.73	0.01	***0.37***
80	0.56	1.07	1.04	0.17	0.67	0.70	0.69	0.01	***0.35***
75	0.86	0.99	0.96	0.17	0.63	0.65	0.64	0.01	***0.32***
70	0.49	0.90	0.88	0.14	0.58	0.60	0.60	0.01	***0.29***
65	0.74	0.81	0.80	0.13	0.53	0.56	0.55	0.01	***0.25***
60	0.47	0.63	0.62	0.06	0.49	0.54	0.51	0.02	***0.11***
55	0.57	0.64	0.62	0.08	0.43	0.48	0.45	0.02	***0.17***
50	0.43	0.57	0.54	0.06	0.38	0.44	0.41	0.02	***0.13***
45	0.40	0.49	0.47	0.05	0.34	0.41	0.37	0.02	***0.10***
40	0.37	0.44	0.41	0.03	0.29	0.37	0.34	0.03	***0.07***
35	0.32	0.38	0.35	0.03	0.25	0.33	0.30	0.03	***0.05***
30	0.25	0.38	0.28	0.03	0.21	0.30	0.27	0.02	***0.00***
25	0.21	0.30	0.23	0.02	0.19	0.26	0.23	0.02	***0.01***
20	0.16	0.25	0.19	0.02	0.04	0.11	0.06	0.02	***0.14***
15	0.12	0.17	0.14	0.02	0.12	0.17	0.15	0.01	***0.00***
10	0.06	0.15	0.11	0.02	0.09	0.14	0.11	0.01	***0.00***
5	0.04	0.15	0.06	0.03	0.06	0.11	0.07	0.02	***-0.01***
2	0.02	0.14	0.04	0.04	0.04	0.11	0.06	0.02	***-0.02***
avg	***0.41***	***0.54***	***0.50***	***0.07***	***0.36***	***0.41***	***0.39***	***0.02***	***0.12***

Source: this study.

Figure 7-2: Example of 3D perspectives showing the wind velocity magnitude pathlines (m/s) and airflow patterns for the prototype D4 for 90° wind.

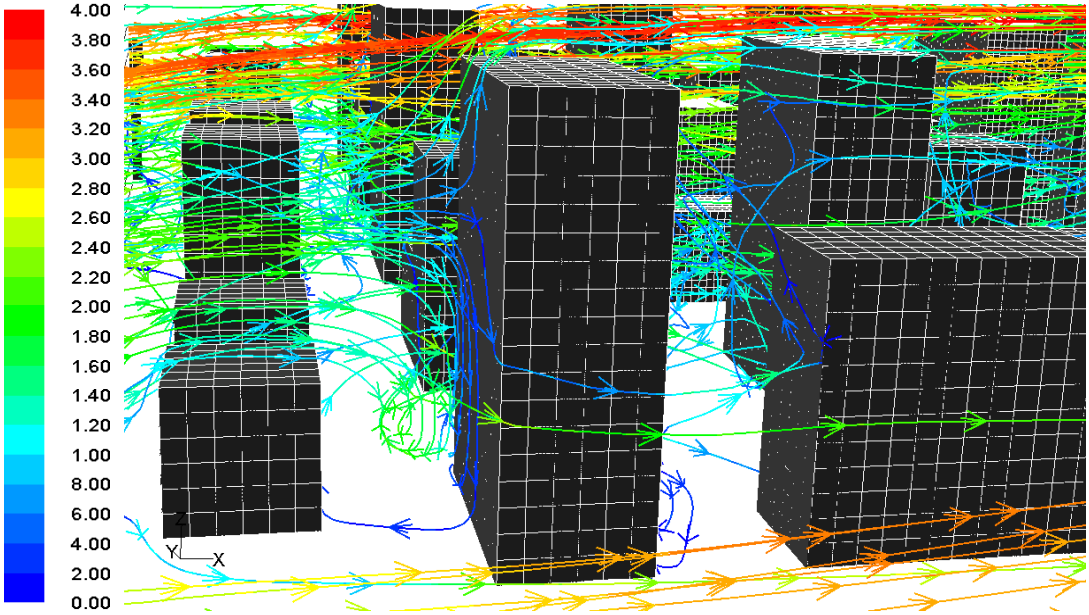

Source: this study.

Figure 7-3: Example of charts depicting the pressure coefficient (Cp) output data for each face of the canyon in a 5m height variation and for the three wind directions investigated for the prototype A1 (H/W= 0.50- see Appendix 5 for all scenarios).

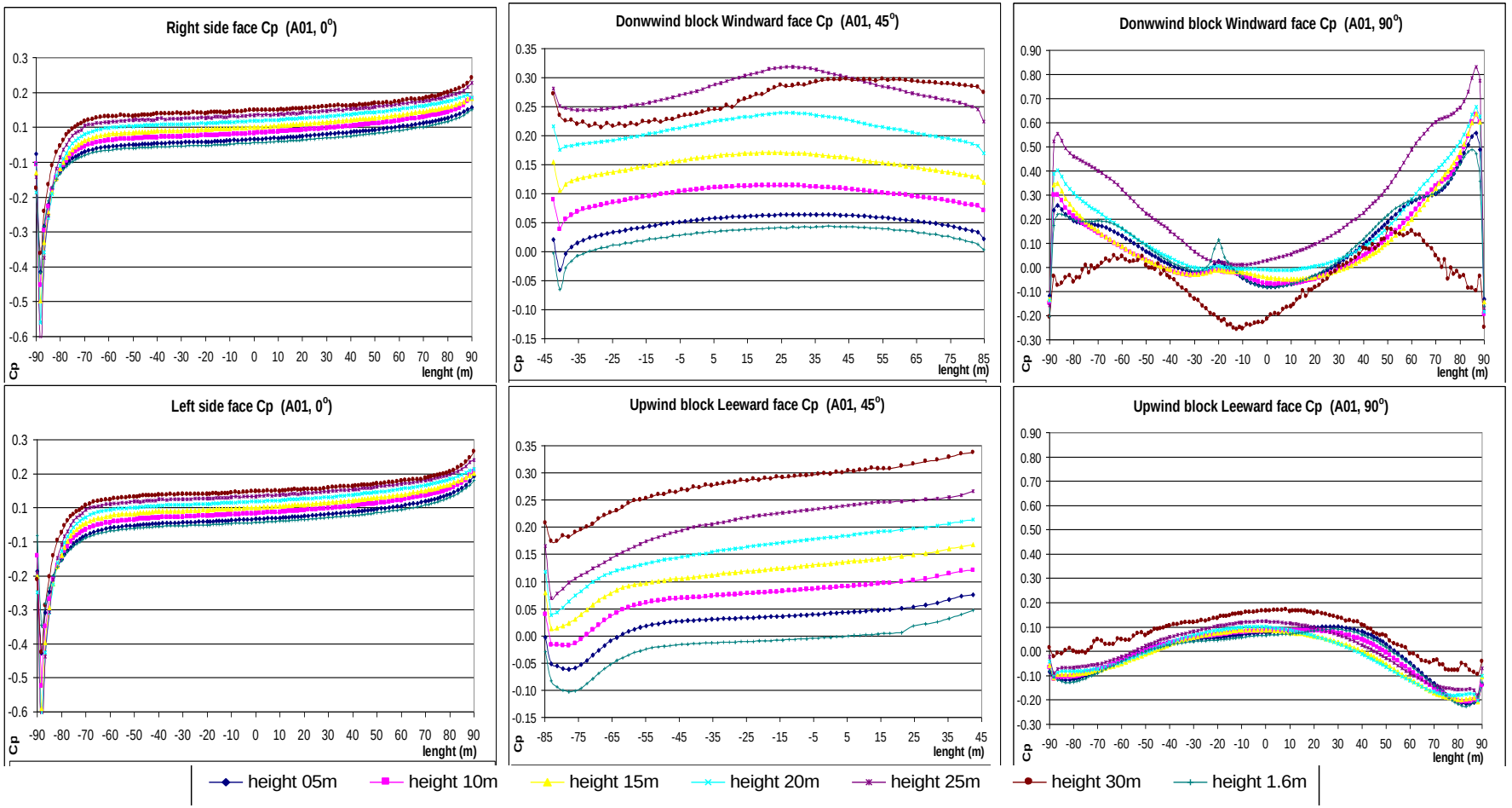

Source: this study.

Figure 7-4: Example of charts depict the wind velocity magnitude and the wind velocity for the x, y and z vector components (m/s) on vertical profiles for the prototype D3 and for 45^{o} wind direction (See Appendix 5 for all scenarios).

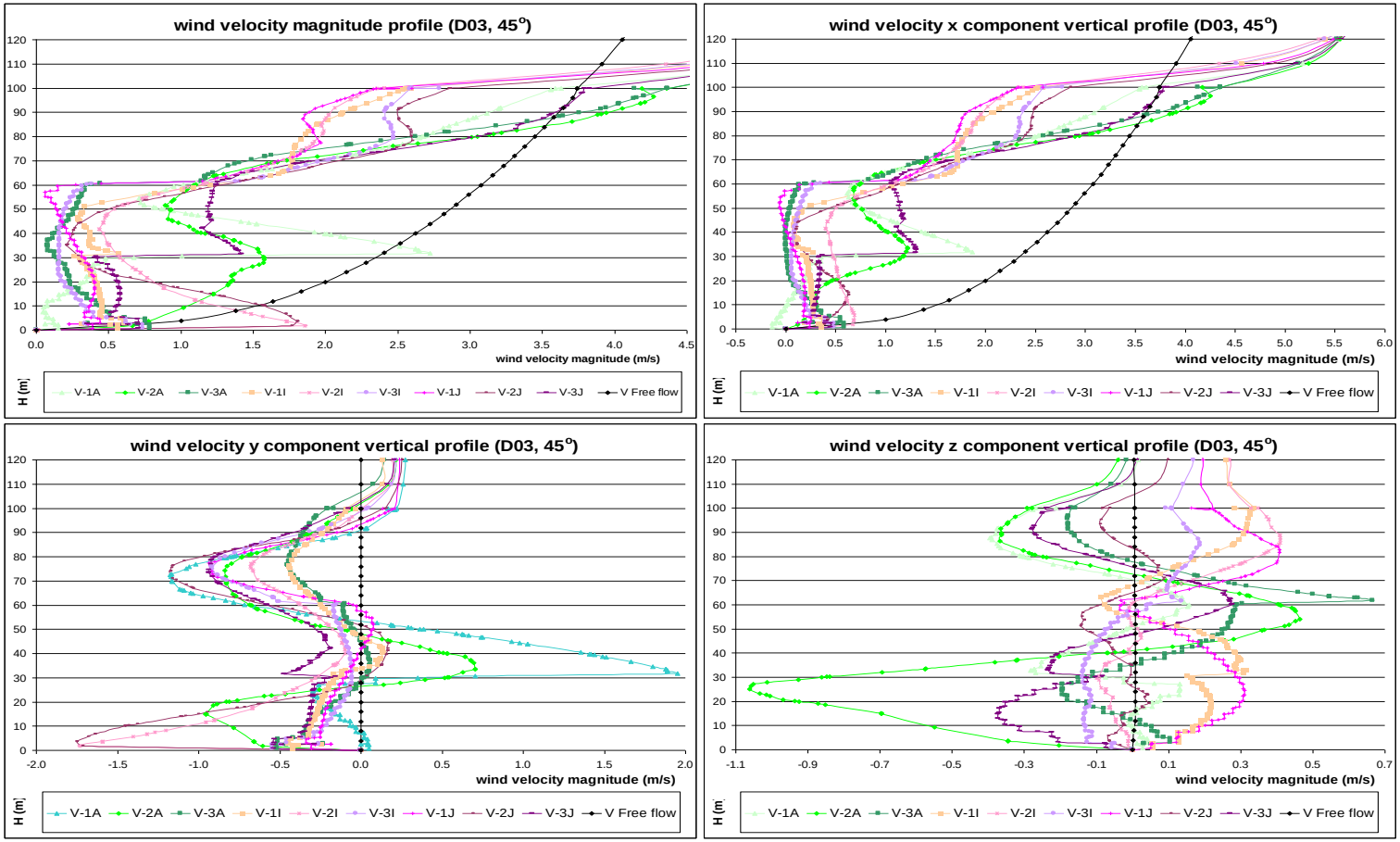

Source: this study.

Table 7-2: Example of correlation matrix tables for a direct comparison between all the urban prototypes' scenarios investigated.

Table 7-8: Correlation coefficient matrix among the urban prototype scenarios regarding the ΔCp results- oblique winds (45°).

45°	A1	A2	A3	A4	B1	B2	B3	B4	C1	C2	C3	C4	D1	D2	D3	D4
ΔCp at top	-0,01	0,03	-0,01	0,01	0,06	-0,06	0,00	0,08	0,01	0,01	0,00	0,00	0,19	0,28	0,20	0,22
	0,06	-0,02	0,04	0,05	0,07	0,17	0,14	0,13	0,01	0,00	0,00	0,00	0,46	0,37	0,29	0,39
ΔCp at middle	0,05	-0,02	0,02	0,04	0,02	0,10	0,06	0,08	0,00	0,00	0,00	0,00	0,20	0,32	0,21	0,28
	0,04	-0,01	0,02	0,04	-0,02	0,03	0,01	0,05	0,00	0,00	0,00	0,00	0,08	0,32	0,28	0,16
ΔCp at bottom	0,02	-0,01	0,01	0,04	-0,02	0,00	0,03	0,03	0,00	0,00	0,00	0,00	0,02	0,26	0,24	0,10
	0,02	-0,01	0,01	0,03	0,02	0,02	0,04	0,04	0,00	0,00	0,00	0,01	0,00	0,18	0,19	0,09
	0,04	-0,01	0,00	0,03	0,04	0,03	0,04	0,03	0,01	0,00	0,00	0,00	0,01	0,19	0,20	0,09
AVG ΔCp	0,03	-0,01	0,01	0,03	0,02	0,04	0,05	0,06	0,00	0,00	0,00	0,00	0,14	0,27	0,23	0,19

Source: this study.

Table 7-9: Correlation coefficient matrix among the urban prototype scenarios regarding the ΔCp results- oblique winds (45°).

	A1	A2	A3	A4	B1	B2	B3	B4	C1	C2	C3	C4	D1	D2	D3	D4
A1																
A2	0,91															
A3	0,77	0,81														
A4	0,92	-0,97	0,92													
B1	0,03	0,27	0,04	-0,16												
B2	0,92	-0,83	0,91	0,91	0,26											
B3	0,77	-0,68	0,82	0,76	0,47	0,92										
B4	0,26	-0,06	0,57	0,28	0,70	0,58	0,61									
C1	0,19	0,12	-0,26	-0,16	0,71	0,12	0,28	0,12								
C2	-0,36	0,57	-0,10	-0,40	0,83	-0,06	0,19	0,69	0,37							
C3	-0,17	0,35	0,14	-0,17	0,82	0,16	0,40	0,78	0,33	0,97						
C4	0,08	-0,31	0,31	0,23	-0,04	0,21	0,28	-0,06	-0,22	-0,21	-0,09					
D1	0,39	-0,18	0,63	0,39	0,68	0,67	0,72	0,98	0,19	0,65	0,77	-0,12				
D2	0,37	-0,24	0,65	0,47	0,20	0,55	0,43	0,80	-0,21	0,35	0,45	-0,36	0,82			
D3	0,52	-0,53	0,68	0,65	-0,06	0,58	0,48	0,44	-0,15	0,04	0,24	-0,14	0,54	0,75		
D4	0,43	-0,22	0,67	0,44	0,60	0,69	0,68	0,97	0,09	0,56	0,67	-0,14	0,98	0,86	0,51	

Source: this study

Figure 7-5: Example of scatter diagram showing the correlation coefficient between the Urban Prototypes C2 ΔCp results and C3 ΔCp results and for oblique winds.

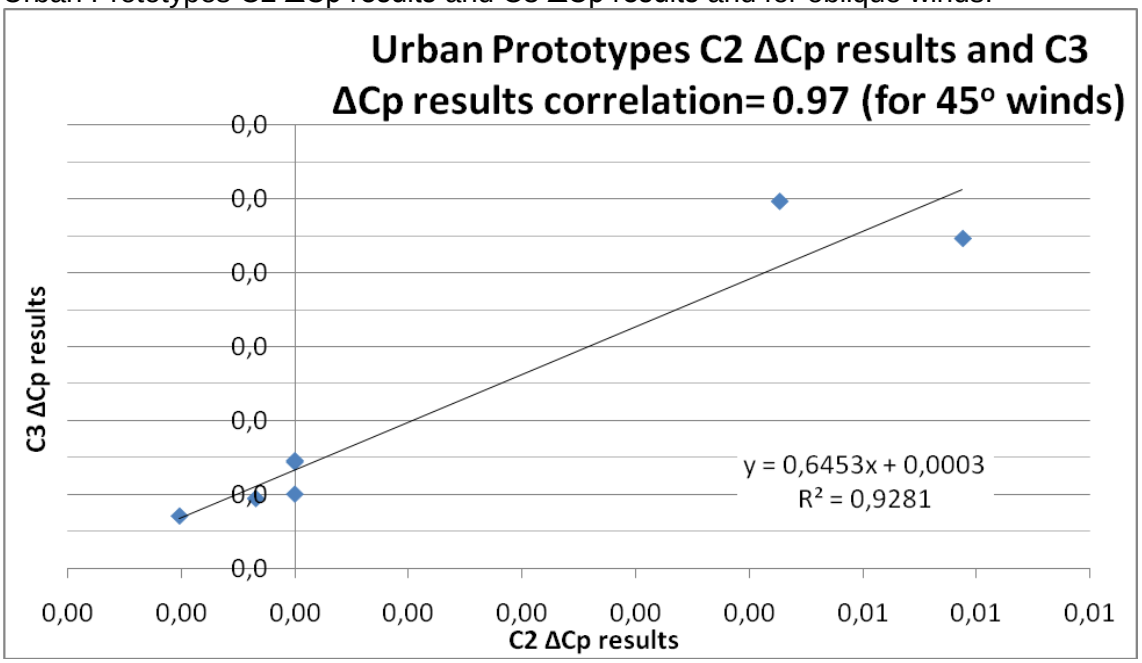

Source: this study

7.3. The groups of prototypes results and analyses

7.3.1. Group 1: prototypes A1, B1, and C1

7.3.1.1 A1, B1, and C1 analysis of the results (0^o)

In general, the results for winds parallel to the canyon's axis were practically symmetrical on both right and left sides. Consequently these sides will not be mentioned when accessing the Cp results unless there is a significant discrepancy between them. This assumption is also valid for the later analysis of parallel winds.

Regarding the A1, B1, and C1 urban prototypes' Cp results, total averages ranging around 0.05 were found for the three scenarios accessed, which are higher than the Cp results described by Liddament[89] (1996). At low height (ground level to 10m) the average Cp result found was 0.02 in all the scenarios. Conversely, the wide (A1), square (B1) and narrow (C1) canyons' results of 0.12, 0.08, and 0.06 at medium height (10 to 20m); and of 0.16, 0.15, and 0.09 at top height (20 to 30m); show that the canyons' width influences the Cp results for parallel winds slightly. The absolute minimum Cp results occurred at the upwind corner where -0.43, -0.07 and -0.06 low peak pressures were found. This drop of pressure is related to flow detachment at the vertical sharp edges, followed by a low pressure bubble of approximately 12m in horizontal length in the three scenarios. After this the flow reattaches and the just quoted averaged Cp results are observed, though a slight increase of 0.05 is perceived along the face as far as the downwind corner. On the basis of this analysis the widest canyon creates a greater flow detachment.

The wind velocity magnitude vertical profiles inside the canyon show when wind acceleration or deceleration occurs. At 4.0m height the ABL input velocity is 1.0m/s. At this same height it was found in the resultant velocity inside the canyon ranged from 0.3m/s to 0.5m/s for the three prototype scenarios. The lowest velocity was found on the upwind side and the highest on the downwind side, at this same height. On the other hand, the average wind velocity at the centre of the A1 and B1 canyon scenarios was 1.45m/s, being practically constant throughout the canyon. This means that the channelling effect accelerates the external wind inside the canyon by approximately 50%. The wind speed inside the C01 canyon ranged from 1.4m/s at the upwind corner to 1.0m/s at the downwind corner, accelerating at the entrance, but decelerating through the canyon. For the three scenarios, the vertical wind velocity inside the canyons decelerates near the walls, reaching around 1,0m/s at 30m height. At this height the ABL input velocity is 2.3m/s. However, above 31m height a sharp

[89] For 10m height rectangular buildings in urban areas, Liddament (1996) gives Cp results of -0.2 for side walls of parallel winds (0^o), though no reference is made to urban density (see topic 2.4 in Chapter 2).

acceleration takes place reaching more than 2.6m/s and continuing to increase. At the centre of the canyon, after the wind accelerates near the ground, the vertical profile inside the canyon meets the ABL input velocity at 12m height. Then, the vertical velocity inside the canyon continues to increase, thought it decelerates as compared to the external flow. Above the blocks, the acceleration recurs and all the vertical profiles present the previously described velocity increase pattern. Finally, the x component of the wind, alongside the mainstream, is the mandatory velocity vector in the definition of the wind velocity magnitude, since the components y and z present low ranges of velocity: approximately 0.20, 0.05, and 0.04m/s for the A1, B1 and C1 scenarios.

Figure 7-6: Wind velocity magnitude and x, y and z wind vector components vertical profiles (A01, 0°, m/s):

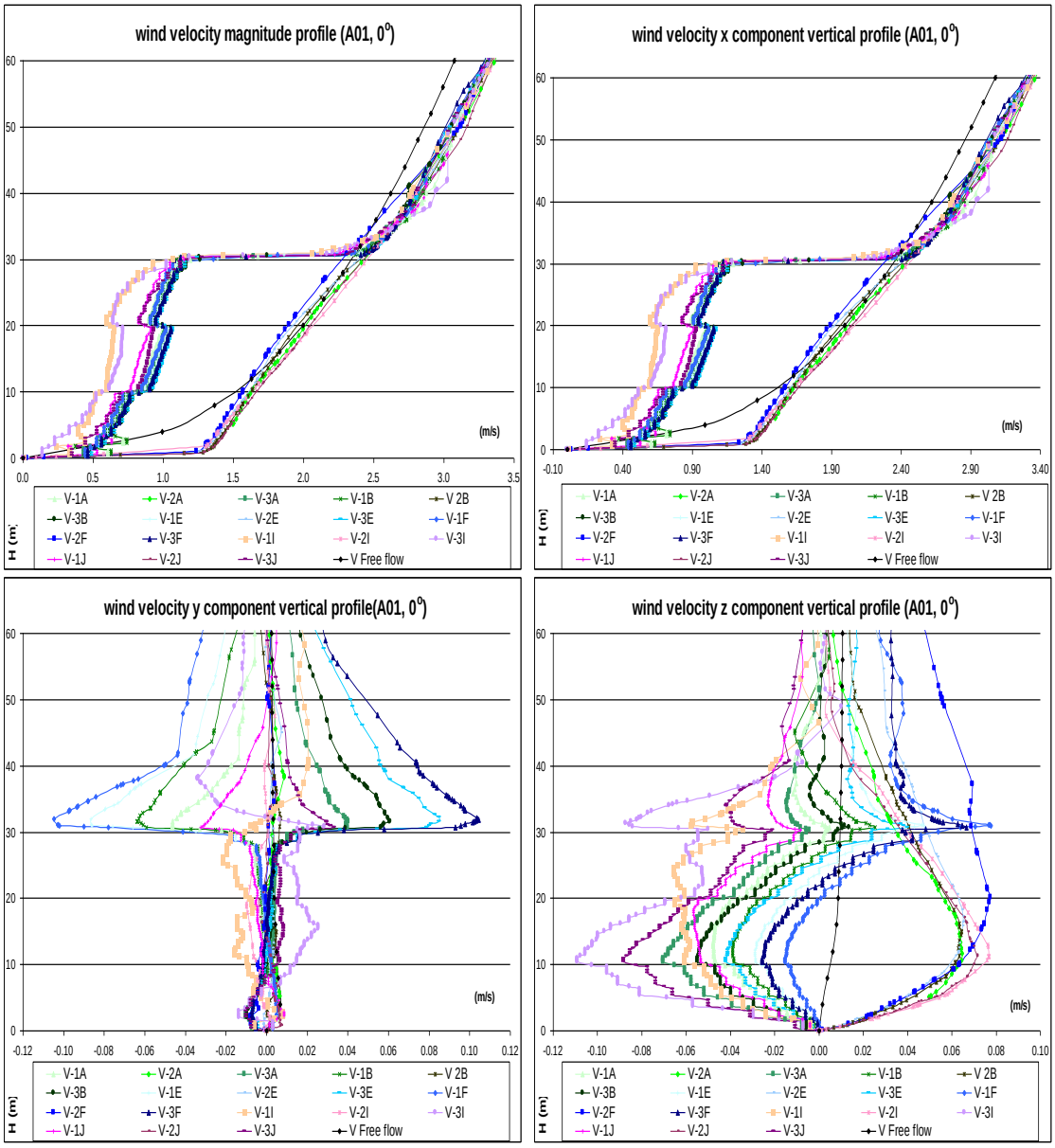

Source: this study.

Figure 7-7: Wind velocity magnitude and x, y and z wind vector components vertical profiles (B01, 0°, m/s):

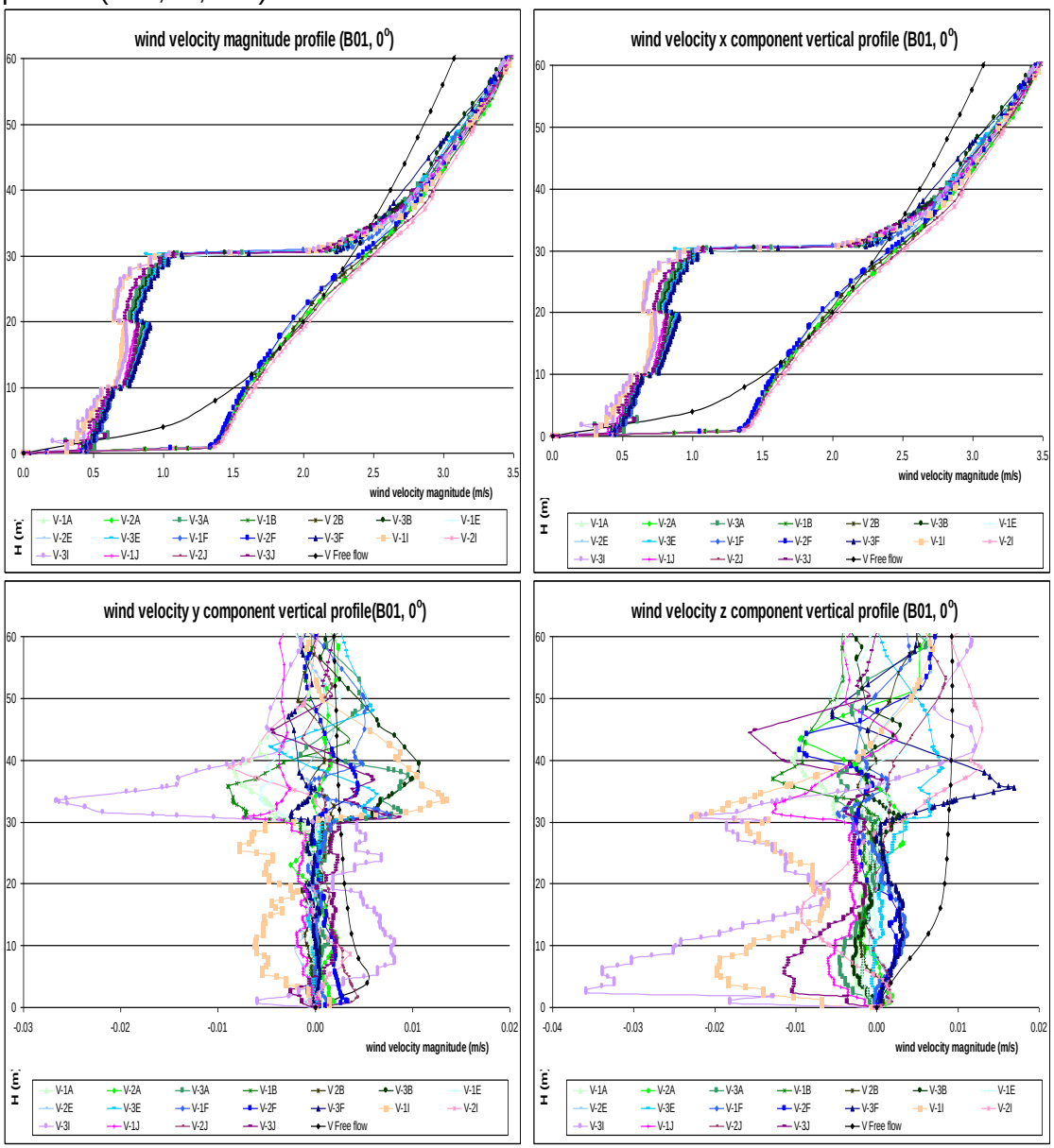

Source: this study.

Figure 7-8: Wind velocity magnitude and x, y and z wind vector components vertical profiles (C01, 0°, m/s):

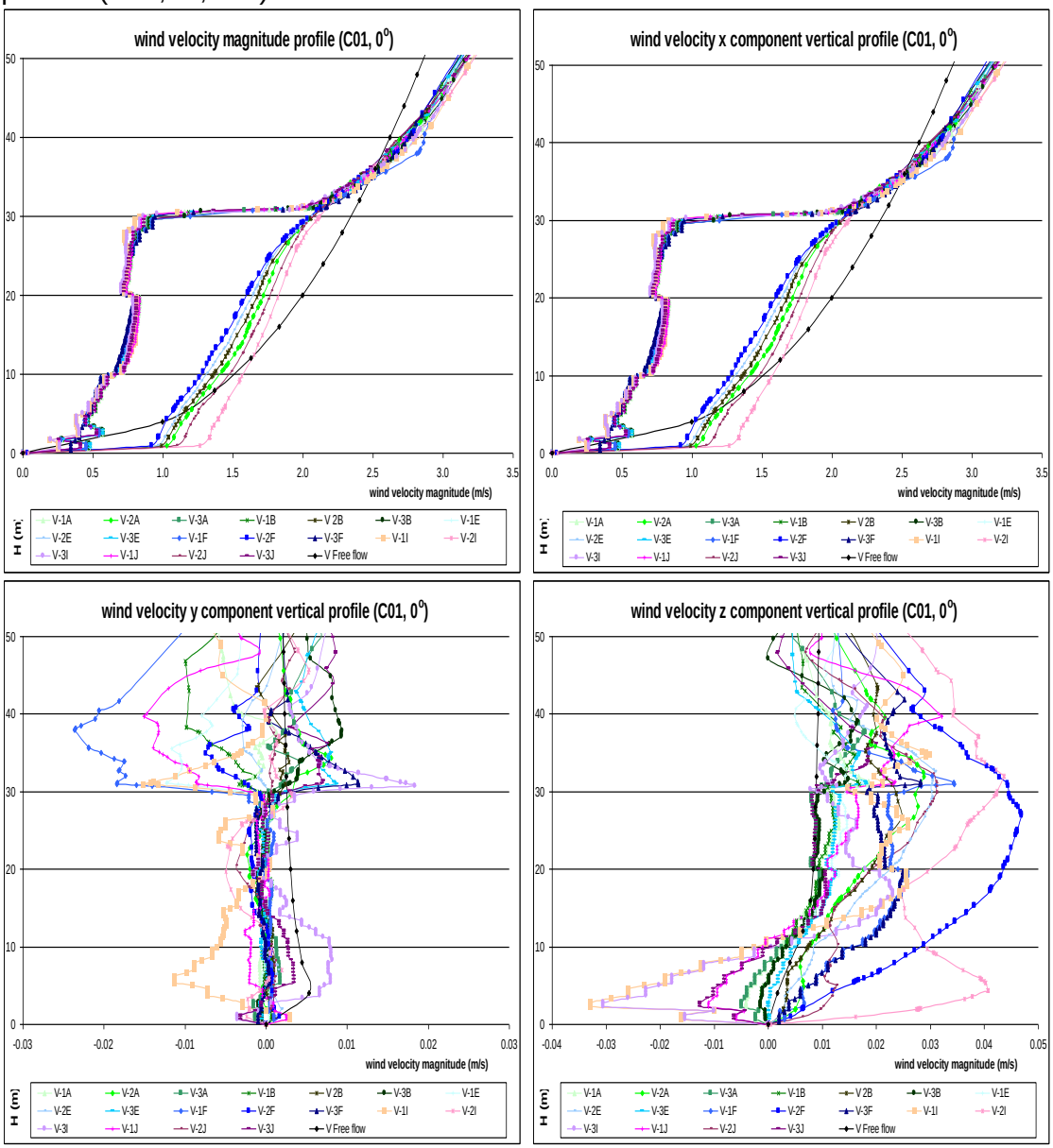

Source: this study.

7.3.1.2. A01, B01, and C01 analysis of the results (90°)

The analysis for winds orthogonal to the canyon's axis focuses on the surfaces of the same canyon, with the windward surface of the upwind block and the leeward one of the opposite block, positioned downwind. The urban prototypes A1, B1, and C1 total average CP results on the windward side were 0.06, 0.11, and 0.03. The wide canyon result agrees with the Cp results from Liddament[90] (1996), though the average results for the square and narrow canyons are also close. A wide Cp range was observed on the windward surfaces, with pressure increase on the sides and a drop in the centre.

[90] For 10m height rectangular buildings in urban areas, Liddament (1996) gives Cp results of +0.06 for the windward walls and -0.30 for the leeward walls in orthogonal winds (90°) (see topic 2.4 in Chapter 2).

Figure 7-9: The wind velocity magnitude pathlines (m/s) for the A1 (top), B1 (middle) and C1 (bottom) prototypes and for 90^{o} winds.

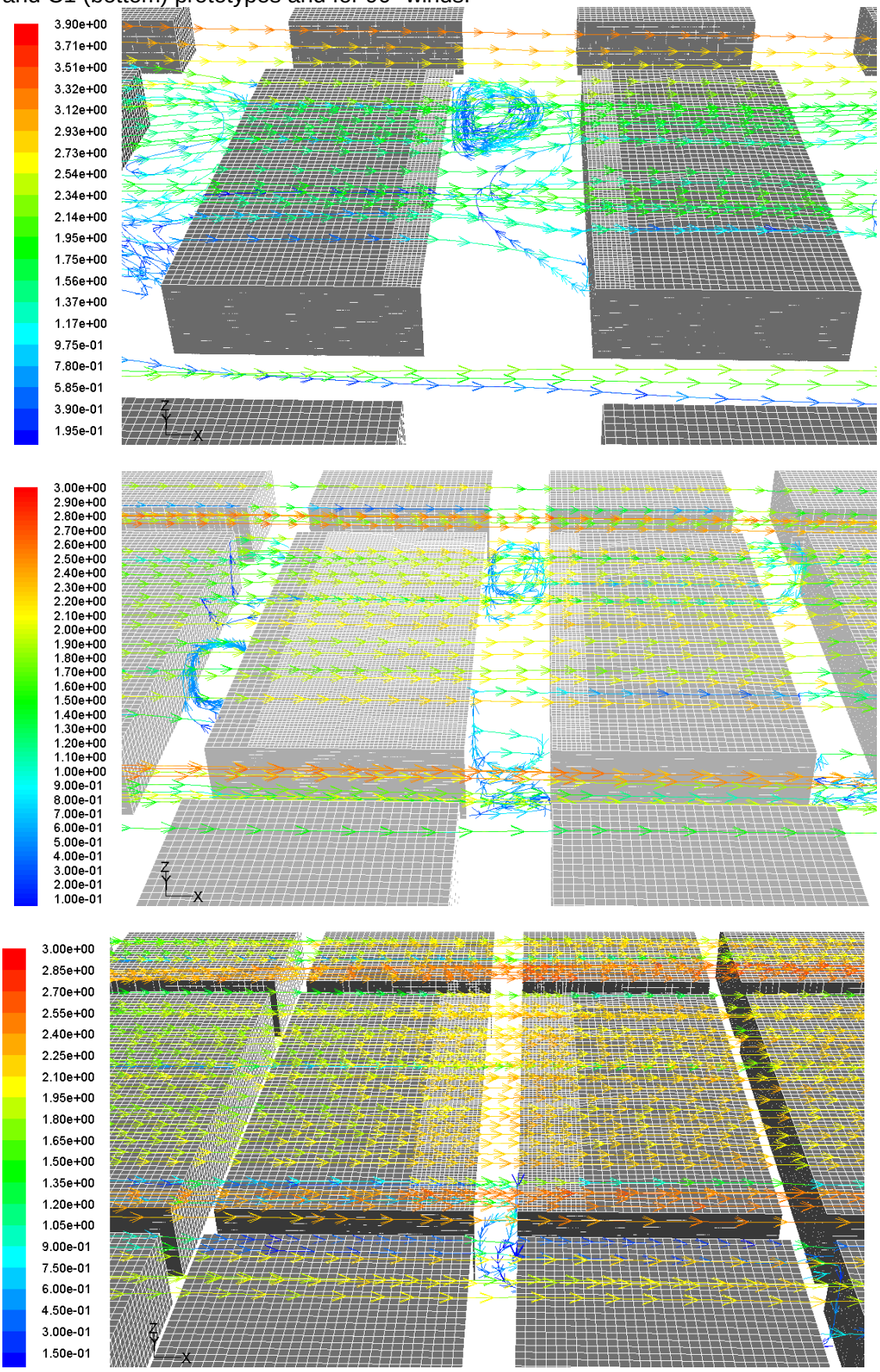

Source: This study.

Symmetry between right and left sides existed at all the heights assessed. At low heights the averaged Cp results were 0.30, 0.20 and 0.02 on both sides of the A1, B1, and C1 scenarios, while in the centre the results were 0.07, 0.09, and 0.01. At medium heights the results were 0.44, 0.24, and 0.08 on the sides, and 0.03, 0.07, and 0.02 in the centre. At top heights the results were 0.48, 0.35, and 0.20 in the sides, and 0.07, 0.15 and 0.03 on the centre. Maximum Cp peaks of 0.83, 0.48, and 0.39 were found at 25m height and 5m away from the side edges. On the other hand, the total averaged Cp results on the leeward sides (0.03, 0.12, and 0.03, respectively, for the A1, B1, and C1 scenarios) do not match those of the reference quoted. This is possibly related to the limitations of the CFD solver adopted in reproducing accurately flow detachments and leeward wakes, which would interfere in the downwind pressure results. Also, while the windward and the leeward total average results are similar, overall leeward results are more homogeneous over the faces, presenting a smaller range of results than that for the windward face. Finally, the B1 square canyon gives greater Cp and wind velocity results due to airflow wake interference in the wide A1, and the skimmed flow in the narrow C1.The wind velocity magnitude vertical profiles show that wind deceleration prevails inside the canyon, and ranges from 50% to 90% at 4.0m height, when airflow velocity at the ABL input is 1.0m/s. Acceleration occur at 2.0m height in the middle of the wide canyon, attaining 100% on the upwind side. In the square and the narrow canyons there is negligible acceleration near ground level.

The analysis of the isolated x, y, and z flow vectors may show why the Cp results on the windward and leeward sides were equal: the bulk of the flow is similar in intensity, but opposite in direction as between the windward and leeward sides. The x flow component, orthogonal to the canyon, presents negative velocity from ground to middle height and positive velocity from middle to top height at the centre of the canyon. This indicates a stream-wise flow at the upper height and a reverse flow at the lower height. The y component vertical profile changes from a positive to a negative velocity on the left side and from a negative to a positive velocity on the right side of the canyon, ranging from -0.5 to +0.5m/s in all three canyon scenarios. The z component has a positive velocity on the leeward (up flow) and a negative ones on the windward side (down flow), with velocity ranges of: +0.30 and -0.50; + 0.25 and -0.50; and +0.15 and -0.30m/s for the A1, B1, and C1 settings, respectively. This shows that the down flow velocity on the windward side is twice that of the up-flow on the leeward side. Finally, the combined analysis of the three wind components describes a spiral, which means that not only a two dimensional vortex occurs inside the canyon, but a three dimensional vortex is observed for orthogonal winds. The spiral flow is symmetrical and divides in two directions: one from the centre to the right, and the other from the centre to the left side of the canyon.

Figure 7-10: Wind velocity magnitude and x, y and z wind vector components vertical profiles (A01, 90°, m/s):

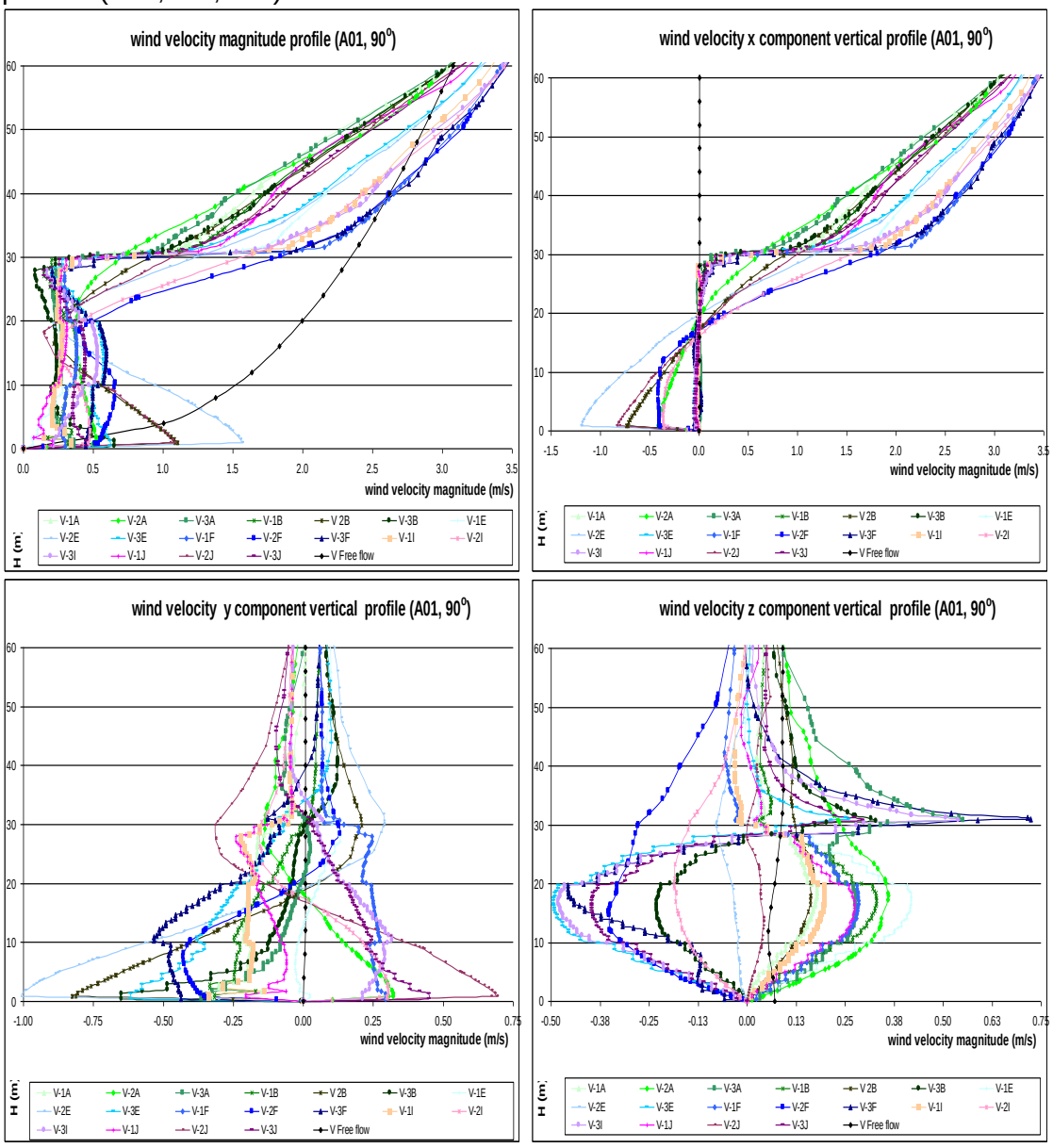

Source: this study.

Figure 7-11: Wind velocity magnitude and x, y and z wind vector components vertical profiles (B01, 90°, m/s):

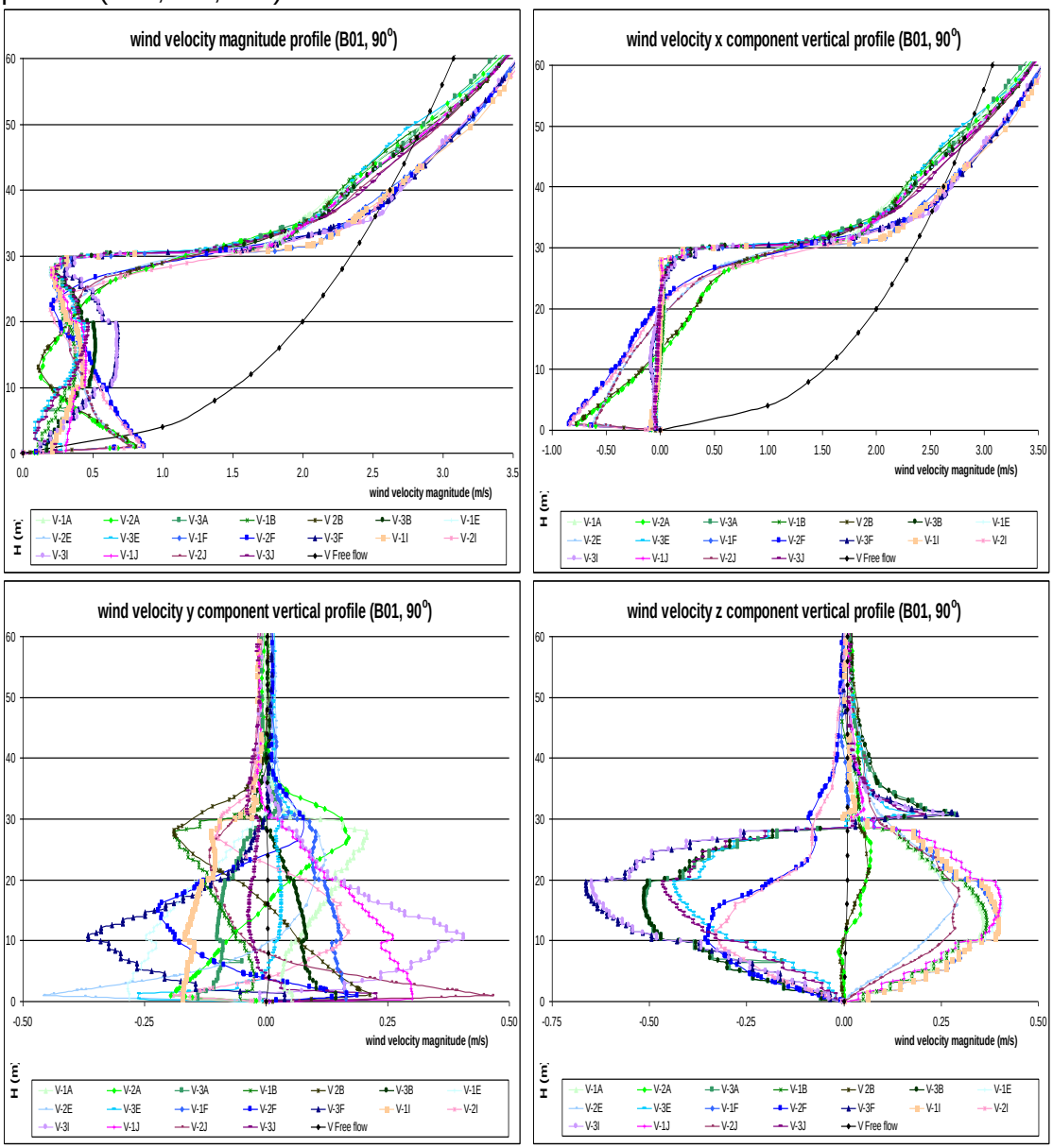

Source: this study.

Figure 7-12: Wind velocity magnitude and x, y and z wind vector components vertical profiles (C01, 90°, m/s):

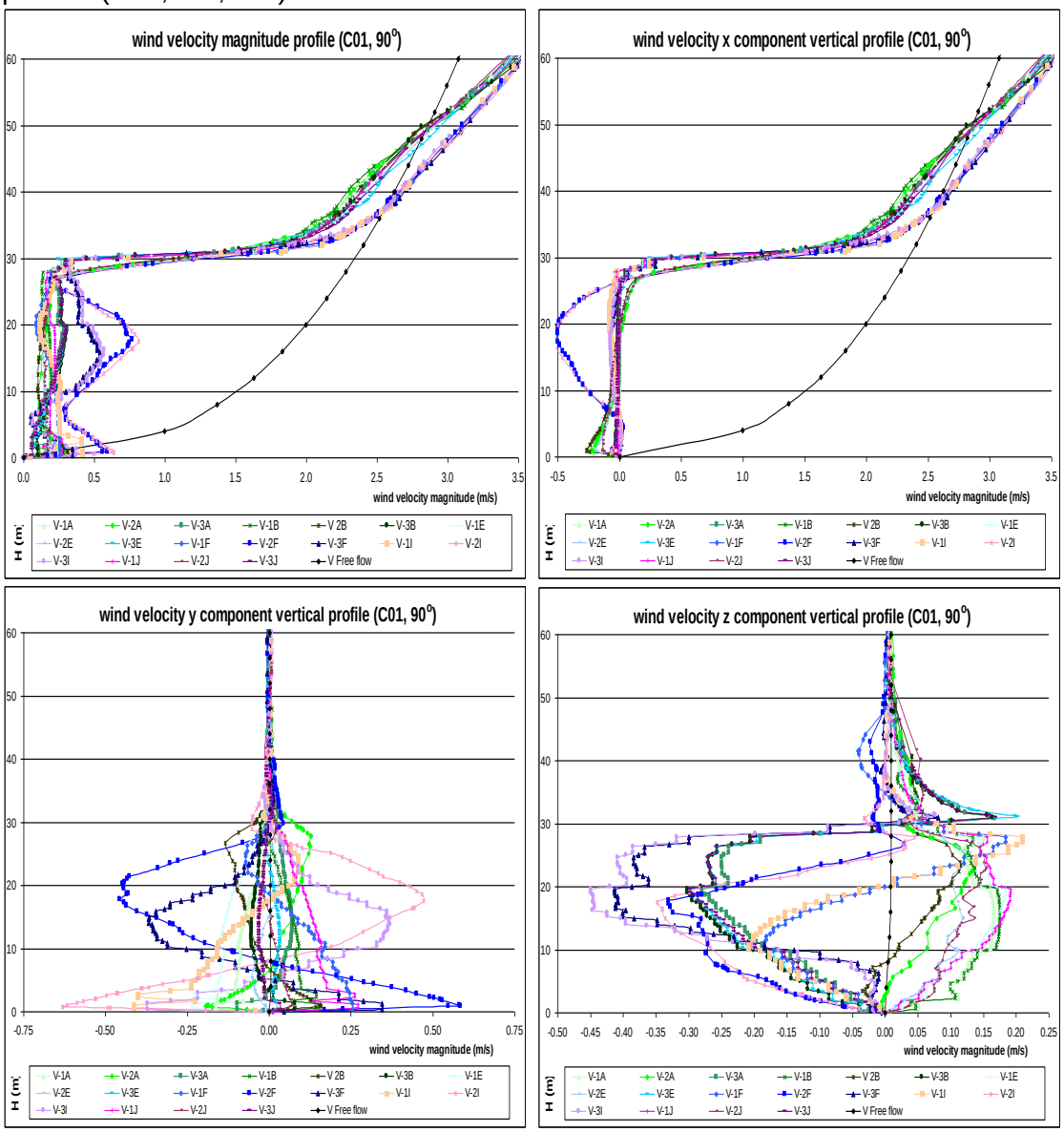

Source: this study.

7.3.1.3. A01, B01, and C01 analysis of the results (45°)

The assessment of winds oblique to the canyon's axis focused on the windward and the leeward faces. The wind flows along a diagonal from the left corner of the upwind block's leeward side to the right corner of the downwind block's windward side. Total averaged Cp results for the A1, B1, and C1 prototypes on the windward surface were 0.16, 0.06, and 0.09, thus agreeing with the results described by Liddament[91] (1996). Conversely, the total averaged Cp average results on the leeward side were higher than those given by the same source: 0.13, 0.04 and 0.09.

[91] For 10m height rectangular buildings in urban areas, Liddament (1996) gives Cp results of +0.12 for the windward walls and Cp results of -0.38 for the leeward walls at oblique winds (45°) (see topic 2.4 in Chapter 2).

Figure 7-13: The wind velocity magnitude pathlines (m/s) for the A1 (top), B1 (middle) and C1 (bottom) prototypes and for 45^{o} winds.

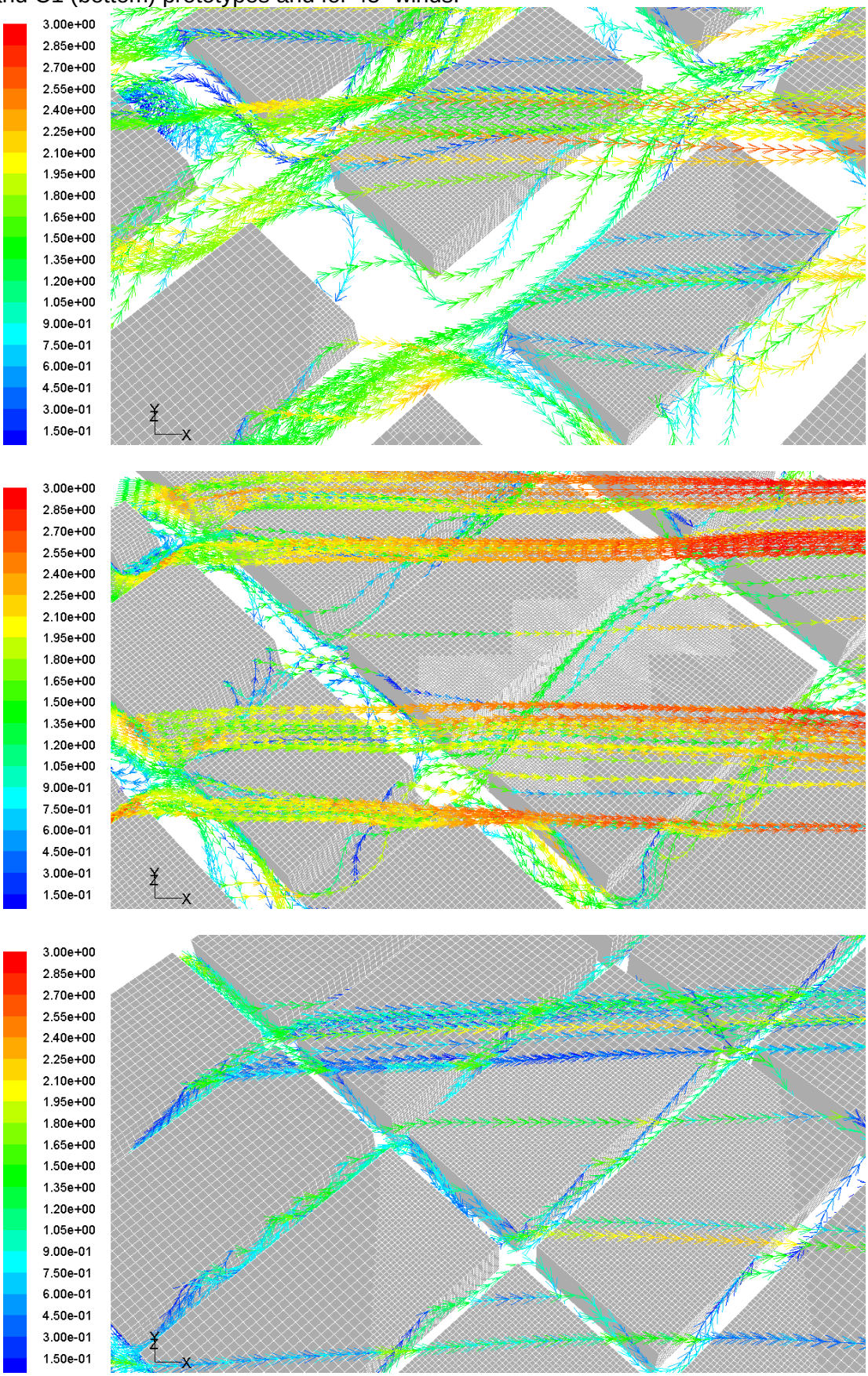

Source: This study.

The wind velocity magnitude vertical profiles show acceleration at the pedestrian level in the A1 and B1 scenario canyon entrance reaching from 100% to 200%. The narrow C1 canyon showed less acceleration: 30%. Detachment flow occurred on the vertical edge of the upwind block left corner from middle to top height, causing a sharp drop in pressure in this area. Both the x and y wind components were positive at low heights and mostly positive at the top height. Conversely, the z component changes it velocity direction from mostly negative from low to middle height to positive from middle to top height near the windward side, with the opposite happening on the leeward side. This shows the existence of a diagonal vortex along the canyon accompanying the airflow.

Figure 7-14: Wind velocity magnitude and x, y and z wind vector components vertical profiles (A01, 45°, m/s):

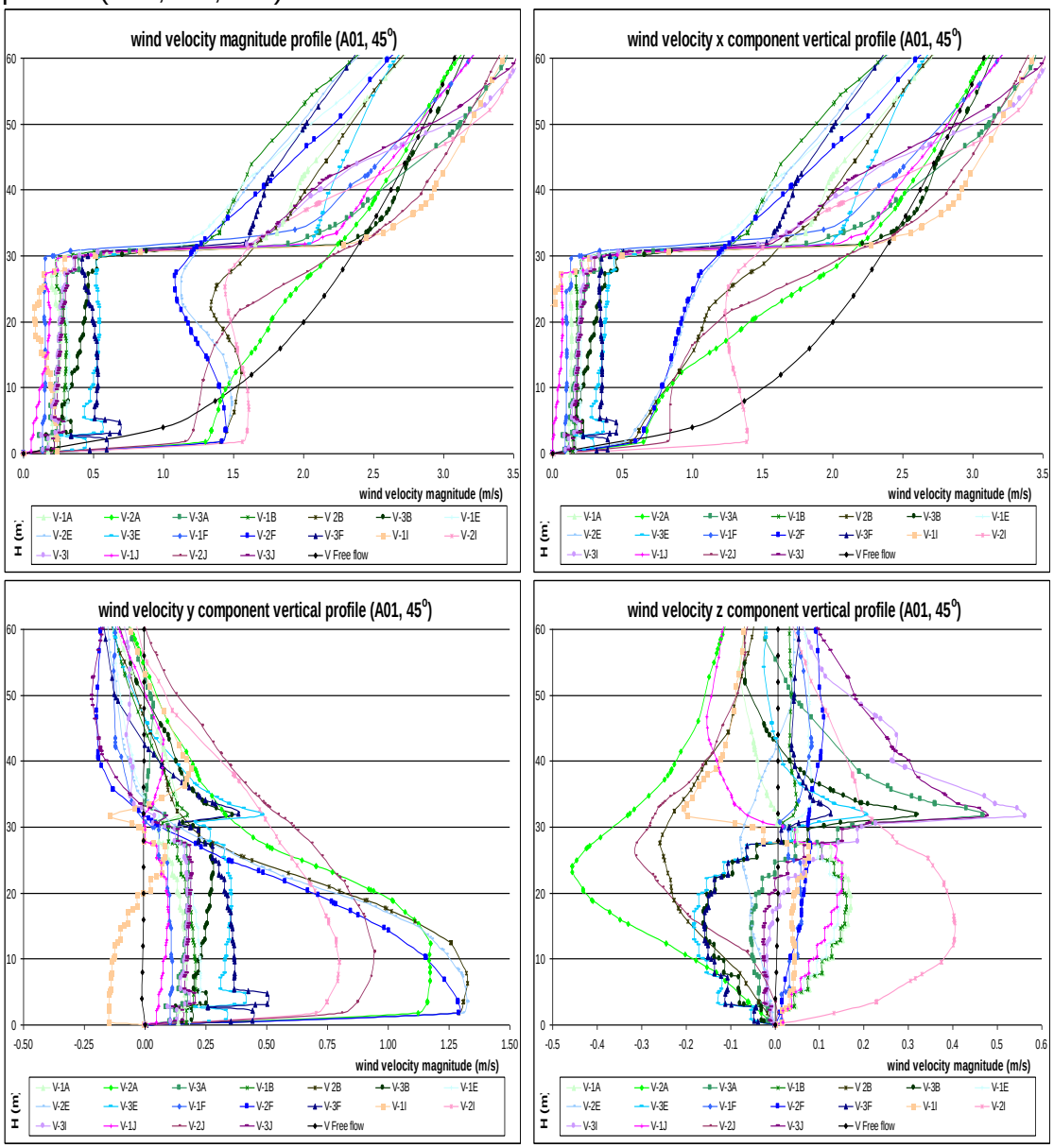

Source: this study.

Figure 7-15: Wind velocity magnitude and x, y and z wind vector components vertical profiles (B01, 45°, m/s):

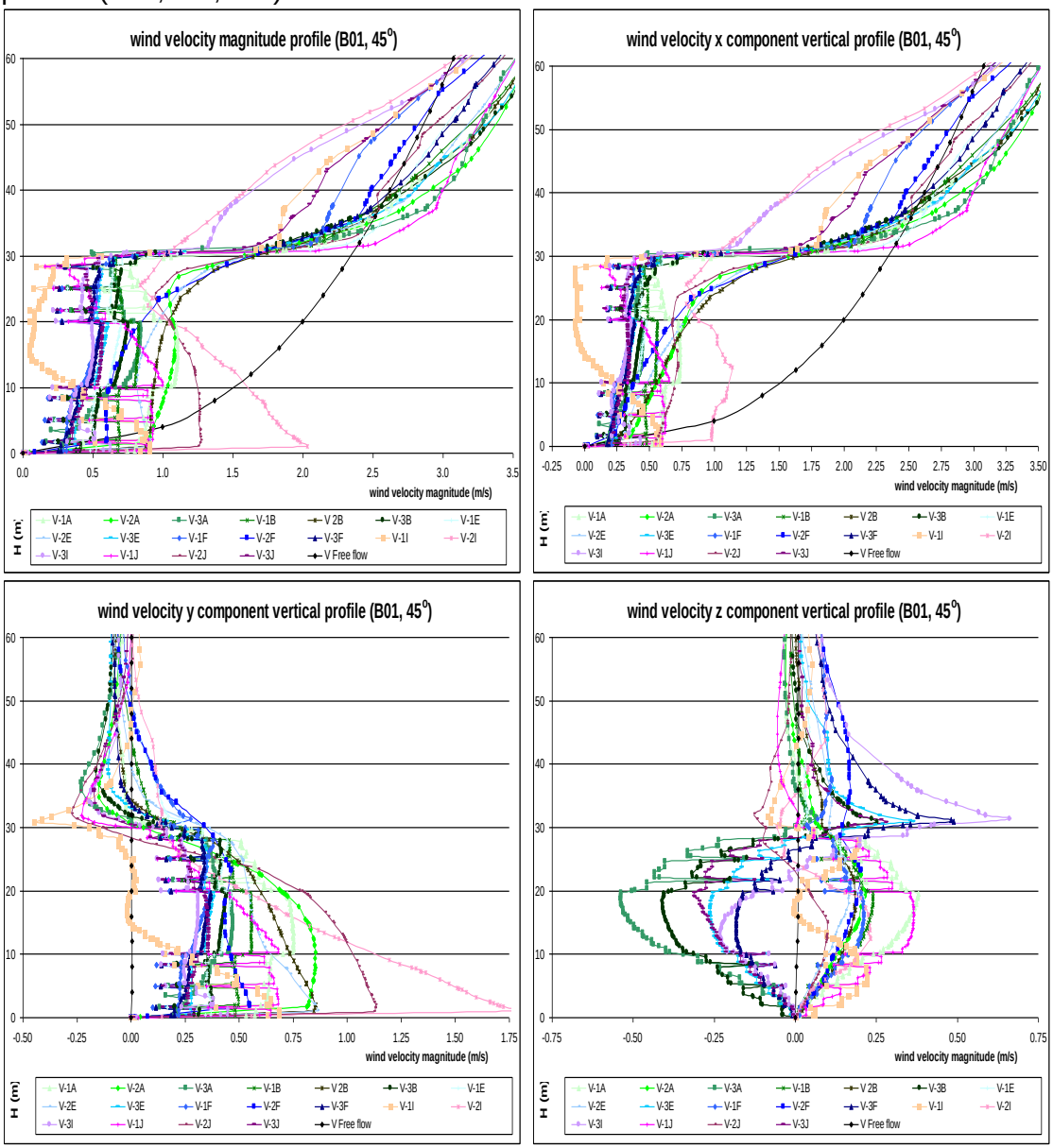

Source: this study.

Figure 7-16: Wind velocity magnitude and x, y and z wind vector components vertical profiles (C01, 45°, m/s):

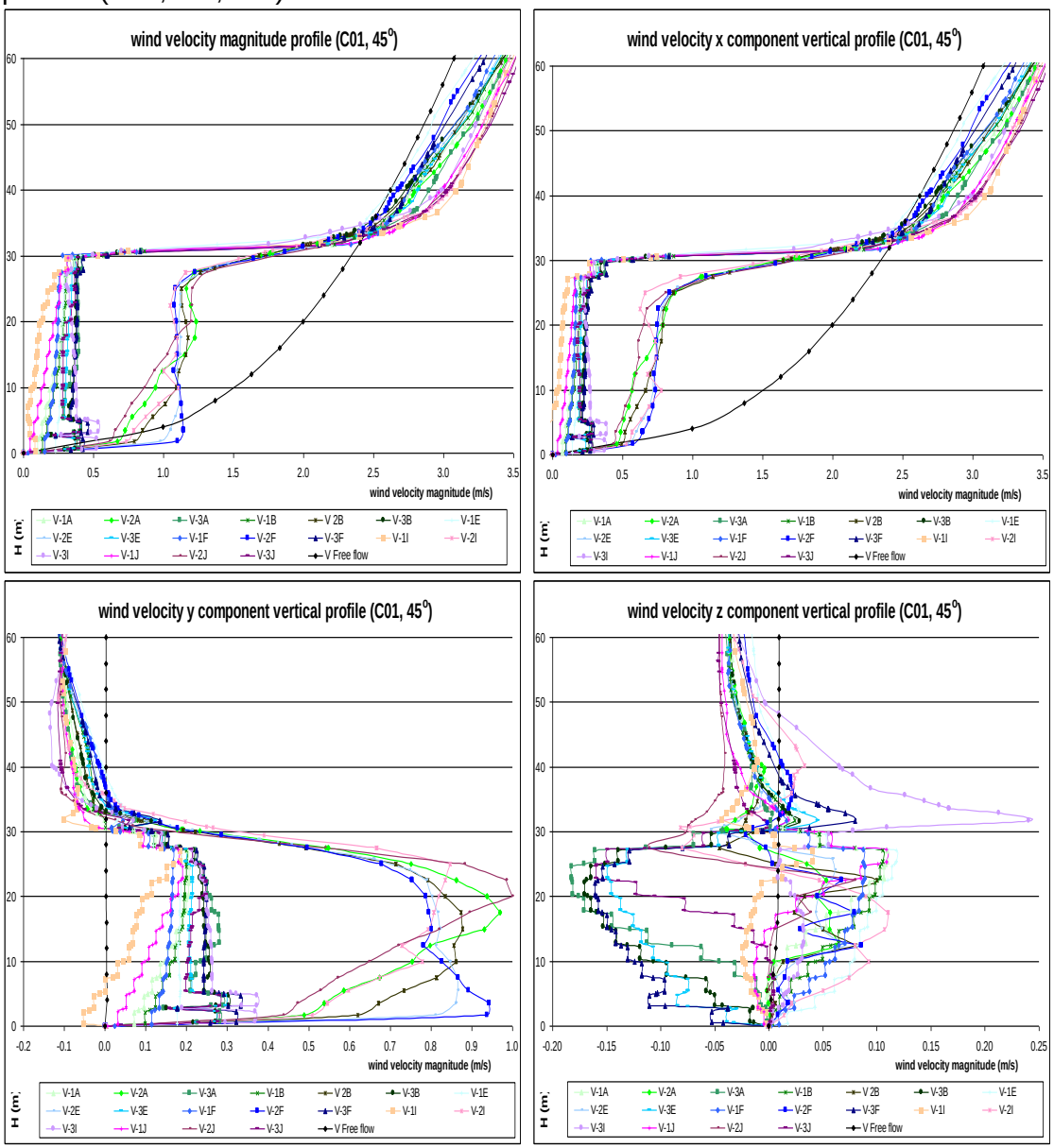

Source: this study.

7.3.2. Group 2: prototypes A2, B2, and C2

7.3.2.1 Analysis for parallel winds (0^o)

With nearly symmetrical results on both the right and left sides of the canyon, the respective total averaged Cp results for the A2 (wide), B2 (square), and C2 (narrow) prototypes were: 0.02, 0.06, and 0.02. These results are higher than those described in the reference literature[92], thought they are similar to the group 1 results.

Further, the ranges of the Cp results for the three scenarios at the low; medium; and top heights were: -0.01, 0.02, and 0.05 in the wide; 0.02, 0.06, and 0.10 in the square; and -0.01, 0.02 and 0.05 in the narrow canyon. This shows little influence of the canyon's width in the Cp results. The absolute minimum Cp results occurred on the upwind side face near the edges, with low peak Cp averaged results of: -0.13, -0.05 and -0.05. As an example of group 1, this indicates flow detachment at the vertical sharp edge creating a low pressure bubble on this corner. Flow reattachment takes place at a 10m horizontal distance and, after this, Cp results show a slight increase of about 0.05 across the face, as far as the downwind corner.

Figure 7-17: Velocity magnitude pathlines for the B2 scenario with parallel winds.

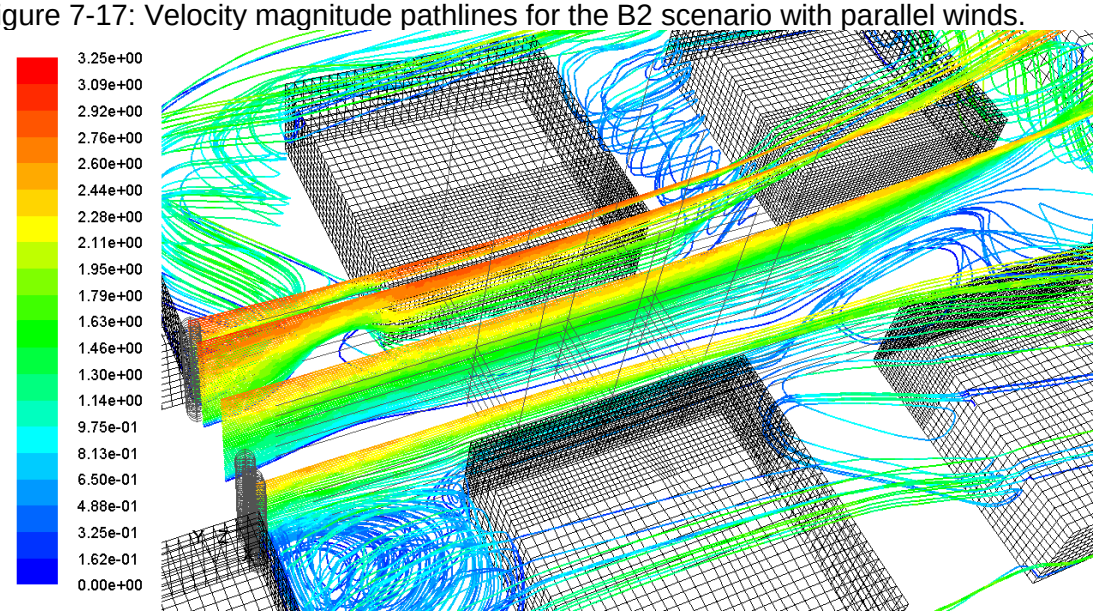

Source: This study.

The wind velocity magnitude vertical profiles show that acceleration occurs near the ground at the centre of the canyon. For instance, at 2m height, the wind speeds in the A2, B2, and C2 scenarios were: 0.95, 1.47 and 0.78m/s, while the related speed at the ABL input was 0.75m/s. As the height increases, the velocity at the centre either

[92] For 10m hight rectangular buildings in urban areas, Liddament (1996) gives Cp results of -0.2 for side walls in parallel winds (0^o) (see topic 2.4 in Chapter 2).

reduces (as in A2 and C2) or accompanies the outside flow. Near the canyon walls deceleration occurs and wind speed ranges from 0.3m/s to 0.6m/s in the three scenarios. The x component of the wind, along with the air stream, is the prevailing vector in the wind velocity magnitude inside the canyon, as both the y and z components show low ranges of velocity: 0.12, 0.05, and 0.07m/s, respectively, in the A2, B2 and C2 prototypes.

Figure 7-18: Wind velocity magnitude and x, y and z wind vector components vertical profiles (A02, 0°, m/s):

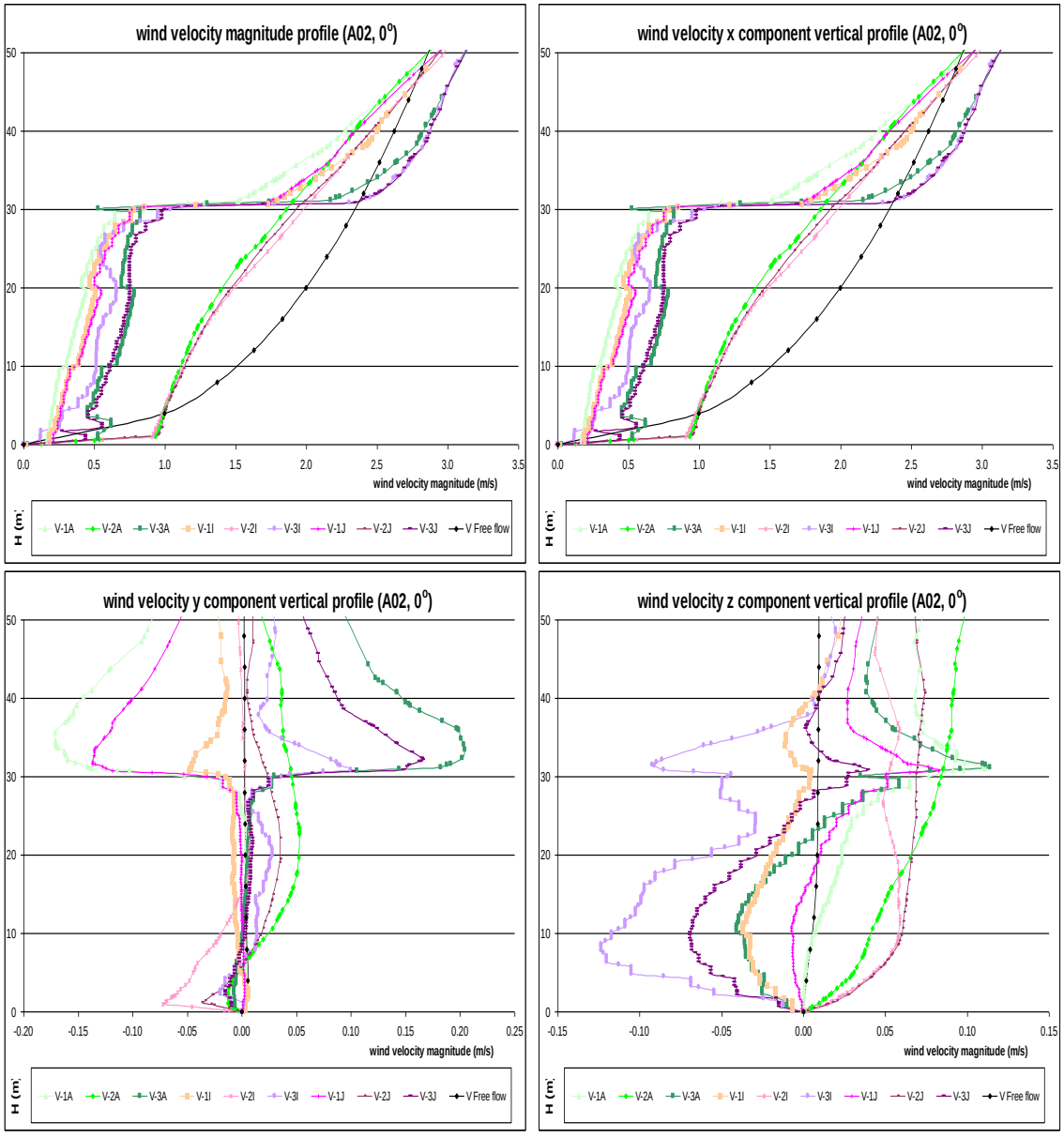

Source: this study.

Figure 7-19: Wind velocity magnitude and x, y and z wind vector components vertical profiles (B02, 0°, m/s):

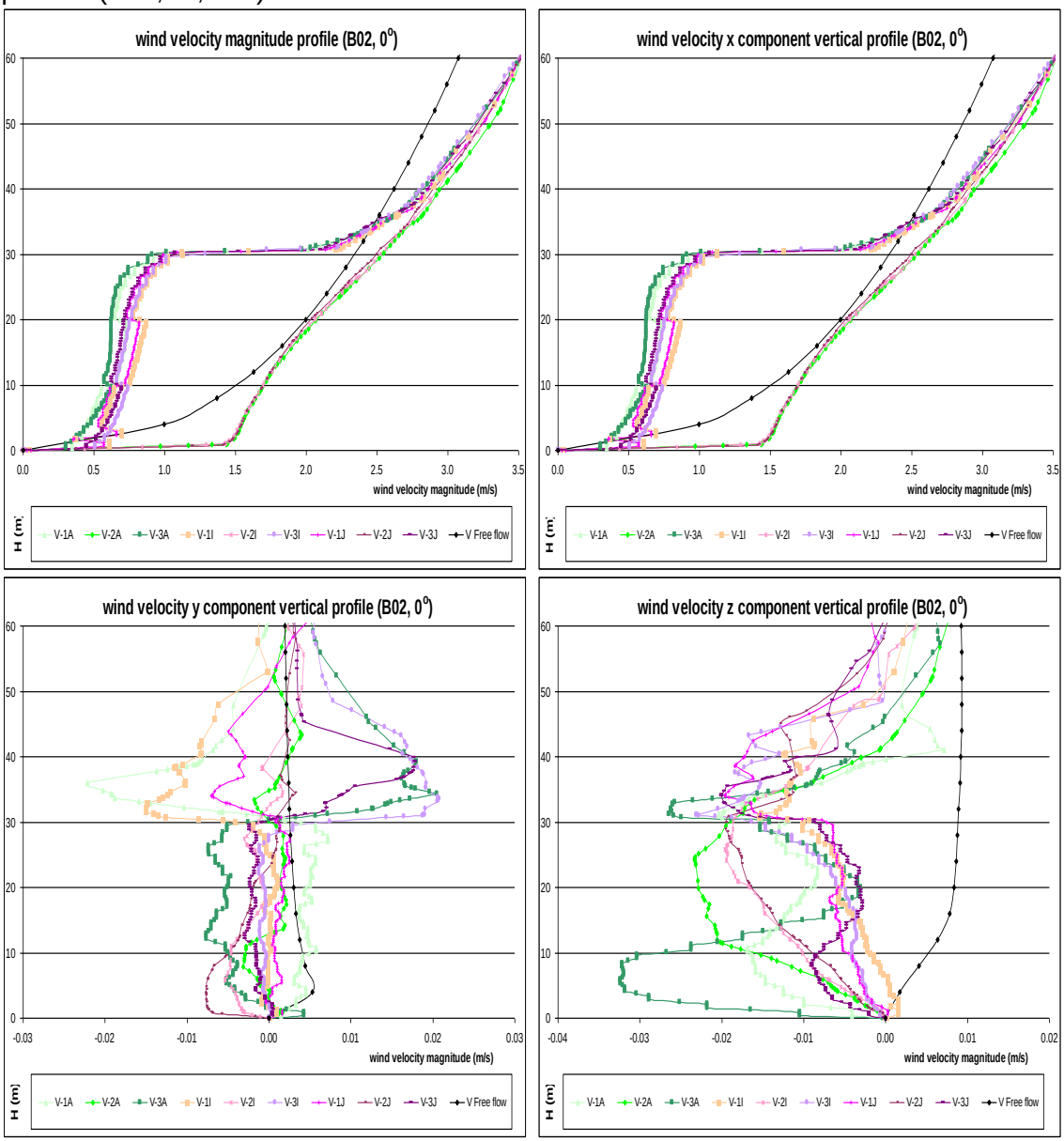

Source: this study.

Figure 7-20: Wind velocity magnitude and x, y and z wind vector components vertical profiles (C02, 0°, m/s):

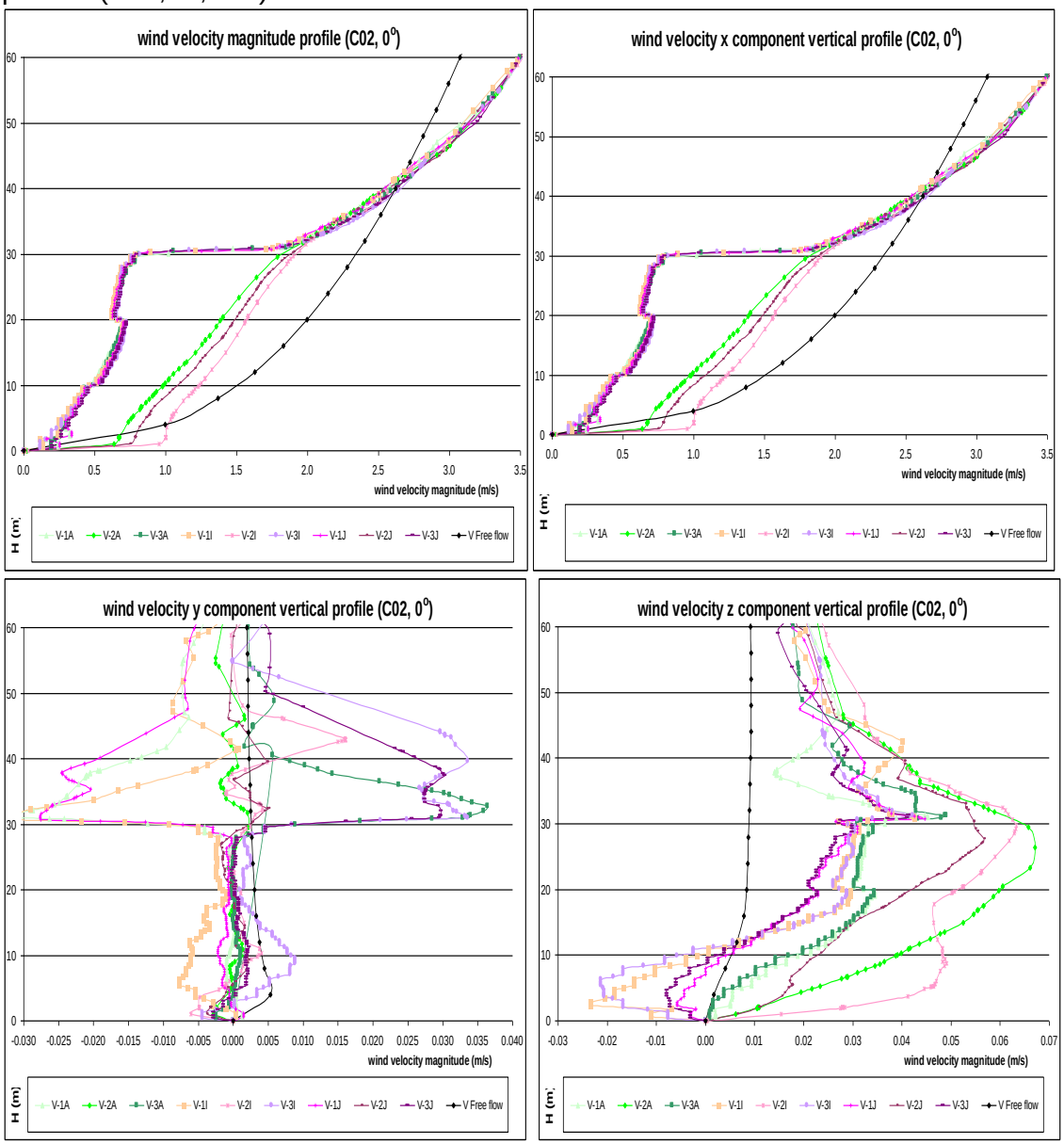

Source: this study.

7.3.2.2 Analysis for orthogonal winds (90°)

The total averaged Cp results for the A2, B2, and C2 prototypes on the windward sides were: 0.40, 0.11, and -0.06. While the result in the A2 wide canyon was greater than that described by Liddament[93] (1996), the results on the B2 square and the C2 narrow canyons were closer to those in the literature.

The Cp distribution on the windward faces varied greatly between the three scenarios. While in the A2 and the B2 canyons great pressure variation was found (as in group 1), the narrow C2 set showed an even Cp distribution with a small pressure range, which arose possibly as a result of the occurrence of the skimming flow. Conversely, the previously commented symmetry of pressure distribution on the windward face, with an equal increase of pressure on the flanks and drop in the centre, did not occur in the A2 scenario - though it did in both the other arrangements. A strong diagonal spiral flow was observed in the A2 prototype, resulting in an irregular flow distribution along the canyon. This flow changed the pressure distribution pattern on the windward wall. For instance, near the lateral edges and at 25m height (where the greatest Cp results were found), the absolute Cp results for the A2, B2, and C2 scenarios were: 0.23 (right side) and 0.78 (left side), 0.36 (on both right and left sides), and 0.02 (on both right and left sides). At the centre the average Cp results were: 0.62; 0.09; and -0.01. In contrast, the maximum peaks were: 1.11, 0.40 and 0.02.

Figure 7-21: Velocity magnitude pathlines for the A2 scenario and orthogonal winds.

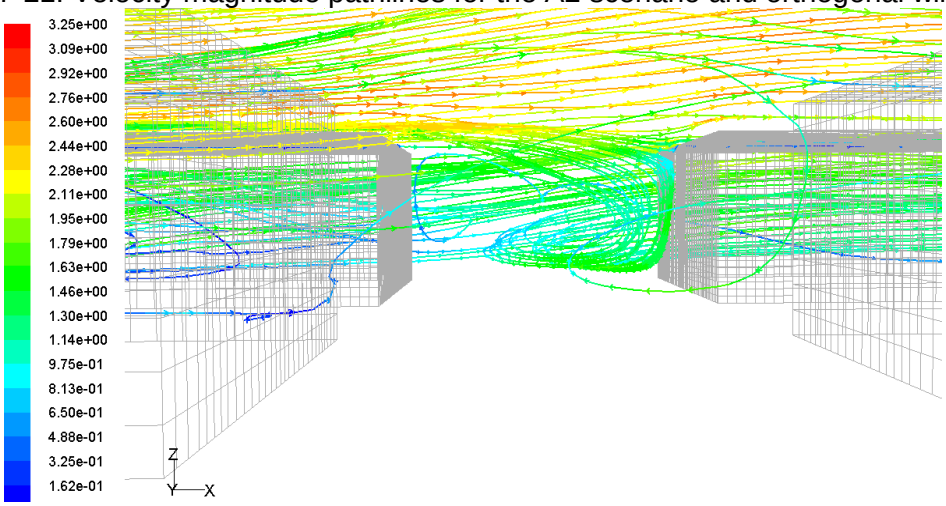

Source: This study.

[93] For 10m height rectangular buildings in urban areas, Liddament (1996) gives Cp results of +0.06 for the windward and of -0.30 for the leeward walls at orthogonal winds (90°) (see topic 2.4 in Chapter 2).

Figure 7-22: The wind velocity magnitude pathlines (m/s) for the A2 (top), B2 (middle) and C2 (bottom) prototypes and for 90^{o} winds.

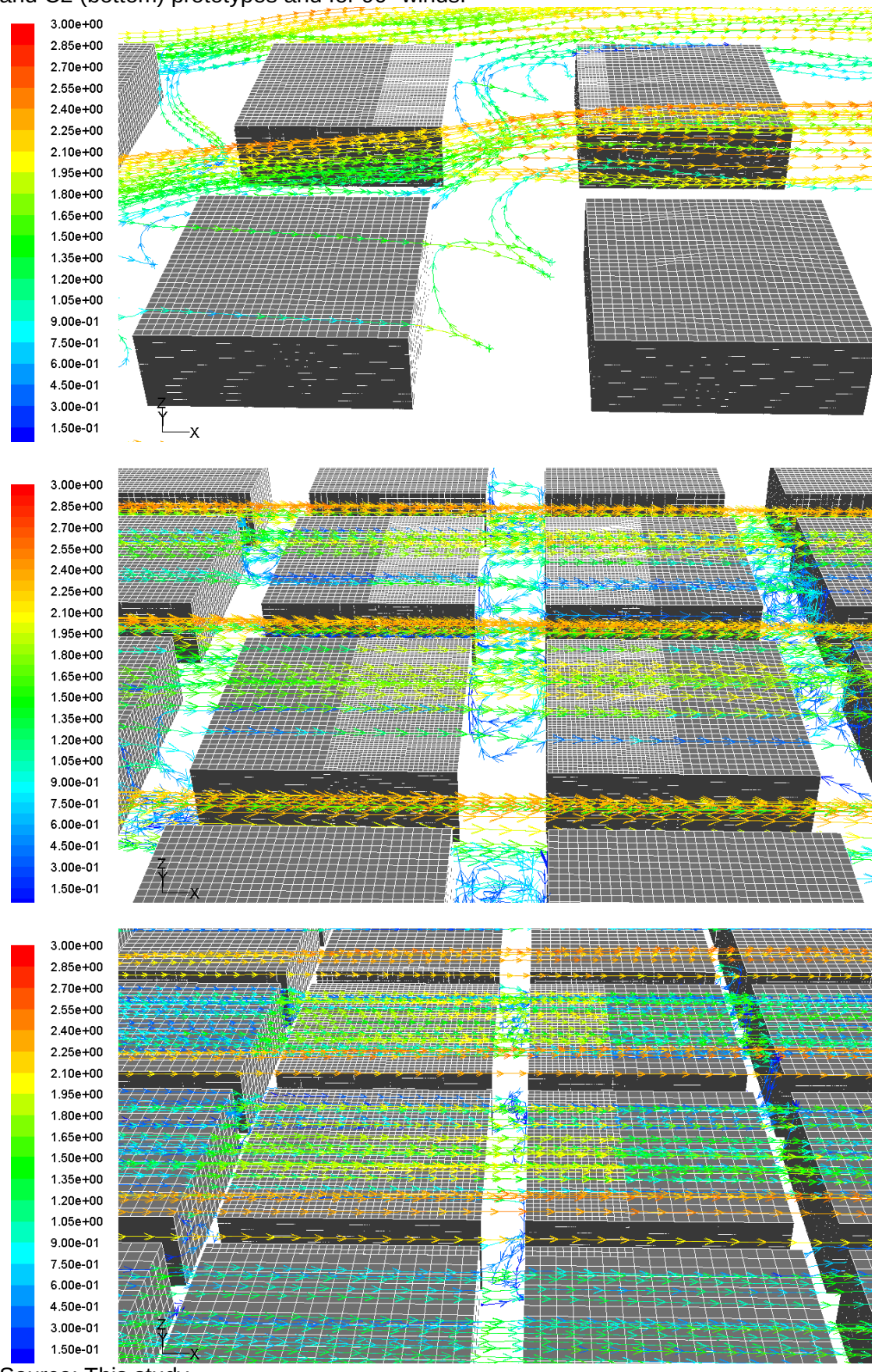

Source: This study.

The total averaged Cp results on the leeward sides (0.04, 0.08, and -0.06 for the A2, B2, and C2 scenarios) were greater than those given by Liddament (1996). Further, the overall leeward results were more homogeneous over that face and the range of results was smaller than those for the windward face. Additionally, it is noticeable that the A2 wide canyon presents a more asymmetrical aspect than either the square or the narrow scenarios. The pressure distribution on the A2 leeward face is a mirrored distribution that on the opposite windward face, indicating a spiral airflow pattern occurring horizontal to the ground.

Figure 7-23: Wind velocity magnitude and x, y and z wind vector components vertical profiles (A02, 90°, m/s):

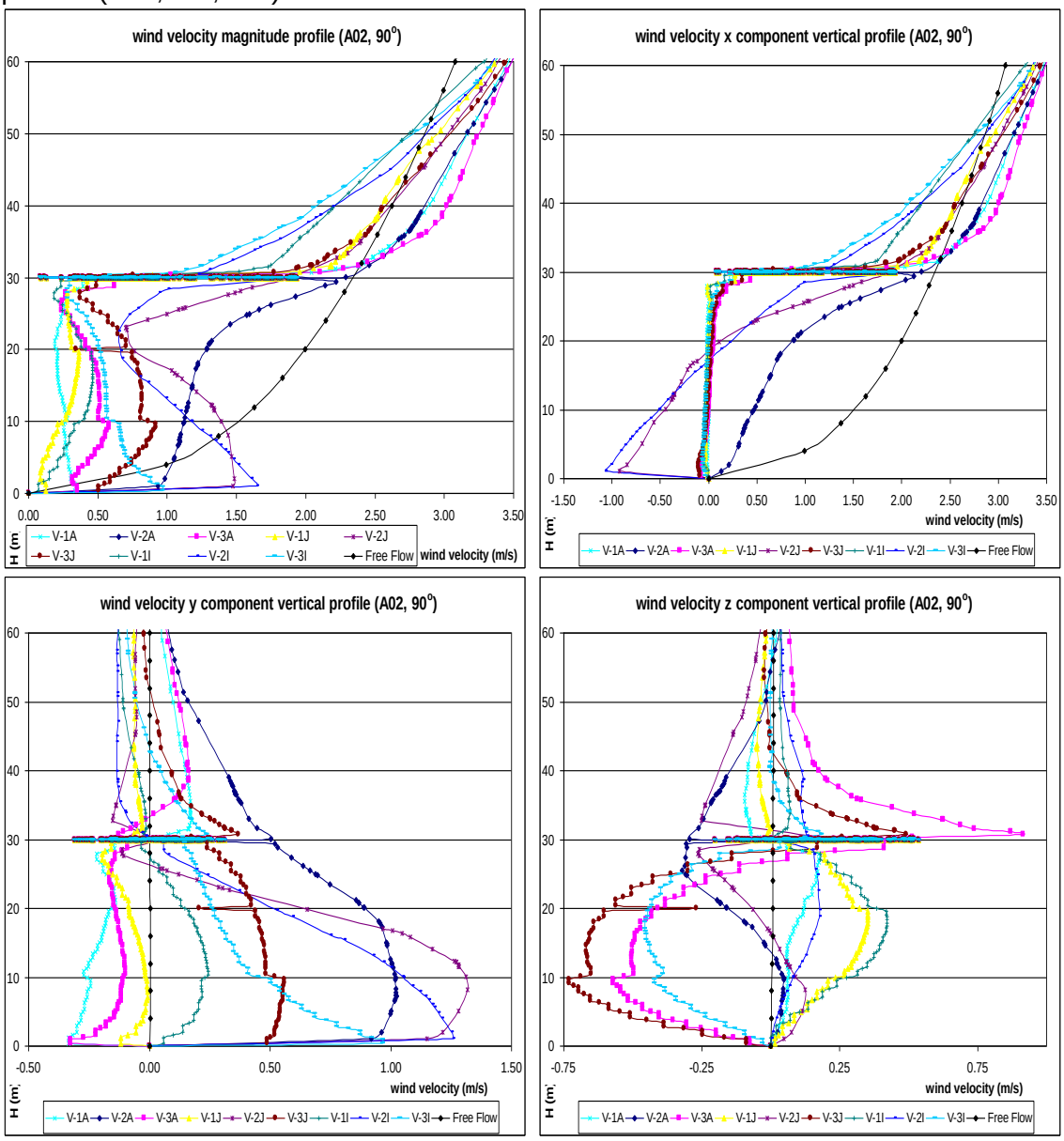

Source: this study.

The wind velocity magnitude vertical profiles show that, while the wind in the centre of the canyon and near the ground accelerates by up to 300% and 50% on both the wide and square scenarios, the narrow one maintains the same input ABL velocity. On the other hand, it was found that wind deceleration inside the canyon prevails near both the windward and the leeward faces, though the velocities on the first are slightly lower than those on the second. In general, the velocity profiles inside the canyons remain constant from ground to top ranging respectively from: 0.20 to 0.70m/s; 0.20 to 0.50m/s; and 0.10 to 0.30m/s in the wide, the square and the narrow canyons.

Figure 7-24: Wind velocity magnitude and x, y and z wind vector components vertical profiles (B02, 90°, m/s):

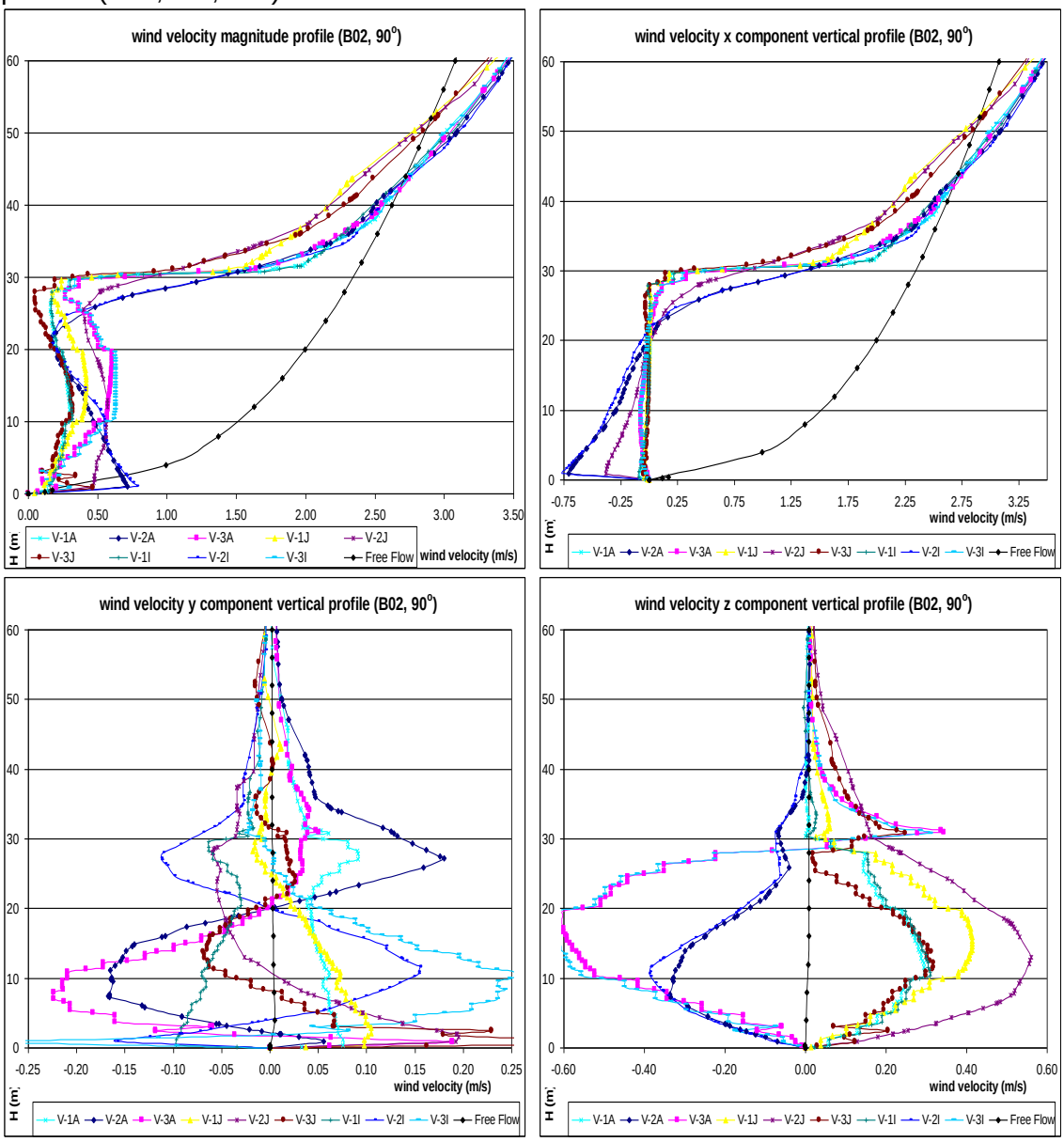

Source: this study.

When assessing the x, y and z wind vector components, it is possible to observe that the x component, orthogonal to the canyon, has negative velocities from the ground to 20m height and positive velocities above it, which indicates an accelerated reverse flow near the ground and a stream wise flow in the upper height, thus forming a clock-wise vortex. The y component behaves in two distinct ways. In the A2 scenario the y velocity vector is all positive below the canyon's height, with the exception of the downwind corners which present some reverse flow. This major flow towards one side is consistent with the asymmetrical pressure distribution on both the windward and leeward faces described above. Conversely, in both the B2 and the C2 scenario, a change of direction is also observed in the y profiles, changing from a positive to a negative velocity at 20m height, though not reflecting as much in the pressure distribution as it does in A2. The results for the z vector component are also characterized by a shift from positive to negative speed with great intensity several times within the canyon's height. The velocity ranges between negative (down) and positive (up) flows were: -0.75 and +0.75; -0.60 and +0.60; and -0.40 and +0.20m/s for the A2, B2, and C2 scenarios. Finally, the combined analysis of the three wind components describes a vortex. While this spiral flow tends to one side for the wide A2 scenario, it is more symmetrical and flows from the centre to both the right and the left sides of the B2 and C2 canyons.

Figure 7-25: Wind velocity magnitude and x, y and z wind vector components vertical profiles (C02, 90°, m/s):

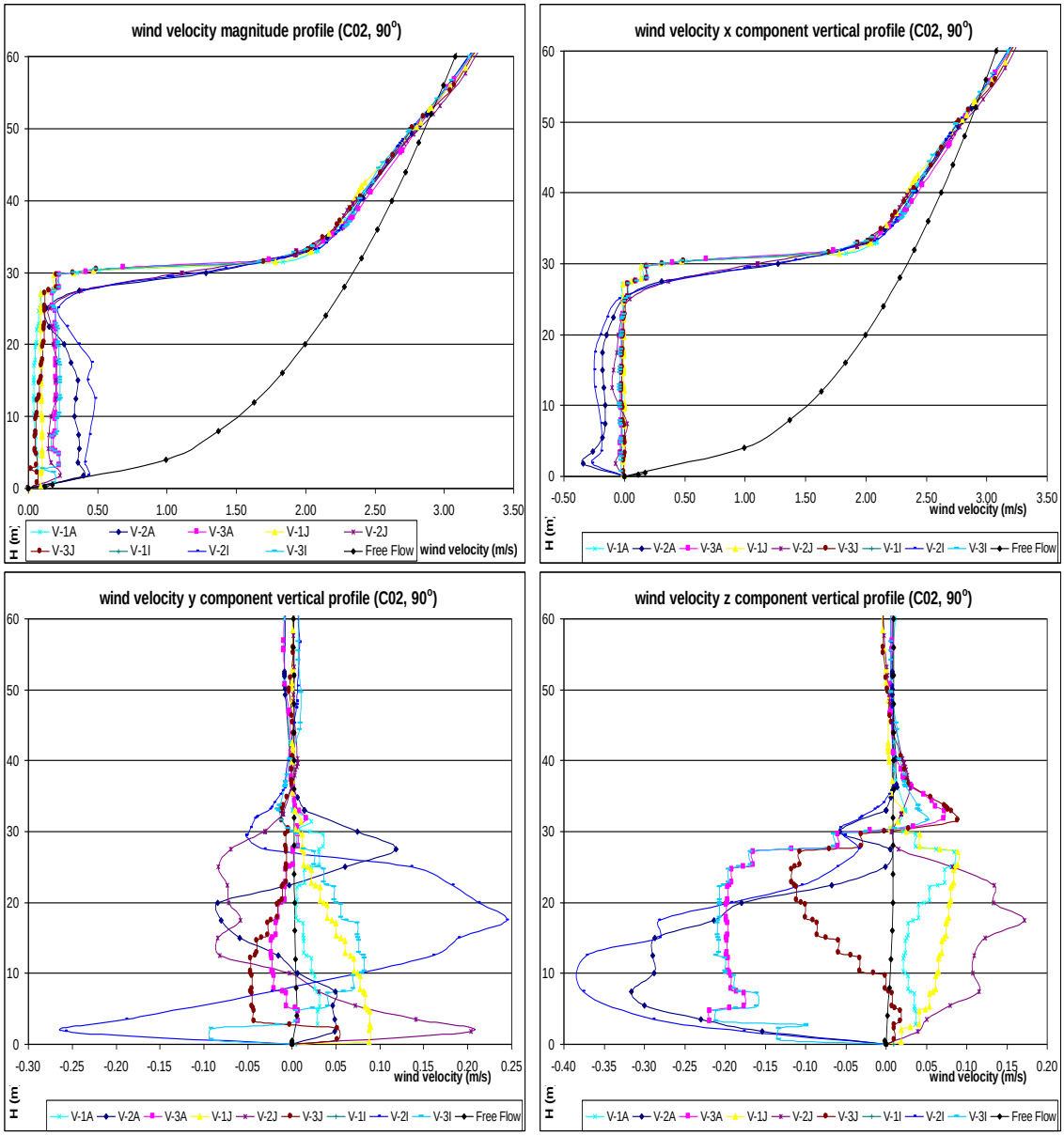

Source: this study.

7.3.2.3 Analysis for oblique winds (45^{o})

The total averaged Cp results on the windward sides of the A2, B2, and C2 prototypes were: 0.10, 0.11, and 0.07, which are close to the reference literature[94] results. The total averaged Cp results on the leeward side were: 0.09, 0.07 and 0.07, which are greater than those mentioned in the literature. As an example of Group 1, the windward and the leeward average results were practically identical in the three cases.

Figure 7-26: The wind velocity magnitude pathlines (m/s) for the B2 scenario (45^{o}).

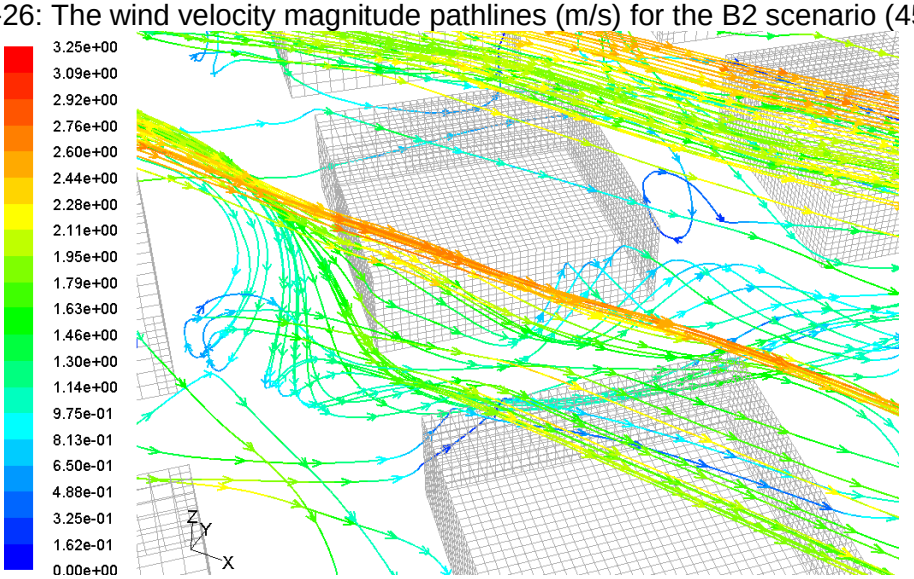

Source: This study.

The wind velocity magnitude vertical profiles show that acceleration happens in the central axis near ground level on the A2 (up to 3x), while it is moderate for the B2 (up to 1.5x), and in the C2 prototype wind speed is similar to the ABL input. Conversely, after accelerating, velocities in the central axis remain constant up to the canyon top. Near walls, wind speed ranges from 0.20 to 0.50m/s on both windward and leeward surfaces. The wind x component vector, at an angle of 135o to the windward side, follows the velocity magnitude profile patterns. The y component indicates flow to one side, following the mainstream in the canyon, but presenting reverse flow near the windward face. Above the canyon reverse flow is noticed. The y velocity ranges up to 1.0, 1.4 and 0.8m/s for the A2, B2, and C2 scenarios. The z vector component shows several changes from positive to negative throughout the canyon height. This indicates an intense diagonal spiral flow towards the mainstream, on which the velocity ranges for positive (up) and negative (down) flows were: +0.50 and -0.10; +0.40 and -0.50; and +0.35 and -0.20m/s.

[94] For 10m height rectangular buildings in urban areas, Liddament (1996) gives Cp results of +0.12 for the windward walls and Cp results of -0.38 for the leeward walls at oblique winds (45^{o}) (see topic 2.4 in Chapter 2).

Figure 7-27: The wind velocity magnitude pathlines (m/s) for the A2 (top), B2 (middle) and C2 (bottom) prototypes and for 45^{o} winds.

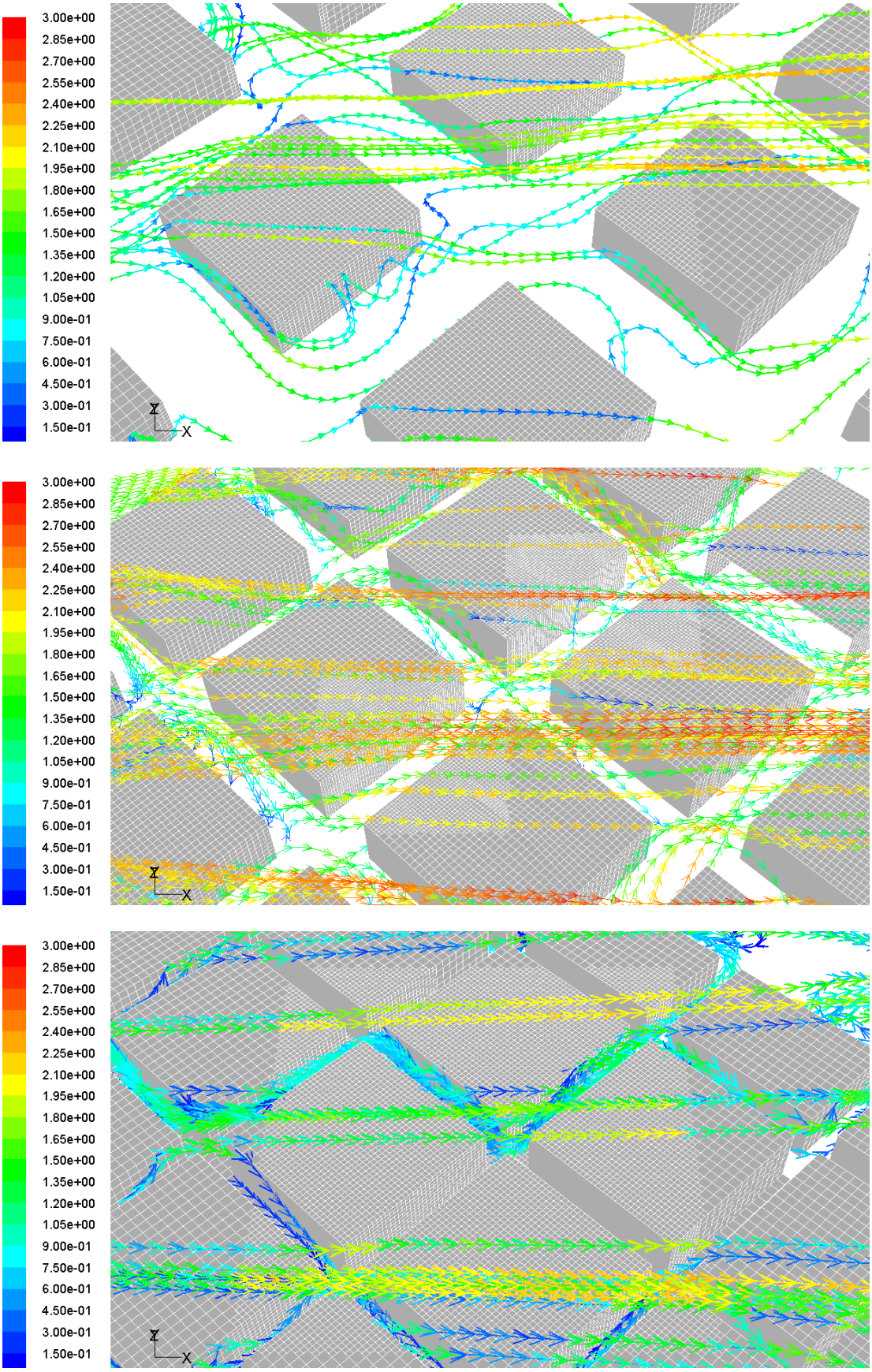

Source: This study.

Figure 7-28: Wind velocity magnitude and x, y and z wind vector components vertical profiles (A02, 45°, m/s):

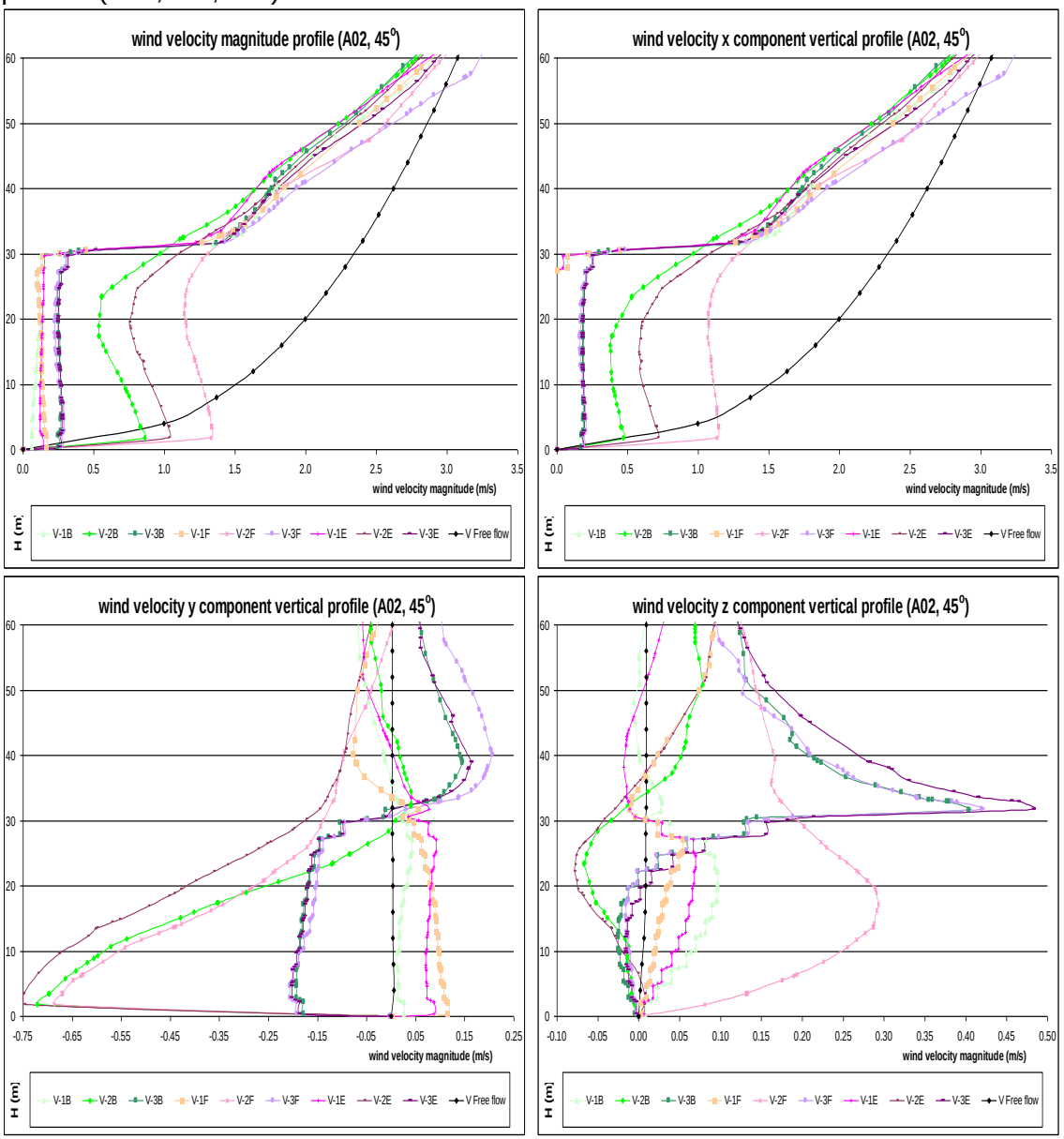

Source: this study.

Figure 7-29: Wind velocity magnitude and x, y and z wind vector components vertical profiles (B02, 45°, m/s):

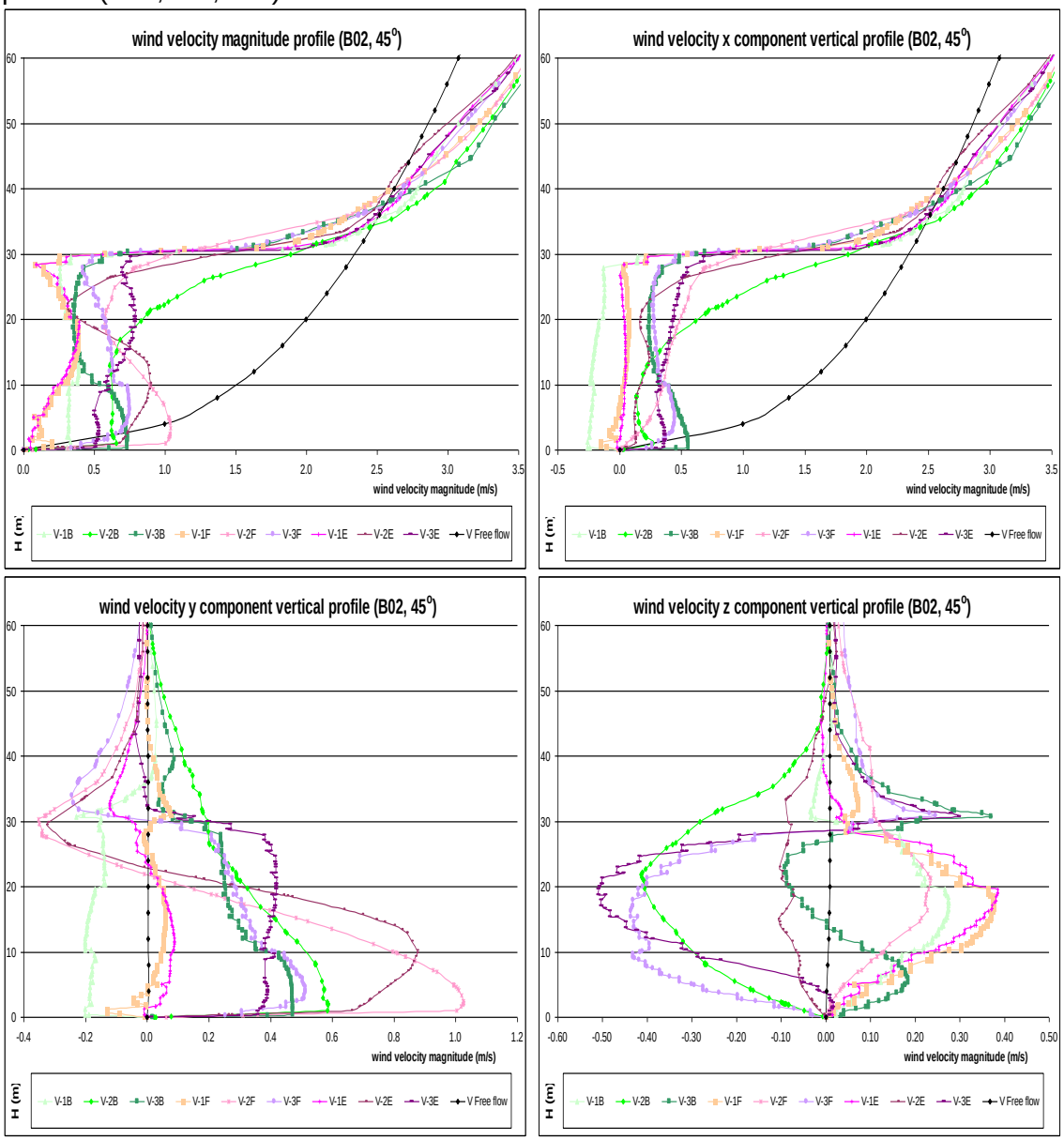

Source: this study.

Figure 7-30: Wind velocity magnitude and x, y and z wind vector components vertical profiles (C02, 45°, m/s):

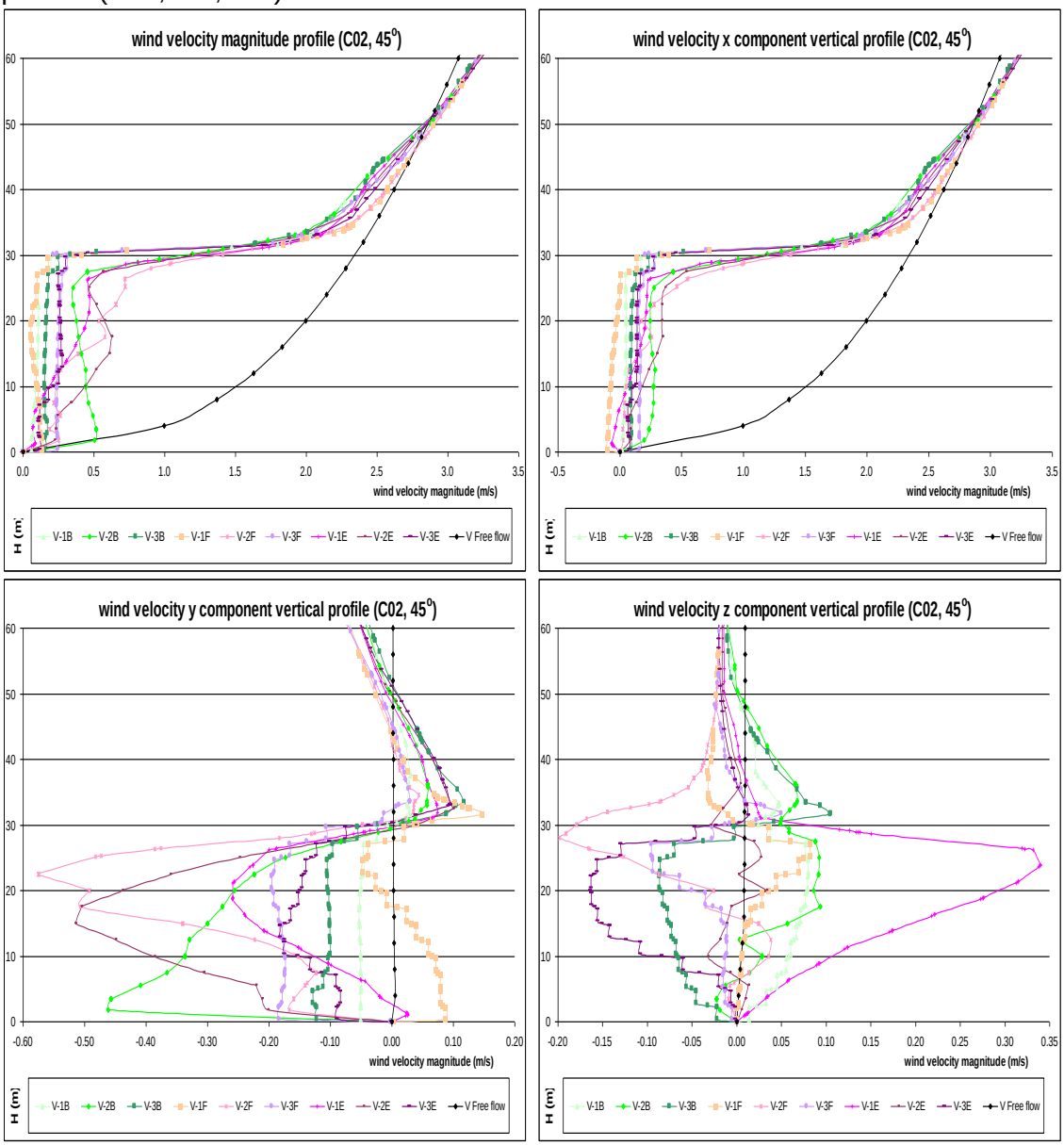

Source: this study.

7.3.3. Group 3: prototypes A3, B3, and C3

7.3.3.1 Analysis of the A03, B03, and C03 results (0^o)

The total averaged Cp results for winds parallel to the A3, B3, and C3 prototypes' faces were: -0.03, -0.01, and 0.00. These results are greater than those given in the reference literature[95]. When considering the Cp distribution across the faces, the A3, B3, and C3 scenarios presented the following range of results (for low, medium, and high heights): -0.02, -0.03, and 0.01; -0.05, -0.01, and 0.03; and -0.03, 0.00 and 0.03. The results show that the canyon's width influences the Cp distribution for parallel winds only slightly. Additionally, absolute minimum Cp results also occurred on the upwind side face near the edges.

Figure 7-31: Wind velocity magnitude and x, y and z wind vector components vertical profiles (A03, 0^o, m/s):

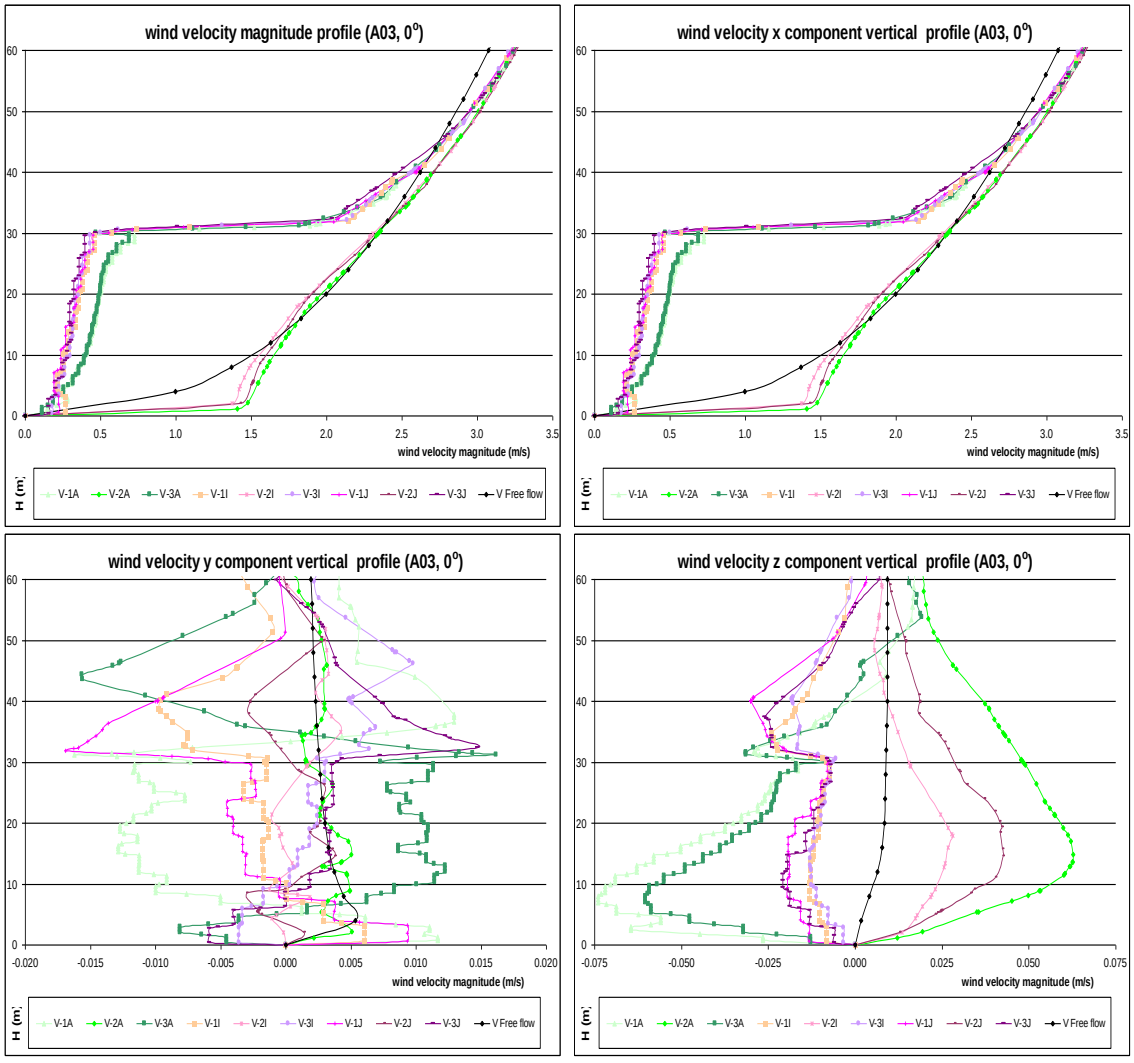

Source: this study.

[95] For 10m high rectangular buildings in urban areas, Liddament (1996) gives Cp results of -0.20 for side walls in parallel winds (0^o) (see topic 2.4 in Chapter 2).

Figure 7-32: Wind velocity magnitude and x, y and z wind vector components vertical profiles (B03, 0°, m/s):

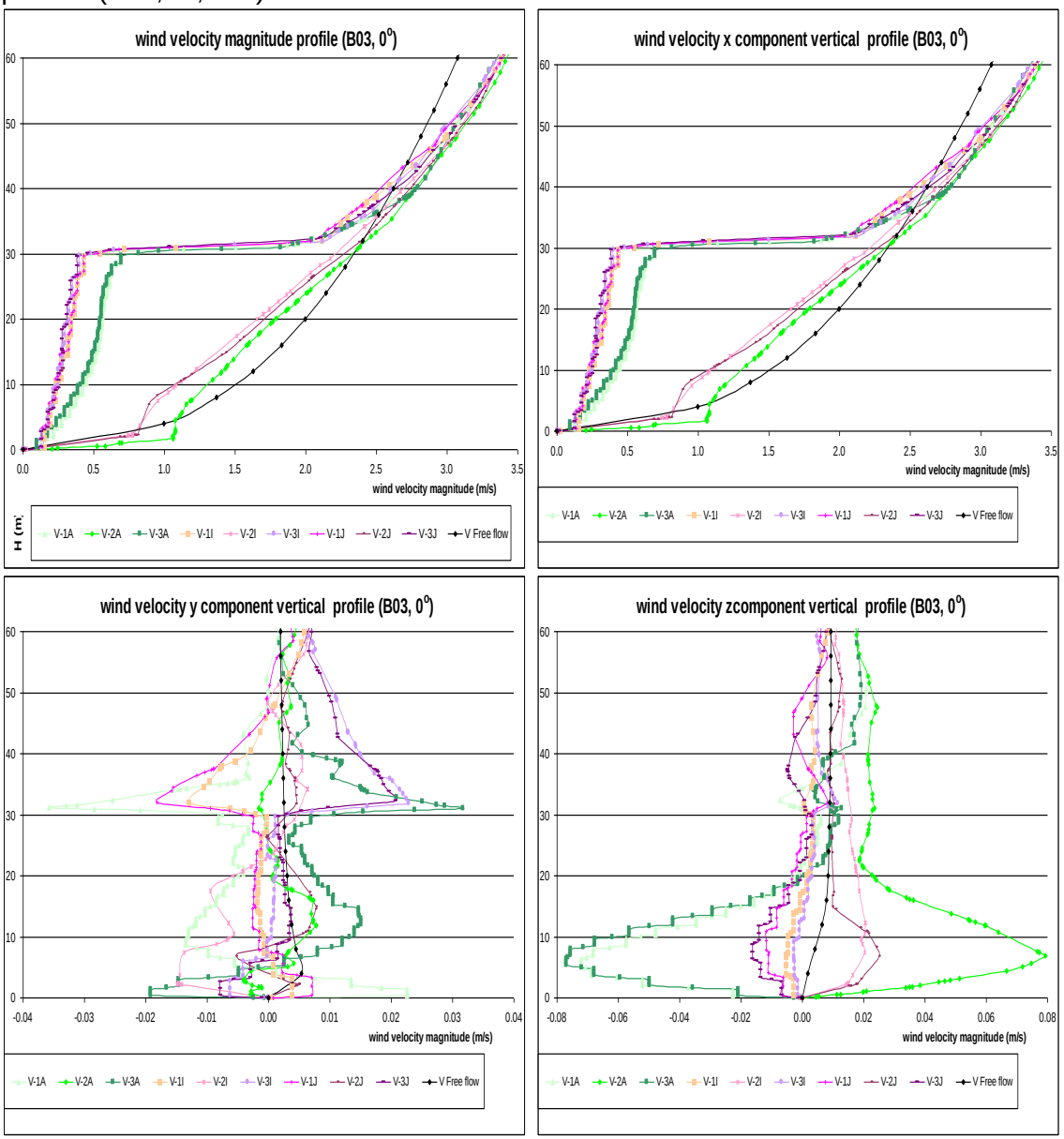

Source: this study.

The vertical wind velocity profiles indicate airflow deceleration near both the windward faces, with wind speed ranging from 0.2 to 0.5m/s up the canyon's height. By contrast, on the central axis, the wide scenario presented 50% of acceleration at 4m height, while in the square and the narrow scenarios airflow speed was maintained at that of the ABL input. The wind x component is the prevailing vector in the velocity magnitude in the three scenarios. Also, while the velocity range in the component y across the canyon is small (±0.02m/s), the z vertical component in the first 10m height reaches -0.08m/s near the walls and +0.08m/s in the centre of the canyon.

Figure 7-33: Wind velocity magnitude and x, y and z wind vector components vertical profiles (C03, 0°, m/s):

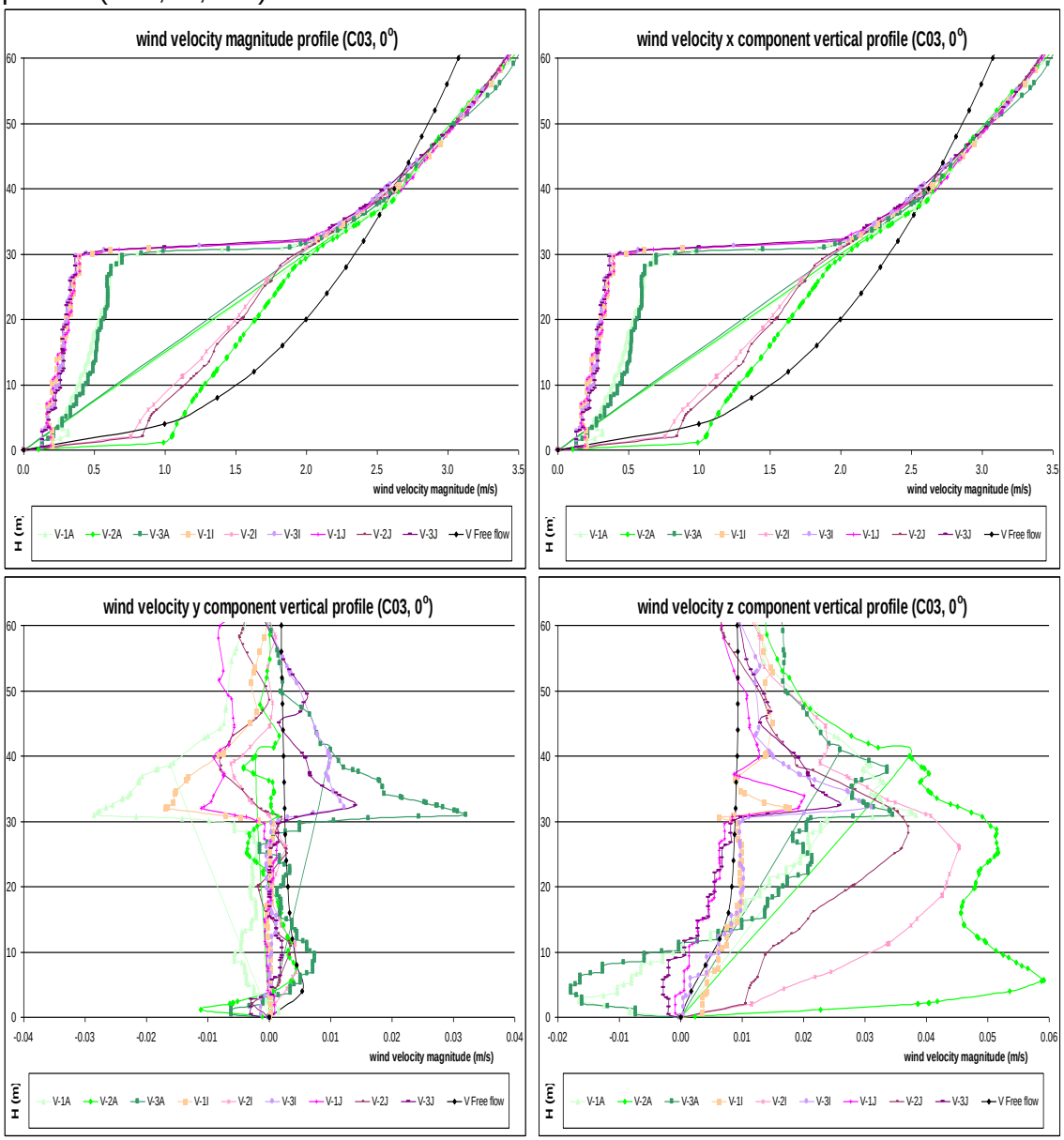

Source: this study.

7.3.3.2. Analysis of the A03, B03, and C03 results (90^{o})

The total averaged Cp results on the A3, B3, and C3 prototypes' windward sides were, respectively: 0.22; 0.11; and 0.03. While the Cp results in the wide canyon are greater than those described by Liddament[96] (1996), the total averaged results for the square and narrow canyons were closer to those in the literature. A great Cp range was found on the windward surfaces (as in groups 1 and 2), with an increase in pressure near the corners and a drop in the centre. Symmetry of results between the sides did not occur in the widest canyon A3. For instance, near the lateral edges at 25m height, the Cp results in the A3, B3, and C3 scenarios were: 0.37 (right) and 0.88 (left); 0.40 (on both sides); and 0.11 (also on both sides). On the other hand, at the centre the Cp results were: 0.24; 0.16; and 0.02. The total averaged Cp results on the leeward sides were: 0.14, 0.10, and 0.01, respectively, for the A3, B3, and C3 scenarios, which are greater than those found in Liddament (1996). Also, overall pressure distribution was more homogeneous over the faces, with a smaller range of results. Additionally, the A3 wide canyon's Cp distribution presented a more asymmetrical aspect than did the square and narrow ones. As an example of the A2 results, the leeward pressure distribution is the mirror image of that on the windward side, indicating a spiral airflow pattern occurring horizontal to the ground.

The wind velocity magnitude vertical profiles show that, whilst wind accelerates near the ground in the centre of the canyon by 150% and 50% in the wide and the square scenarios, the narrow one maintains the same ABL input velocity. It was also found that wind deceleration prevails inside the canyon. Wind velocity remains constant from 0.1 to 0.4m/s from ground to the top near the windward and leeward faces, though the velocities on the former are slightly lower than those on the latter.

The x component of the wind, orthogonal to the canyon, presents negative velocity from ground to 20m height, and positive velocity above that. This indicates an accelerated reverse flow near the ground and a stream wise flow in the upper height, forming a clock-wise vortex. The y component behaves in two ways: in the A3 scenario it tends all to one side below the canyon height (which is coherent with the asymmetrical pressure distribution on both the windward and leeward faces); and in both the B3 and C3 scenarios a shifts from positive to negative speed takes place on the left side and from negative to positive speed on the right side of the canyon. The greatest wind speeds occur in the centre of the canyon. The z vertical vector component shows positive speeds on the leeward and negative on the windward side, while the centre of the canyon presented both up and down flow.

[96] For 10m high rectangular buildings in urban areas, Liddament (1996) gives Cp results of +0.06 for the windward and of -0.30 for the leeward walls in orthogonal winds (90^{o}) (see topic 2.4 in Chapter 2).

Figure 7-34: The wind velocity magnitude pathlines (m/s) for the A3 (top), B3 (middle) and C3 (bottom) prototypes and for 90^{o} winds.

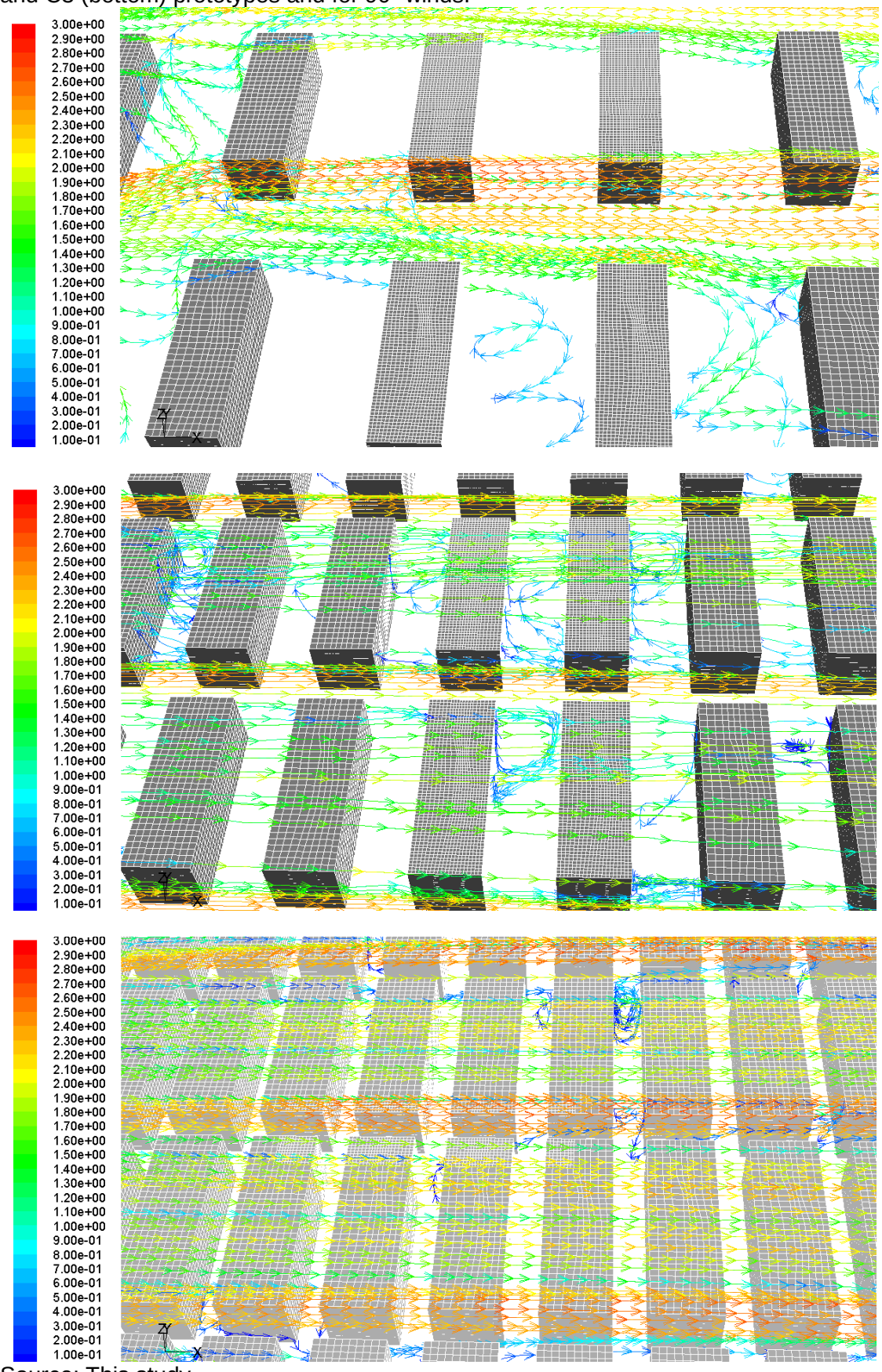

Source: This study.

The velocity ranges for positive (up) and negative (down) flows were: +0.7 and -0.5; +0.5 and -0.4; and +0.35 and -0.4m/s for the A3, B3, and C3 scenarios. The down flow velocity on the windward surface is of equal intensity to the up flow on the leeward side. The combined analysis of the three wind components describes a spiral vortex airflow, which tends all to one side in the wide A3 scenario, splits in two directions in the B3 scenario flowing from the centre towards the right or the left sides, and concentrates near the corners on the C3 ones.

Figure 7-35: Wind velocity magnitude and x, y and z wind vector components vertical profiles (A03, 90°, m/s):

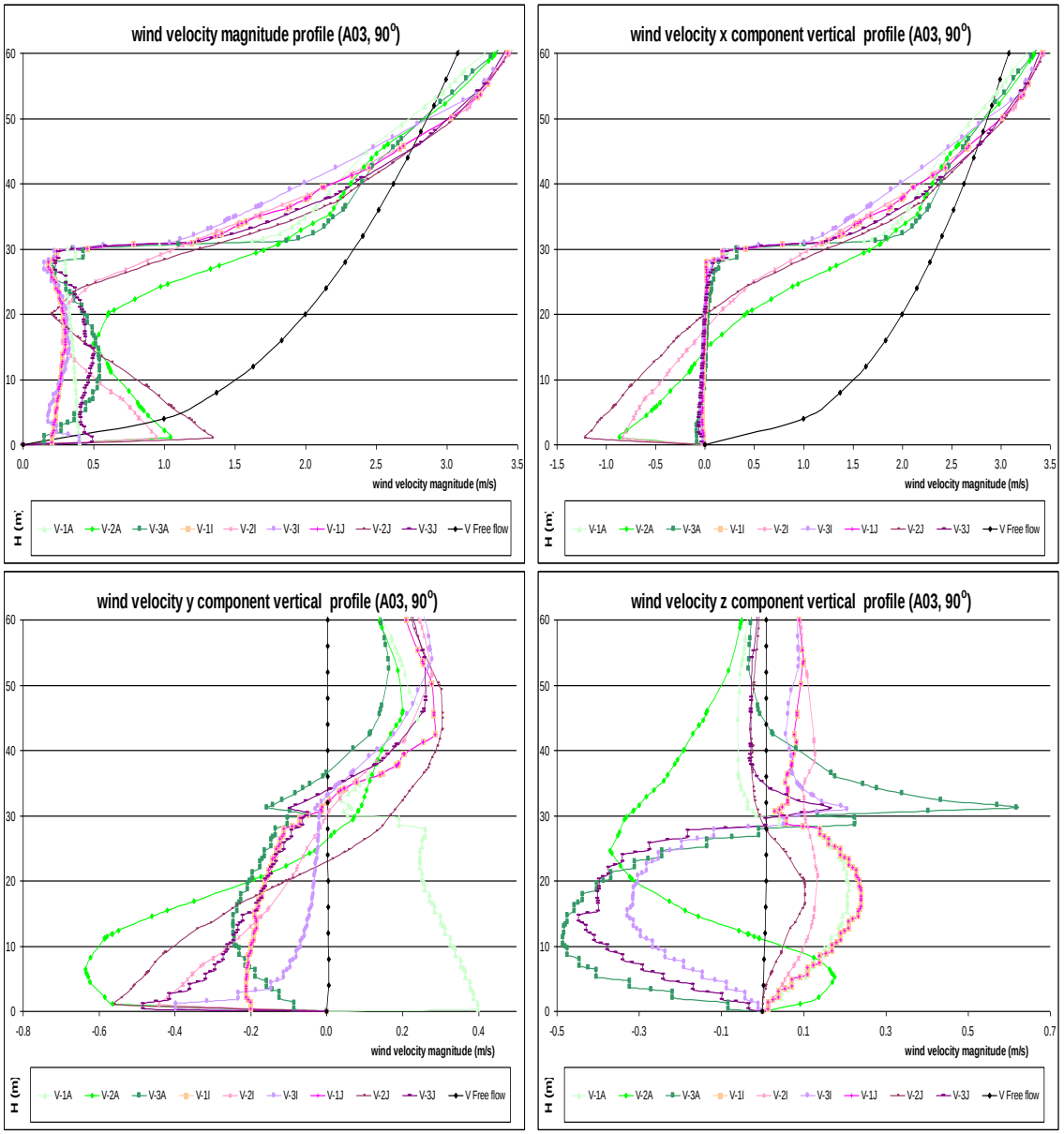

Source: this study.

Figure 7-36: Wind velocity magnitude and x, y and z wind vector components vertical profiles (B03, 90°, m/s):

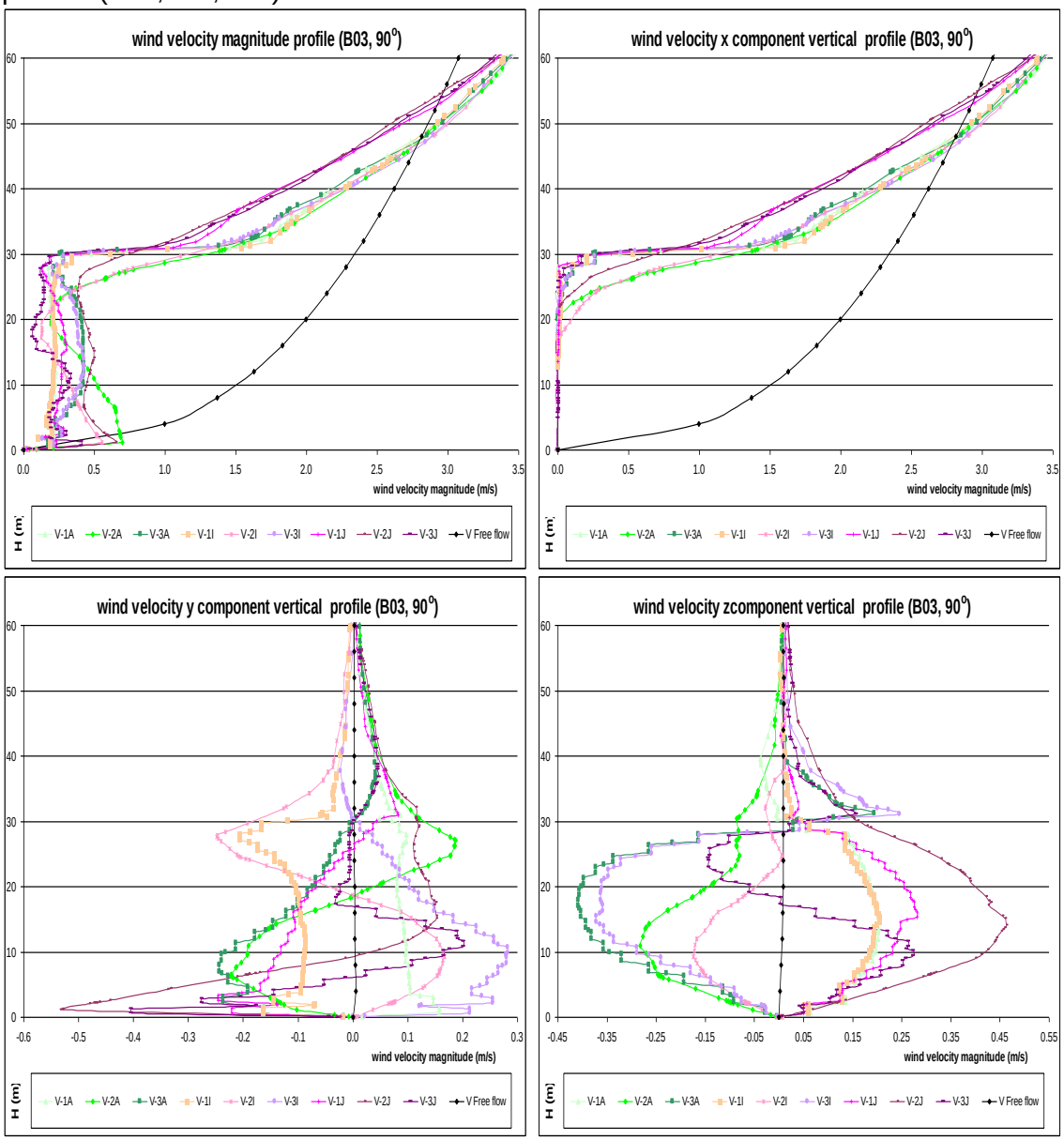

Source: this study.

Figure 7-37: Wind velocity magnitude and x, y and z wind vector components vertical profiles (C03, 90°, m/s):

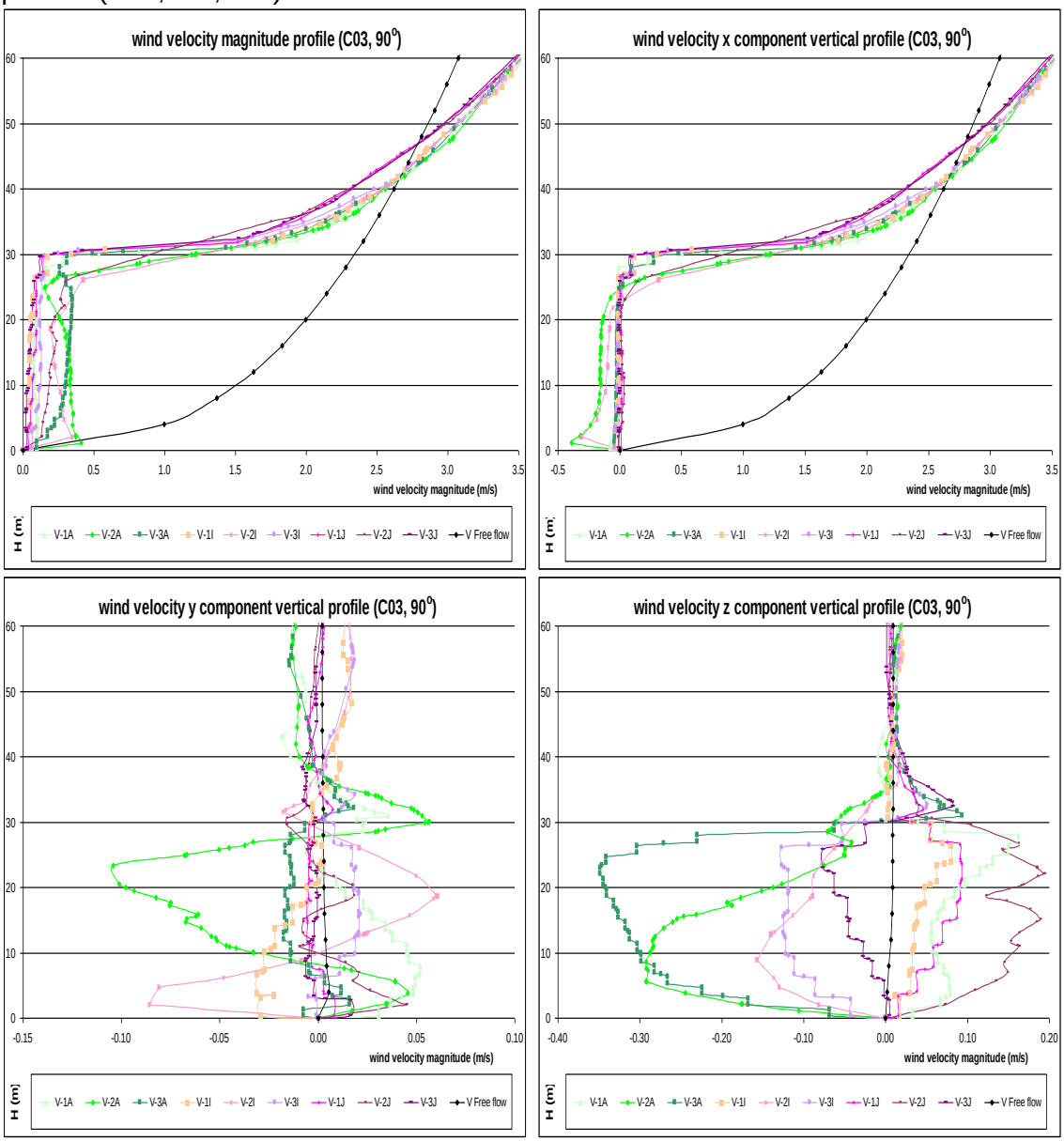

Source: this study.

7.3.3.3. Analysis of the A03, B03, and C03 results (45°)

The Cp results on the A3, B3, and C3 prototypes' windward surfaces presented total averaged results of 0.10, 0.09, and 0.08, which are close to those described by Liddament[97] (1996). Conversely, the total averaged Cp results on the leeward side faces (0.09, 0.04 and 0.08) were higher than the ones given in the literature. Once more, results on the leeward were closer to those in the windward side for 45° winds.

Figure 7-38: Wind velocity magnitude and x, y and z wind vector components vertical profiles (A03, 45°, m/s):

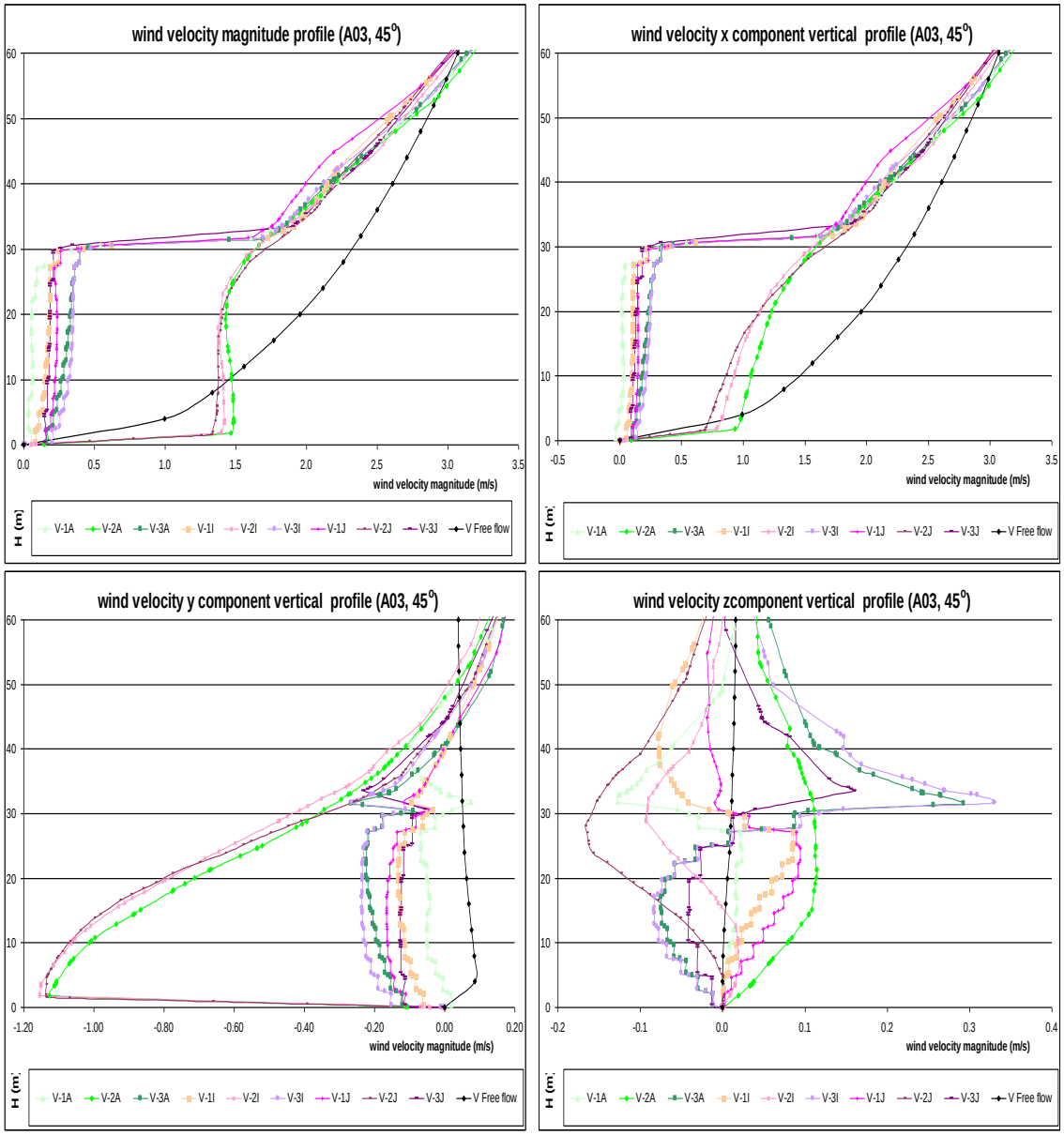

Source: this study.

[97] For 10m high rectangular buildings in urban areas, Liddament (1996) gives Cp results of +0.12 for the windward walls and Cp results of -0.38 for the leeward walls in oblique winds (45°) (see topic 2.4 in Chapter 2).

The wind velocity magnitude vertical profiles show that airflow accelerated in the centre of the canyon at pedestrian level in the three scenarios. The velocity increase factors for the wide, the square and the narrow canyons were: 3.0x, 2.3x, and 1.5x the ABL input velocity at the same height. After accelerating, velocities are kept constant through the canyon's height. Near the windward and the leeward walls wind decelerates and remains constant on the three scenarios. Velocities ranged from 0.35 to 0.50m/s near the windward and from 0.15 to 0.30m/s near the leeward face.

Figure 7-39: Wind velocity magnitude and x, y and z wind vector components vertical profiles (B03, 45°, m/s):

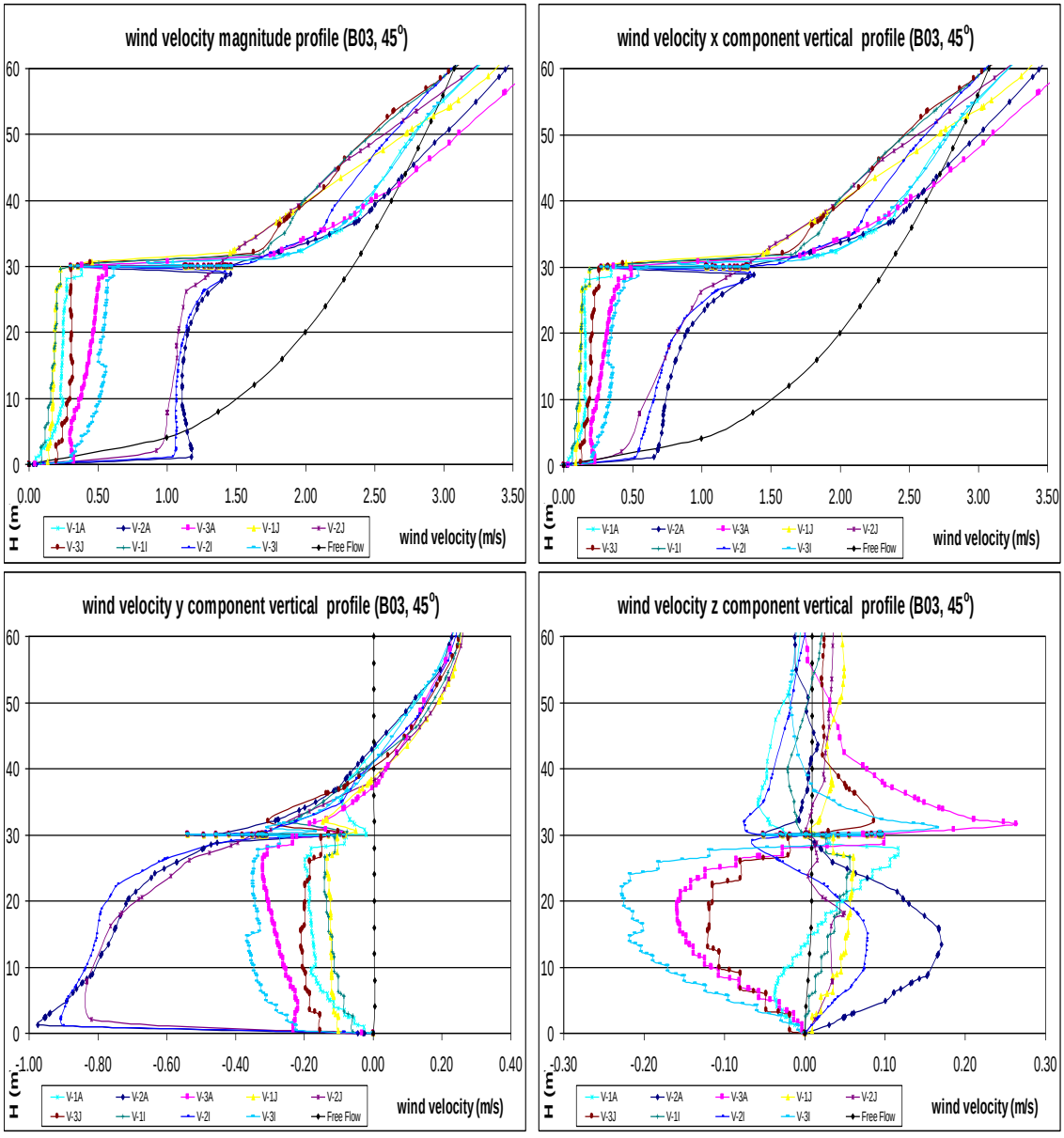

Source: this study.

The wind x vector component, at an angle of 135° towards the windward side, repeats the velocity magnitude profile patterns. The y component tends practically all to one side, with no reverse flow on this axis, and with velocity ranging up to 1.2, 1.0 and 0.8m/s for the A3, B3, and C3 scenarios. The z vertical vector component shows positive velocity on the leeward and negative on the windward side, with both up and down flow in the centre of the canyon. The velocity ranges for the positive (up) and negative (down) flows were: +0.11 and -0.17; +0.17 and -0.21; and +0.08 and -0.16m/s. The combined analysis of the three wind components defines a spiral flow in an ascending diagonal accompanying the mainstream.

Figure 7-40: Wind velocity magnitude and x, y and z wind vector components vertical profiles (C03, 45°, m/s):

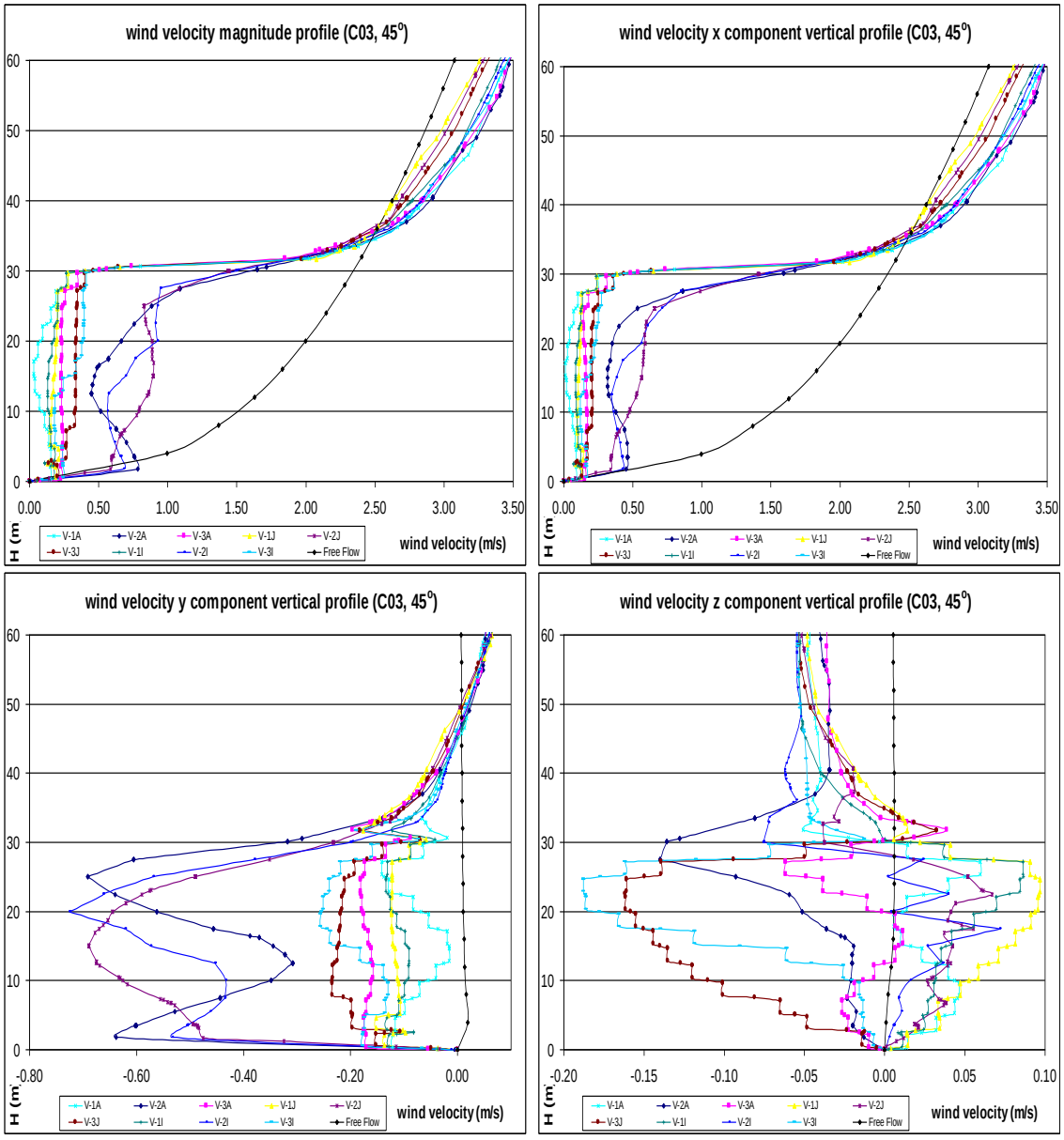

Source: this study.

Figure 7-41: The wind velocity magnitude pathlines (m/s) for the A3 (top), B3 (middle) and C3 (bottom) prototypes and for 45^{o} winds.

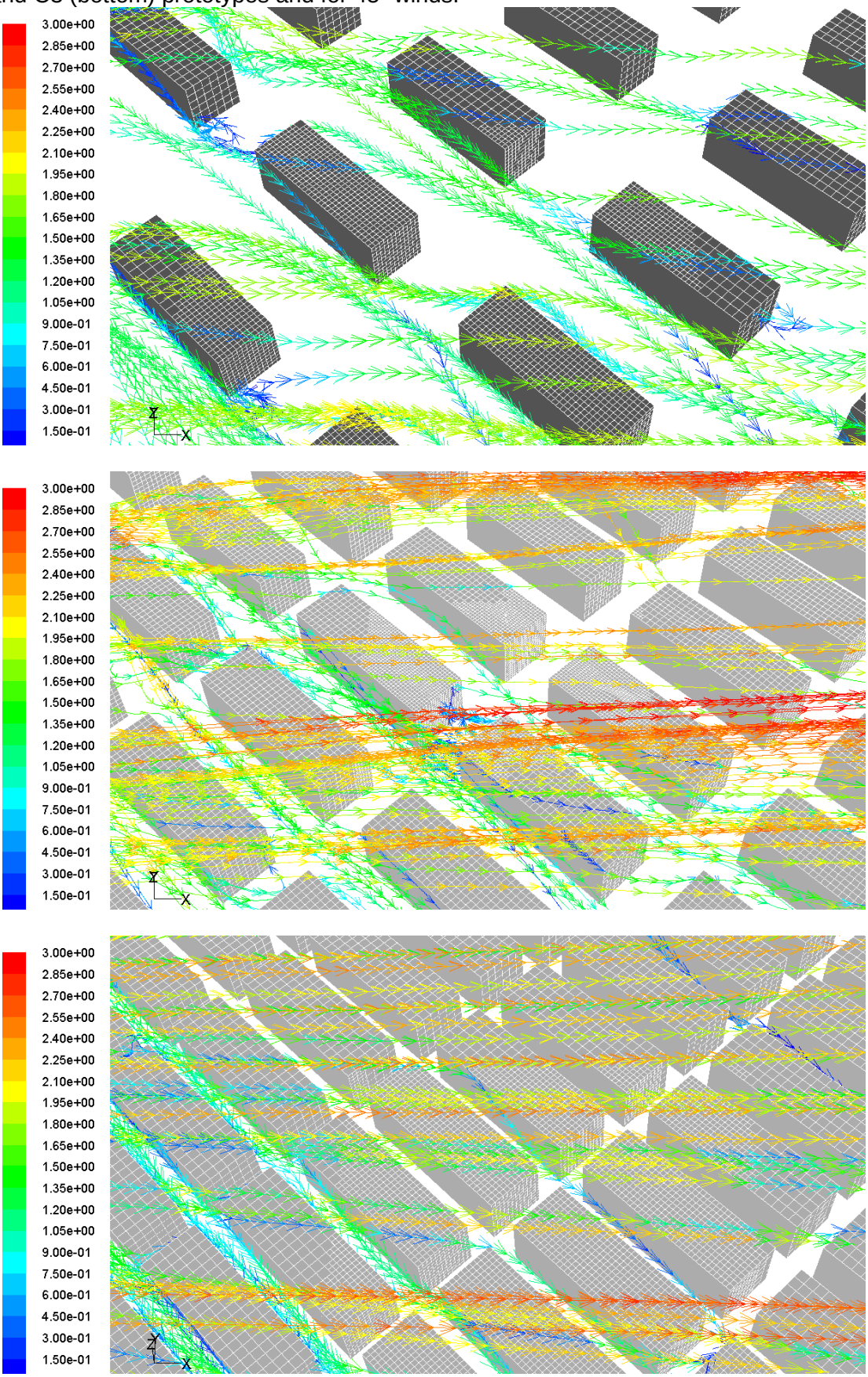

Source: This study.

7.3.4. Group 4: prototypes A4, B4, and C4

Group 4 consists of an array of 30m cubes with variable ground density. Differently than the other prototype scenarios proposed, group 4 has similar cases cited in the literature (Davidson *et al*, 1996; Liddament, 1996; MacDonald *et* al, 1998; Uehara *et al,* 2000; Cheng and Castro, 2002; Cheng *et al*, 2003; Cheng and Meroney, 2003a; Lien *et al*, 2004; Assimakopoulos *et al*, 2006; Cheng *et al*, 2007; Di Sabatino *et al*, 2007; Shi *et al*, 2008; Aristodemou *et al*, 2009). On the other hand, few of these works approach Cp analysis and wind velocity for natural ventilation purposes, keeping the main focus on pollution dispersion in the urban environment.

7.3.4.1. Analysis of the A4, B4, and 04 results (0^o)

Symmetrical distribution of pressure was observed as between the right and left sides of the A4, B4 and C4 cubic prototypes for winds along the canyon. The total averaged Cp results found were: -0.02, 0.05, and 0.02, which are higher than those given in the reference literature[98]. The total averaged Cp results at low, middle, and top heights were: -0.05, -0.02, and 0.02 for the wide; 0.03, 0.05, and 0.07 for the square; and 0.00, 0.02, and 0.04 for the narrow canyons. The Cp lowest peak result occurred on the upwind side face next to the corner (-0.28, -0.06 and -0.05). In fact, the Cp range was rather small, less than 0.15 on the faces, and similar in the three canyon widths adopted, with a slight increase on the faces.

For the three scenarios the velocity magnitude near the walls and at 4.0m height ranged from 0.2m/s to 0.5m/s, while at the ABL input the velocity was 1.0m/s. Flow acceleration by a factor of 1.5x was found at ground level on the upwind side of the A04 (wide) canyon. Conversely, the vertical profiles in the same position for the square and narrow scenarios (B04 and C04) presented flow deceleration. Wind acceleration above the canyon was observed on the vertical profiles near the faces and in the middle of the canyon. The x component of the wind, accompanying the mainstream, is mandatory in the wind velocity magnitude. The components y and z present greater velocity range, from -0.15 to +0.15m/s, as compared to canyons with a larger L/H aspect ratio in which the channelling effects are clearer. This happens due to an increase in wake interference and flow turbulence as a consequence of the short length between blocks in this scenario formed of an array of cubes.

[98] For 10m height square buildings in urban areas, Liddament (1996) gives Cp results of -0.25 for side walls of parallel winds (0^o). See Chapter 02 for further details (see topic 2.4 in Chapter 2).

Figure 7-42: Wind velocity magnitude and x, y and z wind vector components vertical profiles (A04, 0°, m/s):

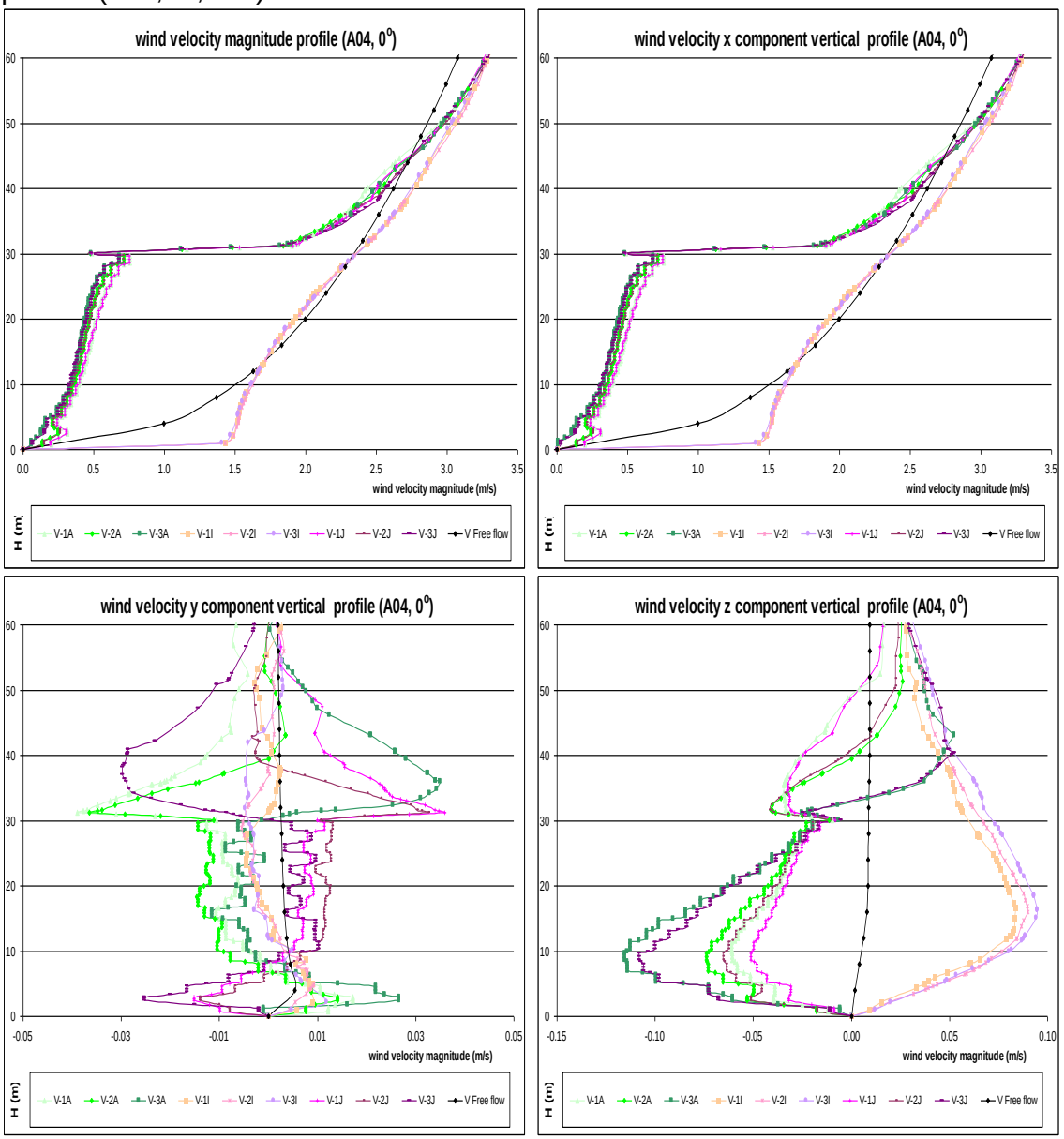

Source: this study.

Figure 7-43: Wind velocity magnitude and x, y and z wind vector components vertical profiles (B04, 0°, m/s):

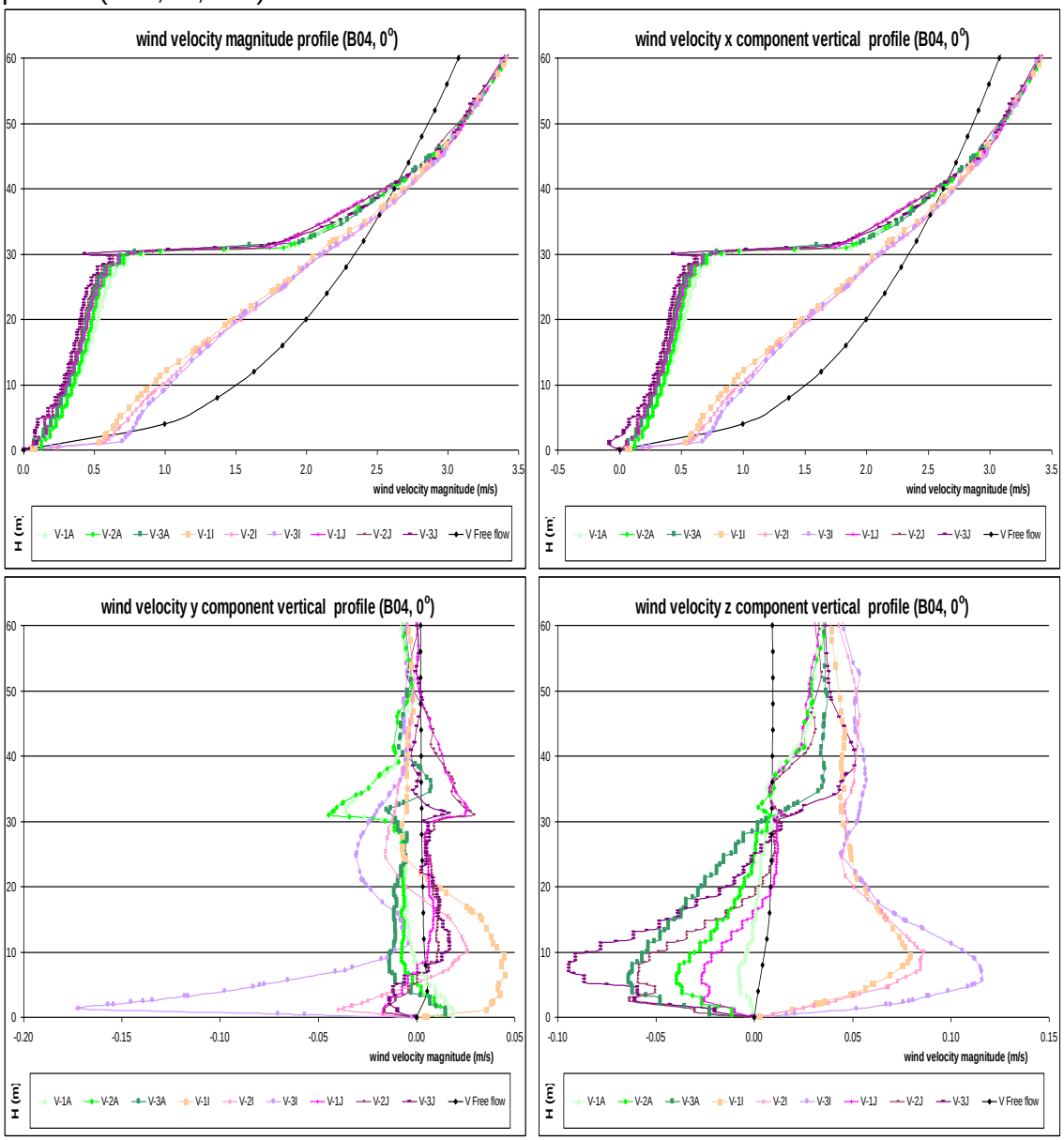

Source: this study.

Figure 7-44: Wind velocity magnitude and x, y and z wind vector components vertical profiles (C04, 0°, m/s):

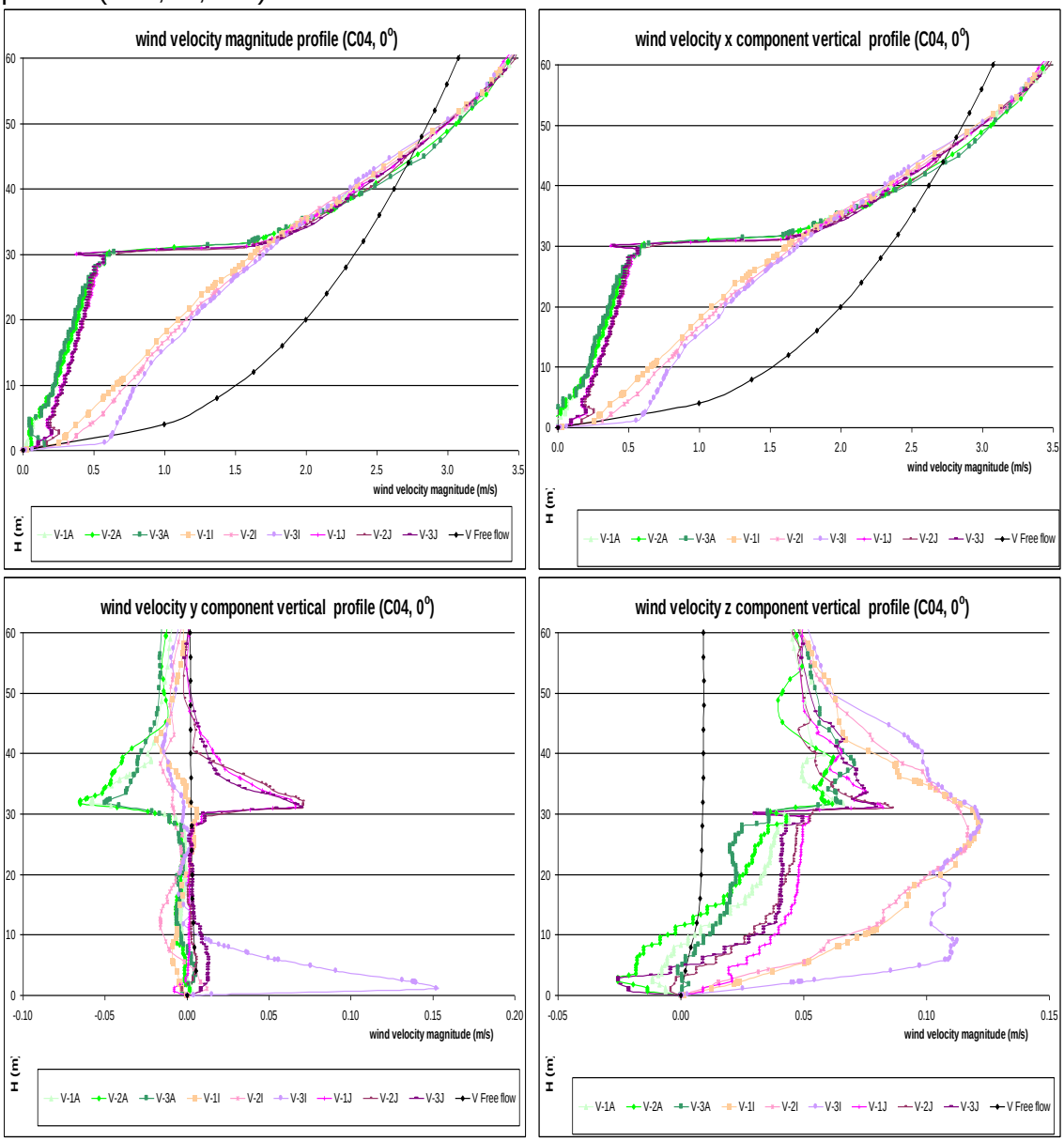

Source: this study.

7.3.4.2. Analysis of the A04, B04, and C04 results (90^{o})

The total averaged Cp results for the windward side of the A4, B4, and C4 prototypes were: 0.18, 0.11, and 0.02. The result in the wider scenario matches well with the Cp results described by Liddament[99] (1996) for arrays of square buildings. Similar pressure distribution patterns to those described in the previous orthogonal wind analysis were also observed in the three cubic arrays of volumes: an increase of pressure on the sides and a drop in the centre, with symmetry between the sides at all the heights assessed. The Cp averaged result variation with height for the A4, B4, and C4 scenarios was: 0.13, 0.06, and -0.02 at low; 0.18, 0.10, and 0.02 at medium and 0.22, 0.16, and 0.06 at top heights. The maximum Cp peak results (0.48, 0.33, and 0.16) were found near the corners at 5m from the side edges and 25m height. The total averaged Cp results found on the A4, B4, and C4 leeward sides (0.00, 0.04, and 0.01) were higher than the Liddament reference results, in accordance with the previous analysis of groups 1, 2 and 3.

Due to the low plot density in group 4 scenarios, greater airflow permeability was found between the blocks. Consequently, there is a relationship between the H/W aspect ratio and the total bulk of pressure on the windward faces: the wider the distance between the blocks the higher is the airflow reaching the windward faces and, therefore, the greater is the pressure on them.

The wind velocity magnitude vertical profiles show wind deceleration inside the canyon. Airflow velocities near the faces range from 0.1 to 0.4m/s. Also, the low plot density does not incite local wind acceleration even at ground level or near sharp edges, indicating an absence of any wind channelling effects. In the canyon centre up to 20m height airflow velocities are lower than the ABL input profile. The assessment of the isolated x wind vector component shows very low velocity near walls and reverse flow at ground level. The y component profiles describes a spiral airflow pattern occurring horizontal to the ground, while positive speed on the leeward and negative speed on the windward side characterize the z component of the flow. For instance, when compared to Group 1 long canyons, the vector components x, y, and z present a 50% reduction in wind velocity magnitude, which may result in fewer intense internal vortices. A clear sinuous airflow pattern is observed in the wide and the square canyons, though it also can be seen in the narrow one, but with less frequency and intensity.

[99] For 10m high square buildings in urban areas, Liddament (1996) gives Cp results of +0.20 for the windward walls and -0.25 for the leeward walls in orthogonal winds (90^{o}) (see topic 2.4 in Chapter 2).

Figure 7-45: The wind velocity magnitude pathlines (m/s) for the A4 (top), B4 (middle) and C4 (bottom) prototypes and for 90^{o} winds.

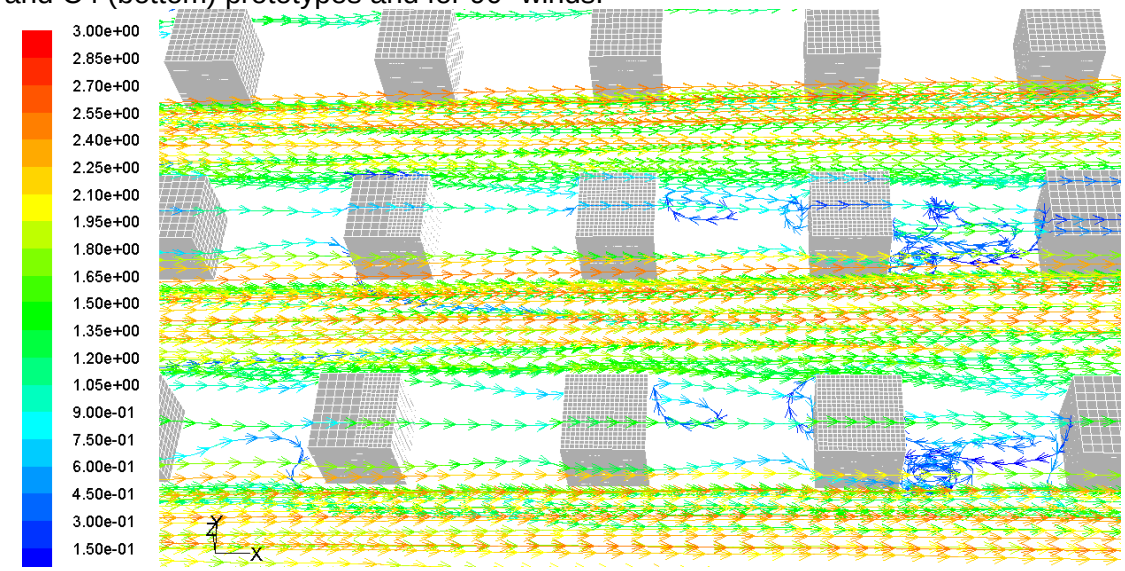

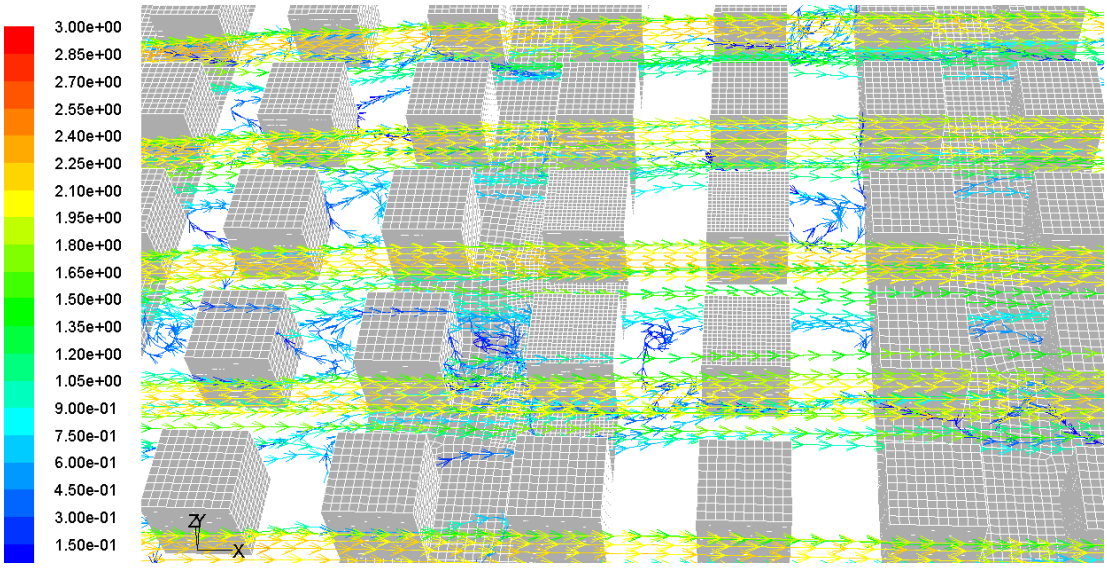

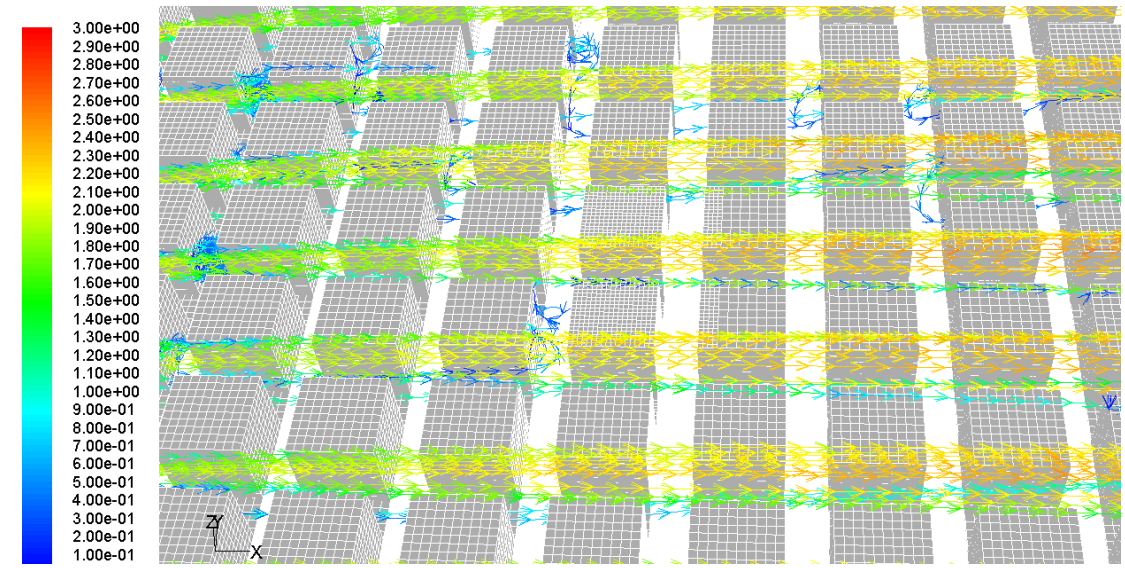

Source: This study.

Figure 7-46: Wind velocity magnitude and x, y and z wind vector components vertical profiles (A04, 90°, m/s):

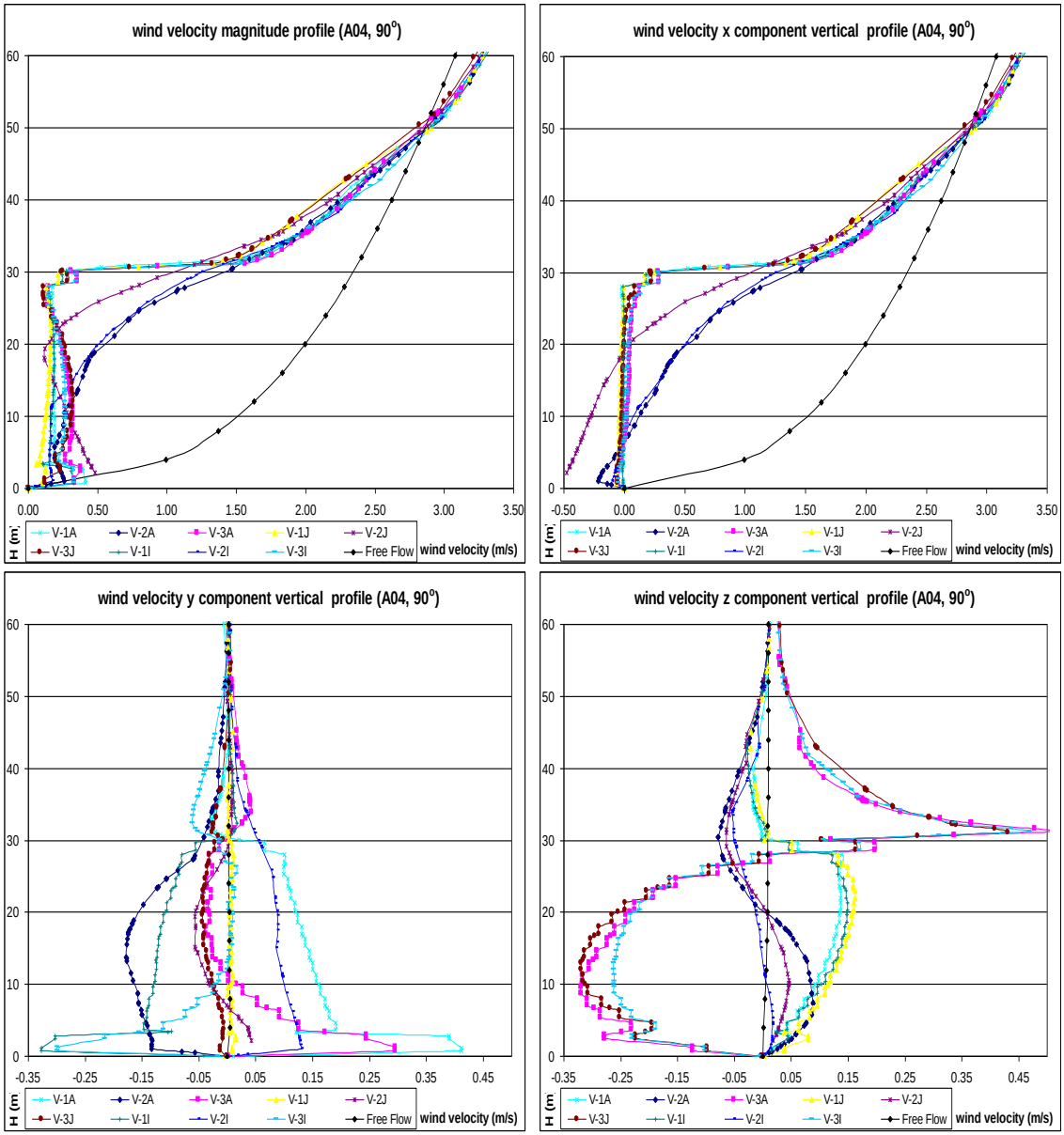

Source: this study.

Figure 7-47: Wind velocity magnitude and x, y and z wind vector components vertical profiles (B04, 90°, m/s):

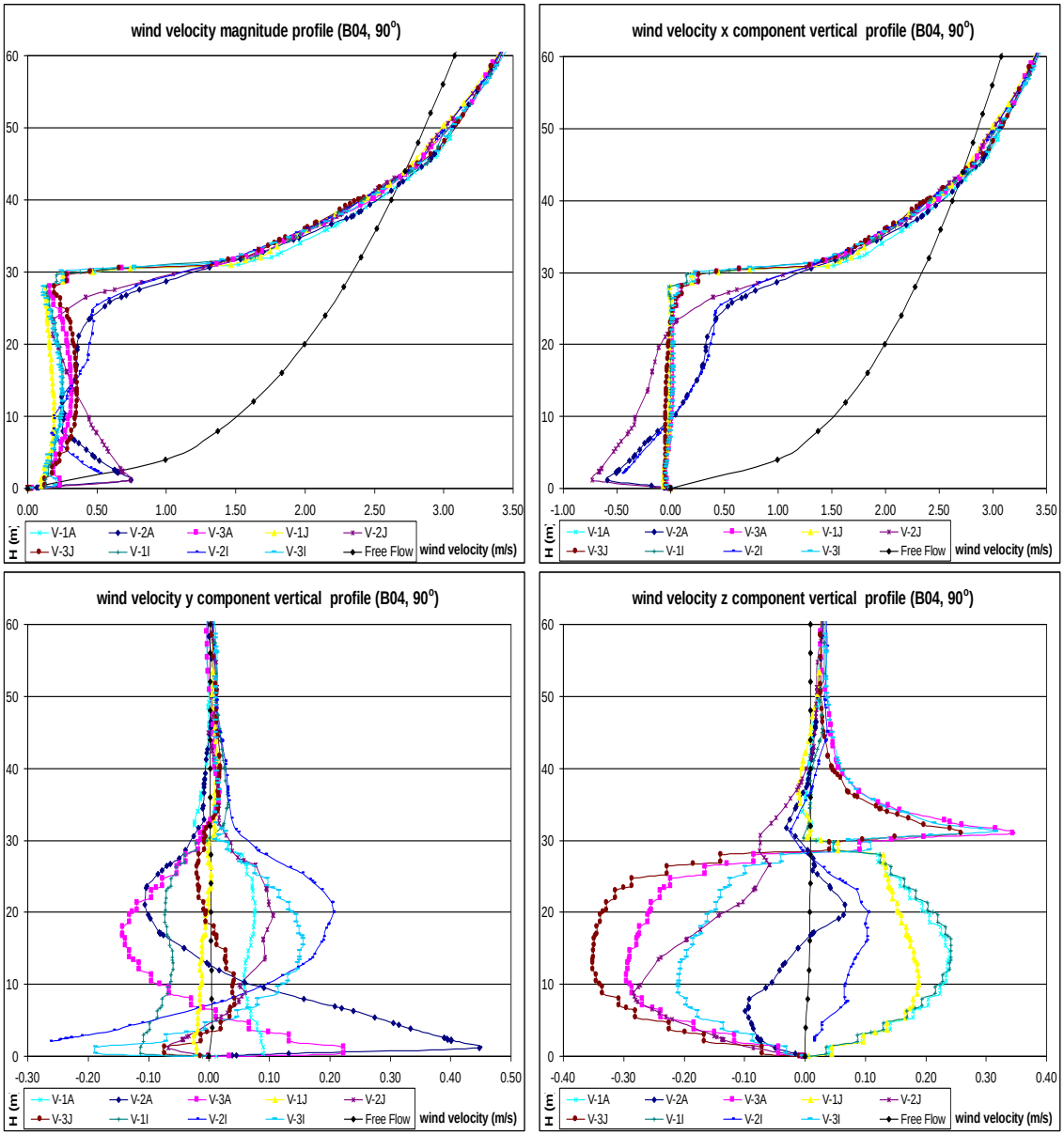

Source: this study.

Figure 7-48: Wind velocity magnitude and x, y and z wind vector components vertical profiles (C04, 90°, m/s):

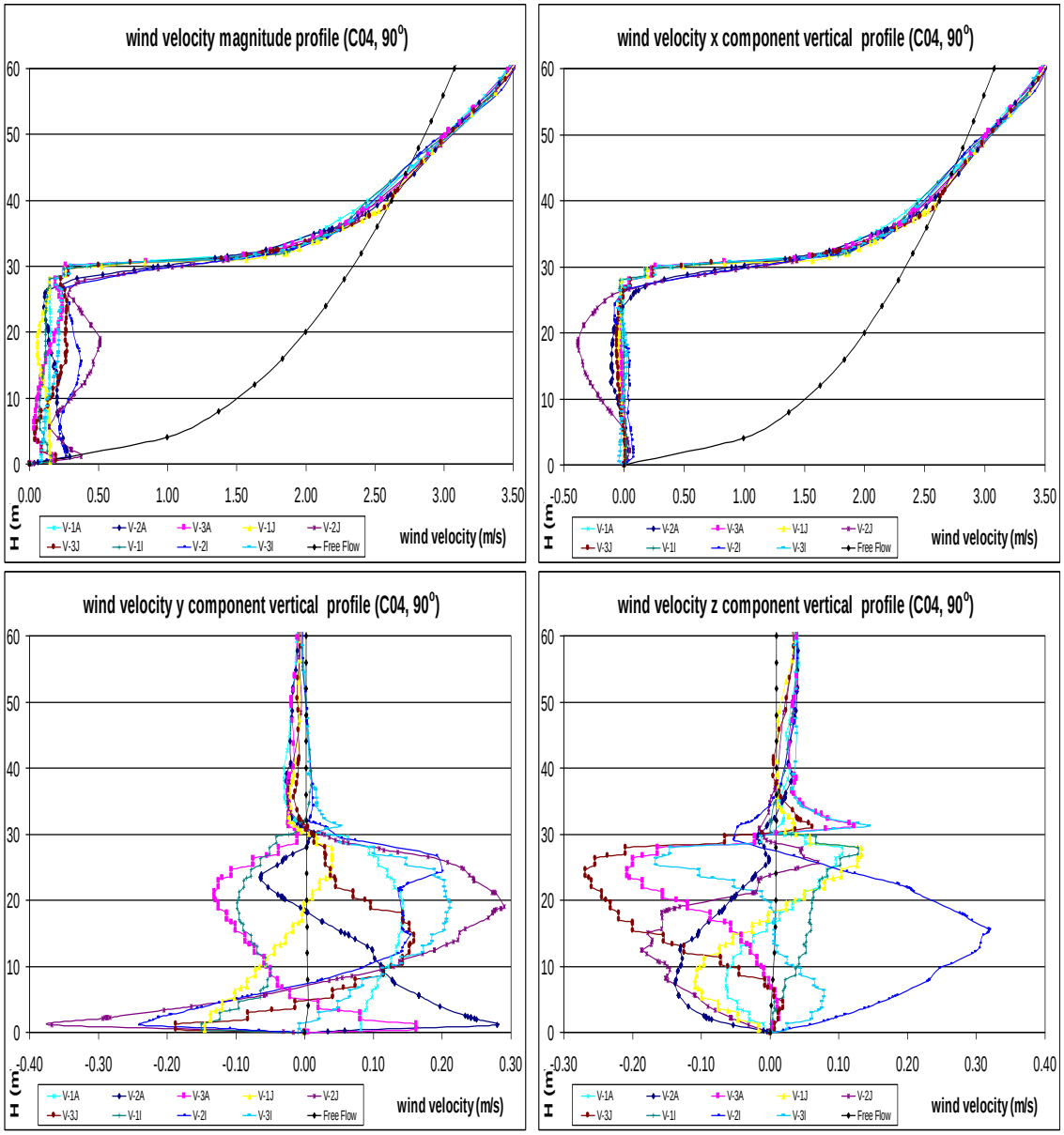

Source: this study.

7.3.4.3. Analysis of the A04, B04, and C04 results (45^{o})

The total averaged Cp results on the A4, B4, and C4 windward surfaces were: 0.07, 0.06 and 0.05, which are in consonance with Liddament's[100] (1996) results for arrays of cubes. Conversely, the averaged Cp results on the leeward side were greater than those given in the same literature and close to those for the windward side: 0.03, 0.02 and 0.05.

The vertical wind velocity magnitude profiles for oblique winds are very similar to the orthogonal results in some aspects, with great wind deceleration inside the canyon, and constant velocity near the faces of between 0.1 and 0.4m/s. The exceptions were the vertical wind profiles in the centre of the wide and the square canyons, which present almost constant wind speed of from 0.5 to 1.0m/s from ground to top. No specific acceleration due to channelling effect was observed whether at ground level or near sharp edges. Both the x and y wind components below 30m height were positive from the canyon's central axis to the windward face and negative from the centre to the leeward face. The z component shows an inversion of wind drection with reverse flow form low to middle height and positive flow from middle to top height near the windward side, the opposite happening on the leeward side. This flow describes a diagonal vortex alongside the blocks, following the mainstream.

[100] For 10m high square buildings in urban areas, Liddament (1996) gives Cp results of +0.05 for the windward walls and Cp results of -0.30 for the leeward walls in oblique winds (45^{o}) (see topic 2.4 in Chapter 2).

Figure 7-49: The wind velocity magnitude pathlines (m/s) for the A4 (top), B4 (middle) and C4 (bottom) prototypes and for 45^{o} winds.

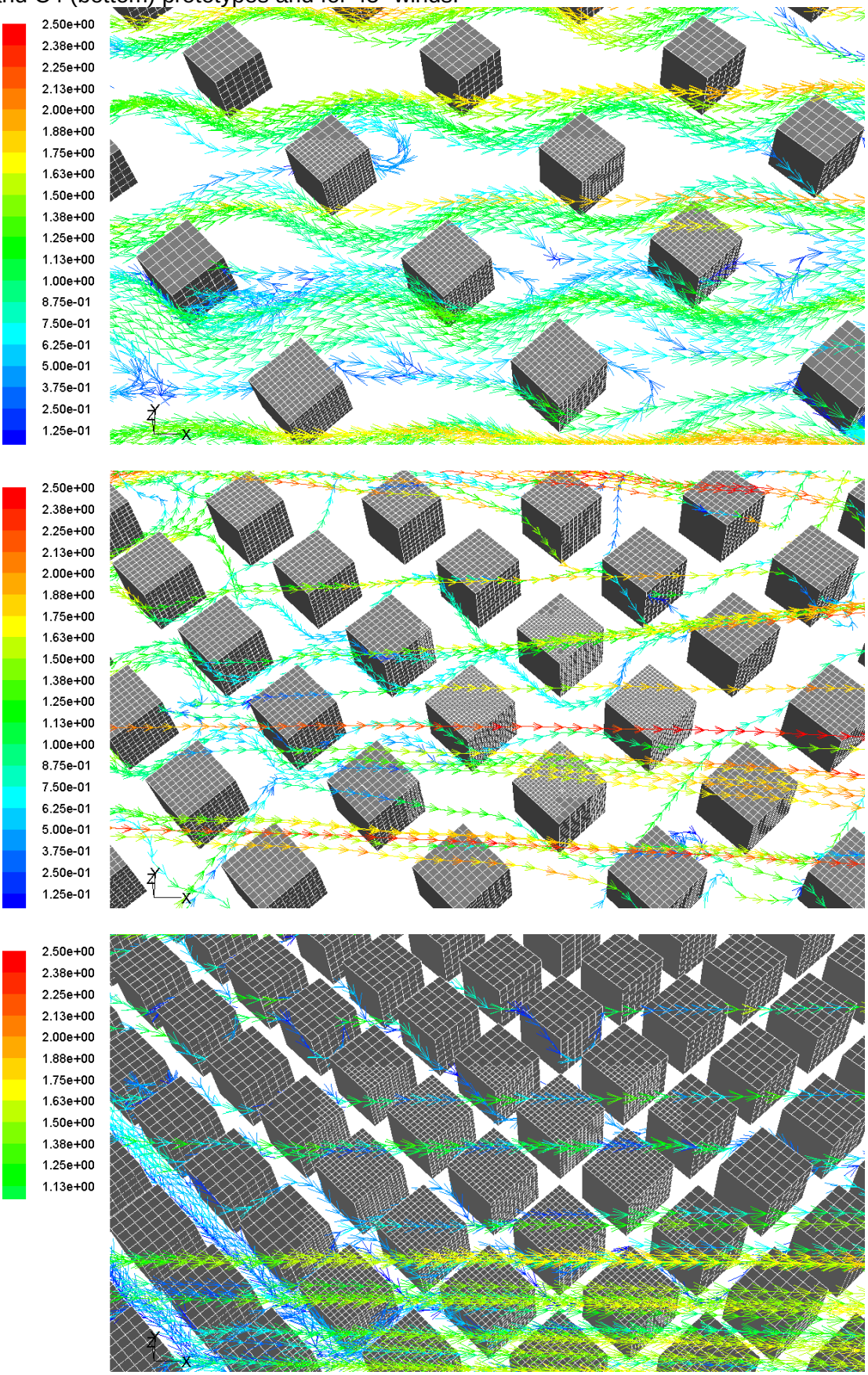

Source: This study.

Figure 7-50: Wind velocity magnitude and x, y and z wind vector components vertical profiles (A04, 45°, m/s):

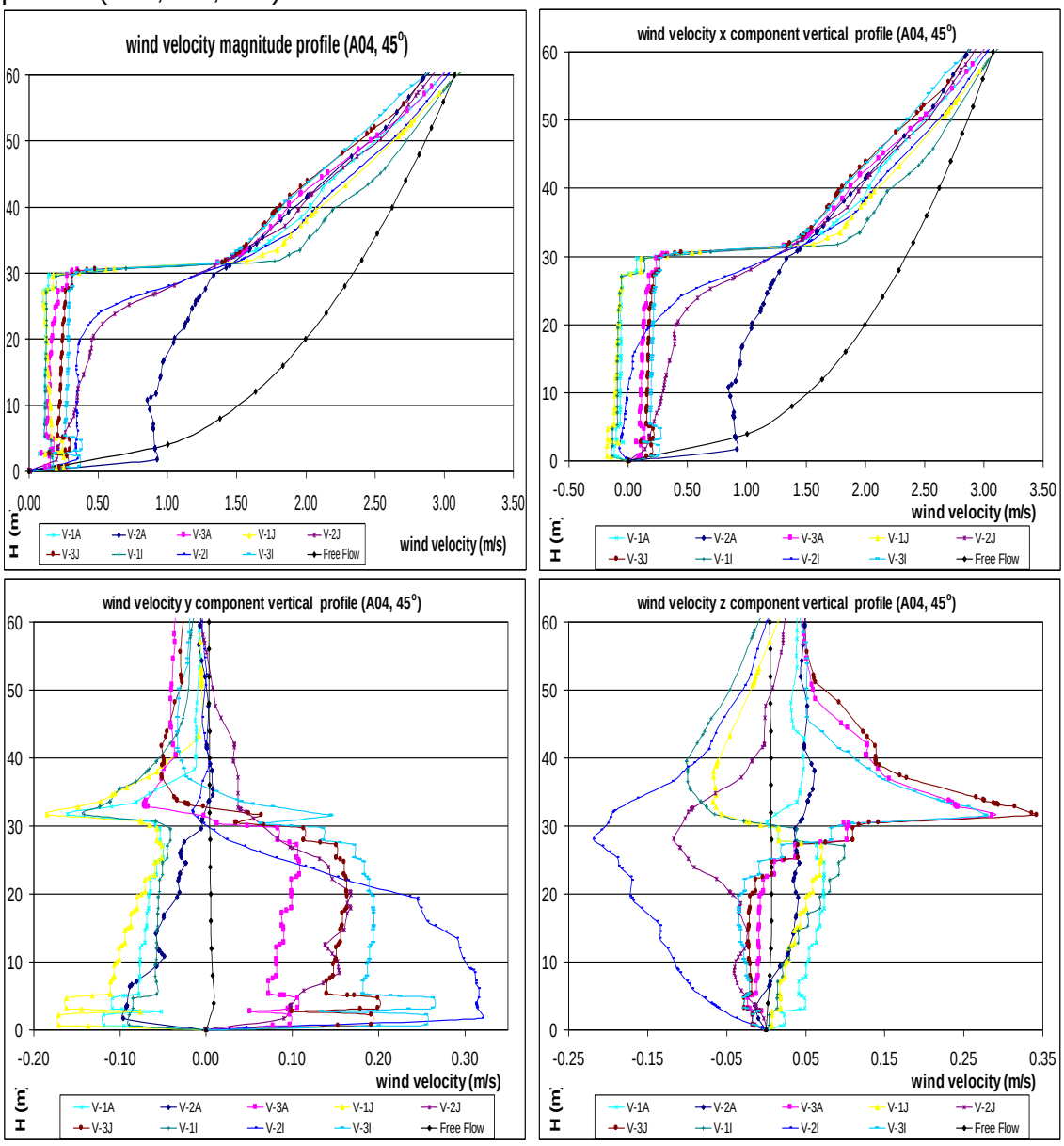

Source: this study.

Figure 7-51: Wind velocity magnitude and x, y and z wind vector components vertical profiles (B04, 45°, m/s):

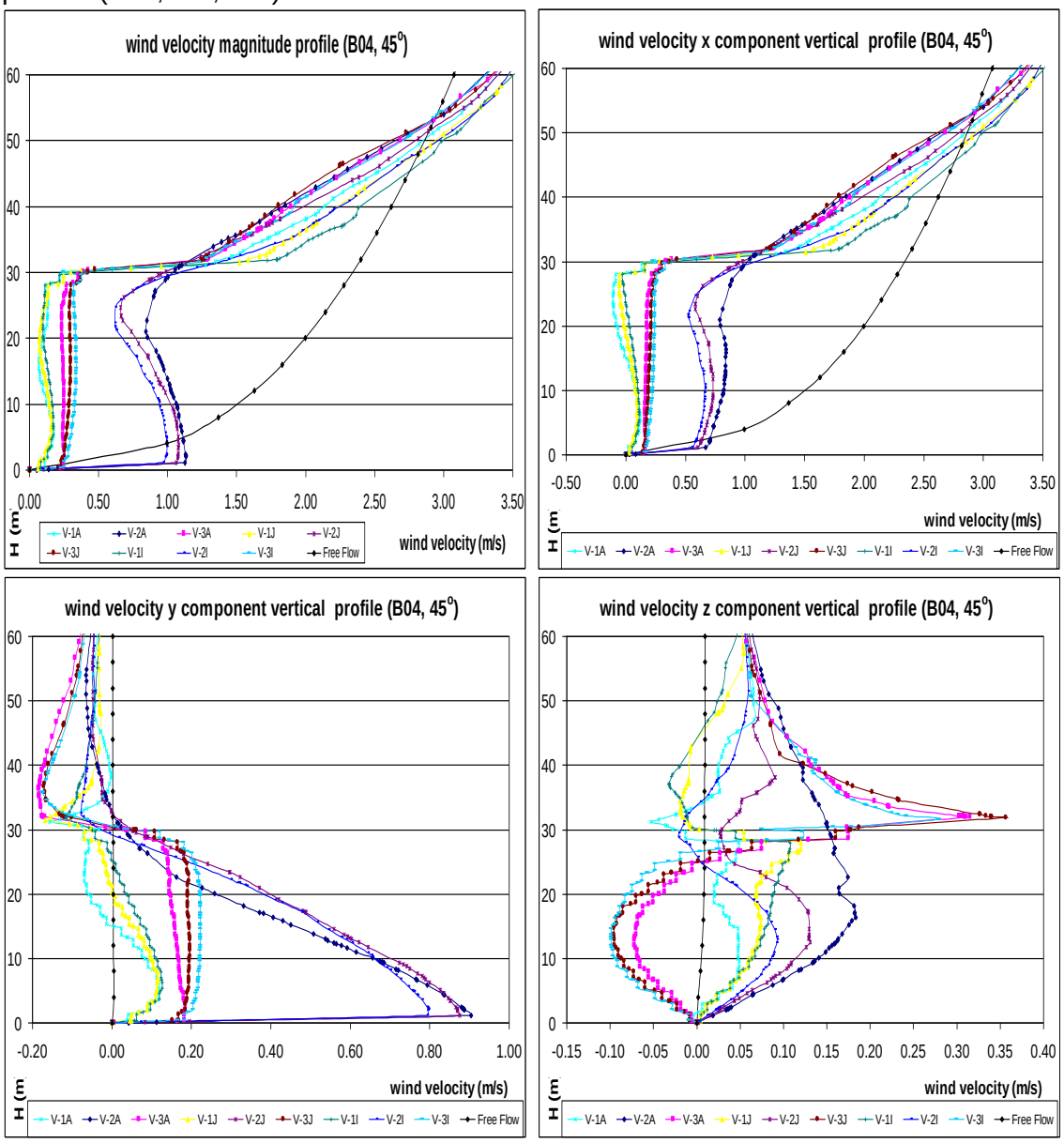

Source: this study.

Figure 7-52: Wind velocity magnitude and x, y and z wind vector components vertical profiles (C04, 45°, m/s):

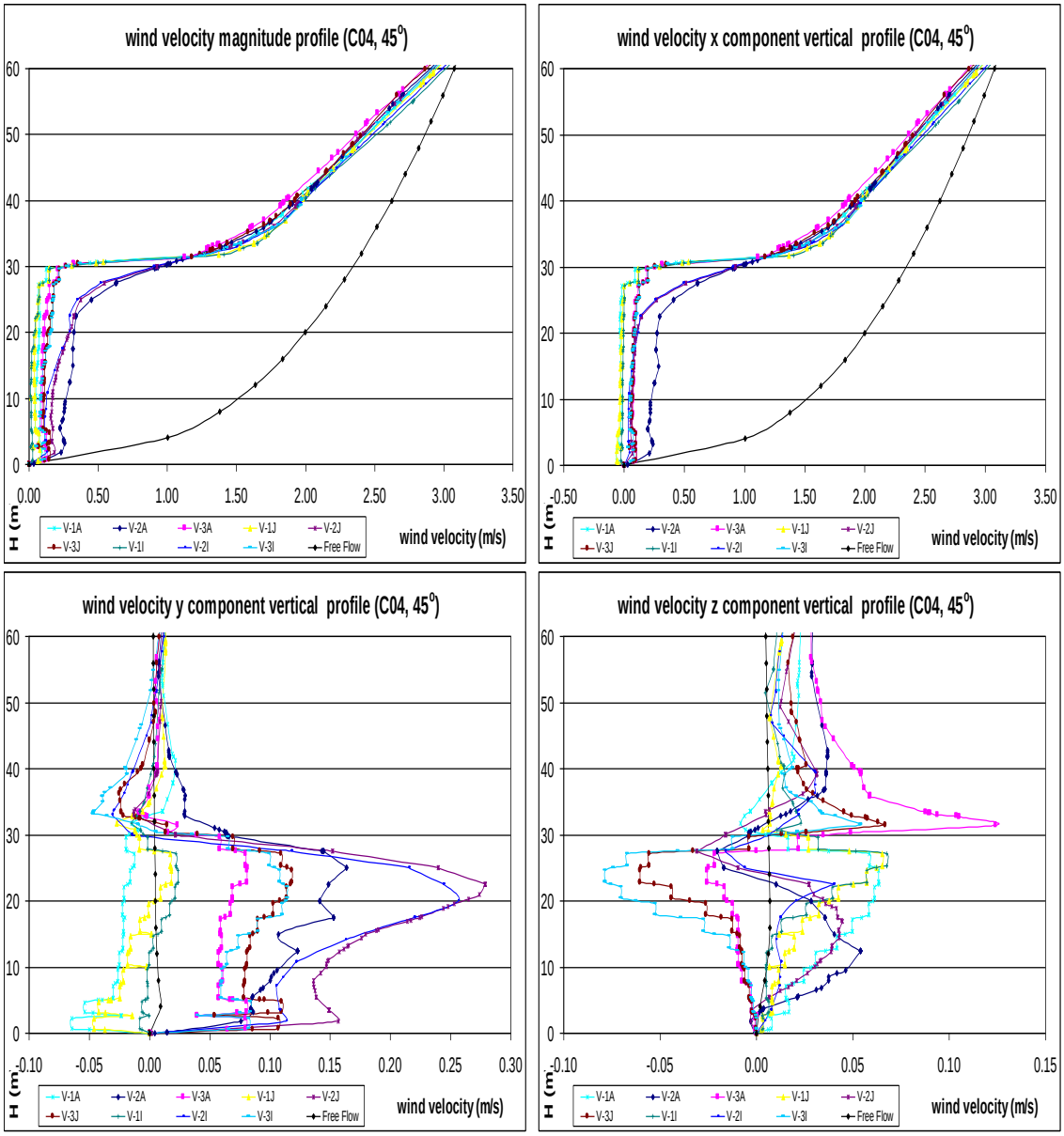

Source: this study.

7.3.5. Group 5: prototype B02 STEP

Here the Group 5 results, which consist of a symmetrical unlevelled canyon, will be presented and discussed. Derived from the previously assessed B2 scenario, the B2 STEP prototypes have constant H/W (0.67), L/W (3.0), A_{roof}/A_{urb} (0.58), and A_{built}/A_{urb} (6.92) aspect ratios. The Group 5 results analysis will be based on the comparison with the B2 scenario results and the contrast of the 5 scenarios among themselves. Five different scenarios were investigated in accordance with the wind direction:

- B2 STEP (0^o): parallel wind alongside the canyon axis. It has low blocks (30m height) on the left and tall blocks (60m height) on the right side;
- B2 STEP-UP (90^o): orthogonal wind facing the step up level;
- B2 STEP-UP (45^o): oblique wind facing the step up level;
- B2 STEP-DOWN (90^o): orthogonal wind facing the step down level; and
- B2 STEP-DOWN (45^o): oblique wind facing the step down level.

7.3.5.1. Analysis of the B2 Step results (0^o)

Below 30m height, both for the 30m high block, on the right, and for the 60m block, on the left, the canyon presented nearly symmetrical total averaged Cp results of 0.06 for parallel winds, which is the same result as was found in the square B2 scenario. Above 30m height the left block shows a Cp increase of up to 0.23, giving a combined averaged Cp of 0.14 on this left face. The upward Cp ranges were, 0.01 (ground to 10m), 0.06 (10 to 20m), and 0.12 (20 to 30m) on both sides, and 0.17 (30 to 40m), 0.22 (40 to 50m), and 0.28 (50 to 60m) on the left side. Also, slight differences between minimum and maximum peak results were observed on the faces.

Figure 7-53: Airflow velocity pathlines released from the vertical axis (m/s, 0^o).

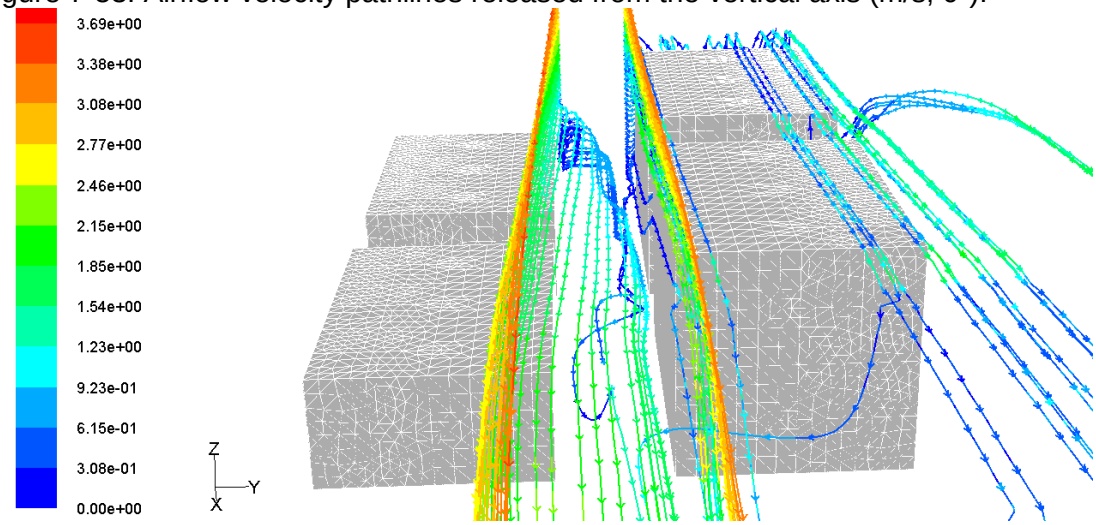

Source: This study.

The wind velocity magnitude vertical profiles show great wind deceleration near the faces and in the centre of the canyon. For instance, wind speeds range from 0.05m/s to 0.2m/s from ground to top near both faces, and from 0.35 to 0.95m/s on the canyon's central axis. Also, while the x component of the wind defines the flow direction along the mainstream, the y and z components indicate a turbulent vortex inside the canyon in a left to right and ground do top diagonal direction.

Figure 7-54: Wind velocity magnitude and x, y and z wind vector components vertical profiles (B02 STEP, 0°, m/s):

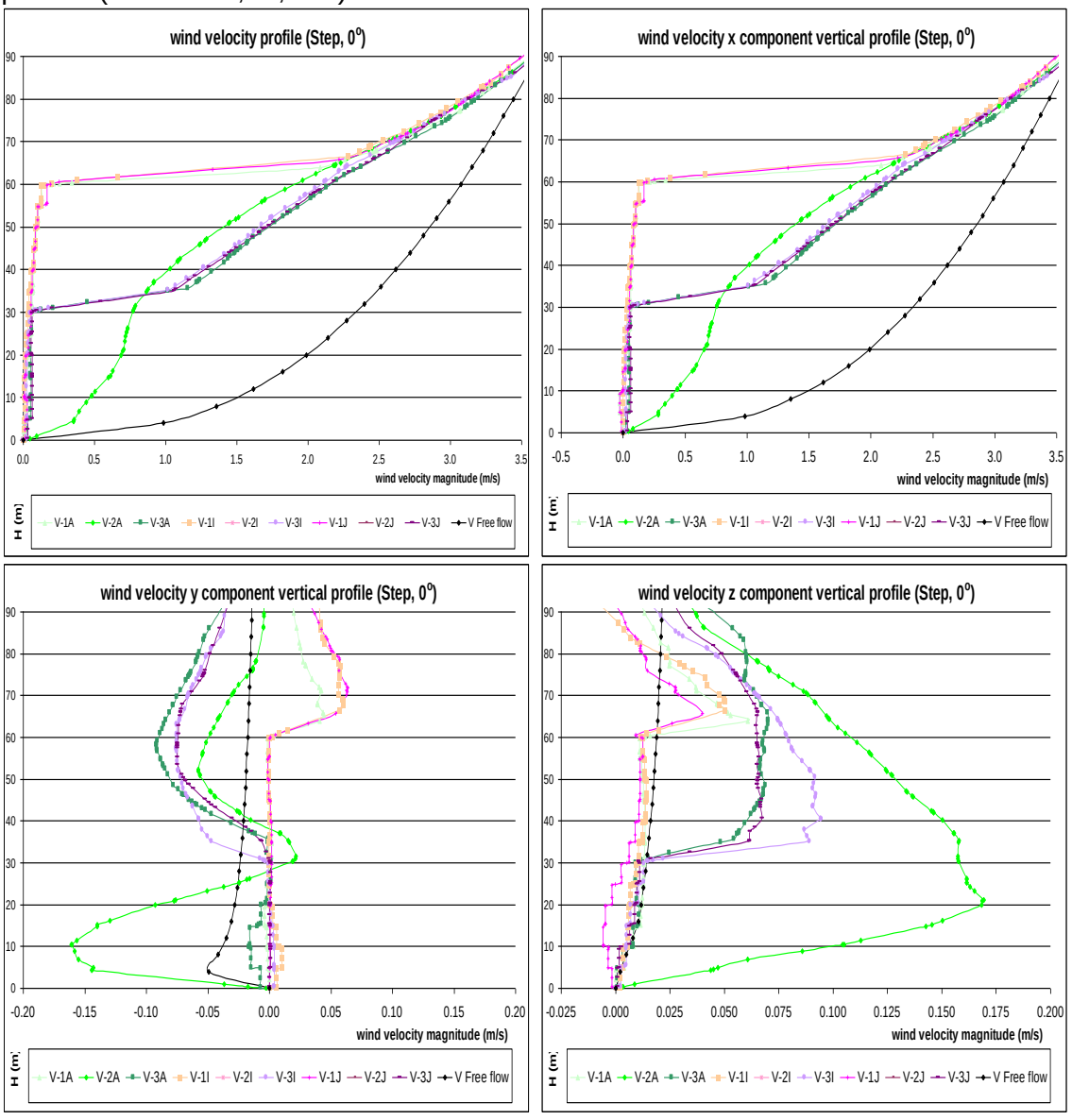

Source: this study.

7.3.5.2. Analysis of the B2 Step-Up results (90^{o})

The airflow outcomes for the B2 Step-Up scenario are characterized by orthogonal winds towards the canyon's axis and the step up level. The results show downwind from the upper side of the windward surface towards the canyon floor. A frontal stagnation point (FS) noticed at 4/5ths of the windward height above the ground directs the flow either upwards or downwards. The up flow escapes over the top side causing both acceleration and flow detachment near the top horizontal edge. Alternatively, the down flow creates a vortex inside the canyon, which eventually escapes at ground level on the blocks' flanks, though less acceleration is observed in this case. The total averaged Cp results for the windward and leeward sides up to 30m height were 0.21 and 0.17. The comparison with the B2 scenario (0.11 and 0.02, respectively) points to an increase of pressure on both sides within the given height. Above 30m height, the total averaged Cp result on the windward side was 0.42, which leads to a total of 0.31 on this side. The Cp upward ranges were, respectively: 0.20 (ground to 10m), 0.18 (10 to 20m), 0.24 (20 to 30m), 0.37 (30 to 40m), 0.50 (40 to 50m), and 0.39 (50 to 60m) on the windward side, and 0.16 (ground to 10m), 0.12 (10 to 20m), and 0.19 (20 to 30m) on the leeward side.

Figure 7-55: Airflow velocity pathlines released from the vertical axis (m/s, 90^{o}).

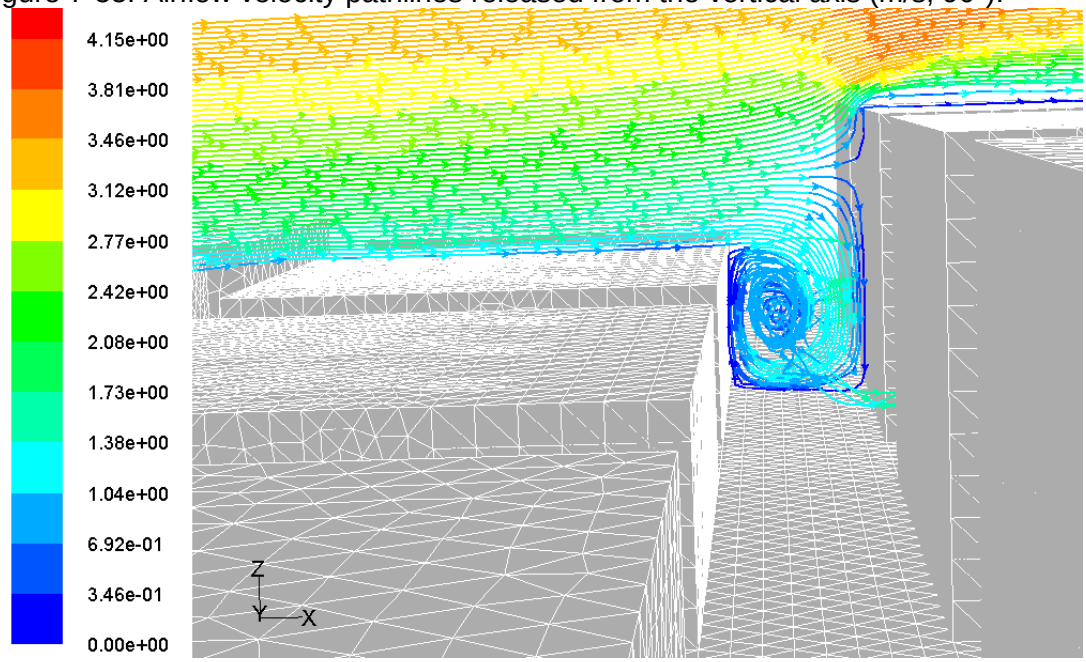

Source: This study.

The wind velocity magnitude vertical profiles show deceleration near the walls with airflow velocities around 0.2 m/s on both the leeward and the windward sides. In the centre of the canyon at 1.45m height the wind is accelerated by a factor of 1.5, attaining 1.5m/s. The x, y, and z wind velocity vector components show that this acceleration forms a diagonal path towards the canyon from the top upwind side to the bottom downwind side. The airflow z vertical profiles are negative near the windward wall and positive near the leeward wall. The y vector component changes from positive to negative velocity several times within the canyon's height. The combined analysis of the three vector components describes a left to right orientated (-y direction) clock-wise spiral flow inside the canyon. Finally, the streamlines above 45m height rise and accelerate as they escape above the windward top side.

Figure 7-56: Wind velocity magnitude and x, y and z wind vector components vertical profiles (B02 STEP UP, 90°, m/s):

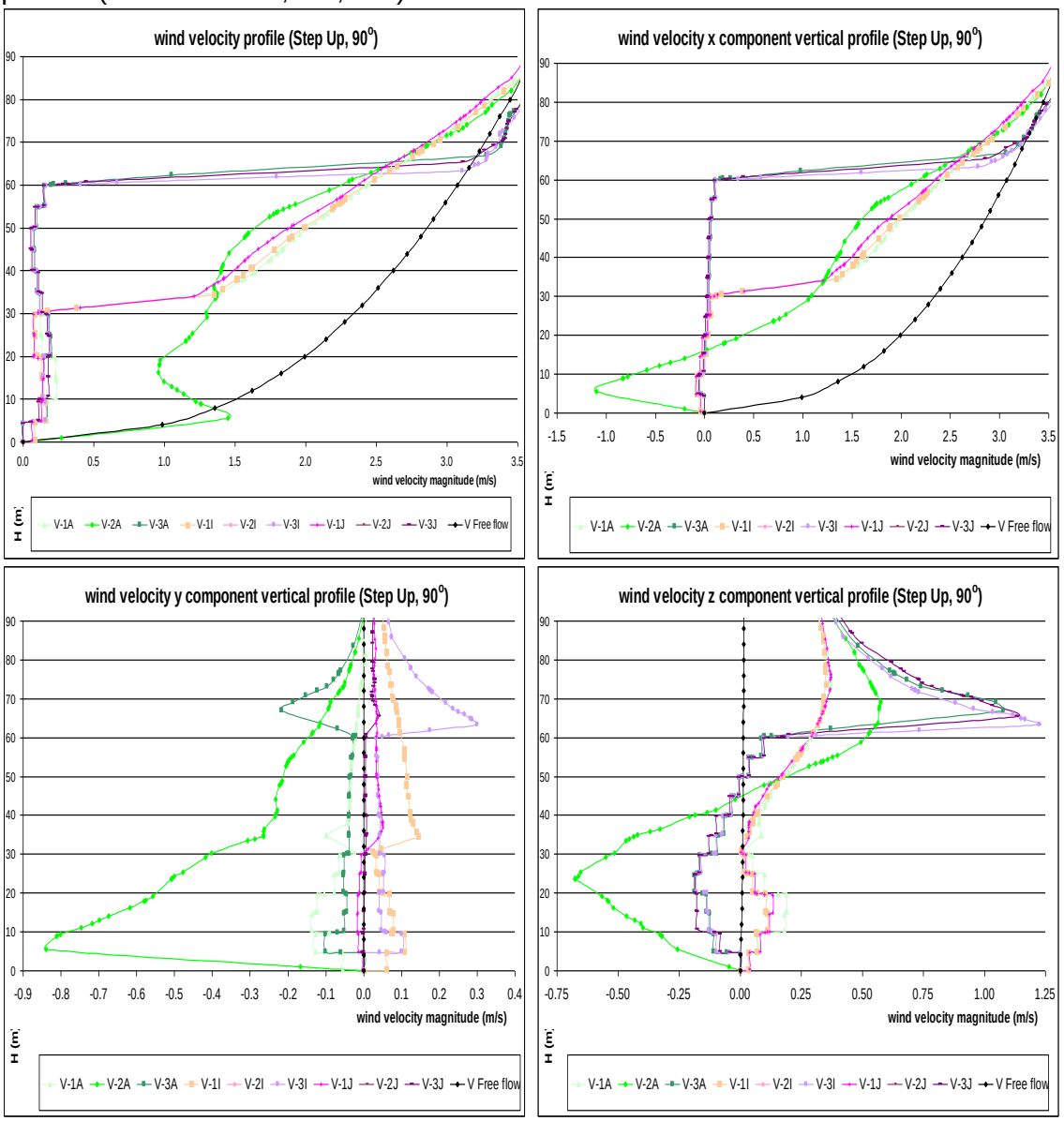

Source: this study.

7.3.5.3. Analysis of the B2 Step-Up results (45°)

The total averaged Cp result on the step-up windward side was 0.45, while on the leeward side it was 0.14. The averaged Cp results for the windward side's lower part (from ground to 30m), and its upper part (from 30m to 60m height) were 0.18 and 0.77. For purpose of comparison, the same results in the B2 scenario were 0.11 and 0.07 for the windward and the leeward faces.

Figure 7-57: Airflow velocity pathlines from the 20m height (Step-Up, m/s, 45°).

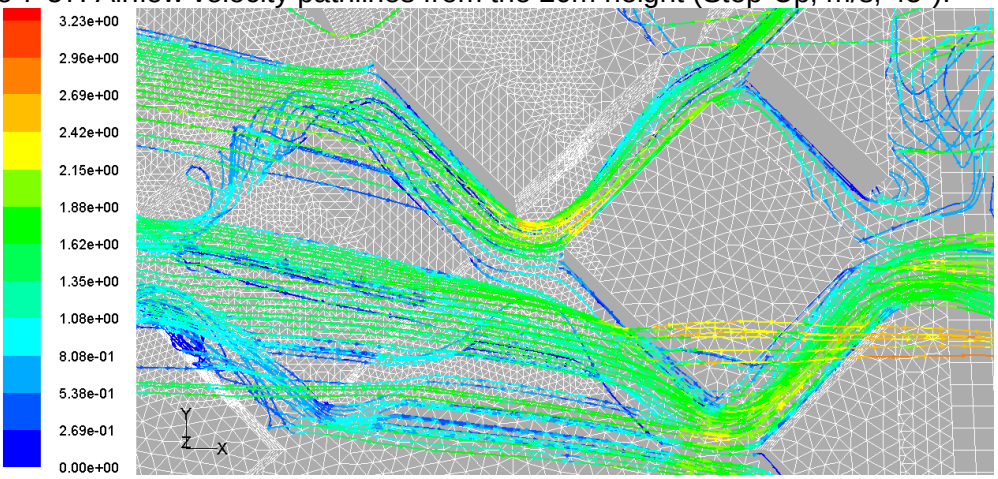

Source: This study.

Figure 7-58: Airflow velocity pathlines from the vertical axis (Step-Up, m/s, 45°).

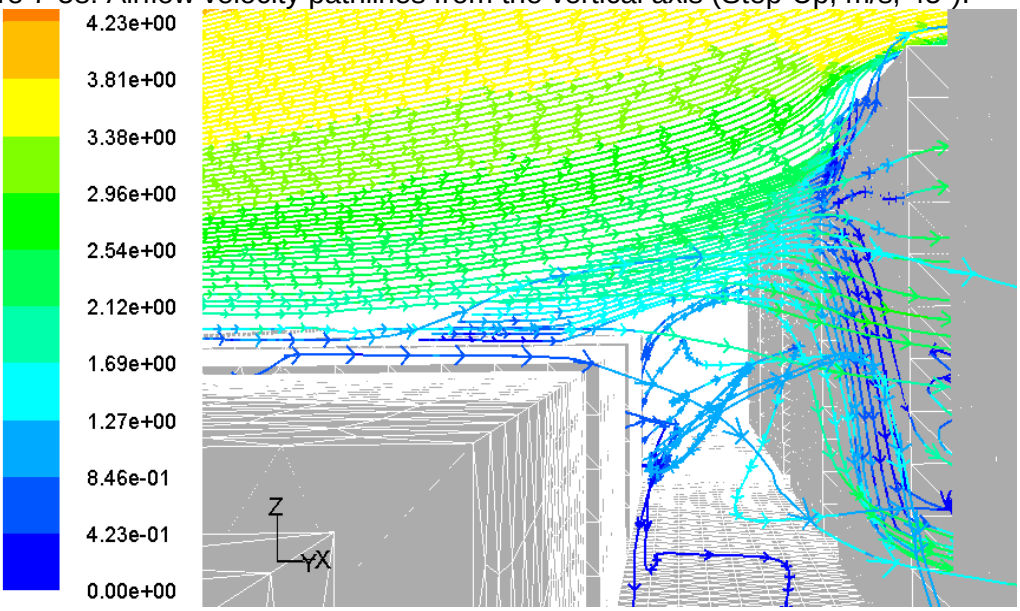

Source: This study.

The average Cp variations towards the height were: -0.03 (0 to 10m), 0.17 (10 to 20m), 0.38 (20 to 30m), 0.64 (30 to 40m), 0.96 (40 to 50m), and 0.72 (50 to 60m) on the windward side and -0.04 (0 to 10m), 0.13 (10 to 20m), and 0.32 (20 to 30m) on the leeward side. It shows that oblique winds towards the B2 step-up scenario produced

higher Cp results in the upper side and lower ones near ground, when compared to the orthogonal wind results. An FS point was noticed at around 4/5ths above the ground. The mainstream, oblique to the blocks, is diverted after meeting the windward side either in an ascending or descending diagonal flow, sweeping the block face. This is related to pressure increase on the downwind block's top height.

Figure 7-59: Wind velocity magnitude and x, y and z wind vector components vertical profiles (B02, STEP UP, 45°, m/s):

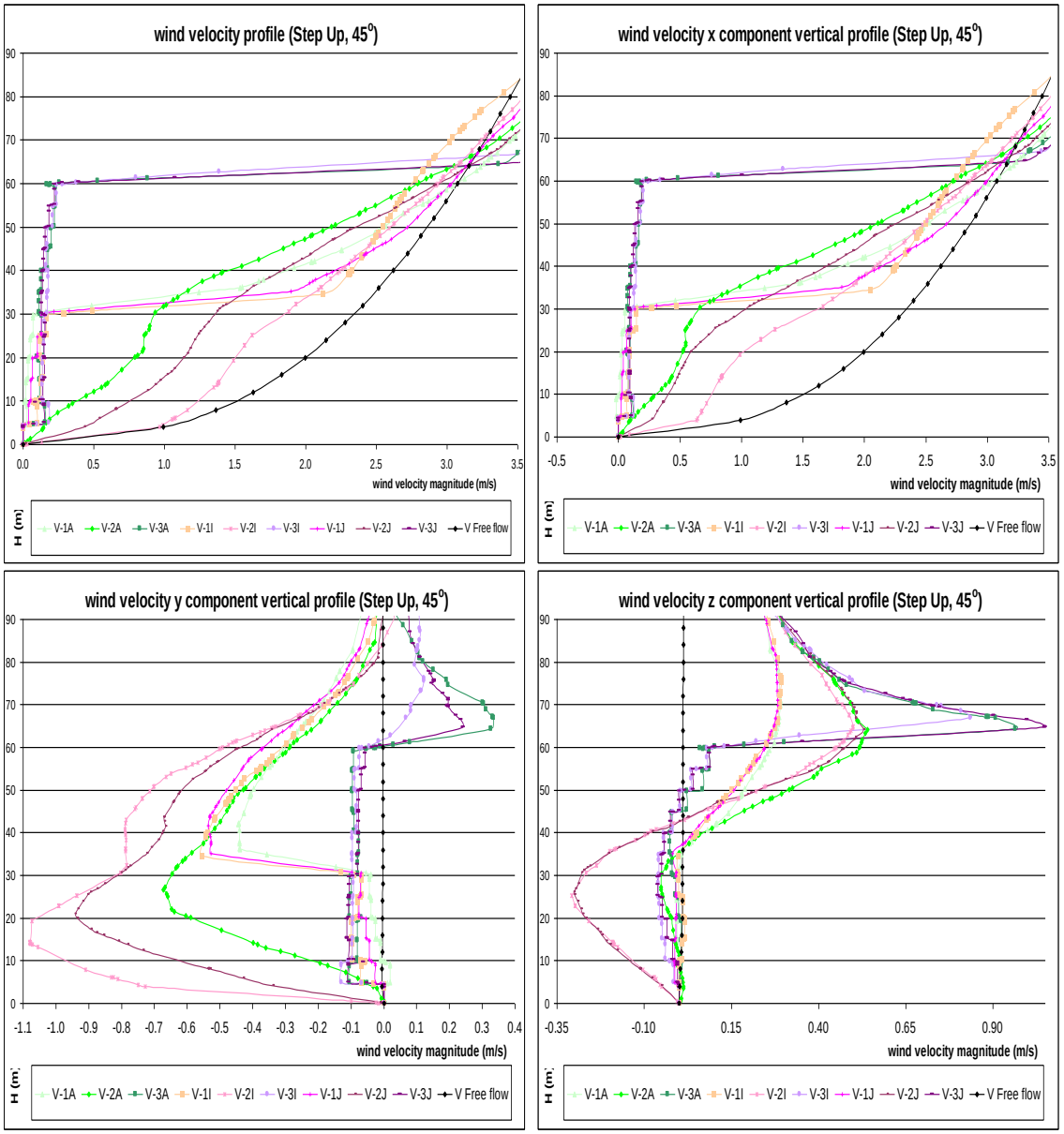

Source: this study.

The wind velocity magnitude vertical profiles show no acceleration inside the canyon. Furthermore, two distinct results are observed: almost still air prevails near the walls, with velocities below 0.20m/s; and the wind velocity along the canyon's central axis follows the ABL input closely, though 0.40 to 0.75% of deceleration occurs. The x

vector component, at an angle of 45° to the windward side, presents the same patterns as the wind velocity magnitude profile. The y component behaves in two distinct ways: while near the windward and the leeward walls speeds are below 0.10m/s, on the central axis the airflow follows the mainstream at 45° attaining up to 1.07m/s at 20m height. The z component presents a similar description to the y vector's, with low speeds near the walls. On the canyon's central axis downward speeds of up to 0.30m/s occur at 20m height.

7.3.5.4. Analysis of the B2 Step-Down results (90°)

The airflow results for winds orthogonal to the B2 step-down scenario show a large leeward wake right after the step, defined by flow deceleration and trailing vortices. The total averaged Cp result on both the windward and the leeward sides up to 30m height was 0.05. The comparison with the B2 scenario (0.11 and 0.08) shows a decrease in pressure in the lower part of the canyon. The total averaged Cp upward ranges were: 0.00 (ground to 10m), 0.05 (10 to 20m), and 0.11 (20 to 30m) on the windward side, and 0.00 (0 to 10m), 0.05 (10 to 20m), 0.10 (20 to 30m), 0.16 (30 to 40m), 0.21 (40 to 50m), and 0.27 (50 to 60m) on the leeward side.

Figure 7-60: Airflow pathlines from a horizontal (top) and vertical (bottom) plane 30m high (Step-Down, m/s, 90°).

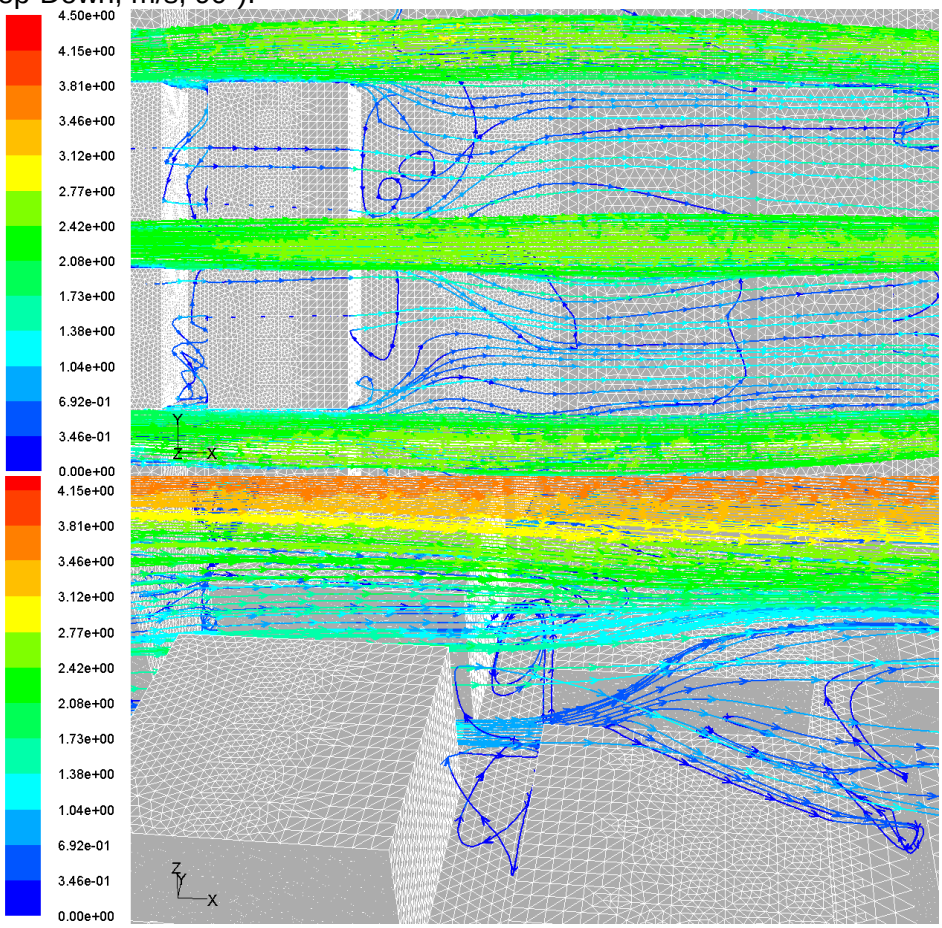

Source: This study.

The wind velocity magnitude vertical profiles indicate great deceleration near the walls, with airflow velocities below 0.20m/s, while in the centre of the canyon airflow at up to 0.50m/s is found. The x vector component indicates reverse flow in the central area. The y vector indicates airflow to the left and right, with velocities ranging from -0.40 to 0.30m/s. In the z vertical vector wind velocities range from -0.10 to 0.45m/s, though upwind prevails. The three wind components change from positive to negative velocities several times from one side of the canyon to the other and also throughout its height. This happens due to highly turbulent vortices within the canyon cavity and above it, and also along the leeward wake.

Figure 7-61: Wind velocity magnitude and x, y and z wind vector components vertical profiles (B02 STEP DOWN, 90°, m/s):

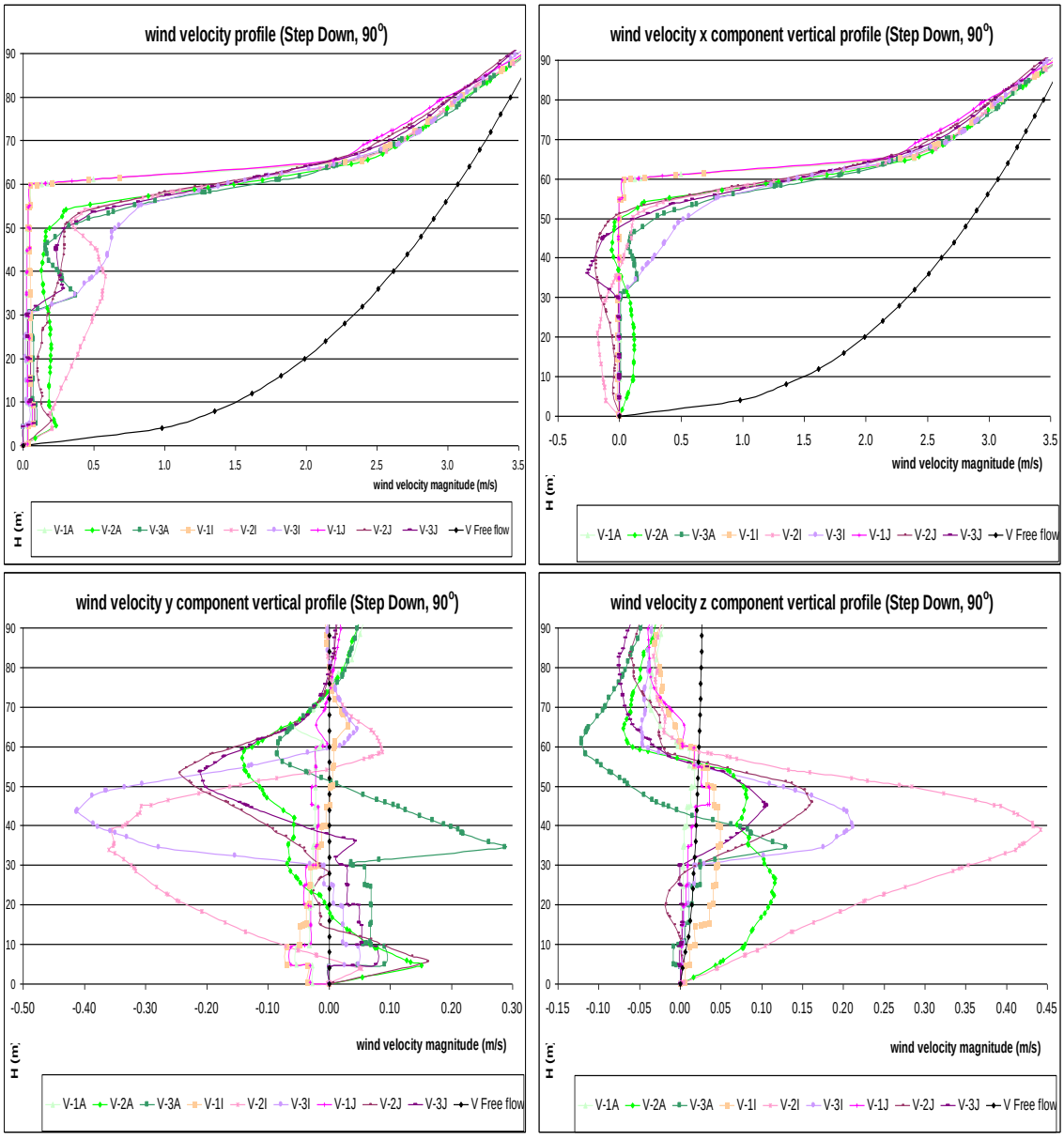

Source: this study.

7.3.5.5. Analysis of the B2 STEP-DOWN results (45^{o})

The airflow path for winds oblique to the canyon's downward step shows a leeward wake accompanying the decrease in the blocks' height, with deceleration and trailing vortices. The total averaged Cp results on the windward and leeward sides up to 30m height were 0.06 and 0.05. Comparison with the B2 scenario (0.11 and 0.08) shows again a decrease of pressure inside the canyon. A total average Cp of 0.22 on the leeward upper side leads to a combined total averaged Cp of 0.13 for this face, which is somewhat higher than the result found for the orthogonal wind direction in this same scenario. The Cp results at different heights were: 0.01 (ground to 10m), 0.06 (10 to 20m), and 0.11 (20 to 30m) on the windward side; and 0.00 (0 to 10m), 0.05 (10 to 20m), 0.10 (20 to 30m), 0.15 (30 to 40m), 0.21 (40 to 50m), and 0.26 (50 to 60m) on the leeward side.

Figure 7-62: Airflow velocity pathlines on a horizontal plane at 05 and 30m height top) and a horizontal plane at 05 and 30m height (Step-Down, m/s, 45^{o}).

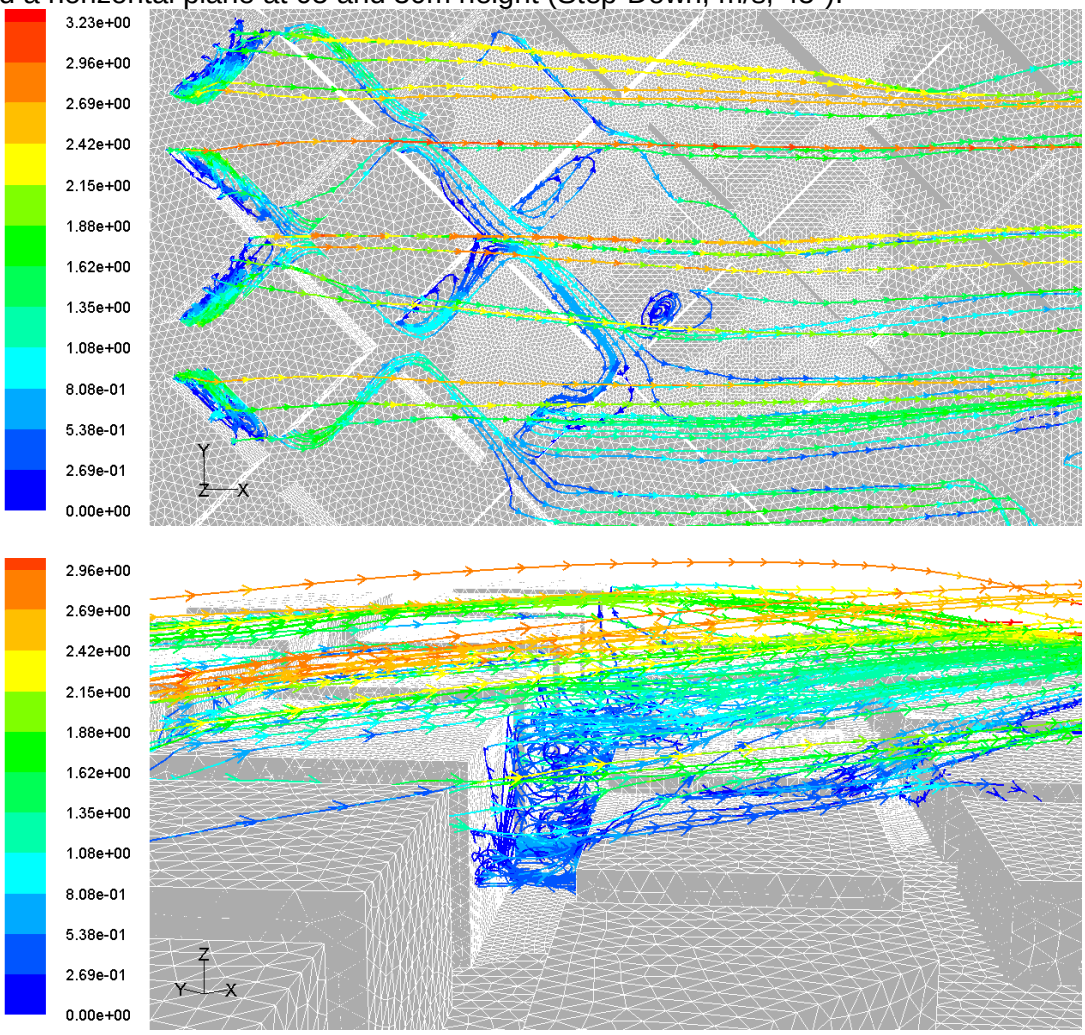

Source: This study.

The analysis of the wind velocity magnitude vertical profiles shows deceleration near the walls, with airflow velocities below 0.20m/s. In the centre of the canyon an airflow of up to 0.50m/s is observed. The x wind velocity vector component indicates reverse flow on the central axis. The y vector presents both stream wise and reverse flows, with velocities ranging from -0.25 to 0.20m/s, and flow direction shifting several times from one side of the canyon to the other. The z vertical component velocity ranges from -0.25 to 0.25m/s, with upwind at the beginning and at the end of the canyon's length and downwind in the central area. This portrays a complete vortex turn along the canyon's axis, which happens at several heights, forming a vertical swirl. This change in the airflow speed and direction can be seen on both the velocity vector and the velocity pathline figures that illustrate this analysis.

Figure 7-63: Wind velocity magnitude and x, y and z wind vector components vertical profiles (B02 STEP DOWN, 45°, m/s):

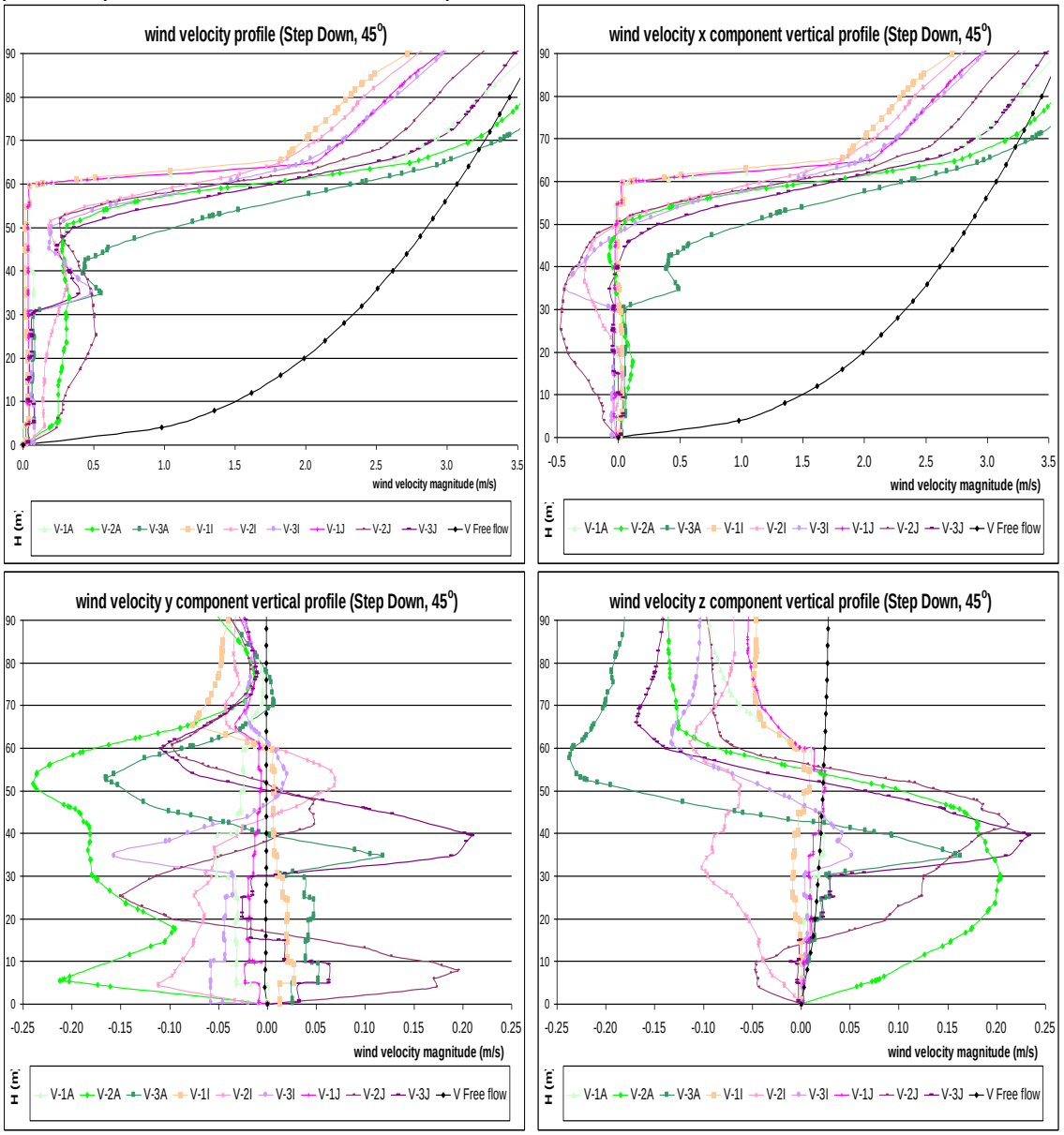

Source: this study.

7.3.6. Analysis for the Group 6: D1, D2, D3 and D4 results

Group 6 constitutes a link between the prototypes and real urban landscapes. This investigation have so far focused on canyon-like scenarios with homogeneous block height or stepped set-up. Now, three different block heights are employed: 30m; 60m; and 90m. The differences in height served to create a mix of asymmetrical volumes throughout the scenario. Further, Group 6 was based on previous prototypes' plot occupation and plan-area density ratios. Some of the aspect ratios are closer to those of a building and street/ canyon scale, while others are on a larger block/ neighbourhood scale. Such analysis may help to identify which are the mandatory urban parameters that will possibly characterize or define the airflow field in the urban environment. The L/H and H/W aspect ratios change from one block to another and, in consequence, averaged results were considered. Ultimately, both the A_{roof}/A_{urb} and the A_{built}/A_{urb} ratios are comparable to those of real urban centres[101].

Although Group 6 scenarios are not symmetrical, they present a common pattern. Only two types of blocks were used in the setting: one with up to 60m and the other with up to 90m height volumes. These blocks were either rotated or mirrored creating several different canyon arrangements. Pressure results are presented for two different canyons, denominated 'canyon A' and 'canyon B'. For instance, the D1 scenario has long blocks just as A2. The D2 scenario is divided in two, just as B2. Then, the plan-area density is decreased in the D3 scenario. The D4 scenario is an approach to the B4 array of cubes, but now with variations in size and height. The D4 scenario is the closest to real urban centres, since it is composed of detached blocks of different heights. This scenario pressure analysis is focused on the vertical faces of three different tower-like blocks, and not on canyon shapes. Tower 1 (T1) is a 30m cube, and the results will be contrasted with those of the previous B4 scenario. Tower 2 (T2) has a 30m square plan and is of 60m height, while tower 3 (T3) has a 30x60m rectangular base and is 90m high.

[101] See table 5-3 in Chapter 5.

7.3.6.1. Prototype D01

Figure 7-64: Output lines and accessed areas used in the prototype D01 for wind incidence at 90°.

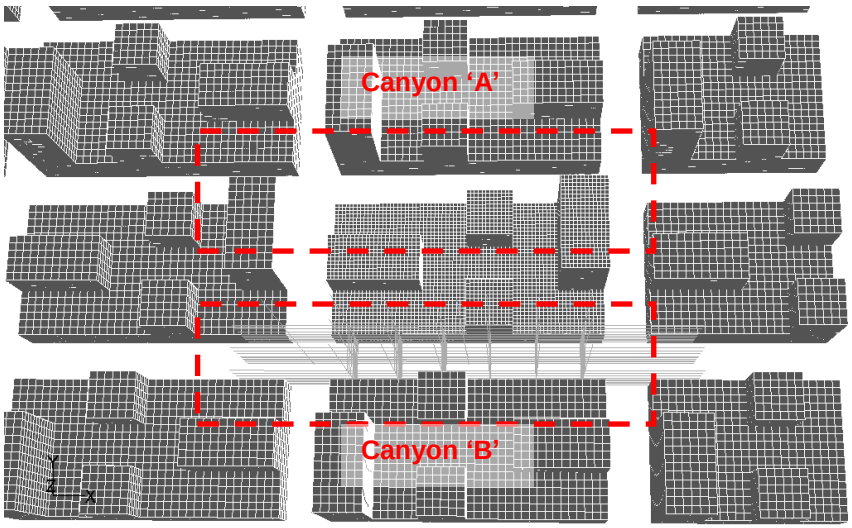

Source: This study.

7.3.6.1.1. Analysis of the D01 results (0°)

In general, the results on the right and the left sides of both the D1 scenarios ('A' and 'B' canyons) assessed were similar, despite the height difference between the models. Both canyons have a 30m lower base and a 60m height middle volume, though the canyon 'A' also has a 90m upper volume on the corners. The Cp analysis covers the three vertical variations.

Figure 7-65: Airflow velocity pathlines from a horizontal rake at 30m H (D01, m/s, 0°).

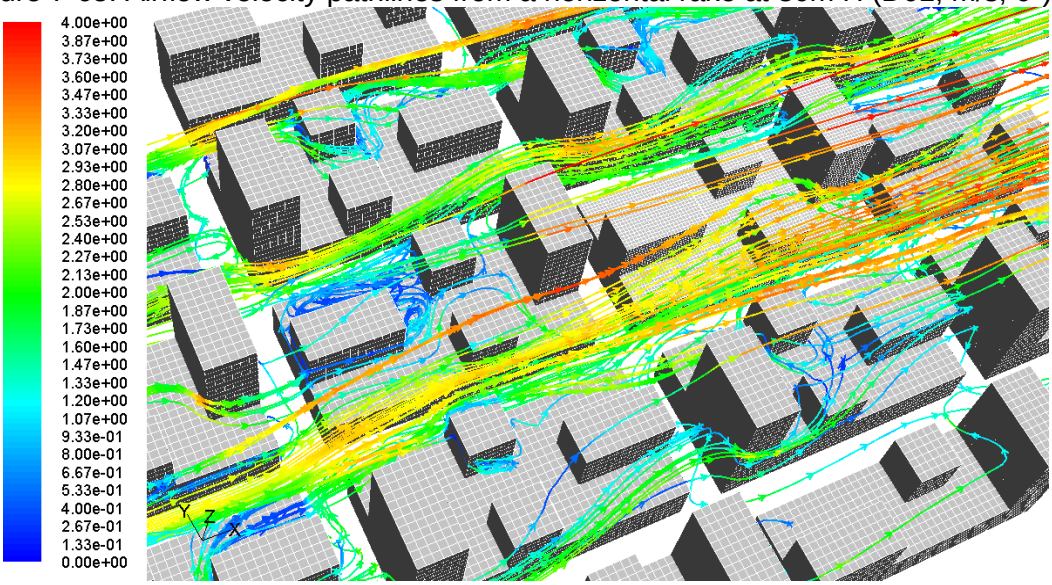

Source: This study.

The total averaged Cp result in the lower base (ground to 30m) on both the right and left sides of canyons ‘A’ and ‘B’ was 0.12, which is twice the result found in the B1 square canyon. This may be explained by down flow and intensification of the channelling effect. Airflow facing blocks above 30m height divert the wind up or down and to the right or left, increasing the flow in and along the canyon. The Cp total average results on the 30 to 60m height middle surfaces were: 0.38 and 0.35 for the right and the left sides. The upper surfaces from 60 to 90m presented a total averaged Cp result of 0.57 on both sides of canyon ‘A’. Finally, total averaged Cp results on the right and left sides were: 0.35 and 0.34 in canyon ‘A’; and 0.24 and 0.23; in canyon ‘B’. A sharp decrease in pressure is observed at most of the upwind vertical edges regardless of the faces’ height. This is related to the flow detachment in the region. After the flow’s reattachment, the pressure on the surfaces increases on an ascendant diagonal as far as the downwind edge. Conversely, there is another drop of pressure on the face’s right side before its height increases. This may occur as a result of horizontal low pressure bubbles caused by lateral horseshoe shaped wakes. Further, the higher the vertical friction area, the greater the airflow deceleration for winds parallel to the vertical walls.

The wind velocity magnitude vertical profiles in canyon ‘A’ show a constant velocity of from 1.2 to 1.5m/s in the centre of the canyon up to a height of 60m. This means that there is acceleration by a factor of 1.5 near the ground, while above 10m height progressive deceleration takes place. Near the walls two kinds of behaviour are to be observed: up to 30m height the wind speed remains constant at around 0.45m/s on the right side and at 0.15m/s on the left side. Possibly the 90m height block near the upwind left side diverts the flow away from its side. Near 60m height faces the wind speed is reduced on both the right and left sides as little as 0.15m/s. Above the blocks all the wind profiles accelerate abruptly in accordance with the same pattern, with velocities above the ABL input. The x wind vector component, alongside the mainstream, shows a similar pattern to the velocity magnitude profile, with no reverse flow. Up to 30m height the y component is rather weak. Conversely, from 30 to 40m height intense velocity vectors of up to +1.0 and -1.0m/s are observed near the left and the right sides. This means that the flow advances laterally above the 30m height blocks on both sides. The z vertical velocity vector profile shows two different patterns: from ground to 30m height an ascending flow occurs at the beginning and the end of this long canyon; while in the centre the flow descends, characterizing a vertical vortex throughout the canyon’s 180m extent. Above 30m height the z component is all ascendant in all the vertical profiles.

Figure 7-66: Wind velocity magnitude and x, y and z wind vector components vertical profiles (D01, 0°, m/s):

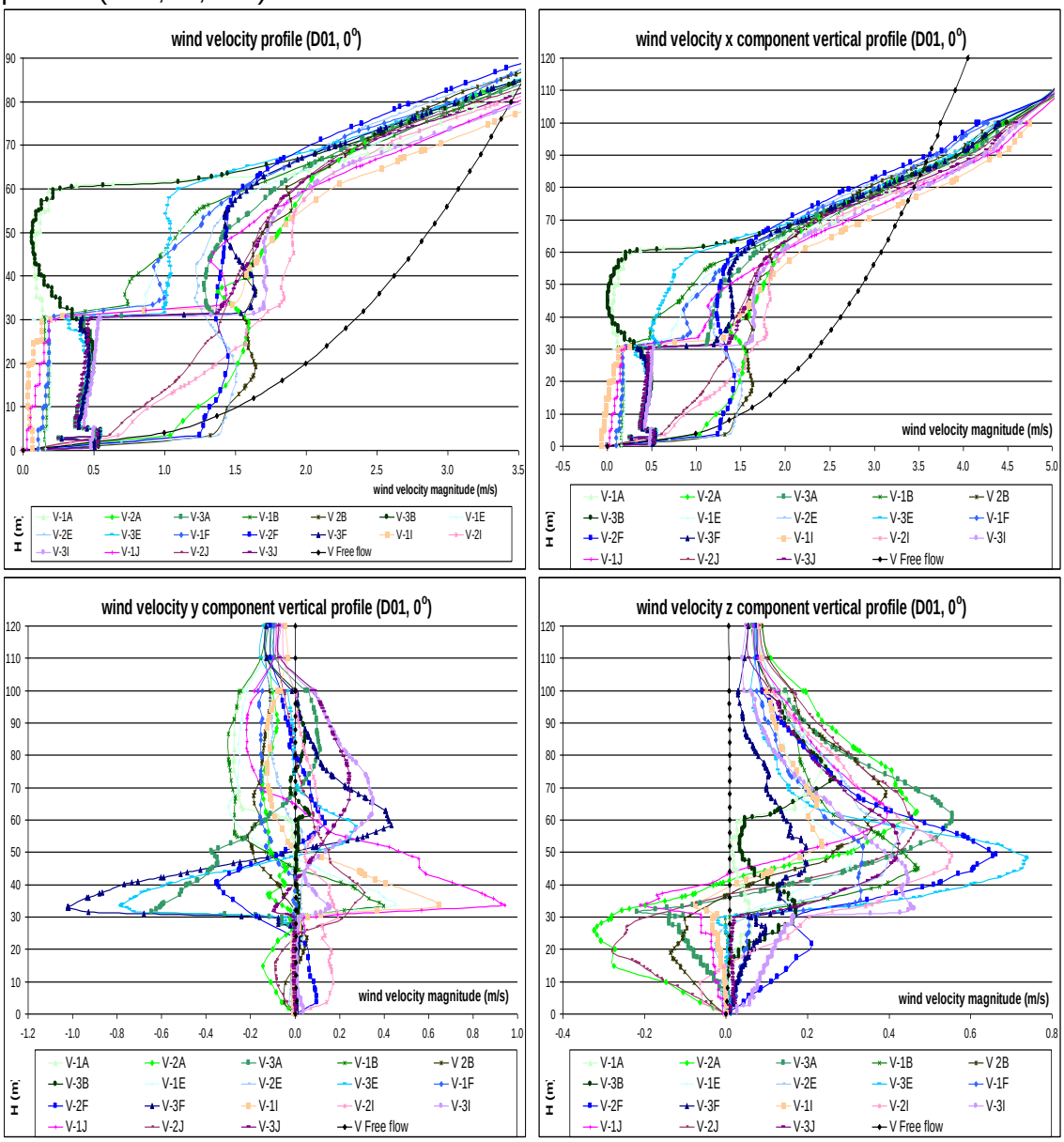

Source: this study.

7.3.6.1.2. Analysis of the D01 results (90°)

For isolated blocks, it is to be expected that the pressure on their sides will be greater than that on the leeward side. In contrast, both the windward and leeward sides of canyons 'A' and 'B' presented the same total averaged Cp result at low height (ground to 30m): 0.12. This result is also similar to that of the B1 square canyon. On the other hand, the windward and leeward Cp difference increases with height and the consequent decrease in the A_{roof}/A_{plot} ratio adopted in this scenario. The following Cp results found for the windward and leeward sides of: 0.45 and 0.40 at middle (30 to 60m); and 0.87 and 0.65 at top (60 to 90m) heights, corroborate this statement. In conclusion, at low heights upwind and downwind face orientation has no effect on Cp

differentiation, excepting in those regions where down-flow and acceleration occur near the ground, as happens in areas near the floor frontal to 90m blocks, on which a clear increase in the Cp result is observed due to down-flow.

Figure 7-67: Airflow velocity pathlines from a horizontal rake at 30m H (D01, m/s,90°).

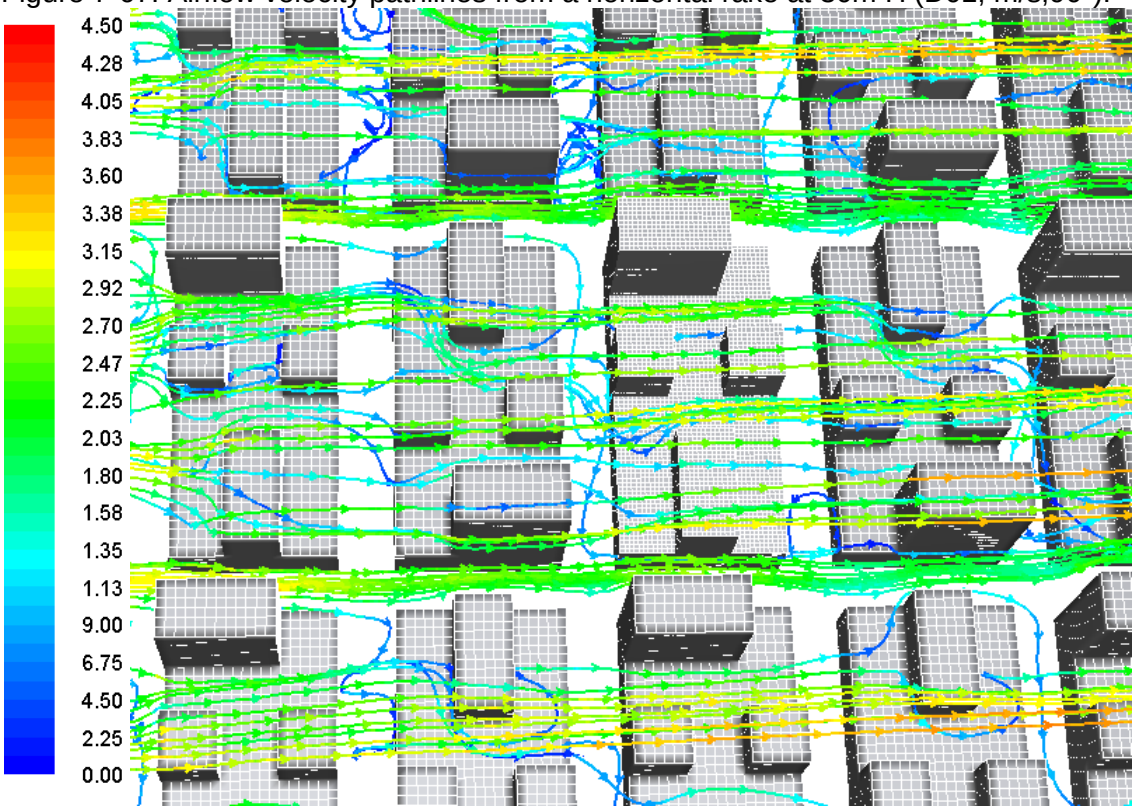

Source: This study.

Figure 7-68: Airflow velocity pathlines from a horizontal rake at 30m H (D01, m/s,90°).

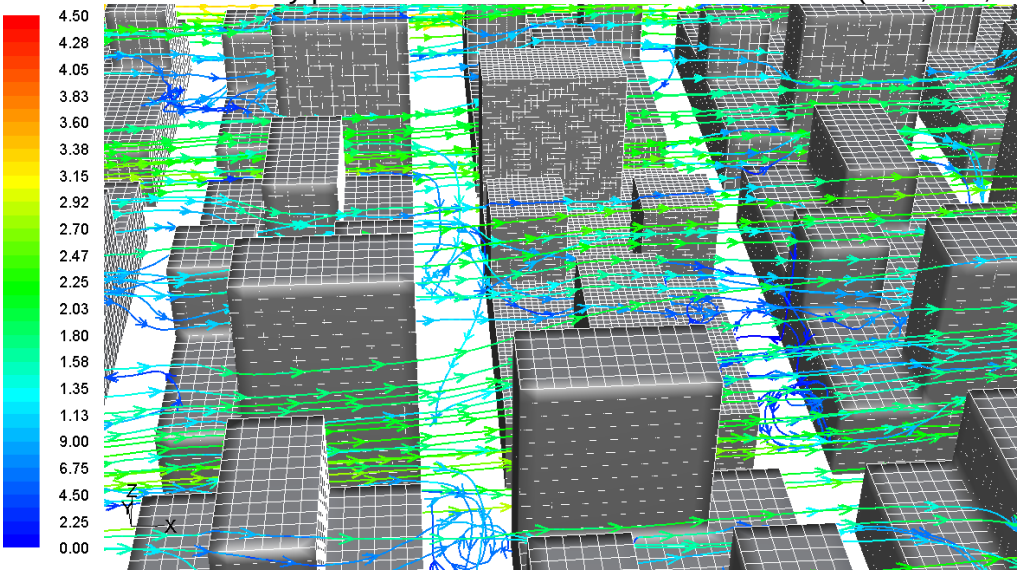

Source: This study.

The wind velocity magnitude vertical profiles in canyon 'B' show deceleration inside the canyon up to 40m height, with wind velocity below 0.50m/s. Exceptions occur in the central area near the ground, where the isolated x wind component shows reverse flows of up to -0.50m/s. The vertical z vector component indicates a descending flow near the windward face, with speeds as low as -0.20m/s, and an ascending flow near the leeward face of up to +0.35m/s. These vectors acting together create a two dimensional clock-wise vortex. Conversely, the lateral y component of the flow, which alternates between positive and negative velocities (or from the left to the right side), indicate the existence of several vortices along and over the canyon.

Figure 7-69: Wind velocity magnitude and x, y and z wind vector components vertical profiles (D01, 90°, m/s):

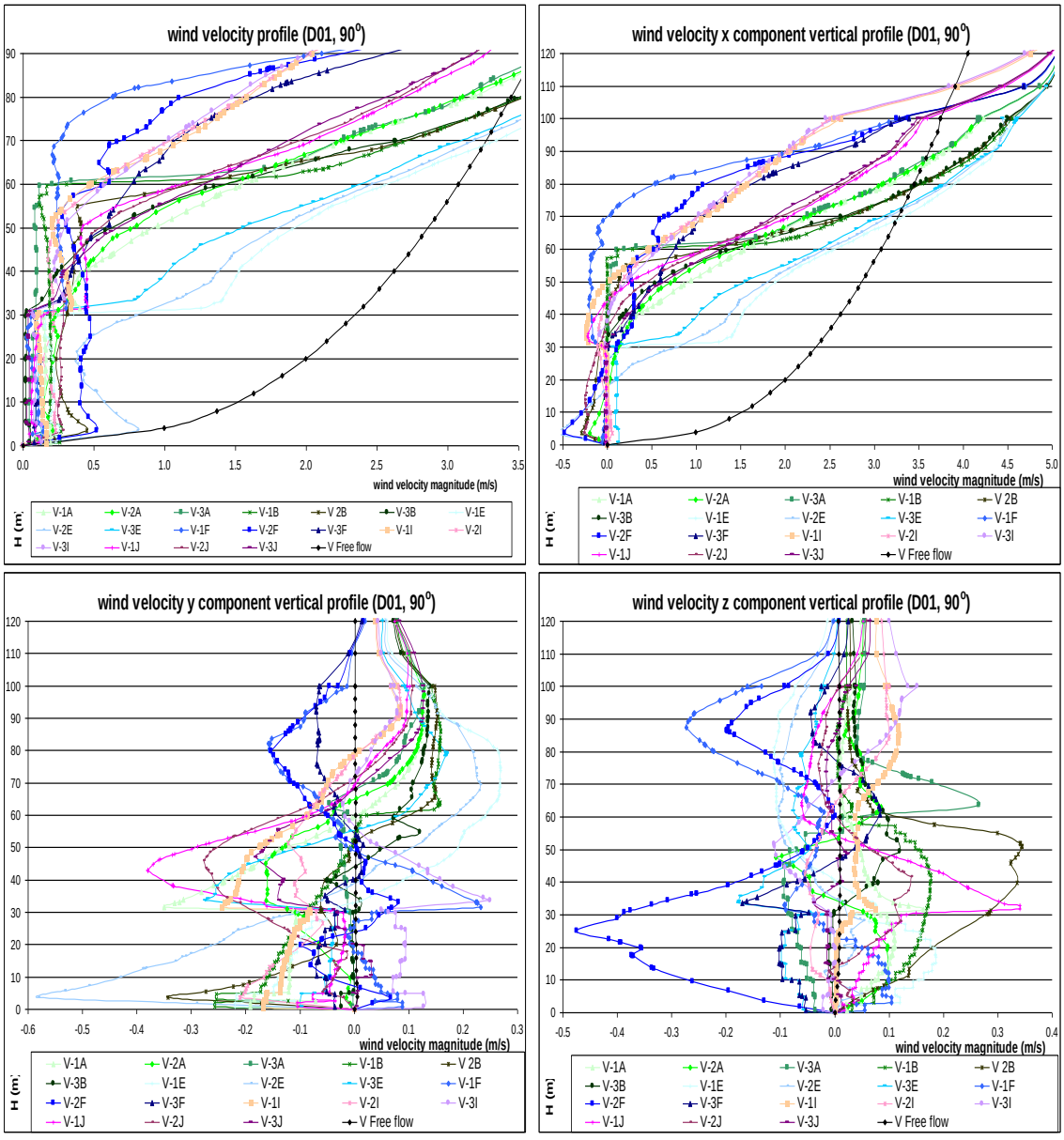

Source: this study.

7.3.6.1.3. Analysis of the D01 results (45^{o})

The D1 prototype assessment for oblique winds comprised also the canyons ‘A’ and ‘B’ and three vertical divisions: low, medium and top heights. The D1 asymmetrical and unlevelled scenario shows greater pressure below 30m height than the B1 symmetrical scenario. The total averaged Cp results for the windward and leeward sides of canyons ‘A’ and ‘B’ were: 0.20 and 0.12 from ground to 30m height, while in B1 they were: 0.06 and 0.04. Further, the total averaged Cp increased with height: 0.52 and 0.43 at medium (30 to 60m); and 1.01 and 0.65 at top (60 to 90m) height. The pressure increase is related to the built height and the diagonal wind direction, which diverts airflow either up or down and creates acceleration at the sharp edges.

Figure 7-70: Airflow velocity pathlines from a horizontal rake at 30m H (D01, m/s, 45^{o}).

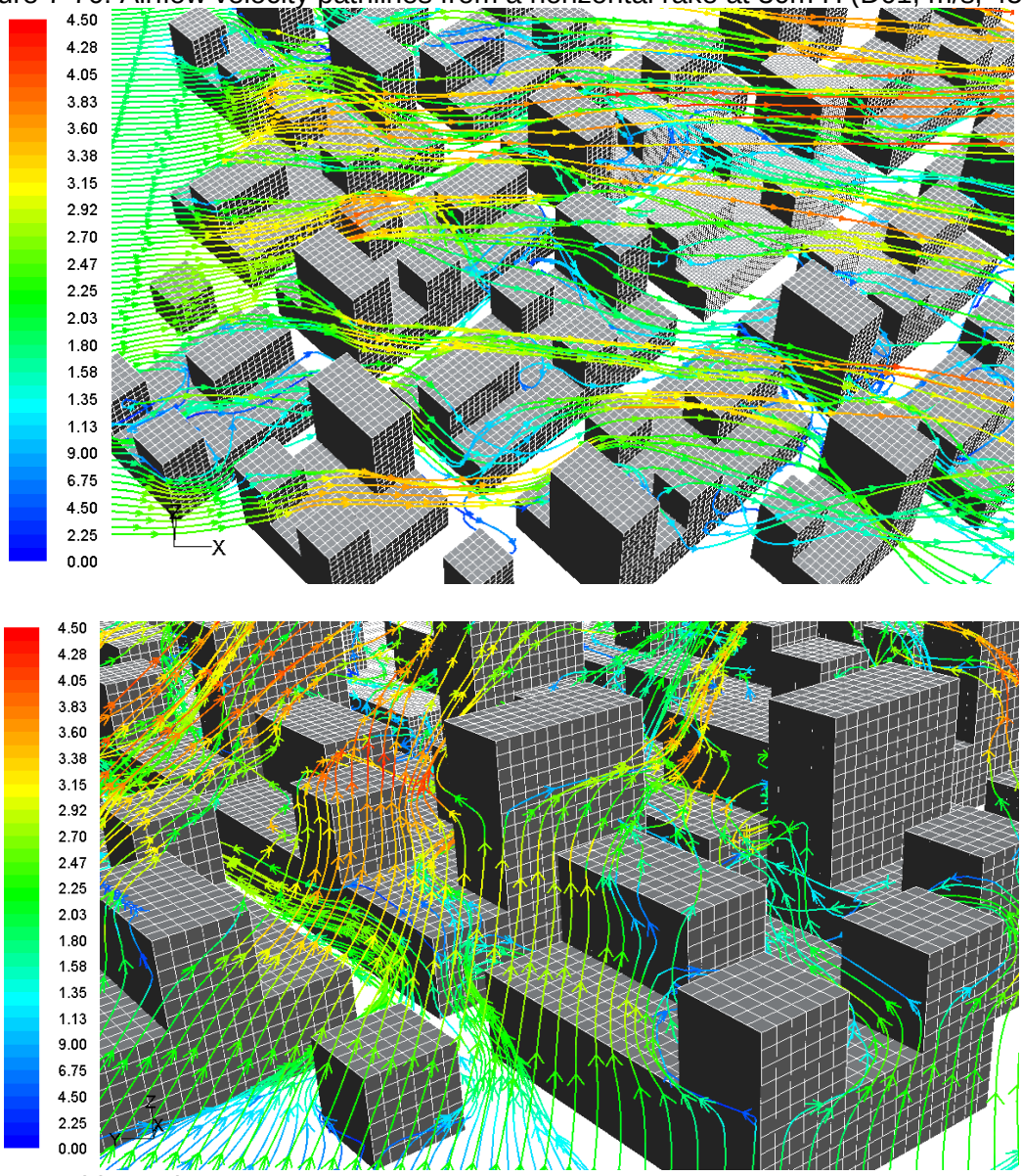

Source: This study.

Figure 7-71: Airflow velocity pathlines from a horizontal rake at 30m H (D01, m/s, 45°).

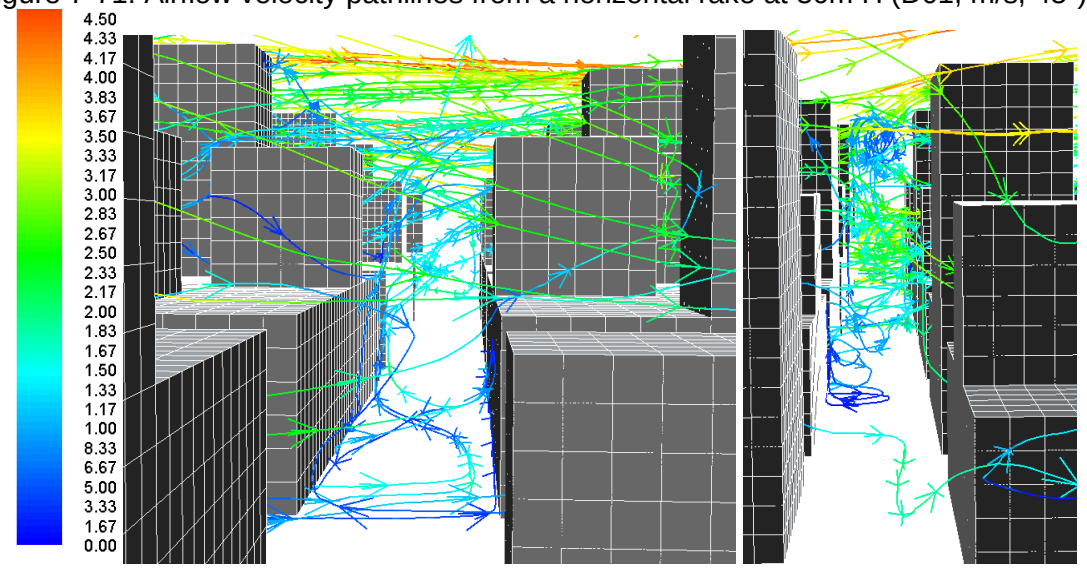

Source: This study.

The canyon 'B' wind velocity magnitude vertical profiles show airflow acceleration in the canyon's central area. At pedestrian level and up to 20m height wind velocity attains 2.33m/s, which is 4x the ABL input velocity. Conversely, near both the faces airflow velocity ranges from 0.20 to 0.50m/s up to 30m height. From 30 to 60m height the velocity ranges from 0.60 to 2.00m/s. Over 60m height considerable acceleration occurs. The x wind component accompanies the wind velocity magnitude pattern, but with reduced intensity. But it presents no negative velocities, which means that there is no reverse flow. The y wind component is entirely positive up to 40m height, and very intense in the canyon's centre, attaining up to +1.90m/s near the ground. Near the walls its velocity ranges from +0.30 to +0.50m/s up to 30m height. From 40 to 70m height the y component shifts to negative velocities of up to -0.80m/s. Over 70m the flow shifts from positive to negative speed. Since the main stream is diagonal to the blocks, this means that the flow divides to go round the 90m height blocks.

Figure 7-72: Wind velocity magnitude and x, y and z wind vector components vertical profiles (D01, 45°, m/s):

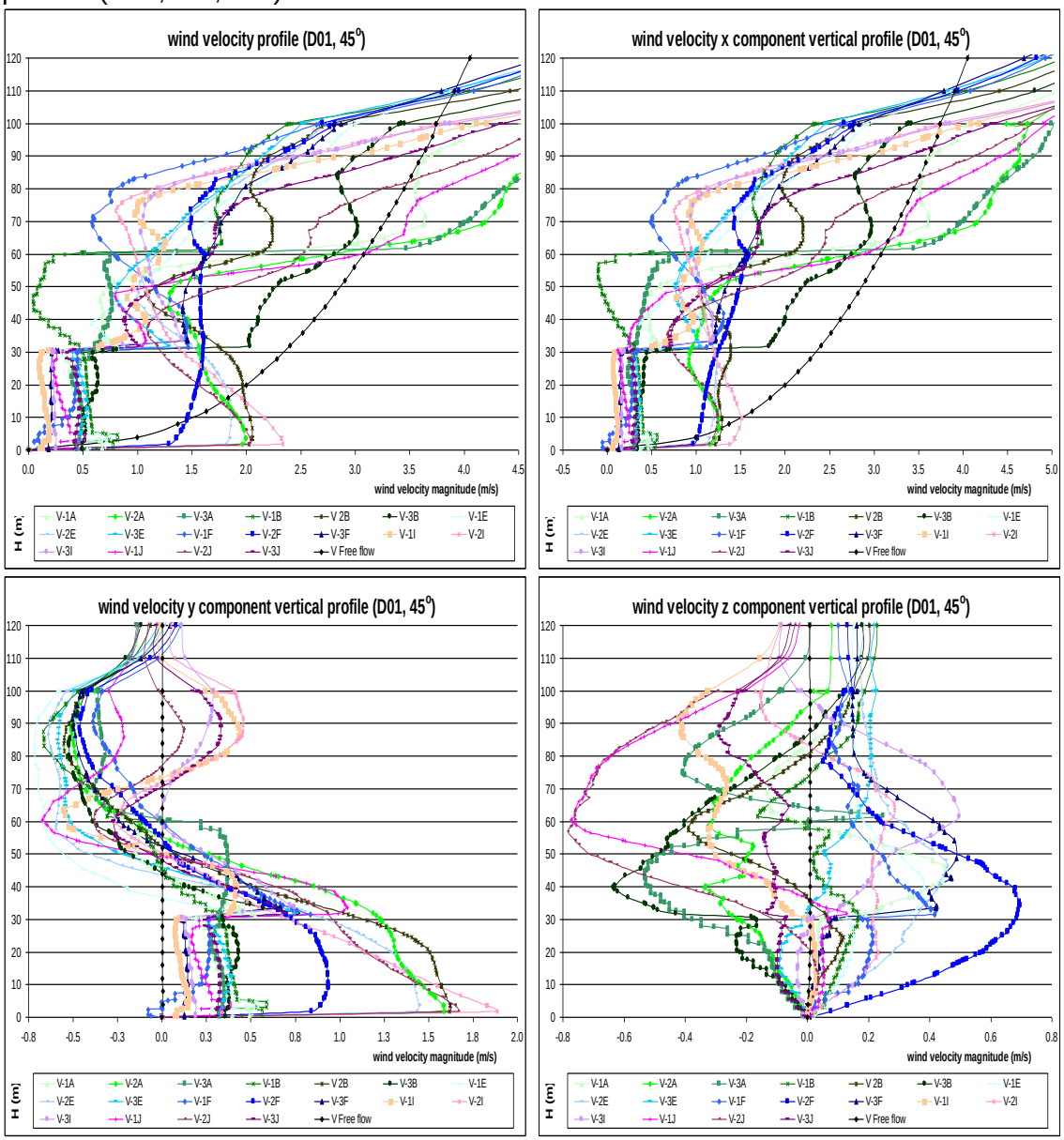

Source: this study.

7.3.6.2. Prototype D02

Figure 7-73: Output lines and accessed areas used in the prototype D02 for wind incidence at 90°.

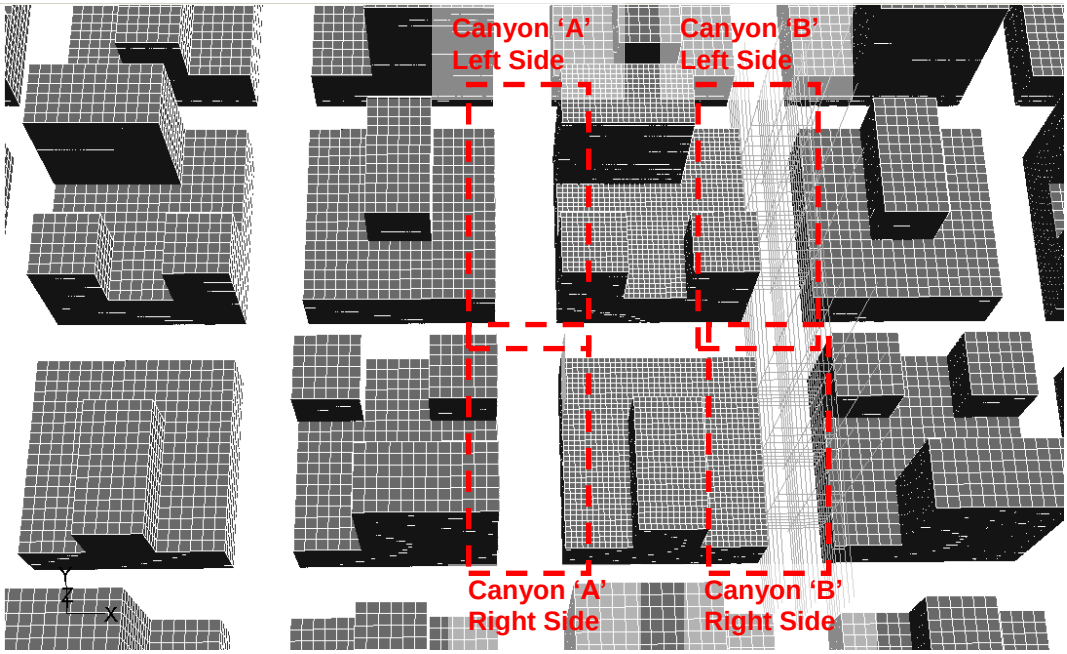

Source: This study.

7.3.6.2.1. Analysis of the D02 results (0°)

Figure 7-74: D02 canyon accessed areas and airflow velocity magnitude pathlines from a horizontal rake at 30m H (D02, m/s, 0°).

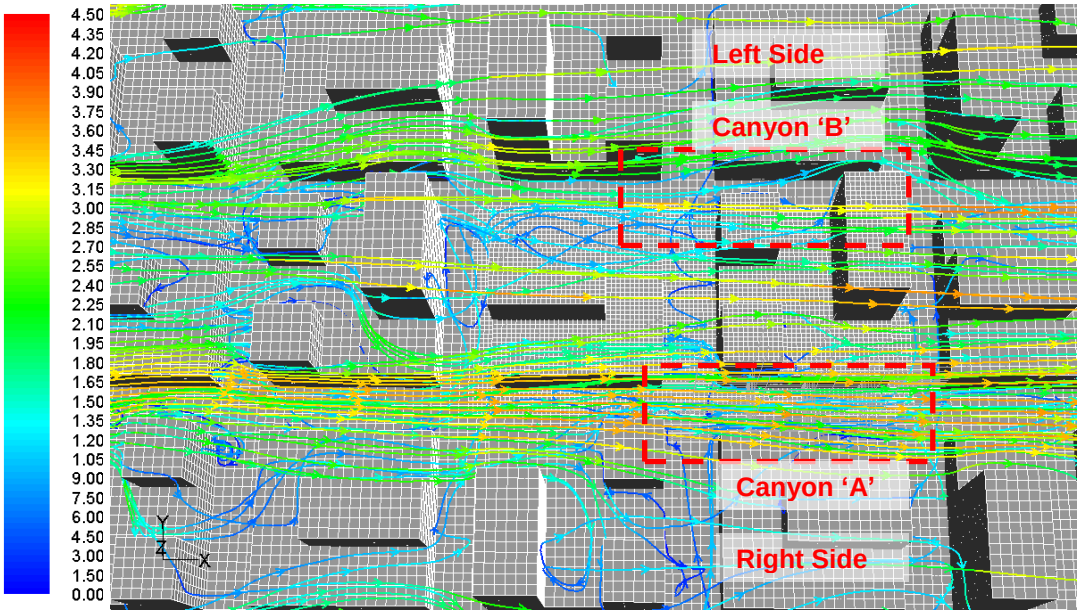

Source: This study.

On the whole, results from parallel winds to both the canyons ‘A’ and ‘B’ were similar, particularly below 30m height. The total averaged Cp result found at low height was 0.09 on both right and left sides of both canyons. This result is lower than the found in D1 scenario (0.12), but greater than the equivalent in plan-area density B1 square scenario (0.06). Also, the canyon ‘A’ averaged Cp results at middle height on both sides were 0.36, showing constant pressure distribution even with height variation. The upper face of canyon ‘B’, with height from 60 to 90m, showed a total averaged Cp result of 0.57. The total Cp averaged results were: 0.09 and 0.17 for the canyon ‘A’ right and left sides; and 0.33 and 0.12; for canyon ‘B’. The Cp distribution in the D1 scenario faces shows pressure decrease in the upwind vertical edges and also before tall blocks; but with less intense airflow channelling effect.

Figure 7-75: Views of airflow pathlines alongside (left) and across (right) the stream (D02, m/s, 0°).

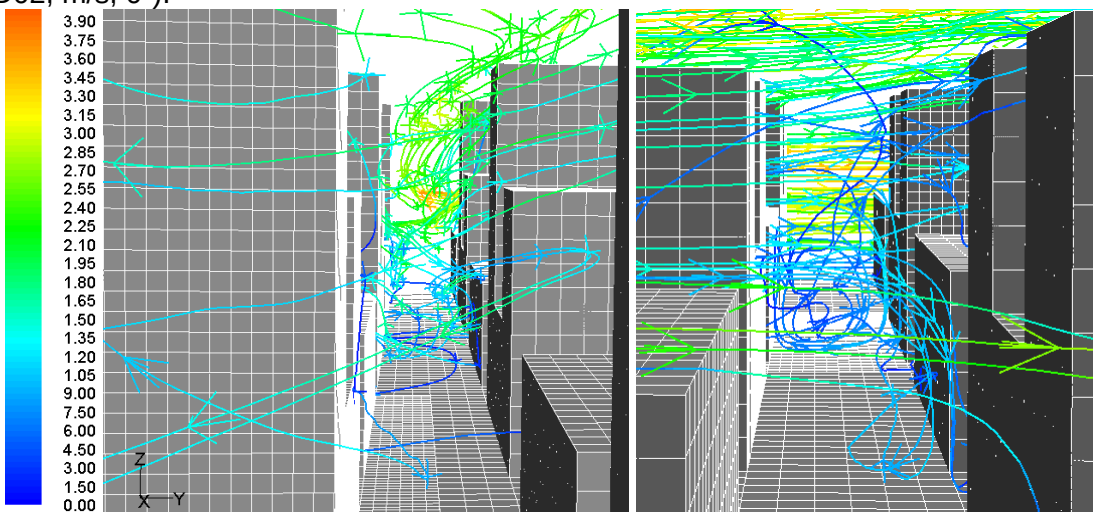

Source: This study.

The wind velocity magnitude vertical profiles in the D2 scenario canyon ‘A’ show velocity reduction when compared to the D1 prototype, though similar airflow patterns were observed: constant wind velocity ranging from 0.75 to 1.25m/s in the centre of the canyon up to 30m height. Near the faces two behaviours are noticed: up to 30m height wind speed remains constant around 0.25m/s on the right side and 0.10m/s on the left side and, over the blocks, intense acceleration takes place. The x component of the wind along the flow shows the same patterns of the velocity magnitude vector, with no reverse flow happening. Conversely, the y component presents some lateral flow up to 30m height. Above it cross flow is more intense, ranging from -0.9 to +0.3m/s. The z vertical velocity vector shows ascending flow pattern with 0.45m/s velocity peak at around 45m height in the centre of the canyon. Both the crossed flow and the continuous ascending vortex alongside the canyon can be seen in the airflow velocity pathline visualization figures.

Figure 7-76: Wind velocity magnitude and x, y and z wind vector components vertical profiles (D02, 0°, m/s):

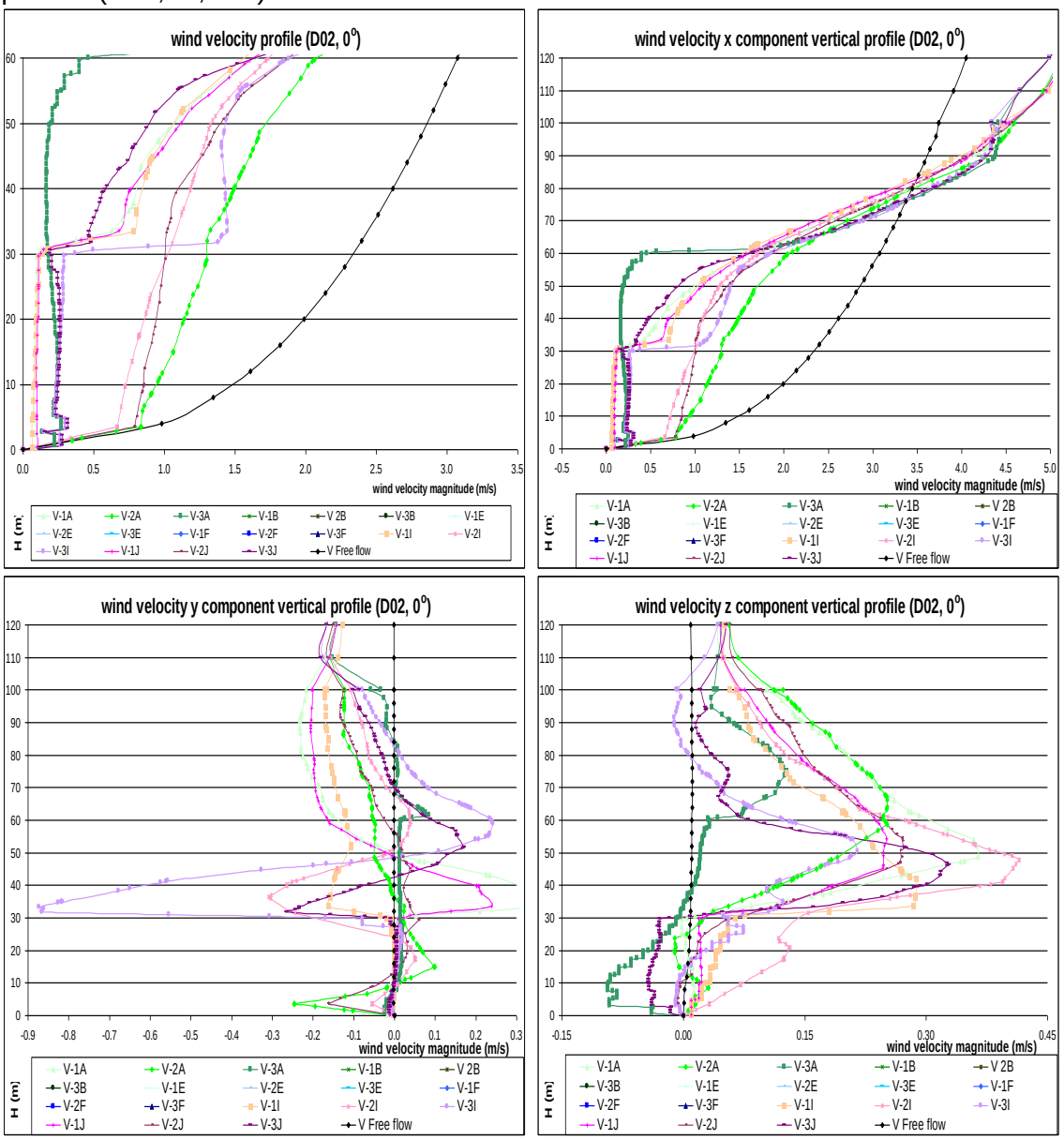

Source: this study.

7.3.6.2.2. Analysis of the D02 results (90^{o})

Four different scenarios were analyzed for winds orthogonal to the D2 prototype: both the left and the right sides of canyons ‘A’ and ‘B’ (positioned upwind and downwind). In this way, faces with 30, 60, and 90m were assessed on both the windward and the leeward sides.

Figure 7-77: D02 output lines and accessed areas for wind incidence at 90^{o}.

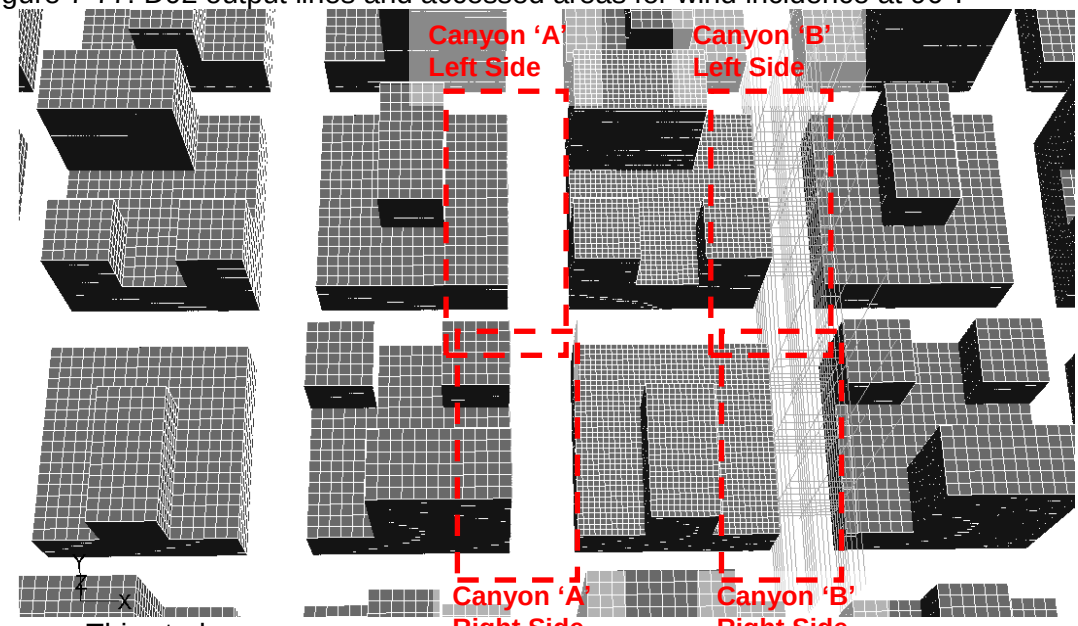

Source: This study.

The block height difference starts to influence the Cp results between the windward and the leeward faces near the ground. For instance, on the left side the 90m height block produces a downward airflow and consequent increase of pressure at a low height, with total averaged Cp results on both the windward and the leeward sides of 0.17. On the other hand, the Cp results for the canyon ‘B’ windward and leeward faces were 0.12 and 0.08. This shows both a reduction and a variation of pressure between them, since canyon ‘B’ is placed in canyon ‘A’ leeward wake. Similar variation was observed between the ‘A’ and the ‘B’ canyons’ right side blocks. Total averaged Cp results on the windward and leeward faces at middle and top heights were, respectively: 0.47 and 0.38; and 0.86 and 0.63, regardless of the block side (right or left) or the canyon’s position (‘A’ or ‘B’). These findings are in agreement with the fact that, for detached blocks, the Cp difference between upwind and downwind faces increases with height and the distance between other obstructions.

Furthermore, it is worthy to mention that both the grid and the mesh refinement in this CFD model were finer in some canyons ‘A’ and ‘B’ faces and coarser in the others. This difference came from the necessity of comparing several scenarios and checking

the Cp results among themselves. On the other hand, the absence of inconsistency or significant difference on the results between diverse mesh refinement levels also served as an indicative that, at this point, further mesh improvement and adaption would not bring more accuracy to the analysis.

Figure 7-78: Airflow velocity pathlines from a horizontal rake at 30m H and views across the canyon (D2, m/s, 90^{o}).

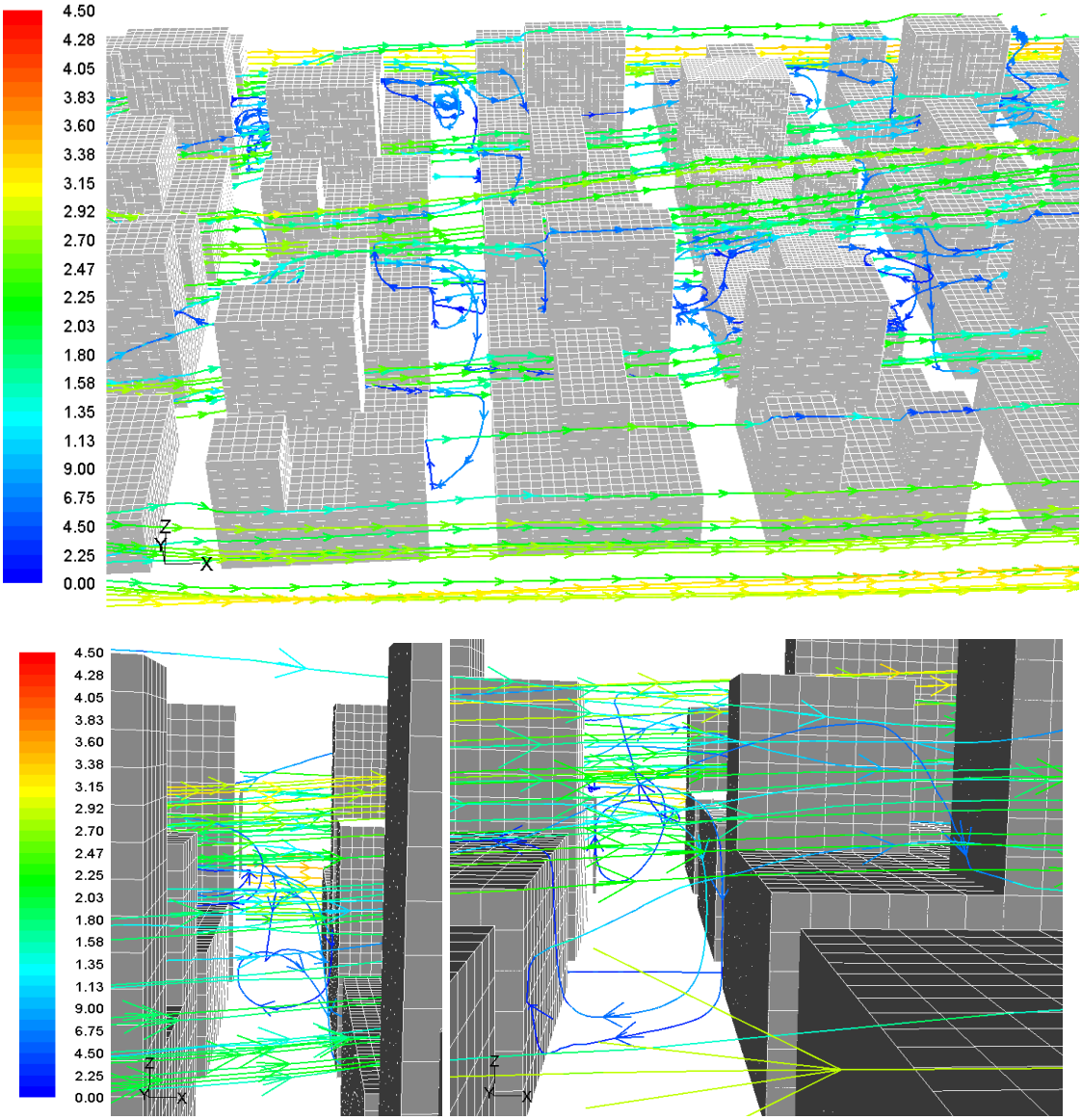

Source: This study.

The wind vertical profile analysis on the D2 scenario compared results from both canyon ‘B’ right and left sides. Up to 30m height it is possible to say that the wind pattern is similar on both sides: deceleration and low speed near walls (from 0.10 to 0.20m/s) with a slightly higher speed on the windward side. In the centre of the canyon wind velocity is equal to the ABL input up to 4m height. Above this, wind speed reduces and remains constant around 0.50m/s up to 30m height. At around 80m height most of

the wind profiles show great acceleration, exceeding the ABL velocity. The vertical profiles positioned behind 90m height blocks show low speeds as far as around 70m, accelerating after this and exceeding the ABL velocity at 110m height.

Figure 7-79: Left side wind velocity magnitude and x, y and z wind vector components vertical profiles (D02, 90°, m/s):

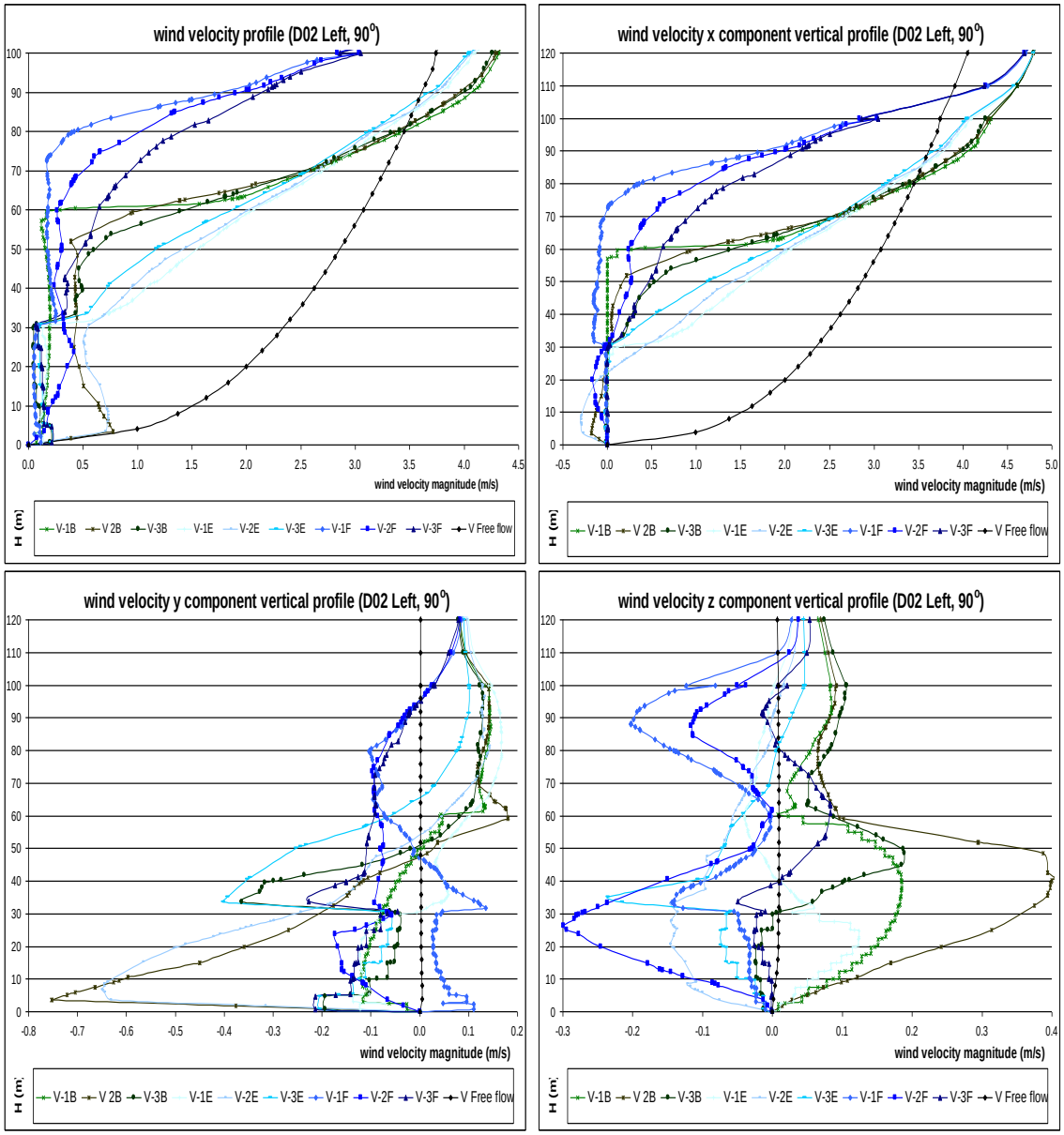

Source: this study.

The isolated x, y, and z vector flow components show similar patterns in both the right and the left canyons. Near the walls the x vector is negligible, while in the centre of the canyon reverse flow occurs on the right and the left sides near the ground with -0.50 and -0.25m/s, and still air is also observed at 20m height. Over 30m flow acceleration takes place along the mainstream. The y velocity vector also presents similar behaviour in both canyons: with a left to right side flow orientation reaching 0.60m/s, in the central areas near the ground. The exception is the wind profile on the

left side near the leeward wall, which shows a reverse flow with 0.1m/s from ground to 30m height. Also, over 30m height the vertical profiles on the right and the left sides present distinct orientations: while in the first the previously described left-right pattern continues, in the second most of the flow changes to the right-left direction across the canyon at 50m height, with the exception of the profiles behind the 60m height blocks. The z vertical component also shows downward flow near the windward side, and upward flow near the leeward side, both with velocities ranging from -0.15 to +0.15m/s. In the centre of the canyon, downward and upward flows takes place within a great range of speeds (+0.40 to -0.30m/s), defining a left to right side oriented vortex across the canyon.

Figure 7-80: Right side wind velocity magnitude and x, y and z wind vector components vertical profiles (D02, 90°, m/s):

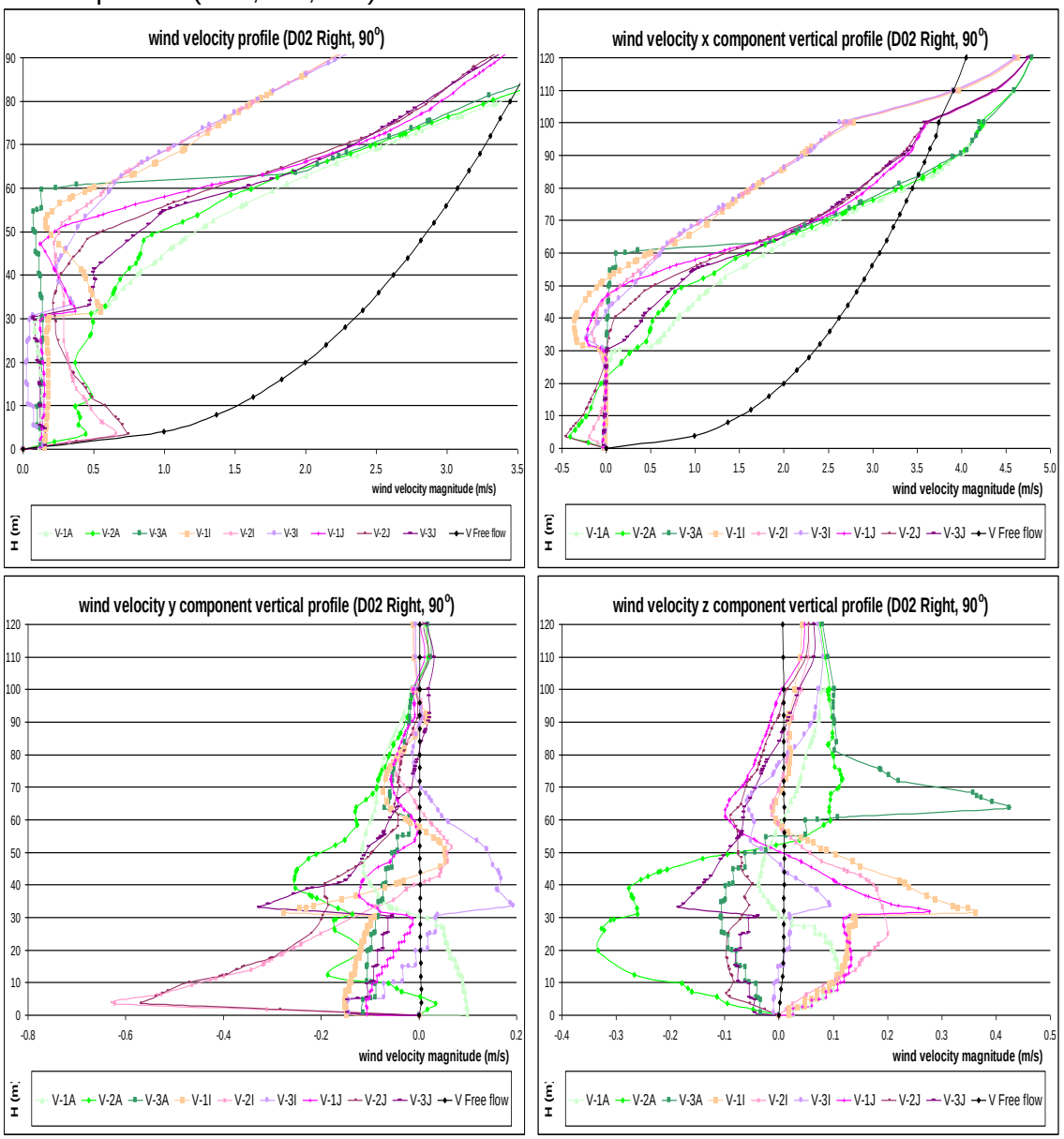

Source: this study.

7.3.6.2.3. Analysis of the D2 results (45^{o})

When airflow meets the 45^{o} windward faces, it is diverted either upwards or downwards on a diagonal through all the blocks. Since the 90m height blocks are located on canyon 'A' downwind side, a trailing wake on the leeward side decreases the wind pressure throughout canyon 'B', while high pressure is found on both sides of canyon 'A'. To illustrate this, the total averaged Cp result at low height on both canyons 'A' windward and leeward faces is 0.12, while on the respective canyon 'B' faces the results are -0.01 and -0.02. Comparatively, Cp results in the symmetrical and square B2 scenario were 0.08 and -0.11. On the other hand, increasing Cp difference between windward and leeward faces was found at middle (0.44 and 0.16); and top heights (0.69 and 0.42).

Figure 7-81: Airflow velocity pathlines from a horizontal rake at 30m H and across the canyon (D2, m/s, 45^{o}).

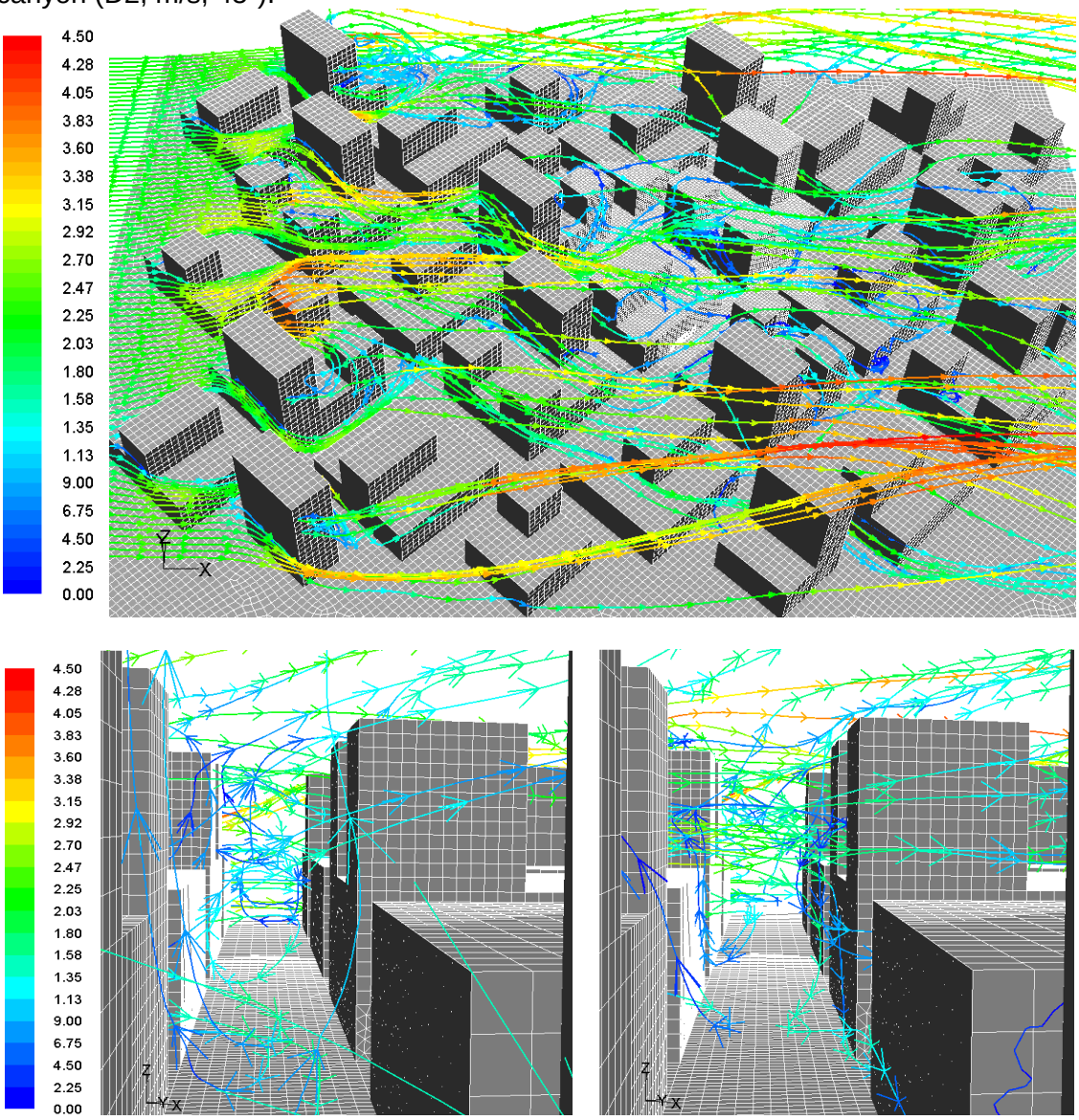

Source: This study.

The wind velocity magnitude vertical profiles in canyon 'A' show that on the central axis acceleration takes place near the ground from the left to the middle of the canyon. The wind speed in this area reaches 1.76m/s, or 2.2x the ABL input velocity (0.80m/s). Conversely, from 10 to 20m height wind velocity abruptly decreases and follows the same pattern as the wind near the walls, with velocities ranging from 0.15 to 0.60m/s up to 60m height. Above this height great acceleration is observed in most of the vertical profiles.

Figure 7-82: Wind velocity magnitude and x, y and z wind vector components vertical profiles (D02, 45°, m/s):

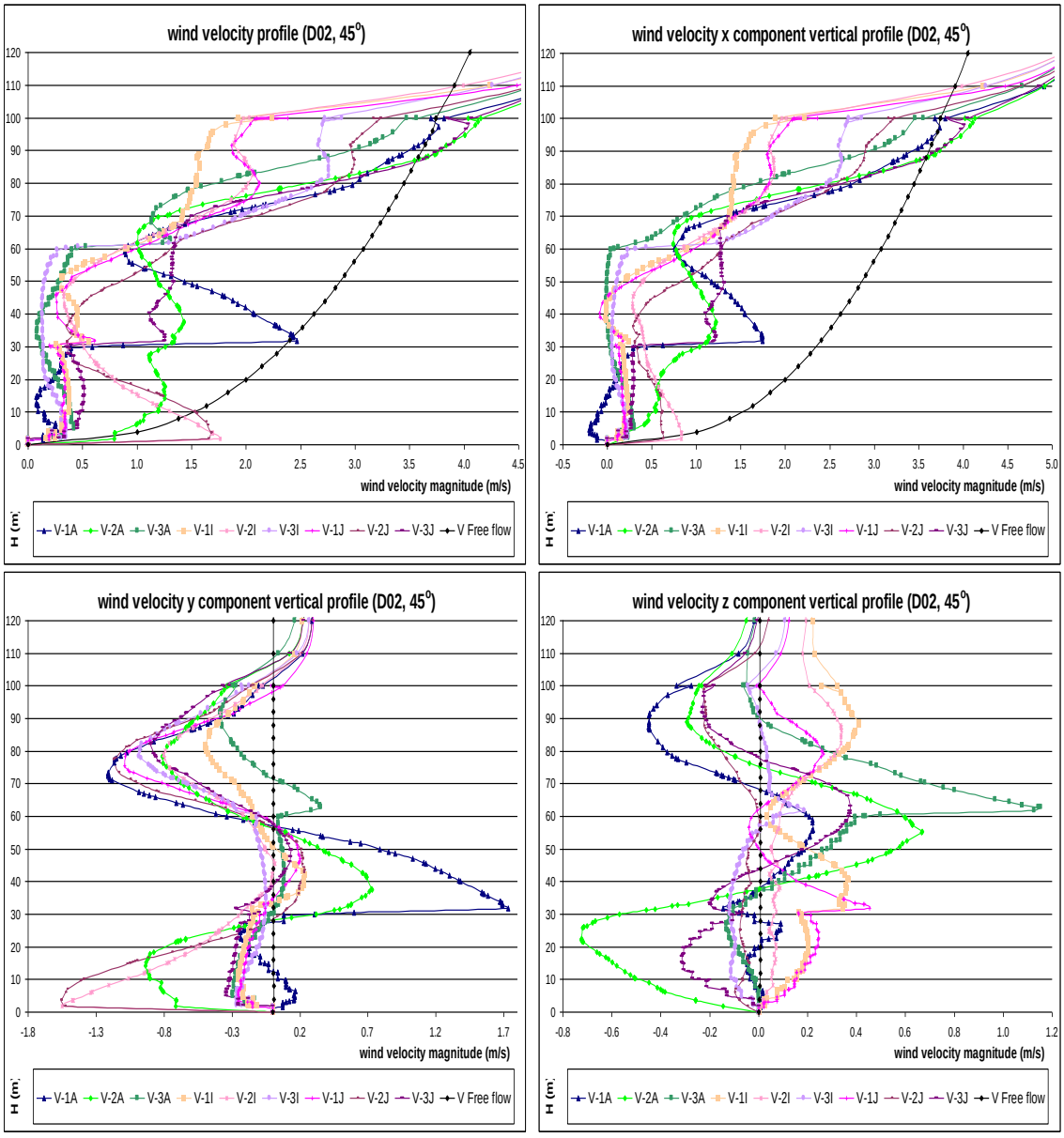

Source: this study.

The wind x vector component follows the same velocity magnitude profile patterns, but with reduced intensity. The y component shows a left-to-right orientation up to 30m height, turning almost completely in the opposite direction from 30 to 60m height, and shifting back above 60m. Wind speed ranges from -1.50 to +1.70m/s in the centre, although near the walls the range is smaller (-0.30 to +0.25m/s). The z vector component indicates a downward flow near the windward faces and in the centre, and an upward flow near the leeward wall up to 30m height. Averaged wind velocities range from -0.40 to +0.25m/s. From 30 to 60m height most of the flow is upwards but above that there is an intense up and down shift of direction

7.3.6.3. Prototype D03

Figure 7-83: Output lines and accessed areas used in the prototype D03 (90^{o}).

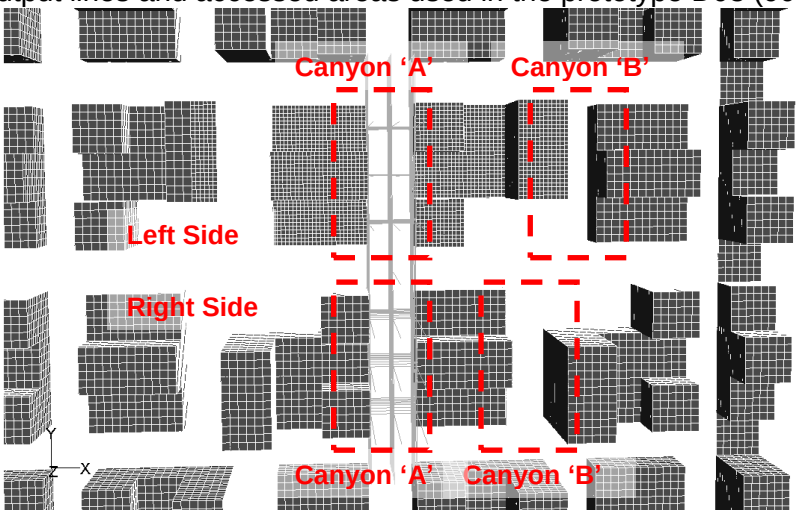

Source: This study.

7.3.6.3.1. Analysis of the D3 results (0^{o})

The D3 Prototype is similar in shape to the previously assessed D2 scenario, but with a reduction in the blocks' volumes, which impacted both the plan-area density and the canyon linearity creating constrained long canyons and square-plan open spaces. Further, D2 and D3 scenarios pressure results were contrasted among themselves.

Canyon 'A' is continuous and 'B' is constrained by other blocks. Also, canyon 'B' has a 90m height block on its right side. On the other hand, similar pressure results were found between right and left sides at low and medium heights. The total averaged Cp result at low height was 0.12 on all block faces, which is greater than in D2 (0.09) and equal to that in D1 (0.12) scenarios. At medium height Cp results ranged from 0.38 to 0.40, which are also greater than those of the D2 prototype (0.36). The pressure result in D3 top height (0.65) was also greater than that in the D2 prototype (0.57).

Figure 7-84: Airflow velocity pathlines from a horizontal rake at 30m H (D3, m/s, 0°).

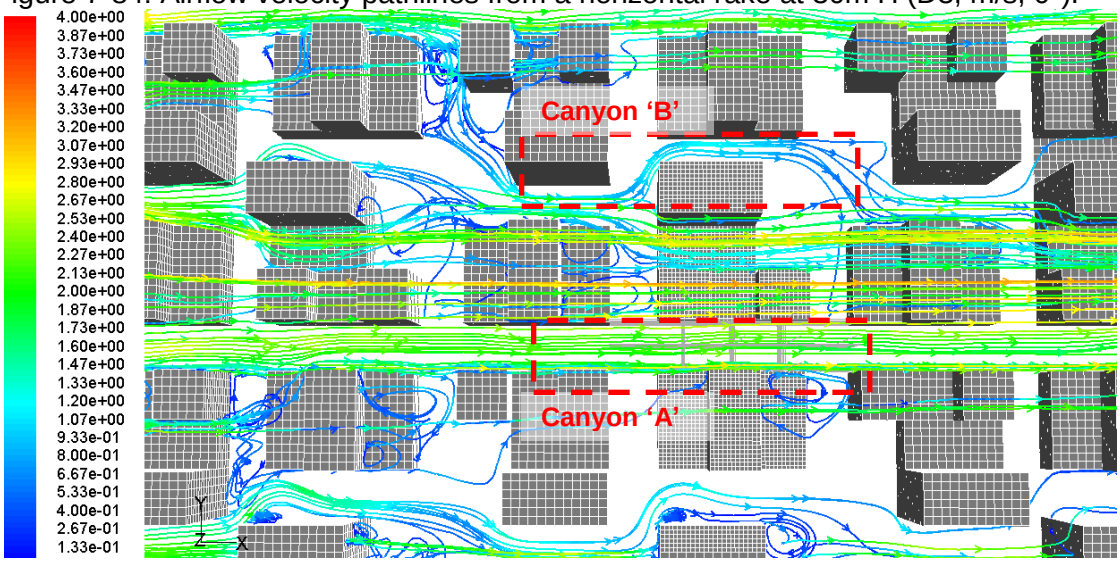

Source: This study.

Figure 7-85: Views of airflow pathlines across the canyons (D3, m/s, 0°).

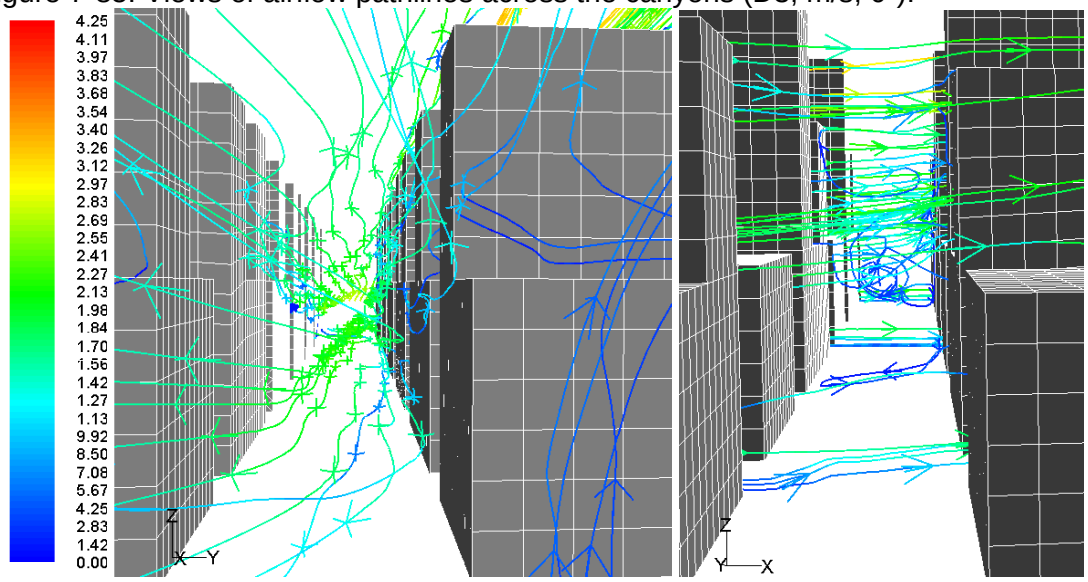

Source: This study.

The wind velocity magnitude vertical profiles in the D3 scenario's canyon 'A' show acceleration in the centre of the canyon near the ground as compared to both the ABL input and that of the previous D1 and D2 scenarios. The almost constant velocity in this area, around 2.25m/s up to 60m height, implies an acceleration factor of up to 2.5x at pedestrian level and 1.5x at 10m height. Near walls airflow speed is unevenly reduced, ranging from 0.10 to 0.40m/s on the right and from 0.40 to 0.65m/s on the left side up to 30m height. Above it acceleration is observed.

The wind x vector component along the flow shows the same patterns as the velocity magnitude profiles, with reduced intensity and no reverse flow. The y component shows a left to right oriented shift across the canyon up to 30m height and, above, another shift and flow acceleration take place. The z vertical velocity vector shows a descending flow near the left faces and ascending flow in the centre of the canyon and near the right faces.

Figure 7-86: Wind velocity magnitude and x, y and z wind vector components vertical profiles (D03, 0°, m/s):

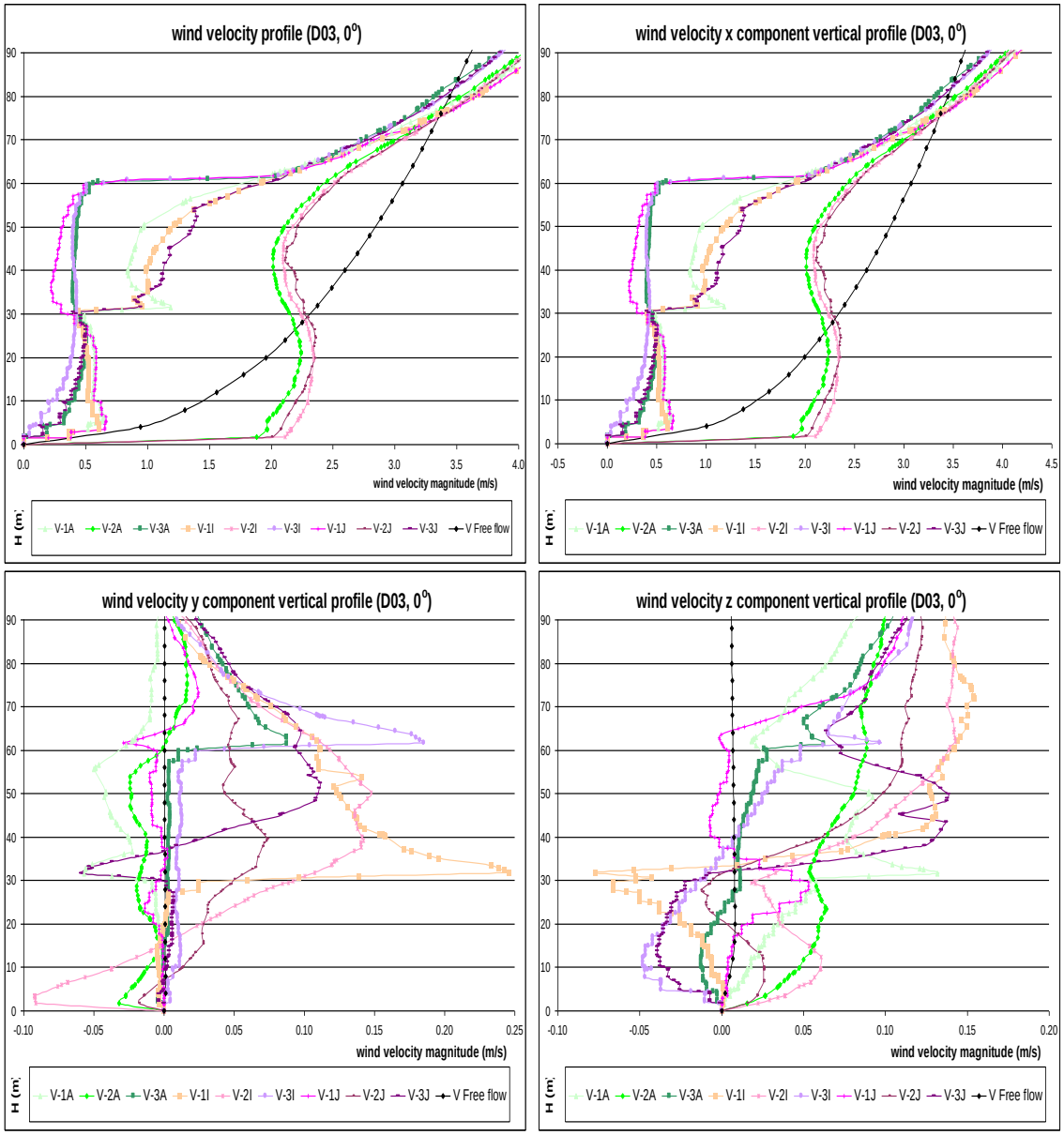

Source: this study.

7.3.6.3.2. Analysis of the D3 results (90°)

Four different scenarios were assessed for winds orthogonal to the D4 prototype: both the left and the right sides of the canyons ‘A’ and ‘B’, positioned in the upwind and the downwind direction. Beyond making the assessment of faces at different heights possible, this scenario aimed at creating empty spaces among blocks, thus reducing the A_{roof}/A_{plot} aspect ratios. This sequence of empty spaces and blocks of different heights seems to create pressure differentials in the canyon in front of 90m blocks, since an FS point is formed on its windward side. Further, the pressure distribution on the downwind side would be reduced by a leeward wake.

Figure 7-87: D03 output lines and accessed areas for wind incidence at 90°.

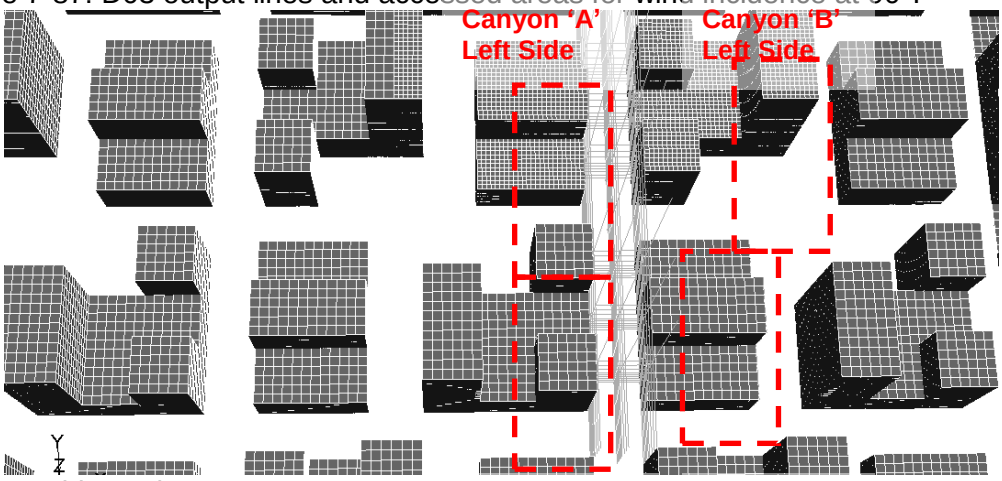

Source: This study.

Overall, pressure distribution on the windward sides agrees well with this statement. For instance, canyon ‘B’ right side showed the greatest total averaged Cp results (0.45), followed by both canyon ‘A’ right (0.29) and left (0.28) sides, while the lowest Cp result was found on canyon ‘B’ left side (0.16), which is positioned after a 90m leeward face. This ranking is also valid for the pressure vertical distribution. At low height the averaged Cp results for the aforementioned order were: 0.15, 0.13, 0.13, and 0.04; and at medium height were: 0.46, 0.45, 0.45, and 0.29. At top height canyon ‘A’ right side Cp result was 0.79. On the other hand, more homogeneous pressure distribution was found in the leeward vertical division on canyon ‘B’ right side and on both sides of canyon ‘A’, though comparatively reduced results were found on canyon ‘B’ left side. For instance, averaged Cp results for the above-mentioned order were: 0.10, 0.13, 0.12, and 0.04 at low height; and 0.34, 0.41, 0.38, and 0.30 at medium height. At top height the Cp result on canyon ‘B’ left side was 0.37. Finally, ΔCp between windward and leeward sides increased with both the height variation and the deliberate plan-area density decrease in this prototype.

Figure 7-88: Airflow velocity pathlines from a rake at 30m height (D3, m/s, 90°).

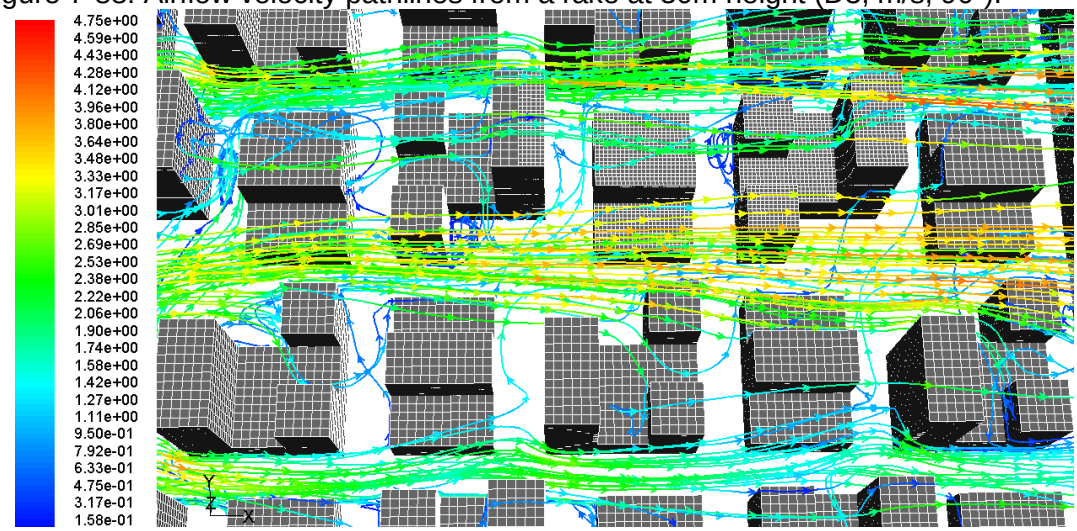

Source: This study.

Figure 7-89: Airflow velocity magnitude pathlines across the canyons (D3, m/s, 90°).

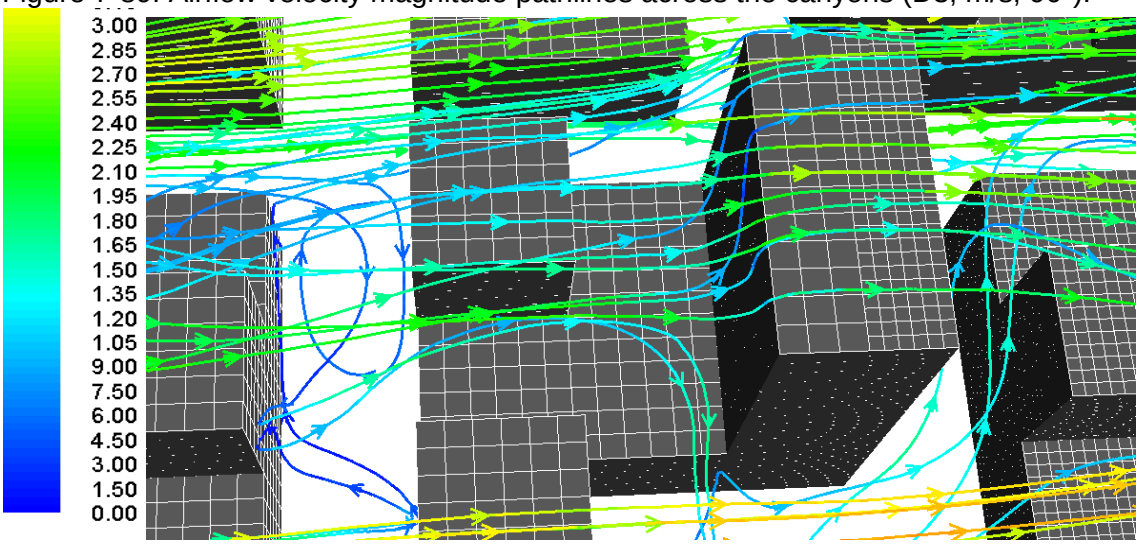

Source: This study.

The wind vertical profiles is presented for both canyons 'A' right and left sides. The results are very similar to those of the D2 prototype in many aspects. For instance, near walls deceleration and low speeds ranging from 0.10 to 0.20m/s are observed, while wind velocity in the centre of the canyon accompanies the ABL input up to 4m height. After this, it reduces and remains constant at around 0.80m/s up to 60m height. Above this most of the wind profiles accelerate and exceed the ABL profile from 70 to 120m height.

The isolated x, y, and z airflow vector components also repeat the D2 scenario findings. Near the walls the x vector is nearly zero, while in the centre of the canyon reverse flow of around -0.75m/s occurs up to 20m height. Both the y component across the stream and the z vertical component alternate positive (straight flow) and negative (reverse flow) velocities at 30, 60 and 90m heights. The profiles in the centre of the canyon present a greater range of speed: from -0.60 to +0.80m/s for the y component and from -0.50 to +0.40m/s for the z component. Once more the combined analysis of the airflow vector components leads to the conclusion that internal vortices with several loops are constrained within the canyon's cavity and/or cross its space in a diagonal flow and then escape from the sides or above the blocks.

Figure 7-90: Wind velocity magnitude and x, y and z wind vector components vertical profiles (D03, 90°, m/s):

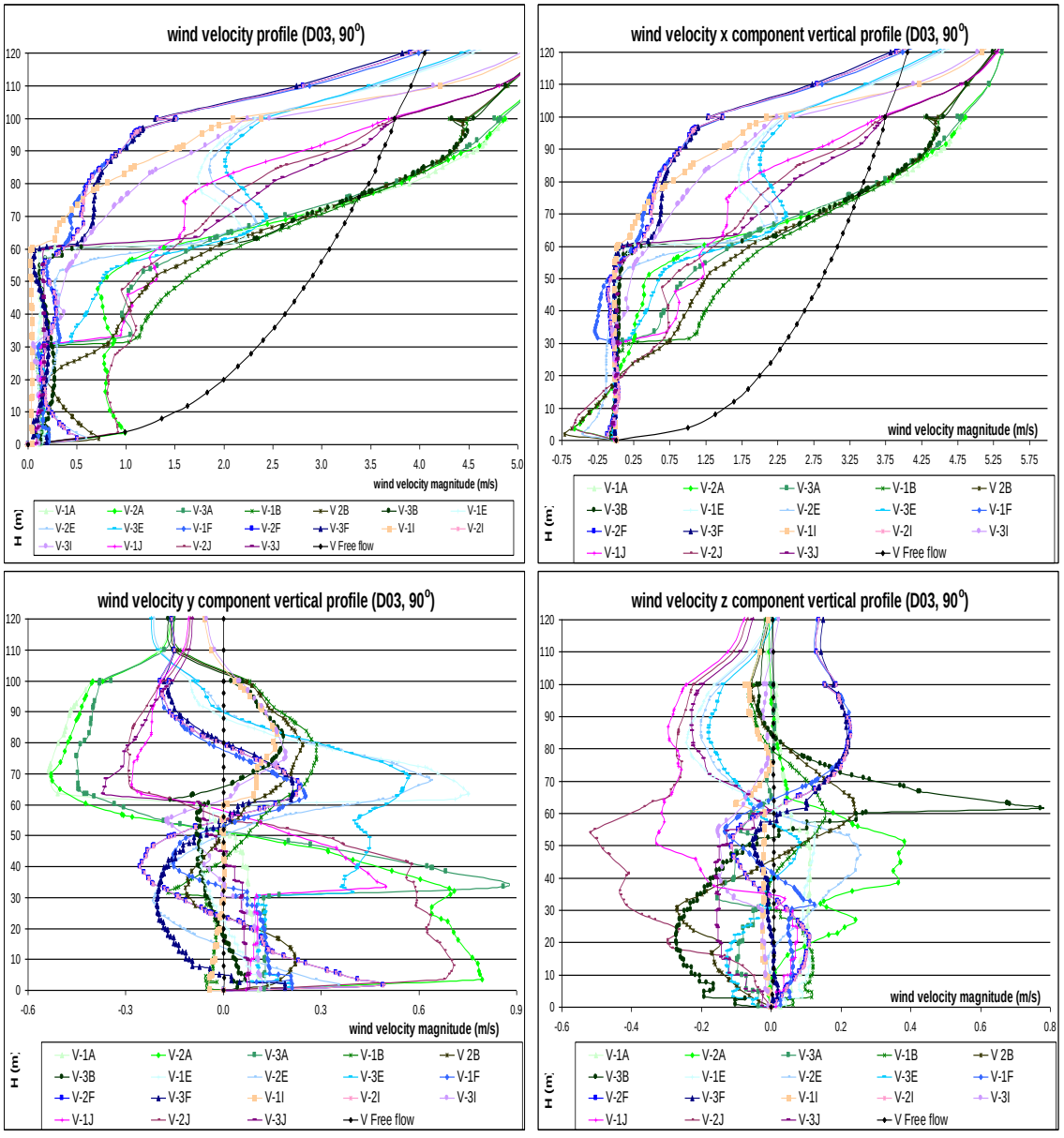

Source: this study.

7.3.6.3.3. Analysis of the D3 results (45°)

The findings for the D3 prototype also repeat much of the D2 scenario analysis: greater pressure results were observed in the canyon 'A' positioned upwind, while canyon 'B', which was downwind and shaded by a 90m height block in its leeward wake, presented lower pressure. The total averaged Cp results on canyon 'A' windward and leeward sides at low height were 0.17 and 0.15. The same sides in canyon 'B' presented lower Cp results: 0.07 and 0.01. The canyon's position continues to influence the results above the low height. For example, in canyon 'A' the windward and the leeward Cp results at medium height were 0.46 and 0.42, while in canyon 'B' they were 0.31 and 0.26. At top height the Cp results were 0.77 and 0.37.

Figure 7-91: Airflow velocity pathlines from a horizontal rake at 30m H (D3, m/s, 45°).

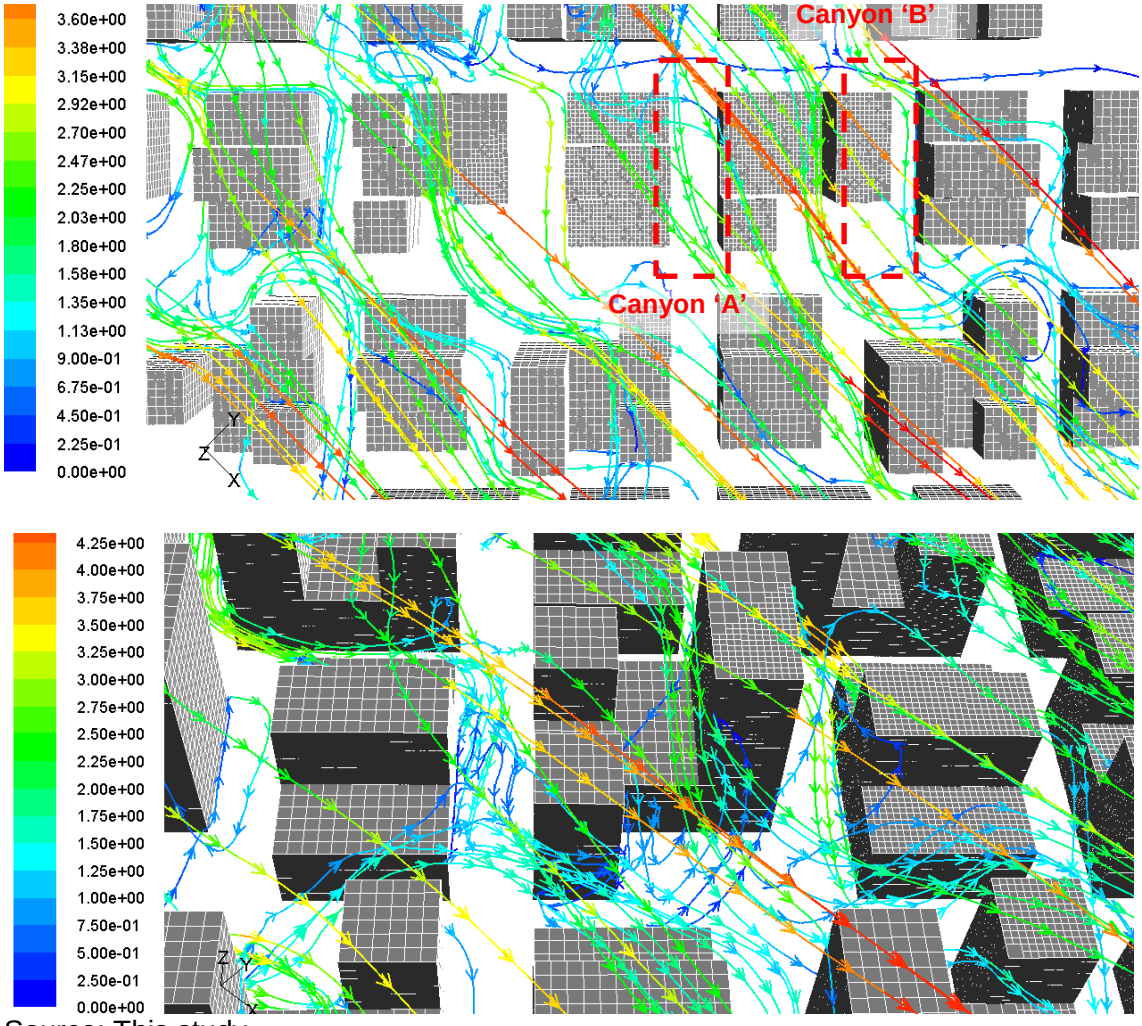

Source: This study.

The wind velocity magnitude vertical profiles in canyon 'A' show acceleration near the ground in the centre of the canyon, with velocity attaining up to 1.80m/s, or 2.25x the airflow speed at the ABL input (0.80m/s). This speed is gradually reduced from 10 to 20m height. Above it a maximum velocity of 0.60m/s is observed up to 60m height,

which is the same near both the windward and the leeward walls. Over 60m height strong acceleration is observed in all the vertical profiles. The x vector component of the wind follows the same velocity magnitude patterns, but no acceleration is observed in the centre of the canyon. The y component follows the left-right orientation up to 90m height, but with different intensity with height. High speed is observed in the centre of the canyon (-1.50m/s) while average speeds of -1.15 to -0.45m/s are observed from 60 to 90m height in most of the vertical profiles. Exceptions of reverse flow (right-to-left oriented) are observed near the upwind leeward corner, with +2.00m/s at 30m height. The z vector component indicates an upward flow of +0.35m/s from the upwind leeward edge to the middle of this face. Apart from that most of the flow is directed downwards from ground to 30m height, with average velocities of -0.35 and a peak of -1.05m/s in the centre of the canyon. Above this height most of the flow is upwards up to 70m height and then an intense up and down shift of direction occurs.

Figure 7-92: Wind velocity magnitude and x, y and z wind vector components vertical profiles (D03, 45°, m/s):

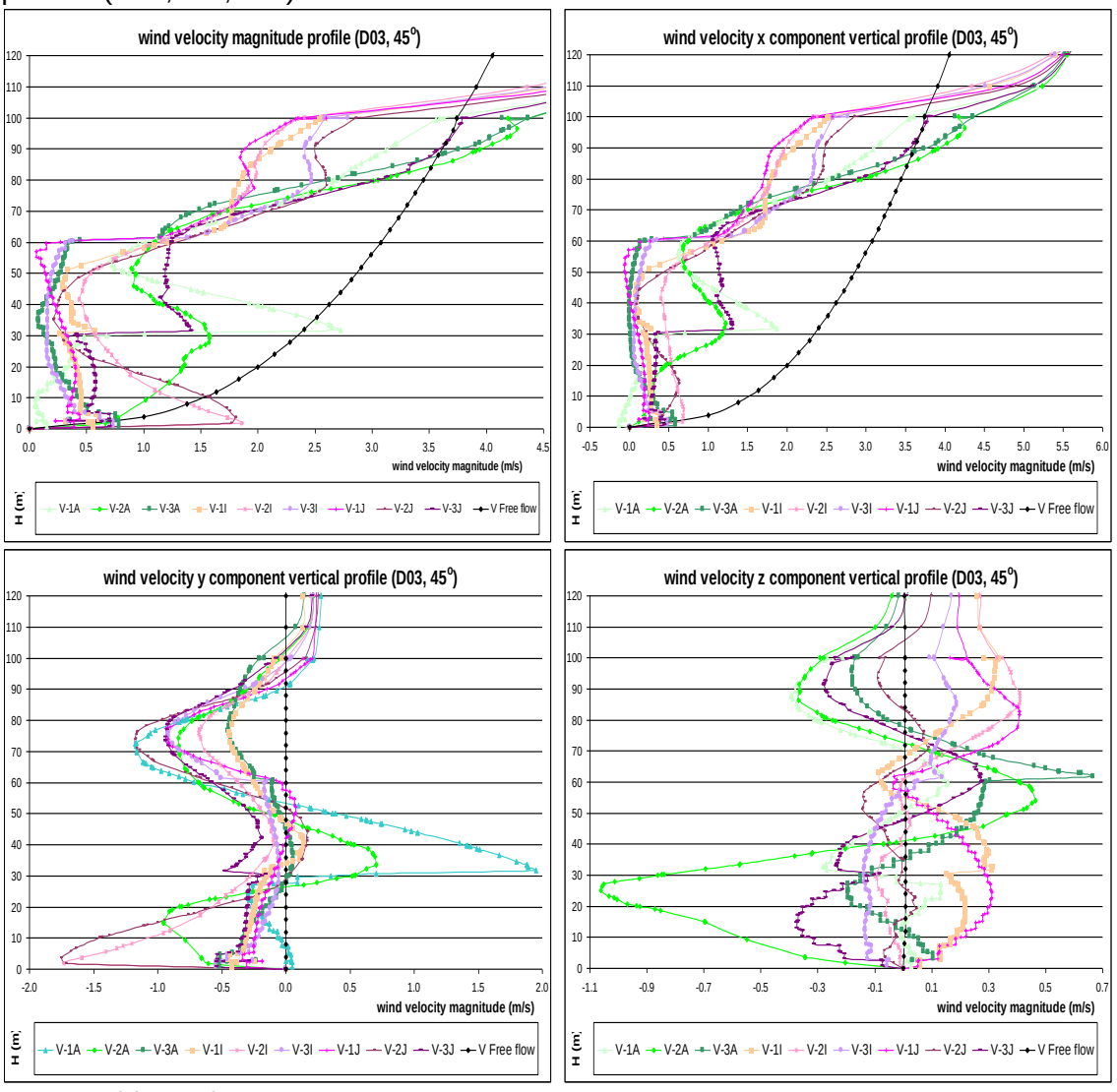

Source: this study.

7.3.6.4. Prototype D04

Figure 7-93: Output lines used in the prototype D04 for wind incidence at 90°.

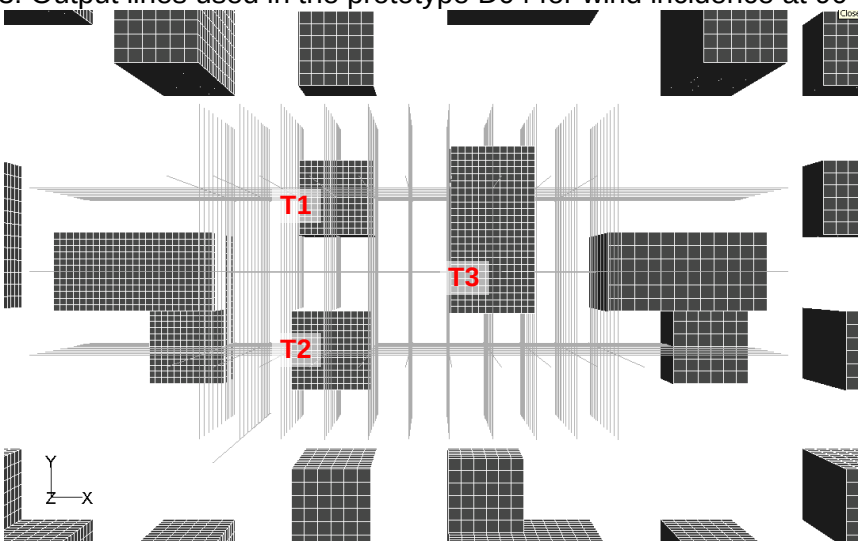

Source: This study.

7.3.6.4.1. Analysis of the D4 results (0°)

The resultant airflow field for parallel winds in the D4 scenario shows channelling flow and acceleration occurring inside the long canyons alongside the main stream and also a decelerated and turbulent flow around the short canyons and square open spaces. This change in the air speed is caused by the 'L' shaped 60m height blocks, which are orthogonal to both the mainstream and the rectangular 90m height blocks positioned alongside the flow. In front of these two high blocks the flow divides in several directions: upwards, downwards, to the left or right side, and reverse vortices are observed either trapped between two blocks or in the leeward trailing wakes.

Figure 7-94: Airflow velocity pathlines from a horizontal rake at 30m H (D4, m/s, 0°).

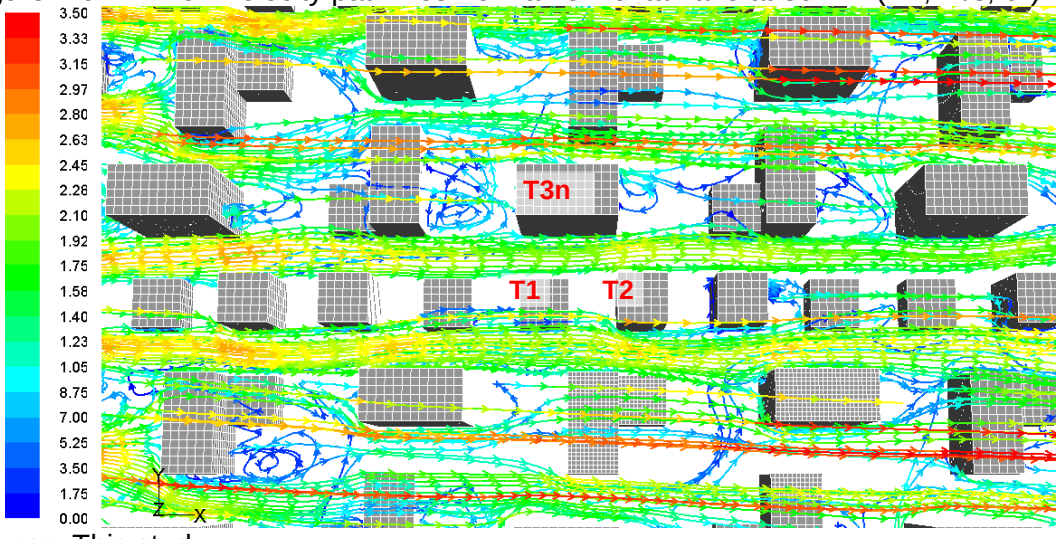

Source: This study.

Close similarity was found between the left and right sides of the T1, T2, and T3w[102] towers. The total averaged Cp results were: 0.14, 0.21, and 0.36. For the T3n[103] tower some difference between the sides was observed: 0.28 and 0.23. At low height, the Cp average results for the right and left sides of the T1, T2, and T3w towers ranged from 0.11 to 0.14, while the results for T3n were: 0.06 and 0.01. For purpose of comparison, the result on both sides of B4 scenario, an array of cubic blocks, was 0.05. At medium height the averaged results for the T2, T3w and T3n right and left sides were: 0.32 and 0.36; 0.40 and 0.38; and 0.23 and 0.29. At top height the averaged results for the T3w and T3n right and left sides were: 0.58 and 0.65; and 0.50 and 0.54.

Figure 7-95: Airflow velocity pathlines alongside the main stream (D4, m/s, 0°).

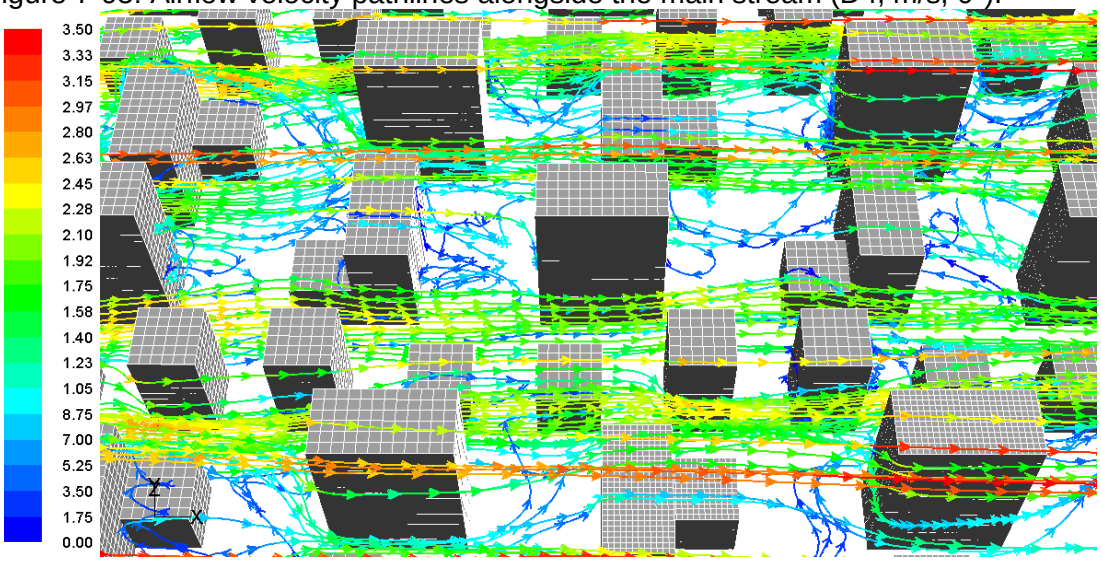

Source: This study.

Figure 7-96: Airflow velocity pathlines alongside the main stream (D04, m/s, 0°).

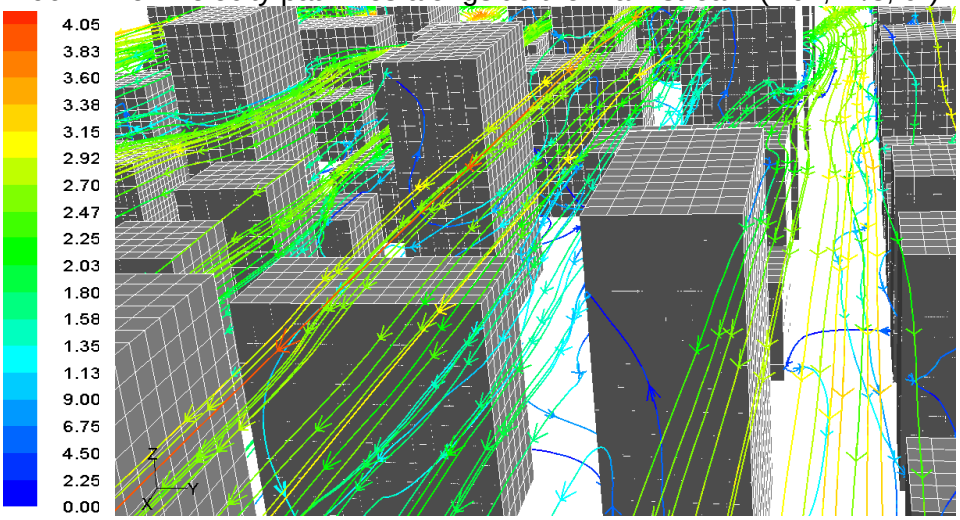

Source: This study.

[102] The T3w is the 90m height block with the wider side of it rectangular base alongside the stream.
[103] The T3n is the 90m height block with the narrower side of it rectangular base alongside the stream.

The wind velocity magnitude vertical profiles show acceleration up to 2x near ground level and on both the right and left sides of T3 block. Also, two other vertical profile patterns were: near the block walls wind speed reduces by between 0.15 and 0.35m/s throughout the block height and then abruptly accelerates. Further, most of the vertical profiles away from the blocks present nearly steady wind velocity ranging from 0.50 to 2.00m/s. Finally, the bulk of the flow accelerates above 60m height while the rest accelerates above 90m. Both bulks converge at 5.00m/s and 120m height, where the ABL input is 4.00m/s.

Figure 7-97: Wind velocity magnitude and x, y and z wind vector components vertical profiles (D04, 0°, m/s):

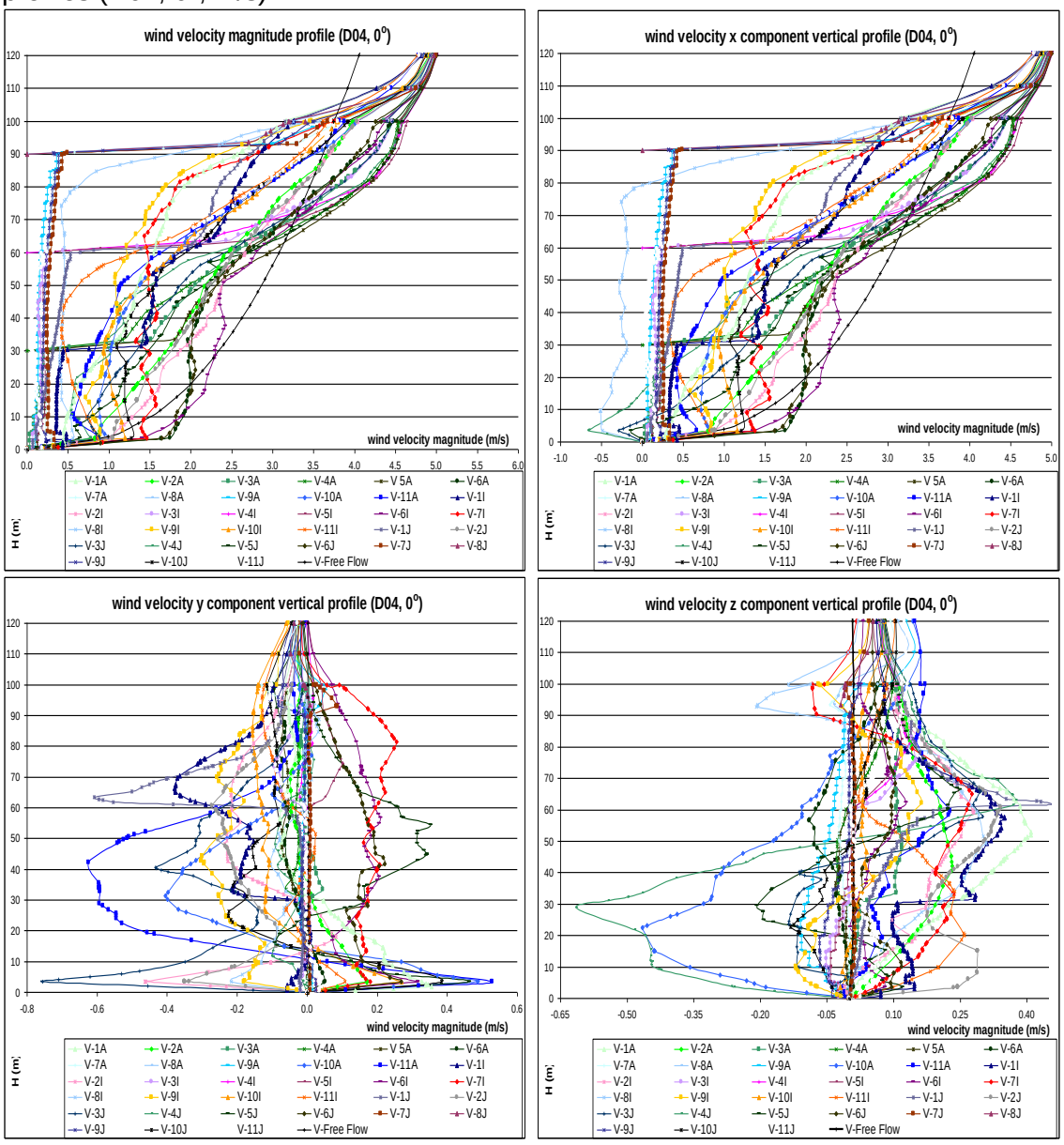

Source: this study.

The x velocity vector component along the flow follows the same patterns and intensity as the velocity magnitude profiles, although reverse flow is observed in two areas: at ground level between T1 and T2 blocks, which constitute a step-up canyon with an internal clock-wise vortex in its cavity; and on a vertical line 15m away from the leeward side of T3 block, from ground to 80m height, reaching -0.50m/s. The y vector shows that the flow near the blocks shifts slightly across the mainstream, with velocities ranging up to -0.60m/s on the right and +0.50m/s on the left side. The z vertical velocity vector shows the existence of clock-wise vortices between T1 and T2 blocks, with a downwind near the T2 windward side and an upwind near the T1 leeward side. A right to left oriented downwind below 60m height also occurs on the T3w upwind side. Attaining -0.65m/s, this represents the FS point downward flow at 2/3rds of this windward face's height. A few profiles present a continuous downwind of up to -0.15m/s while most of them show an upwind flow of up to +0.35m/s. Finally, all the profiles indicate a slight ascending flow of around 0.10m/s above 110m height.

7.3.6.4.2. Analysis of the D4 results (90^{o})

The D4 scenario pressure results from orthogonal winds cover four blocks: T1, T2, T3w and T3n. The ΔCp between the windward and leeward sides were the greatest in the prototype investigation step. This agrees with the fact that ΔCp across a building is related to its height, the surrounding plan-area density and the wind direction.

Figure 7-98: D4 accessed towers for wind incidence at 90^{o}.

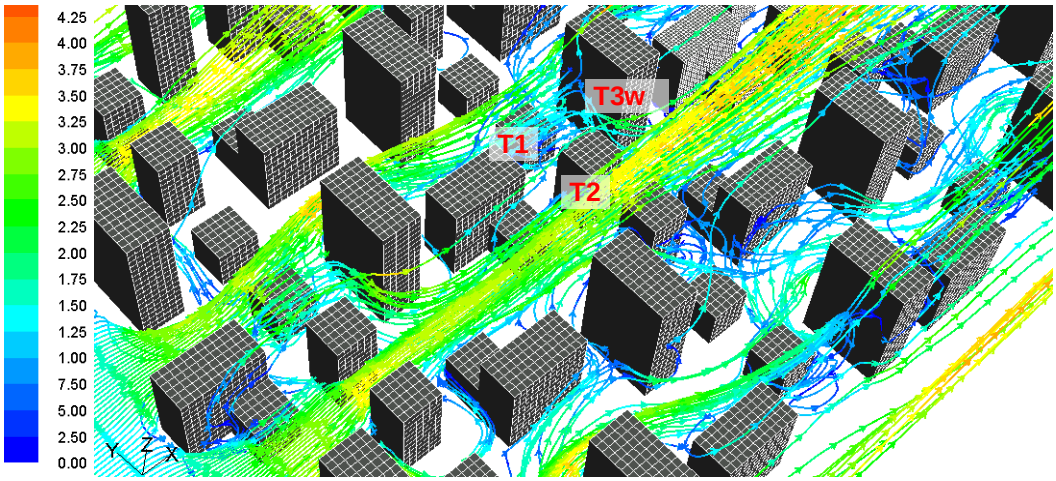

Source: This study.

The D4 scenario airflow field shows a channelling effect, with acceleration inside the canyons along the mainstream and great turbulence on the T3 leeward side. Also, an FS point is observed at around 2/3rds of the T3's height. From this point the flow goes either upwards detaching and accelerating on the horizontal edge while a low

pressure bubble is created on the top surface; or downwards creating a reverse flow trapped in between the upwind blocks until it escapes sideways, where a horse-shoe flow effect is also observed.

Figure 7-99: FS point and detachment on T3 top and side (D04, m/s, 90^{o}).

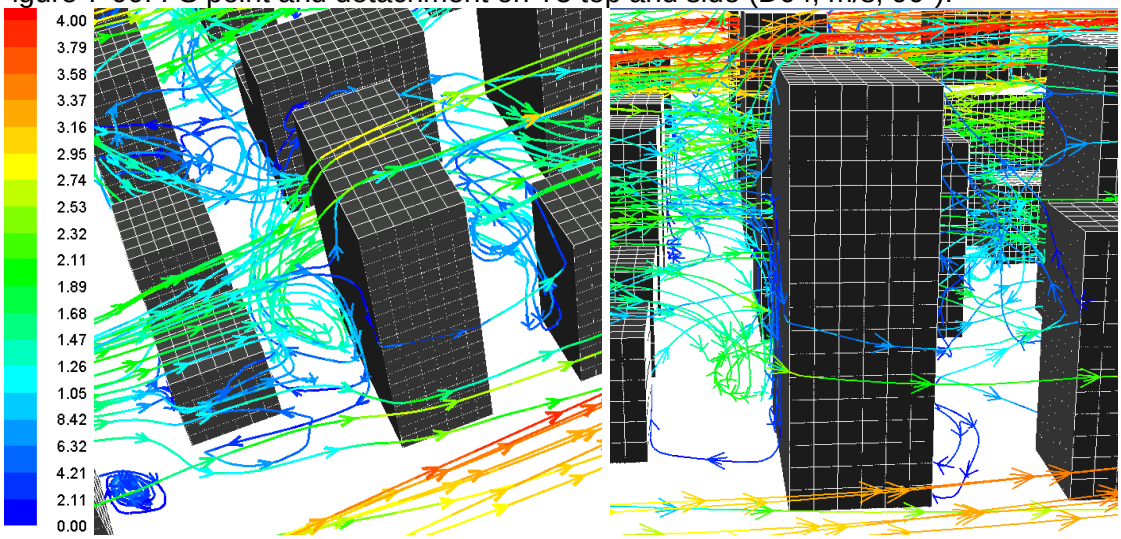

Source: This study.

The total averaged Cp results on the windward and the leeward sides for the D4 scenario T1 block were 0.17 and 0.14. The ΔCp (0.03), is smaller than the former A4 (ΔCp= 0.18) and B4 (ΔCp= 0.07) scenarios, and greater than the C4 (ΔCp= 0.01) one, which consist of arrays of cubes with 0.5, 1.0, and 2.0 H/W aspect ratios. The T1 leeward side is washed-down by a reverse down flow from a downwind 90m block, which may contribute to the increase in pressure. For the T2 block the averaged Cp results found on the windward and the leeward sides at low and medium height were: 0.17 and 0.09; and 0.51 and 0.35. The total averaged Cp results were 0.33 and 0.21. The Cp result on the T2 windward side near the ground matches the result of the T1 block, since both faces are open on the upwind side. On the other hand, for this same height the results on the T2 leeward side are lower than those of T1, since the former is unobstructed on the downwind side and its trail wake can develop fully, creating a lower pressure zone on the rear face. Regarding the T3 90m height block, the windward side averaged Cp results and the total ΔCp are notably greater on the narrow T3n than on the wide T3w at top height. The averaged Cp results on the windward and leeward sides at low, medium and top heights and overall for the T3n were: 0.19 and 0.09; 0.49 and 0.34; 0.87 and 0.58; and 0.50 and 0.32. For the T3w the respective results were: 0.14 and 0.06; 0.46 and 0.30; 0.71 and 0.56; and 0.42 and 0.29.

The wind velocity magnitude vertical profiles analysis shows that near the block faces wind speeds are reduced and kept constant from 0.20 to 0.40 m/s, accelerating rapidly above the blocks. Conversely, acceleration of up to 2.25x is found near the ground and on both the T3 right and left sides, with the vertical profiles keeping constant velocity around 1.5m/s. Some of the vertical profiles (on the right side near the T2 centre) accelerate in a similar pattern, crossing the ABL profile at 3.25m/s and 70m height. Another group of vertical profiles (in the centre of the assessed area, crossing the T1) accelerates at 125m height and 4.05m/s. Finally, these distinct vertical profile bulks are joined at 150m height and 5.50m/s, while the ABL input velocity is 4.40m/s.

Figure 7-100: Wind velocity magnitude and x, y and z wind vector components vertical profiles (D04, 90°, m/s):

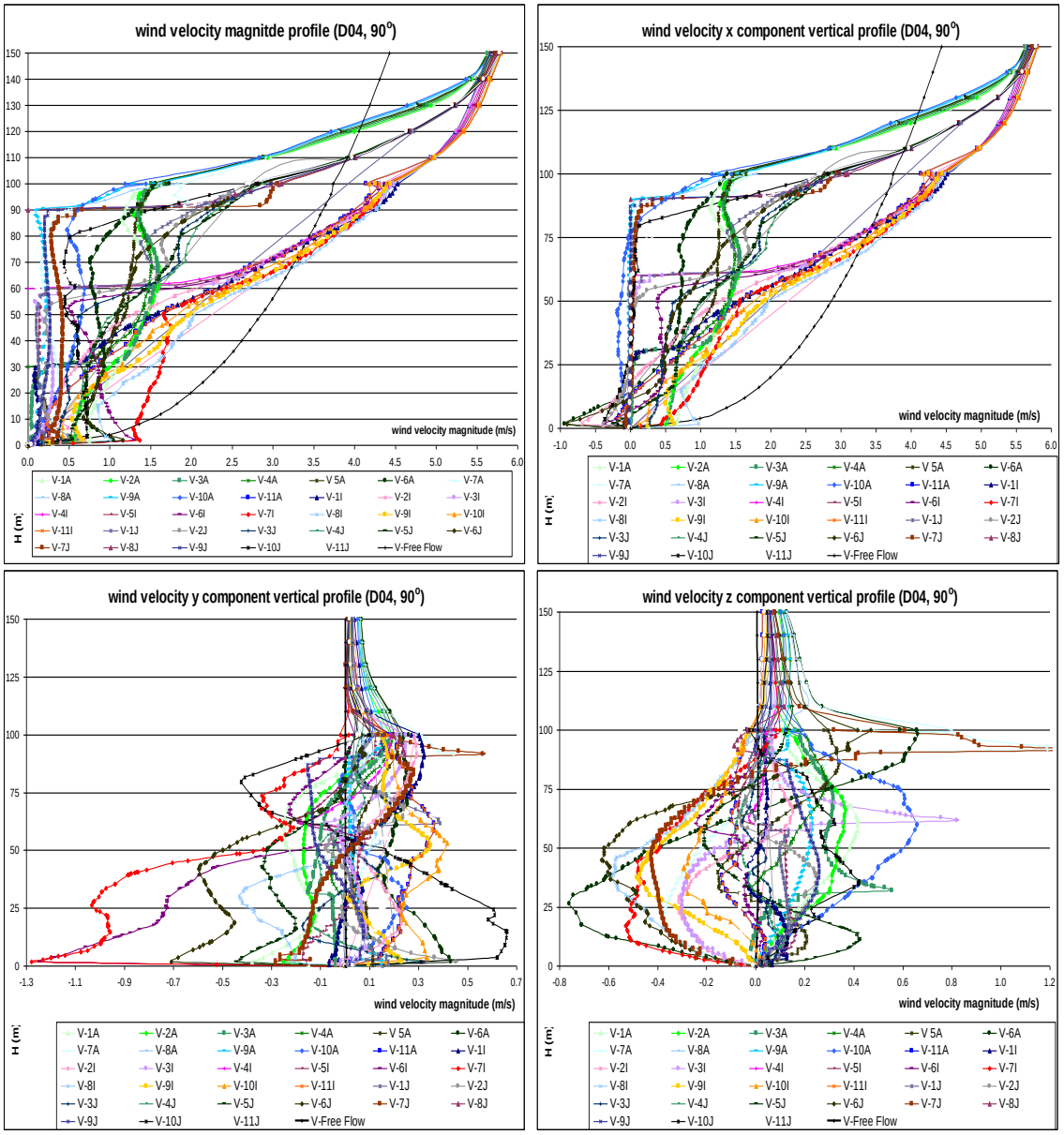

Source: this study.

While the x flow vector is similar in pattern and intensity to the velocity magnitude profile, its analysis shows that reverse flow occurs at ground level on both the windward and the leeward sides of block T3, ranging from -1.00 and -0.35m/s. Reverse flow is also observed on the T1 (0.30m/s) and T2 (0.60m/s) windward sides. The y vector shows a great range of speed near the ground towards the right (-1.30m/s) and the left sides (+0.50m/s). While the most intense flows to the right come from the middle front of the T3 block, those to the left come from the left front to the rear of this same block and also from the T1 and T2 blocks. Overall, the flow across the mainstream shifts direction at 30m and 80m height. The z vertical velocity vector shows down flow of up to -0.60m/s in front of the three assessed blocks. This indicates a clock-wise vortex in their upwind side, and also on T3's right side up to 70m height. There is also a great up and down shift of flow direction at 28, 56 and 82m heights, with up flow peaks over the T1 (+0.56m/s), T2 (+0.82m/s), and T3 (+1.25m/s) blocks.

7.3.6.4.3. Analysis of the D4 results (45^{o})

After reaching the frontal vertical edge of the D4 blocks the pathlines divided into two major directions. On the 90m block's windward side an FS point is clearly observed at around 2/3rds of its height, from where the flow either washes down the oblique faces on an ascending/ descending diagonal or rises and accelerates escaping over the blocks. This last effect seems to occur since in this D4 scenario the wind has no clear corridor to by which to escape, as happens with both the parallel and orthogonal flows. The wind below the canopy height acquires a sinuosity between the blocks which often creates reverse flows and vortices on the leeward side. Conversely, due to this pattern, the upwind bulk of flow and the turbulent and weaker leeward wake mix within a short distance, thereafter continuously repeating the process.

Figure 7-101: Airflow velocity pathlines from a horizontal rake at 30m H (D4, m/s, 45^{o}).

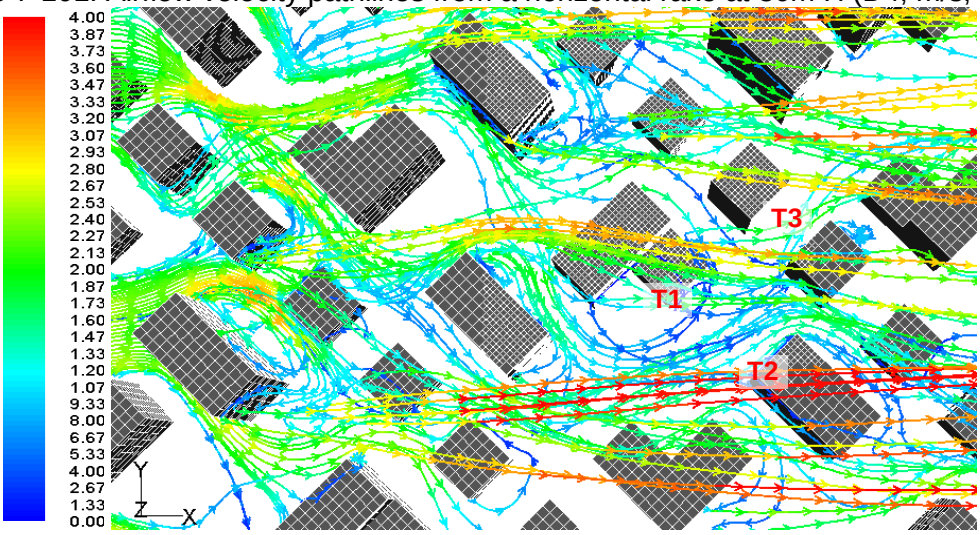

Source: This study.

The pressure distribution analysis covers four blocks: T1, T2, T3w and T3n. The total averaged Cp results on the T1 windward and leeward sides were 0.17 and 0.12. The ΔCp difference (0.05) is similar to that found in the A4 (0.04), B4 (0.04), and C4 (0.01) arrays of cubes. For the T2 60m height block the windward and leeward averaged Cp results were: 0.12 and 0.05 at low; and 0.44 and 0.32 at medium height. For the T3 90m height blocks the ΔCp was greater for the narrow T3n (0.32) than for the wide T3w (0.17), as an example of the orthogonal winds findings. The T3n block Cp results on the windward and the leeward sides positioned at low, medium and top heights were: 0.12 and 0.03; 0.49 and 0.30; and 0.90 and 0.58. For the T3w the results were: 0.14 and 0.05; 0.44 and 0.25; and 0.67 and 0.50.

Figure 7-102: Airflow velocity magnitude pathlines from a horizontal rake at 30m H seem from the windward (above) and the leeward side (below) (D4, m/s, 45o).

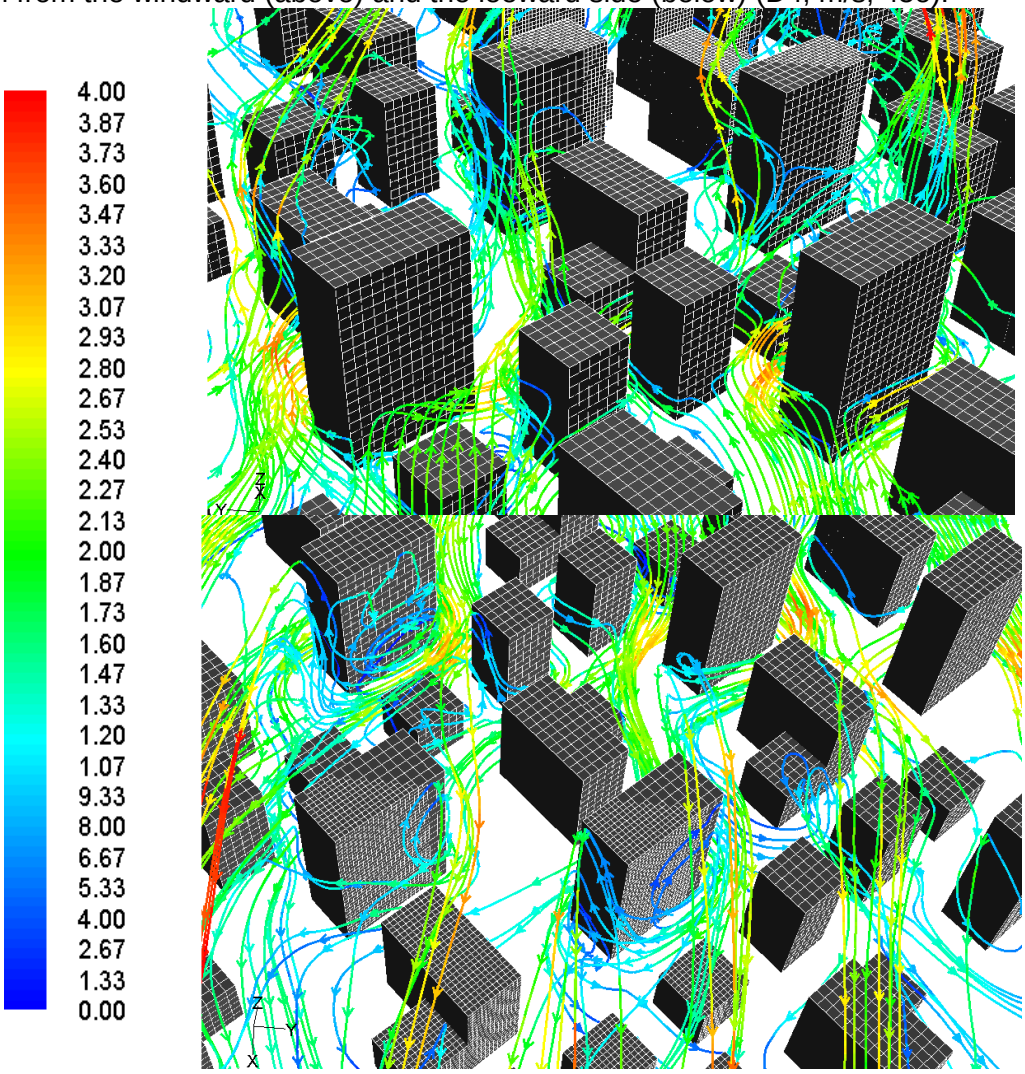

Source: This study.

The wind velocity magnitude vertical profiles show that acceleration takes place at three heights: near the ground, at 60m height and from 110 to 120m height. The accelerated flow near the ground describes a diagonal line between the T1 and T2

blocks and the T3's left side. It starts in the upwind right corner and ends in the downwind left corner. The averaged velocity in these vertical profiles is 1.50m/s, with the exception of the vertical profile between the two blocks (1.80m/s). Also, the ABL velocity at this height was 0.80m/s. On this same diagonal path, the vertical profiles in front of the T2 block showed sharp acceleration above 60m height, reaching 4.15m/s, while the related ABL input was 3.25m/s. Other vertical profiles exceed the ABL velocity of 4.00m/s from 110 to 120m height and eventually all the profiles reach 5.50m/s at around 150m height. Furthermore, near the block faces, wind speed decreases and remains constant throughout their height, with wind speeds around 0.50 and 0.15m/s on the windward and the leeward sides. Above the blocks the assessed vertical profiles present wind speed variation from 0.50 to up to 2.00m/s until reaching the previously described acceleration pattern.

Figure 7-103: Airflow velocity magnitude pathlines close-up showing a FS point (D04, m/s, 45°).

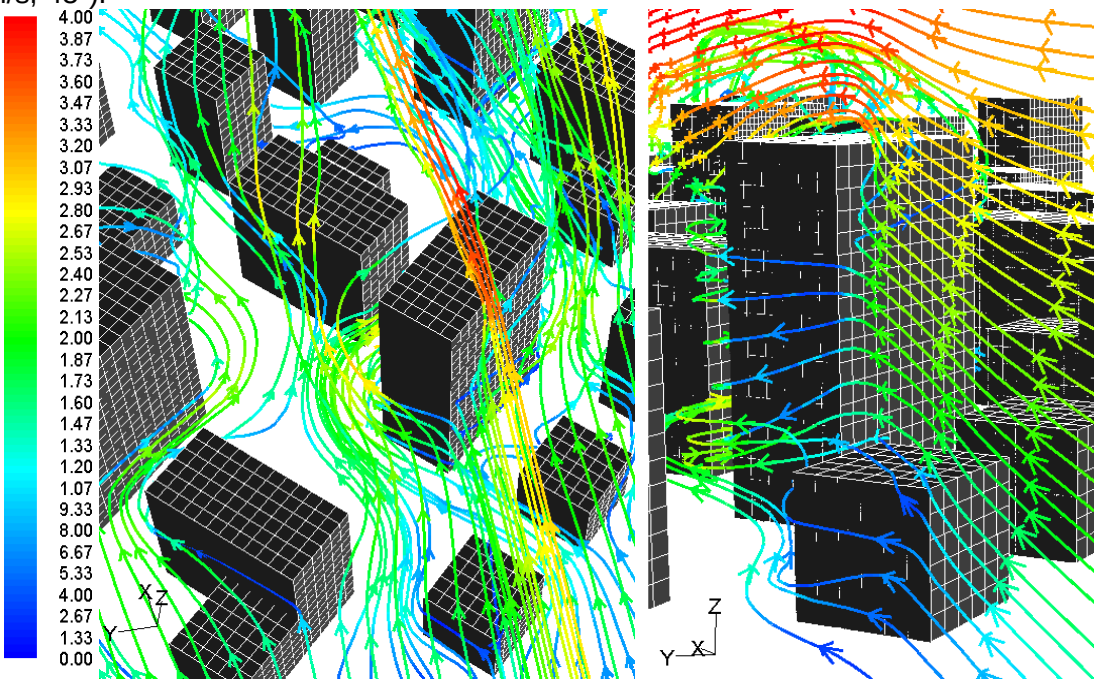

Source: this study.

Once more the x flow vector component follows the velocity magnitude profile pattern and intensity. A reverse flow occurs at ground level and from 30 to 45m height near the T2 block's leeward side (-0.25m/s), and at ground level near the T3 block's windward side (-0.40m/s). The y vector velocity ranges from -1.30 to +1.10m/s near the ground. The y vector flow direction changes continuously along a diagonal line between blocks T1 and T2 and the T3's left side. This pattern indicates the sinuous aspect of the bulk of the flow at ground level. Above ground level the vertical profiles present an accentuated spiral airflow pattern throughout the block's height with two

almost complete changes of direction. From 50 to 75m height practically all the vertical profiles present y negative results, which means, flows occur on a right to left diagonal. From 75 to 110m height another turn occurs in the flow and the pathlines acquire a left to right diagonal direction. Finally, above 110m height the flow returns to the mainstream direction. The z vertical velocity vector repeats the y vector description, adding an ascending or descending pattern to the diagonal flows which range from -0.55 to +0.70m/s. Down winds prevail on the same diagonal path up to 40m height while most of the other vertical profiles present an upwind direction. A partial up and down shift of direction takes place from 40 to 90m height. Above that all the flows stabilize in an almost horizontal pattern following the mainstream direction.

Figure 7-104: Wind velocity magnitude and x, y and z wind vector components vertical profiles (D04, 45°, m/s):

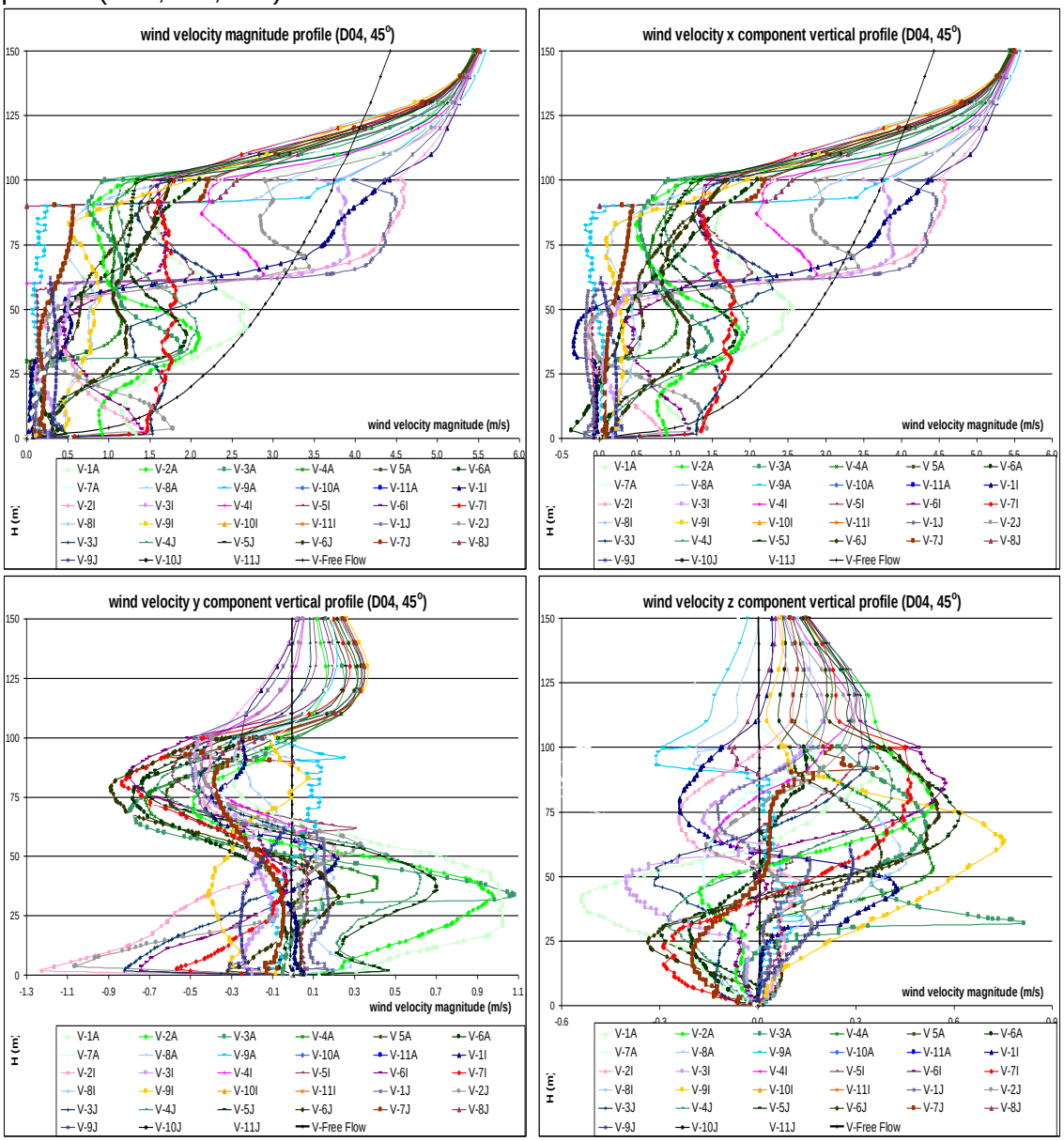

Source: this study.

7.3.7. Urban Prototype combined analysis

Here the direct comparison of the Cp and ΔCp results, the airflow patterns, and the vertical profiles' velocity distribution from groups 01 to 06 of urban prototype CFD simulations will be carried out for each simulated wind direction: 0^o, 45^o and 90^o.

7.3.7.1. Combined analysis for parallel winds (0^o)

In parallel winds, Groups 01 to 04, composed of symmetrical and low height prototypes, presented very low pressure distribution and similar results on both the right and left sides, attaining a maximum Cp of 0.15 at 30m height. It was also noticeable that pressures were slightly higher in the square canyons than in the wide and narrow ones. The uneven Group 05 showed similar results to those of the B2 scenario up to 30m height, on which it was based. Above this height and up to 60m pressure results showed a minimal increase. The asymmetrical and uneven Group 06 prototypes also showed similar results on both the right and left sides, but with higher Cp results for the D1, D2 and D3 canyons, around 0.20 at 30m, 0.45 at 60m, and 0.75 at 90m height, and even higher Cp results in the D4 detached block scenario. The ΔCp was negligible in all six groups. Absolute minimum Cp results occurred on the upwind side face near the vertical edges. This pressure drop is related to flow detachment at the corners, which gives a horseshoe shape to the airflow. Overall, flow reattachment took place within horizontal distance of less than a 5m in all the scenarios.

Regarding the airflow field pattern and velocity analysis great generalized deceleration due to dragging forces was observed near the walls in all the scenarios. On the other hand, acceleration by an averaged factor of 1.5x occurred near the ground and up to 10m height in the canyons' central area, with up-flow along the axis in all the scenarios. Furthermore, above the canopy height great acceleration took place, exceeding the ABL input velocity by a factor of up to 1.25x in all the scenarios.

Finally, for parallel winds, the aspect ratios' order of significance in the definition of pressure on vertical surfaces and the airflow field within the canyons created a contrast. The highest resultant pressures on vertical surfaces were related to the combination of both high surrounding urban built-area density (A_{built}/A_{roof}) and canyon width (H/W), which implies Group 06 scenarios. On the other hand, the highest airflow acceleration ratios were associated with the longest canyons and L/H aspect ratios (for instance, A1 and D1), which allows an intense channelling effect by which both cross and rising flows create continuous vortices alongside the main stream.

7.3.7.2. Combined analysis for orthogonal winds (90^o)

For winds perpendicular to the blocks, the total averaged pressure coefficient difference between the windward and leeward sides was first related to the H/W aspect ratio. For instance, for Groups 01 to 04, the ΔCp increased followed the order: narrow C prototypes (H/W=2.0); square B prototypes (H/W=1.0); and wide A prototypes (H/W=0.5). Narrow canyons presented very low pressure due to skimming flow effect. Furthermore, the ΔCp increased vertically (e.g. from the ground upwards), with its greatest ΔCp found at 4/5ths of the height, at the FS point, in all the scenarios.

Of the four symmetrical prototypes investigated, Group 02 presented the greatest ΔCp, followed by Group 04, while Groups 01 and 03 prototypes both low similar results. This sequence is not related to any of the urban aspect ratios previously mentioned[104] in this investigation. On the other hand, a relationship between the blocks' length and the roof area within the urban perimeter matched this sequence of results well. The conclusion lies in the fact that the airflow inside the canyons comes both from above, being subject to wake interference and skimmed flow due to its H/W aspect ratio, and the sides. The relationship between the canyon's length and the blocks' roof area seems to be indicative of this interaction.

The uneven Group 05 showed lower ΔCp when contrasted to the B2 scenario: 0.26 at 55m, 0.13 at 25m and 0.24 at 05m heights in the B2 Step-up scenario, and 0.01 at 05m heights in the B2 Step-down scenario. On the other hand, Cp results were high on both the windward and leeward sides in the lower part of the Step-up canyon due to the intense downward flow. Furthermore, both the windward and the leeward sides' Cp results were low in the lower part of the step down canyon, this time due to the leeward wake related to the decrease in block height.

Group 06 prototypes showed also low ΔCp up to 25m height, though Cp results were high on both windward and leeward sides. This fact is also related to the intense downward flow. The ΔCp increases above 25m in all the 'D' scenarios. On the other hand, from 55 to 85m height, prototypes D2 and D3 presented greater ΔCp than did prototypes D1 and D4. As mentioned in Chapter 5, prototype D1 was based on B1 block length and canyon width, prototypes D2 and D3 on B2, and prototype D4 on B4 array of cubes. Finally, the relationship between the blocks' length and the roof area was also related to the ΔCp, as example of Groups 01 to 04 demonstrates.

The airflow field is complex, but similar among the groups for orthogonal winds. In general, deceleration is observed near walls, with descending flow on the windward and ascending flow on the leeward side for all scenarios. Furthermore, reverse flow

[104] See Table 5-3 in Chapter 5 for further information about the urban dimensions and aspect ratios.

occurs near the ground in decreasing order of intensity for the wide, the square and the narrow canyons, respectively. When associated with the flow description near walls, a clock-wise vortex occurs across the canyon cavity. Additionally, when associated with the alongside and the up and/ or down flows, a three dimensional spiral is seen. While for the 180m long canyons two spiral vortices are observed (one centre-right and other centre-left oriented), the 90m long blocks show either one spiral vortex towards only one side, or two spirals, one on each side. The airflow field between the arrays of 30m cubes is characterized by several random vortices below their top height. In addition, as the B2 Step-up uneven scenario shows acceleration at ground level, with a diagonal spiral across the canyon intensified by a descending bulk of flow, in the Step down scenario airflow deceleration occurs near walls and in the canyon centre due to a leeward wake. An FS point is clearly observed at 4/5ths of the D4 T1, T2 and T3 blocks' total height. Moreover, great acceleration occurs near the ground at the T2 and T3 vertical corners, also due to downward flow. Above the canopy height great acceleration is also observed in all the group scenarios, which exceeds the ABL velocity by up to 1,5x.

7.3.7.3. Combined analysis for oblique winds (45^{o})

For oblique winds the maximum ΔCp across the Groups 01 to 04 blocks were found at 25m height and for an H/W ratio of 1.00, which means, for the symmetrical and square canyon scenarios. The wide 2.00 canyons presented lower pressure differences, and the narrow 0.50 canyons presented an almost non-existent ΔCp in spite of the other aspect ratio variants. The pressure intensity seems, therefore, to be related to the canyon height and width ratio, with skimmed flow prevailing in the narrow canyon scenarios. Furthermore, the total averaged pressure results were very similar on both the windward and the leeward sides, although their distribution was similar to a reverse mirror image. This may be considered an analytical shortcoming when the total averaged results for a particular height band are taken into account. However, in certain scenarios a differentiated analysis for the right, centre and left sides of the windward and the leeward faces was undertaken, when the differences were significant. Group 05 once again presented coherent results, with greater ΔCp on the Step-up than on the Step-down side. This uneven block height differential should therefore be used as an alternative to direct downward flow when it is desired, e.g. for narrow H/W aspect ratio scenarios.

In Group 06 maximum ΔCp across the blocks were found at 85m height, in the D1 and D4 block T3 scenarios: 0.50 and 0.30. As a rule, in spite of the small difference between the blocks' front and rear sides, the Cp was high on both sides. This is due to the great bulk of downward flow, as has also been mentioned for orthogonal winds.

Regarding the airflow field for oblique winds, the velocities near walls are always reduced, ranging from 0.20 to 0.75m/s. In the centre of the canyon different patterns are observed. Acceleration is seen near the ground in Groups 01 to 03, being greater in the square canyons (up to 3.0x the ABL input at 2m height) than in the wide (up to 2.3x) and the narrow (up to 1.5x) scenarios, which is also in line with the above-mentioned ΔCp magnitude sequence. On the other hand, all the Group 04 arrays of cubes show deceleration near the ground, and constant wind speed from the bottom to the top of the canyon cavity ranging from 1.00 to 1.50m/s, which also explains the low ΔCp in such scenarios The airflow showed a spiral airflow pattern occurring ostly downwards from low to middle height and upwards from middle to top height near the windward side, the opposite occurring on the leeward side. This describes a diagonal vortex along the canyon accompanying the mainstream. Furthermore, detachment flow was observed on the vertical edge of the upwind block's left corner from middle to top height, causing a sharp drop in pressure in this area. Groups 05 and 06 present several airflow field patterns in common with the previous groups' with more intense downward and reverse flow at ground than at the 60 and 90m height windward faces. In general Group 06's airflow pattern presents a sinuous aspect at ground level. Above ground level an ascending or descending diagonal flow pattern is observed. The vertical profiles presented an accentuated inversion of wind direction at 30 to 45m, from 50 to 70m, and from 75 to 110m heights. Finally, above 110m height the flow returns to the direction of the mainstream and above this height stabilizes in an almost horizontal pattern in the same direction.

7.4. The Urban Prototypes correlation assessment

Here the Urban Prototypes CFD outputs from Groups 01 to 06 are compared. This investigation aims to identify if the correlation coefficient strength found between the several urban prototype aspect ratios, and shown in Chapter 5 (see topic 5.8.3), is also valid for the correlation coefficient between the urban prototypes ΔCp results. The correlation coefficients for ΔCp employed the averaged results for 90% of the data (discharging 10% of extreme results)[105].

7.4.1. Correlations between the ΔCp results

Here the ΔCp results for the groups 1 to 6 of the Urban Prototypes and the respective correlation coefficient matrices are shown for each wind direction are presented and assessed.

For instance, in spite of the fact that the ΔCp results for parallel winds were near zero (see Table 7-3), which is expected in CFD calculation for symmetrical scenarios, the scenarios that showed a strong correlation relationship for the aspect ratios continue to show the same relationship for the ΔCp results (Table 7-4): B2 and B3 (0.87), and C2 and C3 (0.99) (Figure 7-105); Further, the correlation relationship for the dissimilar scenarios continued low: A1 and D4 (0.38) (Figure 7-106).

The ΔCp results for orthogonal winds were quite low, reaching an averaged value maximum of 0.10 for the groups 1 to 5 and 0.12 for the group 6 (Table 7-5). Once more the scenarios previously analysed for the aspect ratios continue to show either strong relationship for the ΔCp results (Table 7-6): B2 and B3 (0.97), and C2 and C3 (0.99, see Figure 7-107); and the correlation relationship for the opposite scenarios was kept low: A1 and D4 (0.28, see Figure 7-108), and A4 and C1 (0.60).

Finally, the ΔCp results for oblique winds also manteined the link to the aspect ratios results (Tables 7-7 and 7-8). For example, the scenarios who presented strong relationship before had the same for the ΔCp: B2 and B3 (0.92), and C2 and C3 (0.97, see Figure 7-109); and the correlation relationship for the opposite scenarios continued low: A1 and D4 (0.28, see Figure 7-110), and A4 and C1 (0.43).

[105] Other ΔCp data (such as peaks values, the 8th highest/ lowest results, and the standard deviation) were displayed with the purpose of providing further information about the results.

Table 7-3: Correlation coefficient matrix among the urban prototype scenarios regarding the ΔCp results for parallel winds (0°)[106].

0°	A1	A2	A3	A4	B1	B2	B3	B4	C1	C2	C3	C4	D1	D2	D3	D4
ΔCp at top	0,001	0,001	0,001	0,000	0,001	0,001	0,001	0,010	0,000	0,001	0,001	0,004	0,017	-0,079	0,080	-0,002
	0,001	0,001	0,001	-0,003	0,000	0,000	0,001	0,014	0,000	0,001	0,001	0,003	0,021	-0,081	0,082	-0,008
ΔCp at middle	0,000	0,002	0,000	-0,005	0,000	-0,001	0,002	0,014	0,000	0,002	0,002	0,002	0,028	-0,042	0,017	0,014
	0,000	0,001	0,000	0,000	0,000	0,000	0,001	0,016	0,000	0,001	0,001	0,002	0,027	-0,037	0,018	0,011
ΔCp at bottom	0,000	0,001	0,000	-0,001	0,000	0,000	0,001	0,019	0,000	0,001	0,001	-0,002	-0,016	-0,054	-0,003	-0,004
	0,000	0,001	0,000	-0,001	0,000	0,001	0,001	0,020	0,001	0,001	0,001	-0,005	-0,007	-0,009	-0,008	-0,006
	-0,001	0,001	-0,001	0,001	0,000	-0,001	0,001	0,020	0,001	0,001	0,001	-0,005	-0,006	-0,007	-0,013	-0,007
AVG ΔCp	0,00	0,00	0,00	0,00	0,00	0,00	0,00	0,02	0,00	0,00	0,00	0,00	0,01	-0,04	0,02	0,00

Source: this study.

Table 7-4: Correlation coefficient matrix among the urban prototype scenarios regarding the ΔCp results for parallel winds (0°).

	A1	A2	A3	A4	B1	B2	B3	B4	C1	C2	C3	C4	D1	D2	D3	D4
A1																
A2	0,23															
A3	1,00	0,23														
A4	-0,53	-0,72	-0,53													
B1	0,17	-0,52	0,17	0,57												
B2	0,31	-0,45	0,31	0,23	0,88											
B3	0,23	1,00	0,23	-0,72	-0,52	0.87										
B4	-0,87	-0,29	-0,87	0,37	-0,34	-0,34	-0,29									
C1	-0,73	0,23	-0,73	-0,04	-0,60	-0,55	0,23	0,76								
C2	0,23	1,00	0,23	-0,72	-0,52	-0,45	1,00	-0,29	0,23							
C3	0,23	1,00	0,23	-0,72	-0,52	-0,45	1,00	-0,29	0,23	1,00						
C4	0,94	0,21	0,94	-0,35	0,28	0,26	0,21	-0,96	-0,77	0,21	0,21					
D1	0,70	0,45	0,70	-0,42	-0,01	-0,05	0,45	-0,76	-0,26	0,45	0,45	0,81				
D2	-0,88	0,03	-0,88	0,36	-0,22	-0,30	0,03	0,81	0,88	0,03	0,03	-0,86	-0,44			
D3	0,80	-0,09	0,80	-0,27	0,34	0,39	-0,09	-0,87	-0,77	-0,09	-0,09	0,86	0,61	-0,89		
D4	0,38	0,70	0,38	-0,32	-0,13	-0,21	0,70	-0,35	0,04	0,70	0,70	0,41	0,65	0,02	-0,08	

Source: this study. .

[106] The colours of this scale of significance for the urban prototype ΔCp results correlation coefficient (*r*) strength are based on the Table 5-20 in Chapter 5.

Figure 7-105: Correlation coefficient between the Urban Prototypes C2 ΔCp results and C3 ΔCp results for parallel winds.

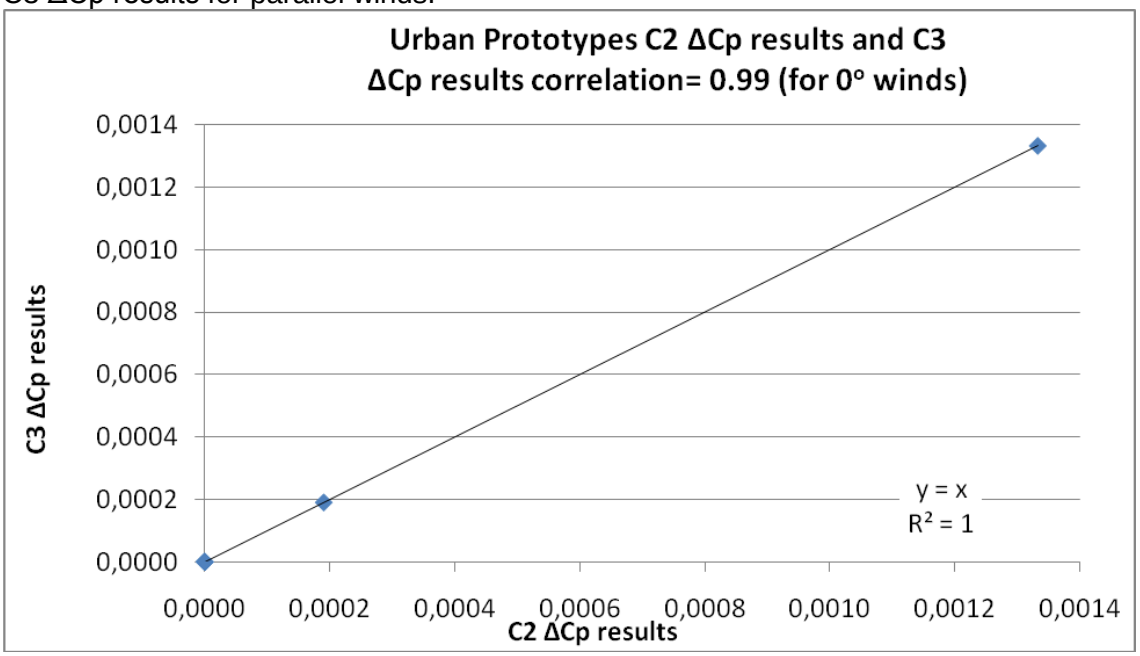

Source: this study

Figure 7-106: Correlation coefficient between the Urban Prototypes A1 ΔCp results and D4 ΔCp results for parallel winds.

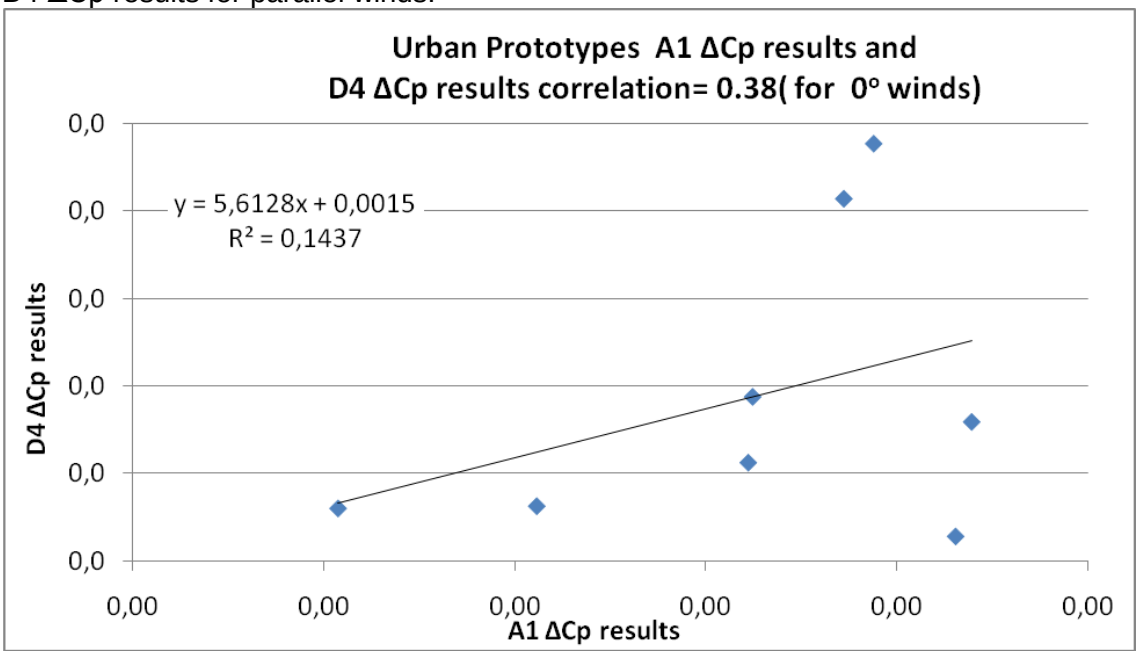

Source: this study

Table 7-5: Correlation coefficient matrix among the urban prototype scenarios regarding the ΔCp results for perpendicular winds (90°).

90°	A1	A2	A3	A4	B1	B2	B3	B4	C1	C2	C3	C4	D1	D2	D3	D4
ΔCp at top	0,12	0,02	0,05	-0,02	-0,07	-0,01	-0,02	0,00	-0,04	0,00	0,01	0,01	0,12	0,13	0,10	0,05
	0,19	0,68	0,21	0,39	0,07	0,16	0,08	0,22	0,02	0,00	0,07	0,04	0,32	0,26	0,28	0,19
ΔCp at middle	0,03	0,48	0,07	0,27	-0,01	0,05	0,01	0,13	0,00	0,00	0,01	0,04	0,18	0,13	0,23	0,16
	0,03	0,34	0,05	0,18	-0,01	0,02	0,02	0,08	0,00	0,00	0,00	0,01	0,10	0,09	0,15	0,16
ΔCp at bottom	0,01	0,29	0,02	0,13	-0,01	0,02	0,00	0,03	0,00	0,00	0,00	-0,01	0,02	0,05	0,10	0,09
	0,04	0,31	0,06	0,13	-0,01	-0,02	-0,01	0,01	-0,01	0,01	-0,01	-0,02	0,00	0,04	0,08	0,07
	0,08	0,38	0,18	0,15	0,01	-0,02	0,00	0,02	0,00	0,00	0,00	-0,02	-0,01	0,04	0,10	0,06
AVG ΔCp	0,07	0,36	0,09	0,17	0,00	0,03	0,01	0,07	-0,01	0,00	0,01	0,01	0,10	0,11	0,15	0,11

Source: this study.

Table 7-6: Correlation coefficient matrix among the urban prototype scenarios regarding the ΔCp results for perpendicular winds (90°)[107].

	A1	A2	A3	A4	B1	B2	B3	B4	C1	C2	C3	C4	D1	D2	D3	D4
A1																
A2	0,33															
A3	0,74	0,71														
A4	0,34	0,99	0,64													
B1	0,46	0,95	0,79	0,92												
B2	0,62	0,80	0,57	0,86	0,81											
B3	0,65	0,86	0,71	0,89	0,88	0,97										
B4	0,52	0,86	0,57	0,92	0,78	0,96	0,94									
C1	0,06	0,94	0,55	0,60	0,91	0,64	0,71	0,68								
C2	-0,59	0,04	-0,19	-0,04	0,03	-0,42	-0,36	-0,38	0,27							
C3	0,90	0,61	0,70	0,65	0,68	0,90	0,88	0,81	0,36	0,97						
C4	0,47	0,45	0,23	0,57	0,31	0,76	0,67	0,83	0,20	-0,68	0,70					
D1	0,72	0,57	0,47	0,66	0,51	0,88	0,83	0,89	0,29	-0,65	0,89	0,94				
D2	0,82	0,54	0,54	0,62	0,54	0,88	0,84	0,86	0,26	-0,67	0,95	0,87	0,99			
D3	0,55	0,80	0,57	0,87	0,70	0,91	0,89	0,98	0,58	-0,45	0,81	0,89	0,92	0,88		
D4	0,28	0,79	0,37	0,87	0,67	0,85	0,85	0,95	0,68	-0,31	0,61	0,82	0,80	0,73	0,92	

Source: this study. .

[107] The colours of this scale of significance for the urban prototype ΔCp results correlation coefficient (*r*) strength are based on the Table 5-20 in Chapter 5.

Figure 7-107: Correlation coefficient between the Urban Prototypes C2 ΔCp results and C3 ΔCp results for orthogonal winds.

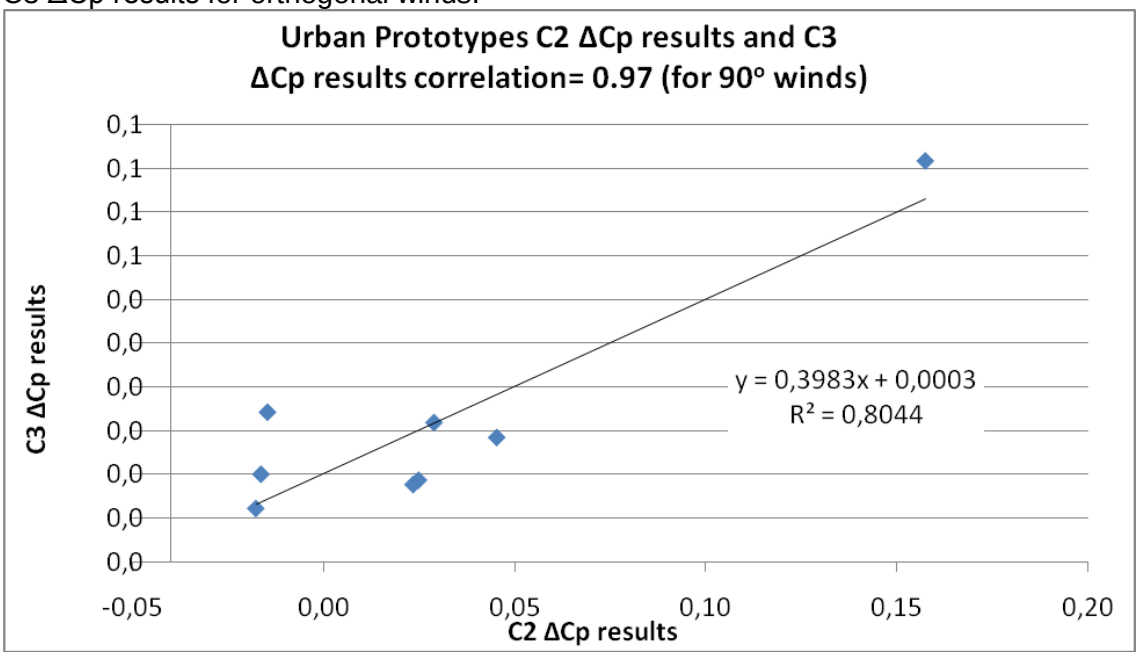

Source: this study

Figure 7-108: Correlation coefficient between the Urban Prototypes A1 ΔCp results and D4 ΔCp results for orthogonal winds.

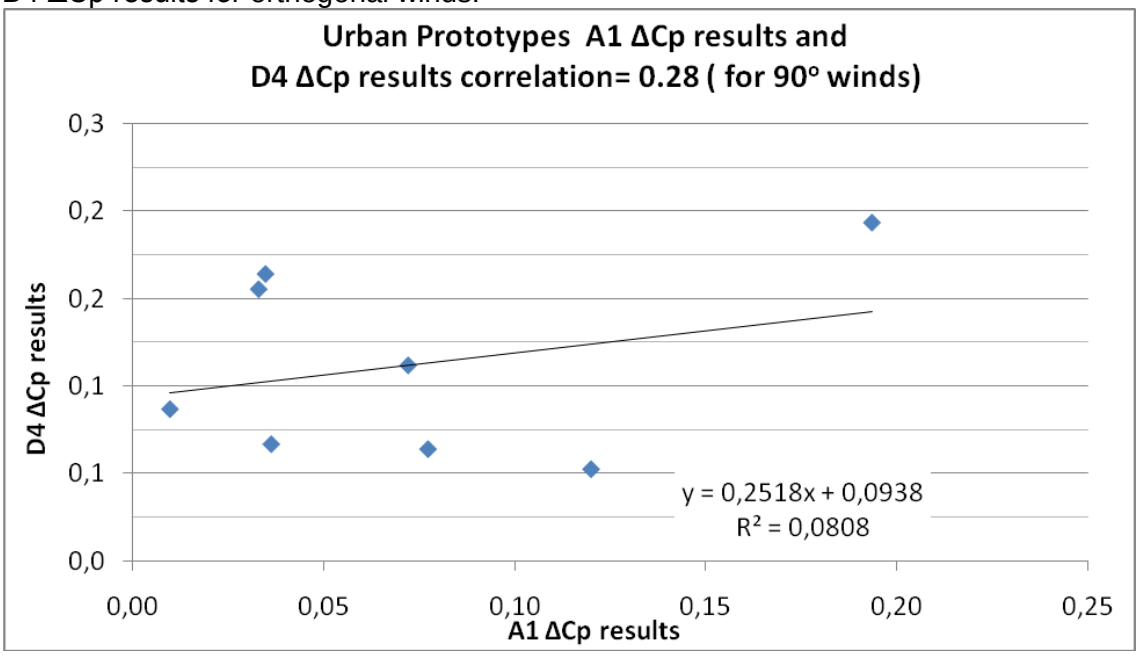

Source: this study

Table 7-7: Correlation coefficient matrix among the urban prototype scenarios regarding the ΔCp results for oblique winds (45°).

45°	A1	A2	A3	A4	B1	B2	B3	B4	C1	C2	C3	C4	D1	D2	D3	D4
ΔCp at top	-0,01	0,03	-0,01	0,01	0,06	-0,06	0,00	0,08	0,01	0,01	0,00	0,00	0,19	0,28	0,20	0,22
	0,06	-0,02	0,04	0,05	0,07	0,17	0,14	0,13	0,01	0,00	0,00	0,00	0,46	0,37	0,29	0,39
ΔCp at middle	0,05	-0,02	0,02	0,04	0,02	0,10	0,06	0,08	0,00	0,00	0,00	0,00	0,20	0,32	0,21	0,28
	0,04	-0,01	0,02	0,04	-0,02	0,03	0,01	0,05	0,00	0,00	0,00	0,00	0,08	0,32	0,28	0,16
ΔCp at bottom	0,02	-0,01	0,01	0,04	-0,02	0,00	0,03	0,03	0,00	0,00	0,00	0,00	0,02	0,26	0,24	0,10
	0,02	-0,01	0,01	0,03	0,02	0,02	0,04	0,04	0,00	0,00	0,00	0,01	0,00	0,18	0,19	0,09
	0,04	-0,01	0,00	0,03	0,04	0,03	0,04	0,03	0,01	0,00	0,00	0,00	0,01	0,19	0,20	0,09
AVG ΔCp	0,03	-0,01	0,01	0,03	0,02	0,04	0,05	0,06	0,00	0,00	0,00	0,00	0,14	0,27	0,23	0,19

Source: this study.

Table 7-8: Correlation coefficient matrix among the urban prototype scenarios regarding the ΔCp results for oblique winds (45°)[108].

	A1	A2	A3	A4	B1	B2	B3	B4	C1	C2	C3	C4	D1	D2	D3	D4
A1																
A2	0,91															
A3	0,77	0,81														
A4	0,92	-0,97	0,92													
B1	0,03	0,27	0,04	-0,16												
B2	0,92	-0,83	0,91	0,91	0,26											
B3	0,77	-0,68	0,82	0,76	0,47	0,92										
B4	0,26	-0,06	0,57	0,28	0,70	0,58	0,61									
C1	0,19	0,12	-0,26	-0,16	0,71	0,12	0,28	0,12								
C2	-0,36	0,57	-0,10	-0,40	0,83	-0,06	0,19	0,69	0,37							
C3	-0,17	0,35	0,14	-0,17	0,82	0,16	0,40	0,78	0,33	0,97						
C4	0,08	-0,31	0,31	0,23	-0,04	0,21	0,28	-0,06	-0,22	-0,21	-0,09					
D1	0,39	-0,18	0,63	0,39	0,68	0,67	0,72	0,98	0,19	0,65	0,77	-0,12				
D2	0,37	-0,24	0,65	0,47	0,20	0,55	0,43	0,80	-0,21	0,35	0,45	-0,36	0,82			
D3	0,52	-0,53	0,68	0,65	-0,06	0,58	0,48	0,44	-0,15	0,04	0,24	-0,14	0,54	0,75		
D4	0,43	-0,22	0,67	0,44	0,60	0,69	0,68	0,97	0,09	0,56	0,67	-0,14	0,98	0,86	0,51	

Source: this study.

[108] The colours of this scale of significance for the urban prototype ΔCp results correlation coefficient (*r*) strength are based on the Table 5-20 in Chapter 5.

Figure 7-109: Correlation coefficient between the Urban Prototypes C2 ΔCp results and C3 ΔCp results for oblique winds.

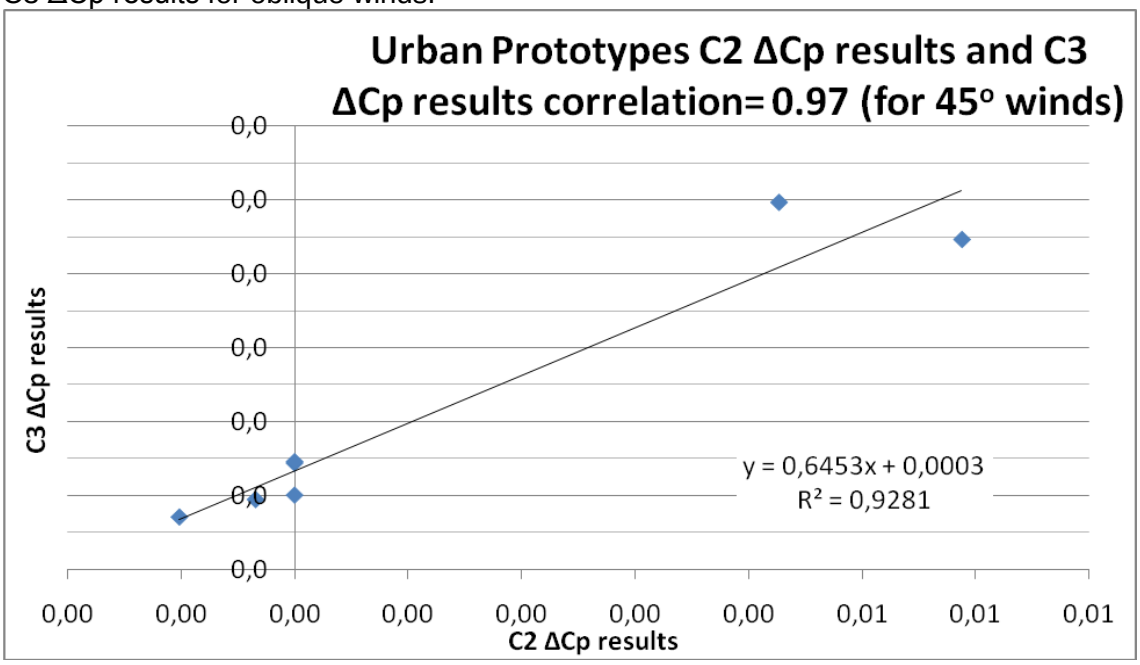

Source: this study

Figure 7-110: Correlation coefficient between the Urban Prototypes A1 ΔCp results and D4 ΔCp results for oblique winds.

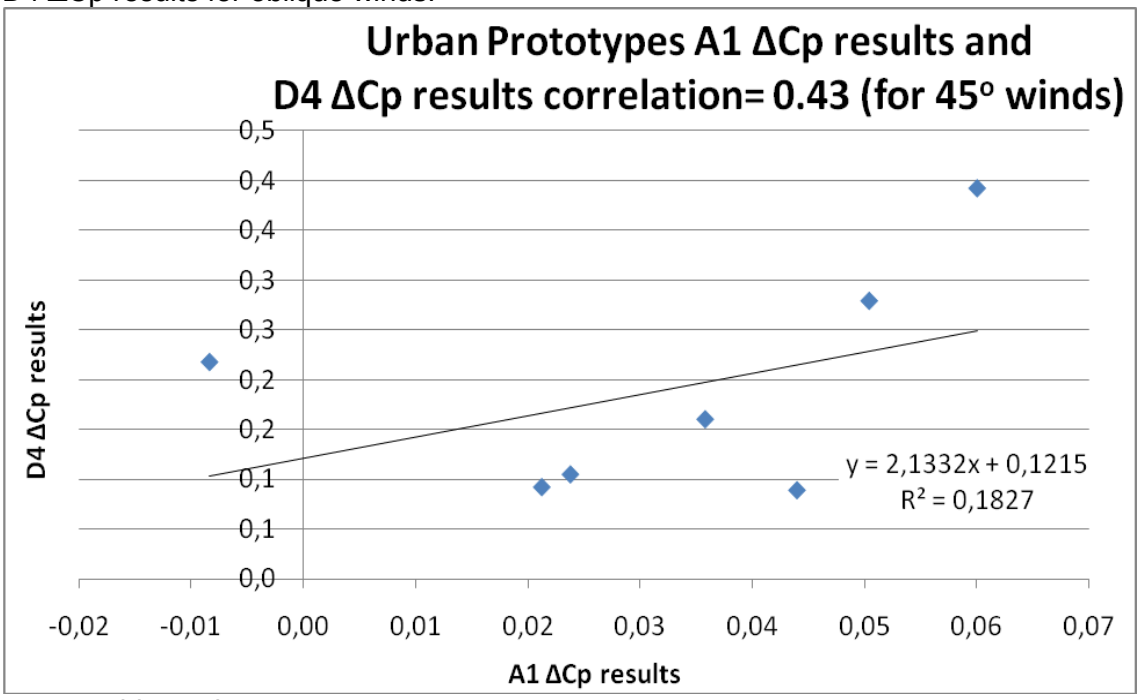

Source: this study.

7.5. Chapter conclusion

The objective proposed for this step of the investigation, i.e. the identification of and relationships between the airflow field patterns and the Cp distribution in several urban scenarios with controlled parameters and aspect ratios for three prevailing wind directions has thus been fulfilled. This investigation was carried out by CFD simulation. Although the range of results among different scenarios for the same group and wind direction are equivalent, it is clear from both the pressure distribution and the airflow field analysis that some of the results are more alike and related to an aspect ratio variation sequence, while other present great vertical or even random variation. The H/W aspect ratio has proved to be the mandatory on the definition of the airflow speed and direction, velocity and pressure inside canyons for both orthogonal and oblique wind directions. Moreover, a correlation coefficient matrix was presented for the urban prototype scenarios relating their ΔCp results. These findings will be tested in the following chapters, which report on the investigation of real urban scenarios.

Chapter 8: Cathays Campus: Results and Analysis

8.1. Introduction

In this chapter, which is part of Step 3 of the proposed methodology, the findings of the Cardiff University Cathays Campus investigation are presented, analysed and discussed. Sets of WT and CFD simulations, and field measurements (FM), were carried-out[109] allowing triangulation of the results and a panoramic view of the airflow field in the canyon formed by the Welsh Assembly and the Cardiff University Law School buildings as well as the ΔCp across this last building. Finally, the results were compared and correlated to the urban prototype outputs, covered in Chapter 7[110].

8.2. On the Cathays Campus results and analyses

First, the Cp and ΔCp results from both WT and CFD simulations for the Cardiff University Law School building are contrasted by means of graphs and tables[111]. The airflow patterns in the Museum Ave. canyon from the CFD are then assessed by the observation of wind velocity magnitude pathlines 3D perspectives, and by wind velocity vertical profiles graphs. Subsequently, wind velocity magnitude and direction from the FM undertaken in the Law School building are compared to the WSA meteorological station (MS) data and, then matched up with CFD wind speed results. Finally, ΔCp results from both WT and CFD simulations are integrated and compared to the urban prototypes' outputs and aspect ratios.

[109] The methods employed for accessing the Cathays Campus were previously covered in topics 5.2, 5.4.2.1, 5.5.3, 5.6.5, 5.7, and 5.8.3.1 of Chapter 5 'Methodology'.
[110] This part corresponds to the Step 2 of the investigation.
[111] Tables with more complete Cp and ΔCp output data from both WT and CFD simulations for each wind direction can be found in Appendix 5.

8.3. Comparison of the WT and CFD results

A total of eight wind directions: N, NE, E, SE, S, SW, W, and NW were applied during the WT and CFD experiments, and the results and analyses are presented in that same sequence.

It is worth bringing out two issues regarding the comparison of the WT and the CFD results: due to the few rows of pressure points used in the WT set of experiments (four on the Museum Avenue- MA- and the Park Place- PP- sides of the Law School building opening on to the roads, and two on the sides opening on the courtyard) it was not possible to create Cp contour plot images for the physical experiment outputs and therefore the comparison is based exclusively on graphs. Further, CFD results cover more points on the same surfaces, e.g., results are shown for more points on the same surface and range from 2.0m to 15.0m high, while for the WT results they range from 6.0, 9.0, or 12.0m to 15m high, depending on the side of the building.

Figure 8-1: The Law School building (marked in red) and the urban canyon assessed (Museum Avenue- marked in green) in the Cathays Campus:

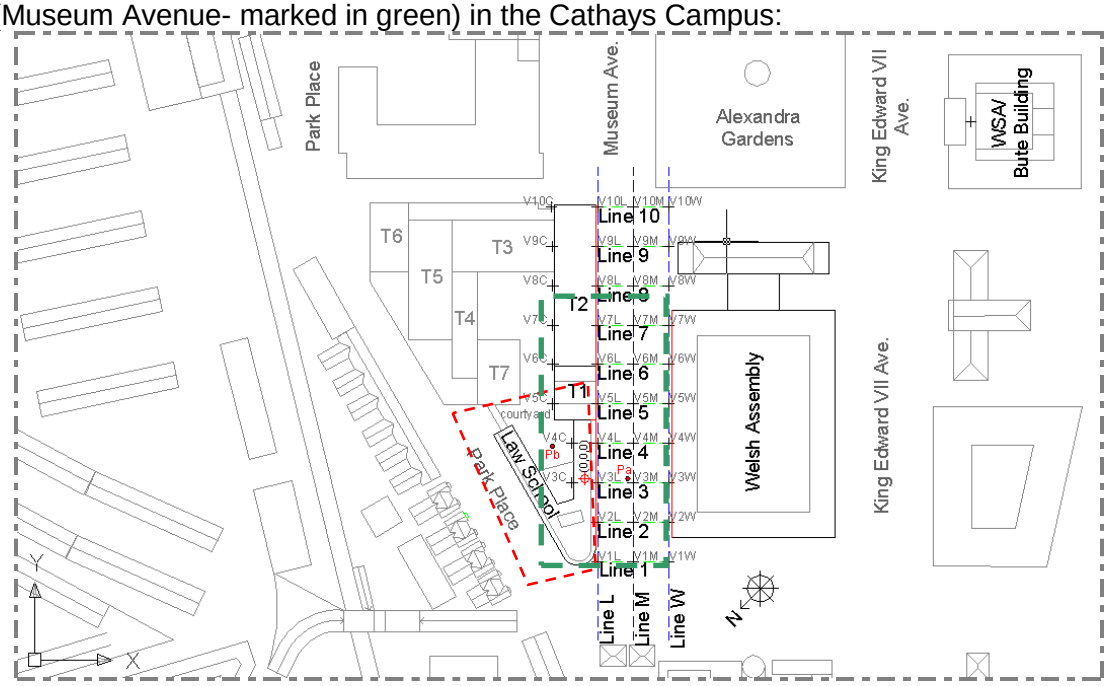

Source: this study.

8.3.1. North winds

North winds are oblique (45^{o}) to Museum Ave. and orthogonal (90^{o}) to Park Place. Both the courtyard side of MA and the external side of PP lie to windward, while the external side of MA and the courtyard side of PP lie to leeward.

The comparison of the Cp distribution for the four façades (MA external and internal, and PP external and internal) from the WT and the CFD simulations showed a reasonable match of both their shapes (with the exception of the Cp results at low height which were not measured in the WT experiments- see Figure 8-2) and range of values (e.g. Cp differences no greater than 0.10). Further, the ΔCp results across the windward and the leeward sides of the Law School agree well on both wings of the building. In contrast, WT data only allowed comparison of ΔCp results from 9.0 to 15.0m height in the MA block and from 12.0 to 15.0m height in the PP block.

Regarding the airflow field, it may be observed that few areas present acceleration (yellow or red pathlines in Figure 8-3), which would represent velocities above 1.80m/s at 15.0m, the input velocity at that height. These areas are concentrated on the horizontal edge at the top of the Welsh Assembly building. Further, the pathlines present a spiral airflow pattern occurring inside the canyon cavity, forming a low pressure bubble on the leeward round corner or the Law School building, bouncing in the windward side of the Welsh Assembly building and then coming back in a spiral along Museum Avenue. Moreover, there is almost no air movement to be seen from these pathlines in the courtyard.

The assessment of the vertical profiles of wind velocity magnitude (Figure 8-4) shows that acceleration occurs near the Welsh Assembly by a factor of 1.5x at 15.0m height. Furthermore, the x, y, and z flow component vectors confirm the spiral airflow pattern and stream oriented vortex, with more intense shifts from positive to negative (or reverse) flow occurring around 20m height in the vertical profiles near the corner of the Welsh Assembly but with practically no air movement in the courtyard up to 15m height.

Figure 8-2: Cp results for N winds: oblique (45º) to the MA and orthogonal (90º) to PP.

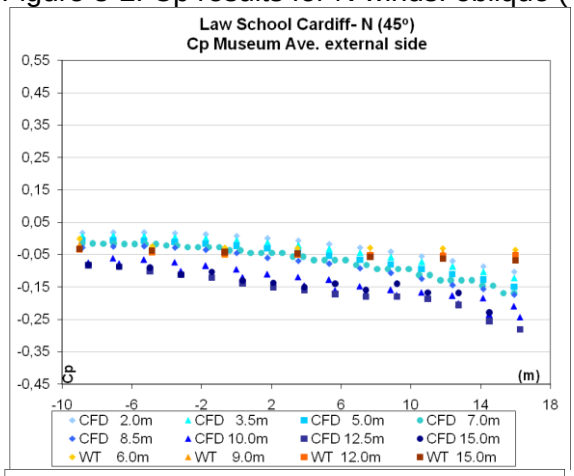

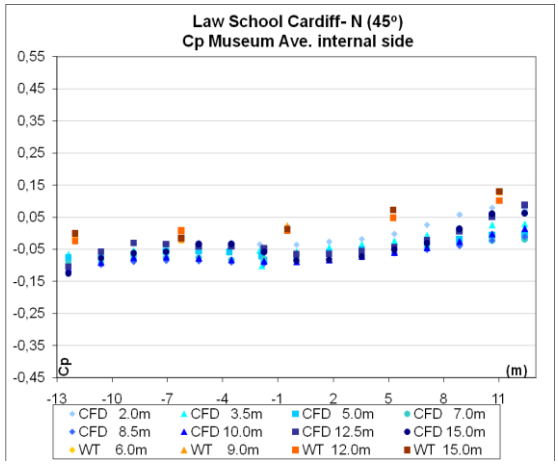

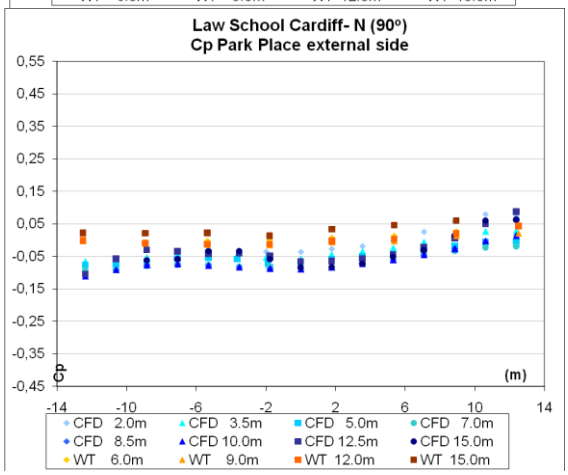

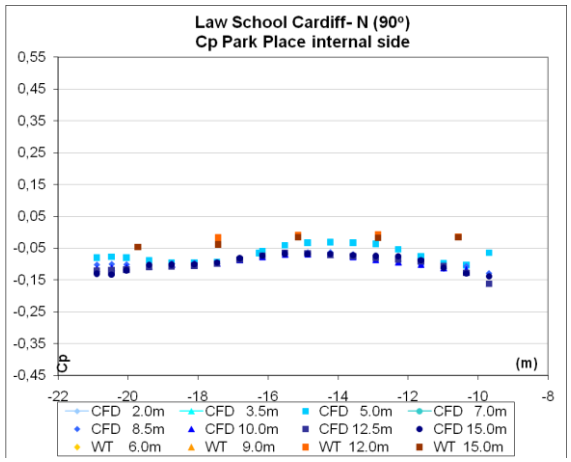

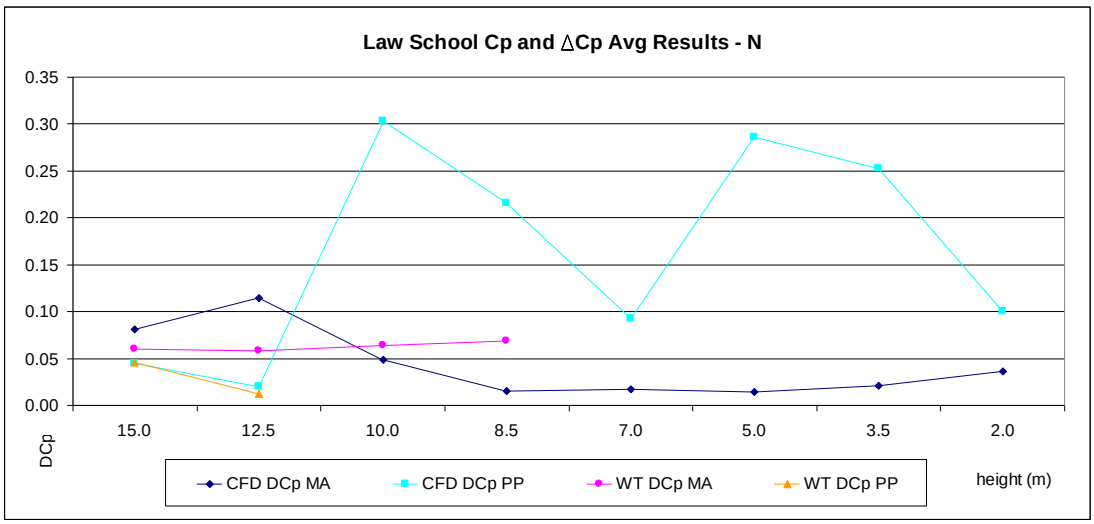

Source: this study.

Figure 8-3: North winds: oblique (45°) to MA and orthogonal (90°) to PP Velocity magnitude airflow pathlines released from horizontal rakes at 05 and 15m height (m/s).

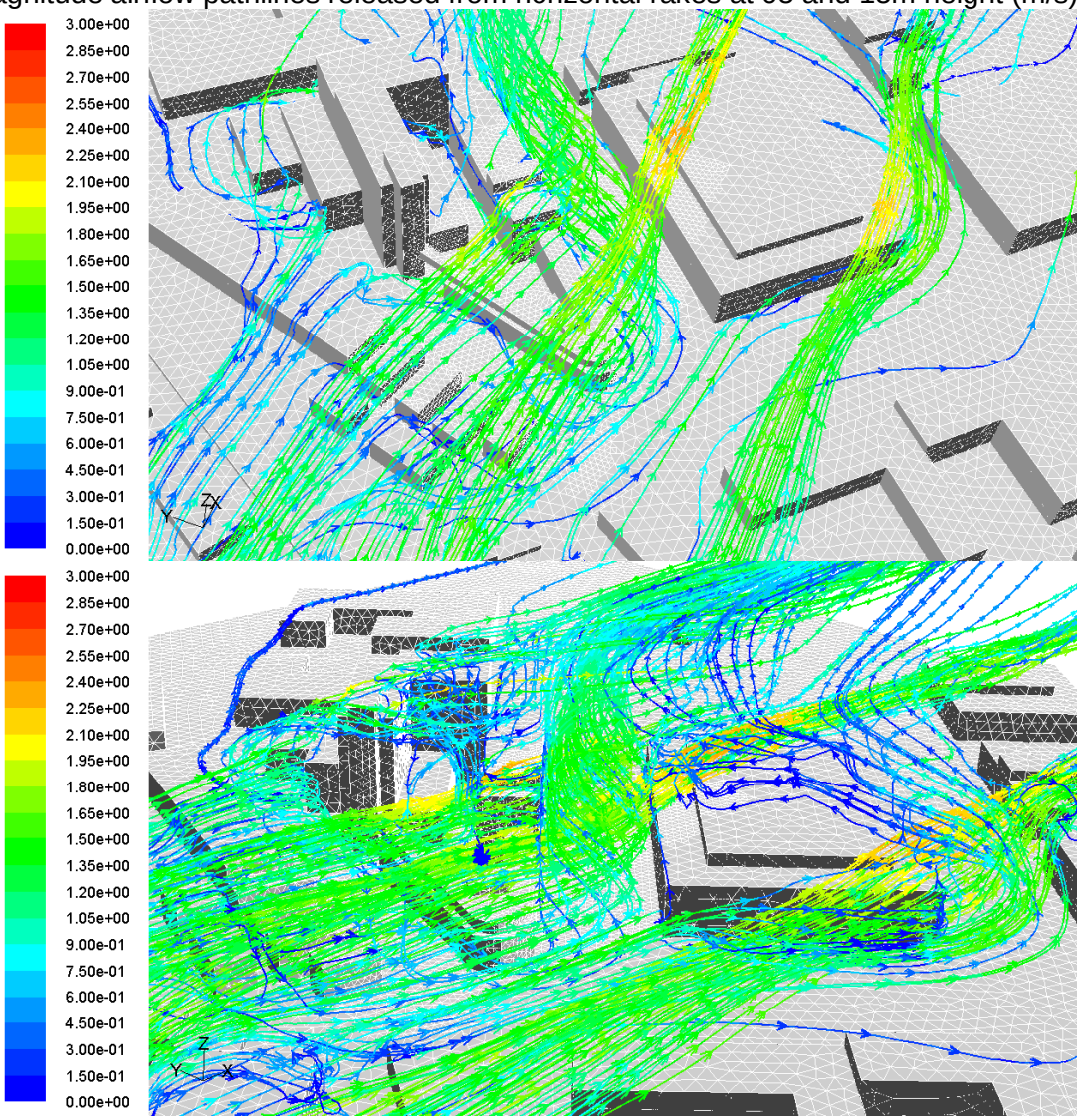

Source: this study.

Figure 8-4: Velocity magnitude and x, y and z vectors vertical profiles[112] for N winds: oblique (45°) to the Museum Ave. (m/s):

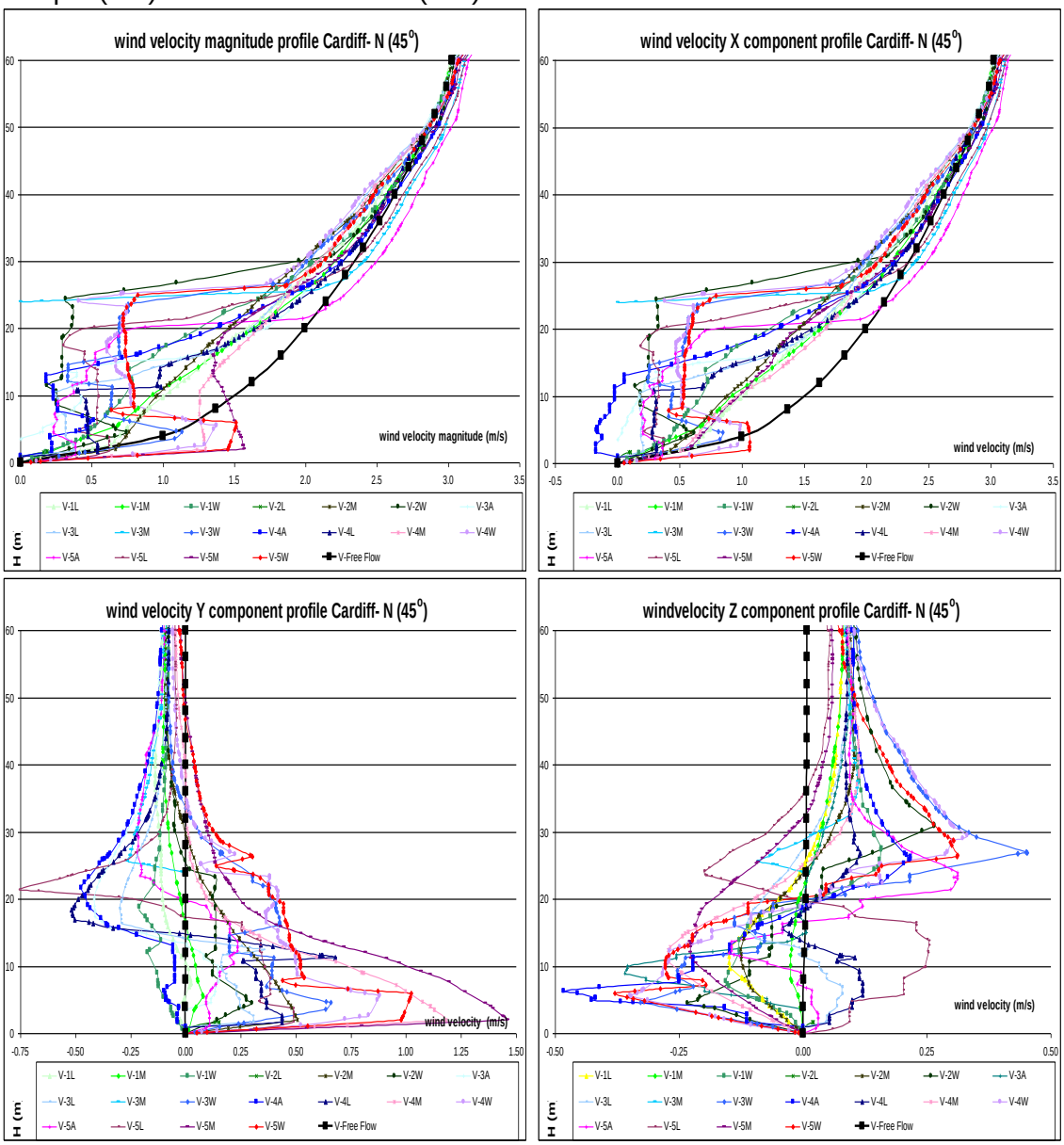

Source: this study.

[112] Where L= Law School; M= middle of the Museum Ave.; W= Welsh Assembly, and A= courtyard.

8.3.2. Northeast winds

Northeast winds are orthogonal (90^o) to Museum Ave. and oblique (45^o) to Park Place. While both the courtyard side of MA and the external side of PP face windward, the external side of MA and the courtyard side of PP face leeward.

The comparison of the WT and the CFD simulations Cp distribution (Figure 8-5) matched well in both shape and range for the PP external face, which corresponds to the open windward side for this wind direction. The faces opening onto the courtyard (MA and PP internal) presented a weaker similarity, while the leeward side of the building open to the MA presented results within the same range. The ΔCp across the PP side of the building also matched well, while the pressure difference from the WT and the CFD simulations found for the MA block showed a disparity of up to 0.30 due to divergences in the MA courtyard face Cp results.

The free airflow comes perpendicular to the canyon with the Welsh Assembly on the downwind side (Figure 8-6). A strong downward flow is observed on its windward face, which results in a clock-wise vortex with an upward flow on the Law School's leeward side and towards the left side (Southeast) of MA. This direction is possibly powered by the low pressure area created in the leeward wake behind tall buildings on the other edge of this canyon. Furthermore, acceleration is observed right above the top of the Law School on PP, and a weak vortex is formed in the courtyard.

The assessment of the vertical profiles of wind velocity magnitude (Figure 8-7) shows a reverse flow occurring near the Welsh Assembly's windward side and near the ground, with an ascending flow near the Law School's leeward side in the canyon, which corroborates the flow vortex description just quoted.

Figure 8-5: Cp results for NE winds: orthogonal (90º) to MA and oblique (45º) to PP.

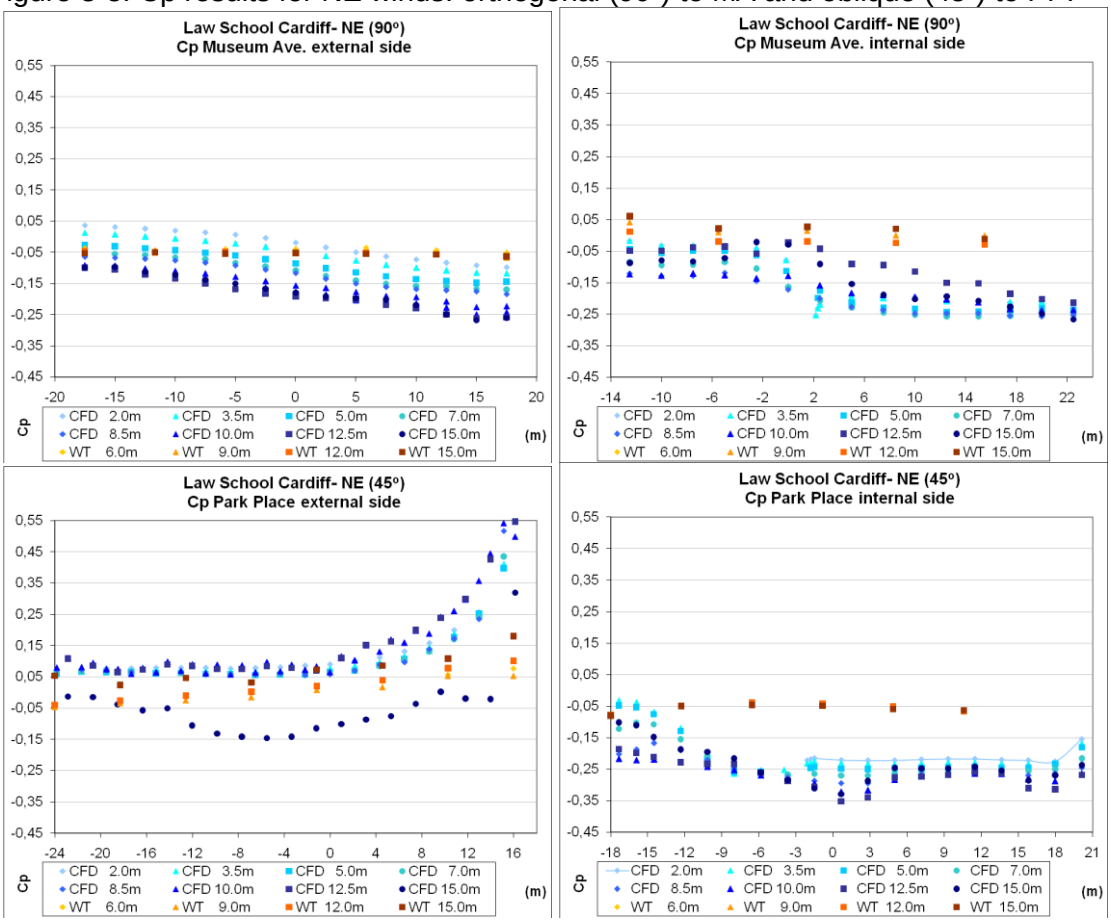

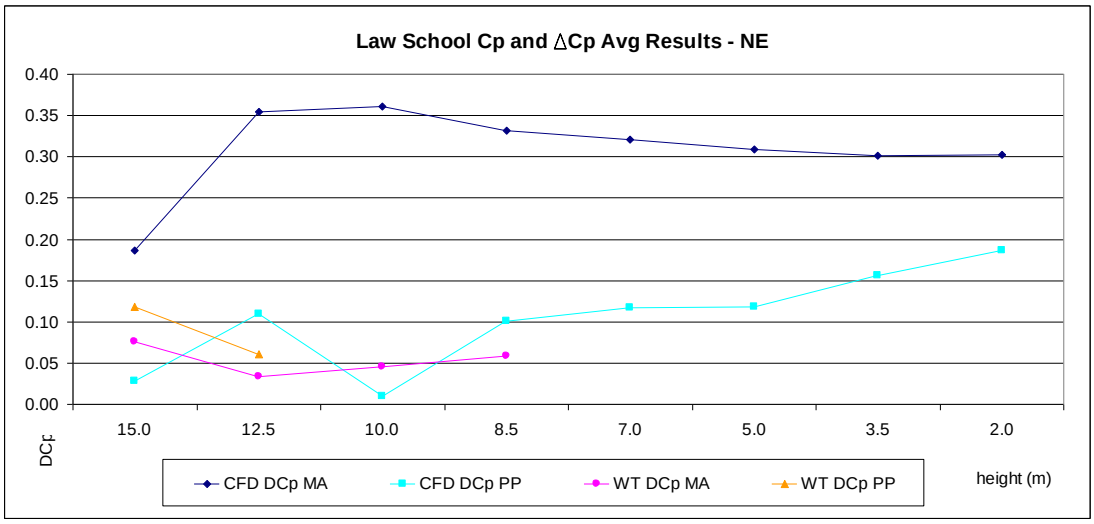

Source: this study.

Figure 8-6: Cp results for Northeast winds: orthogonal (90^{o}) to the Museum Ave. and oblique (45^{o}) to the Park Place. Velocity magnitude airflow pathlines released from horizontal rakes at 05 and 15m height (m/s).

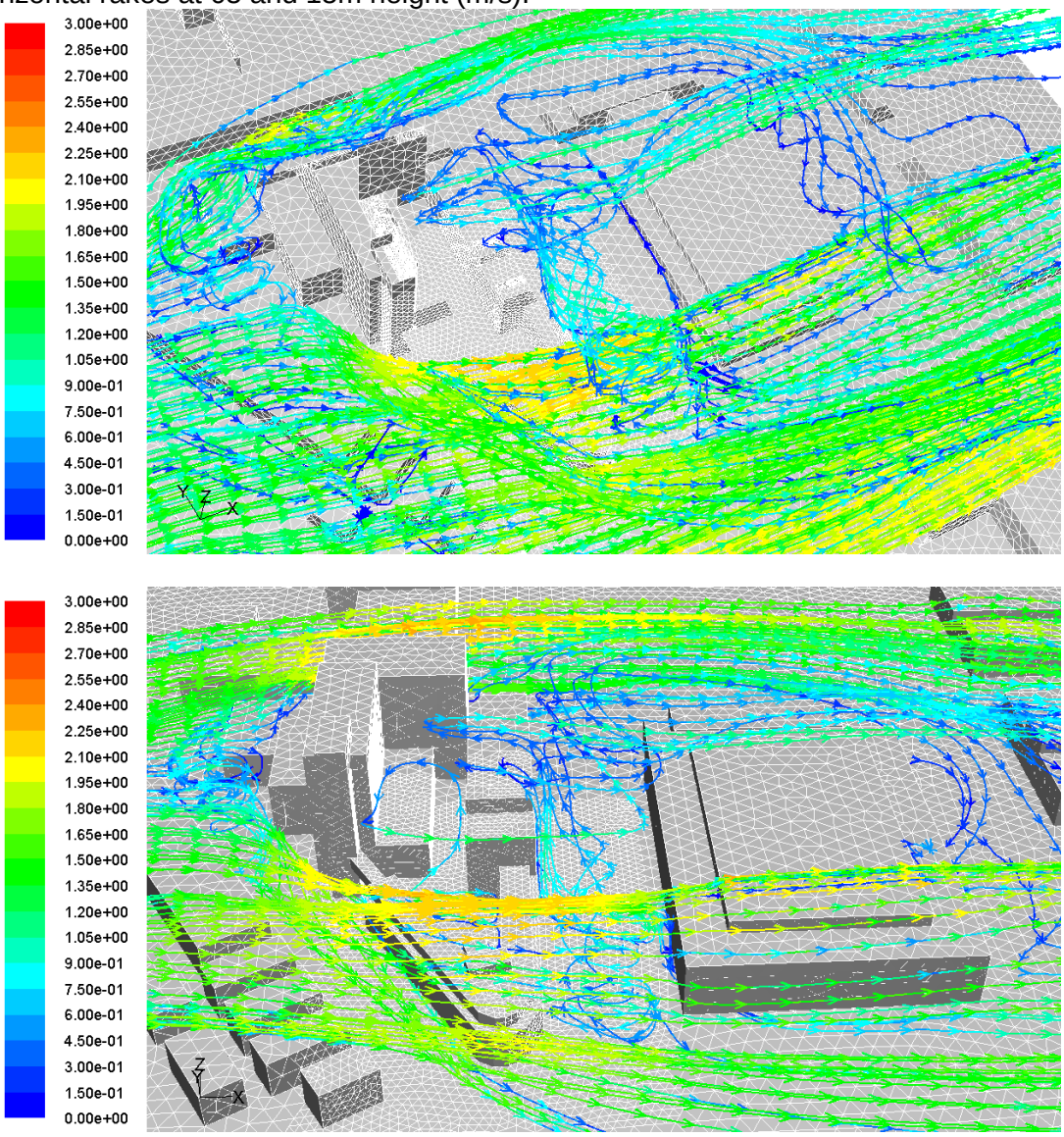

Source: this study.

Figure 8-7: Velocity magnitude and x, y and z vectors vertical profiles for NE winds: orthogonal (90^{o}) to the Museum Ave (m/s):

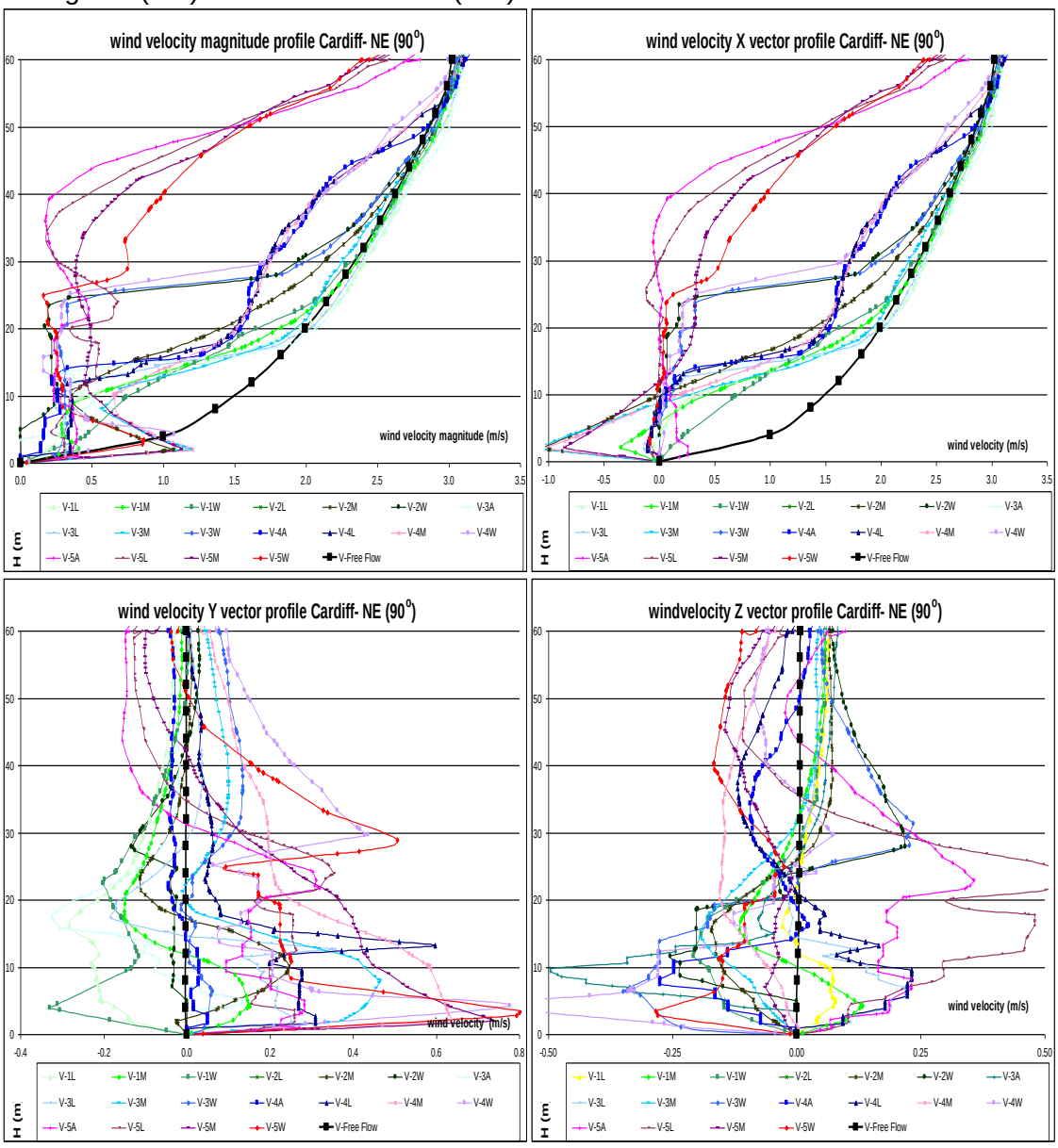

Source: this study.

8.3.3. East winds

East winds are oblique (45^{o}) to Museum Ave. and parallel (0^{o}) to Park Place. The courtyard side of MA faces windward, while the MA's external face faces leeward.

The comparison between the two methods of simulation presents a good match for PP's external face (parallel to the flow), while on the other faces the results on their upper side of the CFD simulations present lower Cp results as contrasted to those of WT (up to 0.30- see Figure 8-8). On the other hand, the ΔCp across the blocks matched well at top height, with a total difference between the CFD and the WT ΔCp resuts of less than 0.05 at 15m and up to 12.5 at 9.0m high.

East winds first reach a few tall buildings positioned upwind in the MA canyon, which creates a leeward wake that surrounds the courtyard area of the Law School building (see Figure 8-9). Within the canyon the pathlines reach the Welsh Assembly's vertical edge on the opposite corner to the area assessed and divide in two directions. The bulk of the flow that goes along the canyon clearly acquires a vortex pattern which washes down the Law School's round corner on the other side of the avenue.

The vertical profiles of the wind velocity magnitude (Figure 8-10) show that some acceleration takes place on the Welsh Assembly's upwind corner. Moreover, the wind vector components describe a reverse flow in the y direction, which means a diagonal flow inside the canyon from the Welsh Assembly's upwind corner to the Law School's downwind corner. The z vector also shows that this flow is directed downwards at the beginning and upwards at this end.

Figure 8-8: Cp results for E winds: oblique (45°) to MA and parallel (0°) to PP.

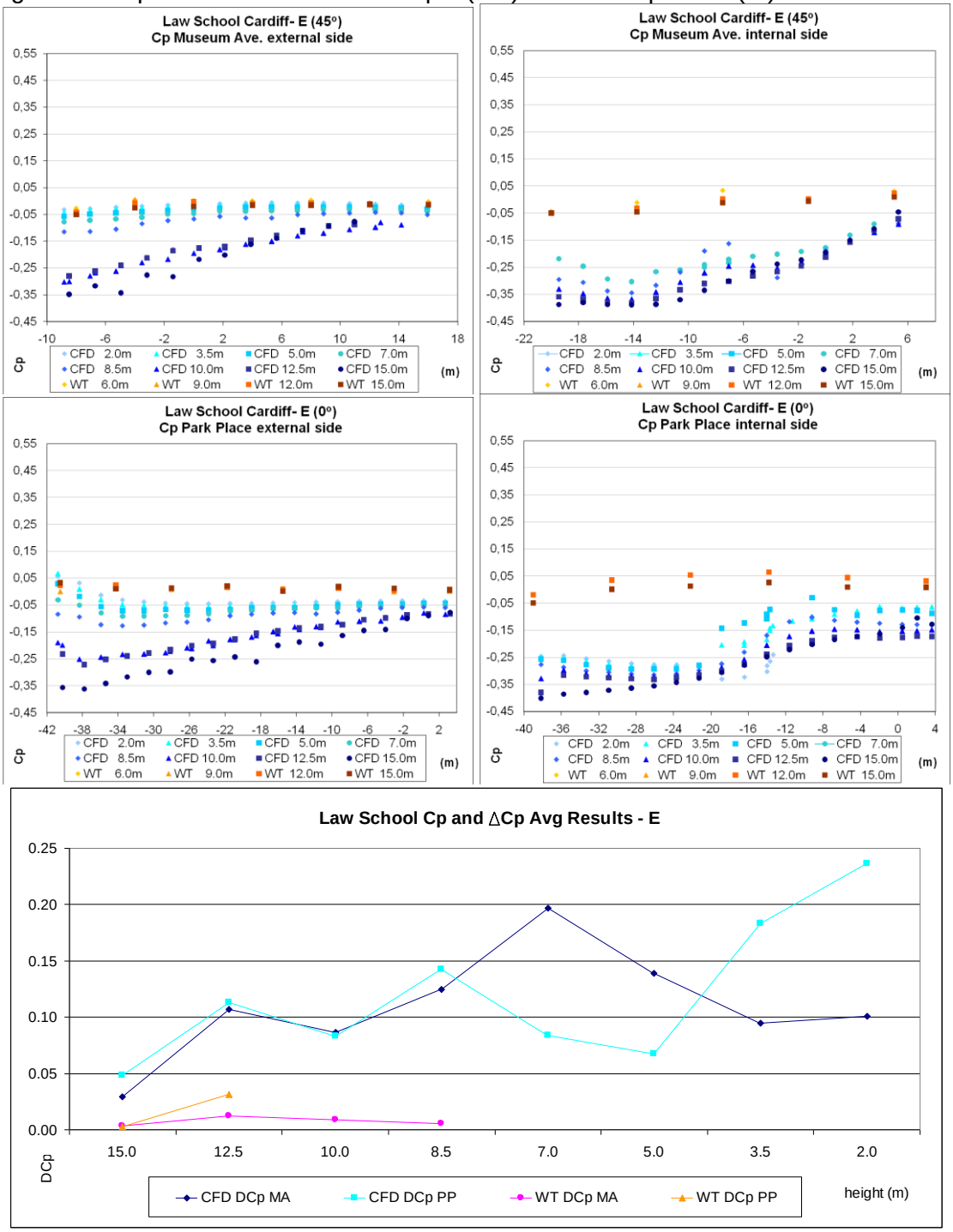

Source: this study.

Figure 8-9: East winds: oblique (45^{o}) to MA and parallel (0^{o}) to PP. Velocity magnitude airflow pathlines released from horizontal rakes at 05 and 15m height (m/s).

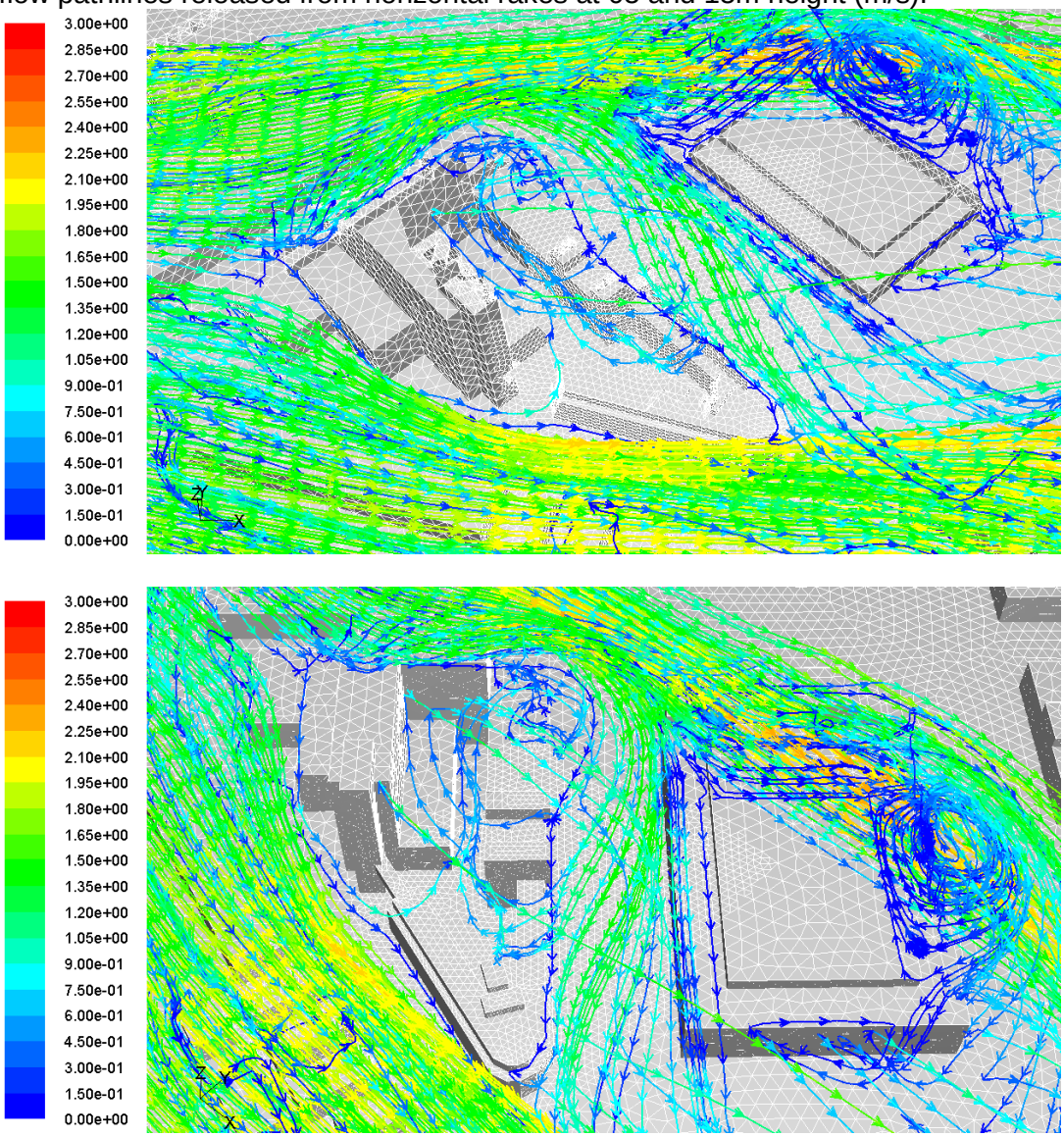

Source: this study.

Figure 8-10: Velocity magnitude and x, y and z vectors vertical profiles for E winds: oblique (45^{o}) to the Museum Ave. (m/s):

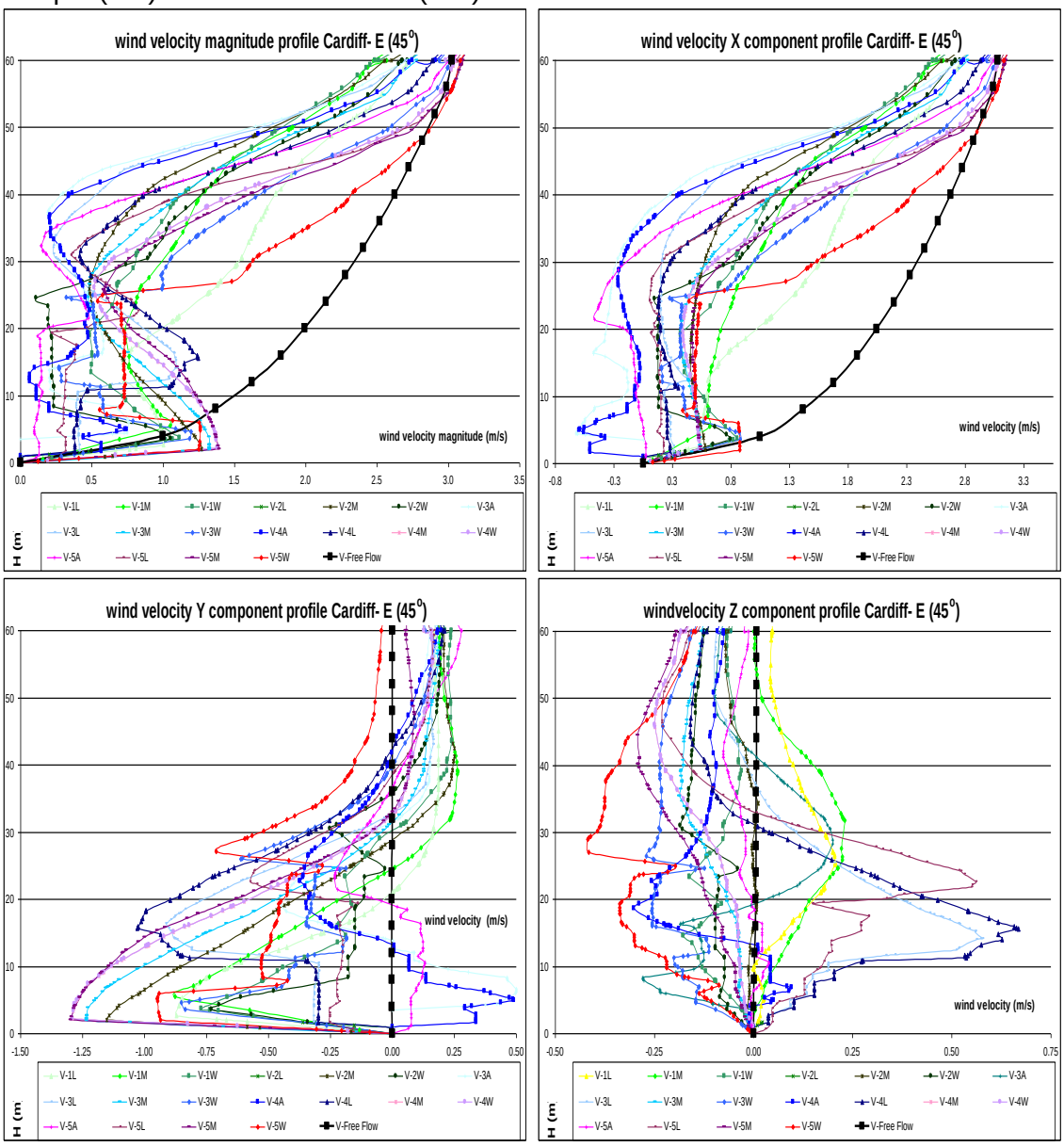

Source: this study.

8.3.4. Southeast winds

Southeast winds are parallel (0^o) to Museum Ave. with the Law School building positioned on its downwind side, and oblique (45^o) to Park Place. While the courtyard side of PP is to windward, the external side of PP is to leeward.

The Cp results on MA's external face match the WT and the CFD simulations well, although the numerical calculation is able to produce lower results due to a low pressure bubble on its upwind corner (Fgure 8-11). This occurs thanks to the level of accuracy that the CFD is able to achieve and which is not absorbed in the WT measurements, as already explained. The Cp results on the PP external face are higher in the CFD than in the WT by up to 0.12. In the courtyard the same event is observed on both the sides: while near the edges the Cp results are accurately matched, in the centre of the faces the CFD results are lower by up to -0.05 on the PP side and -0.25 on the MA side. The ΔCp is almost zero in both simulations across the PP block and for the WT result across the MA block. On the other hand, it reaches up to 0.15 in the CFD results for this latter block.

According to the airflow pathlines observed in Figure 8-12, a channelling effect occurs in both MA and PP canyons. Further, acceleration is seen right at the entrance to this latter one as a result of funnelling and Venture wind effects. A leeward wake created by a few tall buildings positioned upwind also causes a low intensity vortex in the courtyard. The pressure variation in this zone was possibly very difficult to measure accurately because of the small number of pressure taps positioned in the courtyard faces.

The vertical profiles of the wind velocity magnitude (Figure 8-13) show that the acceleration in the centre of MA's upwind side attains up to 1.5x the ABL velocity profile at 2.0m height. Moreover, the wind vector components inside the canyon describe a weak airflow deviation from the upstream direction.

Figure 8-11: Cp results SE winds: parallel (0º) to MA and oblique (45º) to PP.

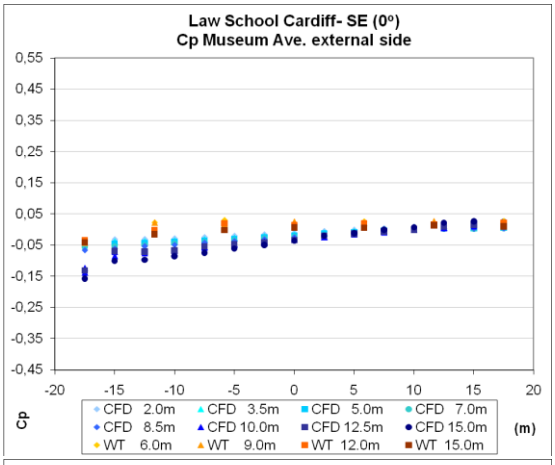

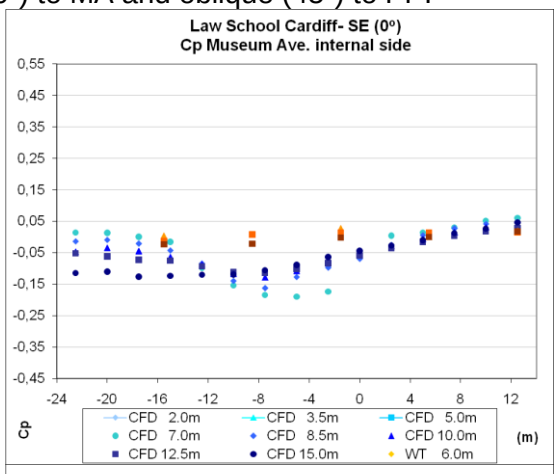

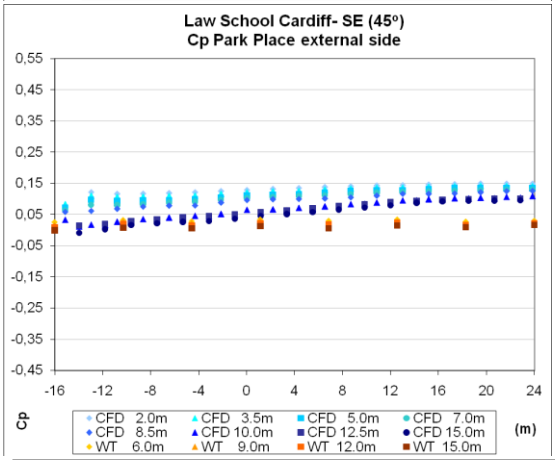

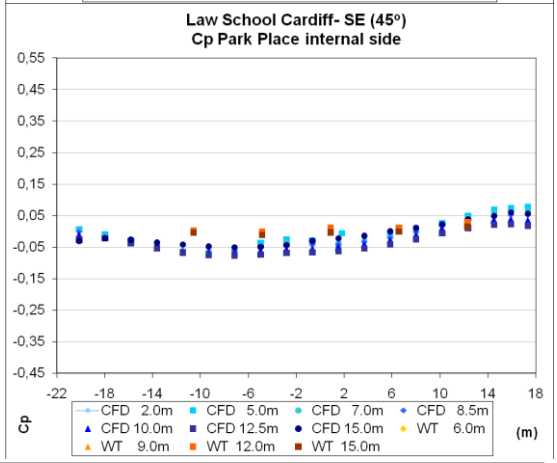

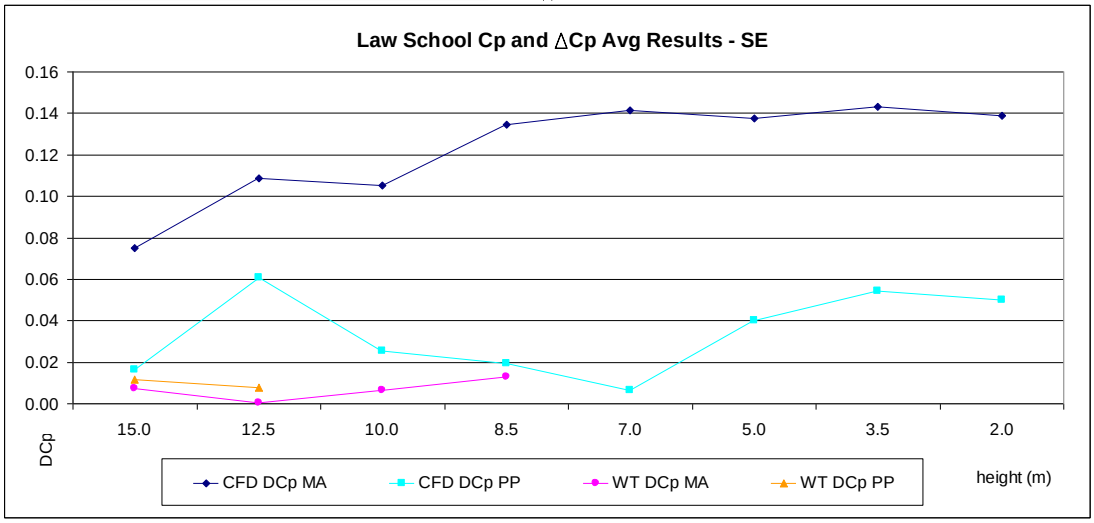

Source: this study.

Figure 8-12: Cp results for Southeast winds: parallel (0^o) to MA and oblique (45^o) to PP. Velocity magnitude airflow pathlines released from horizontal rakes at 05 and 15m height (m/s).

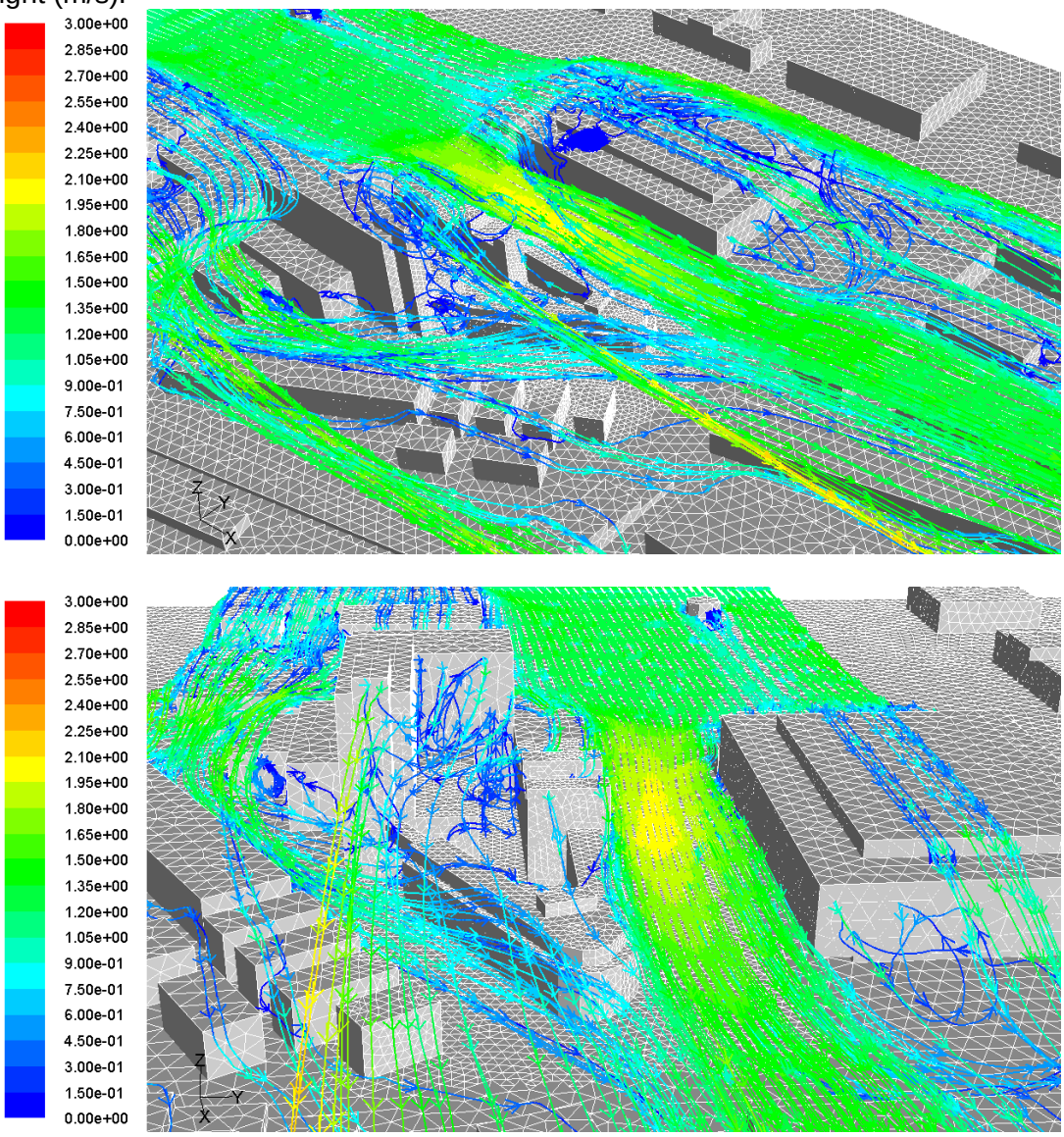

Source: this study.

Figure 8-13: Velocity magnitude and x, y and z vectors vertical profiles for SE winds: parallel (0^o) to the Museum Ave. (m/s):

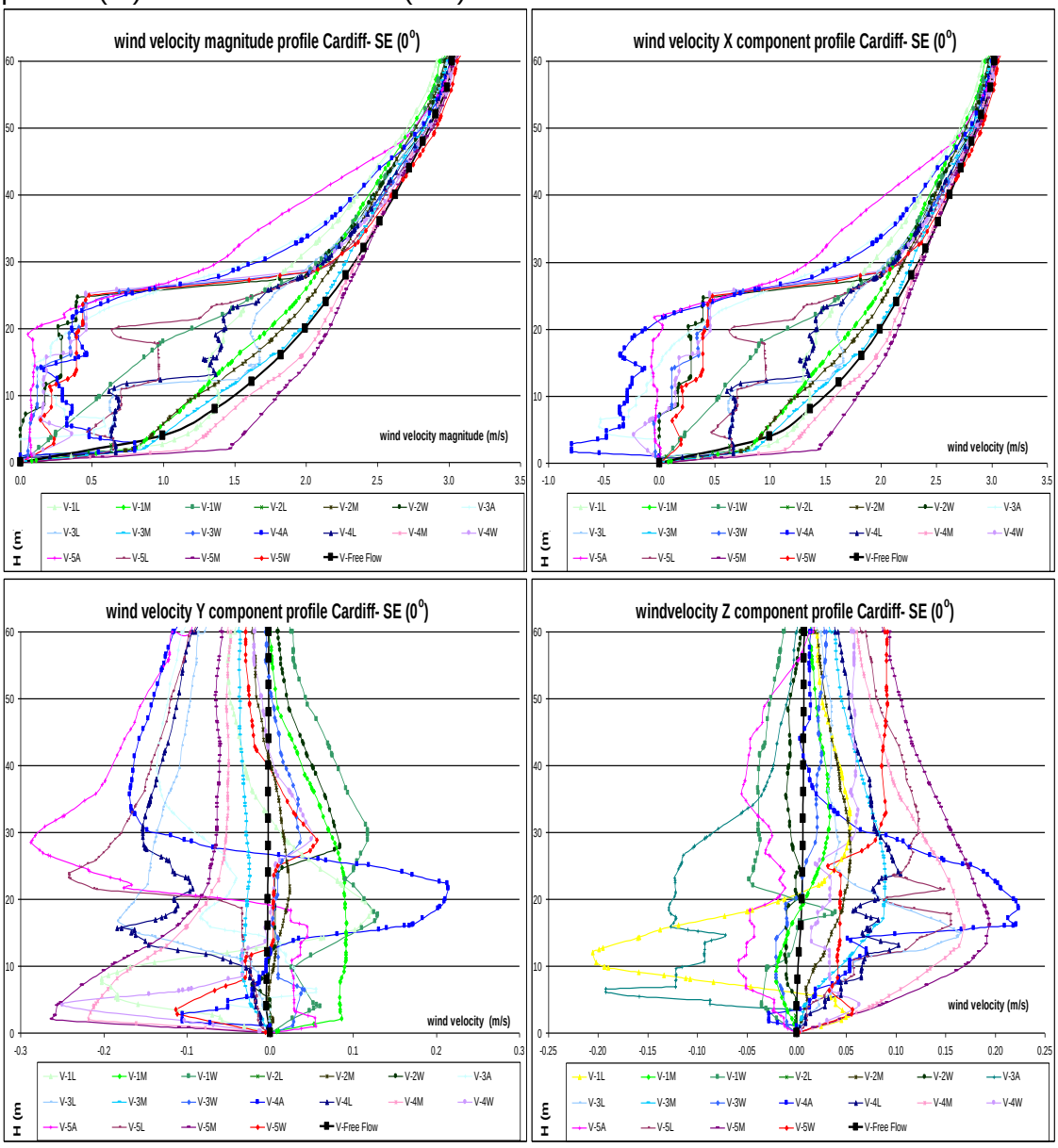

Source: this study

8.3.5. South winds

South winds are oblique (45^{o}) to Museum Ave. and orthogonal (90^{o}) to Park Place. Both the external side of MA and the courtyard side of the PP face the windward, while the courtyard side of MA and the external side of PP face leeward.

All the Cp results between the WT and the CFD simulations showed similarity of shape for the four sides investigated (both MA's and PP's external and courtyard faces), although the absolute difference between them was almost constant at 0.15 (Figure 8-14). On the other hand, the ΔCp matched well at top height. For the Law School wing towards PP this equivalence seems to continue, while for the wing towards MA the ΔCp difference between the results emerges at medium height, attaining the same 0.15 as was found between the pressure coefficient results.

South winds approach the assessed canyon diagonally. Since the Welsh Assembly building is around 7.0m higher than the Law School building, a step downwards scenario takes place inside the canyon. MA is to leeward of a taller building and should, therefore, diminish the bulk of the flow in its interior. On the other hand, some high-rise buildings in the Law School building's quarter deflected flow either upwards, which then accelerated, or downwards into the canyon, and which then seemed to blow throughout its length. Furthermore, it may be observed that the bulk of flow in PP comes from the opposite direction to that in MA (as may be observed in Figures 8-15 and 8-16).

The vertical profiles of wind velocity magnitude (Figure 8-17) show great acceleration of up to 2.5x the ABL velocity profile at 2.0m high. This was not was not captured by the airflow visualization pathlines. The acceleration occurs on the Welsh Assembly's downwind corner just opposite the Law School's round corner, where an existing passageway around this latter building may have created an airflow funnelling effect. Furthermore, the wind vector components describe an even diagonal flow with a slight vertical movement.

Figure 8-14: Cp results for S winds: oblique (45°) to MA and orthogonal (90°) to PP.

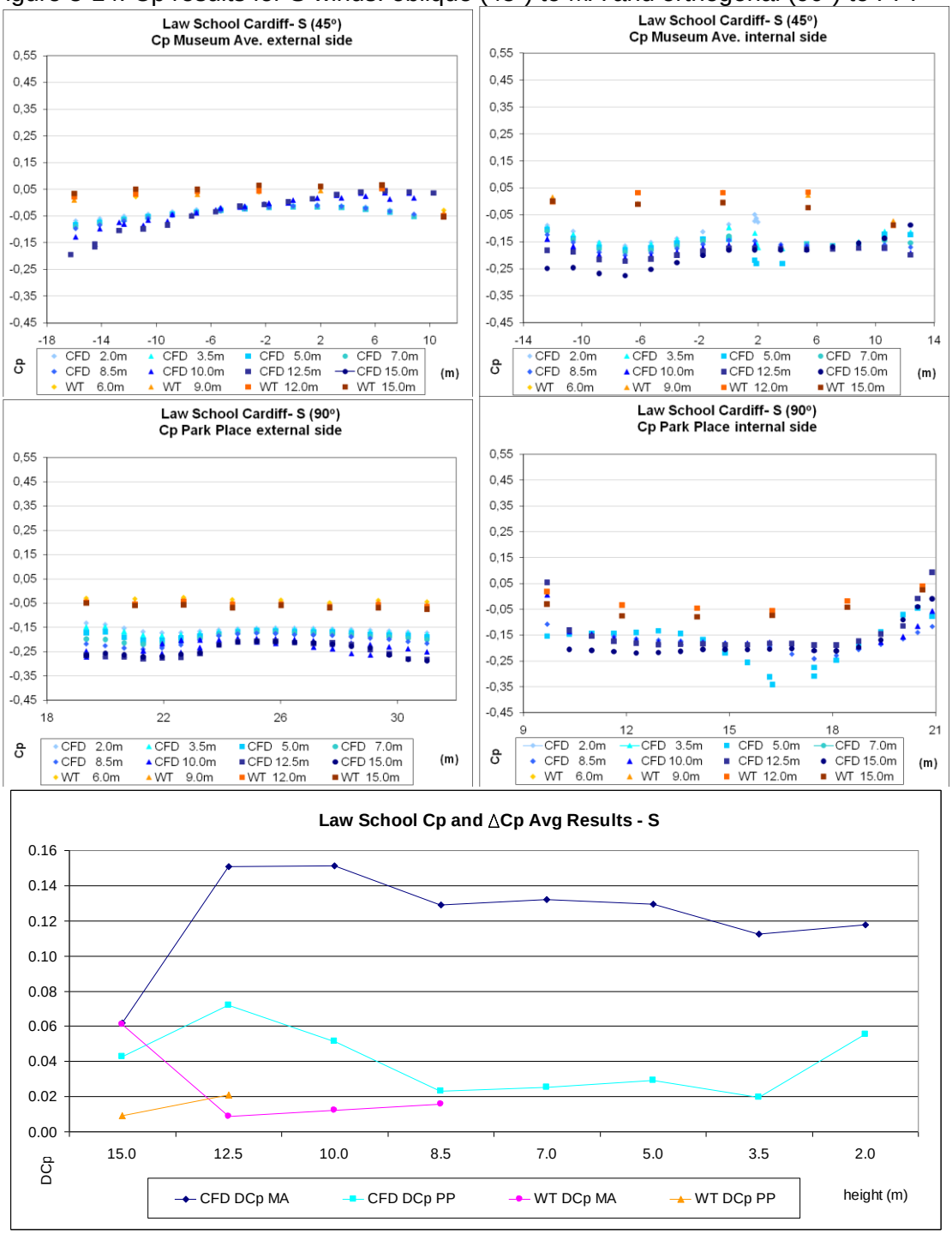

Source: this study.

Figure 8-15: South winds: oblique (45^{o}) to MA and orthogonal (90^{o}) to PP. Velocity magnitude airflow pathlines released from horizontal rakes at 05 (top) and 15m height (bottom) (m/s).

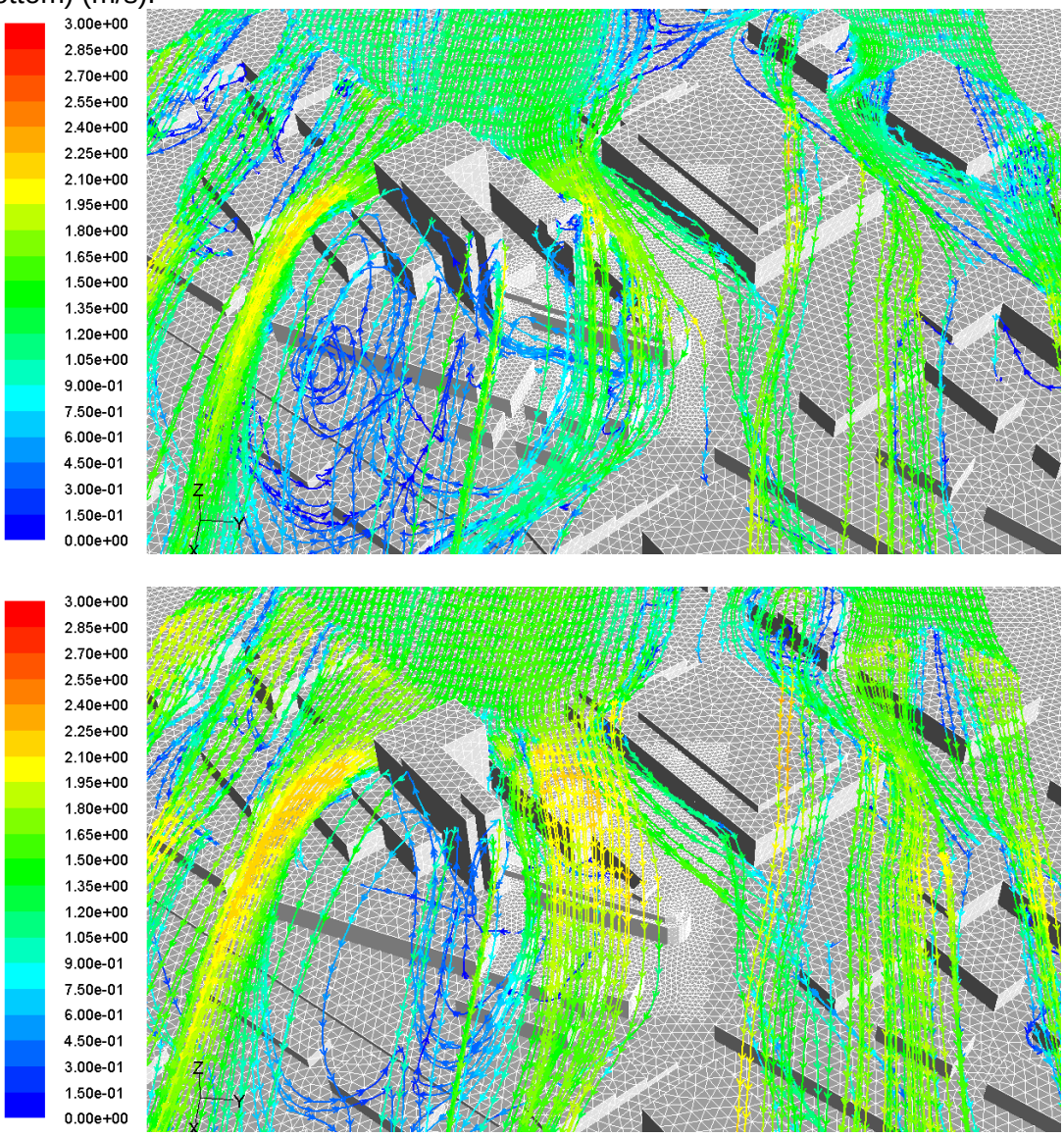

Source: this study.

Figure 8-16: South winds: oblique (45º) to MA and orthogonal (90º) to PP. Velocity magnitude airflow pathlines released from horizontal rakes at 05 (top) and 15m height (bottom) (m/s).

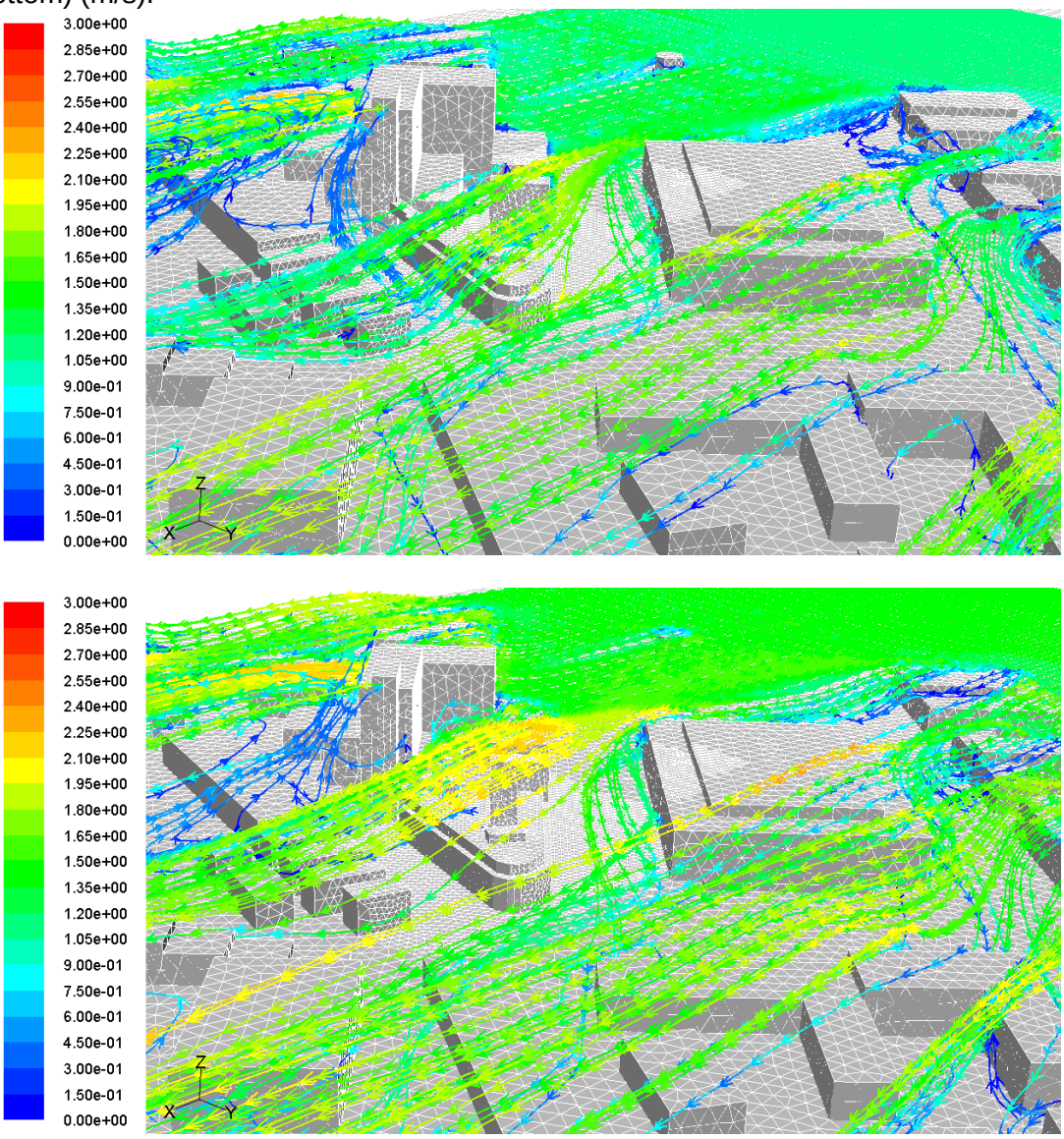

Source: this study.

Figure 8-17: Velocity magnitude and x, y and z vectors vertical profiles for S winds: oblique (45^{o}) to the Museum Ave. (m/s):

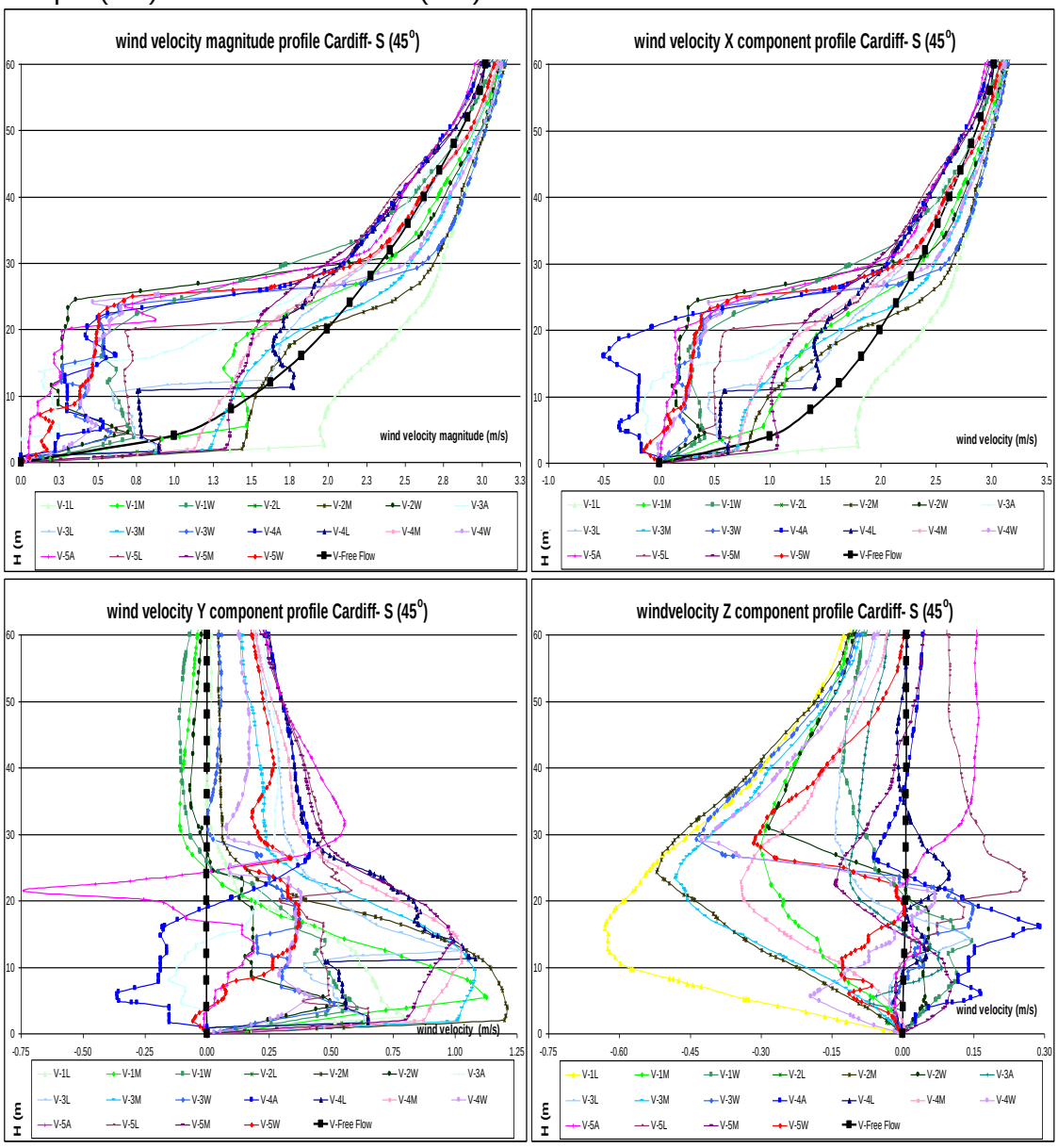

Source: this study.

8.3.6. Southwest winds

Southwest winds are orthogonal (90^{o}) to Museum Ave. and oblique (45^{o}) to Park Place. While both the external side of MA and the courtyard side of PP face windward, the courtyard side of MA and the external side of PP face leeward.

The comparison between the WT and the CFD simulations (Figure 8-18) shows a close similarity in the Cp distribution for the four sides investigated (both the MA's and the PP's external and courtyard faces), although the absolute difference between them was almost constant at 0.15, as an example of the results for South winds described in topic 8.3.5. Furthermore, while on both the MA's and PP's external sides the WT result is greater than the CFD's, the opposite occurs on both the courtyard's sides. The ΔCp across the MA's side of the building also matched well, while the pressure difference between the WT and the CFD simulations found for the MA block showed a disparity of up to 0.20 due to divergences in the courtyard face's Cp results.

The free airflow comes perpendicular to the canyon with the Welsh Assembly on the downwind side (Figures 8-19 and 8-20). A strong downward flow is observed on its windward face, which results in a clock-wise vortex with upward flow on the Law School's leeward side and towards the left side (Southeast) of MA. This direction is possibly powered by the low pressure area created in the leeward wake of tall buildings on the other edge of this canyon. Furthermore, acceleration is observed right above the top of the Law School in PP, and a weak vortex is formed in the courtyard.

The assessment of the vertical profiles of wind velocity magnitude (Figure 8-21) shows a reverse flow taking place near the Welsh Assembly's windward side and near the ground, with ascending flow near the Law School's leeward side on the canyon, which corroborates the flow vortex description just quoted.

Figure 8-18: Cp results for SW winds: orthogonal (90º) to MA and oblique (45º) to PP.

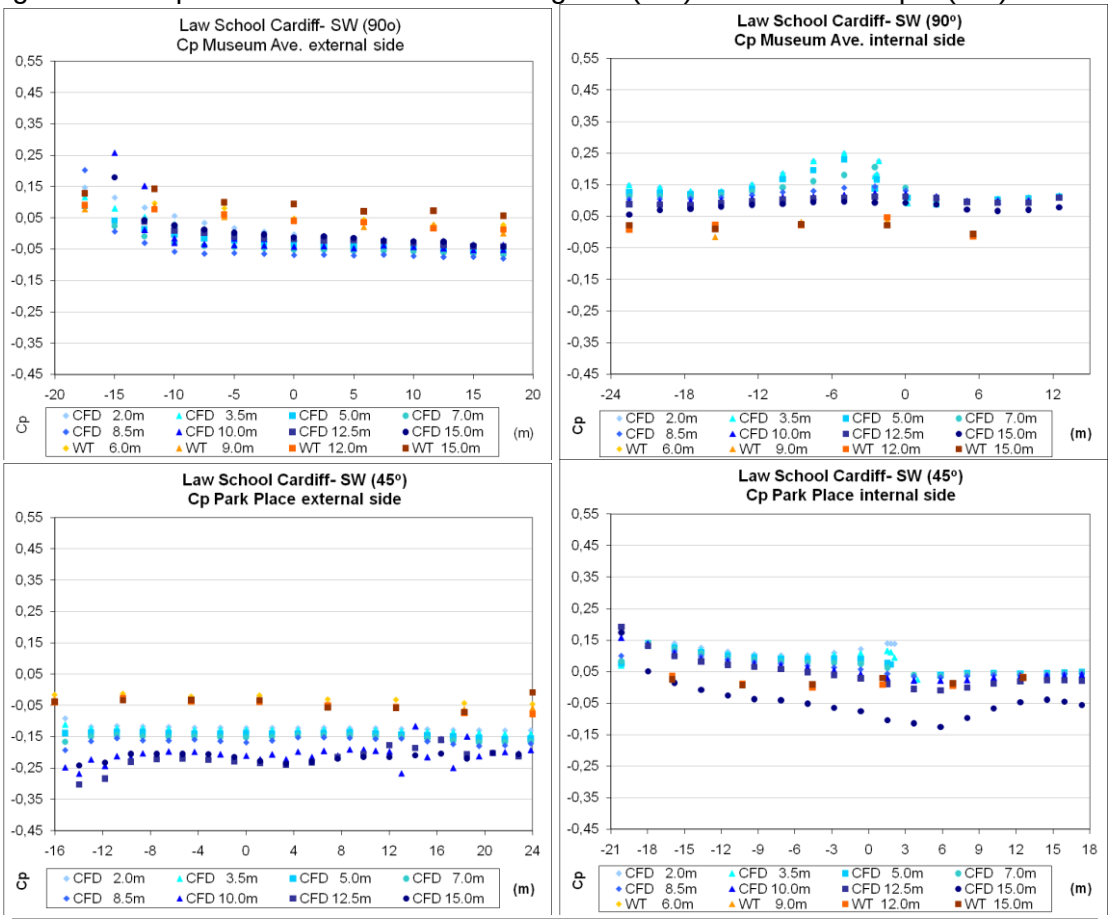

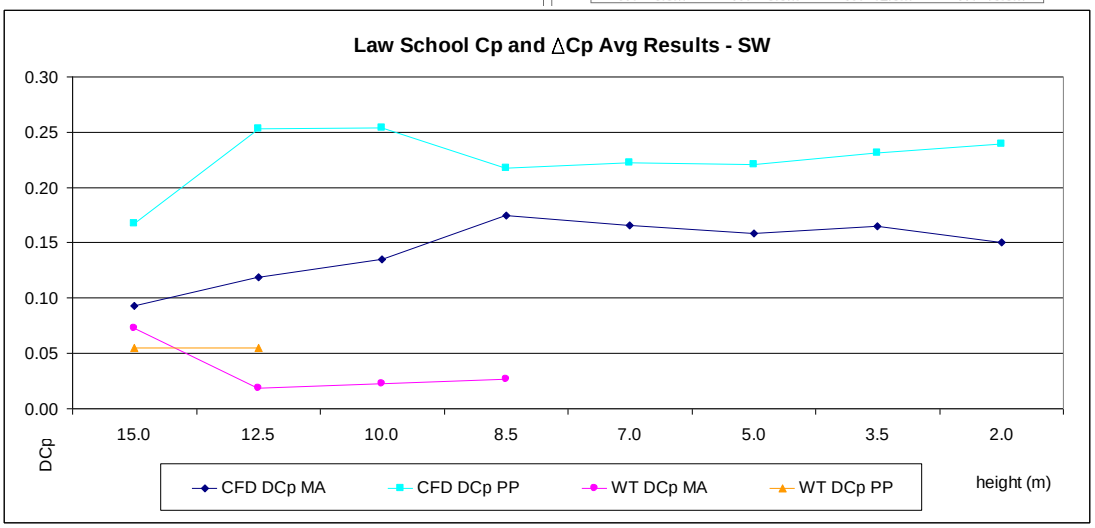

Source: this study.

Figure 8-19: Cp results for Southwest winds: orthogonal (90°) to MA and oblique (45°) to PP. Velocity magnitude airflow pathlines released from horizontal rakes at 05 and 15m height (m/s).

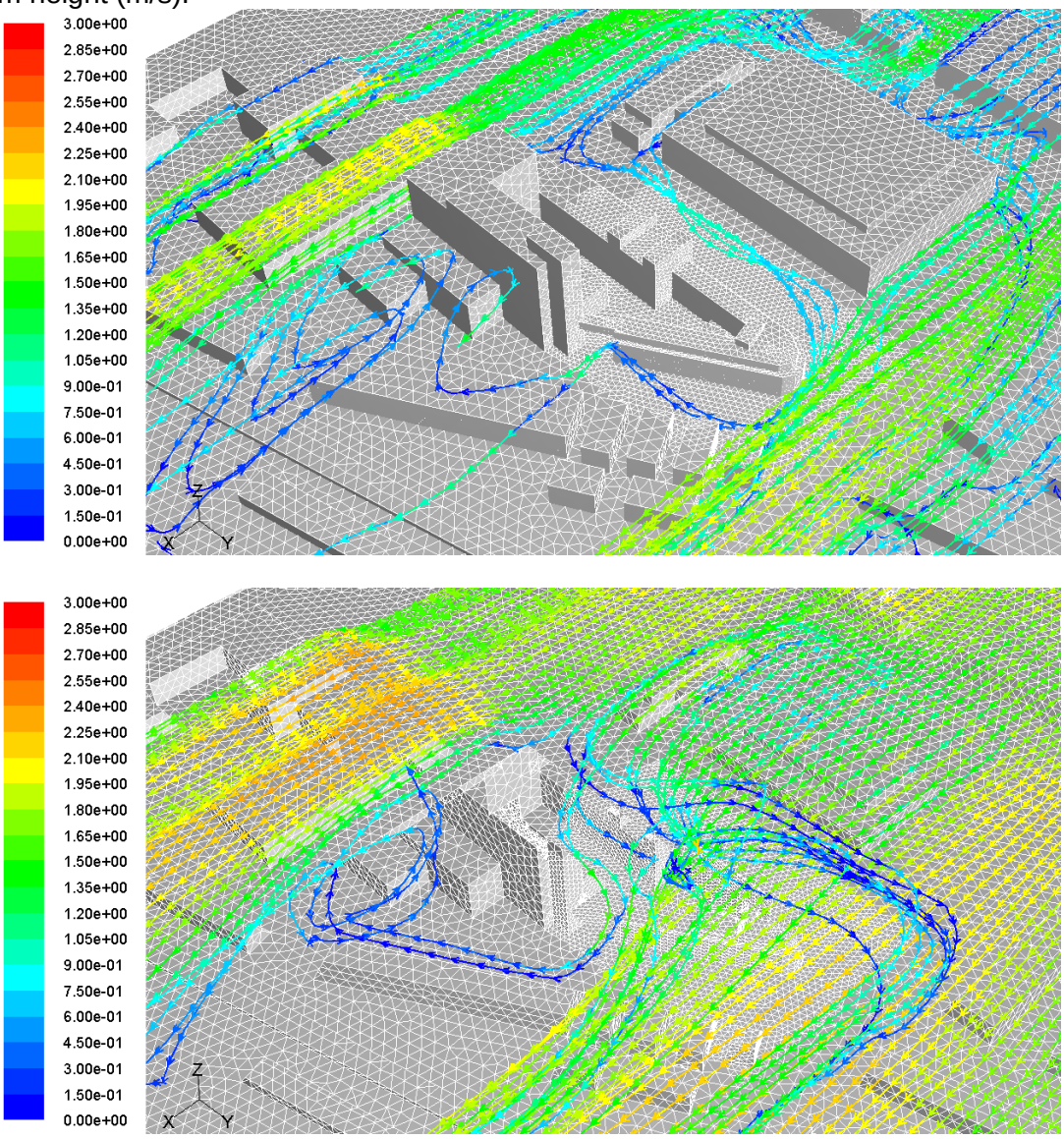

Source: this study.

Figure 8-20: Cp results for SW winds: orthogonal (90°) to MA and oblique (45°) to PP. Velocity magnitude airflow pathlines released from horizontal rakes at 05 and 15m height (m/s).

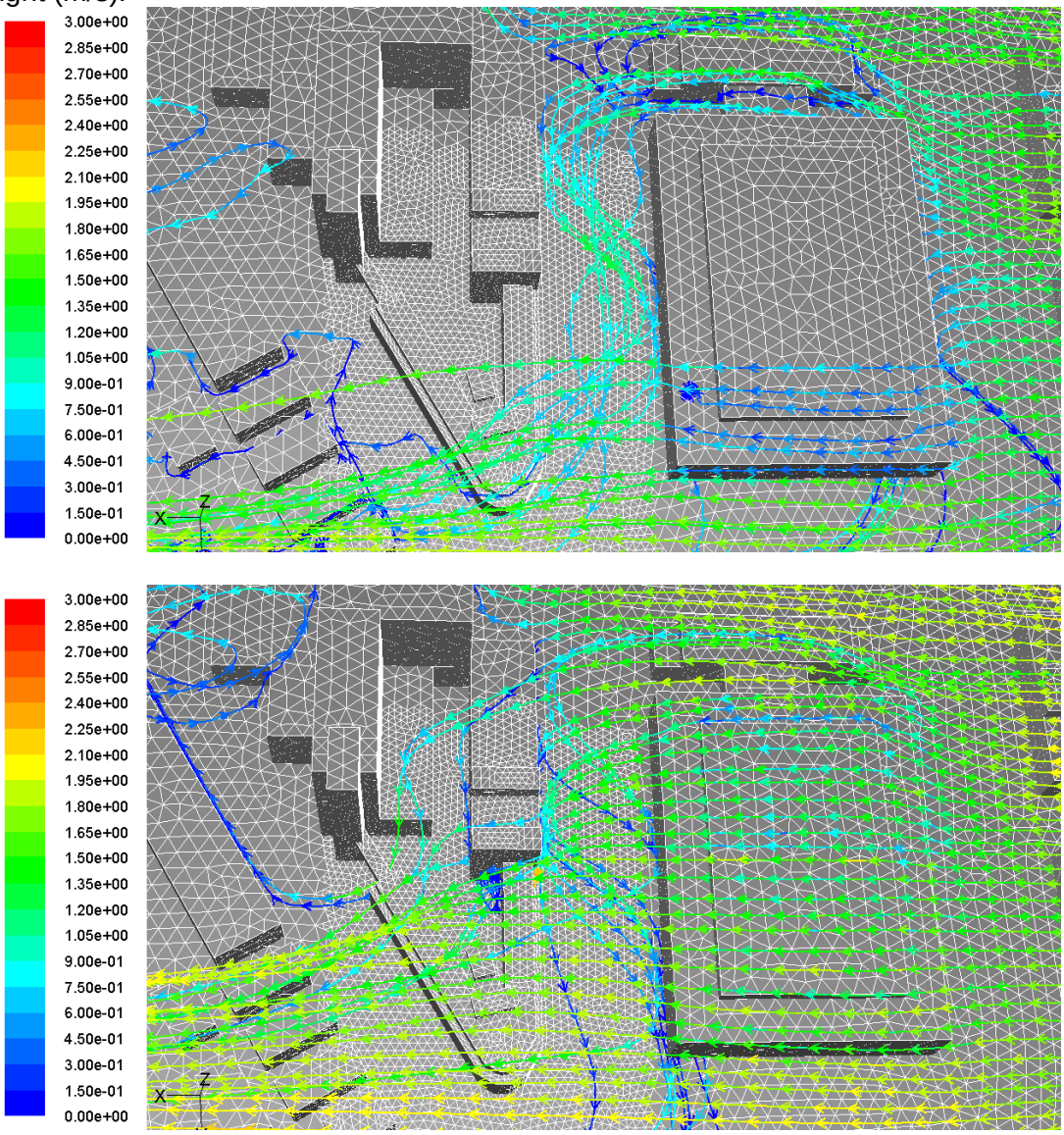

Source: this study.

Figure 8-21: Velocity magnitude and x, y and z vectors vertical profiles for SW winds: orthogonal (90°) to the Museum Ave:

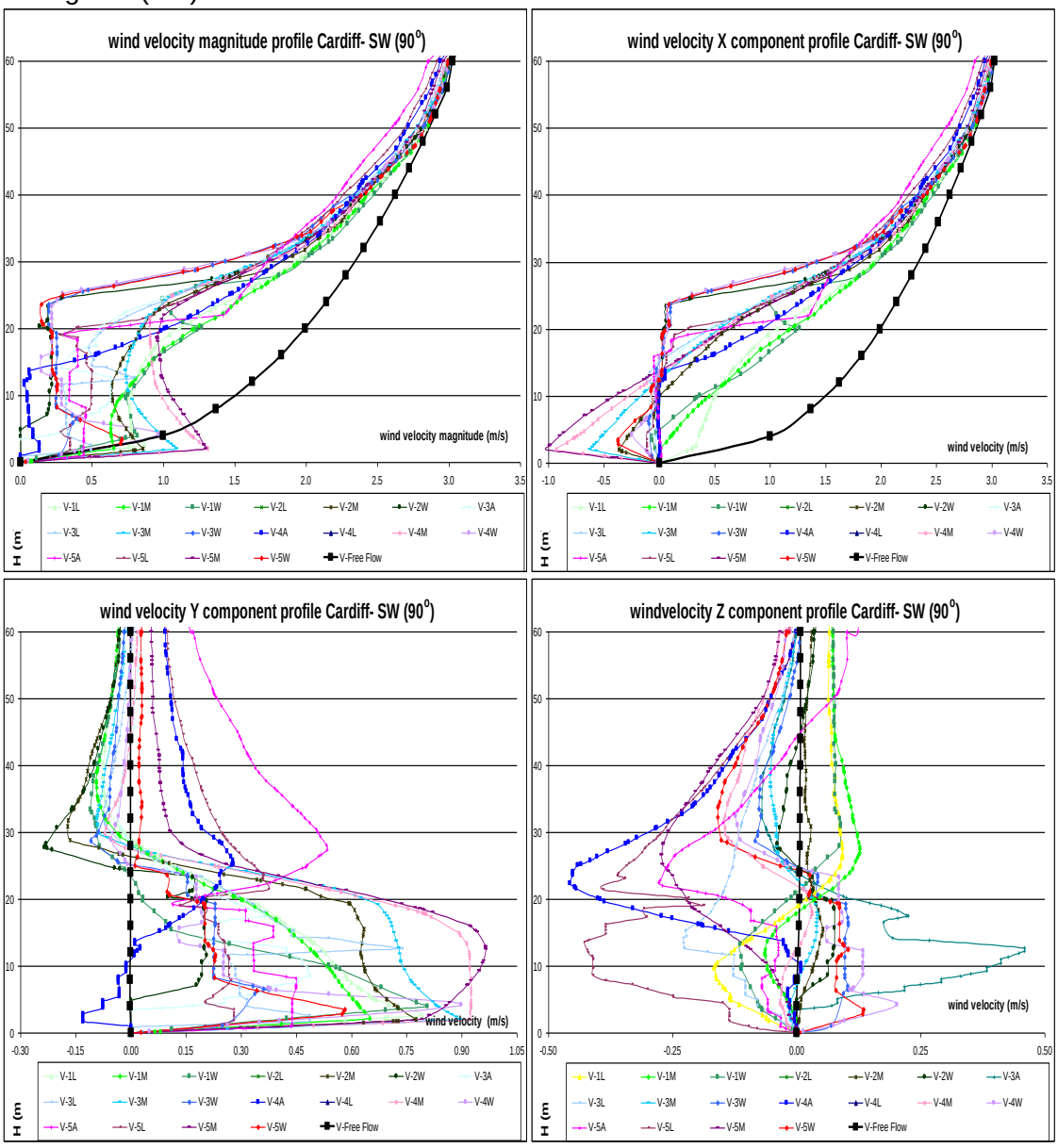

Source: this study.

8.3.7. West winds

West winds are: oblique (45^{o}) to Museum Ave. and parallel (0^{o}) to Park Place. While MA's external side faces windward, its courtyard side faces leeward.

For West winds the Cp results from the CFD simulations showed greater variation and oscillation than those from the WT physical experiments (see Figure 8-22). The four sides investigated (both the MA's and the PP's external and courtyard faces) have points with results in common from both methods of simulation, although divergences of up to 0.25 may be observed in all sets of comparison, which is more than that found in the previous wind direction analyses. On the other hand, the ΔCp matched precisely on both the PP and the MA blocks, with no variation between the WT and the CFD results greater than 0.04.

The West winds approach the canyon being assessed diagonally with the Welsh Assembly building on the upwind side. Once more a step downwards scenario is observed inside the canyon, turning the airflow away from the canyon cavity. Figure 8-23 also shows that a vortex occurs throughout the canyon from the upwind corner to the downwind corner. It first bounces off the Law School's windward side and is then deflected towards the Welsh Assembly's leeward side. In Figure 8-24 may be observed that this twisted flow acquires a vortex shape.

The vertical profiles of wind velocity magnitude and its vector components (Figure 8-25) show several changes of direction in the course of the height of these vertical profiles, which evidences the existence of a constant side-to-side loop in side to side of the canyon forming a spiral shaped flow pattern.

Figure 8-22: Cp results for W winds: oblique (45°) to MA and parallel (0°) to PP.

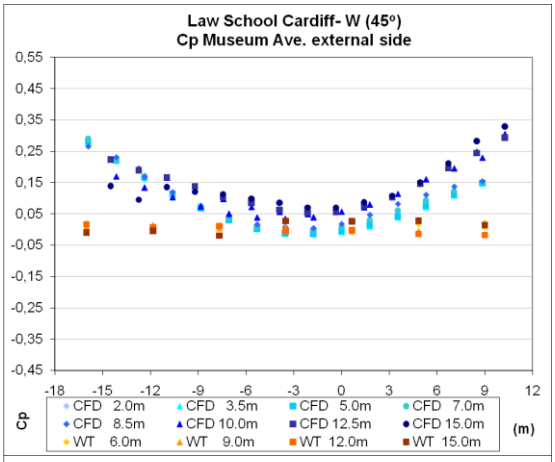

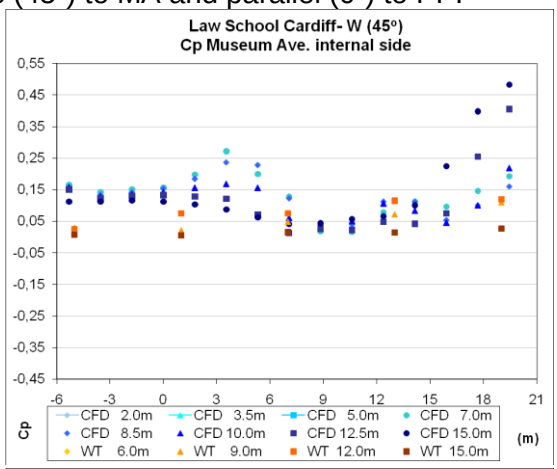

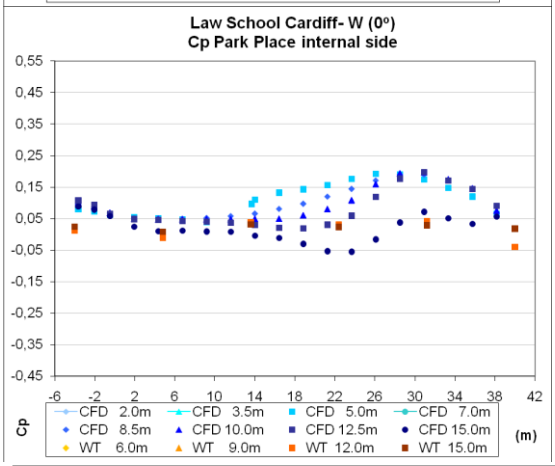

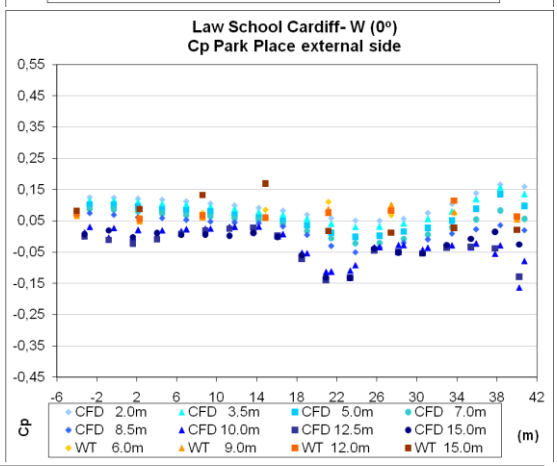

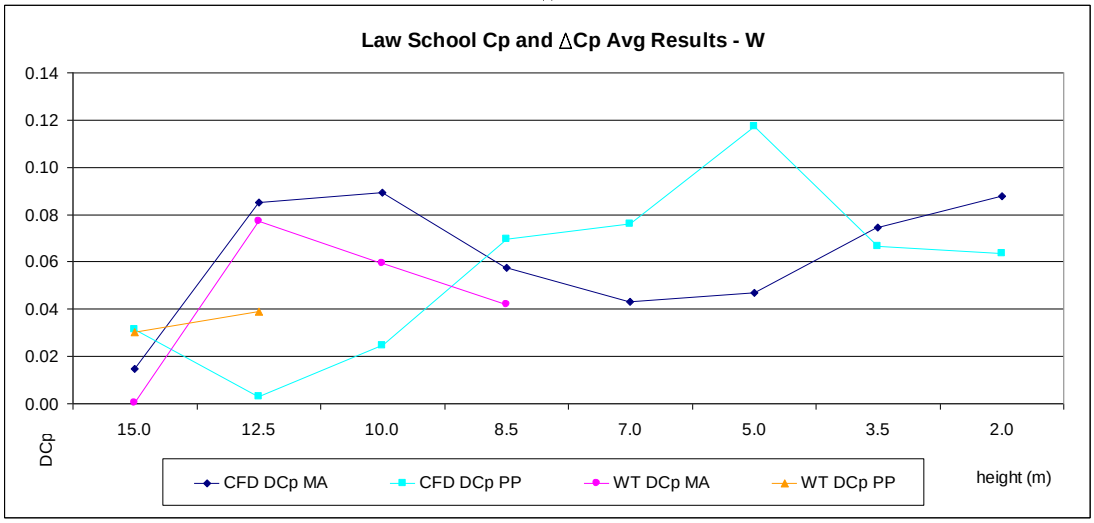

Source: this study.

Figure 8-23: Cp results for West winds: oblique (45°) to MA and parallel (0°) to PP. Velocity magnitude airflow pathlines released from horizontal rakes at 05 and 15m height (m/s).

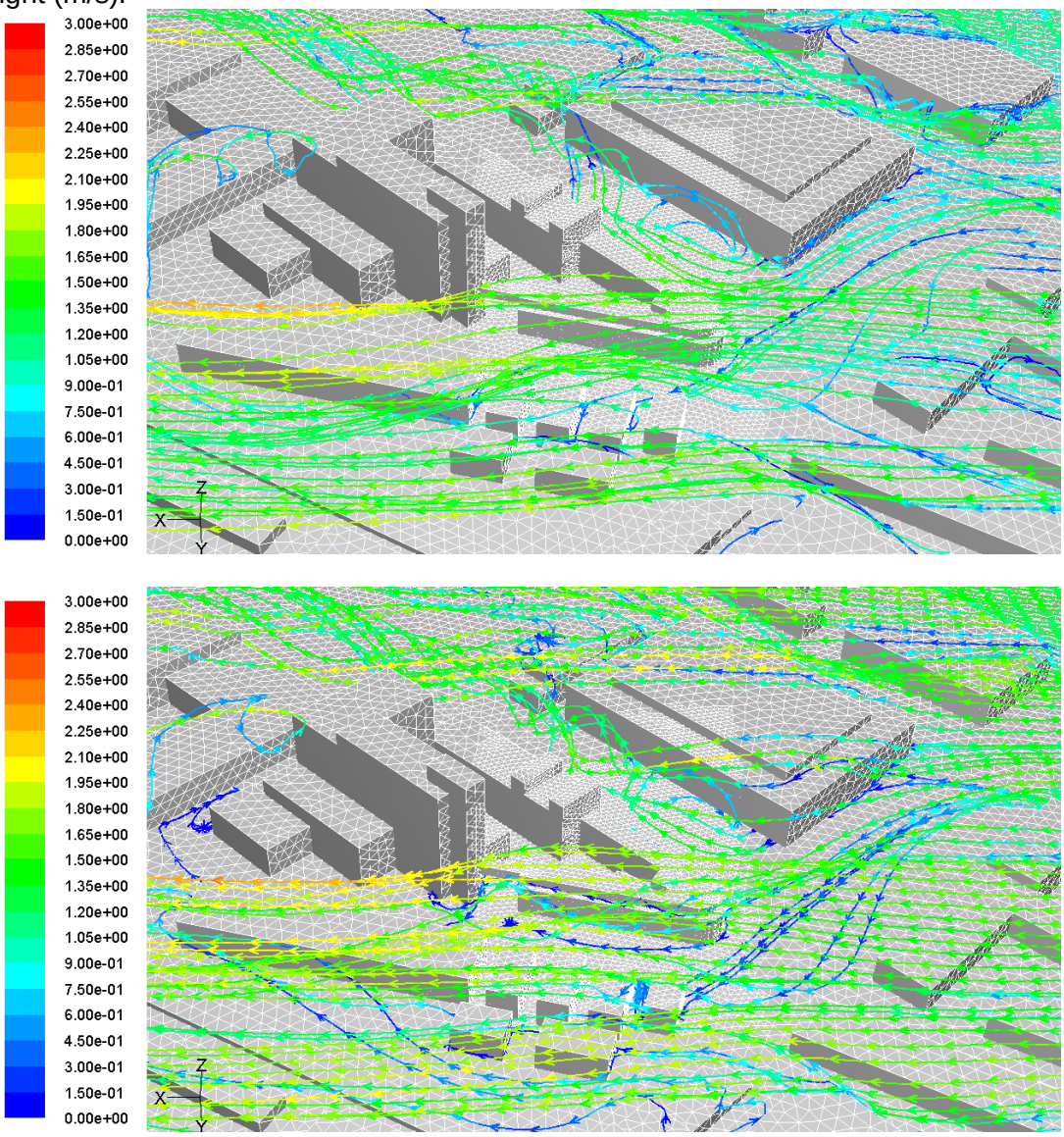

Source: this study.

Figure 8-24: Cp results for West winds: oblique (45^{o}) to MA and parallel (0^{o}) to PP. Velocity magnitude airflow pathlines released from horizontal rakes at 05 and 15m height (m/s).

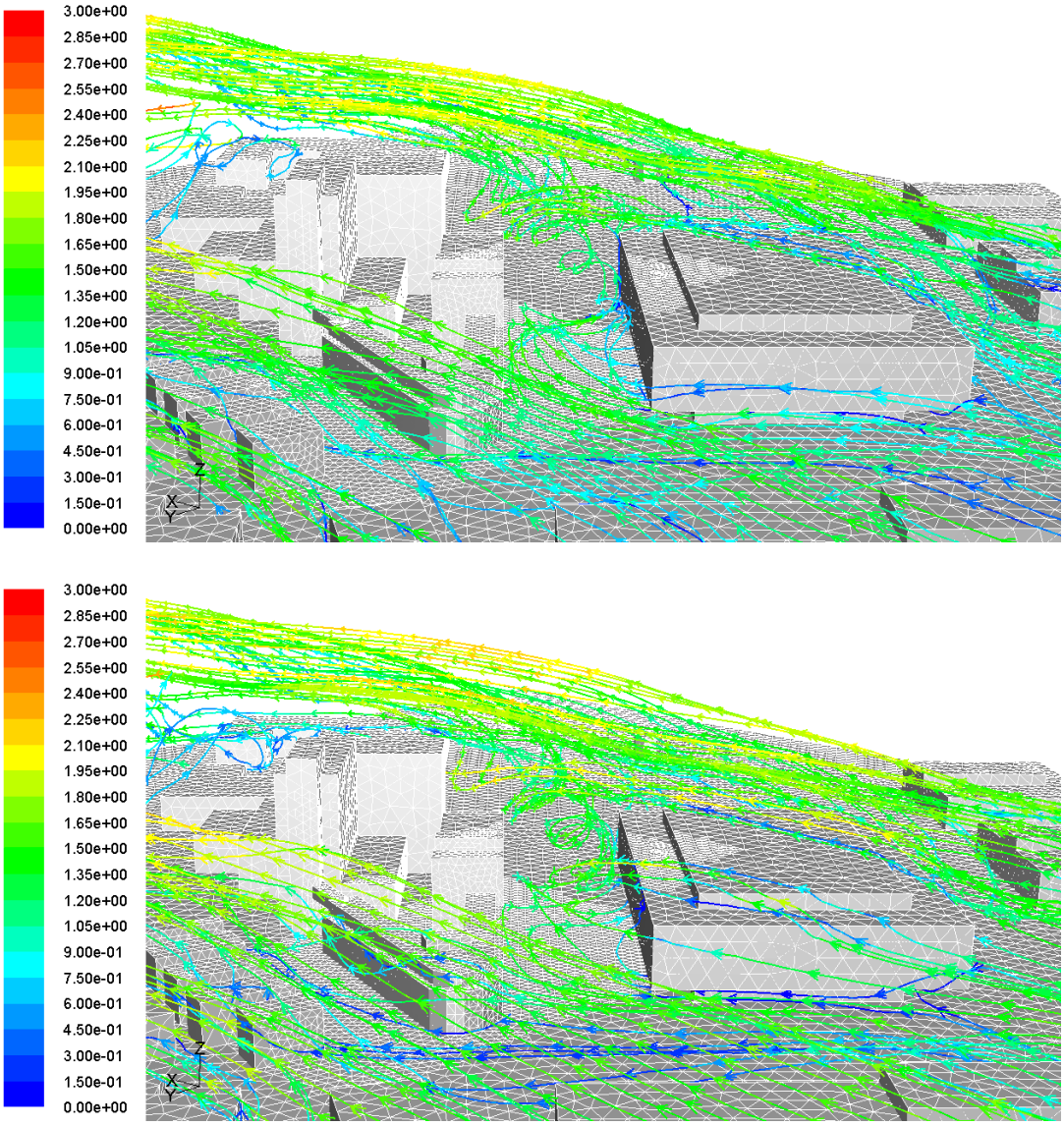

Source: this study.

Figure 8-25: Wind velocity magnitude and x, y and z vectors vertical profiles for W winds: oblique (45°) to the Museum Ave. (m/s):

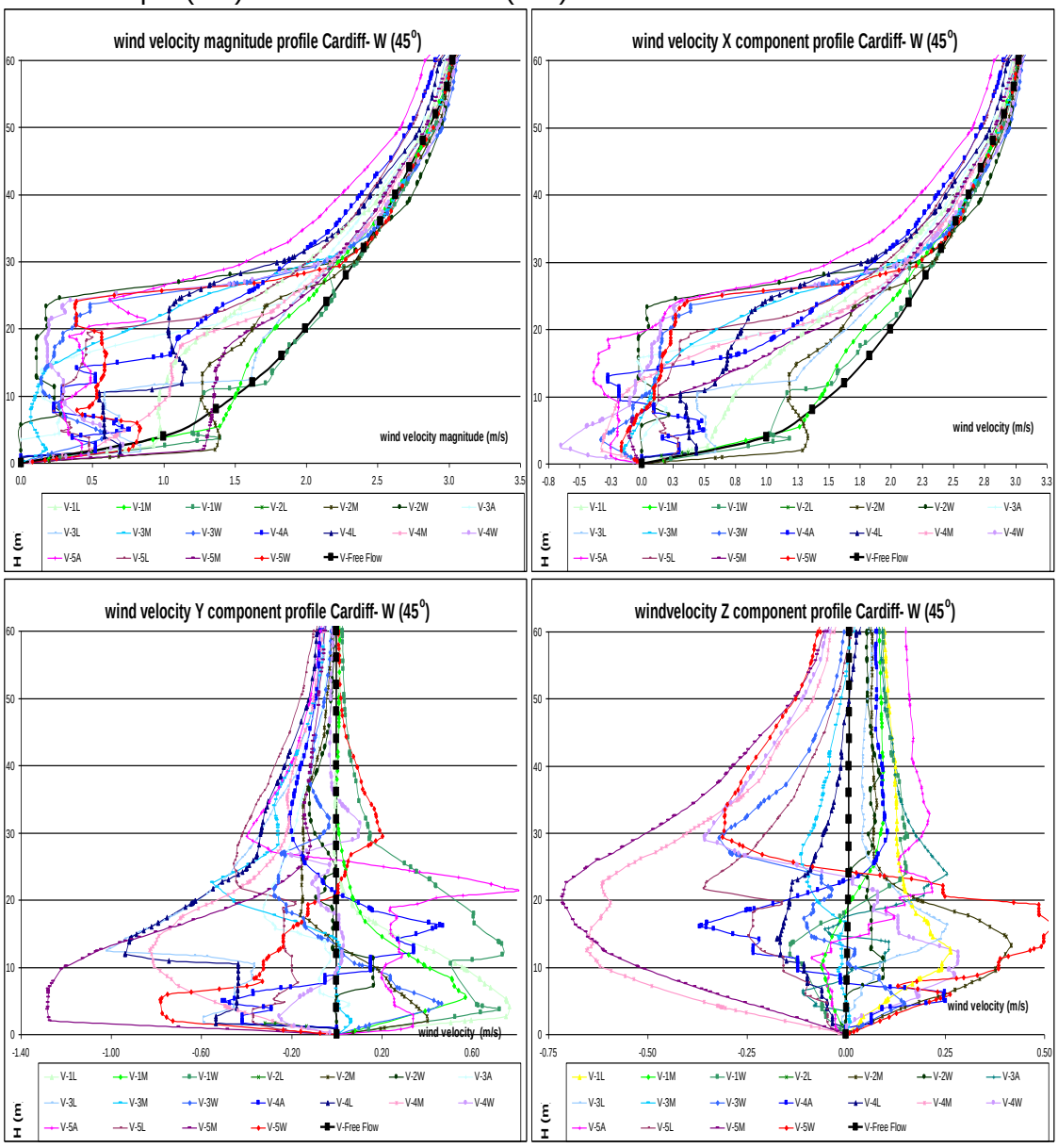

Source: this study.

8.3.8. Northwest winds

Northwest winds are parallel (0^o) to Museum Ave. and oblique (45^o) to Park Place. While the external side of PP lies windward, its courtyard faces leeward.

Good equivalence between the WT and the CFD simulation Cp results was found in the comparison of the four façades (both MA and PP external and the courtyards) since a difference no greater than 0.10 was observed in the range of results (see Figure 8-26). Furthermore, the same level of agreement was reported to occur in the ΔCp results across the windward and leeward sides of both the MA and the PP wings of the Law School building, with a maximum difference of 0.08 between the two methods of simulation employed in this investigation.

Regarding the airflow field, which is parallel to the canyon under investigation, it may be observed that few areas present acceleration (see Figure 8-27). The Northwest winds move towards MA with the Law School building to their upwind side. A spiral airflow pattern occurs from the upwind to the downwind corner of the canyon creating a low pressure bubble near the Welsh Assembly building.

The assessment of the vertical profiles of wind velocity magnitude (Figure 8-28) shows that some acceleration by a factor of 1.2x takes place at 15.0m height at both the beginning and the end of the canyon. The vector flow components register also some reverse flow on the x axis of the flow, inside the courtyard. Furthermore, intense side movement is observed in the y vector, transversely to the canyon and ranging from -0.45 to + 0.65m/s. Finally, both up and down flows seem to occur below 20.0m high. Above this height the airflow is all directed slightly upwards.

Figure 8-26: Cp results NW winds: parallel (0º) to MA and oblique (45º) to PP.

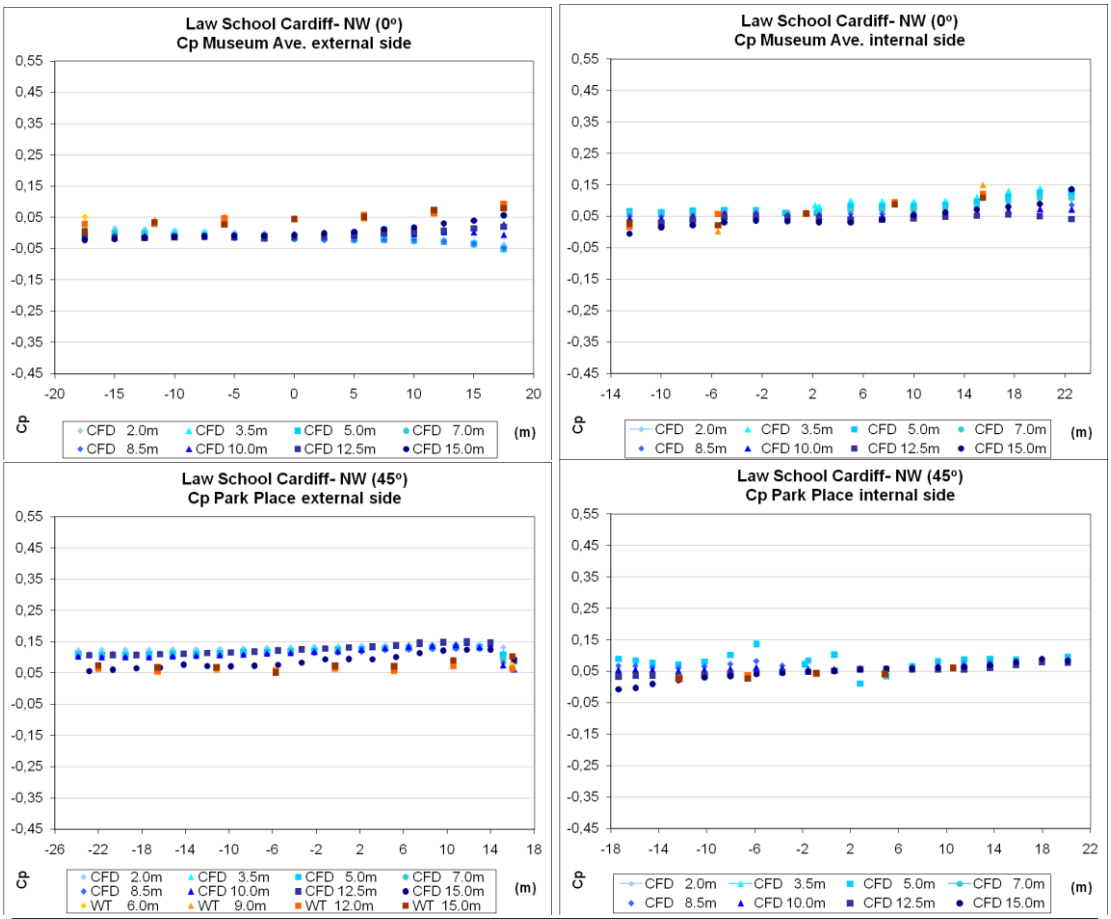

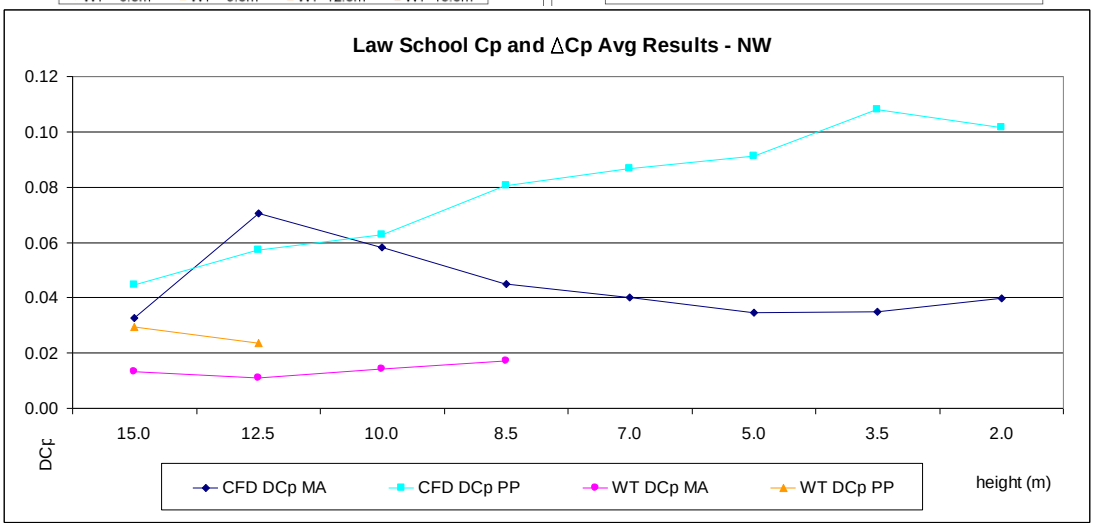

Source: this study.

Figure 8-27: Cp results for NW winds: parallel (0^o) to MA and oblique (45^o) to PP. Velocity magnitude airflow pathlines released from horizontal rakes at 05 and 15m height (m/s).

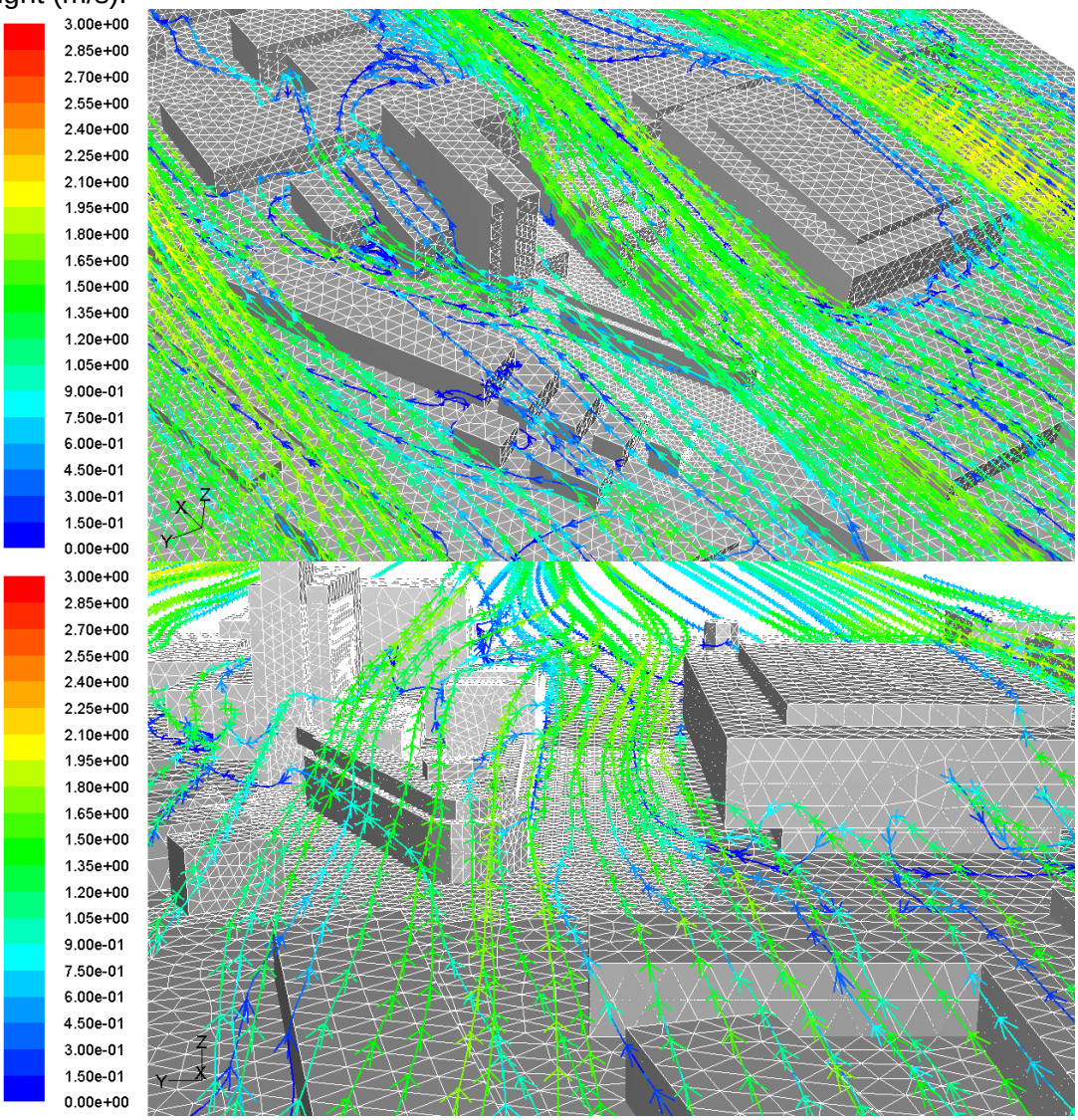

Source: this study.

Figure 8-28: Wind velocity magnitude and x, y and z vectors vertical profiles for NW winds: parallel (0^o) to the Museum Ave. (m/s):

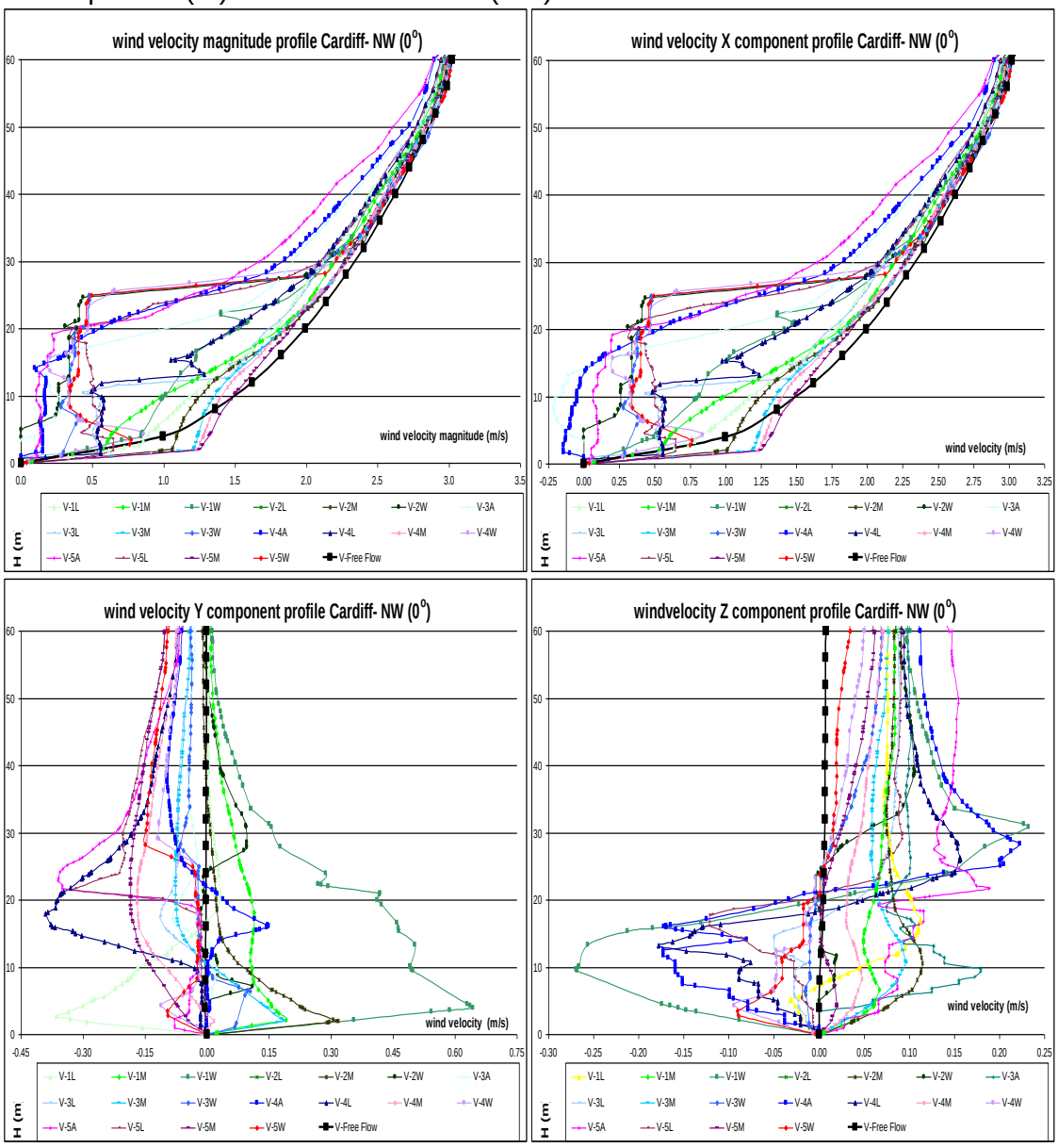

Source: this study.

8.3.9. Notes on the results and analyses

From the former comparative analyses of the Cp and ΔCp results from both CFD and WT simulations for the Cardiff University Law School building and the Museum Ave. urban canyon it may be observed that an absolute averaged difference of 0.10 and no greater than 0.15 was found between the two methods of investigation.

According to descriptions given in the literature[113], this difference is mentioned as acceptable for this purpose and scale of simulation of reality. Further, this difference kept constant on both the windward- leeward sides regardless the wind direction. Conversely, Cp results from Chapter 6[114] pointed to a disparity between the leeward side results from the CFD and WT simulations for orthogonal winds.

Moreover, this step of the research[115] sought to assess the first case study. The comparative analyses of different simulation techniques undertaken in this chapter have the further purpose of achieving an understanding of how an actual urban centre should be investigated. It was found, for instance, that a great number of pressure tap points would make WT physical experiments more accurate. This will be adopted in the second case study, covering the analysis of Paulista Avenue, in the city of São Paulo.

[113] See topics 3.4.4 and 3.5.3 in Chapter 3 for further information.
[114] Chapter 6 covers the two bricks experiments. For further information see topic 6.4.1.
[115] See step 3 of the proposed methodology in topic 5.2 of Chapter 5.

8.4. The field measurement data

Here the data from the Field measurements (FM) undertaken on the external façades of the Law School building at the 3rd floor are shown and contrasted with the WSA meteorological station (MS) data taken on the top of the Bute building, and provided by the CRiBE/ WSA. Two sets of probe were employed simultaneously in the following order: 01T and 02X; 02X and 03T; 02X and 04T; and 02X and 05T (data from the round of measurements taken on the probes 06T and 07X indicated a log error and could not therefore be used in the analysis).

Figure 8-29: The plan of the Law School's 3rd floor showing the positions of the FM probe equipment[116].

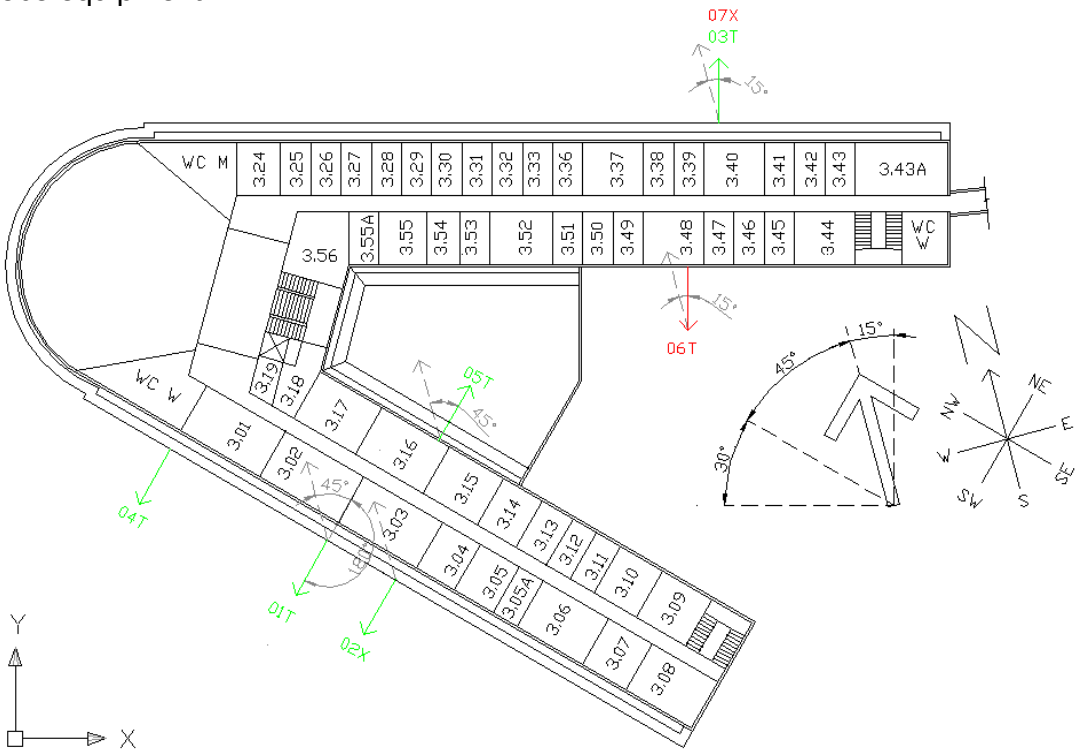

Source: this study.

[116] The pairs of probes that provided valid and comparable data are marked in green, while those which did not present sufficient data on either of the sources, e.g. one of the two probes or the WSA MS, are marked in red.

Table 8-1: Extent of the field measurement data collection for each probe and the period of probes contrasted marked as '[]'.

	22/04/09	23/04/09	24/04/09	25/04/09	26/04/09	27/04/09	28/04/09	29/04/09	30/04/09	01/05/09	02/05/09	03/05/09	04/05/09	05/05/09	06/05/09	07/05/09	08/05/09	Maintenance of the WSA MS set of equipment during this interval	21/05/09	22/05/09	23/05/09	24/05/09	25/05/09	26/05/09	27/05/09	28/05/09	29/05/09	30/05/09	31/05/09	01/06/09	02/06/09	03/06/09	04/06/09	05/06/09
probe 01T		[]	[]																														
probe 02X		[]	[]								[]	[]		[]	[]					[]	[]												
probe 03T											[]	[]																					
probe 04T														[]	[]																		
probe 05T																				[]	[]												
WSA data		[]	[]								[]	[]		[]	[]					[]	[]												

Source: this study.

8.4.1. Comparison of data from probes 02X and 03T.

The data from the WSA MS and the probes 02X and 03T[117] for wind speed and direction are here contrasted.

Figure 8-30: The wind speed direction (WSA MS; probes 02X; and 03T):

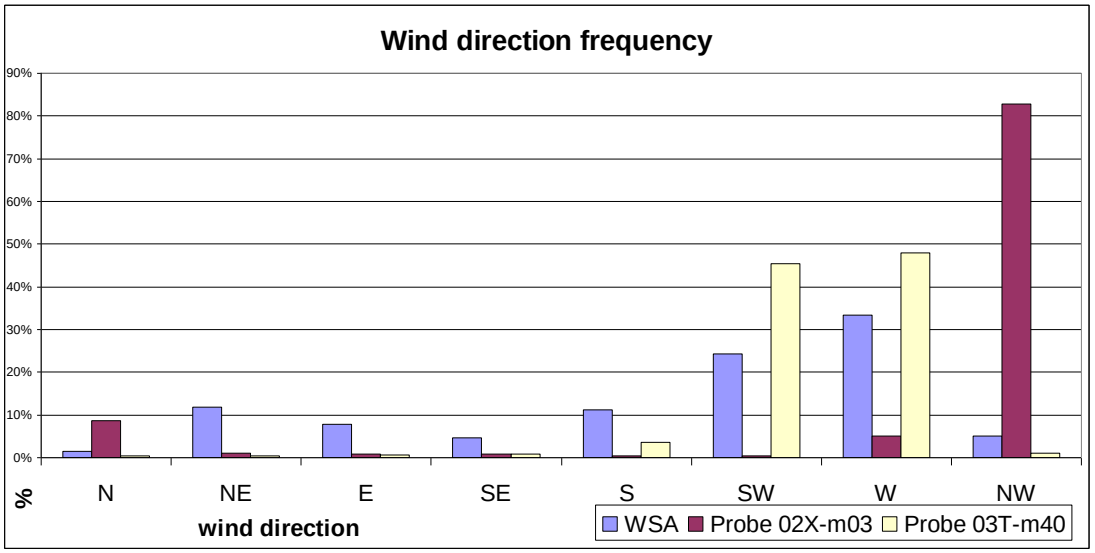

Source: this study.

Figure 8-31: The wind velocity magnitude (WSA MS; probes 02X; and 03T):

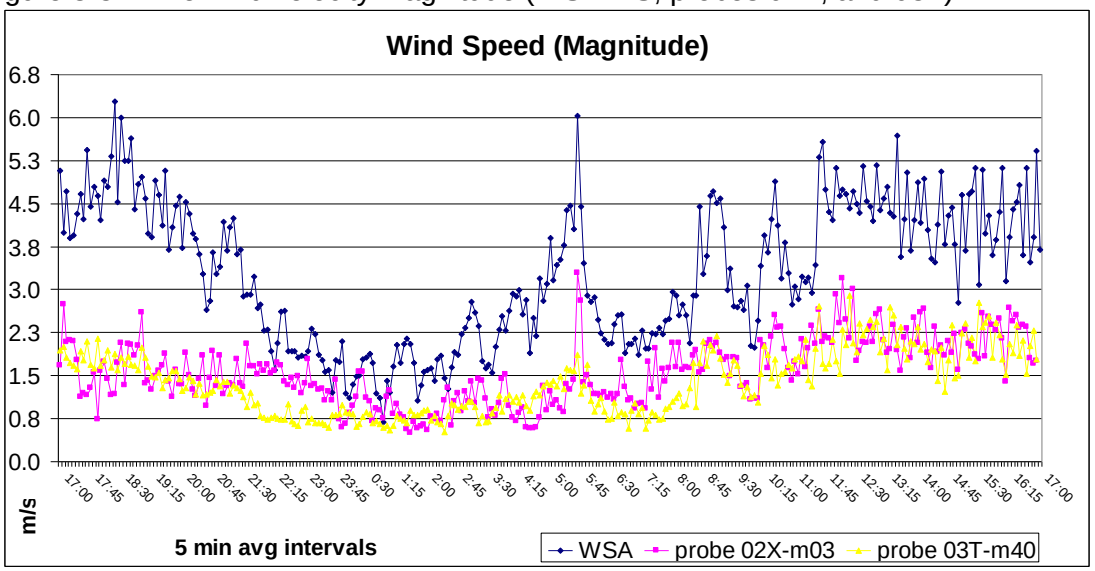

Source: this study.

[117] While probe 02X is positioned on the external side of the MA block in room m-03, probe 03T is positioned on the external side of the PP block in room m-40, both on the 3rd floor of the Law School building.

8.4.2. Comparison between data from probes 02X and 04T.

The data from the WSA MS and the probes 02X and 04T[118] for wind speed and direction are contrasted here.

Figure 8-32: The wind speed direction (WSA MS; probes 02X; and 04T):

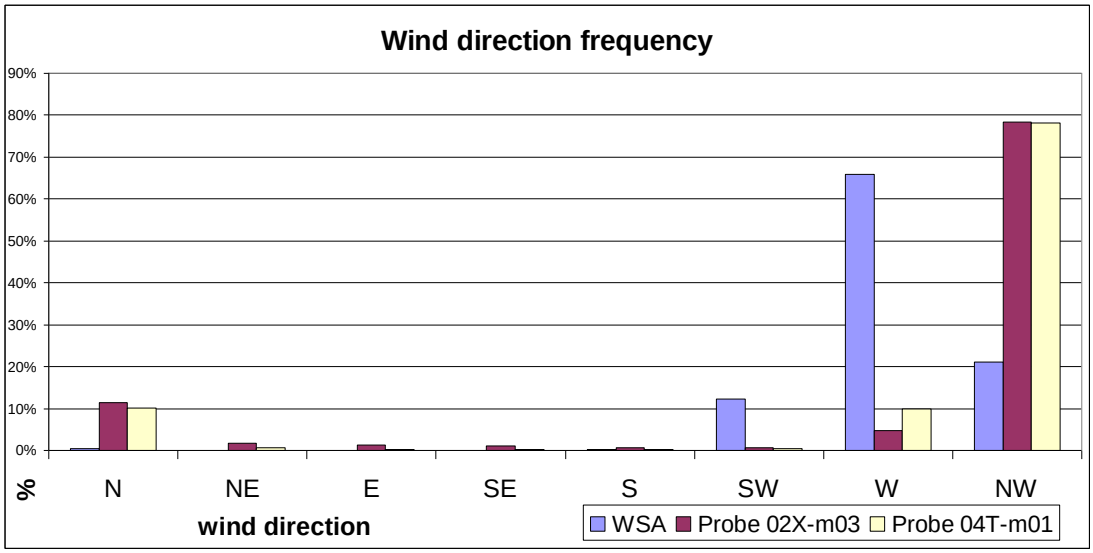

Source: this study.

Figure 8-33: The wind velocity magnitude (WSA MS; probes 02X; and 04T):

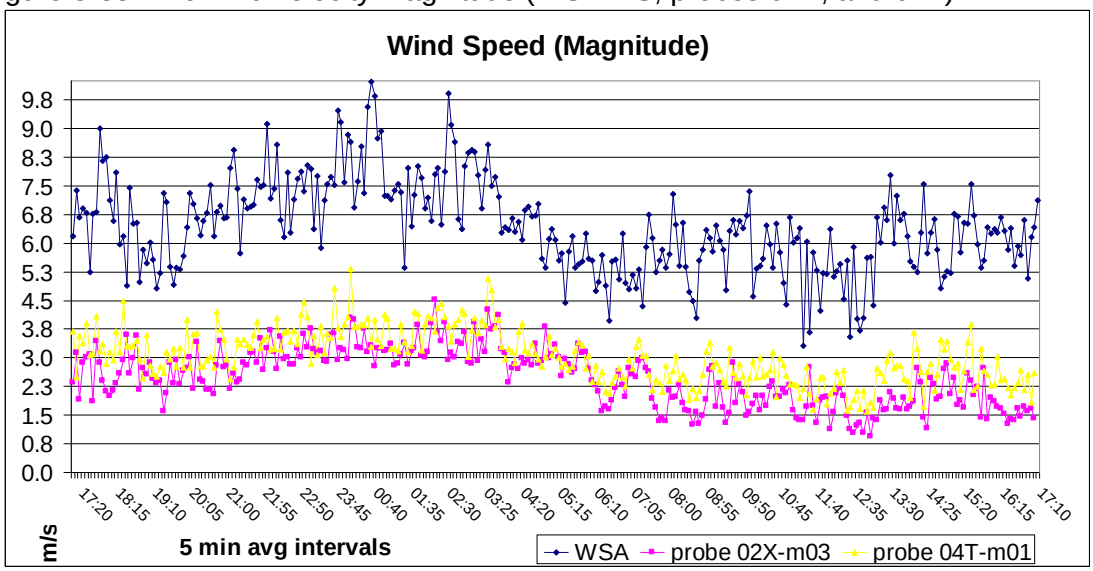

Source: this study.

[118] While the probe 02X is positioned in the external face of the MA block in room m-03, the probe 03T is also positioned in the same block face, but in room m-01Both rooms are on the Law School building 3rd floor.

8.4.3. Comparison between data from probes 02X and 05T.

The data from the WSA MS and the probes 02X and 05T[119] for wind speed and direction are contrasted here.

Figure 8-34: The wind speed direction (WSA MS; probes 02X; and 05T):

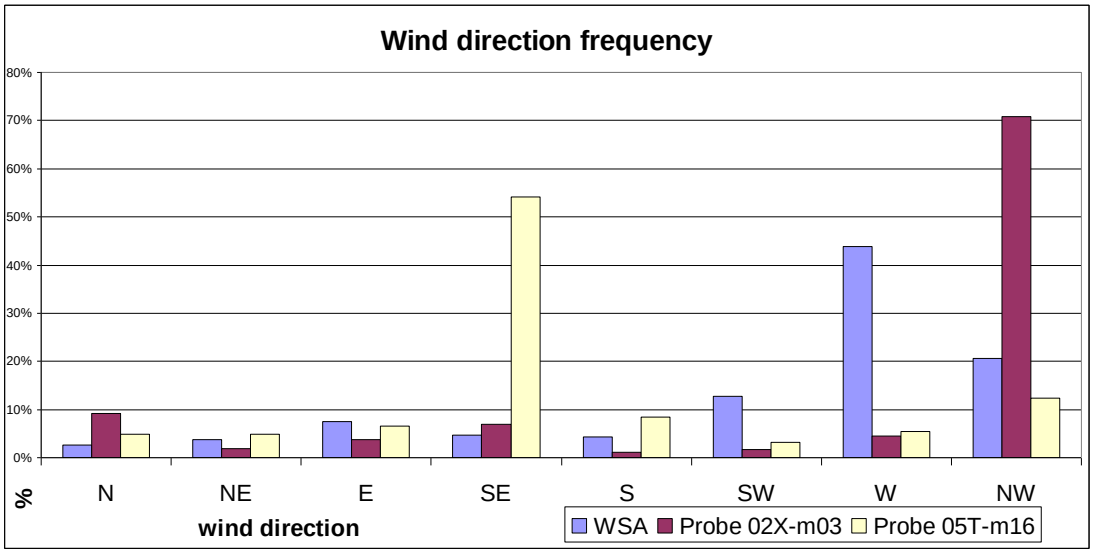

Source: this study.

Figure 8-35: The wind velocity magnitude (WSA MS; probes 02X; and 05T):

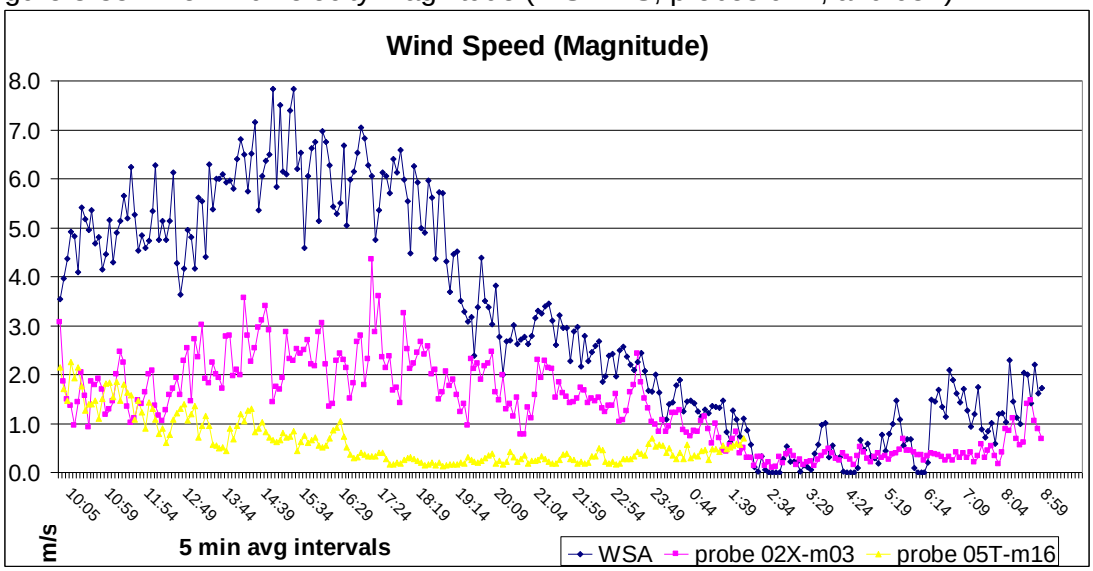

Source: this study.

[119] While the probe 02X is positioned in the external side of the MA block in the room m-03, the probe 03T is positioned in the same block, but in its courtyard side in the room m-16. Both rooms are on the 3rd floor of the Law School building.

8.4.4. Comparison between the FM data and CFD results

Here the FM data from the probes placed on the external façades of the 3rd floor of the Law School building are contrasted to the CFD results.

8.4.4.1. Comparison of data from probes 02x and 03T

In Figure 8-30 a strong incidence of the NW wind on probe 02X, on the MA, may be observed. This occurs since it is associated with the channelling effects that take place in this canyon, diverting N, NE, SW and W winds towards the NW angle. In probe 03T, which is on the external side of PP, the incidence is greater for W winds, which are parallel to its face, and also SW winds, which are also diverted towards the Park Place canyon.

A great decrease in wind speed takes place at around 4/5ths of the canyon's height on both sides of the Law School building (Figure 8-31). Although its association changes according to the time of day and both the wind direction and intensity it is possible, for example, to observe that while the WSA MS wind speed reaches 4.0m/s, the instantaneous wind speed measured by probes 02X and 03T are 2.0m/s and 1.0m/s, respectively. Further, a gust wind peak seems to be related to this same ratio: 6.0m/s, according to the WSA MS, 3.0m/s at probe 02X, and 1.5m/s at probe 03T.

8.4.4.2. Comparison of data from probes 02x and 04T

Both the probes 02X and 04T were placed on the same side of the Museum Ave. While the first was approximately in the middle of the Law School building, the second was near the round corner of this building. Therefore, similar data was expected from these two probes. From Figure 8-32 it may be observed that the data from the WSA MS indicate the prevailing directions for the free wind coming in first from the W and secondly from the NW. Both probes indicate a high incidence of NW wind. Once again this occurs due to channelling effects and the deflection of West winds to the NW.

Regarding the wind speed, the same pattern is to be observed in the data from the three sources (Figure 8-33) although, inside the canyon, great and almost constant deceleration of 45% is found t probe 04T and 60% at probe 02X. This means that the wind speed at the probe near the corner is about 1,4x that at the probe placed in the centre of the Law School building.

8.4.4.3. Comparison of data from probes 02x and 05T

From the wind direction frequency Figure 8-34 can be seen that the prevailing directions for the free wind are first W and secondly NW. While the first probe (02X) remains on the Museum Ave., the second probe (05T) was moved to the internal courtyard. Probe 02X once more indicates a great incidence of NW wind as a result of the W wind's redirection in accordance with the orientation of the NW canyon. On the other hand, the great incidence of SE winds at probe 05T shows the existence of a continuous reverse flow inside the courtyard washing down this façade. This may occur principally for W winds, which impinge on the tall buildings located in the downwind direction immediately beyond the courtyard and which create a downward flow, subsequently trapped in a SE oriented swirl inside the Law School's patio.

The wind speed data show two distinct period contexts (Figure 8-35): one with intense free airflow (from 10.00am until 02.00am of the following day) and another, which follows it, of almost still-air (from 02.00am until 10.00am). In the first period, when the free airflow speed is above 4.00m/s, the velocity at probe 02X decreases by an average of 50%, while at probe 05T the decrease attains 85%. In the second period the wind speed, according to the three data sources, is practically equal as the wind is very weak.

8.4.5. Wind speed decrease inside the canyon

The wind speed decrease ratio consists of the division of the wind velocity magnitude (regardless of the wind direction) inside the canyon as measured at the probes by the free wind speed recorded by the WSA meteorological station (MS) at the same instant of time. The FM data displayed comes from the specific one-day-round data averaged at 5minutes intervals, as just quoted in table 8-1. The CFD velocity magnitude data were obtained from the outputs located at the same points as in the real experiment, but from a time-steady state calculation.

The wind speed decrease ratio analysis and the comparison between the FM and the CFD results allow one to draw several conclusions:

- For reference wind velocities up to 1.0m/s (measured at the WSA meteorological station) and excluding still-air conditions; the wind speeds measured by probes 02X and 03T were almost the same as that of the free airflow, with ratios above 95%;
- For wind speeds from 1.00 to 2.0m/s a decrease from 64.4% to 48.5% is to be observed at probes 02X, 03T, and 04T;

- For wind speeds from 2.00 to 3.0m/s a decrease of about 51% is to be observed at probes 02X and 04T (in MA); 38.4% at probe 03T (in PP); and 24.6% in the courtyard;
- For wind velocity of from 4.00 to 6.00m/s probes 02X and 04T showed a wind speed decrease of about40% while the ratio at probe 03T was approximately 30%;
- For free-airflow velocities above 6.00m/s probe 04T presented a wind speed decrease of about 40% while the ratios at probes 02X and 03T were constant at about 30%;
- The wind speed in the courtyard (probe 05T) reached a maximum of 3m/s, and a decrease of from 25 to 70%; and
- Overall the wind speed decrease of the FM matched that of the CFD results closely. The free-airflow reference velocity used in the numerical simulation was 2.35m/s. For this velocity, the comparison of the decrease ratio of the FM and the CFD for the probes in the same positions were, respectively:
    - probe 02X: 52% and 51%;
    - probe 03T: 38% and 34%;
    - probe 04T: 52% and 44%; and
    - probe 05T: 25% and 22%.

Figure 8-36: The wind speed decrease ratio inside the canyon:

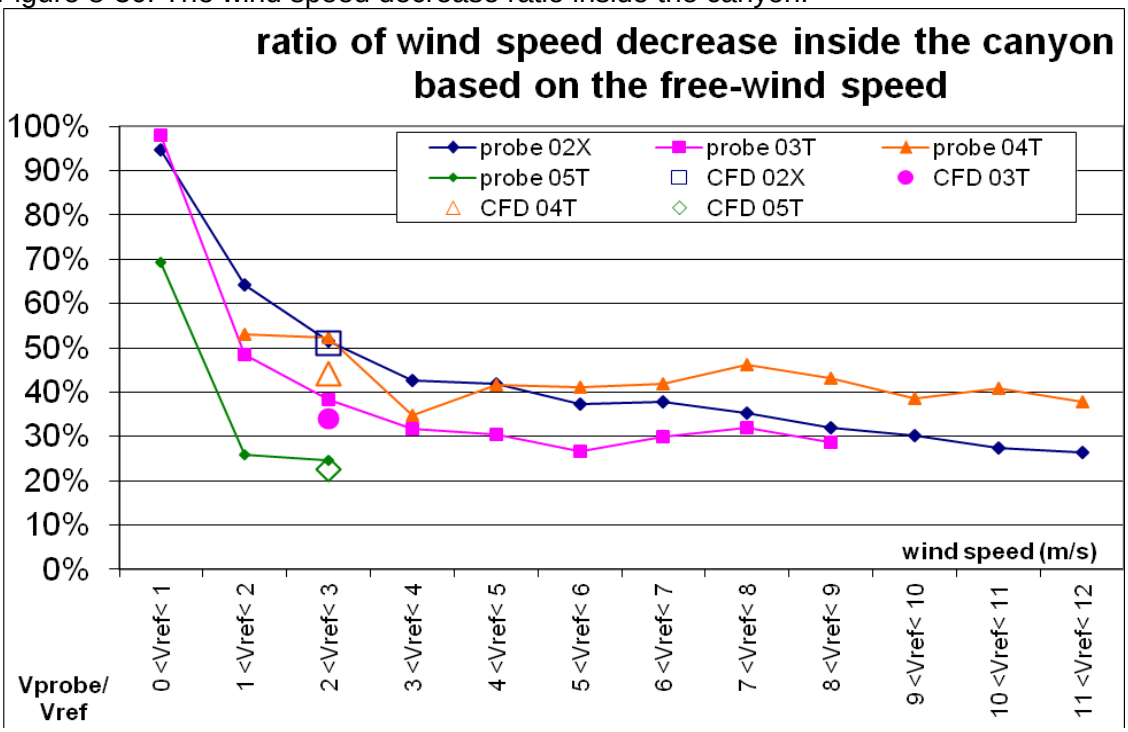

Source: this study.

8.5. Comparison of Cathays Campus and Urban Prototypes

The ΔCp results obtained from the simulation of eight wind directions for the Law School Building in the Cardiff Cathays area will here be directly compared with the results of Groups 01 to 06 of the Urban Prototypes, covered in Chapter 7. This investigation seeks to identify if the relationship found for the aspect ratios between the urban prototypes and the Cardiff Cathays Campus (see topic 5.8.3.1 in Chapter 5) may also be translated into ΔCp results. he correlation coefficients for ΔCp employed the averaged results for 90% of the data (discharging 10% of extreme results)[120].The correlation analysis was undertaken for parallel, orthogonal, and oblique winds, and the scale of significance and correlation coefficient strength employed on this analysis is demonstrated in the topic 5.8.4 in Chapter 5.

8.5.1. Correlation coefficients between the ΔCp results

The correlation coefficients between the Cathays Campus and the Urban Prototypes for ΔCp results shows a strong correlation for S winds (90%- see Figure 8-37), while for SE (83%- see Figure 8-38) and NW (78%- see Figure 8-39) winds they are substantial. These wind directions are respectively at 45^{o} (S) and 0^{o} (both SE and NW) to the Museum Avenue external side. In contrast, the wind directions from E (53%- see Figure 8-40), N (36%- see Figure 8-41) and W (33%- see Figure 8-42) presented moderate to low correlation, while the ones from NE (-30%- see Figure 8-43) and SW (-68%- see Figure 8-44) showed low to moderate reverse correlation. Both the equivalences and disparities found between the aspect ratio and the ΔCp results correlation coefficients may be justified by the same characteristic. The 'V' shape of the Law School Building which forms a oblique courtyard with side high-rise buildings has an impact on both the airflow velocity and the ΔCp results (Figure 8-39). The set out above wind directions that showed good agreement between the two sources of correlations (aspect ratios and ΔCp results) seem to be independent to the Law School Building shape and, therefore, directly comparable to the urban prototypes: the two wind directions parallel to the flow and also the wind direction that is exactly 45^{o} to the façade. Further, while the Law School building wing towards the Museum Avenue is oblique to the North (-45^{o} or 315^{o} or to the azimuth), the Park Place wing is placed at 15^{o} to the North, totalizing an angle of 75^{o} between the two wings., and the results for the other wind directions are to be influenced by this factor. Finally, high-rise buildings towards the E and the NE wind directions may be also a source of divergence in the comparison between the Cathays Campus and the Urban Prototypes CFD results.

[120] Other ΔCp data (such as peaks values, the 8th highest/ lowest results, and the standard deviation) were displayed with the purpose of providing further information about the results.

Table 8-2: The Cathays Campus ΔCp results and Urban Prototypes ΔCp results correlation coefficients (*r*)[121].

Winds Direction		α	Urban Prototypes															
			A1	A2	A3	A4	B1	B2	B3	B4	C1	C2	C3	C4	D1	D2	D3	D4
Cathays Campus	N	45°	0,36	-0,56	0,02	0,35	-0,73	-0,56	-0,12	-0,77	-0,20	-0,96	-0,92	0,26	-0,71	-0,52	-0,16	-0,64
	NE	90°	-0,30	0,55	0,37	0,44	0,56	0,00	0,14	0,06	-0,75	-0,72	-0,21	-0,46	-0,36	-0,37	-0,04	0,09
	E	45°	0,53	-0,69	0,46	0,66	-0,74	0,33	0,05	-0,23	-0,47	-0,73	-0,60	-0,06	-0,15	0,31	0,62	-0,08
	SE	0°	0,83	0,27	0,83	-0,54	-0,12	-0,08	0,27	-0,80	-0,48	0,27	0,27	-0,88	-0,85	0,77	-0,82	-0,31
	S	45°	0,90	-0,98	0,82	0,97	-0,27	0,33	0,69	0,09	-0,10	-0,49	-0,27	0,16	0,24	0,35	0,65	0,26
	SW	90°	-0,68	0,22	-0,20	0,17	0,15	-0,22	-0,11	-0,12	-0,50	-0,75	-0,54	-0,44	-0,49	-0,55	-0,24	0,10
	W	45°	0,33	-0,60	0,20	0,47	-0,86	0,08	-0,06	-0,66	-0,45	-0,13	-0,78	0,11	-0,56	-0,23	0,16	-0,51
	NW	0°	0,78	-0,08	0,74	-0,25	0,43	0,37	-0,08	-0,56	-0,75	-0,08	-0,08	-0,91	-0,65	0,87	-0,96	-0,06

Source: this study.

[121] The colours of this scale of significance for the Cathays Campus ΔCp results and the urban prototype ΔCp results correlation coefficient (*r*) strength are based on the Table 5-20 in Chapter 5.

Figure 8-37: Correlation between Cathays Campus ΔCp results and Urban Prototype A1 ΔCp results for S winds (45° to the Museum Avenue side).

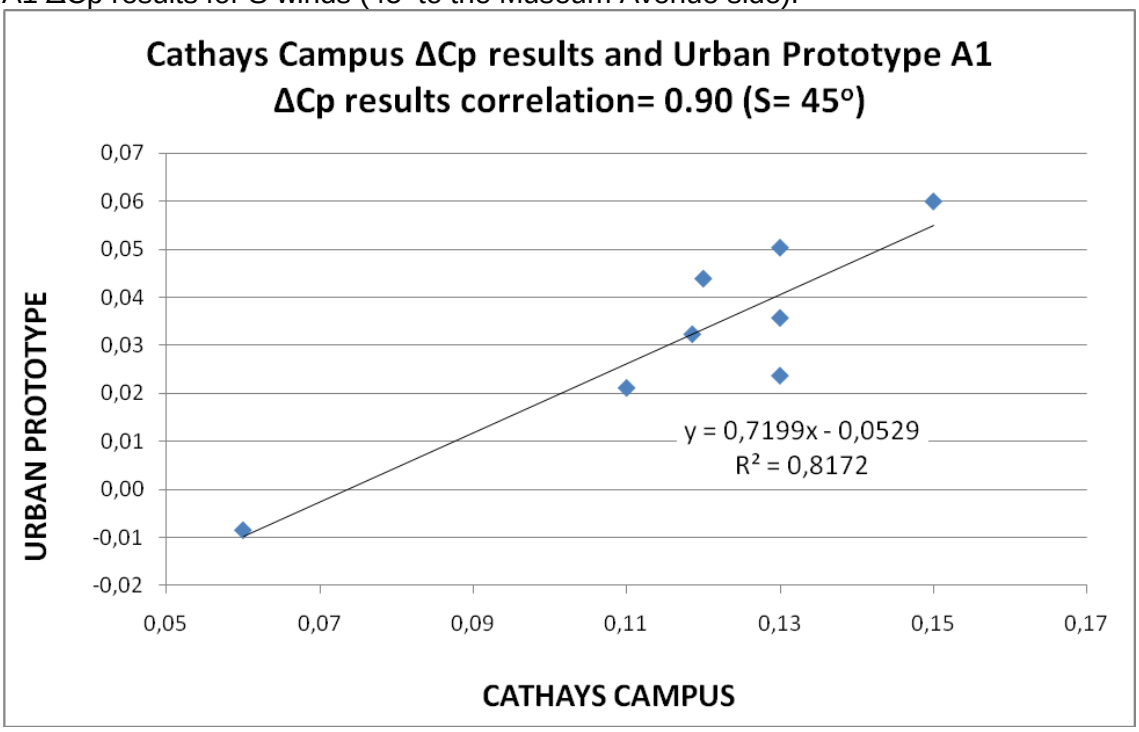

Source: this study.

Figure 8-38: Correlation between Cathays Campus ΔCp results and Urban Prototype A1 ΔCp results for SE winds (0° to the Museum Avenue side).

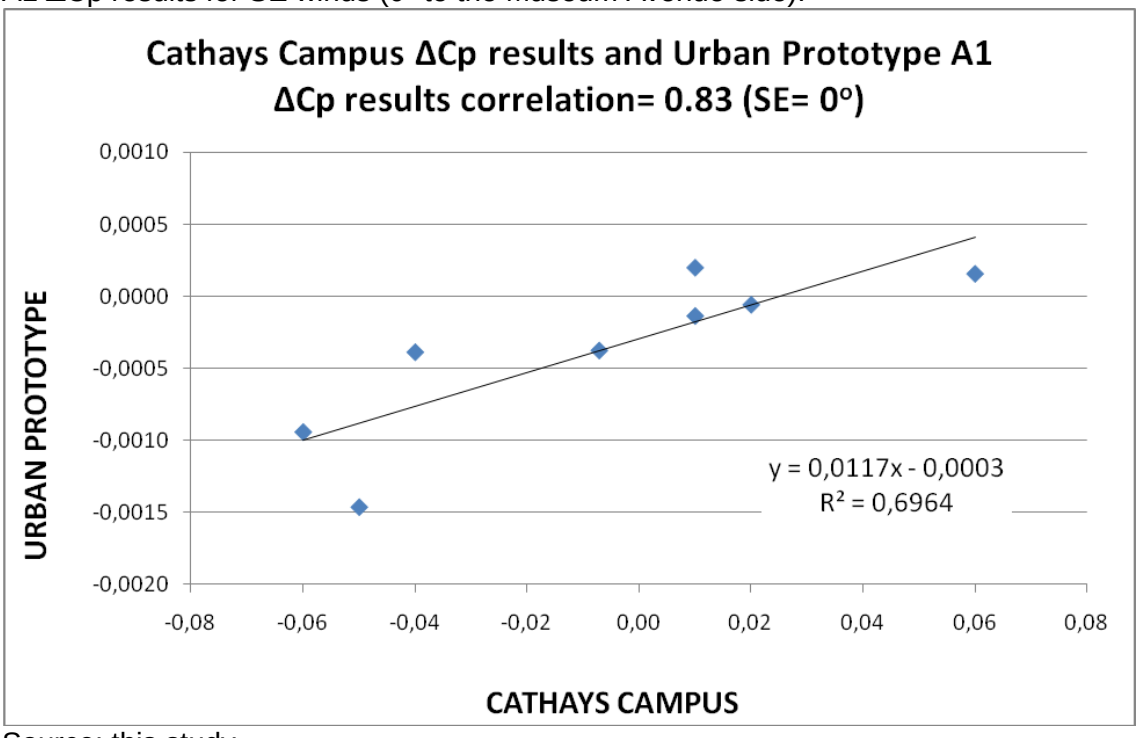

Source: this study.

Figure 8-39: Correlation between Cathays Campus ΔCp results and Urban Prototype A1 ΔCp results for NW winds (0º to the Museum Avenue side).

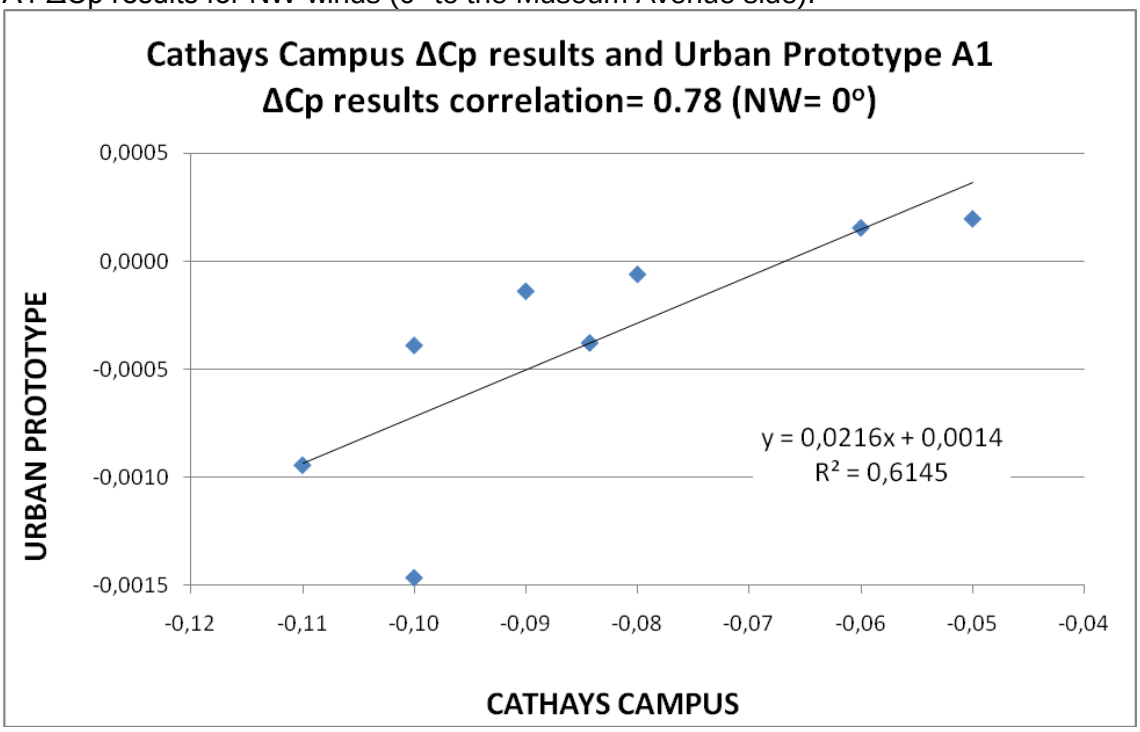

Source: this study.

Figure 8-40: Correlation between Cathays Campus ΔCp results and Urban Prototype A1 ΔCp results for E winds (45º to the Museum Avenue side).

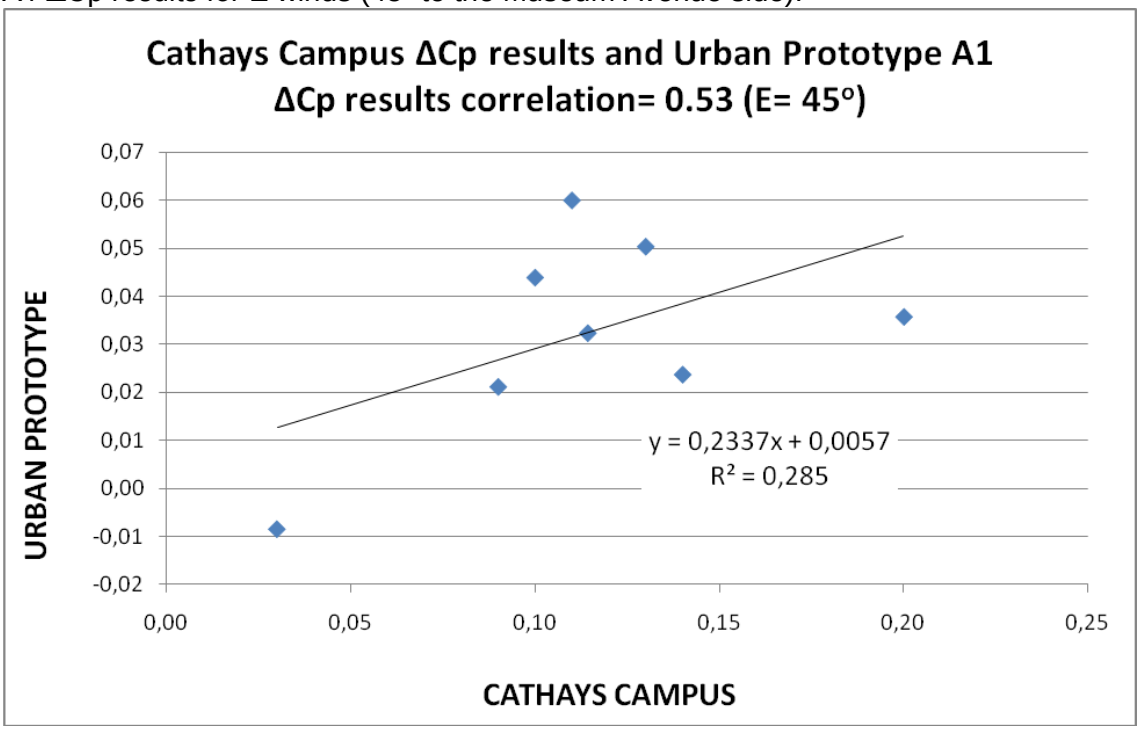

Source: this study.

Figure 8-41: Correlation between Cathays Campus ΔCp results and Urban Prototype A1 ΔCp results for N winds (45° to the Museum Avenue side).

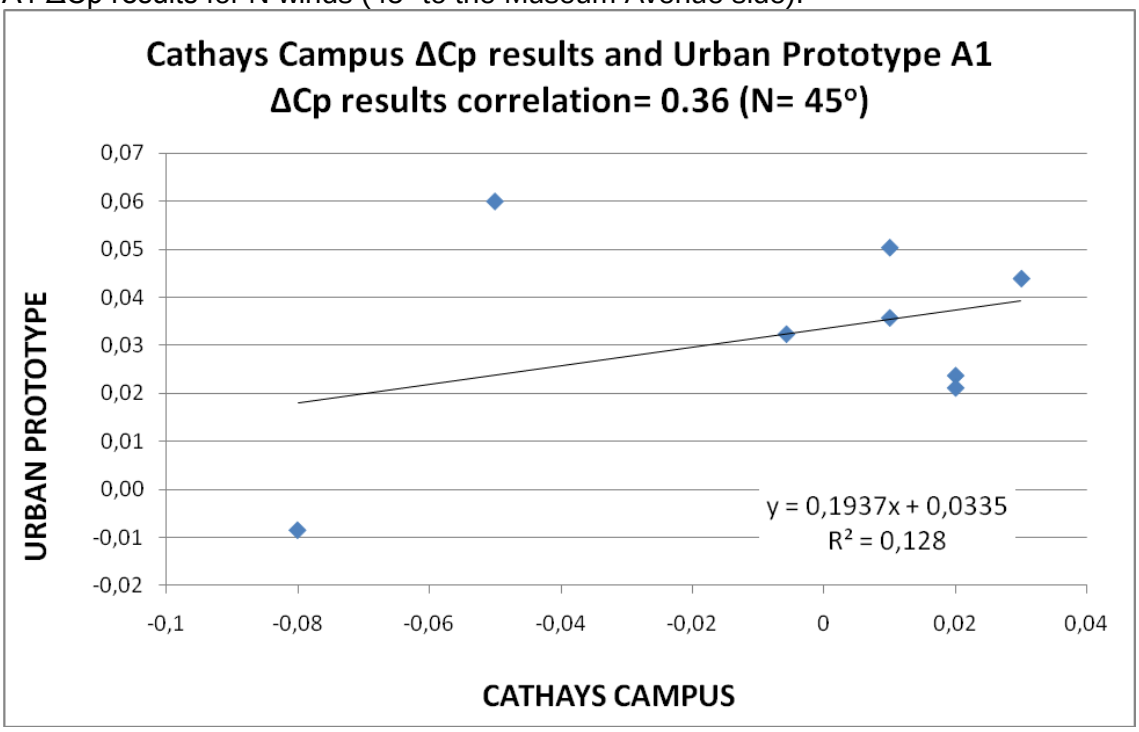

Source: this study.

Figure 8-42: Correlation between Cathays Campus ΔCp results and Urban Prototype A1 ΔCp results for N winds (45° to the Museum Avenue side).

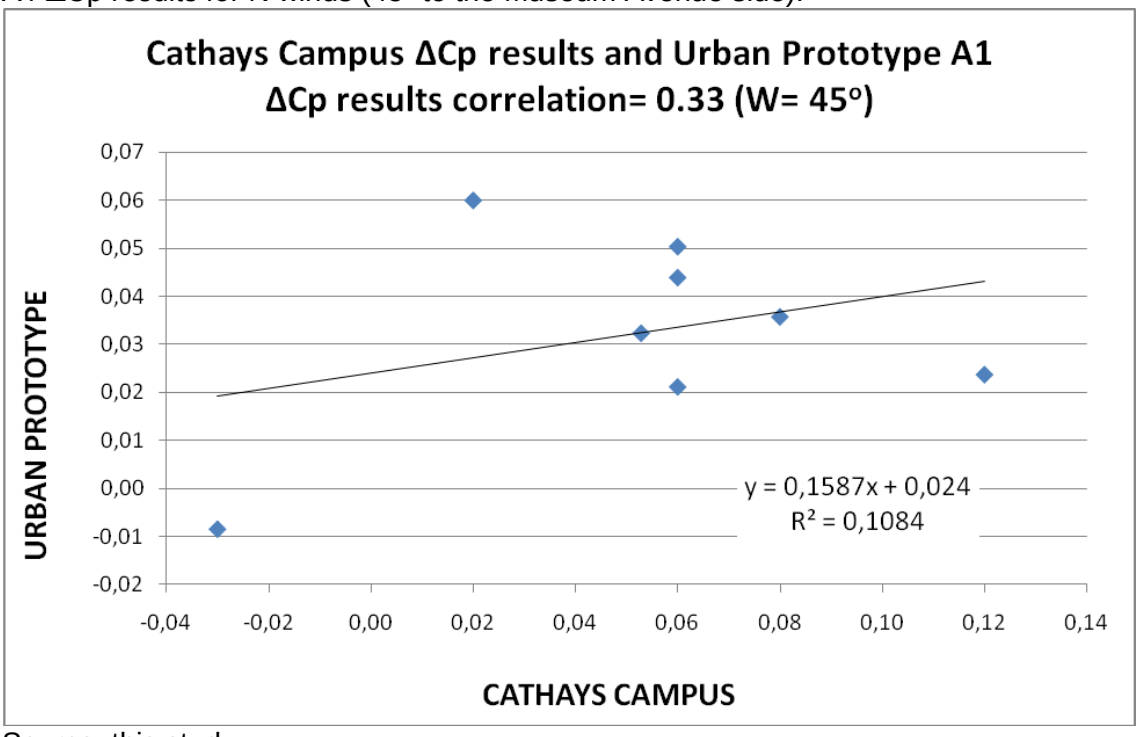

Source: this study.

Figure 8-43: Correlation between Cathays Campus ΔCp results and Urban Prototype A1 ΔCp results for NE winds (90° to the Museum Avenue side).

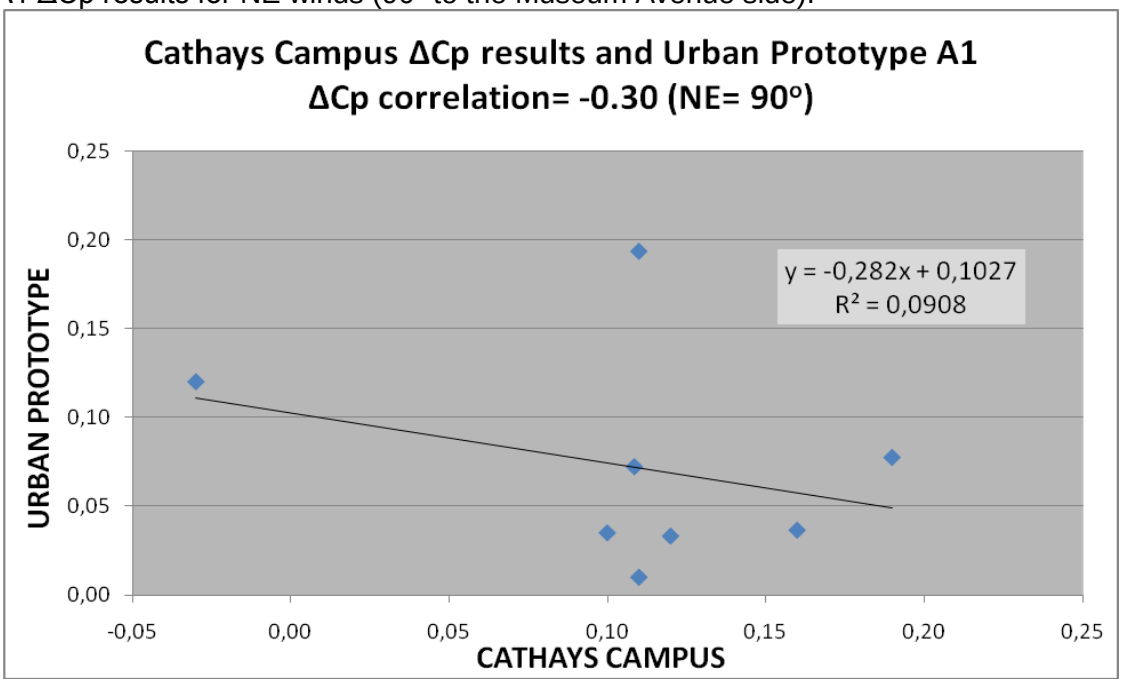

Source: this study.

Figure 8-44: Correlation between Cathays Campus ΔCp results and Urban Prototype A1 ΔCp results for SW winds (90° to the Museum Avenue side).

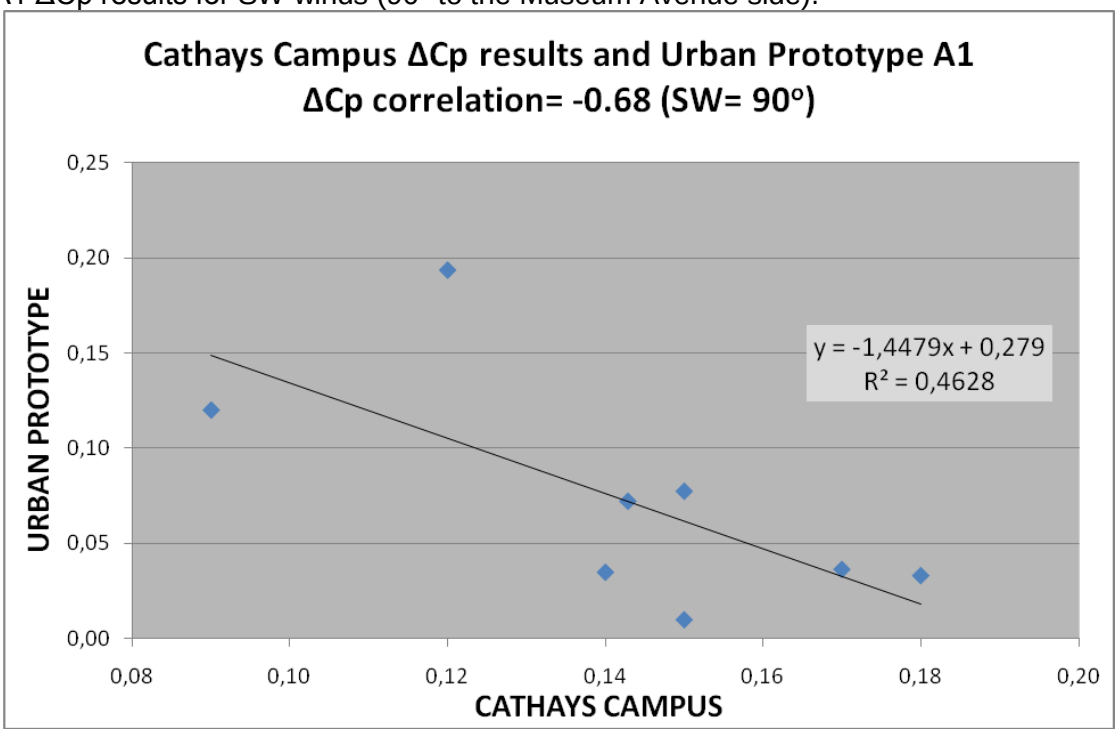

Source: this study.

Figure 8-45: The Law School building and the wind directions that showed strong (in green), low (in yellow) or reverse (in red) correlation coefficients between the Cathays Campus ΔCp results and the Urban Prototype A1 ΔCp results.

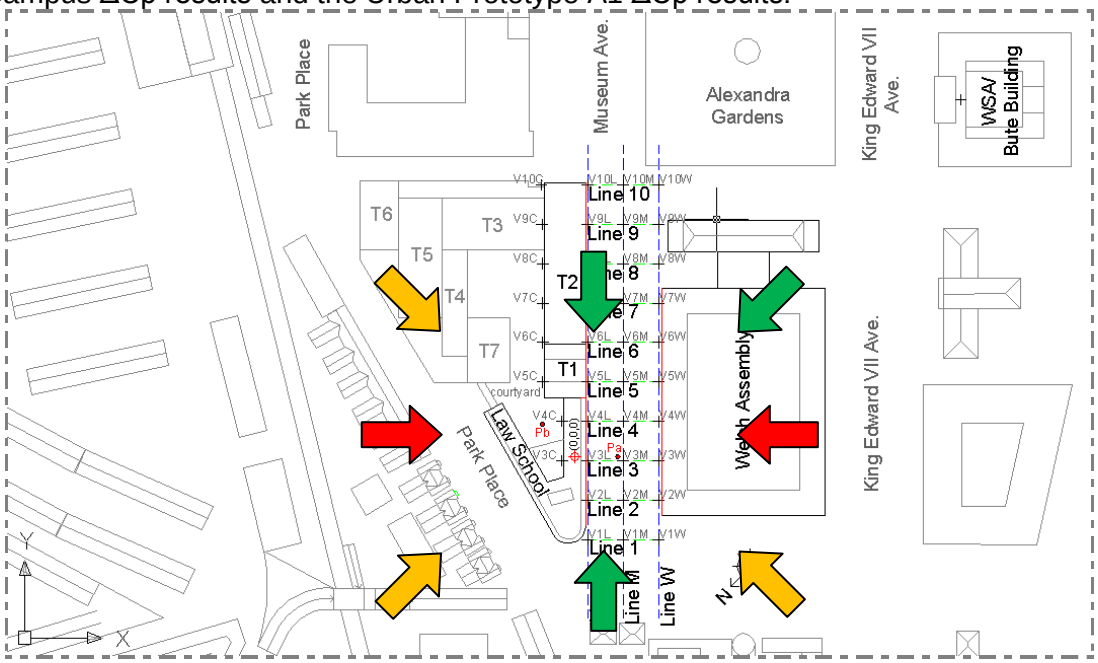

Source: this study.

Figure 8-46: The Urban Prototype A1 and the wind directions simulated.

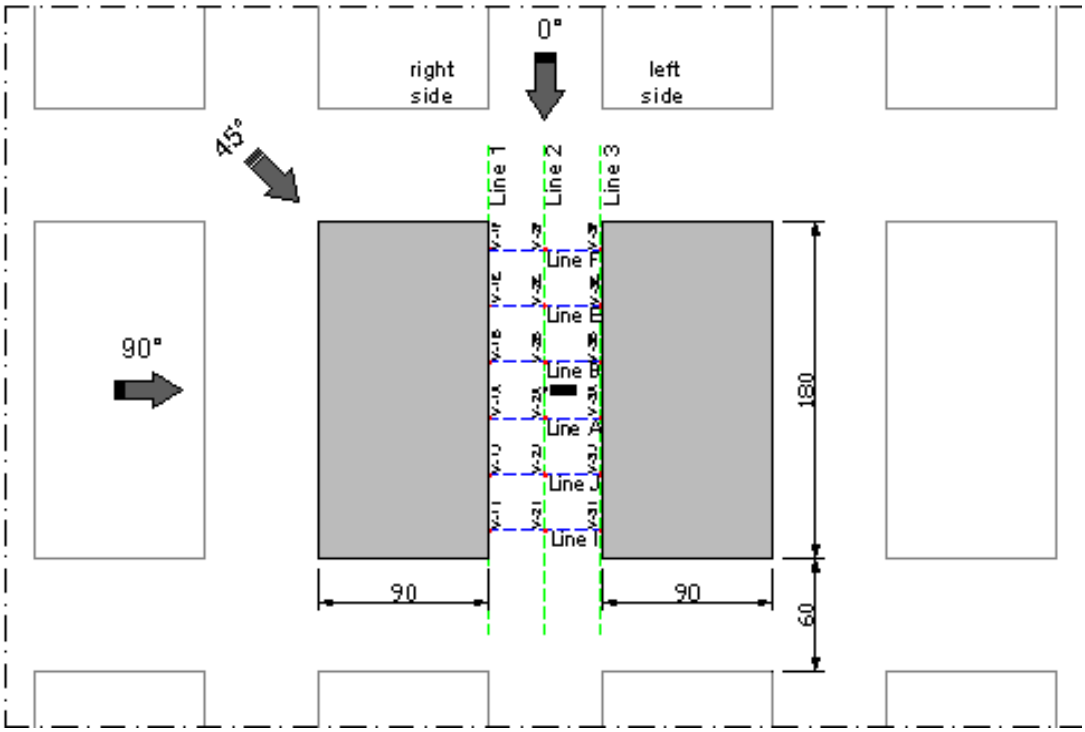

Source: this study.

8.6. Chapter conclusion

A certain level of agreement was found between the WT and the CFD sets of simulation. While topics 8.3.1 to 8.3.8 indicated a comparison between the two methods of simulation case by case, topic 8.3.9 raised some issues relating to the confidence levels of the results and possible further improvements.

Field measurement data demonstrated various modifications in the airflow speed and direction inside the Museum Avenue canyon. A close agreement between these modifications was found between the FM data and the CFD output, in addition to quantifying the airflow velocity decrease due to the existing urban buildings for each wind direction. Moreover, numerical calculation was able to provide visualization of these effects via airflow pathlines.

Finally, a comparison of Cardiff Cathays Campus ΔCp results and the Urban Prototype ΔCp results from the CFD simulations showed strong correlation between this actual urban area and the urban prototype A1 for for three wind directions, while other three showed substantial correlation. This same strength of correlation was previously found between the urban aspect ratios, which turn out finally to be consistent with the hypotheses and objectives of this investigation.

Chapter 9: Paulista Ave.: Results and Analysis

9.1. Introduction

In this chapter the results from both the Paulista Avenue case study WT experiment and the CFD simulation are presented, analyzed and discussed. As mentioned in Chapter 5, this analysis is part of Steps 3 and 4 of the methodology of investigation proposed. A panoramic view of the airflow field below the canopy height in this real urban environment and the ΔCp results from and distribution over the building façades are displayed and compared to examples given in the literature. Finally, the results are correlated to the urban prototypes investigation covered in Chapter 7[122].

9.2. On the Paulista Avenue results and analyses

The Paulista Avenue case study investigation was divided into two sections: a real high-rise office building (CKY Tower), and a proposed Tower Prototype. While Section 1 was assessed by means of both WT and CFD, Section 2 was simulated by WT, alone. Both sections were also simulated in an open field scenario and with the surrounding Paulista Avenue urban area. The CKY Tower WT section investigated three façade finishing's: the existing flat surface, one with horizontal panels (such as balconies or sun-breaks) and another with vertical panels (columns or sun-breaks). The Tower Prototype WT experiment explored two arrangements of central atrium internal partition (shaft 'A' and shaft 'B'). Chapter 5 shows the simulation methods and output post-processing technique employed on each of these two sections[123].

[122] This part corresponds to Step 2 of the investigation.
[123] Further details are found in table 5-5 and in topics 5.2, 5.4.2.2, 5.5.4, 5.6.6, and 5.8.3.2 of Chapter 5.

9.2.1. About the display and analyses of the results

The analysis of the results was based on Cp output data displayed as contour plots (Figure 9-1 and Figure 9-2) and tables depicting the averaged Cp and ΔCp results (Table 9-1 and Table 9-2 [124]).

The wind field inside this high density urban area and around the CKY tower (section 1) was qualitatively visualized and assessed by airflow pathlines from the CFD models (Figure 9-3). It was also depicted by vertical profile charts for wind velocity magnitude and the wind velocity for the x, y and z vector components (Figure 9-4). These vertical profiles were strategically positioned near the tower walls and on the avenue's central axis, and are presented separately for the three wind directions simulated.

Finally, the Paulista Avenue urban aspect ratios and the ΔCp results were directly compared to the same sort of information from the Urban Prototypes just quoted aiming to identifying the statistical correlation coefficient strength between the actual urban environment from Case Study 2 and the similar urban prototypes. Data was plotted in a scatter diagram[125], on which shows the linear relationship between the sources of data by clustering them around a diagonal line (Figure 9-5).

[124] As example of Chapter 7, these tables provide the total averaged Cp maximum and minimum peaks; the averaged results for 90% of the data (discharging 10% of extreme results); the standard deviation among the data; and the ΔCp between the faces and for each 5m height from ground to top, for the total face on both sides of the target tower (right and left faces for parallel winds, or leeward and windward faces for oblique and orthogonal winds), and for both the existing tower and the prototype sections. All tables used in this chapter analyses are found in Appendix 6.

[125] For further information see topic 5.8 in Chapter 5.

Figure 9-1: Example of Cp contour plots: isolated CKY Tower windward face - CFD and WT with flat surface (top right), horizontal panels (bottom left) and vertical panels (bottom right) (90°- see Appendix 7 for all Cp contour plots).

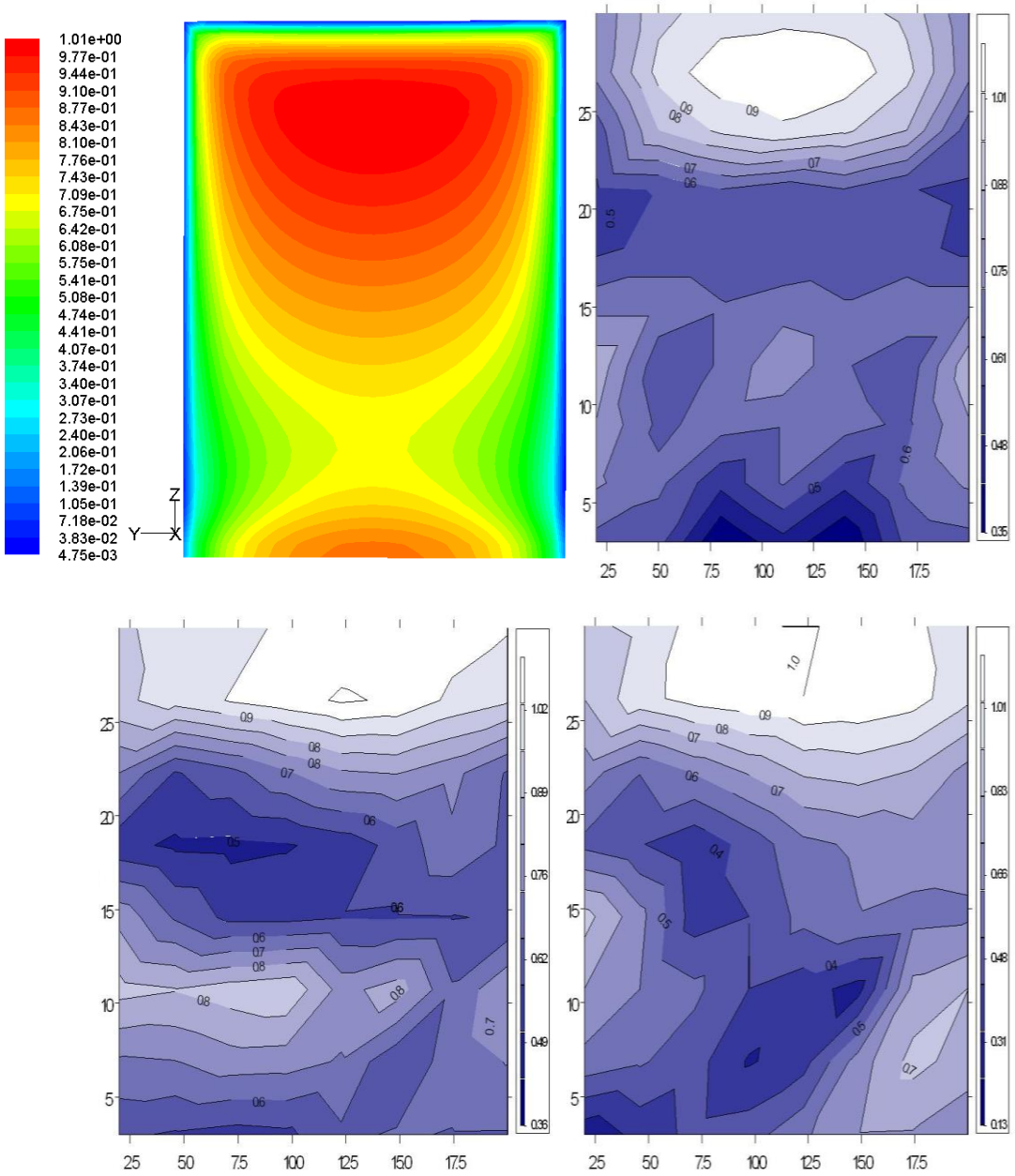

Source: This study.

Figure 9-2: Example of Cp contour plots for the isolated prototype tower shaft 'A' WW and LW sides: horizontal top (above), external side (middle) and internal shaft (bottom) surfaces (WT; 90°)[126].

- Isolated prototype shaft 'A' (90˚)

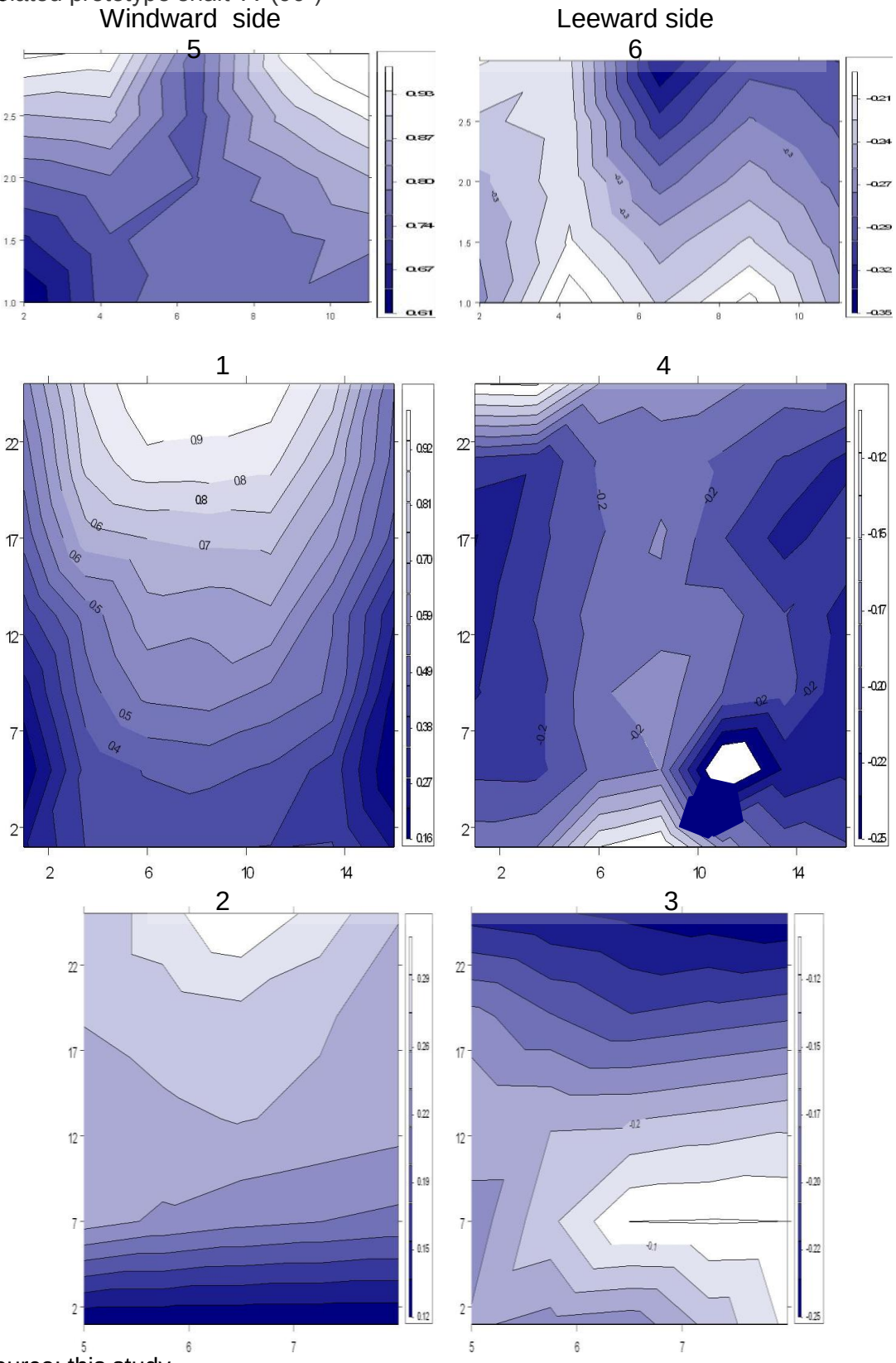

Source: this study.

[126] See Appendix 7 for all Cp contour plots.

Figure 9-3: Example of lines used for extracting data and wind velocity pathlines from a rake at 30m height for aiflow patterns visualization (CFD, S, 45°).

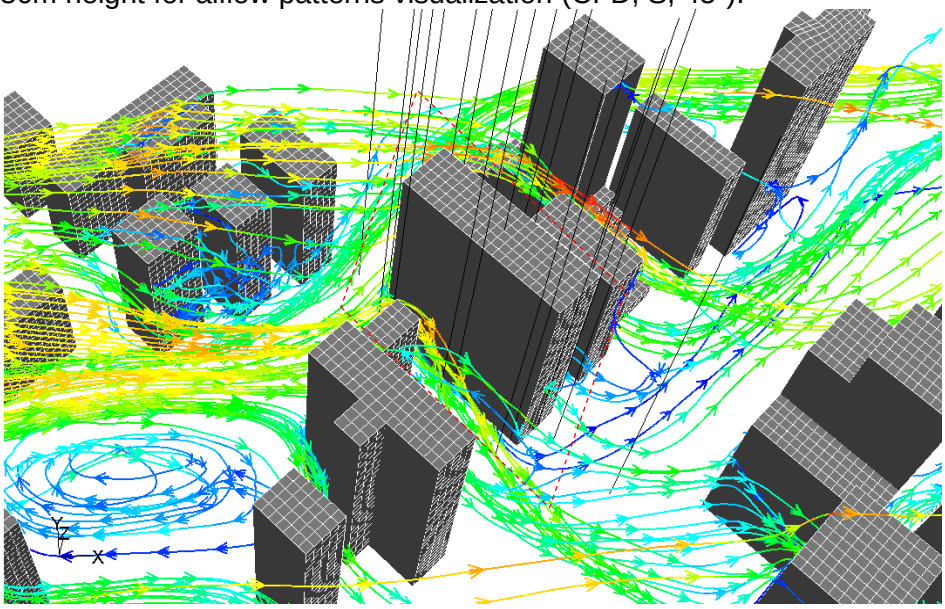

Source: this study.

Table 9-1: Example of table showing Cp and ΔCp results from the CFD simulation for the isolated CKY Tower (45°)[127].

Height	**WW**	**side**			**LW**	**side**			$\Delta X\pi$
(m)	MIN	MAX	AVG	SDEV	MIN	MAX	AVG	SDEV	***AVG***
90 (edge)	0.11	0.45	0.16	0.07	-0.02	0.33	0.03	0.10	***0.13***
84	0.04	0.97	0.63	0.18	0.00	0.20	0.05	0.03	***0.58***
78	0.03	0.99	0.67	0.20	-0.02	0.19	0.05	0.04	***0.62***
72	0.04	0.98	0.69	0.20	-0.03	0.18	0.04	0.03	***0.65***
66	0.05	0.95	0.67	0.20	-0.02	0.17	0.03	0.03	***0.64***
60	0.05	0.92	0.66	0.19	-0.02	0.16	0.03	0.03	***0.63***
54	0.06	0.87	0.63	0.18	-0.01	0.15	0.03	0.02	***0.60***
48	0.06	0.82	0.60	0.17	0.00	0.14	0.03	0.02	***0.57***
42	0.07	0.79	0.58	0.16	0.01	0.14	0.03	0.02	***0.55***
36	0.07	0.73	0.55	0.15	0.01	0.13	0.03	0.02	***0.52***
30	0.08	0.68	0.52	0.13	0.01	0.12	0.03	0.02	***0.50***
24	0.08	0.64	0.50	0.13	0.00	0.11	0.02	0.02	***0.48***
15	0.08	0.56	0.48	0.11	0.00	0.10	0.02	0.02	***0.46***
6	0.11	0.57	0.51	0.10	-0.01	0.09	0.01	0.02	***0.51***
3	0.14	0.62	0.56	0.11	-0.02	0.10	0.00	0.02	***0.55***
Top	0.04	0.97	0.66	0.19	-0.02	0.19	0.04	0.03	***0.62***
Middle	0.06	0.83	0.60	0.17	0.00	0.15	0.03	0.02	***0.58***
Bottom	0.10	0.61	0.52	0.12	0.00	0.10	0.02	0.02	***0.50***
AVG	*0.07*	*0.77*	*0.56*	*0.15*	*-0.01*	*0.16*	*0.03*	*0.03*	***0.53***

Source: this study.

[127] See Appendix 7 for all tables.

Table 9-2: Example of table showing Cp and ΔCp results for the shaft 'A' prototype tower in the urban environment: external, internal, and top faces (WT; N; 45°)[128].

	1 WW frontal face				2 downflow shaft				3 upflow shaft				4 LW rear face			
H (m)	MIN	MAX	AVG	sdev	MIN	MAX	AVG	sdev	MIN	MAX	AVG	sdev	MIN	MAX	AVG	sdev
90	-0.28	0.09	-0.05	0.14	-0.42	-0.40	-0.42	0.01	-0.42	-0.21	-0.29	0.11	-0.59	-0.36	-0.53	0.10
84	-0.34	0.09	-0.14	0.16	-0.42	-0.40	-0.42	0.01	-0.50	-0.46	-0.48	0.02	-0.61	-0.49	-0.58	0.04
72	-0.36	0.08	-0.22	0.17	-0.43	-0.41	-0.43	0.01	-0.44	-0.42	-0.44	0.01	-0.62	-0.55	-0.60	0.03
60	-0.44	-0.19	-0.33	0.10	-0.42	-0.40	-0.42	0.01	-0.42	-0.40	-0.40	0.01	-0.61	-0.51	-0.59	0.04
54	-0.51	0.19	-0.41	0.29	-0.43	-0.42	-0.43	0.01	-0.41	-0.39	-0.39	0.01	-0.61	-0.54	-0.60	0.03
42	-0.48	-0.40	-0.46	0.03	-0.42	-0.38	-0.40	0.02	-0.38	-0.36	-0.36	0.01	-0.62	-0.57	-0.62	0.02
30	-0.46	-0.36	-0.42	0.04	-0.43	-0.42	-0.42	0.00	-0.56	-0.37	-0.37	0.11	-0.62	-0.53	-0.61	0.04
24	-0.45	0.04	-0.39	0.20	-0.43	-0.42	-0.42	0.00	-0.62	-0.37	-0.40	0.13	-0.63	-0.39	-0.60	0.10
15	-0.47	0.00	-0.38	0.18	-0.43	-0.42	-0.43	0.00	-0.58	-0.33	-0.38	0.13	-0.63	-0.34	-0.47	0.12
Top	-0.33	0.09	-0.14	0.16	-0.43	-0.40	-0.42	0.01	-0.46	-0.36	-0.40	0.05	-0.61	-0.47	-0.57	0.05
Middle	-0.48	-0.13	-0.40	0.14	-0.42	-0.40	-0.41	0.01	-0.40	-0.38	-0.39	0.01	-0.62	-0.54	-0.60	0.03
Bottom	-0.46	-0.11	-0.39	0.14	-0.43	-0.42	-0.42	0.00	-0.58	-0.36	-0.39	0.12	-0.62	-0.42	-0.56	0.08
AVG	-0.42	-0.05	-0.31	0.15	-0.43	-0.41	-0.42	0.01	-0.48	-0.37	-0.39	0.06	-0.62	-0.48	-0.58	0.06

	5 WW top surface				6 LW top surface			
	MIN	MAX	AVG	sdev	MIN	MAX	AVG	sdev
Top	-0.07	0.06	0.02	0.06	-0.60	-0.55	-0.58	0.03
Middle	-0.01	0.14	0.06	0.07	-0.61	-0.51	-0.56	0.04
Bottom	-0.02	0.12	0.07	0.07	-0.62	-0.51	-0.57	0.05
AVG	-0.03	0.11	0.05	0.06	-0.61	-0.52	-0.57	0.04

ΔCp AVG Results							
	1 - 3	2 - 4	1 - 4	1 - 2	2 - 3	4 - 3	5 - 6
Top	0.27	0.15	0.43	0.29	-0.17	-0.02	0.60
Middle	-0.01	0.19	0.20	0.01	-0.21	-0.03	0.63
Bottom	-0.01	0.14	0.17	0.03	-0.18	-0.04	0.64
AVG	0.08	0.16	0.27	0.11	-0.19	-0.03	0.62

Source: This study.

[128] See Appendix 7 for all tables.

Figure 9-4: Example of charts depict the wind velocity magnitude and the wind velocity for the x, y and z vector components (m/s) on vertical profiles for 45° wind[129].

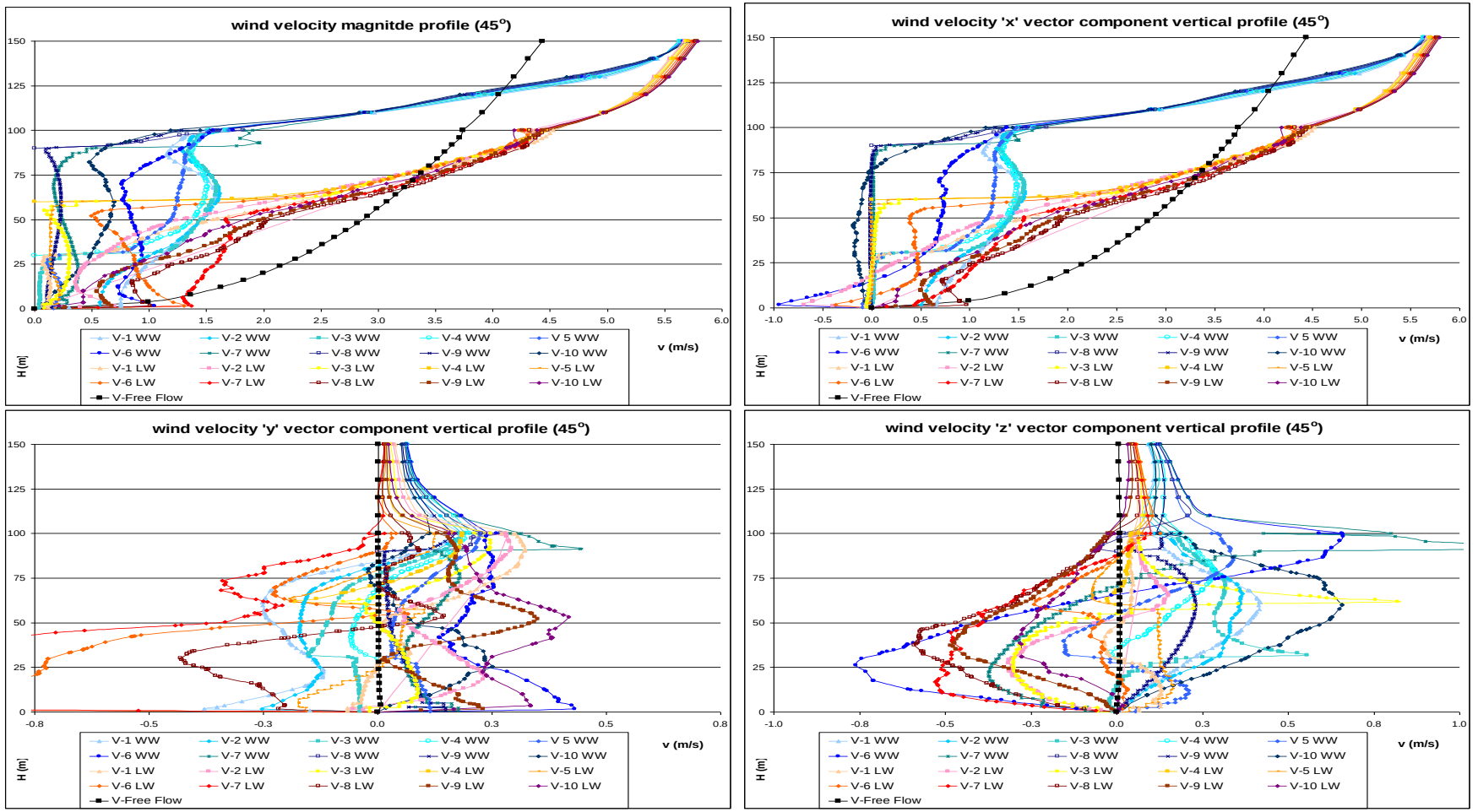

Source: This study.

[129] See Appendix 7 for all tables.

Figure 9-5: Example of a scatter diagram showing the correlation between the Paulista Avenue ΔCp results and the Urban Prototype D4 ΔCp results for NE winds (0^o).

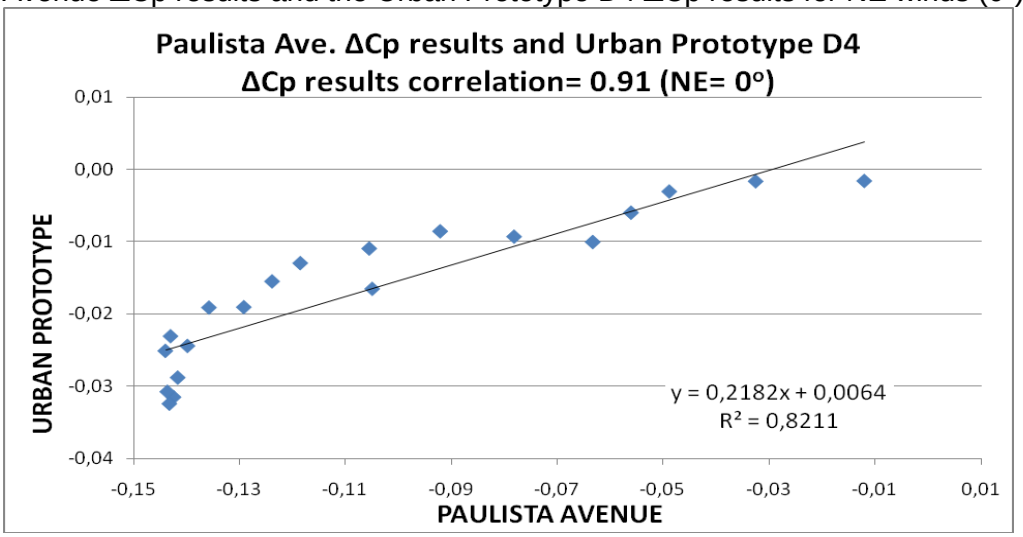

Source: this study.

9.3. Section 1: the CKY Tower

9.3.1. The isolated CKY Tower

Here the results for the isolated CKY Tower from both the CFD and WT experiments are presented and compared among themselves. Three wind directions were simulated: 0^o, 45^o, and 90^o. Further, the physical experiment explored three alternative façades: with a flat surface, with horizontal panels (such as balconies or sun-breaks) and with vertical panels (column ribs or sun-breaks).

9.3.1.1. Results for parallel winds (0˚)

The contour plot Cp comparison shows that the pressure patterns were similar in both the experiments, though the CFD output shows more clearly defined contour lines than do the WT ones. On the other hand, features such as flow detachment on the top side of the upwind vertical sharp edge were seen in all scenarios. Regarding the WT results, the contour plots did not show much variation between the flat, the horizontal panel and the vertical panel surfaces. The Cp results total ranges for these three sets of experiments were: 0.03 to -0.94; 0.00 to -0.82, and 0.07 to -0.72. These results match well with the CFD range: 0.07 to -0.57. In contrast, it is noticeable that a slight decrease in the Cp total range occurs between the flat, the horizontal and the vertical panel surfaces. Furthermore, as regards the WT results, a concentrated low pressure zone on the downwind side near the ground is seen in all three scenarios a discrepancy which may have been caused by any one or a combination of several factors: not enough pressure taps, one pressure tap fault, wind oscillation in the wind tunnel chamber, or even flow detachment at the horizontal surface edge, which was used to attach and hold the tower model in the wind tunnel round table. An example of different results produced by the physical experiment is provided by the ΔCp found between the right and left sides. While in the CFD the total averaged difference was 0.00, showing total symmetry between the sides, on both the WT flat surface and the horizontal panels it was 0.15, and finally on the vertical panel it was 0.25.

Figure 9-6: Cp contour plots: isolated CKY Tower lateral side face - CFD and WT with flat surface (top right), horizontal panels (bottom left) and vertical panels (bottom right) (0^o).

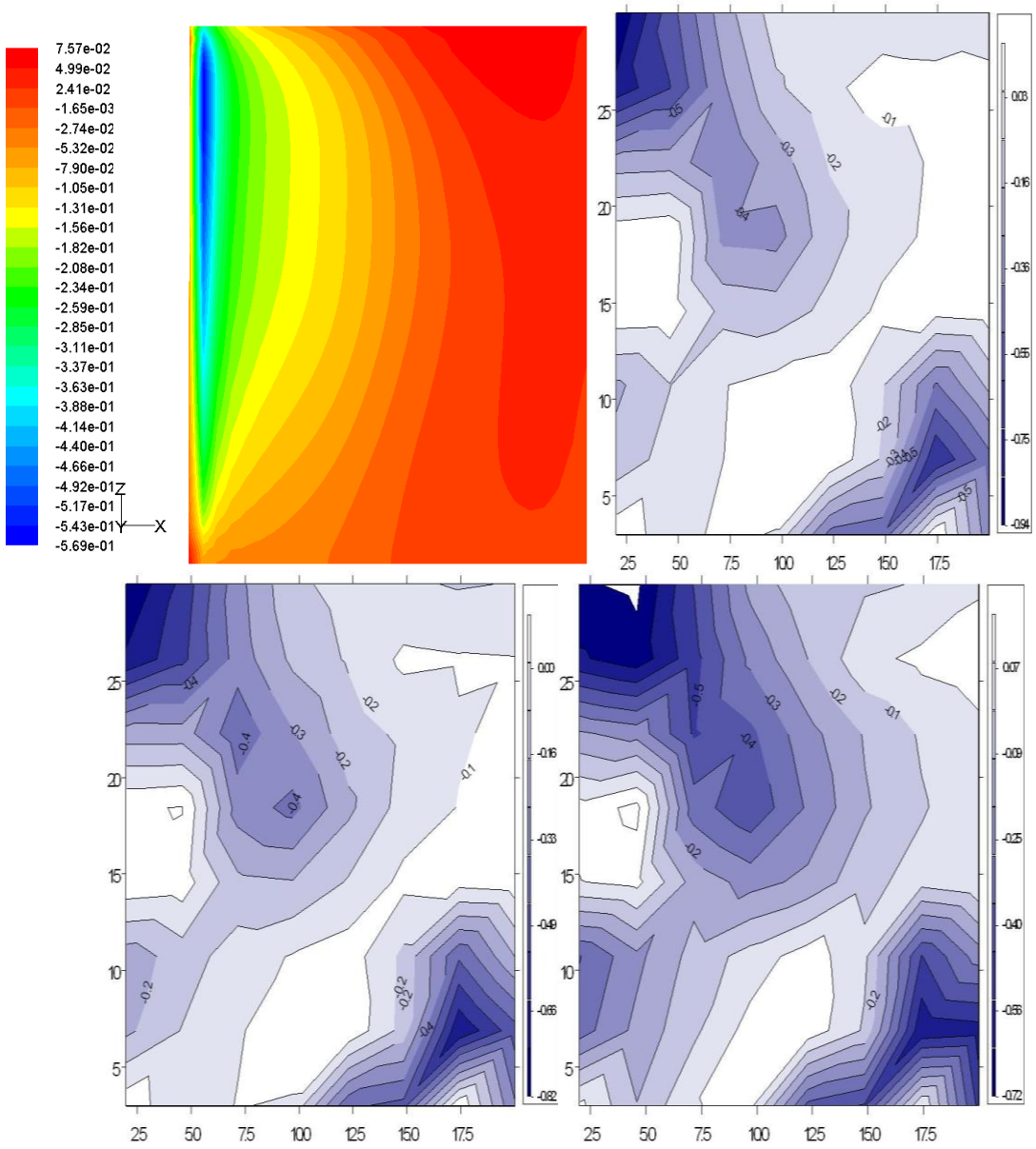

Source: this study.

Regarding the airflow patterns for winds parallel to the isolated tower, it may be said that, although an FS point and downwards flow are not clearly seen, a horse-shoe flow shape is created by the flow detachment at the windward vertical corners, which also causes local flow acceleration and a low pressure bubble on the side walls. Furthermore, a leeward wake is seen in the upwind direction.

Figure 9-7: Wind velocity pathlines from a vertical rake in the central axis (top) and velocity vectors from a horizontal plane at 30m height (bottom- CFD, m/s, 0°).

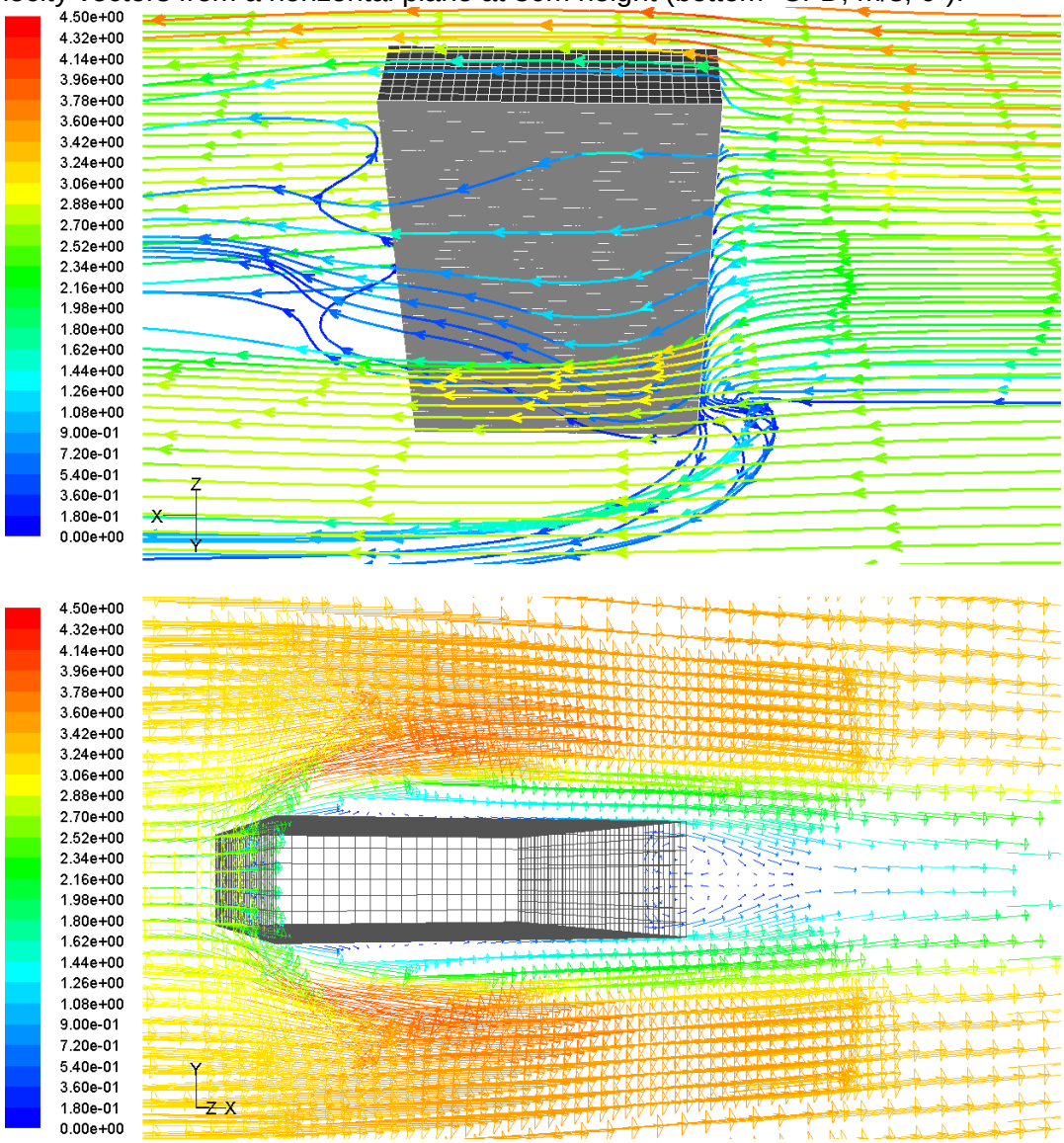

Source: this study.

Figure 9-8: Wind velocity magnitude and x, y and z wind vector components vertical profiles (CFD; 0°)

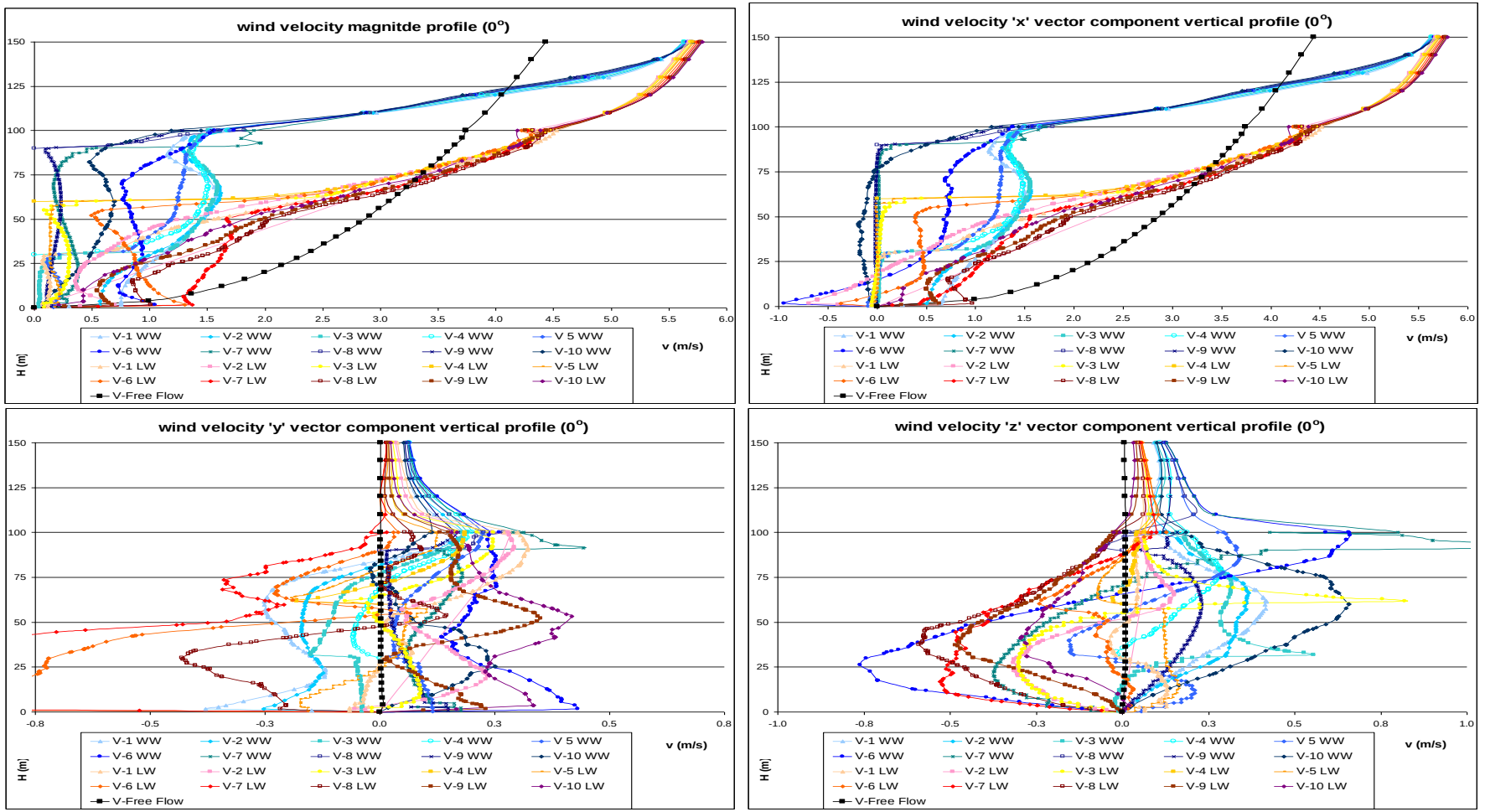

Source: This study.

9.3.1.2. Results for orthogonal winds (90˚)

The Cp distribution for orthogonal winds around the wide side of an isolated rectangular and symmetrical high-rise volume is also known[130] (Holmes, 2001). The CFD Cp contour plots for the CKY Tower windward side show a classic pressure distribution on a bluff-body: great pressure is found at 4/5ths of the total height, which indicates an FS point, and also at ground level, due to the flow's being directed downwards. Furthermore, pressure decreases near the vertical corners due to flow detachment at the sharp edges. The WT Cp contour plots for the flat surface model show also a high pressure zone near the FS point, although its shape is not as clearly delineated as in the numerical calculation. In addition, a more even pressure distribution may be observed in the horizontal direction in the model with horizontal panels, while the model with vertical panels shows an asymmetrical pressure distribution. When comparing the total range of Cp results, practically identical figures were found for the CFD and the three WT surface variation models' (flat, horizontal and vertical panels) maximum Cp: 1.01. The minimum Cp was also close for the three WT experiments: 0.34, while the absolute minimum result for the numerical calculation was 0.04. It is worth of mention that this low peak occurred near the edges, and that the WT models would not have been able to capture these results because of the limitation in the number and position of the pressure taps.

Regarding the leeward side's Cp distribution, in spite of the equivalence of the CFD and WT contour pressure shapes, the range of results was significantly lower in the physical experiment than in the numerical simulation. This is believed to occur as a result of the limitations of the CFD turbulence model[131] adopted in simulating leeward wakes and low pressure bubbles. In consequence, the ΔCp range between the windward and leeward sides was lower in the CFD calculation than in the WT physical experiment, as follows: 0.94 to 0.69 in the CFD; and 1.38 to 0.94 (WT flat surface), 1.52 to 1.05 (WT horizontal panels), and 1.51 to 0.93 (WT vertical panels).

The CFD airflow pathlines clearly identify an FS point, and flow detachment at the vertical edges and on the horizontal top surface, resulting respectively in a horizontal horse-shoe flow pattern and a rising flow. In both places sharp acceleration and low pressure bubbles occur as a consequence. Reverse flow is seen on the windward side at ground level. The leeward wake's length is 3x the tower's height, and flow reattachment to the mainstream takes place after 6x the tower's height. The airflow pattern in the leeward wake forms a descending spiral of decelerated airflow.

[130] See Topic 2.5.1 and Figure 2-6 in Chapter 2 for further information.
[131] See Topic 3.5.3.10 in Chapter 3 for further information.

Figure 9-9: Cp contour plots: isolated CKY Tower windward face - CFD and WT with flat surface (top right), horizontal panels (bottom left) and vertical panels (bottom right) (90°).

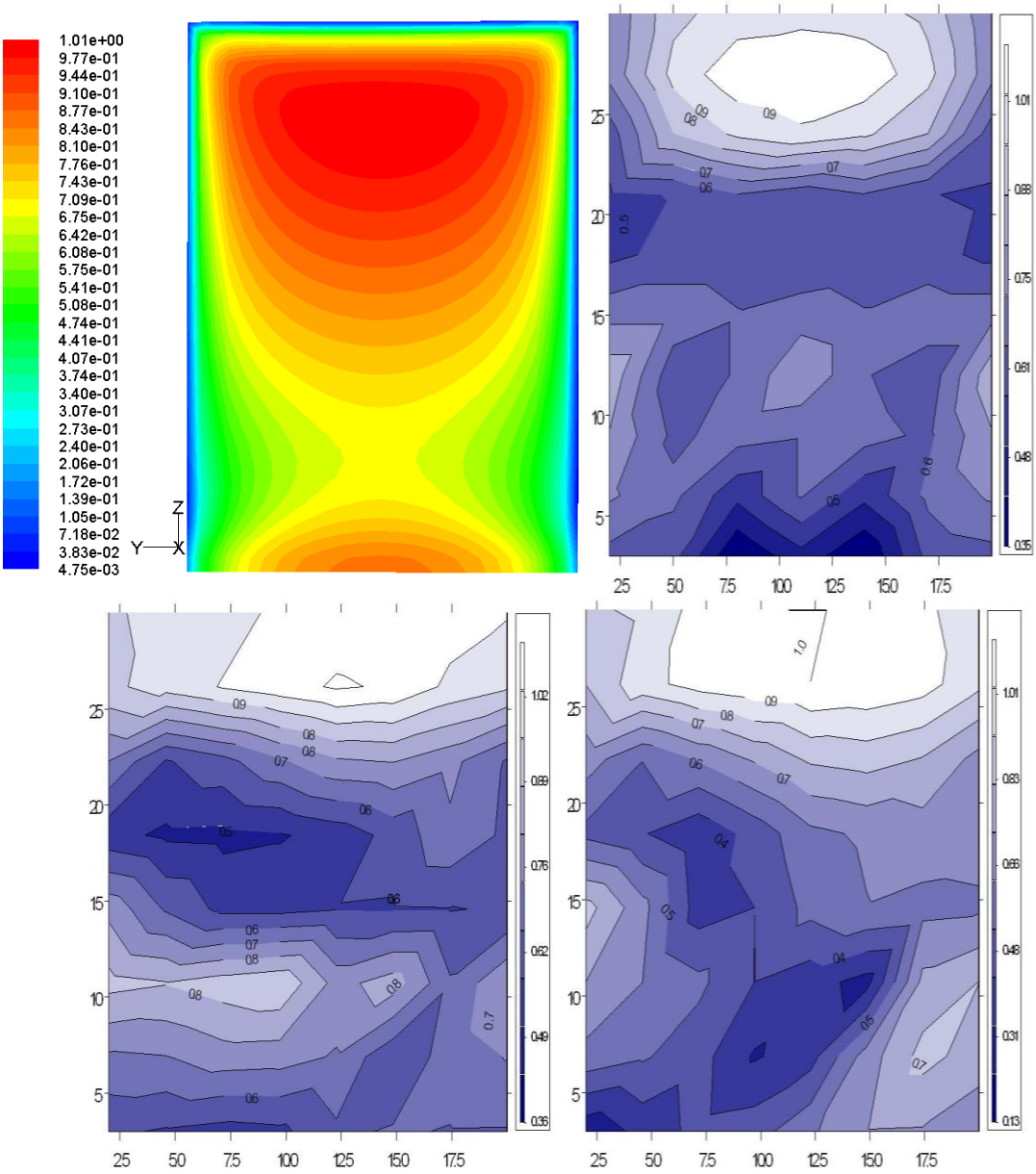

Source: This study.

Figure 9-10: Cp contour plots: isolated CKY Tower leeward face - CFD and WT with flat surface (top right), horizontal panels (bottom left) and vertical panels (bottom right) (90°).

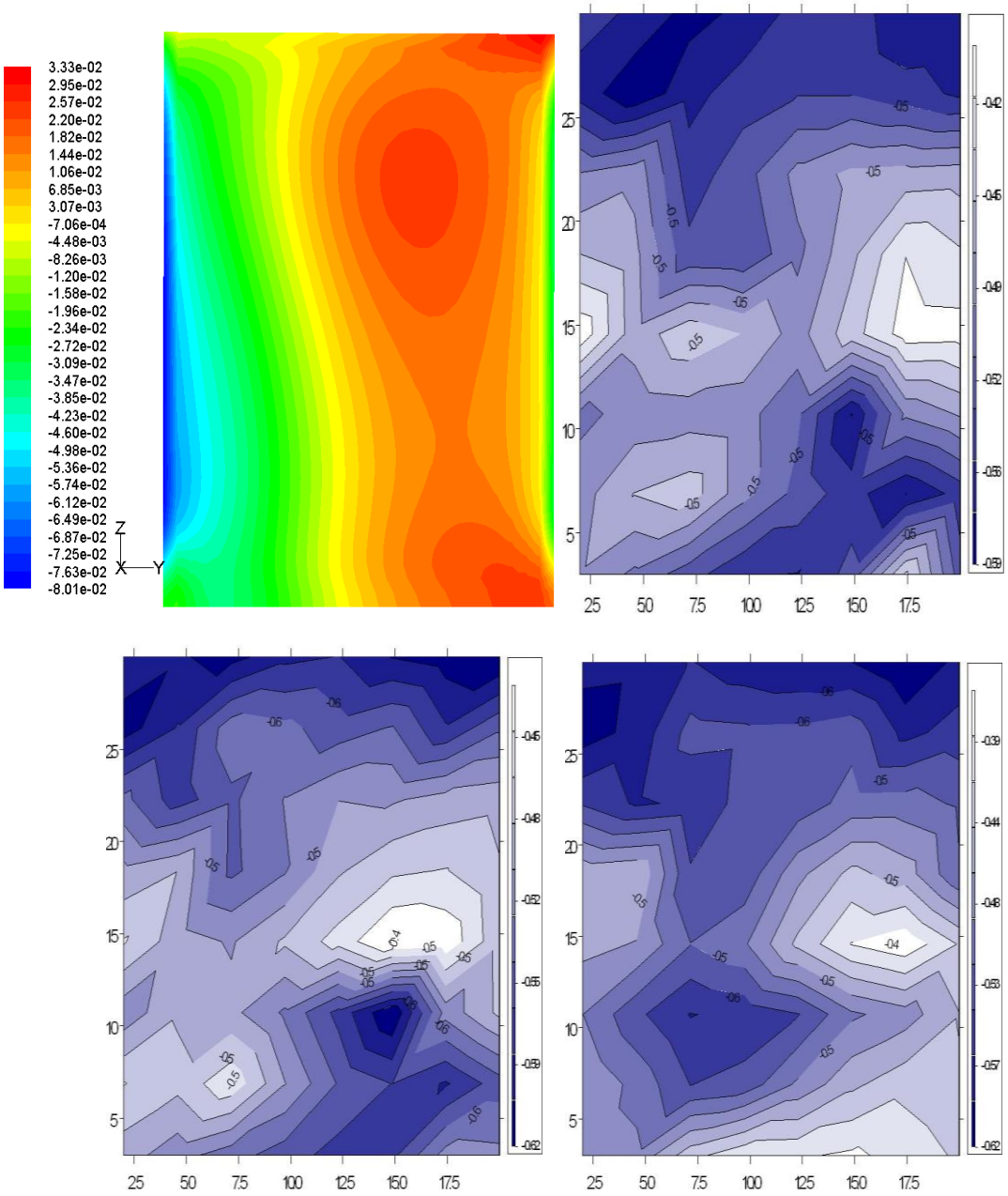

Source: This study.

Figure 9-11: Wind velocity magnitude and x, y and z wind vector components vertical profiles (CFD; 90°)

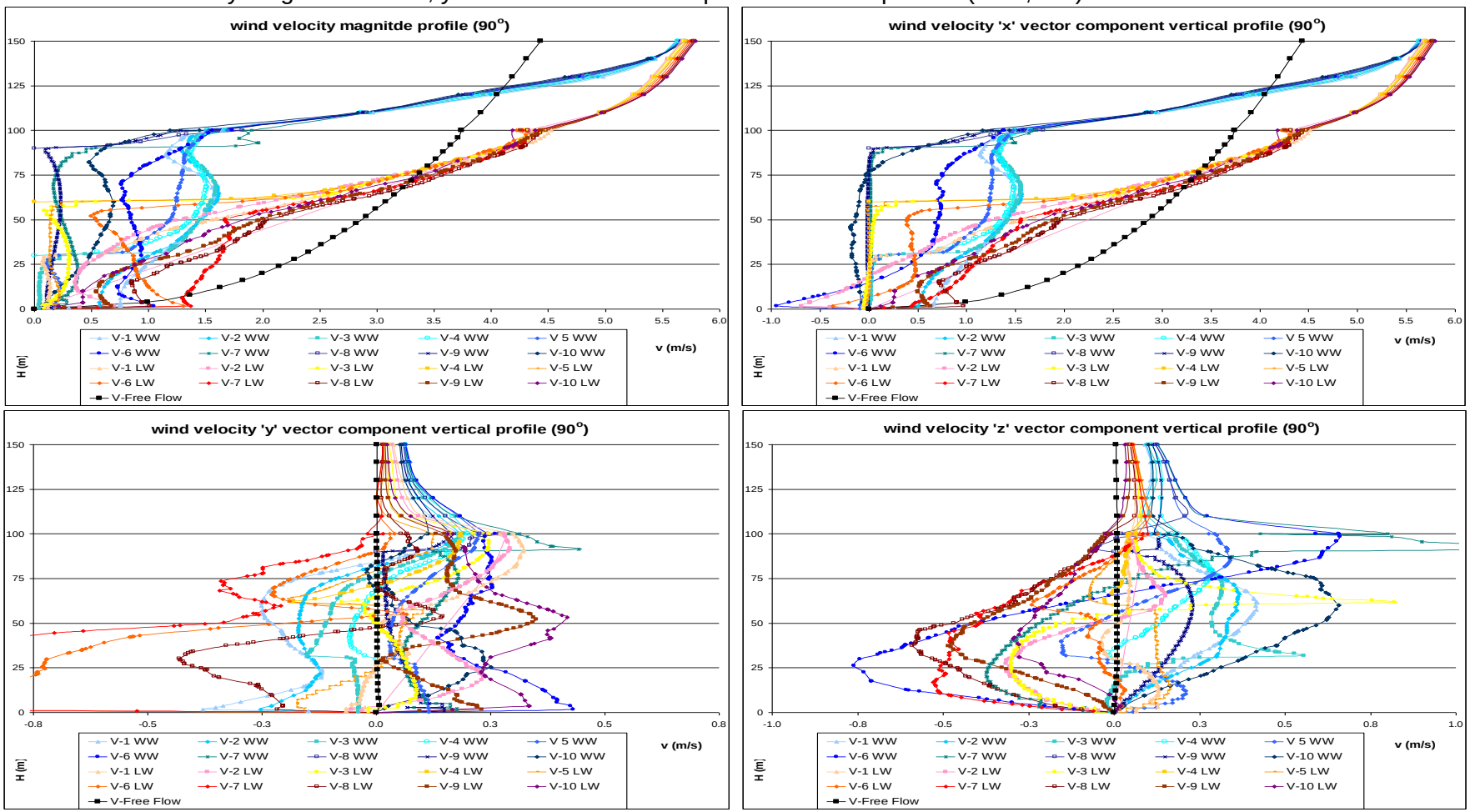

Source: This study.

Figure 9-12: Wind velocity pathlines from a vertical rake in the central axis and a horizontal rake at 50m height (CFD, 90º).

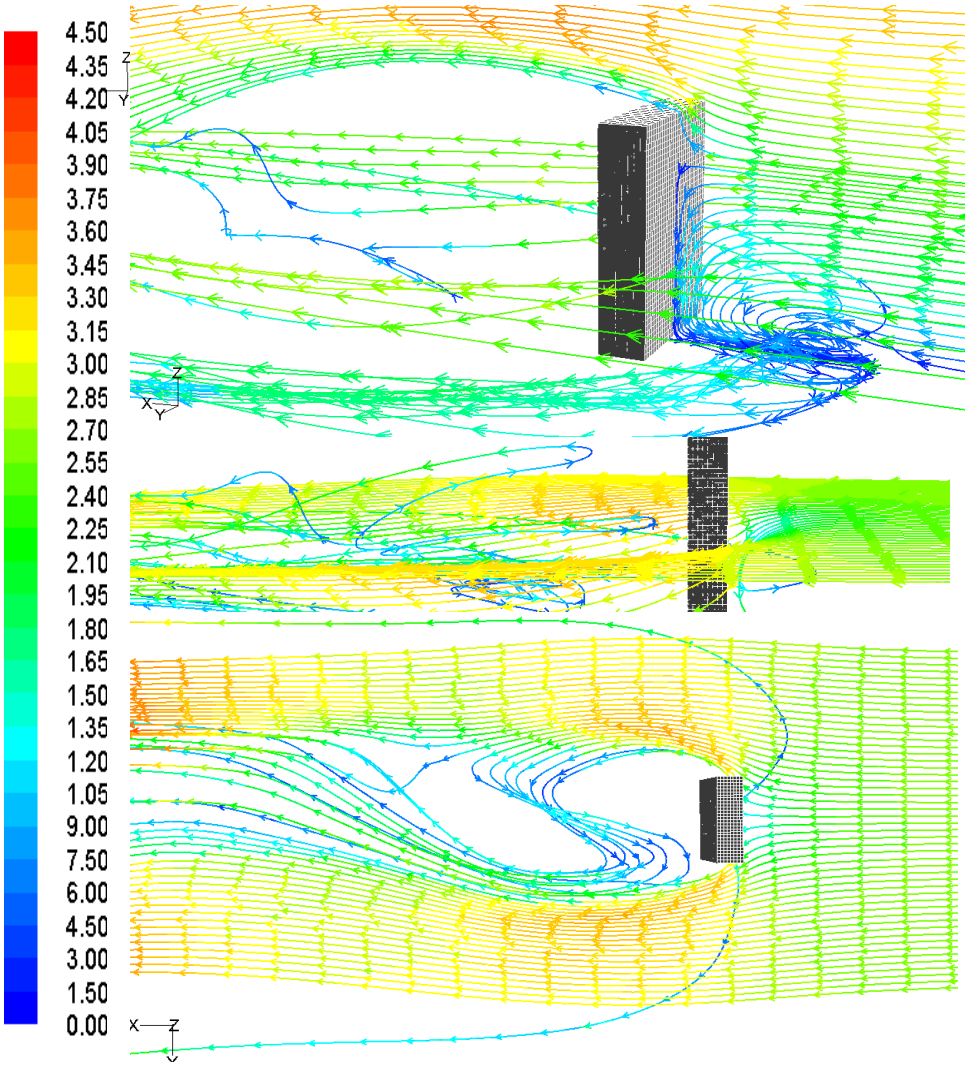

Source: This study.

9.3.1.3. Results for oblique winds (45˚)

For oblique winds, a good agreement was found between the Cp contour plot distribution on the CFD and the WT windward side. This agreement was also reflected in the total averaged CP range of results: 0.99 to 0.03 in the CFD; and 0.99 to 0.06 (WT flat surface), 0.95 to 0.28 (WT horizontal panels), and 0.96 to 0.03 (WT vertical panels). On the leeward side, a good Cp contour plot distribution equivalence was found. Regarding the Cp results, once more the computational calculation was greater than that resulting from the physical experiment: 0.01 to -0.03 in the CFD (leaving aside an isolated high-pressure point on the top-right side); and -0.39 to -0.60 (WT flat surface), -0.42 to -0.60 (WT horizontal panels), and -0.41 to -0.59 (WT vertical panels). Consequently, this disparity in the leeward side results had its impact on the ΔCp range as between windward and leeward sides, as an example of the results for orthogonal winds. The ΔCp range found between windward and leeward sides was: 0.62 to 0.50 in the CFD; and 1.06 to 0.91 (WT flat surface), 1.22 to 1.05 (WT horizontal panels), and 1.11 to 0.94 (WT vertical panels).

Regarding the CFD airflow pattern analysis, when the pathlines meet the oblique block, an FS point is seen at 4/5ths of its total height. From this point the flow washes-up or down the block faces on both the wide and the narrow windward sides. Flow detachment and acceleration by a factor of 2x are to be observed at the frontal vertical edges forming an irregular horse-shoe shape, and reverse flow takes place near ground level on the right side of the wide windward face. The pathlines also present a leeward wake in which deceleration by a factor of 0.5x occurs. Its length exceeds 4x the block's height before it reattaches to the mainstream. Two distinct vertical vortices are found in the wake: while the one from the right side rotates in an anti-clockwise direction, the other from the left side rotates in the opposite direction. Both swirls present up and down flows and their lengths are around equal to the block's height.

Figure 9-13: Cp contour plots: isolated CKY Tower windward face - CFD and WT with flat surface (top right), horizontal panels (bottom left) and vertical panels (bottom right) (45^{o}).

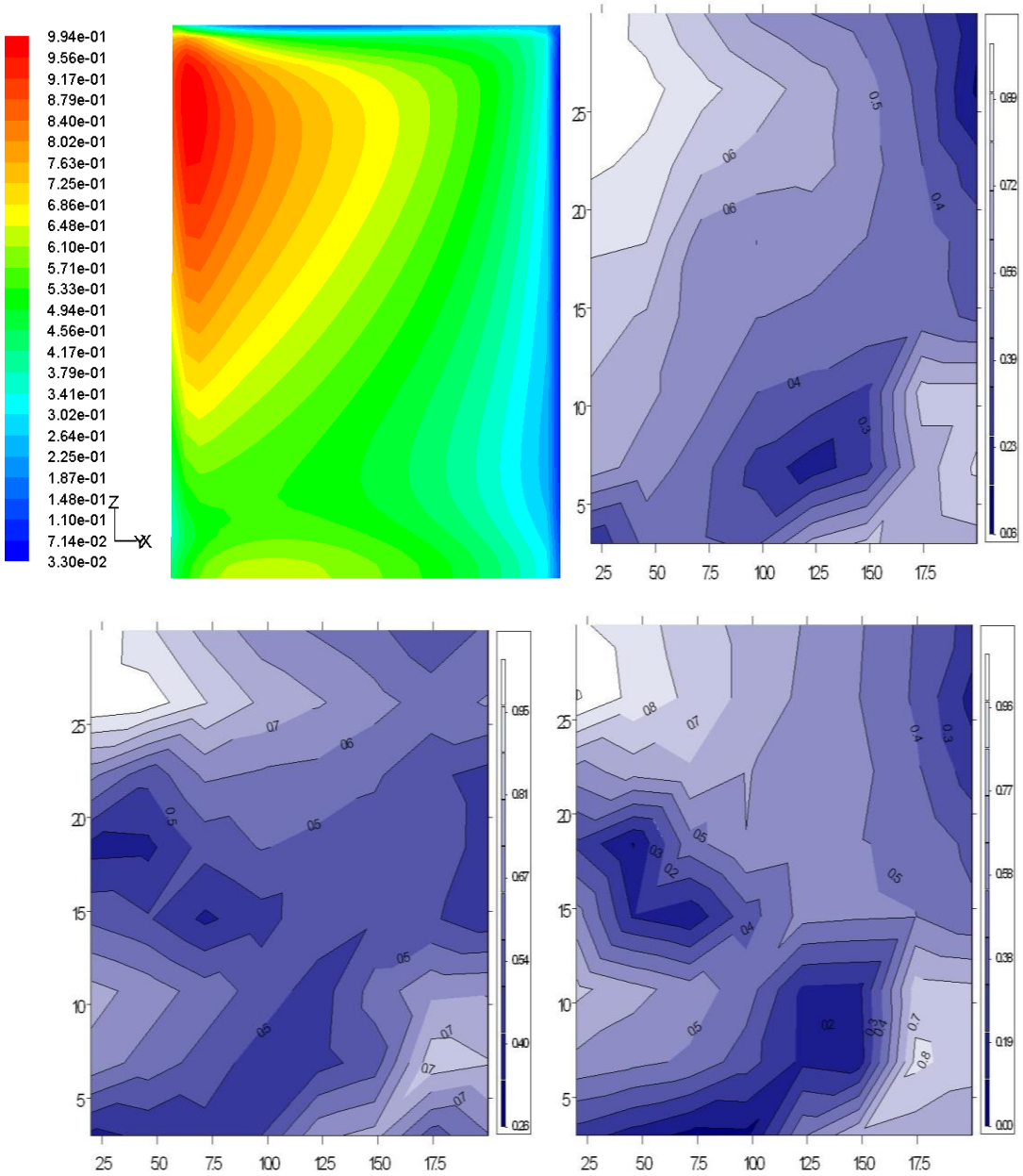

Source: This study.

Figure 9-14: Cp contour plots: isolated CKY Tower leeward face - CFD and WT with flat surface (top right), horizontal panels (bottom left) and vertical panels (bottom right) (45^{o}).

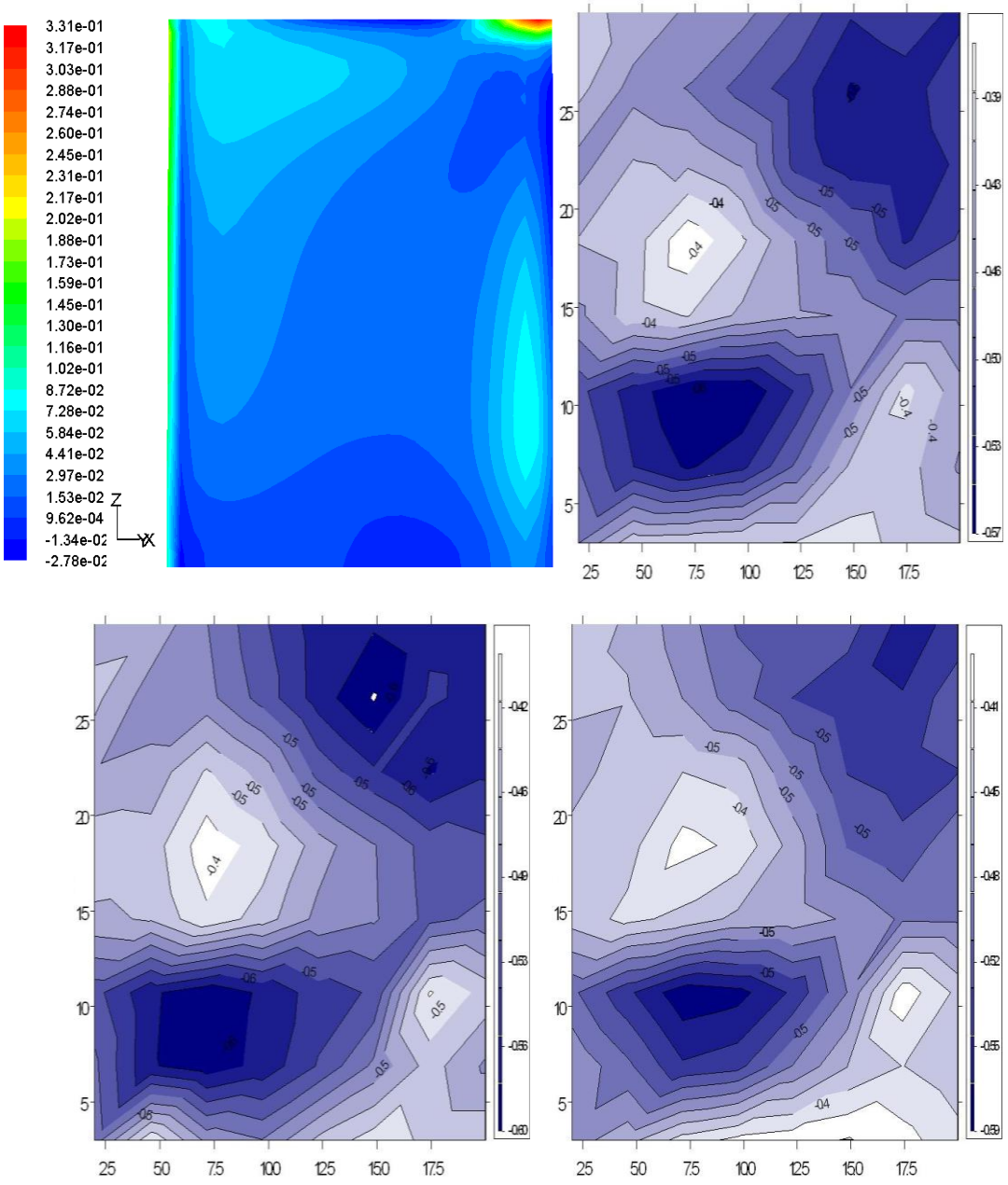

Source: This study.

Figure 9-15: Wind velocity magnitude and x, y and z wind vector components vertical profiles (CFD; 45°)

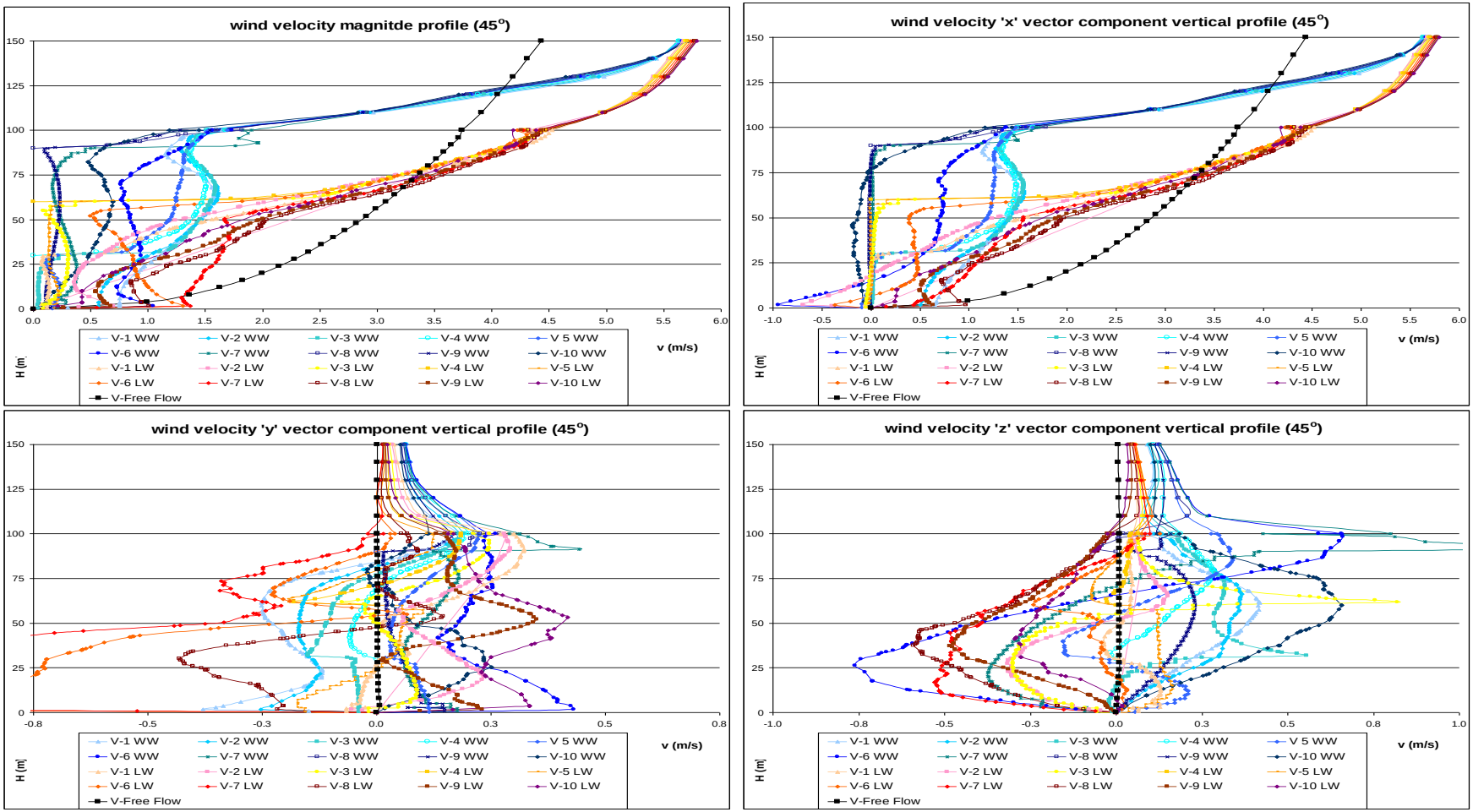

Source: This study.

Figure 9-16: Wind velocity pathlines from a horizontal rake at 40m height (top) and a vertical rake in the central axis (leeward- middle/ windward- bottom) (CFD, 45^{o}).

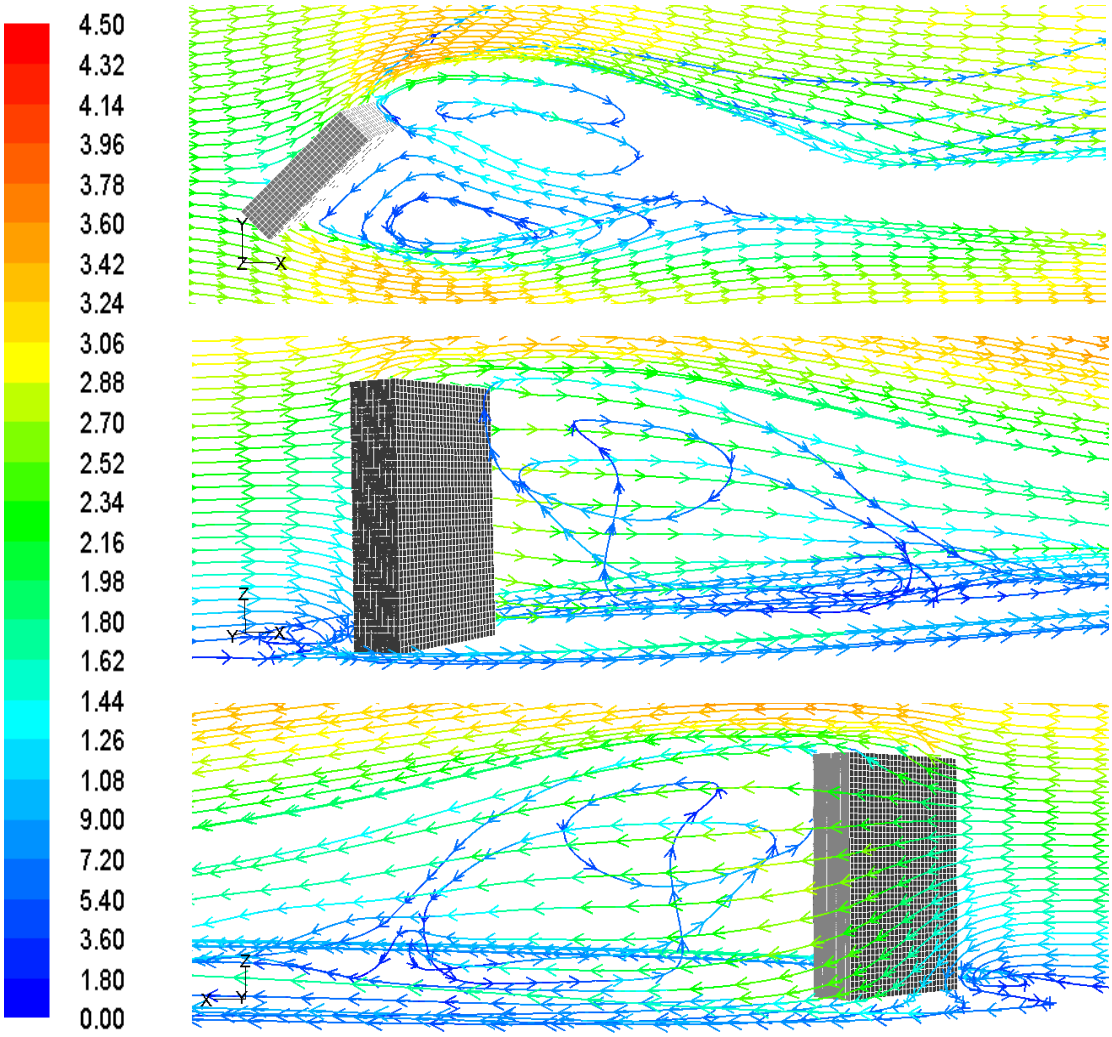

Source: This study.

9.3.2. The CKY Tower in the urban environment

Here the results for the CKY Tower in the urban surroundings of the Paulista Avenue from both CFD and WT experiments are presented and compared among themselves. Five wind directions were simulated, according to the prevailing winds for this region NE (0^o), N and S (45^o), and NW and SE (90^o). Further, the physical experiment explored three alternative façade types: respectively with a flat surface, horizontal panels, and vertical panels.

9.3.2.1. Results for parallel winds (0^o: NE)

First results shown are related to both the right and left sides of the CKY Tower positioned parallel to prevailing North-Easterly winds. As in the analysis for the detached CKY Tower, the contour plot Cp comparison presented similar pressure distributions for both the CFD and the WT sets of experiments, although the computational simulation showed more clearly defined contour lines than did the physical experiment. For instance, a low pressure flow detachment is seen on the top side of the upwind vertical sharp edge in all scenarios and on all sides. Regarding the range of results, there was a considerable difference between the CFD and the WT figures. On the other hand, there was no great variation in the Cp results between the WT models of the three façade types. The total Cp ranges of results for these sets of experiments were: 0.03 to -0.21 (CFD); -0.21 to -0.72 (WT flat surface), -0.24 to -0.73 (WT horizontal panels) and -0.24 to -0.72 (WT vertical panels) on the right side; and -0.08 to -0.35; -0.25 to -0.65, -0.35 to -0.57, and -0.28 to -0.53 on the left side for the same sequence of scenarios. The total averaged ΔCp found between right and left sides were: -0.11, 0.04, 0.02, and 0.04. When contrasted with the isolated tower results, a proportional ΔCp drop of 0.11 is observed in most of the scenarios.

The airflow pathlines and wind velocity vertical profiles illustrate the pressure difference. While an acceleration bulk of flow by a factor of 2.0x strikes the top right side of the CKY Tower windward face, the left side is in the downwind direction of a leeward wake. Near the walls wind velocity ranges from 0.5 to 1.5m/s up to 90m high.

Figure 9-17: Wind velocity pathlines from a rake at 20m height and the assessed vertical profiles (CFD, NE, 0^{o}).

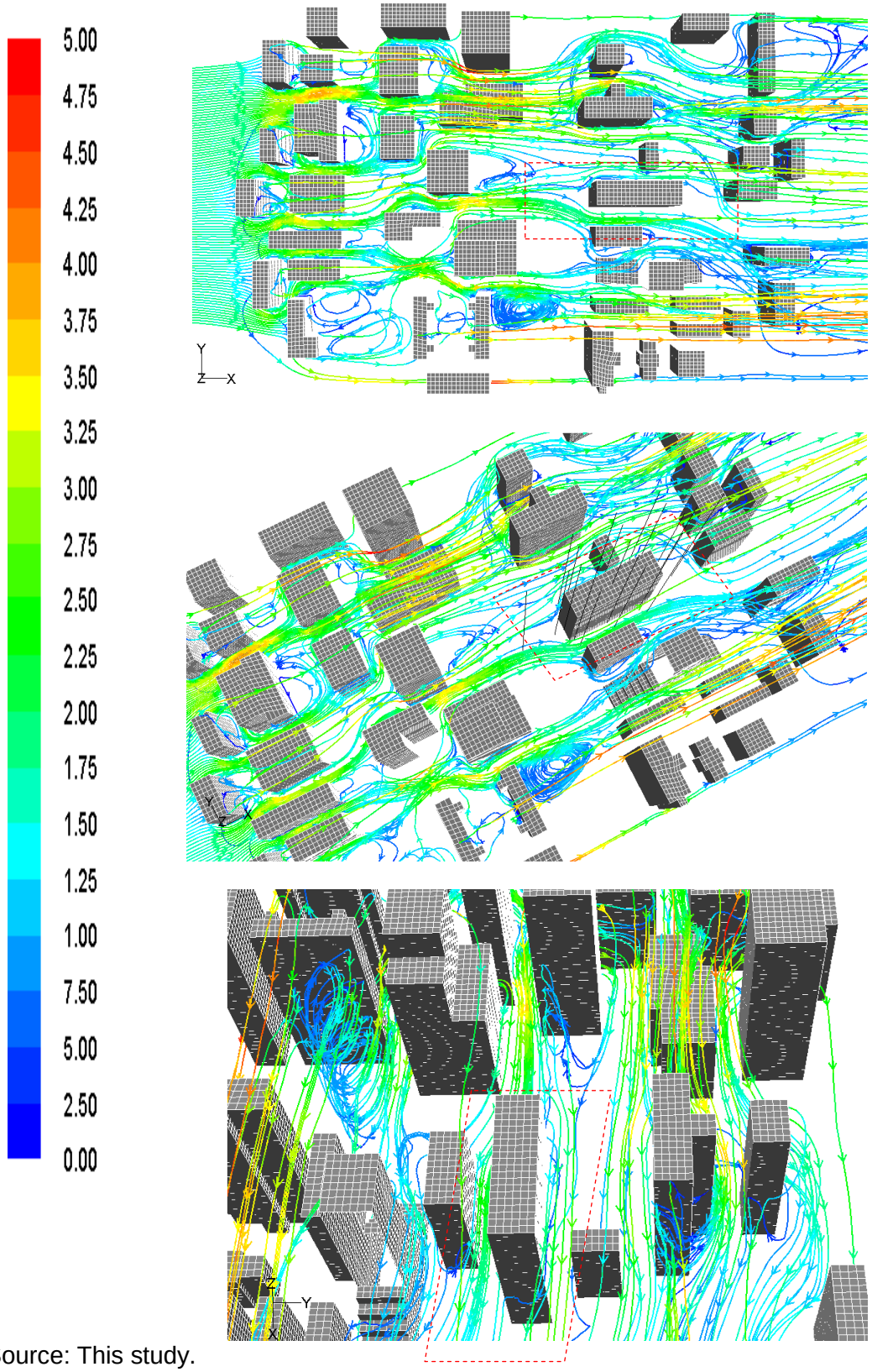

Source: This study.

Figure 9-18: Cp contour plots: CKY Tower in the urban environment right side - CFD and WT with flat surface (top right), horizontal panels (bottom left) and vertical panels (bottom right) (NE, 0°).

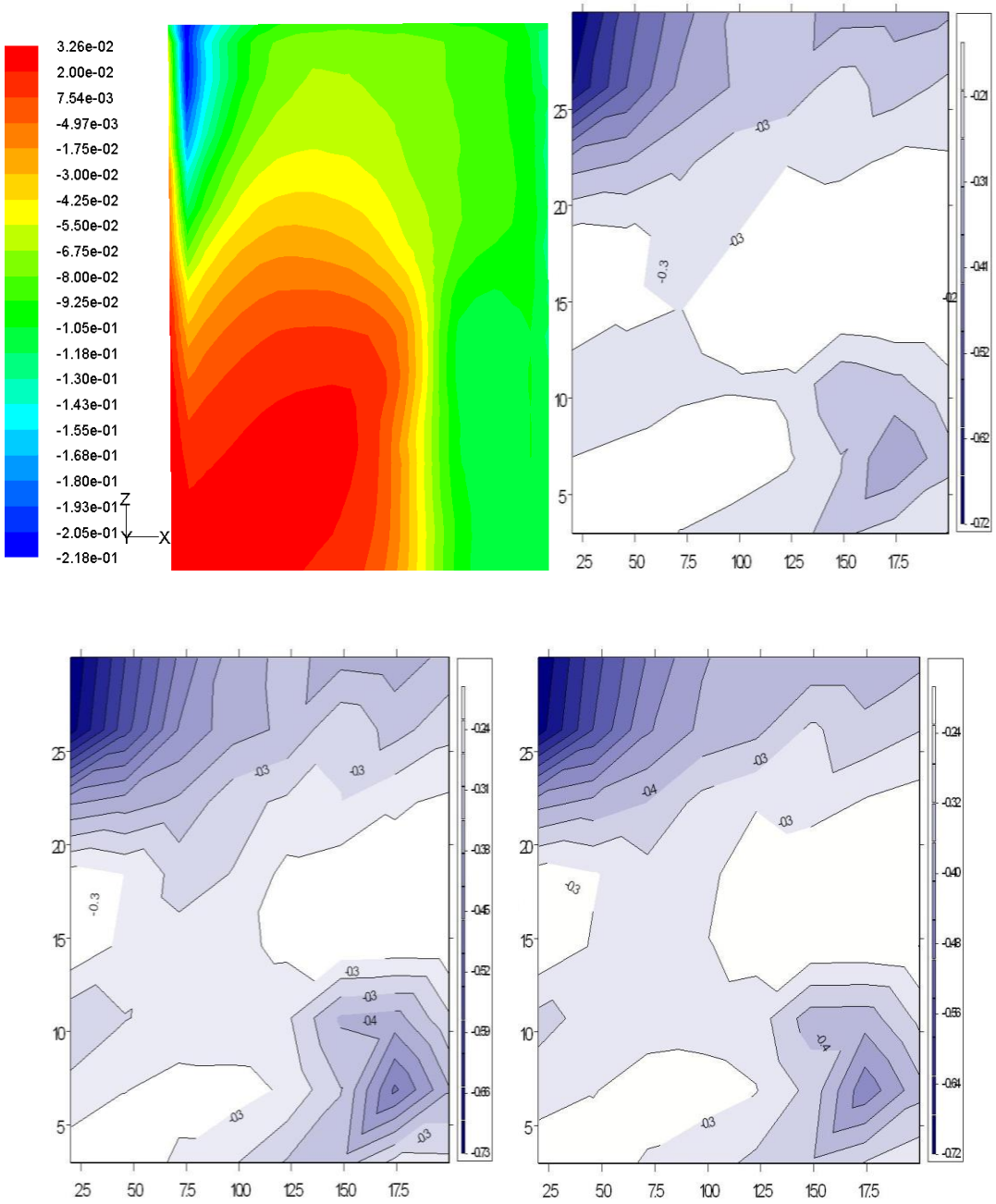

Source: This study.

Figure 9-19: Cp contour plots: CKY Tower in the urban environment left side - CFD and WT with flat surface (top right), horizontal panels (bottom left) and vertical panels (bottom right) (NE, 0^{o}).

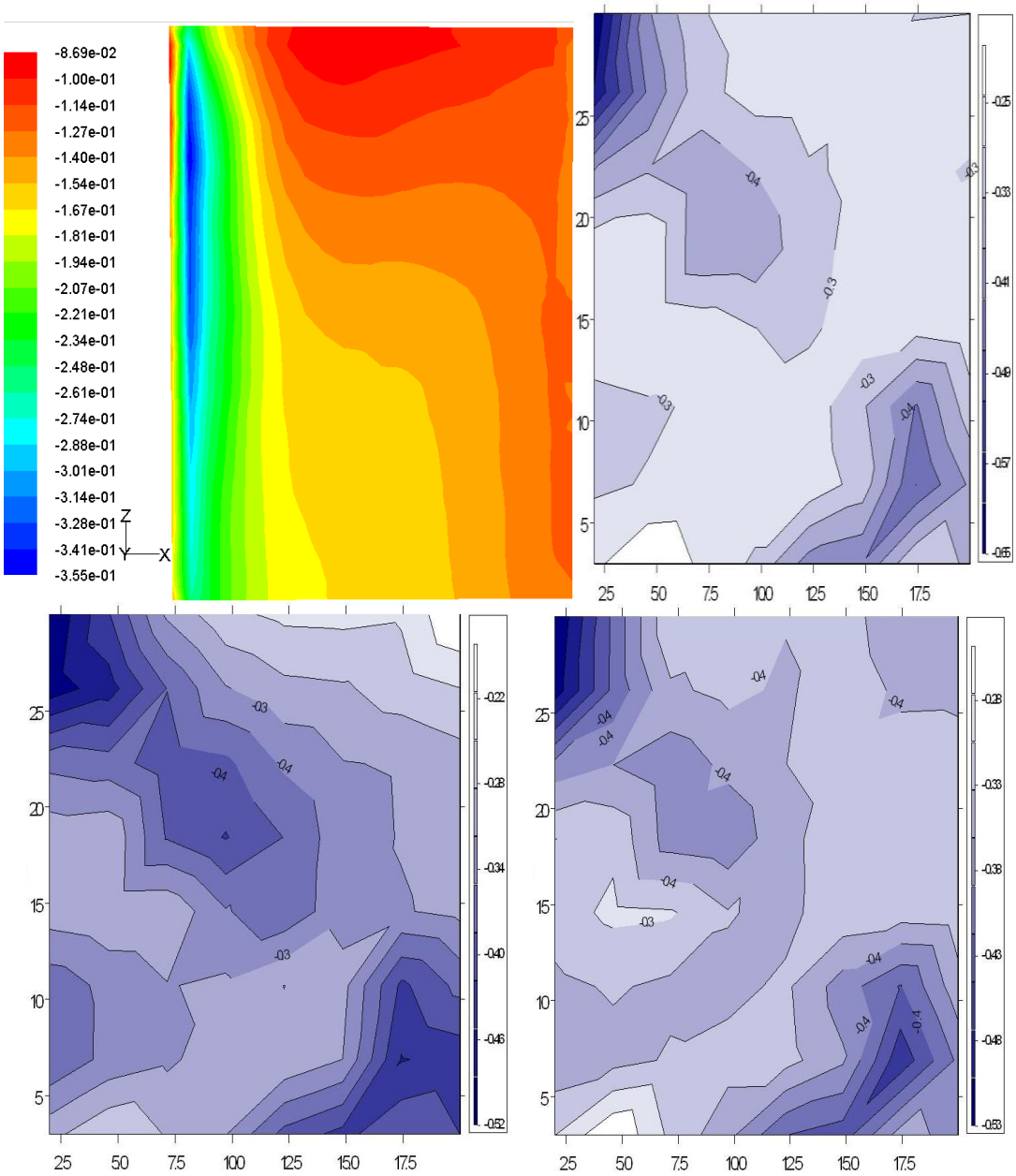

Source: This study.

Figure 9-20: Wind velocity magnitude and x, y and z wind vector components vertical profiles for (CFD; NE; 0^{o})

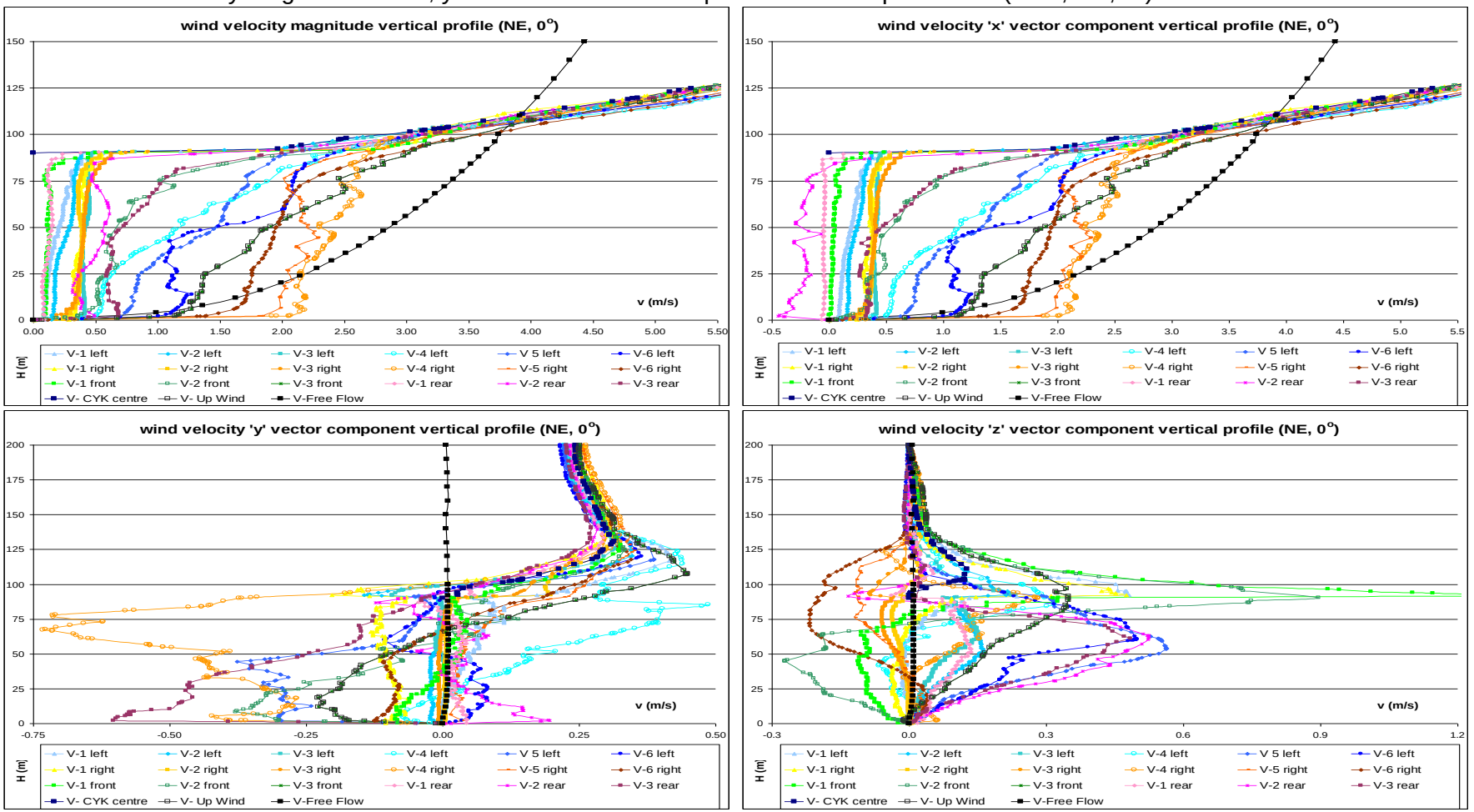

Source: This study.

9.3.2.2. Results for orthogonal winds (90^{o}: NW and SE)

Two wind directions were investigated for prevailing winds orthogonal to the CKY Tower: Northwest and Southeast. These directions are also those with most frequent wind incidence throughout the year in this region[132]. The Cp contour plots are related to both the windward and the leeward faces, and the results from the NW and the SE CFD and WT simulations are directly contrasted between themselves and also with the isolated CKY Tower case study addressed in the previous topics.

On the whole, the pressure distribution contour plots comparing the CFD and the WT windward surfaces matched well. The surrounding upwind buildings create low pressure on most of these surfaces, with the exception of the top left corner for NW winds and the top right corner for SE winds. No FS point is now seen, when contrasted to the wind effects around an isolated tower. The total range of Cp results for these sets of windward surfaces were: 0.10 to -0.67 (CFD); 0.25 to -0.31 (WT flat surface), 0.30 to -0.29 (WT horizontal panels) and 0.31 to -0.31 (WT vertical panels) for the NW winds; and 1.13 to -0.30; 0.49 to -0.31, 0.71 to -0.33, and 0.68 to -0.32 for the SE winds and for the same sequence of scenarios. It may be observed that higher pressures are found for SE winds than for NW ones. This may be explained by the varying proximity of neighbouring buildings in these cases. While in the first example an H/W > 2.0 is observed, in the second the H/W ratio is around 1.0 and, further, the upwind block is narrower than the CKY tower, which would give rise to an air jet directed towards this latter block. Finally, it is clear that the influence of vertical or horizontal panels was irrelevant for the NW winds. On the other hand, for the SE winds it seems that both sorts of panels were useful in increasing the total Cp results.

Regarding the leeward sides some similarity between the WT and the CFD contour plots can be seen, although since it is basically formed by low pressure and unstable turbulent wakes, it is to be expected that a time-averaged result would differ from a time-steady one. Conversely, the total ranges of Cp results for these sets of leeward surfaces were quite close: -0.64 to -0.89 (CFD); -0.28 to -0.50 (WT flat surface), -0.23 to -0.59 (WT horizontal panels) and -0.19 to -0.51 (WT vertical panels) for the NW winds; and 0.00 to -0.24; -0.08 to -0.44, -0.07 to -0.46, and -0.06 to -0.48 for the SE winds and for the same sequence of scenarios.

The total averaged ΔCp found between the windward and the leeward sides were: 0.15 (CFD); 0.25 (WT flat surface), 0.48 (WT horizontal panels) and 0.29 (WT vertical panels) for the NW winds; and 0.17; 0.31, 0.42, and 0.39 for the SE winds and for the same sequence of scenarios. When contrasted to the isolated tower results, an

[132] See topic 5.4.2.2. in Chapter 5.

averaged ΔCp drop of 0.60, 0.75, 0.80, and 0.80 is to be observed in each of the scenarios assessed, which is to be credited to the surrounding urban environment.

The airflow pathlines released from a horizontal rake at 50m height show that, for both the orthogonal wind directions, a strong wind channelling effect takes place in the Paulista Avenue canyon. Consequently, a sequence of decelerated vortices meanders around the towers. When reaching the windward side of tall rectangular base towers, both ascending and descending diagonal airflow patterns are seen. The ascending flow causes acceleration and concentrated increase of pressure on the surfaces. The descending flow shows deceleration throughout its path but, on reaching the ground it accelerates and escapes either through its lateral side or causes reverse vortices. It can also be trapped in others leeward vortices, causing wake interference.

Further, both the wind velocity magnitude vertical profiles show isolated acceleration by a factor of 3.0x at the windward vertical corners up to 10m height, while for all the other vertical profiles the wind velocity ranges from 0.20 to 0.50m/s near walls and from 0.50 to 1.00m/s on each street's central axis. An exception occurs in the leeward side's central profile, where the airflow speed practically accompanies the ABL input's vertical profile. The wind vector components show a rapid change of direction in the flows in both the horizontal and vertical directions, which typically creates ascending and descending spiral vortices along the mainstream.

Figure 9-21: Wind velocity pathlines from a horizontal rake 50m high (CFD, NW, 90º).

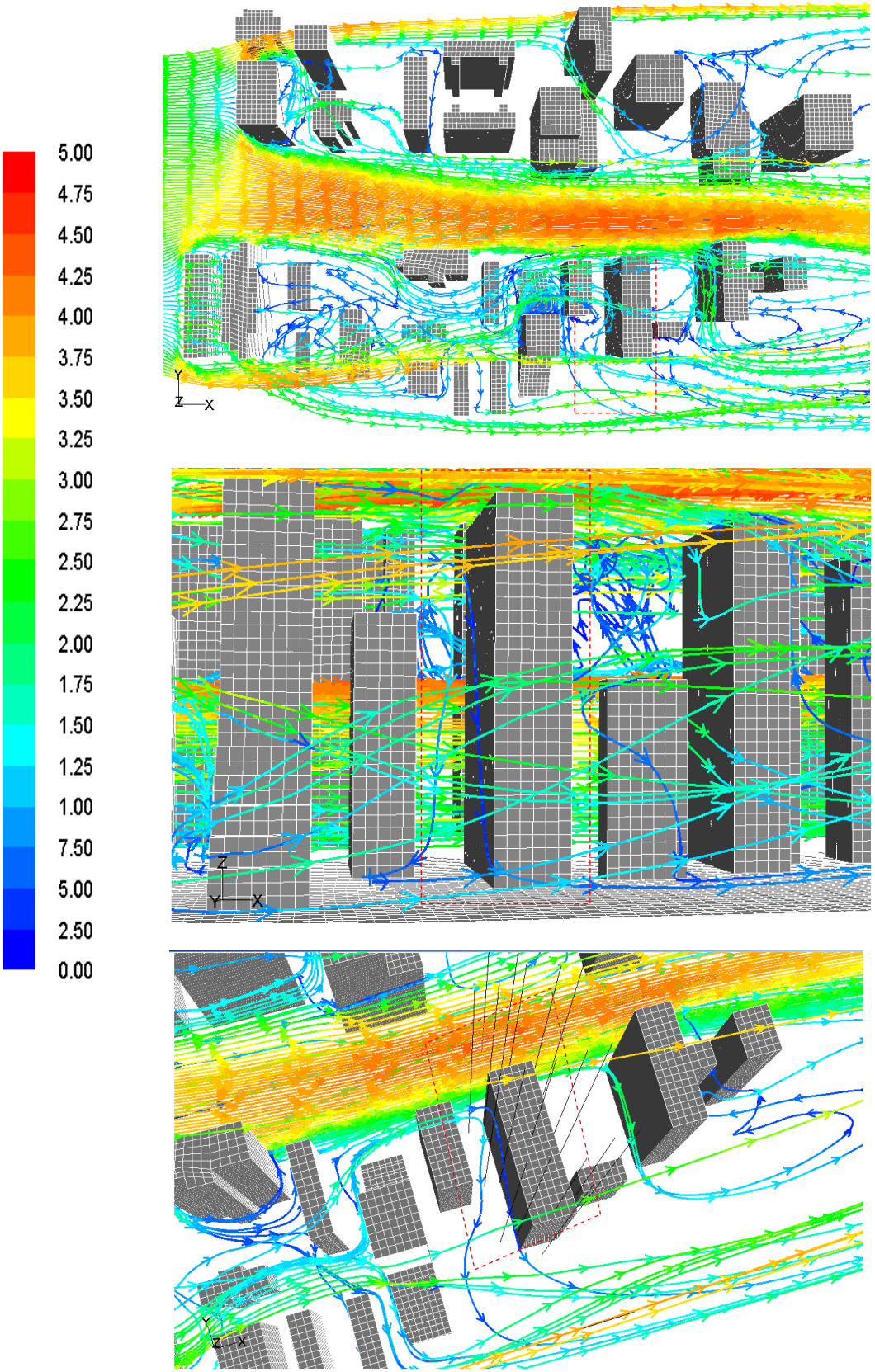

Source: This study.

Figure 9-22: NW: Cp contour plots: windward side of the CKY Tower in the urban environment CFD and WT with flat surface (top right), horizontal panels (bottom left) and vertical panels (bottom right) results (NW, 90^{o})

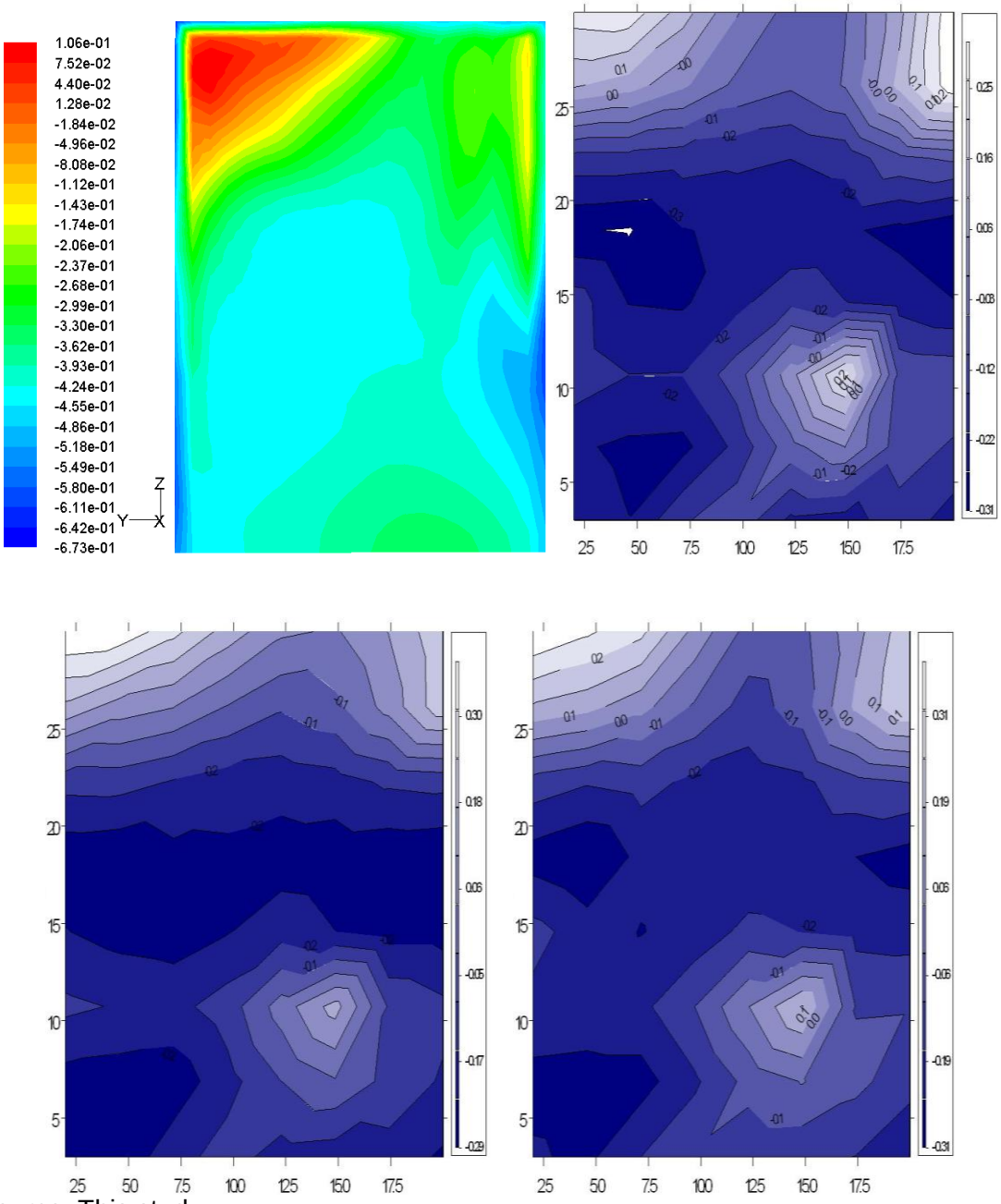

Source: This study.

Figure 9-23: NW: Cp contour plots: leeward side of the CKY Tower in the urban environment CFD and WT with flat surface (top right), horizontal panels (bottom left) and vertical panels (bottom right) results (NW, 90^{o})

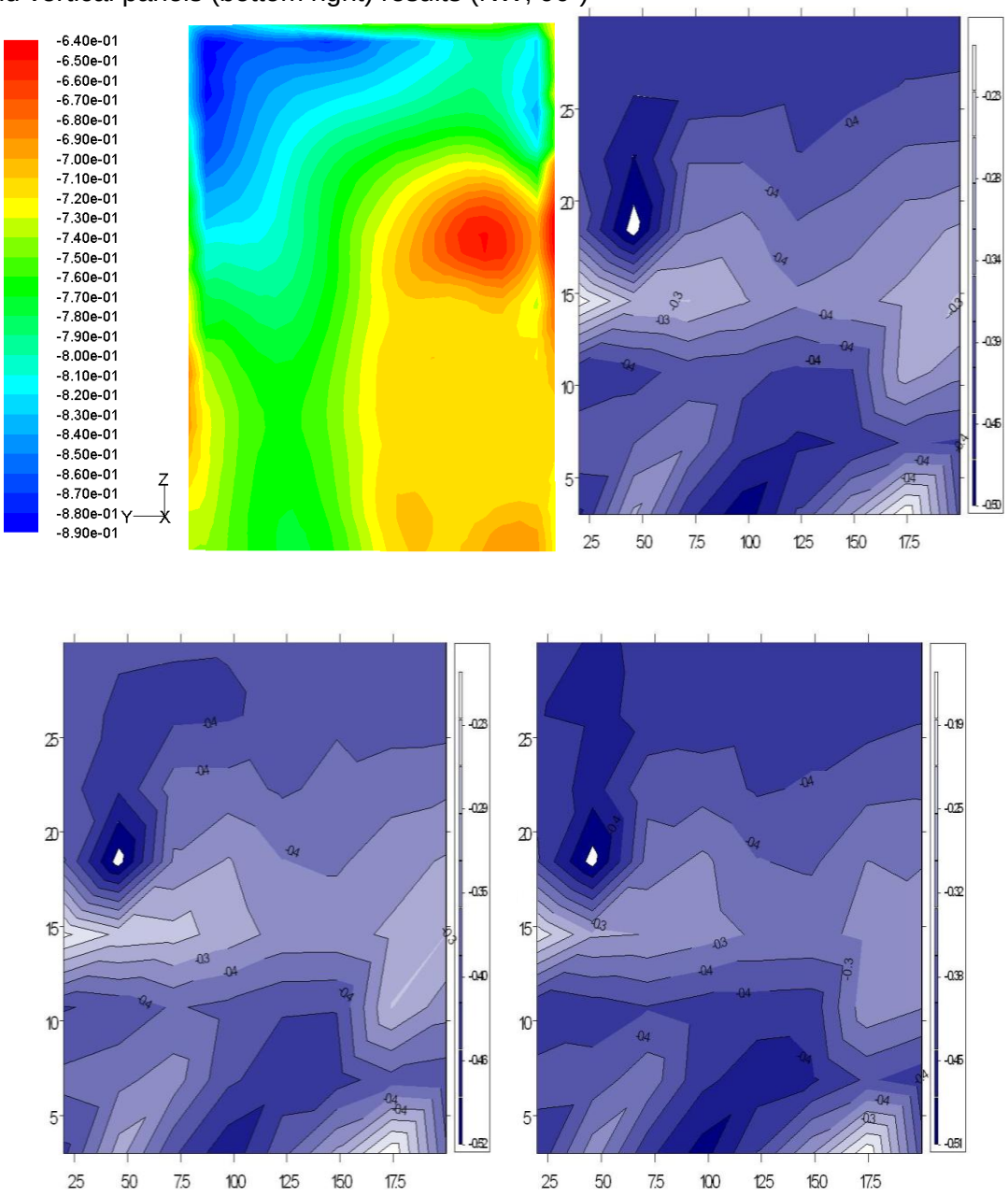

Source: This study.

Figure 9-24: Wind velocity magnitude and x, y and z wind vector components vertical profiles (CFD; NW, 90°)

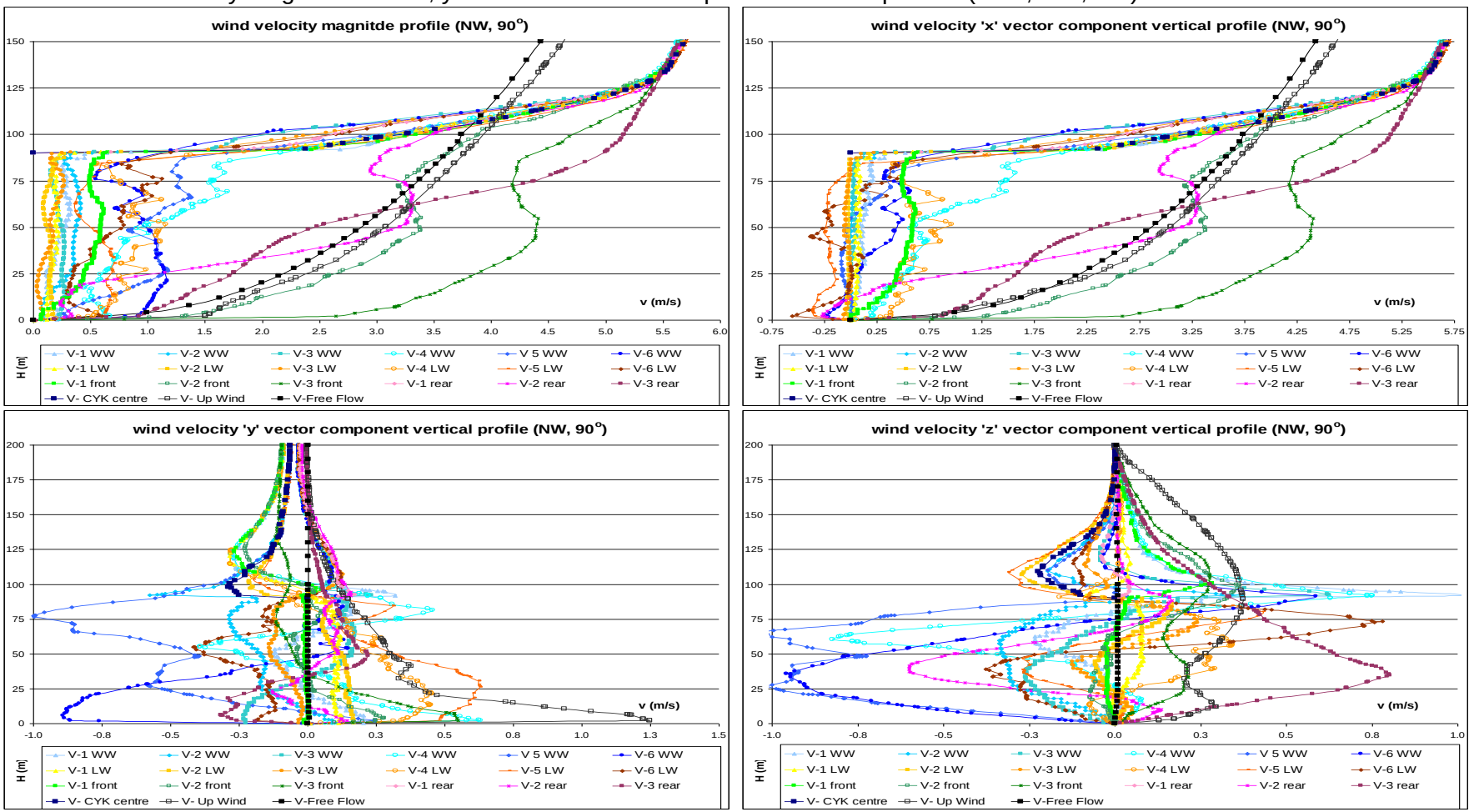

Source: This study.

Figure 9-25: Wind velocity pathlines from a horizontal rake 50m high (CFD, SE, 90°).

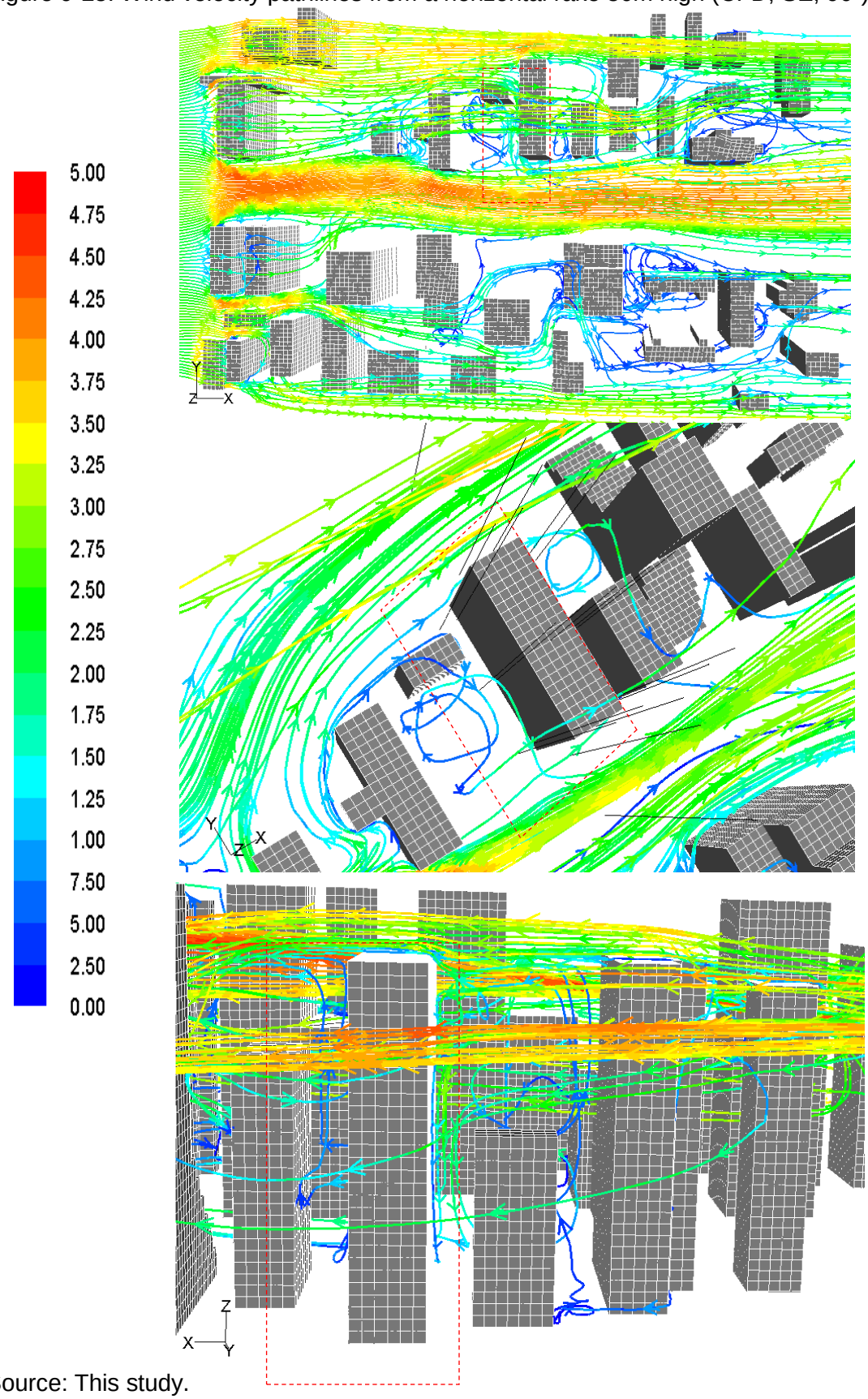

Source: This study.

Figure 9-26: SE: Cp contour plots: windward side of the CKY Tower in the urban environment CFD and WT with flat surface (top right), horizontal panels (bottom left) and vertical panels (bottom right) results (SE, 90^{o})

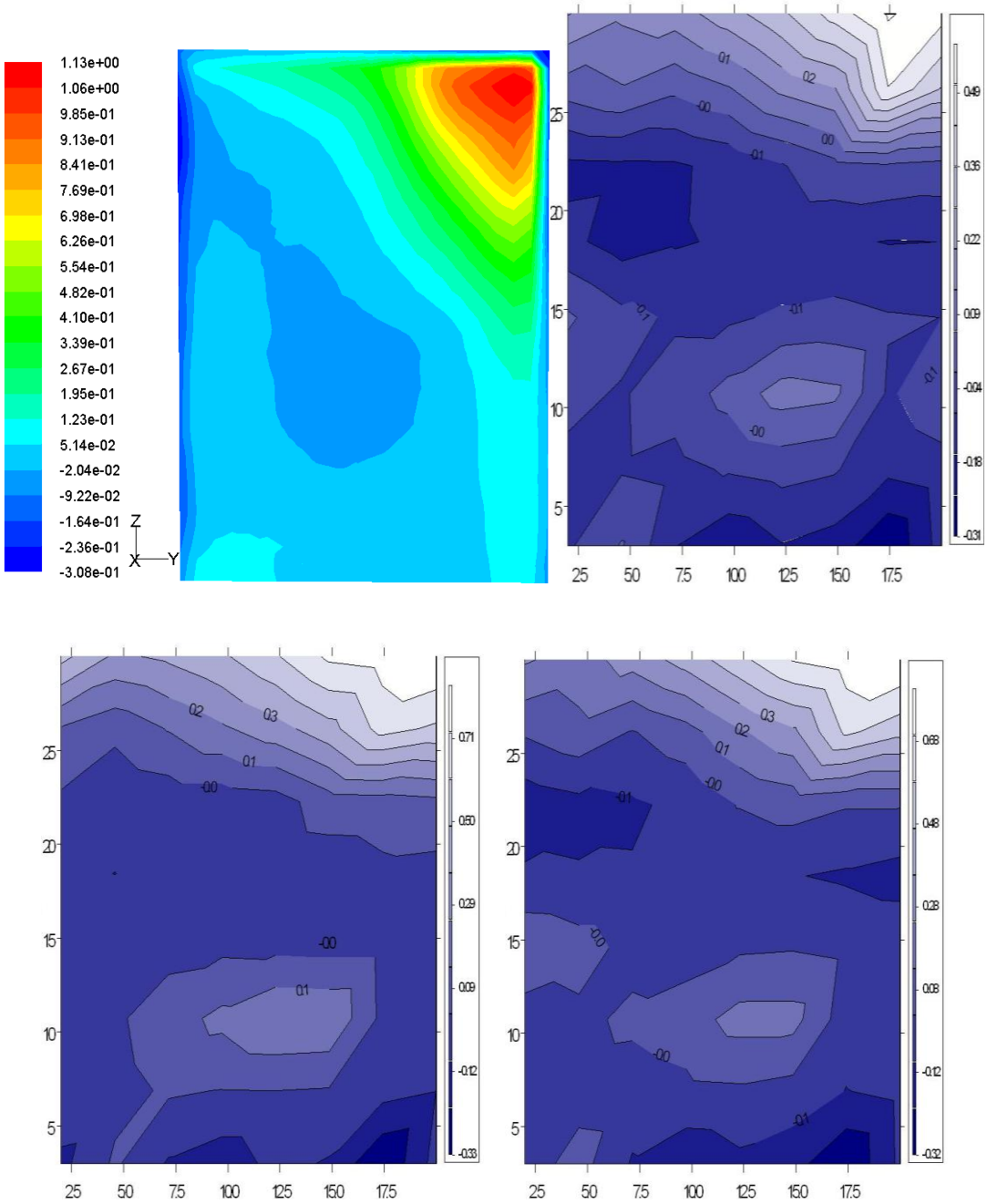

Source: This study.

Figure 9-27: SE: Cp contour plots: leeward side of the CKY Tower in the urban environment CFD and WT with flat surface (top right), horizontal panels (bottom left) and vertical panels (bottom right) results (SE, 90°)

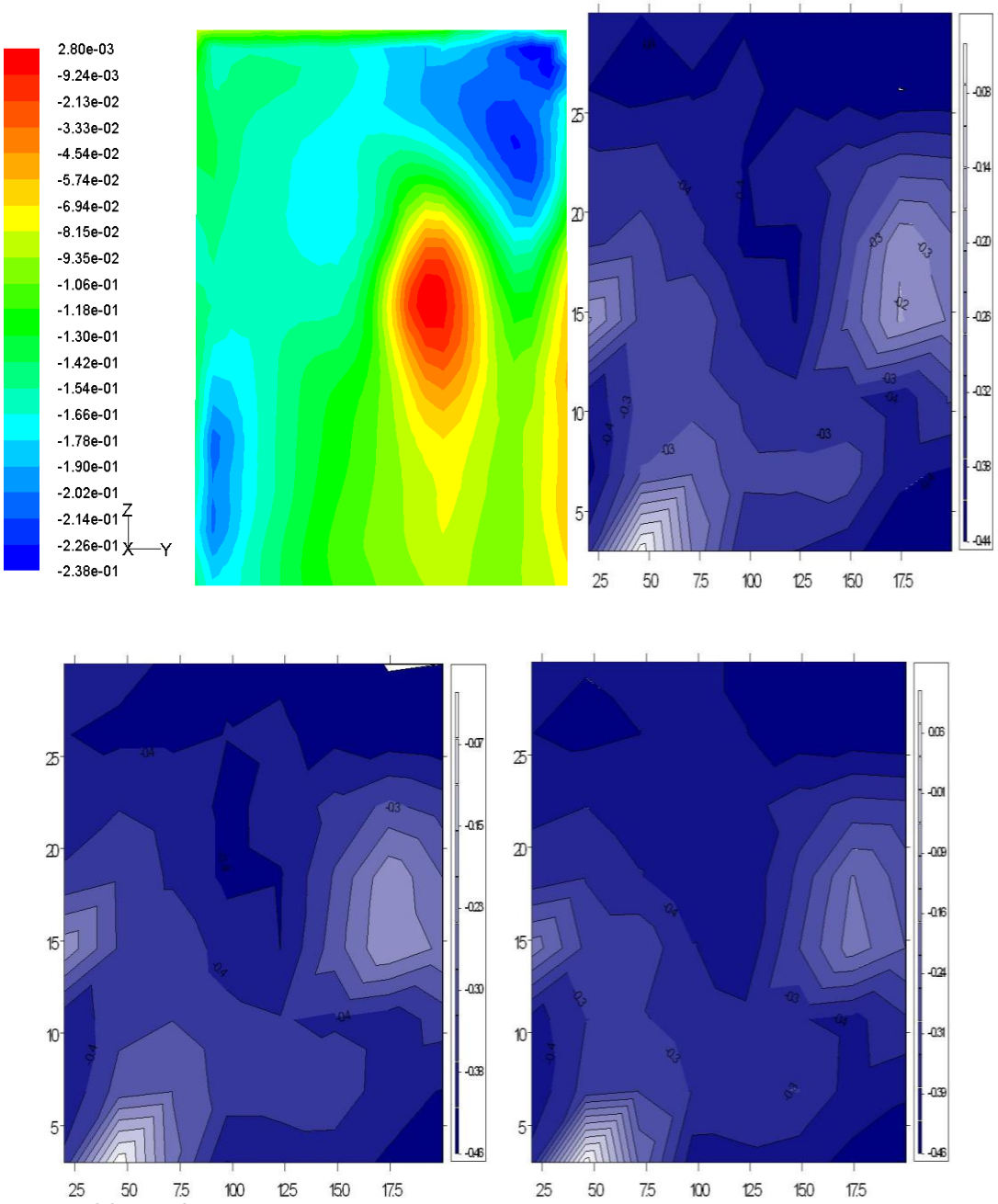

Source: This study.

Figure 9-28: Wind velocity magnitude and x, y and z wind vector components vertical profiles (CFD; SE; 90°)

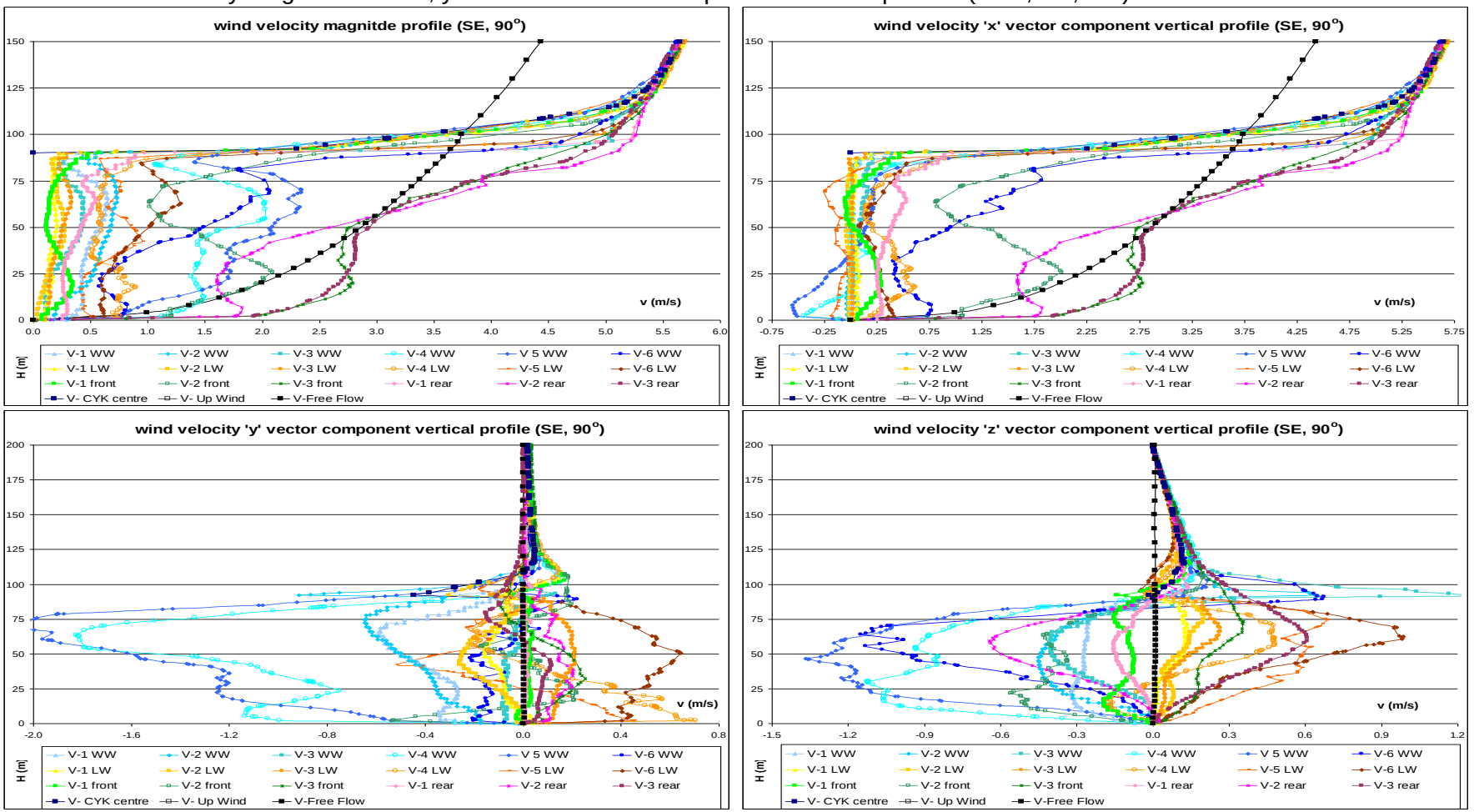

Source: This study.

9.3.2.3. Results for oblique winds (45^{o}: N and S)

To serve as example of the previous topic, two wind directions were investigated for prevailing winds oblique to the CKY Tower: North and South. These directions are also the third and fourth in terms of wind incidence throughout the year in this region. The Cp contour plots are related to both the windward and the leeward faces, and the results from the N and the S CFD and WT simulations are directly contrasted one with the other and with the isolated tower case.

Overall, the Cp contour plots contrasting the CFD and the WT windward flat surfaces matched well for both the N and the S winds. Similar pressure distribution was also maintained between the respective surfaces and the isolated tower simulations. The influence of the horizontal and the vertical panels in the pressure contour distribution was also observed.

Quite different pressure results were found between the N and the S wind directions. The reasons for this lie in the fact that, as previously mentioned for prevailing orthogonal winds, the H/W aspect ratio of the assessed windward surfaces is greater (narrower) for the N direction and smaller (wider) for the S direction. The bulk of the airflow follows a sinuous pattern and the varying proximity of neighbouring buildings in these two cases seems to be as relevant as for orthogonal winds. As a result, the total Cp ranges of results on the windward surfaces were: 0.07 to -0.10 (CFD); 0.05 to -0.47 (WT flat surface), 0.08 to -0.52 (WT horizontal panels) and 0.15 to -0.53 (WT vertical panels) for North winds; and 0.88 to -0.63 (CFD); 0.87 to -0.33 (WT flat surface), 0.68 to -0.14 (WT horizontal panels) and 0.84 to -0.14 (WT vertical panels) for South winds, which are slightly lower than the Cp results from the isolated tower simulation. Regarding the leeward sides less similarity was observed between the WT and the CFD contour plots, and the explanation for this is also in line with the foregoing orthogonal winds assessment. Some disparity was also found in the total range of the Cp results: -0.06 to -0.30 (CFD); -0.26 to -0.54 (WT flat surface), -0.30 to -0.60 (WT horizontal panels) and -0.26 to -0.58 (WT vertical panels) for the N winds; and -0.04 to -0.60; -0.27 to -0.86, -0.22 to -0.89, and -0.34 to -0.84 for the S winds and for the same sequence of scenarios.

The total averaged ΔCp found between the windward and the leeward sides were very similar to the CFD and the WT results in both the North and South wind direction simulations, although the total values for the former were just less than half those of the latter: 0.30 (CFD); 0.29 (WT flat surface), 0.32 (WT horizontal panels) and 0.26 (WT vertical panels) for the N winds; and 0.44, 0.77, 0.88, and 0.82 for the S winds and for

the same sequence of scenarios. When contrasted with the isolated tower results, the ΔCp for the N winds were lower, and those for the S winds higher.

The airflow pathlines released from horizontal rakes show a sinuosity towards the mainstream but that divides into two and turns into either an ascending or a descending diagonal flow after reaching the windward vertical edge of the towers. When this happens, the flow accelerates, which may explain the greater ΔCp for the oblique than for the orthogonal winds in the urban environment. Furthermore, the urban scenario may cause local acceleration due to channelling and Venture wind effects. The leeward airflow patterns are characterized by circular upward and downward swirls which are trapped between these sinuous bulks of flow. This last phenomenon is observed in both the N and the S airflow pathline visualizations.

Both the N and the S wind velocity magnitude vertical profiles show acceleration by a factor of up to 3.0x at the windward vertical corners up to 10m height after the division of the flow in two directions. In the other vertical profiles the wind velocity ranges from 0.20 to 0.50m/s near walls and from 0.50 to 2.00m/s away from them. Reverse flow up to -0.75m/s is found near the leeward sides for North winds. The other wind vector components show a really intense change in the flow direction, attaining from -2.50 to + 2.50m/s across the flow direction and occurring randomly up to 100m height; and vertically from -3.00 (from ground to 50m height) to + 2.50m/s (from 50m to 75m height), though less intense peaks occur at all heights below the canopy height.

Figure 9-29: Wind velocity pathlines from a rake at 30m height (top) and seen from the upwind (middle) and the downwind (bottom) direction (CFD, N, 45^{o}).

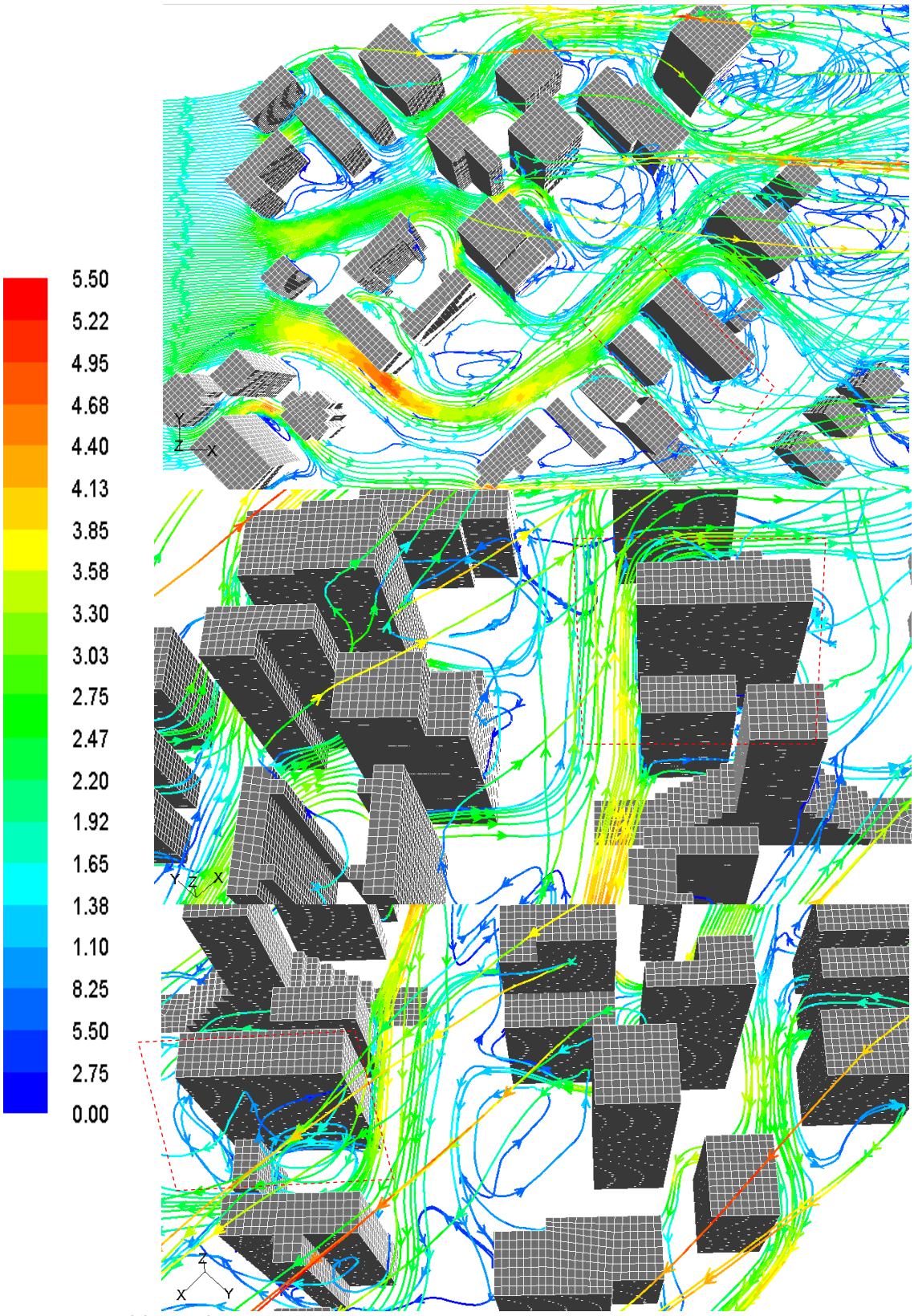

Source: This study.

Figure 9-30: Cp contour plots: windward side of the CKY Tower in the urban environment CFD and WT with flat surface (top right), horizontal panels (bottom left) and vertical panels (bottom right) results (N, 45^{o}).

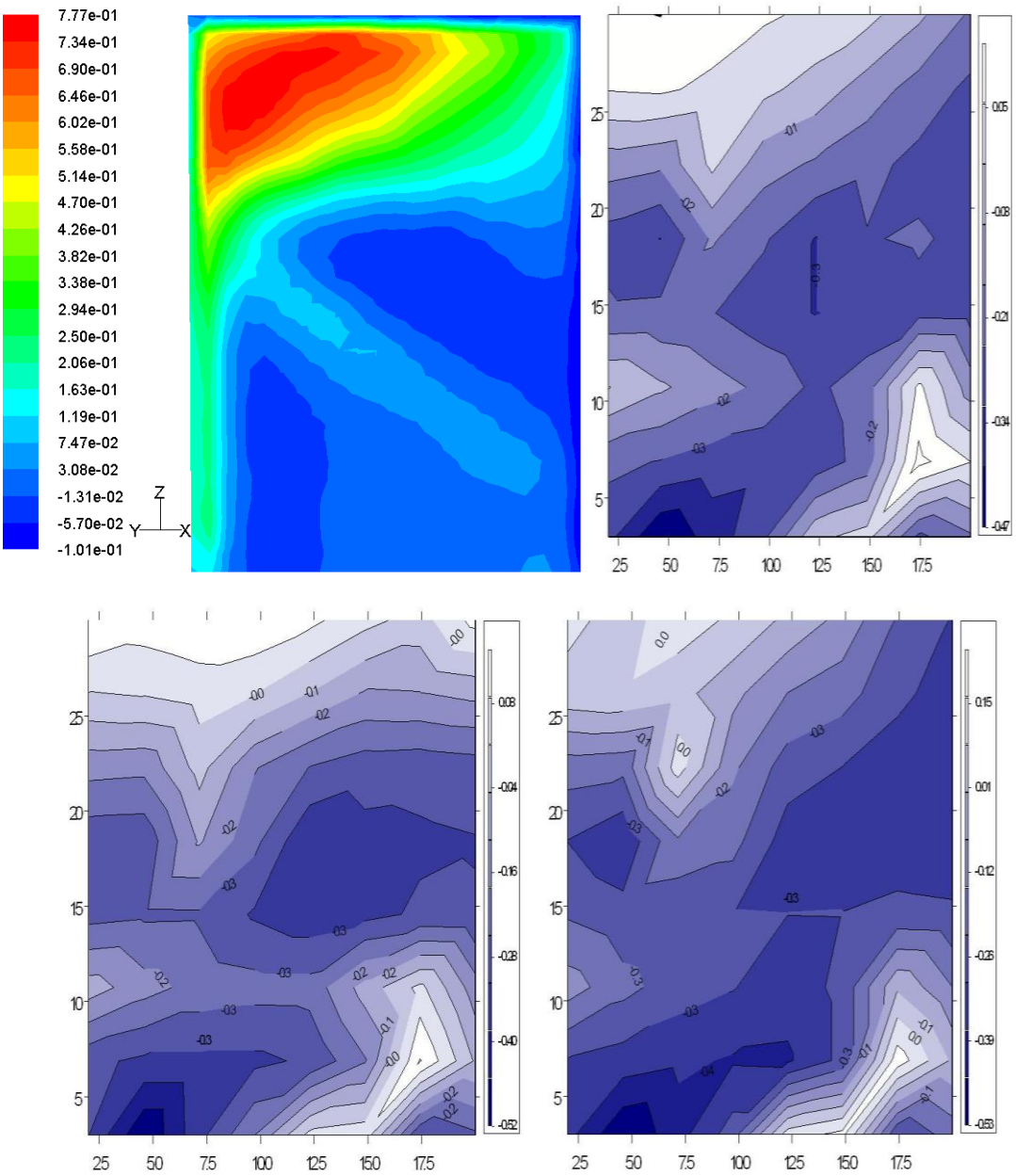

Source: This study.

Figure 9-31: N: Cp contour plots: leeward side of the CKY Tower in the urban environment CFD and WT with flat surface (top right), horizontal panels (bottom left) and vertical panels (bottom right) results (N, 45^{o}).

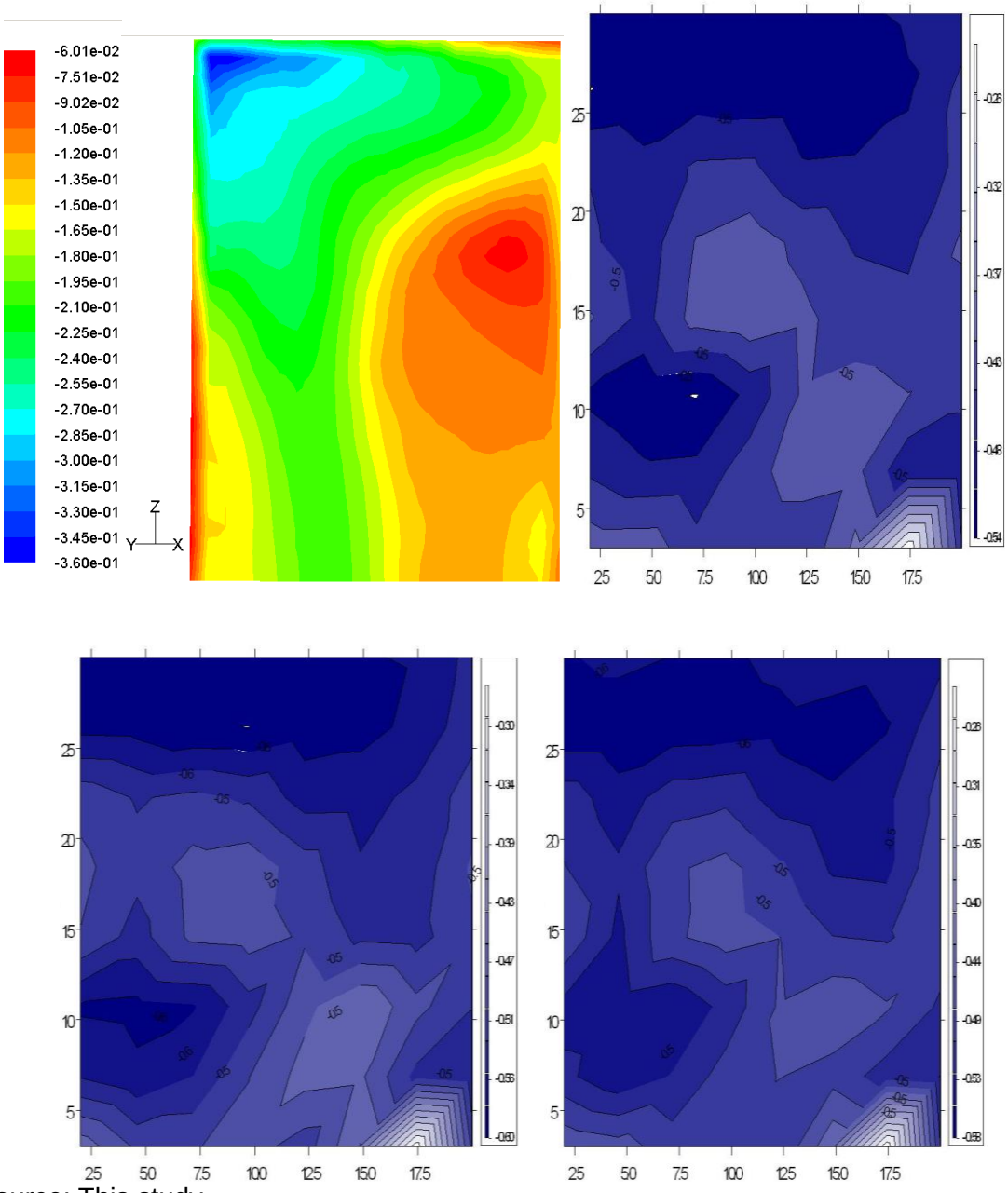

Source: This study.

Figure 9-32: Wind velocity magnitude and x, y and z wind vector components vertical profiles (CFD; N; 45°)

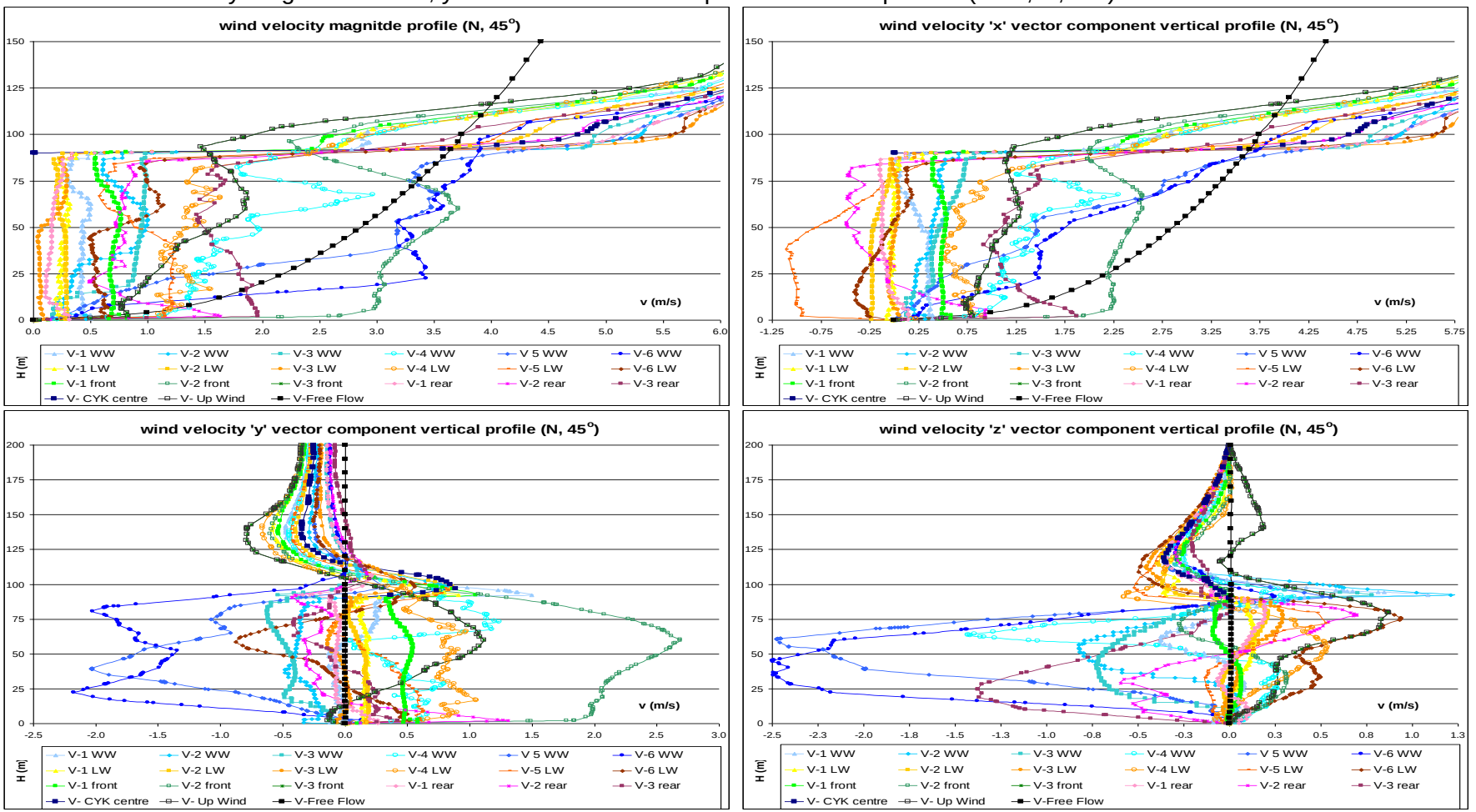

Source: This study.

Figure 9-33: Wind velocity pathlines from a rake at 30m height (top and middle) and seen from the upwind (bottom left) and the downwind (bottom right) direction (CFD, S, 45°).

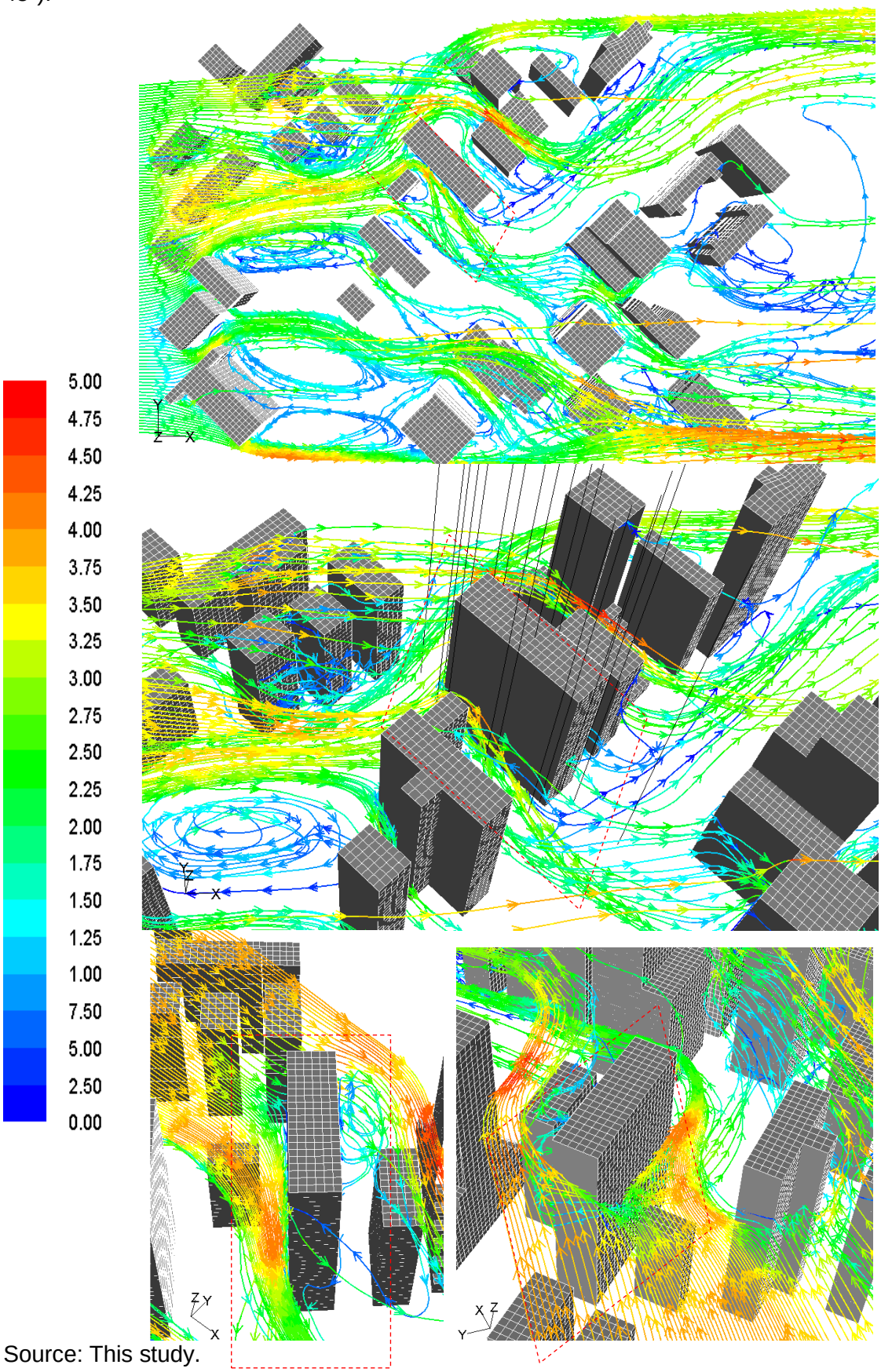

Source: This study.

Figure 9-34: S: Cp contour plots: windward side of the CKY Tower in the urban environment CFD and WT with flat surface (top right), horizontal panels (bottom left) and vertical panels (bottom right) results (S, 45^{o}).

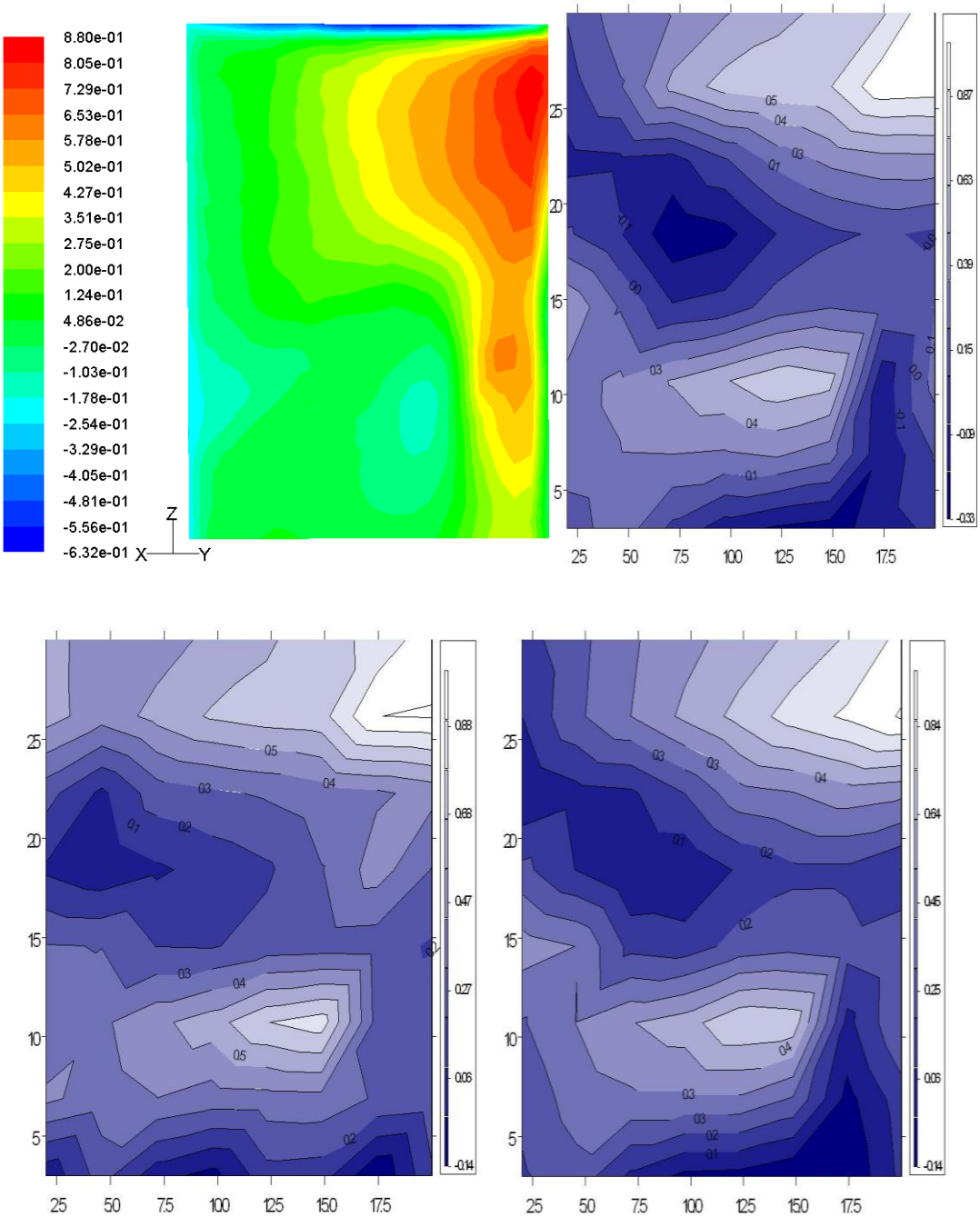

Source: This study.

Figure 9-35: S: Cp contour plots: leeward side of the CKY Tower in the urban environment CFD and WT with flat surface (top right), horizontal panels (bottom left) and vertical panels (bottom right) results (S, 45^{o})

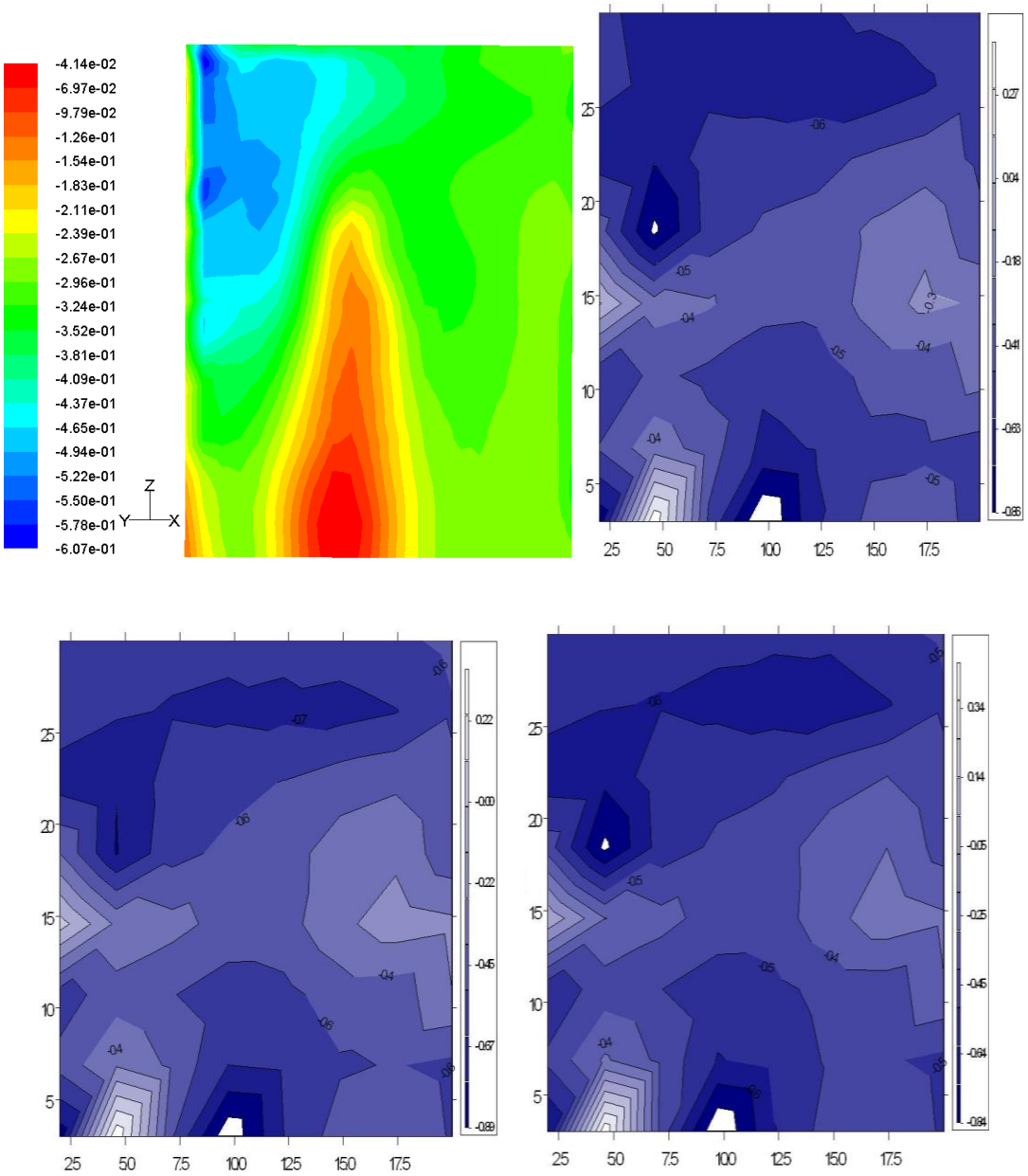

Source: This study.

Figure 9-36: Wind velocity magnitude and x, y and z wind vector components vertical profiles (CFD; S; 45°)

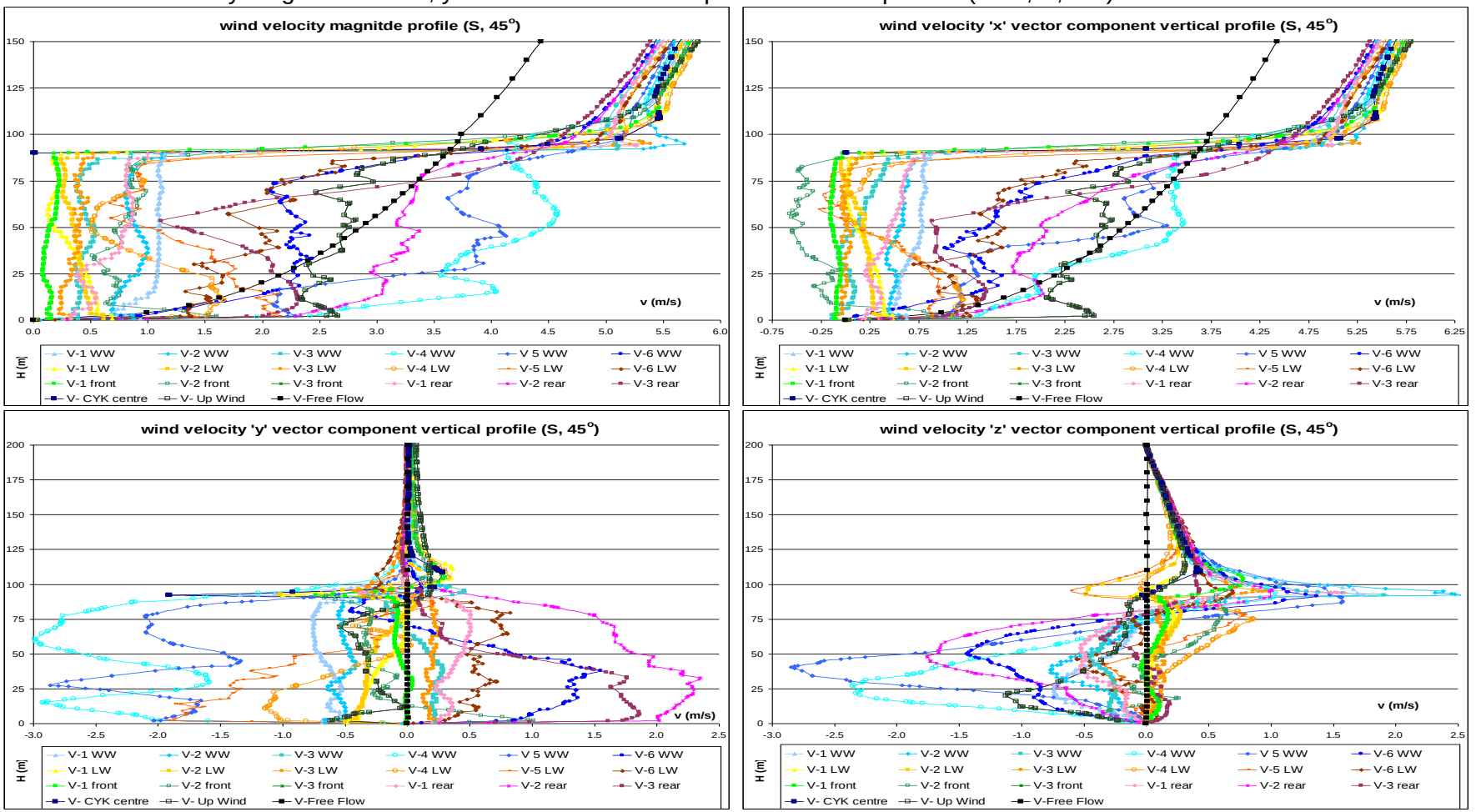

Source: This study.

9.3.3. Some considerations regarding the CKY Tower

The assessment of the airflow for three wind directions around the CKY Tower, an existing corporative office building in the Paulista Avenue, demonstrated that the insertion of a building into an urban environment creates various effects as regards the airflow field velocity and patterns, and the ΔCp results on its sides. For instance, when contrasted with the same tower standing in an isolated setting, the existing urban environment caused a ΔCp decrease ranging from 60 to 84% for incident orthogonal winds; and from 27 to 69% for incident oblique winds. The decrease for parallel winds was negligible, since the ΔCp decrease in both settings was similar.

Regarding the airflow patterns, both the parallel and orthogonal winds have similar effects: wind channelling on the main wide axis, with decelerated vortices meandering around the towers, both ascending and descending airflow patterns on a diagonal after encountering a rectangular volume, with some FS points, acceleration and concentrated increase of pressure on the surfaces. Furthermore, flow detachment at sharp vertical and top horizontal edges are frequent. The occurrence of reverse vortices trapped by other leeward vortices or downward flow defines wake interference. In addition to most of these effects, airflow pathlines for oblique winds also show a sinuous pattern towards the mainstream which divides into two becoming either an ascending or a descending diagonal flow followed by acceleration.

9.4. Section 2: the Prototype Tower

The prototype tower[133] was proposed as an alternative architectonic design to make possible or enhance double-sided cross natural ventilation systems in high-rise towers surrounded by a high-density urban environment. The system is based on wind-driven forces and uses a stack with both positive (top airflow inlet/ wind-catcher) and negative (top airflow outlet) pressure sides. The wind driven inwards was tested in two distribution systems: the crossed-shafts' shaft 'A', which isolates upward and downward winds; and open atrium shaft 'B', which mixes both the inlet and the outlet airflow paths. Buoyancy-driven forces, such as those in a solar chimney outflow stack, were not considered in this simulation due to the impracticality of reproducing this effect in wind tunnel experiment on a reduced physical scale.

[133] For further information on its system and set-up refer to topic 5.4.2.2.2 in Chapter 5.

Figure 9-37: Prototype Tower shaft operating systems and ΔCp schemes.

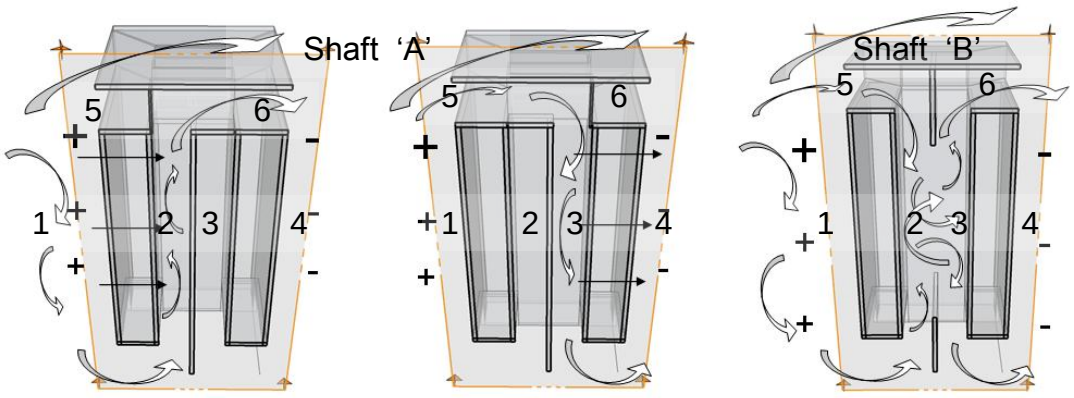

Source: This study.

Several different combinations were employed for the assessment of the ΔCp results[134] between the windward and the leeward faces or between either one of these faces and the internal shaft's faces. These combinations varied also according to the tower prototype shaft operating system, for instance:

- 1- 4: correspond to the ΔCp between the windward and the leeward faces, and are valid for both shafts 'A' and ' B';
- 5- 6: correspond to the ΔCp between the top inlet and the top outlet, and are valid for both shafts 'A' and ' B';
- Shaft 'A' 1-2: ΔCp between the windward face and the internal shaft with low inlet and high outlet openings (ascending flow);
- Shaft 'A' 1-3: ΔCp between the windward face and the internal shaft with high inlet and low outlet openings (descending flow);
- Shaft 'A' 2-4: ΔCp between the internal shaft with low inlet and high outlet openings (ascending flow) and the leeward face;
- Shaft 'A' 3-4: ΔCp between the internal shaft with high inlet and low outlet openings (descending flow) and the leeward face;
- Shaft 'B' 1-2: ΔCp between the windward face and the internal atrium with both low and high inlet and outlet openings; and
- Shaft 'B' 3-4: ΔCp between the windward face and the internal atrium with both low and high inlet and outlet openings.

[134] Tables showing the averaged ΔCp results at low, middle, and top heights, and the total averaged ΔCp result for each wind direction and for the Prototype Tower both isolated and in the urban environment and the respective Cp contour plot figures can also be found in Appendix 6.

9.4.1. The isolated Prototype Tower

Here the Cp results for the set of experiments with the prototype tower isolated in the WT chamber are presented as contour plots. This simulation sought to achieve two goals: to create a standard for later comparison with the set of experiments with the prototype tower in the urban environment; and also to check the potential of both the shaft 'A' and 'B' scenarios. Four wind directions were studied in this first approach: 0^o, 45^o, 67.5^o, and 90^o.

Figure 9-38: The Prototype Tower isolated in the WT chamber.

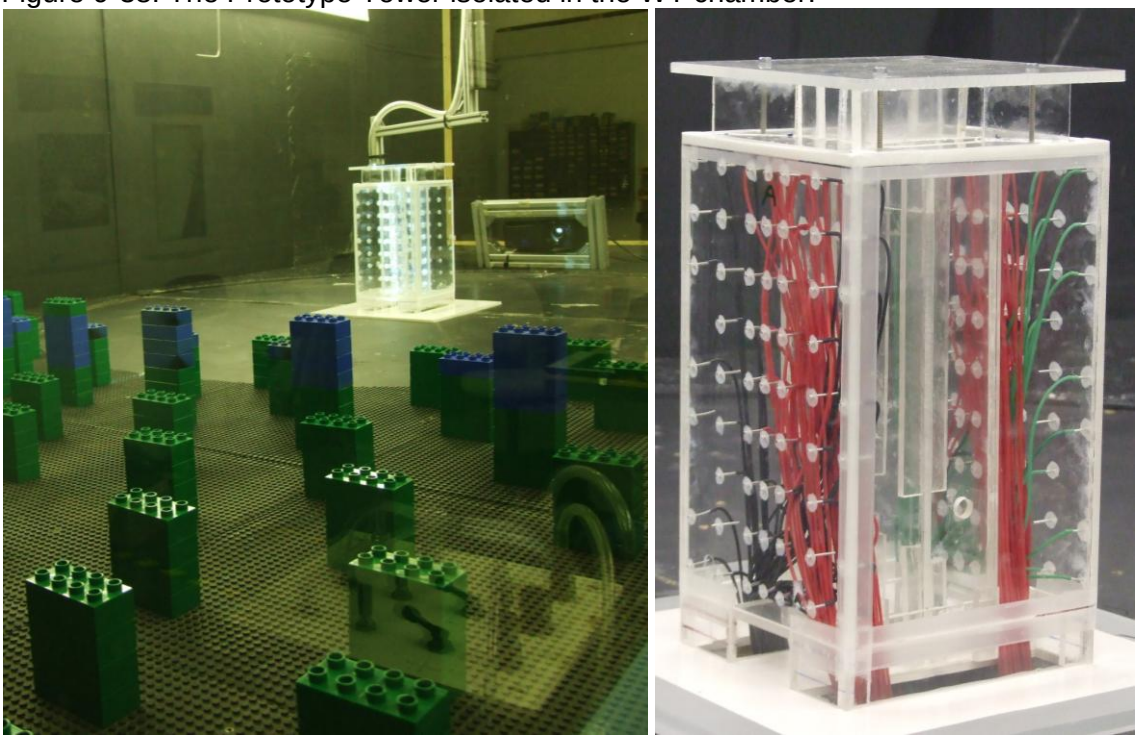

Source: This study.

9.4.1.1. Results for parallel winds (0˚)

The Cp distribution for parallel winds around a rectangular symmetrical volume should be as even as possible between the lateral sides. This was observed in the results from the Prototype Tower isolated in the WT. The total averaged ΔCp results between the lateral sides 1-4 are close to zero (-0.04 and 0.01). On the other hand, the ΔCp results from the proposed shaft 'A' system provide an alternative which increases the pressure differential and make natural cross ventilation for parallel winds possible. For instance, ΔCp results of up to -0.25 were found at medium and top heights between sides 1-2 (shaft 'A' system: ascending flow from the shaft's lower opening serving as inlet, and windows as outlet) and sides 1-3 (shaft 'A' system: descending flow from the shaft's upper opening serving as inlet, and windows as outlet). This pressure difference would potentially make double cross ventilation with fresh air on

these floors possible. At low height, ΔCp drop to a maximum of -0.10. When the shafts are operated as 'B', which means, both shafts are joined forming an atrium, the average ΔCp results between sides 1-2 are -0.09 and between sides 3-4 are 0.00. The ΔCp found between the cowl inlet/ windward and outlet/ leeward sides (5-6) was -0.07 for shaft 'A' and -0.01 for shaft 'B'.

9.4.1.2. Results for orthogonal winds (90˚)

The contour plots and Cp results for orthogonal winds around the windward wide side of the isolated, rectangular and symmetrical Prototype Tower high-rise volume match well with the descriptions found in the literature (Holmes, 2001). The averaged ΔCp results at top, middle, and low heights between the windward and the leeward sides (1-4) were: 1.00, 0.80, and 0.65, with a total averaged result of 0.80. On the other hand, for deep floor plans (ceiling height/ floor length < 1/5), double-sided crossed ventilation becomes inefficient[135], which happens in the Prototype Tower 30m square floor-plan. When operating as shaft 'A', the system would overcome this by ensuring a practically constant ΔCp result of 0.40 on any side (windward or leeward) and at any height (low, middle or top), with the exception of the combination 1-3, which would produce higher results closer to those of 1-4. The open atrium shaft 'B' would produce less intense ΔCp with total averaged results of 0.25, although lower results were found near the ground than at the top (1-2) and at middle heights than at either the ground level or top heights (3-4). The ΔCp found between the cowl inlet/ windward and outlet/ leeward (5-6) was 1.06 for shaft 'A' and 0.77 for shaft 'B'

9.4.1.3. Results for oblique winds (45˚)

The contour plots and Cp results for oblique winds around the isolated, Prototype Tower ensures averaged ΔCp results between the windward and the leeward sides (1-4) at top, middle, and low heights of: 0.76, 0.63, and 0.52, with an overal average of 0.64. When operating as shaft 'A', the system shows total averaged ΔCp results of: 0.48 (1- 2), 0.78 (1-3), 0.39 (2- 4), and 0.30 (3- 4) with practically constant averaged results at low, middle and top heights. When operating as shaft 'B', the same pattern of averaged ΔCp results from oblique winds is observed: decreased ΔCp averaged results around 0.25, with lower results near the ground for sides 1-2, and at middle height for sides 3-4. The cowl inlet/ windward and outlet/ leeward sides ΔCp found (5-6) was 1.12 for shaft 'A' and 0.79 for shaft 'B'.

[135] See Topic 4.5.3 in Chapter 4 for further information.

9.4.1.4. Results for skewed winds (67.5˚)

The simulation with skewed winds at 67.5˚ sought to ascertain the kinds of airflow behavior occurring in the wind-catcher/ purge at the top of the structure and their impact on the pressure results of shafts ‘A’ and ‘B’. This isolated Prototype Tower simulated in the WT was the only experiment that employed a wind direction other than the three used hitherto: 0˚, 45˚, and 90˚. The contour plots rendered a pressure distribution which was in fact intermediate between the results produced by the orthogonal and the oblique winds.

The averaged ΔCp results between the windward and the leeward sides (1-4) at top, middle, and low heights of: 1.06, 0.89, and 0.73, with an overall average of 0.89 were the highest found so far among the isolated Prototype Tower set of experiments. When operating as shaft ‘A’, the system showed total averaged ΔCp results slightly higher than those of the orthogonal and oblique winds: 0.44 (1-2), 0.87 (1-3), 0.45 (2-4), and 0.47 (3-4) with an absolute difference of ±0.10 for the low and top heights. When operating as shaft ‘B’, the same pattern of averaged ΔCp results as that of the orthogonal and oblique winds is to be observed: ΔCp averaged results of around 0.25, with lower results near the ground for sides 1-2, and at middle height for sides 3-4. The ΔCp found between the cowl inlet/ windward and outlet/ leeward (5-6) was 0.86 for shaft ‘A’ and 0.79 for shaft ‘B’.

Figure 9-39: Isolated prototype shaft ‘A’: Cp contour plots for the isolated prototype tower shaft ‘A’ right and left sides: horizontal top (above), external side (middle) and internal shaft (bottom) surfaces (WT; 0^{o})

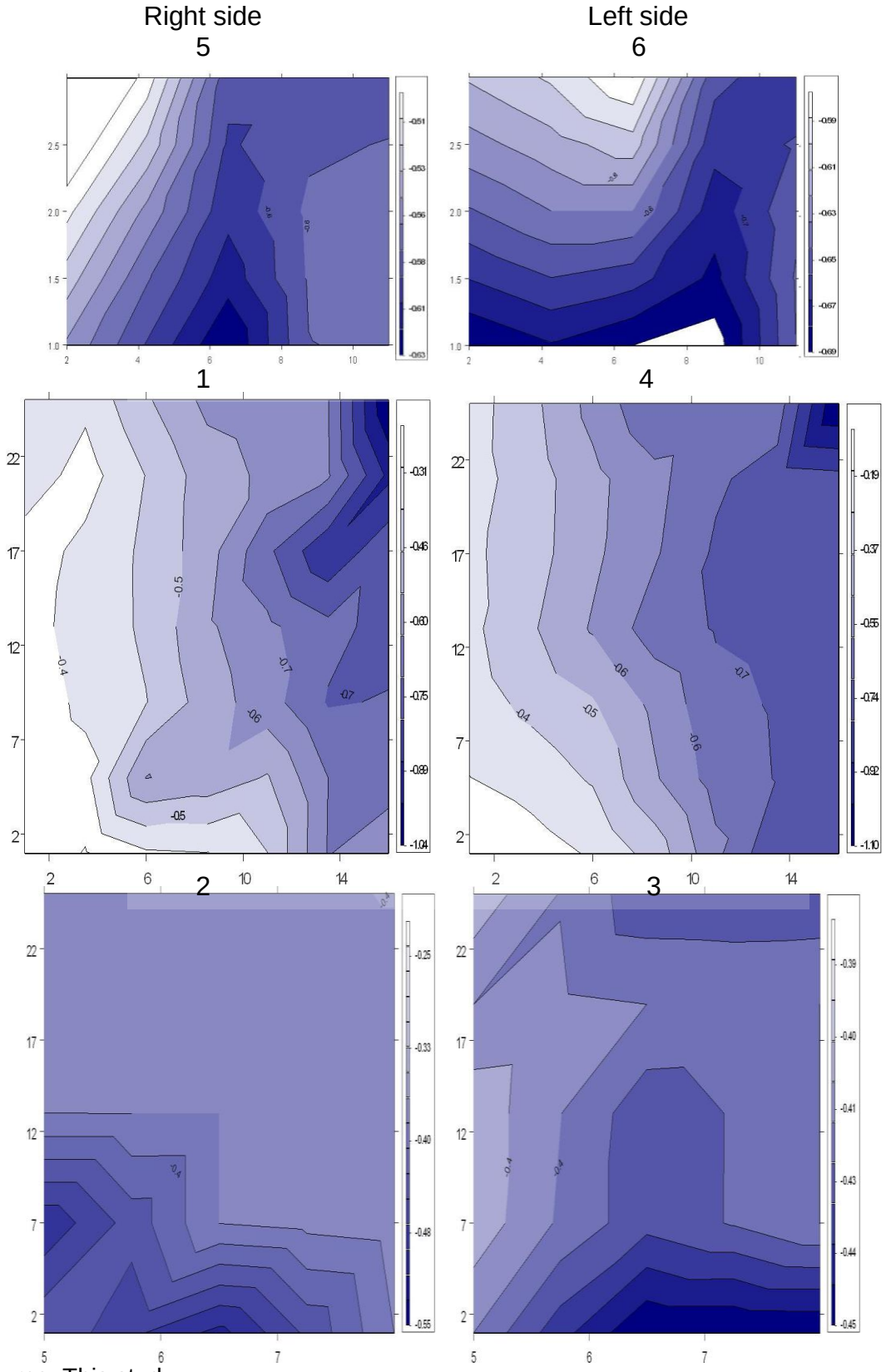

Source: This study.

Figure 9-40: Isolated prototype shaft ‘B’: Cp contour plots for the isolated prototype tower shaft ‘B’ right and left sides: horizontal top (above), external side (middle) and internal shaft (bottom) surfaces (WT; 0^{o}).

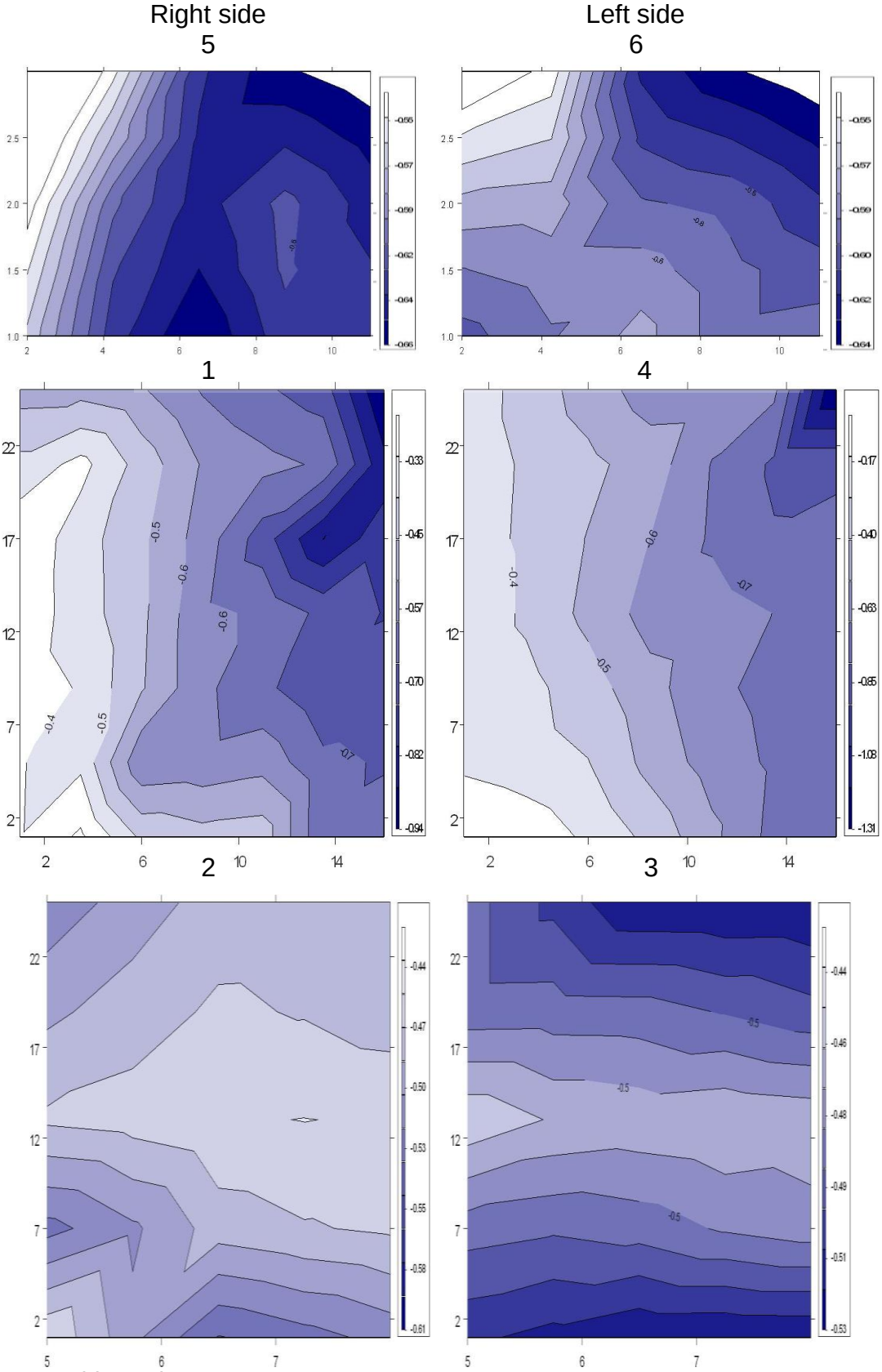

Source: This study.

Figure 9-41: Isolated prototype shaft ‘A’: Cp contour plots for the isolated prototype tower shaft ‘A’ WW and LW sides: horizontal top (above), external side (middle) and internal shaft (bottom) surfaces (WT; 90^{o}).

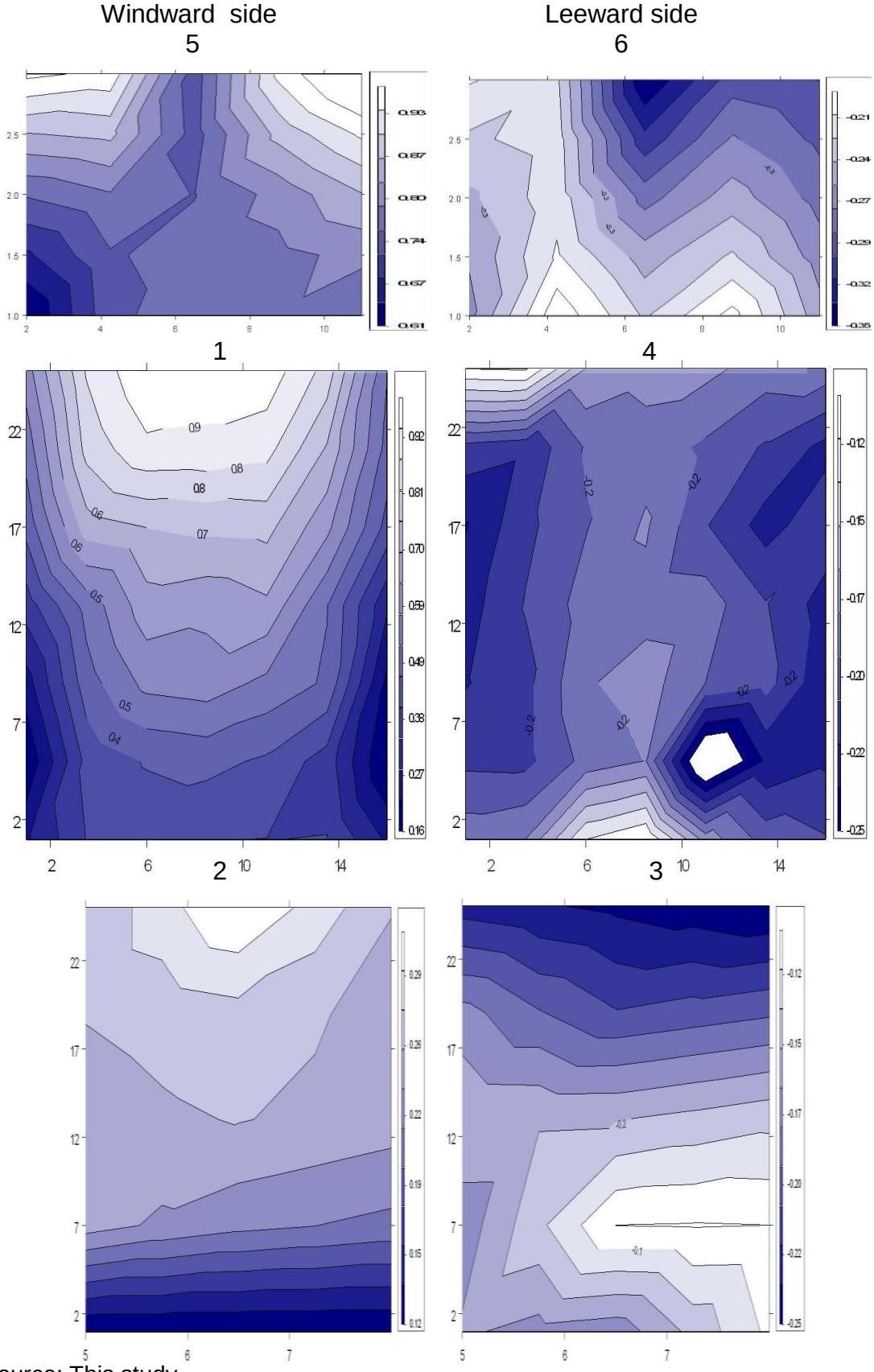

Source: This study.

Figure 9-42: Isolated prototype shaft ‘B’: Cp contour plots for the isolated prototype tower shaft ‘B’ WW and LW sides: horizontal top (above), external side (middle) and internal shaft (bottom) surfaces (WT; 90^{o}).

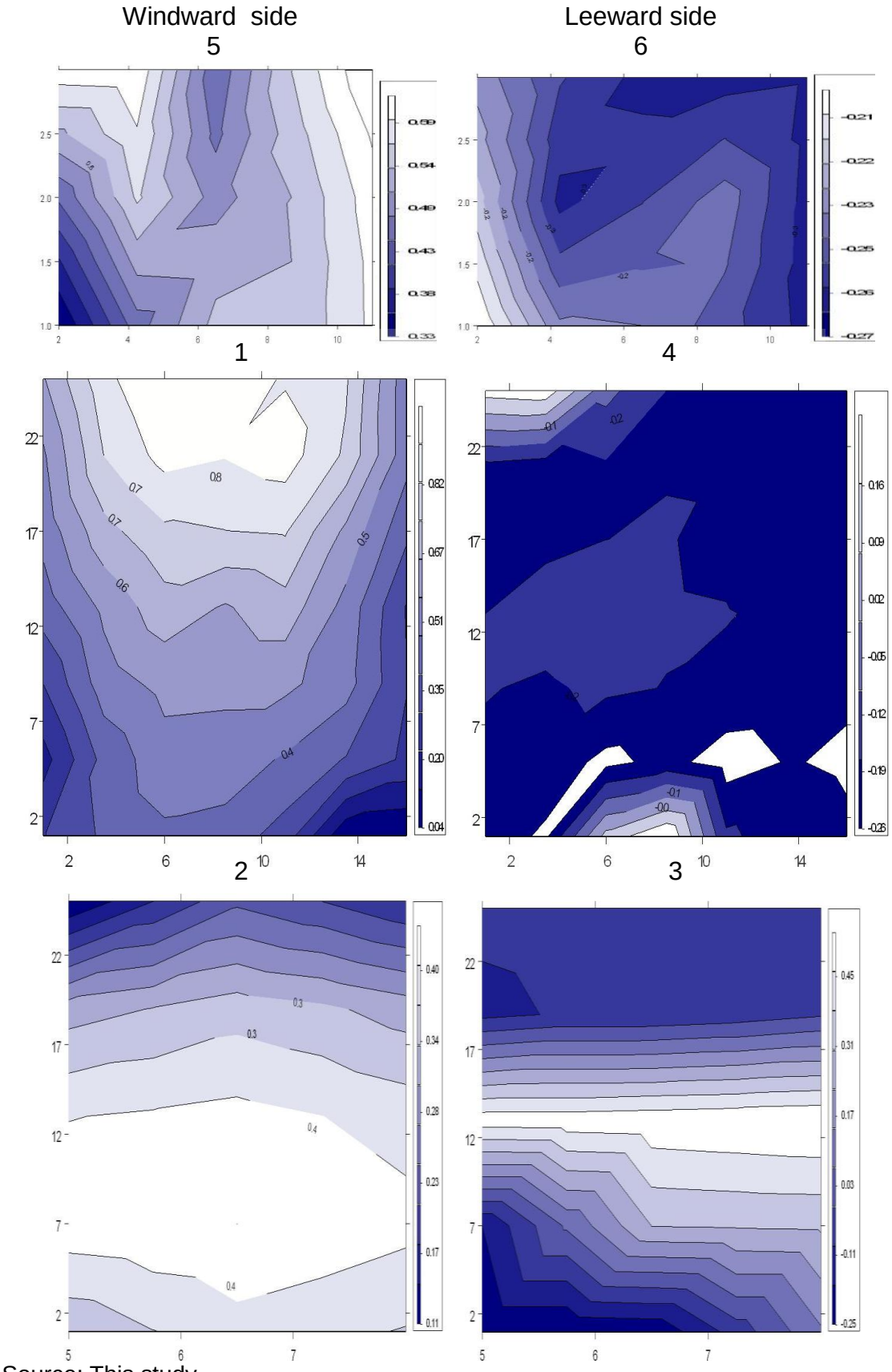

Source: This study.

Figure 9-43: Isolated prototype shaft ‘A’: Cp contour plots for the isolated prototype tower shaft ‘A’ WW and LW sides: horizontal top (above), external side (middle) and internal shaft (bottom) surfaces (WT; 45^{o})

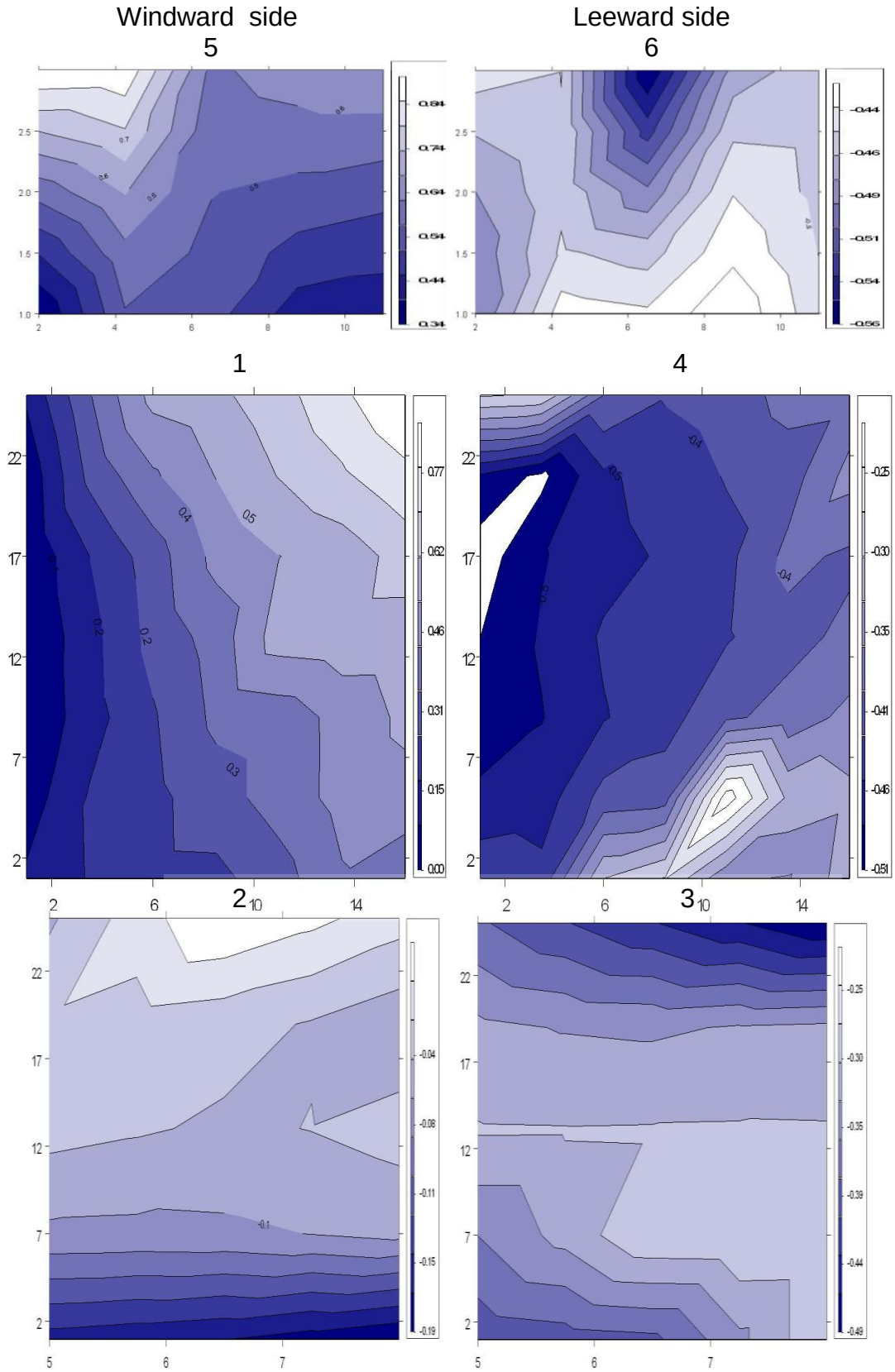

Source: This study.

Figure 9-44: Isolated prototype shaft ‘B’: Cp contour plots for the isolated prototype tower shaft ‘B’ WW and LW sides: horizontal top (above), external side (middle) and internal shaft (bottom) surfaces (WT; 45^{o})

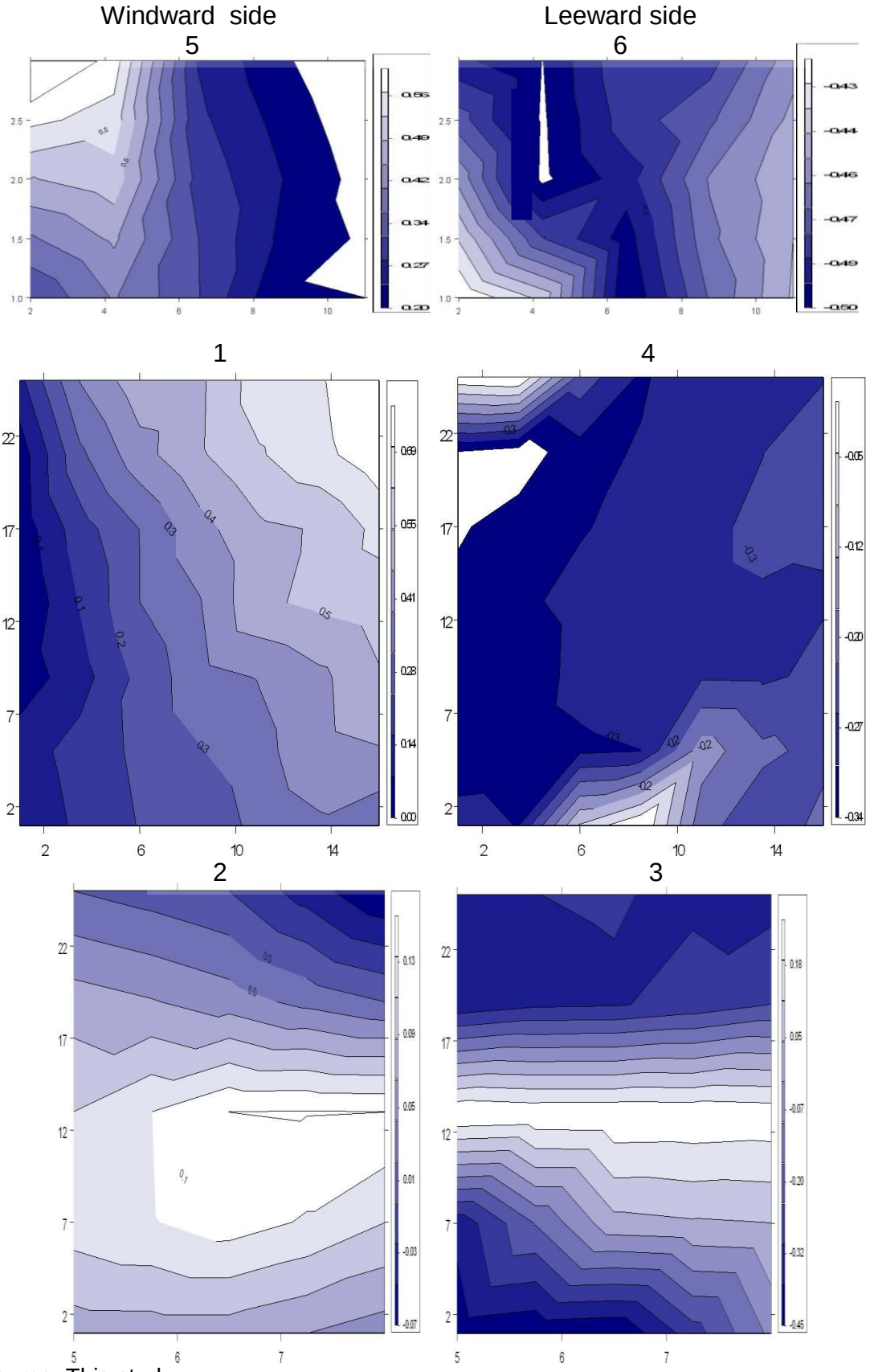

Source: This study.

Figure 9-45: Isolated prototype shaft ‘A’: Cp contour plots for the isolated prototype tower shaft ‘A’ WW and LW sides: horizontal top (above), external side (middle) and internal shaft (bottom) surfaces (WT; 67.5^{o})

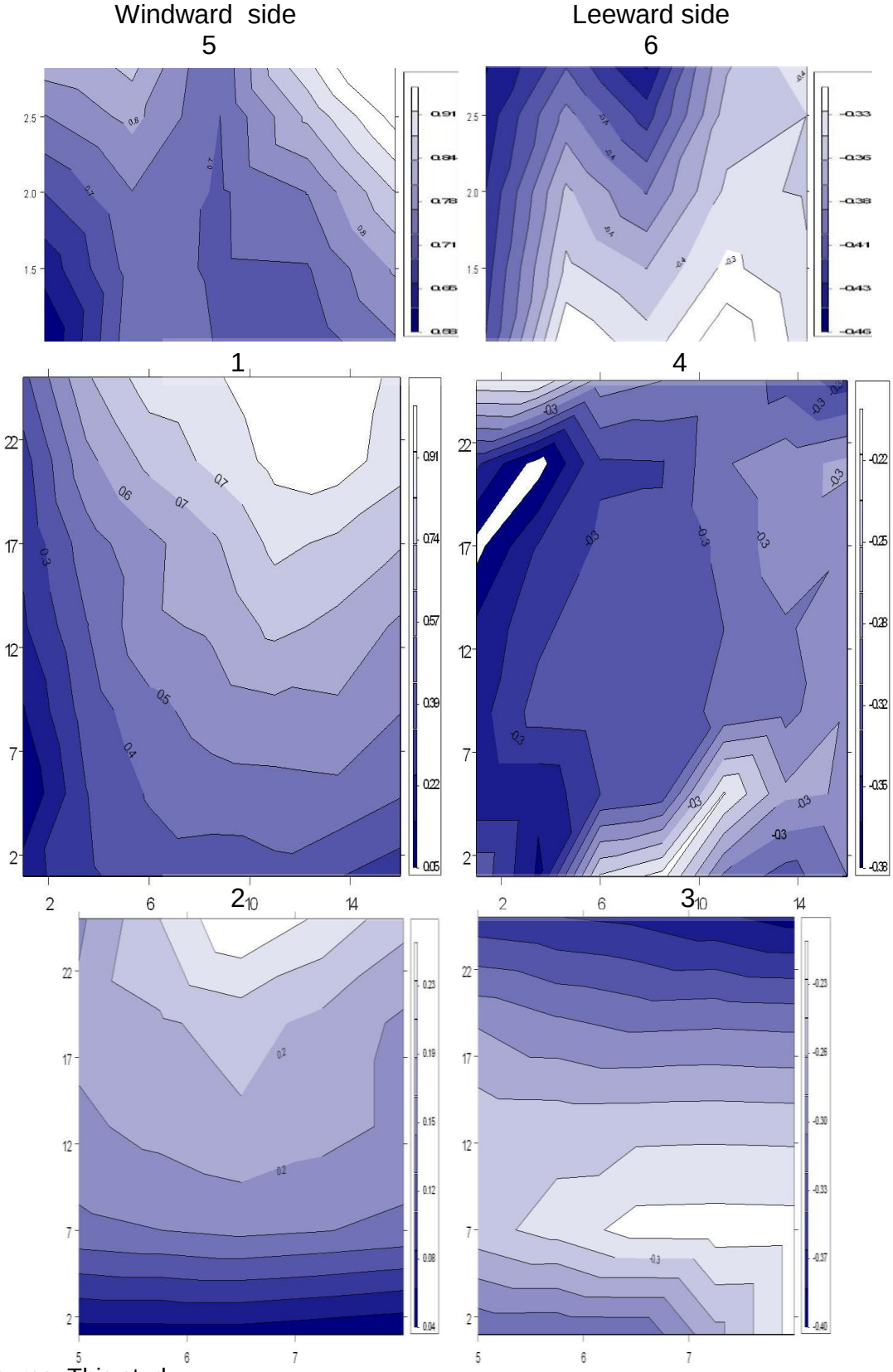

Source: This study.

Figure 9-46: Isolated prototype shaft ‘B’: Cp contour plots for the isolated prototype tower shaft ‘B’ WW and LW sides: horizontal top (above), external side (middle) and internal shaft (bottom) surfaces (WT; 67.5^{o})

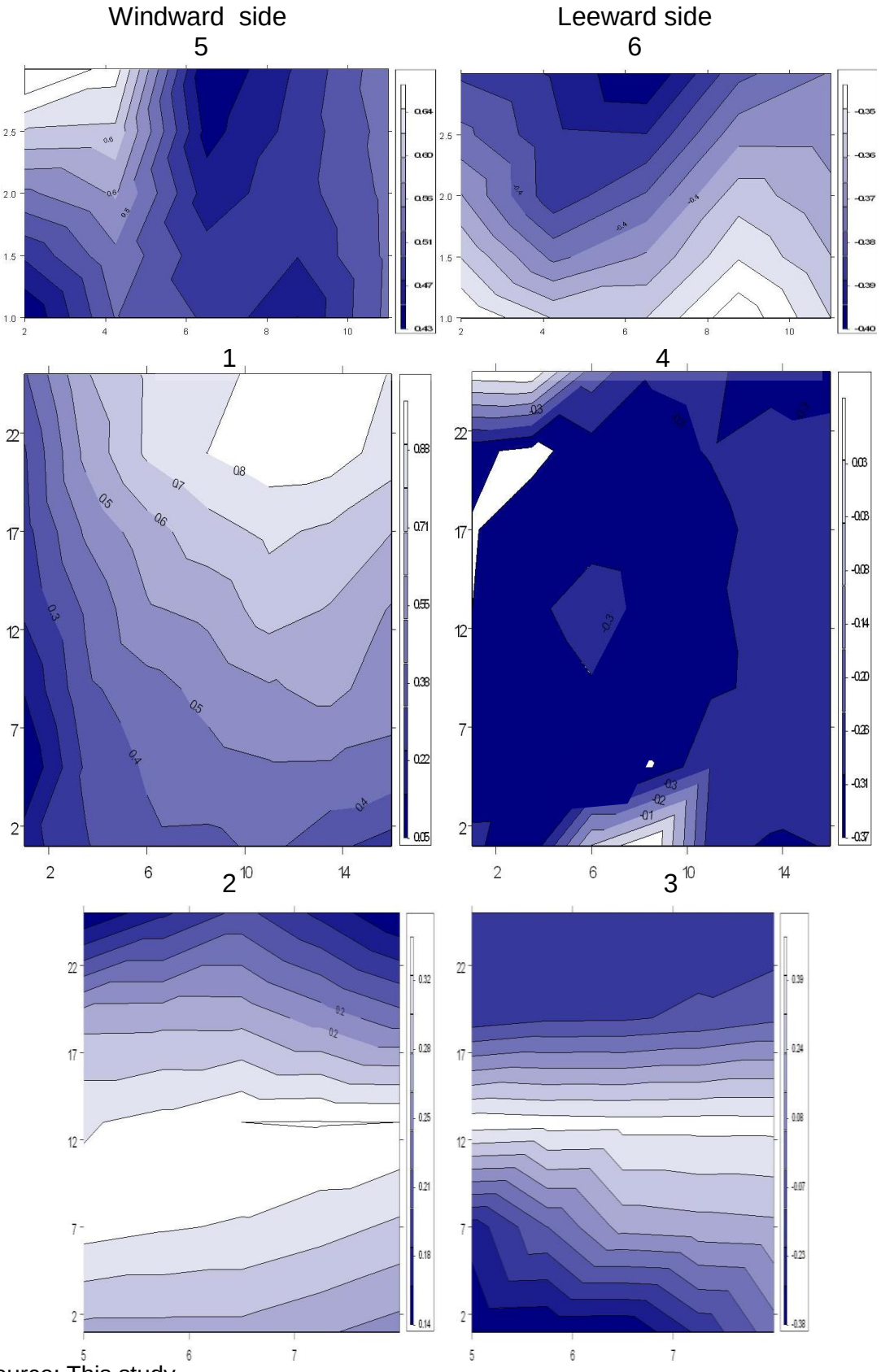

Source: This study.

9.4.2. The Prototype Tower in the urban environment

Here the results of the set of experiments carried out in the wind tunnel with the Prototype Tower surrounded by the Paulista Avenue urban environment are presented and compared among them and with the isolated tower case base. Eight wind directions were simulated in order to explore the potential of the proposed shaft systems in any scenario: NE and SW (0^o), N, S, E and W (45^o), and NW and SE (90^o).

Figure 9-47: The Prototype Tower surrounded by the Paulista Avenue urban area.

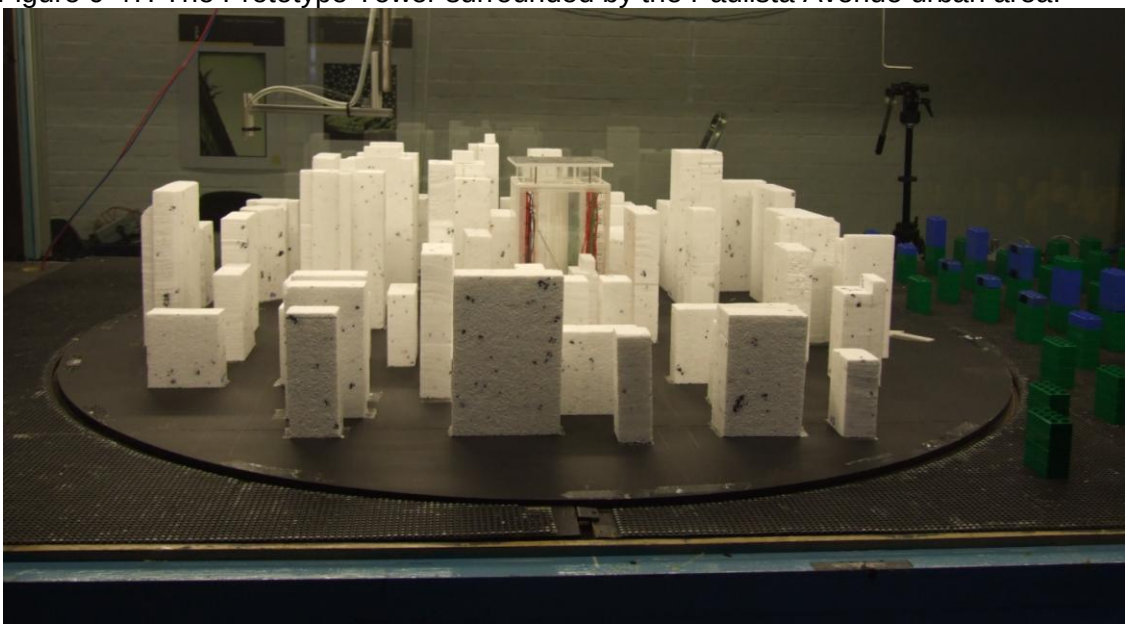

Source: This study

9.4.2.1. Results for parallel winds (0^o: NE and SW)

The first results shown are related to both the right and the left sides of the Prototype Tower, which are positioned along the North-East/ South-West axis. This characterizes winds parallel to the pressure taps. Regarding the contour plot distribution, there was no great interference of the urban surroundings in the results of the external faces 1-4. For instance, the right side for NE winds and the left side for SW winds (the same side, but rotated) showed both contour plots and Cp range (from -0.30 to -1.00) similar to the previous isolated tower scenario. The other side presented some contour plot alteration, but with no considerable difference in the range of Cp results. The ΔCp was close to zero in the NE wind as in the previous parallel wind assessments. It also ranged from -0.05 to 0.02 in the SW wind. When employing the shafts 'A' and 'B' stack and atrium systems, the resultant ΔCp for NE winds remain low, ranging up to -0.07 on average. When operating with the shaft 'B' open atrium system for SW winds, the resultant ΔCp once more approximated to zero. On the other hand, a

greater pressure differential is created by the SW wind and shaft mode ‘A’: the resultant ΔCp at top and middle heights and ground level were: -0.37, -0.17 and -0.03 for ΔCp between sides 1-2; -0.30, -0.11 and -0.12 for ΔCp between sides 1-3, and 0.36, 0.09 and -0.02 for ΔCp between sides 2-4. Finally, the ΔCp found for the cowl inlet/ windward and outlet/ leeward sides (5-6) was 0.08 operating as shaft ‘A’ and 0.04 as shaft ‘B’.

To ventilate this large floor-plan section naturally in an urban context and during prevailing parallel winds, a pressure differential must be created between the internal shaft face and the external faces and between the top and the bottom. Moreover, both the ΔCp between sides 1-2 and 2-4 mean an upward flow inside the shaft, with the inlet area near the ground and the outlet at the top cowl. For this scenario, double-cross ventilation would occur with the fresh airflow blowing from the shaft opening in the direction of the external façade window. This system does not take into account the solar chimney effect and the resultant buoyancy-driven force in the pressure differential. Furthermore, since the pressure is greater at top height, an NPL should be carefully balanced, working with larger openings at lower height and smaller openings at top height in order to control and ensure an equal flow and, therefore, an even ACH for each storey. Another alternative would be to place full air conditioned areas (such as stores, meeting rooms, and auditoriums) or unoccupied areas (such as parking basements) at a low height, and work with natural double-cross ventilation in the upper 2/3rds of the tower’s height. An advantage of a high-rise building vertical zoning lies in the fact that, in high-density urban areas, ground level is shaded more frequently than the middle and the top heights and, therefore, the solar heat loads would be smaller under such conditions, and affect the HVAC system dimensioning and operation.

Figure 9-48: Prototype tower with shaft ‘A’ surrounded by urban area: : Cp contour plots for the prototype tower shaft ‘A’ WW and LW sides in urban area: base top (above), external side (middle) and internal shaft (bottom) surfaces (WT; NE; 0^{o})

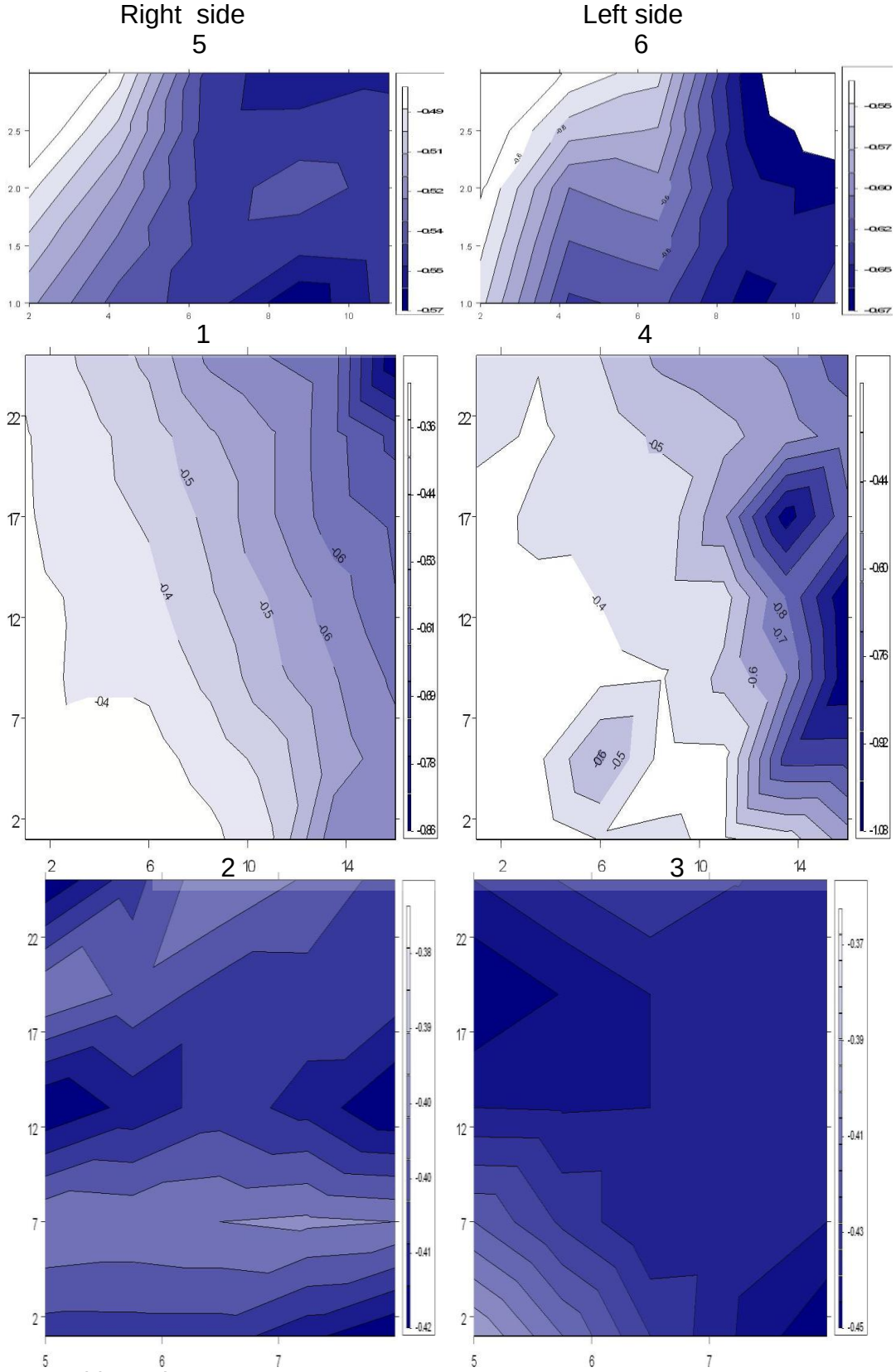

Source: This study.

Figure 9-49: Prototype tower with shaft ‘B’ surrounded by urban area: Cp contour plots for the prototype tower shaft ‘B’ WW and LW sides in urban area: base top (above), external side (middle) and internal shaft (bottom) surfaces (WT; NE 0^{o})

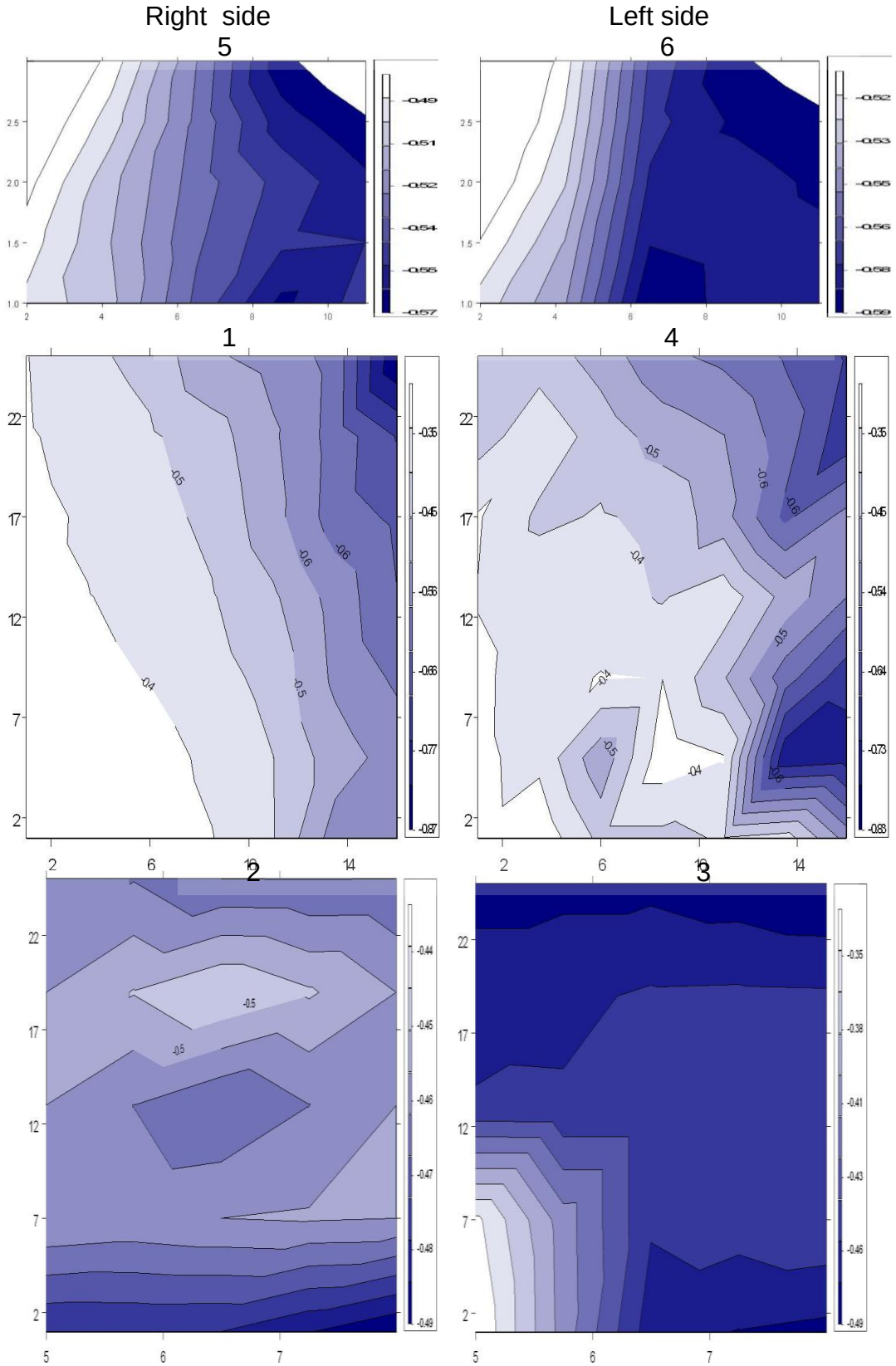

Source: This study.

Figure 9-50: Prototype tower with shaft ‘A’ surrounded by urban area: Cp contour plots for the prototype tower shaft ‘A’ Right and Left sides in urban area: base top (above), external side (middle) and internal shaft (bottom) surfaces (WT;SW; 0^{o})

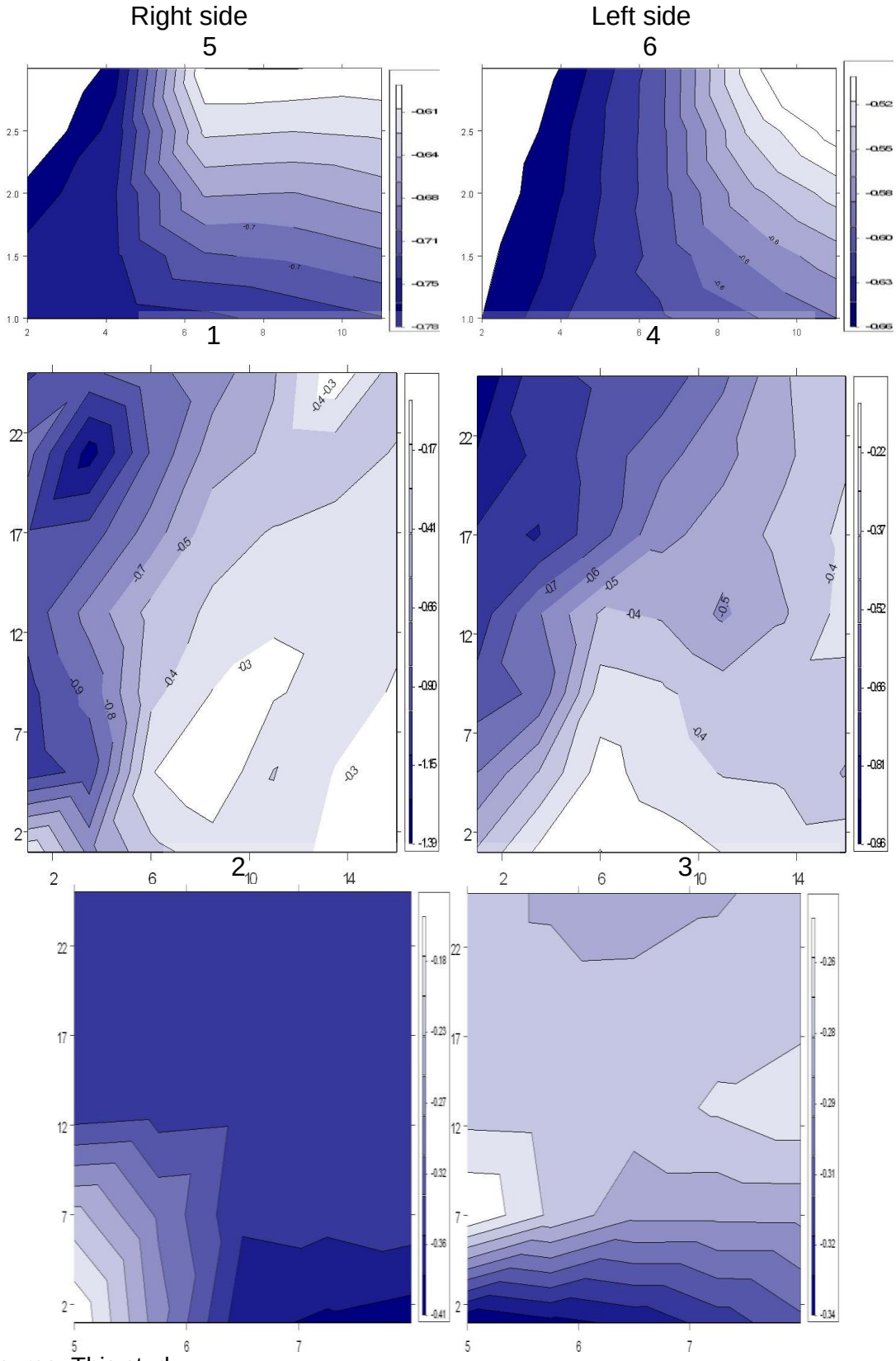

Source: This study.

Figure 9-51: Prototype tower with shaft ‘B’ surrounded by urban area: Cp contour plots for the prototype tower shaft ‘B’ Right and Left sides in urban area: base top (above), external side (middle) and internal shaft (bottom) surfaces (WT; SW; 0^{o})

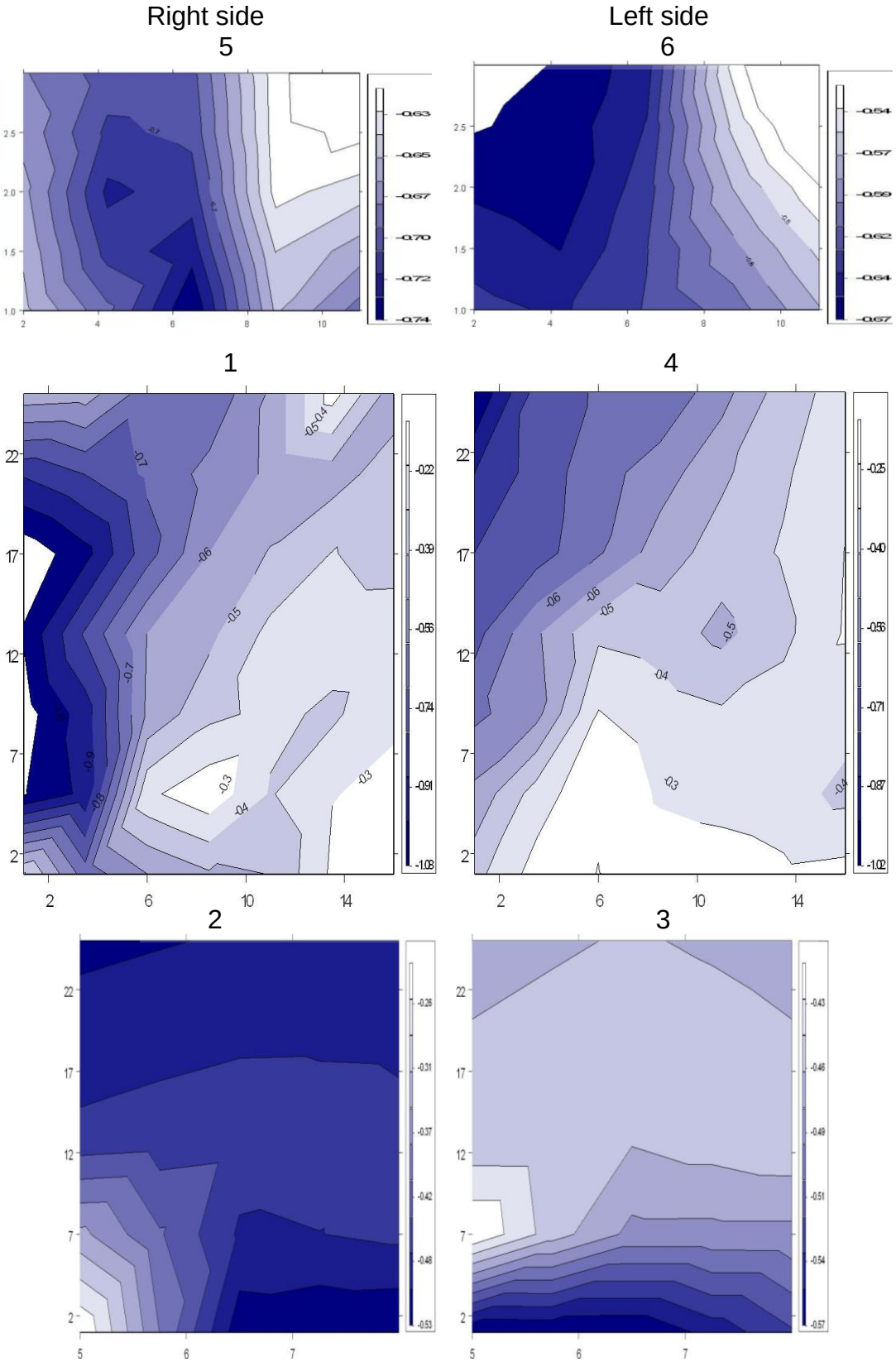

Source: This study.

9.4.2.2. Results for orthogonal winds (90°: NW and SE)

Northwest and Southeast are the wind directions orthogonal to the prototype pressure taps. These are also the wind directions with greatest incidence throughout the year in this region[136]. The averaged ΔCp results at top, middle, and low heights between the windward and the leeward sides (1-4) were: 0.17, 0.06, and 0.05, with an overall average result of 0.10 for the NW; and 0.50, 0.15, and 0.09, an overall average result of 0.20 for the SE. This shows an overall average ΔCp decrease of around 90% for the NW, and 75% for the SE winds, when contrasted to the isolated Prototype Tower scenario addressed in topic 9.4.1.2. The same pressure decrease was found in the CKY Tower investigation, and is to be explained by the difference in the H/W aspect ratios between the NW and SE façades. While on the former face a narrow proportion of around 2.0 is found, with a higher tower in the upwind direction, on the latter a square proportion of around 1.0 makes a more open SE field possible. If the ΔCp is taken as that between the cowl inlet/ windward and outlet/ leeward sides (5-6), the results found for the NW winds shafts 'A' and 'B' were, respectively: 0.42 and 0.31, and those for the SE wind shafts 'A' and 'B': 0.89 and 0.62.

As regards the pressure distribution throughout the height of the tower, the resultant ΔCp found for the NW wind at top and middle heights and ground level were quite similar: 0.14, -0.07 and -0.03 for ΔCp between faces 1-2; 0.07, -0.08 and -0.02 for faces 1-3; and 0.10, 0.11 and 0.09 for faces 2-4, and when the system operates as either shaft 'A' or 'B'. On the other hand, the results found for the SE wind were somewhat different when the system operates as shaft 'A' or 'B'. The resultant ΔCp at top and middle heights and ground level for shaft 'A' were: 0.20, -0.01 and -0.01 for faces 1-2; 0.36, 0.07 and 0.02 for faces 1-3; 0.16, 0.08 and 0.04 for faces 2-4; and 0.16, 0.08 and 0.04 for faces 3-4. The results for shaft 'B' were: 0.46, -0.18 and -0.13 for faces 1- 2; and 0.10, 0.00 and 0.05 for faces 3-4.

The greatest ΔCp is found on the windward side at top height and with the system operating as shaft 'B' for both wind directions. Under such a scenario, double-crossed flow occurs across the building from the windward side inlet openings to the shaft outlet openings. On the other hand, at medium and low heights the internal airflow is weakened in the same proportion and its direction is inverted. If the system operates as in the crossed shafts 'A' scenario, the rear part of the building may present a constant ΔCp around 0.15 from the ground to the top in both wind directions, when the solution of ΔCp between faces 2-4 is adopted. This implies an ascending flow inside the shaft feeding the inlet openings and the internal flow across the building from

[136] See Topic 5.4.2.2 in Chapter 5 for further information.

the shaft to the leeward outlet openings. In addition, the solution for the front block would be the ΔCp between faces 1-3, where a descending flow takes place from the top wind-catcher to the ground outlet opening. This scenario ensures a higher ΔCp near the top and a lower one near the ground. Once more, since pressure is greater at top height, different sizes of openings should be used at top, middle and bottom heights in order to balance the NPL and regulate the ACH rates on each floor.

Figure 9-52: Prototype tower with shaft ‘A’ surrounded by urban area: Cp contour plots for the prototype tower shaft ‘A’ WW and LW sides in urban area: base top (above), external side (middle) and internal shaft (bottom) surfaces (WT; NW; 90^{o})

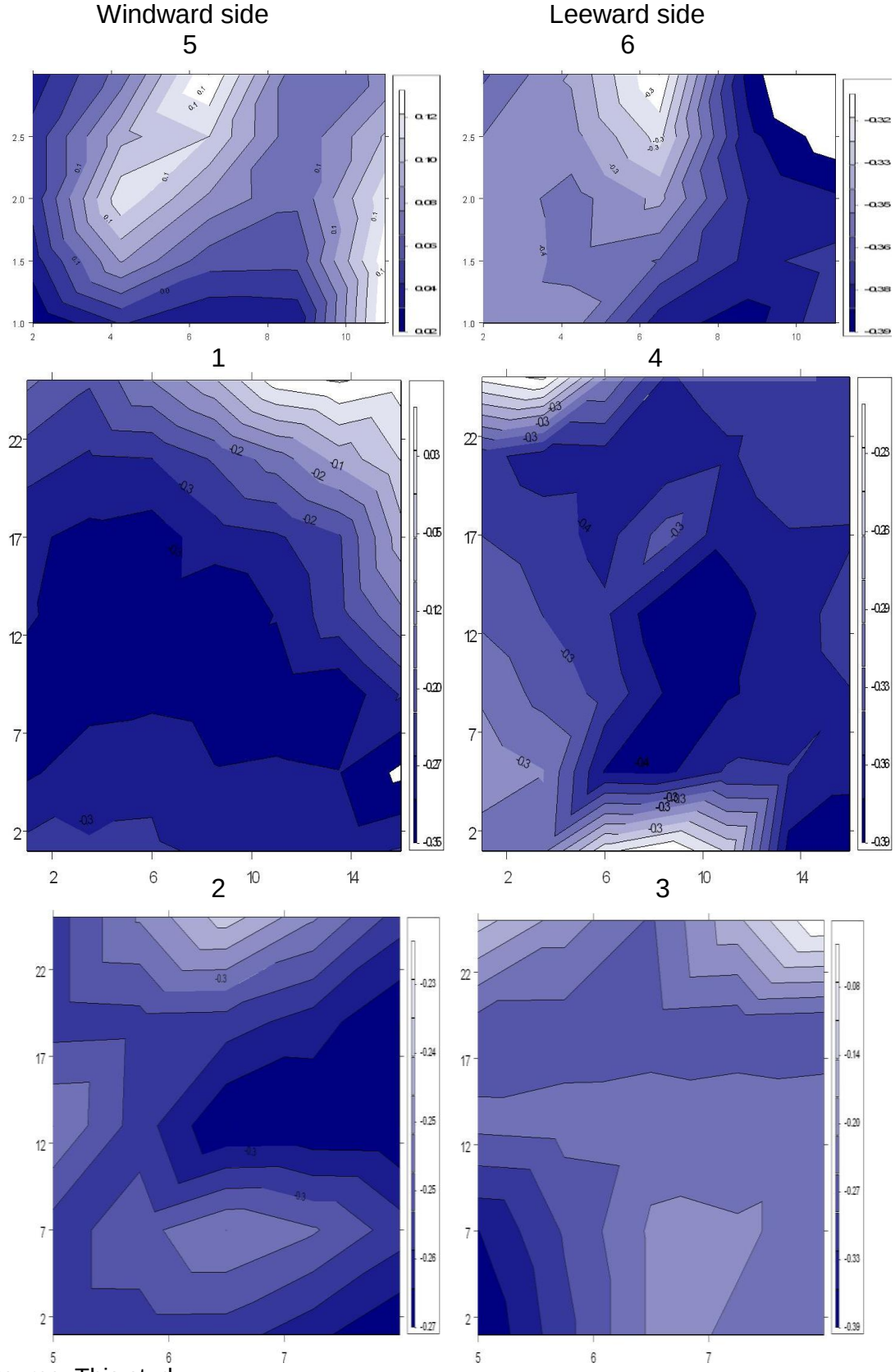

Source: This study.

Figure 9-53: Prototype tower with shaft ‘B’ surrounded by urban area: Cp contour plots for the prototype tower shaft ‘B’ WW and LW sides in urban area: base top (above), external side (middle) and internal shaft (bottom) surfaces (WT; NW; 90^{o})

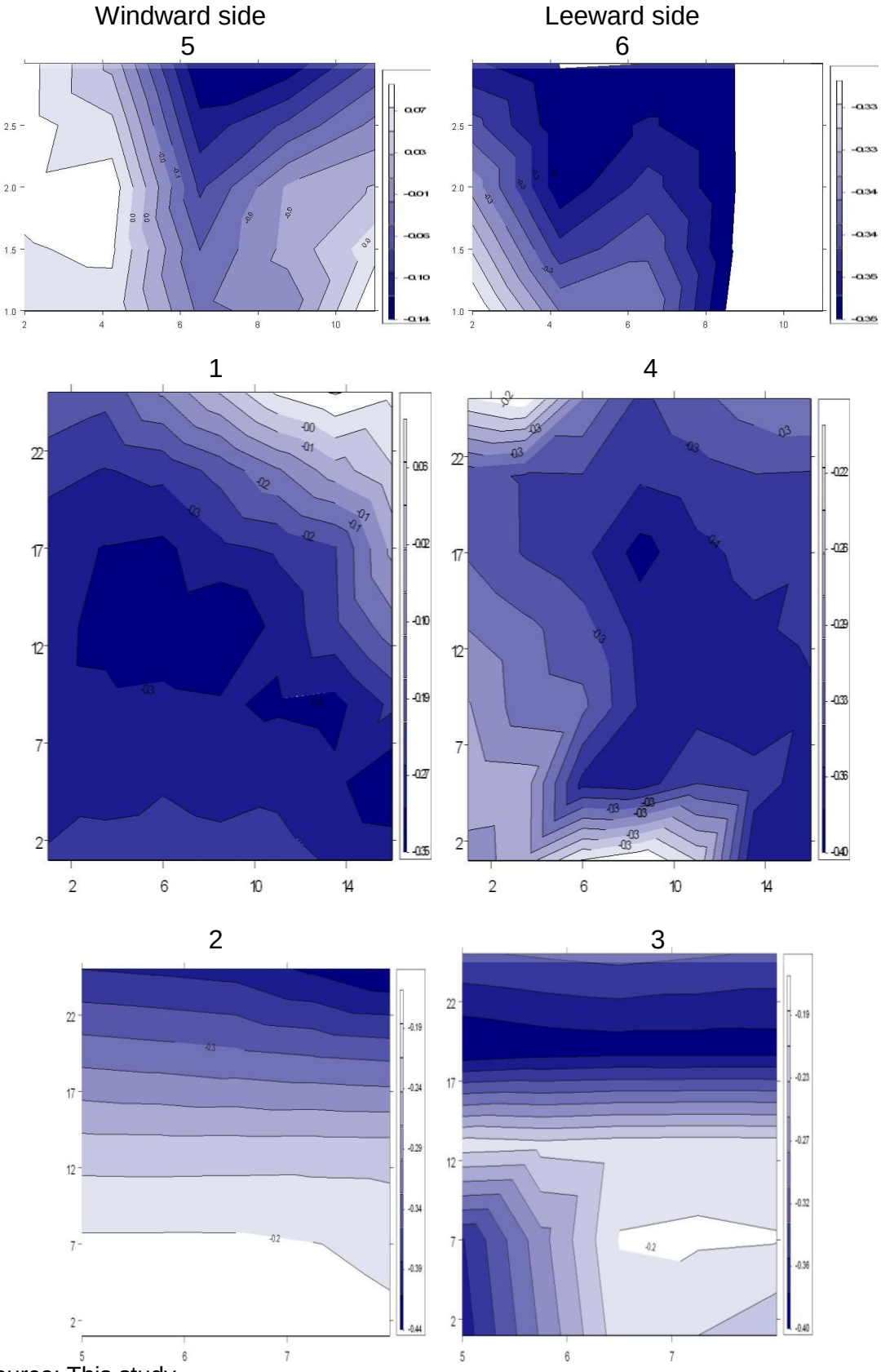

Source: This study.

Figure 9-54: Prototype tower with shaft ‘A’ surrounded by urban area: Cp contour plots for the prototype tower shaft ‘A’ WW and LW sides in urban area: base top (above), external side (middle) and internal shaft (bottom) surfaces (WT; SE; 90^{o})

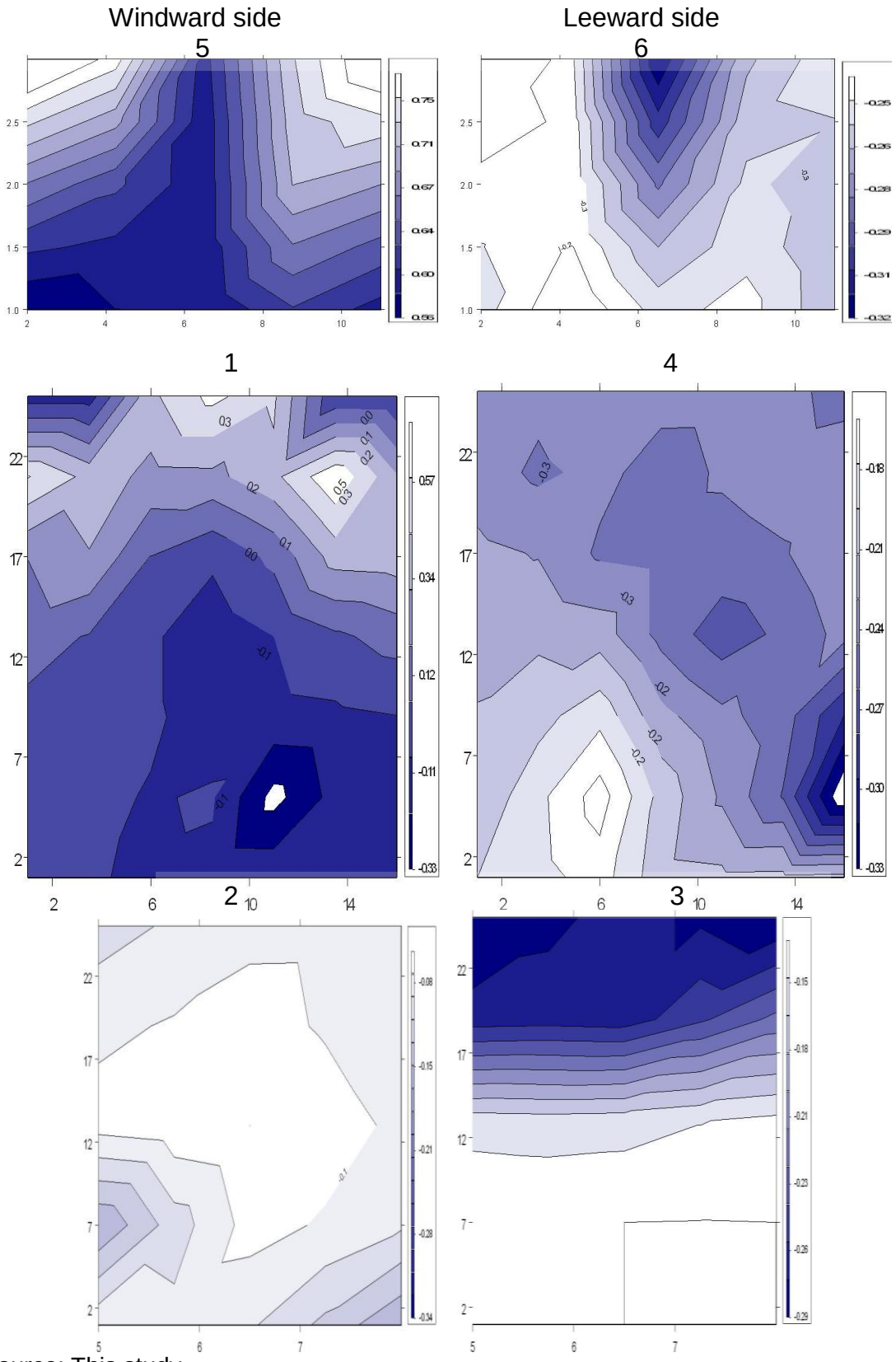

Source: This study.

Figure 9-55: Prototype tower with shaft ‘B’ surrounded by urban area: Cp contour plots for the prototype tower shaft ‘B’ WW and LW sides in urban area: base top (above), external side (middle) and internal shaft (bottom) surfaces (WT; SE; 90^{o})

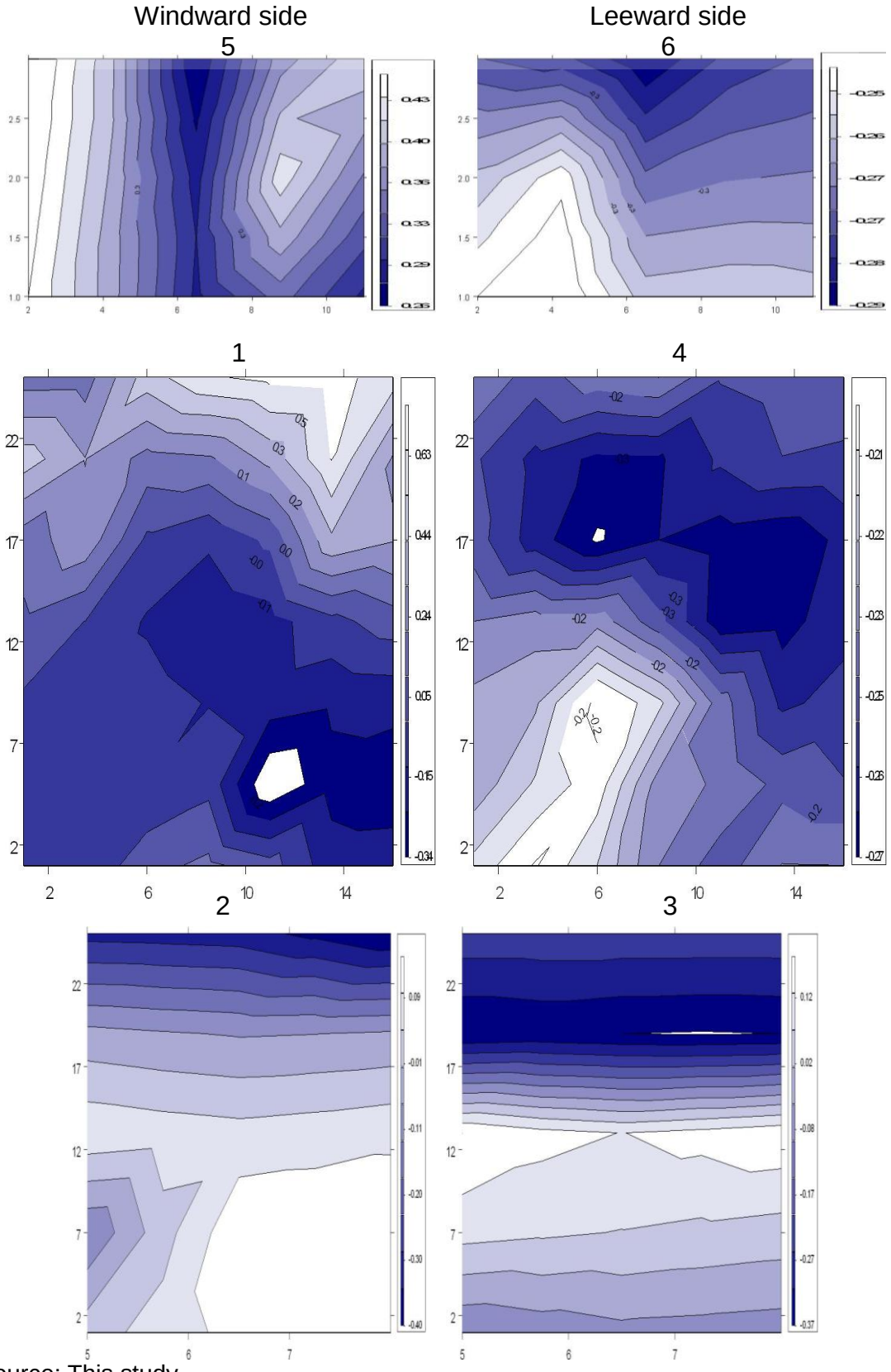

Source: This study.

9.4.2.3. Results for oblique winds (45^{o}: N, S, E, and W)

Winds oblique to the Prototype Tower were simulated on two axes: North/ South and East/ West. Each of them is first discussed separately and then contrasted one to other and with the isolated Prototype Tower results.

Starting with the axis North/ South, the pressure difference between the cowl inlet/ windward and outlet/ leeward sides (5-6) found for N winds were: 0.62 for shaft 'A' and 0.33 for shaft 'B'; while the ΔCp for S winds were: 0.95 and 0.73. The averaged ΔCp results at top, middle, and low heights between the windward and the leeward sides (1-4) of the Prototype Tower were: 0.43, 0.20, and 0.17, with a total averaged result of 0.27 for N winds. For S winds the averaged ΔCp results at the same positions were: 0.63, 0.33, and 0.17 with a total averaged result of 0.38. It may be observed that the pressure is greater for winds from the South than from the North. Since the Paulista Ave. is positioned along the NW/ SE axis, the greater frontal northward distance should also result in greater pressure and, consequently, greater ΔCp. Paulista Ave. presents an H/W aspect ratio of around 1.00, while towards the S the H/W aspect ratio is irregular, ranging from 3.00 to 0.50. Figures 9-13 and 9-14 presenting the CFD airflow velocity magnitude pathlines from the CKY Tower simulation for N and S prevailing wind, show in fact that the prevailing northerly winds reache the Paulista Ave. at 45^{o} and acquire a sinuous course. When it reaches the target tower, the bulk of the flow decelerates and is weakened. The same does not happen for the S winds. In spite of the H/W variation, both the A_{roof}/A_{plot} and the A_{built}/A_{plot} aspect ratios of the surrounding buildings are lower for this wind direction, resulting in a bulk of flow with greater intensity and acceleration reaching the target tower. When contrasted with the isolated tower case-base, the ΔCp reduction due to the urban area on the faces 1-4 ranges from 14% at the top, to 47% in the middle, and 67% near the ground for Southerly winds. For Noutherly winds the reductions were, respectively: 41%, 68%, and 67%. The ΔCp reduction rates show that, in fact, near ground results are quite similar, while a difference begins to appear at mid height and becomes considerable at top height.

As regards the prevailing winds on the East/ West axis, the ΔCp between the cowl inflow and outflow sides 5 and 6 found for East winds and for shafts 'A' and 'B' were, correspondingly, 0.52 and 0.41. For W winds the same Cp differences were: 0.73 and 0.41. The averaged ΔCp results between the windward and the leeward sides (1-4) at top, middle, and low heights were: 0.34, 0.32, and 0.17, with a total averaged result of 0.28 for E winds. For W winds the respective averaged ΔCp results were: 0.26, 0.27, and 0.26 with a total averaged result of 0.26. Both the results show a decrease when contrasted to the former two wind directions, which is reflected in the reduction in the ΔCp due to the urban environment when contrasted with the isolated

tower case-base: 46% at the top, 50% in the middle, and 67% near the ground for E winds; and 65%, 57%, and 50% for W winds. The reduction in ΔCp rates show that, in fact, near ground results are quite similar, while a difference starts to occur at mid- and becomes considerable at top height. As regards the performance of the shaft systems for oblique winds, the analysis will be made for each wind direction individually.

Starting with North winds, total averaged ΔCp of 0.16 evenly distributed throughout the floors was found when contrasting faces 2-4, and with the shaft operating as 'A'. This scheme represents the ΔCp between the leeward face and the internal shaft face with an internal ascending flow. When the shaft operates as 'B', an open atrium, pressure decrease and uneven distribution take place.

On the other hand, for South winds, the open atrium shaft 'B' which mixes airflow inlet and outlet at both low and top heights, allowed a higher and constant ΔCp of around 0.34 between the leeward and the atrium faces. Further, the ΔCp between the windward face and the internal shaft face vary from 0.54 at the top to -0.22 near the ground, which implies an internal NPL that causes double-sided cross ventilation from outside to inside the atrium at top height and from the atrium to the outside at low height. This same airflow pattern is maintained if the system operates as shaft 'A' for South winds, but ΔCp results then drop by approximately half.

For East winds the best ΔCp results were found with the shaft system operating as 'A'. Under this condition, the ΔCp between the windward face and the internal shaft face operating with ascending flow attains constant results of around 0.26 throughout the tower's height. In addition, the ΔCp between the leeward face and the internal shaft face operating with descending flow attains an average result of 0.14, although it is greater at top height and lower at low height. On the other hand, when operating as an open atrium (shaft 'B') the respective total averaged ΔCp results between the windward face and the atrium and between the atrium and the leeward sides are 0.06 and 0.17.

Finally, for West winds a similar panorama to that depicted for East winds is observed, although a greater pressure difference is found. When the system operates as shaft 'A' the ΔCp between the windward face and the internal shaft face reaches an average of 0.38 throughout the tower's height, while the ΔCp between the leeward face and the internal shaft face attains an average absolute result of 0.11 with the same decrease of pressure from top to low height. Further, when the system operates as an open atrium (shaft 'B') the respective total averaged ΔCp results between the windward face and the atrium and between the atrium and the leeward sides are 0.31 and 0.10.

Figure 9-56: Prototype tower with shaft ‘A’ surrounded by urban area : Cp contour plots for the prototype tower shaft ‘A’ WW and LW sides in urban area: base top (above), external side (middle) and internal shaft (bottom) surfaces (WT; N; 45^{o}).

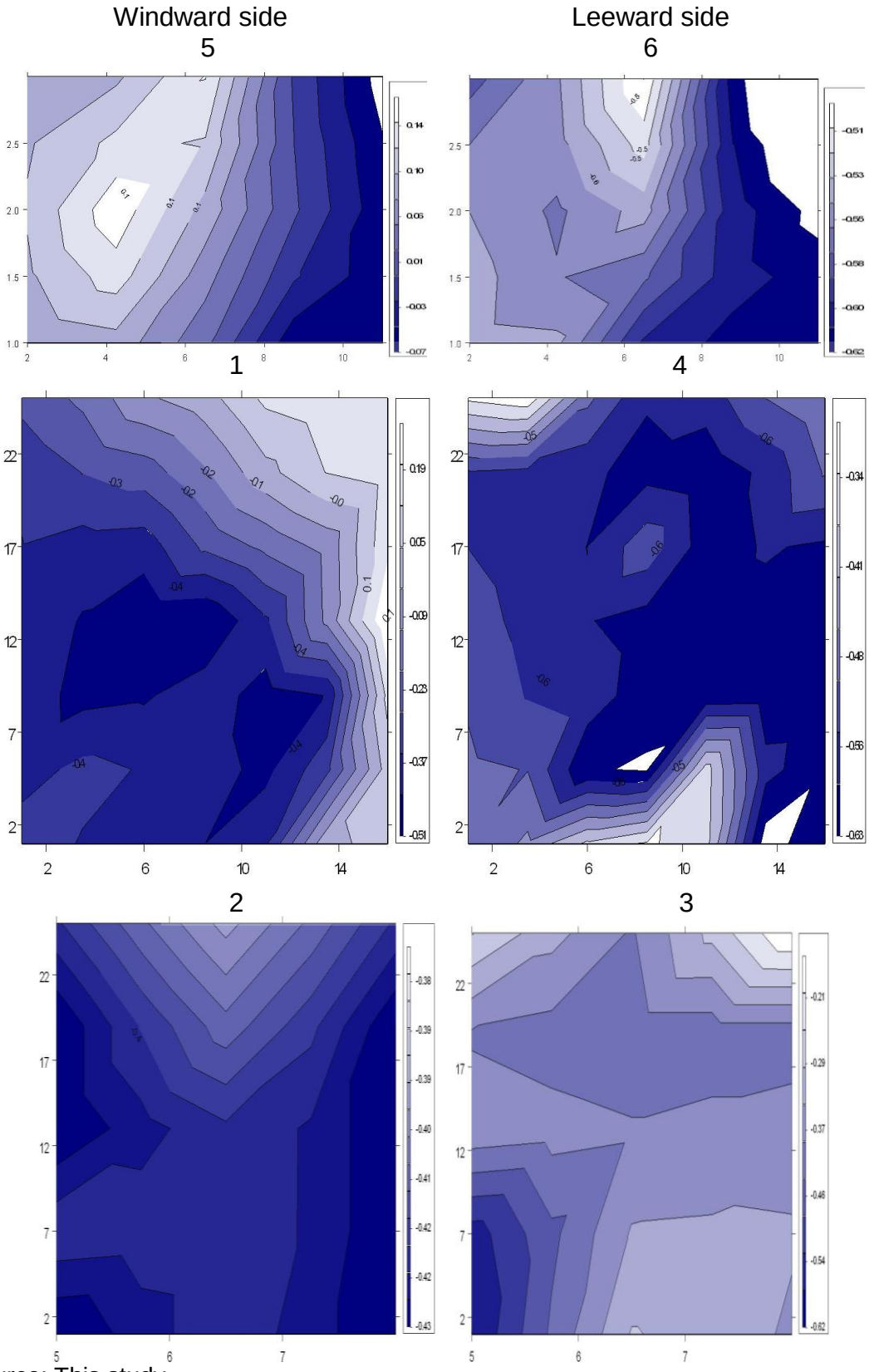

Source: This study.

Figure 9-57: Prototype tower with shaft ‘B’ surrounded by urban area : Cp contour plots for the prototype tower shaft ‘B’ WW and LW sides in urban area: base top (above), external side (middle) and internal shaft (bottom) surfaces (WT; N; 45^{o})

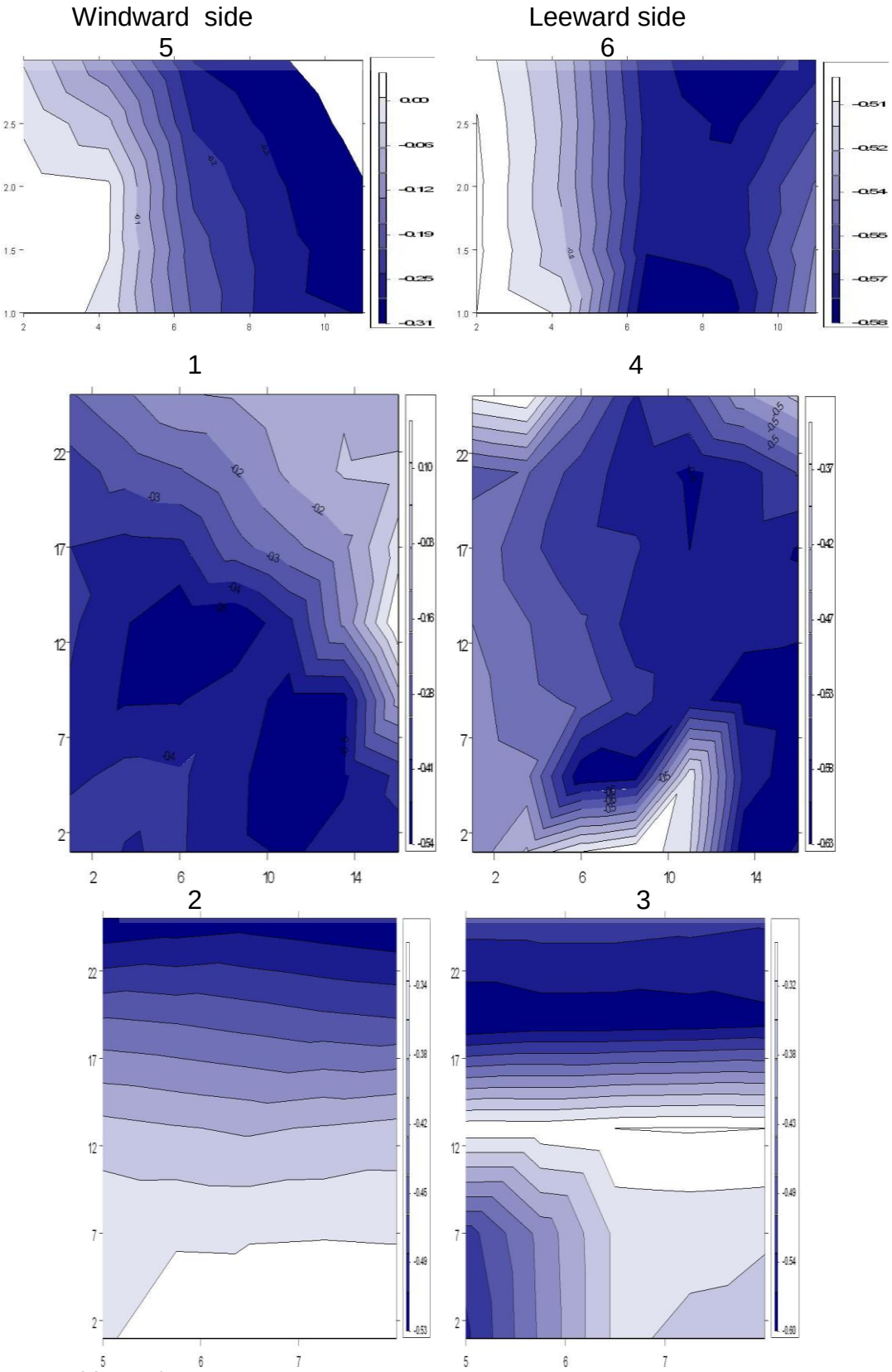

Source: This study.

Figure 9-58: Prototype tower with shaft ‘A’ surrounded by urban area: Cp contour plots for the prototype tower shaft ‘A’ WW and LW sides in urban area: base top (above), external side (middle) and internal shaft (bottom) surfaces (WT; S; 45^{o})

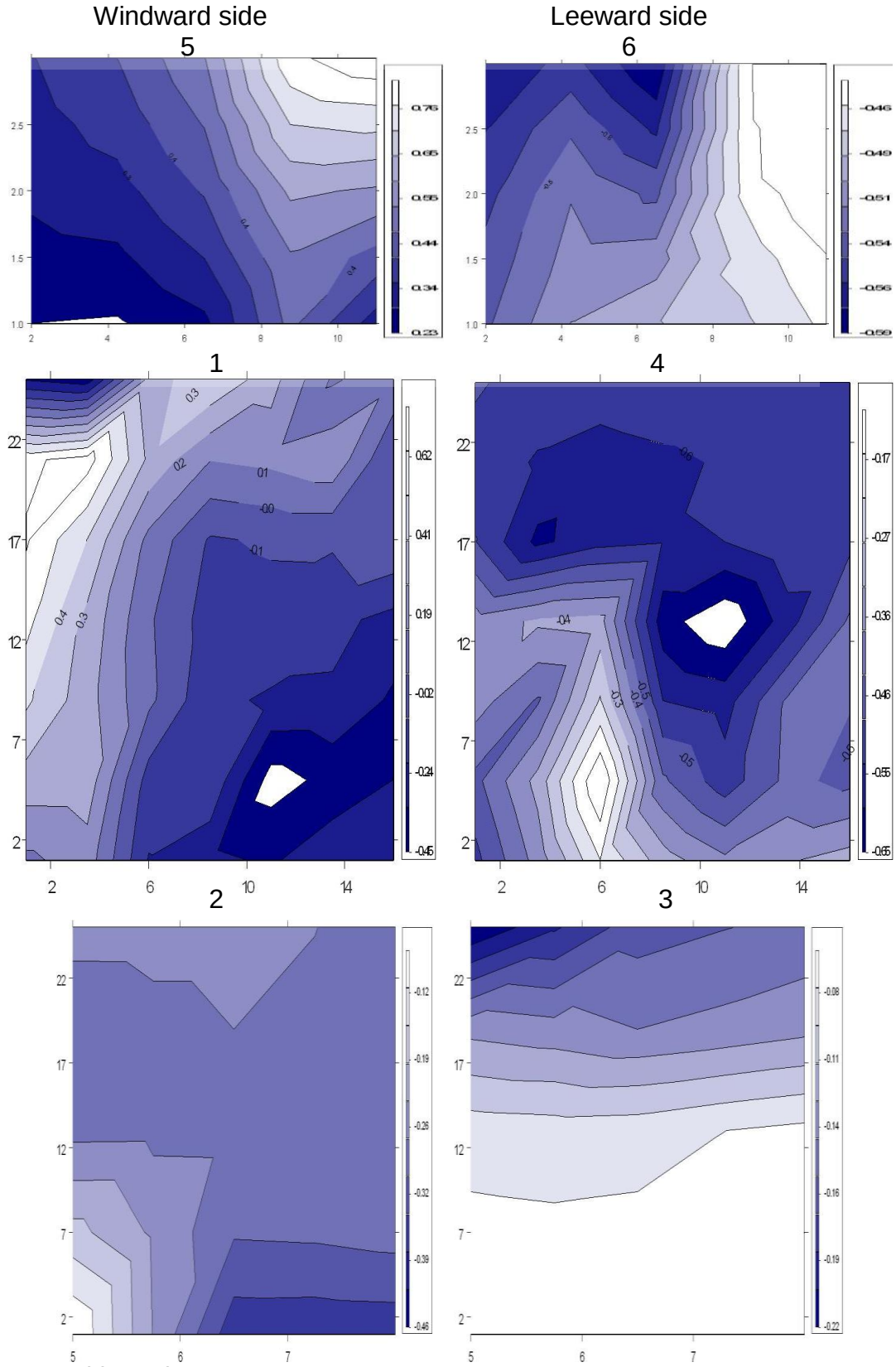

Source: This study.

Figure 9-59: Prototype tower with shaft ‘B’ surrounded by urban area: Cp contour plots for the prototype tower shaft ‘B’ WW and LW sides in urban area: base top (above), external side (middle) and internal shaft (bottom) surfaces (WT; S; 45^{o})

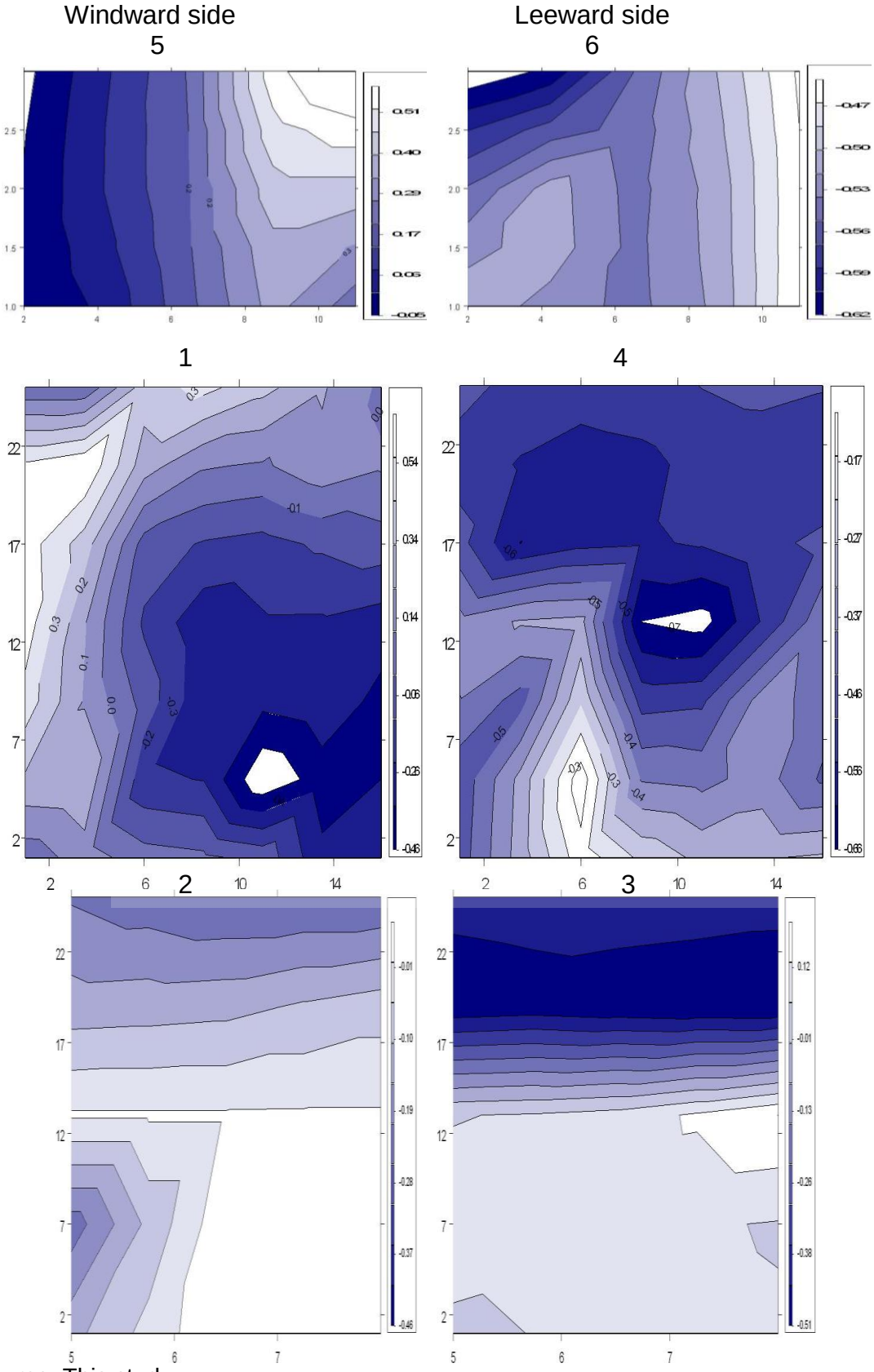

Source: This study.

Figure 9-60: Prototype tower with shaft ‘A’ surrounded by urban area: Cp contour plots for the prototype tower shaft ‘A’ WW and LW sides in urban area: base top (above), external side (middle) and internal shaft (bottom) surfaces (WT; E; 45^{o})

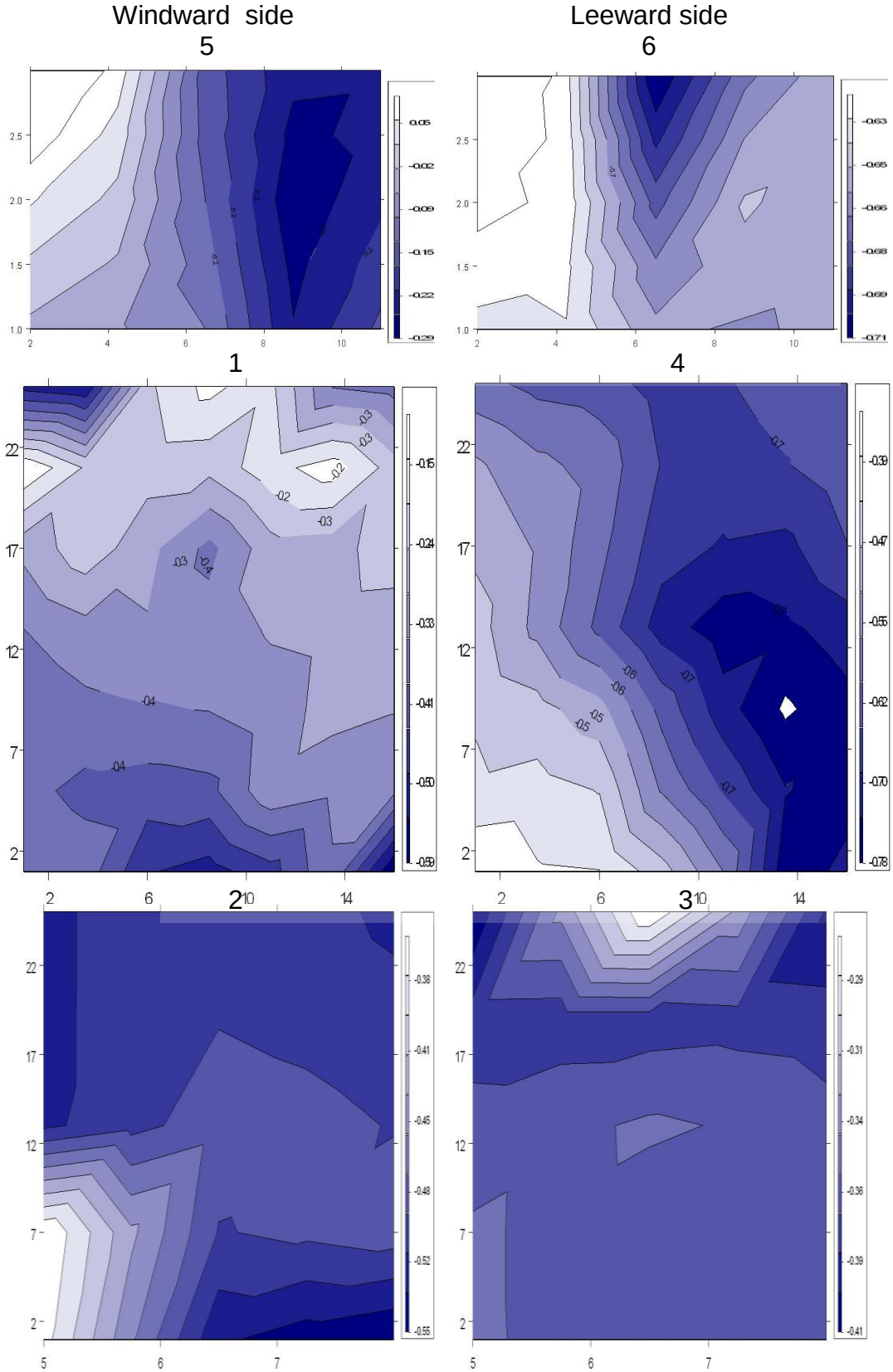

Source: This study.

Figure 9-61: Prototype tower with shaft ‘B’ surrounded by urban area: Cp contour plots for the prototype tower shaft ‘B’ WW and LW sides in urban area: base top (above), external side (middle) and internal shaft (bottom) surfaces (WT; E; 45^{o}).

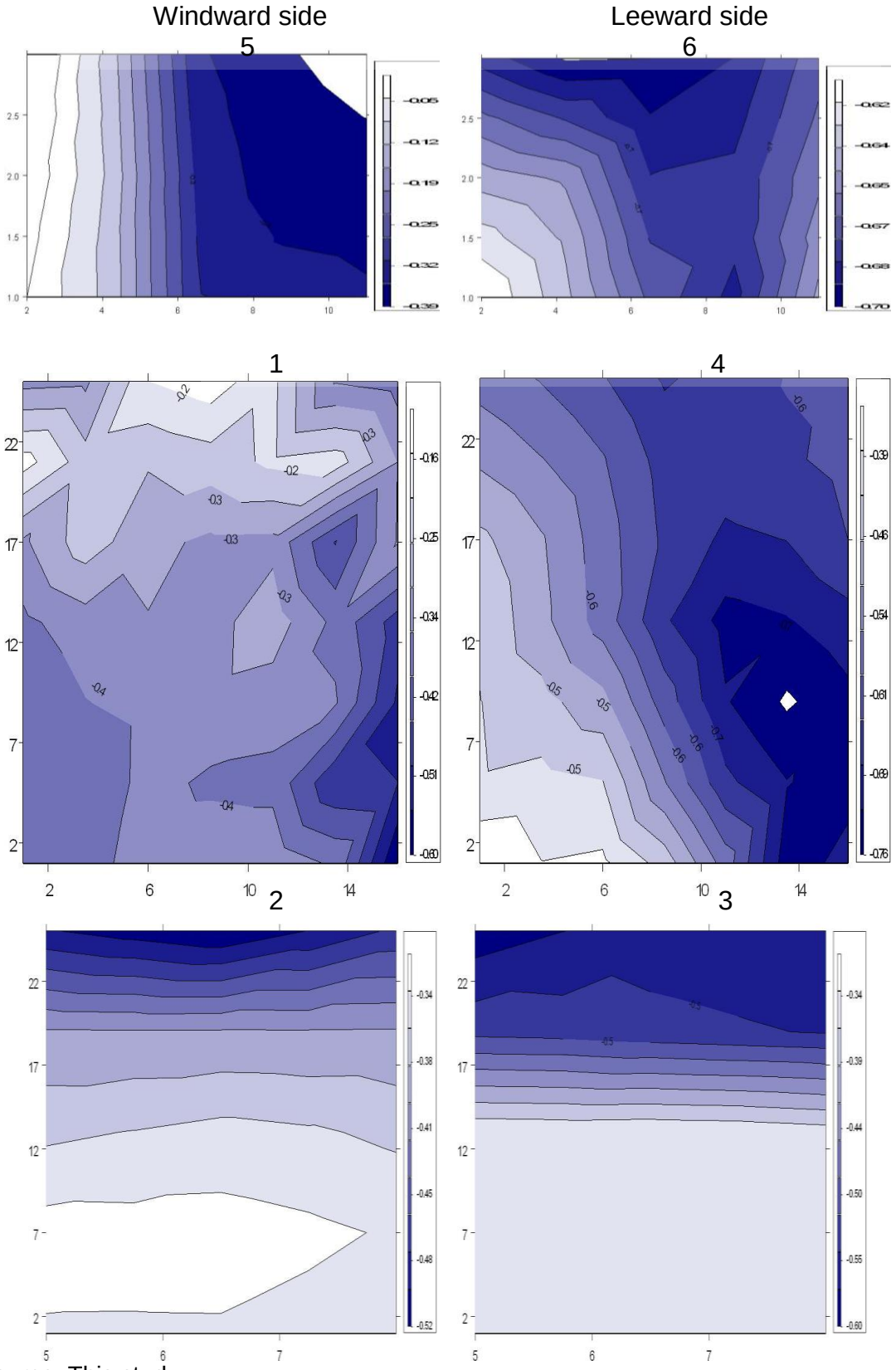

Source: This study.

Figure 9-62: Prototype tower with shaft ‘A’ surrounded by urban area: Cp contour plots for the prototype tower shaft ‘A’ WW and LW sides in urban area: base top (above), external side (middle) and internal shaft (bottom) surfaces (WT; W; 45^{o})

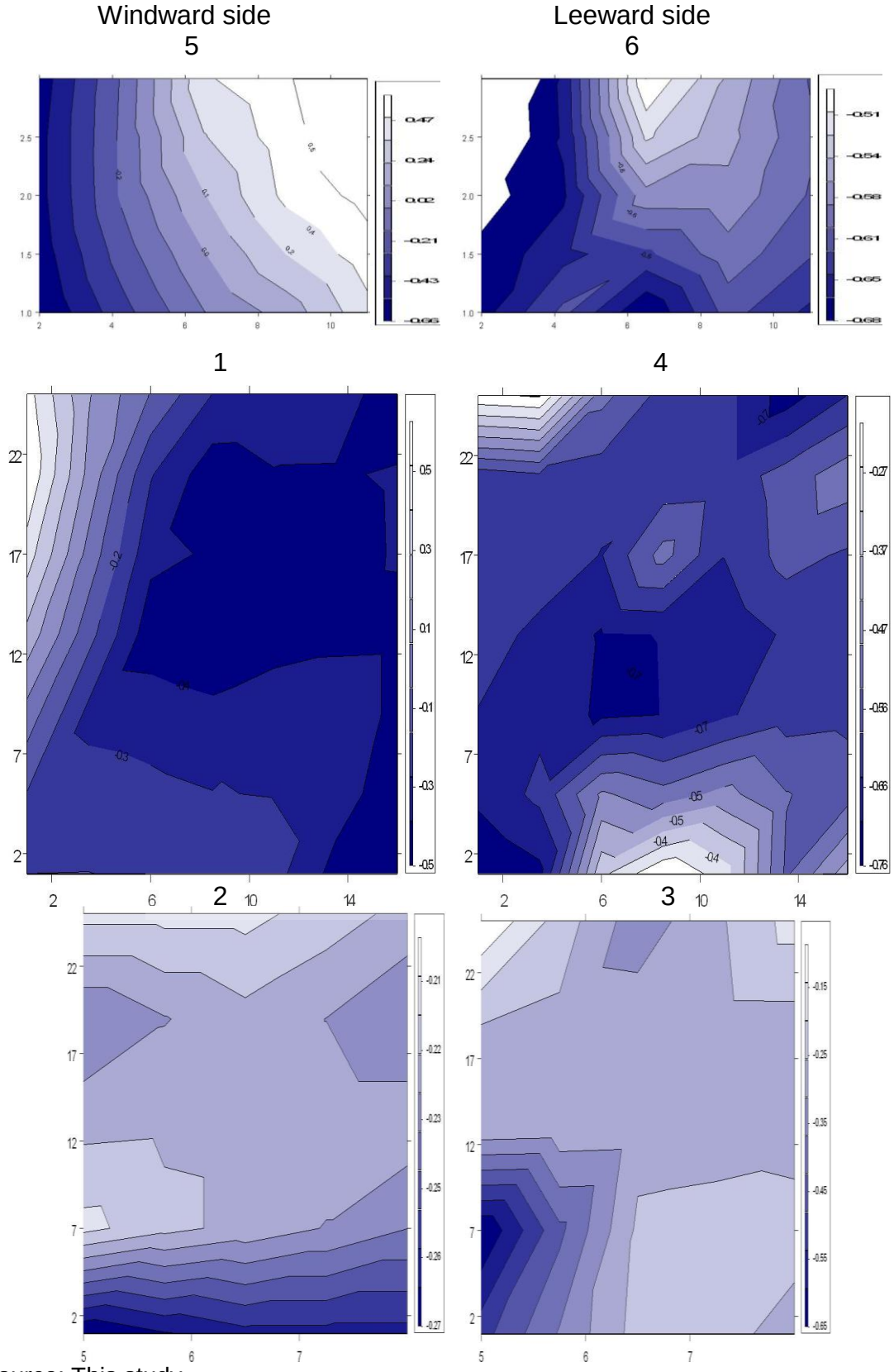

Source: This study.

Figure 9-63: Prototype tower with shaft ‘B’ surrounded by urban area: Cp contour plots for the prototype tower shaft ‘B’ WW and LW sides in urban area: base top (above), external side (middle) and internal shaft (bottom) surfaces (WT; W; 45^{o})

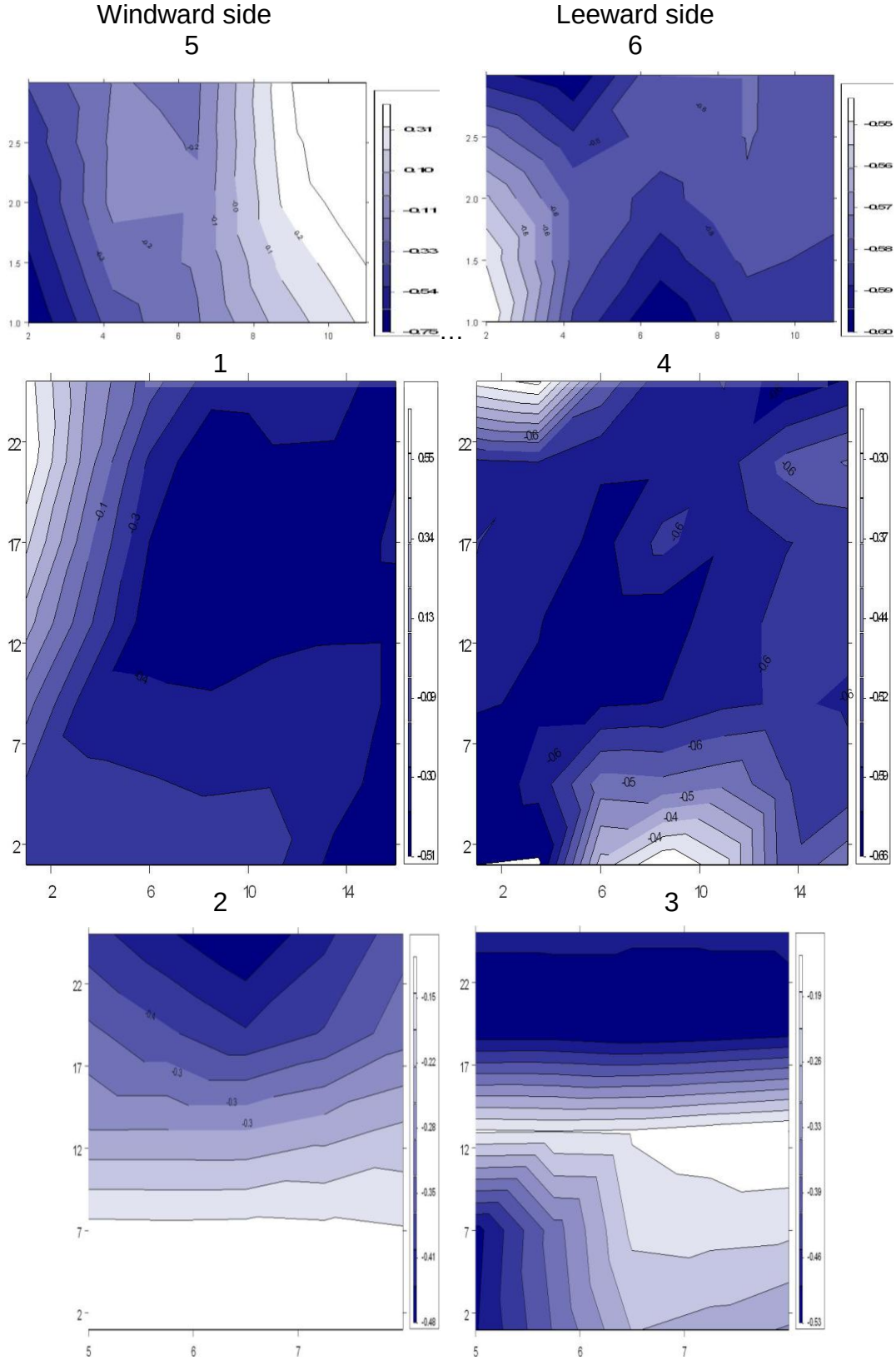

Source: This study.

9.4.3. Some considerations about the Prototype Tower

Regarding the ΔCp between the inlet and the outlet sides of the wind-catcher/ air-purge cowl, a practically constant decrease of 28% was found in the shaft 'B' operating mode when contrasted to the findings for shaft 'A'. The air wedge cavity space is the same in both systems. The difference between one inlet system and the other consists of having one opening in shaft 'B', while in shaft 'A' only half of this area works as inlet and it is also divided into six equal voids. It seems that the concentrated pressure increase exceeds the discharge coefficient pressure losses in shaft 'A'.

9.5. Paulista Avenue and Urban Prototypes ΔCp results combined analysis.

Here the ΔCp results obtained from both the Paulista Avenue CKY Tower and the Prototype Tower will be directly compared with the results obtained from the Urban Prototype Groups 1 to 6, covered in Chapter 7. It is worthy to note that, while the CKY Tower scenario was investigated by both WT and CFD techniques, the Prototype Tower experiment was carried out in the WT, and the Urban Prototype's were only simulated by CFD. This analysis aims to identify the relationship between the final ΔCp results and the urban aspect ratios so as to ascertain the existence of patterns that would help architects, building designers, and urban planners in developing both building and urban projects of high-rise and high-density areas. The analyses are based in both the previous topics of this chapter.

9.5.1. Combined analysis for parallel winds (0^o)

For prevailing winds parallel to isolated towers, it is to be expected that the ΔCp difference between the right and the left sides will always be close to zero, unless deliberate action is taken to modify this condition. For instance, the results covered in topic 9.3.1 show that both the horizontal and the vertical panels may contribute to the creation of an effective pressure difference. When the same tower is inserted in an urban context, turbulence and airflow detachment and deflection may interfere in this condition, also causing a ΔCp difference between the sides (topic 9.3.2).

An almost constant ΔCp variation was found in the urban canyons assessed as in the urban area of the rectangular CKY Tower on the Paulista Ave. Overall, results varied within a very narrow range: from 0.10 to -0.05 regardless of the aspect ratio and the tower's height, or whether it was a canyon or an asymmetrical built environment. An exception to this was found in the mid to low portion of the CKY Tower faces simulated by CFD, which showed a ΔCp variation of up to 0.16. This result is possibly related to the proximity of a low building to one of its sides, and may also be associated

with the steady-state nature of this simulation. For instance, the same geometry in the WT attains a maximum ΔCp of 0.08.

The Prototype Tower ΔCp differences between the right and the left sides also approximated to zero, ranging from 0.05 to -0.03. On the other hand, when coupled to a shaft system, the ΔCp between the potential inflow and outflow sides could reach as much as 0.45, with a range of from 0.30 to -0.30. The negative pressure difference means a change in the direction of flow direction inside the building, e.g., either from the external side to the shaft or the opposite.

9.5.2. Combined analysis for orthogonal winds (90^{o})

The analysis of the ΔCp results together with that of both the CKY Tower and the Urban Prototype may allow observing which results corroborate each other for orthogonal winds. Further, in order to make it easier to identify their common urban aspect ratios, the analysis was divided according to the following variation in height: 'low' from ground level to 30m, 'middle' from 30 to 60m and 'top' height from 60 to 90m.

Starting with the comparative analysis of the CKY Tower and the Urban Prototypes, for instance, at low height most of the Urban Prototypes' ΔCp results range from zero to 0.10. The Group 6 Urban Prototype scenarios; ΔCp results are all close to 0.10. The ΔCp results of both the CFD CKY Tower models simulated for NW and SE winds also match those of Group 6. On the other hand, the ΔCp results of both the CKY Tower NW and SE models simulated in the WT were higher, ranging in growing magnitude from 0.15 at ground level to 0.25 at 30m height for the NW winds; and from 0.27 at ground level to 0.39 at 30m height for the SE winds. At medium height, once more Group 6's D1, D3, D4-T2, and D4-T3 results are close to all the four CKY Tower NW results: CFD with flat surface, WT with flat surface, WT with horizontal panels, and WT with vertical panels. The results from the CFD CKY Tower SE model also match well, all of them ranging from 0.08 to 0.16 at 35m, and from 0.10 to 0.18 at 60m. Exceptions were the three CKY Tower SE models simulated in the WT, which once again registered higher ΔCp results: from 0.35 to 0.25 for the same height variation. At top height there is a perfect match of both the CFD CKY Tower's NW and SE models and Group 6's D1 model, ranging from 0.29 at 65m height to 0.41 at 85m height. Group 6's D4-T3 model starts with similar results, but at 85m height it drops to 0.17. The WT CKY Tower's NW models start and end this sequence with similar results, but show an increase of up to +0.10 between these heights. The three WT CKY Tower's SE models start this sequence with a ΔCp of 0.35 at 65m height, but end this sequence at 85m with different results: 0.54 for the model with flat surface, 0.60 for the vertical panel, and 0.69 for the horizontal panel.

The comparison between the Prototype Tower and the Urban Prototypes also shows many similarities to the CKY Tower comparison: at low height ΔCp results between the windward and the leeward sides (1-4) from both the Prototype Tower models simulated for NW and SE winds also match the results described previously. For this height, higher ΔCp results are observed in the following sequences of the SE model operating as shaft 'B': at 10m, ΔCp results between the 2- 4 and the 3-4 faces are 0.30 and 0.14; at 20m, between the 2- 4 and the 3-4 faces they are 0.21 and 0.18; at 30m, between the 2- 4 and the 3-4 faces they are 0.30 and 0.24. At medium height, the ΔCp results from Group 6's D1, D3, D4-T2, and D4-T3 are within the range of the results of the Prototype Tower's NW and SE models: from 0.03 at 35m to 0.05 at 60m height for the NW model, and from 0.11 at 35m to 0.17 at 60m height for the SE model. Many shaft systems also produced results within these ranges at medium height: the SE model shaft 'A' between faces 1-3, 2-4 and 3-4; the NW model shaft 'A' between faces 2-4; and the NW model shaft 'B' between faces 2-4 and 3-4. Once again, the ΔCp results from the SE model shaft 'B' between faces 2- 4 and 3-4 produced higher results, around 0.30. At top height this same pattern is maintained: the ΔCp results from Group 6's D1 and D4-T3 scenarios are within the range of the results comparing the Prototype Tower's NW and SE models: from 0.08 at 60m to 0.27 at 85m height for the NW model, and from 0.25 at 60m to 0.56 at 85m height for the SE model. The shaft arrangements that also produced results which were within these ranges at top height were: the SE model shaft 'A' between faces 1-2 and 1-3; the SE model shaft 'B' between faces 1-2 and 1-3; the NW model shaft 'A' between faces 3-4; and the NW model shaft 'B' between faces 1-2, 1-3 and 2-4.

In conclusion, a relationship between the ΔCp results of both the Paulista Avenue CKY Tower and the Prototype Tower and the Urban Prototype's Group 6 was observed. Regarding the urban aspect ratios, there is also equivalence between these scenarios in three categories: H/W= 1.00 to 1.10; A_{roof}/A_{built}= 0.24 to 0.25; and A_{built}/A_{built}= 4.00 to 4.62.

9.5.3. Combined analysis for oblique winds (45^{o})

The analysis for oblique winds adopted the same criteria as were used for the previous topic: it differentiated by height variation, as follows: 'low' from ground to 30m; 'middle' from 30 to 60m; and 'top' height from 60 to 90m. Furthermore, the aim was to observe which results match each other and also which are the urban aspect ratios they have in common.

Starting with the comparative analysis of the CKY Tower and the Urban Prototypes, for instance, at low height most of the Urban Prototypes' ΔCp results range from zero to 0.10. Exceptions are those of scenarios B2, B4 and D4-T3 above 25m,

which attain 0.17. As for the CKY Tower two distinct analyses must be made. For North winds, while both the CFD and the WT N scenario models start with ΔCp results near 0.15 at ground level, at 30m four different results are observed: 0.14 for the CFD model with flat surface; 0.28 for the WT model with flat surface, 0.20 for the WT model with vertical panels, and 0.34 for the WT model with horizontal panels. The ΔCp results for South winds are greater than those for North winds. In addition, the CFD and the WT S scenario models start and end with four different ΔCp results near the ground (0.29 for the CFD model with flat surface; 0.31 for the WT model with flat surface, 0.39 for the WT model with vertical panels, and 0.43 for the WT model with horizontal panels) and at 30m height (0.26 for the CFD model with flat surface; 0.46 for the WT model with flat surface, 0.53 for the WT model with vertical panels, and 0.54 for the WT model with horizontal panels). At medium height the ΔCp results of the Urban Prototypes D1 and D3 range from 0.05 to 0.10, while those of the scenarios D4-T2 and D4-T3 range from 0.15 to 0.25. The CKY Tower presents more homogeneous results, although distinct among themselves. The ΔCp results for the North scenario start with four different ΔCp results at 35m height (0.15 for the CFD model with flat surface; 0.31 for the WT model with flat surface, 0.23 for the WT model with vertical panels, and 0.27 for the WT model with horizontal panels) and end at 60m with three similar results around 0.15 (the three WT scenarios: with flat surface, vertical and horizontal panels) and the CFD flat surface result of 0.26. The ΔCp results for the three WT scenarios for the South wind (with flat surface, vertical and horizontal panels) range from 0.46 to 0.54 and remain constant from 35m to 60m height. Conversely, the CKY Tower CFD scenario ranges from 0.31 at 30m to 0.66 at 60m height. At top height the ΔCp results from the CFD CKY Tower for North winds are between those of Group 6's D4-T3 (ranging from 0.24 at 65m to 0.30 at 85m height) and D1 scenarios (ranging from 0.36 at 65m to 0.50 at 85m height). On the other hand, the ΔCp results from the CFD CKY Tower for North winds range from 0.45 at 65m to 0.76 at 85m height.

As regards the Prototype Tower, at low height ΔCp results between the windward and the leeward sides (1-4) of North winds range from 0.10 at ground level to 0.20 at 30m height, while those of South winds range from 0.06 at ground level to 0.30 at 30m height. Three shaft systems produced results ranging from 0.27 up to 0.41 at low height: for South winds operating as shaft 'A' between faces 3-4; and as shaft 'B' between faces 2-4 and 3-4. At medium height, the ΔCp results of Group 6 matched the sequence of results of the Prototype Tower for North winds closely, ranging from 0.19 at 35m to 0.24 at 60m height. While the other Urban Prototypes's scenarios (D1, D3 and D4-T2) were below this range, the ΔCp results from the Prototype Tower for South winds ranged from 0.29 at 35m to 0.45 at 60m height. The same three shaft systems (for South winds operating as shaft 'A' between faces 3-4; and as shaft 'B' between

faces 2-4 and 3-4) produced the highest results at medium height, which ranged from 0.38 up to 0.48. Six other shafts produced results ranging from -0.11 to -0.31 at medium height: for N winds and operating as shaft 'A' between faces 1-3 and as shaft 'B' between faces 1-2 and 1-3; for S winds and operating as shaft 'A' between faces 1-3 and as shaft 'B' between faces 1-2 and 1-3. At top height the Urban Prototype's D4-T3 ΔCp results are practically constant at 0.28 from 65m to 85m height, as for the Prototype Tower the ΔCp results range from 0.32 to 0.48 for North winds and 0.50 to 0.76 for South winds, with the Urban Prototype D1 varying between these last two. Furthermore, at top height for oblique winds the following ranges of ΔCp results were associated with the sequence of shaft arrangements:

- ΔCp ranging from 0.00 to 0.15: South winds and prototype tower operating as shaft 'B' between faces 3-4; and North winds operating as shaft 'A' between faces 3-4, and as shaft 'B' between faces 2-4 and 3-4;
- ΔCp ranging from 0.15 to 0.30: South winds and prototype tower operating as shaft 'A' between faces 1-3 and 2-4, and as shaft 'B' between faces 1-2; and North winds operating as shaft 'A' between faces 1-2 and 2-4, and as shaft 'B' between faces 1-2;
- ΔCp ranging from 0.30 to 0.45: South winds and prototype tower operating as shaft 'A' between faces 1-2 and 3-4, and as shaft 'B' between faces 2-4; and North winds operating as shaft 'B' between faces 1-3; and
- ΔCp ranging from 0.45 to 0.60: South winds and prototype tower operating as shaft 'B' between faces 1-3.

9.6. CKY Tower and the Urban Prototypes correlation assessment

The Paulista Avenue CFD outputs were directly compared to the results from the Urban Prototype's Groups 1 to 6 here. The scale of significance and correlation coefficient strength employed here is described in the topic 5.8.4 in Chapter 5. This investigation sought to identify if the correlation coefficient strength previously found between this actual urban environment aspect ratio and the urban prototypes aspect ratios is also translated into the same level of correlation coefficient strength for the ΔCp results. The correlation coefficients for ΔCp employed the averaged results for 90% of the data (discharging 10% of extreme results)[137].

[137] Other ΔCp data (such as peaks values, the 8th highest/ lowest results, and the standard deviation) were displayed with the purpose of providing further information about the results.

9.6.1. Correlation coefficients between the ΔCp results

The correlation coefficients for the ΔCp results seen on table 9-4 showed a strong relationship for all wind directions between the Paulista Ave. and the Urban Prototype D4. Further, at least two out five wind directions with the same rank for the other prototypes from the Group 6: D1, D2, and D3 showed strong statistical similarity. Strong relationship was also found for the Prototype scenarios A1, A3, C3, and C4. The other prototype scenarios showed from substantial to low relationship levels.

Strong correlation was found between the Paulista Avenue and the Urban Prototype D4 on both the aspect ratio (0.95) and the ΔCp: 0.91 for NE (0^o), 0.90 and 0.94 for N and S (90^o), and 0.92 and 0.93 for NW and SE (45^o) winds. It is possible to say that, according to the urban aspect ratios, both the urban scenarios were similar, with respective H/W= 1.10 and 1.31, A_{roof}/A_{built}= 0.25 and 0.30, and A_{built}/A_{built}= 4.03 and 4.98. These results can be observed in figures 9-64 to 9-68.

Figure 9-64: Correlation between the Paulista Avenue ΔCp results and the Urban Prototype D4 ΔCp results for NE winds (0^o).

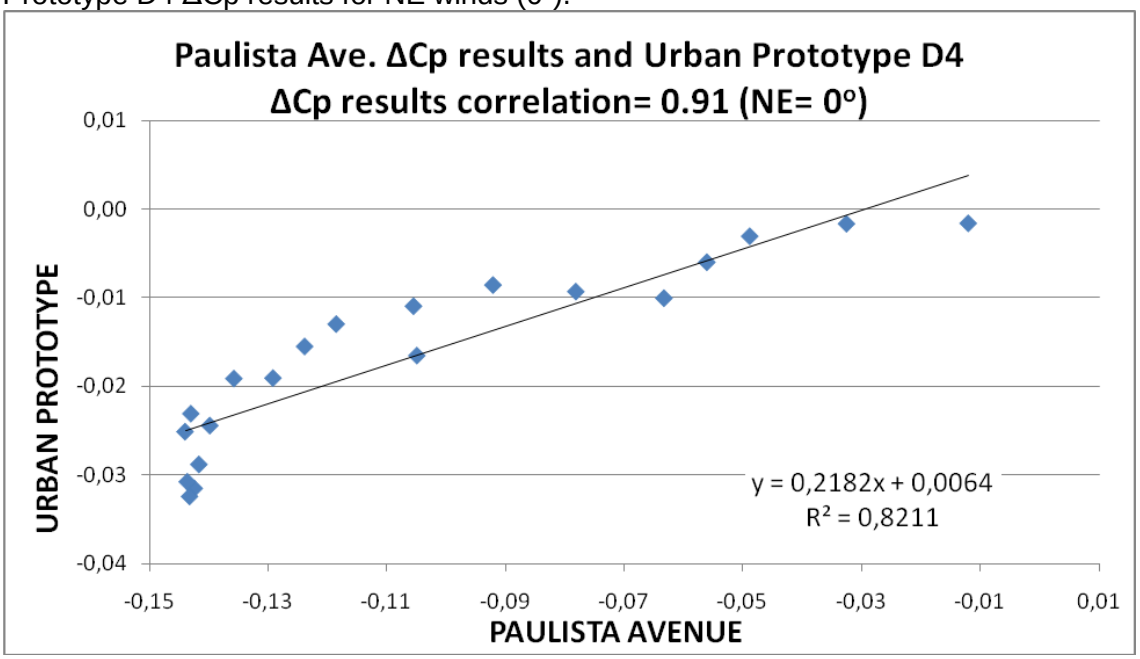

Source: this study.

Figure 9-65: Correlation between the Paulista Avenue ΔCp results and the Urban Prototype D4 ΔCp results for N winds (45°).

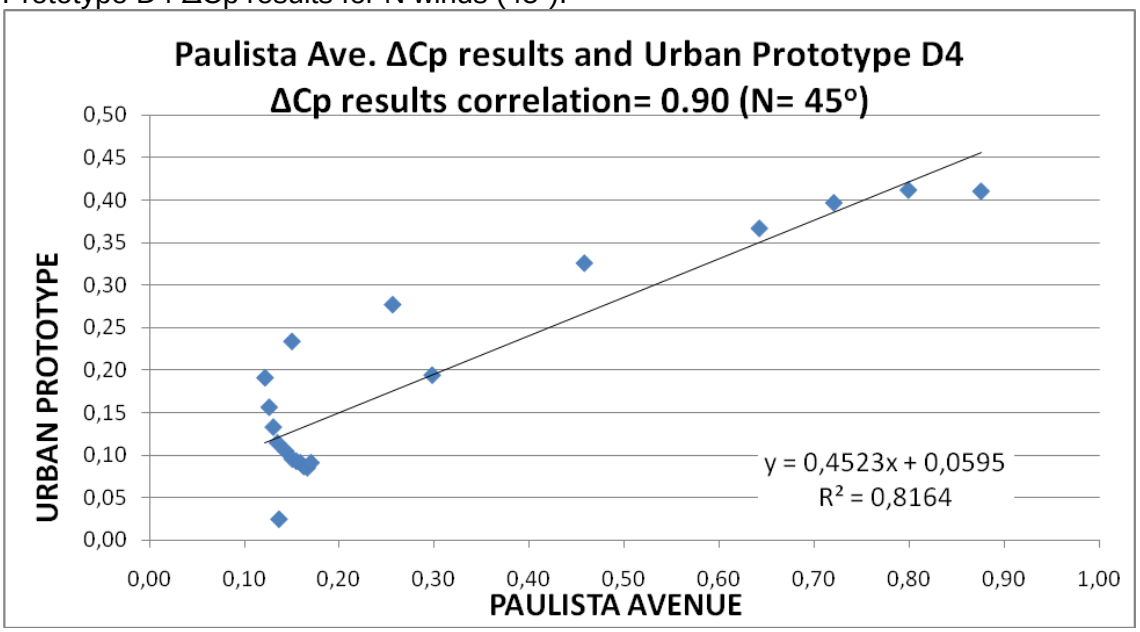

Source: this study.

Figure 9-66: Correlation between the Paulista Avenue ΔCp results and the Urban Prototype D4 ΔCp results for S winds (45°).

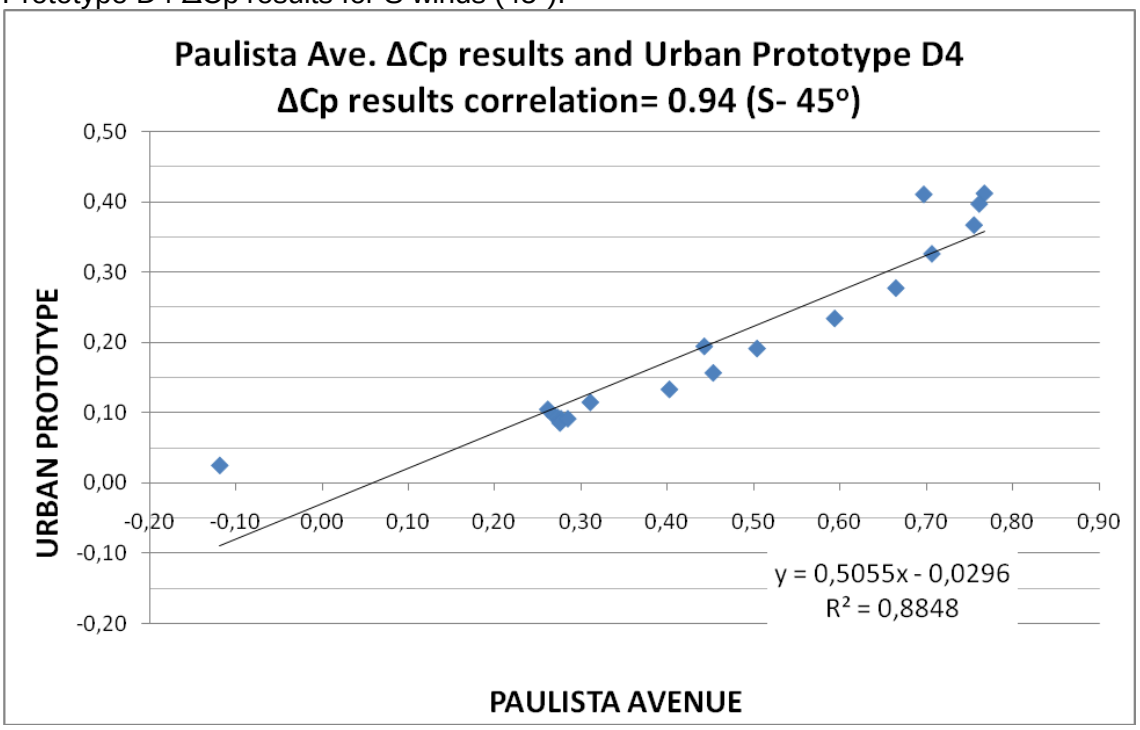

Source: this study.

Figure 9-67: Correlation between the Paulista Avenue ΔCp results and the Urban Prototype D4 ΔCp results for NW winds (90º).

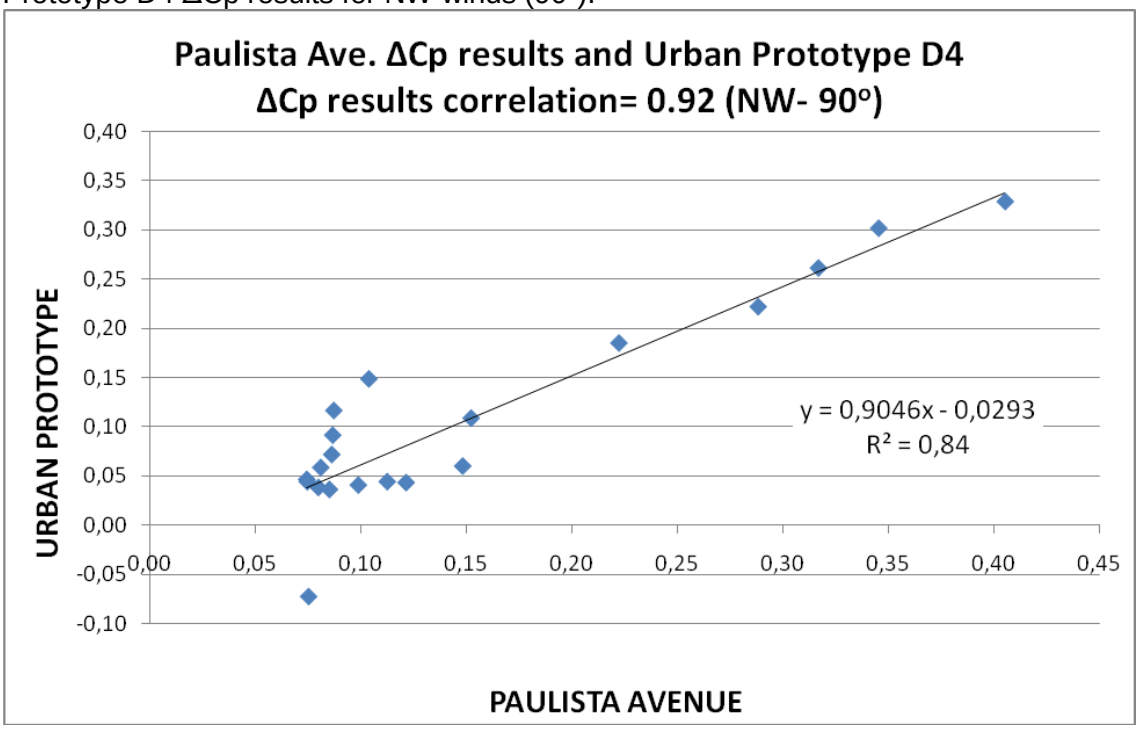

Source: this study.

Figure 9-68: Correlation between the Paulista Avenue ΔCp results and the Urban Prototype D4 ΔCp results for SE winds (90º).

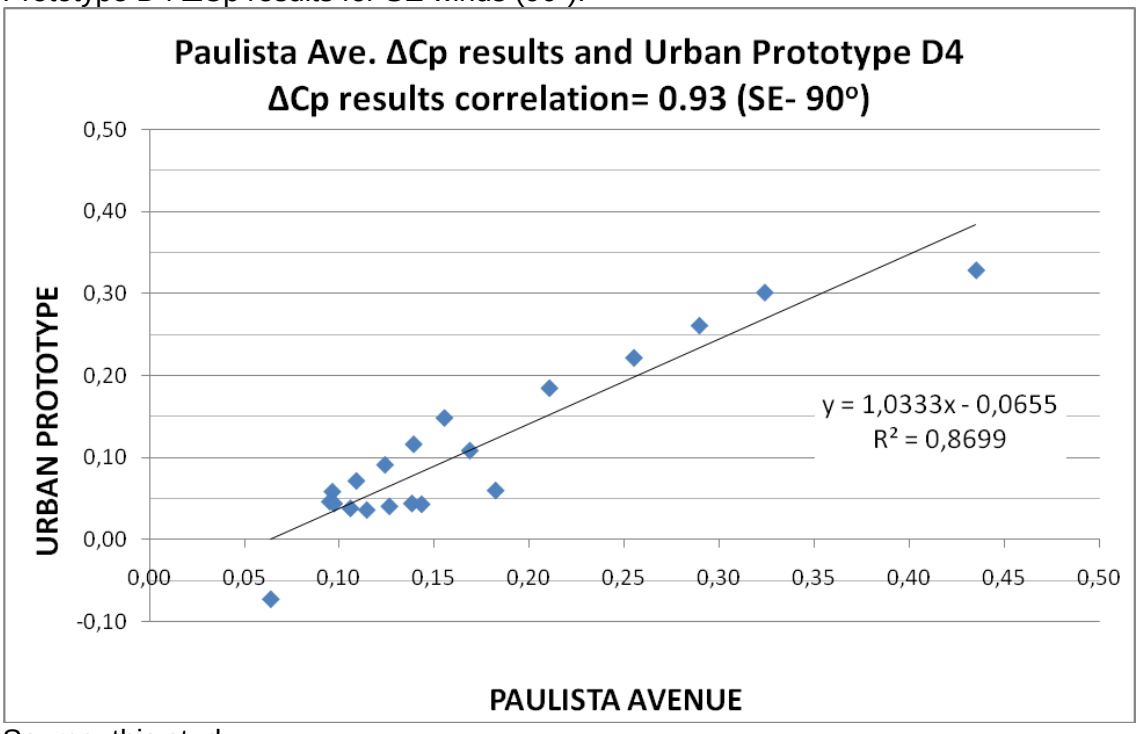

Source: this study.

Table 9-3: The Paulista Avenue CKY Tower and the Urban Prototypes correlation coefficients between the ΔCp results[138].

Winds Direction		α	Urban Prototypes															
			A1	A2	A3	A4	B1	B2	B3	B4	C1	C2	C3	C4	D1	D2	D3	D4
Paulista Avenue	N	45°	-0,18	0,40	0,09	-0,22	0,56	0,14	0,35	0,31	0,38	-0,98	0,29	-0,18	0,94	0,71	0,48	0,90
	S	45°	0,48	-0,27	0,69	0,48	0,59	0,23	0,69	0,56	0,10	0,50	0,61	-0,12	0,89	0,88	0,58	0,94
	NE	0°	0,74	0,03	0,74	-0,25	0,43	0,44	0,03	-0,92	-0,79	0,03	0,03	0,84	0,48	0,79	0,92	0,91
	SE	90°	0,57	-0,03	0,40	0,02	0,03	0,39	0,34	0,32	-0,35	-0,73	0,72	0,55	0,61	0,80	0,89	0,92
	SW	90°	-0,92	0,02	0,45	0,07	0,12	0,46	0,42	0,35	-0,28	-0,72	0,78	0,52	0,65	0,82	0,90	0,93

Source: this study.

[138] The colours of this scale of significance for the Paulista Avenue CKY Tower ΔCp results and the urban prototype ΔCp results correlation coefficient (*r*) strength are based on the Table 5-20 in Chapter 5.

Table 9-4: Paulista Ave. and Urban Prototypes Group 6 correlation coefficients for the ΔCp results, and the ΔCp standard deviation (NE- 0°).

Northeast		**Paulista Avenue**	**Urban Prototypes**							
Parallel Winds 0°		**NE** CFD	**D1**	SDEV NE-D1	**D2**	SDEV NE-D2	**D3**	SDEV NE-D3	**D4**	SDEV NE-D4
height	(m)	ΔXπ	ΔXπ	%	ΔXπ	%	ΔXπ	%	ΔXπ	%
ΔCp at	90	-0,01	0,01	1%	0,08	4%	0,08	4%	0,00	3%
ΔCp at	85	-0,03	0,02	4%	0,08	5%	0,08	4%	0,00	4%
ΔCp at	80	-0,05	0,02	5%	0,08	6%	0,08	5%	0,00	5%
ΔCp at	75	-0,06	0,02	5%	0,08	6%	0,08	5%	−0,01	5%
ΔCp at	70	-0,06	0,02	6%	0,08	6%	0,08	5%	−0,01	5%
ΔCp at	65	-0,08	0,02	7%	0,08	7%	0,08	6%	−0,01	6%
ΔCp at	60	-0,09	0,03	9%	0,04	8%	0,01	6%	−0,01	6%
ΔCp at	55	-0,11	0,02	9%	0,04	8%	0,02	7%	−0,01	6%
ΔCp at	50	-0,12	0,02	10%	0,04	9%	0,02	8%	−0,01	7%
ΔCp at	45	-0,12	0,03	11%	0,04	10%	0,02	8%	−0,02	7%
ΔCp at	40	-0,13	0,03	11%	0,04	10%	0,02	9%	−0,02	8%
ΔCp at	35	-0,14	0,02	11%	0,04	10%	0,02	9%	−0,02	8%
ΔCp at	30	-0,14	-0,03	8%	0,07	10%	0,00	9%	-0,02	8%
ΔCp at	25	-0,14	-0,01	9%	0,06	10%	0,00	9%	-0,03	8%
ΔCp at	20	-0,14	-0,01	9%	0,04	10%	-0,01	9%	-0,03	8%
ΔCp at	15	-0,14	-0,01	10%	0,01	10%	-0,01	9%	-0,03	8%
ΔCp at	10	-0,14	-0,01	10%	0,01	10%	-0,01	9%	-0,03	8%
ΔCp at	5	-0,14	-0,01	10%	0,01	10%	-0,01	9%	-0,03	8%
ΔCp at	2	-0,14	-0,01	10%	0,01	10%	-0,03	9%	-0,02	8%
AVG ΔCp	**>>>**	**-0,10**	**0,01**	8,1%	**0,05**	8,4%	**0,03**	7,4%	**-0,02**	6,7%
Correlation >>>			**0,48**		**0,79**		**0,92**		**0,91**	

Source: this study.

Table 9-5: Paulista Ave. and Urban Prototypes Group 6 correlation coefficients for the ΔCp results, and the ΔCp standard deviation (N- 45°).

North		Paulista Avenue	Urban Prototypes							
Oblique Winds 45°		**N**	**D1**	SDEV	**D2**	SDEV	**D3**	SDEV	**D4**	SDEV
		CFD		NE-D1		NE-D2		NE-D3		NE-D4
height	(m)	ΔXπ	ΔXπ	%	ΔXπ	%	ΔXπ	%	ΔXπ	%
ΔCp at	90	0,14	-0,12	18%	0,15	14%	0,08	11%	0,02	9%
ΔCp at	85	0,88	0,50	27%	0,41	26%	0,32	23%	0,41	21%
ΔCp at	80	0,80	0,51	21%	0,39	25%	0,31	22%	0,41	20%
ΔCp at	75	0,72	0,46	18%	0,37	22%	0,29	20%	0,40	18%
ΔCp at	70	0,64	0,42	16%	0,35	20%	0,26	18%	0,37	16%
ΔCp at	65	0,46	0,36	7%	0,34	17%	0,24	14%	0,33	13%
ΔCp at	60	0,26	0,13	9%	0,29	10%	0,18	8%	0,28	9%
ΔCp at	55	0,15	0,12	2%	0,32	12%	0,20	10%	0,23	9%
ΔCp at	50	0,12	0,10	2%	0,32	13%	0,20	10%	0,19	9%
ΔCp at	45	0,13	0,08	3%	0,32	13%	0,40	15%	0,16	12%
ΔCp at	40	0,13	0,07	5%	0,31	12%	0,22	10%	0,13	9%
ΔCp at	35	0,13	0,06	5%	0,30	11%	0,24	10%	0,11	9%
ΔCp at	30	0,14	0,00	10%	0,26	11%	0,25	10%	0,10	8%
ΔCp at	25	0,15	0,00	11%	0,21	9%	0,22	8%	0,10	7%
ΔCp at	20	0,15	0,00	11%	0,20	8%	0,20	8%	0,09	7%
ΔCp at	15	0,16	0,00	11%	0,16	7%	0,19	7%	0,09	6%
ΔCp at	10	0,16	0,01	11%	0,20	8%	0,19	7%	0,09	7%
ΔCp at	5	0,17	0,01	11%	0,18	8%	0,23	8%	0,09	7%
ΔCp at	2	0,17	-0,08	17%	0,21	13%	0,25	11%	0,09	10%
AVG ΔCp		**0,30**	**0,14**	11,3%	**0,28**	13,7%	**0,24**	12,1%	**0,19**	10,8%
Correlation >>>			**0,94**		**0,71**		**0,48**		**0,90**	

Source: this study.

Table 9-6: Paulista Ave. and Urban Prototypes Group 6 correlation coefficients for the ΔCp results, and the ΔCp standard deviation (S- 45°).

South		Paulista Avenue	Urban Prototypes							
Oblique Winds 45°		**S**	**D1**	SDEV	**D2**	SDEV	**D3**	SDEV	**D4**	SDEV
		CFD		NE-D1		NE-D2		NE-D3		NE-D4
height	(m)	ΔXπ	ΔXπ	%	ΔXπ	%	ΔXπ	%	ΔXπ	%
ΔCp at	90	-0,12	-0,12	0%	0,15	13%	0,08	12%	0,02	11%
ΔCp at	85	0,70	0,50	14%	0,41	23%	0,32	20%	0,41	18%
ΔCp at	80	0,77	0,51	19%	0,39	24%	0,31	21%	0,41	19%
ΔCp at	75	0,76	0,46	21%	0,37	23%	0,29	21%	0,40	19%
ΔCp at	70	0,76	0,42	24%	0,35	22%	0,26	20%	0,37	18%
ΔCp at	65	0,71	0,36	25%	0,34	20%	0,24	19%	0,33	17%
ΔCp at	60	0,66	0,13	38%	0,29	22%	0,18	19%	0,28	17%
ΔCp at	55	0,59	0,12	34%	0,32	19%	0,20	17%	0,23	15%
ΔCp at	50	0,50	0,10	29%	0,32	17%	0,20	14%	0,19	13%
ΔCp at	45	0,45	0,08	26%	0,32	15%	0,40	14%	0,16	13%
ΔCp at	40	0,40	0,07	24%	0,31	14%	0,22	12%	0,13	11%
ΔCp at	35	0,31	0,06	18%	0,30	12%	0,24	10%	0,11	10%
ΔCp at	30	0,26	0,00	19%	0,26	12%	0,25	10%	0,10	9%
ΔCp at	25	0,27	0,00	19%	0,21	12%	0,22	10%	0,10	9%
ΔCp at	20	0,27	0,00	19%	0,20	12%	0,20	9%	0,09	9%
ΔCp at	15	0,28	0,00	19%	0,16	12%	0,19	9%	0,09	8%
ΔCp at	10	0,28	0,01	19%	0,20	11%	0,19	9%	0,09	9%
ΔCp at	5	0,28	0,01	19%	0,18	11%	0,23	9%	0,09	9%
ΔCp at	2	0,28	-0,08	26%	0,21	17%	0,25	13%	0,09	12%
AVG ΔCp		**0,44**	**0,14**	21,6%	**0,28**	16,4%	**0,24**	14,2%	**0,19**	12,8%
Correlation >>>			**0,89**		**0,88**		**0,58**		**0,94**	

Source: this study.

Table 9-7: Paulista Ave. and Urban Prototypes Group 6 correlation coefficients for the ΔCp results, and the ΔCp standard deviation (NW- 90°).

Northwest		**Paulista Avenue**	**Urban Prototypes**						
Orthogonal Winds 90°		**NW** CFD	**D1**	SDEV NE-D1	**D2**	SDEV NE-D2	**D3**	SDEV NE-D3	**D4**	SDEV NE-D4
height	(m)	ΔXπ	ΔXπ	%	ΔXπ	%	ΔXπ	%	ΔXπ	%
ΔCp at	90	0,08	-0,06	10%	-0,06	9%	-0,12	10%	-0,07	9%
ΔCp at	85	0,41	0,17	17%	0,26	11%	0,37	12%	0,33	12%
ΔCp at	80	0,35	0,19	11%	0,30	11%	0,35	11%	0,30	11%
ΔCp at	75	0,32	0,20	9%	0,29	10%	0,32	11%	0,26	10%
ΔCp at	70	0,29	0,20	6%	0,27	10%	0,29	10%	0,22	9%
ΔCp at	65	0,22	0,19	2%	0,25	10%	0,25	9%	0,18	8%
ΔCp at	60	0,15	0,19	3%	0,23	9%	0,11	7%	0,06	7%
ΔCp at	55	0,10	0,18	5%	0,21	7%	0,17	6%	0,15	6%
ΔCp at	50	0,09	0,16	5%	0,17	6%	0,13	5%	0,12	5%
ΔCp at	45	0,09	0,14	4%	0,14	5%	0,10	4%	0,09	4%
ΔCp at	40	0,09	0,13	3%	0,13	5%	0,07	4%	0,07	4%
ΔCp at	35	0,08	0,11	2%	0,11	4%	0,05	4%	0,06	3%
ΔCp at	30	0,07	0,10	2%	0,09	4%	0,00	4%	0,05	3%
ΔCp at	25	0,07	0,08	0%	0,08	4%	0,01	4%	0,04	3%
ΔCp at	20	0,08	0,07	1%	0,08	4%	0,00	4%	0,04	3%
ΔCp at	15	0,09	0,06	2%	0,08	3%	0,00	4%	0,04	3%
ΔCp at	10	0,10	0,07	2%	0,10	4%	-0,01	4%	0,04	4%
ΔCp at	5	0,11	0,09	1%	0,15	6%	-0,01	6%	0,04	5%
ΔCp at	2	0,12	0,11	1%	0,17	7%	-0,02	7%	0,04	6%
AVG ΔCp		**0,15**	**0,12**	4,5%	**0,16**	6,7%	**0,11**	6,6%	**0,11**	6,1%
Correlation >>>			**0,61**		**0,80**		**0,89**		**0,92**	

Source: this study.

Table 9-8: Paulista Ave. and Urban Prototypes Group 6 correlation coefficients for the ΔCp results, and the ΔCp standard deviation (SE- 90°).

Southeast		**Paulista Avenue**	**Urban Prototypes**							
Orthogonal Winds 90°		**SE** CFD	**D1**	SDEV NE-D1	**D2**	SDEV NE-D2	**D3**	SDEV NE-D3	**D4**	SDEV NE-D4
height	(m)	ΔXπ	ΔXπ	%	ΔXπ	%	ΔXπ	%	ΔXπ	%
ΔCp at	90	0,06	-0,06	9%	-0,06	8%	-0,12	9%	-0,07	9%
ΔCp at	85	0,44	0,17	19%	0,26	12%	0,37	12%	0,33	12%
ΔCp at	80	0,32	0,19	9%	0,30	10%	0,35	11%	0,30	11%
ΔCp at	75	0,29	0,20	7%	0,29	10%	0,32	11%	0,26	10%
ΔCp at	70	0,25	0,20	4%	0,27	10%	0,29	10%	0,22	9%
ΔCp at	65	0,21	0,19	1%	0,25	11%	0,25	9%	0,18	8%
ΔCp at	60	0,18	0,19	0%	0,23	10%	0,11	8%	0,06	7%
ΔCp at	55	0,16	0,18	2%	0,21	8%	0,17	7%	0,15	6%
ΔCp at	50	0,14	0,16	1%	0,17	7%	0,13	6%	0,12	5%
ΔCp at	45	0,12	0,14	1%	0,14	6%	0,10	5%	0,09	5%
ΔCp at	40	0,11	0,13	1%	0,13	6%	0,07	5%	0,07	4%
ΔCp at	35	0,10	0,11	1%	0,11	5%	0,05	4%	0,06	4%
ΔCp at	30	0,09	0,10	0%	0,09	5%	0,00	5%	0,05	4%
ΔCp at	25	0,10	0,08	1%	0,08	4%	0,01	4%	0,04	3%
ΔCp at	20	0,11	0,07	3%	0,08	3%	0,00	4%	0,04	3%
ΔCp at	15	0,11	0,06	4%	0,08	3%	0,00	4%	0,04	3%
ΔCp at	10	0,13	0,07	4%	0,10	4%	-0,01	5%	0,04	4%
ΔCp at	5	0,14	0,09	3%	0,15	5%	-0,01	6%	0,04	5%
ΔCp at	2	0,14	0,11	3%	0,17	6%	-0,02	7%	0,04	6%
AVG ΔCp		**0,17**	**0,12**	3,9%	**0,16**	7,1%	**0,11**	7,0%	**0,11**	6,3%
Correlation >>>			**0,65**		**0,82**		**0,90**		**0,93**	

Source: this study.

Figure 9-69: The Paulista Ave. (top) and the wind directions which showed strong correlation (in green) to the Urban Prototype D4 (bottom) ΔCp results.

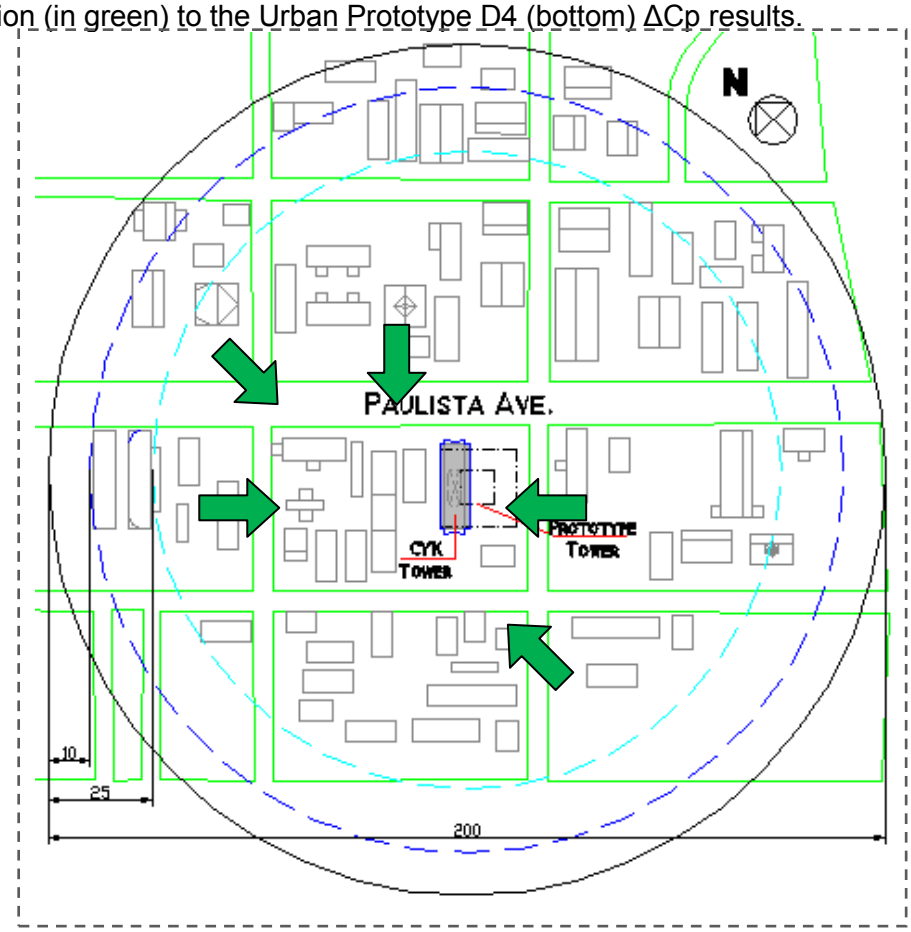

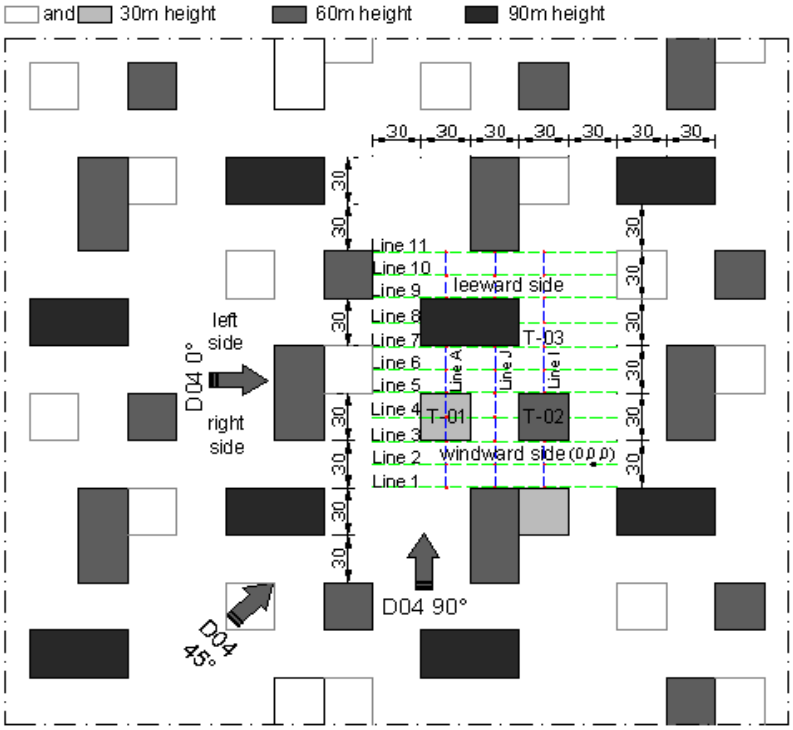

Source: this study.

9.7. Chapter conclusion

This chapter presents an assessment of the Paulista Avenue urban environment with two variables: the existing CKY Tower and a proposed Prototype Tower. This constitutes of one of the case studies, planned in Step 3 of the methodology. The sets of experiments consisted of the investigation of the airflow field around isolated towers within the Paulista Avenue urban environment for three prevailing wind directions.

These simulations were carried out by means of CFD and/ or WT, and casting light on several issues related to airflow patterns in high-density urban environments and around high-rise buildings, and the resultant Cp and ΔCp. Close agreement was found between the CFD and the WT Results. The combined analysis between the Paulista Avenue CKY Tower and the Urban Prototypes[139] CFD simulations showed strong statistical strength between the ΔCp results from this actual urban area and the D4 urban prototype scenario, agreeing with the strong statistical strength between the physical aspect ratios and previously covered in Chapter 5. This agreement is consistent with the hypotheses and the objectives of this investigation, set-out in Chapter 1.

This chapter is supported by the critical literature review presented in Part 2. Based on these considerations, it may be affirmed that the objective proposed for this chapter has been successfully achieved.

[139] The Urban Prototypes consisted of the Step 2 of the methodology: Study of a large quantity of urban prototypes with simplified volumetric shape simulated in CFD, and which was covered in Chapter 7.

Part 05: Conclusion

Chapter 10: Final Conclusions and Further Investigations

10.1. Introduction

This chapter contains the final conclusions of the thesis. An over-all view of the chapters of 'Part 04: Results and Analyses' chapters are presented here. The main findings of this investigation are discussed on the theoretical level. Further implications and contributions of the theory, as well as the limitations of this study are addressed. Finally, suggestions for future research are offered.

10.2. Airflow in the urban environment

The results presented and the analyses undertaken in Chapters 6, 7, 8 and 9 of this thesis demonstrate that a considerable decrease in the airflow velocity and its applicability for the purpose of natural ventilation occurs in urban areas. The assessment of two case studies based on actual urban areas corroborates this statement. In such scenarios, the analysis of the surrounding urban aspect ratios with and without future buildings was essential for the achievement of the final results.

10.2.1. The airflow speed and direction and ΔCp potential on urban areas

The research findings show that the airflow in low-density urban canyon areas such as, for instance, Museum Ave. in the Cardiff University Cathays Campus, decreases by from 45% to 50% when free airflow is at 3m/s. Further, the resulting ΔCp found ranges: from 0.00 to 0.10 for 0^o winds, from 0.10 to 0.25 for 45^o winds; and from 0.05 to up to 0.35 for 90^o winds.

10.2.2. The airflow speed and direction and ΔCp potential in high-density urban areas

With regard to the airflow patterns in high-rise building urban areas, such as the Paulista Avenue in São Paulo, it was found that[140]:

- For parallel winds, the decrease in airflow velocity magnitude ranges from 15% to 50% with local acceleration of up to 2x[141]. The resulting ΔCp ranges: from 0.00 to 0.10 at low, medium and top heights;
- For orthogonal winds, the decrease in airflow velocity magnitude ranges from 15% to 33% with local acceleration of up to 3x. The resulting ΔCp ranges: from 0.05 to 0.25, 0.10 to 0.35, and 0.30 to 0.60, respectively, at low, medium and top heights; and
- For oblique winds, the decrease in airflow velocity magnitude ranges from 15% to 66% with local acceleration of up to 3x. The resulting ΔCp ranges: from 0.10 to 0.35, 0.10 to 0.60, and 0.25 to 0.75, respectively, at low, medium and top heights.

10.2.2.1. Final considerations for winds at 0^o

For winds parallel to buildings and along canyons the ΔCp between right and left sides was found to be practically zero. In this case, architectonic ornaments such as wings, oblique faces or external blocks projecting outside create ΔCp by forcing airflow inwards at the high-pressure inlet and outwards at the low-pressure outlet. Cp results are greater in blocks of uneven height and also in square canyons, e.g. those with H/W= 1.0, than in narrower or wider ones. Further, channelling effects cause acceleration by a factor of up to 1.5x, which occurs from ground level up to 10m height on the canyon's central axis[142].

10.2.2.2. Final considerations for winds at 90^o

For winds orthogonal to buildings and across canyons the pressure differential between windward and leeward sides accompanied the expected sequence in decrease of ΔCp magnitude for wide, square, and narrow canyons. The ΔCp also increased with height, i.e., from ground level upwards. A clock-wise three-dimensional vortex across the canyon was fully developed in all three varieties of canyon. In the longest canyons, e.g., with L/H>3, the occurrence of two vortices from the centre to both sides was observed. For short canyons the spiral vortex tends to follow the same

[140] For further information see topics 9.3 and 9.4 in Chapter 9

[141] Wind velocity decrease based on the findings of the CFD simulations carried out in the steps 3 and 4 of the proposed method of research and based on a free airflow velocity of at 3m/s at 10m high related to the input ABL wind profile. See topic 5.6.1.2 in Chapter 5 for further information.

[142] For further details, see topic 7.3.7.1 in Chapter 7; and topic 9.5.1 in Chapter 9.

direction throughout the grid, forming a sinuous pattern. Wake interference in wide canyons, e.g. those with H/W ≥ 2.0, was clearly observed, while skimming flow for narrow canyons, e.g. with H/W ≤ 0.5 did limit the airflow within their cavities. Moreover, for large and well-defined urban canyons, the urban aspect ratio defined by the canyon's length and the roof area L/Aroof ≈ 1.2 was related to greater ΔCp, regardless of the other urban aspect ratios investigated[143].

10.2.2.3. Final considerations for winds at 45°

For winds oblique to buildings and across canyons a three-dimensional vortex forming a spiral diagonally across the canyon created a strong and well-defined sinuous pattern. After meeting the vertical windward edge the flow is divided into two and takes either a descending or ascending path according to its height towards the FS point (usually at around 4/5ths of the total height). Wind speed in the centre of the canyon was constant from ground level up to the canopy height ranging from 0.5 to 1.5 m/s, except near the walls, where the speed decelerated and ranged from 0.2 to 0.5m/s. In general, ΔCp between windward and leeward sides was found to be lower than those found for oblique winds, although the same urban aspect ratio defined by the canyon length and the roof area L/Aroof ≈ 1.2 was observed and related to greater ΔCp incidence as well, regardless of the other urban aspect ratios investigated[144].

10.3. The comparison between the results of the research methods

Of all the sets of experiments conducted in the WT, and by CFD and FM during the four steps of this investigation it may be affirmed that:

- The overall results show that the CFD pre-processing, solving and post-processing parameters adopted in the simulation sets were appropriate and did not interfere in the results;
- The Cp contour plots found in the CFD experimental sets were similar and comparable to those from WT physical experiments in Steps 1, 3 and 4 of the research method;
- WT and CFD Cp results for simulations with isolated bluff bodies, such as the two bricks and the CKY Tower, matched well on the windward, lateral and top sides. For these scenarios CFD Cp results were over-estimated on the leeward side, giving higher values than the WT results[145];
- For investigations with complex scenarios, such as the two urban area case studies, whose results contrasted with those of WT and CFD, it was

[143] For further information, see topic 7.3.7.2 in Chapter 7.
[144] For further information see topic 7.3.7.3 in Chapter 7.
[145] For further information see topics 3.5.3.10, 3.5.3.11 and 3.5.4 in Chapter 3.

observed that the Cp results from CFD showed either overall higher values or values within the same range on either one of the sides when contrasted with WT results. In the last analysis, both occurrences reflected a ΔCp range of results common to both the WT and the CFD experiments.

- This consistency in the ΔCp results for complex scenarios extends also to the urban prototype results, for which CFD experiments were carried out alone;
- Airflow field patterns around either isolated bluff bodies, such as the two bricks and the CKY Tower, or within urban areas, such as the urban Prototype Tower, showed close agreement between the WT (via helium bubble airflow visualization) and the CFD (by means of airflow velocity magnitude pathlines) sets of experiments;
- Airflow patterns and velocity magnitude found in the CFD sets of experiments for Case Study 1 matched well with the results observed in both the WT and the FM undertaken '*in locus*'; and
- Due to the successful triangulation of the research methods conducted for the case study just mentioned, Case Study 2 could be carried out by means of WT and CFD, since the results o both methods agreed well with the FM output data.

10.4. Theoretical discussion of the findings of the main objective

The main objective of this thesis is to investigate the relationship between the physical dimensions of urban areas and the resulting airflow patterns and wind speed and direction and pressure coefficients on buildings and/ or bocks' envelopes. In order to accomplish this objective a large number of simulations and experiments involving urban prototypes and two case studies were carried out using CFD, WT and FM.

10.4.1. Implications and contributions for the theory

A relationship was found between the urban aspect ratios and the ΔCp results in urban areas. This relationship was demonstrated by statistical methods using data on the variables concerned, thus verifying the strength of the correlation coefficient between them. A scale of significance for the assessment of the correlation coefficient strength between the urban aspect ratios was presented[146]. Strong correlation coefficients were found between the investigations into similar scenarios of the urban prototypes and the two case studies as regards both the aspect ratios and the ΔCp results. On the other hand, low correlation coefficients for the same variables were identified when contrasting dissimilar scenarios.

10.4.2. Potential for further contributions for the theory

Based on the information just quoted it may be affirmed that it is possible to create an empirical scale that permits the ΔCp results to be estimated on the basis of the urban physical dimensions' aspect ratios and a local source of data on wind speed and direction by using the method of research presented in this investigation. Although this empirical method needs further development and testing before being used as a practical tool, the relationship found between the various physical dimensions which characterize the urban environment in terms of its urban aspect ratios have proved to be related to the resultant ΔCp in buildings when associated with air flow data.

An empirical scale to provide a rule of thumb based on the urban aspect ratios and wind data for estimating ΔCp across buildings in urban environments and, therefore, estimating the potential of specific urban environments for naturally ventilate buildings would be helpful for architects, building engineers and urban planners. With such a tool, these professionals would be able to make decisions as to the potential of a specific building project for the application of natural ventilation strategies without having to engage in CFD and WT experiments in the initial stages of a project. These methods of experimentation are highly complex and specialized and not, therefore, available during the early stages of a project in architects' or engineers' offices.

[146] See Table 5.20 and topic 5.8.4 in Chapter 5.

10.5. Limitations of this study

Set out below are those subjects which are either beyond the scope of this research or are recognised as shortcomings characteristic of investigations related to this thesis's investigations, but which nevertheless deserve mention:

- Since external airflow is subject to various other parameters which are neither considered in the objectives proposed nor covered by the methods of analysis used, it is not the intention of this research to provide general guidelines for all the conceivable applications of this topic. Consequently, the possible practical applications which may be derived from this outcome lie exclusively within the scope defined by its methodology;
- Another limitation of the results achieved by this research lies in the fact that both wind velocity and direction change constantly in urban areas, and are thus unpredictable. Therefore, the results obtained, related to specific wind direction input are indicative of instantaneous modification of airflow speed and direction and wind pressures and do not constitute the complete picture;
- Although urban aspect ratios comparing two different areas can be correlated, trees, moving vehicles, and other urban barriers may cause a varying impact in terms of the final external airflow patterns, e.g. the wind speed and direction, thereby creating limitations in the application of the results of this investigation; and
- This research was limited to wind-driven forces only during the analysis of external airflow in urban environments, which means that isothermal conditions prevailed as regards all air and surface temperatures and buoyancy driven forces were not explored.

10.6. Future research in the field

As a continuation of the limitations of this study, several topics that call for investigation related to this subject may be listed, in decreasing order of importance:

- The need to carry out more urban prototype experiments based on the research method proposed and this investigation's results in order to provide sufficient information to build and validate an empirical scale and/ or mathematical model that can be employed in building projects;
- The need to carry out more urban prototype experiments covering wind directions other than 0^o, 45^o, and 90^o, such, e.g., as 22.5^o;
- The need to explore the sky-view factor (SVF) as a useful aspect ratio to estimate the potential for natural ventilation in urban areas; and

- The need to apply the methodology proposed in new case studies covering differing and contrasting actual urban scenarios, such as:
  - The Moroccan Medina of Fez, with its irregular and narrow lanes built in the course of centuries;
  - The 19th century Paris boulevard city planned by Haussmann;
  - The orthogonal superblocks of Brasilia, planned during the 1960s and which follows the precepts of Modern Architecture;
  - A high-density skyscraper urban area, such as that of Hong Kong;
  - The London 2012 Olympic Village facilities centre; and
  - A typical residential neighbourhood of blocks, for instance on the outskirts of Rio de Janeiro, which grew up haphazardly, without urban planning.

Table 10-1: Results of the research hypotheses and questions:

Research hypotheses and questions	Results	Find more
For urban areas where regional wind direction is known, can the resultant air flow below the urban canopy layer be associated with urban dimensional aspect ratios?	The assessment of the airflow field in two actual urban areas and a large number of urban prototype scenarios via WT and CFD simulations and FM with further contrast of results allowed a comprehensive understanding of the relationship between urban shapes and aspect ratios and the possible airflow pattern for a given wind direction.	Topics 7.1 to 7.9, 8.3 and 8.4, and 9.3 to 9.5.
Is it possible, by using the surrounding urban aspect ratio, to estimate ΔCp over the surface of the constructed envelope? If so, how accurately?	Taken together, several urban aspect ratios can provide the basis for an estimation of a range of Cp results to be found on external façades of urban buildings. Strong correlation coefficients (above 0.80) were found between urban prototype scenarios and the urban areas investigated in this thesis.	Topics 7.11, 8.5, and 9.6
Can the mapping of potential ΔCp on building façades assist in the design process of selecting strategies for wind-driven natural ventilation systems?	Knowing the Cp and the ΔCp distribution on a building or ventilation system surface for the prevailing wind directions is a key point in the design of natural ventilation systems and in defining strategies based on wind-driven forces, though buoyancy-driven forces should not be neglected or underestimated.	Topics 4.4. to 4.10.
With regard to high-rise buildings in urban areas, may it be expected that the choice of different ventilation strategies and façade elements based on the external pressure variation results should maximise the natural resources provided by the external micro-climate and increase the potential for natural ventilation systems?	The Paulista Ave. case study of an area located amidst high-rise urban buildings showed that pressure distribution in high-density urban areas may jeopardize ventilation strategies if the immediate built surrounding areas are no taken into account. The Tower Prototype investigation demonstrated alternatives to overcome drawbacks and propose solutions to achieve ΔCp levels that make the employment of double-sided cross ventilation in large, tall buildings in dense urban areas possible.	Topics 9.3, 9.4 and 9.5.
Is it possible to produce a rule-of-thumb based on urban dimensions to guide professionals in the design of new buildings which use natural ventilation systems effectively?	Although both case studies investigated in this thesis found a good correlation level with the urban prototypes that have the same aspect ratios and also resulted in similar ΔCp results, a scale or rule-of-thumb based on empirical data would require validation and more detailed testing before being implemented.	Topics 3.2, 3.4, .11, 8.5, and 9.6

Source: this study. .

10.7. Chapter conclusion

Chapter 10 presents the final conclusions of this thesis. A short description of the main findings on the topic ‘airflow in the urban environment’ and airflow patterns, wind velocity and ΔCp potential on urban areas is covered, specifically for wind incidence at 0^o, 45^o and 90^o. Further, discussions of the results of the research methods adopted in this investigation, their implications for and contributions to the theory, the limitations of this study and its potential for future research in the field are presented.

Finally, the findings of the various steps in the investigation of the subject of the potential harnessing of airflow in the urban environment, covering different methods of research and case studies, finally demonstrated a direct, close relationship between the urban scenarios’ physical dimensions and both airflow patterns and wind speed and direction and ΔCp results on the building envelopes.

10.8. Personal statement

The completion of this research project is more than just one more step in my academic and professional life. This has in fact been a personal enterprise that has changed my way of thinking, planning, appraising and understanding architecture, the urban environment, and life as a whole.

This pursuit started with the questionings of an undergraduate student of architecture and urban planning who was unable to find answers as to how to design buildings to be environmentally comfortable and sustainable. Further, I sought answers for the mismatch between the sub-tropical climate and ordinary architectonic solutions that practically oblige people to live and work in air-conditioned buildings.

All these questionings brought me to the WSA of Cardiff University, where I found the optimal intellectual and technical environment for the development of my research. Once more I need to thank the supervisor of this investigation, Professor Phil Jones, as also the WSA and the CRiBE lecturers and researchers who gave me their support. Without their know-how I would not have been be able to find the answers to my questions or to bring this thesis to a sactisfactory conclusion.

As an architect working in professional practice I have always sougt to attain the best for the end-users of the buildings and residences for whose design I have been responsible. In urban centres people spend most of their life indoors, and creating a good built environment directly affects people's health, safety, happiness and life quality diretctly. This is a great responsibility for us, architects and building technicians. I do hope this thesis will prove to be of as much value to my esteemed colleagues in both their professional practise and academic research as it has been for me.

References

A'zami, A. 2005. Badgir in traditional Iranian Architecture. In: *Proceedings of Passive and Low Energy Cooling for the Building Environment.* International conference. Santorini, May, pp. 1021-1026.

Ahmad, M. et al. 2005. Wind tunnel simulation studies on dispersion at urban street canyons and intersections – A review. *Journal of Wind Engineering and Industrial Aerodynamics* 93 (September), pp. 697-717.

Aristodemou, E. et al. 2009.A comparison of mesh-adaptive LES with wind tunnel data for past buildings: mean flows and velocity fluctuations. *Atmospheric Environment* 43, pp. 6238-6253.

Armitt, J. and Counihan, J. 1968. The simulation of the atmospheric boundary layer in a wind tunnel. *Atmospheric Environment* 2, pp. 49-71.

Arnfield, A. J. and Mills, G. 1994. An analysis of the circulation characteristics and energy budget of a dry, asymmetric, east, west urban canyon. I. Circulation characteristics. *International Journal of Climatology* 14, pp. 119-134.

ASHRAE. 2001. *2001 ASHRAE Handbook* – Fundamentals. American Society of Heating, Refrigerating and Air-Conditioning Engineers Handbook. Atlanta: ASHRAE.

Assimakopoulos, V. D. et al. 2006. Experimental validation of a computational fluid dynamics code to predict the wind speed in street canyons for passive cooling purposes. *Solar Energy* 80, pp. 423-434.

Awbi, H. B. 1998a. Calculation of convective heat transfer coefficients of room surfaces for natural convection. *Energy and Buildings* 28, pp. 219-227.

Awbi, H. B. 1998b. Chapter 7 – Ventilation. *Renewable and Sustainable Energy Reviews* 2, pp. 157-188.

Awbi, H. B. 1991. *Ventilation of Buildings*. London: E & FN Spon.

Awbi, H. B. 2003. *Ventilation of Buildings*. 2 ed. London: Spon Press.

Axley, J. W. 2006. Analytical methods and computing tools for ventilation. In: Santamouris, M. and Wouters, P. *Building Ventilation*: The State-of-the-Art. London: Earthscan, pp. 39-106.

Badran, A. A. 2003. Performance of cool towers under various climates in Jordan. *Energy and Buildings* 35, pp. 1031-1035.

Bady, M. et al. 2008.Towards the application of indoor ventilation efficiency indices to evaluate the air quality of urban areas. *Building and Environment* 42(12), pp. 1991-2004.

Bahadori, M. N. 1985. An improved design of wind towers for natural ventilation and passive cooling. *Solar Energy* 35(2), pp. 119-129.

Bansal, N. K. et al. 1993. Solar chimney for enhanced stack ventilation. *Building and Environment* 28(3), pp. 373-377.

Bansal, N. K. et al. 1994. A study of solar chimney assisted wind tower system for natural ventilation in buildings. *Building and Environment* 29(4), pp. 495-500.

Barnard, N. 2002. *Thermal mass and night ventilation – Utilising "hidden" thermal mass*. *International Journal of Ventilation* 1(2), pp. 81-90.

Barrow, M. 2009. *Statistics for economics, accounting and business studies 5th ed*. Essex: Pearson Education, p 475.

Bastos, L. E. G. and Barroso-Krause, C. 2008. Potential of natural ventilation in a tropical climate. *International Journal of Ventilation* 6(1), pp. 87-93.

Belarbi, R., et al. 2006. Modeling of water spray evaporation: application to passive cooling of buildings. Solar Energy 80, pp 1540-1552.

Beranek, W. J. and van Koten, H. 1979. Visual techniques for the determination of wind environment. *Journal of Wind Engineering and Industrial Aerodynamics* 4(3-4), pp. 295-306.

Bogo, A. et al. 1994. Bioclimatologia aplicada ao projeto de edificações visando o conforto térmico. *Relatório interno n^{o} 2/94*. Núcleo de Pesquisa em Construção, UFSC, Florianópolis [online]. Available at: http://www.labeee.ufsc.br/sites/default/files/publicacoes/relatorios_pesquisa/RP_Bioclimatologia.pdf. [Retrieved in: 01 September 2011].

Bouchair, A. 1994. Solar chimney for promoting cooling ventilation in Southern Algeria. *Building Services Engineers Research Technology* 15(2), pp. 81-93.

Bradley *et al*. 2001. A method to assess the variation of urban canyon geometry from Sky view factor transects. *Atmospheric Science Letters*. Doi: 10.1006/ asle.2001.0031. Pp. 261-272.

BS-EM-13779. 2005. *Ventilation for Non-Residential Buildings*. Performance Requirements for Ventilation and Room-Conditioning Systems. London: BSI.

Campbell M. J., and Swinscow T. D. V. 2009. *Statistics at square one*. US: Wiley-Blackwell, pp 119.

Caretto, L. S., et al. 1972. Two calculation procedures for steady, three-dimensional flows with recirculation. In: *Proceedings of the Third International Conference in Numerical Methods in Fluid Dynamics*. Paris, 3-7 July.

Chan, A. T. et al. 2003. Strategic guidelines for street canyon geometry to achieve sustainable street air quality — Part II: multiple canopies and canyons. *Atmospheric Environment* 37, pp. 2761–2772.

Chan, A. T. et al. 2001. Strategic guidelines for street canyon geometry to achieve sustainable street air quality. *Atmospheric Environment* 35, pp. 4089-4098.

Chandra, S. et al. 1986. *Cooling with Ventilation*. A Product of the Solar Technical Information Program Published by Solar Energy Research Institute, Operated for the U.S. Department of Energy. Cocoa, Florida: Florida Solar Energy Center.

Chang, P. C. et al. 1971. Turbulent diffusion in a city street. In: *Proceedings of the Symposium on Air Pollution and Turbulent Diffusion*. Las Cruces, New Mexico, 7-10 December, pp. 137-144.

Charles, K. E. 2003. Fanger's Thermal Comfort and Draught Models. National Research Council Canada- NRC. IRC-RR-162 [online]. Available at: http://www.nrc-cnrc.gc.ca/obj/irc/doc/pubs/rr/rr162/rr162.pdf [Retrieved in: 01 March 2009].

Cheng, Y. and Meroney R. N. (2003a). The effect of surroundings with different separation distances on surface pressures on low-rise buildigns. *Journal of Wind Engineering and Industrial Aerodynamics* 91, pp. 1039-1050.

Cheng, Y. and Meroney R. N. (2003b). Concentration and flow distributions in urban street canyon: wind tunnel and computational data. *Journal of Wind Engineering and Industrial Aerodynamics* 91, pp. 1141-1154.

Cheng, Y. et al. (2003). A comparison of LES with k-e RANS model for the prediction of a fully developed turbulent flow over a matrix of cubes. *Journal of Wind Engineering and Industrial Aerodynamics* 91, pp. 1301-1328.

Cheng, Y. et al. (2007). Flow over cube arrays of different packing densities. *Journal of Wind Engineering and Industrial Aerodynamics* 95, pp. 715-740.

Chegung, J. C. K. 1984. Effect of tall building edge configurations on local surface wind pressures. In: *3rd International Conference on Tall Buildings*. Hong Kong and Guangzhou, 10-15 December.

CIBSE A. 2006. *Environmental Design*: CIBSE Guide A. Chartered Institution of Building Services Engineers. 7 ed. London: CIBSE.

CIBSE AM 10. 2007. CIBSE Applications Manual 10: Natural Ventilation in Non Domestic Buildings. Chartered Institution of Building Services Engineers. London: CIBSE.

CIBSE B. 2005. Heating, Ventilating, Air Conditioning and Refrigeration: CIBSE Guide B [Editor, Ken Butcher]. Chartered Institution of Building Services Engineers. London: CIBSE.

CIBSE B1. 2002. *Heating:* CIBSE Guide B1. Chartered Institution of Building Services Engineers. London: CIBSE.

CIBSE B2. 2001. *Ventilation and Air Conditioning*: CIBSE Guide B2. Chartered Institution of Building Services Engineers. London: CIBSE.

CIBSE F. 2004. *Energy efficiency in Buildings*: CIBSE Guide F. Chartered Institution of Building Services Engineers. 2 ed. London: CIBSE.

Coleman, H. W. and Stern, F. 1997. Uncertainties in CFD code validation. ASME *Journal of Fluids Engineering* 119, pp. 795-803.

Cook, M. J. et al. 2003. CFD modelling of natural ventilation combined wind and buoyancy forces. *International Journal of Ventilation* 1(3), pp. 169-180.

Cook, N. J. 1985. *Designer's Guide to Wind Loading of Building Structures*. London: Butterworths.

Cook, N. J. 1977/1978. Determination of the model scale factor in wind-tunnel simulations of the adiabatic atmospheric boundary layer. *Journal of Industrial Aerodynamics* 2, pp. 311-321.

Costelloe, B. and Finn, D. 2003. Indirect evaporative cooling potential in air–water systems in temperate climates. *Energy and Buildings* 35, pp. 573-591.

Costelloe, B. and Finn, D. 2007. Thermal effectiveness characteristics of low approach indirect evaporative cooling systems in buildings. *Energy and Buildings* 39, pp. 1235-1243.

Costola, D. and Etheridge, D. W. 2008. Unsteady natural ventilation at model scale—Flow reversal and discharge coefficients of a short stack and an orifice. *Building and Environment* 43, pp. 1491–1506.

Croft, A. and Davison, R. 2010. *Foundation Maths*. 5 ed. Harlow, England: Pearson.

Cunningham, W. and Thompson, T. 1986. Passive cooling with natural draft cooling towers in combination with solar chimneys. In: *Proceedings of the Passive and Low Energy Architecture* PLEA`86. Pecs, Hungary, 1-5 September.

Dowdy, S. et al. 2004. Statistics for research, 3rd edition. New Jersey, John Wiley & Sons, Inc. Pp. 431.

Davidson, M. J. et al. 1996. Wind tunnel simulations of plume dispersion through groups of obstacles. *Atmospheric Environment* 30 (22), pp. 3715-3731.

De Dear, R. J. and Brager, G. S. 2002. Thermal comfort in naturally ventilated buildings: Revisions to ASHRAE Standard 55. *Energy and Buildings* 34, pp. 549-561.

De Faria, L. 2008. Airflow effects in urban canyons. In: *Research Student Conference Day*. The Welsh School of Architecture. Cardiff, 05 November.

De Faria, L. and Romero, M. 2005. Office buildings revitalization in the city of São Paulo. In: *CISBAT 2005* - Science Day. Ecole Polytechnique Federale de Lausanne. Lausanne, 28-29 September.

De Gids, W. 2002. Methods for vent sizing in the pre-design stage. Result of WG A2. IEA energy conservations in buildings and community systems programme. Buildings and construction research. *Technical Report 13* [online] May 2002. Available at: http://hybvent.civil.auc.dk/index.htm. [Retrieved in: 12 March 2011].

Deaves, D. M. 1981. Terrain-dependence of longitudinal rms velocities in the neutral atmosphere. *Journal of Wind Engineering and Industrial Aerodynamics* 8, pp. 259-274.

Deaves, D. M. and Harris, R. I. 1978. A mathematical model of the structure of strong winds. *CIRIA Report 76*. Construction Industry Research and Information Association.

Delsante, A. and Li, Y. 1999. Natural ventilation induces by combined wind and thermal forces in a two-zone building. In: *Proceedings of IEA Annex 35 Hybvent Forum*. Sydney, Australia, 28 September, pp. 181-190.

Delsante, A. and Vik, T. A. 2001. Hybrid ventilation: State-of-the-art review. International Energy Agency (IEA) – IEA-ECBCS Energy Conservation in Buildings and Community System, Annex 35 HybVent. *Hybrid Ventilation in New and Retrofitted Office Buildings*, pp. 1-135.

DePaul, F.S.C. 1986. Measurements of wind velocities in a street canyon, *Atmospheric Environment* 20, pp. 455–459.

DePaul, F. T. and Sheih, C. M. 1986. Measurements of wind velocities in a street canyon. *Atmospheric Environment* 20, pp. 445-459.

Di Sabatino, S. et al. 2007. Simulation of pollutant dispersion within idealised urban-type geometries with CFD and integral models. *Atmospheric Environment* 41, pp. 8316-8329.

Dixon, N. S. et al. 2006. Evaluation of a turbulent flow and dispersion model in a typical street canyon in York, UK. *Atmospheric Environment* 40, pp. 958–972

Eicker, U. et al. 2005. Passive and low energy cooling of office buildings. *International Journal of Ventilation* 4(3), pp. 203-214.

Elfatih, I. et al. 2003. Performance of porous evaporators for building cooling application. *Energy and Buildings* 35, pp. 941-949.

Elman, H. et al. 2005. *Finite Elements and Fast Iterative Solvers with Applications in Incompressible Fluid Dynamics*. Series Numerical Mathematics and Scientific Computation. Oxford: Oxford Science Publications.

Elmualim, A. A. et al. 1999. Evaluation of dichroic material for enhancing light pipe/natural ventilation and daylighting in an integrated system. *Applied Energy* 62, pp. 253-366.

Erell, E. 2007. Radiative cooling. In: Santamouris, M. ed. *Advances in Passive Cooling*. London: Earthscan, pp. 262-296.

Etheridge, D. W. 2000a. Unsteady flow effects due to fluctuating wind pressures in natural ventilation design - instantaneous flow rates. *Building and Environment* 35, pp. 321-337.

Etheridge, D. W. 2000b. Unsteady flow effects due to fluctuating wind pressures in natural ventilation design - mean flow rates. *Building and Environment* 35, pp. 111-133.

Etheridge, D. W. 2002. Nondimensional methods for natural ventilation design. *Building and Environment* 37, pp. 1057-1072.

Etheridge, D. W. 2004. Natural Ventilation through Large Openings - Measurements at Model Scale and Envelope Flow Theory. *International Journal of Ventilation* 2(4), pp. 325-342.

FANGER, P. O. 1972. Thermal Comfort: Analysis and Applications in Environmental Engineering. McGraw-Hill, NY.

Fanger, P. O. 1988. Air turbulence and the sensation of draught. *Energy and Buildings*, 12, pp21-30.

Fluent. 2005. *Fluent 6.2 User´s Guide*. Lebanon: Fluent Inc.

Franke, J et al. 2007. Best practice guideline for the CFD simulation of flows in the urban environment. COST Action 732, Quality Assurance and Improvement of Microscale Meteorological Models.

Frota, A. B. 1995. *Manual de Conforto Térmico*. São Paulo: Studio Nobel.

Gan, G. and Riffat, S. B. 1998. A numerical study of solar chimney for natural ventilation of buildings with heat recovery. *Applied Thermal Engineering* 18, pp. 1171-1187.

Gan, G. and Riffat, S. B. 1999. Numerical simulation of closed wet cooling towers for chilled ceiling systems. *Applied Thermal Engineering* 19, pp. 1279-1296.

Gan, G. et al. 2001. Application of CFD to closed-wet cooling towers. *Applied Thermal Engineering* 21(1), pp. 79-92.

Georgakis, Ch. and Santamouris, M. 2004. On the air flow in urban canyons for ventilation purposes. *The International Journal of Ventilation* 3(1), pp. 53-66.

Georgakis C. and Santamouris, M. 2005. Wind and Temperature in the Urban Environment. In: Ghiaus, C.; Allard, F. *Natural Ventilation in the Urban Environment: Assessment and Design*. URBVENT. London: Earthscan, pp. 81-102.

Germano, M. et al. 2005b. Natural ventilation potential of urban buildings. *International Journal of Ventilation* 4(1), pp. 49-56.

Germano, M. et al. 2005a. Natural Ventilation Potential. In: Ghiaus, C.; Allard, F. *Natural Ventilation in the Urban Environment: Assessment and Design*. URBVENT. London: Earthscan, pp. 195-227.

Geros, V. et al. 1999. Experimental evaluation of night ventilation phenomena. *Energy and Buildings* 29, pp. 141-154.

Geros, V. et al. 2005. On the cooling potential of night ventilation techniques in the urban environment. *Energy and Buildings* 37, pp. 243-257.

Ghiabaklou, Z. 2003. Thermal comfort prediction for a new passive cooling system. *Building and Environment* 38, pp. 883-891.

Ghiaus, C. et al. 2004. URBVENT Natural ventilation in urban areas. *Final Technical Report. Project N^{o} NNE4-2000-00238*. LEPTAB, Université de La Rochelle, France.

Ghiaus, C. and Allard, F. 2005. The physics of natural ventilation. In: Ghiaus, C.; Allard, F. *Natural Ventilation in the Urban Environment: Assessment and Design*. URBVENT. London: Earthscan, pp. 36-80.

Ghiaus, C. et al. 2005a. Outdoor-Indoor Pollutant Transfer. In: Ghiaus, C.; Allard, F. *Natural Ventilation in the Urban Environment: Assessment and Design*. URBVENT. London: Earthscan, pp. 125-135.

Ghiaus, C. et al. 2005b. Natural ventilation of urban buildings – Summary of URBVENT project. In: *International Conference Passive and Low Energy Cooling for the Built Environment*. Santorini, Greece, 19-21 May, pp. 29-33.

Ghiaus, C. and Roulet, C. 2005. Strategies for Natural Ventilation. In: Ghiaus, C.; Allard, F. *Natural Ventilation in the Urban Environment: Assessment and Design*. URBVENT. London: Earthscan, pp. 136-157.

Ghiaus, C. And Allard, F. 2006. Potential for free-cooling by ventilation. *Solar Energy,* 80, pp. 402-413.

Givoni, B. 1976. *Man, Climate and Architecture*. 2 ed. London: Applied Science Publishers.

Givoni, B. 1991. Impact of planted areas on urban environmental quality: A review. *Atmospheric Environment* 25B(3), pp. 289-299.

Givoni, B. 1993. Semiempirical model of a building with a passive evaporative cool tower. *Solar Energy* 50(5), pp. 425-434.

Givoni, B. 1994. *Passive and Low Energy Cooling of Building*s. New York: John Wiley & Sons.

Givoni, B. 1998a. *Climate Considerations in Building and Urban Design*. New York: Van Nostrand Reinhold.

Givoni, B. 1998b. Effectiveness of mass and night ventilation in lowering the indoor daytime temperatures. Part I: 1993 experimental periods. *Energy and Buildings* 28, pp. 25-32.

Gratia, E. and de Herde, A. 2007. Guidelines for improving natural daytime ventilation in an office building with a double-skin façade. *Solar Energy* 81(4), pp. 435-448.

Heikkinen et al. 2002. Performance simulation of hybrid ventilation concepts. International Energy Agency (IEA) – AIVC IEA-ECBCS Annex 35 HybVent. *Hybrid Ventilation in New and Retrofitted Office Buildings*: Technical report. pp. 1-47.

Heiselberg, P. 1999. The hybrid ventilation process: Theoretical and experimental work. International Energy Agency (IEA) – AIVC IEA-ECBCS Annex 35 HybVent. *Air Infiltration Review*: A quarterly Newsletter from the IEA Air Infiltration and Ventilation Centre 21(1). pp. 1-16.

Heiselberg, P. et al. 1999. Characteristics of air flow through windows. In: *The First International One day Forum on Natural and Hybrid Ventilation*. HybVent Forum 1999. Sydney, Australia, 28 September.

Heiselberg, P. 2002. *Principles of Hybrid Ventilation*. IEA, Annex 35, Hybrid Ventilation Centre, Aalborg Univerity.

Heiselberg, P. 2006. Hybrid Ventilation in Non-residential Buildings. In: Santamouris, M. and Wouters, P. *Building Ventilation*: The State-of-the-Art. London: Earthscan, pp. 191-216.

Heiselberg, P., and Tjelflaat, P. O., 1999. Design procedure for hybrid ventilation. In In: *The First International One day Forum on Natural and Hybrid Ventilation*. HybVent Forum 1999. Sydney, Australia, 28 September.

Heiselberg, P. and Sandberg, M. 2006. Evaluation of discharge coefficients for window openings in wind driven natural ventilation. *International Journal of Ventilation* 5(1), pp. 43-52.

Holmes, J. D. 2001. *Wind Loading of Structures*. New York: Spon Press.

Hoydysh, W. G. and Dabberdt, W. F. 1988. Kinematics and dispersion characteristics of flows in asymmetric street canyons. *Atmospheric Environment* 22, pp. 2677-2689.

Huang, Y.; JIN, M.; SUN, Y. (2007). Numerical studies on airflow and pollutant dispersion in urban street canyons formed by oblique roof buildings. *Journal of Hydrodynamics* 19(1), pp. 100-106.

Humphreys, M. A. and Nicol, J. F. 2002. The validity of ISO-PMV for predicting comfort votes in every-day thermal environments. *Energy and Buildings* 34(6), pp. 667-684.

Hunt, G. R. and Syrios, K. 2004. Roof-mounted ventilation towers-design criteria for enhanced buoyancy-driven ventilation. *International Journal of Ventilation* 3(3), pp. 193–208.

Hunter, L. J., Watson, I. D. and Johnson, G.T. (1991) Modelling air flow regimes in urban canyons. *Energy and Buildings* 15-16, pp. 315-324.

Jeong, Y. and Haghighat, F. 2002. Modelling of a hybrid-ventilated building – Using ESP-r. International Journal of Ventilation 1(2), pp. 127-140.

Jeong, S. and Andrews, M. 2002. Application of the k–e turbulence model to the high Reynolds number skimming flow field of an urban street canyon. *Atmospheric Environment* 36, pp. 1137–1145.

Ji, Y. et al. 2007. CFD modelling of natural displacement ventilation in an enclosure connected to an atrium. *Building and Environment* 42, pp. 1158-1172.

Jiang and Chen. 2004. Buoyancy-driven single-sided natural ventilation in buildings with large openings. *International Journal of Heat and Mass Transfer.* 46, pp. 973-988.

Johnson, G. T. and Hunter, L. L. 1998. Urban wind flows: Wind tunnel and numerical simulations — A preliminary comparison. *Environmental Modelling & Software* 13, pp. 279–286.

Johnson, G. T. and Hunter, L. J. 1999. Some insights into typical urban canyon airflows. *Atmospheric Environment* 33, pp. 3991-3999.

Jones, P. and Yeang, K. 1999. Use of the wind wing-wall as a device for low-energy passive comfort cooling in a high-rise tower in the warm-humid tropics. In: PLEA' 99-Sustaining the future: Energy-Ecology-Architecture. Brisbane, Australia, 22-24 September.

Jones, P. 2001. Ventilation and Air Conditioning. The Chartered Institution of Building Services, London.

Jones, P. J. et al. 2004. Pedestrian wind environment around high-rise residential buildings in Hong-kong. *Indoor and Built Environment.* 13, pp. 259-269.

Kastner-Klein, P. and Plate, E. J. 1999. Wind-tunnel study of concentration fields in street canyons. *Atmospheric Environment* 33, pp. 3973-3979.

Kastner-Klein, P., M. Ketzel, R. Berkowicz, E. Fedorovich, and R. Britter. 2003: The modelling of turbulence from traffic in urban dispersion models – Part II: Evaluation against laboratory and full-scale concentration measurements in street canyons. *Environmental Fluid Mechanics,* 3, pp. 145-172.

Kastner-Klein, P. and Rotarch, M. W. 2004: Mean flow and turbulence characteristics in an urban roughness sublayer. *Boundary-Layer Meteorology,* 111, pp. 55-84.

Keeping, M. and Shiers, D. E. 2004. *Sustainable Property Development*: A Guide to Real Estate and the Environment. Oxford: Blackwell.

Khan, N. et al. 2008. Performance testing and comparison of turbine ventilators. *Renewable Energy* 33, p. 2441-2447.

Koch-Nielsen, H. 2002. *Stay Cool*: A Design Guide for the Built Environment in Hot Climates. London: James & James.

Kolokotroni, M. and Santamouris, M. 2007. Ventilation for cooling. In: Santamouris, M. ed. *Advances in Passive Cooling.* London: Earthscan, pp. 140-189.

Kottegoda, T. N., and Rosso, R. 2009. Applied statistics for civil and environmental engineers 2nd ed. Oxford: Wiley-Blackwell, pp 736.

Kurabuchi, T. et al. 2004. Local dynamic similarity model of cross-ventilation. Part 1 – theoretical framework. *International Journal of Ventilation* 2(4), pp. 371-382.

Kurabuchi, T. et al. 2006. A study on the effects of porosity on discharge coefficients in cross-ventilation buildings based on wind tunnel experiments. *International Journal of Ventilation* 5(1), pp. 67-78.

Launder. B. E. and Spalding, D. B. 1976. *Mathematical Models of Turbulence*. London: Academic Press.

Levermore, G. J. 2002. Technical note: The exponential limit to the cooling of buildings by natural ventilation. *Building Services Engineering Research & Technology* 23(2), pp. 119-125.

Li. A. et al. 2003. 3DFLOW Development and validation for three cases- downward mixing, partition and displacement ventilation. *International Journal of Ventilation* 2(2), pp. 111-124.

Li, X-X. et al. 2005a. Impact of building configuration on air quality in street canyon. *Atmospheric Environment* 38(25), pp. 4519-4530.

Li, X-X. et al. 2005b. Development of a k-e model for the determination of air exchange rates for street canyons. *Atmospheric Environment* 39, pp. 7285-7296.

Li, X-X. et al. 2006. Recent progress in CFD modelling of wind field and pollutant transport in street canyons. *Atmospheric Environment* 40(29), pp. 5640-5658.

Li. D. H. W. et al. 2008. An analysis of luminous efficacies under the CIE standard skies. *Renewable Energy.* 33, pp. 2357-2365.

Liddament, M. W. 1996. *A Guide to Energy Efficient Ventilation.* AIVC. Coventry: Oscar Faber.

Liddament, M. et al. 2006. Achieving natural and hybrid ventilation in practice. *International Journal of Ventilation* 5(1), pp. 115-130.

Lien F. S. et al. 2004. Simulation of mean flow and turbulence over a 2D building array using high-resolution CFD and a distributed drag force approach. *Journal of Wind Engineering and Industrial Aerodynamics* 92, pp. 117-158.

Linden, P. F. and Kaye, N. B. 2006. Interacting turbulent plumes in a naturally ventilated enclosure. *International Journal of Ventilation* 4(4), pp. 301-310.

Lissen, J. M. S. et al. (2008). Flow pattern effects on night cooling ventilation. *International Journal of Ventilation* 6(1), pp. 21-30.

Liu, C.-H. et al. 2005. On the prediction of air and pollutant exchange rates in street canyons of different aspect ratios using large-eddy simulation. *Atmospheric Environment* 39, pp. 1567–1574.

MacDonald, A. J. 1975. *Wind Loading on Building*. London: Applied Science Publisher.

Martilli, A. et al. 2002. An urban surface exchange parameterisation for mesoscale models. *Boundary-Layer Meteorology* 104, pp. 261–304.

Masi, M. and Ochoa, A. *Il Vento. Climatizzazione Naturale degli Edifici e Impianti a Energia Pulita*. Roma: DEI Tipografia del Genio Civile.

Mathews, E. H. et al. 1994. Integrated simulation of buildings and evaporative cooling systems. *Building and Environment* 29(2), pp. 197-206.

McCartney, K. and Nicol, F. 2002. Developing an adaptive control algorithm for Europe. *Energy and Buildings* 34, pp. 623-635.Melaragno, M. G. 1982. Wind in Architectural and Environmental Design. New York: Van Nostrand Reinhold.

Meroney, R. N. et al. 1999. Wind-tunnel and numerical modelling of flow and dispersion about several building shapes. *Journal of Wind Engineering and Industrial Aerodynamics* 81, pp. 333-345.

Monteiro, C. A. F. and Mendonça, F. 2003. *Clima Urbano*. São Paulo: Contexto.

Nakamura, Y. Oke, T. R. 1988. Wind, temperature and stability conditions in an east-west oriented urban canyon. *Atmospheric Environment* 22(12), pp. 2691-2700.

Navon, R. and Arkin, H. 1994. Feasibility of direct- indirect evaporative cooling for residences, based on studies with a desert cooler. *Building and Environment* 29(3), pp. 393-399.

Nayak, J. K. et al. 1982. The relative performance of different approaches to the passive cooling of roofs. *Building and Environment* 17(2), pp. 145-161.

Nishizawa et al. 2008. A wind tunnel full-scale building model comparison between experimental and CFD results based on the standard k-e turbulence representation. *International Journal of Ventilation.* 2(4), pp. 419-430.

Ng, E. 2008. An investigation into parameters affecting an optimum ventilation design of high density cities. *International Journal of Ventilation.* 6(4), pp. 349-365.

Nozu, T. et al. 2008. LES of the flow and building wall pressures in the center of Tokyo. *Journal of Wind Engineering and Industrial Aerodynamics* 96, pp. 1762–1773.

Ohba, M. et al. 2006. Experimental study on predicting wind-driven cross-ventilation flow rates and discharge coefficients based on the local dynamic similarity model. *International Journal of Ventilation* 5(1), pp. 105-114.

Oliveira, J. T. et al. 2009. Estimation of passive cooling efficiency for environmental design in Brazil. Energy and *Buildings.* 41, pp. 809-813.

Oliveira, A. P. et al. 2002. Annual and diurnal wind patterns in the city of São Paulo. *Atmospheric Environment* 39, pp. 04-15.

Oke, T. R. 1978. *Boundary Layer Climates*. London: Methuen & Co.

Oke, T. R. 1988. Street design and urban canopy layer climate. *Energy and Buildings* 11, pp. 103-113.

Oke, T. R. 1973. City size and the urban heat island. *Atmospheric Environment* 7(8), pp. 769-779.

Olgyay, V. 1963. *Design with Climate*. Princeton: Princeton University Press.

Olgyay, V. 1973. *Design with Climate*. Bioclimatic Approach to Architectural Regionalism. New Jersey: Princeton University Press.

Paiva, C. 2003. Para ver a Avenida. Fachada inclinada sobre a Avenida Paulista. Edifício CYK, São Paulo-SP. *Finestra* 34.

Parker, J. and Teekaram, A. 2005. BSRIA BG 2/2005: Wind-Driven Natural Ventilation Systems. Bracknell: BSRIA.

Pearlmutter, D. et al. 1996. Refining the use of evaporation in an experimental down-draft cool tower. *Energy and Buildings* 23, pp. 191-197.

Plate, E. J. 1999. Methods of investigating urban wind fields-physical models. *Atmospheric Environment* 33, pp. 3981-3989.

Plate, E. and Kiefer, H. 2001. Wind loads in urban areas. *Journal of Wind Engineering and Industrial Aerodynamics* 89, pp. 1233–1256.

Pollet, I. and Renson, P. 2008. Nightcooling - Practical experiences in offices and the need for standard implementation into energy performance legislation. *International Journal of Ventilation* 6(4), pp. 359-366.

Riffat, S. B. and Zhu, J. 2004. Mathematical model of indirect evaporative cooler using porous ceramic and heat pipe. *Applied Thermal Engineering* 24, pp. 457-470.

Romero, M. and De Faria, L. 2004. Energy consumption potential of office buildings in the city of São Paulo. In: *XXI PLEA* - International Conference Passive and Low

Energy Architecture - Built Environment and Environmental Buildings. Eindhoven, Netherlands, 19-22 September.

Rotarch, M. W. 1995. Profiles of turbulence statistics In and above an urban street canyon. *Atmospheric Environment* 29(13), pp. 1473-1486.

Roulet, C. 2005. The role of ventilation. In: Ghiaus, C.; Allard, F. *Natural Ventilation in the Urban Environment: Assessment and Design*. URBVENT. London: Earthscan, pp. 20-35.

Sandberg, M. 2004. An alternative view on the theory of cross-ventilation. International *Journal of Ventilation* 2(4), pp. 409-418.

Santamouris, M. et al. 1996. On the efficiency of night ventilation techniques for thermostatically controlled buildings. *Solar Energy* 56(6), pp. 479-483.

Santamouris, M. et al. 1997. On the coupling of thermostatically controlled buildings with ground and night ventilation passive dissipation techniques. *Solar Energy* 60(3/4), pp. 191-197.

Santamouris M, et. Al. 1999. Thermal and airflow characteristics in a deep pedestrian canyon under hot weather conditions. *Atmospheric Environment.* 33, pp. 4503-4521.

Santamouris, M. 2005. Energy in the Urban Built Environment: the role of Natural Ventilation. In: Ghiaus, C.; Allard, F. *Natural Ventilation in the Urban Environment: Assessment and Design*. URBVENT. London: Earthscan, pp. 1-19.

Santamouris, M. 2006a. Special issue of the solar energy program devoted to natural ventilation in urban areas. *Solar Energy* 80, pp. 369-370.

Santamouris, M. 2006b. Ventilation for Comfort and Cooling: the State of the Art. In: Santamouris, M. and Wouters, P. *Building Ventilation*: The State-of-the-Art. London: Earthscan, pp. 217-246.

Schild, P. 2006. Heat Recovery. In: Santamouris, M. and Wouters, P. *Building Ventilation*: The State-of-the-Art. London: Earthscan, pp. 177-190.

Senthooran, S. et al. 2004. A computational model to calculate the flow-induced pressure fluctuations on buildings. *Journal of Wind Engineering and Industrial Aerodynamics* 92, pp. 1131–1145.

Sherman, M. H. and Chan, W. R. 2006. Building Air Tightness: Research and Practice. In: Santamouris, M. and Wouters, P. *Building Ventilation*: The State-of-the-Art. London: Earthscan, pp. 137-162.

Shi, R. F. et al. 2008. Large eddy simulation of wind field and plume dispersion in building array. *Atmospheric Environment* 42, pp. 1083–1097.

Sini, J.-F. et al. 1996. Pollutant dispersion and thermal effects in urban street canyons. *Atmospheric Environment* 30, pp. 2659–2677.

Syrios, K and Hunt, G. R. 2008. Urban canyon influence on building natural ventilation. *International Journal of Ventilation* 6 (1), pp. 43-49.

Sodha, M. S. et al. 1986. Thermal performance of an evaporatively cooled multi-storey building. *Building and Environment* 21(2), pp. 71-79.

Summers, D. M. et al. 1986. Validation of a computer simulation of wind flow over a building model. *Building and Environment* 21(2), pp. 97-111.

Sun et al. 2008. Experimental and CFD study of ventilation flow rate of a Monodraught^{TM} windcatcher. *Energy and Buildings,* 40, pp. 1110-1116.

Tarifa, J. R. and Azevedo, T. R. 2001. *Os Climas na Cidade de São Paulo*: Teoria e Prática. 4 ed. São Paulo: GEOUSP – Coleção Novos Caminhos.

Tiwari, G. N. et al. 1994. A comparison of passive cooling techniques. *Building and Environment* 29(1), pp. 21-31.

The Lancet. 18th of September, 1880. Hall's patent ventilator and chimney-cowl. Reviews- New Inventions- Analytical Records, pp. 462.

Cunningham, W. and Thompson, T. 1986. Passive cooling with natural draft cooling towers in combination with solar chimneys. In: *Proceedings of the Passive and Low Energy Architecture* PLEA`86. Pecs, Hungary, 1-5 September.

Tominaga, Y. et al. 2008. Comparison of various k-e models and LES applied to flow around a high-rise building model with 1:1:2 shape placed within the surface boundary layer. *Journal of Wind Engineering and Industrial Aerodynamics* 96, pp. 389-411.

Twinn, C. 1997. Specifying environmental conditions for naturally ventilated buildings – A consultants view. In: Clements-Croome, D. *Naturally Ventilated Buildings.* Buildings for the Senses, the Economy and Society. London: E & FN Spon, pp. 151-164.

Uehara, K. et al. 2000. Wind tunnel experiments on how thermal stratification affects flow in and above urban street canyons. *Atmospheric Environment* 34, pp. 1553-1562.

Vardoulakis, B. et al. 2003. Modelling air quality in street canyons: a review. *Atmospheric Environment* 37 (2), pp. 155-182.

Wagner, A. et al. 2008. Monitoring Results of a Naturally Ventilated and Passively Cooled Office Building in Frankfurt, Germany. *International Journal of Ventilation*. 6 (1), pp 3-20.

Walton, A. and Cheng, Y. 2002. LES of pollution dispersion in an urban street canyon - Part II. Idealised canyon simulation. *Atmospheric Environment* 36, pp. 3615-3627.

Wang, J.-S. and Huang, Z. 2006. Numerical study on flow and dispersion in urban street canyons of asymmetrical configurations. *Journal of Hydrodynamics* 18(3) Ser. B, Supplement 1, pp. 146-150.

Wang, J.-S., Zhao, B-Q.; Chun, Y. E. (2006). Optimizing layout of urban street canyon using numerical simulation coupling with mathematical optimization. *Journal of Hydrodynamics* 18(3), pp. 345-351.

Warner, R. M. 2008. *Applied Statistics*: From Bivariate Through Multivariate Techniques. Los Angeles: Sage.

Wedding, J. B. et al. 1977. A wind tunnel study of gaseous pollutants in city street canyons. *Journal of Air Pollution Control Association* 27, pp. 557-566.

Wilson, M. and Nicol, F. 2005. Noise Level and Natural Ventilation Potential in Street Canyons. In: Ghiaus, C.; Allard, F. *Natural Ventilation in the Urban Environment: Assessment and Design*. URBVENT. London: Earthscan, pp. 103-124.

Wouters, P., N. Heijmans, C. Delmotte, and L. Vandaele. 1999. Classification of hybrid ventilation concepts. In: *The First International One day Forum on Natural and Hybrid Ventilation*. HybVent Forum 1999. Sydney, Australia, 28 September.

Wouters, P. et al. 2006. Ventilation standards and regulations. In: Santamouris, M. and Wouters, P. *Building Ventilation*: The State-of-the-Art. London: Earthscan, pp. 281-297.

Yamartino, R. J. and Wiegang, G. 1986. Development and evaluation of simple models for the flow, turbulence and pollutant concentration fields whitin an urban street canyon. *Atmospheric Environment* 20(11), pp. 2137-2156.

Yassin, M. F. et al. 2008. Impact of street intersections on air quality in an urban environment. *Atmospheric Environment* 42(20), pp. 4948-4963.

Yeang, K. 1996. *The Skyscraper Bioclimatically Considered*: a Design Pimer. London: Academy Editions.

Zuo, W. and Chen, Q. 2007b. Validation of fast fluid dynamics for room airflow. In: *Proceedings of the 10th International IBPSA Conference* (Building Simulation 2007). Beijing, China, 3-6 September, pp. 980-983.

Zuo, W. and Chen, Q. 2007a. Real time airflow simulation in buildings. In: *Proceedings of the 6th International Indoor Air Quality, Ventilation and Energy Conservation in Buildings Conference* (IAQVEC 2007), Vol. 2. Sendai, Japan, 28-31 October, pp. 459-466.

Zuo, W. and Chen, Q. 2008. Real-time airflow simulation in buildings by using graphic processing units. In: *Abstracts of the 1st International Conference on Energy and Environment* (COBEE 2008), T11-01. Dalian, China, 4-6 August, p. 274.

Appendix 1: The Brazilian Macro-Scale Wind System

Large atmospheric scales (synoptic and general planetary) defines the major wind distribution over the seasons for the Brazilian territory (Bastos and Barroso-Krause, 2008), but presenting regional phenomenon's variations due to topography. Other local factors, such as site roughness, urbanization, vegetation and water masses, are responsible for micro-scale wind variations through the day. Due to the scarcity of wind data in most of the Brazilian cities suitable for the architectural practice, Bastos creates a map plotting the potential yearly average wind zoning for each region. This map was based on wind data produced by the government agencies to assess the wind power potential through the country, which comprised hourly annual data for average wind speed and direction identified at fifty meters height plus information about terrain roughness. This information was combined in order to produce a potential range of wind velocity at 1.5m and 6m height for each of the seventeen regional sub-divisions of the country defined by this researcher. His findings overlaps the official bioclimatic zoning map defined by the Brazilian Standards "Norm NBR 15220-3" (ABNT, 2005), which has a poor distinction between the wind description for coast and country-side.

Table 1 Potential range of wind velocity for regional Brazilian housing

Region	Region portion	Prevailing wind direction:	Wind velocity range (m/s)			Terrain roughness
			at 1.5m	at 6.0m	at 50.0m	
Western and Central Amazon Basin	V1 General	E	< 0.53	< 1.7	< 3.5	0.8
	V1' North	E – NE	2.2 – 3.3	3.7 – 5.5	6.0 – 9.0	0.2
Eastern Amazon Basin	V2 General	E – NE	< 0.8	< 1.9	< 3.5	0.5
	V2' Hills	E – SE	1.8 – 2.0	4.0 – 5.0	7.5 – 9.0	0.5
North-Northeaster Atlantic Coast	V3 North	E	1.4 – 2.0	4.2 – 6.3	5.0 – 7.5	0.4
	V3' South	E	2.6 – 3.9	4.4 – 6.6	6.0 – 9.0	0.2
Northeaster-Southeaster Coast	V4 Rio (RJ)	E – SE	-	< 1.4	3.5 – 4.0	0.3
	V4' Hills	S	< 0.67	< 3.0	~ 6.5	1.0
	V4'' North	E	2.5 – 2.9	4.7 – 5.3	8.0 – 9.0	0.3
	V4''' NE (RJ), S (ES)	E	3.1 – 4.7	4.2 – 6.0	3.5 – 6.0	-
Northeaster-Southeaster Hills	V5 General	-	1.5 – 2.0	3.1 – 4.2	5.5 – 7.7	0.4
	V5' Central and South	-	1.6 – 2.0	3.6 – 4.5	6.5 – 8.5	0.4
Central Plateau Region	V6 North	E – SE	1.1 – 1.5	1.8 – 2.5	3.5 – 4.0	0.2
	V6' South	E – SE	1.8 – 2.2	3.1 – 3.7	5.0 – 6.0	0.2
Southern Plateau Region	V7 General	SE	1.4 – 1.7	3.0 – 3.6	5.5 – 6.6	0.45
	V7' Hills	SE	1.8 – 2.0	3.8 – 4.4	7.0 – 8.0	0.45
	V7'' Coast	E – NE	> 3.0	> 4.6	> 7.0	0.1

Source: Bastos and Barroso-Krause, 2008.

Appendix 2: Buildings and Natural Ventilation

Figure 1: Check-list for decision making regarding natural, hybrid or mechanical ventilation systems

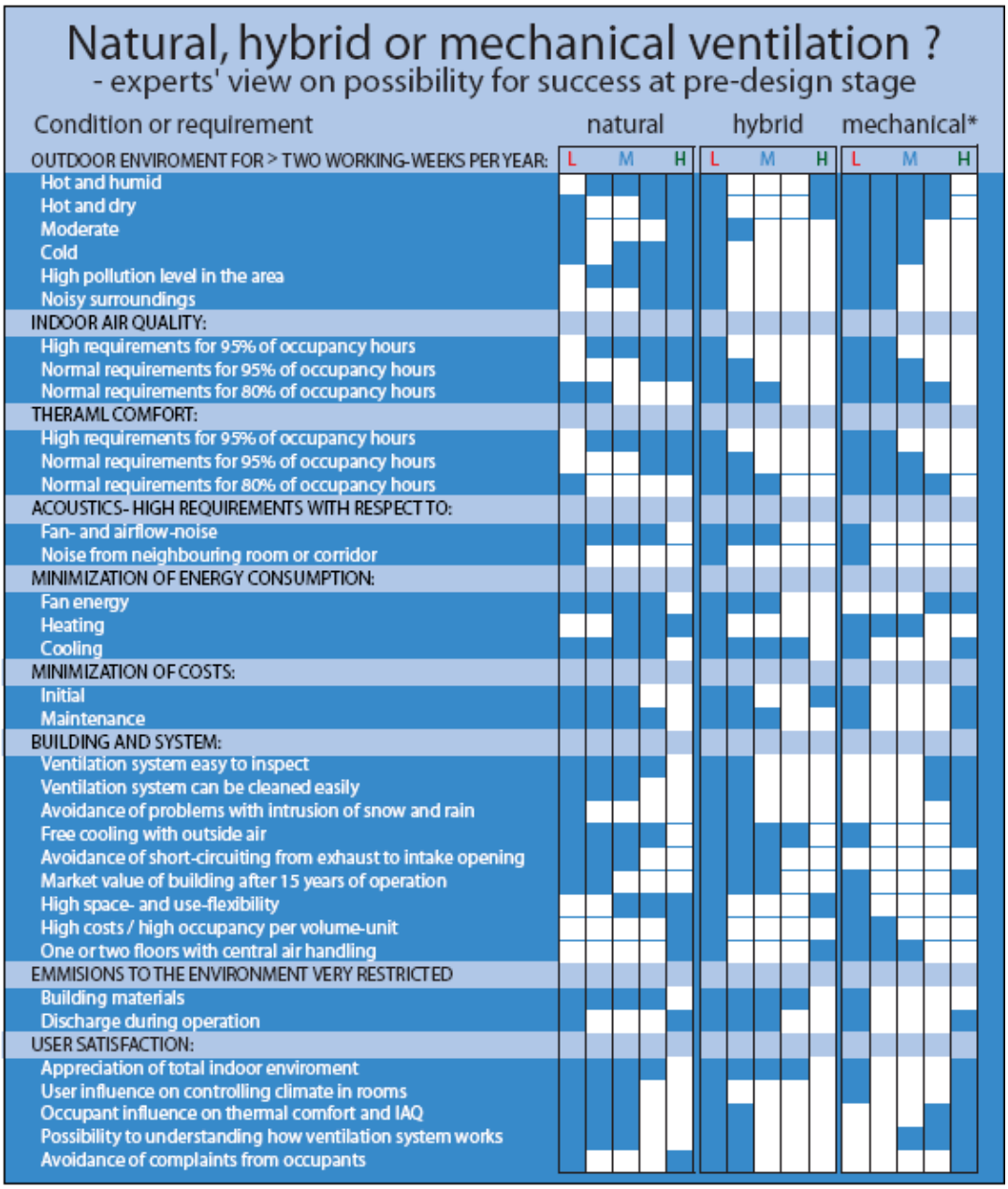

Source: Heiselberg (2002, 29).

Figure 2: Recommendation and limitation check-list for natural ventilation systems

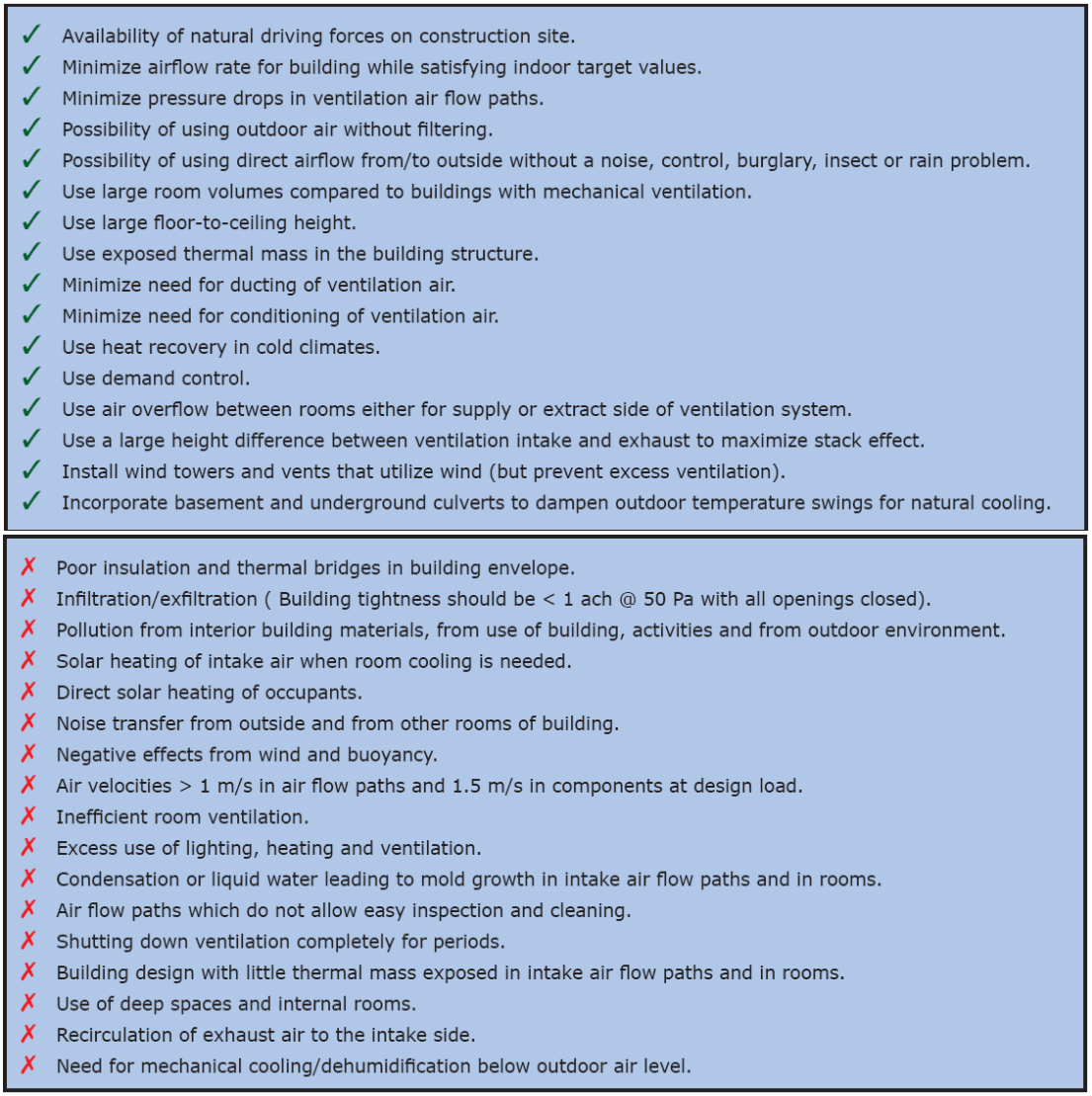

Source: Heiselberg (2002, 10).

Appendix 3: Output Standard Deviation for all sets of experiment carried out in the wind tunnel

Table 1: Output Standard Deviation from all sets of experiment carried out in wind tunnel

	wind	n° of	AVG
	angles	experiments	SDEV
Two bricks test	3	12	1,9%
Law School	3	16	0,3%
Paulista Ave. CKY Tower- isolated	3	9	1,0%
Paulista Ave. CKY Tower- urban	3	24	0,5%
Paulista Ave. Prot. Tower Shaft 'A'- isolated	3	4	0,9%
Paulista Ave. Prot. Tower Shaft 'B'- isolated	3	4	1,0%
Paulista Ave. Prot. Tower Shaft 'A'- urban	3	8	0,5%
Paulista Ave. Prot. Tower Shaft 'B'- urban	3	8	0,5%
Total AVG SDEV from the WT simulations >			**0,8%**

Source: This study.

Table 2: Output SDEV from the two bricks experiments carried out in WT

H/W	wind	SDEV	SDEV
ratio	angle	round 1-5	round 6-10
2,00	0°	1,1%	1,2%
2,00	45°	1,4%	1,6%
2,00	90°	1,5%	1,5%
1,00	0°	1,3%	1,4%
1,00	45°	1,8%	1,4%
1,00	90°	2,4%	1,7%
0,50	0°	1,7%	1,7%
0,50	45°	2,1%	2,0%
0,50	90°	2,5%	4,7%
0,66	0°	1,3%	1,3%
0,66	45°	1,9%	1,8%
0,66	90°	2,3%	4,7%
Total AVG SDEV from the WT simulations >		**1,8%**	**2,1%**

Source: This study.

Table 3: Output SDEV from the Cathays Campus experiments carried out in WT

Cathays Campus	wind	wind	
Law School	incidence	angle	SDEV
Museum Ave.	N	45°	0,2%
Park Place	N	90°	0,3%
Museum Ave.	NE	90°	0,2%
Park Place	NE	45°	0,3%
Museum Ave.	E	45°	0,2%
Park Place	E	0°	0,2%
Museum Ave.	SE	0°	0,2%
Park Place	SE	45°	0,2%
Museum Ave.	S	45°	0,7%
Park Place	S	90°	0,3%
Museum Ave.	SW	90°	0,4%
Park Place	SW	45°	0,3%
Museum Ave.	W	45°	0,3%
Park Place	W	0°	0,2%
Museum Ave.	NW	0°	0,3%
Park Place	NW	45°	0,3%
Total AVG SDEV from the WT simulations >			**1,8%**

Source: This study

Table 4: Output SDEV from the CKY Tower in isolation experiment carried out in WT

Paulista				SDEV	
CKY Tower	wind	wind		height	
Isolated	incidence	angle	low	middle	top
flat surf.		0°	0,7%	0,6%	0,6%
H panels		0°	0,8%	0,8%	0,8%
V panels		0°	0,7%	0,7%	1,1%
flat surf.		90°	1,7%	1,4%	1,8%
H panels		90°	1,1%	1,1%	1,0%
V panels		90°	0,9%	0,8%	1,5%
flat surf.		45°	1,1%	0,7%	1,0%
H panels		45°	0,9%	0,9%	0,8%
V panels		45°	0,9%	0,7%	0,8%
			1,0%	**0,9%**	**1,0%**
Total AVG SDEV from the WT simulations >				***1,0%***	

Source: This study

Table 5: Output SDEV from the CKY Tower in the urban environment experiment carried out in WT

Paulista CKY Tower	wind	wind		height	
Urban	incidence	angle	low	middle	top
flat surf.	N	45°	0,4%	0,4%	0,5%
H panels	N	45°	0,4%	0,3%	0,6%
V panels	N	45°	0,4%	0,4%	0,5%
flat surf.	NE	0°	0,3%	0,3%	0,3%
H panels	NE	0°	0,3%	0,3%	0,4%
V panels	NE	0°	0,3%	0,3%	0,3%
flat surf.	E	45°	0,4%	0,5%	0,6%
H panels	E	45°	0,4%	0,4%	0,6%
V panels	E	45°	0,4%	0,3%	0,5%
flat surf.	SE	90°	0,6%	0,5%	0,8%
H panels	SE	90°	0,5%	0,3%	0,6%
V panels	SE	90°	0,4%	0,4%	0,6%
flat surf.	S	45°	0,9%	0,6%	0,9%
H panels	S	45°	0,6%	0,6%	0,7%
V panels	S	45°	0,7%	0,6%	0,9%
flat surf.	SW	0°	0,7%	0,4%	0,7%
H panels	SW	0°	0,5%	0,3%	0,7%
V panels	SW	0°	0,4%	0,4%	0,4%
flat surf.	W	45°	0,8%	0,6%	0,8%
H panels	W	45°	0,8%	0,5%	0,6%
V panels	W	45°	0,5%	0,5%	0,6%
flat surf.	NW	90°	0,5%	0,4%	0,3%
H panels	NW	90°	0,4%	0,4%	0,5%
V panels	NW	90°	0,4%	0,3%	0,6%
			0,5%	**0,4%**	**0,6%**
Total AVG SDEV from the WT simulations >				***0,5%***	

Source: This study

Table 6: Output SDEV from the Prototype Tower in isolation (Shaft A) experiment carried out in WT

Paulista			SDEV		
Prototype		side 01	side 01	side 02	side 02
Tower	wind	top cowl &	external	top cowl &	external
Isolated	angle	int face	face	int face	face
Shaft 'A'	0^o	1,3%	1,5%	1,2%	1,0%
Shaft 'A'	45^o	1,0%	1,0%	0,7%	0,5%
Shaft 'A'	67.5^o	1,4%	1,0%	0,5%	0,5%
Shaft 'A'	90^o	1,4%	0,8%	0,6%	0,4%
		1,3%	**1,1%**	**0,8%**	**0,6%**
Total AVG SDEV from the WT simulations >			***0,9%***		

Source: This study

Table 7: Output SDEV from the Prototype Tower in isolation (Shaft B) experiment carried out in WT

Paulista			SDEV		
Prototype		side 01	side 01	side 02	side 02
Tower	wind	top cowl &	external	top cowl &	external
Isolated	angle	int face	face	int face	face
Shaft 'B'	0^o	0,8%	1,5%	1,0%	1,1%
Shaft 'B'	45^o	0,9%	1,3%	0,6%	0,6%
Shaft 'B'	67.5^o	1,7%	1,0%	0,8%	0,7%
Shaft 'B'	90^o	1,8%	1,1%	0,8%	0,6%
		1,3%	**1,2%**	**0,8%**	**0,8%**
Total AVG SDEV from the WT simulations >			***1,0%***		

Source: This study

Table 8: Output SDEV from the Prototype Tower in the urban environment (Shaft A) experiment carried out in WT

Paulista				SDEV		
Prototype			side 01	side 01	side 02	side 02
Tower	wind	wind	top cowl &	external	top cowl &	external
Urban	incidence	angle	int face	face	int face	face
Shaft 'A'	N	45°	0,5%	0,2%	0,5%	0,5%
Shaft 'A'	NE	0°	0,6%	0,2%	0,4%	0,2%
Shaft 'A'	E	45°	0,7%	0,5%	0,6%	0,4%
Shaft 'A'	SE	90°	0,3%	0,3%	1,0%	0,4%
Shaft 'A'	S	45°	0,5%	0,6%	1,1%	0,6%
Shaft 'A'	SW	0°	0,6%	0,6%	0,6%	0,5%
Shaft 'A'	W	45°	0,6%	0,4%	0,6%	0,5%
Shaft 'A'	NW	90°	1,0%	0,4%	0,3%	0,3%
			0,6%	**0,4%**	**0,6%**	**0,4%**
Total AVG SDEV from the WT simulations >				***0,5%***		

Source: This study

Table 9: Output SDEV from the Prototype Tower in the urban environment (Shaft B) experiment carried out in WT:

Paulista				SDEV		
Prototype			side 01	side 01	side 02	side 02
Tower	wind	wind	top cowl &	external	top cowl &	external
Shaft 'B'	N	45°	0,4%	0,4%	0,4%	0,5%
Shaft 'B'	NE	0°	0,3%	0,4%	0,3%	0,4%
Shaft 'B'	E	45°	0,7%	0,5%	0,4%	0,5%
Shaft 'B'	SE	90°	0,4%	0,3%	1,4%	0,8%
Shaft 'B'	S	45°	0,5%	0,5%	0,9%	1,2%
Shaft 'B'	SW	0°	0,6%	0,5%	0,5%	0,8%
Shaft 'B'	W	45°	0,5%	0,4%	0,5%	0,5%
Shaft 'B'	NW	90°	0,4%	0,4%	0,3%	0,4%
			0,5%	**0,4%**	**0,6%**	**0,6%**
Total AVG SDEV from the WT simulations >				***0,5%***		

Source: This study

Appendix 4: Urban Prototypes graphs and tables

In Appendix 4 the CP and ΔCp graphs and tables which support the analysis of Chapter 7: 'Urban Prototypes: Results and Analysis' are presented. These data cover in details the output from all the CFD simulations carried out for the six groups of the urban prototypes and for each simulated wind direction (0^o, 45^o, and 90^o).

Figure 1: A1 scenario Cp results for parallel, orthogonal and oblique winds (H/W= 0.50; 0°, 45°, 90°)

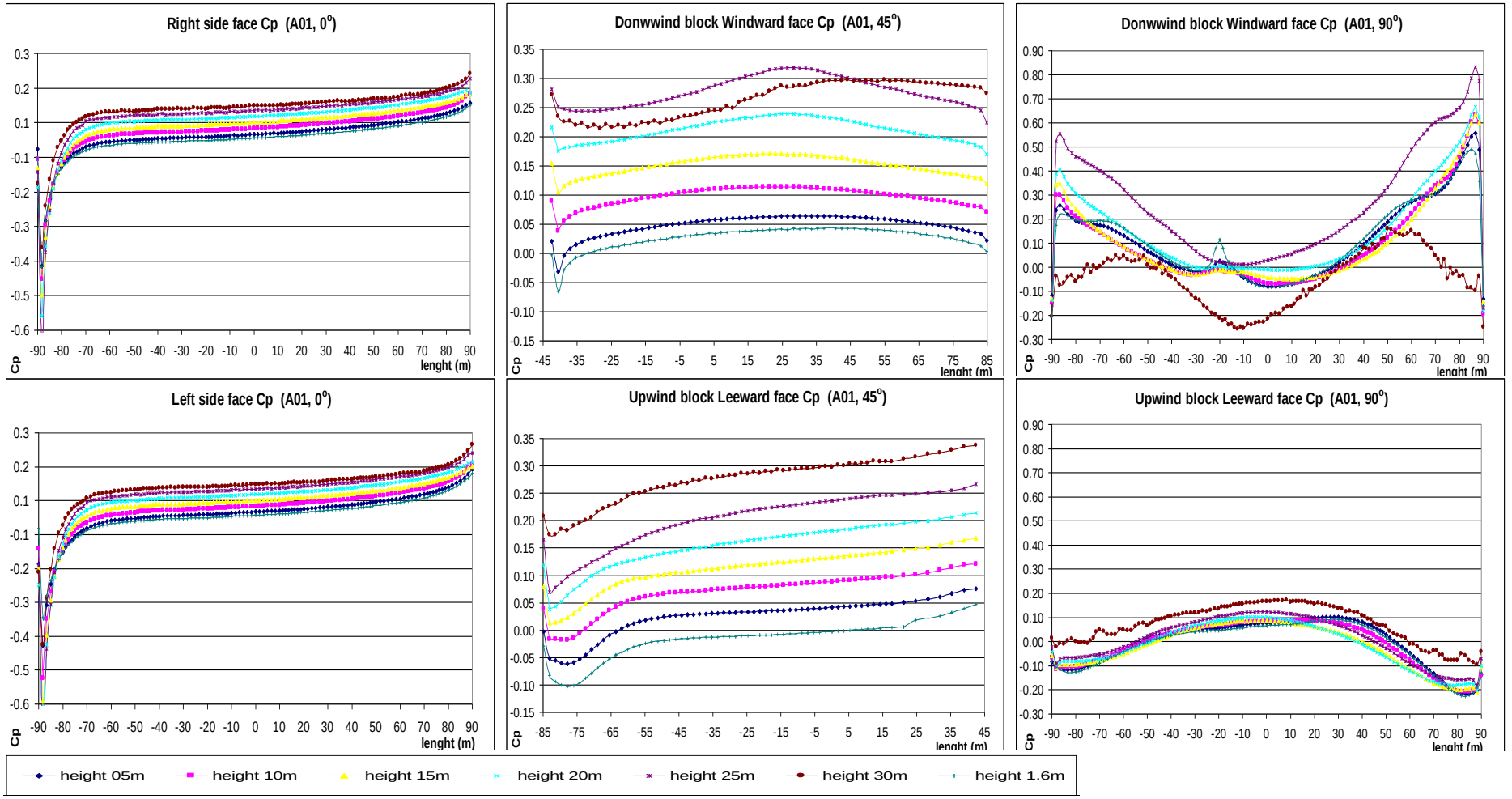

Source: this study.

Figure 2: B1 scenario Cp results for parallel, orthogonal and oblique winds (H/W= 1.00; 0°, 45°, 90°)

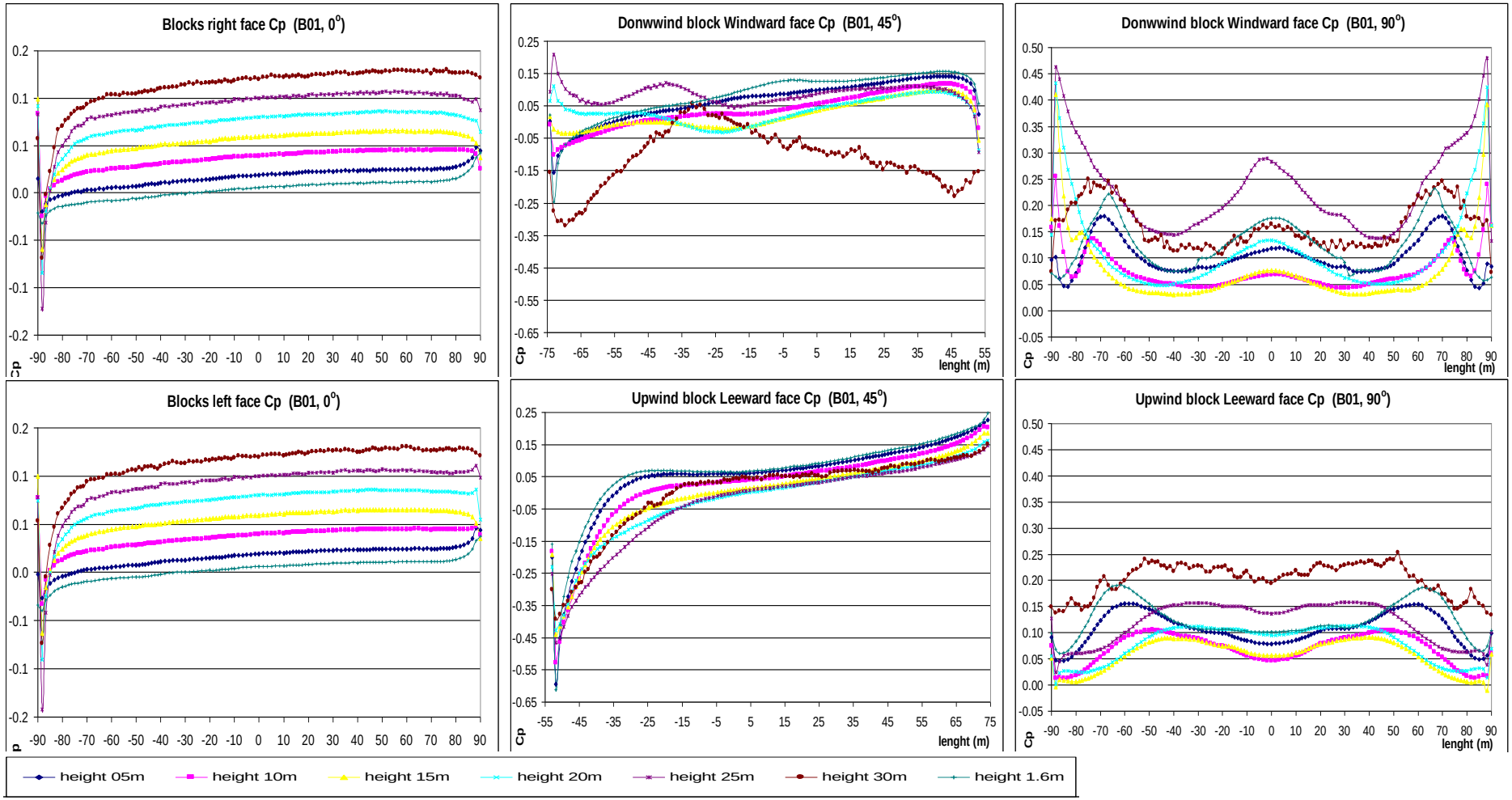

Source: this study.

Figure 3: C1 scenario Cp results for parallel, orthogonal and oblique winds (H/W= 2.00; 0°, 45°, 90°)

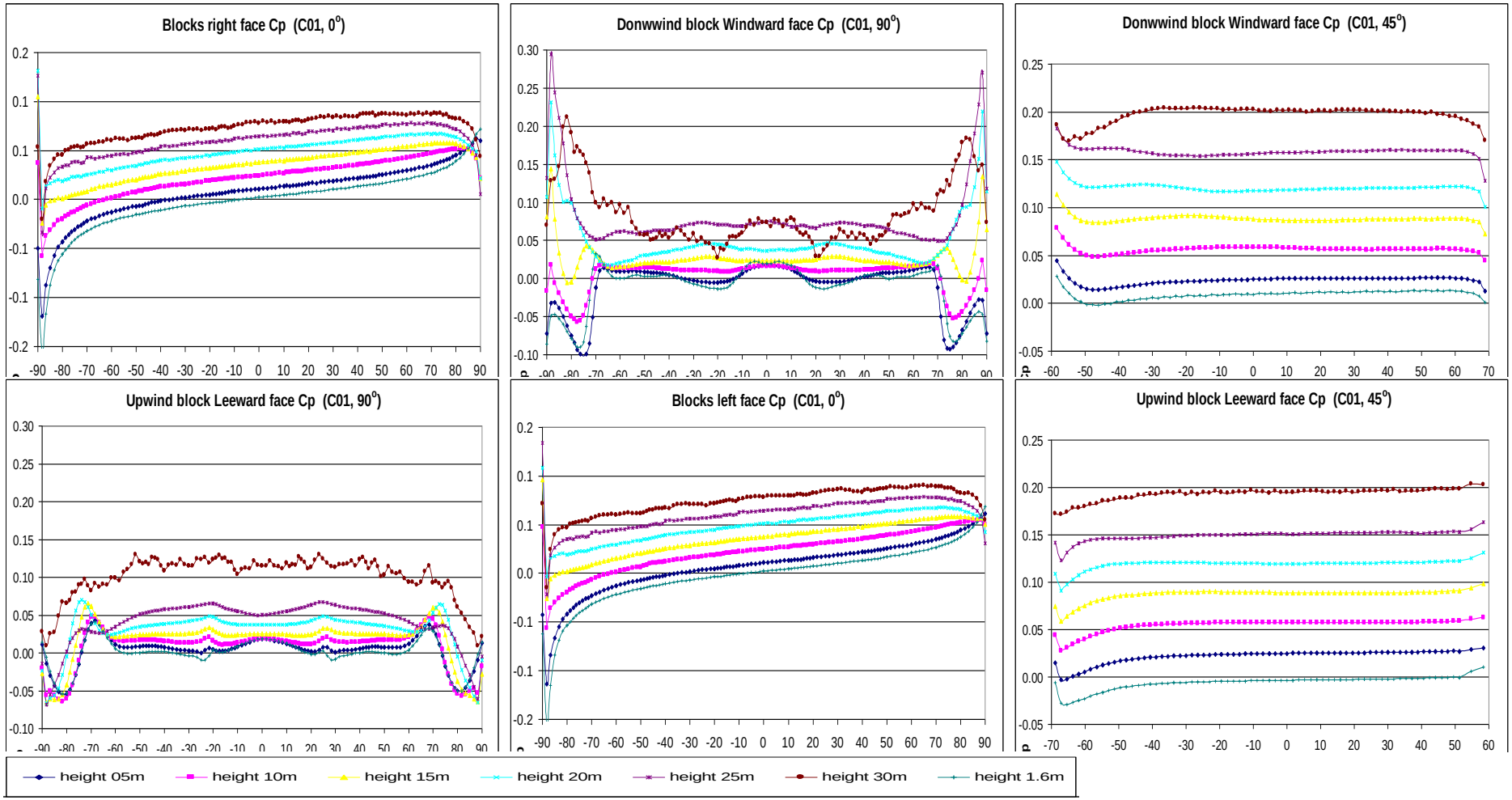

Source: this study.

Table 1: Cp results for the A1, B1, and C1 for parallel winds (0^o)

		Parallel wind incidence (0^o)												
		Right side Cp						Left side Cp						⊿Cp
	(m)	min $_{peak}$	max $_{peak}$	low $_{8th}$	high $_{8th}$	avg $_{90\%}$	sdev	min $_{peak}$	max $_{peak}$	low $_{8th}$	high $_{8th}$	avg $_{90\%}$	sdev	
A1	30	-0.31	0.19	0.00	0.15	0.10	0.06	-0.38	0.22	-0.02	0.16	0.10	0.07	***0.00***
	25	-0.59	0.18	-0.04	0.14	0.08	0.08	-0.66	0.19	-0.06	0.15	0.08	0.09	***0.00***
	20	-0.51	0.14	-0.14	0.13	0.07	0.08	-0.61	0.16	-0.20	0.15	0.07	0.09	***0.00***
	15	-0.45	0.13	-0.07	0.11	0.05	0.07	-0.54	0.15	-0.09	0.12	0.05	0.08	***0.00***
	10	-0.40	0.13	-0.13	0.11	0.03	0.06	-0.47	0.16	-0.16	0.12	0.03	0.07	***0.00***
	5	-0.37	0.11	-0.06	0.08	0.02	0.06	-0.38	0.14	-0.10	0.09	0.02	0.06	***0.00***
	2	-0.37	0.10	-0.07	0.07	0.01	0.05	-0.30	0.13	-0.09	0.08	0.01	0.06	***0.00***
avg	**>**	**-0.43**	**0.14**	**-0.07**	**0.11**	**0.05**	**0.07**	**-0.47**	**0.16**	**-0.10**	**0.12**	**0.05**	**0.08**	***0.00***
B1	30	-0.07	0.13	0.07	0.13	0.12	0.03	-0.07	0.13	0.07	0.13	0.12	0.03	***0.00***
	25	-0.12	0.11	0.06	0.11	0.10	0.03	-0.14	0.11	0.05	0.11	0.10	0.03	***0.00***
	20	-0.08	0.09	0.02	0.09	0.08	0.02	-0.09	0.09	0.02	0.09	0.08	0.02	***0.00***
	15	-0.06	0.10	0.03	0.07	0.06	0.02	-0.06	0.10	0.03	0.07	0.06	0.02	***0.00***
	10	-0.02	0.08	0.01	0.05	0.04	0.01	-0.03	0.08	0.01	0.05	0.04	0.01	***0.00***
	5	-0.02	0.05	0.00	0.03	0.02	0.01	-0.03	0.05	0.00	0.03	0.02	0.01	***0.00***
	2	-0.03	0.04	-0.01	0.02	0.01	0.01	-0.04	0.04	-0.02	0.01	0.01	0.01	***0.00***
avg	**>**	**-0.06**	**0.09**	**0.02**	**0.07**	**0.06**	**0.02**	**-0.07**	**0.08**	**0.02**	**0.07**	**0.06**	**0.02**	***0.00***
C1	30	-0.02	0.09	0.05	0.09	0.08	0.02	-0.02	0.09	0.05	0.09	0.08	0.01	***0.00***
	25	-0.03	0.13	0.03	0.08	0.06	0.02	-0.02	0.13	0.04	0.08	0.06	0.02	***0.00***
	20	-0.01	0.13	0.02	0.07	0.05	0.02	0.00	0.11	0.02	0.07	0.05	0.02	***0.00***
	15	-0.02	0.11	0.00	0.06	0.04	0.02	-0.03	0.10	0.00	0.06	0.04	0.02	***0.00***
	10	-0.06	0.05	-0.03	0.05	0.02	0.02	-0.06	0.05	-0.03	0.05	0.02	0.02	***0.00***
	5	-0.12	0.06	-0.04	0.05	0.01	0.03	-0.11	0.06	-0.04	0.04	0.01	0.03	***0.00***
	2	-0.16	0.07	-0.06	0.04	0.00	0.03	-0.16	0.07	-0.05	0.04	0.00	0.03	***0.00***
avg	**>**	**-0.06**	**0.09**	**0.00**	**0.06**	**0.04**	**0.02**	**-0.06**	**0.09**	**0.00**	**0.06**	**0.04**	**0.02**	***0.00***
AVG	***>***	***-0.18***	***0.11***	***-0.02***	***0.08***	***0.05***	***0.03***	***-0.20***	***0.11***	***-0.03***	***0.08***	***0.05***	***0.04***	***0.00***

Source: this study.

Table 2: Cp results for the A01, B01, and C01 for oblique winds (45^{o})

		Oblique wind incidence (45^{o})												
		Windward side Cp						Leewardside Cp						***ΔCp***
	(m)	min $_{peak}$	max $_{peak}$	low $_{8th}$	high $_{8th}$	avg $_{90\%}$	sdev	min $_{peak}$	max $_{peak}$	low $_{8th}$	high $_{8th}$	avg $_{90\%}$	sdev	
A1	30	0.21	0.30	0.22	0.30	0.28	0.03	0.17	0.34	0.20	0.32	0.28	0.04	***-0.01***
	25	0.22	0.32	0.25	0.32	0.28	0.03	0.07	0.27	0.12	0.25	0.22	0.05	***0.06***
	20	0.17	0.24	0.18	0.24	0.21	0.02	0.04	0.21	0.06	0.21	0.16	0.04	***0.05***
	15	0.11	0.17	0.13	0.17	0.15	0.02	0.01	0.17	0.05	0.15	0.12	0.04	***0.04***
	10	0.04	0.11	0.07	0.11	0.10	0.02	-0.02	0.12	-0.02	0.11	0.08	0.03	***0.02***
	5	-0.03	0.06	0.02	0.06	0.05	0.02	-0.06	0.08	-0.04	0.05	0.03	0.03	***0.02***
	2	-0.07	0.04	0.00	0.04	0.03	0.02	-0.10	0.05	-0.08	0.02	-0.01	0.03	***0.04***
avg	**>**	**0.09**	**0.18**	**0.12**	**0.18**	**0.16**	**0.02**	**0.02**	**0.18**	**0.04**	**0.16**	**0.13**	**0.04**	***0.03***
B1	30	-0.25	0.18	-0.04	0.15	0.11	0.07	-0.39	0.15	-0.29	0.11	0.05	0.12	***0.06***
	25	-0.09	0.21	0.05	0.12	0.09	0.03	-0.47	0.15	-0.32	0.11	0.02	0.14	***0.07***
	20	-0.09	0.11	-0.03	0.09	0.03	0.04	-0.43	0.16	-0.35	0.14	0.01	0.12	***0.02***
	15	-0.06	0.10	-0.03	0.10	0.00	0.04	-0.44	0.19	-0.27	0.14	0.02	0.12	***-0.02***
	10	-0.10	0.12	-0.07	0.12	0.03	0.05	-0.53	0.20	-0.36	0.18	0.05	0.13	***-0.02***
	5	-0.16	0.14	-0.05	0.14	0.08	0.06	-0.59	0.23	-0.21	0.18	0.07	0.12	***0.02***
	2	-0.25	0.18	-0.04	0.15	0.11	0.07	-0.61	0.25	-0.16	0.19	0.07	0.12	***0.04***
avg	**>**	**-0.14**	**0.15**	**-0.03**	**0.12**	**0.06**	**0.05**	**-0.49**	**0.19**	**-0.28**	**0.15**	**0.04**	**0.12**	***0.02***
C1	30	0.17	0.20	0.18	0.20	0.20	0.01	0.17	0.20	0.18	0.20	0.19	0.01	***0.01***
	25	0.13	0.18	0.15	0.16	0.16	0.01	0.12	0.16	0.14	0.15	0.15	0.00	***0.01***
	20	0.10	0.15	0.12	0.13	0.12	0.00	0.09	0.13	0.11	0.12	0.12	0.01	***0.00***
	15	0.07	0.11	0.09	0.09	0.09	0.00	0.06	0.10	0.08	0.09	0.09	0.01	***0.00***
	10	0.04	0.08	0.05	0.06	0.06	0.00	0.03	0.06	0.04	0.06	0.06	0.01	***0.00***
	5	0.01	0.04	0.02	0.03	0.03	0.00	0.00	0.03	0.01	0.03	0.02	0.01	***0.00***
	2	0.00	0.03	0.00	0.01	0.01	0.00	-0.03	0.01	-0.02	0.00	0.00	0.01	***0.01***
avg	**>**	**0.08**	**0.11**	**0.09**	**0.10**	**0.09**	**0.01**	**0.06**	**0.10**	**0.08**	**0.09**	**0.09**	**0.01**	***0.00***
AVG	***>***	***0.01***	***0.15***	***0.06***	***0.13***	***0.11***	***0.03***	***-0.14***	***0.16***	***-0.05***	***0.13***	***0.09***	***0.06***	***0.02***

Source: this study.

Table 3: Cp results for the A01, B01, and C01 for orthogonal winds (90°)

		Orthogonal wind incidence (90°)												
		Windward side Cp						Leewardside Cp						⊿Cp
	(m)	min peak	max peak	low 8th	high 8th	avg 90%	sdev	min peak	max peak	low 8th	high 8th	avg 90%	sdev	
A1	30	-0.26	0.16	-0.24	0.14	-0.03	0.11	-0.10	0.17	-0.08	0.17	0.09	0.08	***-0.12***
	25	-0.17	0.83	0.01	0.65	0.22	0.22	-0.18	0.12	-0.15	0.12	0.02	0.09	***0.19***
	20	-0.14	0.64	-0.05	0.45	0.03	0.17	-0.20	0.10	-0.18	0.10	-0.01	0.09	***0.03***
	15	-0.14	0.64	-0.05	0.45	0.03	0.17	-0.21	0.09	-0.19	0.09	-0.01	0.09	***0.03***
	10	-0.19	0.63	-0.07	0.54	0.03	0.17	-0.21	0.09	-0.20	0.09	0.02	0.09	***0.01***
	5	-0.13	0.56	-0.08	0.41	0.07	0.16	-0.22	0.10	-0.20	0.10	0.03	0.09	***0.04***
	2	-0.20	0.49	-0.08	0.39	0.10	0.15	-0.23	0.09	-0.20	0.09	0.02	0.09	***0.08***
avg	**>**	**-0.18**	**0.56**	**-0.08**	**0.43**	**0.06**	**0.16**	**-0.19**	**0.11**	**-0.17**	**0.11**	**0.03**	**0.09**	***0.04***
B1	30	0.07	0.25	0.11	0.24	0.14	0.04	0.13	0.25	0.15	0.24	0.21	0.03	***-0.07***
	25	0.13	0.48	0.14	0.37	0.21	0.08	0.03	0.16	0.06	0.16	0.14	0.04	***0.07***
	20	0.05	0.43	0.05	0.36	0.09	0.07	0.00	0.11	0.02	0.11	0.10	0.03	***-0.01***
	15	0.03	0.41	0.03	0.16	0.05	0.06	-0.01	0.09	0.01	0.09	0.07	0.03	***-0.01***
	10	0.04	0.26	0.04	0.16	0.06	0.04	0.01	0.10	0.01	0.10	0.07	0.03	***-0.01***
	5	0.04	0.18	0.06	0.17	0.09	0.03	0.05	0.16	0.05	0.15	0.11	0.03	***-0.01***
	2	0.06	0.23	0.07	0.20	0.12	0.04	0.06	0.19	0.07	0.18	0.11	0.03	***0.01***
avg	**>**	**0.06**	**0.32**	**0.07**	**0.24**	**0.11**	**0.05**	**0.04**	**0.15**	**0.05**	**0.15**	**0.12**	**0.03**	***0.00***
C1	30	0.03	0.21	0.04	0.18	0.07	0.04	0.01	0.13	0.03	0.13	0.11	0.03	***-0.04***
	25	0.05	0.29	0.05	0.15	0.07	0.04	-0.07	0.07	-0.02	0.06	0.05	0.03	***0.02***
	20	0.02	0.23	0.02	0.16	0.04	0.03	-0.07	0.07	-0.06	0.06	0.04	0.03	***0.00***
	15	-0.01	0.14	0.00	0.04	0.02	0.02	-0.07	0.07	-0.06	0.05	0.02	0.03	***0.00***
	10	-0.06	0.02	-0.05	0.02	0.01	0.02	-0.06	0.05	-0.06	0.05	0.02	0.03	***0.00***
	5	-0.10	0.02	-0.08	0.02	0.00	0.03	-0.06	0.04	-0.05	0.03	0.01	0.02	***-0.01***
	2	-0.09	0.03	-0.08	0.02	0.00	0.03	-0.05	0.04	-0.05	0.03	0.00	0.02	***0.00***
avg	**>**	**-0.02**	**0.14**	**-0.02**	**0.08**	**0.03**	**0.03**	**-0.05**	**0.07**	**-0.04**	**0.06**	**0.04**	**0.03**	***-0.01***
AVG	***>***	***-0.05***	***0.34***	***-0.01***	***0.25***	***0.07***	***0.08***	***-0.07***	***0.11***	***-0.05***	***0.11***	***0.06***	***0.05***	***0.01***

Source: this study.

Figure 4: A2 scenario Cp results for parallel, orthogonal and oblique winds (H/W= 0.50; 0°, 45°, 90°)

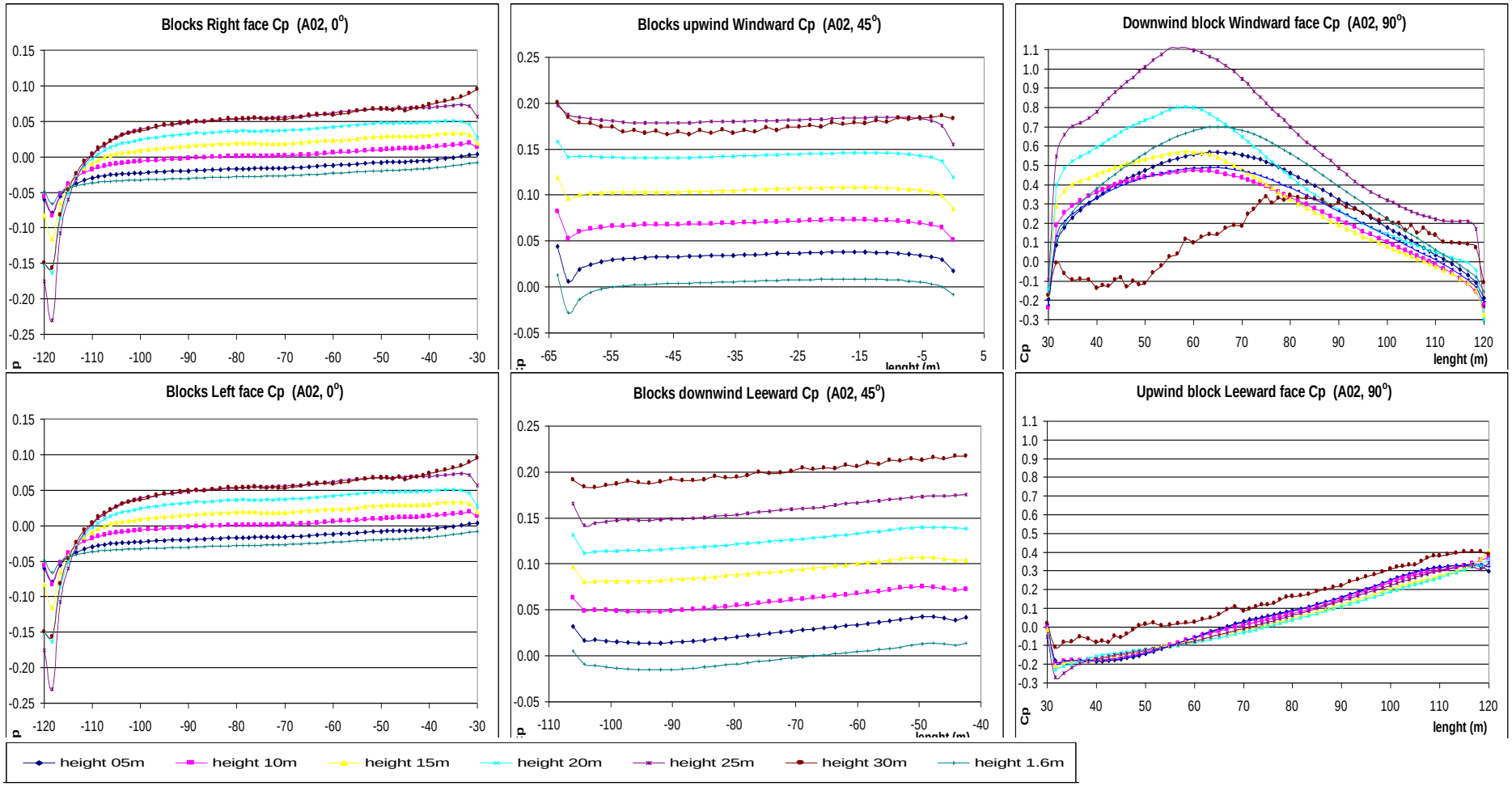

Source: this study.

Figure 5: B2 scenario Cp results for parallel, orthogonal and oblique winds (H/W= 0.50; 0°, 45°, 90°)

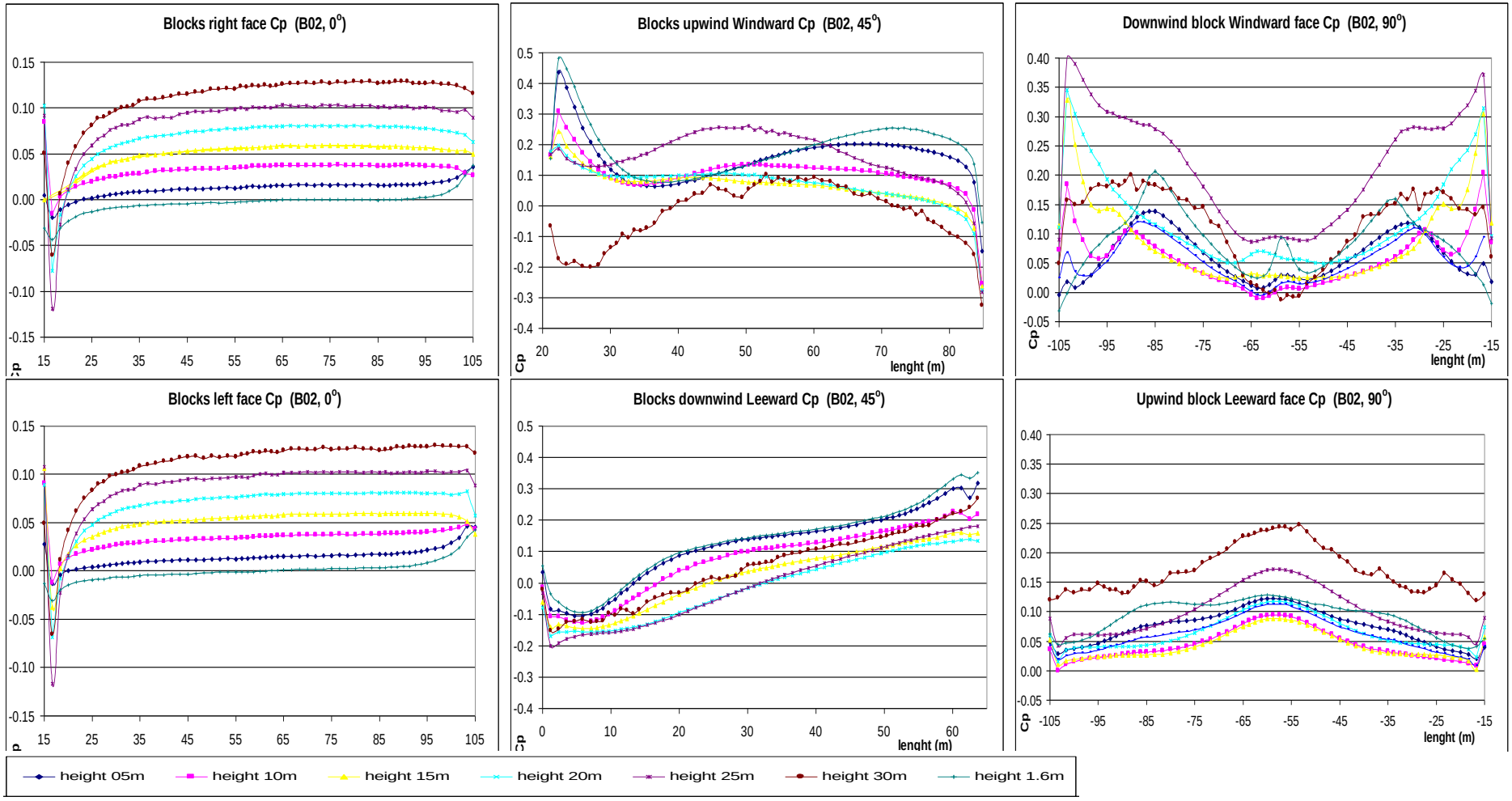

Source: this study.

Figure 6: C2 scenario Cp results for parallel, orthogonal and oblique winds (H/W= 0.50; 0°, 45°, 90°)

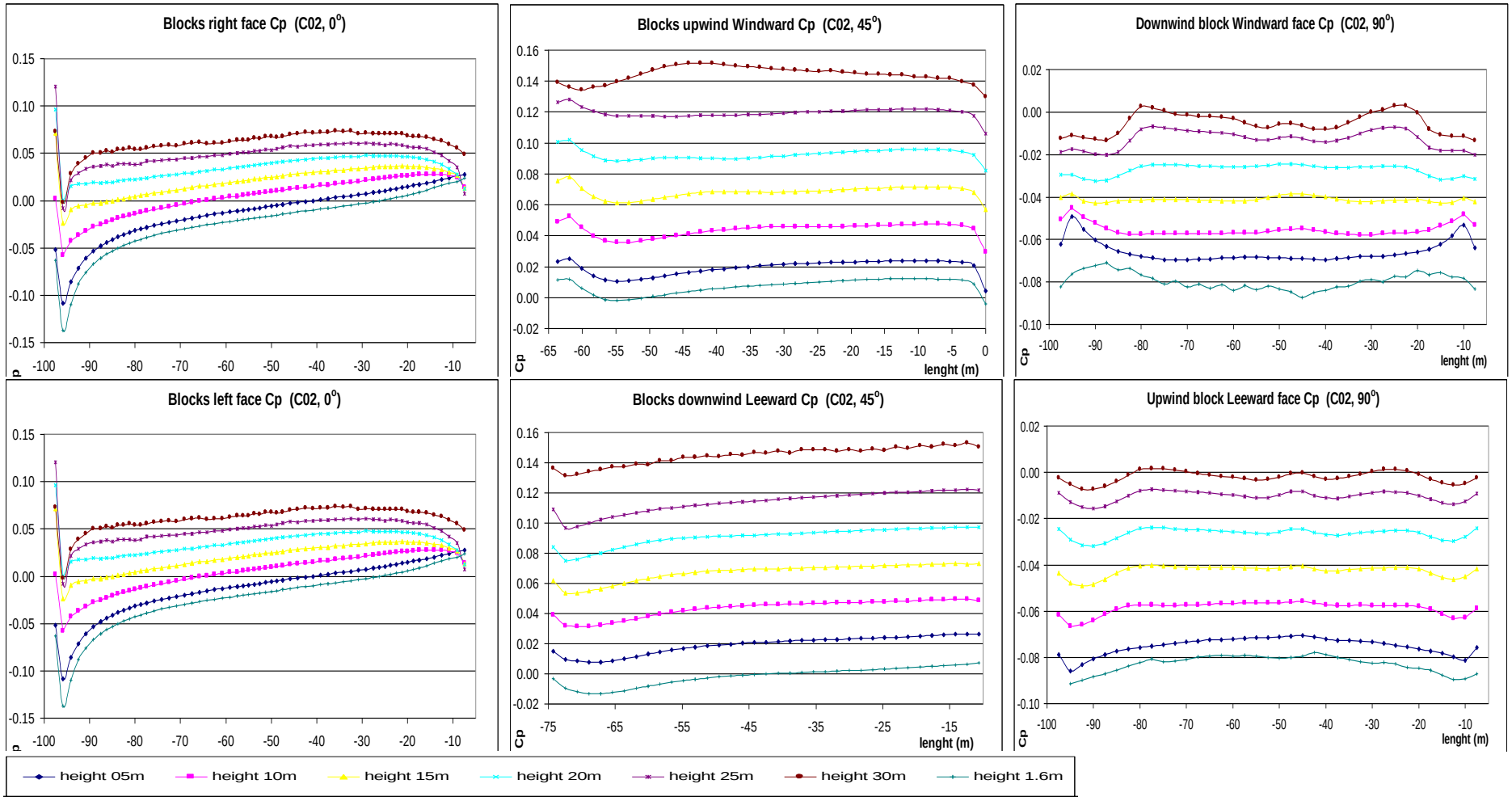

Source: this study.

Table 4: Cp results for the A02, B02, and C02 for parallel winds (0^o)

		Parallel wind incidence (0^o)												
		Right side Cp						Left side Cp						*ΔCp*
	(m)	$\min_{peak}$	$\max_{peak}$	low_{8th}	$high_{8th}$	$avg_{90\%}$	sdev	$\min_{peak}$	$\max_{peak}$	low_{8th}	$high_{8th}$	$avg_{90\%}$	sdev	
A2	30	-0.16	0.10	0.00	0.07	0.05	0.04	-0.16	0.10	0.00	0.07	0.05	0.04	***0.00***
	25	-0.23	0.07	0.00	0.07	0.05	0.05	-0.23	0.07	0.00	0.07	0.05	0.05	***0.00***
	20	-0.16	0.05	-0.05	0.05	0.04	0.04	-0.16	0.05	-0.05	0.05	0.04	0.04	***0.00***
	15	-0.12	0.03	-0.01	0.03	0.02	0.03	-0.12	0.03	-0.01	0.03	0.02	0.03	***0.00***
	10	-0.08	0.02	-0.04	0.02	0.00	0.02	-0.08	0.02	-0.04	0.02	0.00	0.02	***0.00***
	5	-0.08	0.00	-0.03	0.00	-0.02	0.01	-0.08	0.00	-0.03	0.00	-0.02	0.01	***0.00***
	2	-0.07	-0.01	-0.04	-0.02	-0.03	0.01	-0.07	-0.01	-0.04	-0.02	-0.03	0.01	***0.00***
avg	**>**	**-0.13**	**0.04**	**-0.02**	**0.03**	**0.02**	**0.03**	**-0.13**	**0.04**	**-0.02**	**0.03**	**0.02**	**0.03**	***0.00***
B2	30	-0.06	0.13	0.08	0.13	0.12	0.03	-0.07	0.13	0.08	0.13	0.12	0.03	***0.00***
	25	-0.12	0.10	0.07	0.10	0.10	0.03	-0.12	0.11	0.07	0.10	0.10	0.03	***0.00***
	20	-0.08	0.10	0.03	0.08	0.08	0.03	-0.07	0.09	0.03	0.08	0.08	0.02	***0.00***
	15	0.00	0.06	0.04	0.06	0.06	0.01	-0.04	0.11	0.04	0.06	0.06	0.02	***0.00***
	10	-0.02	0.08	0.01	0.04	0.04	0.01	-0.01	0.09	0.02	0.04	0.04	0.01	***0.00***
	5	-0.02	0.04	0.00	0.02	0.01	0.01	-0.01	0.05	0.00	0.02	0.01	0.01	***0.00***
	2	-0.04	0.04	-0.01	0.00	0.00	0.01	-0.03	0.04	-0.01	0.01	0.00	0.01	***0.00***
avg	**>**	**-0.05**	**0.08**	**0.03**	**0.06**	**0.06**	**0.02**	**-0.05**	**0.09**	**0.03**	**0.06**	**0.06**	**0.02**	***0.00***
C2	30	0.00	0.07	0.05	0.07	0.06	0.01	0.00	0.07	0.05	0.07	0.06	0.01	***0.00***
	25	-0.01	0.12	0.04	0.06	0.05	0.02	-0.01	0.12	0.04	0.06	0.05	0.02	***0.00***
	20	0.00	0.10	0.02	0.05	0.04	0.01	0.00	0.10	0.02	0.05	0.04	0.01	***0.00***
	15	-0.02	0.07	0.00	0.04	0.02	0.02	-0.02	0.07	0.00	0.04	0.02	0.02	***0.00***
	10	-0.06	0.03	-0.03	0.03	0.01	0.02	-0.06	0.03	-0.03	0.03	0.01	0.02	***0.00***
	5	-0.11	0.03	-0.05	0.02	-0.01	0.03	-0.11	0.03	-0.05	0.02	-0.01	0.03	***0.00***
	2	-0.14	0.02	-0.06	0.01	-0.02	0.03	-0.14	0.02	-0.06	0.01	-0.02	0.03	***0.00***
avg	**>**	**-0.05**	**0.06**	**-0.01**	**0.04**	**0.02**	**0.02**	**-0.05**	**0.06**	**-0.01**	**0.04**	**0.02**	**0.02**	***0.00***
AVG	***>***	***-0.07***	***0.06***	***0.00***	***0.04***	***0.03***	***0.02***	***-0.07***	***0.06***	***0.00***	***0.04***	***0.03***	***0.02***	***0.00***

Source: this study.

Table 5: Cp results for the A02, B02, and C02 for oblique winds (45°)

		Oblique wind incidence (45°)												
		Windward side Cp						Leewardside Cp						ΔCp
	(m)	min_{peak}	max_{peak}	low_{8th}	$high_{8th}$	$avg_{90\%}$	sdev	min_{peak}	max_{peak}	low_{8th}	$high_{8th}$	$avg_{90\%}$	sdev	
A2	30	0.18	0.22	0.19	0.21	0.20	0.01	0.17	0.20	0.17	0.18	0.17	0.01	***0.03***
	25	0.14	0.18	0.15	0.17	0.16	0.01	0.16	0.20	0.18	0.18	0.18	0.01	***-0.02***
	20	0.11	0.14	0.11	0.14	0.13	0.01	0.12	0.16	0.14	0.15	0.14	0.00	***-0.02***
	15	0.08	0.11	0.08	0.10	0.09	0.01	0.09	0.12	0.10	0.11	0.11	0.00	***-0.01***
	10	0.05	0.08	0.05	0.07	0.06	0.01	0.05	0.08	0.06	0.07	0.07	0.01	***-0.01***
	5	0.01	0.04	0.02	0.04	0.03	0.01	0.01	0.04	0.03	0.04	0.03	0.01	***-0.01***
	2	-0.02	0.01	-0.01	0.01	0.00	0.01	-0.03	0.01	0.00	0.01	0.01	0.01	***-0.01***
avg	**>**	**0.08**	**0.11**	**0.08**	**0.11**	**0.09**	**0.01**	**0.08**	**0.12**	**0.10**	**0.11**	**0.10**	**0.01**	***-0.01***
B2	30	-0.15	0.27	-0.12	0.18	0.06	0.11	-0.32	0.10	-0.17	0.08	0.00	0.10	***0.06***
	25	-0.20	0.18	-0.16	0.15	0.00	0.12	-0.28	0.26	0.08	0.25	0.17	0.09	***-0.17***
	20	-0.17	0.14	-0.16	0.13	0.00	0.10	-0.28	0.20	-0.02	0.14	0.09	0.06	***-0.10***
	15	-0.14	0.16	-0.14	0.14	0.04	0.10	-0.26	0.24	0.02	0.10	0.08	0.06	***-0.03***
	10	-0.13	0.23	-0.12	0.21	0.11	0.11	-0.25	0.31	0.06	0.17	0.11	0.06	***0.00***
	5	-0.10	0.32	-0.08	0.26	0.14	0.12	-0.15	0.44	0.07	0.20	0.17	0.08	***-0.02***
	2	-0.09	0.35	-0.06	0.28	0.15	0.12	-0.05	0.48	0.08	0.25	0.18	0.09	***-0.03***
avg	**>**	**-0.14**	**0.24**	**-0.12**	**0.19**	**0.07**	**0.11**	**-0.23**	**0.29**	**0.02**	**0.17**	**0.11**	**0.08**	***-0.04***
C2	30	0.13	0.15	0.14	0.15	0.15	0.01	0.13	0.15	0.14	0.15	0.15	0.01	***0.00***
	25	0.11	0.13	0.12	0.12	0.12	0.00	0.10	0.12	0.11	0.12	0.12	0.01	***0.00***
	20	0.08	0.10	0.09	0.10	0.09	0.00	0.07	0.10	0.08	0.10	0.09	0.01	***0.00***
	15	0.06	0.08	0.06	0.07	0.07	0.00	0.05	0.07	0.06	0.07	0.07	0.01	***0.00***
	10	0.03	0.05	0.04	0.05	0.05	0.00	0.03	0.05	0.04	0.05	0.05	0.00	***0.00***
	5	0.00	0.03	0.01	0.02	0.02	0.00	0.00	0.03	0.01	0.02	0.02	0.00	***0.00***
	2	0.00	0.01	0.00	0.01	0.01	0.00	0.00	0.01	0.00	0.01	0.01	0.00	***0.00***
avg	**>**	**0.06**	**0.08**	**0.07**	**0.07**	**0.07**	**0.00**	**0.06**	**0.08**	**0.06**	**0.07**	**0.07**	**0.01**	***0.00***
AVG	***>***	***0.00***	***0.14***	***0.01***	***0.13***	***0.08***	***0.04***	***-0.03***	***0.16***	***0.06***	***0.12***	***0.10***	***0.03***	***-0.02***

Source: this study.

Table 6: Cp results for the A02, B02, and C02 for orthogonal winds (90°)

		Orthogonal wind incidence (90°)												
		Windward side Cp						Leewardside Cp						ΔCp
	(m)	min peak	max peak	low 8th	high 8th	avg 90%	sdev	min peak	max peak	low 8th	high 8th	avg 90%	sdev	
A2	30	-0.17	0.34	-0.11	0.32	0.15	0.16	-0.11	0.40	-0.06	0.38	0.13	0.16	***0.02***
	25	-0.23	1.11	0.22	1.06	0.71	0.34	-0.27	0.34	-0.16	0.30	0.03	0.18	***0.68***
	20	-0.30	0.81	0.00	0.80	0.48	0.29	-0.23	0.36	-0.19	0.31	0.00	0.16	***0.48***
	15	-0.28	0.57	-0.02	0.55	0.36	0.23	-0.21	0.41	-0.17	0.27	0.01	0.17	***0.34***
	10	-0.24	0.47	-0.11	0.47	0.33	0.20	-0.19	0.37	-0.18	0.33	0.04	0.18	***0.29***
	5	-0.20	0.57	0.04	0.55	0.37	0.21	-0.18	0.33	-0.18	0.32	0.06	0.18	***0.31***
	2	-0.16	0.70	0.06	0.68	0.43	0.25	-0.19	0.31	-0.18	0.29	0.05	0.17	***0.38***
avg	**>**	**-0.23**	**0.65**	**0.01**	**0.63**	**0.40**	**0.24**	**-0.20**	**0.36**	**-0.16**	**0.31**	**0.04**	**0.17**	***0.36***
B2	30	-0.01	0.20	0.00	0.18	0.14	0.07	0.12	0.25	0.13	0.24	0.16	0.04	***-0.01***
	25	0.09	0.40	0.09	0.32	0.24	0.10	0.04	0.17	0.06	0.16	0.09	0.04	***0.16***
	20	0.05	0.35	0.05	0.27	0.10	0.07	0.02	0.12	0.04	0.12	0.05	0.03	***0.05***
	15	0.02	0.33	0.03	0.15	0.06	0.07	0.00	0.09	0.02	0.08	0.03	0.02	***0.02***
	10	-0.01	0.20	0.00	0.12	0.06	0.04	0.00	0.09	0.01	0.09	0.03	0.03	***0.02***
	5	0.00	0.14	0.02	0.12	0.06	0.04	0.02	0.12	0.04	0.12	0.08	0.03	***-0.02***
	2	-0.03	0.21	0.03	0.16	0.09	0.05	0.04	0.13	0.05	0.12	0.10	0.03	***-0.02***
avg	**>**	**0.01**	**0.26**	**0.03**	**0.19**	**0.11**	**0.06**	**0.03**	**0.14**	**0.05**	**0.13**	**0.08**	**0.03**	***0.03***
C2	30	-0.01	0.00	-0.01	0.00	-0.01	0.01	-0.01	0.00	0.00	0.00	0.00	0.00	***0.00***
	25	-0.02	-0.01	-0.02	-0.01	-0.01	0.00	-0.02	-0.01	-0.01	-0.01	-0.01	0.00	***0.00***
	20	-0.03	-0.02	-0.03	-0.02	-0.03	0.00	-0.03	-0.02	-0.03	-0.02	-0.03	0.00	***0.00***
	15	-0.04	-0.04	-0.04	-0.04	-0.04	0.00	-0.05	-0.04	-0.05	-0.04	-0.04	0.00	***0.00***
	10	-0.06	-0.05	-0.06	-0.05	-0.06	0.00	-0.07	-0.06	-0.06	-0.06	-0.06	0.00	***0.00***
	5	-0.07	-0.05	-0.07	-0.06	-0.07	0.00	-0.09	-0.07	-0.08	-0.07	-0.07	0.00	***0.01***
	2	-0.09	-0.07	-0.08	-0.08	-0.08	0.00	-0.09	-0.08	-0.09	-0.08	-0.08	0.00	***0.00***
avg	**>**	**-0.06**	**-0.05**	**-0.06**	**-0.06**	**-0.06**	**0.00**	**-0.07**	**-0.06**	**-0.07**	**-0.06**	**-0.06**	**0.00**	***0.00***
AVG	***>***	***-0.09***	***0.29***	***0.00***	***0.26***	***0.16***	***0.10***	***-0.07***	***0.15***	***-0.05***	***0.13***	***0.03***	***0.07***	***0.13***

Source: this study.

Figure 7: A3 scenario Cp results for parallel, orthogonal and oblique winds (H/W= 0.50; 0°, 45°, 90°)

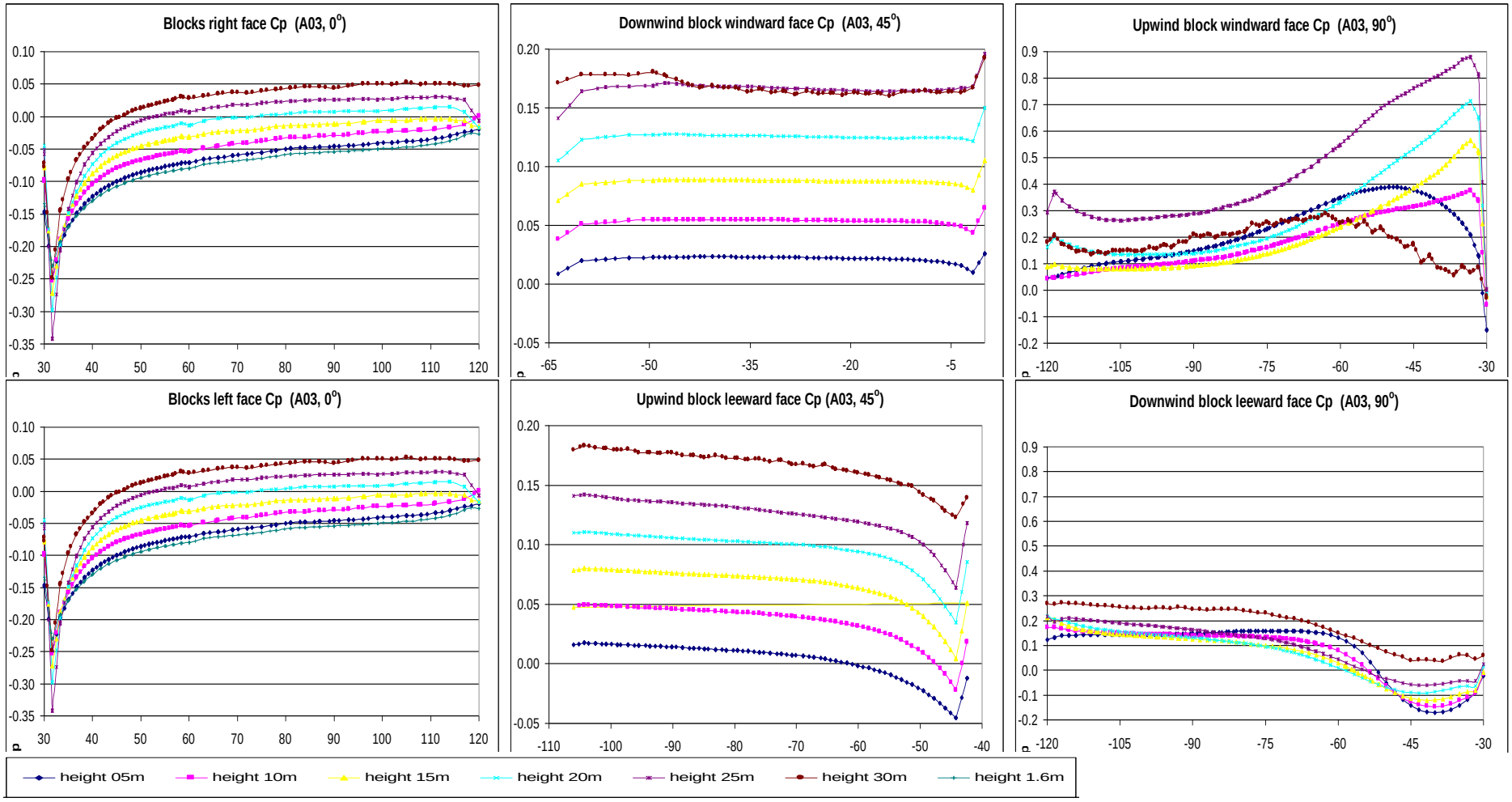

Source: this study.

Figure 8: B3 scenario Cp results for parallel, orthogonal and oblique winds (H/W= 0.50; 0°, 45°, 90°)

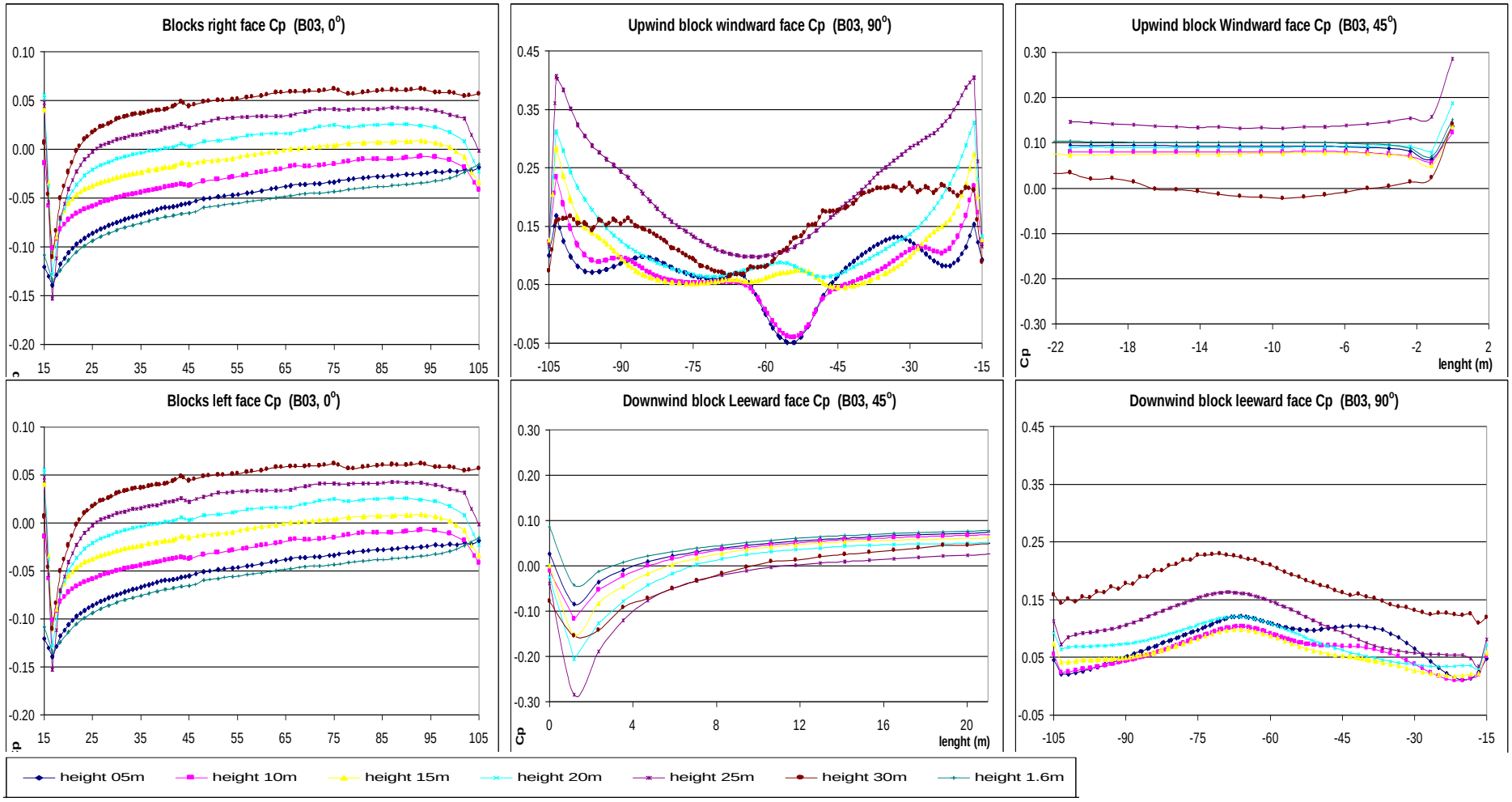

Source: this study.

Figure 9: C3 scenario Cp results for parallel, orthogonal and oblique winds (H/W= 0.50; 0°, 45°, 90°)

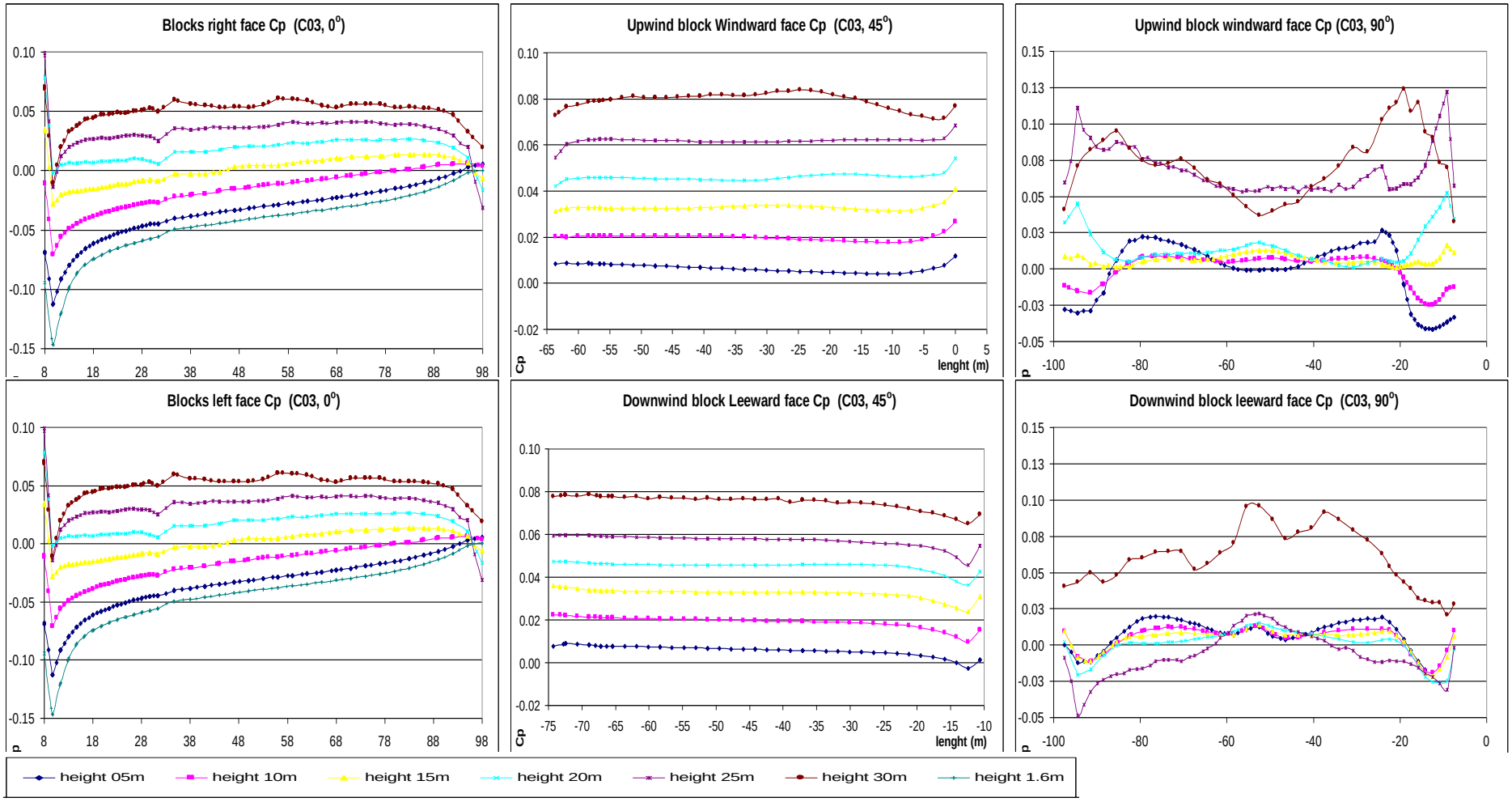

Source: this study.

Table 7: Cp results for the A03, B03, and C03 for parallel winds (0^o)

		Parallel wind incidence (0^o)												
		Right side Cp						Left side Cp						ΔCp
	(m)	min_{peak}	max_{peak}	low_{8th}	$high_{8th}$	$avg_{90\%}$	sdev	min_{peak}	max_{peak}	low_{8th}	$high_{8th}$	$avg_{90\%}$	sdev	
A3	30	-0.25	0.05	-0.14	0.05	0.03	0.06	-0.25	0.05	-0.14	0.05	0.03	0.06	**0.00**
	25	-0.34	0.03	-0.20	0.03	0.01	0.07	-0.34	0.03	-0.20	0.03	0.01	0.07	**0.00**
	20	-0.30	0.01	-0.17	0.01	-0.01	0.06	-0.30	0.01	-0.17	0.01	-0.01	0.06	**0.00**
	15	-0.27	0.00	-0.18	0.00	-0.03	0.05	-0.27	0.00	-0.18	0.00	-0.03	0.05	**0.00**
	10	-0.25	0.00	-0.18	-0.02	-0.05	0.05	-0.25	0.00	-0.18	-0.02	-0.05	0.05	**0.00**
	5	-0.25	-0.02	-0.20	-0.03	-0.07	0.05	-0.25	-0.02	-0.20	-0.03	-0.07	0.05	**0.00**
	2	-0.23	-0.03	-0.19	-0.04	-0.07	0.04	-0.23	-0.03	-0.19	-0.04	-0.07	0.04	**0.00**
avg	**>**	**-0.27**	**0.01**	**-0.18**	**0.00**	**-0.03**	**0.06**	**-0.27**	**0.01**	**-0.18**	**0.00**	**-0.03**	**0.06**	**0.00**
B3	30	-0.11	0.06	-0.04	0.06	0.05	0.03	-0.11	0.06	-0.04	0.06	0.05	0.03	**0.00**
	25	-0.15	0.05	-0.06	0.04	0.03	0.04	-0.15	0.05	-0.06	0.04	0.03	0.04	**0.00**
	20	-0.13	0.06	-0.06	0.03	0.01	0.03	-0.13	0.06	-0.06	0.03	0.01	0.03	**0.00**
	15	-0.11	0.04	-0.06	0.01	-0.01	0.02	-0.11	0.04	-0.06	0.01	-0.01	0.02	**0.00**
	10	-0.10	-0.01	-0.08	-0.01	-0.03	0.02	-0.10	-0.01	-0.08	-0.01	-0.03	0.02	**0.00**
	5	-0.14	-0.02	-0.12	-0.02	-0.05	0.03	-0.14	-0.02	-0.12	-0.02	-0.05	0.03	**0.00**
	2	-0.14	-0.02	-0.12	-0.03	-0.06	0.03	-0.14	-0.02	-0.12	-0.03	-0.06	0.03	**0.00**
avg	**>**	**-0.13**	**0.02**	**-0.08**	**0.01**	**-0.01**	**0.03**	**-0.13**	**0.02**	**-0.08**	**0.01**	**-0.01**	**0.03**	**0.00**
C3	30	-0.01	0.07	0.02	0.06	0.05	0.01	-0.01	0.07	0.02	0.06	0.05	0.01	**0.00**
	25	-0.03	0.10	0.01	0.04	0.03	0.02	-0.03	0.10	0.01	0.04	0.03	0.02	**0.00**
	20	-0.02	0.08	0.00	0.03	0.02	0.01	-0.02	0.08	0.00	0.03	0.02	0.01	**0.00**
	15	-0.03	0.04	-0.02	0.01	0.00	0.01	-0.03	0.04	-0.02	0.01	0.00	0.01	**0.00**
	10	-0.07	0.01	-0.05	0.01	-0.02	0.02	-0.07	0.01	-0.05	0.01	-0.02	0.02	**0.00**
	5	-0.11	0.01	-0.09	0.00	-0.04	0.03	-0.11	0.01	-0.09	0.00	-0.04	0.03	**0.00**
	2	-0.15	0.00	-0.12	-0.01	-0.04	0.03	-0.15	0.00	-0.12	-0.01	-0.04	0.03	**0.00**
avg	**>**	**-0.06**	**0.04**	**-0.04**	**0.02**	**0.00**	**0.02**	**-0.06**	**0.04**	**-0.04**	**0.02**	**0.00**	**0.02**	**0.00**
AVG	**>**	**-0.15**	**0.02**	**-0.10**	**0.01**	**-0.01**	**0.03**	**-0.15**	**0.02**	**-0.10**	**0.01**	**-0.01**	**0.03**	**0.00**

Source: this study.

Table 8: Cp results for the A03, B03, and C03 for oblique winds (45^{o})

		Oblique wind incidence (45o)												
		Windward side Cp						Leewardside Cp						
	(m)	min peak	max peak	low 8th	high 8th	avg 90%	sdev	min peak	max peak	low 8th	high 8th	avg 90%	sdev	DCp
A3	30	0.16	0.18	0.16	0.18	0.16	0.01	0.12	0.18	0.13	0.18	0.17	0.02	-0.01
	25	0.14	0.19	0.16	0.17	0.17	0.01	0.06	0.14	0.08	0.14	0.13	0.02	0.04
	20	0.11	0.20	0.12	0.17	0.13	0.01	0.03	0.12	0.05	0.11	0.10	0.02	0.02
	15	0.07	0.15	0.08	0.12	0.09	0.01	0.00	0.08	0.02	0.08	0.07	0.02	0.02
	10	0.04	0.11	0.05	0.05	0.05	0.01	-0.02	0.05	0.00	0.05	0.04	0.02	0.01
	5	0.01	0.06	0.02	0.02	0.02	0.00	-0.05	0.02	-0.03	0.02	0.01	0.02	0.01
	2	0.00	0.00	0.00	0.00	0.00	0.00	0.00	0.00	0.00	0.00	0.00	0.00	0.00
avg	**>**	**0.09**	**0.15**	**0.10**	**0.12**	**0.10**	**0.01**	**0.03**	**0.10**	**0.04**	**0.10**	**0.09**	**0.02**	**0.02**
B3	30	-0.02	0.14	-0.01	0.08	0.04	0.04	-0.15	0.06	-0.03	0.06	0.04	0.06	0.00
	25	0.13	0.29	0.14	0.14	0.14	0.03	-0.29	0.03	-0.03	0.01	0.00	0.08	0.14
	20	0.08	0.19	0.09	0.09	0.09	0.02	-0.21	0.05	-0.04	0.05	0.03	0.07	0.06
	15	0.05	0.14	0.07	0.08	0.07	0.01	-0.15	0.07	0.02	0.07	0.07	0.04	0.01
	10	0.05	0.12	0.08	0.08	0.08	0.01	-0.12	0.07	-0.01	0.06	0.05	0.05	0.03
	5	0.06	0.14	0.09	0.09	0.09	0.01	-0.08	0.07	0.03	0.06	0.05	0.04	0.04
	2	0.07	0.15	0.10	0.11	0.10	0.01	-0.04	0.09	0.05	0.07	0.06	0.03	0.04
avg	**>**	0.06	0.17	0.08	0.10	0.09	0.02	-0.15	0.06	0.00	0.05	0.04	0.05	0.05
C3	30	**0.07**	**0.08**	**0.08**	**0.08**	**0.08**	**0.00**	**0.06**	**0.08**	**0.07**	**0.08**	**0.08**	**0.00**	**0.00**
	25	0.05	0.07	0.06	0.06	0.06	0.00	0.05	0.06	0.06	0.06	0.06	0.00	0.00
	20	0.04	0.05	0.04	0.05	0.05	0.00	0.04	0.05	0.04	0.05	0.05	0.00	0.00
	15	0.03	0.04	0.03	0.03	0.03	0.00	0.02	0.04	0.03	0.03	0.03	0.00	0.00
	10	0.02	0.03	0.02	0.02	0.02	0.00	0.01	0.02	0.02	0.02	0.02	0.00	0.00
	5	0.00	0.01	0.00	0.01	0.01	0.00	0.00	0.01	0.00	0.01	0.01	0.00	0.00
	2	0.00	0.00	0.00	0.00	0.00	0.00	0.00	0.00	0.00	0.00	0.00	0.00	0.00
avg	**>**	**0.07**	**0.08**	**0.08**	**0.08**	**0.08**	**0.00**	**0.06**	**0.08**	**0.07**	**0.08**	**0.08**	**0.00**	**0.00**
AVG	**>**	**0.06**	**0.11**	**0.07**	**0.08**	**0.07**	**0.01**	**-0.03**	**0.06**	**0.02**	**0.06**	**0.05**	**0.02**	**0.02**

Source: this study.

Table 9: Cp results for the A03, B03, and C03 for orthogonal winds (90°)

		Orthogonal wind incidence (90°)												
		Windward side Cp						Leewardside Cp						ΔCp
	(m)	min peak	max peak	low 8th	high 8th	avg 90%	sdev	min peak	max peak	low 8th	high 8th	avg 90%	sdev	
A3	30	-0.03	0.29	0.07	0.27	0.19	0.06	0.04	0.27	0.05	0.26	0.23	0.08	***-0.05***
	25	0.00	0.88	0.26	0.86	0.36	0.21	-0.06	0.22	-0.04	0.20	0.15	0.08	***0.21***
	20	-0.02	0.71	0.13	0.68	0.19	0.18	-0.09	0.22	-0.07	0.19	0.12	0.09	***0.07***
	15	-0.02	0.57	0.08	0.54	0.13	0.14	-0.12	0.21	-0.10	0.18	0.12	0.10	***0.01***
	10	-0.06	0.37	0.05	0.36	0.15	0.10	-0.15	0.17	-0.11	0.16	0.14	0.09	***0.02***
	5	-0.15	0.39	0.05	0.39	0.20	0.12	-0.17	0.16	-0.12	0.16	0.14	0.09	***0.06***
	2	-0.14	0.39	0.20	0.37	0.28	0.23	-0.21	0.19	-0.16	0.12	0.10	0.09	***0.18***
avg	**>**	**-0.06**	**0.51**	**0.12**	**0.50**	**0.22**	**0.15**	**-0.11**	**0.21**	**-0.08**	**0.18**	**0.14**	**0.09**	***0.07***
B3	30	0.06	0.22	0.07	0.22	0.15	0.05	0.11	0.23	0.13	0.22	0.17	0.04	***-0.02***
	25	0.10	0.41	0.10	0.40	0.20	0.09	0.04	0.16	0.06	0.16	0.11	0.03	***0.08***
	20	0.06	0.33	0.06	0.31	0.09	0.07	0.03	0.12	0.04	0.12	0.08	0.03	***0.01***
	15	0.05	0.28	0.05	0.25	0.07	0.06	0.02	0.10	0.02	0.09	0.05	0.02	***0.02***
	10	-0.04	0.23	-0.04	0.21	0.07	0.06	0.01	0.10	0.02	0.10	0.07	0.03	***0.00***
	5	-0.05	0.17	-0.05	0.15	0.08	0.05	0.01	0.12	0.02	0.12	0.09	0.03	***-0.01***
	2	0.00	0.00	0.00	0.00	0.00	0.00	0.00	0.00	0.00	0.00	0.00	0.00	***0.00***
avg	**>**	**0.03**	**0.27**	**0.03**	**0.25**	**0.11**	**0.06**	**0.04**	**0.14**	**0.05**	**0.13**	**0.10**	**0.03**	***0.01***
C3	30	0.03	0.12	0.05	0.09	0.07	0.02	0.02	0.10	0.04	0.08	0.06	0.02	***0.01***
	25	0.05	0.12	0.05	0.11	0.06	0.02	-0.05	0.02	-0.02	0.01	-0.01	0.02	***0.07***
	20	0.00	0.05	0.00	0.04	0.01	0.01	-0.03	0.02	-0.02	0.01	0.00	0.01	***0.01***
	15	0.00	0.02	0.00	0.01	0.01	0.00	-0.02	0.01	-0.01	0.01	0.01	0.01	***0.00***
	10	-0.03	0.01	-0.02	0.01	0.01	0.01	-0.02	0.01	-0.01	0.01	0.01	0.01	***0.00***
	5	-0.04	0.03	-0.04	0.02	0.00	0.02	-0.02	0.02	0.00	0.02	0.01	0.01	***-0.01***
	2	0.00	0.00	0.00	0.00	0.00	0.00	0.00	0.00	0.00	0.00	0.00	0.00	***0.00***
avg	**>**	**0.00**	**0.06**	**0.01**	**0.05**	**0.03**	**0.02**	**-0.02**	**0.03**	**0.00**	**0.02**	**0.01**	**0.01**	***0.03***
AVG	***>***	***-0.01***	***0.27***	***0.05***	***0.25***	***0.11***	***0.07***	***-0.03***	***0.12***	***-0.01***	***0.11***	***0.08***	***0.04***	***0.03***

Source: this study.

Figure 10: A4 scenario Cp results for parallel, orthogonal and oblique winds (H/W= 0.50; 0°, 45°, 90°):

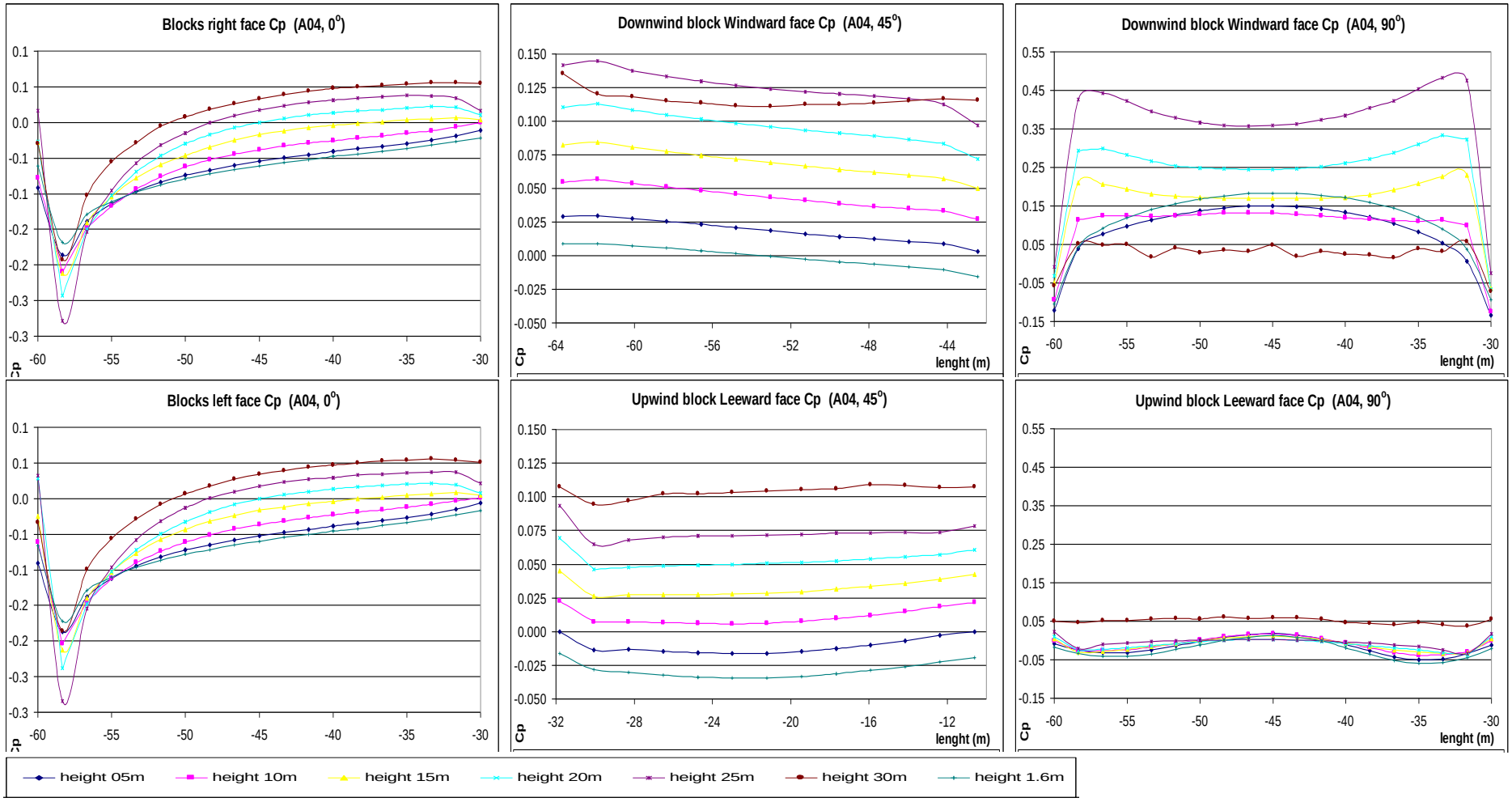

Source: this study.

Figure 11: B4 scenario Cp results for parallel, orthogonal and oblique winds (H/W= 0.50; 0°, 45°, 90°):

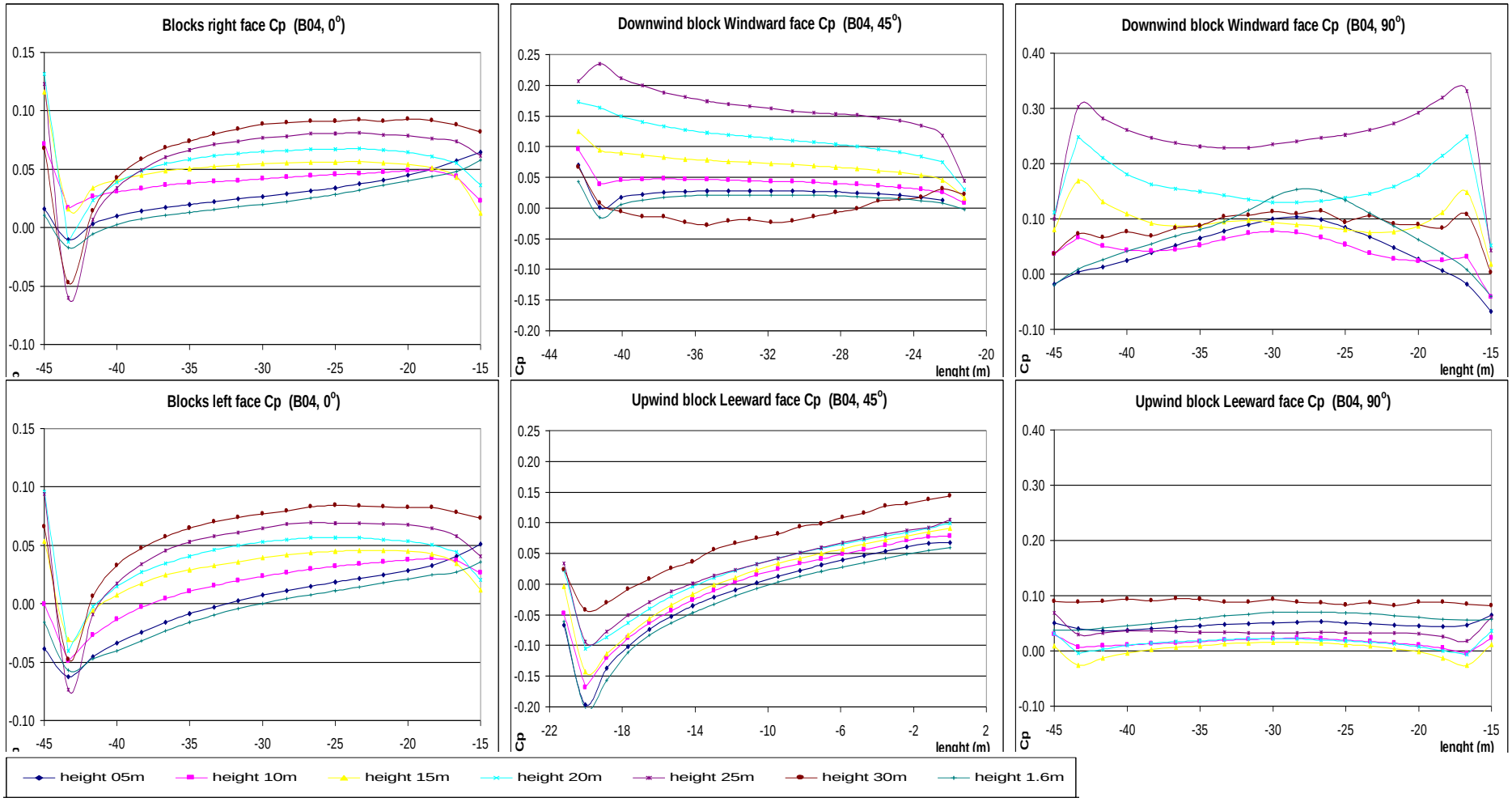

Source: this study.

Figure 12: C4 scenario Cp results for parallel, orthogonal and oblique winds (H/W= 0.50; 0°, 45°, 90°):

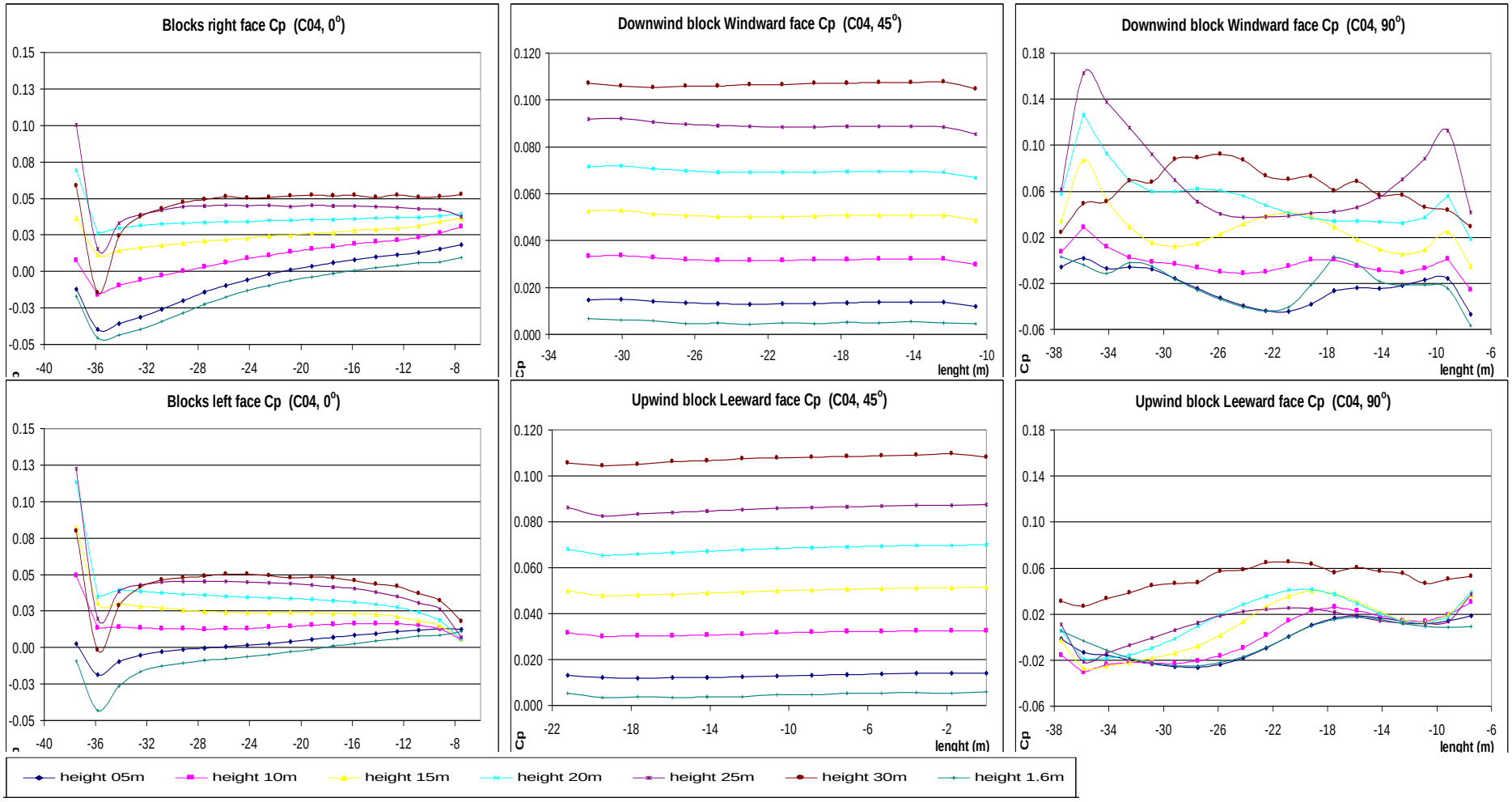

Source: this study.

Table 10: Cp results for the A04, B04, and C04 for parallel winds (0^o)

		Parallel wind incidence (0^o)												
		Right side Cp						**Left side Cp**						***ΔCp***
	(m)	min_{peak}	max_{peak}	low_{8th}	$high_{8th}$	$avg_{90\%}$	sdev	min_{peak}	max_{peak}	low_{8th}	$high_{8th}$	$avg_{90\%}$	sdev	
A4	30	-0.19	0.06	0.01	0.05	0.03	0.06	-0.19	0.06	0.01	0.05	0.03	0.06	***0.00***
	25	-0.28	0.04	0.00	0.03	0.02	0.08	-0.28	0.04	0.00	0.03	0.02	0.08	***0.00***
	20	-0.24	0.02	-0.07	0.02	0.00	0.07	-0.24	0.03	-0.07	0.02	0.00	0.07	***-0.01***
	15	-0.21	0.01	-0.03	0.00	-0.02	0.06	-0.21	0.01	-0.03	0.00	-0.02	0.06	***0.00***
	10	-0.21	0.00	-0.09	-0.02	-0.04	0.05	-0.20	0.00	-0.09	-0.01	-0.04	0.05	***0.00***
	5	-0.19	-0.01	-0.07	-0.04	-0.05	0.04	-0.19	-0.01	-0.07	-0.04	-0.05	0.04	***0.00***
	2	-0.17	-0.02	-0.07	-0.05	-0.06	0.04	-0.17	-0.02	-0.07	-0.05	-0.06	0.04	***0.00***
avg	**>**	**-0.21**	**0.01**	**-0.05**	**0.00**	**-0.02**	**0.06**	**-0.21**	**0.02**	**-0.05**	**0.00**	**-0.02**	**0.06**	***0.00***
B4	30	-0.05	0.09	0.07	0.09	0.08	0.03	-0.05	0.08	0.07	0.08	0.07	0.03	***0.01***
	25	-0.06	0.12	0.07	0.08	0.07	0.04	-0.07	0.09	0.05	0.07	0.06	0.04	***0.01***
	20	-0.01	0.13	0.04	0.07	0.06	0.03	-0.04	0.10	0.02	0.06	0.05	0.03	***0.01***
	15	0.01	0.12	0.05	0.05	0.05	0.02	-0.03	0.05	0.03	0.04	0.04	0.02	***0.02***
	10	0.02	0.07	0.03	0.05	0.04	0.01	-0.05	0.04	0.00	0.04	0.02	0.02	***0.02***
	5	-0.01	0.06	0.02	0.03	0.03	0.02	-0.06	0.05	-0.01	0.02	0.01	0.03	***0.02***
	2	-0.02	0.06	0.01	0.03	0.02	0.02	-0.06	0.04	-0.02	0.01	0.00	0.03	***0.02***
avg	**>**	**-0.02**	**0.09**	**0.04**	**0.06**	**0.05**	**0.02**	**-0.05**	**0.06**	**0.02**	**0.04**	**0.04**	**0.03**	***0.02***
C4	30	-0.01	0.06	0.05	0.05	0.05	0.02	0.00	0.08	0.04	0.05	0.05	0.02	***0.00***
	25	0.02	0.10	0.04	0.04	0.04	0.01	0.01	0.12	0.04	0.04	0.04	0.02	***0.00***
	20	0.03	0.07	0.03	0.04	0.04	0.01	0.01	0.11	0.03	0.04	0.03	0.02	***0.00***
	15	0.01	0.04	0.02	0.03	0.02	0.01	0.01	0.08	0.02	0.02	0.02	0.01	***0.00***
	10	-0.02	0.03	0.00	0.02	0.01	0.01	0.01	0.05	0.01	0.02	0.01	0.01	***0.00***
	5	-0.04	0.02	-0.01	0.01	0.00	0.02	-0.02	0.01	0.00	0.01	0.00	0.01	***-0.01***
	2	-0.05	0.01	-0.02	0.00	-0.01	0.02	-0.04	0.01	-0.01	0.00	0.00	0.01	***-0.01***
avg	**>**	**-0.01**	**0.05**	**0.02**	**0.03**	**0.02**	**0.01**	**-0.01**	**0.07**	**0.02**	**0.03**	**0.02**	**0.01**	***0.00***
AVG	***>***	***-0.08***	***0.05***	***0.00***	***0.03***	***0.02***	***0.03***	***-0.09***	***0.05***	***0.00***	***0.02***	***0.01***	***0.03***	***0.00***

Source: this study.

Table 11: Cp results for the A04, B04, and C04 for oblique winds (45^{o})

		Oblique wind incidence (45^{o})												
		Windward side Cp						Leewardside Cp						*ΔCp*
	(m)	min $_{peak}$	max $_{peak}$	low $_{8th}$	high $_{8th}$	avg $_{90\%}$	sdev	min $_{peak}$	max $_{peak}$	low $_{8th}$	high $_{8th}$	avg $_{90\%}$	sdev	
A4	30	0.11	0.14	0.11	0.11	0.11	0.01	0.09	0.11	0.11	0.11	0.11	0.00	***0.01***
	25	0.10	0.14	0.12	0.12	0.12	0.01	0.06	0.09	0.07	0.07	0.07	0.01	***0.05***
	20	0.07	0.11	0.09	0.10	0.10	0.01	0.05	0.07	0.05	0.06	0.05	0.01	***0.04***
	15	0.05	0.08	0.07	0.07	0.07	0.01	0.03	0.05	0.03	0.03	0.03	0.01	***0.04***
	10	0.03	0.06	0.04	0.05	0.04	0.01	0.01	0.02	0.01	0.01	0.01	0.01	***0.04***
	5	0.00	0.03	0.02	0.02	0.02	0.01	-0.02	0.00	-0.01	-0.01	-0.01	0.01	***0.03***
	2	-0.02	0.01	0.00	0.00	0.00	0.01	-0.03	-0.02	-0.03	-0.03	-0.03	0.01	***0.03***
avg	**>**	**0.05**	**0.08**	**0.06**	**0.07**	**0.07**	**0.01**	**0.03**	**0.05**	**0.03**	**0.03**	**0.03**	**0.01**	***0.03***
B4	30	-0.03	0.07	-0.01	0.00	-0.01	0.02	-0.04	0.14	0.04	0.10	0.07	0.06	***-0.08***
	25	0.04	0.23	0.15	0.17	0.16	0.04	-0.09	0.10	0.01	0.06	0.04	0.06	***0.13***
	20	0.03	0.17	0.09	0.14	0.11	0.03	-0.10	0.10	-0.04	0.08	0.03	0.06	***0.08***
	15	0.02	0.13	0.07	0.08	0.07	0.02	-0.14	0.09	0.00	0.05	0.02	0.07	***0.05***
	10	0.01	0.10	0.03	0.05	0.04	0.02	-0.17	0.08	-0.06	0.06	0.01	0.07	***0.03***
	5	0.01	0.10	0.03	0.05	0.04	0.02	-0.20	0.07	-0.04	0.03	0.00	0.07	***0.04***
	2	-0.02	0.04	0.02	0.02	0.02	0.01	-0.20	0.06	-0.05	0.02	-0.01	0.07	***0.03***
avg	**>**	**0.01**	**0.12**	**0.05**	**0.07**	**0.06**	**0.02**	**-0.14**	**0.09**	**-0.02**	**0.06**	**0.02**	**0.06**	***0.04***
C4	30	0.10	0.11	0.11	0.11	0.11	0.00	0.10	0.11	0.11	0.11	0.11	0.00	***0.00***
	25	0.09	0.09	0.09	0.09	0.09	0.00	0.08	0.09	0.09	0.09	0.09	0.00	***0.00***
	20	0.07	0.07	0.07	0.07	0.07	0.00	0.07	0.07	0.07	0.07	0.07	0.00	***0.00***
	15	0.05	0.05	0.05	0.05	0.05	0.00	0.05	0.05	0.05	0.05	0.05	0.00	***0.00***
	10	0.03	0.03	0.03	0.03	0.03	0.00	0.03	0.03	0.03	0.03	0.03	0.00	***0.00***
	5	0.01	0.01	0.01	0.01	0.01	0.00	0.00	0.01	0.00	0.00	0.00	0.00	***0.01***
	2	0.00	0.01	0.00	0.00	0.00	0.00	0.00	0.01	0.00	0.00	0.00	0.00	***0.00***
avg	**>**	**0.05**	**0.05**	**0.05**	**0.05**	**0.05**	**0.00**	**0.05**	**0.05**	**0.05**	**0.05**	**0.05**	**0.00**	***0.00***
AVG	***>***	***0.04***	***0.09***	***0.06***	***0.06***	***0.06***	***0.01***	***-0.02***	***0.06***	***0.02***	***0.05***	***0.04***	***0.02***	***0.02***

Source: this study.

Table 12: Cp results for the A04, B04, and C04 for orthogonal winds (90°)

		Orthogonal wind incidence (90°)												
		Windward side Cp						Leewardside Cp						ΔCp
	(m)	min peak	max peak	low 8th	high 8th	avg 90%	sdev	min peak	max peak	low 8th	high 8th	avg 90%	sdev	
A4	30	-0.07	0.06	0.02	0.04	0.03	0.03	0.04	0.06	0.05	0.06	0.05	0.01	***-0.02***
	25	-0.02	0.48	0.37	0.40	0.38	0.13	-0.03	0.02	-0.01	0.00	0.00	0.01	***0.39***
	20	-0.07	0.33	0.24	0.30	0.26	0.10	-0.04	0.01	-0.02	0.00	-0.01	0.01	***0.27***
	15	-0.06	0.23	0.17	0.18	0.17	0.08	-0.03	0.01	-0.02	0.00	-0.01	0.02	***0.18***
	10	-0.12	0.13	0.11	0.13	0.12	0.07	-0.04	0.02	-0.03	0.01	-0.01	0.02	***0.13***
	5	-0.13	0.15	0.10	0.13	0.12	0.08	-0.05	0.02	-0.02	-0.01	-0.01	0.02	***0.13***
	2	-0.10	0.18	0.12	0.17	0.15	0.08	-0.06	0.01	-0.04	-0.02	0.00	0.02	***0.15***
avg	**>**	**-0.08**	**0.22**	**0.16**	**0.19**	**0.18**	**0.08**	**-0.03**	**0.02**	**-0.01**	**0.01**	**0.00**	**0.02**	***0.17***
B4	30	0.00	0.11	0.08	0.09	0.09	0.03	0.08	0.10	0.09	0.09	0.09	0.00	***0.00***
	25	0.04	0.33	0.24	0.26	0.25	0.06	0.02	0.07	0.03	0.03	0.03	0.01	***0.22***
	20	0.05	0.25	0.13	0.21	0.15	0.04	-0.01	0.04	0.00	0.02	0.02	0.01	***0.13***
	15	0.02	0.17	0.09	0.09	0.09	0.03	-0.03	0.02	0.00	0.01	0.01	0.01	***0.08***
	10	-0.04	0.08	0.03	0.07	0.05	0.03	0.00	0.03	0.01	0.02	0.02	0.01	***0.03***
	5	-0.07	0.10	0.03	0.07	0.06	0.05	0.04	0.06	0.04	0.05	0.05	0.01	***0.01***
	2	-0.04	0.15	0.05	0.10	0.08	0.06	0.04	0.07	0.06	0.06	0.06	0.01	***0.02***
avg	**>**	**0.00**	**0.17**	**0.09**	**0.13**	**0.11**	**0.04**	**0.02**	**0.05**	**0.03**	**0.04**	**0.04**	**0.01**	***0.07***
C4	30	0.02	0.09	0.06	0.07	0.07	0.02	0.03	0.07	0.05	0.06	0.05	0.01	***0.01***
	25	0.04	0.16	0.04	0.07	0.05	0.04	-0.02	0.04	0.01	0.02	0.01	0.01	***0.04***
	20	0.02	0.13	0.03	0.06	0.05	0.02	-0.02	0.04	-0.01	0.04	0.02	0.02	***0.04***
	15	0.00	0.09	0.02	0.03	0.03	0.02	-0.03	0.04	0.00	0.02	0.01	0.02	***0.01***
	10	-0.03	0.03	-0.01	0.00	0.00	0.01	-0.03	0.03	-0.02	0.02	0.00	0.02	***-0.01***
	5	-0.05	0.00	-0.03	-0.02	-0.02	0.01	-0.03	0.02	-0.02	0.01	0.00	0.02	***-0.02***
	2	-0.06	0.00	-0.02	-0.01	-0.02	0.02	-0.02	0.02	-0.01	0.01	0.00	0.02	***-0.02***
avg	**>**	**-0.01**	**0.07**	**0.01**	**0.03**	**0.02**	**0.02**	**-0.02**	**0.04**	**0.00**	**0.03**	**0.01**	**0.02**	***0.01***
AVG	***>***	***-0.03***	***0.16***	***0.09***	***0.12***	***0.10***	***0.05***	***-0.01***	***0.04***	***0.01***	***0.02***	***0.02***	***0.01***	***0.08***

Source: this study.

Figure 13: B02 STEP UP scenario Cp results for parallel, orthogonal and oblique winds (H/W= 0.67; 0°, 45°, 90°):

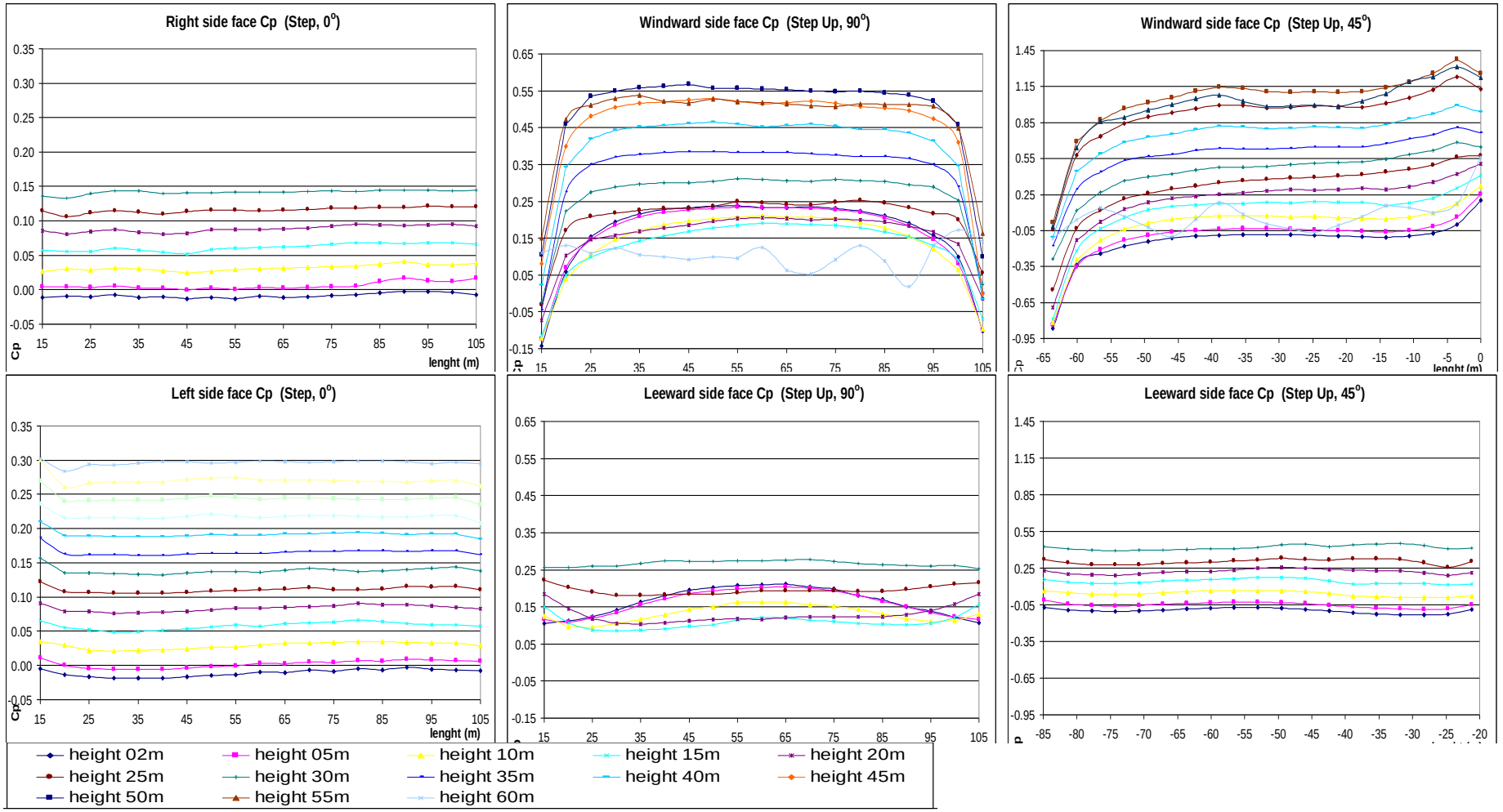

Source: this study.

Figure 14: B02 STEP UP scenario Cp results for parallel, orthogonal and oblique winds (H/W= 0.67; 0°, 45°, 90°):

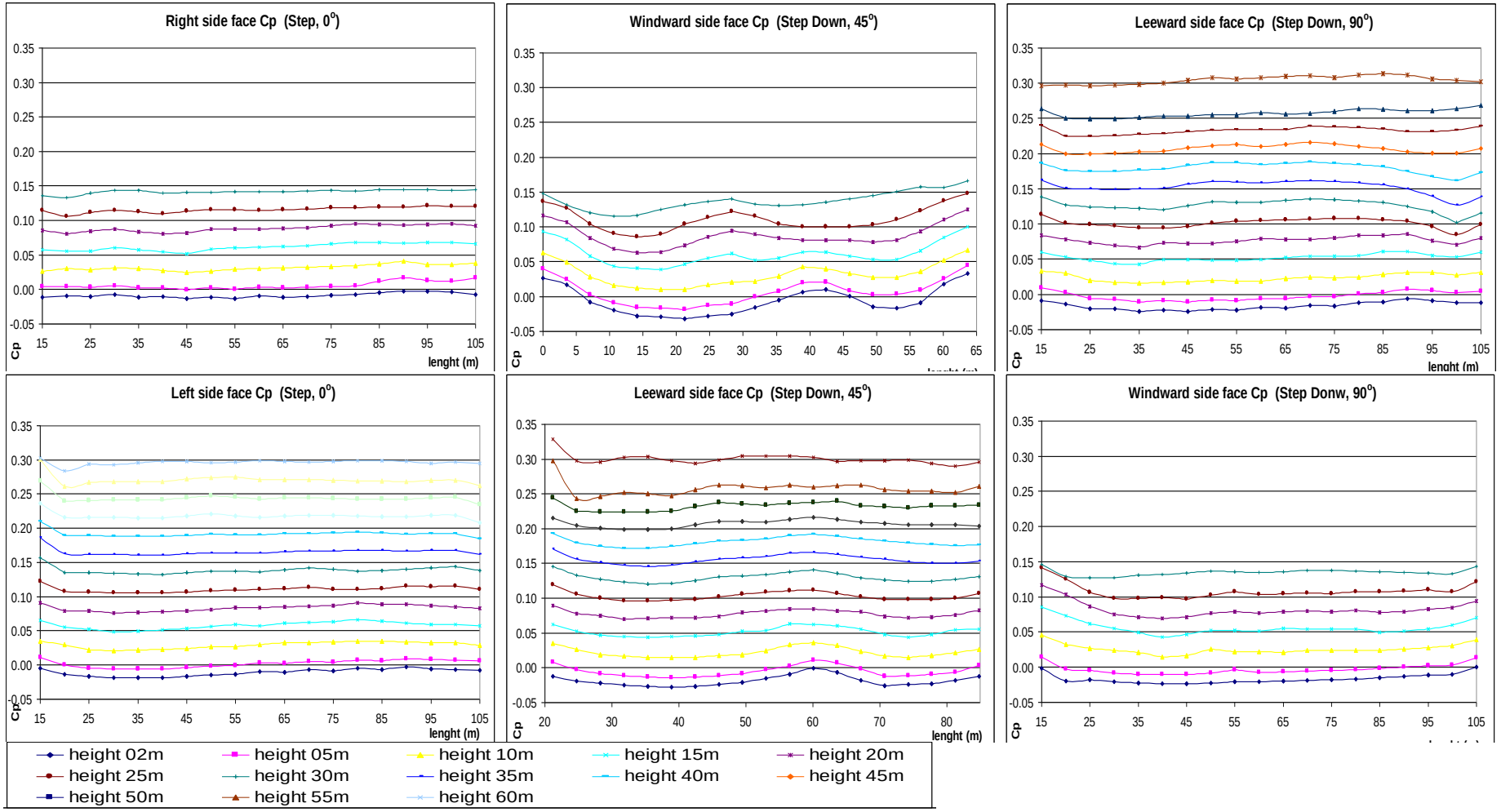

Source: this study.

Table 13: Cp results for the B2 STEP scenario for parallel winds (0^o)

B2 STEP	Parallel wind incidence (0^o)								
	Right side Cp				Left ide Cp				⊿Cp
(m)	low 8th	high 8th	avg 90%	sdev	low 8th	high 8th	avg 90%	sdev	
60	-	-	-	-	0.30	0.30	0.30	0.00	-
55	-	-	-	-	0.27	0.27	0.27	0.01	-
50	-	-	-	-	0.24	0.25	0.24	0.01	-
45	-	-	-	-	0.22	0.22	0.22	0.00	-
40	-	-	-	-	0.19	0.19	0.19	0.00	-
35	-	-	-	-	0.16	0.17	0.16	0.00	-
30	0.14	0.14	0.14	0.00	0.13	0.14	0.14	0.00	***0.00***
25	0.11	0.12	0.12	0.00	0.11	0.11	0.11	0.00	***-0.01***
20	0.08	0.09	0.09	0.00	0.08	0.09	0.08	0.00	***0.00***
15	0.06	0.07	0.06	0.01	0.05	0.06	0.06	0.01	***0.00***
10	0.03	0.04	0.03	0.00	0.02	0.03	0.03	0.00	***0.00***
5	0.00	0.01	0.00	0.01	0.00	0.01	0.00	0.01	***0.00***
2	-0.01	-0.01	-0.01	0.00	-0.02	-0.01	-0.01	0.01	***0.00***
avg	***0.06***	***0.07***	***0.06***	***0.00***	***0.13***	***0.14***	***0.14***	***0.00***	***0.00***

Source: this study.

Table 14: Cp results for the B2 STEP UP for orthogonal winds (90^o)

B2 STEP UP	Orthogonal wind incidence (90^o)								
	Windward side Cp				Leeward side Cp				⊿Cp
(m)	low 8th	high 8th	avg 90%	sdev	low 8th	high 8th	avg 90%	sdev	
60	-	-	-	-	0.09	0.12	0.10	0.03	-
55	-	-	-	-	0.51	0.52	0.51	0.10	-
50	-	-	-	-	0.46	0.56	0.55	0.12	-
45	-	-	-	-	0.48	0.52	0.51	0.13	-
40	-	-	-	-	0.35	0.46	0.45	0.12	-
35	-	-	-	-	0.35	0.38	0.37	0.11	-
30	0.26	0.27	0.27	0.01	0.25	0.31	0.30	0.08	***0.03***
25	0.19	0.19	0.19	0.01	0.22	0.25	0.23	0.06	***0.04***
20	0.11	0.14	0.12	0.02	0.13	0.20	0.18	0.06	***0.06***
15	0.10	0.11	0.10	0.02	0.13	0.19	0.16	0.08	***0.06***
10	0.10	0.16	0.13	0.02	0.06	0.21	0.18	0.09	***0.05***
5	0.13	0.19	0.17	0.03	0.15	0.23	0.21	0.09	***0.04***
2	0.14	0.20	0.17	0.04	0.16	0.23	0.22	0.10	***0.05***
avg	***0.15***	***0.18***	***0.17***	***0.02***	***0.26***	***0.32***	***0.31***	***0.09***	***0.05***

Source: this study.

Table 15: Cp results for the B2 STEP UP for oblique winds (45°)

B2 STEP UP	Oblique wind incidence (45°)								
	Windward side Cp				Leeward side Cp				⊿Cp
(m)	low 8th	high 8th	avg 90%	sdev	low 8th	high 8th	avg 90%	sdev	
60	-	-	-	-	-0.01	0.14	0.06	0.13	-
55	-	-	-	-	0.98	1.08	1.01	0.24	-
50	-	-	-	-	0.87	1.26	1.11	0.25	-
45	-	-	-	-	0.93	0.99	0.98	0.23	-
40	-	-	-	-	0.59	0.92	0.81	0.20	-
35	-	-	-	-	0.59	0.65	0.63	0.19	-
30	0.40	0.43	0.42	0.02	0.27	0.62	0.49	0.19	***0.07***
25	0.29	0.32	0.31	0.02	0.30	0.42	0.38	0.22	***0.07***
20	0.19	0.25	0.22	0.02	0.02	0.35	0.28	0.22	***0.05***
15	0.12	0.16	0.14	0.02	0.15	0.19	0.17	0.21	***0.04***
10	0.01	0.07	0.04	0.02	-0.13	0.09	0.06	0.19	***0.02***
5	-0.06	-0.04	-0.05	0.02	-0.06	-0.04	-0.05	0.18	***0.00***
2	-0.10	-0.08	-0.10	0.02	-0.11	-0.08	-0.10	0.17	***0.00***
avg	***0.12***	***0.16***	***0.14***	***0.02***	***0.34***	***0.51***	***0.45***	***0.20***	***0.04***

Source: this study.

Table 16: Cp results for the B2 STEP-DOWN for orthogonal winds (90°)

B2 STEP DOWN	Orthogonal wind incidence (90°)								
	Windward side Cp				Leeward side Cp				⊿Cp
(m)	low 8th	high 8th	avg 90%	sdev	low 8th	high 8th	avg 90%	sdev	
60	-	-	-	-	0.30	0.31	0.31	0.01	-
55	-	-	-	-	0.25	0.26	0.26	0.01	-
50	-	-	-	-	0.23	0.24	0.23	0.00	-
45	-	-	-	-	0.20	0.21	0.21	0.01	-
40	-	-	-	-	0.17	0.19	0.18	0.01	-
35	-	-	-	-	0.15	0.16	0.16	0.01	-
30	0.13	0.14	0.14	0.00	0.12	0.13	0.13	0.01	***0.01***
25	0.10	0.11	0.11	0.01	0.10	0.11	0.10	0.01	***0.00***
20	0.07	0.09	0.08	0.01	0.07	0.08	0.08	0.01	***0.00***
15	0.05	0.06	0.05	0.01	0.05	0.06	0.05	0.01	***0.00***
10	0.02	0.03	0.02	0.01	0.02	0.03	0.02	0.01	***0.00***
5	-0.01	0.00	0.00	0.01	-0.01	0.00	-0.01	0.01	***0.00***
2	-0.02	-0.02	-0.02	0.01	-0.02	-0.01	-0.02	0.01	***0.00***
avg	***0.05***	***0.06***	***0.05***	***0.01***	***0.13***	***0.14***	***0.13***	***0.01***	***-0.08***

Source: this study.

Table 17: Cp results for the B2 Step-Down for oblique winds (45°)

B2 STEP DOWN	Oblique wind incidence (45°)								
	Windward side Cp				Leeward side Cp				⊿Cp
(m)	low 8th	high 8th	avg 90%	sdev	low 8th	high 8th	avg 90%	sdev	
60	-	-	-	-	0.30	0.30	0.30	0.01	-
55	-	-	-	-	0.25	0.26	0.26	0.01	-
50	-	-	-	-	0.22	0.24	0.23	0.01	-
45	-	-	-	-	0.20	0.21	0.21	0.01	-
40	-	-	-	-	0.17	0.19	0.18	0.01	-
35	-	-	-	-	0.15	0.16	0.16	0.01	-
30	0.13	0.15	0.13	0.01	0.12	0.14	0.13	0.01	***0.01***
25	0.10	0.12	0.10	0.02	0.10	0.11	0.10	0.01	***0.00***
20	0.07	0.11	0.08	0.02	0.07	0.08	0.08	0.01	***0.01***
15	0.05	0.06	0.06	0.02	0.05	0.06	0.05	0.01	***0.01***
10	0.01	0.05	0.03	0.02	0.01	0.03	0.02	0.01	***0.01***
5	-0.01	0.01	0.00	0.02	-0.01	0.00	-0.01	0.01	***0.01***
2	-0.03	0.00	-0.01	0.02	-0.02	-0.01	-0.02	0.01	***0.01***
avg	***0.05***	***0.07***	***0.06***	***0.02***	***0.12***	***0.14***	***0.13***	***0.01***	***-0.07***

Source: this study.

Figure 15: Canyon 'A' and canyon ‘B’ Cp results for the right and left faces (D01, 0°)

- Canyon 'A' Cp for the right and left faces (D01, 0°):

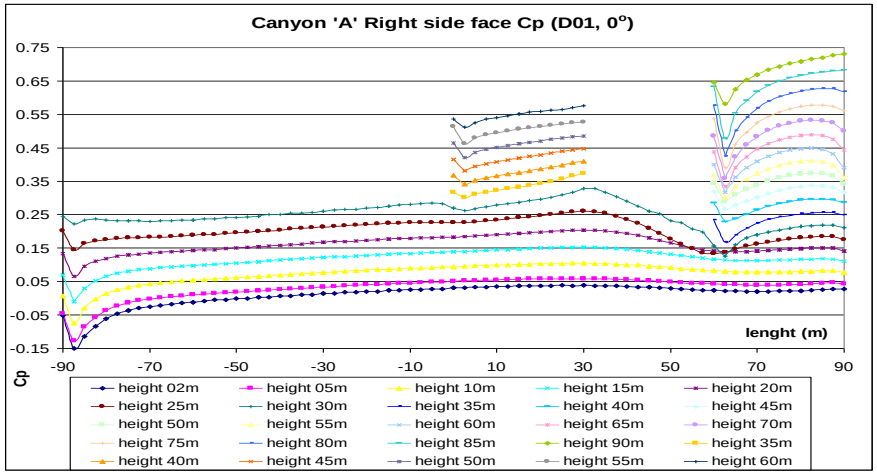

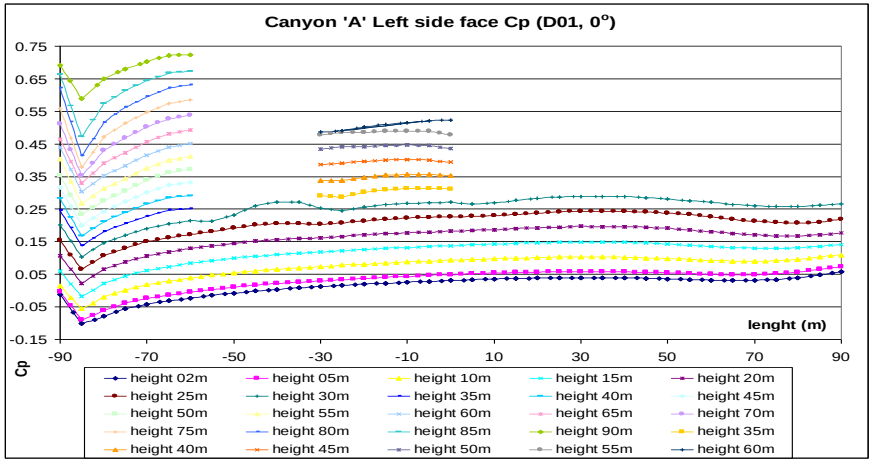

- Canyon 'B' Cp for the right and left faces (D01, 0°):

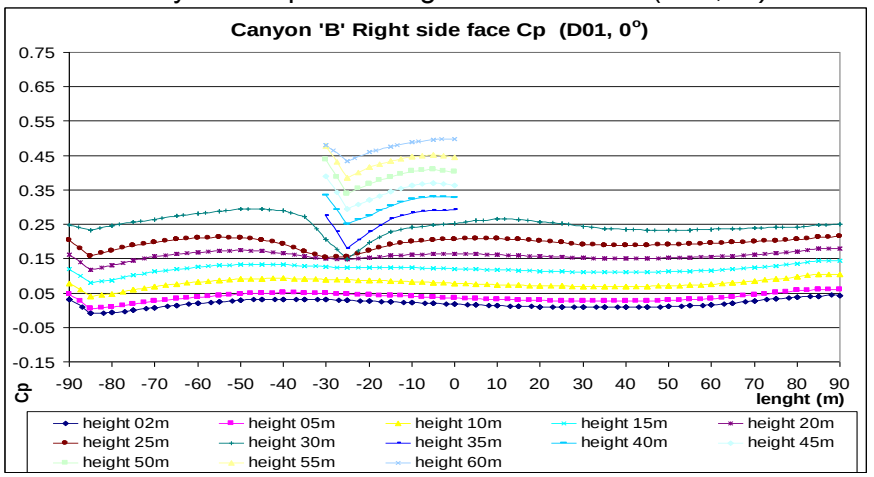

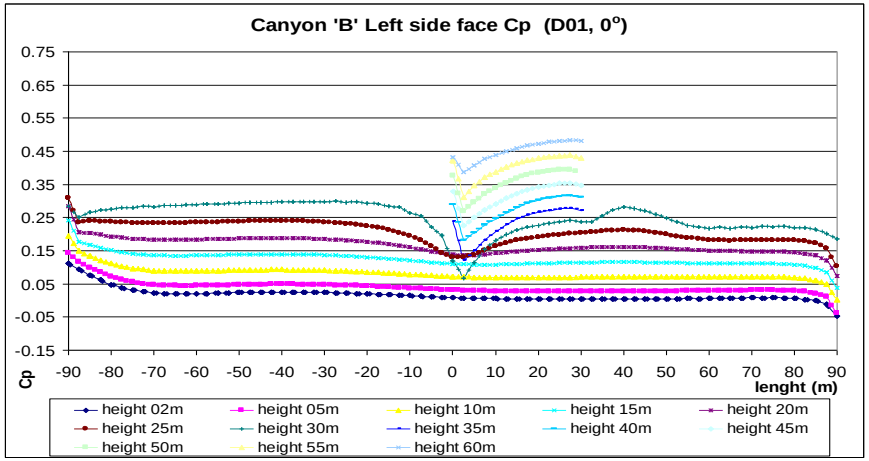

Source: this study.

Figure 16: Canyon 'A' and canyon ‘B’ Cp results for the windward and leeward faces (D01, 90°)

- Canyon 'A' Cp for the WW and LW faces (D01, 90°):

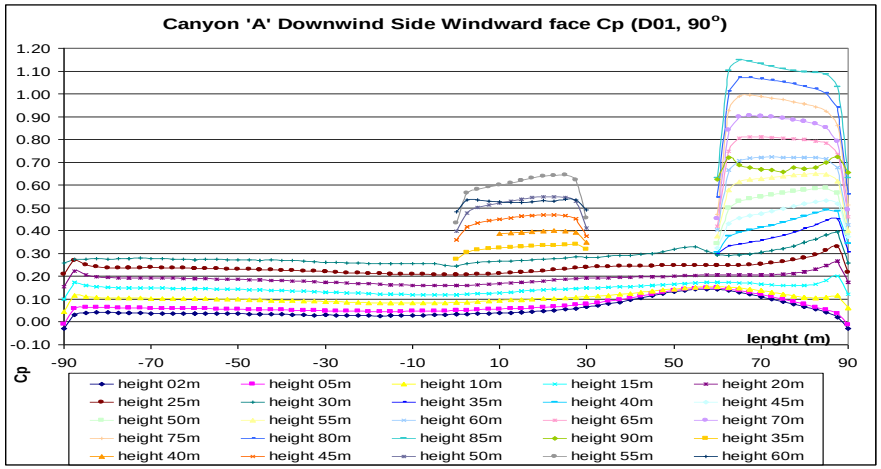

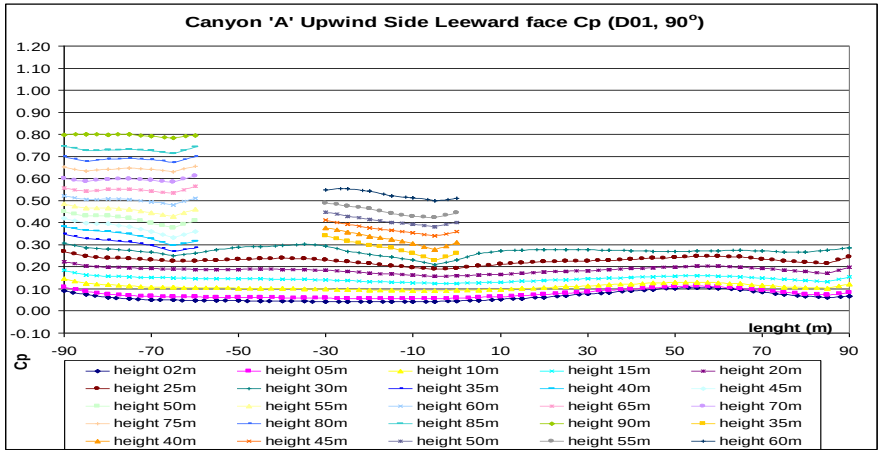

- Canyon 'B' Cp for the WW and LW faces (D01, 90°):

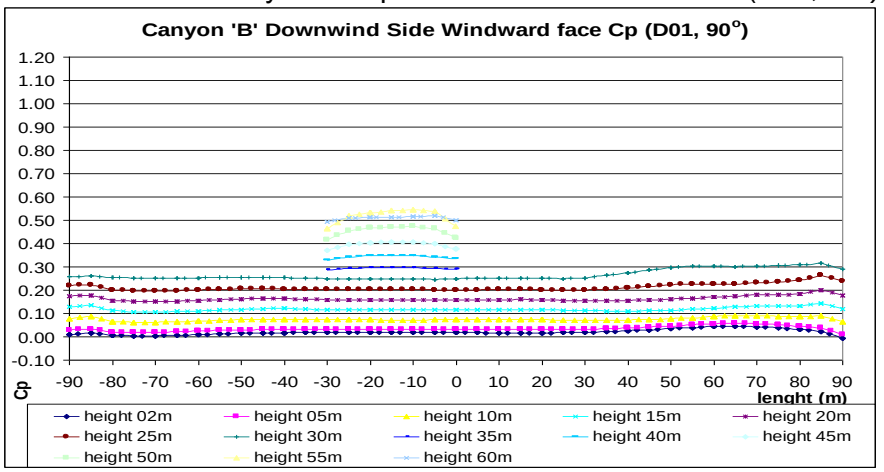

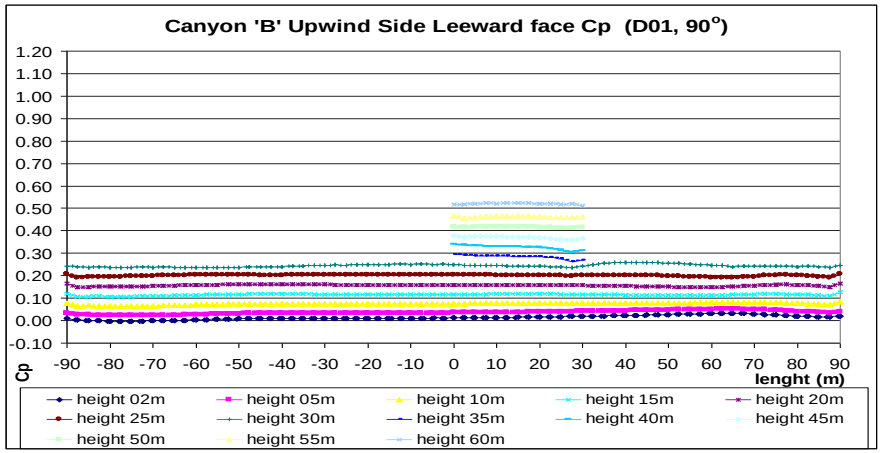

Source: this study.

Figure 17: Canyon 'A' and canyon ‘B’ Cp results for the windward and leeward faces (D01, 45°)

- Canyon 'A' Cp for the WW and LW faces (D01, 45°):

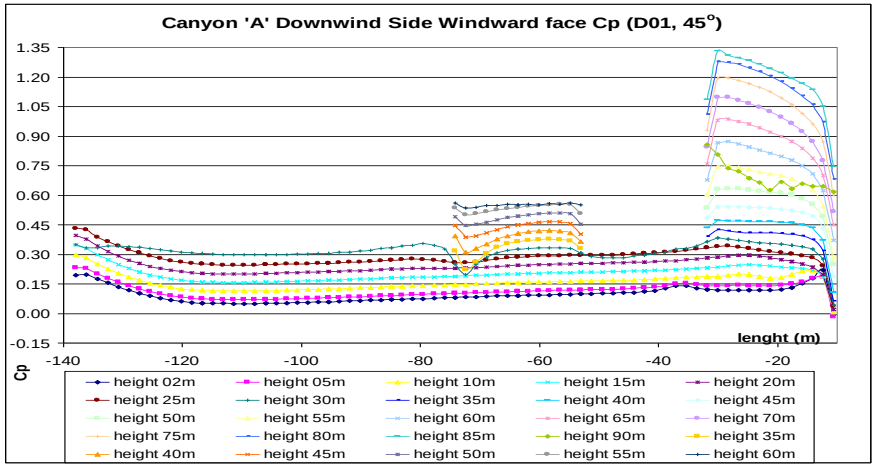

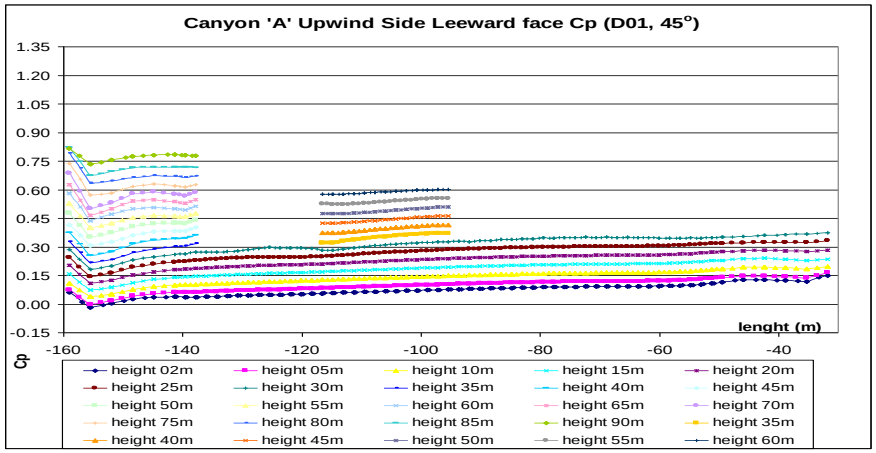

- Canyon 'B' Cp for the WW and LW faces (D01, 45°):

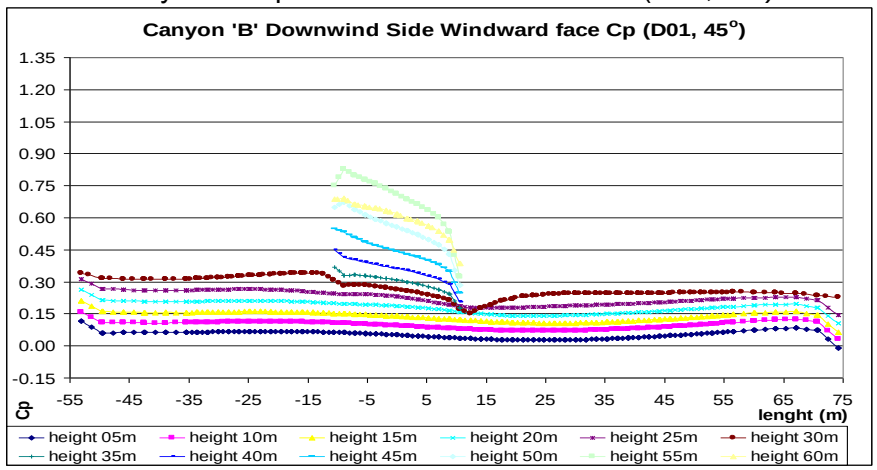

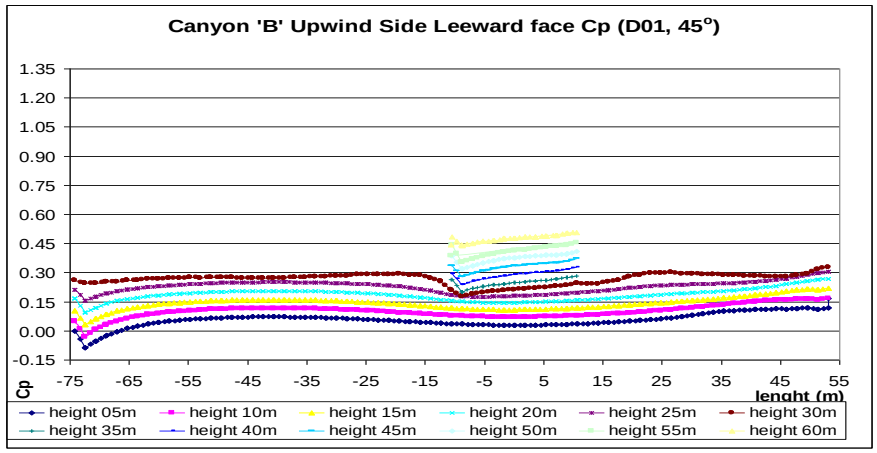

Source: this study.

Figure 18: Canyon 'A' and canyon 'B' Cp results for the right and the left faces (D02, 0°)

- Canyon 'A' Cp for the right and left faces (D02, 0°):
- Canyon 'B' Cp for the right and left faces (D02, 0°):

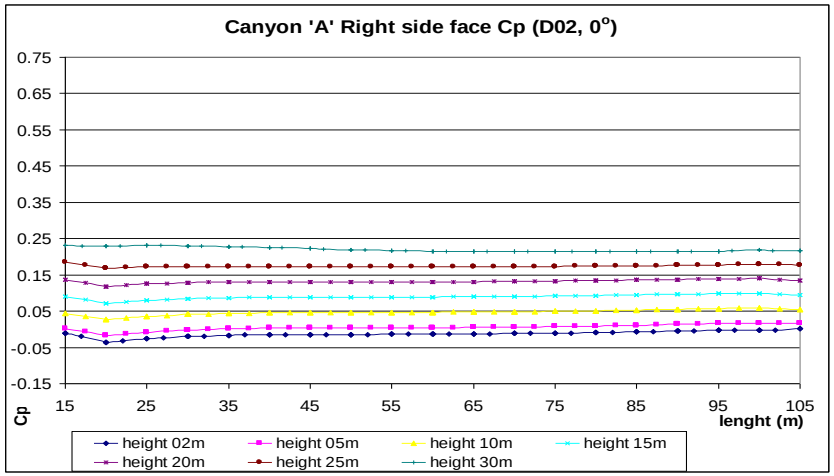

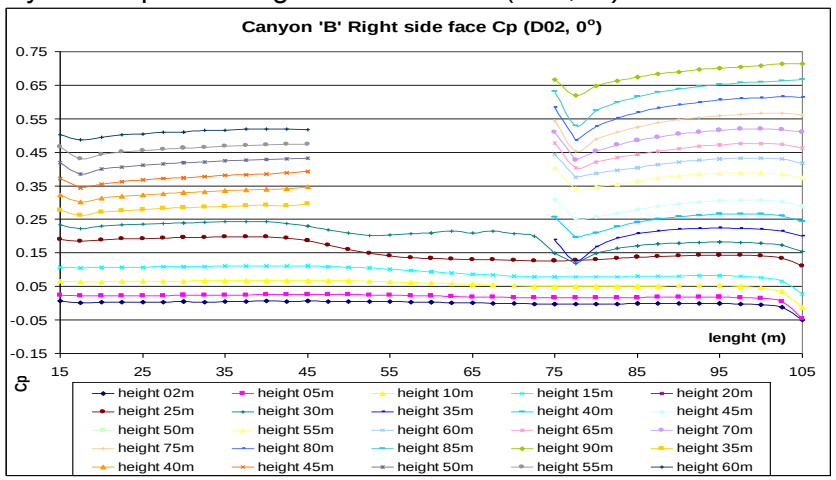

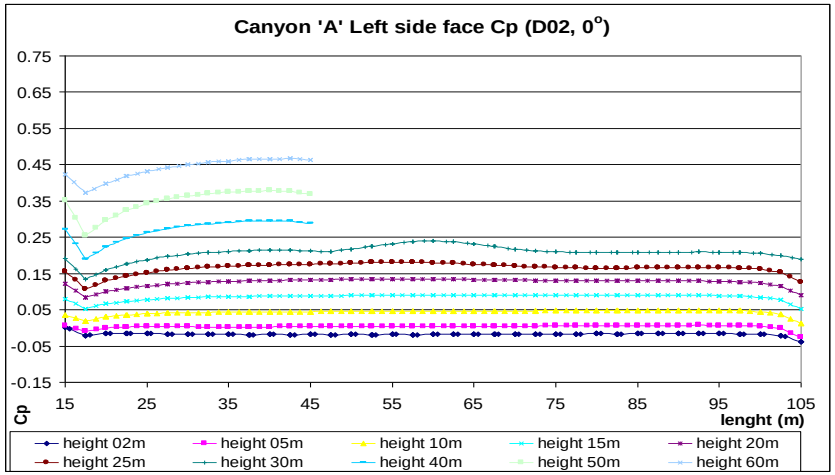

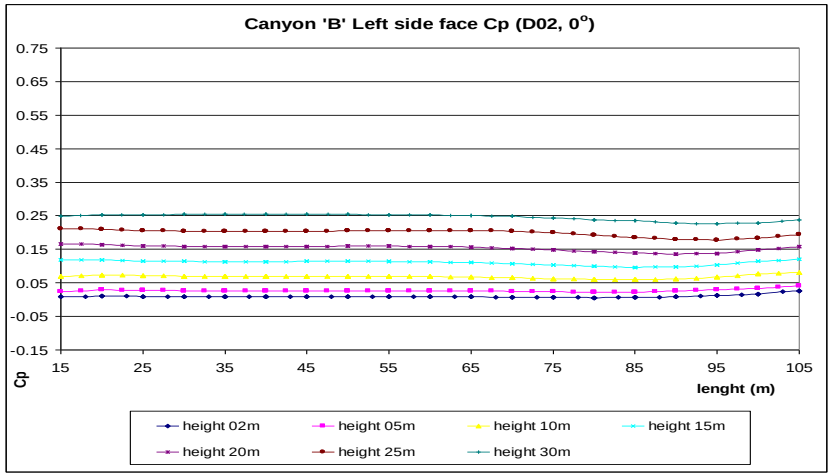

Source: this study.

Figure 19: Right side canyon ‘A’ and canyon ‘B’ Cp results for the WW and the LW faces (D02, 90^{o})

- Right canyon ‘A’ Cp for the WW and LW faces (D02, 90^{o}):
- Right canyon 'B' Cp for the WW and LW faces (D02, 90^{o}):

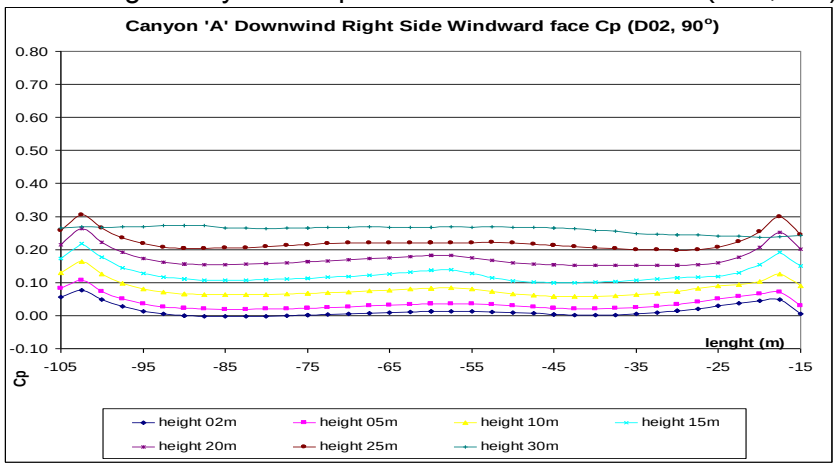

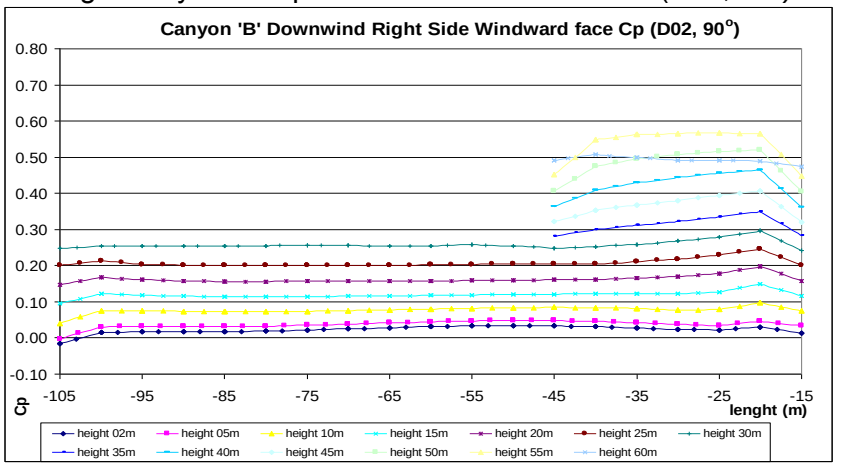

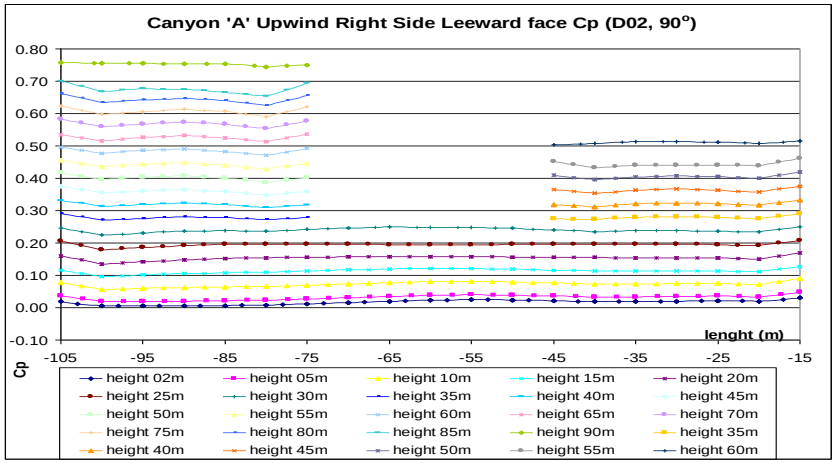

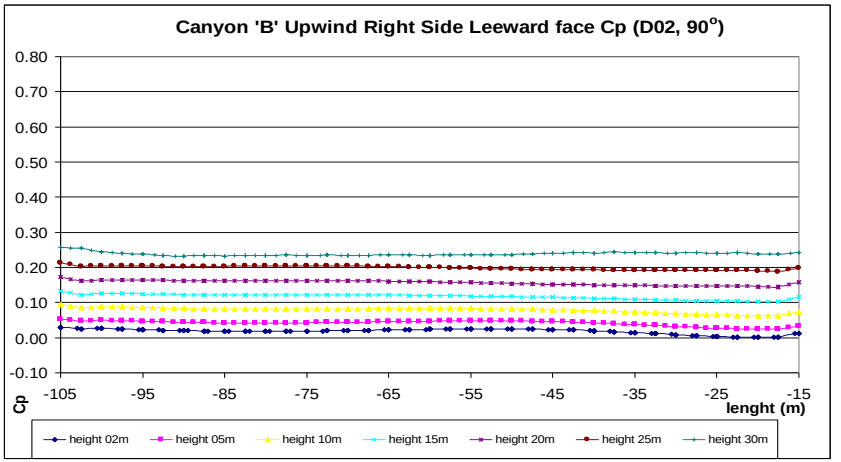

Source: this study.

Figure 20: Left side canyon ‘A’ and canyon ‘B’ Cp results for the WW and the LW faces (D02, 90°)

- Left canyon ‘A’ Cp for the WW and LW faces (D02, 90°):
- Leftt canyon 'B' Cp for the WW and LW faces (D02, 90°):

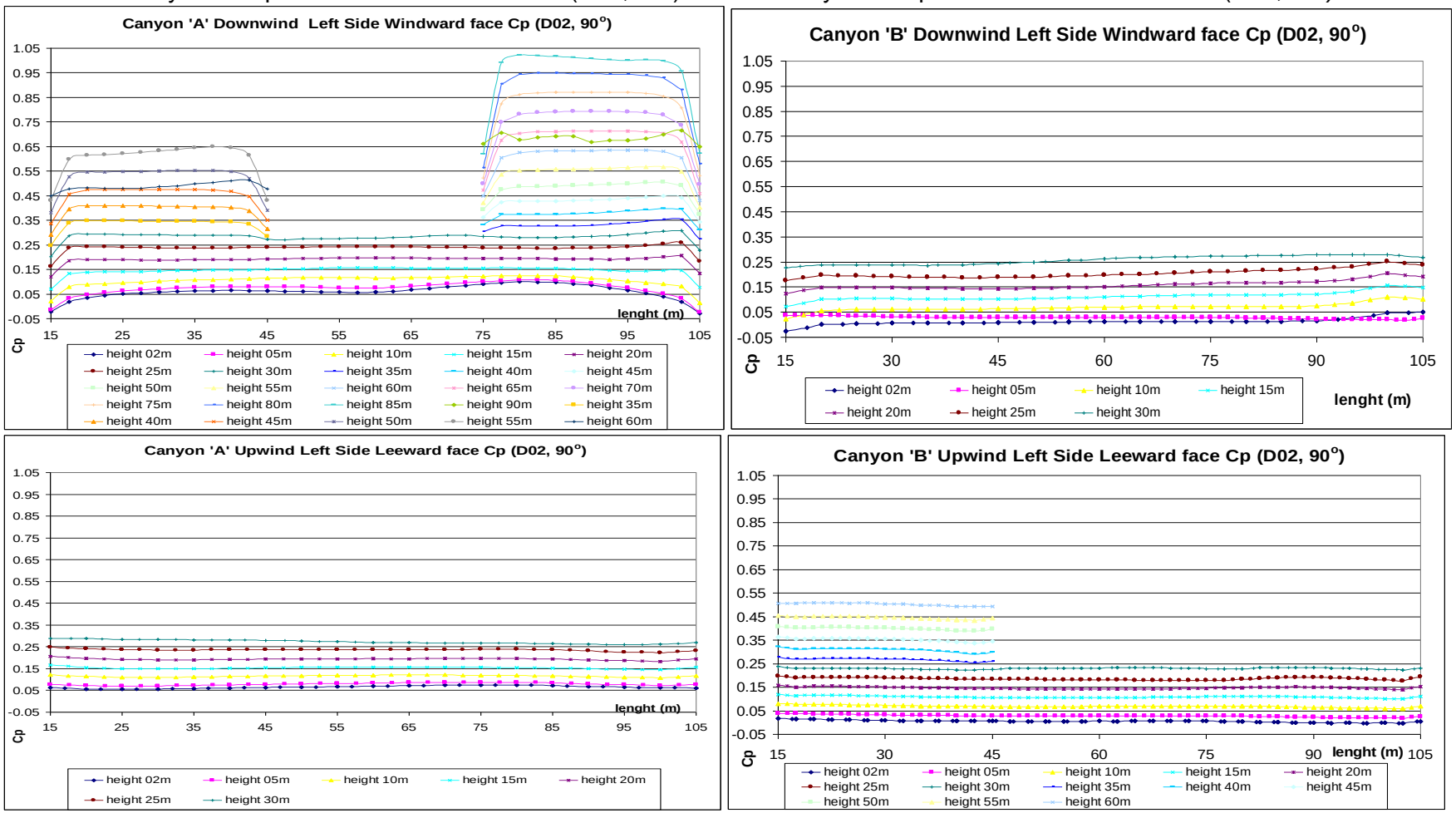

Source: this study.

Figure 21: Canyon ‘A’ and canyon ‘B’ Cp results for the WW and the LW faces (D03, 0°)

- Canyon ‘A’ Cp for the WW and LW faces (D02, 45°):

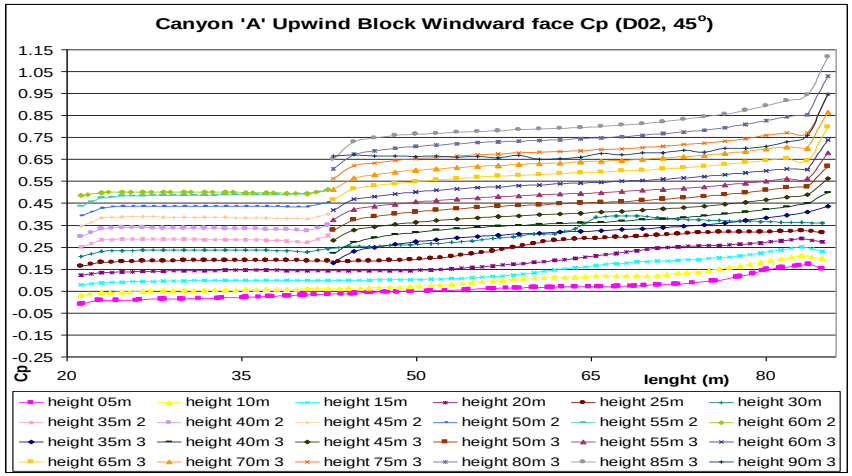

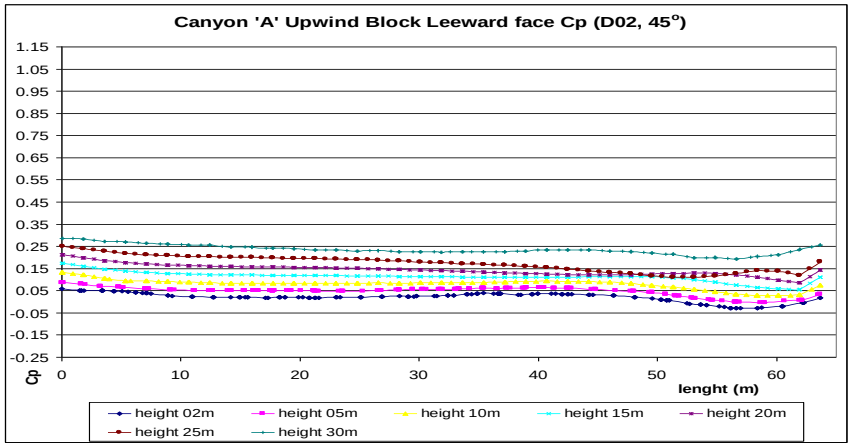

- Canyon 'B' Cp for the WW and LW faces (D02, 45°):

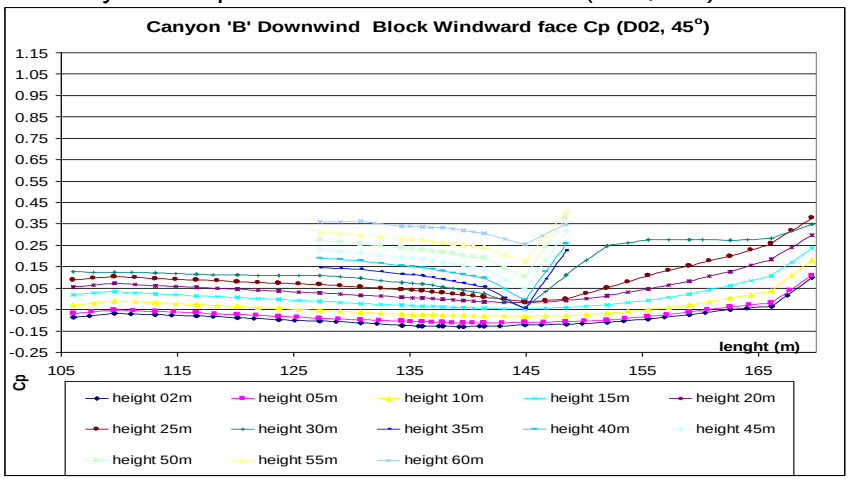

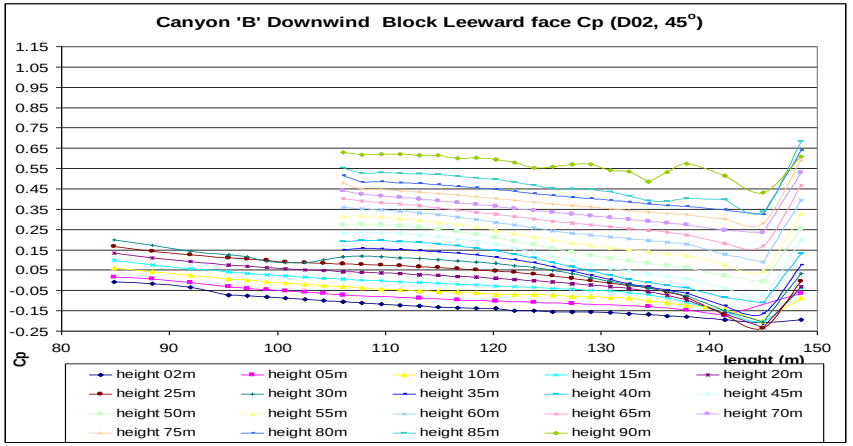

Source: this study.

Figure 22: Canyon ‘A’ and canyon ‘B’ Cp results for the WW and the LW faces (D03, 0°)

- Canyon ‘A’ Cp for the WW and LW faces (D03, 0°):
- Canyon 'B' Cp for the WW and LW faces (D03, 0°):

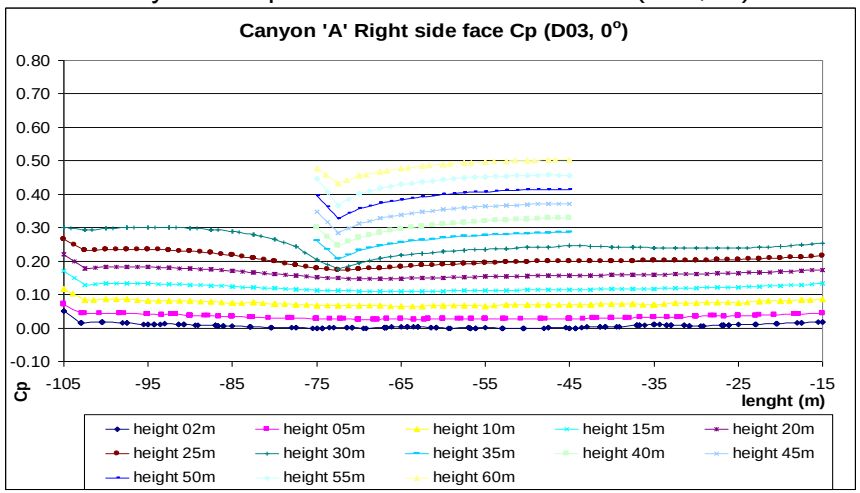

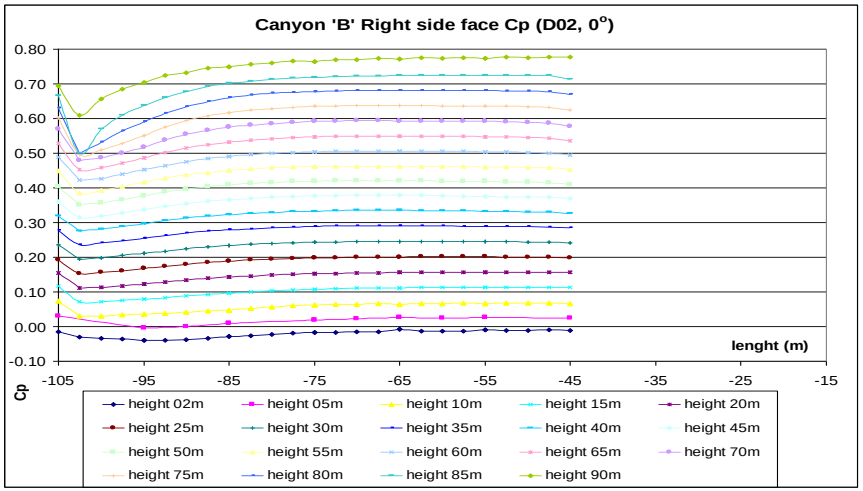

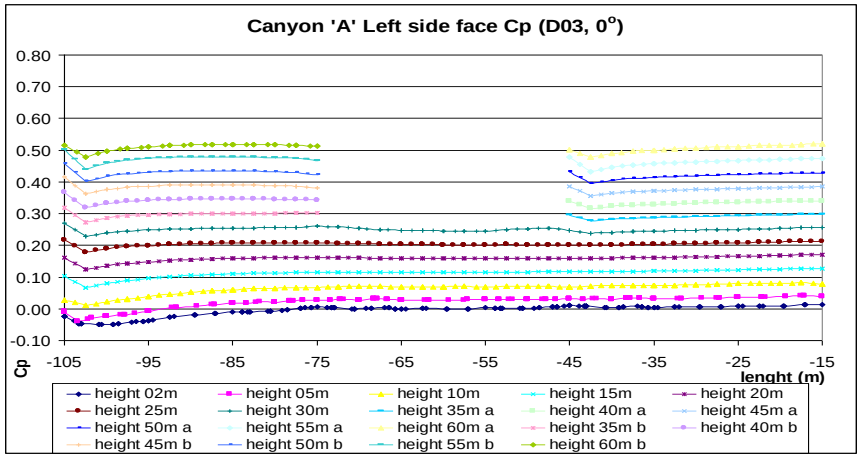

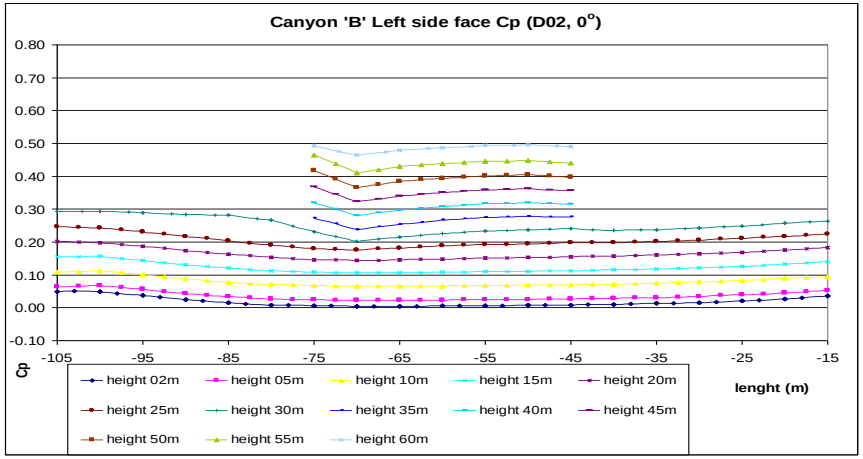

Source: this study.

Figure 23: Right side canyon ‘A’ and canyon ‘B’ Cp results for the WW and the LW faces (D03, 90°)

- Right canyon ‘A’ Cp for the WW and LW faces (D03, 90°):
- Right canyon 'B' Cp for the WW and LW faces (D03, 90°):

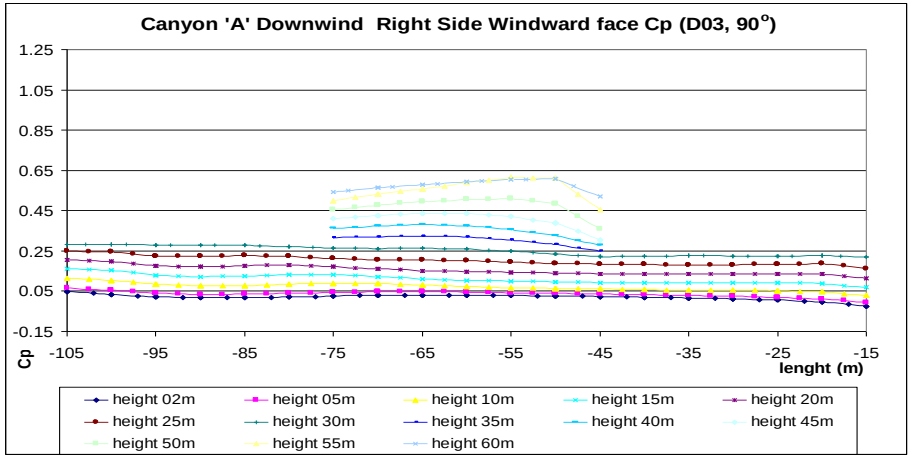

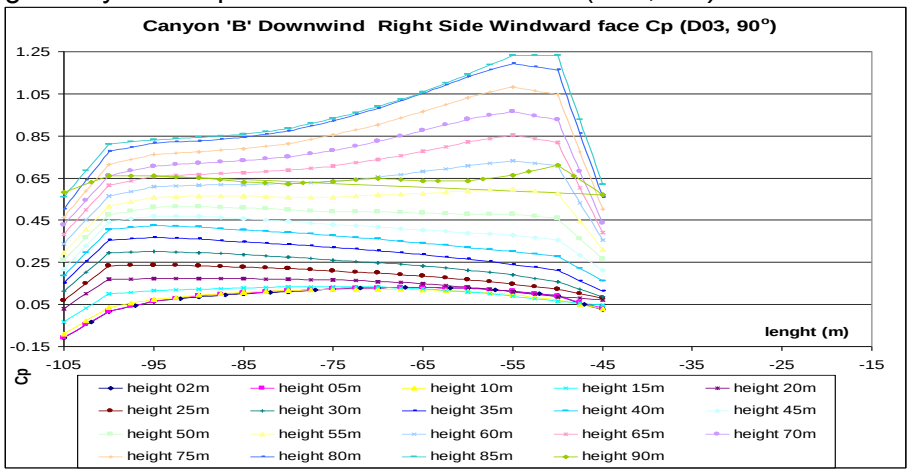

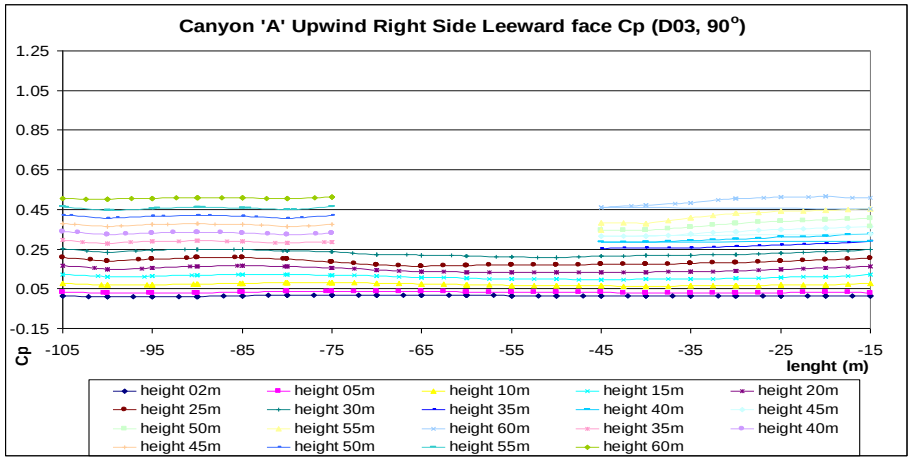

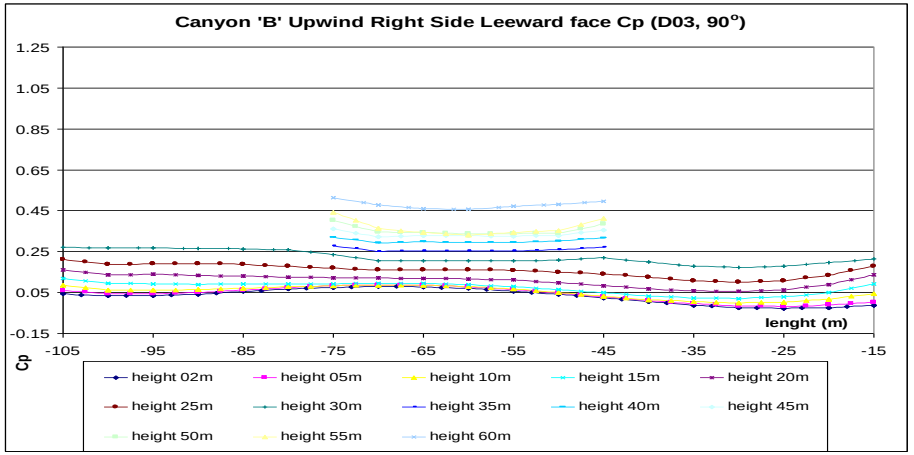

Source: this study.

Figure 24: Left side canyon ‘A’ and canyon ‘B’ Cp results for the WW and the LW faces (D03, 90°)

- Left canyon ‘A’ Cp for the WW and LW faces (D03, 90°):

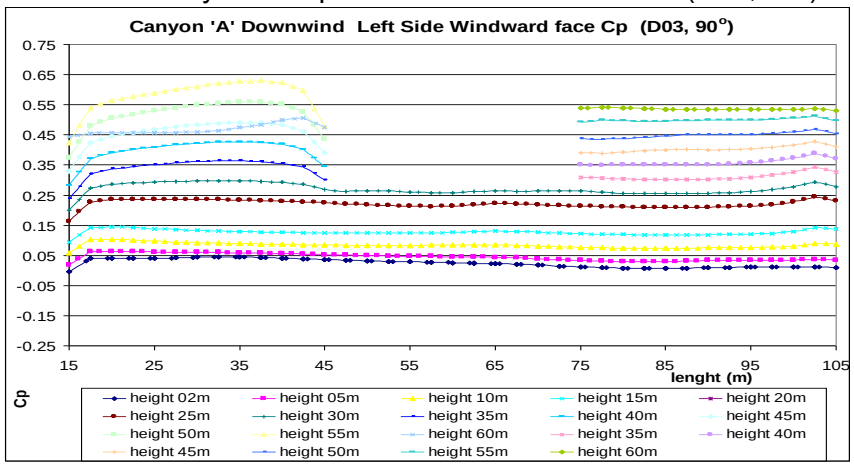

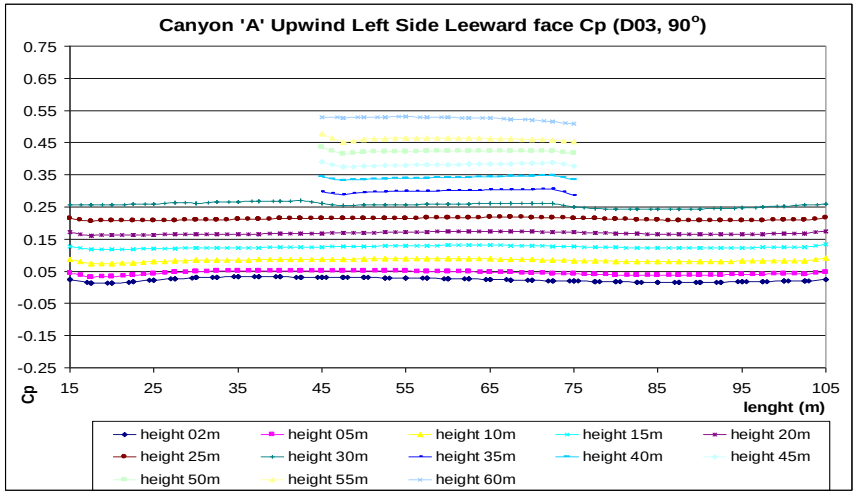

- Left canyon 'B' Cp for the WW and LW faces (D03, 90°):

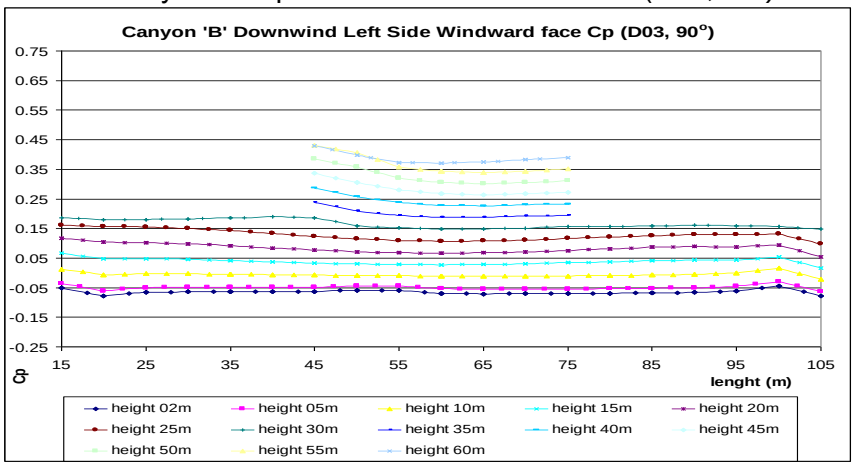

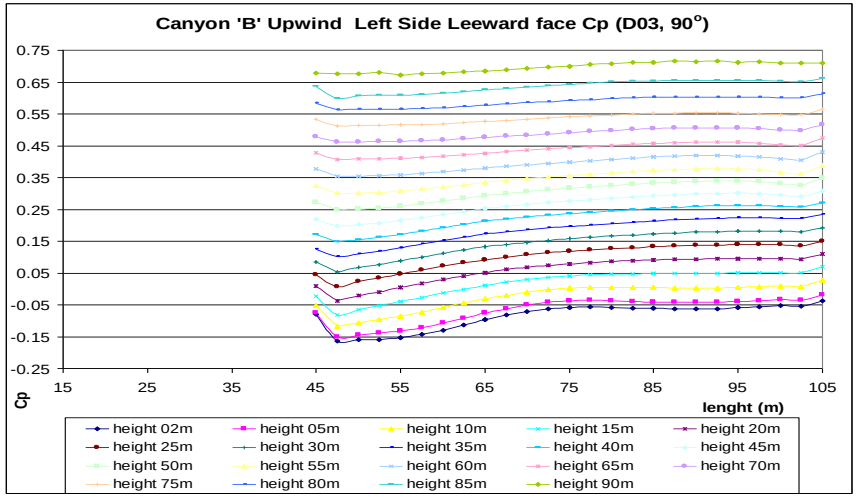

Source: this study.

Figure 25: Canyon ‘A’ and canyon ‘B’ Cp results for the WW and the LW faces (D03, 45°)

- Canyon ‘A’ Cp for the WW and LW faces (D03, 45°):

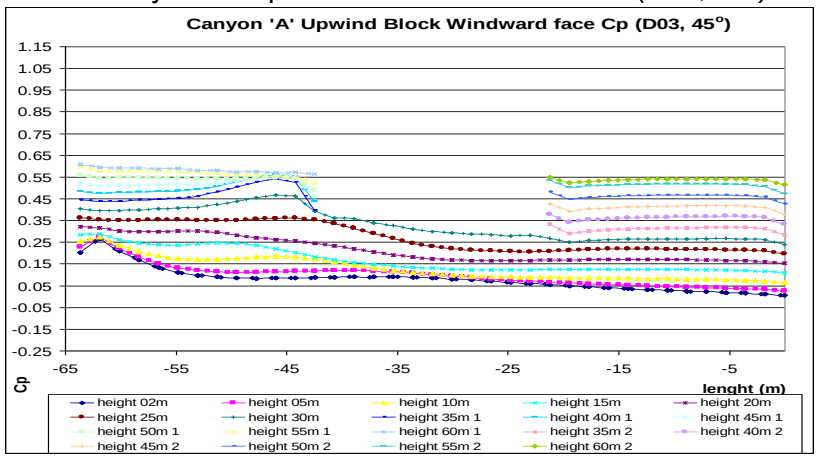

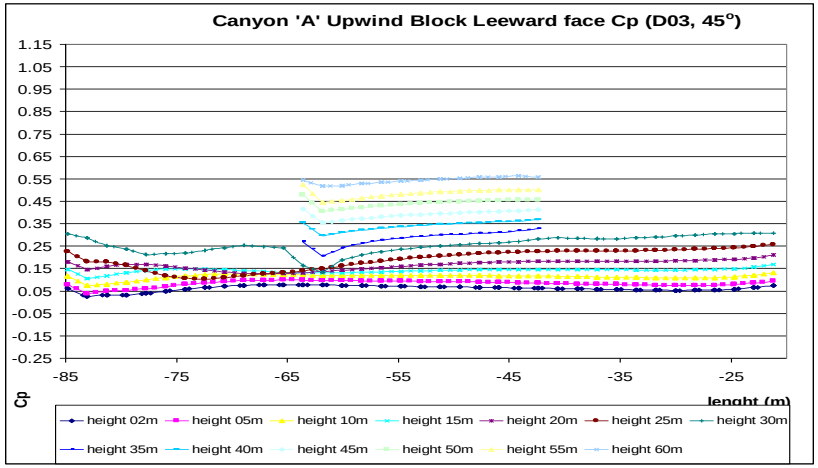

- Canyon 'B' Cp for the WW and LW faces (D03, 45°):

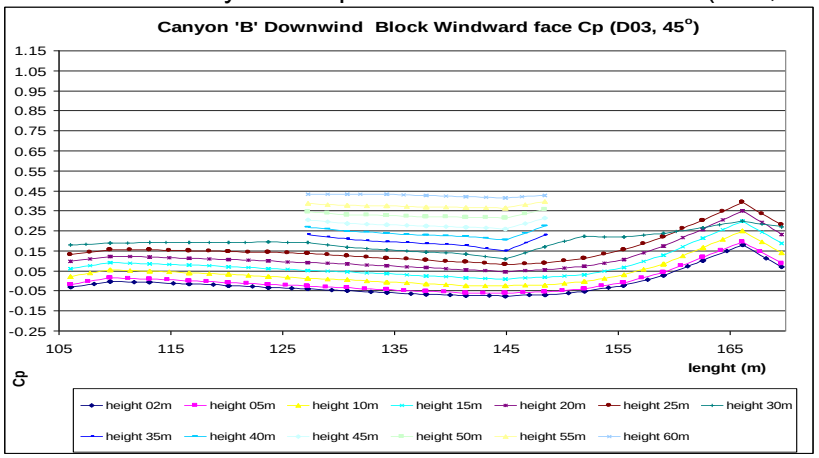

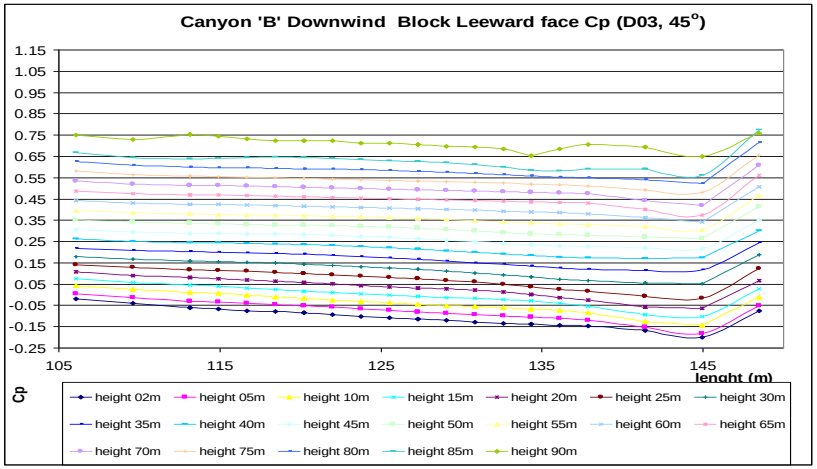

Source: this study.

Figure 26: T-01 windward, leeward, right and left side Cp results (D04, 0°)

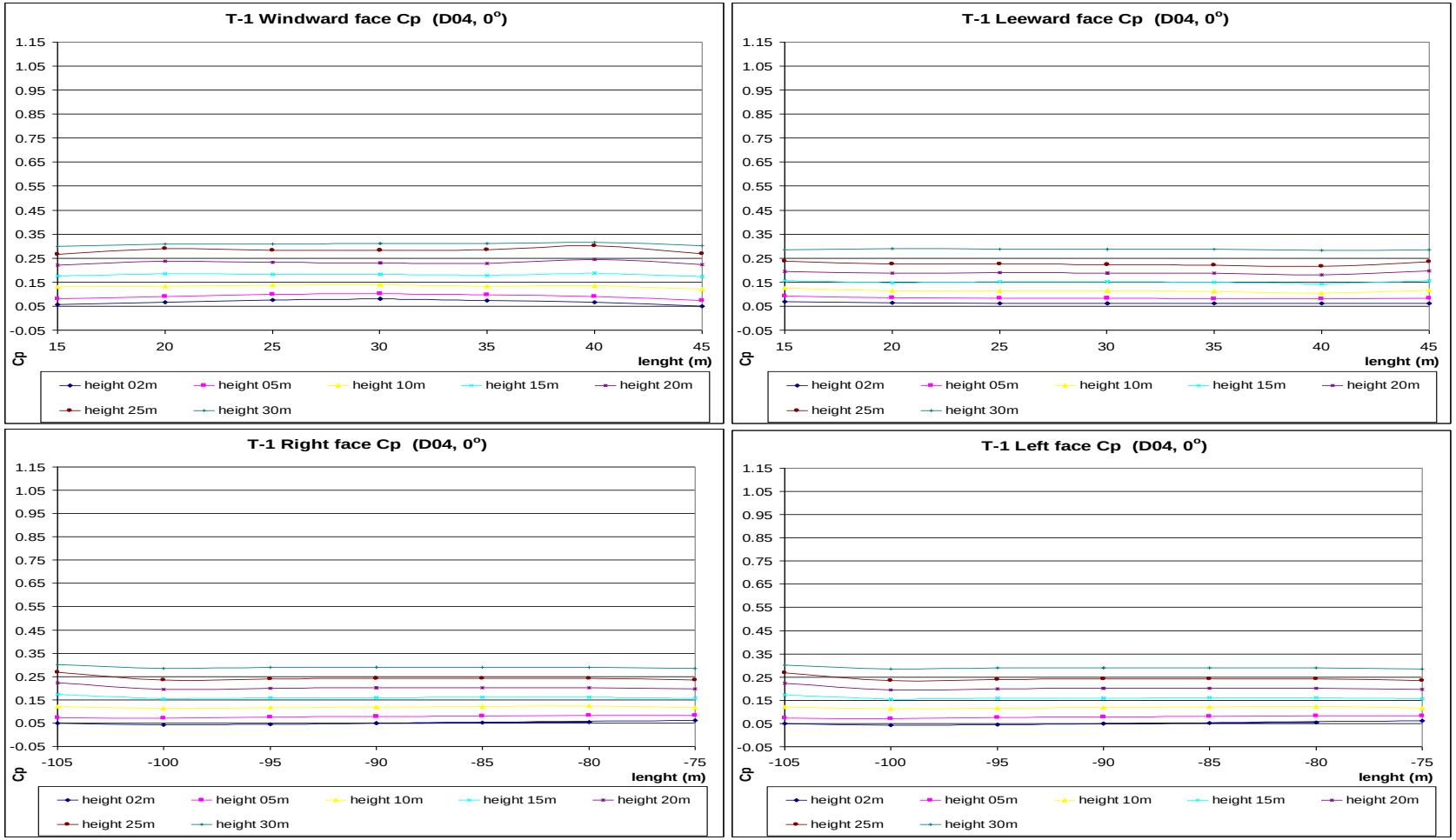

Source: this study.

Figure 27: T-02 windward, leeward, right and left side Cp results (D04, 0°)

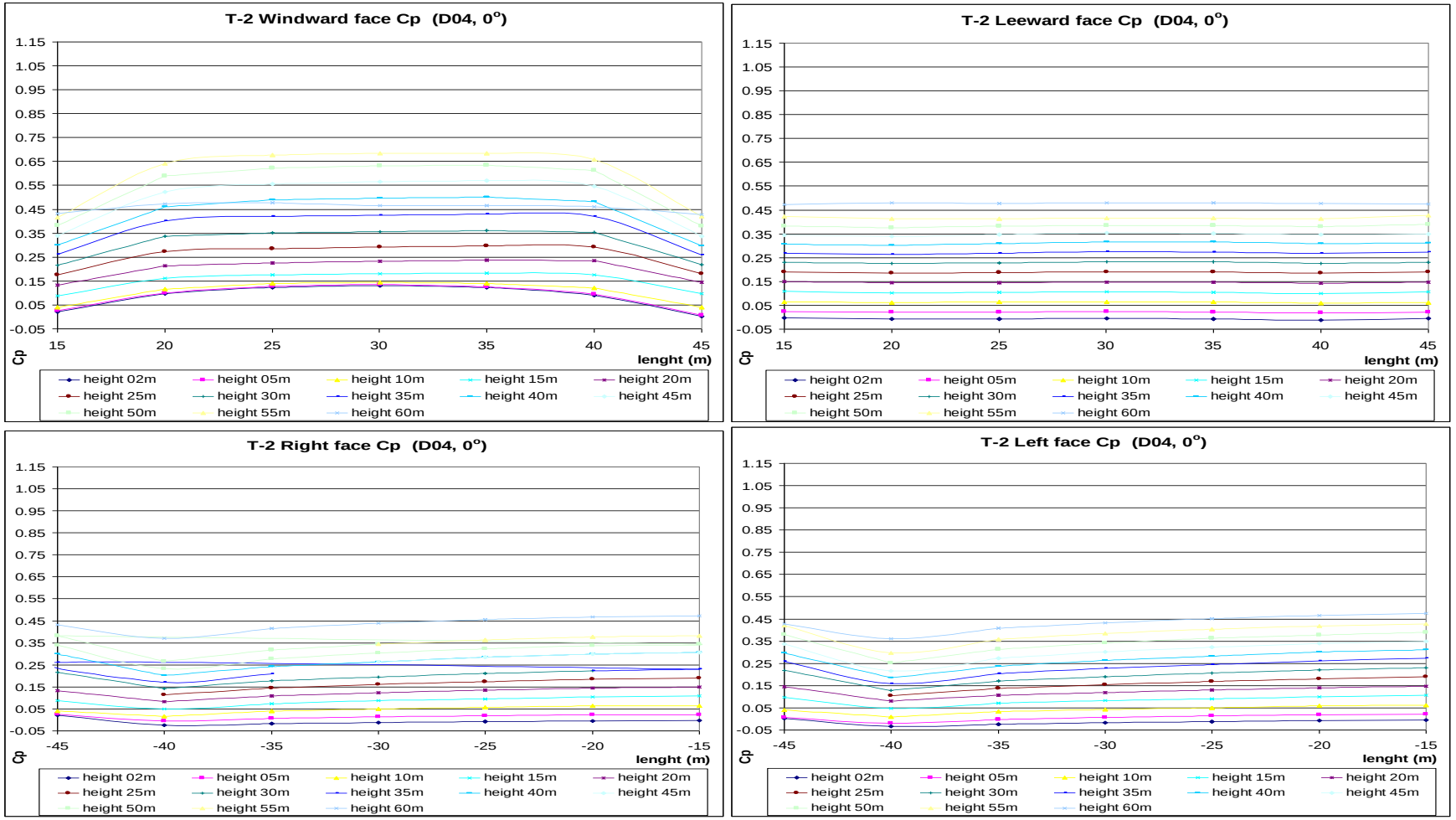

Source: this study.

Figure 28: T-03 windward, leeward, right and left side Cp results (D04, 0°)

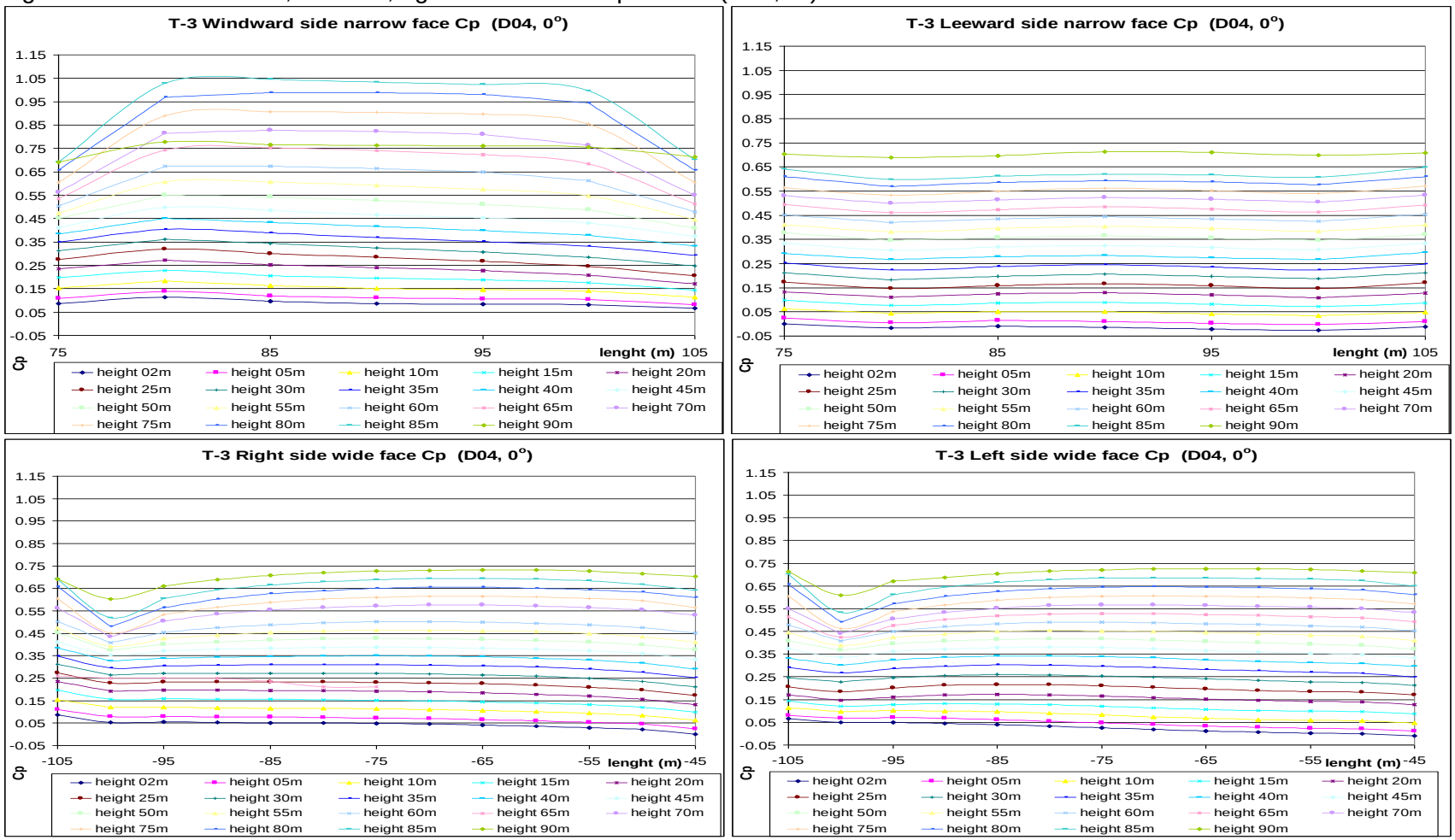

Source: this study.

Figure 29: T-02 windward, leeward, right and left side Cp results 90°)

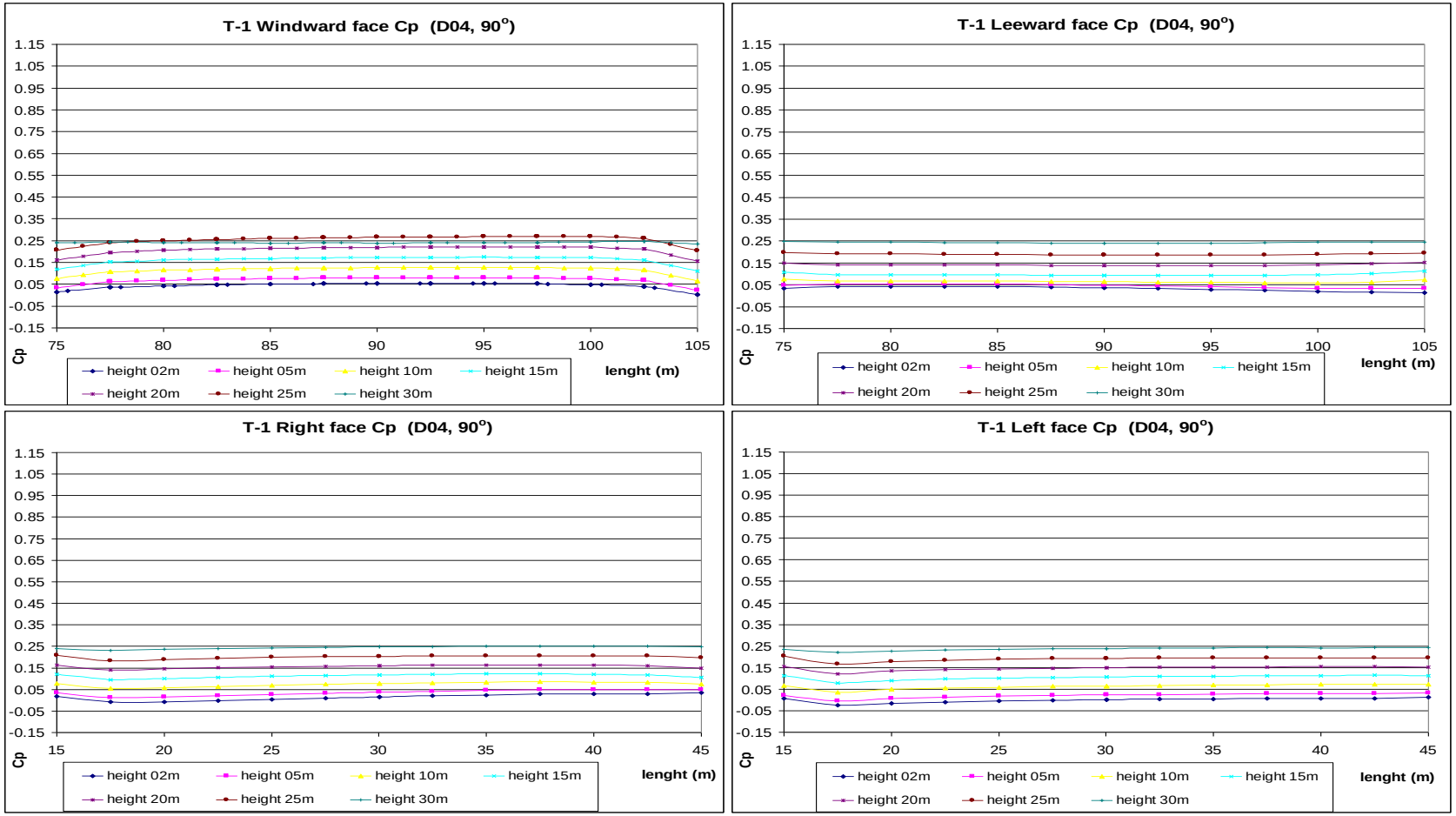

Source: this study.

Figure 30: T-02 windward, leeward, right and left side Cp results 90^{o})

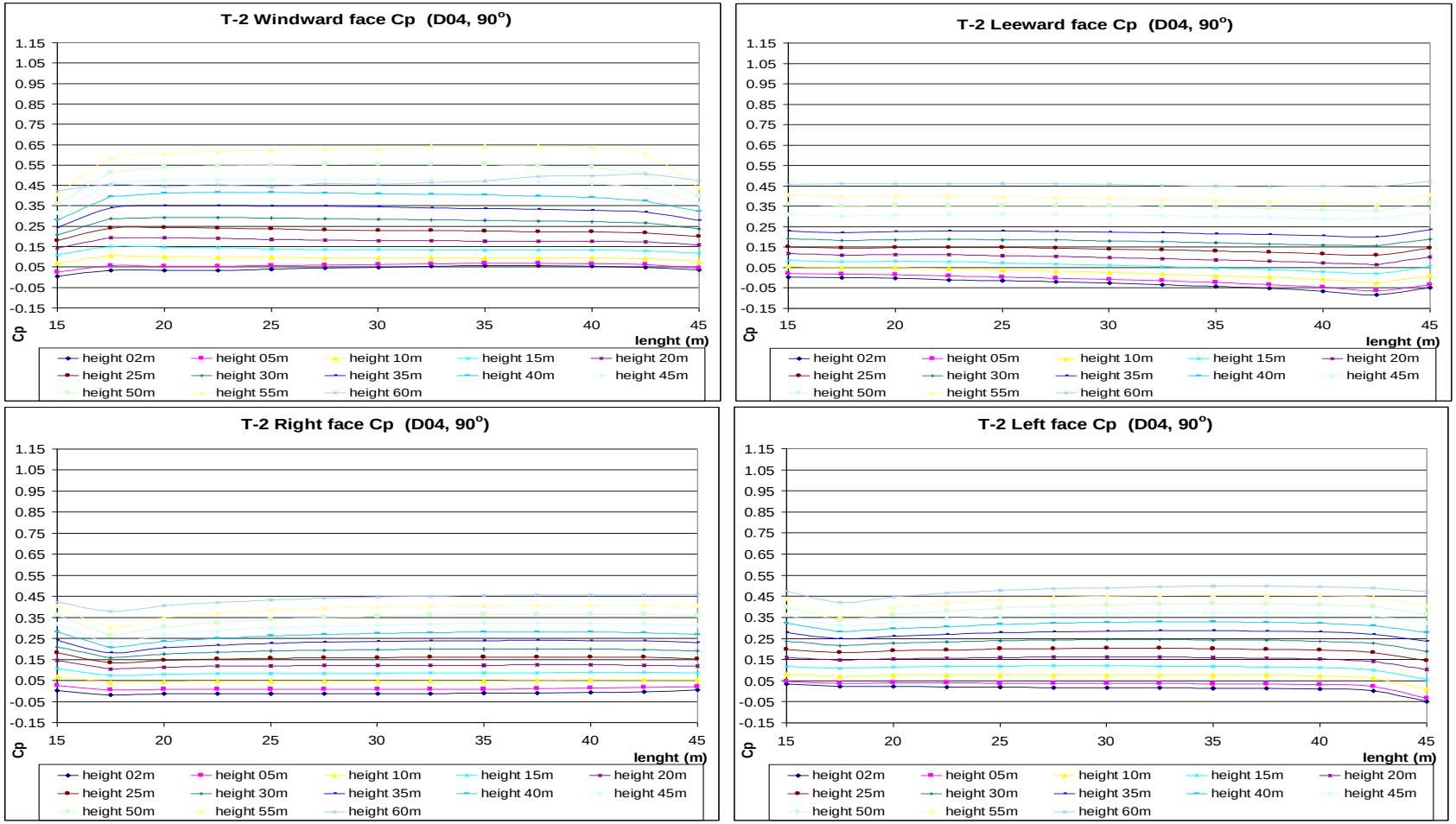

Source: this study.

Figure 31: T-03 windward, leeward, right and left side Cp results (D04, 90°)

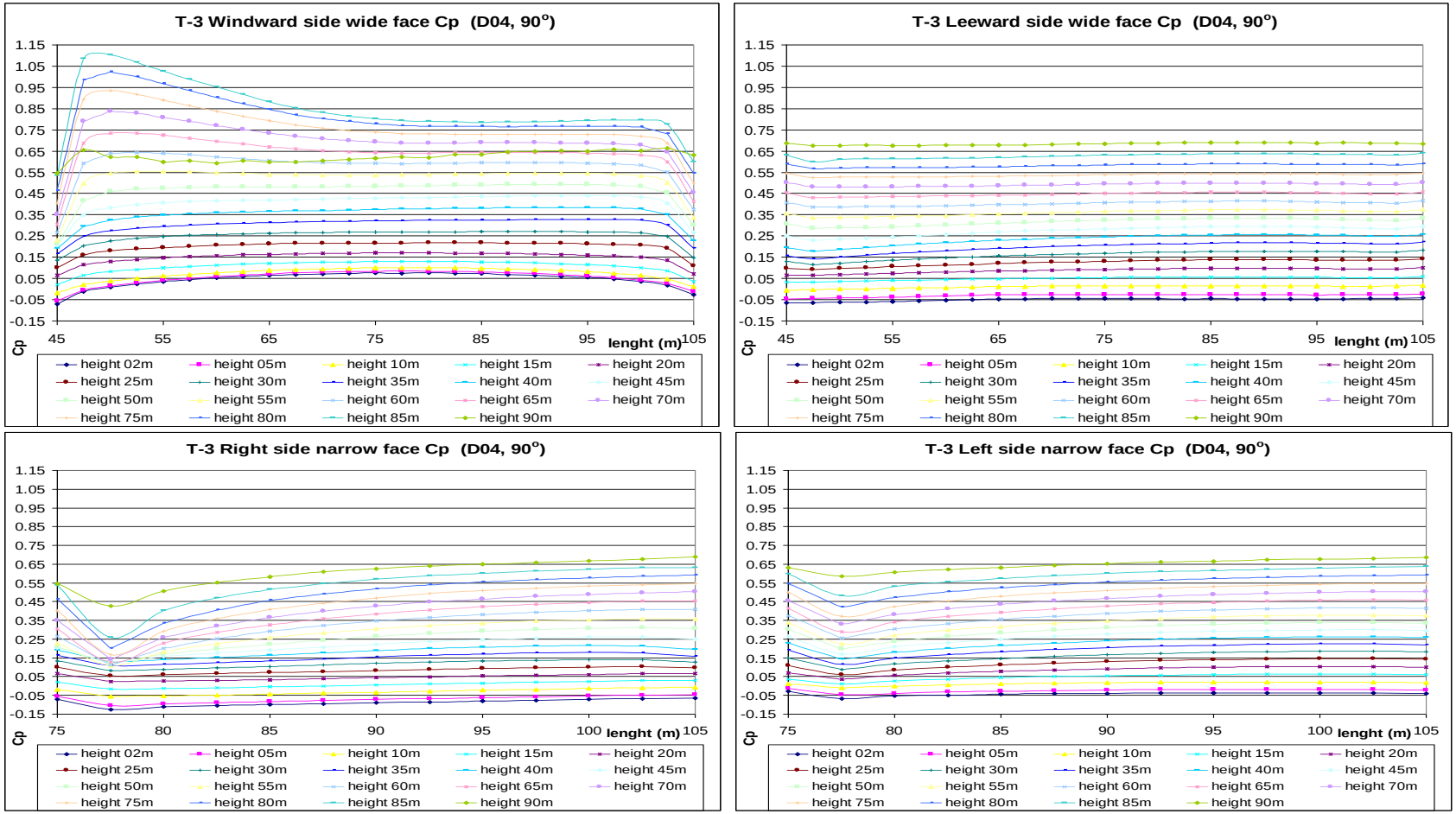

Source: this study.

Figure 32: T-01 windward, leeward, right and left side Cp results (D04, 45°)

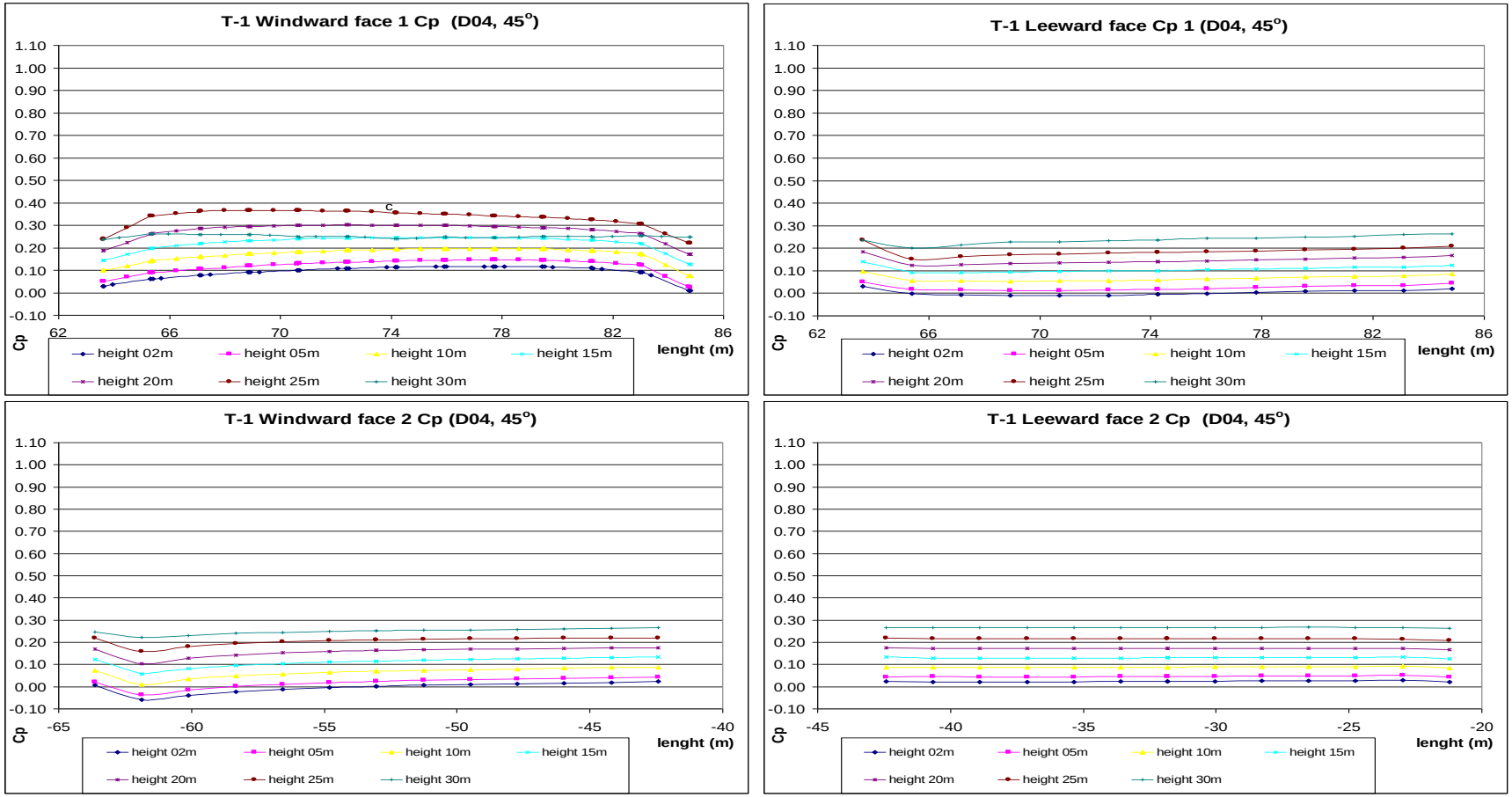

Source: this study.

Figure 33: T-02 windward, leeward, right and left side Cp results (D04, 45°)

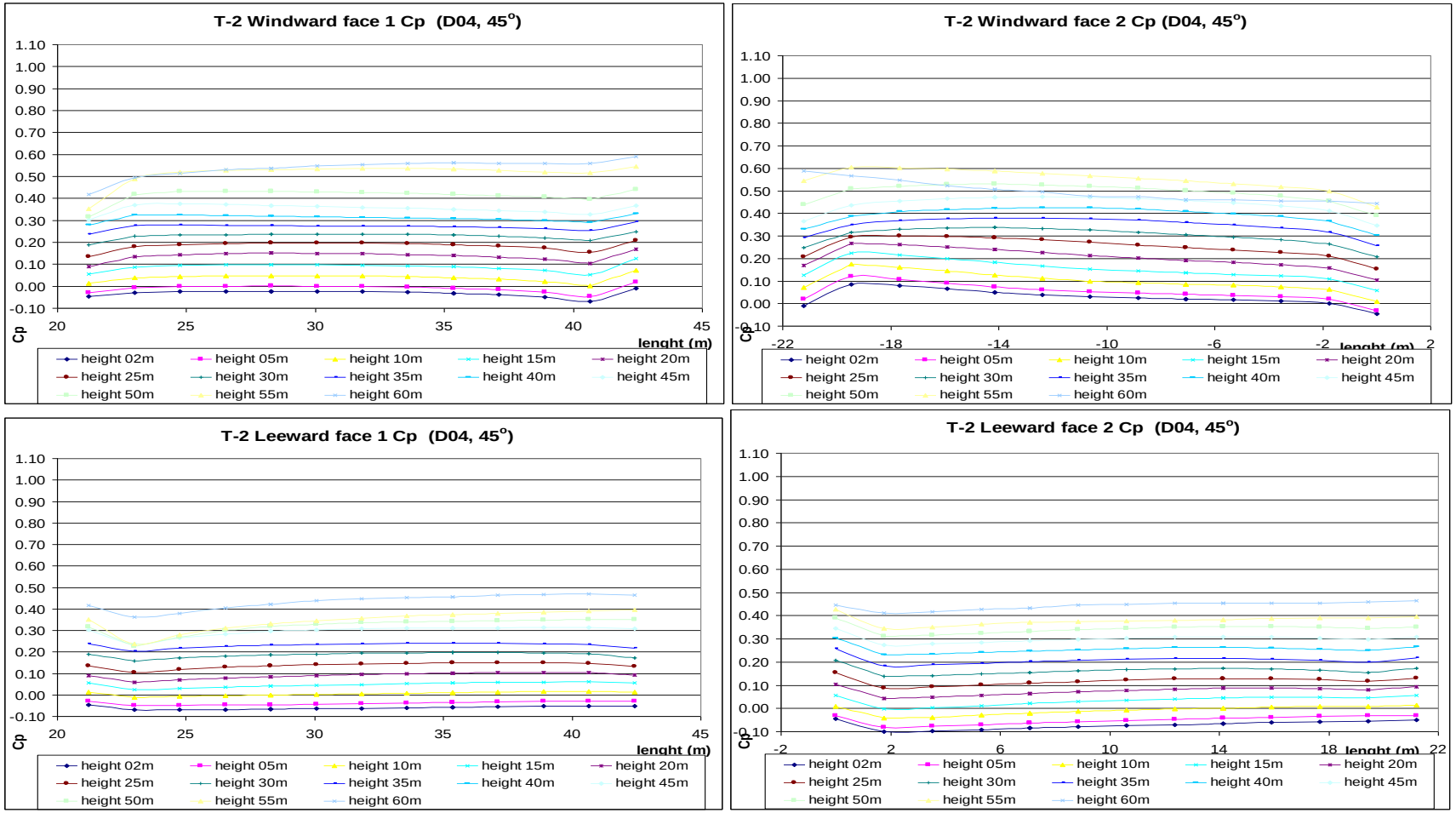

Source: this study.

Figure 34: T-03 windward, leeward, right and left side Cp results (D04, 45°)

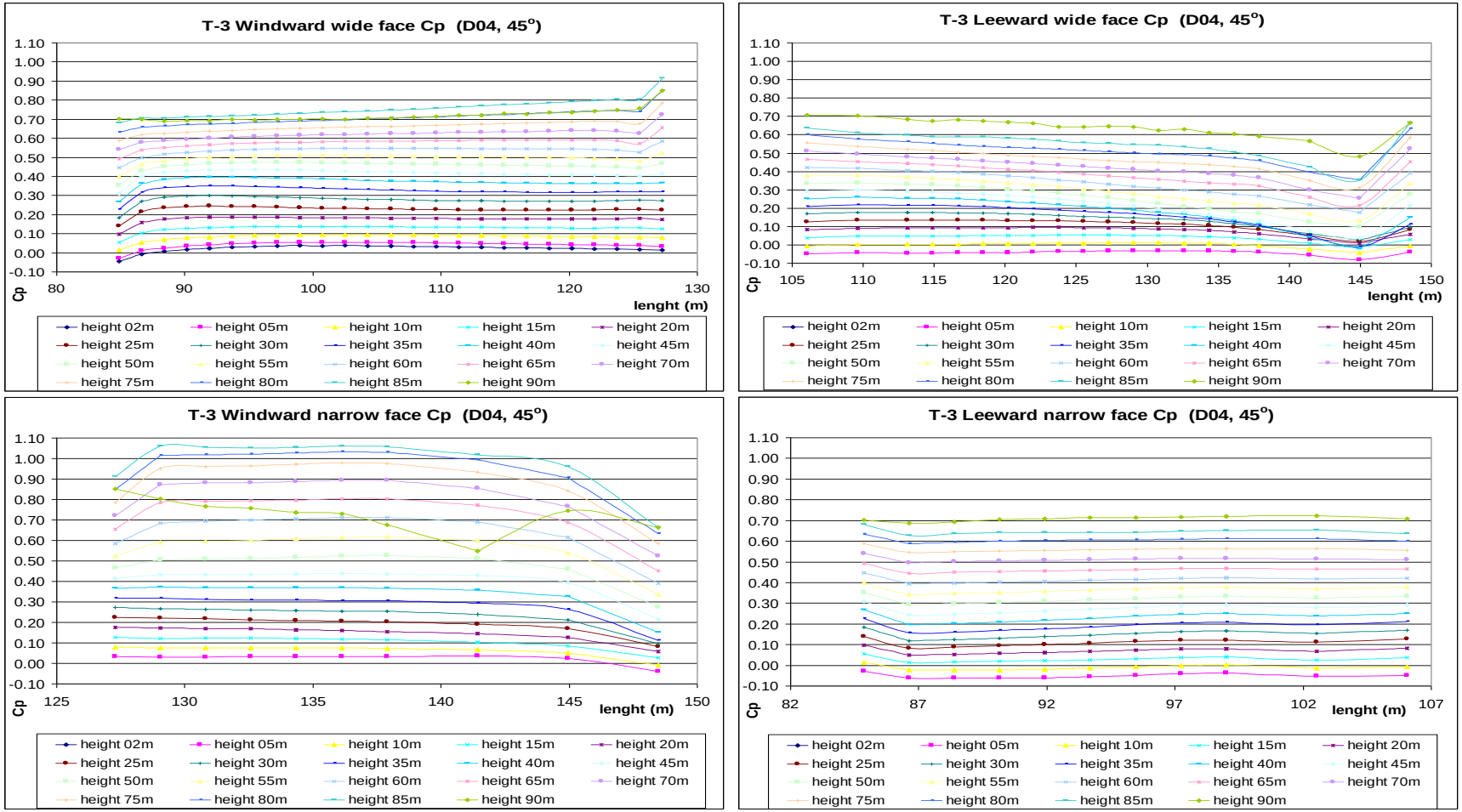

Source: this study.

Table 18: Cp results for the D1 scenario (wind at 0°)

D1- Canyon 'A'	Parallel wind incidence (0°)								
	Right side Cp				Left ide Cp				⊿Cp
(m)	low 8th	high 8th	avg 90%	sdev	low 8th	high 8th	avg 90%	sdev	
90	0.65	0.72	0.69	0.04	0.59	0.72	0.69	0.04	***0.01***
85	0.59	0.68	0.65	0.06	0.47	0.67	0.63	0.07	***0.02***
80	0.50	0.63	0.60	0.06	0.41	0.63	0.58	0.07	***0.02***
75	0.50	0.57	0.55	0.05	0.38	0.58	0.53	0.07	***0.02***
70	0.42	0.53	0.50	0.05	0.35	0.53	0.48	0.06	***0.02***
65	0.42	0.49	0.46	0.04	0.33	0.49	0.44	0.05	***0.02***
60	0.45	0.51	0.49	0.03	0.40	0.48	0.45	0.03	***0.03***
55	0.42	0.47	0.45	0.03	0.37	0.45	0.42	0.03	***0.02***
50	0.38	0.43	0.41	0.02	0.33	0.41	0.38	0.03	***0.02***
45	0.34	0.39	0.37	0.02	0.29	0.36	0.34	0.02	***0.03***
40	0.30	0.35	0.33	0.02	0.25	0.32	0.30	0.02	***0.03***
35	0.26	0.31	0.29	0.02	0.21	0.28	0.26	0.02	***0.02***
30	0.16	0.33	0.24	0.04	0.10	0.29	0.26	0.04	***-0.03***
25	0.14	0.26	0.20	0.03	0.06	0.24	0.21	0.04	***-0.01***
20	0.11	0.20	0.15	0.03	0.02	0.20	0.17	0.04	***-0.02***
15	0.03	0.15	0.12	0.03	-0.02	0.15	0.13	0.04	***-0.01***
10	0.00	0.10	0.08	0.03	-0.06	0.11	0.09	0.04	***-0.01***
5	-0.06	0.06	0.04	0.03	-0.09	0.07	0.05	0.04	***-0.01***
2	-0.08	0.04	0.02	0.03	-0.10	0.06	0.03	0.04	***-0.01***
avg	***0.29***	***0.38***	***0.35***	***0.03***	***0.23***	***0.37***	***0.34***	***0.04***	***0.01***

Source: this study.

Table 19: Cp results for the D1 canyon 'B' scenario for parallel winds (0°)

D1- Canyon 'B'	Parallel wind incidence (0°)								
	Right side Cp				Left ide Cp				⊿Cp
(m)	low 8th	high 8th	avg 90%	sdev	low 8th	high 8th	avg 90%	sdev	
60	0.43	0.50	0.48	0.02	0.39	0.48	0.46	0.03	***0.02***
55	0.39	0.45	0.44	0.03	0.31	0.44	0.42	0.04	***0.02***
50	0.34	0.41	0.40	0.03	0.27	0.39	0.37	0.04	***0.02***
45	0.29	0.37	0.35	0.03	0.23	0.35	0.33	0.04	***0.03***
40	0.25	0.33	0.31	0.03	0.18	0.32	0.28	0.04	***0.03***
35	0.18	0.29	0.27	0.04	0.12	0.28	0.25	0.05	***0.03***
30	0.15	0.29	0.25	0.03	0.07	0.30	0.26	0.05	***-0.01***
25	0.15	0.21	0.20	0.02	0.13	0.31	0.21	0.03	***-0.01***
20	0.12	0.18	0.16	0.01	0.10	0.25	0.16	0.02	***0.00***
15	0.08	0.14	0.12	0.01	0.06	0.21	0.12	0.02	***0.00***
10	0.04	0.10	0.08	0.01	0.03	0.17	0.07	0.02	***0.00***
5	0.01	0.06	0.04	0.01	-0.02	0.13	0.03	0.02	***0.00***
2	-0.01	0.04	0.02	0.01	-0.02	0.11	0.01	0.02	***0.01***
avg	***0.19***	***0.26***	***0.24***	***0.02***	***0.14***	***0.29***	***0.23***	***0.03***	***0.01***

Source: this study.

Table 20: Cp results for the D1 scenario (wind at 90°)

D1- Canyon 'A'	Orthogonal wind incidence (90°)								
	Windward side Cp				Leeward side Cp				⊿Cp
(m)	low 8th	high 8th	avg 90%	sdev	low 8th	high 8th	avg 90%	sdev	
90	0.66	0.70	0.67	0.02	0.79	0.80	0.80	0.00	***-0.12***
85	1.03	1.13	1.10	0.17	0.71	0.74	0.73	0.01	***0.37***
80	0.56	1.07	1.04	0.17	0.67	0.70	0.69	0.01	***0.35***
75	0.86	0.99	0.96	0.17	0.63	0.65	0.64	0.01	***0.32***
70	0.49	0.90	0.88	0.14	0.58	0.60	0.60	0.01	***0.29***
65	0.74	0.81	0.80	0.13	0.53	0.56	0.55	0.01	***0.25***
60	0.47	0.63	0.62	0.06	0.49	0.54	0.51	0.02	***0.11***
55	0.57	0.64	0.62	0.08	0.43	0.48	0.45	0.02	***0.17***
50	0.43	0.57	0.54	0.06	0.38	0.44	0.41	0.02	***0.13***
45	0.40	0.49	0.47	0.05	0.34	0.41	0.37	0.02	***0.10***
40	0.37	0.44	0.41	0.03	0.29	0.37	0.34	0.03	***0.07***
35	0.32	0.38	0.35	0.03	0.25	0.33	0.30	0.03	***0.05***
30	0.25	0.38	0.28	0.03	0.21	0.30	0.27	0.02	***0.00***
25	0.21	0.30	0.23	0.02	0.19	0.26	0.23	0.02	***0.01***
20	0.16	0.25	0.19	0.02	0.04	0.11	0.06	0.02	***0.14***
15	0.12	0.17	0.14	0.02	0.12	0.17	0.15	0.01	***0.00***
10	0.06	0.15	0.11	0.02	0.09	0.14	0.11	0.01	***0.00***
5	0.04	0.15	0.06	0.03	0.06	0.11	0.07	0.02	***-0.01***
2	0.02	0.14	0.04	0.04	0.04	0.11	0.06	0.02	***-0.02***
avg	***0.41***	***0.54***	***0.50***	***0.07***	***0.36***	***0.41***	***0.39***	***0.02***	***0.12***

Source: this study.

Table 21: Cp results for the D1 canyon 'B' scenario for orthogonal wind incidence (90°)

D1- Canyon 'B'	Orthogonal wind incidence (90°)								
	Windward side Cp				Leeward side Cp				⊿Cp
(m)	low 8th	high 8th	avg 90%	sdev	low 8th	high 8th	avg 90%	sdev	
60	0.51	0.52	0.51	0.01	0.52	0.52	0.52	0.00	***-0.01***
55	0.52	0.54	0.53	0.03	0.46	0.46	0.46	0.00	***0.07***
50	0.45	0.47	0.46	0.02	0.41	0.42	0.42	0.00	***0.05***
45	0.40	0.41	0.40	0.01	0.36	0.37	0.37	0.01	***0.03***
40	0.34	0.35	0.34	0.01	0.31	0.33	0.33	0.01	***0.02***
35	0.29	0.30	0.29	0.00	0.27	0.29	0.29	0.01	***0.01***
30	0.25	0.31	0.25	0.02	0.24	0.26	0.24	0.01	***0.01***
25	0.20	0.24	0.20	0.02	0.19	0.20	0.20	0.00	***0.00***
20	0.15	0.18	0.16	0.01	0.15	0.16	0.16	0.00	***0.00***
15	0.11	0.13	0.12	0.01	0.11	0.12	0.12	0.00	***0.00***
10	0.06	0.09	0.07	0.01	0.07	0.08	0.08	0.00	***0.00***
5	0.02	0.06	0.03	0.01	0.02	0.05	0.03	0.01	***0.00***
2	0.00	0.04	0.02	0.01	0.00	0.03	0.01	0.01	***0.01***
avg	***0.25***	***0.28***	***0.26***	***0.01***	***0.24***	***0.25***	***0.25***	***0.01***	***0.01***

Source: this study.

Table 22: Cp results for the D1 scenario (wind at 45^{o})

D1- Canyon 'A'	Oblique wind incidence (45^{o})								
	Windward side Cp				Leeward side Cp				⊿Cp
(m)	low $_{8th}$	high $_{8th}$	avg $_{90\%}$	sdev	low $_{8th}$	high $_{8th}$	avg $_{90\%}$	sdev	
90	0.63	0.74	0.66	0.07	0.73	0.78	0.78	0.02	***-0.12***
85	1.08	1.29	1.22	0.15	0.67	0.82	0.72	0.04	***0.50***
80	0.97	1.28	1.17	0.16	0.63	0.71	0.67	0.04	***0.51***
75	0.93	1.18	1.09	0.16	0.57	0.74	0.62	0.04	***0.47***
70	0.78	1.10	1.00	0.15	0.50	0.69	0.58	0.05	***0.42***
65	0.76	0.97	0.90	0.14	0.47	0.63	0.54	0.04	***0.36***
60	0.59	0.71	0.67	0.07	0.51	0.59	0.54	0.02	***0.13***
55	0.56	0.65	0.62	0.07	0.46	0.54	0.50	0.02	***0.12***
50	0.47	0.57	0.55	0.06	0.41	0.49	0.46	0.02	***0.10***
45	0.44	0.50	0.49	0.06	0.37	0.44	0.41	0.02	***0.08***
40	0.36	0.44	0.43	0.06	0.31	0.39	0.37	0.03	***0.07***
35	0.34	0.39	0.38	0.07	0.27	0.34	0.32	0.03	***0.06***
30	0.20	0.38	0.33	0.05	0.18	0.37	0.33	0.04	***0.00***
25	0.25	0.39	0.28	0.05	0.14	0.33	0.28	0.04	***0.00***
20	0.20	0.34	0.25	0.05	0.11	0.28	0.24	0.04	***0.01***
15	0.16	0.33	0.20	0.04	0.07	0.24	0.19	0.03	***0.00***
10	0.11	0.25	0.16	0.04	0.04	0.19	0.15	0.03	***0.02***
5	0.07	0.20	0.11	0.04	0.00	0.15	0.10	0.03	***0.01***
2	0.05	0.20	0.00	0.04	-0.02	0.15	0.08	0.03	***-0.08***
avg	***0.47***	***0.63***	***0.55***	***0.08***	***0.34***	***0.47***	***0.41***	***0.03***	***0.14***

Source: this study.

Table 23: Cp results for the D1 canyon 'B' scenario for oblique winds (45 ^{o})

D1- Canyon 'B'	Oblique wind incidence (45^{o})								
	Windward side Cp				Leeward side Cp				⊿Cp
(m)	low $_{8th}$	high $_{8th}$	avg $_{90\%}$	sdev	low $_{8th}$	high $_{8th}$	avg $_{90\%}$	sdev	
60	0.45	0.69	0.61	0.07	0.44	0.50	0.48	0.02	***0.13***
55	0.43	0.83	0.70	0.12	0.35	0.44	0.41	0.03	***0.29***
50	0.35	0.67	0.55	0.10	0.32	0.40	0.38	0.02	***0.17***
45	0.30	0.53	0.44	0.07	0.28	0.36	0.34	0.02	***0.10***
40	0.25	0.41	0.36	0.05	0.24	0.32	0.29	0.02	***0.07***
35	0.21	0.33	0.31	0.04	0.20	0.28	0.25	0.02	***0.06***
30	0.17	0.34	0.25	0.05	0.19	0.30	0.27	0.03	***-0.02***
25	0.18	0.27	0.22	0.03	0.18	0.29	0.24	0.03	***-0.01***
20	0.14	0.21	0.18	0.03	0.13	0.26	0.19	0.03	***-0.01***
15	0.11	0.16	0.14	0.02	0.07	0.21	0.14	0.03	***0.00***
10	0.07	0.12	0.10	0.02	0.01	0.16	0.10	0.03	***0.00***
5	0.03	0.08	0.06	0.02	-0.04	0.12	0.06	0.04	***0.00***
2	-0.15	-0.10	-0.12	0.09	-0.27	-0.11	-0.17	0.14	***0.05***
avg	***0.19***	***0.35***	***0.29***	***0.05***	***0.16***	***0.27***	***0.23***	***0.04***	***0.06***

Source: this study.

Table 24: Cp results for the D2 scenario (wind at 0°)

D2- Canyon 'A'	Parallel wind incidence (0°)								
	Right side Cp				Left ide Cp				⊿Cp
(m)	low 8th	high 8th	avg 90%	sdev	low 8th	high 8th	avg 90%	sdev	
90	0.66	0.71	0.69	0.03	-	-	-	-	-
85	0.60	0.66	0.64	0.04	-	-	-	-	-
80	0.53	0.61	0.59	0.04	-	-	-	-	-
75	0.51	0.56	0.55	0.03	-	-	-	-	-
70	0.45	0.52	0.51	0.03	-	-	-	-	-
65	0.43	0.47	0.46	0.02	-	-	-	-	-
60	0.44	0.48	0.47	0.01	-	-	-	-	-
55	0.40	0.43	0.42	0.01	-	-	-	-	-
50	0.36	0.39	0.38	0.01	-	-	-	-	-
45	0.31	0.35	0.33	0.02	-	-	-	-	-
40	0.26	0.30	0.29	0.02	-	-	-	-	-
35	0.23	0.26	0.25	0.02	-	-	-	-	-
30	0.15	0.24	0.18	0.03	0.23	0.25	0.25	0.01	***-0.07***
25	0.13	0.20	0.14	0.03	0.18	0.21	0.20	0.01	***-0.06***
20	0.10	0.15	0.11	0.02	0.14	0.17	0.16	0.01	***-0.05***
15	0.08	0.11	0.10	0.02	0.10	0.12	0.11	0.01	***-0.01***
10	0.04	0.07	0.05	0.02	0.06	0.08	0.07	0.01	***-0.02***
5	0.01	0.03	0.02	0.01	0.02	0.04	0.03	0.00	***-0.01***
2	0.00	0.01	0.00	0.01	0.01	0.03	0.01	0.00	***-0.01***
avg	***0.30***	***0.34***	***0.33***	***0.02***	***0.10***	***0.13***	***0.12***	***0.01***	***-0.03***

Source: this study.

Table 25: Cp results for the D2 canyon 'B' scenario for parallel winds (0°)

D2- Canyon 'B'	Parallel wind incidence (0°)								
	Right side Cp				Left ide Cp				⊿Cp
(m)	low 8th	high 8th	avg 90%	sdev	low 8th	high 8th	avg 90%	sdev	
60	-	-	-	-	0.40	0.47	0.45	0.03	-
55	-	-	-	-	-	-	-	-	-
50	-	-	-	-	0.30	0.38	0.36	0.04	-
45	-	-	-	-	-	-	-	-	-
40	-	-	-	-	0.23	0.29	0.28	0.03	-
35	-	-	-	-	-	-	-	-	-
30	0.21	0.23	0.22	0.01	0.16	0.24	0.21	0.02	***0.01***
25	0.17	0.18	0.17	0.00	0.13	0.18	0.17	0.01	***0.01***
20	0.13	0.14	0.13	0.00	0.10	0.13	0.13	0.01	***0.00***
15	0.08	0.10	0.09	0.01	0.07	0.09	0.09	0.01	***0.00***
10	0.04	0.06	0.05	0.01	0.03	0.05	0.05	0.01	***0.00***
5	-0.01	0.02	0.00	0.01	0.00	0.01	0.00	0.00	***0.00***
2	-0.02	0.00	-0.01	0.01	-0.02	-0.01	-0.02	0.00	***0.00***
avg	***0.09***	***0.10***	***0.09***	***0.01***	***0.14***	***0.18***	***0.17***	***0.02***	***0.00***

Source: this study.

Table 26: Cp results for the D2 scenario (wind at 90^{o})

D2- Right Side Canyon 'A'	**Orthogonal wind incidence (90^{o})**								
	Windward side Cp				**Leeward side Cp**				***⊿Cp***
(m)	low $_{8th}$	high $_{8th}$	avg $_{90\%}$	sdev	low $_{8th}$	high $_{8th}$	avg $_{90\%}$	sdev	
90	-	-	-	-	0.74	0.76	0.75	0.00	**-**
85	-	-	-	-	0.65	0.69	0.67	0.01	**-**
80	-	-	-	-	0.63	0.66	0.64	0.01	**-**
75	-	-	-	-	0.59	0.62	0.61	0.01	**-**
70	-	-	-	-	0.55	0.58	0.57	0.01	**-**
65	-	-	-	-	0.51	0.53	0.53	0.01	**-**
60	-	-	-	-	0.49	0.51	0.50	0.01	**-**
55	-	-	-	-	0.43	0.45	0.44	0.01	**-**
50	-	-	-	-	0.39	0.41	0.40	0.01	**-**
45	-	-	-	-	0.35	0.37	0.36	0.01	**-**
40	-	-	-	-	0.31	0.32	0.32	0.01	**-**
35	-	-	-	-	0.27	0.28	0.28	0.00	**-**
30	0.24	0.27	0.27	0.01	0.22	0.25	0.24	0.01	***0.03***
25	0.20	0.26	0.22	0.02	0.18	0.21	0.20	0.01	***0.02***
20	0.15	0.22	0.16	0.03	0.13	0.16	0.15	0.01	***0.01***
15	0.10	0.19	0.12	0.03	0.10	0.12	0.11	0.01	***0.00***
10	0.06	0.13	0.07	0.02	0.06	0.08	0.07	0.01	***0.00***
5	0.02	0.07	0.03	0.02	0.02	0.04	0.03	0.01	***0.00***
2	0.00	0.05	0.01	0.02	0.00	0.03	0.02	0.01	***-0.01***
avg	***0.11***	***0.17***	***0.12***	***0.02***	***0.35***	***0.37***	***0.36***	***0.01***	***0.01***

Source: this study.

Table 27: Cp results for the D2 right side canyon 'B' scenario for orthogonal winds (90^{o})

D2- Right Side Canyon 'B'	**Orthogonal wind incidence (90^{o})**								
	Windward side Cp				**Leeward side Cp**				***⊿Cp***
(m)	low $_{8th}$	high $_{8th}$	avg $_{90\%}$	sdev	low $_{8th}$	high $_{8th}$	avg $_{90\%}$	sdev	
60	0.49	0.50	0.49	0.01	-	-	-	-	**-**
55	0.55	0.56	0.56	0.04	-	-	-	-	**-**
50	0.47	0.51	0.50	0.04	-	-	-	-	**-**
45	0.35	0.39	0.37	0.03	-	-	-	-	**-**
40	0.41	0.45	0.43	0.03	-	-	-	-	**-**
35	0.30	0.33	0.32	0.02	-	-	-	-	**-**
30	0.25	0.27	0.25	0.01	0.23	0.24	0.24	0.01	***0.02***
25	0.20	0.22	0.20	0.01	0.19	0.20	0.20	0.01	***0.00***
20	0.16	0.18	0.16	0.01	0.19	0.20	0.20	0.01	***-0.04***
15	0.11	0.13	0.12	0.01	0.10	0.13	0.12	0.01	***0.00***
10	0.07	0.08	0.08	0.01	0.06	0.09	0.08	0.01	***0.00***
5	0.03	0.05	0.04	0.01	0.02	0.05	0.04	0.01	***-0.01***
2	0.01	0.03	0.02	0.01	0.00	0.03	0.02	0.01	***0.00***
avg	***0.26***	***0.28***	***0.27***	***0.02***	***0.12***	***0.13***	***0.13***	***0.01***	***0.00***

Source: this study.

Table 28: Cp results for the D2 left side canyon 'A' scenario for orthogonal winds (90°)

D2- Left Side Canyon 'A'	Orthogonal wind incidence (90°)								
	Windward side Cp				Leeward side Cp				⊿Cp
(m)	low 8th	high 8th	avg 90%	sdev	low 8th	high 8th	avg 90%	sdev	
90	0.67	0.70	0.68	0.02	-	-	-	-	-
85	0.96	1.02	1.00	0.14	-	-	-	-	-
80	0.58	0.95	0.94	0.13	-	-	-	-	-
75	0.81	0.87	0.87	0.12	-	-	-	-	-
70	0.50	0.79	0.79	0.10	-	-	-	-	-
65	0.67	0.71	0.71	0.09	-	-	-	-	-
60	0.46	0.57	0.56	0.04	-	-	-	-	-
55	0.57	0.60	0.59	0.06	-	-	-	-	-
50	0.46	0.53	0.52	0.05	-	-	-	-	-
45	0.39	0.46	0.45	0.04	-	-	-	-	-
40	0.36	0.40	0.39	0.03	-	-	-	-	-
35	0.33	0.35	0.34	0.02	-	-	-	-	-
30	0.23	0.31	0.28	0.02	0.26	0.29	0.27	0.01	***0.01***
25	0.24	0.25	0.24	0.02	0.22	0.24	0.24	0.00	***0.00***
20	0.13	0.20	0.19	0.02	0.18	0.20	0.19	0.00	***0.00***
15	0.08	0.16	0.15	0.02	0.14	0.16	0.15	0.00	***0.00***
10	0.02	0.12	0.11	0.02	0.11	0.12	0.12	0.00	***0.00***
5	0.03	0.10	0.08	0.03	0.07	0.09	0.08	0.01	***0.00***
2	0.02	0.10	0.06	0.03	0.06	0.29	0.15	0.07	***-0.09***
avg	***0.39***	***0.48***	***0.47***	***0.05***	***0.15***	***0.20***	***0.17***	***0.02***	***-0.01***

Source: this study.

Table 29: Cp results for the D2 left side canyon 'B' scenario for orthogonal winds (90°)

D2- Left Side Canyon 'B'	Orthogonal wind incidence (90°)								
	Windward side Cp				Leeward side Cp				⊿Cp
(m)	low 8th	high 8th	avg 90%	sdev	low 8th	high 8th	avg 90%	sdev	
60	0.49	0.51	0.50	0.01	-	-	-	-	-
55	0.43	0.45	0.45	0.01	-	-	-	-	-
50	0.39	0.41	0.40	0.01	-	-	-	-	-
45	0.34	0.36	0.36	0.01	-	-	-	-	-
40	0.29	0.32	0.31	0.01	-	-	-	-	-
35	0.26	0.27	0.27	0.01	-	-	-	-	-
30	0.22	0.24	0.23	0.00	0.23	0.28	0.26	0.02	***-0.03***
25	0.00	0.02	0.01	0.00	0.19	0.25	0.20	0.02	***-0.19***
20	0.14	0.15	0.15	0.00	0.14	0.20	0.15	0.02	***-0.01***
15	0.10	0.12	0.11	0.00	0.09	0.16	0.11	0.02	***0.00***
10	0.06	0.08	0.07	0.00	0.04	0.11	0.07	0.02	***0.00***
5	0.02	0.04	0.03	0.00	0.02	0.04	0.03	0.00	***0.00***
2	0.00	0.02	0.01	0.00	-0.03	0.05	0.01	0.01	***-0.01***
avg	***0.21***	***0.23***	***0.22***	***0.01***	***0.10***	***0.16***	***0.12***	***0.01***	***-0.03***

Source: this study.

Table 30: Cp results for the D2 scenario (wind at 45^{o})

D2- Block 'A'	**Oblique wind incidence (45^{o})**								
	Windward side Cp				**Leeward side Cp**				***⊿Cp***
(m)	low $_{8th}$	high $_{8th}$	avg $_{90\%}$	sdev	low $_{8th}$	high $_{8th}$	avg $_{90\%}$	sdev	
90	0.66	0.73	0.67	0.05	-	-	-	-	**-**
85	0.75	0.92	0.80	0.08	-	-	-	-	**-**
80	0.67	0.85	0.74	0.07	-	-	-	-	**-**
75	0.63	0.77	0.69	0.07	-	-	-	-	**-**
70	0.57	0.71	0.64	0.06	-	-	-	-	**-**
65	0.53	0.65	0.59	0.06	-	-	-	-	**-**
60	0.49	0.55	0.52	0.02	-	-	-	-	**-**
55	0.47	0.54	0.51	0.03	-	-	-	-	**-**
50	0.43	0.51	0.47	0.03	-	-	-	-	**-**
45	0.39	0.47	0.43	0.03	-	-	-	-	**-**
40	0.34	0.44	0.39	0.03	-	-	-	-	**-**
35	0.31	0.39	0.34	0.03	-	-	-	-	**-**
30	0.23	0.39	0.27	0.06	0.20	0.28	0.23	0.02	***0.04***
25	0.18	0.32	0.21	0.06	0.11	0.23	0.18	0.04	***0.03***
20	0.14	0.28	0.15	0.05	0.10	0.19	0.14	0.03	***0.01***
15	0.09	0.24	0.11	0.05	0.06	0.15	0.11	0.02	***-0.01***
10	0.04	0.20	0.08	0.05	0.03	0.11	0.08	0.02	***0.00***
5	0.01	0.16	0.06	0.04	0.00	0.08	0.05	0.02	***0.01***
2	-0.01	0.13	0.03	0.04	-0.03	0.05	0.02	0.02	***0.01***
avg	***0.36***	***0.49***	***0.41***	***0.05***	***0.07***	***0.16***	***0.12***	***0.02***	***0.01***

Source: this study.

Table 31: Cp results for the D2 Block 'B' scenario for oblique winds (45 ^{o}).

D2- Block 'B'	**Oblique wind incidence (45^{o})**								
	Windward side Cp				**Leeward side Cp**				***⊿Cp***
(m)	low $_{8th}$	high $_{8th}$	avg $_{90\%}$	sdev	low $_{8th}$	high $_{8th}$	avg $_{90\%}$	sdev	
60	0.25	0.36	0.33	0.03	0.13	0.36	0.26	0.08	***0.08***
55	0.18	0.31	0.27	0.05	0.08	0.32	0.21	0.08	***0.06***
50	0.10	0.27	0.23	0.06	0.02	0.27	0.17	0.09	***0.05***
45	0.04	0.23	0.18	0.06	-0.04	0.23	0.14	0.10	***0.04***
40	0.00	0.19	0.14	0.06	-0.08	0.19	0.11	0.10	***0.03***
35	-0.05	0.22	0.10	0.06	-0.13	0.15	0.08	0.10	***0.03***
30	-0.04	0.32	0.11	0.10	-0.15	0.14	0.08	0.09	***0.03***
25	-0.01	0.32	0.07	0.08	-0.17	0.13	0.05	0.09	***0.02***
20	-0.02	0.24	0.03	0.07	-0.16	0.09	0.01	0.07	***0.03***
15	-0.05	0.17	-0.01	0.06	-0.15	0.08	0.00	0.06	***-0.01***
10	-0.08	0.11	-0.05	0.05	-0.14	0.02	-0.07	0.05	***0.02***
5	-0.11	0.04	-0.09	0.04	-0.15	-0.01	-0.08	0.05	***-0.01***
2	-0.13	0.02	-0.10	0.04	-0.19	-0.03	-0.14	0.05	***0.04***
avg	***0.01***	***0.22***	***0.09***	***0.06***	***0.04***	***0.26***	***0.17***	***0.07***	***0.03***

Source: this study.

Table 32: Cp results for the D3 scenario (wind at 0°)

D3- Canyon 'B'	Parallel wind incidence (0°)								
	Right side Cp				Left ide Cp				⊿Cp
(m)	low 8th	high 8th	avg 90%	sdev	low 8th	high 8th	avg 90%	sdev	
60	0.46	0.50	0.49	0.02	0.49	0.52	0.51	0.01	***-0.02***
55	0.41	0.46	0.44	0.03	0.46	0.48	0.47	0.01	***-0.02***
50	0.36	0.41	0.40	0.02	0.41	0.43	0.43	0.01	***-0.03***
45	0.32	0.37	0.35	0.02	0.37	0.39	0.38	0.01	***-0.03***
40	0.27	0.33	0.31	0.02	0.33	0.34	0.34	0.01	***-0.03***
35	0.23	0.28	0.27	0.02	0.29	0.30	0.30	0.01	***-0.03***
30	0.20	0.30	0.24	0.03	0.24	0.26	0.25	0.01	***-0.01***
25	0.18	0.24	0.20	0.02	0.19	0.21	0.20	0.01	***0.00***
20	0.15	0.18	0.16	0.01	0.14	0.17	0.16	0.01	***0.00***
15	0.11	0.13	0.12	0.01	0.08	0.13	0.12	0.01	***0.00***
10	0.07	0.09	0.07	0.01	0.03	0.08	0.07	0.02	***0.00***
5	0.03	0.04	0.03	0.01	-0.02	0.04	0.03	0.02	***0.00***
2	0.00	0.02	0.01	0.01	-0.05	0.01	0.00	0.02	***0.00***
avg	***0.21***	***0.26***	***0.24***	***0.02***	***0.23***	***0.26***	***0.25***	***0.01***	***-0.01***

Source: this study.

Table 33: Cp results for the D3 canyon 'A' scenario for parallel winds (0°)

D3- Canyon 'A'	Parallel wind incidence (0°)								
	Right side Cp				Left ide Cp				⊿Cp
(m)	low 8th	high 8th	avg 90%	sdev	low 8th	high 8th	avg 90%	sdev	
90	0.68	0.78	0.77	0.04	-	-	-	-	**-**
85	0.61	0.72	0.72	0.05	-	-	-	-	**-**
80	0.53	0.68	0.68	0.05	-	-	-	-	**-**
75	0.53	0.64	0.63	0.04	-	-	-	-	**-**
70	0.49	0.59	0.59	0.03	-	-	-	-	**-**
65	0.47	0.55	0.54	0.03	-	-	-	-	**-**
60	0.43	0.51	0.50	0.02	0.46	0.50	0.49	0.01	***0.01***
55	0.40	0.46	0.46	0.02	0.41	0.45	0.44	0.01	***0.02***
50	0.36	0.42	0.42	0.02	0.37	0.40	0.40	0.01	***0.02***
45	0.33	0.38	0.37	0.02	0.32	0.36	0.35	0.01	***0.02***
40	0.28	0.34	0.33	0.02	0.28	0.32	0.31	0.01	***0.02***
35	0.25	0.29	0.29	0.02	0.24	0.28	0.27	0.01	***0.02***
30	0.20	0.25	0.24	0.02	0.20	0.29	0.24	0.03	***0.00***
25	0.16	0.20	0.20	0.02	0.18	0.24	0.20	0.02	***0.00***
20	0.11	0.16	0.15	0.01	0.14	0.20	0.16	0.02	***-0.01***
15	0.07	0.11	0.11	0.01	0.11	0.16	0.12	0.01	***-0.01***
10	0.03	0.07	0.06	0.01	0.07	0.11	0.07	0.01	***-0.01***
5	0.00	0.03	0.02	0.01	0.02	0.07	0.03	0.01	***-0.01***
2	-0.04	-0.01	-0.02	0.01	0.00	0.05	0.01	0.01	***-0.03***
avg	***0.31***	***0.38***	***0.37***	***0.02***	***0.22***	***0.26***	***0.24***	***0.02***	***0.00***

Source: this study.

Table 34: Cp results for the D3 scenario (wind at 90^{o})

D3- Right Side Canyon 'B'	**Orthogonal wind incidence (90^{o})**								
	Windward side Cp				**Leeward side Cp**				***⊿Cp***
(m)	low $_{8th}$	high $_{8th}$	avg $_{90\%}$	sdev	low $_{8th}$	high $_{8th}$	avg $_{90\%}$	sdev	
90	0.57	0.68	0.64	0.03	-	-	-	-	**-**
85	0.62	1.23	0.91	0.18	-	-	-	-	**-**
80	0.56	1.19	0.89	0.18	-	-	-	-	**-**
75	0.50	1.08	0.83	0.16	-	-	-	-	**-**
70	0.44	0.96	0.76	0.14	-	-	-	-	**-**
65	0.39	0.85	0.69	0.12	-	-	-	-	**-**
60	0.35	0.73	0.63	0.10	0.46	0.50	0.48	0.02	***0.15***
55	0.31	0.60	0.56	0.08	0.33	0.41	0.35	0.03	***0.21***
50	0.27	0.52	0.49	0.07	0.34	0.38	0.34	0.02	***0.14***
45	0.22	0.47	0.42	0.07	0.32	0.36	0.33	0.01	***0.09***
40	0.19	0.42	0.37	0.07	0.29	0.32	0.30	0.01	***0.07***
35	0.15	0.37	0.31	0.07	0.25	0.27	0.25	0.01	***0.05***
30	0.11	0.30	0.25	0.06	0.17	0.27	0.21	0.03	***0.04***
25	0.08	0.24	0.20	0.05	0.10	0.20	0.16	0.03	***0.04***
20	0.07	0.17	0.16	0.04	0.06	0.15	0.12	0.03	***0.04***
15	0.03	0.14	0.12	0.04	0.02	0.11	0.09	0.03	***0.03***
10	-0.03	0.12	0.10	0.05	0.00	0.09	0.06	0.03	***0.04***
5	-0.05	0.13	0.11	0.06	-0.02	0.09	0.05	0.04	***0.06***
2	-0.11	0.13	0.10	0.06	-0.03	0.08	0.04	0.04	***0.06***
avg	***0.25***	***0.54***	***0.45***	***0.09***	***0.18***	***0.25***	***0.21***	***0.02***	***0.08***

Source: this study.

Table 35: Cp results for the D3 right side canyon 'A' scenario for orthogonal winds (90^{o})

D3- Right Side Canyon 'A'	**Orthogonal wind incidence (90^{o})**								
	Windward side Cp				**Leeward side Cp**				***⊿Cp***
(m)	low $_{8th}$	high $_{8th}$	avg $_{90\%}$	sdev	low $_{8th}$	high $_{8th}$	avg $_{90\%}$	sdev	
60	0.56	0.60	0.58	0.03	0.49	0.51	0.50	0.01	***0.08***
55	0.53	0.60	0.56	0.05	0.42	0.45	0.44	0.02	***0.12***
50	0.48	0.50	0.49	0.04	0.39	0.41	0.40	0.01	***0.09***
45	0.41	0.43	0.42	0.04	0.35	0.36	0.36	0.01	***0.07***
40	0.36	0.37	0.37	0.03	0.31	0.32	0.32	0.01	***0.05***
35	0.30	0.32	0.32	0.02	0.27	0.28	0.27	0.01	***0.04***
30	0.22	0.28	0.26	0.02	0.21	0.25	0.23	0.01	***0.03***
25	0.18	0.23	0.20	0.02	0.21	0.25	0.23	0.01	***-0.03***
20	0.13	0.18	0.15	0.02	0.17	0.21	0.18	0.01	***-0.04***
15	0.09	0.13	0.10	0.02	0.10	0.12	0.11	0.01	***0.00***
10	0.05	0.09	0.07	0.02	0.06	0.08	0.07	0.01	***0.00***
5	0.02	0.61	0.18	0.16	0.03	0.04	0.03	0.00	***0.15***
2	0.01	0.03	0.02	0.01	0.01	0.02	0.01	0.00	***0.01***
avg	***0.56***	***0.60***	***0.58***	***0.03***	***0.49***	***0.51***	***0.50***	***0.01***	***0.08***

Source: this study.

Table 36: Cp results for the D3 left side canyon 'B' scenario for orthogonal winds (90°)

D3- Left Side Canyon 'B'	Orthogonal wind incidence (90°)								
	Windward side Cp				Leeward side Cp				⊿Cp
(m)	low 8th	high 8th	avg 90%	sdev	low 8th	high 8th	avg 90%	sdev	
90	-	-	-	-	0.68	0.71	0.70	0.02	-
85	-	-	-	-	0.61	0.66	0.64	0.02	-
80	-	-	-	-	0.56	0.60	0.59	0.02	-
75	-	-	-	-	0.51	0.55	0.54	0.02	-
70	-	-	-	-	0.46	0.51	0.49	0.02	-
65	-	-	-	-	0.41	0.46	0.44	0.02	-
60	0.37	0.42	0.38	0.02	0.35	0.42	0.40	0.02	***-0.02***
55	0.34	0.42	0.35	0.03	0.30	0.38	0.36	0.03	***-0.01***
50	0.30	0.37	0.31	0.03	0.25	0.34	0.32	0.03	***-0.01***
45	0.26	0.32	0.27	0.02	0.21	0.30	0.28	0.04	***0.00***
40	0.23	0.27	0.23	0.02	0.15	0.26	0.24	0.04	***0.00***
35	0.19	0.22	0.19	0.01	0.12	0.22	0.20	0.04	***0.00***
30	0.15	0.19	0.16	0.01	0.07	0.18	0.16	0.04	***0.00***
25	0.11	0.16	0.13	0.02	0.03	0.14	0.12	0.04	***0.01***
20	0.07	0.12	0.08	0.01	-0.02	0.10	0.08	0.04	***0.01***
15	0.03	0.06	0.04	0.01	-0.05	0.05	0.04	0.04	***0.00***
10	-0.01	0.02	-0.01	0.01	-0.11	0.01	0.00	0.04	***-0.01***
5	-0.06	-0.03	-0.05	0.01	-0.14	-0.04	-0.04	0.04	***-0.01***
2	-0.08	-0.04	-0.07	0.01	-0.16	-0.05	-0.06	0.04	***0.00***
avg	***0.15***	***0.19***	***0.16***	***0.02***	***0.22***	***0.31***	***0.29***	***0.03***	***0.00***

Source: this study.

Table 37: Cp results for the D3 left side canyon 'A' scenario for orthogonal winds (90°)

D3- Left Side Canyon 'A'	Orthogonal wind incidence (90°)								
	Windward side Cp				Leeward side Cp				⊿Cp
(m)	low 8th	high 8th	avg 90%	sdev	low 8th	high 8th	avg 90%	sdev	
60	0.49	0.52	0.50	0.01	0.52	0.53	0.53	0.01	***-0.03***
55	0.46	0.57	0.55	0.03	0.46	0.46	0.46	0.00	***0.09***
50	0.41	0.51	0.49	0.03	0.42	0.42	0.42	0.00	***0.07***
45	0.38	0.45	0.44	0.02	0.38	0.39	0.38	0.00	***0.05***
40	0.34	0.40	0.38	0.02	0.34	0.35	0.34	0.00	***0.04***
35	0.29	0.35	0.33	0.02	0.29	0.30	0.30	0.01	***0.03***
30	0.25	0.30	0.26	0.02	0.24	0.27	0.26	0.01	***0.01***
25	0.21	0.24	0.22	0.01	0.21	0.22	0.21	0.00	***0.01***
20	0.13	0.16	0.15	0.01	0.16	0.17	0.17	0.00	***-0.02***
15	0.12	0.14	0.13	0.01	0.12	0.13	0.12	0.00	***0.00***
10	0.07	0.10	0.08	0.01	0.08	0.09	0.08	0.00	***0.00***
5	0.03	0.06	0.04	0.01	0.04	0.05	0.04	0.01	***0.00***
2	0.01	0.04	0.02	0.01	0.01	0.03	0.02	0.01	***0.00***
avg	***0.25***	***0.30***	***0.28***	***0.02***	***0.25***	***0.26***	***0.26***	***0.00***	***0.02***

Source: this study.

Table 38: Cp results for the D3 scenario (wind at 45^{o})

D3- Block 'A'	**Oblique wind incidence (45^{o})**								
	Windward side Cp				**Leeward side Cp**				***⊿Cp***
(m)	low $_{8th}$	high $_{8th}$	avg $_{90\%}$	sdev	low $_{8th}$	high $_{8th}$	avg $_{90\%}$	sdev	
90	0.74	0.78	0.75	0.03	-	-	-	-	**-**
85	0.86	0.97	0.90	0.05	-	-	-	-	**-**
80	0.77	0.91	0.84	0.05	-	-	-	-	**-**
75	0.72	0.83	0.77	0.05	-	-	-	-	**-**
70	0.64	0.76	0.71	0.05	-	-	-	-	**-**
65	0.59	0.69	0.65	0.04	-	-	-	-	**-**
60	0.54	0.59	0.57	0.02	0.52	0.56	0.55	0.01	***0.03***
55	0.51	0.56	0.54	0.02	0.44	0.50	0.49	0.02	***0.05***
50	0.46	0.51	0.50	0.02	0.41	0.48	0.44	0.02	***0.06***
45	0.42	0.48	0.46	0.02	0.36	0.42	0.39	0.02	***0.06***
40	0.36	0.45	0.42	0.03	0.30	0.37	0.35	0.02	***0.07***
35	0.33	0.41	0.38	0.03	0.20	0.32	0.29	0.03	***0.08***
30	0.26	0.46	0.30	0.07	0.16	0.31	0.26	0.04	***0.05***
25	0.21	0.36	0.24	0.07	0.11	0.24	0.20	0.05	***0.03***
20	0.16	0.31	0.18	0.06	0.13	0.19	0.17	0.02	***0.01***
15	0.12	0.28	0.13	0.06	0.12	0.15	0.14	0.01	***-0.01***
10	0.12	0.28	0.13	0.06	0.09	0.13	0.12	0.01	***0.01***
5	0.04	0.22	0.10	0.05	0.05	0.10	0.09	0.01	***0.02***
2	0.02	0.21	0.08	0.06	0.03	0.08	0.06	0.01	***0.02***
avg	***0.32***	***0.44***	***0.36***	***0.04***	***0.22***	***0.30***	***0.27***	***0.02***	***0.04***

Source: this study.

Table 39: Cp results for the D3 Block 'B' scenario for oblique winds (45 ^{o})

D3- Block 'B'	**Oblique wind incidence (45^{o})**								
	Windward side Cp				**Leeward side Cp**				***⊿Cp***
(m)	low $_{8th}$	high $_{8th}$	avg $_{90\%}$	sdev	low $_{8th}$	high $_{8th}$	avg $_{90\%}$	sdev	
60	0.42	0.43	0.43	0.01	0.36	0.44	0.41	0.03	***0.02***
55	0.36	0.39	0.37	0.01	0.32	0.39	0.36	0.03	***0.01***
50	0.31	0.35	0.33	0.01	0.27	0.35	0.32	0.03	***0.01***
45	0.26	0.30	0.28	0.02	-0.01	0.12	0.08	0.05	***0.20***
40	0.20	0.27	0.24	0.02	0.17	0.26	0.22	0.03	***0.01***
35	0.15	0.23	0.19	0.03	0.12	0.21	0.17	0.04	***0.02***
30	0.11	0.30	0.19	0.05	0.05	0.18	0.13	0.04	***0.07***
25	0.08	0.39	0.14	0.08	-0.01	0.12	0.08	0.05	***0.06***
20	0.05	0.35	0.10	0.08	-0.06	0.09	0.04	0.05	***0.06***
15	0.01	0.30	0.06	0.07	-0.09	0.05	0.00	0.05	***0.06***
10	-0.03	0.25	0.02	0.07	-0.09	0.05	0.00	0.05	***0.03***
5	-0.06	0.20	-0.02	0.07	-0.15	-0.03	-0.07	0.05	***0.06***
2	-0.07	0.18	-0.03	0.06	-0.17	-0.06	-0.11	0.04	***0.08***
avg	***0.42***	***0.43***	***0.43***	***0.01***	***0.36***	***0.44***	***0.41***	***0.03***	***0.02***

Source: this study.

Table 40: Cp results for the D04 for parallel winds (0^o)

D4- Tower 1	Parallel wind incidence (0^o)								
	Right side Cp				Left side Cp				⊿Cp
(m)	low 8th	high 8th	avg 90%	sdev	low 8th	high 8th	avg 90%	sdev	
30	0.26	0.27	0.26	0.01	0.26	0.27	0.27	0.01	***0.00***
25	0.21	0.22	0.22	0.01	0.22	0.22	0.22	0.01	***-0.01***
20	0.17	0.18	0.18	0.01	0.17	0.18	0.18	0.01	***0.00***
15	0.12	0.14	0.13	0.01	0.13	0.14	0.14	0.01	***-0.01***
10	0.09	0.10	0.09	0.01	0.09	0.10	0.10	0.01	***-0.01***
5	0.04	0.05	0.05	0.01	0.05	0.06	0.06	0.01	***-0.01***
2	0.02	0.03	0.03	0.01	0.02	0.04	0.03	0.01	***-0.01***
avg	***0.14***	***0.14***	***0.14***	***0.01***	***0.14***	***0.15***	***0.14***	***0.01***	***-0.01***

Source: this study.

Table 41: Cp results for the D4 scenario Tower 2 for parallel winds (0 o)

D4- Tower 2	Parallel wind incidence (0^o)								
	Right side Cp				Left side Cp				⊿Cp
(m)	low 8th	high 8th	avg 90%	sdev	low 8th	high 8th	avg 90%	sdev	
60	0.44	0.47	0.46	0.03	0.39	0.44	0.43	0.03	***0.03***
55	0.38	0.44	0.42	0.04	0.37	0.39	0.38	0.02	***0.04***
50	0.34	0.40	0.38	0.03	0.29	0.35	0.34	0.03	***0.04***
45	0.30	0.35	0.34	0.03	0.29	0.31	0.30	0.02	***0.04***
40	0.26	0.31	0.30	0.03	0.22	0.27	0.26	0.03	***0.04***
35	0.23	0.27	0.26	0.03	0.22	0.24	0.23	0.02	***0.03***
30	0.19	0.23	0.22	0.02	0.18	0.21	0.20	0.02	***0.02***
25	0.16	0.19	0.18	0.02	0.16	0.17	0.16	0.02	***0.02***
20	0.12	0.15	0.14	0.02	0.11	0.13	0.13	0.01	***0.02***
15	0.09	0.11	0.10	0.02	0.08	0.09	0.09	0.01	***0.02***
10	0.05	0.07	0.06	0.02	0.04	0.06	0.05	0.01	***0.01***
5	0.01	0.03	0.02	0.02	0.01	0.02	0.01	0.01	***0.01***
2	-0.01	0.01	0.00	0.01	-0.01	0.00	-0.01	0.01	***0.01***
avg	***0.20***	***0.23***	***0.22***	***0.02***	***0.18***	***0.21***	***0.20***	***0.02***	***0.00***

Source: this study.

Table 42: Cp results for the D4 scenario Tower 3 narrow for parallel winds (0 ^{o})

D4- Tower 3 Narrow	Parallel wind incidence (0^{o})								
	Right side Cp				Left side Cp				⊿Cp
(m)	low $_{8th}$	high $_{8th}$	avg $_{90\%}$	sdev	low $_{8th}$	high $_{8th}$	avg $_{90\%}$	sdev	
90	0.67	0.73	0.72	0.03	0.66	0.73	0.72	0.03	***0.00***
85	0.61	0.69	0.68	0.04	0.61	0.69	0.68	0.05	***0.00***
80	0.57	0.65	0.64	0.04	0.56	0.66	0.64	0.05	***0.00***
75	0.54	0.61	0.60	0.04	0.53	0.61	0.60	0.04	***-0.01***
70	0.50	0.57	0.55	0.03	0.50	0.58	0.56	0.04	***-0.01***
65	0.68	0.74	0.52	0.09	0.24	0.25	0.53	0.02	***-0.01***
60	0.45	0.49	0.48	0.02	0.45	0.50	0.49	0.02	***-0.01***
55	0.42	0.45	0.44	0.02	0.43	0.46	0.45	0.02	***-0.01***
50	0.37	0.42	0.41	0.01	0.38	0.43	0.42	0.02	***-0.01***
45	0.35	0.38	0.37	0.01	0.36	0.39	0.38	0.02	***-0.02***
40	0.30	0.34	0.33	0.01	0.32	0.35	0.34	0.02	***-0.02***
35	0.27	0.30	0.29	0.01	0.29	0.31	0.31	0.02	***-0.02***
30	0.22	0.26	0.25	0.01	0.24	0.27	0.27	0.02	***-0.02***
25	0.18	0.21	0.20	0.01	0.21	0.23	0.23	0.02	***-0.03***
20	0.14	0.17	0.16	0.01	0.16	0.20	0.19	0.02	***-0.03***
15	0.10	0.13	0.12	0.02	0.13	0.16	0.15	0.02	***-0.03***
10	0.06	0.10	0.08	0.02	0.09	0.12	0.11	0.02	***-0.03***
5	0.02	0.07	0.05	0.02	0.05	0.08	0.07	0.02	***-0.03***
2	0.00	0.05	0.02	0.02	0.03	0.05	0.05	0.02	***-0.02***
avg	***0.34***	***0.39***	***0.37***	***0.03***	***0.33***	***0.37***	***0.36***	***0.02***	***0.01***

Source: this study.

Table 43: Cp results for D4 orthogonal winds (90^{o})

D4- Tower 1	Orthogonal wind incidence (90^{o})								
	Windward side Cp				Leeward side Cp				⊿Cp
(m)	low $_{8th}$	high $_{8th}$	avg $_{90\%}$	sdev	low $_{8th}$	high $_{8th}$	avg $_{90\%}$	sdev	
30	0.27	0.28	0.28	0.00	0.26	0.27	0.26	0.00	***0.01***
25	0.24	0.28	0.27	0.02	0.20	0.21	0.21	0.01	***0.07***
20	0.20	0.23	0.22	0.01	0.16	0.17	0.16	0.00	***0.06***
15	0.15	0.18	0.18	0.01	0.12	0.13	0.12	0.01	***0.05***
10	0.11	0.13	0.13	0.01	0.09	0.09	0.09	0.01	***0.04***
5	0.06	0.09	0.09	0.01	0.06	0.07	0.07	0.01	***0.02***
2	0.03	0.07	0.06	0.01	0.04	0.05	0.05	0.01	***0.01***
avg	***0.16***	***0.18***	***0.17***	***0.01***	***0.14***	***0.14***	***0.14***	***0.00***	***0.04***

Source: this study.

Table 44: Cp results for the D4 scenario Tower 2 for orthogonal winds (90 ^{o})

D4- Tower 2	**Orthogonal wind incidence (90^{o})**								
	Windward side Cp				**Leeward side Cp**				***⊿Cp***
(m)	low $_{8th}$	high $_{8th}$	avg $_{90\%}$	sdev	low $_{8th}$	high $_{8th}$	avg $_{90\%}$	sdev	
60	0.44	0.49	0.46	0.02	0.45	0.46	0.46	0.01	***0.00***
55	0.58	0.64	0.62	0.07	0.37	0.40	0.40	0.01	***0.23***
50	0.40	0.55	0.55	0.06	0.33	0.36	0.35	0.01	***0.20***
45	0.44	0.48	0.47	0.05	0.30	0.31	0.31	0.01	***0.17***
40	0.32	0.41	0.40	0.04	0.25	0.27	0.26	0.01	***0.14***
35	0.32	0.35	0.34	0.03	0.21	0.23	0.22	0.01	***0.12***
30	0.24	0.29	0.28	0.02	0.16	0.19	0.18	0.01	***0.10***
25	0.22	0.24	0.23	0.02	0.12	0.15	0.14	0.01	***0.09***
20	0.16	0.19	0.18	0.01	0.07	0.11	0.10	0.02	***0.08***
15	0.13	0.14	0.13	0.01	0.04	0.08	0.06	0.02	***0.07***
10	0.08	0.10	0.10	0.01	-0.01	0.05	0.03	0.02	***0.07***
5	0.05	0.07	0.06	0.01	-0.03	0.02	-0.01	0.03	***0.07***
2	0.03	0.06	0.04	0.01	-0.05	0.00	-0.03	0.03	***0.07***
avg	***0.26***	***0.31***	***0.30***	***0.03***	***0.17***	***0.20***	***0.19***	***0.01***	***0.11***

Source: this study.

Table 45: Cp results for the D4 scenario Tower 3 Wide for orthogonal winds (90 ^{o})

D4- Tower 3 Wide	**Orthogonal wind incidence (90^{o})**								
	Windward side Cp				**Leeward side Cp**				***⊿Cp***
(m)	low $_{8th}$	high $_{8th}$	avg $_{90\%}$	sdev	low $_{8th}$	high $_{8th}$	avg $_{90\%}$	sdev	
90	0.60	0.65	0.62	0.03	0.68	0.69	0.68	0.01	***-0.06***
85	0.78	1.07	0.80	0.13	0.61	0.64	0.63	0.01	***0.17***
80	0.55	1.00	0.77	0.12	0.57	0.59	0.58	0.01	***0.19***
75	0.69	0.89	0.74	0.11	0.53	0.54	0.54	0.01	***0.20***
70	0.46	0.83	0.69	0.10	0.48	0.50	0.49	0.01	***0.20***
65	0.60	0.72	0.64	0.09	0.44	0.46	0.45	0.01	***0.19***
60	0.38	0.64	0.59	0.08	0.39	0.41	0.41	0.01	***0.19***
55	0.50	0.55	0.54	0.07	0.34	0.37	0.36	0.01	***0.18***
50	0.30	0.49	0.48	0.06	0.29	0.33	0.32	0.02	***0.16***
45	0.35	0.44	0.43	0.05	0.24	0.30	0.28	0.02	***0.14***
40	0.23	0.38	0.37	0.04	0.19	0.26	0.24	0.02	***0.13***
35	0.25	0.33	0.32	0.04	0.16	0.22	0.21	0.02	***0.11***
30	0.15	0.27	0.27	0.03	0.12	0.18	0.17	0.02	***0.10***
25	0.16	0.22	0.21	0.03	0.10	0.14	0.13	0.02	***0.08***
20	0.07	0.17	0.16	0.03	0.07	0.10	0.09	0.01	***0.07***
15	0.07	0.13	0.12	0.03	0.04	0.06	0.05	0.01	***0.06***
10	0.01	0.10	0.09	0.03	0.00	0.02	0.01	0.01	***0.07***
5	0.00	0.08	0.07	0.03	-0.04	-0.02	-0.03	0.01	***0.09***
2	-0.01	0.08	0.06	0.03	-0.06	-0.04	-0.05	0.01	***0.11***
avg	***0.32***	***0.48***	***0.42***	***0.06***	***0.27***	***0.30***	***0.29***	***0.01***	***0.12***

Source: this study.

Table 46: Cp results for the D4 for oblique winds (45°)

D4- Tower 1	Oblique wind incidence (45°)								
	Windward side Cp				Leeward side Cp				ΔCp
(m)	low 8th	high 8th	avg 90%	sdev	low 8th	high 8th	avg 90%	sdev	
30	0.21	0.29	0.28	0.03	0.19	0.21	0.20	0.01	***0.08***
25	0.16	0.24	0.23	0.03	0.15	0.17	0.16	0.01	***0.07***
20	0.10	0.19	0.18	0.03	0.11	0.13	0.12	0.01	***0.06***
15	0.06	0.14	0.13	0.03	0.07	0.08	0.07	0.01	***0.05***
10	0.03	0.09	0.08	0.03	0.03	0.04	0.03	0.01	***0.05***
5	-0.01	0.07	0.05	0.03	0.01	0.02	0.01	0.01	***0.04***
2	0.11	0.18	0.17	0.03	0.12	0.13	0.12	0.01	***0.05***
avg	***0.11***	***0.18***	***0.17***	***0.03***	***0.12***	***0.13***	***0.12***	***0.01***	***0.05***

Source: this study.

Table 47: Cp results for the D4 scenario Tower 2 for oblique winds (45°)

D4- Tower 2	Oblique wind incidence (45°)								
	Windward side Cp				Leeward side Cp				ΔCp
(m)	low 8th	high 8th	avg 90%	sdev	low 8th	high 8th	avg 90%	sdev	
60	0.48	0.55	0.52	0.04	0.42	0.46	0.45	0.02	***0.07***
55	0.52	0.57	0.54	0.05	0.34	0.39	0.37	0.03	***0.17***
50	0.42	0.48	0.47	0.03	0.29	0.35	0.34	0.03	***0.13***
45	0.38	0.42	0.41	0.03	0.28	0.31	0.30	0.02	***0.10***
40	0.31	0.37	0.36	0.02	0.24	0.27	0.27	0.01	***0.10***
35	0.29	0.33	0.32	0.02	0.21	0.23	0.22	0.01	***0.10***
30	0.23	0.29	0.27	0.03	0.16	0.18	0.18	0.01	***0.10***
25	0.19	0.25	0.23	0.03	0.12	0.14	0.13	0.01	***0.09***
20	0.13	0.21	0.17	0.03	0.06	0.10	0.09	0.02	***0.09***
15	0.10	0.15	0.12	0.03	0.02	0.05	0.05	0.01	***0.07***
10	0.02	0.07	0.04	0.03	-0.02	0.01	0.00	0.01	***0.04***
5	0.00	0.05	0.02	0.03	-0.06	-0.03	-0.04	0.01	***0.06***
2	-0.02	0.02	0.00	0.02	-0.08	-0.05	-0.06	0.01	***0.06***
avg	***0.23***	***0.29***	***0.27***	***0.03***	***0.15***	***0.19***	***0.18***	***0.02***	***0.09***

Source: this study.

Table 48: Cp results for the D4 scenario Tower 3 for oblique winds (45 ^{o})

D4- Tower 3	**Oblique wind incidence (45^{o})**								
	Windward side Cp				**Leeward side Cp**				***⊿Cp***
(m)	low $_{8th}$	high $_{8th}$	avg $_{90\%}$	sdev	low $_{8th}$	high $_{8th}$	avg $_{90\%}$	sdev	
90	0.68	0.76	0.72	0.06	0.63	0.70	0.68	0.03	***0.04***
85	0.83	0.93	0.90	0.08	0.53	0.63	0.60	0.04	***0.30***
80	0.75	0.89	0.86	0.08	0.50	0.61	0.56	0.04	***0.30***
75	0.73	0.83	0.81	0.08	0.45	0.55	0.51	0.04	***0.30***
70	0.65	0.77	0.75	0.07	0.40	0.51	0.47	0.04	***0.28***
65	0.62	0.69	0.69	0.06	0.36	0.46	0.42	0.04	***0.26***
60	0.54	0.63	0.62	0.06	0.31	0.42	0.38	0.04	***0.24***
55	0.51	0.56	0.55	0.05	0.26	0.37	0.34	0.04	***0.22***
50	0.45	0.50	0.49	0.05	0.21	0.34	0.29	0.04	***0.19***
45	0.41	0.44	0.43	0.04	0.17	0.29	0.25	0.05	***0.17***
40	0.34	0.38	0.37	0.04	0.12	0.25	0.22	0.05	***0.15***
35	0.31	0.33	0.32	0.04	0.11	0.21	0.19	0.04	***0.13***
30	0.24	0.28	0.27	0.03	0.09	0.17	0.15	0.03	***0.11***
25	0.21	0.23	0.22	0.03	0.07	0.13	0.12	0.02	***0.10***
20	0.14	0.18	0.17	0.02	0.04	0.09	0.08	0.02	***0.09***
15	0.11	0.13	0.13	0.02	0.02	0.05	0.04	0.01	***0.09***
10	0.05	0.09	0.08	0.02	-0.02	0.01	0.00	0.01	***0.09***
5	0.03	0.04	0.04	0.02	-0.06	-0.04	-0.05	0.01	***0.09***
2	0.01	0.03	0.02	0.01	-0.07	-0.06	-0.07	0.01	***0.09***
avg	***0.40***	***0.46***	***0.44***	***0.05***	***0.22***	***0.30***	***0.27***	***0.03***	***0.17***

Source: this study.

Appendix 5: Cardiff Cathatys Campus Graphs and Tables

In Appendix 5 the CP and ΔCp contour plots, graphs and tables which support the assessment of Chapter 8: 'Cathays Campus: Results and Analysis' are presented. These data cover in details the output from all the wind tunnel and CFD simulations carried out for the Caste Study1: the Cardiff University Cathays Campus area, and specifically the urban canyon in the Museum Avenue formed by the Welsh Assembly building and the Law School building, and for eight wind directions (0^o, 45^o, and 90^o).

Figure 1: The Law School building (marked in red) and the assessed urban canyon (Museum Avenue- marked in green) in the Cathays Campus

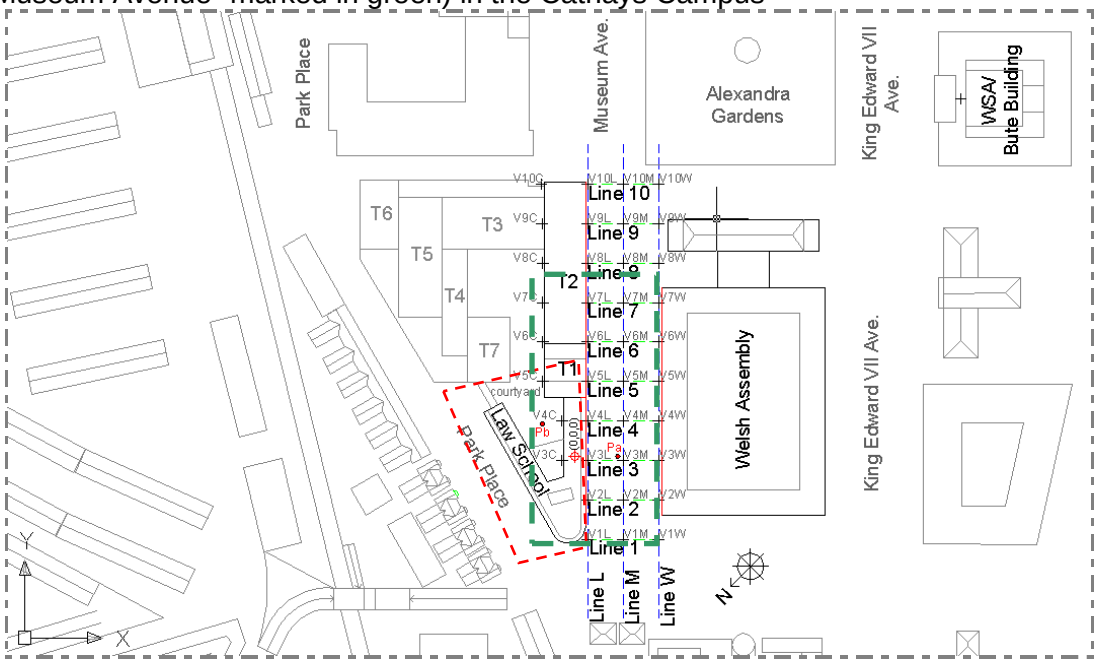

Source: this study.

Table 1: Cp results for North winds: oblique (45°) to the Museum Ave. and orthogonal (90°) to the Park Place:

N	CFD Law School (45°) Museum Ave. side Cp				Museum Ave. side courtyard Cp					WT Law School (45°) Museum Ave. side Cp				Museum Ave. side courtyard Cp				
line h (m)	min peak	max peak	avg 90%	sdev	min peak	max peak	avg 90%	sdev	△Cp	min peak	max peak	avg 90%	sdev	min peak	max peak	avg 90%	sdev	△Cp
15.0	-0.17	-0.08	-0.13	0.03	-0.12	0.09	-0.05	0.05	0.08	-0.07	-0.03	-0.05	0.01	-0.01	0.13	0.01	0.06	0.06
12.5	-0.20	-0.08	-0.15	0.04	-0.10	0.01	-0.03	0.03	0.11	-0.05	-0.03	-0.05	0.01	-0.03	0.10	0.01	0.05	0.06
10.0	-0.23	-0.06	-0.13	0.04	-0.11	-0.01	-0.08	0.02	0.05	-	-	-	-	-	-	-	-	-
8.5	-0.17	-0.02	-0.07	0.05	-0.11	-0.02	-0.08	0.03	0.02	-0.05	-0.02	-0.04	0.01	-0.02	0.13	0.02	0.06	0.07
7.0	-0.17	-0.02	-0.06	0.05	-0.09	0.00	-0.07	0.02	0.02	-	-	-	-	-	-	-	-	-
5.0	-0.15	-0.01	-0.04	0.04	-0.08	0.03	-0.06	0.04	0.01	-0.03	0.00	0.00	0.01	-	-	-	-	-
3.5	-0.12	0.01	-0.02	0.04	-0.10	0.08	-0.04	0.05	0.02	-	-	-	-	-	-	-	-	-
2.0	-0.10	0.02	-0.01	0.04	-0.10	0.08	-0.04	0.05	0.04	-	-	-	-	-	-	-	-	-
△Cp	-0.17	-0.03	-0.08	0.04	-0.10	0.03	-0.06	0.04	0.04	-0.05	-0.02	-0.04	0.01	-0.02	0.12	0.02	0.06	0.06

N	CFD Law School (90°) Park Place. side Cp				Park Place side courtyard Cp					WT Law School (90°) Park Place. side Cp				Park Place side courtyard Cp				
line h (m)	min peak	max peak	avg 90%	sdev	min peak	max peak	avg 90%	sdev	△Cp	min peak	max peak	avg 90%	sdev	min peak	max peak	avg 90%	sdev	△Cp
15.0	-0.08	0.24	-0.05	0.09	-0.14	-0.07	-0.09	0.02	0.04	0.01	0.16	0.03	0.08	-0.05	-0.02	-0.02	0.01	0.05
12.5	-0.09	0.23	-0.08	0.14	-0.16	-0.06	-0.10	0.02	0.02	-0.01	0.04	0.00	0.02	-0.05	-0.01	-0.01	0.02	0.01
10.0	-0.06	0.21	0.21	0.09	-0.16	-0.07	-0.10	0.02	0.30	-	-	-	-	-	-	-	-	-
8.5	-0.08	0.23	0.12	0.14	-0.13	-0.06	-0.10	0.02	0.22	-0.02	0.02	0.00	0.01	-	-	-	-	-
7.0	-0.06	0.25	0.00	0.11	-0.11	-0.05	-0.09	0.02	0.09	-	-	-	-	-	-	-	-	-
5.0	0.21	0.24	0.21	0.01	-0.10	-0.03	-0.07	0.02	0.29	-0.01	0.05	0.00	0.02	-	-	-	-	-
3.5	-0.07	0.27	0.22	0.10	-0.09	-0.01	-0.04	0.03	0.25	-	-	-	-	-	-	-	-	-
2.0	-0.03	0.24	0.09	0.12	-0.08	0.01	-0.01	0.03	0.10	-	-	-	-	-	-	-	-	-
△Cp	-0.03	0.24	0.09	0.10	-0.12	-0.04	-0.07	0.02	0.16	0.00	0.07	0.01	0.03	-0.05	-0.01	-0.02	0.02	0.03

Source: this study.

Table 2: Cp results for South winds: oblique (45^{o}) to the Museum Ave. and orthogonal (90o) to the Park Place:

S	CFD Law School (45^{o}) Museum Ave. side Cp				Museum Ave. side courtyard Cp					WT Law School (45^{o}) Museum Ave. side Cp				Museum Ave. side courtyard Cp				
line h (m)	min peak	max peak	avg 90%	sdev	min peak	max peak	avg 90%	sdev	△Cp	min peak	max peak	avg 90%	sdev	min peak	max peak	avg 90%	sdev	△Cp
15.0	-0.36	-0.02	-0.13	0.10	-0.28	-0.17	-0.19	0.04	0.06	-0.05	0.07	0.05	0.04	-0.09	0.00	-0.01	0.04	0.06
12.5	-0.19	0.04	-0.03	0.07	-0.22	-0.17	-0.18	0.02	0.15	-0.05	0.06	0.04	0.04	-0.09	0.03	0.03	0.05	0.01
10.0	-0.15	0.04	-0.02	0.05	-0.21	-0.14	-0.17	0.02	0.15	-	-	-	-	-	-	-	-	-
8.5	-0.10	-0.01	-0.03	0.02	-0.20	-0.12	-0.16	0.02	0.13	-0.04	0.06	0.03	0.03	-0.07	0.03	0.02	0.04	0.02
7.0	-0.09	-0.02	-0.03	0.02	-0.23	-0.11	-0.16	0.03	0.13	-	-	-	-	-	-	-	-	-
5.0	-0.08	-0.02	-0.03	0.02	-0.22	-0.10	-0.16	0.03	0.13	-0.03	0.05	0.00	0.03	-	-	-	-	-
3.5	-0.08	-0.01	-0.03	0.02	-0.17	-0.05	-0.14	0.04	0.11	-	-	-	-	-	-	-	-	-
2.0	-0.07	-0.01	-0.02	0.02	-0.17	-0.05	-0.14	0.04	0.12	-	-	-	-	-	-	-	-	-
△Cp	-0.14	0.00	-0.04	0.04	-0.21	-0.11	-0.16	0.03	0.12	-0.04	0.06	0.03	0.03	-0.08	0.02	0.01	0.04	0.03

S	CFD Law School (90^{o}) Park Place. side Cp				Park Place side courtyard Cp					WT Law School (90^{o}) Park Place. side Cp				Park Place side courtyard Cp				
line h (m)	min peak	max peak	avg 90%	sdev	min peak	max peak	avg 90%	sdev	△Cp	min peak	max peak	avg 90%	sdev	min peak	max peak	avg 90%	sdev	△Cp
15.0	-0.29	-0.21	-0.25	0.03	-0.22	0.02	-0.21	0.07	0.04	-0.07	-0.05	-0.06	0.01	-0.08	-0.03	-0.07	0.02	0.01
12.5	-0.28	-0.21	-0.25	0.03	-0.19	0.09	-0.18	0.07	0.07	-0.07	-0.04	-0.05	0.01	-0.06	0.02	-0.03	0.03	0.02
10.0	-0.27	-0.20	-0.23	0.03	-0.21	0.01	-0.18	0.05	0.05	-	-	-	-	-	-	-	-	-
8.5	-0.24	-0.17	-0.20	0.02	-0.24	-0.11	-0.17	0.03	0.02	-0.07	-0.04	-0.05	0.01	-	-	-	-	-
7.0	-0.22	-0.17	-0.19	0.02	-0.28	-0.11	-0.16	0.05	0.03	-	-	-	-	-	-	-	-	-
5.0	-0.20	-0.16	-0.18	0.01	-0.34	-0.04	-0.15	0.08	0.03	-0.05	-0.03	0.00	0.01	-	-	-	-	-
3.5	-0.18	-0.15	-0.17	0.01	-66.9	0.02	-0.15	19.57	0.02	-	-	-	-	-	-	-	-	-
2.0	-0.17	-0.13	-0.16	0.01	-57.0	8.12	-0.10	21.75	0.06	-	-	-	-	-	-	-	-	-
△Cp	-0.23	-0.17	-0.20	0.02	-15.7	1.00	-0.16	5.21	0.04	-0.06	-0.04	-0.04	0.01	-0.07	-0.01	-0.05	0.03	0.02

Source: this study.

Table 3: Cp results for East winds: oblique (45°) to the Museum Ave. and parallel (0°) to the Park Place:

E	CFD Law School (45°) Museum Ave. side Cp				Museum Ave. side courtyard Cp					WT Law School (45°) Museum Ave. side Cp				Museum Ave. side courtyard Cp				
line h (m)	min peak	max peak	avg 90%	sdev	min peak	max peak	avg 90%	sdev	△Cp	min peak	max peak	avg 90%	sdev	min peak	max peak	avg 90%	sdev	△Cp
15.0	-0.40	-0.09	-0.28	0.10	-0.39	-0.07	-0.31	0.10	0.03	-0.05	-0.01	-0.02	0.01	-0.05	0.01	-0.01	0.03	0.00
12.5	-0.40	-0.09	-0.19	0.08	-0.38	-0.09	-0.30	0.11	0.11	-0.04	0.00	-0.01	0.01	-0.05	0.02	0.00	0.03	0.01
10.0	-0.34	-0.09	-0.18	0.07	-0.37	-0.09	-0.26	0.07	0.09	-	-	-	-	-	-	-	-	-
8.5	-0.11	-0.04	-0.06	0.02	-0.34	-0.07	-0.19	0.10	0.12	-0.04	0.01	-0.01	0.01	-0.04	0.03	0.00	0.03	0.01
7.0	-0.08	-0.03	-0.04	0.01	-0.38	-0.04	-0.24	0.07	0.20	-	-	-	-	-	-	-	-	-
5.0	-0.06	-0.02	-0.03	0.01	-0.35	0.29	-0.17	0.17	0.14	-0.03	0.00	0.00	0.01	-	-	-	-	-
3.5	-0.04	-0.01	-0.02	0.01	-0.18	-0.02	-0.11	0.05	0.09	-	-	-	-	-	-	-	-	-
2.0	-0.03	-0.01	-0.01	0.01	-0.18	-0.02	-0.11	0.05	0.10	-	-	-	-	-	-	-	-	-
△Cp	-0.18	-0.05	-0.10	0.04	-0.32	-0.01	-0.21	0.09	0.11	-0.04	0.00	-0.01	0.01	-0.05	0.02	0.00	0.03	0.01

E	CFD Law School (0°) Park Place. side Cp				Park Place side courtyard Cp					WT Law School (0°) Park Place. side Cp				Park Place side courtyard Cp				
line h (m)	min peak	max peak	avg 90%	sdev	min peak	max peak	avg 90%	sdev	△Cp	min peak	max peak	avg 90%	sdev	min peak	max peak	avg 90%	sdev	△Cp
15.0	-0.36	-0.08	-0.23	0.09	-0.40	-0.10	-0.28	0.10	0.05	0.00	0.03	0.01	0.01	0.00	0.03	0.01	0.01	0.00
12.5	-0.27	-0.08	-0.16	0.06	-0.38	-0.17	-0.27	0.07	0.11	0.01	0.03	0.01	0.01	0.03	0.06	0.04	0.01	0.03
10.0	-0.27	-0.08	-0.17	0.06	-0.33	-0.15	-0.25	0.08	0.08	-	-	-	-	-	-	-	-	-
8.5	-0.13	-0.06	-0.08	0.02	-0.31	-0.10	-0.23	0.09	0.14	0.00	0.02	0.01	0.01	-	-	-	-	-
7.0	-0.09	-0.03	-0.06	0.02	-0.30	0.08	-0.15	0.12	0.08	-	-	-	-	-	-	-	-	-
5.0	-0.07	0.03	-0.06	0.02	-0.29	-0.03	-0.12	0.10	0.07	0.00	0.02	0.00	0.01	-	-	-	-	-
3.5	-0.06	0.07	-0.05	0.02	-0.28	-0.06	-0.23	0.09	0.18	-	-	-	-	-	-	-	-	-
2.0	-0.05	0.06	-0.04	0.02	-0.33	-0.24	-0.27	0.03	0.24	-	-	-	-	-	-	-	-	-
△Cp	-0.16	-0.02	-0.11	0.04	-0.33	-0.10	-0.23	0.08	0.12	0.00	0.03	0.01	0.01	0.02	0.05	0.03	0.01	0.02

Source: this study.

Table 4: Cp results for West winds: oblique (45°) to the Museum Ave. and parallel (0°) to the Park Place:

W	CFD Law School (45°) Museum Ave. side Cp				Museum Ave. side courtyard Cp					WT Law School (45°) Museum Ave. side Cp				Museum Ave. side courtyard Cp				
line h (m)	min peak	max peak	avg 90%	sdev	min peak	max peak	avg 90%	sdev	△Cp	min peak	max peak	avg 90%	sdev	min peak	max peak	avg 90%	sdev	△Cp
15.0	0.07	0.28	0.11	0.05	0.02	0.40	0.08	0.09	0.03	-0.02	0.03	0.02	0.02	0.01	0.03	0.01	0.01	0.00
12.5	0.05	0.24	0.10	0.06	0.01	0.22	0.11	0.06	0.00	-0.02	0.02	0.00	0.01	0.03	0.12	0.07	0.04	0.08
10.0	0.04	0.25	0.10	0.06	0.03	0.17	0.12	0.05	0.02	-	-	-	-	-	-	-	-	-
8.5	0.00	0.27	0.08	0.08	0.04	0.24	0.14	0.05	0.07	0.00	0.01	0.01	0.01	0.02	0.11	0.05	0.04	0.04
7.0	0.00	0.29	0.07	0.08	0.02	0.27	0.15	0.07	0.08	-	-	-	-	-	-	-	-	-
5.0	-0.01	0.28	0.06	0.08	0.14	0.44	0.18	0.10	0.12	-0.01	0.02	0.00	0.01	-	-	-	-	-
3.5	-0.02	0.28	0.06	0.08	-0.17	0.23	0.12	0.14	0.07	-	-	-	-	-	-	-	-	-
2.0	-0.01	0.27	0.06	0.08	-0.17	0.23	0.12	0.14	0.06	-	-	-	-	-	-	-	-	-
△Cp	0.01	0.27	0.08	0.07	-0.01	0.28	0.13	0.09	0.06	-0.01	0.02	0.00	0.01	0.02	0.09	0.05	0.03	0.04

W	CFD Law School (0°) Park Place. side Cp				Park Place side courtyard Cp					WT Law School (0°) Park Place. side Cp				Park Place side courtyard Cp				
line h (m)	min peak	max peak	avg 90%	sdev	min peak	max peak	avg 90%	sdev	△Cp	min peak	max peak	avg 90%	sdev	min peak	max peak	avg 90%	sdev	△Cp
15.0	-0.13	0.02	0.00	0.04	-0.14	0.22	0.03	0.10	0.03	0.01	0.17	0.05	0.06	0.01	0.03	0.02	0.01	0.03
12.5	-0.14	0.03	-0.03	0.05	0.05	0.49	0.14	0.14	0.17	0.06	0.11	0.07	0.02	-0.01	0.04	0.03	0.02	0.04
10.0	-0.16	0.03	-0.02	0.05	0.12	0.49	0.18	0.13	0.20	-	-	-	-	-	-	-	-	-
8.5	-0.05	0.08	0.03	0.04	0.12	0.47	0.22	0.13	0.19	0.05	0.10	0.06	0.02	-	-	-	-	-
7.0	-0.02	0.09	0.05	0.04	0.12	0.48	0.24	0.13	0.19	-	-	-	-	-	-	-	-	-
5.0	0.00	0.13	0.07	0.04	0.10	0.48	0.28	0.13	0.22	0.06	0.11	0.00	0.02	-	-	-	-	-
3.5	0.03	0.16	0.08	0.03	0.05	0.49	0.40	0.13	0.31	-	-	-	-	-	-	-	-	-
2.0	0.05	0.17	0.10	0.03	0.22	0.50	0.47	0.07	0.37	-	-	-	-	-	-	-	-	-
△Cp	-0.05	0.09	0.04	0.04	0.08	0.45	0.24	0.12	0.21	0.04	0.12	0.05	0.03	0.00	0.04	0.03	0.02	0.03

Source: this study.

Table 5: Cp results for Northeast winds: orthogonal (90°) to the Museum Ave. and oblique (45°) to the Park Place:

NE	CFD Law School (90°) Museum Ave. side Cp				Museum Ave. side courtyard Cp					WT Law School (90°) Museum Ave. side Cp				Museum Ave. side courtyard Cp				
line h (m)	min peak	max peak	avg 90%	sdev	min peak	max peak	avg 90%	sdev	△Cp	min peak	max peak	avg 90%	sdev	min peak	max peak	avg 90%	sdev	△Cp
15.0	-0.27	-0.10	-0.17	0.05	-0.27	-0.02	-0.14	0.08	0.03	-0.06	-0.05	-0.05	0.00	-0.01	0.06	0.02	0.03	0.08
12.5	-0.26	-0.10	-0.19	0.05	-0.21	-0.02	-0.08	0.06	0.11	-0.06	-0.05	-0.05	0.01	-0.03	0.01	-0.02	0.02	0.03
10.0	-0.25	-0.09	-0.17	0.04	-0.24	-0.12	-0.18	0.04	0.01	-	-	-	-	-	-	-	-	-
8.5	-0.19	-0.07	-0.12	0.04	-0.26	-0.12	-0.22	0.05	0.10	-0.07	-0.04	-0.05	0.01	0.00	0.04	0.01	0.02	0.06
7.0	-0.17	-0.05	-0.11	0.04	-0.26	-0.08	-0.23	0.07	0.12	-	-	-	-	-	-	-	-	-
5.0	-0.15	-0.03	-0.09	0.04	-0.24	-0.04	-0.20	0.08	0.12	-0.05	-0.04	0.00	0.01	-	-	-	-	-
3.5	-0.12	0.01	-0.05	0.04	-0.25	-0.02	-0.21	0.07	0.16	-	-	-	-	-	-	-	-	-
2.0	-0.10	0.04	-0.02	0.05	-0.25	-0.02	-0.21	0.07	0.19	-	-	-	-	-	-	-	-	-
△Cp	-0.19	-0.05	-0.11	0.04	-0.25	-0.06	-0.18	0.07	0.10	-0.06	-0.04	-0.04	0.01	-0.01	0.04	0.00	0.02	0.06

NE	CFD Law School (45°) Park Place. side Cp				Park Place side courtyard Cp					WT Law School (45°) Park Place. side Cp				Park Place side courtyard Cp				
line h (m)	min peak	max peak	avg 90%	sdev	min peak	max peak	avg 90%	sdev	△Cp	min peak	max peak	avg 90%	sdev	min peak	max peak	avg 90%	sdev	△Cp
15.0	-0.15	0.32	-0.06	0.09	-0.33	-0.10	-0.25	0.06	0.19	0.02	0.18	0.06	0.05	-0.08	-0.05	-0.05	0.01	0.12
12.5	0.06	0.55	0.09	0.12	-0.35	-0.19	-0.27	0.04	0.35	-0.04	0.10	0.01	0.05	-0.08	-0.04	-0.05	0.01	0.06
10.0	0.06	0.54	0.09	0.11	-0.32	-0.22	-0.27	0.03	0.36	-	-	-	-	-	-	-	-	-
8.5	0.05	0.52	0.07	0.09	-0.30	-0.17	-0.26	0.04	0.33	-0.05	0.05	0.00	0.04	-	-	-	-	-
7.0	0.06	0.44	0.07	0.08	-0.27	-0.10	-0.25	0.06	0.32	-	-	-	-	-	-	-	-	-
5.0	0.05	0.40	0.07	0.08	-0.26	-0.05	-0.24	0.07	0.31	-0.05	0.08	0.00	0.04	-	-	-	-	-
3.5	0.06	0.41	0.07	0.08	-0.26	-0.03	-0.23	0.05	0.30	-	-	-	-	-	-	-	-	-
2.0	0.07	0.40	0.08	0.07	-0.23	-0.15	-0.22	0.02	0.30	-	-	-	-	-	-	-	-	-
△Cp	0.03	0.45	0.06	0.09	-0.29	-0.13	-0.25	0.05	0.31	-0.03	0.10	0.02	0.05	-0.08	-0.04	-0.05	0.01	0.09

Source: this study.

Table 6: Cp results for Southwest winds: orthogonal (90°) to the Museum Ave. and oblique (45°) to the Park Place:

SW	CFD Law School (90°) Museum Ave. side Cp				Museum Ave. side courtyard Cp					WT Law School (90°) Museum Ave. side Cp				Museum Ave. side courtyard Cp				
line h (m)	min peak	max peak	avg 90%	sdev	min peak	max peak	avg 90%	sdev	△Cp	min peak	max peak	avg 90%	sdev	min peak	max peak	avg 90%	sdev	△Cp
15.0	-0.04	0.18	-0.01	0.05	0.06	0.10	0.08	0.01	0.09	0.06	0.14	0.09	0.03	-0.01	0.02	0.02	0.01	0.07
12.5	-0.04	0.04	-0.02	0.02	0.09	0.11	0.10	0.01	0.12	0.01	0.09	0.04	0.03	-0.01	0.05	0.02	0.02	0.02
10.0	-0.05	0.26	-0.03	0.06	0.10	0.12	0.11	0.01	0.13	-	-	-	-	-	-	-	-	-
8.5	-0.08	0.20	-0.07	0.06	0.10	0.14	0.11	0.02	0.17	0.00	0.09	0.04	0.03	-0.01	0.04	0.02	0.02	0.03
7.0	-0.07	0.09	-0.05	0.04	0.10	0.21	0.12	0.03	0.17	-	-	-	-	-	-	-	-	-
5.0	-0.06	0.09	-0.03	0.04	0.09	0.23	0.12	0.04	0.16	0.03	0.10	0.00	0.03	-	-	-	-	-
3.5	-0.04	0.12	-0.02	0.04	0.09	0.25	0.15	0.05	0.16	-	-	-	-	-	-	-	-	-
2.0	-0.04	0.15	0.00	0.05	0.09	0.25	0.15	0.05	0.15	-	-	-	-	-	-	-	-	-
△Cp	-0.05	0.14	-0.03	0.04	0.09	0.18	0.12	0.03	0.15	0.02	0.10	0.04	0.03	-0.01	0.04	0.02	0.02	0.04

SW	CFD Law School (45°) Park Place. side Cp				Park Place side courtyard Cp					WT Law School (45°) Park Place. side Cp				Park Place side courtyard Cp				
line h (m)	min peak	max peak	avg 90%	sdev	min peak	max peak	avg 90%	sdev	△Cp	min peak	max peak	avg 90%	sdev	min peak	max peak	avg 90%	sdev	△Cp
15.0	-0.31	-0.20	-0.21	0.02	-0.31	0.44	-0.12	0.15	0.10	-0.07	-0.01	-0.04	0.02	0.01	0.03	0.02	0.01	0.05
12.5	-0.33	-0.16	-0.22	0.04	-0.02	0.48	0.08	0.12	0.30	-0.08	-0.03	-0.05	0.02	0.00	0.04	0.01	0.02	0.06
10.0	-0.32	-0.12	-0.21	0.03	0.05	0.39	0.11	0.09	0.32	-	-	-	-	-	-	-	-	-
8.5	-0.19	-0.15	-0.16	0.01	0.08	0.34	0.14	0.07	0.30	-0.06	-0.02	-0.04	0.01	-	-	-	-	-
7.0	-0.17	-0.14	-0.15	0.01	0.09	0.35	0.18	0.07	0.33	-	-	-	-	-	-	-	-	-
5.0	-0.16	-0.13	-0.14	0.01	0.10	0.35	0.20	0.07	0.34	-0.05	-0.01	0.00	0.01	-	-	-	-	-
3.5	-0.14	-0.11	-0.13	0.01	0.06	0.35	0.25	0.08	0.38	-	-	-	-	-	-	-	-	-
2.0	-0.13	-0.09	-0.12	0.01	0.17	0.35	0.29	0.05	0.42	-	-	-	-	-	-	-	-	-
△Cp	-0.22	-0.14	-0.17	0.02	0.03	0.38	0.14	0.09	0.31	-0.06	-0.02	-0.03	0.02	0.00	0.03	0.01	0.01	0.05

Source: this study.

Table 7 Cp results for Southeast winds: parallel (0°) to the Museum Ave. and oblique (45°) to the Park Place:

SE	CFD Law School (0°) Museum Ave. side Cp				Museum Ave. side courtyard Cp					WT Law School (0°) Museum Ave. side Cp				Museum Ave. side courtyard Cp				
line h (m)	min peak	max peak	avg 90%	sdev	min peak	max peak	avg 90%	sdev	△Cp	min peak	max peak	avg 90%	sdev	min peak	max peak	avg 90%	sdev	△Cp
15.0	-0.10	0.03	-0.03	0.04	-0.12	0.05	-0.04	0.06	0.02	-0.04	0.01	0.01	0.02	-0.02	0.02	0.00	0.02	0.01
12.5	-0.07	0.01	-0.03	0.03	-0.13	0.03	-0.09	0.05	0.06	-0.03	0.02	0.02	0.02	-0.01	0.02	0.01	0.01	0.00
10.0	-0.14	0.01	-0.04	0.04	-0.13	0.04	-0.07	0.05	0.03	-	-	-	-	-	-	-	-	-
8.5	-0.07	0.00	-0.03	0.02	-0.16	0.05	-0.05	0.06	0.02	-0.04	0.03	0.02	0.02	0.00	0.03	0.01	0.01	0.01
7.0	-0.06	0.00	-0.02	0.02	-0.19	0.06	-0.03	0.09	0.01	-	-	-	-	-	-	-	-	-
5.0	-0.05	0.01	-0.02	0.02	0.00	0.07	0.02	0.02	0.04	-0.03	0.03	0.00	0.02	-	-	-	-	-
3.5	-0.04	0.01	-0.02	0.02	-0.34	0.20	0.04	0.15	0.05	-	-	-	-	-	-	-	-	-
2.0	-0.04	0.01	-0.01	0.02	-0.34	0.20	0.04	0.15	0.05	-	-	-	-	-	-	-	-	-
△Cp	-0.07	0.01	-0.02	0.03	-0.18	0.09	-0.02	0.08	0.03	-0.04	0.02	0.01	0.02	-0.01	0.02	0.01	0.01	0.01

SE	CFD Law School (45°) Park Place. side Cp				Park Place side courtyard Cp					WT Law School (45°) Park Place. side Cp				Park Place side courtyard Cp				
line h (m)	min peak	max peak	avg 90%	sdev	min peak	max peak	avg 90%	sdev	△Cp	min peak	max peak	avg 90%	sdev	min peak	max peak	avg 90%	sdev	△Cp
15.0	-0.01	0.10	0.05	0.03	-0.05	0.06	-0.02	0.04	0.07	0.00	0.02	0.01	0.01	-0.01	0.02	0.00	0.01	0.01
12.5	0.01	0.10	0.06	0.03	-0.08	0.02	-0.04	0.03	0.11	0.01	0.02	0.02	0.01	0.00	0.03	0.01	0.01	0.01
10.0	0.01	0.11	0.07	0.03	-0.07	0.04	-0.04	0.04	0.11	-	-	-	-	-	-	-	-	-
8.5	0.06	0.13	0.10	0.02	-0.07	0.05	-0.03	0.04	0.13	0.02	0.03	0.02	0.00	-	-	-	-	-
7.0	0.06	0.13	0.11	0.02	-0.07	0.07	-0.03	0.04	0.14	-	-	-	-	-	-	-	-	-
5.0	0.07	0.13	0.12	0.02	-0.07	0.08	-0.02	0.05	0.14	0.03	0.03	0.00	0.00	-	-	-	-	-
3.5	0.08	0.14	0.13	0.02	-0.08	0.08	-0.02	0.05	0.14	-	-	-	-	-	-	-	-	-
2.0	0.08	0.15	0.13	0.02	-0.05	0.17	0.00	0.05	0.14	-	-	-	-	-	-	-	-	-
△Cp	0.05	0.12	0.10	0.02	-0.07	0.07	-0.03	0.04	0.12	0.01	0.03	0.01	0.00	-0.01	0.02	0.00	0.01	0.01

Source: this study.

Table 8: Cp results for Northwest winds: parallel (0°) to the Museum Ave. and oblique (45°) to the Park Place:

NW	CFD Law School (0°) Museum Ave. side Cp				Museum Ave. side courtyard Cp					WT Law School (0°) Museum Ave. side Cp				Museum Ave. side courtyard Cp				
line h (m)	min peak	max peak	avg 90%	sdev	min peak	max peak	avg 90%	sdev	△Cp	min peak	max peak	avg 90%	sdev	min peak	max peak	avg 90%	sdev	△Cp
15.0	-0.02	0.04	-0.01	0.02	-0.01	0.14	0.04	0.03	0.04	0.00	0.08	0.05	0.03	0.02	0.11	0.06	0.04	0.01
12.5	-0.02	0.01	-0.01	0.01	0.03	0.06	0.04	0.01	0.06	0.03	0.09	0.05	0.02	0.02	0.12	0.06	0.04	0.01
10.0	-0.01	0.02	-0.01	0.01	0.04	0.07	0.05	0.01	0.06	-	-	-	-	-	-	-	-	-
8.5	-0.05	-0.01	-0.02	0.01	0.05	0.09	0.06	0.01	0.08	0.03	0.08	0.05	0.02	0.00	0.15	0.06	0.06	0.02
7.0	-0.05	0.00	-0.02	0.01	0.05	0.11	0.07	0.02	0.09	-	-	-	-	-	-	-	-	-
5.0	-0.05	0.00	-0.02	0.01	0.06	0.12	0.08	0.02	0.09	0.04	0.09	0.00	0.02	-	-	-	-	-
3.5	-0.04	0.01	-0.01	0.01	0.06	0.14	0.10	0.02	0.11	-	-	-	-	-	-	-	-	-
2.0	-0.04	0.02	0.00	0.01	0.06	0.14	0.10	0.02	0.10	-	-	-	-	-	-	-	-	-
△Cp	-0.04	0.01	-0.01	0.01	0.04	0.11	0.07	0.02	0.08	0.03	0.09	0.03	0.02	0.01	0.13	0.06	0.05	0.01

NW	CFD Law School (45°) Park Place. side Cp				Park Place side courtyard Cp					WT Law School (45°) Park Place. side Cp				Park Place side courtyard Cp				
line h (m)	min peak	max peak	avg 90%	sdev	min peak	max peak	avg 90%	sdev	△Cp	min peak	max peak	avg 90%	sdev	min peak	max peak	avg 90%	sdev	△Cp
15.0	0.06	0.12	0.08	0.02	-0.01	0.09	0.05	0.03	0.03	0.05	0.10	0.07	0.02	0.03	0.06	0.04	0.01	0.03
12.5	0.09	0.15	0.12	0.02	0.03	0.08	0.05	0.01	0.07	0.06	0.07	0.06	0.01	0.03	0.06	0.04	0.01	0.02
10.0	0.06	0.15	0.12	0.02	0.05	0.08	0.06	0.01	0.06	-	-	-	-	-	-	-	-	-
8.5	0.08	0.13	0.11	0.01	0.05	0.09	0.07	0.01	0.04	0.05	0.07	0.06	0.01	-	-	-	-	-
7.0	0.10	0.13	0.11	0.01	-0.49	0.10	0.07	0.15	0.04	-	-	-	-	-	-	-	-	-
5.0	0.11	0.13	0.12	0.01	0.01	0.14	0.08	0.03	0.03	0.06	0.08	0.00	0.01	-	-	-	-	-
3.5	0.11	0.14	0.12	0.01	-0.15	0.14	0.09	0.08	0.03	-	-	-	-	-	-	-	-	-
2.0	0.12	0.14	0.13	0.01	-0.20	0.11	0.09	0.11	0.04	-	-	-	-	-	-	-	-	-
△Cp	0.09	0.14	0.12	0.01	-0.09	0.10	0.07	0.05	0.04	0.06	0.08	0.05	0.01	0.03	0.06	0.04	0.01	0.03

Source: this study.

Appendix 6: Paulista Avenue Graphs and Figures

In Appendix 6 the CP and ΔCp contour plots, graphs and tables which support the analysis of Chapter 9: ‘Paulista Ave.: Results and Analysis’ are presented. These data cover in details the output all the the wind tunnel and CFD simulations carried out for the Caste Study 2: Paulista Avenue from both the CKY Tower and the Prototype Tower, and for each simulated wind direction (0^o, 45^o, and 90^o).

Table 1: Cp results for the isolated CKY Tower - CFD (0^o)

Height	**Right side**				**Left side**				$\Delta X\pi$
(m)	MIN	MAX	AVG	SDEV	MIN	MAX	AVG	SDEV	***AVG***
90	-0.34	0.08	0.03	0.10	-0.34	0.08	0.03	0.10	***0.00***
84	-0.55	0.06	-0.01	0.14	-0.55	0.06	-0.01	0.14	***0.00***
78	-0.57	0.06	-0.03	0.14	-0.57	0.06	-0.03	0.14	***0.00***
72	-0.56	0.05	-0.05	0.13	-0.56	0.05	-0.05	0.13	***0.00***
66	-0.53	0.04	-0.06	0.13	-0.53	0.04	-0.06	0.13	***0.00***
60	-0.51	0.04	-0.06	0.12	-0.51	0.04	-0.06	0.12	***0.00***
54	-0.48	0.04	-0.06	0.12	-0.48	0.04	-0.06	0.12	***0.00***
48	-0.45	0.03	-0.06	0.11	-0.45	0.03	-0.06	0.11	***0.00***
42	-0.43	0.03	-0.05	0.11	-0.43	0.03	-0.05	0.11	***0.00***
36	-0.40	0.03	-0.04	0.10	-0.40	0.03	-0.04	0.10	***0.00***
30	-0.36	0.03	-0.03	0.09	-0.36	0.03	-0.03	0.09	***0.00***
24	-0.33	0.03	-0.03	0.08	-0.33	0.03	-0.03	0.08	***0.00***
15	-0.26	0.03	-0.01	0.07	-0.26	0.03	-0.01	0.07	***0.00***
6	-0.17	0.02	-0.01	0.04	-0.17	0.02	-0.01	0.04	***0.00***
3	-0.09	0.04	0.00	0.03	-0.09	0.04	0.00	0.03	***0.00***
Top	-0.55	0.05	-0.04	0.13	-0.55	0.05	-0.04	0.13	***0.00***
Middle	-0.46	0.03	-0.05	0.11	-0.46	0.03	-0.05	0.11	***0.00***
Bottom	-0.24	0.03	-0.02	0.06	-0.24	0.03	-0.02	0.06	***0.00***
AVG	*-0.40*	*0.04*	*-0.03*	*0.10*	*-0.40*	*0.04*	*-0.03*	*0.10*	***0.00***

Source: This study.

Table 2: Cp results for the isolated CKY Tower - WT (0^o)

Height	**Right side**				**Left side**				$\Delta X\pi$
(m)	MIN	MAX	AVG	SDEV	MIN	MAX	AVG	SDEV	***AVG***
90	-0.92	0.00	-0.21	-0.04	-0.95	-0.12	-0.40	-0.25	***0.19***
84	-0.79	0.01	-0.21	-0.03	-0.82	-0.07	-0.36	-0.27	***0.15***
72	-0.76	0.00	-0.21	-0.08	-0.80	0.00	-0.33	-0.22	***0.13***
60	-0.42	0.03	-0.09	-0.04	-0.61	-0.02	-0.24	-0.17	***0.16***
54	-0.31	0.04	-0.05	0.01	-0.62	-0.01	-0.21	-0.12	***0.17***
42	-0.04	0.05	0.01	0.02	-0.47	0.00	-0.16	-0.08	***0.17***
30	-0.14	0.05	-0.04	-0.03	-0.42	-0.05	-0.20	-0.13	***0.16***
24	-0.68	0.01	-0.17	-0.09	-0.75	-0.03	-0.31	-0.23	***0.14***
15	-0.61	0.00	-0.14	-0.02	-0.61	-0.02	-0.27	-0.21	***0.13***
3	-0.51	0.01	-0.13	-0.02	-0.71	0.05	-0.24	-0.18	***0.11***
Top	-0.82	0.00	-0.21	-0.05	-0.86	-0.06	-0.36	-0.24	***0.16***
Middle	-0.26	0.04	-0.04	0.00	-0.57	-0.01	-0.21	-0.12	***0.17***
Bottom	-0.48	0.02	-0.12	-0.04	-0.62	-0.01	-0.26	-0.19	***0.14***
AVG	*-0.52*	*0.02*	*-0.12*	*-0.03*	*-0.68*	*-0.03*	*-0.28*	*-0.18*	***0.15***

Source: This study.

Table 3: Cp results for the isolated CKY Tower with horizontal panel; WT (0^o)

Height	**Right side**				**Left side**				$\Delta X\pi$
(m)	MIN	MAX	AVG	SDEV	MIN	MAX	AVG	SDEV	***AVG***
90	-0.71	-0.04	-0.12	0.25	-0.92	-0.20	-0.26	0.29	***0.14***
84	-0.64	-0.03	-0.09	0.23	-0.79	-0.08	-0.30	0.31	***0.21***
72	-0.64	-0.04	-0.12	0.22	-0.77	-0.02	-0.28	0.30	***0.16***
60	-0.45	0.00	-0.04	0.16	-0.65	-0.02	-0.22	0.25	***0.18***
54	-0.28	0.02	-0.02	0.11	-0.59	0.00	-0.17	0.23	***0.14***
42	-0.06	0.04	0.01	0.04	-0.52	-0.02	-0.10	0.19	***0.10***
30	-0.13	0.05	-0.07	0.06	-0.48	-0.07	-0.15	0.17	***0.09***
24	-0.64	-0.02	-0.09	0.22	-0.77	-0.04	-0.28	0.29	***0.19***
15	-0.57	-0.02	-0.07	0.20	-0.70	-0.05	-0.24	0.26	***0.18***
3	-0.47	-0.02	-0.06	0.17	-0.70	0.02	-0.20	0.28	***0.14***
Top	-0.66	-0.04	-0.11	0.23	-0.82	-0.10	-0.28	0.30	***0.17***
Middle	-0.26	0.02	-0.02	0.10	-0.59	-0.02	-0.16	0.23	***0.14***
Bottom	-0.45	0.00	-0.07	0.16	-0.66	-0.04	-0.22	0.25	***0.15***
AVG	*-0.46*	*-0.01*	*-0.07*	*0.17*	*-0.69*	*-0.05*	*-0.22*	*0.26*	***0.15***

Source: This study.

Table 4: Cp results for the isolated CKY Tower with vertical panels; WT (0^o)

Height	**Right side**				**Left side**				$\Delta X\pi$
(m)	MIN	MAX	AVG	SDEV	MIN	MAX	AVG	SDEV	***AVG***
90	-0.61	0.18	0.01	0.32	-0.87	-0.21	-0.29	0.28	***0.30***
84	-0.55	0.17	-0.12	0.28	-0.83	-0.11	-0.36	0.31	***0.24***
72	-0.47	0.10	-0.12	0.24	-0.82	-0.03	-0.36	0.32	***0.24***
60	-0.32	0.11	0.00	0.17	-0.70	-0.05	-0.30	0.26	***0.30***
54	-0.28	0.16	0.03	0.17	-0.66	-0.02	-0.23	0.24	***0.26***
42	-0.16	0.14	0.05	0.11	-0.60	-0.03	-0.15	0.21	***0.20***
30	-0.26	0.13	0.02	0.14	-0.52	-0.11	-0.21	0.18	***0.23***
24	-0.44	0.07	-0.08	0.22	-0.81	-0.06	-0.33	0.30	***0.25***
15	-0.40	0.13	-0.09	0.22	-0.71	-0.08	-0.31	0.23	***0.22***
3	-0.36	0.14	-0.03	0.20	-0.76	0.12	-0.23	0.32	***0.20***
Top	-0.54	0.15	-0.08	0.28	-0.84	-0.12	-0.34	0.30	***0.26***
Middle	-0.26	0.14	0.03	0.15	-0.65	-0.04	-0.23	0.24	***0.26***
Bottom	-0.37	0.12	-0.05	0.20	-0.70	-0.03	-0.27	0.26	***0.22***
AVG	*-0.39*	*0.13*	*-0.03*	*0.21*	*-0.73*	*-0.06*	*-0.28*	*0.26*	***0.25***

Source: This study.

Table 5: Cp results for the isolated CKY Tower - CFD (45°)

Height	**WW**	**side**			**LW**	**side**			$\Delta X\pi$
(m)	MIN	MAX	AVG	SDEV	MIN	MAX	AVG	SDEV	***AVG***
90 (edge)	0.11	0.45	0.16	0.07	-0.02	0.33	0.03	0.10	***0.13***
84	0.04	0.97	0.63	0.18	0.00	0.20	0.05	0.03	***0.58***
78	0.03	0.99	0.67	0.20	-0.02	0.19	0.05	0.04	***0.62***
72	0.04	0.98	0.69	0.20	-0.03	0.18	0.04	0.03	***0.65***
66	0.05	0.95	0.67	0.20	-0.02	0.17	0.03	0.03	***0.64***
60	0.05	0.92	0.66	0.19	-0.02	0.16	0.03	0.03	***0.63***
54	0.06	0.87	0.63	0.18	-0.01	0.15	0.03	0.02	***0.60***
48	0.06	0.82	0.60	0.17	0.00	0.14	0.03	0.02	***0.57***
42	0.07	0.79	0.58	0.16	0.01	0.14	0.03	0.02	***0.55***
36	0.07	0.73	0.55	0.15	0.01	0.13	0.03	0.02	***0.52***
30	0.08	0.68	0.52	0.13	0.01	0.12	0.03	0.02	***0.50***
24	0.08	0.64	0.50	0.13	0.00	0.11	0.02	0.02	***0.48***
15	0.08	0.56	0.48	0.11	0.00	0.10	0.02	0.02	***0.46***
6	0.11	0.57	0.51	0.10	-0.01	0.09	0.01	0.02	***0.51***
3	0.14	0.62	0.56	0.11	-0.02	0.10	0.00	0.02	***0.55***
Top	0.04	0.97	0.66	0.19	-0.02	0.19	0.04	0.03	***0.62***
Middle	0.06	0.83	0.60	0.17	0.00	0.15	0.03	0.02	***0.58***
Bottom	0.10	0.61	0.52	0.12	0.00	0.10	0.02	0.02	***0.50***
AVG	*0.07*	*0.77*	*0.56*	*0.15*	*-0.01*	*0.16*	*0.03*	*0.03*	***0.53***

Source: This study.

Table 6: Cp results for the isolated CKY Tower - WT (45°)

Height	**WW**	**side**			**LW**	**side**			$\Delta X\pi$
(m)	MIN	MAX	AVG	SDEV	MIN	MAX	AVG	SDEV	***AVG***
90	0.17	0.88	0.53	0.48	-0.54	-0.44	-0.49	-0.48	***1.02***
84	0.15	0.88	0.59	0.63	-0.54	-0.44	-0.50	-0.50	***1.08***
72	0.06	0.85	0.57	0.66	-0.56	-0.43	-0.51	-0.51	***1.08***
60	0.39	0.79	0.57	0.54	-0.54	-0.42	-0.48	-0.49	***1.05***
54	0.35	0.74	0.52	0.47	-0.53	-0.39	-0.46	-0.45	***0.98***
42	0.36	0.68	0.51	0.48	-0.49	-0.41	-0.45	-0.45	***0.96***
30	0.13	0.63	0.46	0.48	-0.55	-0.41	-0.50	-0.49	***0.96***
24	0.00	0.83	0.51	0.55	-0.55	-0.45	-0.50	-0.51	***1.01***
15	0.09	0.71	0.43	0.49	-0.54	-0.35	-0.47	-0.49	***0.90***
3	0.24	0.66	0.46	0.41	-0.48	0.33	-0.33	-0.43	***0.79***
Top	0.13	0.87	0.56	0.59	-0.55	-0.44	-0.50	-0.50	***1.06***
Middle	0.37	0.74	0.53	0.50	-0.52	-0.41	-0.46	-0.46	***0.99***
Bottom	0.11	0.70	0.46	0.48	-0.53	-0.22	-0.45	-0.48	***0.91***
AVG	*0.20*	*0.77*	*0.52*	*0.52*	*-0.53*	*-0.35*	*-0.47*	*-0.48*	***0.99***

Source: This study.

Table 7: Cp results for the isolated CKY Tower with horizontal panel; WT (45°)

Height	**WW**	**side**			**LW**	**side**			$\Delta X\pi$
(m)	MIN	MAX	AVG	SDEV	MIN	MAX	AVG	SDEV	***AVG***
90	0.48	0.95	0.60	0.16	-0.57	-0.47	-0.56	0.04	***1.16***
84	0.58	0.94	0.70	0.14	-0.60	-0.47	-0.55	0.04	***1.24***
72	0.45	0.91	0.68	0.16	-0.59	-0.47	-0.57	0.05	***1.25***
60	0.26	0.57	0.47	0.10	-0.58	-0.43	-0.50	0.05	***0.96***
54	0.38	0.52	0.50	0.06	-0.53	-0.42	-0.47	0.04	***0.96***
42	0.35	0.50	0.47	0.06	-0.54	-0.42	-0.48	0.04	***0.95***
30	0.49	0.70	0.53	0.08	-0.57	-0.43	-0.56	0.06	***1.09***
24	0.31	0.90	0.58	0.20	-0.60	-0.48	-0.52	0.04	***1.09***
15	0.42	0.72	0.55	0.11	-0.58	0.72	-0.52	0.48	***1.06***
3	-0.43	0.71	0.50	0.38	-0.52	0.43	-0.46	0.35	***0.96***
Top	0.50	0.93	0.66	0.15	-0.59	-0.47	-0.56	0.05	***1.22***
Middle	0.33	0.53	0.48	0.07	-0.55	-0.42	-0.48	0.04	***0.96***
Bottom	0.20	0.76	0.54	0.19	-0.57	0.06	-0.51	0.23	***1.05***
AVG	*0.34*	*0.74*	*0.56*	*0.14*	*-0.57*	*-0.28*	*-0.52*	*0.11*	***1.08***

Source: This study.

Table 8: Cp results for the isolated CKY Tower with vertical panels; WT (45°)

Height	**WW**	**side**			**LW**	**side**			$\Delta X\pi$
(m)	MIN	MAX	AVG	SDEV	MIN	MAX	AVG	SDEV	***AVG***
90	0.25	0.88	0.61	0.22	-0.56	-0.45	-0.51	0.04	***1.12***
84	0.19	0.96	0.60	0.26	-0.54	-0.45	-0.51	0.04	***1.11***
72	0.07	0.92	0.57	0.29	-0.56	-0.44	-0.53	0.05	***1.09***
60	-0.04	0.59	0.45	0.22	-0.53	-0.41	-0.48	0.05	***0.93***
54	0.08	0.55	0.47	0.17	-0.53	-0.41	-0.45	0.04	***0.92***
42	0.10	0.51	0.48	0.19	-0.51	-0.42	-0.46	0.03	***0.94***
30	0.13	0.68	0.56	0.19	-0.58	-0.41	-0.51	0.07	***1.07***
24	0.00	0.82	0.52	0.29	-0.56	-0.45	-0.51	0.04	***1.03***
15	0.06	0.74	0.46	0.23	-0.54	0.74	-0.48	0.47	***0.94***
3	-0.45	0.63	0.28	0.39	-0.49	0.33	-0.44	0.30	***0.72***
Top	0.17	0.92	0.59	0.25	-0.55	-0.45	-0.52	0.04	***1.11***
Middle	0.04	0.55	0.47	0.19	-0.52	-0.42	-0.46	0.04	***0.93***
Bottom	-0.07	0.72	0.46	0.27	-0.54	0.05	-0.48	0.22	***0.94***
AVG	*0.05*	*0.73*	*0.51*	*0.24*	*-0.54*	*-0.27*	*-0.49*	*0.10*	***0.99***

Source: This study.

Table 9: Cp results for the isolated CKY Tower - CFD (90°)

Height	**WW**	**side**			**LW**	**side**			$\Delta X\pi$
(m)	MIN	MAX	AVG	SDEV	MIN	MAX	AVG	SDEV	***AVG***
90 (edge)	0.00	0.12	0.03	0.03	-0.01	0.03	0.02	0.00	***0.03***
84	0.05	0.92	0.91	0.20	-0.05	0.02	0.03	0.01	***0.90***
78	0.06	0.99	0.97	0.22	-0.06	0.02	0.03	0.01	***0.96***
72	0.06	1.01	0.98	0.23	-0.07	0.02	0.03	0.01	***0.96***
66	0.06	0.98	0.94	0.22	-0.08	0.02	0.04	0.01	***0.93***
60	0.06	0.96	0.91	0.22	-0.08	0.02	0.03	0.01	***0.91***
54	0.06	0.91	0.87	0.20	-0.08	0.02	0.03	0.01	***0.86***
48	0.05	0.86	0.82	0.19	-0.08	0.02	0.03	0.00	***0.81***
42	0.05	0.82	0.78	0.19	-0.08	0.02	0.03	0.00	***0.78***
36	0.04	0.77	0.73	0.17	-0.08	0.02	0.03	0.00	***0.73***
30	0.03	0.72	0.68	0.16	-0.08	0.01	0.02	0.00	***0.68***
24	0.03	0.70	0.65	0.16	-0.08	0.01	0.02	0.00	***0.65***
15	0.01	0.69	0.63	0.17	-0.08	0.02	0.03	0.00	***0.63***
6	0.05	0.78	0.71	0.18	-0.05	0.02	0.03	0.00	***0.71***
3	0.14	0.85	0.78	0.18	-0.04	0.02	0.02	0.00	***0.78***
Top	0.05	0.81	0.77	0.18	-0.05	0.02	0.01	0.02	***0.94***
Middle	0.05	0.86	0.82	0.19	-0.08	0.02	0.00	0.03	***0.82***
Bottom	0.05	0.75	0.69	0.17	-0.06	0.02	0.00	0.02	***0.69***
AVG	*0.05*	*0.81*	*0.76*	*0.18*	*-0.07*	*0.02*	*0.00*	*0.02*	***0.75***

Source: This study.

Table 10: Cp results for the isolated CKY Tower - WT (90°)

Height	**WW**	**side**			**LW**	**side**			$\Delta X\pi$
(m)	MIN	MAX	AVG	SDEV	MIN	MAX	AVG	SDEV	***AVG***
90	0.58	0.94	0.83	0.87	-0.58	-0.54	-0.56	-0.56	***1.39***
84	0.62	1.03	0.88	0.94	-0.58	-0.54	-0.56	-0.56	***1.44***
72	0.55	0.93	0.78	0.83	-0.56	-0.50	-0.53	-0.53	***1.31***
60	0.24	0.61	0.45	0.48	-0.55	-0.43	-0.48	-0.46	***0.93***
54	0.20	0.56	0.44	0.47	-0.53	-0.44	-0.48	-0.49	***0.92***
42	0.22	0.73	0.52	0.60	-0.49	-0.42	-0.45	-0.45	***0.97***
30	0.31	0.83	0.67	0.74	-0.58	-0.43	-0.50	-0.50	***1.17***
24	0.44	0.76	0.65	0.72	-0.58	-0.48	-0.51	-0.49	***1.16***
15	-0.56	0.73	0.45	0.63	-0.56	-0.47	-0.51	-0.52	***0.96***
3	-0.43	0.64	0.36	0.46	-0.55	0.56	-0.36	-0.53	***0.72***
Top	0.58	0.97	0.83	0.88	-0.57	-0.53	-0.55	-0.55	***1.38***
Middle	0.22	0.63	0.47	0.52	-0.53	-0.43	-0.47	-0.47	***0.94***
Bottom	-0.06	0.74	0.53	0.64	-0.57	-0.21	-0.47	-0.51	***1.00***
AVG	*0.25*	*0.78*	*0.61*	*0.68*	*-0.56*	*-0.39*	*-0.50*	*-0.51*	***1.11***

Source: This study.

Table 11: Cp results for the isolated CKY Tower with horizontal panel; WT (90°)

Height	**WW**	**side**			**LW**	**side**			$\Delta X\pi$
(m)	MIN	MAX	AVG	SDEV	MIN	MAX	AVG	SDEV	***AVG***
90	0.88	0.99	0.96	0.04	-0.62	-0.58	-0.60	0.01	***1.56***
84	0.88	1.02	0.95	0.05	-0.62	-0.55	-0.57	0.02	***1.53***
72	0.70	0.97	0.92	0.09	-0.58	-0.51	-0.56	0.02	***1.48***
60	0.36	0.60	0.57	0.09	-0.57	-0.48	-0.53	0.04	***1.10***
54	0.49	0.67	0.52	0.07	-0.56	-0.48	-0.50	0.03	***1.02***
42	0.48	0.71	0.56	0.07	-0.52	-0.45	-0.48	0.03	***1.04***
30	0.56	0.90	0.84	0.12	-0.61	-0.45	-0.52	0.05	***1.36***
24	0.49	0.79	0.75	0.10	-0.60	-0.47	-0.57	0.04	***1.32***
15	0.62	0.72	0.66	0.04	-0.56	0.62	-0.50	0.43	***1.16***
3	-0.50	0.64	0.62	0.42	-0.58	0.67	-0.53	0.46	***1.16***
Top	0.82	0.99	0.95	0.06	-0.61	-0.54	-0.58	0.02	***1.52***
Middle	0.44	0.66	0.55	0.08	-0.55	-0.47	-0.50	0.03	***1.05***
Bottom	0.29	0.76	0.72	0.17	-0.58	0.09	-0.53	0.24	***1.25***
AVG	*0.52*	*0.80*	*0.74*	*0.10*	*-0.58*	*-0.31*	*-0.54*	*0.10*	***1.28***

Source: This study.

Table 12: Cp results for the isolated CKY Tower with vertical panels; WT (90°)

Height	**WW**	**side**			**LW**	**side**			$\Delta X\pi$
(m)	MIN	MAX	AVG	SDEV	MIN	MAX	AVG	SDEV	***AVG***
90	0.82	1.01	0.95	0.08	-0.62	-0.57	-0.59	0.02	***1.54***
84	0.76	1.01	0.97	0.09	-0.61	-0.54	-0.57	0.03	***1.54***
72	0.64	0.96	0.89	0.13	-0.60	-0.50	-0.55	0.03	***1.44***
60	0.25	0.66	0.57	0.15	-0.58	-0.50	-0.52	0.03	***1.09***
54	0.33	0.61	0.51	0.11	-0.56	-0.45	-0.46	0.04	***0.97***
42	0.28	0.77	0.55	0.14	-0.53	-0.39	-0.47	0.04	***1.02***
30	0.13	0.70	0.53	0.20	-0.58	-0.44	-0.51	0.05	***1.04***
24	0.00	0.82	0.52	0.29	-0.56	-0.45	-0.51	0.04	***1.03***
15	0.06	0.74	0.46	0.23	-0.54	0.74	-0.48	0.47	***0.94***
3	-0.53	0.65	0.28	0.42	-0.50	0.70	-0.44	0.44	***0.72***
Top	0.74	0.99	0.94	0.10	-0.61	-0.54	-0.57	0.03	***1.51***
Middle	0.29	0.68	0.54	0.13	-0.56	-0.45	-0.48	0.04	***1.03***
Bottom	-0.09	0.73	0.45	0.28	-0.54	0.14	-0.48	0.25	***0.93***
AVG	*0.31*	*0.80*	*0.64*	*0.17*	*-0.57*	*-0.28*	*-0.51*	*0.10*	***1.16***

Source: This study.

Table 13: Cp results for the CKY Tower in urban environment; CFD (NE; 0^o)

Height	**Right side**				**Left side**				$\Delta X\pi$
(m)	MIN	MAX	AVG	SDEV	MIN	MAX	AVG	SDEV	***AVG***
90 (edge)	-0.25	-0.09	-0.10	0.04	-0.22	-0.08	-0.09	0.03	***-0.01***
84	-0.31	-0.09	-0.11	0.05	-0.22	-0.05	-0.08	0.03	***-0.03***
78	-0.34	-0.11	-0.12	0.05	-0.21	-0.04	-0.08	0.03	***-0.04***
72	-0.35	-0.11	-0.12	0.06	-0.18	-0.04	-0.07	0.03	***-0.05***
66	-0.34	-0.12	-0.13	0.05	-0.15	-0.01	-0.07	0.03	***-0.06***
60	-0.34	-0.13	-0.13	0.05	-0.12	-0.01	-0.06	0.03	***-0.07***
54	-0.33	-0.13	-0.14	0.05	-0.12	-0.01	-0.04	0.03	***-0.09***
48	-0.33	-0.13	-0.15	0.05	-0.12	0.01	-0.03	0.04	***-0.12***
42	-0.33	-0.12	-0.15	0.05	-0.11	0.02	-0.01	0.05	***-0.14***
36	-0.31	-0.13	-0.16	0.04	-0.12	0.02	0.00	0.05	***-0.16***
30	-0.30	-0.13	-0.16	0.04	-0.12	0.03	0.01	0.06	***-0.17***
24	-0.29	-0.13	-0.16	0.04	-0.11	0.03	0.01	0.06	***-0.17***
15	-0.28	-0.13	-0.16	0.03	-0.11	0.03	0.01	0.06	***-0.17***
6	-0.27	-0.13	-0.16	0.03	-0.11	0.03	0.01	0.06	***-0.17***
3	-0.27	-0.13	-0.16	0.03	-0.11	0.03	0.01	0.06	***-0.17***
Top	-0.34	-0.11	-0.12	0.05	-0.19	-0.04	-0.07	0.03	***-0.04***
Middle	-0.33	-0.13	-0.14	0.05	-0.12	0.01	-0.03	0.04	***-0.12***
Bottom	-0.28	-0.13	-0.16	0.03	-0.11	0.03	0.01	0.06	***-0.17***
AVG	*-0.31*	*-0.12*	*-0.14*	*0.04*	*-0.14*	*0.00*	*-0.03*	*0.04*	***-0.11***

Source: This study.

Table 14: Cp results for the CKY Tower in urban environment; WT (NE; 0^o)

Height	**Right side**				**Left side**				$\Delta X\pi$
(m)	MIN	MAX	AVG	SDEV	MIN	MAX	AVG	SDEV	***AVG***
90	-0.65	-0.31	-0.33	0.12	-0.72	-0.33	-0.38	0.13	***-0.05***
84	-0.60	-0.31	-0.32	0.11	-0.67	-0.29	-0.37	0.13	***-0.04***
72	-0.55	-0.32	-0.33	0.09	-0.64	-0.28	-0.32	0.13	***0.01***
60	-0.44	-0.30	-0.33	0.05	-0.30	-0.23	-0.24	0.03	***0.09***
54	-0.42	-0.30	-0.31	0.05	-0.28	-0.22	-0.24	0.02	***0.08***
42	-0.35	-0.29	-0.31	0.02	-0.26	-0.21	-0.22	0.02	***0.09***
30	-0.40	-0.30	-0.33	0.03	-0.32	-0.22	-0.27	0.04	***0.06***
24	-0.51	-0.31	-0.33	0.07	-0.48	-0.25	-0.26	0.08	***0.07***
15	-0.47	-0.31	-0.32	0.06	-0.47	-0.23	-0.26	0.08	***0.06***
3	-0.46	-0.25	-0.33	0.07	-0.32	-0.22	-0.26	0.03	***0.06***
Top	-0.60	-0.31	-0.33	0.11	-0.68	-0.30	-0.36	0.13	***-0.03***
Middle	-0.40	-0.30	-0.32	0.04	-0.28	-0.22	-0.23	0.02	***0.09***
Bottom	-0.46	-0.29	-0.33	0.06	-0.39	-0.23	-0.26	0.06	***0.06***
AVG	*-0.49*	*-0.30*	*-0.32*	*0.07*	*-0.45*	*-0.25*	*-0.28*	*0.07*	***0.04***

Source: This study.

Table 15: Cp results for the CKY Tower in urban environment with horizontal panels; WT (NE; 0^o)

Height	**Right side**				**Left side**				$\Delta X\pi$
(m)	MIN	MAX	AVG	SDEV	MIN	MAX	AVG	SDEV	***AVG***
90	-0.51	-0.22	-0.28	0.10	-0.72	-0.37	-0.40	0.13	***-0.12***
84	-0.50	-0.27	-0.32	0.09	-0.71	-0.32	-0.40	0.14	***-0.08***
72	-0.47	-0.31	-0.34	0.07	-0.69	-0.30	-0.35	0.14	***-0.01***
60	-0.43	-0.32	-0.35	0.05	-0.35	-0.25	-0.27	0.03	***0.07***
54	-0.42	-0.31	-0.34	0.04	-0.32	-0.25	-0.26	0.03	***0.08***
42	-0.41	-0.31	-0.33	0.03	-0.30	-0.24	-0.25	0.02	***0.07***
30	-0.40	-0.31	-0.34	0.03	-0.35	-0.25	-0.30	0.03	***0.04***
24	-0.47	-0.33	-0.35	0.06	-0.57	-0.28	-0.30	0.10	***0.06***
15	-0.44	-0.31	-0.35	0.05	-0.44	-0.26	-0.30	0.07	***0.05***
3	-0.43	-0.28	-0.34	0.06	-0.37	-0.25	-0.30	0.04	***0.05***
Top	-0.50	-0.26	-0.31	0.09	-0.71	-0.33	-0.38	0.14	***-0.07***
Middle	-0.42	-0.31	-0.34	0.04	-0.32	-0.25	-0.26	0.03	***0.07***
Bottom	-0.44	-0.31	-0.35	0.05	-0.43	-0.26	-0.30	0.06	***0.05***
AVG	*-0.45*	*-0.29*	*-0.33*	*0.06*	*-0.49*	*-0.28*	*-0.31*	*0.08*	***0.02***

Source: This study.

Table 16: Cp results for the CKY Tower in urban area with vertical panels; WT (NE; 0^o)

Height	**Right side**				**Left side**				$\Delta X\pi$
(m)	MIN	MAX	AVG	SDEV	MIN	MAX	AVG	SDEV	***AVG***
90	-0.53	-0.32	-0.36	0.07	-0.72	-0.37	-0.39	0.13	***-0.02***
84	-0.51	-0.34	-0.36	0.06	-0.70	-0.32	-0.40	0.14	***-0.04***
72	-0.50	-0.35	-0.35	0.06	-0.68	-0.30	-0.34	0.14	***0.01***
60	-0.41	-0.33	-0.34	0.03	-0.33	-0.24	-0.27	0.03	***0.07***
54	-0.40	-0.33	-0.34	0.03	-0.31	-0.24	-0.26	0.02	***0.08***
42	-0.37	-0.32	-0.34	0.02	-0.30	-0.24	-0.25	0.02	***0.09***
30	-0.39	-0.33	-0.36	0.02	-0.35	-0.24	-0.29	0.04	***0.07***
24	-0.49	-0.35	-0.36	0.05	-0.54	-0.28	-0.30	0.10	***0.06***
15	-0.45	-0.34	-0.35	0.04	-0.45	-0.26	-0.29	0.07	***0.06***
3	-0.45	-0.28	-0.37	0.05	-0.35	-0.25	-0.29	0.04	***0.08***
Top	-0.51	-0.34	-0.36	0.06	-0.70	-0.33	-0.37	0.14	***-0.02***
Middle	-0.40	-0.33	-0.34	0.02	-0.31	-0.24	-0.26	0.02	***0.08***
Bottom	-0.44	-0.33	-0.36	0.04	-0.42	-0.26	-0.29	0.06	***0.07***
AVG	*-0.45*	*-0.33*	*-0.35*	*0.04*	*-0.48*	*-0.27*	*-0.31*	*0.07*	***0.04***

Source: This study.

Table 17: Cp results for the CKY Tower in urban environment; CFD (N, 45°)

Height	**WW**	**side**			**LW**	**side**			$\Delta X\pi$
(m)	MIN	MAX	AVG	SDEV	MIN	MAX	AVG	SDEV	***AVG***
90 (edge)	-0.10	0.03	-0.05	0.03	-0.24	-0.09	-0.19	0.05	***0.14***
84	-0.02	0.75	0.61	0.21	-0.34	-0.17	-0.26	0.04	***0.88***
78	-0.05	0.78	0.55	0.23	-0.30	-0.17	-0.25	0.03	***0.80***
72	-0.07	0.74	0.42	0.22	-0.28	-0.16	-0.23	0.04	***0.64***
66	-0.04	0.66	0.26	0.19	-0.27	-0.13	-0.20	0.05	***0.46***
60	-0.06	0.53	0.08	0.13	-0.26	-0.09	-0.17	0.06	***0.26***
54	-0.08	0.40	0.00	0.11	-0.24	-0.07	-0.15	0.07	***0.15***
48	-0.08	0.34	-0.02	0.10	-0.23	-0.08	-0.14	0.06	***0.12***
42	-0.09	0.27	0.00	0.08	-0.23	-0.09	-0.14	0.05	***0.13***
36	-0.10	0.24	0.00	0.07	-0.21	-0.08	-0.13	0.04	***0.13***
30	-0.10	0.22	0.01	0.06	-0.21	-0.07	-0.14	0.04	***0.14***
24	-0.09	0.23	0.01	0.06	-0.21	-0.06	-0.14	0.04	***0.15***
15	-0.08	0.22	0.01	0.06	-0.20	-0.07	-0.15	0.03	***0.16***
6	-0.10	0.22	0.01	0.06	-0.20	-0.07	-0.15	0.03	***0.17***
3	-0.09	0.16	0.02	0.05	-0.20	-0.07	-0.15	0.03	***0.17***
Top	-0.05	0.73	0.46	0.21	-0.30	-0.16	-0.23	0.04	***0.69***
Middle	-0.08	0.36	0.01	0.10	-0.24	-0.08	-0.15	0.06	***0.16***
Bottom	-0.09	0.21	0.01	0.06	-0.21	-0.07	-0.15	0.03	***0.16***
AVG	*-0.08*	*0.39*	*0.13*	*0.11*	*-0.24*	*-0.10*	*-0.17*	*0.04*	***0.30***

Source: This study.

Table 18: Cp results for the CKY Tower in urban environment; WT (N, 45°)

Height	**WW**	**side**			**LW**	**side**			$\Delta X\pi$
(m)	MIN	MAX	AVG	SDEV	MIN	MAX	AVG	SDEV	***AVG***
90	-0.22	0.05	-0.02	0.10	-0.53	-0.49	-0.53	0.02	***0.51***
84	-0.28	-0.01	-0.07	0.10	-0.54	-0.48	-0.53	0.02	***0.46***
72	-0.30	0.01	-0.11	0.12	-0.54	-0.46	-0.52	0.03	***0.41***
60	-0.35	-0.10	-0.30	0.08	-0.51	-0.44	-0.47	0.02	***0.17***
54	-0.35	-0.19	-0.29	0.05	-0.50	-0.44	-0.48	0.02	***0.19***
42	-0.34	-0.27	-0.30	0.03	-0.49	-0.42	-0.47	0.02	***0.17***
30	-0.32	-0.05	-0.20	0.11	-0.53	-0.40	-0.48	0.05	***0.28***
24	-0.33	0.04	-0.20	0.14	-0.53	-0.42	-0.52	0.04	***0.31***
15	-0.33	0.04	-0.31	0.15	-0.50	0.04	-0.48	0.20	***0.18***
3	-0.46	-0.03	-0.29	0.13	-0.47	-0.26	-0.46	0.08	***0.17***
Top	-0.27	0.02	-0.07	0.11	-0.54	-0.48	-0.52	0.02	***0.46***
Middle	-0.35	-0.19	-0.30	0.05	-0.50	-0.43	-0.47	0.02	***0.18***
Bottom	-0.36	0.00	-0.25	0.13	-0.51	-0.26	-0.48	0.09	***0.23***
AVG	*-0.32*	*-0.06*	*-0.20*	*0.10*	*-0.51*	*-0.39*	*-0.49*	*0.04*	***0.29***

Source: This study.

Table 19: Cp results for the CKY Tower in urban environment with horizontal panels; WT (N, 45^o)

Height	**WW**	**side**			**LW**	**side**			$\Delta X\pi$
(m)	MIN	MAX	AVG	SDEV	MIN	MAX	AVG	SDEV	***AVG***
90	-0.07	0.07	0.05	0.05	-0.59	-0.55	-0.58	0.01	***0.63***
84	-0.14	0.00	-0.05	0.06	-0.60	-0.54	-0.59	0.02	***0.53***
72	-0.21	0.00	-0.13	0.09	-0.60	-0.52	-0.57	0.03	***0.44***
60	-0.39	-0.11	-0.37	0.10	-0.56	-0.50	-0.52	0.02	***0.15***
54	-0.38	-0.14	-0.34	0.08	-0.55	-0.50	-0.51	0.02	***0.17***
42	-0.39	-0.30	-0.34	0.04	-0.55	-0.49	-0.52	0.02	***0.18***
30	-0.35	-0.09	-0.18	0.09	-0.58	-0.47	-0.53	0.04	***0.34***
24	-0.32	0.05	-0.29	0.16	-0.58	-0.47	-0.56	0.04	***0.27***
15	-0.39	0.06	-0.32	0.16	-0.57	0.06	-0.54	0.22	***0.22***
3	-0.51	0.04	-0.31	0.17	-0.52	-0.30	-0.50	0.08	***0.19***
Top	-0.14	0.03	-0.04	0.07	-0.59	-0.54	-0.58	0.02	***0.54***
Middle	-0.39	-0.18	-0.35	0.07	-0.55	-0.50	-0.52	0.02	***0.17***
Bottom	-0.39	0.01	-0.28	0.14	-0.56	-0.30	-0.53	0.10	***0.26***
AVG	*-0.31*	*-0.05*	*-0.22*	*0.09*	*-0.57*	*-0.44*	*-0.54*	*0.05*	***0.32***

Source: This study.

Table 20: Cp results for the CKY Tower in urban area with vertical panels; WT (N; 45^o)

Height	**WW**	**side**			**LW**	**side**			$\Delta X\pi$
(m)	MIN	MAX	AVG	SDEV	MIN	MAX	AVG	SDEV	***AVG***
90	-0.32	0.04	-0.04	0.14	-0.56	-0.54	-0.55	0.01	***0.51***
84	-0.35	0.00	-0.14	0.14	-0.58	-0.52	-0.57	0.02	***0.43***
72	-0.37	0.01	-0.20	0.15	-0.57	-0.50	-0.55	0.02	***0.35***
60	-0.41	0.08	-0.38	0.17	-0.54	-0.49	-0.51	0.02	***0.13***
54	-0.37	-0.19	-0.34	0.06	-0.54	-0.48	-0.51	0.02	***0.17***
42	-0.33	-0.28	-0.32	0.02	-0.54	-0.47	-0.50	0.02	***0.18***
30	-0.36	-0.13	-0.30	0.09	-0.55	-0.45	-0.50	0.04	***0.20***
24	-0.39	0.07	-0.31	0.18	-0.54	-0.46	-0.54	0.03	***0.23***
15	-0.40	0.10	-0.36	0.19	-0.55	0.10	-0.51	0.23	***0.15***
3	-0.53	0.15	-0.31	0.21	-0.51	-0.26	-0.49	0.09	***0.18***
Top	-0.35	0.02	-0.13	0.14	-0.57	-0.52	-0.56	0.02	***0.43***
Middle	-0.37	-0.13	-0.34	0.08	-0.54	-0.48	-0.51	0.02	***0.16***
Bottom	-0.42	0.05	-0.32	0.17	-0.54	-0.27	-0.51	0.10	***0.19***
AVG	*-0.38*	*-0.02*	*-0.26*	*0.13*	*-0.55*	*-0.42*	*-0.52*	*0.05*	***0.26***

Source: This study.

Table 21: Cp results for the CKY Tower in urban environment; CFD (S, 45^o)

Height	**WW**	**side**			**LW**	**side**			$\Delta X\pi$
(m)	MIN	MAX	AVG	SDEV	MIN	MAX	AVG	SDEV	***AVG***
90 (edge)	-0.63	0.05	-0.47	0.15	-0.54	-0.28	-0.36	0.05	***-0.12***
84	-0.14	0.78	0.31	0.24	-0.55	-0.20	-0.39	0.08	***0.70***
78	-0.15	0.88	0.39	0.28	-0.54	-0.21	-0.38	0.08	***0.77***
72	-0.19	0.83	0.41	0.27	-0.51	-0.22	-0.35	0.08	***0.76***
66	-0.15	0.77	0.38	0.26	-0.56	-0.22	-0.33	0.09	***0.71***
60	-0.18	0.72	0.34	0.25	-0.50	-0.22	-0.32	0.09	***0.66***
54	-0.19	0.66	0.27	0.22	-0.49	-0.17	-0.32	0.09	***0.59***
48	-0.21	0.57	0.19	0.19	-0.46	-0.15	-0.31	0.09	***0.50***
42	-0.20	0.55	0.09	0.19	-0.47	-0.14	-0.31	0.09	***0.40***
36	-0.21	0.58	0.02	0.21	-0.42	-0.12	-0.29	0.08	***0.31***
30	-0.24	0.60	-0.03	0.24	-0.37	-0.11	-0.29	0.07	***0.26***
24	-0.24	0.52	-0.02	0.22	-0.35	-0.10	-0.29	0.07	***0.27***
15	-0.23	0.45	0.01	0.18	-0.33	-0.07	-0.27	0.08	***0.28***
6	-0.22	0.34	0.02	0.13	-0.31	-0.04	-0.25	0.09	***0.28***
3	-0.22	0.32	0.03	0.12	-0.30	-0.04	-0.25	0.09	***0.28***
Top	-0.16	0.81	0.37	0.26	-0.54	-0.21	-0.36	0.08	***0.73***
Middle	-0.20	0.62	0.18	0.21	-0.47	-0.16	-0.31	0.09	***0.50***
Bottom	-0.23	0.45	0.00	0.18	-0.33	-0.07	-0.27	0.08	***0.27***
AVG	*-0.23*	*0.57*	*0.13*	*0.21*	*-0.45*	*-0.15*	*-0.31*	*0.08*	***0.44***

Source: This study.

Table 22: Cp results for the CKY Tower in urban environment; WT (S, 45^o)

Height	**WW**	**side**			**LW**	**side**			$\Delta X\pi$
(m)	MIN	MAX	AVG	SDEV	MIN	MAX	AVG	SDEV	***AVG***
90	-0.67	-0.52	-0.62	0.05	0.04	0.86	0.43	0.27	***1.04***
84	-0.71	-0.56	-0.67	0.05	0.03	0.81	0.58	0.29	***1.24***
72	-0.66	-0.52	-0.62	0.05	-0.18	0.78	0.41	0.34	***1.03***
60	-0.84	-0.31	-0.53	0.18	-0.33	0.13	-0.07	0.16	***0.46***
54	-0.86	-0.32	-0.48	0.17	-0.31	0.07	-0.02	0.13	***0.46***
42	-0.50	-0.05	-0.37	0.14	-0.18	0.35	0.11	0.16	***0.48***
30	-0.62	-0.22	-0.54	0.14	-0.08	0.66	0.32	0.23	***0.86***
24	-0.61	-0.34	-0.52	0.09	-0.24	0.52	0.24	0.26	***0.77***
15	-0.68	-0.27	-0.56	0.13	-0.52	0.28	0.21	0.28	***0.77***
3	-0.82	0.27	-0.55	0.36	-0.27	0.23	-0.06	0.16	***0.49***
Top	-0.68	-0.53	-0.63	0.05	-0.03	0.82	0.47	0.30	***1.11***
Middle	-0.73	-0.23	-0.46	0.16	-0.27	0.18	0.01	0.15	***0.47***
Bottom	-0.68	-0.14	-0.54	0.18	-0.28	0.42	0.18	0.23	***0.72***
AVG	*-0.70*	*-0.30*	*-0.55*	*0.13*	*-0.20*	*0.47*	*0.22*	*0.23*	***0.77***

Source: This study.

Table 23 Cp results for the CKY Tower in urban environment with horizontal panels; WT (S, 45°)

Height	**WW**	**side**			**LW**	**side**			$\Delta X\pi$
(m)	MIN	MAX	AVG	SDEV	MIN	MAX	AVG	SDEV	***AVG***
90	-0.65	-0.53	-0.62	0.04	0.39	0.84	0.52	0.15	***1.14***
84	-0.69	-0.57	-0.67	0.04	0.43	0.88	0.60	0.17	***1.27***
72	-0.65	-0.52	-0.64	0.05	0.29	0.82	0.46	0.19	***1.10***
60	-0.88	-0.32	-0.54	0.20	-0.12	0.17	0.14	0.10	***0.68***
54	-0.76	-0.36	-0.50	0.13	0.01	0.42	0.12	0.14	***0.62***
42	-0.51	-0.05	-0.36	0.15	0.10	0.25	0.19	0.06	***0.54***
30	-0.62	-0.19	-0.53	0.14	0.19	0.76	0.38	0.21	***0.91***
24	-0.63	-0.34	-0.55	0.09	0.18	0.54	0.35	0.12	***0.89***
15	-0.69	-0.27	-0.56	0.13	-0.54	0.41	0.28	0.32	***0.85***
3	-0.84	0.22	-0.56	0.35	-0.13	0.21	0.15	0.14	***0.72***
Top	-0.66	-0.54	-0.64	0.05	0.37	0.85	0.53	0.17	***1.17***
Middle	-0.72	-0.24	-0.47	0.16	0.00	0.28	0.15	0.10	***0.62***
Bottom	-0.70	-0.15	-0.55	0.18	-0.08	0.48	0.29	0.20	***0.84***
AVG	*-0.69*	*-0.31*	*-0.55*	*0.13*	*0.10*	*0.53*	*0.32*	*0.16*	***0.88***

Source: This study.

Table 24: Cp results for the CKY Tower in urban area with vertical panels; WT (S; 45°)

Height	**WW**	**side**			**LW**	**side**			$\Delta X\pi$
(m)	MIN	MAX	AVG	SDEV	MIN	MAX	AVG	SDEV	***AVG***
90	-0.63	-0.52	-0.61	0.04	0.11	0.77	0.44	0.23	***1.06***
84	-0.69	-0.56	-0.65	0.04	0.08	0.83	0.52	0.27	***1.17***
72	-0.64	-0.51	-0.63	0.05	-0.03	0.78	0.49	0.29	***1.12***
60	-0.80	-0.30	-0.53	0.17	-0.09	0.19	0.04	0.10	***0.57***
54	-0.84	-0.34	-0.48	0.16	-0.05	0.21	0.06	0.08	***0.55***
42	-0.51	-0.06	-0.35	0.14	0.02	0.39	0.19	0.13	***0.54***
30	-0.61	-0.21	-0.52	0.14	0.10	0.70	0.39	0.20	***0.91***
24	-0.59	-0.35	-0.55	0.08	-0.04	0.54	0.33	0.20	***0.88***
15	-0.66	-0.26	-0.56	0.12	-0.52	0.30	0.23	0.29	***0.79***
3	-0.75	0.34	-0.56	0.37	-0.14	0.22	0.08	0.14	***0.64***
Top	-0.66	-0.53	-0.63	0.04	0.05	0.80	0.49	0.26	***1.12***
Middle	-0.72	-0.24	-0.45	0.16	-0.04	0.26	0.10	0.10	***0.55***
Bottom	-0.65	-0.12	-0.55	0.18	-0.15	0.44	0.26	0.21	***0.81***
AVG	*-0.67*	*-0.30*	*-0.54*	*0.13*	*-0.05*	*0.50*	*0.28*	*0.19*	***0.82***

Source: This study.

Table 25: Cp results for the CKY Tower in urban environment; CFD (NW, 90^o)

Height	**WW**	**side**			**LW**	**side**			$\Delta X\pi$
(m)	MIN	MAX	AVG	SDEV	MIN	MAX	AVG	SDEV	***AVG***
90 (edge)	-0.43	-0.21	-0.26	0.05	-0.42	-0.30	-0.34	0.03	***0.08***
84	-0.36	0.23	-0.01	0.15	-0.47	-0.32	-0.42	0.03	***0.41***
78	-0.36	0.21	-0.06	0.13	-0.47	-0.31	-0.40	0.03	***0.35***
72	-0.35	0.13	-0.09	0.11	-0.45	-0.33	-0.38	0.03	***0.29***
66	-0.31	0.09	-0.13	0.08	-0.44	-0.27	-0.35	0.04	***0.22***
60	-0.26	0.01	-0.18	0.06	-0.42	-0.24	-0.33	0.06	***0.15***
54	-0.25	-0.06	-0.21	0.05	-0.40	-0.22	-0.31	0.06	***0.10***
48	-0.29	-0.10	-0.22	0.04	-0.38	-0.24	-0.31	0.05	***0.09***
42	-0.34	-0.16	-0.22	0.03	-0.37	-0.26	-0.31	0.03	***0.09***
36	-0.37	-0.16	-0.22	0.04	-0.36	-0.27	-0.30	0.03	***0.08***
30	-0.37	-0.19	-0.23	0.04	-0.35	-0.27	-0.30	0.02	***0.07***
24	-0.35	-0.20	-0.23	0.03	-0.34	-0.28	-0.30	0.02	***0.07***
15	-0.35	-0.19	-0.22	0.03	-0.35	-0.29	-0.30	0.02	***0.09***
6	-0.35	-0.16	-0.19	0.04	-0.35	-0.28	-0.31	0.02	***0.11***
3	-0.34	-0.15	-0.19	0.04	-0.35	-0.27	-0.31	0.03	***0.12***
Top	-0.35	0.17	-0.07	0.12	-0.46	-0.31	-0.39	0.03	***0.32***
Middle	-0.30	-0.09	-0.21	0.04	-0.38	-0.25	-0.31	0.05	***0.10***
Bottom	-0.35	-0.18	-0.21	0.04	-0.35	-0.28	-0.30	0.02	***0.09***
AVG	*-0.34*	*-0.06*	*-0.18*	*0.06*	*-0.39*	*-0.28*	*-0.33*	*0.03*	***0.15***

Source: This study.

Table 26: Cp results for the CKY Tower in urban environment; WT (NW, 90^o)

Height	**WW**	**side**			**LW**	**side**			$\Delta X\pi$
(m)	MIN	MAX	AVG	SDEV	MIN	MAX	AVG	SDEV	***AVG***
90	-0.10	0.25	0.05	0.13	-0.43	-0.42	-0.43	0.00	***0.48***
84	-0.10	0.24	0.05	0.12	-0.44	-0.42	-0.43	0.01	***0.48***
72	-0.15	0.15	-0.04	0.11	-0.44	-0.40	-0.41	0.02	***0.38***
60	-0.31	-0.26	-0.28	0.02	-0.50	-0.35	-0.39	0.05	***0.11***
54	-0.30	-0.25	-0.27	0.02	-0.50	-0.33	-0.38	0.06	***0.11***
42	-0.28	-0.20	-0.24	0.03	-0.35	-0.24	-0.31	0.04	***0.07***
30	-0.21	0.20	-0.17	0.15	-0.43	-0.28	-0.41	0.06	***0.24***
24	-0.25	-0.04	-0.14	0.09	-0.43	-0.38	-0.43	0.02	***0.29***
15	-0.28	0.00	-0.20	0.09	-0.45	-0.18	-0.39	0.09	***0.19***
3	-0.26	-0.15	-0.24	0.04	-0.47	-0.23	-0.40	0.08	***0.16***
Top	-0.11	0.22	0.02	0.12	-0.44	-0.41	-0.42	0.01	***0.44***
Middle	-0.30	-0.24	-0.26	0.02	-0.45	-0.30	-0.36	0.05	***0.10***
Bottom	-0.25	0.00	-0.19	0.09	-0.45	-0.27	-0.41	0.06	***0.22***
AVG	*-0.22*	*-0.01*	*-0.14*	*0.08*	*-0.44*	*-0.33*	*-0.40*	*0.04*	***0.25***

Source: This study.

Table 27: Cp results for the CKY Tower in urban environment with horizontal panels; WT (NW, 90^o)

Height	**WW**	**side**			**LW**	**side**			$\Delta X\pi$
(m)	MIN	MAX	AVG	SDEV	MIN	MAX	AVG	SDEV	***AVG***
90	-0.01	0.30	0.16	0.12	-0.43	-0.41	-0.43	0.01	***0.59***
84	-0.07	0.18	0.02	0.09	-0.44	-0.41	-0.42	0.01	***0.44***
72	-0.12	0.07	-0.02	0.07	-0.44	-0.40	-0.41	0.01	***0.39***
60	-0.29	-0.25	-0.27	0.02	-0.48	-0.35	-0.38	0.05	***0.11***
54	-0.28	-0.24	-0.27	0.01	-0.52	-0.33	-0.36	0.06	***0.09***
42	-0.27	-0.23	-0.25	0.02	-0.36	-0.24	-0.32	0.04	***0.07***
30	-0.22	0.10	-0.16	0.11	-0.42	-0.27	-0.41	0.06	***0.25***
24	-0.24	-0.04	-0.17	0.08	-0.44	-0.38	-0.42	0.02	***0.25***
15	-0.27	-0.04	-0.21	0.08	-0.45	-0.16	-0.39	0.10	***0.18***
3	-0.27	-0.17	-0.21	0.04	-0.45	-0.23	-0.40	0.08	***0.19***
Top	-0.07	0.18	0.05	0.09	-0.44	-0.41	-0.42	0.01	***0.48***
Middle	-0.28	-0.24	-0.26	0.01	-0.45	-0.31	-0.35	0.05	***0.09***
Bottom	-0.25	-0.04	-0.19	0.08	-0.44	-0.26	-0.40	0.06	***0.22***
AVG	*-0.07*	*0.18*	*0.05*	*0.09*	*-0.44*	*-0.41*	*-0.42*	*0.01*	***0.48***

Source: This study.

Table 28: Cp results for the CKY Tower in urban area with vertical panels; WT (NW; 90^o)

Height	**WW**	**side**			**LW**	**side**			$\Delta X\pi$
(m)	MIN	MAX	AVG	SDEV	MIN	MAX	AVG	SDEV	***AVG***
90	-0.10	0.31	0.17	0.15	-0.44	-0.42	-0.43	0.01	***0.60***
84	-0.11	0.19	0.05	0.12	-0.45	-0.41	-0.43	0.01	***0.48***
72	-0.15	0.11	-0.01	0.10	-0.45	-0.41	-0.42	0.01	***0.41***
60	-0.31	-0.21	-0.27	0.03	-0.47	-0.35	-0.38	0.04	***0.11***
54	-0.30	-0.21	-0.24	0.03	-0.51	-0.33	-0.36	0.06	***0.12***
42	-0.25	-0.17	-0.21	0.03	-0.36	-0.23	-0.33	0.04	***0.12***
30	-0.20	0.15	-0.17	0.13	-0.43	-0.29	-0.41	0.06	***0.24***
24	-0.25	-0.03	-0.11	0.09	-0.45	-0.39	-0.43	0.02	***0.32***
15	-0.28	-0.05	-0.19	0.08	-0.46	-0.13	-0.39	0.11	***0.21***
3	-0.26	-0.16	-0.18	0.04	-0.46	-0.18	-0.39	0.09	***0.22***
Top	-0.12	0.20	0.07	0.12	-0.45	-0.41	-0.43	0.01	***0.50***
Middle	-0.29	-0.20	-0.24	0.03	-0.45	-0.30	-0.36	0.05	***0.12***
Bottom	-0.25	-0.02	-0.16	0.09	-0.45	-0.25	-0.41	0.07	***0.25***
AVG	*-0.22*	*-0.01*	*-0.11*	*0.08*	*-0.45*	*-0.32*	*-0.40*	*0.04*	***0.29***

Source: This study.

Table 29: Cp results for the CKY Tower in urban environment; CFD (SE, 90°)

Height	**WW**	**side**			**LW**	**side**			$\Delta X\pi$
(m)	MIN	MAX	AVG	SDEV	MIN	MAX	AVG	SDEV	***AVG***
90 (edge)	-0.31	0.01	-0.04	0.08	-0.17	-0.08	-0.10	0.03	***0.06***
84	-0.21	1.13	0.26	0.42	-0.24	-0.13	-0.17	0.03	***0.44***
78	-0.29	0.99	0.15	0.39	-0.22	-0.13	-0.17	0.02	***0.32***
72	-0.29	0.89	0.09	0.34	-0.23	-0.13	-0.17	0.03	***0.25***
66	-0.22	0.72	0.05	0.27	-0.22	-0.13	-0.16	0.02	***0.21***
60	-0.19	0.54	0.02	0.21	-0.19	-0.07	-0.16	0.03	***0.18***
54	-0.17	0.40	0.00	0.15	-0.17	-0.03	-0.16	0.05	***0.16***
48	-0.16	0.29	0.00	0.11	-0.16	0.00	-0.14	0.06	***0.14***
42	-0.17	0.19	-0.01	0.08	-0.17	-0.01	-0.12	0.05	***0.11***
36	-0.14	0.13	-0.02	0.06	-0.17	-0.03	-0.11	0.05	***0.10***
30	-0.13	0.11	-0.01	0.05	-0.19	-0.05	-0.11	0.04	***0.09***
24	-0.13	0.11	-0.01	0.05	-0.21	-0.06	-0.10	0.04	***0.10***
15	-0.16	0.11	0.01	0.05	-0.20	-0.06	-0.10	0.04	***0.11***
6	-0.11	0.11	0.04	0.05	-0.19	-0.07	-0.10	0.03	***0.14***
3	-0.08	0.10	0.04	0.05	-0.18	-0.07	-0.10	0.03	***0.14***
Top	-0.25	0.93	0.14	0.36	-0.22	-0.13	-0.17	0.03	***0.31***
Middle	-0.16	0.31	0.00	0.12	-0.17	-0.03	-0.14	0.05	***0.14***
Bottom	-0.12	0.11	0.01	0.05	-0.19	-0.06	-0.10	0.04	***0.12***
AVG	*-0.18*	*0.39*	*0.04*	*0.16*	*-0.19*	*-0.07*	*-0.13*	*0.04*	***0.17***

Source: This study.

Table 30: Cp results for the CKY Tower in urban environment; WT (SE, 90°)

Height	**WW**	**side**			**LW**	**side**			$\Delta X\pi$
(m)	MIN	MAX	AVG	SDEV	MIN	MAX	AVG	SDEV	***AVG***
90	-0.43	-0.40	-0.41	0.01	0.10	0.49	0.24	0.15	***0.66***
84	-0.44	-0.41	-0.42	0.01	0.00	0.45	0.12	0.17	***0.53***
72	-0.42	-0.38	-0.40	0.01	-0.15	0.18	-0.06	0.14	***0.34***
60	-0.43	-0.27	-0.35	0.06	-0.20	-0.15	-0.20	0.02	***0.15***
54	-0.43	-0.24	-0.35	0.06	-0.19	-0.15	-0.17	0.01	***0.18***
42	-0.43	-0.22	-0.32	0.08	-0.13	-0.04	-0.11	0.03	***0.21***
30	-0.39	-0.30	-0.38	0.03	-0.10	0.06	-0.05	0.06	***0.33***
24	-0.40	-0.31	-0.35	0.04	-0.17	0.03	-0.13	0.08	***0.22***
15	-0.42	-0.29	-0.36	0.05	-0.40	-0.10	-0.14	0.10	***0.22***
3	-0.42	-0.08	-0.36	0.12	-0.31	-0.04	-0.16	0.08	***0.20***
Top	-0.43	-0.40	-0.41	0.01	-0.02	0.37	0.10	0.15	***0.51***
Middle	-0.43	-0.24	-0.34	0.06	-0.18	-0.11	-0.16	0.02	***0.18***
Bottom	-0.41	-0.24	-0.36	0.06	-0.25	-0.01	-0.12	0.08	***0.24***
AVG	*-0.42*	*-0.29*	*-0.37*	*0.05*	*-0.15*	*0.08*	*-0.06*	*0.09*	***0.31***

Source: This study.

Table 31: Cp results for the CKY Tower in urban environment with horizontal panels; WT (SE, 90^{o})

Height	**WW**	**side**			**LW**	**side**			$\Delta X\pi$
(m)	MIN	MAX	AVG	SDEV	MIN	MAX	AVG	SDEV	***AVG***
90	-0.46	-0.41	-0.42	0.02	0.27	0.71	0.43	0.16	***0.85***
84	-0.46	-0.42	-0.43	0.02	0.05	0.58	0.26	0.20	***0.69***
72	-0.42	-0.40	-0.41	0.01	-0.07	0.33	0.01	0.17	***0.41***
60	-0.45	-0.27	-0.38	0.06	-0.13	-0.05	-0.11	0.03	***0.27***
54	-0.43	-0.23	-0.37	0.07	-0.12	-0.04	-0.09	0.03	***0.27***
42	-0.44	-0.22	-0.34	0.08	-0.08	-0.05	-0.07	0.01	***0.27***
30	-0.40	-0.31	-0.39	0.04	-0.04	0.22	0.00	0.12	***0.39***
24	-0.43	-0.32	-0.37	0.04	-0.13	0.04	-0.04	0.06	***0.33***
15	-0.41	-0.29	-0.38	0.05	-0.41	-0.01	-0.03	0.14	***0.35***
3	-0.44	-0.07	-0.37	0.12	-0.33	0.00	-0.09	0.11	***0.29***
Top	-0.45	-0.41	-0.42	0.02	0.08	0.54	0.23	0.18	***0.65***
Middle	-0.44	-0.24	-0.36	0.07	-0.11	-0.05	-0.09	0.02	***0.27***
Bottom	-0.42	-0.25	-0.38	0.06	-0.23	0.06	-0.04	0.11	***0.34***
AVG	*-0.44*	*-0.30*	*-0.39*	*0.05*	*-0.09*	*0.18*	*0.03*	*0.10*	***0.42***

Source: This study.

Table 32: Cp results for the CKY Tower in urban area with vertical panels; WT (SE; 90^{o})

Height	**WW**	**side**			**LW**	**side**			$\Delta X\pi$
(m)	MIN	MAX	AVG	SDEV	MIN	MAX	AVG	SDEV	***AVG***
90	-0.45	-0.41	-0.42	0.02	0.14	0.68	0.37	0.21	***0.79***
84	-0.46	-0.42	-0.43	0.01	0.00	0.55	0.16	0.21	***0.59***
72	-0.43	-0.40	-0.42	0.01	-0.14	0.28	0.06	0.17	***0.48***
60	-0.43	-0.27	-0.37	0.06	-0.18	-0.09	-0.15	0.03	***0.23***
54	-0.43	-0.24	-0.37	0.06	-0.15	-0.09	-0.11	0.02	***0.26***
42	-0.42	-0.21	-0.32	0.08	-0.08	0.06	-0.05	0.05	***0.26***
30	-0.39	-0.29	-0.38	0.03	-0.05	0.15	0.00	0.07	***0.37***
24	-0.42	-0.32	-0.37	0.04	-0.13	0.07	-0.07	0.08	***0.30***
15	-0.42	-0.30	-0.36	0.04	-0.40	-0.05	-0.09	0.12	***0.28***
3	-0.44	0.06	-0.37	0.17	-0.32	0.02	-0.11	0.10	***0.26***
Top	-0.45	-0.41	-0.42	0.01	0.00	0.50	0.20	0.20	***0.62***
Middle	-0.43	-0.24	-0.35	0.07	-0.14	-0.04	-0.10	0.03	***0.25***
Bottom	-0.42	-0.21	-0.37	0.07	-0.22	0.05	-0.07	0.09	***0.30***
AVG	*-0.43*	*-0.29*	*-0.38*	*0.05*	*-0.12*	*0.17*	*0.01*	*0.11*	***0.39***

Source: This study.

Table 33: Cp and ΔCp results for the shaft 'A' prototype tower isolated: external, internal, and top faces (WT; 0°)

	1 Right face				2 downflow shaft				3 upflow shaft				4 Left face			
H (m)	MIN	MAX	AVG	sdev	MIN	MAX	AVG	sdev	MIN	MAX	AVG	sdev	MIN	MAX	AVG	sdev
90	-1.10	-0.33	-0.65	0.24	-0.43	-0.41	-0.43	0.01	-0.40	-0.38	-0.39	0.01	-1.04	-0.41	-0.62	0.21
84	-0.83	-0.33	-0.62	0.18	-0.41	-0.40	-0.41	0.01	-0.40	-0.38	-0.39	0.01	-0.97	-0.35	-0.57	0.20
72	-0.75	-0.35	-0.65	0.16	-0.42	-0.42	-0.42	0.00	-0.39	-0.39	-0.39	0.00	-0.76	-0.35	-0.57	0.15
60	-0.76	-0.44	-0.63	0.13	-0.41	-0.40	-0.40	0.01	-0.41	-0.39	-0.40	0.01	-0.89	-0.42	-0.57	0.18
54	-0.77	-0.35	-0.69	0.16	-0.43	-0.41	-0.42	0.01	-0.40	-0.39	-0.40	0.00	-0.77	-0.36	-0.59	0.15
42	-0.74	-0.43	-0.58	0.13	-0.41	-0.39	-0.39	0.01	-0.38	-0.36	-0.37	0.01	-0.74	-0.42	-0.58	0.12
30	-0.74	-0.36	-0.59	0.15	-0.43	-0.41	-0.42	0.01	-0.49	-0.39	-0.40	0.05	-0.71	-0.35	-0.53	0.13
24	-0.78	-0.26	-0.51	0.20	-0.43	-0.41	-0.42	0.01	-0.55	-0.25	-0.38	0.15	-0.69	-0.34	-0.59	0.14
15	-0.80	-0.19	-0.41	0.25	-0.45	-0.42	-0.45	0.02	-0.50	-0.40	-0.44	0.05	-0.66	-0.31	-0.39	0.14
Top	-0.89	-0.34	-0.64	0.19	-0.42	-0.41	-0.42	0.01	-0.40	-0.38	-0.39	0.01	-0.92	-0.37	-0.58	0.19
Middle	-0.76	-0.41	-0.63	0.14	-0.42	-0.40	-0.40	0.01	-0.40	-0.38	-0.39	0.01	-0.80	-0.40	-0.58	0.15
Bottom	-0.78	-0.27	-0.50	0.20	-0.44	-0.41	-0.43	0.01	-0.51	-0.35	-0.41	0.09	-0.68	-0.33	-0.50	0.14
AVG	-0.81	-0.34	-0.59	0.18	-0.43	-0.41	-0.42	0.01	-0.44	-0.37	-0.39	0.03	-0.80	-0.37	-0.56	0.16

	5 Right top surface				6 Left top surface			
	MIN	MAX	AVG	sdev	MIN	MAX	AVG	sdev
Top	-0.69	-0.65	-0.69	0.02	-0.63	-0.56	-0.60	0.03
Middle	-0.68	-0.64	-0.65	0.02	-0.58	-0.56	-0.57	0.01
Bottom	-0.66	-0.59	-0.61	0.04	-0.59	-0.51	-0.56	0.05
AVG	-0.68	-0.63	-0.65	0.02	-0.60	-0.54	-0.58	0.03

	ΔCp AVG Results						
	1 - 3	2 - 4	1 - 4	1 - 2	2 - 3	4 - 3	5 - 6
Top	-0.25	0.16	-0.06	-0.22	-0.20	-0.03	-0.09
Middle	-0.25	0.18	-0.05	-0.23	-0.19	-0.01	-0.08
Bottom	-0.10	0.07	0.00	-0.07	-0.10	-0.02	-0.05
AVG	-0.20	0.14	-0.04	-0.18	-0.16	-0.02	-0.07

Source: This study.

Table 34: Cp and ΔCp results for the shaft 'B' prototype tower isolated: external, internal, and top faces (WT; 0°)

	1 Right face				2 downflow shaft				3 upflow shaft				4 Left face			
H (m)	MIN	MAX	AVG	sdev	MIN	MAX	AVG	sdev	MIN	MAX	AVG	sdev	MIN	MAX	AVG	sdev
90	-1.31	-0.33	-0.66	0.31	-0.52	-0.49	-0.52	0.02	-0.52	-0.49	-0.49	0.02	-0.94	-0.54	-0.64	0.14
84	-0.91	-0.33	-0.57	0.21	-0.50	-0.49	-0.50	0.01	-0.50	-0.48	-0.49	0.01	-0.90	-0.38	-0.58	0.16
72	-0.85	-0.34	-0.60	0.19	-0.50	-0.49	-0.49	0.00	-0.50	-0.48	-0.49	0.01	-0.77	-0.36	-0.60	0.15
60	-0.83	-0.44	-0.64	0.15	-0.49	-0.47	-0.49	0.01	-0.49	-0.48	-0.48	0.00	-0.88	-0.44	-0.60	0.16
54	-0.77	-0.30	-0.67	0.18	-0.47	-0.46	-0.47	0.01	-0.48	-0.47	-0.47	0.01	-0.76	-0.35	-0.62	0.15
42	-0.76	-0.39	-0.59	0.14	-0.49	-0.44	-0.45	0.03	-0.49	-0.44	-0.45	0.03	-0.73	-0.42	-0.64	0.12
30	-0.78	-0.38	-0.60	0.15	-0.49	-0.48	-0.49	0.01	-0.53	-0.48	-0.49	0.03	-0.71	-0.39	-0.57	0.12
24	-0.76	-0.29	-0.52	0.18	-0.53	-0.50	-0.52	0.02	-0.61	-0.50	-0.54	0.06	-0.69	-0.39	-0.63	0.12
15	-0.76	-0.17	-0.43	0.23	-0.52	-0.51	-0.52	0.01	-0.54	-0.47	-0.52	0.03	-0.67	-0.33	-0.49	0.13
Top	-1.02	-0.33	-0.61	0.24	-0.51	-0.49	-0.50	0.01	-0.50	-0.48	-0.49	0.01	-0.87	-0.43	-0.61	0.15
Middle	-0.79	-0.38	-0.63	0.15	-0.48	-0.46	-0.47	0.01	-0.49	-0.46	-0.47	0.01	-0.79	-0.40	-0.62	0.14
Bottom	-0.77	-0.28	-0.51	0.19	-0.51	-0.50	-0.51	0.01	-0.56	-0.49	-0.52	0.04	-0.69	-0.37	-0.56	0.12
AVG	-0.86	-0.33	-0.59	0.19	-0.50	-0.48	-0.49	0.01	-0.52	-0.48	-0.49	0.02	-0.78	-0.40	-0.60	0.14

	5 Right top surface				6 Left top surface			
	MIN	MAX	AVG	sdev	MIN	MAX	AVG	sdev
Top	-0.62	-0.59	-0.61	0.01	-0.64	-0.57	-0.62	0.03
Middle	-0.62	-0.59	-0.60	0.01	-0.61	-0.60	-0.60	0.01
Bottom	-0.66	-0.55	-0.64	0.06	-0.64	-0.55	-0.60	0.05
AVG	-0.63	-0.58	-0.62	0.03	-0.63	-0.57	-0.61	0.03

	ΔCp AVG Results						
	1 - 3	2 - 4	1 - 4	1 - 2	2 - 3	4 - 3	5 - 6
Top	-0.12	0.10	0.00	-0.11	-0.12	-0.01	0.00
Middle	-0.17	0.15	-0.01	-0.16	-0.15	0.00	0.01
Bottom	0.00	0.05	0.05	-0.01	-0.05	0.01	-0.04
AVG	-0.09	0.10	0.01	-0.09	-0.11	0.00	-0.01

Source: This study.

Table 35: Cp and ΔCp results for the shaft 'A' prototype tower isolated: external, internal, and top faces (WT; 22.5°)

	1 WW frontal face				2 downflow shaft				3 upflow shaft				4 LW rear face			
H (m)	MIN	MAX	AVG	sdev	MIN	MAX	AVG	sdev	MIN	MAX	AVG	sdev	MIN	MAX	AVG	sdev
90	0.37	0.91	0.81	0.18	0.15	0.23	0.18	0.04	-0.39	-0.36	-0.37	0.02	-0.34	-0.24	-0.30	0.04
84	0.29	0.91	0.79	0.20	0.15	0.18	0.16	0.02	-0.40	-0.34	-0.35	0.03	-0.38	-0.28	-0.31	0.03
72	0.26	0.78	0.67	0.21	0.15	0.18	0.16	0.01	-0.32	-0.30	-0.32	0.01	-0.38	-0.30	-0.32	0.03
60	0.46	0.72	0.62	0.11	0.17	0.18	0.17	0.01	-0.30	-0.30	-0.30	0.00	-0.34	-0.29	-0.33	0.02
54	0.21	0.65	0.57	0.17	0.15	0.17	0.15	0.01	-0.27	-0.27	-0.27	0.00	-0.36	-0.29	-0.32	0.03
42	0.38	0.57	0.54	0.07	0.14	0.14	0.14	0.00	-0.25	-0.23	-0.24	0.01	-0.33	-0.31	-0.32	0.01
30	0.39	0.53	0.47	0.05	0.13	0.14	0.13	0.00	-0.27	-0.24	-0.24	0.02	-0.36	-0.29	-0.30	0.03
24	0.05	0.43	0.40	0.16	0.10	0.11	0.10	0.01	-0.32	-0.24	-0.25	0.05	-0.36	-0.24	-0.31	0.04
15	0.18	0.38	0.32	0.07	0.04	0.05	0.05	0.01	-0.33	-0.24	-0.33	0.05	-0.36	-0.22	-0.30	0.05
Top	0.31	0.87	0.75	0.20	0.15	0.20	0.17	0.02	-0.37	-0.33	-0.34	0.02	-0.37	-0.27	-0.31	0.03
Middle	0.35	0.65	0.58	0.12	0.15	0.16	0.15	0.01	-0.27	-0.26	-0.27	0.01	-0.34	-0.30	-0.32	0.02
Bottom	0.21	0.45	0.40	0.09	0.09	0.10	0.09	0.01	-0.31	-0.24	-0.27	0.04	-0.36	-0.25	-0.31	0.04
AVG	0.29	0.65	0.58	0.14	0.13	0.15	0.14	0.01	-0.32	-0.28	-0.30	0.02	-0.36	-0.27	-0.31	0.03

	5 WW top surface				6 LW top surface			
	MIN	MAX	AVG	sdev	MIN	MAX	AVG	sdev
Top	0.58	0.74	0.71	0.06	-0.42	-0.33	-0.36	0.04
Middle	0.64	0.76	0.73	0.05	-0.37	-0.35	-0.36	0.01
Bottom	0.72	0.91	0.84	0.10	-0.46	-0.37	-0.42	0.05
AVG	0.65	0.80	0.76	0.07	-0.42	-0.35	-0.38	0.03

	ΔXπ AVG Results						
	1 - 3	2 - 4	1 - 4	1 - 2	2 - 3	4 - 3	5 - 6
Top	1.10	0.48	1.07	0.59	0.03	0.51	1.07
Middle	0.84	0.48	0.90	0.42	-0.05	0.42	1.09
Bottom	0.67	0.40	0.70	0.30	-0.03	0.37	1.26
AVG	0.87	0.45	0.89	0.44	-0.02	0.43	1.14

Source: This study.

Table 36: Cp and ΔCp results for the shaft 'B' prototype tower isolated: external, internal, and top faces (WT; 22.5°)

	1 WW frontal face				2 downflow shaft				3 upflow shaft				4 LW rear face			
H (m)	MIN	MAX	AVG	sdev	MIN	MAX	AVG	sdev	MIN	MAX	AVG	sdev	MIN	MAX	AVG	sdev
90	0.37	0.88	0.74	0.17	0.14	0.20	0.14	0.04	-0.22	-0.18	-0.19	0.02	-0.35	0.01	-0.31	0.16
84	0.30	0.88	0.78	0.20	0.14	0.24	0.21	0.05	-0.24	-0.21	-0.22	0.02	-0.36	-0.28	-0.31	0.03
72	0.29	0.79	0.72	0.20	0.22	0.26	0.26	0.02	-0.20	-0.09	-0.16	0.06	-0.35	-0.30	-0.33	0.02
60	0.49	0.69	0.64	0.08	0.27	0.28	0.28	0.01	0.32	0.39	0.34	0.03	-0.34	-0.30	-0.33	0.01
54	0.23	0.64	0.56	0.16	0.30	0.32	0.32	0.01	0.34	0.36	0.34	0.01	-0.37	-0.29	-0.32	0.03
42	0.39	0.59	0.50	0.07	0.27	0.29	0.28	0.01	0.25	0.31	0.28	0.03	-0.34	-0.31	-0.33	0.02
30	0.40	0.51	0.47	0.05	0.28	0.31	0.30	0.01	-0.27	0.14	0.11	0.23	-0.35	-0.27	-0.34	0.03
24	0.05	0.43	0.41	0.16	0.28	0.30	0.29	0.01	-0.36	0.02	-0.25	0.20	-0.35	-0.24	-0.33	0.05
15	0.18	0.42	0.33	0.08	0.24	0.26	0.26	0.01	-0.38	-0.03	-0.37	0.20	-0.34	0.03	-0.30	0.15
Top	0.32	0.85	0.74	0.19	0.16	0.23	0.20	0.04	-0.22	-0.16	-0.19	0.03	-0.36	-0.19	-0.32	0.07
Middle	0.37	0.64	0.57	0.11	0.28	0.30	0.29	0.01	0.31	0.35	0.32	0.02	-0.35	-0.30	-0.33	0.02
Bottom	0.21	0.45	0.40	0.10	0.27	0.29	0.28	0.01	-0.33	0.04	-0.17	0.21	-0.35	-0.16	-0.32	0.08
AVG	0.30	0.65	0.57	0.13	0.24	0.27	0.26	0.02	-0.08	0.08	-0.01	0.09	-0.35	-0.22	-0.32	0.06

	5 WW top surface				6 LW top surface			
	MIN	MAX	AVG	sdev	MIN	MAX	AVG	sdev
Top	0.43	0.52	0.49	0.04	-0.36	-0.35	-0.35	0.01
Middle	0.46	0.56	0.50	0.04	-0.39	-0.36	-0.38	0.01
Bottom	0.43	0.64	0.48	0.11	-0.40	-0.38	-0.39	0.01
AVG	0.44	0.57	0.49	0.06	-0.38	-0.36	-0.37	0.01

	ΔCp AVG Results						
	1 - 3	2 - 4	1 - 4	1 - 2	2 - 3	4 - 3	5 - 6
Top	0.93	0.52	1.06	0.54	-0.13	0.39	0.84
Middle	0.24	0.62	0.89	0.28	-0.65	-0.03	0.88
Bottom	0.57	0.61	0.73	0.12	-0.15	0.45	0.87
AVG	0.58	0.58	0.89	0.31	-0.31	0.27	0.86

Source: This study.

Table 37: Cp and ΔCp results for the shaft 'A' prototype tower isolated: external, internal, and top faces (WT; 45°)

	1 WW frontal face				2 downflow shaft				3 upflow shaft				4 LW rear face			
H (m)	MIN	MAX	AVG	sdev	MIN	MAX	AVG	sdev	MIN	MAX	AVG	sdev	MIN	MAX	AVG	sdev
90	0.10	0.85	0.58	0.25	-0.07	0.00	-0.04	0.03	-0.55	-0.43	-0.49	0.06	-0.48	-0.34	-0.44	0.06
84	0.03	0.77	0.53	0.24	-0.06	-0.04	-0.06	0.01	-0.47	-0.41	-0.43	0.03	-0.55	-0.39	-0.48	0.05
72	0.02	0.68	0.48	0.25	-0.07	-0.05	-0.05	0.01	-0.39	-0.37	-0.38	0.01	-0.56	-0.46	-0.50	0.04
60	0.19	0.52	0.43	0.13	-0.06	-0.05	-0.05	0.01	-0.38	-0.37	-0.37	0.01	-0.53	-0.44	-0.51	0.03
54	0.00	0.57	0.38	0.22	-0.07	-0.06	-0.06	0.01	-0.36	-0.35	-0.35	0.00	-0.56	-0.44	-0.49	0.04
42	0.16	0.45	0.37	0.11	-0.09	-0.06	-0.06	0.01	-0.35	-0.33	-0.33	0.01	-0.53	-0.45	-0.49	0.03
30	0.22	0.46	0.29	0.10	-0.09	-0.07	-0.09	0.01	-0.41	-0.34	-0.34	0.04	-0.54	-0.40	-0.47	0.05
24	0.05	0.46	0.31	0.15	-0.15	-0.11	-0.14	0.02	-0.45	-0.28	-0.33	0.09	-0.52	-0.28	-0.42	0.09
15	0.10	0.41	0.24	0.10	-0.21	-0.18	-0.19	0.01	-0.46	-0.33	-0.44	0.07	-0.49	-0.33	-0.41	0.07
Top	0.05	0.77	0.53	0.25	-0.07	-0.03	-0.05	0.02	-0.47	-0.40	-0.43	0.03	-0.53	-0.40	-0.48	0.05
Middle	0.12	0.51	0.39	0.15	-0.07	-0.06	-0.06	0.01	-0.36	-0.35	-0.35	0.01	-0.54	-0.44	-0.50	0.04
Bottom	0.12	0.44	0.28	0.12	-0.15	-0.12	-0.14	0.01	-0.44	-0.32	-0.37	0.07	-0.52	-0.34	-0.43	0.07
AVG	0.10	0.57	0.40	0.17	-0.10	-0.07	-0.08	0.01	-0.42	-0.36	-0.38	0.04	-0.53	-0.39	-0.47	0.05

	5 WW top surface				6 LW top surface			
	MIN	MAX	AVG	sdev	MIN	MAX	AVG	sdev
Top	0.38	0.58	0.47	0.08	-0.55	-0.49	-0.51	0.03
Middle	0.54	0.71	0.63	0.08	-0.52	-0.50	-0.51	0.01
Bottom	0.65	0.93	0.68	0.15	-0.62	-0.51	-0.55	0.06
AVG	0.52	0.74	0.59	0.11	-0.56	-0.50	-0.52	0.03

	ΔCp AVG Results						
	1 - 3	2 - 4	1 - 4	1 - 2	2 - 3	4 - 3	5 - 6
Top	0.96	0.43	1.01	0.58	-0.05	0.38	0.98
Middle	0.74	0.44	0.89	0.45	-0.14	0.29	1.14
Bottom	0.65	0.29	0.71	0.42	-0.07	0.23	1.24
AVG	0.78	0.39	0.87	0.48	-0.09	0.30	1.12

Source: This study.

Table 38: Cp and ΔCp results for the shaft 'B' prototype tower isolated: external, internal, and top faces (WT; 45°)

	1 WW frontal face				2 downflow shaft				3 upflow shaft				4 LW rear face			
H (m)	MIN	MAX	AVG	sdev	MIN	MAX	AVG	sdev	MIN	MAX	AVG	sdev	MIN	MAX	AVG	sdev
90	0.12	0.69	0.48	0.19	-0.07	0.01	-0.01	0.04	-0.35	-0.32	-0.33	0.01	-0.31	-0.06	-0.27	0.11
84	0.04	0.68	0.48	0.21	-0.05	0.06	0.01	0.06	-0.39	-0.35	-0.38	0.02	-0.34	-0.24	-0.30	0.03
72	0.04	0.61	0.45	0.22	0.01	0.06	0.04	0.03	-0.37	-0.26	-0.33	0.06	-0.33	-0.26	-0.30	0.03
60	0.19	0.46	0.36	0.11	0.08	0.10	0.08	0.01	0.12	0.18	0.14	0.03	-0.32	-0.26	-0.29	0.02
54	0.00	0.52	0.34	0.19	0.09	0.13	0.13	0.02	0.16	0.18	0.17	0.01	-0.33	-0.27	-0.29	0.02
42	0.13	0.40	0.34	0.10	0.09	0.11	0.10	0.01	0.06	0.11	0.09	0.02	-0.32	-0.28	-0.28	0.02
30	0.17	0.41	0.27	0.09	0.09	0.12	0.10	0.01	-0.37	-0.01	-0.03	0.21	-0.33	-0.24	-0.29	0.03
24	0.11	0.39	0.27	0.10	0.07	0.09	0.08	0.01	-0.42	-0.08	-0.27	0.17	-0.32	-0.17	-0.27	0.06
15	0.09	0.33	0.23	0.08	0.04	0.06	0.06	0.01	-0.45	-0.12	-0.42	0.18	-0.29	-0.05	-0.22	0.10
Top	0.07	0.66	0.47	0.20	-0.04	0.05	0.01	0.04	-0.37	-0.31	-0.34	0.03	-0.33	-0.19	-0.29	0.06
Middle	0.11	0.46	0.34	0.14	0.09	0.11	0.11	0.01	0.12	0.15	0.13	0.02	-0.32	-0.27	-0.29	0.02
Bottom	0.12	0.38	0.26	0.09	0.07	0.09	0.08	0.01	-0.41	-0.07	-0.24	0.19	-0.31	-0.15	-0.26	0.06
AVG	0.10	0.50	0.36	0.14	0.04	0.08	0.07	0.02	-0.22	-0.08	-0.15	0.08	-0.32	-0.20	-0.28	0.05

	5 WW top surface				6 LW top surface			
	MIN	MAX	AVG	sdev	MIN	MAX	AVG	sdev
Top	0.20	0.35	0.31	0.06	-0.50	-0.43	-0.47	0.03
Middle	0.23	0.48	0.34	0.11	-0.50	-0.46	-0.49	0.02
Bottom	0.20	0.56	0.27	0.19	-0.50	-0.48	-0.49	0.01
AVG	0.21	0.46	0.31	0.12	-0.50	-0.46	-0.48	0.02

	ΔCp AVG Results						
	1 - 3	2 - 4	1 - 4	1 - 2	2 - 3	4 - 3	5 - 6
Top	0.82	0.30	0.76	0.46	0.05	0.35	0.78
Middle	0.21	0.39	0.63	0.24	-0.42	-0.03	0.83
Bottom	0.50	0.34	0.52	0.18	-0.02	0.32	0.76
AVG	0.51	0.34	0.64	0.29	-0.13	0.22	0.79

Source: This study.

Table 39: Cp and ΔCp results for the shaft 'A' prototype tower isolated: external, internal, and top faces (WT; 90°)

	1 WW frontal face				2 downflow shaft				3 upflow shaft				4 LW rear face			
H (m)	MIN	MAX	AVG	sdev	MIN	MAX	AVG	sdev	MIN	MAX	AVG	sdev	MIN	MAX	AVG	sdev
90	0.49	0.92	0.85	0.18	0.24	0.29	0.24	0.03	-0.25	-0.23	-0.24	0.01	-0.19	-0.12	-0.18	0.03
84	0.47	0.88	0.85	0.17	0.23	0.25	0.23	0.01	-0.25	-0.23	-0.23	0.01	-0.23	-0.18	-0.20	0.02
72	0.47	0.81	0.78	0.17	0.23	0.25	0.24	0.01	-0.21	-0.18	-0.20	0.02	-0.23	-0.19	-0.20	0.01
60	0.61	0.69	0.68	0.03	0.23	0.26	0.26	0.02	-0.19	-0.18	-0.19	0.01	-0.23	-0.18	-0.20	0.02
54	0.28	0.64	0.61	0.17	0.23	0.24	0.23	0.00	-0.16	-0.15	-0.16	0.00	-0.23	-0.19	-0.19	0.02
42	0.49	0.59	0.56	0.04	0.21	0.22	0.22	0.00	-0.13	-0.12	-0.12	0.01	-0.21	-0.18	-0.19	0.01
30	0.44	0.53	0.51	0.03	0.20	0.23	0.21	0.01	-0.18	-0.12	-0.12	0.03	-0.23	-0.17	-0.18	0.03
24	0.16	0.42	0.41	0.14	0.18	0.19	0.18	0.01	-0.25	-0.13	-0.19	0.06	-0.25	-0.18	-0.21	0.02
15	0.26	0.39	0.38	0.06	0.12	0.12	0.12	0.00	-0.18	-0.13	-0.17	0.03	-0.21	-0.12	-0.18	0.04
Top	0.48	0.87	0.83	0.17	0.23	0.26	0.24	0.02	-0.23	-0.21	-0.23	0.01	-0.22	-0.16	-0.19	0.02
Middle	0.46	0.64	0.62	0.08	0.22	0.24	0.24	0.01	-0.16	-0.15	-0.16	0.01	-0.23	-0.18	-0.19	0.02
Bottom	0.29	0.45	0.43	0.08	0.17	0.18	0.17	0.01	-0.20	-0.13	-0.16	0.04	-0.23	-0.16	-0.19	0.03
AVG	0.41	0.65	0.62	0.11	0.21	0.23	0.22	0.01	-0.20	-0.16	-0.18	0.02	-0.22	-0.17	-0.19	0.02

	5 WW top surface				6 LW top surface			
	MIN	MAX	AVG	sdev	MIN	MAX	AVG	sdev
Top	0.61	0.76	0.74	0.06	-0.27	-0.21	-0.23	0.03
Middle	0.73	0.79	0.76	0.03	-0.26	-0.23	-0.24	0.01
Bottom	0.72	0.93	0.92	0.12	-0.35	-0.23	-0.29	0.06
AVG	0.69	0.83	0.81	0.07	-0.29	-0.22	-0.26	0.03

	ΔCp AVG Results						
	1 - 3	2 - 4	1 - 4	1 - 2	2 - 3	4 - 3	5 - 6
Top	1.05	0.43	1.02	0.59	0.03	0.46	0.97
Middle	0.77	0.43	0.81	0.38	-0.04	0.39	1.00
Bottom	0.60	0.36	0.62	0.26	-0.03	0.33	1.22
AVG	0.81	0.41	0.82	0.41	-0.01	0.40	1.06

Source: This study.

Table 40: Cp and ΔCp results for the shaft 'B' prototype tower isolated: external, internal, and top faces (WT; 90°)

	1 WW frontal face				2 downflow shaft				3 upflow shaft				4 LW rear face			
H (m)	MIN	MAX	AVG	sdev	MIN	MAX	AVG	sdev	MIN	MAX	AVG	sdev	MIN	MAX	AVG	sdev
90	0.46	0.90	0.82	0.16	0.11	0.22	0.17	0.05	-0.10	-0.07	-0.09	0.01	-0.24	0.12	-0.18	0.16
84	0.47	0.87	0.81	0.17	0.22	0.28	0.26	0.03	-0.14	-0.12	-0.13	0.01	-0.24	-0.17	-0.20	0.02
72	0.43	0.85	0.79	0.20	0.30	0.33	0.30	0.02	-0.13	-0.05	-0.10	0.04	-0.21	-0.17	-0.19	0.02
60	0.57	0.74	0.71	0.07	0.33	0.36	0.34	0.01	0.37	0.39	0.38	0.01	-0.26	-0.18	-0.19	0.03
54	0.27	0.63	0.58	0.16	0.36	0.38	0.37	0.01	0.42	0.45	0.43	0.01	-0.23	-0.15	-0.18	0.03
42	0.49	0.56	0.53	0.03	0.38	0.39	0.39	0.01	0.35	0.37	0.36	0.01	-0.21	-0.17	-0.19	0.02
30	0.44	0.55	0.48	0.05	0.38	0.40	0.39	0.01	-0.18	0.25	0.24	0.24	-0.25	-0.18	-0.20	0.03
24	0.16	0.46	0.42	0.14	0.37	0.39	0.38	0.01	-0.25	0.14	-0.22	0.22	-0.26	-0.21	-0.24	0.02
15	0.04	0.42	0.38	0.16	0.32	0.36	0.34	0.02	-0.25	0.09	-0.24	0.19	-0.25	0.16	-0.21	0.18
Top	0.46	0.87	0.81	0.18	0.21	0.28	0.24	0.03	-0.12	-0.08	-0.11	0.02	-0.23	-0.07	-0.19	0.07
Middle	0.44	0.64	0.61	0.09	0.36	0.37	0.37	0.01	0.38	0.40	0.39	0.01	-0.23	-0.16	-0.19	0.03
Bottom	0.21	0.48	0.43	0.12	0.36	0.38	0.37	0.01	-0.23	0.16	-0.07	0.22	-0.25	-0.08	-0.22	0.08
AVG	0.37	0.66	0.61	0.13	0.31	0.34	0.33	0.02	0.01	0.16	0.07	0.08	-0.24	-0.11	-0.20	0.06

	5 WW top surface				6 LW top surface			
	MIN	MAX	AVG	sdev	MIN	MAX	AVG	sdev
Top	0.33	0.57	0.50	0.09	-0.25	-0.21	-0.23	0.02
Middle	0.48	0.54	0.50	0.03	-0.27	-0.24	-0.26	0.01
Bottom	0.44	0.59	0.55	0.08	-0.26	-0.25	-0.25	0.00
AVG	0.42	0.57	0.52	0.07	-0.26	-0.23	-0.25	0.01

	ΔCp AVG Results						
	1 - 3	2 - 4	1 - 4	1 - 2	2 - 3	4 - 3	5 - 6
Top	0.91	0.43	1.00	0.56	-0.08	0.35	0.74
Middle	0.22	0.56	0.80	0.24	-0.58	-0.02	0.76
Bottom	0.50	0.58	0.65	0.06	-0.14	0.44	0.81
AVG	0.54	0.53	0.81	0.29	-0.27	0.26	0.77

Source: This study.

Table 41: Cp and ΔCp results for the shaft 'A' prototype tower in the urban environment: external, internal, and top faces (WT; N; 45°)

	1 WW frontal face				2 downflow shaft				3 upflow shaft				4 LW rear face			
H (m)	MIN	MAX	AVG	sdev	MIN	MAX	AVG	sdev	MIN	MAX	AVG	sdev	MIN	MAX	AVG	sdev
90	-0.28	0.09	-0.05	0.14	-0.42	-0.40	-0.42	0.01	-0.42	-0.21	-0.29	0.11	-0.59	-0.36	-0.53	0.10
84	-0.34	0.09	-0.14	0.16	-0.42	-0.40	-0.42	0.01	-0.50	-0.46	-0.48	0.02	-0.61	-0.49	-0.58	0.04
72	-0.36	0.08	-0.22	0.17	-0.43	-0.41	-0.43	0.01	-0.44	-0.42	-0.44	0.01	-0.62	-0.55	-0.60	0.03
60	-0.44	-0.19	-0.33	0.10	-0.42	-0.40	-0.42	0.01	-0.42	-0.40	-0.40	0.01	-0.61	-0.51	-0.59	0.04
54	-0.51	0.19	-0.41	0.29	-0.43	-0.42	-0.43	0.01	-0.41	-0.39	-0.39	0.01	-0.61	-0.54	-0.60	0.03
42	-0.48	-0.40	-0.46	0.03	-0.42	-0.38	-0.40	0.02	-0.38	-0.36	-0.36	0.01	-0.62	-0.57	-0.62	0.02
30	-0.46	-0.36	-0.42	0.04	-0.43	-0.42	-0.42	0.00	-0.56	-0.37	-0.37	0.11	-0.62	-0.53	-0.61	0.04
24	-0.45	0.04	-0.39	0.20	-0.43	-0.42	-0.42	0.00	-0.62	-0.37	-0.40	0.13	-0.63	-0.39	-0.60	0.10
15	-0.47	0.00	-0.38	0.18	-0.43	-0.42	-0.43	0.00	-0.58	-0.33	-0.38	0.13	-0.63	-0.34	-0.47	0.12
Top	-0.33	0.09	-0.14	0.16	-0.43	-0.40	-0.42	0.01	-0.46	-0.36	-0.40	0.05	-0.61	-0.47	-0.57	0.05
Middle	-0.48	-0.13	-0.40	0.14	-0.42	-0.40	-0.41	0.01	-0.40	-0.38	-0.39	0.01	-0.62	-0.54	-0.60	0.03
Bottom	-0.46	-0.11	-0.39	0.14	-0.43	-0.42	-0.42	0.00	-0.58	-0.36	-0.39	0.12	-0.62	-0.42	-0.56	0.08
AVG	-0.42	-0.05	-0.31	0.15	-0.43	-0.41	-0.42	0.01	-0.48	-0.37	-0.39	0.06	-0.62	-0.48	-0.58	0.06

	5 WW top surface				6 LW top surface			
	MIN	MAX	AVG	sdev	MIN	MAX	AVG	sdev
Top	-0.07	0.06	0.02	0.06	-0.60	-0.55	-0.58	0.03
Middle	-0.01	0.14	0.06	0.07	-0.61	-0.51	-0.56	0.04
Bottom	-0.02	0.12	0.07	0.07	-0.62	-0.51	-0.57	0.05
AVG	-0.03	0.11	0.05	0.06	-0.61	-0.52	-0.57	0.04

	ΔCp AVG Results						
	1 - 3	2 - 4	1 - 4	1 - 2	2 - 3	4 - 3	5 - 6
Top	0.27	0.15	0.43	0.29	-0.17	-0.02	0.60
Middle	-0.01	0.19	0.20	0.01	-0.21	-0.03	0.63
Bottom	-0.01	0.14	0.17	0.03	-0.18	-0.04	0.64
AVG	0.08	0.16	0.27	0.11	-0.19	-0.03	0.62

Source: This study.

Table 42: Cp and ΔCp results for the shaft 'B' prototype tower in the urban environment: external, internal, and top faces (WT; N; 45°)

	1 WW frontal face				2 downflow shaft				3 upflow shaft				4 LW rear face			
H (m)	MIN	MAX	AVG	sdev	MIN	MAX	AVG	sdev	MIN	MAX	AVG	sdev	MIN	MAX	AVG	sdev
90	-0.29	-0.10	-0.14	0.07	-0.53	-0.52	-0.53	0.00	-0.54	-0.53	-0.53	0.01	-0.58	-0.38	-0.49	0.09
84	-0.36	-0.09	-0.21	0.10	-0.52	-0.46	-0.49	0.03	-0.56	-0.56	-0.56	0.00	-0.59	-0.51	-0.57	0.04
72	-0.40	-0.04	-0.25	0.14	-0.47	-0.45	-0.46	0.01	-0.60	-0.58	-0.59	0.01	-0.62	-0.50	-0.59	0.04
60	-0.45	-0.21	-0.35	0.10	-0.42	-0.41	-0.41	0.01	-0.46	-0.44	-0.46	0.01	-0.59	-0.55	-0.57	0.02
54	-0.54	0.10	-0.45	0.26	-0.40	-0.39	-0.39	0.00	-0.33	-0.32	-0.32	0.00	-0.60	-0.50	-0.59	0.04
42	-0.50	-0.43	-0.49	0.03	-0.37	-0.35	-0.37	0.01	-0.36	-0.34	-0.34	0.01	-0.61	-0.53	-0.58	0.03
30	-0.51	-0.40	-0.47	0.04	-0.36	-0.36	-0.36	0.00	-0.53	-0.37	-0.37	0.10	-0.61	-0.49	-0.55	0.05
24	-0.51	-0.40	-0.42	0.04	-0.36	-0.34	-0.35	0.01	-0.59	-0.39	-0.40	0.11	-0.63	-0.40	-0.61	0.10
15	-0.48	-0.36	-0.43	0.04	-0.36	-0.35	-0.35	0.01	-0.55	-0.37	-0.40	0.10	-0.61	-0.37	-0.44	0.10
Top	-0.35	-0.07	-0.20	0.10	-0.50	-0.48	-0.49	0.01	-0.57	-0.55	-0.56	0.01	-0.60	-0.46	-0.55	0.06
Middle	-0.50	-0.18	-0.43	0.13	-0.40	-0.39	-0.39	0.01	-0.38	-0.36	-0.37	0.01	-0.60	-0.53	-0.58	0.03
Bottom	-0.50	-0.39	-0.44	0.04	-0.36	-0.35	-0.35	0.01	-0.56	-0.37	-0.39	0.10	-0.62	-0.42	-0.54	0.09
AVG	-0.45	-0.21	-0.36	0.09	-0.42	-0.40	-0.41	0.01	-0.50	-0.43	-0.44	0.04	-0.61	-0.47	-0.56	0.06

	5 WW top surface				6 LW top surface			
	MIN	MAX	AVG	sdev	MIN	MAX	AVG	sdev
Top	-0.28	0.00	-0.19	0.12	-0.58	-0.51	-0.55	0.03
Middle	-0.28	-0.01	-0.18	0.12	-0.57	-0.53	-0.55	0.02
Bottom	-0.31	-0.14	-0.28	0.09	-0.58	-0.53	-0.56	0.02
AVG	-0.29	-0.05	-0.22	0.11	-0.58	-0.52	-0.55	0.03

	ΔCp AVG Results						
	1 - 3	2 - 4	1 - 4	1 - 2	2 - 3	4 - 3	5 - 6
Top	0.36	0.06	0.35	0.29	0.01	0.07	0.36
Middle	-0.06	0.19	0.15	-0.04	-0.21	-0.02	0.37
Bottom	-0.05	0.18	0.09	-0.09	-0.15	0.04	0.28
AVG	0.08	0.14	0.20	0.06	-0.11	0.03	0.33

Source: This study.

Table 43: Cp and ΔCp results for the shaft 'A' prototype tower in the urban environment: external, internal, and top faces (WT; NE; 0°)

	1 Right side face				2 downflow shaft				3 upflow shaft				4 Left side face			
H (m)	MIN	MAX	AVG	sdev	MIN	MAX	AVG	sdev	MIN	MAX	AVG	sdev	MIN	MAX	AVG	sdev
90	-0.86	-0.41	-0.58	0.15	-0.42	-0.40	-0.41	0.01	-0.44	-0.43	-0.44	0.01	-0.81	-0.45	-0.62	0.13
84	-0.73	-0.40	-0.53	0.11	-0.41	-0.40	-0.41	0.01	-0.45	-0.44	-0.45	0.00	-0.76	-0.43	-0.55	0.11
72	-0.67	-0.40	-0.51	0.10	-0.41	-0.40	-0.41	0.01	-0.45	-0.44	-0.44	0.01	-0.64	-0.40	-0.51	0.09
60	-0.62	-0.43	-0.49	0.07	-0.41	-0.40	-0.41	0.00	-0.44	-0.44	-0.44	0.00	-1.08	-0.45	-0.47	0.28
54	-0.65	-0.39	-0.48	0.09	-0.42	-0.41	-0.42	0.00	-0.44	-0.44	-0.44	0.00	-1.08	-0.39	-0.47	0.29
42	-0.56	-0.42	-0.46	0.06	-0.41	-0.38	-0.40	0.02	-0.44	-0.42	-0.43	0.01	-0.61	-0.42	-0.44	0.08
30	-0.55	-0.38	-0.44	0.06	-0.40	-0.40	-0.40	0.00	-0.44	-0.42	-0.44	0.01	-0.94	-0.40	-0.43	0.23
24	-0.59	-0.38	-0.41	0.09	-0.41	-0.40	-0.41	0.00	-0.45	-0.37	-0.41	0.04	-0.81	-0.36	-0.42	0.19
15	-0.58	-0.36	-0.39	0.10	-0.42	-0.41	-0.41	0.01	-0.45	-0.40	-0.43	0.03	-0.64	-0.39	-0.45	0.08
Top	-0.75	-0.40	-0.54	0.12	-0.41	-0.40	-0.41	0.01	-0.45	-0.44	-0.44	0.01	-0.74	-0.42	-0.56	0.11
Middle	-0.61	-0.41	-0.48	0.07	-0.41	-0.40	-0.41	0.01	-0.44	-0.43	-0.44	0.01	-0.92	-0.42	-0.46	0.21
Bottom	-0.58	-0.37	-0.42	0.08	-0.41	-0.40	-0.41	0.00	-0.45	-0.40	-0.43	0.03	-0.80	-0.38	-0.43	0.17
AVG	-0.65	-0.40	-0.48	0.09	-0.41	-0.40	-0.41	0.01	-0.45	-0.42	-0.44	0.01	-0.82	-0.41	-0.48	0.16

	5 Right top surface				6 Left top surface			
	MIN	MAX	AVG	sdev	MIN	MAX	AVG	sdev
Top	-0.57	-0.52	-0.55	0.02	-0.65	-0.57	-0.62	0.03
Middle	-0.55	-0.52	-0.54	0.01	-0.66	-0.59	-0.62	0.03
Bottom	-0.56	-0.49	-0.55	0.04	-0.67	-0.55	-0.60	0.06
AVG	-0.56	-0.51	-0.55	0.02	-0.66	-0.57	-0.61	0.04

	ΔCp AVG Results						
	1 - 3	2 - 4	1 - 4	1 - 2	2 - 3	4 - 3	5 - 6
Top	-0.09	0.15	0.02	-0.13	-0.11	0.04	0.07
Middle	-0.04	0.05	-0.02	-0.07	-0.02	0.03	0.08
Bottom	0.01	0.03	0.02	-0.01	-0.01	0.02	0.04
AVG	-0.04	0.08	0.01	-0.07	-0.05	0.03	0.07

Source: This study.

Table 44: Cp and ΔCp results for the shaft 'B' prototype tower in the urban environment: external, internal, and top faces (WT; NE; 0°)

	1 WW frontal face				2 downflow shaft				3 upflow shaft				4 LW rear face			
H (m)	MIN	MAX	AVG	sdev	MIN	MAX	AVG	sdev	MIN	MAX	AVG	sdev	MIN	MAX	AVG	sdev
90	-0.87	-0.40	-0.55	0.15	-0.47	-0.46	-0.47	0.00	-0.49	-0.48	-0.48	0.00	-0.69	-0.46	-0.58	0.08
84	-0.74	-0.40	-0.49	0.12	-0.46	-0.46	-0.46	0.00	-0.48	-0.47	-0.47	0.01	-0.76	-0.42	-0.53	0.11
72	-0.68	-0.39	-0.48	0.11	-0.46	-0.45	-0.46	0.00	-0.47	-0.46	-0.46	0.01	-0.59	-0.40	-0.48	0.07
60	-0.62	-0.41	-0.46	0.08	-0.45	-0.45	-0.45	0.00	-0.47	-0.46	-0.47	0.00	-0.64	-0.43	-0.46	0.08
54	-0.66	-0.39	-0.45	0.10	-0.47	-0.46	-0.46	0.00	-0.46	-0.46	-0.46	0.00	-0.59	-0.40	-0.43	0.08
42	-0.56	-0.40	-0.44	0.06	-0.46	-0.44	-0.45	0.01	-0.46	-0.44	-0.44	0.01	-0.55	-0.40	-0.41	0.06
30	-0.53	-0.37	-0.42	0.06	-0.46	-0.46	-0.46	0.00	-0.46	-0.36	-0.45	0.05	-0.83	-0.37	-0.39	0.20
24	-0.58	-0.36	-0.41	0.09	-0.48	-0.47	-0.47	0.01	-0.47	-0.35	-0.37	0.06	-0.71	-0.35	-0.39	0.15
15	-0.57	-0.35	-0.40	0.09	-0.49	-0.48	-0.48	0.00	-0.48	-0.35	-0.47	0.07	-0.56	-0.37	-0.46	0.06
Top	-0.76	-0.40	-0.51	0.13	-0.46	-0.46	-0.46	0.00	-0.48	-0.47	-0.47	0.00	-0.68	-0.43	-0.53	0.09
Middle	-0.61	-0.40	-0.45	0.08	-0.46	-0.45	-0.46	0.00	-0.46	-0.46	-0.46	0.00	-0.59	-0.41	-0.43	0.07
Bottom	-0.56	-0.36	-0.41	0.08	-0.48	-0.47	-0.47	0.00	-0.47	-0.36	-0.43	0.06	-0.70	-0.36	-0.41	0.14
AVG	-0.65	-0.39	-0.46	0.10	-0.47	-0.46	-0.46	0.00	-0.47	-0.43	-0.45	0.02	-0.66	-0.40	-0.46	0.10

	5 WW top surface				6 LW top surface			
	MIN	MAX	AVG	sdev	MIN	MAX	AVG	sdev
Top	-0.56	-0.50	-0.54	0.02	-0.59	-0.53	-0.57	0.03
Middle	-0.55	-0.51	-0.53	0.02	-0.58	-0.53	-0.56	0.02
Bottom	-0.57	-0.49	-0.53	0.04	-0.59	-0.52	-0.56	0.04
AVG	-0.56	-0.50	-0.53	0.03	-0.59	-0.53	-0.56	0.03

	ΔCp AVG Results						
	1 - 3	2 - 4	1 - 4	1 - 2	2 - 3	4 - 3	5 - 6
Top	-0.04	0.07	0.02	-0.05	-0.06	0.01	0.03
Middle	0.00	-0.02	-0.02	0.00	0.02	0.00	0.04
Bottom	0.02	-0.06	0.00	0.06	0.02	-0.05	0.03
AVG	0.00	-0.01	0.00	0.01	-0.01	-0.01	0.03

Source: This study.

Table 45: Cp and ΔCp results for the shaft 'A' prototype tower in the urban environment: external, internal, and top faces (WT; E; 45°)

	1 WW frontal face				2 downflow shaft				3 upflow shaft				4 LW rear face			
H (m)	MIN	MAX	AVG	sdev	MIN	MAX	AVG	sdev	MIN	MAX	AVG	sdev	MIN	MAX	AVG	sdev
90	-0.53	-0.15	-0.36	0.16	-0.41	-0.29	-0.40	0.07	-0.52	-0.50	-0.52	0.01	-0.68	-0.61	-0.65	0.02
84	-0.30	-0.15	-0.24	0.05	-0.41	-0.37	-0.37	0.02	-0.52	-0.50	-0.51	0.01	-0.69	-0.55	-0.64	0.05
72	-0.31	-0.21	-0.30	0.04	-0.38	-0.38	-0.38	0.00	-0.52	-0.50	-0.51	0.01	-0.67	-0.53	-0.64	0.06
60	-0.41	-0.26	-0.33	0.05	-0.38	-0.37	-0.38	0.00	-0.51	-0.49	-0.50	0.01	-0.73	-0.56	-0.70	0.07
54	-0.37	-0.32	-0.34	0.02	-0.37	-0.36	-0.37	0.01	-0.52	-0.49	-0.50	0.01	-0.74	-0.49	-0.72	0.11
42	-0.37	-0.31	-0.36	0.02	-0.36	-0.33	-0.35	0.02	-0.51	-0.48	-0.49	0.01	-0.78	-0.52	-0.65	0.10
30	-0.42	-0.34	-0.37	0.03	-0.37	-0.36	-0.37	0.01	-0.50	-0.38	-0.49	0.07	-0.76	-0.47	-0.62	0.11
24	-0.46	-0.38	-0.40	0.04	-0.37	-0.36	-0.36	0.00	-0.52	-0.39	-0.40	0.07	-0.75	-0.45	-0.57	0.12
15	-0.59	-0.37	-0.52	0.09	-0.37	-0.36	-0.37	0.01	-0.55	-0.39	-0.53	0.09	-0.75	-0.39	-0.49	0.15
Top	-0.38	-0.17	-0.30	0.09	-0.40	-0.34	-0.38	0.03	-0.52	-0.50	-0.51	0.01	-0.68	-0.56	-0.64	0.04
Middle	-0.38	-0.30	-0.34	0.03	-0.37	-0.36	-0.36	0.01	-0.51	-0.49	-0.50	0.01	-0.75	-0.52	-0.69	0.09
Bottom	-0.49	-0.36	-0.43	0.05	-0.37	-0.36	-0.37	0.01	-0.52	-0.38	-0.48	0.08	-0.75	-0.44	-0.56	0.13
AVG	-0.42	-0.28	-0.36	0.06	-0.38	-0.35	-0.37	0.02	-0.52	-0.46	-0.50	0.03	-0.73	-0.51	-0.63	0.09

	5 WW top surface				6 LW top surface			
	MIN	MAX	AVG	sdev	MIN	MAX	AVG	sdev
Top	-0.67	-0.64	-0.66	0.01	-0.23	-0.06	-0.13	0.07
Middle	-0.66	-0.63	-0.66	0.01	-0.29	-0.02	-0.17	0.12
Bottom	-0.71	-0.63	-0.67	0.04	-0.25	0.05	-0.12	0.16
AVG	-0.68	-0.63	-0.66	0.02	-0.26	-0.01	-0.14	0.12

	ΔCp AVG Results						
	1 - 3	2 - 4	1 - 4	1 - 2	2 - 3	4 - 3	5 - 6
Top	0.21	0.26	0.35	0.08	-0.13	0.13	-0.53
Middle	0.16	0.32	0.35	0.02	-0.19	0.14	-0.49
Bottom	0.05	0.19	0.13	-0.07	-0.08	0.11	-0.55
AVG	0.14	0.26	0.27	0.01	-0.14	0.12	-0.52

Source: This study.

Table 46: Cp and ΔCp results for the shaft 'B' prototype tower in the urban environment: external, internal, and top faces (WT; E; 45°)

	1 WW frontal face				2 downflow shaft				3 upflow shaft				4 LW rear face			
H (m)	MIN	MAX	AVG	sdev	MIN	MAX	AVG	sdev	MIN	MAX	AVG	sdev	MIN	MAX	AVG	sdev
90	-0.40	-0.16	-0.34	0.10	-0.59	-0.56	-0.57	0.01	-0.52	-0.48	-0.50	0.02	-0.69	-0.59	-0.65	0.03
84	-0.38	-0.16	-0.25	0.07	-0.60	-0.59	-0.59	0.01	-0.47	-0.44	-0.46	0.01	-0.67	-0.56	-0.64	0.04
72	-0.33	-0.26	-0.30	0.03	-0.55	-0.53	-0.54	0.01	-0.41	-0.41	-0.41	0.00	-0.66	-0.51	-0.63	0.06
60	-0.50	-0.27	-0.34	0.09	-0.41	-0.39	-0.40	0.01	-0.39	-0.38	-0.39	0.01	-0.70	-0.54	-0.66	0.07
54	-0.49	-0.32	-0.35	0.07	-0.38	-0.37	-0.37	0.00	-0.38	-0.37	-0.38	0.01	-0.71	-0.47	-0.68	0.10
42	-0.37	-0.33	-0.35	0.02	-0.38	-0.34	-0.36	0.02	-0.36	-0.34	-0.36	0.01	-0.76	-0.51	-0.64	0.10
30	-0.50	-0.35	-0.36	0.07	-0.37	-0.37	-0.37	0.00	-0.36	-0.35	-0.35	0.01	-0.74	-0.47	-0.61	0.11
24	-0.51	-0.36	-0.40	0.06	-0.39	-0.38	-0.38	0.00	-0.38	-0.36	-0.36	0.01	-0.73	-0.45	-0.55	0.11
15	-0.60	-0.34	-0.37	0.09	-0.39	-0.38	-0.39	0.00	-0.37	-0.36	-0.36	0.00	-0.73	-0.39	-0.48	0.14
Top	-0.37	-0.19	-0.30	0.07	-0.58	-0.56	-0.57	0.01	-0.47	-0.44	-0.46	0.01	-0.67	-0.55	-0.64	0.04
Middle	-0.45	-0.31	-0.34	0.06	-0.39	-0.36	-0.38	0.01	-0.38	-0.37	-0.37	0.01	-0.72	-0.51	-0.66	0.09
Bottom	-0.54	-0.35	-0.38	0.07	-0.38	-0.38	-0.38	0.00	-0.37	-0.36	-0.36	0.01	-0.73	-0.44	-0.55	0.12
AVG	-0.45	-0.28	-0.34	0.06	-0.45	-0.43	-0.44	0.01	-0.40	-0.39	-0.40	0.01	-0.71	-0.50	-0.61	0.08

	5 WW top surface				6 LW top surface			
	MIN	MAX	AVG	sdev	MIN	MAX	AVG	sdev
Top	-0.69	-0.62	-0.65	0.02	-0.33	-0.05	-0.22	0.13
Middle	-0.69	-0.65	-0.67	0.02	-0.38	-0.11	-0.27	0.13
Bottom	-0.70	-0.69	-0.70	0.00	-0.39	-0.12	-0.28	0.14
AVG	-0.69	-0.66	-0.67	0.02	-0.36	-0.09	-0.26	0.14

	ΔCp AVG Results						
	1 - 3	2 - 4	1 - 4	1 - 2	2 - 3	4 - 3	5 - 6
Top	0.16	0.07	0.34	0.27	-0.18	-0.11	-0.43
Middle	0.03	0.28	0.32	0.03	-0.29	-0.01	-0.40
Bottom	-0.02	0.17	0.17	0.00	-0.19	-0.02	-0.41
AVG	0.06	0.17	0.28	0.10	-0.22	-0.05	-0.41

Source: This study.

Table 47: Cp and ΔCp results for the shaft 'A' prototype tower in the urban environment: external, internal, and top faces (WT; SE; 90°)

	1 WW frontal face				2 downflow shaft				3 upflow shaft				4 LW rear face			
H (m)	MIN	MAX	AVG	sdev	MIN	MAX	AVG	sdev	MIN	MAX	AVG	sdev	MIN	MAX	AVG	sdev
90	-0.16	0.51	-0.06	0.33	-0.12	-0.10	-0.10	0.01	-0.29	-0.27	-0.29	0.01	-0.26	-0.24	-0.25	0.00
84	0.14	0.57	0.30	0.14	-0.11	-0.08	-0.10	0.02	-0.28	-0.22	-0.23	0.04	-0.26	-0.24	-0.25	0.00
72	0.01	0.38	0.05	0.15	-0.11	-0.09	-0.10	0.01	-0.27	-0.23	-0.27	0.02	-0.26	-0.24	-0.26	0.01
60	-0.13	0.22	-0.08	0.17	-0.10	-0.08	-0.09	0.01	-0.21	-0.20	-0.20	0.00	-0.26	-0.24	-0.26	0.01
54	-0.17	0.06	-0.11	0.11	-0.10	-0.08	-0.09	0.01	-0.17	-0.16	-0.17	0.00	-0.27	-0.23	-0.25	0.02
42	-0.16	-0.04	-0.12	0.05	-0.11	-0.09	-0.10	0.01	-0.16	-0.15	-0.16	0.01	-0.26	-0.21	-0.24	0.02
30	-0.15	-0.06	-0.13	0.03	-0.16	-0.09	-0.11	0.04	-0.15	-0.15	-0.15	0.00	-0.26	-0.20	-0.23	0.03
24	-0.33	-0.08	-0.14	0.10	-0.34	-0.13	-0.13	0.12	-0.15	-0.15	-0.15	0.00	-0.33	-0.18	-0.22	0.06
15	-0.18	-0.09	-0.12	0.03	-0.16	-0.10	-0.11	0.03	-0.16	-0.15	-0.15	0.01	-0.22	-0.19	-0.22	0.01
Top	-0.01	0.48	0.10	0.21	-0.11	-0.09	-0.10	0.01	-0.28	-0.24	-0.26	0.02	-0.26	-0.24	-0.25	0.01
Middle	-0.16	0.08	-0.10	0.11	-0.10	-0.08	-0.10	0.01	-0.18	-0.17	-0.17	0.00	-0.27	-0.23	-0.25	0.02
Bottom	-0.22	-0.08	-0.13	0.06	-0.22	-0.11	-0.12	0.06	-0.16	-0.15	-0.15	0.00	-0.27	-0.19	-0.22	0.03
AVG	-0.13	0.16	-0.04	0.12	-0.14	-0.09	-0.10	0.03	-0.21	-0.19	-0.20	0.01	-0.27	-0.22	-0.24	0.02

	5 WW top surface				6 LW top surface			
	MIN	MAX	AVG	sdev	MIN	MAX	AVG	sdev
Top	-0.27	-0.25	-0.26	0.01	0.56	0.59	0.57	0.01
Middle	-0.27	-0.25	-0.26	0.01	0.58	0.71	0.63	0.06
Bottom	-0.32	-0.25	-0.27	0.04	0.59	0.75	0.69	0.09
AVG	-0.29	-0.25	-0.26	0.02	0.58	0.68	0.63	0.05

	ΔCp AVG Results						
	1 - 3	2 - 4	1 - 4	1 - 2	2 - 3	4 - 3	5 - 6
Top	0.36	0.15	0.35	0.20	0.01	0.16	-0.83
Middle	0.07	0.15	0.15	-0.01	-0.07	0.08	-0.89
Bottom	0.02	0.10	0.09	-0.01	-0.07	0.04	-0.96
AVG	0.15	0.14	0.20	0.06	-0.05	0.09	-0.89

Source: This study.

Table 48: Cp and ΔCp results for the shaft 'B' prototype tower in the urban environment: external, internal, and top faces (WT; SE; 90°)

	1 WW frontal face				2 downflow shaft				3 upflow shaft				4 LW rear face			
H (m)	MIN	MAX	AVG	sdev	MIN	MAX	AVG	sdev	MIN	MAX	AVG	sdev	MIN	MAX	AVG	sdev
90	0.10	0.58	0.50	0.21	-0.40	-0.32	-0.33	0.04	-0.24	-0.24	-0.24	0.00	-0.25	-0.24	-0.25	0.00
84	0.21	0.63	0.26	0.16	-0.21	-0.17	-0.19	0.02	-0.31	-0.30	-0.30	0.01	-0.26	-0.25	-0.26	0.00
72	-0.09	0.34	-0.02	0.18	-0.11	-0.09	-0.10	0.01	-0.37	-0.37	-0.37	0.00	-0.27	-0.25	-0.26	0.01
60	-0.19	0.26	-0.15	0.22	-0.06	-0.03	-0.04	0.01	-0.14	-0.08	-0.12	0.03	-0.27	-0.26	-0.27	0.01
54	-0.22	0.03	-0.17	0.11	0.01	0.03	0.03	0.01	0.07	0.12	0.11	0.02	-0.26	-0.24	-0.25	0.01
42	-0.21	-0.09	-0.17	0.05	0.03	0.05	0.05	0.01	0.06	0.08	0.06	0.01	-0.26	-0.21	-0.23	0.02
30	-0.25	-0.10	-0.11	0.06	-0.15	0.08	0.08	0.13	0.00	0.04	0.02	0.02	-0.25	-0.21	-0.22	0.02
24	-0.34	-0.05	-0.14	0.12	-0.34	0.07	-0.11	0.21	-0.04	-0.02	-0.02	0.02	-0.25	-0.22	-0.24	0.01
15	-0.20	0.07	-0.11	0.13	-0.03	0.09	0.06	0.06	-0.12	-0.09	-0.10	0.02	-0.25	-0.21	-0.24	0.01
Top	0.07	0.52	0.25	0.18	-0.24	-0.19	-0.21	0.02	-0.31	-0.30	-0.30	0.00	-0.26	-0.25	-0.25	0.01
Middle	-0.21	0.07	-0.16	0.13	-0.01	0.02	0.01	0.01	0.00	0.04	0.01	0.02	-0.26	-0.24	-0.25	0.01
Bottom	-0.27	-0.03	-0.12	0.10	-0.17	0.08	0.01	0.13	-0.05	-0.02	-0.03	0.02	-0.25	-0.22	-0.23	0.01
AVG	-0.13	0.19	-0.01	0.14	-0.14	-0.03	-0.06	0.06	-0.12	-0.09	-0.11	0.01	-0.26	-0.23	-0.25	0.01

	5 WW top surface				6 LW top surface			
	MIN	MAX	AVG	sdev	MIN	MAX	AVG	sdev
Top	-0.26	-0.25	-0.26	0.01	0.29	0.43	0.34	0.06
Middle	-0.27	-0.25	-0.27	0.01	0.32	0.42	0.37	0.04
Bottom	-0.29	-0.28	-0.28	0.01	0.26	0.39	0.34	0.06
AVG	-0.27	-0.26	-0.27	0.01	0.29	0.41	0.35	0.06

	ΔCp AVG Results						
	1 - 3	2 - 4	1 - 4	1 - 2	2 - 3	4 - 3	5 - 6
Top	0.55	0.05	0.50	0.46	0.05	0.10	-0.60
Middle	-0.18	0.26	0.08	-0.18	-0.26	0.00	-0.64
Bottom	-0.09	0.24	0.11	-0.13	-0.20	0.05	-0.62
AVG	0.10	0.18	0.23	0.05	-0.14	0.05	-0.62

Source: This study.

Table 49: Cp and ΔCp results for the shaft 'A' prototype tower in the urban environment: external, internal, and top faces (WT; S; 45°)

	1 WW frontal face				2 downflow shaft				3 upflow shaft				4 LW rear face			
H (m)	MIN	MAX	AVG	sdev	MIN	MAX	AVG	sdev	MIN	MAX	AVG	sdev	MIN	MAX	AVG	sdev
90	-0.38	0.44	0.06	0.34	-0.30	-0.28	-0.28	0.01	-0.22	-0.16	-0.17	0.03	-0.53	-0.50	-0.52	0.01
84	-0.19	0.62	0.20	0.26	-0.29	-0.28	-0.29	0.01	-0.15	-0.14	-0.14	0.00	-0.56	-0.52	-0.55	0.02
72	-0.05	0.59	0.01	0.26	-0.31	-0.29	-0.30	0.01	-0.15	-0.14	-0.14	0.01	-0.58	-0.53	-0.56	0.02
60	-0.19	0.34	-0.12	0.22	-0.30	-0.29	-0.29	0.00	-0.11	-0.11	-0.11	0.00	-0.60	-0.52	-0.56	0.04
54	-0.27	0.55	-0.16	0.33	-0.30	-0.30	-0.30	0.00	-0.10	-0.09	-0.10	0.00	-0.65	-0.39	-0.45	0.12
42	-0.23	0.18	-0.21	0.17	-0.30	-0.29	-0.30	0.00	-0.11	-0.08	-0.09	0.01	-0.59	-0.30	-0.48	0.12
30	-0.40	0.33	-0.16	0.27	-0.32	-0.21	-0.31	0.06	-0.09	-0.08	-0.09	0.01	-0.58	-0.24	-0.46	0.14
24	-0.45	0.22	-0.29	0.26	-0.46	-0.18	-0.31	0.14	-0.08	-0.08	-0.08	0.00	-0.48	-0.17	-0.45	0.13
15	-0.37	0.11	-0.32	0.21	-0.38	-0.12	-0.38	0.15	-0.09	-0.08	-0.09	0.00	-0.52	-0.21	-0.37	0.09
Top	-0.21	0.55	0.09	0.29	-0.30	-0.28	-0.29	0.01	-0.17	-0.15	-0.15	0.01	-0.56	-0.52	-0.54	0.02
Middle	-0.23	0.36	-0.16	0.24	-0.30	-0.29	-0.30	0.00	-0.11	-0.09	-0.10	0.01	-0.61	-0.40	-0.50	0.09
Bottom	-0.41	0.22	-0.26	0.24	-0.39	-0.17	-0.33	0.12	-0.09	-0.08	-0.09	0.00	-0.52	-0.21	-0.43	0.12
AVG	-0.28	0.37	-0.11	0.26	-0.33	-0.25	-0.31	0.04	-0.12	-0.11	-0.11	0.01	-0.57	-0.38	-0.49	0.08

	5 WW top surface				6 LW top surface			
	MIN	MAX	AVG	sdev	MIN	MAX	AVG	sdev
Top	-0.54	-0.47	-0.51	0.03	0.23	0.42	0.29	0.09
Middle	-0.54	-0.46	-0.51	0.04	0.31	0.57	0.44	0.11
Bottom	-0.59	-0.46	-0.56	0.07	0.38	0.76	0.54	0.19
AVG	-0.56	-0.46	-0.53	0.04	0.31	0.58	0.43	0.13

	ΔCp AVG Results						
	1 - 3	2 - 4	1 - 4	1 - 2	2 - 3	4 - 3	5 - 6
Top	0.24	0.25	0.63	0.38	-0.39	-0.14	-0.80
Middle	-0.06	0.20	0.33	0.13	-0.40	-0.20	-0.95
Bottom	-0.17	0.09	0.17	0.08	-0.34	-0.25	-1.11
AVG	0.00	0.18	0.38	0.20	-0.37	-0.19	-0.95

Source: This study.

Table 50: Cp and ΔCp results for the shaft 'B' prototype tower in the urban environment: external, internal, and top faces (WT; S; 45°)

	1 WW frontal face				2 downflow shaft				3 upflow shaft				4 LW rear face			
H (m)	MIN	MAX	AVG	sdev	MIN	MAX	AVG	sdev	MIN	MAX	AVG	sdev	MIN	MAX	AVG	sdev
90	-0.04	0.40	0.17	0.19	-0.28	-0.24	-0.28	0.02	-0.42	-0.40	-0.42	0.01	-0.54	-0.50	-0.52	0.02
84	0.06	0.54	0.16	0.18	-0.27	-0.14	-0.20	0.07	-0.49	-0.46	-0.48	0.01	-0.57	-0.53	-0.55	0.02
72	-0.14	0.46	-0.10	0.25	-0.17	-0.12	-0.16	0.02	-0.51	-0.50	-0.50	0.00	-0.59	-0.52	-0.55	0.03
60	-0.22	0.23	-0.20	0.20	-0.09	-0.07	-0.08	0.01	-0.09	-0.06	-0.09	0.01	-0.60	-0.53	-0.57	0.03
54	-0.33	0.50	-0.28	0.35	-0.05	-0.05	-0.05	0.00	-0.01	0.12	0.02	0.06	-0.66	-0.40	-0.43	0.13
42	-0.37	0.06	-0.28	0.17	-0.03	-0.03	-0.03	0.00	0.00	0.00	0.00	0.00	-0.56	-0.31	-0.48	0.10
30	-0.40	0.29	-0.26	0.27	-0.26	-0.02	-0.02	0.14	-0.01	0.03	0.01	0.02	-0.51	-0.24	-0.40	0.11
24	-0.46	0.19	-0.32	0.25	-0.46	-0.02	-0.26	0.22	0.02	0.03	0.03	0.00	-0.49	-0.17	-0.39	0.12
15	-0.35	0.08	-0.04	0.17	-0.16	-0.01	-0.04	0.08	-0.02	0.01	0.00	0.02	-0.49	-0.18	-0.32	0.09
Top	-0.04	0.47	0.07	0.21	-0.24	-0.17	-0.21	0.04	-0.47	-0.45	-0.47	0.01	-0.57	-0.51	-0.54	0.02
Middle	-0.30	0.27	-0.25	0.24	-0.06	-0.05	-0.06	0.01	-0.03	0.02	-0.02	0.03	-0.61	-0.41	-0.49	0.09
Bottom	-0.40	0.19	-0.21	0.23	-0.29	-0.02	-0.11	0.14	0.00	0.02	0.01	0.01	-0.50	-0.20	-0.37	0.11
AVG	-0.25	0.31	-0.13	0.23	-0.20	-0.08	-0.13	0.06	-0.17	-0.14	-0.16	0.02	-0.56	-0.37	-0.47	0.07

	5 WW top surface				6 LW top surface			
	MIN	MAX	AVG	sdev	MIN	MAX	AVG	sdev
Top	-0.55	-0.47	-0.54	0.03	-0.05	0.26	0.11	0.13
Middle	-0.54	-0.52	-0.53	0.01	0.05	0.40	0.22	0.14
Bottom	-0.62	-0.51	-0.56	0.05	0.04	0.51	0.24	0.24
AVG	-0.57	-0.50	-0.54	0.03	0.01	0.39	0.19	0.17

	ΔCp AVG Results						
	1 - 3	2 - 4	1 - 4	1 - 2	2 - 3	4 - 3	5 - 6
Top	0.54	0.32	0.61	0.29	-0.07	0.26	-0.64
Middle	-0.23	0.44	0.24	-0.20	-0.47	-0.04	-0.74
Bottom	-0.22	0.26	0.16	-0.10	-0.38	-0.12	-0.80
AVG	0.03	0.34	0.34	0.00	-0.31	0.03	-0.73

Source: This study.

Table 51: Cp and ΔCp results for the shaft 'A' prototype tower in the urban environment: external, internal, and top faces (WT; SW; 0°)

	1 Right face				2 downflow shaft				3 upflow shaft				4 Left face			
H (m)	MIN	MAX	AVG	sdev	MIN	MAX	AVG	sdev	MIN	MAX	AVG	sdev	MIN	MAX	AVG	sdev
90	-0.96	-0.37	-0.71	0.19	-0.29	-0.28	-0.28	0.01	-0.35	-0.35	-0.35	0.00	-1.04	-0.20	-0.72	0.27
84	-0.90	-0.38	-0.63	0.18	-0.29	-0.27	-0.28	0.01	-0.36	-0.35	-0.35	0.01	-1.39	-0.38	-0.61	0.34
72	-0.82	-0.36	-0.60	0.17	-0.28	-0.28	-0.28	0.00	-0.36	-0.35	-0.35	0.00	-1.02	-0.43	-0.58	0.23
60	-0.78	-0.43	-0.51	0.13	-0.29	-0.28	-0.28	0.00	-0.35	-0.35	-0.35	0.00	-0.91	-0.34	-0.41	0.23
54	-0.78	-0.34	-0.45	0.17	-0.28	-0.27	-0.28	0.00	-0.36	-0.35	-0.35	0.01	-0.98	-0.32	-0.39	0.28
42	-0.63	-0.30	-0.40	0.13	-0.28	-0.27	-0.28	0.01	-0.34	-0.34	-0.34	0.00	-0.76	-0.28	-0.32	0.20
30	-0.47	-0.29	-0.38	0.07	-0.29	-0.26	-0.29	0.02	-0.36	-0.24	-0.35	0.06	-1.05	-0.22	-0.25	0.36
24	-0.55	-0.25	-0.34	0.12	-0.31	-0.26	-0.30	0.03	-0.41	-0.21	-0.36	0.10	-1.01	-0.17	-0.24	0.35
15	-0.43	-0.22	-0.28	0.07	-0.34	-0.31	-0.33	0.01	-0.40	-0.18	-0.38	0.12	-0.68	-0.22	-0.36	0.15
Top	-0.89	-0.37	-0.65	0.18	-0.29	-0.28	-0.28	0.01	-0.36	-0.35	-0.35	0.00	-1.15	-0.34	-0.64	0.28
Middle	-0.73	-0.36	-0.45	0.14	-0.28	-0.27	-0.28	0.00	-0.35	-0.34	-0.35	0.00	-0.88	-0.31	-0.37	0.24
Bottom	-0.48	-0.25	-0.34	0.08	-0.31	-0.27	-0.31	0.02	-0.39	-0.21	-0.36	0.10	-0.92	-0.20	-0.28	0.29
AVG	-0.70	-0.33	-0.48	0.14	-0.29	-0.27	-0.29	0.01	-0.37	-0.30	-0.35	0.03	-0.98	-0.29	-0.43	0.27

	5 Right top surface				6 Left top surface			
	MIN	MAX	AVG	sdev	MIN	MAX	AVG	sdev
Top	-0.66	-0.59	-0.62	0.02	-0.75	-0.74	-0.74	0.00
Middle	-0.65	-0.56	-0.59	0.04	-0.75	-0.66	-0.70	0.04
Bottom	-0.66	-0.52	-0.61	0.07	-0.78	-0.61	-0.67	0.10
AVG	-0.66	-0.56	-0.61	0.04	-0.76	-0.67	-0.70	0.05

	ΔCp AVG Results						
	1 - 3	2 - 4	1 - 4	1 - 2	2 - 3	4 - 3	5 - 6
Top	-0.30	0.36	-0.01	-0.37	-0.29	0.07	0.12
Middle	-0.11	0.09	-0.08	-0.17	-0.03	0.07	0.10
Bottom	0.03	-0.02	-0.05	-0.03	0.08	0.06	0.06
AVG	-0.12	0.14	-0.05	-0.19	-0.08	0.07	0.09

Source: This study.

Table 52: Cp and ΔΧπ results for the shaft 'B' prototype tower in the urban environment: external, internal, and top faces (WT; SW; 0°)

	1 Right face				2 downflow shaft				3 upflow shaft				4 Left face			
H (m)	MIN	MAX	AVG	sdev	MIN	MAX	AVG	sdev	MIN	MAX	AVG	sdev	MIN	MAX	AVG	sdev
90	-1.02	-0.37	-0.70	0.21	-0.48	-0.47	-0.48	0.00	-0.51	-0.50	-0.50	0.01	-0.75	-0.27	-0.53	0.17
84	-0.89	-0.35	-0.62	0.18	-0.48	-0.47	-0.47	0.00	-0.50	-0.49	-0.49	0.01	-0.80	-0.41	-0.63	0.13
72	-0.82	-0.33	-0.55	0.18	-0.47	-0.46	-0.47	0.00	-0.49	-0.48	-0.48	0.01	-1.08	-0.46	-0.63	0.24
60	-0.71	-0.41	-0.50	0.12	-0.47	-0.46	-0.46	0.01	-0.47	-0.46	-0.46	0.00	-0.98	-0.37	-0.53	0.23
54	-0.74	-0.32	-0.44	0.16	-0.47	-0.46	-0.47	0.00	-0.47	-0.46	-0.47	0.00	-1.07	-0.35	-0.50	0.29
42	-0.58	-0.31	-0.38	0.10	-0.47	-0.45	-0.47	0.01	-0.48	-0.47	-0.47	0.00	-0.86	-0.39	-0.42	0.20
30	-0.39	-0.31	-0.37	0.03	-0.49	-0.43	-0.49	0.03	-0.48	-0.36	-0.47	0.07	-1.05	-0.32	-0.35	0.32
24	-0.51	-0.26	-0.33	0.09	-0.54	-0.45	-0.52	0.05	-0.49	-0.30	-0.41	0.10	-1.01	-0.22	-0.29	0.33
15	-0.43	-0.25	-0.28	0.06	-0.57	-0.53	-0.57	0.02	-0.53	-0.26	-0.52	0.15	-0.69	-0.25	-0.49	0.15
Top	-0.91	-0.35	-0.62	0.19	-0.47	-0.47	-0.47	0.00	-0.50	-0.49	-0.49	0.01	-0.88	-0.38	-0.60	0.18
Middle	-0.68	-0.35	-0.44	0.12	-0.47	-0.46	-0.46	0.01	-0.47	-0.47	-0.47	0.00	-0.97	-0.37	-0.48	0.24
Bottom	-0.44	-0.27	-0.33	0.06	-0.53	-0.47	-0.52	0.03	-0.50	-0.31	-0.47	0.11	-0.92	-0.27	-0.38	0.27
AVG	-0.68	-0.32	-0.46	0.13	-0.49	-0.47	-0.49	0.01	-0.49	-0.42	-0.48	0.04	-0.92	-0.34	-0.49	0.23

	5 Right top surface				6 Left top surface			
	MIN	MAX	AVG	sdev	MIN	MAX	AVG	sdev
Top	-0.64	-0.58	-0.63	0.03	-0.74	-0.66	-0.69	0.03
Middle	-0.67	-0.57	-0.62	0.04	-0.72	-0.63	-0.68	0.04
Bottom	-0.67	-0.54	-0.65	0.07	-0.70	-0.63	-0.68	0.04
AVG	-0.66	-0.56	-0.64	0.05	-0.72	-0.64	-0.68	0.04

ΔΧπ AVG Results							
	1 - 3	2 - 4	1 - 4	1 - 2	2 - 3	4 - 3	5 - 6
Top	-0.13	0.12	0.03	-0.15	-0.10	0.02	0.06
Middle	0.03	0.02	0.04	0.02	-0.02	0.00	0.06
Bottom	0.14	-0.15	0.05	0.19	0.09	-0.06	0.02
AVG	0.01	0.00	0.02	0.02	-0.01	-0.01	0.05

Source: This study.

Table 53: Cp and ΔXπ results for the shaft 'A' prototype tower in the urban environment: external, internal, and top faces (WT; W; 45°)

	1 WW frontal face				2 downflow shaft				3 upflow shaft				4 LW rear face			
H (m)	MIN	MAX	AVG	sdev	MIN	MAX	AVG	sdev	MIN	MAX	AVG	sdev	MIN	MAX	AVG	sdev
90	-0,48	0,44	-0,30	0,31	-0,23	-0,22	-0,22	0,00	-0,38	-0,15	-0,23	0,12	-0,74	-0,28	-0,63	0,19
84	-0,45	0,50	-0,40	0,35	-0,24	-0,23	-0,24	0,00	-0,39	-0,37	-0,39	0,01	-0,64	-0,53	-0,61	0,04
72	-0,47	0,42	-0,41	0,37	-0,24	-0,23	-0,24	0,00	-0,32	-0,30	-0,32	0,01	-0,67	-0,60	-0,65	0,03
60	-0,50	-0,12	-0,41	0,15	-0,23	-0,21	-0,23	0,01	-0,33	-0,30	-0,32	0,01	-0,68	-0,51	-0,63	0,07
54	-0,50	0,17	-0,47	0,29	-0,23	-0,23	-0,23	0,00	-0,32	-0,31	-0,31	0,01	-0,71	-0,62	-0,70	0,04
42	-0,38	-0,33	-0,34	0,02	-0,23	-0,22	-0,23	0,01	-0,30	-0,29	-0,29	0,01	-0,73	-0,65	-0,70	0,03
30	-0,37	-0,30	-0,34	0,03	-0,24	-0,22	-0,23	0,01	-0,65	-0,29	-0,29	0,21	-0,72	-0,61	-0,67	0,05
24	-0,46	-0,20	-0,26	0,10	-0,24	-0,22	-0,24	0,01	-0,56	-0,29	-0,44	0,14	-0,70	-0,43	-0,47	0,11
15	-0,42	-0,20	-0,21	0,10	-0,27	-0,26	-0,26	0,01	-0,52	-0,28	-0,31	0,13	-0,76	-0,27	-0,44	0,21
Top	-0,47	0,45	-0,37	0,34	-0,24	-0,23	-0,23	0,00	-0,37	-0,28	-0,31	0,05	-0,68	-0,47	-0,63	0,09
Middle	-0,46	-0,09	-0,41	0,15	-0,23	-0,22	-0,23	0,01	-0,32	-0,30	-0,31	0,01	-0,71	-0,60	-0,68	0,05
Bottom	-0,41	-0,23	-0,27	0,07	-0,25	-0,23	-0,25	0,01	-0,58	-0,28	-0,35	0,16	-0,73	-0,44	-0,53	0,12
AVG	-0,45	0,04	-0,35	0,19	-0,24	-0,23	-0,23	0,01	-0,42	-0,29	-0,32	0,07	-0,71	-0,50	-0,61	0,08

	5 WW top surface				6 LW top surface			
	MIN	MAX	AVG	sdev	MIN	MAX	AVG	sdev
Top	-0,66	0,32	-0,10	0,36	-0,68	-0,61	-0,64	0,03
Middle	-0,23	0,42	0,12	0,27	-0,67	-0,53	-0,60	0,06
Bottom	-0,25	0,47	0,34	0,38	-0,67	-0,51	-0,58	0,08
AVG	-0,38	0,40	0,12	0,34	-0,67	-0,55	-0,61	0,06

ΔXπ AVG Results							
	1 - 3	2 - 4	1 - 4	1 - 2	2 - 3	4 - 3	5 - 6
Top	-0,06	0,40	0,26	-0,14	-0,32	0,08	0,54
Middle	-0,10	0,45	0,27	-0,18	-0,37	0,08	0,72
Bottom	0,08	0,28	0,26	-0,03	-0,18	0,10	0,93
AVG	-0,03	0,38	0,26	-0,11	-0,29	0,09	0,73

Source: This study.

Table 54: Cp and ΔXπ results for the shaft 'B' prototype tower in the urban environment: external, internal, and top faces (WT; W; 45°)

	1 WW frontal face				2 downflow shaft				3 upflow shaft				4 LW rear face			
H (m)	MIN	MAX	AVG	sdev	MIN	MAX	AVG	sdev	MIN	MAX	AVG	sdev	MIN	MAX	AVG	sdev
90	-0,49	0,50	-0,33	0,34	-0,48	-0,36	-0,40	0,06	-0,49	-0,49	-0,49	0,00	-0,65	-0,30	-0,60	0,15
84	-0,50	0,55	-0,42	0,38	-0,48	-0,34	-0,36	0,07	-0,53	-0,52	-0,52	0,00	-0,62	-0,51	-0,57	0,04
72	-0,50	0,44	-0,41	0,39	-0,41	-0,33	-0,34	0,05	-0,53	-0,51	-0,52	0,01	-0,64	-0,57	-0,61	0,04
60	-0,51	-0,15	-0,44	0,14	-0,32	-0,27	-0,32	0,03	-0,29	-0,27	-0,29	0,01	-0,64	-0,57	-0,60	0,02
54	-0,50	0,17	-0,47	0,29	-0,28	-0,24	-0,28	0,02	-0,22	-0,19	-0,22	0,01	-0,65	-0,58	-0,61	0,03
42	-0,40	-0,34	-0,37	0,02	-0,21	-0,20	-0,20	0,01	-0,24	-0,20	-0,20	0,02	-0,63	-0,59	-0,63	0,02
30	-0,37	-0,32	-0,34	0,02	-0,18	-0,17	-0,17	0,00	-0,51	-0,25	-0,25	0,15	-0,63	-0,56	-0,60	0,03
24	-0,46	-0,20	-0,28	0,10	-0,17	-0,15	-0,16	0,01	-0,52	-0,31	-0,46	0,10	-0,65	-0,44	-0,45	0,09
15	-0,42	-0,21	-0,22	0,10	-0,17	-0,16	-0,17	0,01	-0,50	-0,29	-0,33	0,11	-0,66	-0,30	-0,49	0,16
Top	-0,50	0,49	-0,39	0,37	-0,45	-0,34	-0,37	0,06	-0,52	-0,50	-0,51	0,01	-0,64	-0,46	-0,59	0,07
Middle	-0,47	-0,11	-0,43	0,15	-0,27	-0,23	-0,26	0,02	-0,25	-0,22	-0,24	0,02	-0,64	-0,58	-0,61	0,02
Bottom	-0,42	-0,24	-0,28	0,07	-0,17	-0,16	-0,17	0,01	-0,51	-0,29	-0,35	0,12	-0,65	-0,43	-0,51	0,09
AVG	-0,46	0,05	-0,37	0,20	-0,30	-0,25	-0,27	0,03	-0,42	-0,34	-0,36	0,05	-0,64	-0,49	-0,57	0,06

	5 WW top surface				6 LW top surface			
	MIN	MAX	AVG	sdev	MIN	MAX	AVG	sdev
Top	-0,75	0,23	-0,23	0,36	-0,60	-0,55	-0,58	0,02
Middle	-0,21	0,26	-0,07	0,20	-0,58	-0,57	-0,58	0,00
Bottom	-0,24	0,31	-0,23	0,31	-0,60	-0,58	-0,59	0,01
AVG	-0,40	0,26	-0,18	0,29	-0,60	-0,57	-0,58	0,01

ΔXπ AVG Results							
	1 - 3	2 - 4	1 - 4	1 - 2	2 - 3	4 - 3	5 - 6
Top	0,12	0,23	0,21	-0,02	-0,09	0,14	0,35
Middle	-0,19	0,35	0,19	-0,16	-0,38	-0,03	0,51
Bottom	0,07	0,35	0,23	-0,11	-0,17	0,18	0,36
AVG	0,00	0,31	0,21	-0,10	-0,21	0,10	0,41

Source: This study.

Table 55: Cp and ΔXπ results for the shaft 'A' prototype tower in the urban environment: external, internal and top faces (WT; NW; 90°)

	1 WW frontal face				2 downflow shaft				3 upflow shaft				4 LW rear face			
H (m)	MIN	MAX	AVG	sdev	MIN	MAX	AVG	sdev	MIN	MAX	AVG	sdev	MIN	MAX	AVG	sdev
90	-0.23	0.03	-0.09	0.10	-0.26	-0.24	-0.26	0.01	-0.27	-0.08	-0.16	0.10	-0.36	-0.23	-0.35	0.06
84	-0.27	-0.03	-0.21	0.09	-0.27	-0.25	-0.26	0.01	-0.34	-0.31	-0.31	0.02	-0.37	-0.34	-0.36	0.01
72	-0.29	-0.06	-0.25	0.09	-0.27	-0.26	-0.26	0.01	-0.29	-0.28	-0.28	0.00	-0.37	-0.34	-0.36	0.01
60	-0.34	-0.28	-0.32	0.02	-0.26	-0.23	-0.25	0.02	-0.26	-0.26	-0.26	0.00	-0.37	-0.33	-0.36	0.02
54	-0.35	-0.17	-0.32	0.07	-0.27	-0.25	-0.27	0.01	-0.26	-0.24	-0.25	0.01	-0.39	-0.33	-0.36	0.02
42	-0.34	-0.33	-0.33	0.00	-0.27	-0.24	-0.26	0.01	-0.24	-0.22	-0.22	0.01	-0.38	-0.34	-0.37	0.02
30	-0.33	-0.30	-0.31	0.01	-0.26	-0.25	-0.26	0.01	-0.36	-0.23	-0.24	0.07	-0.37	-0.31	-0.36	0.02
24	-0.35	-0.28	-0.30	0.02	-0.26	-0.25	-0.26	0.01	-0.37	-0.22	-0.35	0.08	-0.37	-0.30	-0.37	0.03
15	-0.29	-0.26	-0.27	0.01	-0.27	-0.26	-0.26	0.01	-0.39	-0.23	-0.25	0.09	-0.38	-0.23	-0.31	0.07
Top	-0.26	-0.02	-0.18	0.09	-0.26	-0.25	-0.26	0.01	-0.30	-0.22	-0.25	0.04	-0.37	-0.30	-0.36	0.03
Middle	-0.34	-0.26	-0.32	0.03	-0.27	-0.24	-0.26	0.01	-0.25	-0.24	-0.24	0.01	-0.38	-0.34	-0.37	0.02
Bottom	-0.32	-0.28	-0.30	0.01	-0.26	-0.25	-0.26	0.01	-0.37	-0.23	-0.28	0.08	-0.37	-0.28	-0.35	0.04
AVG	-0.31	-0.19	-0.27	0.05	-0.27	-0.25	-0.26	0.01	-0.31	-0.23	-0.26	0.04	-0.37	-0.31	-0.36	0.03

	5 WW top surface				6 LW top surface			
	MIN	MAX	AVG	sdev	MIN	MAX	AVG	sdev
Top	0.02	0.12	0.03	0.04	-0.38	-0.35	-0.37	0.02
Middle	0.06	0.11	0.09	0.02	-0.38	-0.32	-0.35	0.02
Bottom	0.06	0.12	0.06	0.03	-0.39	-0.32	-0.35	0.04
AVG	0.05	0.12	0.06	0.03	-0.38	-0.33	-0.36	0.02

ΔXπ AVG Results							
	1 - 3	2 - 4	1 - 4	1 - 2	2 - 3	4 - 3	5 - 6
Top	0.07	0.10	0.17	0.08	-0.10	-0.01	0.40
Middle	-0.08	0.11	0.04	-0.07	-0.12	-0.01	0.44
Bottom	-0.02	0.09	0.05	-0.04	-0.07	0.02	0.41
AVG	-0.01	0.10	0.09	-0.01	-0.10	0.00	0.42

Source: This study.

Table 56: Cp and $\Delta X\pi$ results for the shaft 'B' prototype tower in the urban environment: external, internal and top faces (WT; NW; 90°)

	1 WW frontal face				2 downflow shaft				3 upflow shaft				4 LW rear face			
H (m)	MIN	MAX	AVG	sdev	MIN	MAX	AVG	sdev	MIN	MAX	AVG	sdev	MIN	MAX	AVG	sdev
90	-0.21	0.06	-0.06	0.11	-0.44	-0.39	-0.40	0.02	-0.34	-0.33	-0.34	0.01	-0.35	-0.23	-0.32	0.05
84	-0.26	-0.01	-0.19	0.09	-0.39	-0.34	-0.35	0.02	-0.37	-0.36	-0.36	0.01	-0.36	-0.33	-0.34	0.01
72	-0.28	-0.05	-0.23	0.10	-0.34	-0.32	-0.33	0.01	-0.40	-0.39	-0.39	0.00	-0.37	-0.33	-0.36	0.01
60	-0.33	-0.27	-0.30	0.03	-0.30	-0.29	-0.29	0.00	-0.38	-0.37	-0.38	0.01	-0.40	-0.35	-0.37	0.02
54	-0.35	-0.16	-0.31	0.07	-0.25	-0.25	-0.25	0.00	-0.22	-0.22	-0.22	0.00	-0.37	-0.31	-0.36	0.03
42	-0.32	-0.31	-0.31	0.00	-0.23	-0.22	-0.23	0.01	-0.20	-0.19	-0.19	0.00	-0.38	-0.33	-0.37	0.02
30	-0.30	-0.28	-0.29	0.01	-0.22	-0.21	-0.21	0.00	-0.36	-0.21	-0.21	0.08	-0.37	-0.28	-0.36	0.04
24	-0.34	-0.27	-0.28	0.03	-0.21	-0.19	-0.20	0.01	-0.35	-0.22	-0.34	0.07	-0.37	-0.28	-0.37	0.04
15	-0.28	-0.24	-0.26	0.01	-0.21	-0.20	-0.21	0.01	-0.37	-0.22	-0.25	0.08	-0.37	-0.22	-0.28	0.07
Top	-0.25	0.00	-0.16	0.10	-0.39	-0.35	-0.36	0.02	-0.37	-0.36	-0.36	0.01	-0.36	-0.30	-0.34	0.02
Middle	-0.33	-0.25	-0.31	0.04	-0.26	-0.25	-0.26	0.01	-0.27	-0.26	-0.26	0.00	-0.38	-0.33	-0.36	0.02
Bottom	-0.31	-0.26	-0.28	0.02	-0.21	-0.20	-0.21	0.01	-0.36	-0.22	-0.27	0.08	-0.37	-0.26	-0.34	0.05
AVG	-0.30	-0.17	-0.25	0.05	-0.29	-0.27	-0.28	0.01	-0.33	-0.28	-0.30	0.03	-0.37	-0.29	-0.35	0.03

	5 WW top surface				6 LW top surface			
	MIN	MAX	AVG	sdev	MIN	MAX	AVG	sdev
Top	-0.05	0.07	0.01	0.05	-0.35	-0.33	-0.34	0.01
Middle	-0.08	0.07	0.01	0.06	-0.35	-0.34	-0.34	0.01
Bottom	-0.14	0.01	-0.13	0.08	-0.35	-0.35	-0.35	0.00
AVG	-0.09	0.05	-0.04	0.07	-0.35	-0.34	-0.34	0.01

	$\Delta X\pi$ AVG Results						
	1 - 3	2 - 4	1 - 4	1 - 2	2 - 3	4 - 3	5 - 6
Top	0.20	-0.02	0.18	0.20	0.02	0.00	0.35
Middle	-0.05	0.11	0.06	-0.05	-0.10	0.01	0.35
Bottom	-0.01	0.13	0.06	-0.07	-0.07	0.06	0.22
AVG	0.05	0.07	0.10	0.03	-0.05	0.02	0.31

Source: This study.